



日中笹川医学奨学金制度
第44期〈学位取得コース〉研究者

報 告 書

2022年4月～2024年3月

公益財団法人 日中医学協会

日中笹川医学奨学金制度＜学位取得コース＞：第 44 期研究者

研究者 No.	氏 名	所 属 機 関	受 け 入 れ 機 関	指導責任者	掲載頁
		研究テーマ			
G 4401	李 君鵬	吉林省人民医院・主治医師	東北大学大学院医学系研究科 消化器外科学分野	亀井 尚 教授	p. 1
		胃癌、食道胃接合部癌における癌微小免疫環境の解析と至適治療の確立			
G 4402	黄 璐嬌	四川省医学科学院・四川省人民医院・主管技師	筑波大学医学医療系国際発達ケア： エンパワメント科学研究室	安梅 勅江 教授	p. 7
		高齢栄養リスクの指数と高齢入院者の入院時間、入院費用との関係			
G 4403	楊 勇	懷化市第一人民医院・主治医師	千葉大学社会精神保健教育研究センター	橋本 謙二 副センター 長・教授	p. 13
		脳疾患の病因解明と新規治療法の開発			
G 4404	蔣 夢恬	東京医科歯科大学大学院医歯学総合研究科 ・博士課程学生	東京医科歯科大学大学院医歯学総合研究科 生体補綴歯科学分野	若林 則幸 教授	p. 70
		暗条件下での血清及び唾液中の二酸化チタンの殺菌効果に及ぼす 3 種類のイオン性抗菌剤の影響に関する研究			
G 4405	陳 曹傑	慶應義塾大学大学院医学研究科・博士課程学生	慶應義塾大学医学部形成外科学	貴志 和生 教授	p. 88
		創傷治癒とオートファジーの関係			
G 4406	趙 宏波	中国医学科学院腫瘍医院深圳医院・副主任医師	東海大学医学部外科学系消化器外科学	小柳 和夫 教授	p. 119
		食道癌術後縫合不全に対する ICG 蛍光イメージング法の有用性の検討			
G 4407	周 英	金沢大学大学院人間社会環境研究科 ・博士課程学生	金沢大学大学院人間社会環境研究科	堤 敦朗 教授	p. 162
		日本における精神科医療通訳が受ける心理的影響に関する研究：質的研究			
G 4408	劉 天驕	成都市婦女児童センター医院・幹事	京都大学大学院医学研究科 分子遺伝学分野	篠原 隆司 教授	p. 178
		α-Klotho を要因とする老化過程における精子幹細胞の微小環境制御			
G 4409	馬 快	大阪大学大学院医学系研究科・博士課程学生	大阪大学大学院医学系研究科腎臓内科学 国立成育医療研究センター研究所 RI 管理室/移植免疫研究室	猪阪 善隆 教授 李 小康 室長	p. 219
		腎移植における腎臓線維化発生機序の解明と新規治療法の開発に関する研究			
G 4410	徐 勇	長崎大学大学院医歯薬学総合研究科・博士課程学生	長崎大学原爆後障害医療研究所 生物学研究分野	李 桃生 教授	p. 272
		ニカラベンによる間葉系幹細胞の放射線損傷の軽減			
G 4411	李 佩霖	長崎大学大学院医歯薬学総合研究科・博士課程学生	長崎大学大学院医歯薬学総合研究科 移植・消化器外科学	江口 晋 教授	p. 330
		小分子誘導肝前駆細胞 (CLiP) からの 3D 胆管形成			

日中笹川医学奨学金制度<学位取得コース>評価書

課程博士：指導教官用



第 44 期

研究者番号：G4401

作成日：2024年3月10日

氏名	李君鵬	LI JUNPENG	性別	M	生年月日	1983/01/15
所属機関(役職)	吉林省人民医院急診外科(主治医師)					
研究先(指導教官)	東北大学大学院医学系研究科消化器外科学分野(亀井尚教授)					
研究テーマ	SIRP α -CD47 経路が食道癌に与える影響の解明と治療標的としての有用性の検討 The impact of the immune checkpoint SIRP α -CD47 on esophageal cancer and its efficacy as a therapeutic target.					
専攻種別	<input type="checkbox"/> 論文博士			<input checked="" type="checkbox"/> 課程博士		

研究者評価(指導教官記入欄)

成績状況	優 良 可 不可	取得単位数
	(優) 学業成績係数=	12/30
学生本人が行った研究の概要	食道癌手術患者における SIRP α ・CD47 の発現を 120 名の手術検体の免疫染色にて評価し、長期予後との関連について検討をおこなった。特に CD47 については臨床で実際に使用されている PD-L1 発現の染色評価基準に準じて CPS・TPS で評価するという新たな試みをおこなった。その結果、食道癌周囲の免疫細胞の SIRP α の高発現や癌微小環境内の腫瘍や免疫細胞の CD47 高発現が食道癌患者の予後不良因子であるという知見を新たに得ることが出来た。また、In vitro 実験のため食道癌細胞株の培養・継代・保存の手技を獲得し、細胞増殖試験や蛋白抽出などの手技も取得したため今後の細胞実験の準備は整っている。	
総合評価	【良かった点】 実験についてはいつも積極的に取り組む姿勢を評価したい。当初に設定した研究テーマで思うような結果が得られず途中でテーマを変更し課題に当たってもらったが、それまでの研究で得た知識も生かし、スピード感を持って結果を得ることが出来た。また、実験だけでなくグループ内のミーティングや抄読会などにも積極的に参加し、自身の専門的知識の獲得と周囲との円滑なコミュニケーションの獲得に努めていたことは素晴らしい姿勢であった。	
	【改善すべき点】 特にないが、独自で研究を進め発表をおこなっていくためには、英語のスキルはもう少し向上することが望まれる。	
	【今後の展望】 今回の結果を基に、In vitro でマクロファージの食道癌細胞に対する貪食機能の評価を、チェックポイント阻害剤を用いて評価・検討していく予定である。	
学位取得見込	奨学金支援の終了後、2年以内に博士学位を取得見込みである。	
評価者(指導教官名) 東北大学大学院消化器外科学教授 亀井 尚		

日中笹川医学奨学金制度<学位取得コース>報告書 研究者用



第44期

研究者番号: G4401

作成日: 2024年3月7日

氏名	李君鹏	LI JUNPENG	性別	M	生年月日	1983/01/15
所属機関(役職)	吉林省人民医院急診外科(主治医師)					
研究先(指導教官)	東北大学大学院医学系研究科消化器外科学分野(亀井 尚 教授)					
研究テーマ	SIRP α -CD47経路が食道癌に与える影響の解明と治療標的としての有用性の検討 The impact of the immune checkpoint SIRP α -CD47 on esophageal cancer and its efficacy as a therapeutic target.					
専攻種別	論文博士	<input type="checkbox"/>	課程博士	<input checked="" type="checkbox"/>		
<p>1. 研究概要(1)</p> <p>1) 目的(Goal) This study aimed to conduct a detailed evaluation of the expression of SIRPα and CD47 in cancer cells and immune cells within the cancer microenvironment of ESCC (esophageal squamous cell carcinoma) surgical specimens using immunohistochemistry. Furthermore, it investigated the relationship between the CD47-SIRPα pathway and the long-term prognosis after ESCC surgery. Additionally, the study aimed to stratify the risk for esophageal cancer and to prove the utility of this stratification as a therapeutic target.</p> <p>2) 戦略(Approach) Esophageal cancer is one of the major causes of death worldwide, including in Japan. Particularly in East Asia and Africa, the incidence of esophageal squamous cell carcinoma (ESCC) is high, and its prognosis is known to be poor. In Japan, according to data from 2015, the incidence rate was 31.2 cases per 100,000 men and 5.9 cases per 100,000 women. In 2019, there were 11,619 deaths due to esophageal cancer, accounting for 3.1% of all cancer deaths, highlighting the need for the development of new treatments and improved intervention strategies. Recently, the inhibition of the PD-1/PD-L1 pathway through anti-PD1 antibody drugs has been widely used in cancer immunotherapy, and several immune checkpoints other than the PD-1/PD-L1 pathway have been reported and are attracting attention as therapeutic targets.</p> <p>Signal-regulatory protein alpha (SIRPα) and Cluster of Differentiation 47 (CD47) are known as immune checkpoints that control innate immunity. It has been reported that the binding of these two proteins suppresses the phagocytic activity of myeloid cells such as macrophages. In the field of oncology, high expression of CD47 in various tumors has been reported as a poor prognostic factor, and inhibition of the SIRPα-CD47 pathway is being focused on as a new therapeutic strategy. However, in esophageal cancer, a detailed examination of the SIRPα-CD47 pathway has not yet been conducted.</p> <p>3) 材料と方法(Materials and methods) Our institution targeted 100 patients with ESCC (esophageal squamous cell carcinoma) who underwent esophagectomy. From the resected specimens, slides including the deepest part of the tumor were selected for immunohistochemical staining of SIRPα and CD47. The expression of SIRPα in immune cells was classified into high and low expression groups using a cutoff value of 3% positivity. For CD47, the expression status in both tumor cells and immune cells was evaluated using Combined Positive Score (CPS) and Tumor Proportion Score (TPS), with a cutoff value of 10% used to categorize into high and low expression groups. Long-term survival was compared between the groups using 5-year overall survival (5y-OS) and 5-year recurrence-free survival (5y-RFS) rates.</p> <p>4) 実験結果(Results) In this study, 79 males and 21 females were included, with an average age of 68.7 years. The median follow-up period was 61 months. The high SIRPα expression group (48 patients) showed a statistically significant poorer 5-year overall survival rate (5y-OS) compared to the low expression group (52 patients) (56.4% vs. 82.8%, P=0.0098). For CD47, high expression in both CPS and TPS was significantly associated with poorer 5y-OS (48.8% vs. 89.5%, P<0.0001, and 48.4% vs. 87.5%, P<0.0001). The 5-year recurrence-free survival (5y-RFS) was also significantly worse in the high expression groups for both SIRPα and CD47. Furthermore, multivariate analysis using the Cox proportional hazards model identified high expression of CD47 and high expression of SIRPα as poor prognostic factors for overall survival (OS), and high expression of CD47 as a poor prognostic factor for recurrence-free survival (RFS).</p>						

5) 考察 (Discussion)

This study investigated the importance of SIRP α and CD47 expression in esophageal squamous cell carcinoma (ESCC) and its implications for prognosis. Our main findings are:

Impact of High SIRP α and CD47 Expression: We found that high levels of SIRP α and CD47 in ESCC are associated with worse survival rates. This suggests that these proteins play a significant role in the progression of this cancer.

Potential Therapeutic Targets: The link between high expression of SIRP α and CD47 and poor outcomes highlights the potential of these molecules as targets for new treatments in ESCC.

Use in Clinical Practice: Identifying patients with high SIRP α and CD47 expression could help in choosing more effective treatments, as these patients might have more aggressive cancer.

Limitations and Future Research: Our study, while informative, has limitations due to its retrospective design and small sample size. Further research with larger groups of patients is needed to confirm our findings and understand the mechanisms behind them. We plan to investigate the expression levels of SIRP α and CD47 in esophageal squamous cell carcinoma (ESCC) and conduct cellular experiments to verify the reduction in macrophage phagocytic ability using anti-CD47 and anti-SIRP α antibodies. In conclusion, SIRP α and CD47 are important in understanding ESCC and could be key targets for improving treatment strategies for this cancer.

6) 参考文献 (References)

1. Huang, C.-Y., Ye, Z.-H., Huang, M.-Y., & Lu, J.-J. (2020). Regulation of CD47 expression in cancer cells. *Translational Oncology*, 13, Article 100862.
2. Koga, N., Hu, Q., Sakai, A., Takada, K., Nakanishi, R., Hisamatsu, Y., Ando, K., Kimura, Y., Oki, E., Oda, Y., & Mori, M. (2021). Clinical significance of signal regulatory protein alpha (SIRP α) expression in esophageal squamous cell carcinoma. *Cancer Science*. <https://doi.org/10.1111/cas.14971>.
3. Son, J., Hsieh, R. C.-E., Lin, H. Y., Krause, K. J., Yuan, Y., Biter, A. B., Welsh, J., Curran, M. A., & Hong, D. S. (2022). Inhibition of the CD47-SIRP α axis for cancer therapy: A systematic review and meta-analysis of emerging clinical data. *Frontiers in Immunology*. <https://doi.org/10.3389/fimmu.2022.1027235>.
4. Zhao, C.-L., Yu, S., Wang, S.-H., Li, S.-G., Wang, Z.-J., & Han, S.-N. (2018). Characterization of cluster of differentiation 47 expression and its potential as a therapeutic target in esophageal squamous cell cancer. *Oncology Letters*, 15, 2017-2023. <https://doi.org/10.3892/ol.2017.7447>.
5. Logtenberg, M. E. W., Scheeren, F. A., & Schumacher, T. N. (2020). The CD47-SIRP α Immune Checkpoint. *Immunity*, 52(5), 742-752. <https://doi.org/10.1016/j.immuni.2020.04.011>.

2. 執筆論文 Publication of thesis ※記載した論文を添付してください。Attach all of the papers listed below.

論文名 1 Title						
掲載誌名 Published journal						
	年	月	巻(号)	頁 ~	頁	言語 Language
第1著者名 First author	第2著者名 Second author		第3著者名 Third author			
その他著者名 Other authors						
論文名 2 Title						
掲載誌名 Published journal						
	年	月	巻(号)	頁 ~	頁	言語 Language
第1著者名 First author	第2著者名 Second author		第3著者名 Third author			
その他著者名 Other authors						
論文名 3 Title						
掲載誌名 Published journal						
	年	月	巻(号)	頁 ~	頁	言語 Language
第1著者名 First author	第2著者名 Second author		第3著者名 Third author			
その他著者名 Other authors						
論文名 4 Title						
掲載誌名 Published journal						
	年	月	巻(号)	頁 ~	頁	言語 Language
第1著者名 First author	第2著者名 Second author		第3著者名 Third author			
その他著者名 Other authors						
論文名 5 Title						
掲載誌名 Published journal						
	年	月	巻(号)	頁 ~	頁	言語 Language
第1著者名 First author	第2著者名 Second author		第3著者名 Third author			
その他著者名 Other authors						

3. 学会発表 Conference presentation ※筆頭演者として総会・国際学会を含む主な学会で発表したものを記載してください

※Describe your presentation as the principal presenter in major academic meetings including general meetings or international meetings

学会名 Conference					
演題 Topic					
開催日 date	年	月	日	開催地 venue	
形式 method	<input type="checkbox"/> 口頭発表 Oral	<input type="checkbox"/> ポスター発表 Poster	言語 Language	<input type="checkbox"/> 日本語	<input type="checkbox"/> 英語 <input type="checkbox"/> 中国語
共同演者名 Co-presenter					
学会名 Conference					
演題 Topic					
開催日 date	年	月	日	開催地 venue	
形式 method	<input type="checkbox"/> 口頭発表 Oral	<input type="checkbox"/> ポスター発表 Poster	言語 Language	<input type="checkbox"/> 日本語	<input type="checkbox"/> 英語 <input type="checkbox"/> 中国語
共同演者名 Co-presenter					
学会名 Conference					
演題 Topic					
開催日 date	年	月	日	開催地 venue	
形式 method	<input type="checkbox"/> 口頭発表 Oral	<input type="checkbox"/> ポスター発表 Poster	言語 Language	<input type="checkbox"/> 日本語	<input type="checkbox"/> 英語 <input type="checkbox"/> 中国語
共同演者名 Co-presenter					
学会名 Conference					
演題 Topic					
開催日 date	年	月	日	開催地 venue	
形式 method	<input type="checkbox"/> 口頭発表 Oral	<input type="checkbox"/> ポスター発表 Poster	言語 Language	<input type="checkbox"/> 日本語	<input type="checkbox"/> 英語 <input type="checkbox"/> 中国語
共同演者名 Co-presenter					

4. 受賞(研究業績) Award (Research achievement)

名称 Award name	国名 Country		受賞年 Year of	年	月
	国名 Country		受賞年 Year of	年	月

5. 本研究テーマに関わる他の研究助成金受給 Other research grants concerned with your research theme

受給実績 Receipt record	<input type="checkbox"/> 有 <input checked="" type="checkbox"/> 無
助成機関名称 Funding agency	
助成金名称 Grant name	
受給期間 Supported period	年 月 ~ 年 月
受給額 Amount received	円
受給実績 Receipt record	<input type="checkbox"/> 有 <input type="checkbox"/> 無
助成機関名称 Funding agency	
助成金名称 Grant name	
受給期間 Supported period	年 月 ~ 年 月
受給額 Amount received	円

6. 他の奨学金受給 Another awarded scholarship

受給実績 Receipt record	<input type="checkbox"/> 有 <input checked="" type="checkbox"/> 無
助成機関名称 Funding agency	
奨学金名称 Scholarship name	
受給期間 Supported period	年 月 ~ 年 月
受給額 Amount received	円

7. 研究活動に関する報道発表 Press release concerned with your research activities

※記載した記事を添付してください。Attach a copy of the article described below

報道発表 Press release	<input type="checkbox"/> 有 <input checked="" type="checkbox"/> 無	発表年月日 Date of release	
発表機関 Released medium			
発表形式 Release method	・新聞 ・雑誌 ・Web site ・記者発表 ・その他()		
発表タイトル Released title			

8. 本研究テーマに関する特許出願予定 Patent application concerned with your research theme

出願予定 Scheduled	<input type="checkbox"/> 有 <input checked="" type="checkbox"/> 無	出願国 Application	
出願内容(概要) Application contents			

9. その他 Others

--

指導責任者(記名) 亀井尚

日中笹川医学奨学金制度<学位取得コース>評価書

課程博士：指導教官用



第 44 期

研究者番号：G4402

作成日：2024年3月1日

氏名	黄璐嬌	HUANG LUJIAO	性別	F	生年月日	1988/09/10
所属機関（役職）	四川省医学科学院・四川省人民医院臨床栄養科（主管技師）					
研究先（指導教官）	筑波大学大学院人間総合科学研究科生命システム医学専攻 国際発達ケア：エンパワメント科学研究室（安梅 勅江 教授）					
研究テーマ	社会資本と生活の質の変化：多民族社会における縦断的研究 Social Capital and Changes in Quality of Life: A Longitudinal Study in Multi-Ethnic Populations					
専攻種別	<input type="checkbox"/> 論文博士			<input checked="" type="checkbox"/> 課程博士		

研究者評価（指導教官記入欄）

成績状況	(優) 良 可 不可 学業成績係数=3.98	取得単位数 34
		取得単位数/取得すべき単位数総数 34/30
学生本人が行った研究の概要	黄璐嬌さんは、博士課程の単位取得において優秀な成績を修めた。研究テーマは、ベースラインの社会資本が、中国の多民族社会における生活の質の変化に影響を与える重要な要因であること、そして社会資本と生活の質の関係は多民族地域では異質性を有することを包括的な視点から捉えようとするものである。ベースラインの社会資本がすでに高いレベルの人々は、生活の質の改善の余地が限られており、天井効果が存在する可能性がある。本研究は、多民族地域における健康増進の指針として示唆深いものである。	
総合評価	【良かった点】 1. 研究仮説が明確で豊富な情報を提供し、適切な研究デザインと調査方法を用い、この分野における研究の方向性を示した。 2. 最先端の集団調査のスキルと方法を習得した。 3. 異分野間のチームワーク能力を身につけた。	
	【改善すべき点】 1. タイムマネジメントをさらに効率的にする。 2. さらに高度な統計スキルを学び、分析の幅を広げる。	
	【今後の展望】 黄璐嬌さんが研究内容をさらに充実・深化させ、学術的価値を高めてくれることを確信している。卒業後も研究に従事し、日中医療交流の架け橋として活躍し、多民族国家の健康増進に貢献することを期待している。	
学位取得見込	博士学位取得見込です。	
		評価者（指導教官名） 安梅勅江

日中笹川医学奨学金制度＜学位取得コース＞報告書 研究者用



第44期

研究者番号: G4402

作成日: 2024年3月 1 日

氏名	黄璐娇	HUANG LUJIAO	性別	F	生年月日 1988/09/10
所属機関(役職)	四川省医学科学院・四川省人民医院臨床栄養科(主管技師)				
研究先(指導教官)	筑波大学大学院人間総合科学研究科生命システム医学専攻 国際発達ケア: エンパワメント科学研究室(安梅 勅江 教授)				
研究テーマ	社会資本と生活の質の変化: 多民族社会における縦断的研究 Social Capital and Changes in Quality of Life: A Longitudinal Study in Multi-Ethnic Populations				
専攻種別	論文博士	<input type="checkbox"/>	課程博士	<input checked="" type="checkbox"/>	

1. 研究概要(1)

1) 目的(Goal)

To explore the association of Social capital with changes in Quality of life in multi-ethnic populations and to clarify the heterogeneity in the effects of Social capital on Quality of life across subgroups in multi-ethnic populations

2) 戦略(Approach)

This longitudinal study was based on the China Multi-Ethnic Cohort (CMEC), five provinces of Southwest China were included. The baseline survey was conducted between May 2018 and September 2019 and a total of 99556 participants were recruited. Data were collected with an electronic questionnaire and face-to-face interviews, medical examinations, and clinical laboratory tests. The repeated survey was conducted between August 2020 and July 2021 involving approximately 10% (11161) of the baseline participants. The on-site survey were mostly the same as the baseline survey, except for an expanded and refined questionnaire.

3) 材料と方法(Materials and methods)

a. Participants

Inclusion criteria:

- ①Adults aged 30-79 years old
- ②Permanent residents who have lived for more than six months

Exclusion criteria:

- ①Inability to provide a unique identity card
- ②Severe physical or mental illness (such as schizophrenia)
- ③Refusal to comply with study requirements

b. Measurements

Social Capital (SC)

SC was measured using a validated Chinese version of Health-related Social Capital Measurement. According to the purpose and feasibility of this study, 5 items were chosen to measure family SC and community/society SC. The answers consisted of 5-point Likert scales ranging from 1 (strongly disagree) to 5 (strongly agree). A higher total score indicates the stronger SC.

Quality of Life (QoL)

QoL was measured using EQ-5D-5L scale. EQ-5D instrument comprises a short descriptive system questionnaire and a visual analogue scale (EQ VAS). The descriptive system comprises 5 dimensions(Mobility, Self-Care, Usual Activities, Pain/Discomfort, Anxiety/Depression), each dimension has five response levels(no problems, slight problems, moderate problems, severe problems, unable to/extreme problems). The EQ VAS is a 0-100 score scale where participants are asked to indicate their overall health, providing a quantitative measure of the patient's perception of their overall health

Changes in Quality of Life

As continuous variables using QoL index value & VAS score: $\Delta QoL = QoL(\text{Repeated-survey}) - QoL(\text{Baseline-survey})$; As categorical variables according to the Pareto Classification of Health Change (PCHC), there are 4 possibilities: Better, Worse, Unchanged, Mixed (better on one dimension, but worse on another)

c. Statistical analysis

Descriptive statistics: Mean±SD, Percentiles(interquartile range) and frequency distributions were conducted to show the demographic characteristics, SC score, QoL index value or QoL VAS score. T-test, ANOVA or Nonparametric tests were used to compare between groups .

Change analysis: Multiple linear regression models and logistic regression models

1. 研究概要(2)

4) 実験結果 (Results)

At baseline, the proportion of participants reporting “no problem”(level 1) in mobility, self-care, pain/discomfort, usual activities, and anxiety/depression were 85.0%, 95.0%, 66.9%, 90.4%, and 87.7%, respectively. By year two, the proportion of participants achieving “no problem”(level 1) in mobility, pain/discomfort, and anxiety/depression had a slightly increase except for “usual activities”. Analysis according to Pareto Classification of Health Change (PCHC) showed that more than a quarter of participants (25.2%) reported improvement(better) in QoL after 2 years. However, there were 19% reported a level below baseline QoL at follow-up. The remaining more than half of the participants either had no change or had a mixed change of the dimensions of EQ-5D.

Taking changes in QoL as a continuous variable, after controlling for potential confounding factors, the Linear regression model indicated a negative association between social capital and changes in QoL. Taking changes in QoL as a categorical variable, after controlling for potential confounding factors, the Multinomial logistic regression model indicated that comparison with “unchanged group”, the higher the social capital at baseline the less likely(OR=0.974) it is to get better QoL. However, No statistically significant associations were found between social capital and “mixed group” or “worse group” when comparison with “unchanged group”.

5) 考察 (Discussion)

This study found better social capital at baseline is associated with less positive improvement in quality of life over 2 years among multi-ethnics in southwest China after adjust for potential confounders. This suggests that those with already higher levels of social capital at baseline have less room for improvement in quality of life. There may be a ceiling effect, wherein social capital has diminishing returns on quality of life, it is difficult for them to significantly improve further. This could relate to theories around social support already being adequate for those starting with better social capital. The stress-buffering hypothesis argues good social support protects against life stressors negatively impacting health and well-being. Those starting with poorer social capital have more uncertainty (a stressor), leaving more room for building networks to improve quality of life.

Heterogeneity exists in the SC-changes in QoL relationships. The marginal returns from SC on QoL may differ between Han majority versus ethnic minority groups due to variances in socioeconomic position, social integration, lifestyles and access to resources.

Urbanization trends have likely disrupted traditional social connections among certain minorities. Those with higher social capital pre-transition may perceive greater subsequent worsening in QoL and wellbeing.

Several limitations exist in this study. First, the study variables were restricted to baseline social capital and changes in quality of life scores. In observational data, where the baseline outcome is a confounder or mediator, change-score analyses evaluate obscure estimates, which may differ in magnitude and direction from the total and direct causal effects. Second, the two-wave data cannot show long-term trajectories. More timepoints are needed to analyze how changes in social capital might shape trajectories in quality of life.

6) 参考文献 (References)

- [1] CDC. Health-Related Quality of Life (HRQOL). 2023. Available from: <https://www.cdc.gov/hrqol/concept.htm>.
- [2] Whoqol Group. The World Health Organization quality of life assessment (WHOQOL): position paper from the World Health Organization. *Soc SciMed*. 1995;41(10):1403-9. [https://doi.org/10.1016/0277-9536\(95\)00112-k](https://doi.org/10.1016/0277-9536(95)00112-k).
- [3] Karimi M, Brazier J. Health, health-related quality of life, and quality of life: what is the difference? *PharmacoEconomics*. 2016;34(7):645-9. <https://doi.org/10.1007/s40273-016-0389-9>
- [4] Development of the World Health Organization WHOQOL-BREF quality of life assessment. The WHOQOL Group. *Psychol Med* 1998; 28:551-8.
- [5] Macran S, Weatherly H, Kind P. Measuring population health: a comparison of three generic health status measures. *Med Care*. 2003;41(2):21831. <https://doi.org/10.1097/01.MLR.0000044901.57067.19>.
- [6] Cunillera O, Tresserras R, Rajmil L, Vilagut G, Brugulat P, Herdman M, et al. Discriminative capacity of the EQ-5D, SF-6D, and SF-12 as measures of health status in population health survey. *Qual Life Res*. 2010;19(6):853-64. <https://doi.org/10.1007/s11136-010-9639-z>
- [7] Wang, D., Xie, S., Wu, J. et al. The trend in quality of life of Chinese population: analysis based on population health surveys from 2008 to 2020. *BMC Public Health* 23, 167 (2023). <https://doi.org/10.1186/s12889-023-15075-2>.
- [8] Reeve BB, Graves KD, Lin L, Potosky AL, Ahn J, Henke DM, Pan W, Fall-Dickson JM. Health-related quality of life by race, ethnicity, and country of origin among cancer survivors. *J Natl Cancer Inst*. 2023 Mar 9;115(3):258-267. doi: 10.1093/jnci/djac230.

2. 執筆論文 Publication of thesis ※記載した論文を添付してください。Attach all of the papers listed below.

論文名 1 Title						
掲載誌名 Published journal						
	年	月	巻(号)	頁 ~	頁	言語 Language
第1著者名 First author			第2著者名 Second author			第3著者名 Third author
その他著者名 Other authors						
論文名 2 Title						
掲載誌名 Published journal						
	年	月	巻(号)	頁 ~	頁	言語 Language
第1著者名 First author			第2著者名 Second author			第3著者名 Third author
その他著者名 Other authors						
論文名 3 Title						
掲載誌名 Published journal						
	年	月	巻(号)	頁 ~	頁	言語 Language
第1著者名 First author			第2著者名 Second author			第3著者名 Third author
その他著者名 Other authors						
論文名 4 Title						
掲載誌名 Published journal						
	年	月	巻(号)	頁 ~	頁	言語 Language
第1著者名 First author			第2著者名 Second author			第3著者名 Third author
その他著者名 Other authors						
論文名 5 Title						
掲載誌名 Published journal						
	年	月	巻(号)	頁 ~	頁	言語 Language
第1著者名 First author			第2著者名 Second author			第3著者名 Third author
その他著者名 Other authors						

3. 学会発表 Conference presentation ※筆頭演者として総会・国際学会を含む主な学会で発表したものを記載してください。

※Describe your presentation as the principal presenter in major academic meetings including general meetings or international meetings

学会名 Conference					
演題 Topic					
開催日 date	年	月	日	開催地 venue	
形式 method	<input type="checkbox"/> 口頭発表 Oral	<input type="checkbox"/> ポスター発表 Poster	言語 Language	<input type="checkbox"/> 日本語	<input type="checkbox"/> 英語 <input type="checkbox"/> 中国語
共同演者名 Co-presenter					
学会名 Conference					
演題 Topic					
開催日 date	年	月	日	開催地 venue	
形式 method	<input type="checkbox"/> 口頭発表 Oral	<input type="checkbox"/> ポスター発表 Poster	言語 Language	<input type="checkbox"/> 日本語	<input type="checkbox"/> 英語 <input type="checkbox"/> 中国語
共同演者名 Co-presenter					
学会名 Conference					
演題 Topic					
開催日 date	年	月	日	開催地 venue	
形式 method	<input type="checkbox"/> 口頭発表 Oral	<input type="checkbox"/> ポスター発表 Poster	言語 Language	<input type="checkbox"/> 日本語	<input type="checkbox"/> 英語 <input type="checkbox"/> 中国語
共同演者名 Co-presenter					
学会名 Conference					
演題 Topic					
開催日 date	年	月	日	開催地 venue	
形式 method	<input type="checkbox"/> 口頭発表 Oral	<input type="checkbox"/> ポスター発表 Poster	言語 Language	<input type="checkbox"/> 日本語	<input type="checkbox"/> 英語 <input type="checkbox"/> 中国語
共同演者名 Co-presenter					

4. 受賞(研究業績) Award (Research achievement)

名称 Award name	国名		受賞年	年	月
	Country name		Year of award		
名称 Award name	国名		受賞年	年	月
	Country name		Year of award		

5. 本研究テーマに関わる他の研究助成金受給 Other research grants concerned with your research theme

受給実績 Receipt record	<input type="checkbox"/> 有 <input checked="" type="checkbox"/> 無
助成機関名称 Funding agency	
助成金名称 Grant name	
受給期間 Supported period	年 月 ~ 年 月
受給額 Amount received	円
受給実績 Receipt record	<input type="checkbox"/> 有 <input checked="" type="checkbox"/> 無
助成機関名称 Funding agency	
助成金名称 Grant name	
受給期間 Supported period	年 月 ~ 年 月
受給額 Amount received	円

6. 他の奨学金受給 Another awarded scholarship

受給実績 Receipt record	<input type="checkbox"/> 有 <input checked="" type="checkbox"/> 無
助成機関名称 Funding agency	
奨学金名称 Scholarship name	
受給期間 Supported period	年 月 ~ 年 月
受給額 Amount received	円

7. 研究活動に関する報道発表 Press release concerned with your research activities

※記載した記事を添付してください。Attach a copy of the article described below

報道発表 Press release	<input type="checkbox"/> 有 <input checked="" type="checkbox"/> 無	発表年月日 Date of release	
発表機関 Released medium			
発表形式 Release method	・新聞 ・雑誌 ・Web site ・記者発表 ・その他()		
発表タイトル Released title			

8. 本研究テーマに関する特許出願予定 Patent application concerned with your research theme

出願予定 Scheduled application	<input type="checkbox"/> 有 <input checked="" type="checkbox"/> 無	出願国 Application country	
出願内容(概要) Application contents			

9. その他 Others

None

指導責任者(記名) 安梅 勅江

日中笹川医学奨学金制度＜学位取得コース＞評価書

課程博士：指導教官用



第 44 期

研究者番号：G4403

作成日：2024年2月21日

氏名	楊 勇	YANG YONG	性別	M	生年月日	1986/07/22
所属機関（役職）	懐化市第一人民医院神経外科（主治医師）					
研究先（指導教官）	千葉大学社会精神保健教育研究センター 病態解析研究部門（橋本 謙二 副センター長・教授）					
研究テーマ	脳疾患の病因解明と新規治療法の開発 Study of brain disorders and development of new therapeutic drugs					
専攻種別	<input type="checkbox"/> 論文博士			<input checked="" type="checkbox"/> 課程博士		

研究者評価（指導教官記入欄）

成績状況	<input checked="" type="radio"/> 優 <input type="radio"/> 良 <input type="radio"/> 可 <input type="radio"/> 不可 学業成績係数=	取得単位数
学生本人が行った研究の概要	楊勇君は、千葉大学大学院在籍中に、うつ病モデルにおける迷走神経や脾臓神経の役割に関する実験を行いました。以前、私の研究室は炎症に重要な役割を果たしている $\alpha 7$ ニコチン受容体遺伝子欠損マウスがうつ様行動を示すことを報告した。楊君は、この遺伝子欠損マウスの横隔膜下の迷走神経の切断あるいは脾臓神経を障害すると、うつ様行動が消失することを見出し、またこの現象に腸内細菌叢や微生物が生成する代謝物が関与している可能性を見出した。このように、うつ病における迷走神経・脾臓神経を介する臓器-脳連関の重要性を明らかにした。さらに、肝障害モデル（肝における虚血再灌流障害モデルと胆管結紮・閉塞性胆汁うっ滞モデル）におけるうつ病との関連を見出し、肝-脳連関の重要性を提唱した。	
総合評価	【良かった点】 上記にあるように、新しい研究成果を発表し、うつ病における臓器-脳連関の重要性を提唱し、これらは国際誌に原著論文（筆頭著者として4本）として掲載された。さらに、原著論文2本を筆頭著者として論文投稿中である。このように、多くの研究成果を発表していることは良かった点である。	
	【改善すべき点】 特に改善する個所は無い。	
	【今後の展望】 現在、貴州省人民病院で脳外科医として勤務しており、臨床研究で益々の活躍を期待している。さらに、日中の医学交流にも尽力すると期待している。	
学位取得見込	楊勇君は、2023年3月末に千葉大学で学位（医学博士）を取得した。	
評価者（指導教官名） 橋本 謙二		

日中笹川医学奨学金制度<学位取得コース>報告書 研究者用



第44期

研究者番号: G4403

作成日: 2024年3月1日

氏名	杨 勇	YANG YONG	性別	M	生年月日	1986/07/22
所属機関(役職)	懐化市第一人民医院神経外科(主治医師)					
研究先(指導教官)	千葉大学社会精神保健教育研究センター病態解析研究部門(橋本 謙二 副センター長・教授)					
研究テーマ	脳疾患の病因解明と新規治療法の開発 Study of brain disorders and development of new therapeutic drugs					
専攻種別	論文博士	<input type="checkbox"/>	課程博士	<input checked="" type="checkbox"/>		
1. 研究概要(1)						
<p>1) 目的(Goal) うつ病は代表的な精神疾患であるが、未だ病因は明らかでなく、現在の治療薬に奏功しない治療抵抗性うつ病患者が存在する。近年、うつ病などの精神疾患の病因に腸-脳相関の異常が寄与している可能性が指摘されている。一方、肝臓疾患患者ではうつ症状を呈するが、その機序は明らかでない。</p> <p>2) 戦略(Approach) 今回、二つの実系を行うことにより、うつ病における臓器-脳連関の役割を調べた。A7ニコチン受容体は炎症に重要な役割を果たしており、この遺伝子欠損マウスはうつ様行動を示すことを報告した(参考文献1-2)。最初の実験は、この遺伝子欠損マウスにおける迷走神経および脾臓神経の役割を調べることであった。次に、肝障害患者はうつ症状を呈することが知られているが、その機序は明らかでない。今回、二つの肝障害モデルを用いて、腸-肝-脳連関の役割を調べた。</p> <p>3) 材料と方法(Materials and methods) まずは、A7ニコチン受容体遺伝子欠損マウスおよび野生型マウスを用いた。まずは、横隔膜下の迷走神経切断を行い、うつ様行動、腸内細菌叢や代謝物解析を行った。次に、同様に遺伝子欠損マウスの脾臓神経を傷害させた後、うつ様行動、腸内細菌叢および代謝物解析を行った。次に、肝における虚血再灌流障害モデルと胆管結紮・閉塞性胆汁うっ滞モデルを用いて、うつ様行動における肝-脳連関の役割を調べた。</p> <p>4) 実験結果(Results) A7ニコチン受容体遺伝子欠損マウスのうつ様行動は、横隔膜下の迷走神経切断あるいは脾臓神経障害の前処置により、起きないことを見出した。さらに、腸内細菌叢・代謝物の解析により、これらの効果に、腸内細菌叢や代謝物の関与が示唆された。これらの研究成果は、昨年原著論文として発表し(参考文献3)、もう一つは現在論文投稿中である(参考文献4)。肝における虚血再灌流障害モデルマウスが、うつ様行動を示すことを見出し、この効果は迷走神経切断により生じないことから、迷走神経を介する肝-脳連関が重要であることを明らかにした(参考文献5)。さらに、胆管結紮・閉塞性胆汁うっ滞モデルマウスもうつ様行動を示すことを見出し、迷走神経切断により、うつ様行動が消失することを見出した。迷走神経を介する肝-脳連関の重要性を見出した(論文投稿中)。さらに興味深いことに、千葉大学で開発した新規抗うつ薬アールケタミンは、これらの二つのモデルにおけるうつ様行動を単回投与で改善することを見出した(参考文献4)。</p> <p>5) 考察(Discussion) 本研究により、$\alpha 7$ニコチン受容体はうつ様行動に重要な役割を果たしており、迷走神経および脾臓神経が遺伝子欠損マウスのうつ様行動に重要な役割を果たしていることが分かった。また腸内細菌叢や代謝物を含む腸-脳相関が関与している可能性が示唆された。今後、消化器系だけの受容体遺伝子欠損マウスを用いた研究が重要であると思われる。さらに、二つの肝障害モデルにおいても、迷走神経を介する腸-脳相関がうつ様行動に関与している可能性を見出した。さらに、国内外で臨床試験実施中である新規抗うつ薬アールケタミンが二つのモデルにおいても、即効性の抗うつ化を示したことは特筆すべきことである。うつ症状は、精神疾患だけでなく、様々な内科疾患患者でも観察されることから、適応が広まると考えている。これまでうつ病は、脳の病気であると信じられていたが、今後は末梢臓器を含めた身体疾患であることを知る必要があろう。</p> <p>6) 参考文献(References) (1) Zhang, J.C., Yao, W., Ren, Q., Yang, C., Chao, D., Ma, M., Wu, J., and Hashimoto, K. (2016) Depression-like phenotype by deletion of $\alpha 7$ nicotinic acetylcholine receptor: Role of BDNF-TrkB in nucleus accumbens. <i>Sci. Rep.</i> 6, 36705. (2) Pu, Y., Tan, Y., Qu, Y., Chang, L., Wang, S., Wei, Y., Wang, X., and Hashimoto, K. (2021) A role of the subdiaphragmatic vagus nerve in depression-like phenotypes in mice after fecal microbiota transplantation from Chrna7 knock-out mice with depression-like phenotypes. <i>Brain Behav. Immun.</i> 94, 318-326. (3) Yang, Y., Eguchi, A., Wan, X., Chang, L., Wang, X., Qu, Y., Mori, C. and Hashimoto, K. (2023) A role of gut-microbiota-brain axis via subdiaphragmatic vagus nerve in depression-like phenotypes in Chrna7 gene knock-out mice. <i>Prog. Neuropsychopharmacol. Biol. Psychiatry</i> 120, 110652. (4) Yang, Y., Eguchi, A., Wan, X., Mori, C., and Hashimoto, K. (2024) Depression-like phenotypes in mice with hepatic ischemia/reperfusion injury: A role of gut-microbiota-liver-brain axis via vagus nerve. <i>J. Affect. Disord.</i> 345, 157-167. (5) Yang, Y., Eguchi, A., Mori, C., and Hashimoto, K. (2024) Depression-like phenotypes in mice following common bile duct ligation: Insights into the gut-liver-brain axis via the vagus nerve. <i>Neurobiol. Dis.</i> 192, 106433.</p>						

2. 執筆論文 Publication of thesis ※記載した論文を添付してください。Attach all of the papers listed below.

論文名 1 Title	Abnormalities in gut microbiota composition and short-chain fatty acids in mice after repeated administration of colony stimulating factor 1 receptor inhibitor PLX5622					
掲載誌名 Published journal	Eur. Arch. Psychiatry Clin. Neurosci.					
	2022 年 4 月	272 巻(号)	483 頁 ~	495 頁	言語 Language	English
第1著者名 First author	Yong Yang	第2著者名 Second author	Tamaki Ishima		第3著者名 Third author	Xiayun Wan
その他著者名 Other authors	Yan Wei, Lijia Chang, Jiancheng Zhang, Youge Qu, Kenji Hashimoto					
論文名 2 Title	A role of gut-microbiota-brain axis via subdiaphragmatic vagus nerve in depression-like phenotypes in Chrna7 gene knock-out mice.					
掲載誌名 Published journal	Prog. Neuropsychopharmacol. Biol. Psychiatry					
	2023 年 1 月	120 巻(号)	110652 頁 ~	頁	言語 Language	English
第1著者名 First author	Yong Yang	第2著者名 Second author	Akifumi Eguchi		第3著者名 Third author	Xiayun Wan
その他著者名 Other authors	Lijia Chang, Xingming Wang, Youge Qu, Chisato Mori, Kenji Hashimoto					
論文名 3 Title	Depression-like phenotypes in mice with hepatic ischemia/reperfusion injury: A role of gut-microbiota-liver-brain axis via vagus nerve.					
掲載誌名 Published journal	J. Affect. Disord.					
	2024 年 1 月	345 巻(号)	157 頁 ~	167 頁	言語 Language	English
第1著者名 First author	Yong Yang	第2著者名 Second author	Akifumi Eguchi		第3著者名 Third author	Xiayun Wan
その他著者名 Other authors	Chisato Mori, Kenji Hashimoto					
論文名 4 Title	Depression-like phenotypes in mice following common bile duct ligation: Insights into the gut-liver-brain axis via the vagus nerve.					
掲載誌名 Published journal	Neurobiol. Dis					
	2024 年 2 月	192 巻(号)	106433 頁 ~	頁	言語 Language	English
第1著者名 First author	Yong Yang	第2著者名 Second author	Akifumi Eguchi		第3著者名 Third author	Chisato Mori
その他著者名 Other authors	Kenji Hashimoto					
論文名 5 Title	Key role of the gut-microbiota-brain axis via the subdiaphragmatic vagus nerve in demyelination of the cuprizone-treated mouse brain					
掲載誌名 Published journal	Neurobiol. Dis					
	2023 年 1 月	176 巻(号)	105951 頁 ~	頁	言語 Language	English
第1著者名 First author	Xingming Wang	第2著者名 Second author	Akifumi Eguchi		第3著者名 Third author	Yong Yang
その他著者名 Other authors	Lijia Chang, Xiayun Wan, Jiajing Shan, Youge QU, Li Ma, Chisato Mori, Jianjun Yang, Kenji Hashimoto					

3. 学会発表 Conference presentation ※筆頭演者として総会・国際学会を含む主な学会で発表したものを記載してください。

※Describe your presentation as the principal presenter in major academic meetings including general meetings or international meeting

学会名 Conference	無し				
演題 Topic					
開催日 date	年	月	日	開催地 venue	
形式 method	<input type="checkbox"/> 口頭発表 Oral	<input type="checkbox"/> ポスター発表 Poster	言語 Language	<input type="checkbox"/> 日本語	<input type="checkbox"/> 英語 <input type="checkbox"/> 中国語
共同演者名 Co-presenter					
学会名 Conference					
演題 Topic					
開催日 date	年	月	日	開催地 venue	
形式 method	<input type="checkbox"/> 口頭発表 Oral	<input type="checkbox"/> ポスター発表 Poster	言語 Language	<input type="checkbox"/> 日本語	<input type="checkbox"/> 英語 <input type="checkbox"/> 中国語
共同演者名 Co-presenter					
学会名 Conference					
演題 Topic					
開催日 date	年	月	日	開催地 venue	
形式 method	<input type="checkbox"/> 口頭発表 Oral	<input type="checkbox"/> ポスター発表 Poster	言語 Language	<input type="checkbox"/> 日本語	<input type="checkbox"/> 英語 <input type="checkbox"/> 中国語
共同演者名 Co-presenter					
学会名 Conference					
演題 Topic					
開催日 date	年	月	日	開催地 venue	
形式 method	<input type="checkbox"/> 口頭発表 Oral	<input type="checkbox"/> ポスター発表 Poster	言語 Language	<input type="checkbox"/> 日本語	<input type="checkbox"/> 英語 <input type="checkbox"/> 中国語
共同演者名 Co-presenter					

4. 受賞(研究業績) Award (Research achievement)

名称 Award name	国名 Country		受賞年 Year of award	年	月
	国名 Country		受賞年 Year of award	年	月

5. 本研究テーマに関わる他の研究助成金受給 Other research grants concerned with your research theme

受給実績 Receipt record	<input type="checkbox"/> 有 <input checked="" type="checkbox"/> 無
助成機関名称 Funding agency	
助成金名称 Grant name	
受給期間 Supported period	年 月 ~ 年 月
受給額 Amount received	円
受給実績 Receipt record	<input type="checkbox"/> 有 <input checked="" type="checkbox"/> 無
助成機関名称 Funding agency	
助成金名称 Grant name	
受給期間 Supported period	年 月 ~ 年 月
受給額 Amount received	円

6. 他の奨学金受給 Another awarded scholarship

受給実績 Receipt record	<input checked="" type="checkbox"/> 有 <input type="checkbox"/> 無
助成機関名称 Funding agency	国立大学法人千葉大学
奨学金名称 Scholarship name	千葉大学全方位イノベーション創発博士人材養成プロジェクト
受給期間 Supported period	2022 年 4 月 ~ 2023 年 3 月
受給額 Amount received	2,040,000 円

7. 研究活動に関する報道発表 Press release concerned with your research activities

※記載した記事を添付してください。Attach a copy of the article described below

報道発表 Press release	<input type="checkbox"/> 有 <input checked="" type="checkbox"/> 無	発表年月日 Date of release	
発表機関 Released medium			
発表形式 Release method	・新聞 ・雑誌 ・Web site ・記者発表 ・その他()		
発表タイトル Released title			

8. 本研究テーマに関する特許出願予定 Patent application concerned with your research theme

出願予定 Scheduled	<input type="checkbox"/> 有 <input checked="" type="checkbox"/> 無	出願国 Application	
出願内容(概要) Application contents			

9. その他 Others

特になし

指導責任者(記名) 橋本 謙二



Microglial depletion and abnormalities in gut microbiota composition and short-chain fatty acids in mice after repeated administration of colony stimulating factor 1 receptor inhibitor PLX5622

Yong Yang¹ · Tamaki Ishima¹ · Xiayun Wan¹ · Yan Wei¹ · Lijia Chang¹ · Jiancheng Zhang¹ · Youge Qu¹ · Kenji Hashimoto¹

Received: 7 July 2021 / Accepted: 27 August 2021 / Published online: 4 September 2021
© Springer-Verlag GmbH Germany, part of Springer Nature 2021

Abstract

PLX5622, a brain-penetrant highly specific inhibitor of the colony-stimulating factor 1 receptor (CSF1R), is used to eliminate microglia in the brain. Considering the role of microglia and gut microbiota in the brain homeostasis, this study was undertaken to investigate whether repeated intragastric administration of PLX5622 (65 mg/kg/day for consecutive 7 days) could affect the composition of gut microbiota and the concentration of short-chain fatty acids (SCFAs) in fresh feces of adult mice. Repeated administration of PLX5622 caused significant reductions of the expression of genes and proteins for microglial markers in the prefrontal cortex (PFC) and hippocampus compared to control mice although the elimination of brain's microglia was partial. There was a significant alteration in the β -diversity of intestine microbiota in the PLX5622-treated group. Linear discriminant analysis effect size identified eight significant enriched bacteria as microbial markers for PLX5622-treated group. Repeated administration of PLX5622 affected the relative abundance of several bacteria at the genus and species levels. Furthermore, repeated administration of PLX5622 caused a significant change in lactic acid compared to control group. Interestingly, we found significant correlations between microglial markers in the brain and the relative abundance of several bacteria, suggesting microbiome–microglia crosstalk through the brain–gut axis. These data demonstrate that repeated administration of PLX5622 leads to an abnormal composition of the gut microbiota and lactic acid in adult mice. Therefore, abnormalities in the composition of gut microbiota after repeated treatment of PLX5622 should be considered for behavioral and biological functions in animals treated with CSF1R inhibitors.

Keywords Brain–gut–microbiota axis · CSF1R · Gut microbiota · Microglia

Introduction

Microglia are the mononuclear phagocytes in the natural immune system of the central nervous system (CNS) [1, 2]. Despite the fact that microglia were thought to be mainly in charge of the handling of cellular fragments and answering to neural injury, accumulating evidence suggests that microglia play a role in the pathogenesis of numerous psychiatric and neurological disorders [3–5]. Penetration of myeloid cells into the substantial tissue of brain is very rare in normal healthy CNS conditions following the establishment of

the blood–brain barrier in adult mice [6, 7], indicating that microglia are considered essential macrophages that represent the unique tissue-specificity of the CNS.

Colony stimulating factor 1 receptor (CSF1R) is predominantly expressed on microglia within CNS, and it is necessary for their survival, differentiation and proliferation [3, 8–10]. Microglia were absent in *Csf1r* knock-out (KO) mice [6, 11], suggesting that CSF1R plays a crucial role in the microglia. Interestingly, the extensive treatment of CSF1R inhibitor PLX3397 resulted in probable 99% of microglia in the brain were eliminated, suggesting that microglia in the adult brain are physiologically dependent on CSF1R signaling [12].

PLX5622 is a new inhibitor of CSF1R, which can permeate the brain ($IC_{50} = 0.016 \mu M$). PLX5622 is selective for CSF1R over the kinase insert domain receptor (KDR), Aurora C, Kit, and FMS-related tyrosine kinase 3 (FLT3)

✉ Kenji Hashimoto
hashimoto@faculty.chiba-u.jp

¹ Division of Clinical Neuroscience, Chiba University Center for Forensic Mental Health, Chiba 260-8670, Japan

($IC_{50s} = 1.1, 1, 0.86$ and $0.39 \mu\text{M}$, respectively), and it is greater than 100-fold selective for CSF1R over a panel of 230 kinases [13, 14]. Thus, CSF1R inhibitors (PLX3397 and PLX5622) have been used widely to eliminate microglia in the CNS without significant effects on peripheral immune cells [3, 15–21]. Although CSF1R is expressed in the microglial cells and macrophages, the role of CSF1R in the gut microbiome is currently unknown.

The brain-gut-microbiota axis is a vital multi-organ two-way signal transduction interaction system between the brain and the host's intestinal microbiota homeostasis [22–27]. An increasing number of preclinical studies have shown a disturbance of intestine microbiota in rodents with depression-like behaviors [28–34]. Short-chain fatty acids (SCFAs), the main metabolic products derived from microbiota in the alimentary canal, play an indispensable role in the metabolic functions in humans and rodents [35–37]. Increasing preclinical findings suggest the role of gut microbiota in the maturation and function of microglia in the CNS [38–40]. Interestingly, clinical trials of small molecule CSF1R inhibitors in patients with cancer are underway [41, 42]. However, there are no reports demonstrating the alterations in the distribution of intestine microbiota and SCFAs in rodents after repeated administration of CSF1R inhibitors such as PLX5622.

The present study was attempted to investigate whether the repeated administration of PLX5622 alters the distribution of the gut microbiota and the concentration of SCFAs in fecal samples of adult mice. In this study, we examined the effects of the repeated intragastric administration of PLX5622 on the composition of gut microbiota and SCFAs in adult mice. Additionally, we examined correlations between microglia markers in the brain, and certain intestine bacteria since brain–gut–microbiota axis plays a key role in the immune system [22, 26].

Methods

Animals

Male adult C57BL/6NCr mice ($n = 16$, 8 weeks old, 21–27 g) were purchased from Japan SLC Inc. (Hamamatsu, Shizuoka, Japan). All the experimental animals were acclimatized to standard laboratory conditions (4/cage), maintain alternating cycles of 12 h of light and 12 h of darkness (7:00–19:00 light), and under controlled conditions for humidity and temperature. Animals were given free admittance to chow and water. The animal protocol was approved by Chiba University of Institutional Animal Care and Use Committee (Permission number was 2–447).

Treatment and sample collection

PLX5622 was purchased from MedChemExpress (Monmouth Junction, NJ, USA). Dietary administration of PLX5622 (1200 ppm in chow) is reported to eliminate approximately 90% of microglia in the brain [14]. It is also shown that dietary administration of PLX5622 (300 ppm in chow) could eliminate the part of the microglia in the brain [13]. The dosage (65 mg/kg/day) by intragastric administration is equal to the 300 ppm in chow daily dosage, eliminating the part of microglia in the brain [13]. The dosage (65 mg/kg/day) of PLX5622 was used in this study.

Briefly, PLX5622 stock solution was dissolved in dimethyl sulfoxide (DMSO) at a concentration of 130 mg/ml; 2% hydroxypropyl methylcellulose (Sigma-Aldrich Co., Ltd, St. Louis, MO, USA), and 25% polysorbate 80 (FUJIFILM Co., Tokyo, Japan) were prepared to make a diluent. The daily intragastric administration, by adding 1 volume of compound stock solution (130 mg/ml) into 19 volumes of diluent, dilutes the PLX5622 stock solution 20 times to make a working solution of 6.5 mg/ml. The vehicle solution was prepared with a mixture of DMSO and diluent. Mice were weighed body weight before intragastric administration every day. According to daily changes in the mice's body weight, animals were treated daily by intragastric administration with 0.1 ml solution (6.5 mg/ml) per 0.01 kg body weight (final dosage at 65 mg/kg body weight) [13].

Mice were treated with either vehicle solution (10 ml/kg/day) or PLX5622 (65 mg/kg/day) for 7 consecutive days (day 1–day 7). Fresh fecal samples were collected in the morning of day 8 (9:00–10:00) to prevent the influence of circadian rhythm effect on the microbiota. Mouse brain was collected by decapitation, subsequently prefrontal cortex (PFC) and hippocampus were dissected on ice. Then, all kinds of samples quickly frozen in liquid nitrogen and stored at -80°C until assays (Fig. 1A).

Quantification of mRNA expression

We measured the gene expression of microglial markers such as Iba1 (or AIF-1), TGF- β 1 and CSF1R in the mouse brain. We used a quantitative RT-PCR system (Step One Plus, Thermo Fisher Scientific, Yokohama, Japan). All specific mRNA transcripts were quantitatively analyzed by TaqManGene Expression assays (Thermo Fisher Scientific, Yokohama, Japan). Expression levels of *Aif1* (Mm00479862_g1), *Tgfb1* (Mm01178820_m1), *Csf1r* (Mm01266652_m1) were measured. Total RNA was extracted using an RNase-Free DNase Set and an RNeasy

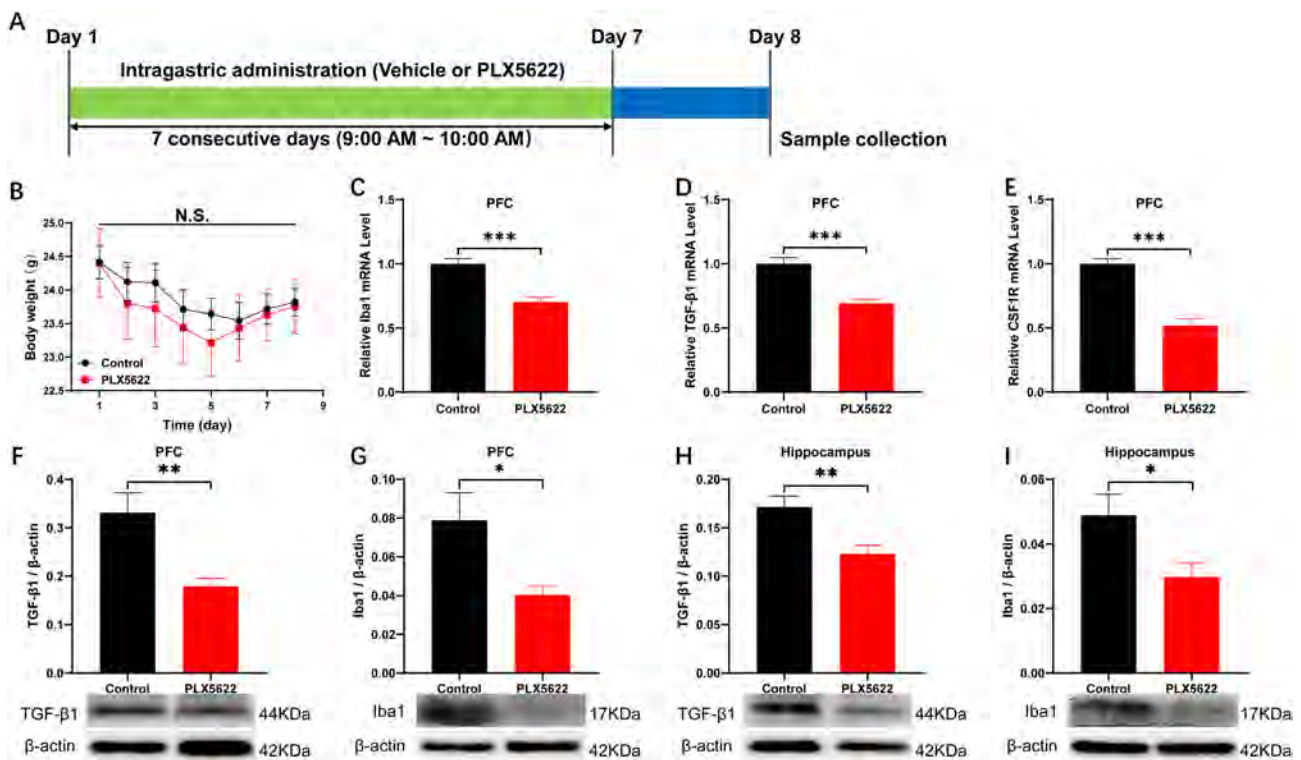


Fig. 1 Experiment design, collection of cerebrum and fecal samples, body weight changes, expression of microglial markers in the brain. **A** Intragastric administration of either vehicle or PLX5622 for consecutive 7 days (day 1—day 7). Collection of feces, prefrontal cortex (PFC) and hippocampus were performed on day 8. **B** Body weighing of two groups from the first day to the eighth day. Repeated measure ANOVA, $F_{(7,14)}=0.166$, $P=0.690$. **C** The level of Iba1 mRNA in the PFC (unpaired t test, $t=5.449$, $df=14$, $P<0.0001$). **D** The level of TGF- β 1 mRNA in the PFC (unpaired t test, $t=5.279$, $df=14$, $P=0.0001$). **E** The level of CSF1R mRNA in the PFC (unpaired t

test, $t=7.183$, $df=14$, $P<0.0001$). **F** Western blot analysis of TGF- β 1 in the PFC (unpaired t test, $t=3.430$, $df=14$, $P=0.0041$). **G** Western blot analysis of Iba1 in the PFC (unpaired t test, $t=2.589$, $df=14$, $P=0.0214$). **H** Western blot analysis of TGF- β 1 in the hippocampus (unpaired t test, $t=3.390$, $df=14$, $P=0.0044$). **I** Western blot analysis of Iba1 in the hippocampus (unpaired t test, $t=2.445$, $df=14$, $P=0.0283$). The data are shown as means \pm SEM ($n=8$). ANOVA: analysis of variance. N.S. not significant; * $P<0.05$; ** $P<0.01$; *** $P<0.001$

Mini Kit (Qiagen, Hilden, Germany). The purity of total RNA was assessed by Bio photometer plus (Eppendorf, Hamburg, Germany). The cDNA libraries were obtained by reverse transcription-PCR using a High-Capacity cDNA Reverse Transcription Kit (#4368813 Thermo Fisher Scientific, Yokohama, Japan). All specimens were detected twice, and arithmetic means were used for quantification. The data of arithmetic mean were normalized to Vic-labeled *Actb* mRNA (#4352341E: pre-developed TaqMan Assay Reagents, Thermo Fisher Scientific, Yokohama, Japan).

Western blot analysis of TGF- β 1 and Iba1

Western blot analysis was performed as previously reported [30, 43]. The tissues were homogenized in freezing Laemmli lysis buffer, each specimen was performed separately, centrifuged at $3000\times g$ (RCF) at 4°C for 5 min to collect the supernatants. Use a DC protein assay kit (Bio-Rad,

Hercules, CA, USA) to measure aliquots (60 μg) of proteins; and boiled at 95°C for 10 min with a quarter volume of 125 mM Tris-HCl, pH 6.8; 0.1% bromophenol blue; 4% sodium dodecyl sulfate; 10% β -mercaptoethanol and 20% glycerol. Proteins were separated using 10% sodium dodecyl sulfate-polyacrylamide gel electrophoresis (SDS-PAGE) (catalog #: 4568125, Mini-PROTEAN TGX™ Stain-Free Gels; Bio-Rad) and then were transferred onto polyvinylidene difluoride membranes using a Trans-Blot Mini Cell apparatus (Bio-Rad).

For immunodetection, the polyvinylidene difluoride membranes were sealed with blocking solution [5% skim milk in TBS + 0.1% Tween-20 (TBST)] at room temperature for 1 h, the membranes for detecting TGF- β 1 were incubated with the appropriate dilution of the primary antibody against TGF- β 1 (1:2000, Catalog No.: ab179695, 1 $\mu\text{g}/\text{mL}$, Abcam, Cambridge, MA, USA), while the membranes for detecting Iba1 were incubated with the appropriate dilution of the primary antibody against Iba1 (1:1000, Cat No.:

016-20001, 1 µg/mL, FUJIFILM, Tokyo, Japan) and β-actin (1:10,000; Cat number: A5441 Sigma-Aldrich Co., Ltd, St Louis, MO, USA) at 4 °C overnight. The next day, wash the polyvinylidene difluoride membranes in three washes of TBST, 10 min each. Then the polyvinylidene difluoride membranes were selectively incubated with a recommended dilution of labeled secondary antibody in 5% blocking buffer in TBST [anti-mouse antibody (1:5000, catalog No.: NA931, GE Healthcare) or a horseradish peroxidase-conjugated anti-rabbit antibody (1:5000, catalog No.: NA934, GE Healthcare)] at room temperature for 1 h. After three final washes in TBST, 10 min each. The bands in the polyvinylidene difluoride membranes were detected using enhanced chemiluminescence plus a Western Blotting Detection system (GE Healthcare Bioscience).

The membranes for detecting TGF-β1 were incubated in elution buffer (62.5 mM Tris-HCl, pH 6.8, 2% sodium dodecyl sulfate, and 100 mM β-mercaptoethanol) at 60 °C for 30 min and then washed three times (10 min at a time) in TBST. The stripped membranes were sealed with blocking solution [5% skim milk in TBS + 0.1% Tween-20 (TBST)] for 1 h and then were incubated with the appropriate dilution of primary antibody directed against β-actin (1:10,000; Cat No.: A5441 Sigma-Aldrich Co., Ltd, St Louis, MO, USA) at 4 °C overnight. The following day, washing the membranes for three times (10 min at a time) in TBST and were incubated with a horseradish peroxidase-conjugated anti-mouse antibody (1:5000, catalog No.: NA931, GE Healthcare) for 1 h at room temperature. After three final washes in TBST, 10 min each. The bands in the polyvinylidene difluoride membranes were detected using enhanced chemiluminescence plus a Western Blotting Detection system (GE Healthcare Bioscience).

Images were produced using a ChemiDoc™ Touch Imaging System (170-01401; Bio-Rad Laboratories, Hercules, CA, USA), and immunoreactive bands were quantified using Image Lab™3.0 software (Bio-Rad Laboratories).

16S ribosome RNA sequencing

DNA extraction from fecal samples and 16S ribosome RNA analysis were performed by MyMetagenome Co., Ltd. (Tokyo, Japan), as previously reported [30, 33, 43–48]. DNA extraction from mouse fecal samples and the 16S ribosome RNA analysis were carried out in reference to the procedure of the previous reports [49, 50]. Briefly, PCR was carried out using 27Fmod 5'-AGRGTGGATYMTGGCTCAG-3' and 338R 5'-TGCTGCCTCCCGTAGGAGT-3' to amplify the V1–V2 region of the bacterial 16S ribosome RNA gene. The 16S amplicons were then sequenced using MiSeq reference to the Illumina protocol. Use the GLSEARCH program to search for similarities between the Ribosome Database Project and the genome database of the National Center for

Biotechnology Information (NCBI) and classify and identify OTUs. The 16S rRNA sequencing data have been deposited to the NCBI Sequence Read Archive and are available at the accession number PRJNA746230.

The abundance and diversity of the microbial community are reflected by α-diversity analyses, including Observed_otus, Chao1, Ace, Shannon, and Shannon_e. β-diversity analysis including principal components analysis (PCA) was used to access similarity or dissimilarity of two communities.

Linear discriminant analysis (LDA) effect size (LEfSe) was used to identify microbiota as a biomarker discovery. Microbiota-based biomarker discoveries were performed with LEfSe using the online galaxy platform [51]. The LDA scores (LDA > 3.5) derived from LEfSe analysis were considered significantly to be increased or decreased bacterial taxa in the gut microbiota between the two groups.

Measurement of the concentration of SCFAs in fresh fecal samples

SCFAs are the primary metabolites produced by bacterial fermentation of dietary fiber in the gastrointestinal tract. As previously reported, SCFAs (i.e., acetic acid, propionic acid, n-butyric acid, lactic acid, and succinic acid) in fresh fecal samples were measured at Techno Suruga Laboratory, Co., Ltd. (Shizuoka, Japan) [30, 34, 46, 47]. The concentration of the SCFAs was measured by gas chromatography with a flame ionization detector. The concentration of SCFAs were displayed as milligrams per gram of feces.

Statistical analysis

The data are shown as the mean ± standard error of the mean (S.E.M.). Statistical analysis was performed using SPSS version 20.0 software (SPSS, Tokyo, Japan). The data of body weight were analyzed using repeated measure analysis of variance (ANOVA), followed by Fisher's least significant difference (LSD) test. The gut microbiota data for α-diversity and the relative abundance at different levels in this study were analyzed using the Mann–Whitney *U* test. The results of Western blot analyses, RT-PCR and the concentration of the SCFAs were statistically analyzed using the unpaired Student's *t* test. Correlations between bacterial relative abundance and SCFAs, correlations between bacterial relative abundance and the expression of microglial markers, and correlations between bacterial relative abundance and mRNA levels of Iba1, TGF-β1, and CSF1R in the brain were all statistically analyzed using Spearman's correlation analysis. *P* values under 0.05 were considered statistically significant.

Results

Effects of PLX5622 on the body weight and the expression of gene and protein for microglial markers in the brain

It is well known that Iba1 and CSF1R are specific markers for microglia in the CNS. In the CNS, TGF- β 1 is also indispensable for the maturation of microglia, the maintenance of homeostasis of adult microglia and the control of microglia activation [52–54]. Repeated measure ANOVA identified significant changes of body weight which declined slowly over time and then increased gradually in two groups; however, there were no changes between the two groups at each time point (Fig. 1B). The levels of *Aif1* mRNA ($P < 0.001$), *Tgfb1* mRNA ($P = 0.001$), and *Csf1r* mRNA ($P < 0.001$) in the PFC of mice treated with PLX5622 were significantly lower than those of the control group (Fig. 1C–E). The reduction of mRNA for *Aif1*, *Tgfb1*, and *Csf1r* in the PFC of mice treated with PLX5622 were ~70%, ~69% and ~51% of control group, respectively.

Western blot statistical analysis showed that the expressions of TGF- β 1 and Iba1 in the PFC and hippocampus of the mice treated with PLX5622 were significantly lower than that of the control group. (Fig. 1F–I). These findings indicated that elimination of microglia in the PFC and hippocampus after repeated intragastric administration of PLX5622 (65 mg/kg/day for 7 consecutive days) was partial.

Effects of PLX5622 on the composition diversity of gut microbiota

The intestinal microbiota composition between PLX5622-treated mice and control mice was analyzed using both α -diversity and β -diversity. Mann–Whitney U test revealed no differences in the Observed_OTUs, Chao1, Ace, Shannon, and Shannon_e indices between PLX5622-treated mice and control mice (Fig. 2A–E). Regarding β -diversity, the bacterial population composition of intestine microbiota between the two groups was analyzed by PCA. Based on the OTU level, PCA analysis showed a significant separation in the bacterial population composition ($R = 0.2009$, $P = 0.022$) (Fig. 2F).

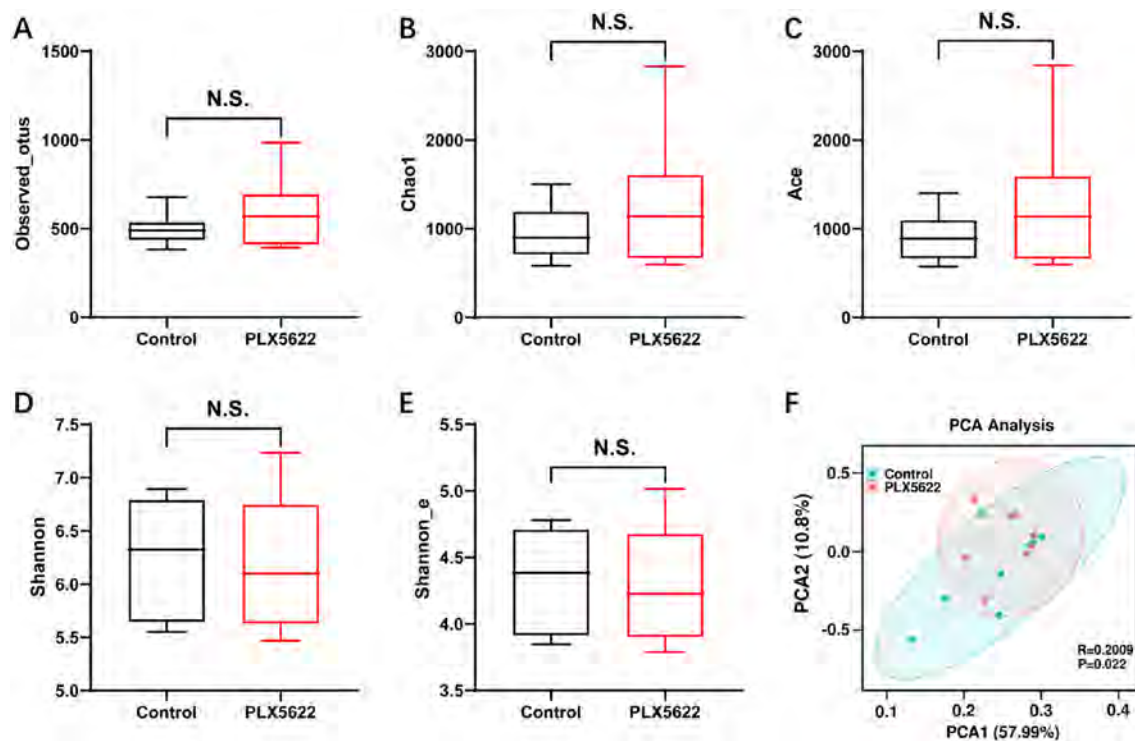


Fig. 2 Effects of PLX5622 on the composition diversity of gut microbiota. **A** α -diversity index of observed_otu (Mann–Whitney U test, $U = 24$, $P = 0.4418$). **B** α -diversity index of Chao1 (Mann–Whitney U test, $U = 26$, $P = 0.5737$). **C** α -diversity index of Ace (Mann–Whitney U test, $U = 22$, $P = 0.3282$). **D** α -diversity index of Shannon (Mann–Whitney U test, $U = 29$, $P = 0.7984$). **E** α -diversity index of

Shannon_e (Mann–Whitney U test, $U = 29$, $P = 0.7984$). **F** PCA based on OTU level ($R = 0.2009$, $P = 0.022$). For all box plots, the middle line in the box addresses the median, the box addresses the interquartile range, and the whisker addresses the most extreme and least values. The number of each group was 8. *N.S.* not significant

Effects of PLX5622 on the LefSe algorithm of gut microbiota

Cladogram presented the relationship between biomarker taxa (layers of the cladogram represent different levels, with phyla, class, order, family, and genera from inside to outside) generated by LefSe analysis (Fig. 3A). Furthermore, we identified eight taxonomic biomarkers, the species *Clostridium disporicum*, the genus *Clostridium*, the species *Barnesiella viscericola*, the genus *Barnesiella*, the family *Barnesiellaceae*, the species *Gabonibacter massiliensis*, the genus *Gabonibacter*, and the species *Lactobacillus intestinalis* were statistically significantly enriched in PLX5622-treated group compared to control group (Fig. 3B).

Effects of PLX5622 on the composition of the gut microbiota at the levels of genus and species

At the genus level, the composition of the gut microbiota was altered after repeated intragastric administration of PLX5622 (Fig. 4A). Both *Clostridium* and *Enterorhabdus* in the PLX5622-treated group were significantly higher in abundance than in the control group (Fig. 4B, D). By contrast, the relative abundance of *Anaerotignum* in the PLX5622-treated group was significantly lower than in the control group (Fig. 4C).

At the species level, repeated intragastric administration of PLX5622 also altered the composition of the gut microbiota. The relative abundance of *Lactobacillus intestinalis*, *Clostridium disporicum*, and *Enterorhabdus caecimuris* were higher in the PLX5622-treated group than that of control group. Whereas, compared with the control group, the

relative abundance of *Bacteroides acidifaciens* and *Bacteroides caecimuris* were lower in the PLX5622-treated group (Fig. 5A–F).

Measurement of SCFAs content in fecal samples

The concentration of lactic acid in the PLX5622-treated group was significantly higher than those in the control group (Table 1). In contrast, there were no changes in succinic acid, acetic acid, propionic acid, and n-butyric acid (Table 1).

Correlations between the bacterial relative abundance and lactic acid or microglia markers

There was a significant negative correlation between the concentration of lactic acid and the relative abundance of the genus *Anaerotignum* between the PLX5622-treated group and the control group (Fig. 6A). A negative correlation was determined between the concentration of lactic acid and the relative abundance of the species *Bacteroides acidifaciens* between the PLX5622-treated group and control group (Fig. 6B).

Next, we used the heat maps to show correlations between microglial markers in PFC and hippocampal tissues and the relative abundance of bacteria that differed significantly at the genus and species levels. A heat map showed the correlations between the data of RT-PCR and Western Blot of *Aif1* or *Tgfb1* expression in the PFC and hippocampus and the relative bacterial abundance that differ significantly at

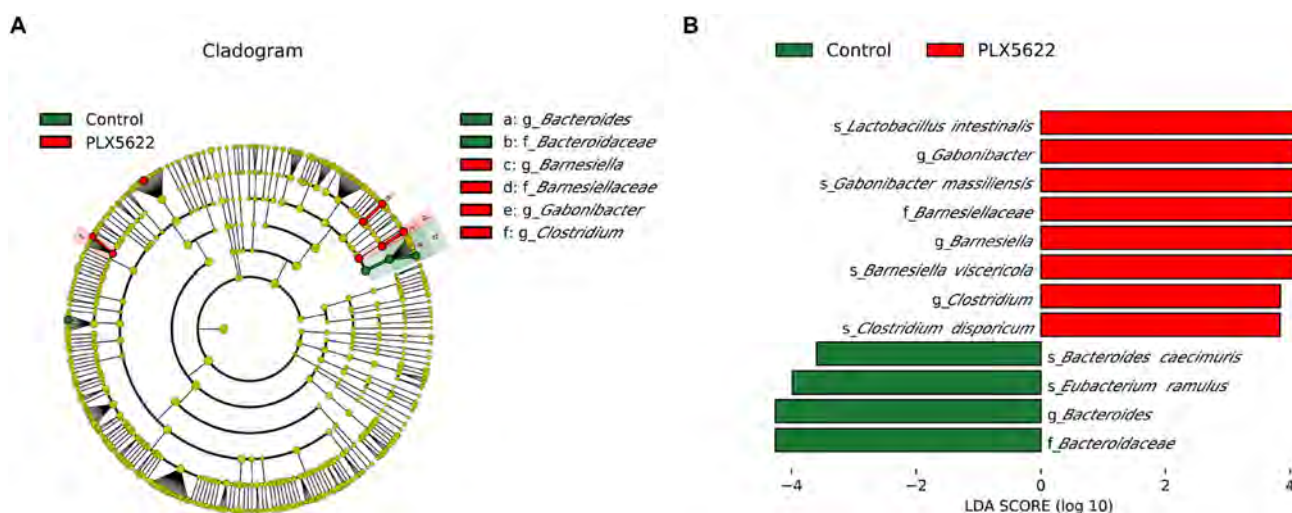


Fig. 3 LefSe determined bacteria biomarkers of gut microbiota in two groups. **A** Functional branching diagram generated from LefSe (LDA score > 3.5, $P < 0.05$) showed differences between the two

groups at taxonomic level. **B** Histogram represents enriched taxa with LDA score more than 3.5 and $P < 0.05$ obtained from LefSe between two groups

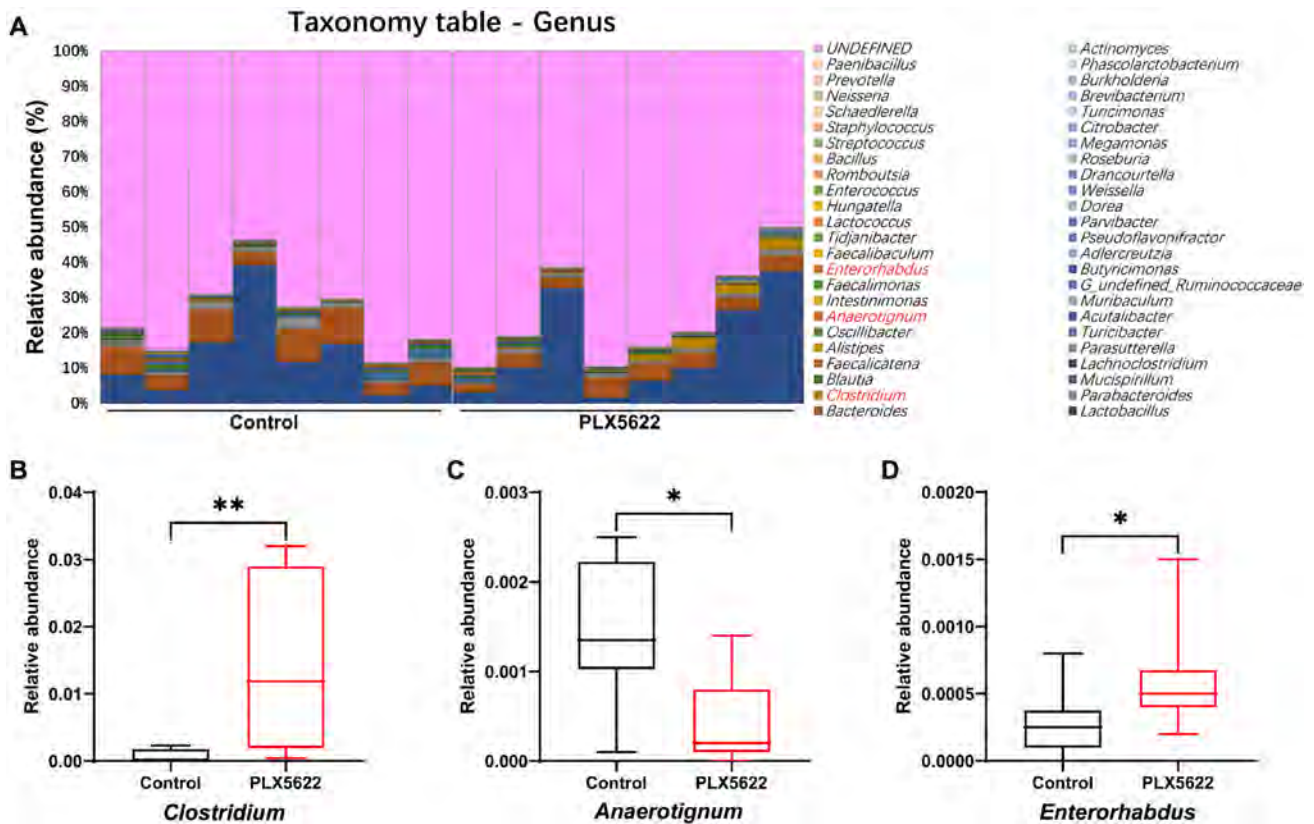


Fig. 4 PLX5622 altered the composition of mice gut microbiota at the genus levels. **A** Gut bacteria composition at the genus level in the two groups. **B** Relative abundance of genus *Clostridium* in two groups. (Mann–Whitney U test, $U=6$, $P=0.0037$). **C** Relative abundance of genus *Anaerotignum* in two groups (Mann–Whitney U test, $U=9$, $P=0.0131$). **D** Relative abundance of genus *Enterorhabdus* in

two groups (Mann–Whitney U test, $U=11.50$, $P=0.0284$). For all box plots, the middle line in the box addresses the median, the box addresses the interquartile range, and the whisker addresses the most extreme and least values. The number of each group was 8. * $P < 0.05$; ** $P < 0.01$

the genus and species levels (Fig. 6C). There were significant positive correlations between *Tgfb1* mRNA levels in the PFC and the relative abundance of the species *Bacteroides caecimuris*. There were significant negative correlations between *Tgfb1* mRNA levels in the PFC and the relative abundance of the genus *Clostridium* (or the species *Clostridium disporicum*) (Fig. 6C).

There were significant positive correlations between *Aif1* mRNA levels in the PFC and the relative abundance of the species *Bacteroides acidifaciens* (or the species *Bacteroides caecimuris*). There were significant negative correlations between *Aif1* mRNA levels in the PFC and the relative abundance of the genus *Clostridium*, the genus *Enterorhabdus*, the species *Clostridium disporicum*, and the species *Enterorhabdus caecimuris* (Fig. 6C).

A positive correlation was identified between *Csflr* mRNA levels in the PFC and the relative abundance of the species *Bacteroides caecimuris*. Furthermore, *Csflr* mRNA levels in the PFC were significant negatively correlated with the relative abundance of the genus *Clostridium*,

the genus *Enterorhabdus*, and the species *Clostridium disporicum* (Fig. 6C).

We found that the abundance of genus *Anaerotignum* and species *Bacteroides caecimuris* were positively correlated with TGF- β 1 expression in the PFC at the protein level. Negative correlations were determined between the abundance of the genus *Clostridium*, the genus *Enterorhabdus*, the species *Lactobacillus intestinalis*, the species *Clostridium disporicum*, or the species *Enterorhabdus caecimuris* and TGF- β 1 protein expression in the PFC. The plentitude of the species *Bacteroides acidifaciens* was positively correlated with Iba1 expression in the PFC (Fig. 6C).

Negative correlations were determined between the plentitude of the genus *Clostridium*, the genus *Enterorhabdus*, or the species *Lactobacillus intestinalis*, the species *Enterorhabdus caecimuris*, and TGF- β 1 protein expression in the hippocampal tissues. The abundance of the genus *Anaerotignum* was positively correlated with Iba1 protein expression in the hippocampal tissues (Fig. 6C).

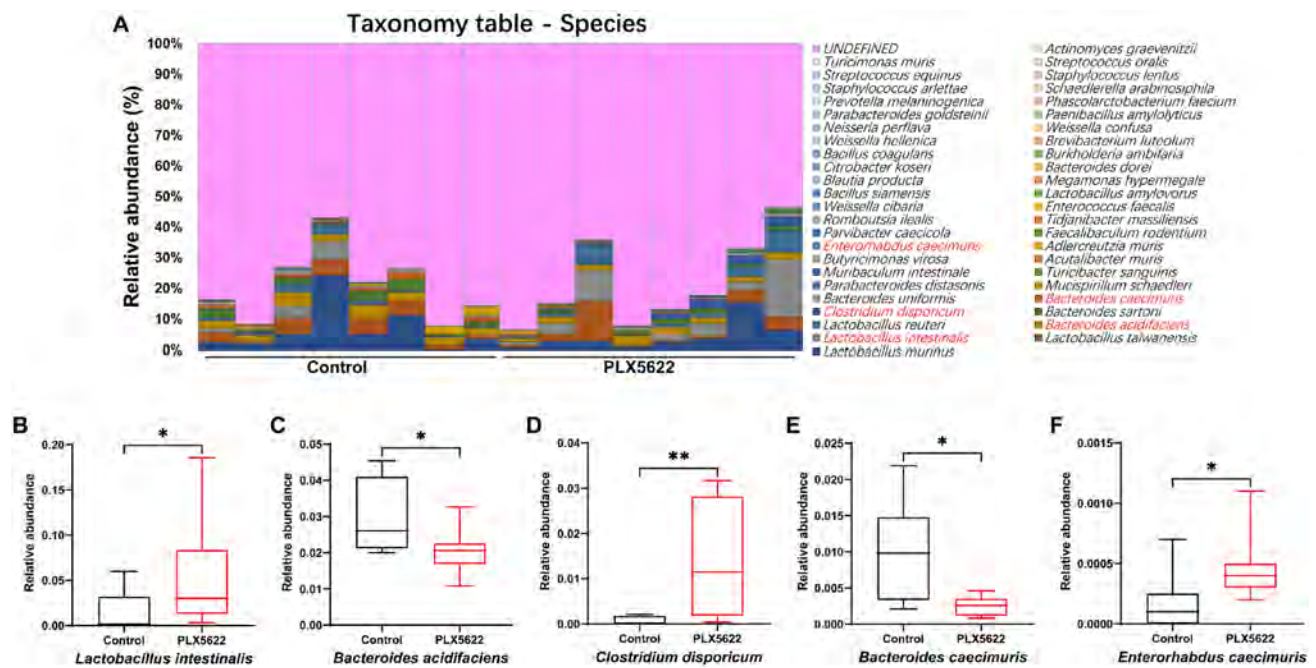


Fig. 5 Effects of PLX5622 on the composition of mice gut microbiota at the species level. **A** Gut bacteria composition at the species level in the two groups. **B** Relative abundance of species *Lactobacillus intestinalis* in two groups (Mann–Whitney *U* test, $U=13$, $P=0.0499$). **C** Relative abundance of species *Bacteroides acidifaciens* (Mann–Whitney *U* test, $U=12.50$, $P=0.0409$). **D** Relative abundance of species *Clostridium disporicum* in two groups (Mann–Whitney *U* test, $U=6$, $P=0.0042$). **E** Relative abundance

of species *Bacteroides caecimuris* in two groups (Mann–Whitney *U* test, $U=8.50$, $P=0.0115$). **F** Relative abundance of species *Enterorhabdus caecimuris* in two groups (Mann–Whitney *U* test, $U=9$, $P=0.0109$). For all box plots, the middle line in the box addresses the median, the box addresses the interquartile range, and the whisker addresses the most extreme and least values. The number of each group was 8. * $P < 0.05$; ** $P < 0.01$

Table 1 The concentration of short-chain fatty acids (SCFAs) in the feces

SCFAs (mg/g)	Control	PLX5622	Student's <i>t</i> test
Lactic acid	0.228 ± 0.026	0.424 ± 0.073	$t = 2.537$, $df = 14$, $P = 0.024$
Succinic acid	0.235 ± 0.031	0.387 ± 0.101*	$t = 1.533$, $df = 13$, $P = 0.149$
Propionic acid	0.370 ± 0.026	0.428 ± 0.043	$t = 1.142$, $df = 14$, $P = 0.273$
Acetic acid	1.629 ± 0.178	1.424 ± 0.161	$t = 0.853$, $df = 14$, $P = 0.408$
n-butyric acid	0.453 ± 0.057	0.494 ± 0.134	$t = 0.284$, $df = 14$, $P = 0.781$

The values represent as the mean ± SEM ($n=8$)

Bold was statistically significant

*One sample from PLX5622-treated group was under the limitation of detection for succinic acid

Discussion

In this study, we demonstrated the partial elimination of microglia in the brain after repeated oral administration of PLX5622 (65 mg/kg/day for consecutive 7 days), consistent with a previous report [13]. We found that repeated administration to PLX5622 in adult mice caused a significant change in the β -diversity of the gut microbiota. Furthermore, the LEfSe algorithm identified the species *Clostridium disporicum*, the genus *Clostridium*, the species *Barnesiella viscericola*, the genus *Barnesiella*, the

family *Barnesiellaceae*, the species *Gabonibacter massiliensis*, the genus *Gabonibacter*, and the species *Lactobacillus intestinalis* as specific microbial biomarkers in the PLX5622-treated group. Repeated administration of PLX5622 caused the alteration of the relative abundance of several microbes at distinct taxa such as genus and species. Moreover, we found higher levels of lactic acid in the feces' samples from the PLX5622-treated group, although levels of other SCFAs were not altered. We found significant negative correlations between lactic acid levels and the relative abundance of *Anaerostignum* (or *Bacteroides acidifaciens*) in feces from the two groups. Very

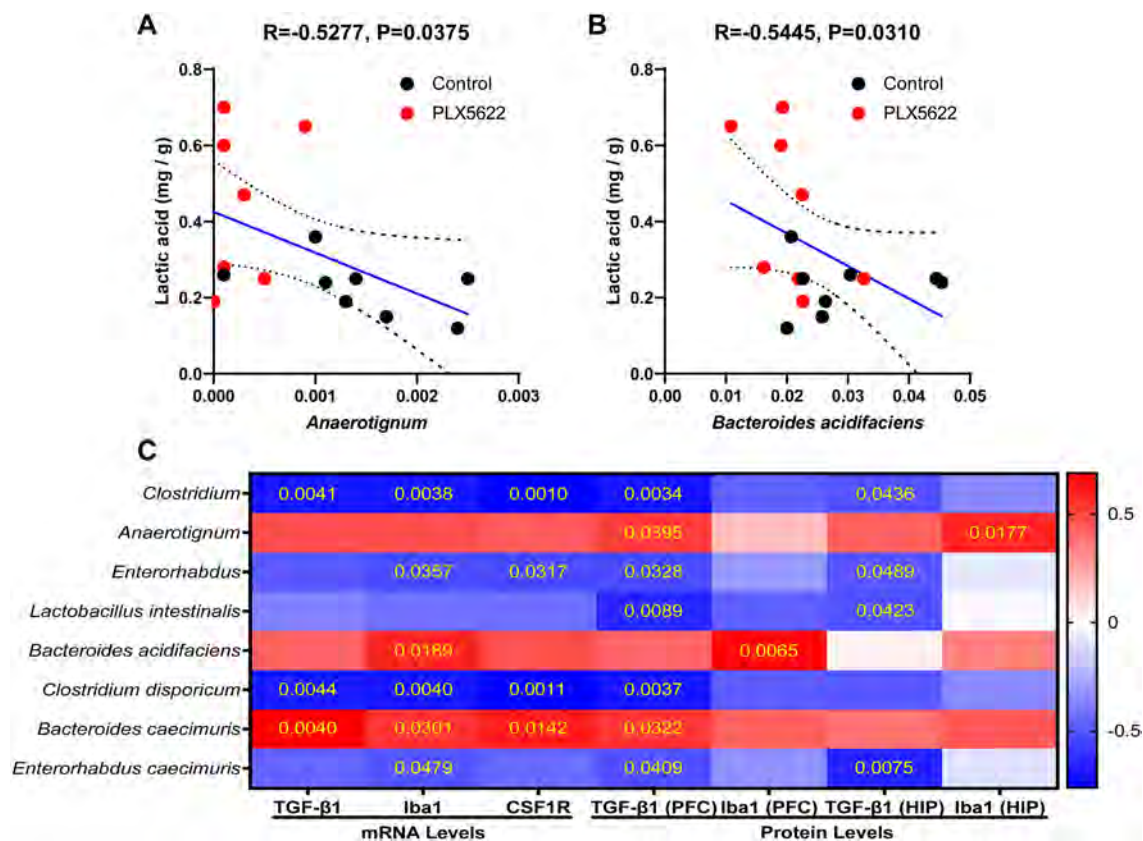


Fig. 6 Correlations between the relative abundance of bacteria and the results of SCFA or the expression of microglial markers. **A** A negative correlation was determined between the genus *Anaerotignum* abundance and lactic acid level of feces in two groups. **B** A negative correlation was found between the species *Bacteroides*

acidifaciens abundance and lactic acid level of feces in two groups. **C** The heat map displayed the correlation coefficient between bacterial abundance and the western blot and RT-PCR results in the PFC and hippocampus. The data are shown as means \pm SEM ($n=8$). * $P<0.05$; ** $P<0.01$; *** $P<0.001$. *HIP* hippocampus

interestingly, we found significant correlations between microglial markers in the brain and the relative abundance of the microbiome in the two groups, suggesting a possible connection between gut bacteria and microglia functions in the brain. Taken together, the present data suggest that repeated administration of PLX5622 could alter the gut microbiota constitution and SCFAs such as lactic acid in the host, despite the elimination of microglia in the brain by PLX5622 injection was partial.

In the current study, we determined alterations in the relative abundance of specific bacteria at the species level. We found a more abundant *Lactobacillus intestinalis*, *Clostridium disporicum*, and *Enterorhabdus caecimuris* in the PLX5622-treated group compared with the control group. Previously, we demonstrated that the species *Lactobacillus intestinalis* might be accountable for the depression-like phenotype in mice subjected to fecal microbiota transplantation (FMT) from mice with depression-like phenotypes [30]. It seems that a high abundance of *Lactobacillus intestinalis* in PLX5622-treated mice may lead to depression-like behaviors in adult mice, although further study is needed.

Clostridium disporicum is a Gram-positive, rod-shaped, and anaerobic bacterium [55]. A case report shows an orthopedic hardware infection with *Clostridium disporicum* [56]. *Enterorhabdus caecimuris* were isolated from a spontaneous colitis mouse model, suggesting a possible role of this bacteria in inflammatory bowel colitis [57]. Although the precise functions of *Clostridium disporicum* and *Enterorhabdus caecimuris* are currently unknown, it seems that PLX5622 could increase the relative abundance of the above microbes in the host. Further study is required to explore how alterations in the abundance of these three bacteria after repeated administration of PLX5622 can influence biochemical and behavioral functions in rodents.

Here, we found lower abundances of the species *Bacteroides acidifaciens* and *Bacteroides caecimuris* in PLX5622-treated mice than control mice. *Bacteroides acidifaciens* is known to be one of the dominating commensal microbes that facilitate IgA antibody creation in the digestive organ [58]. Interestingly, *Bacteroides acidifaciens* significantly increased in the excrement of *Atg7ΔCD11c* mice that had alleviated insulin resistance and reduced body weight and

fat mass, suggesting that *Bacteroides acidifaciens* may be a microbiome for regulating metabolic functions such as diabetes and obesity [59]. A recent study revealed that *Bacteroides acidifaciens* may assume a part in the gut–liver axis in rodents [60]. Furthermore, a recent study in healthy control subjects showed a significant decline in *Bacteroides acidifaciens* in non-responder to Vitamin D supplementation [61]. It is also reported that *Bacteroides caecimuris* were enriched in the gut of mice with retinal disease [62] and that higher exposure to 24-h O₃ was related to higher *Bacteroides caecimuris* in youthful grown-ups dwelling in Southern California [63]. Although the exact mechanism by which repeated administration of PLX5622 results in a reduction of relative abundance of these two *Bacteroides* microbes remains unclear, the abnormal composition of these microbes may likely affect biochemical and behavioral outcomes in PLX5622-treated mice.

In this study, we found higher levels of lactic acid in mice treated with PLX5622, although other SCFA did not alter. Interestingly, we found that lactic acid level was negatively correlated with the *Bacteroides acidifaciens* abundance. The detailed mechanisms underlying the negative correlation between lactic acid and *Bacteroides acidifaciens* remain unclear. Given the role of SCFAs in energy sources for the host, it seems that higher levels of lactic acid and lower levels of *Bacteroides acidifaciens* may contribute to abnormal metabolic system in the host. Further study is required to verify the role of *Bacteroides acidifaciens* in the metabolic system.

Importantly, we found significant correlations between several bacterial abundances in feces and microglial markers in the brain. Recent preclinical findings showed the crucial role of gut microbe in the regulations of microglial maturation and function [38–40]. A recent study showed that gut commensal-derived butyrate reversed obesity-induced social deficits and anxiety-like behaviors through regulation of microglial homeostasis [64]. Although the precise mechanisms underlying connections between the bacterial abundance and microglial markers in the brain are unknown, it is possible that the gut microbiota might play a vital role in the physiological functions of microglia in the CNS through the brain–gut–microbiota axis. We recently reported the critical role of the subdiaphragmatic vagus nerve on the brain–gut–microbiota axis in depression-like behaviors [30, 33, 44, 47]. Further study on the role of vagus nerve on the association between the gut microbiota and microglial functions in the CNS would be of interest.

In this study, we used the dosage (65 mg/kg/day for consecutive 7 days) of PLX5622, although the elimination of microglia by this dosage was partial, consistent with the previous report using PLX5622 (300 ppm in chow) [13]. It is noteworthy that elimination of microglia by PLX5622 could cause abnormal composition of gut microbe and SCFAs

alterations in the host's feces. Notably, dietary administration of PLX5622 (1200 ppm in chow) is reported to reduce approximately 90% of the brain's microglia [14, 65]. Given the important role of microglia in the brain–gut–microbiota axis in CNS functions, it is possible that repeated administration of CSF1R inhibitors such as PLX5622 could cause the marked elimination of microglia in the brain, as well as abnormal composition of gut microbe and SCFAs of the host, resulting in alterations in behavioral and physiological functions in the host. A recent study demonstrated that repeated treatment with PLX5622 (1200 ppm for 3 weeks) produced long-lasting alterations in the myeloid and lymphoid compartments of the bone marrow [66], indicating that CSF1R inhibition by PLX5622 is not microglia specific. Given the substantial and long-term effects on circulating and tissue macrophages by PLX5622, it is likely that these changes could affect the experimental data using PLX5622. Future detailed studies are necessary to ascertain the effects of PLX5622 on non-microglia cells.

As aforementioned in the introduction, clinical trials of small molecule CSF1R inhibitors in patients with cancer are underway [41, 42]. In this study, we found that CSF1R inhibitor could affect the composition of gut microbiota and SCFAs in the host. Therefore, abnormalities in the composition of gut microbiota and SCFAs after administration of CSF1R inhibitors should be taken into consideration for clinical outcomes in patients treated with CSF1R inhibitors.

In conclusion, the present study shows that repeated administration of PLX5622 caused abnormal composition of the gut microbiota in adult mice, and that the certain gut microbiota were correlated with expression of microglial markers in the brain. Given the role of the brain–gut–microbiota axis in host homeostasis, we propose that abnormalities in the composition of gut microbiota and SCFAs by CSF1R inhibitors such as PLX5622 should be considered to investigate biochemical and behavioral tests in animals treated with CSF1R inhibitors.

Acknowledgements This study was supported by Japan Society for the Promotion of Science (JSPS) (to K.H., 21H00184 and 21H02846).

Declarations

Conflict of interest The authors report no biomedical financial interests or potential conflicts of interest.

References

1. Glezer I, Simard AR, Rivest S (2007) Neuroprotective role of the innate immune system by microglia. *Neuroscience* 147:867–883. <https://doi.org/10.1016/j.neuroscience.2007.02.055>
2. Gogoleva VS, Drutskaya MS, Atratkhany KS (2019) The role of microglia in the homeostasis of the central nervous system and

- neuroinflammation. *Mol Biol (Mosk)* 53:790–798. <https://doi.org/10.1134/S0026898419050057>
3. Rosin JM, Vora SR, Kurrasch DM (2018) Depletion of embryonic microglia using the CSF1R inhibitor PLX5622 has adverse sex-specific effects on mice, including accelerated weight gain, hyperactivity and anxiolytic-like behaviour. *Brain Behav Immun* 73:682–697. <https://doi.org/10.1016/j.bbi.2018.07.023>
 4. Spangenberg EE, Green KN (2017) Inflammation in Alzheimer's disease: lessons learned from microglia-depletion models. *Brain Behav Immun* 61:1–11. <https://doi.org/10.1016/j.bbi.2016.07.003>
 5. Wolf SA, Boddeke HW, Kettenmann H (2017) Microglia in physiology and disease. *Annu Rev Physiol* 79:619–643. <https://doi.org/10.1146/annurev-physiol-022516-034406>
 6. Ginhoux F, Greter M, Leboeuf M, Nandi S, See P, Gokhan S, Mehler MF, Conway SJ, Ng LG, Stanley ER, Samokhvalov IM, Merad M (2010) Fate mapping analysis reveals that adult microglia derive from primitive macrophages. *Science* 330:841–845. <https://doi.org/10.1126/science.1194637>
 7. Mildner A, Schmidt H, Nitsche M, Merkler D, Hanisch UK, Mack M, Heikenwalder M, Brück W, Priller J, Prinz M (2007) Microglia in the adult brain arise from Ly-6ChiCCR2⁺ monocytes only under defined host conditions. *Nat Neurosci* 10:1544–1553. <https://doi.org/10.1038/nn2015>
 8. Chitu V, Gokhan Ş, Nandi S, Mehler MF, Stanley ER (2016) Emerging roles for CSF-1 receptor and its ligands in the nervous system. *Trends Neurosci* 39:378–393. <https://doi.org/10.1016/j.tins.2016.03.005>
 9. Li J, Chen K, Zhu L, Pollard JW (2006) Conditional deletion of the colony stimulating factor-1 receptor (c-fms proto-oncogene) in mice. *Genesis* 44:328–335. <https://doi.org/10.1002/dvg.20219>
 10. Patel S, Player MR (2009) Colony-stimulating factor-1 receptor inhibitors for the treatment of cancer and inflammatory disease. *Curr Top Med Chem* 9:599–610. <https://doi.org/10.2174/156802609789007327>
 11. Erbllich B, Zhu L, Etgen AM, Dobrenis K, Pollard JW (2011) Absence of colony stimulation factor-1 receptor results in loss of microglia, disrupted brain development and olfactory deficits. *PLoS ONE* 6:e26317. <https://doi.org/10.1371/journal.pone.0026317>
 12. Elmore MR, Najafi AR, Koike MA, Dagher NN, Spangenberg EE, Rice RA, Kitazawa M, Matusow B, Nguyen H, West BL, Green KN (2014) Colony-stimulating factor 1 receptor signaling is necessary for microglia viability, unmasking a microglia progenitor cell in the adult brain. *Neuron* 82:380–397. <https://doi.org/10.1016/j.neuron.2014.02.040>
 13. Lee S, Shi XQ, Fan A, West B, Zhang J (2018) Targeting macrophage and microglia activation with colony stimulating factor 1 receptor inhibitor is an effective strategy to treat injury-triggered neuropathic pain. *Mol Pain* 14:1744806918764979. <https://doi.org/10.1177/1744806918764979>
 14. Spangenberg E, Severson PL, Hohsfield LA, Crapser J, Zhang J, Burton EA, Zhang Y, Spevak W, Lin J, Phan NY, Habets G, Rymar A, Tsang G, Walters J, Nespi M, Singh P, Broome S, Ibrahim P, Zhang C, Bollag G, West BL, Green KN (2019) Sustained microglial depletion with CSF1R inhibitor impairs parenchymal plaque development in an Alzheimer's disease model. *Nat Commun* 10:3758. <https://doi.org/10.1038/s41467-019-11674-z>
 15. Cavnar MJ, Zeng S, Kim TS, Sorenson EC, Ocuin LM, Balachandran VP, Seifert AM, Greer JB, Popow R, Crawley MH, Cohen NA, Green BL, Rossi F, Besmer P, Antonescu CR, DeMatteo RP (2013) KIT oncogene inhibition drives intratumoral macrophage M2 polarization. *J Exp Med* 210:2873–2886. <https://doi.org/10.1084/jem.20130875>
 16. Coniglio SJ, Eugenin E, Dobrenis K, Stanley ER, West BL, Symons MH, Segall JE (2012) Microglial stimulation of glioblastoma invasion involves epidermal growth factor receptor (EGFR) and colony stimulating factor 1 receptor (CSF-1R) signaling. *Mol Med* 18:519–527. <https://doi.org/10.2119/molmed.2011.00217>
 17. Dagher NN, Najafi AR, Kayala KM, Elmore MR, White TE, Medeiros R, West BL, Green KN (2015) Colony-stimulating factor 1 receptor inhibition prevents microglial plaque association and improves cognition in 3xTg-AD mice. *J Neuroinflammation* 12:139. <https://doi.org/10.1186/s12974-015-0366-9>
 18. Green KN, Crapser JD, Hohsfield LA (2020) To kill a microglia: a case for CSF1R inhibitors. *Trends Immunol* 41:771–784. <https://doi.org/10.1016/j.it.2020.07.001>
 19. Janova H, Arinrad S, Balmuth E, Mitjans M, Hertel J, Habes M, Bittner RA, Pan H, Goebbels S, Begemann M, Gerwig UC, Langner S, Werner HB, Kittel-Schneider S, Homuth G, Davatzikos C, Völzke H, West BL, Reif A, Grabe HJ, Boretius S, Ehrenreich H, Nave KA (2018) Microglia ablation alleviates myelin-associated catatonic signs in mice. *J Clin Invest* 128:734–745. <https://doi.org/10.1172/JCI97032>
 20. Walzl I, Käufer C, Gerhauser I, Chhatbar C, Ghita L, Kalinke U, Löscher W (2018) Microglia have a protective role in viral encephalitis-induced seizure development and hippocampal damage. *Brain Behav Immun* 74:186–204. <https://doi.org/10.1016/j.bbi.2018.09.006>
 21. Zhang K, Yang C, Chang L, Sakamoto A, Suzuki T, Fujita Y, Qu Y, Wang S, Pu Y, Tan Y, Wang X, Ishima T, Shirayama Y, Hatano M, Tanaka KF, Hashimoto K (2020) Essential role of microglial transforming growth factor-β1 in antidepressant actions of (R)-ketamine and the novel antidepressant TGF-β1. *Transl Psychiatry* 10:32. <https://doi.org/10.1038/s41398-020-0733-x>
 22. Cryan JF, O'Riordan KJ, Cowan CSM, Sandhu KV, Bastiaanssen TFS, Boehme M, Codagnone MG, Cussotto S, Fulling C, Golubeva AV, Guzzetta KE, Jaggard M, Long-Smith CM, Lyte JM, Martin JA, Molinero-Perez A, Moloney G, Morelli E, Morillas E, O'Connor R, Cruz-Pereira JS, Peterson VL, Rea K, Ritz NL, Sherwin E, Spichak S, Teichman EM, van de Wouw M, Ventura-Silva AP, Wallace-Fitzsimons SE, Hyland N, Clarke G, Dinan TG (2019) The microbiota-gut-brain axis. *Physiol Rev* 99:1877–2013. <https://doi.org/10.1152/physrev.00018.2018>
 23. Cussotto S, Sandhu KV, Dinan TG, Cryan JF (2018) The neuroendocrinology of the microbiota-gut-brain axis: a behavioural perspective. *Front Neuroendocrinol* 51:80–101. <https://doi.org/10.1016/j.yfrne.2018.04.002>
 24. Dinan TG, Cryan JF (2017) Brain-gut-microbiota axis and mental health. *Psychosom Med* 79:920–926. <https://doi.org/10.1097/PSY.0000000000000519>
 25. Fung TC, Olson CA, Hsiao EY (2017) Interactions between the microbiota, immune and nervous systems in health and disease. *Nat Neurosci* 20:145–155. <https://doi.org/10.1038/nn.4476>
 26. Long-Smith C, O'Riordan KJ, Clarke G, Stanton C, Dinan TG, Cryan JF (2020) Microbiota-gut-brain axis: new therapeutic opportunities. *Annu Rev Pharmacol Toxicol* 60:477–502. <https://doi.org/10.1146/annurev-pharmtox-010919-023628>
 27. Wei Y, Chang L, Hashimoto K (2021) Molecular mechanisms underlying the antidepressant actions of arketamine: beyond the NMDA receptor. *Mol Psychiatry*. <https://doi.org/10.1038/s41380-021-01121-1>
 28. Jianguo L, Xueyang J, Cui W, Changxin W, Xuemei Q (2019) Altered gut metabolome contributes to depression-like behaviors in rats exposed to chronic unpredictable mild stress. *Transl Psychiatry* 9:40. <https://doi.org/10.1038/s41398-019-0391-z>
 29. Szyzkowicz JK, Wong A, Anisman H, Merali Z, Audet MC (2017) Implications of the gut microbiota in vulnerability to the social avoidance effects of chronic social defeat in male mice. *Brain Behav Immun* 66:45–55. <https://doi.org/10.1016/j.bbi.2017.06.009>
 30. Wang S, Ishima T, Zhang J, Qu Y, Chang L, Pu Y, Fujita Y, Tan Y, Wang X, Hashimoto K (2020) Ingestion of *Lactobacillus*

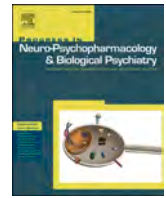
- intestinalis* and *Lactobacillus reuteri* causes depression- and anhedonia-like phenotypes in antibiotic-treated mice via the vagus nerve. *J Neuroinflammation* 17:241. <https://doi.org/10.1186/s12974-020-01916-z>
31. Yang C, Fang X, Zhan G, Huang N, Li S, Bi J, Jiang R, Yang L, Miao L, Zhu B, Luo A, Hashimoto K (2019) Key role of gut microbiota in anhedonia-like phenotype in rodents with neuropathic pain. *Transl Psychiatry* 9:57. <https://doi.org/10.1038/s41398-019-0379-8>
 32. Yang C, Fujita Y, Ren Q, Ma M, Dong C, Hashimoto K (2017) *Bifidobacterium* in the gut microbiota confer resilience to chronic social defeat stress in mice. *Sci Rep* 7:45942. <https://doi.org/10.1038/srep45942>
 33. Zhang J, Ma L, Chang L, Pu Y, Qu Y, Hashimoto K (2020) A key role of the subdiaphragmatic vagus nerve in the depression-like phenotype and abnormal composition of gut microbiota in mice after lipopolysaccharide administration. *Transl Psychiatry* 10:186. <https://doi.org/10.1038/s41398-020-00878-3>
 34. Zhang K, Fujita Y, Chang L, Qu Y, Pu Y, Wang S, Shirayama Y, Hashimoto K (2019) Abnormal composition of gut microbiota is associated with resilience versus susceptibility to inescapable electric stress. *Transl Psychiatry* 9:231. <https://doi.org/10.1038/s41398-019-0571-x>
 35. Dalile B, Van Oudenhove L, Vervliet B, Verbeke K (2019) The role of short-chain fatty acids in microbiota-gut-brain communication. *Nat Rev Gastroenterol Hepatol* 16:461–478. <https://doi.org/10.1038/s41575-019-0157-3>
 36. den Besten G, van Eunen K, Groen AK, Venema K, Reijngoud DJ, Bakker BM (2013) The role of short-chain fatty acids in the interplay between diet, gut microbiota, and host energy metabolism. *J Lipid Res* 54:2325–2340. <https://doi.org/10.1194/jlr.R036012>
 37. Morrison DJ, Preston T (2016) Formation of short chain fatty acids by the gut microbiota and their impact on human metabolism. *Gut Microbes* 7:189–200. <https://doi.org/10.1080/19490976.2015.1134082>
 38. Abdel-Haq R, Schlachetzki J, Glass CK, Mazmanian SK (2019) Microbiome-microglia connections via the gut–brain axis. *J Exp Med* 216:41–59. <https://doi.org/10.1084/jem.20180794>
 39. Ma Q, Xing C, Long W, Wang HY, Liu Q, Wang RF (2019) Impact of microbiota on central nervous system and neurological diseases: the gut–brain axis. *J Neuroinflammation* 16:53. <https://doi.org/10.1186/s12974-019-1434-3>
 40. Wang Y, Wang Z, Wang Y, Li F, Jia J, Song X, Qin S, Wang R, Jin F, Kitazato K, Wang Y (2018) The gut–microglia connection: implications for central nervous system diseases. *Front Immunol* 9:2325. <https://doi.org/10.3389/fimmu.2018.02325>
 41. Cannarile MA, Weisser M, Jacob W, Jegg AM, Ries CH, Rüttinger D (2017) Colony-stimulating factor 1 receptor (CSF1R) inhibitors in cancer therapy. *J Immunother Cancer* 5:53. <https://doi.org/10.1186/s40425-017-0257-y>
 42. Denny WA, Flanagan JU (2021) Small-molecule CSF1R kinase inhibitors; review of patents 2015-present. *Expert Opin Ther Pat* 31:107–117. <https://doi.org/10.1080/13543776.2021.1839414>
 43. Wang S, Qu Y, Chang L, Pu Y, Zhang K, Hashimoto K (2020) Antibiotic-induced microbiome depletion is associated with resilience in mice after chronic social defeat stress. *J Affect Disord* 260:448–457. <https://doi.org/10.1016/j.jad.2019.09.064>
 44. Pu Y, Tan Y, Qu Y, Chang L, Wang S, Wei Y, Wang X, Hashimoto K (2021) A role of the subdiaphragmatic vagus nerve in depression-like phenotypes in mice after fecal microbiota transplantation from *Chrna7* knock-out mice with depression-like phenotypes. *Brain Behav Immun* 94:318–326. <https://doi.org/10.1016/j.bbi.2020.12.032>
 45. Qu Y, Zhang K, Pu Y, Chang L, Wang S, Tan Y, Wang X, Zhang J, Ohnishi T, Yoshikawa T, Hashimoto K (2020) Betaine supplementation is associated with the resilience in mice after chronic social defeat stress: a role of brain–gut–microbiota axis. *J Affect Disord* 272:66–76. <https://doi.org/10.1016/j.jad.2020.03.095>
 46. Shinno-Hashimoto H, Hashimoto Y, Wei Y, Chang L, Fujita Y, Ishima T, Matsue H, Hashimoto K (2021) Abnormal composition of microbiota in the gut and skin of imiquimod-treated mice. *Sci Rep* 11:11265. <https://doi.org/10.1038/s41598-021-90480-4>
 47. Wang S, Ishima T, Qu Y, Shan J, Chang L, Wei Y, Zhang J, Pu Y, Fujita Y, Tan Y, Wang X, Ma L, Wan X, Hammock BD, Hashimoto K (2021) Ingestion of *Faecalibaculum rodentium* causes depression-like phenotypes in resilient *Ephx2* knock-out mice: a role of brain-gut-microbiota axis via the subdiaphragmatic vagus nerve. *J Affect Disord* 292:565–573. <https://doi.org/10.1016/j.jad.2021.06.006>
 48. Pu Y, Yang J, Chang L, Qu Y, Wang S, Zhang K, Xiong Z, Zhang J, Tan Y, Wang X, Fujita Y, Ishima T, Wang D, Hwang SH, Hammock BD, Hashimoto K (2020) Maternal glyphosate exposure causes autism-like behaviors in offspring through increased expression of soluble epoxide hydrolase. *Proc Natl Acad Sci U S A* 117:11753–11759. <https://doi.org/10.1073/pnas.1922287117>
 49. Kim SW, Suda W, Kim S, Oshima K, Fukuda S, Ohno H, Morita H, Hattori M (2013) Robustness of gut microbiota of healthy adults in response to probiotic intervention revealed by high-throughput pyrosequencing. *DNA Res* 20:241–253. <https://doi.org/10.1093/dnares/dst006>
 50. Shibagaki N, Suda W, Clavaud C, Bastien P, Takayasu I, Iioka E, Kurokawa R, Yamashita N, Hattori Y, Shindo C, Breton L, Hattori M (2017) Aging-related changes in the diversity of women's skin microbiomes associated with oral bacteria. *Sci Rep* 7:10567. <https://doi.org/10.1038/s41598-017-10834-9>
 51. Segata N, Izard J, Waldron L, Gevers D, Miropolsky L, Garrett WS, Huttenhower C (2011) Metagenomic biomarker discovery and explanation. *Genome Biol* 12:R60. <https://doi.org/10.1186/gb-2011-12-6-r60>
 52. Priller J, Prinz M (2019) Targeting microglia in brain disorders. *Science* 365:32–33. <https://doi.org/10.1126/science.aau9100>
 53. Spittau B, Dokalis N, Prinz M (2020) The role of TGF- β signaling in microglia maturation and activation. *Trends Immunol* 41:836–848. <https://doi.org/10.1016/j.it.2020.07.003>
 54. Zöller T, Schneider A, Kleimeyer C, Masuda T, Potru PS, Pfeifer D, Blank T, Prinz M, Spittau B (2018) Silencing of TGF β signaling in microglia results in impaired homeostasis. *Nat Commun* 9:4011. <https://doi.org/10.1038/s41467-018-06224-y>
 55. Horn N (1987) *Clostridium disporicum* sp. nov., a Saccharolytic species able to form two spores per cell, isolated from a rat cecum. *Int J Syst Bacteriol* 37:398–401. <https://doi.org/10.1099/00207713-37-4-398>
 56. McBride JA, Sterkel AK, Rehrauer WM, Smith JA (2017) First described case of prosthetic joint infection with *Clostridium disporicum*. *Anaerobe* 48:56–58. <https://doi.org/10.1016/j.anaerobe.2017.06.022>
 57. Clavel T, Duck W, Charrier C, Wenning M, Elson C, Haller D (2010) *Enterorhabdus caecimuris* sp. nov., a member of the family *Coriobacteriaceae* isolated from a mouse model of spontaneous colitis, and emended description of the genus *Enterorhabdus*. *Int J Syst Evol Microbiol* 60:1527–1531. <https://doi.org/10.1099/ijs.0.015016-0>
 58. Yanagibashi T, Hosono A, Oyama A, Tsuda M, Suzuki A, Hachimura S, Takahashi Y, Momose Y, Itoh K, Hirayama K, Takahashi K, Kaminogawa S (2013) IgA production in the large intestine is modulated by a different mechanism than in the small intestine: *Bacteroides acidifaciens* promotes IgA production in the large intestine by inducing germinal center formation and increasing the number of IgA⁺ B cells. *Immunobiology* 218:645–651. <https://doi.org/10.1016/j.imbio.2012.07.033>
 59. Yang JY, Lee YS, Kim Y, Lee SH, Ryu S, Fukuda S, Hase K, Yang CS, Lim HS, Kim MS, Kim HM, Ahn SH, Kwon BE, Ko

- HJ, Kweon MN (2017) Gut commensal *Bacteroides acidifaciens* prevents obesity and improves insulin sensitivity in mice. *Mucosal Immunol* 10:104–116. <https://doi.org/10.1038/mi.2016.42>
60. Wu L, Yan Q, Chen F, Cao C, Wang S (2021) *Bupleuri radix* extract ameliorates impaired lipid metabolism in high-fat diet-induced obese mice via gut microbiota-mediated regulation of FGF21 signaling pathway. *Biomed Pharmacother* 135:111187. <https://doi.org/10.1016/j.biopha.2020.111187>
61. Singh P, Rawat A, Alwakeel M, Sharif E, Al Khodor S (2020) The potential role of vitamin D supplementation as a gut microbiota modifier in healthy individuals. *Sci Rep* 10:21641. <https://doi.org/10.1038/s41598-020-77806-4>
62. Kutsyr O, Maestre-Carballa L, Lluesma-Gomez M, Martinez-Garcia M, Cuenca N, Lax P (2021) Retinitis pigmentosa is associated with shifts in the gut microbiome. *Sci Rep* 11:6692. <https://doi.org/10.1038/s41598-021-86052-1>
63. Fouladi F, Bailey MJ, Patterson WB, Sioda M, Blakley IC, Fodor AA, Jones RB, Chen Z, Kim JS, Lurmann F, Martino C, Knight R, Gilliland FD, Alderete TL (2020) Air pollution exposure is associated with the gut microbiome as revealed by shotgun metagenomic sequencing. *Environ Int* 138:105604. <https://doi.org/10.1016/j.envint.2020.105604>
64. Duan C, Huang L, Zhang C, Zhang L, Xia X, Zhong Z, Wang B, Wang Y, Man Hoi MP, Ding W, Yang Y (2021) Gut commensal-derived butyrate reverses obesity-induced social deficits and anxiety-like behaviors via regulation of microglial homeostasis. *Eur J Pharmacol* 908:174338. <https://doi.org/10.1016/j.ejphar.2021.174338>
65. Clayton K, Delpuch JC, Herron S, Iwahara N, Ericsson M, Saito T, Saido TC, Ikezu S, Ikezu T (2021) Plaque associated microglia hyper-secrete extracellular vesicles and accelerate tau propagation in a humanized APP mouse model. *Mol Neurodegener* 16:18. <https://doi.org/10.1186/s13024-021-00440-9>
66. Lei F, Cui N, Zhou C, Chodosh J, Vavvas DG, Paschalis EI (2020) CSF1R inhibition by a small-molecule inhibitor is not microglia specific; affecting hematopoiesis and the function of macrophages. *Proc Natl Acad Sci U S A* 117:23336–23338. <https://doi.org/10.1073/pnas.1922788117>



Contents lists available at ScienceDirect

Progress in Neuropsychopharmacology & Biological Psychiatry

journal homepage: www.elsevier.com/locate/pnp

A role of gut–microbiota–brain axis via subdiaphragmatic vagus nerve in depression-like phenotypes in *Chrna7* knock-out mice

Yong Yang^a, Akifumi Eguchi^b, Xiayun Wan^a, Lijia Chang^a, Xingming Wang^a, Youge Qu^a, Chisato Mori^{b,c}, Kenji Hashimoto^{a,*}

^a Division of Clinical Neuroscience, Chiba University Center for Forensic Mental Health, Chiba 260-8670, Japan

^b Department of Sustainable Health Science, Chiba University Center for Preventive Medical Sciences, Chiba 263-8522, Japan

^c Department of Bioenvironmental Medicine, Graduate School of Medicine, Chiba University, Chiba 260-8670, Japan

ARTICLE INFO

Keywords:

$\alpha 7$ nAChR
Brain-gut axis
Gut microbiota
Metabolites
Vagus nerve

ABSTRACT

The $\alpha 7$ subtype of the nicotinic acetylcholine receptor ($\alpha 7$ nAChR; coded by *Chrna7*) is known to regulate the cholinergic ascending anti-inflammatory pathway. We previously reported that *Chrna7* knock-out (KO) mice show depression-like behaviors through abnormal composition of gut microbiota and systemic inflammation. Given the role of subdiaphragmatic vagus nerve in gut–microbiota–brain axis, we investigated whether subdiaphragmatic vagotomy (SDV) could affect depression-like behaviors, abnormal composition of gut microbiota, and microbes-derived metabolites in *Chrna7* KO mice. SDV blocked depression-like behaviors and reduced expression of synaptic proteins in the medial prefrontal cortex (mPFC) of *Chrna7* KO mice. LEfSe (linear discriminant analysis effect size) analysis revealed that the species *Lactobacillus* sp. *BL302*, the species *Lactobacillus hominis*, and the species *Lactobacillus reuteri*, were identified as potential microbial markers in the KO + SDV group. There were several genus and species altered among the three groups [wild-type (WT) + sham group, KO + sham group, KO + SDV group]. Furthermore, there were several plasma metabolites altered among the three groups. Moreover, there were correlations between relative abundance of several microbiome and behavioral data (or synaptic proteins). Network analysis showed correlations between relative abundance of several microbiome and plasma metabolites (or behavioral data). These data suggest that *Chrna7* KO mice produce depression-like behaviors and reduced expression of synaptic proteins in the mPFC through gut–microbiota–brain axis via subdiaphragmatic vagus nerve.

1. Introduction

Depression is the most prevalent mental disorder with an estimated 5.0% of adults and 5.7% of elderly adults (>60 years old) worldwide. Furthermore, depression is a leading cause of disability worldwide, and it is a major contributor to the overall global burden of disease (WHO, 2021). Although the precise neurobiology underlying depression remains unclear, inflammation is known to play an important role in depression (Brydges et al., 2022; Haroon et al., 2012; Hashimoto, 2009; Hashimoto, 2015; Liu et al., 2020; Lucido et al., 2021; Mac Giollabhui et al., 2021; Miller and Raison, 2016; Shan and Hashimoto, 2022; Toenders et al., 2022; Zhang et al., 2016a).

Nicotinic acetylcholine receptor (nAChR) is a kind of ionotropic

ligand-gated ion channels widely distributed in various cells of the central nervous system (CNS), peripheral nervous system (PNS), enteric nervous system, neuromuscular junction and immune system, which consist of pentameric combinations of α and/or β subunits (Dani, 2015; Dani and Bertrand, 2007). Among its many subtypes, $\alpha 7$ nAChRs, encoded by the *Chrna7* gene, mediates systemic inflammatory homeostasis between the CNS and the immune system through a vagus nerve mediated way known as the “cholinergic anti-inflammatory pathway” (Andersson and Tracey, 2012; Lei and Duan, 2021; Martelli et al., 2014; Olofsson et al., 2012; Piovesana et al., 2021; Ulloa, 2005; Wang et al., 2003; Wu et al., 2021). We previously reported that *Chrna7* KO mice show depression-like phenotypes through systemic inflammation (Pu et al., 2021b; Zhang et al., 2016b).

Abbreviations: *Chrna7*, $\alpha 7$ subtype of the nicotinic acetylcholine receptor; CNS, central nervous system; FMT, fecal microbiota transplantation; FST, forced swimming test; LPS, lipopolysaccharide; mPFC, medial prefrontal cortex; SDV, subdiaphragmatic vagotomy; SPT, sucrose preference test.

* Corresponding author.

E-mail address: hashimoto@faculty.chiba-u.jp (K. Hashimoto).

<https://doi.org/10.1016/j.pnpbp.2022.110652>

Received 13 June 2022; Received in revised form 26 September 2022; Accepted 27 September 2022

Available online 30 September 2022

0278-5846/© 2022 Elsevier Inc. All rights reserved.

Increasing evidence suggests altered composition of intestinal microbiota in rodents with depressive-like phenotypes (Chang et al., 2022; Hashimoto, 2020; Huang et al., 2019; Park et al., 2013; Qu et al., 2017; Wang et al., 2020a, 2020b; Wong et al., 2016; Yang et al., 2017, 2019; Zhang et al., 2017; Zhang et al., 2019), and patients with depression (Caso et al., 2021; Jiang et al., 2015; Li et al., 2022; Nikolova et al., 2021; Sanada et al., 2020; Wei et al., 2022a, 2022b; Wong et al., 2016; Zheng et al., 2016). Fecal microbiota transplantation (FMT) of certain intestinal microbiota from depressed patients or rodents with depressive-like phenotypes causes depression-like phenotypes in mice (Kelly et al., 2016; Pu et al., 2021b; Pu et al., 2022; Wang et al., 2020a; Yang et al., 2019; Zheng et al., 2016). Furthermore, microbial-derived metabolites, including short-chain fatty acids (SCFAs), tryptophan-derived metabolites, bile acids and D-amino acids, could regulate a number of physiological functions such as behaviors (Bartoli et al., 2021; Chang et al., 2022; Hashimoto, 2022; Li et al., 2022; Pu et al., 2021a; Tran and Mohajeri, 2021; Wan et al., 2022a, 2022b). Vagus nerve is known to play a key role in the bi-directional communication between the gut microbiota and the brain (Bonaz et al., 2018; Cawthon and de La Serre, 2018; Chang et al., 2022; Cryan et al., 2019; Forsythe et al., 2014). We reported that subdiaphragmatic vagotomy (SDV) blocked the onset of depression-like behavior and altered composition of intestinal microbiota in mice after lipopolysaccharide (LPS) administration (Zhang et al., 2020). Subsequently, we reported that SDV blocked the onset of depression-like behaviors in mice after FMT from mice with depression-like behaviors (Pu et al., 2021a; Wang et al., 2020a; Wang et al., 2021). Collectively, it is likely that subdiaphragmatic vagus nerve plays a key role in depression-like behaviors (Chang et al., 2022; Wei et al., 2022b). However, there are no reports showing the role of subdiaphragmatic vagus nerve in depression-like phenotypes in *Chrna7* KO mice.

The aim of present study was to evaluate whether SDV could affect depression-like phenotypes and reduced expression of synaptic proteins in the medial prefrontal cortex (mPFC) of *Chrna7* KO mice. Furthermore, we performed 16S rRNA analysis for gut microbiota composition and untargeted metabolomics analysis of plasma samples.

2. Materials and methods

2.1. Animals

Mice deficient in $\alpha 7$ nAChR (coded by *Chrna7* gene, C57BL/6 background) were purchased from the Jackson Laboratory (Bar Harbor, ME, USA) (Zhang et al., 2016b). Adult male wild-type (WT) and *Chrna7* KO mice used in this study were littermates. All the experimental mice were aged 9 weeks, body weight 21–27 g. All the experimental mice were acclimatized to standard laboratory conditions (3 or 4/ cage), maintain alternating cycles of 12 h of light and 12 h of darkness (lights on from 7:00–19:00), and under constant room temperature of 23 ± 1 °C and controlled humidity of $55 \pm 5\%$. Animals were given free admittance to chow and water. The experimental protocol of present study was approved by the Chiba University Institutional Animal Care and Use Committee (Permission number 3–399). The experimental mice were all firstly deeply anesthetized with inhaled isoflurane and then rapidly sacrificed by cervical dislocation. All efforts were made to minimize animals suffering.

2.2. Bilateral subdiaphragmatic vagotomy (SDV)

Bilateral SDV or sham surgery was performed under continuous inhalation anesthesia with 4–5% isoflurane by using an inhalation small animal anesthesia apparatus (KN-1071 NARCOBIT-E; Natsume Seisakusho, Tokyo, Japan), as previously method (Pu et al., 2021a; Wang et al., 2020a, 2021; Zhang et al., 2020) with a slight modification. Briefly, each mouse was placed in the right-side decubitus position, the skin is disinfected with iodophor disinfectant and sterile tissue is laid.

Starting from the midline alba of the abdomen, about 1 cm incision parallel to the costal arch was made at 0.5 cm below the left costal arch. The incision was gently opened with Mini incision spreader to expose the underlying liver tissue. The liver tissue was carefully pushed upward using a small sterilized cotton ball moistened with physiological saline solution and with the aid of an animal surgical microscope (Leica, Heidelberg, Germany), the fascia between the caudate lobe and the left lobe of the liver was sharply cut to fully expose the esophagus and the surrounding surgical field of view. In this case, the dorsal and ventral branches running along the esophagus under the diaphragm of the vagus nerve can be clearly identified and can be severed after careful separation. After that, no bleeding was detected, and no additional injury of esophagus, liver and other organs was checked, the liver tissue was returned to its original normal position, and 0.5 ml physiological saline solution was injected into the abdominal cavity. Then 5–0 surgical silk sutures were used to suture the abdominal incision muscle and skin layers layer by layer, ensuring aseptic operation throughout the operation. The successful implementation of SDV was confirmed by a significant increase in stomach volume on the 14th postoperative day due to loss of vagus nerve innervation.

During the sham operation, the abdominal wall incision of the same size was made in the same way at the same site. After the dorsal and ventral branches of the subdiaphragmatic vagus nerve were also softly exposed but not cut off, no bleeding and no additional damage of other organs was checked. After the abdominal organs were restored to their normal positions, 0.5 ml normal saline was also injected into the abdominal cavity, then the incision was sutured layer by layer using the same method.

2.3. Behavioral tests

Male WT and *Chrna7* KO mice born in the same litter were subjected to behavioral tests, as previously method (Pu et al., 2021a; Wang et al., 2020a, 2021). Behavioral tests including locomotion test (LMT), forced swimming test (FST), and 1% sucrose preference test (1% SPT) (Fig. 1A).

In order to monitor the locomotor activity of the mice, we adopted an automatic animal movement analysis system (SCANET MV-40; MEL-QUEST Co., Ltd., Toyama, Japan). The cumulative ambulatory activity counts were automatic document continuously over a total stage of 60 min (10 min \times 6 times) after the mice were placed into the experimental cube boxes [33 cm (height) \times 56 cm (width) \times 56 cm (length)]. To avoid experimental interference, the cube boxes were cleaned up during the test interval.

A mouse automated forced-swim apparatus (SCANET MV-40; MEL-QUEST Co., Ltd., Toyama, Japan) was used to perform FST. Mice were placed into an inescapable transparent tank [31 cm (height) \times 23 cm (diameter)] that is filled with tap water at a temperature of 23 ± 1 °C and a depth of 15 cm. Then their escape related mobility behavior was measured immediately. The immobility times were automatic document and calculated using the analytical software of the apparatus over a total stage of 6 min (1 min \times 6 times).

For 1% SPT, which was carried out in the separate animal's home cage. Each mouse was presented with two dual bearing sipper bottles, one bottle contained tap water, and the second contained a 1% sucrose solution. After 24 h of every mouse exposed to the respective two bottles containing different solution, replaced the positions of two bottles for each other to lower any confound produced by a side bias. After another 24 h, all food and bottles were deprived lasting 4 h, then performed 1 h exposure to two identical bottles (containing tap water and 1% sucrose solution), which were weighed before and after the exposure period. The 1% sucrose preference was calculated as a percentage of 1% sucrose solution intake weight over the total liquid intake weight.

2.4. Western blotting analysis of synaptic proteins (PSD-95 and GluA1)

Western blotting analysis was performed as previously method (Pu

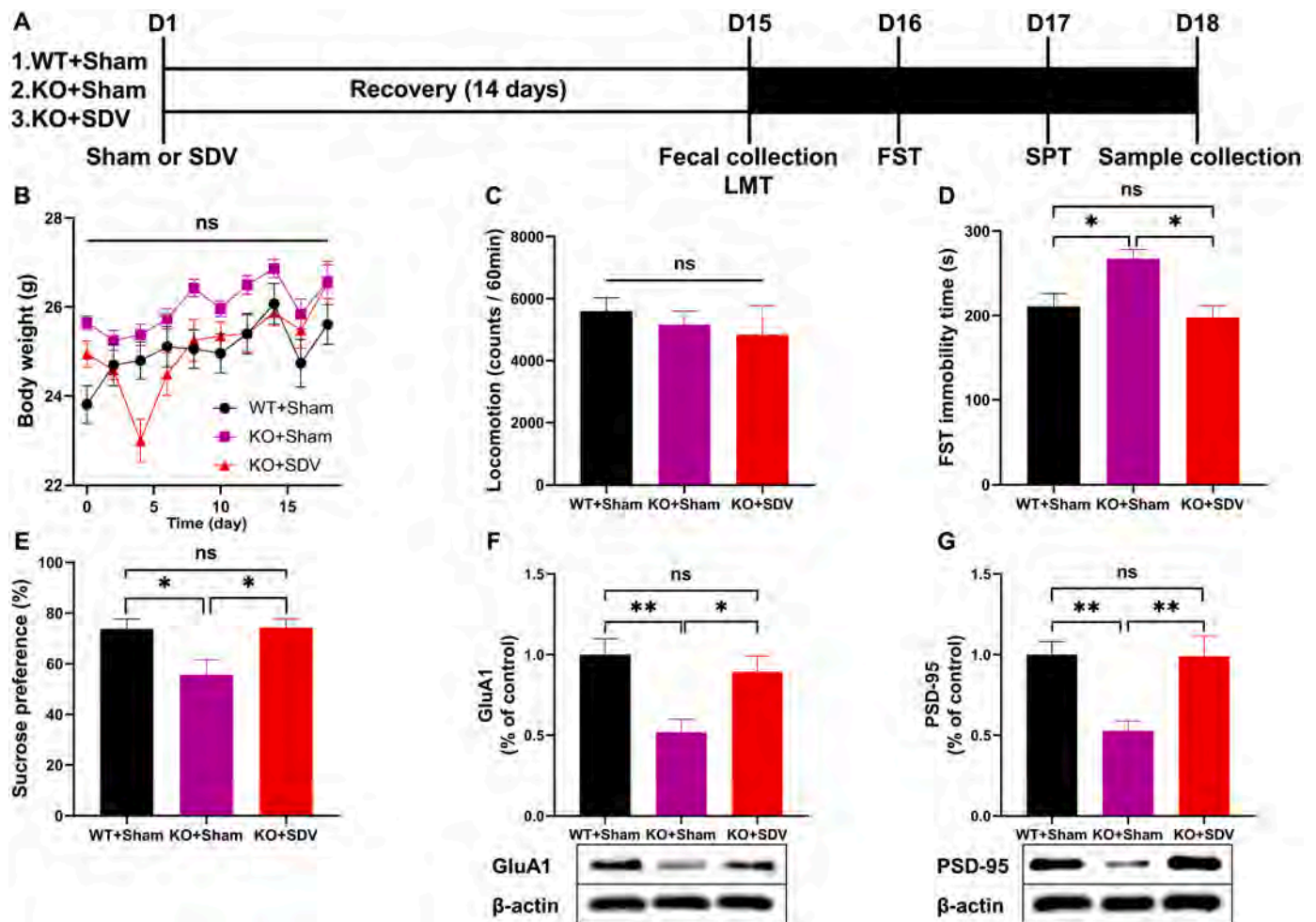


Fig. 1. Effects of bilateral SDV on depression-like phenotypes and reduced expression of synaptic proteins in *Chrna7* KO mice.

(A): Experimental schedule. On day 1, bilateral SDV or sham was performed, and they were recovered 14 days. On day 15, fresh feces samples were collected, and subsequently LMT was performed. FST and SPT were performed on day 16 and day 17, respectively. On day 18, medial prefrontal cortex (mPFC) and plasma samples were collected. (B): Body weight (repeated measure ANOVA, $F_{(2, 21)} = 2.424$, $P = 0.1129$). (C): LMT (one-way ANOVA, $F_{(2,21)} = 0.4278$, $P = 0.6575$). (D): FST (one-way ANOVA, $F_{(2, 21)} = 6.050$, $P = 0.0084$). (E): SPT (one-way ANOVA, $F_{(2, 21)} = 5.312$, $P = 0.0136$). (F): Western blot analysis of GluA1 in the mPFC (one-way ANOVA, $F_{(2, 21)} = 6.805$, $P = 0.0053$) and the representative bands. (G): Western blot analysis of PSD-95 in the mPFC (one-way ANOVA, $F_{(2, 21)} = 8.191$, $P = 0.0023$) and the representative bands. The data are shown as means \pm S.E.M (WT + sham group: $n = 10$, KO + sham group: $n = 7$, KO + SDV group: $n = 7$). ANOVA: analysis of variance. ns: not significant; * $P < 0.05$; ** $P < 0.01$; *** $P < 0.001$.

et al., 2021a; Wang et al., 2020a, 2021; Yang et al., 2022b). The mPFC tissues were mechanically homogenized just right in ice-cold Laemmli lysis buffer. To avoid cross-contamination, each specimen was prepared separately, liquid supernatants were collected after centrifugation at $3000 \times g$ (RCF) at 4°C for 5 min. The total protein concentration extracted from each sample was detected on a spectrophotometer (Molecular Devices Emax Precision Microplate Reader; Molecular Devices., San Jose, CA, USA) using a DC protein assay kit (Bio-Rad, Hercules, CA, USA). By adding a quarter volume of sample buffer (125 mM Tris-HCl, pH 6.8; 0.1% bromophenol blue; 4% sodium dodecyl sulfate; and 10% β -mercaptoethanol and 20% glycerol) and Laemmli Lysis buffer in appropriate proportions to balance the total protein concentration of each sample, then incubate them at 95°C for 10 min.

Considering the size of target protein, we chose 10% sodium dodecyl sulfate-polyacrylamide gel electrophoresis (SDS-PAGE) (catalog #: 4568125, Mini-PROTEAN TGX™ Stain-Free Gels; Bio-Rad, USA) separated the proteins by gel electrophoresis. Then a Trans-Blot Mini Cell apparatus (Bio-Rad) was used to electrotransfer the target protein onto polyvinylidene difluoride membranes.

For immunodetection, the polyvinylidene difluoride membranes were blocked with blocker [5% skim milk in TBS + 0.1% Tween-20

(TBST)] at room temperature for 1 h, the membranes for detecting postsynaptic density protein 95 (PSD-95) were incubated with the recommended dilution of the primary antibody against PSD-95 (1:1000, Catalog No.: 51-6,900, 1 $\mu\text{g}/\text{mL}$, Invitrogen, Camarillo, CA, USA) and β -actin (1:10,000; Cat number: A5441 Sigma-Aldrich Co., Ltd., St Louis, MO, USA) at 4°C overnight. The next day, wash the polyvinylidene difluoride membranes in three washes of TBST, 10 min each. Then the polyvinylidene difluoride membranes were selectively incubated with a recommended dilution of labeled secondary antibody [anti-mouse antibody (1:5000, catalog No.: NA931, GE Healthcare) or a horseradish peroxidase-conjugated anti-rabbit antibody (1:5000, catalog No.: NA934, GE Healthcare)] in 5% blocking buffer in TBST at room temperature for 1 h. After three final washes in TBST, 10 min each. The bands in the polyvinylidene difluoride membranes were detected using enhanced chemiluminescence plus a Western Blotting Detection system (GE Healthcare Bioscience).

The membranes for detecting anti-glutamate receptor 1 (AMPA subtype: GluA1) were incubated in elution buffer (62.5 mM Tris-HCl, pH 6.8, 2% sodium dodecyl sulfate, and 100 mM β -mercaptoethanol) (preheat in incubator at 60°C for 10 min, shake 50 times /min) at 60°C for 30 min and then washed three times (10 min at a time) in TBST. The

stripped membranes were blocked with blocker [5% skim milk in TBS + 0.1% Tween-20 (TBST)] at room temperature for 1 h and then were incubated with the recommended dilution of primary antibody directed against GluA1 (1:1,000; Cat No.: ab31232, Abcam, Cambridge, MA, USA) at 4 °C overnight. The following day, washing the membranes for three times (10 min at a time) in TBST and were incubated with a recommended dilution of horseradish peroxidase-conjugated anti-rabbit antibody (1:5000, catalog No.: NA934, GE Healthcare) for 1 h at room temperature. After three final washes in TBST, 10 min each. The bands in the polyvinylidene difluoride membranes were detected using enhanced chemiluminescence plus a Western Blotting Detection system (GE Healthcare Bioscience). Images were produced using a ChemiDoc™ Touch Imaging System (170-01401; Bio-Rad Laboratories, Hercules, CA, USA), and immunoreactive bands were quantified using Image Lab™ 3.0 software (Bio-Rad Laboratories).

2.5. Collection of fresh fecal samples and 16S ribosome RNA sequencing

We collected fresh fecal samples from mice before behavioral test LMT (Fig. 1A). To avoid cross-contamination, fecal samples from each mouse were collected separately. After the mice defecated, fresh fecal samples were collected immediately and were quickly intromitted into individual sterilized screw cap microtubes and then were stored at -80 °C until use.

Extraction of total DNA from mouse feces samples and subsequent 16S rRNA analysis were performed at MyMetagenome Co., Ltd. (Tokyo, Japan). The specific operation scheme can be carried out according to the procedure previously reported (Pu et al., 2021b; Wang et al., 2020a, 2021; Yang et al., 2022b). In brief, in order to amplify the V1-V2 hypervariable region of the bacterial 16S ribosome RNA gene, the universal primers 27F-mod (5'-AGRGTGATYMTGGCTCAG-3') and 338R (5'-TGCTGCCTCCCGTAGGAGT-3') have been used in the process of PCR. Then used an Illumina MiSeq Platform to sequence the 16S amplicons. The similarities between the genome database of the National Center for Biotechnology Information (NCBI) and the Ribosome Database Project were searched by using the GLSEARCH program. Finally, OTUs were classified and identified.

α -diversity analysis such as Observed_otus, Chao1, Ace, Shannon, and Shannon_e was used to reflect the abundance and diversity of intestinal microbial communities. β -diversity analysis including Principal Co-ordinates Analysis (PCoA) was used to access similarity or dissimilarity of the three intestinal microbial communities. Linear discriminant analysis (LDA) effect size (LEfSe) was used for identifying certain bacteria as potential microbial biomarkers discovery. Microbiota-based potential biomarker discoveries were performed with LEfSe using the online galaxy platform (Segata et al., 2011). The LDA scores (LDA > 4.0 and $P < 0.05$) derived from LEfSe analysis were considered significantly to be enriched or deficient bacterial taxa in the intestinal microbiota among the three groups.

2.6. Untargeted metabolomics analysis of plasma samples and data preprocessing

Untargeted metabolomics profiles from plasma samples were analysis by using ultra-performance liquid chromatography-tandem quadrupole time-of-flight mass spectrometry (UPLC-QTOF/MS) technique. The acquisition was operated on an ExionLC™ AD system (SCIEX, Tokyo, Japan) coupled to a X500R QTOF system (SCIEX, Tokyo, Japan), as previously reported (Wan et al., 2022a, 2022b). With the help of R statistical environment Ver 4.0.5. and Mass Spectrometry-Data Independent AnaLysis (MS-DIAL) software version 4.60 (Tsugawa et al., 2015), metabolomics profiles data was analyzed. Metabolites were detected at least 50% from the analyzed samples and the coefficient of variation (CV) values of 30% of metabolites in pooled quality control (QC) samples, and annotation level 2 proposed by Schymanski et al. (2014) were used for data analysis.

2.7. Statistical analysis

Statistical analysis of the data was performed using SPSS version 20.0 software (SPSS, Tokyo, Japan). The data were shown as the mean \pm standard error of the mean (S.E.M.). Data for behavioral tests and the expression levels of synaptic proteins were analyzed using one-way analysis of variance (ANOVA), followed by Fisher's least significant difference (LSD) test. The data of body weight were analyzed using repeated measure ANOVA, followed by Fisher's LSD test. Metabolites, the α -diversity of intestinal microbiota, and the abundance of gut microbiota at the phylum level, genus level, and species level among the three groups were analyzed using the Kruskal-Wallis test, followed by the Dunn's test for post-hoc analysis. Pairwise comparison of metabolomics data among the three groups were analyzed by Wilcoxon rank sum test. Bioinformatic analysis of PCoA, LEfSe algorithm of intestinal microbiota, Volcanic plot analysis of metabolomics and Correlation networks were all performed by using the OmicStudio tools (<https://www.omicstudio.cn/tool>).

Correlations between the plasma metabolites and the intestinal microbiota at species level, depression-like phenotypes and the expression of synaptic proteins in the brain, and correlations between the relative abundance of species bacteria and the expression levels of synaptic proteins in the mPFC and depression-like phenotypes were analyzed using Spearman's correlation analysis. P -value for comparison <0.05 was regarded as significant.

3. Results

3.1. Effects of bilateral SDV on depression-like phenotypes, and the expression of synaptic proteins in the brain

Effects of bilateral SDV in depression-like phenotypes in *Chrna7* KO mice were investigated (Fig. 1A). Body weight after surgery was not different among the three groups (Fig. 1B). There were no changes in locomotion among the three groups (Fig. 1C). The immobility time of FST in the KO + sham group was significantly higher than that of WT + sham group and KO + SDV group (Fig. 1D). In the SPT, sucrose preference of KO + sham group was significantly lower than that of WT + sham and KO + SDV groups (Fig. 1E). There were no differences in FST immobility time and sucrose preference of SPT between WT + sham group and KO + SDV group (Fig. 1D and E).

It is well known that synaptic proteins such as PSD-95 and GluA1 are decreased in the mPFC of rodents with depression-like phenotypes (Pu et al., 2021b; Wang et al., 2020a, 2020b, 2021; Yang et al., 2015; Zhang et al., 2014). Western blotting analysis showed that the expressions of PSD-95 and GluA1 in the mPFC of the KO + sham group were significantly lower than those of WT + sham group and KO + SDV group (Fig. 1F and G). There were no differences in expressions of GluA1 and PSD-95 in the mPFC between WT + sham group and KO + SDV group (Fig. 1F and G).

These data suggest that bilateral SDV significantly blocked depression-like phenotypes and reduced expression of synaptic proteins in the mPFC of *Chrna7* KO mice.

3.2. Effects of bilateral SDV on the composition diversity of intestinal microbiota

For α -diversity, Kruskal-Wallis test revealed no statistically significant differences in the Observed_otus, Chao1, Ace, Shannon, and Shannon_e indices among the three group (Fig. 2A-E). Regarding β -diversity, the bacterial population composition of intestine microbiota in the three groups was analyzed by PCoA. Based on the OUT level, PCoA analysis showed a significant separation in the bacterial population composition through Analysis of similarities (ANOSIM) assessment ($R = 0.3500$, $P = 0.001$) (Fig. 2F).

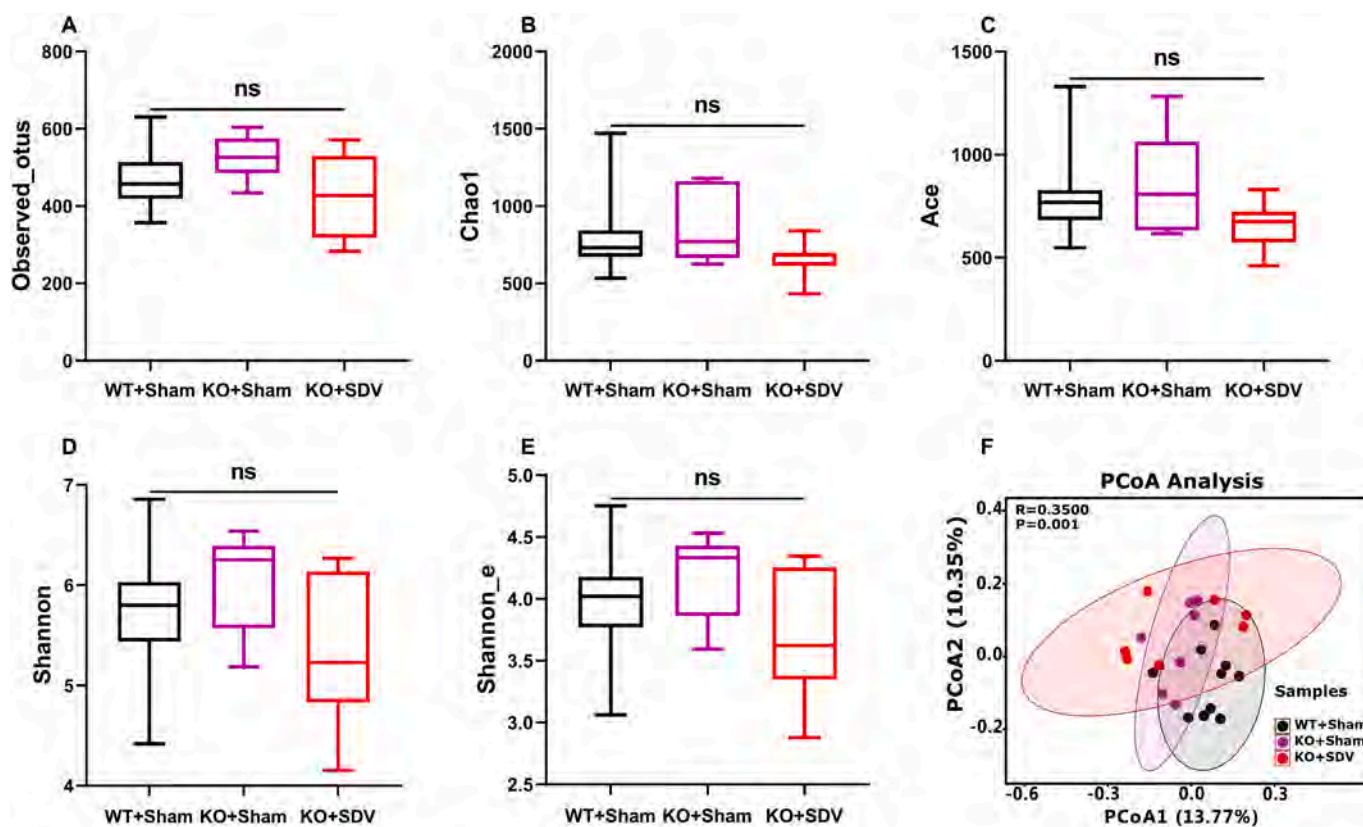


Fig. 2. Effects of bilateral SDV on the diversity of gut microbiota composition.

(A): Observed_otus (Kruskal-Wallis test, $P = 0.2028$). (B): Chao1 (Kruskal-Wallis test, $P = 0.1920$). (C): Ace (Kruskal-Wallis test, $P = 0.2305$). (D): Shannon (Kruskal-Wallis test, $P = 0.1941$). (E): Shannon_e (Kruskal-Wallis test, $P = 0.1941$). (F): PCoA based on OTU level (ANOSIM, Bray-Curtis dissimilarity matrix) ($R = 0.3500$, $P = 0.001$). For all box plots, the middle line in the box addresses the median, the box addresses the interquartile range, and the whisker addresses the most extreme and least values. ns: not significant.

3.3. Effects of bilateral SDV on the LEfSe algorithm of intestinal microbiota

Cladogram presented the relationship between biomarker taxa (layers of the cladogram represent different levels, with phylum, class, order, family, genus, and species from inside to outside) generated by LEfSe analysis (Fig. 3A). Furthermore, we identified 5 taxonomic biomarkers, the species *Porphyromonadaceae bacterium C941*, the genus *G_undefined_Porphyromonadaceae*, the species *Gabonibacter massiliensis*, the genus *Gabonibacter*, and the species *Prevotella sp. oral taxon 317* for the WT + sham group. Furthermore, we identified 6 taxonomic biomarkers, the species *Gabonia massiliensis*, the genus *Gabonia*, the family *Porphyromonadaceae*, the order *Bacteroidales*, the class *Bacteroidia*, and the phylum *Bacteroidetes* for the KO + sham group. Moreover, we identified 8 taxonomic biomarkers, the species *Lactobacillus hominis*, the species *Lactobacillus reuteri*, the species *Lactobacillus sp. BL302*, the genus *Lactobacillus*, the family *Lactobacillaceae*, the order *Lactobacillales*, the class *Bacilli*, and the phylum *Firmicutes* for the KO + SDV group (Fig. 3B).

3.4. Effects of bilateral SDV on the intestinal microbiota at the levels of phylum, genus, and species

At the phylum level, the composition of the intestinal microbiota in *Chrna7* KO mice was altered after SDV (Fig. 4A). Compared with WT + sham group and KO + sham group, the relative abundance of *Firmicutes* in the KO + SDV group were significantly higher, although there were no significant differences between WT + sham group and KO + sham group (Fig. 4B). Although there were no significant differences in the relative

abundance of *Tenericutes* between KO + SDV group and KO + sham group, the relative abundance of *Tenericutes* in the KO + SDV group were significantly lower than that in the WT + sham group (Fig. 4C).

At the genus level, the composition of the gut microbiota in *Chrna7* KO mice was altered after SDV (Fig. 5A). The relative abundance of *Faecalibaculum* in the KO + SDV group were statistically significantly lower than in the WT + sham group and KO + sham group (Fig. 5B). The relative abundance of *Candidatus Arthromitus*, *Bifidobacterium*, *G_undefined_Burkholderiales*, and *Muribaculum* in the KO + SDV group was lower than that in the WT + sham group, whereas the relative abundance of *Ihubacter* in the KO + SDV group was higher than that in the WT + sham group (Fig. 5C, F, and I-5J). The relative abundance of *Turicibacter* in the KO + SDV group were lower than in the KO + sham group (Fig. 5D). The relative abundance of *Lactobacillus* in the KO + SDV group were higher than in the KO + sham group (Fig. 5G). The relative abundance of *Lactococcus* in the KO + sham group and the KO + SDV group were lower than that in the WT + sham group (Fig. 5E).

At the species level, we screened out 15 bacteria with statistical differences based on their relative abundance (Fig. 6A). There were significant differences in the relative abundance of *Lactobacillus intestinalis*, *Lactobacillus hominis*, *Faecalibaculum rodentium*, *Lactobacillus sp. BL302*, *Bacteroides sp. TP-5*, *Candidatus Arthromitus sp. SFB-mouse*, *Turicibacter sp. LA62*, *Lactobacillus reuteri*, *Lactococcus lactis*, *Lactobacillus sp. NBRC 14512*, *Clostridium sp. Culture Jar-56*, *Lachnospiraceae bacterium 607*, *Clostridiales bacterium CIEAF 030*, *Bifidobacterium pseudolongum* and *Muribaculum intestinale* (Fig. 6B-6P). Among these microbes, the relative abundance of three microbiome (*Lactobacillus intestinalis*, *Lactobacillus sp. BL302*, *Turicibacter sp. LA62*) was significantly different between KO + sham group and KO + SDV group (Fig. 6B, E, and H).

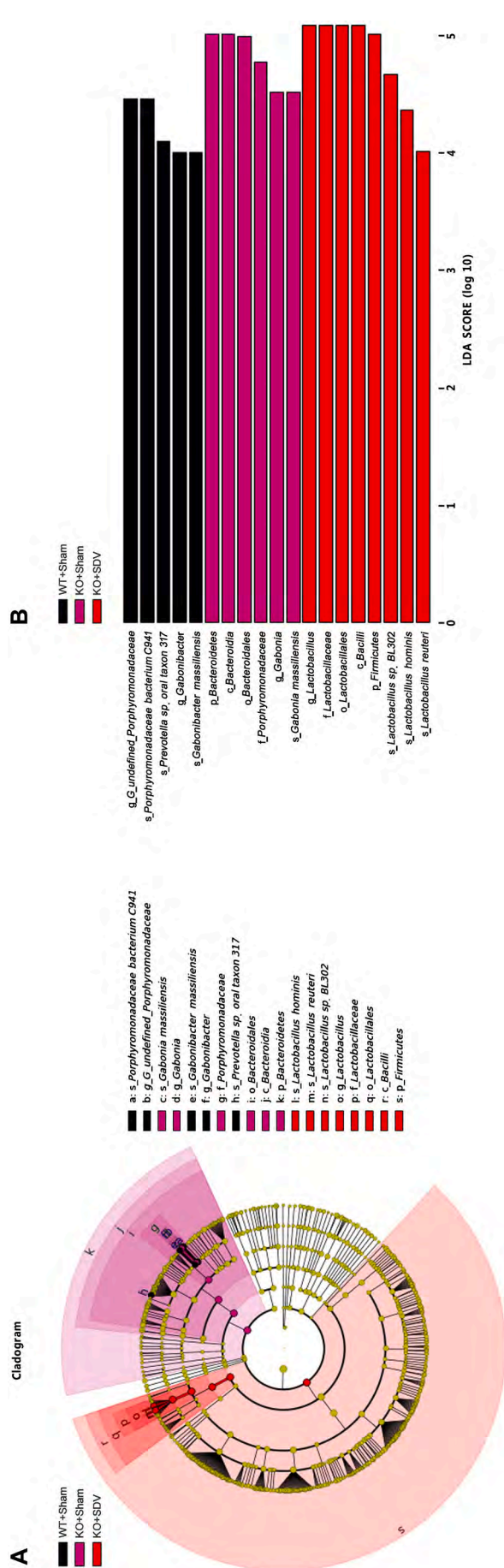


Fig. 3. LEfSe analysis for potential bacteria biomarkers of gut microbiota. (A): Functional branching diagram generated from LEfSe showing the differences of the three groups at different taxonomic levels. (B): Histogram representing the enriched taxa with LDA score > 4.0 and $P < 0.05$ obtained from LEfSe of the three groups.

3.5. Untargeted metabolomic profiles analysis of plasma samples

Considering the close interaction between intestinal microbiome and host metabolism, we conducted untargeted metabolomics profiles analysis from plasma samples. After the quality control and removal of low-abundance peaks, a subset of 175 metabolites was annotated. After log10 transformation of the concentration of metabolomics data, Kruskal-Wallis test was performed among the three groups. We identified 24 metabolites with statistical differences (Fig. 7A-D).

Then we conducted pairwise comparison of metabolomics data among the three groups, and screened out the metabolites with significant up-regulation and down-regulation obtained in each two groups through the form of Volcano plot [the threshold was set as: $P < 0.05$ and fold change (FC) > 2]. When comparing the WT + sham group with the KO + sham group, we confirmed that 3 annotation metabolites were significantly up-regulated and 7 annotation metabolites were significantly down-regulated (Fig. 8A). When comparing the WT + sham group with the KO + SDV group, we confirmed that 9 annotation metabolites were significantly up-regulated and 8 annotation metabolites were significantly down-regulated (Fig. 8B). When the KO + sham group compared with the KO + SDV group, we confirmed 9 significantly up-regulated annotated metabolites and 4 significantly down-regulated metabolites (Fig. 8C).

Finally, we further used UpSet plot listed out that there were 11 kinds of annotated metabolites with statistical differences between WT + sham group and KO + sham group, 17 kinds of annotated metabolites with statistical differences between the KO + sham group and KO + SDV group, and 27 kinds of annotated metabolites with statistical differences between WT + sham group and KO + SDV group. In addition, 6 kinds of annotated metabolites showed significant differences between the WT + sham group and the KO + sham group, and between the WT + sham group and the KO + SDV group. Furthermore, 9 kinds of annotated metabolites showed significant differences between the KO + sham group and the KO + SDV group, and between the WT + sham group and the KO + SDV group (Fig. 8D).

3.6. Correlations between the gut microbiota and plasma metabolites (or FST, synapse proteins)

There was a widely correlation between the plasma metabolites and the gut microbiota of the three groups, indicating the existence of a close relationship between the plasma metabolites and the gut microbiota. Furthermore, we evaluated the association between plasma metabolites and the gut microbiota at the species level. After screening the data by setting the threshold of $P < 0.05$ and the absolute value of $R \geq 0.5$, a Correlation Network was developed to indicate the correlation between the plasma metabolites and the intestinal microbiota at species level, depression-like phenotypes and the expression of synaptic proteins in the brain, all of which significantly differences among the three groups in the present study (Fig. 9A).

Two differentially relative abundant of gut bacteria (*Lactobacillus intestinalis* and *Bacteroides* sp. TP-5) were positively correlated with 1,5-anhydro-D-sorbitol (Fig. 9A). Three differentially relative abundant of gut bacteria (*Faecalibaculum rodentium*, *Turcibacter* sp. LA62 and *Muribaculum intestinale*) were negatively correlated with 1,5-anhydro-D-sorbitol (Fig. 9A). There were positive correlations between the relative abundance of species *Lactobacillus intestinalis*, *Lactobacillus hominis*, *Lactobacillus* sp. BL302, *Lactobacillus* sp. NBRC 14512, and *Clostridiales bacterium CIEAF 030* and L-citrulline. In contrast, there were negative correlations between the relative abundance of species *Faecalibaculum rodentium* and L-citrulline (Fig. 9A).

The relative abundance of species *Lachnospiraceae bacterium 607* was positively correlated with succinic anhydride while the relative abundances of species *Lactobacillus hominis*, *Lactobacillus* sp. BL302, *Bacteroides* sp. TP-5, *Lactobacillus reuteri*, and *Clostridiales bacterium CIEAF 030* were negatively correlated with succinic anhydride (Fig. 9A). The

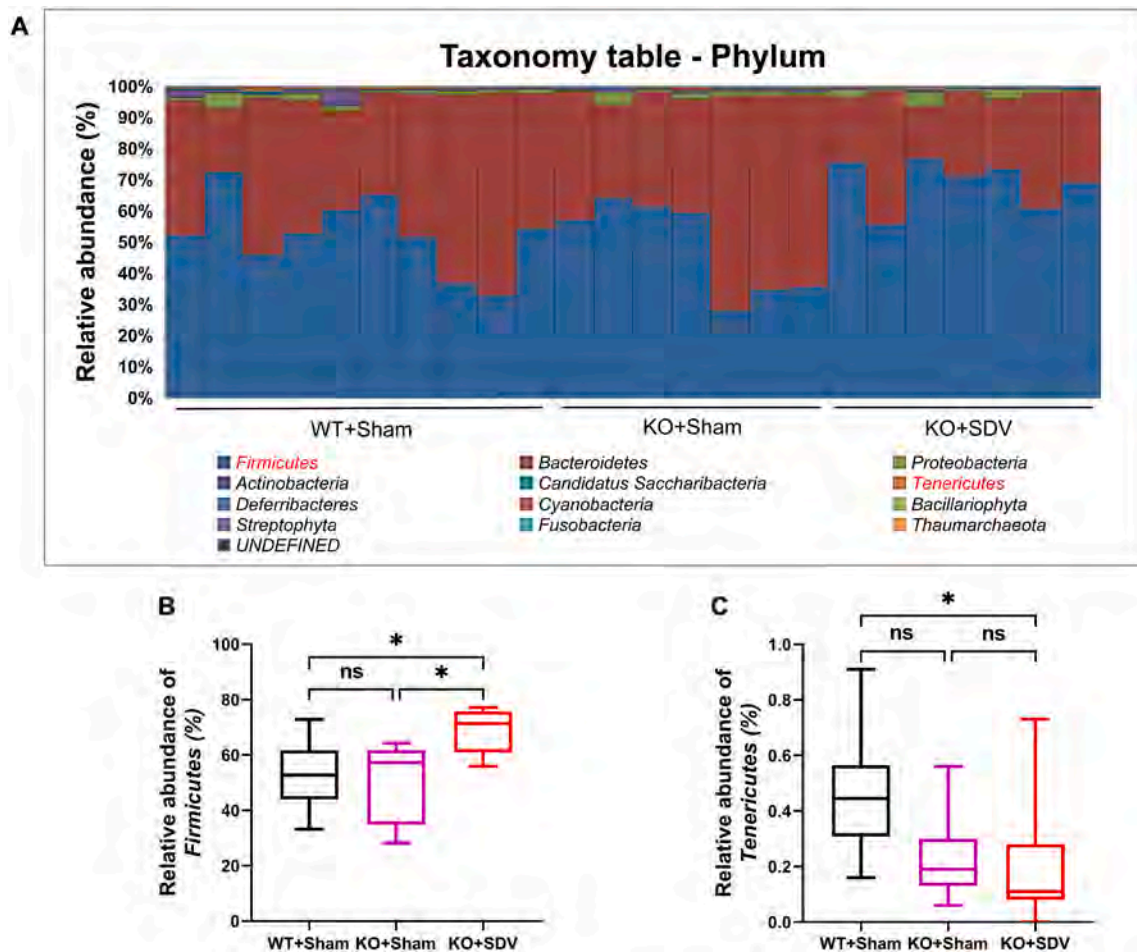


Fig. 4. Effects of bilateral SDV on gut microbiota at the phylum levels.

(A): Gut bacteria composition at the phylum level in the three groups. (B): Relative abundance of the phylum *Firmicutes* (Kruskal-Wallis test, $P = 0.0126$). (C): Relative abundance of the phylum *Tenericutes* (Kruskal-Wallis test, $P = 0.0258$). For all box plots, the middle line in the box addresses the median, the box addresses the interquartile range, and the whisker addresses the most extreme and least values. $*P < 0.05$. ns: not significant.

species *Lactobacillus intestinalis*, *Lactobacillus hominis*, *Lactobacillus* sp. BL302, *Lactobacillus reuteri* and *Lactobacillus* sp. NBRC 14512 were positively correlated with taurocholic acid. In contrast, the species *Faecalibaculum rodentium* and *Turicibacter* sp. LA62 were negatively correlated with taurocholic acid (Fig. 9A).

There was only a significant positive correlation between the FST data and the concentration of ethyl hydrogen sulfate (Fig. 9A). There was no correlation between changes in SPT and changes in metabolite concentration (data not shown). There was a positive correlation between GluA1 expression levels in mPFC and the concentration of 2-oxindole (Fig. 9A). Furthermore, there were positive correlations between PSD-95 expression levels in mPFC and the concentration of L-citrulline, D-ornithine, 2,6-dihydroxybenzoic acid or resorcinol. In contrast, there were no negative correlations between expressions of GluA1 and PSD-95 in the mPFC and plasma metabolites (Fig. 9A).

Similarly, we used a Correlation Network to investigate correlations between the relative abundance of the gut bacteria that differed significantly at the species levels among the three groups and depression-like phenotypes or the expression of synaptic proteins (Fig. 9B). After screening the data by setting the threshold of $P < 0.05$ and the absolute value of $R \geq 0.5$. There were significant negative correlations between the FST data and the relative abundance of the species *Lactobacillus intestinalis*, *Lactobacillus* sp. BL302, *Bacteroides* sp. TP-5, and *Lactobacillus* sp. NBRC 14512 in the three groups (Fig. 9B), suggesting a role of these species in behavioral despair. There were statistically significant positive correlations between the SPT data and the relative abundance of

species *Bacteroides* sp. TP-5 in the three experimental groups (Fig. 9B), suggesting a role of *Bacteroides* sp. TP-5 in anhedonia-like behavior. Furthermore, there were positive or negative correlation between expression levels of synaptic proteins in the mPFC and the relative abundance of species bacteria (Fig. 9B).

4. Discussion

The major findings of this study are as follows: First, SDV blocked depression-like behaviors and reduced expression of synaptic proteins (i. e., GluA1 and PSD-95) in the mPFC of *Chrna7* KO mice. Second, there were no changes in α -diversity among the three groups. However, there was a significant difference in β -diversity among the three groups. LEfSe analysis revealed that the species *Lactobacillus* sp. BL302, the species *Lactobacillus hominis*, and the species *Lactobacillus reuteri*, were identified as potential microbial markers in the KO + SDV group. Furthermore, there were several genus and species altered among the three groups. Third, there were several metabolites altered among the three groups. Fourth, there were correlations between relative abundance of several microbiome and behavioral data (or synaptic proteins). Network analysis showed correlations between several microbiome and blood metabolites or behavioral data. Collectively, these data suggest that subdiaphragmatic vagus nerve plays a crucial role in depression-like phenotypes in *Chrna7* KO mice through gut-microbiota-brain axis including microbiome-derived metabolites.

β -diversity data among the three groups suggest that SDV is a driving

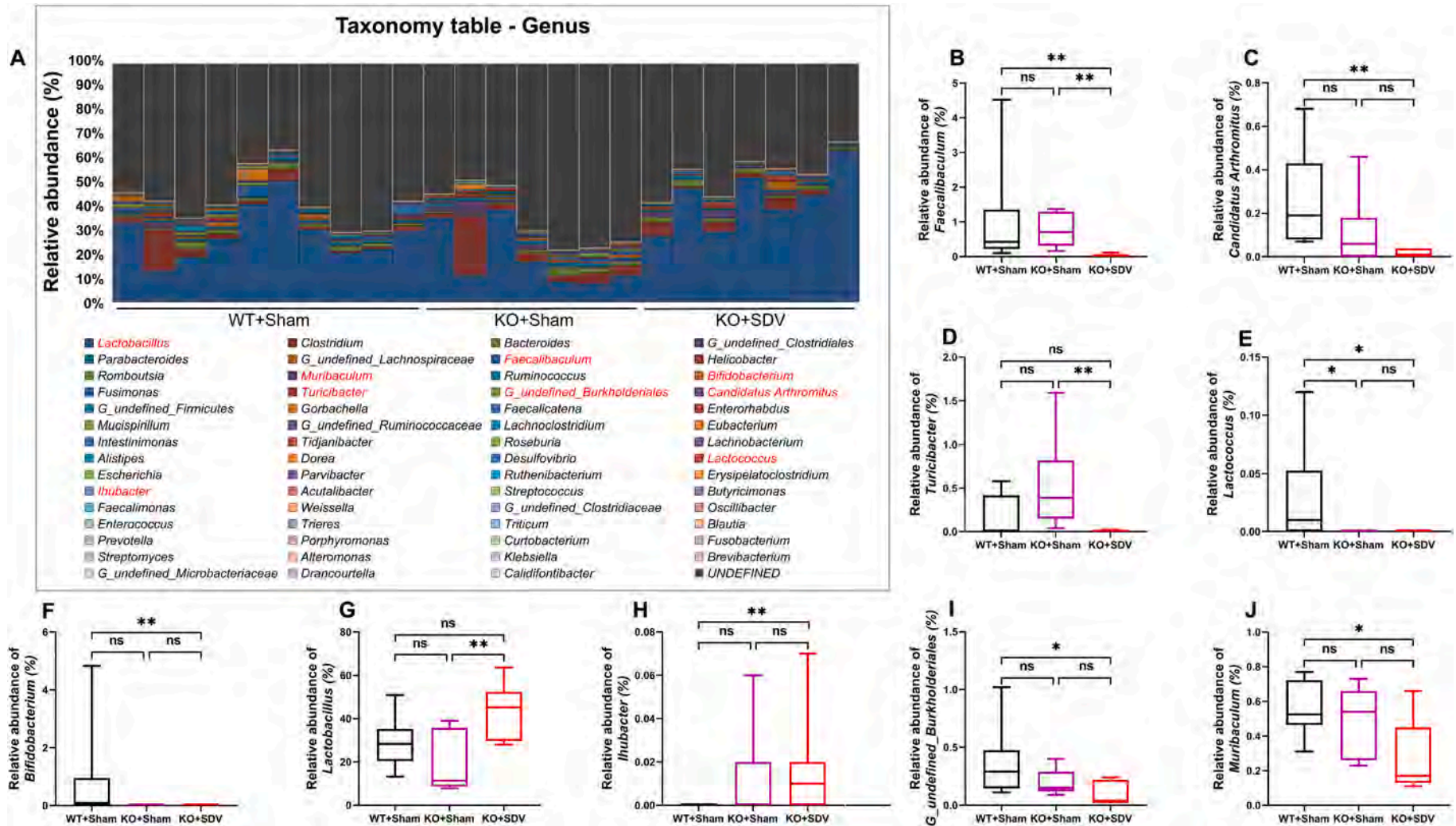


Fig. 5. Effects of bilateral SDV on gut microbiota at the genus levels.

(A): Gut bacteria composition at the genus level in the three groups. (B): Relative abundance of the genus *Faecalibaculum* (Kruskal-Wallis test, $P = 0.0009$). (C): Relative abundance of the genus *Candidatus Arthromitus* (Kruskal-Wallis test, $P = 0.0021$). (D): Relative abundance of the genus *Turicibacter* (Kruskal-Wallis test, $P = 0.0030$). (E): Relative abundance of the genus *Lactococcus* (Kruskal-Wallis test, $P = 0.0053$). (F): Relative abundance of the genus *Bifidobacterium* (Kruskal-Wallis test, $P = 0.0086$). (G): Relative abundance of the genus *Lactobacillus* (Kruskal-Wallis test, $P = 0.0102$). (H): Relative abundance of the genus *Ihubacter* (Kruskal-Wallis test, $P = 0.0131$). (I): Relative abundance of the genus *G_undefined_Burkholderiales* (Kruskal-Wallis test, $P = 0.0132$). (J): Relative abundance of the genus *Muribaculum* (Kruskal-Wallis test, $P = 0.0395$). For all box plots, the middle line in the box addresses the median, the box addresses the interquartile range, and the whisker addresses the most extreme and least values. * $P < 0.05$; ** $P < 0.01$. ns: not significant.

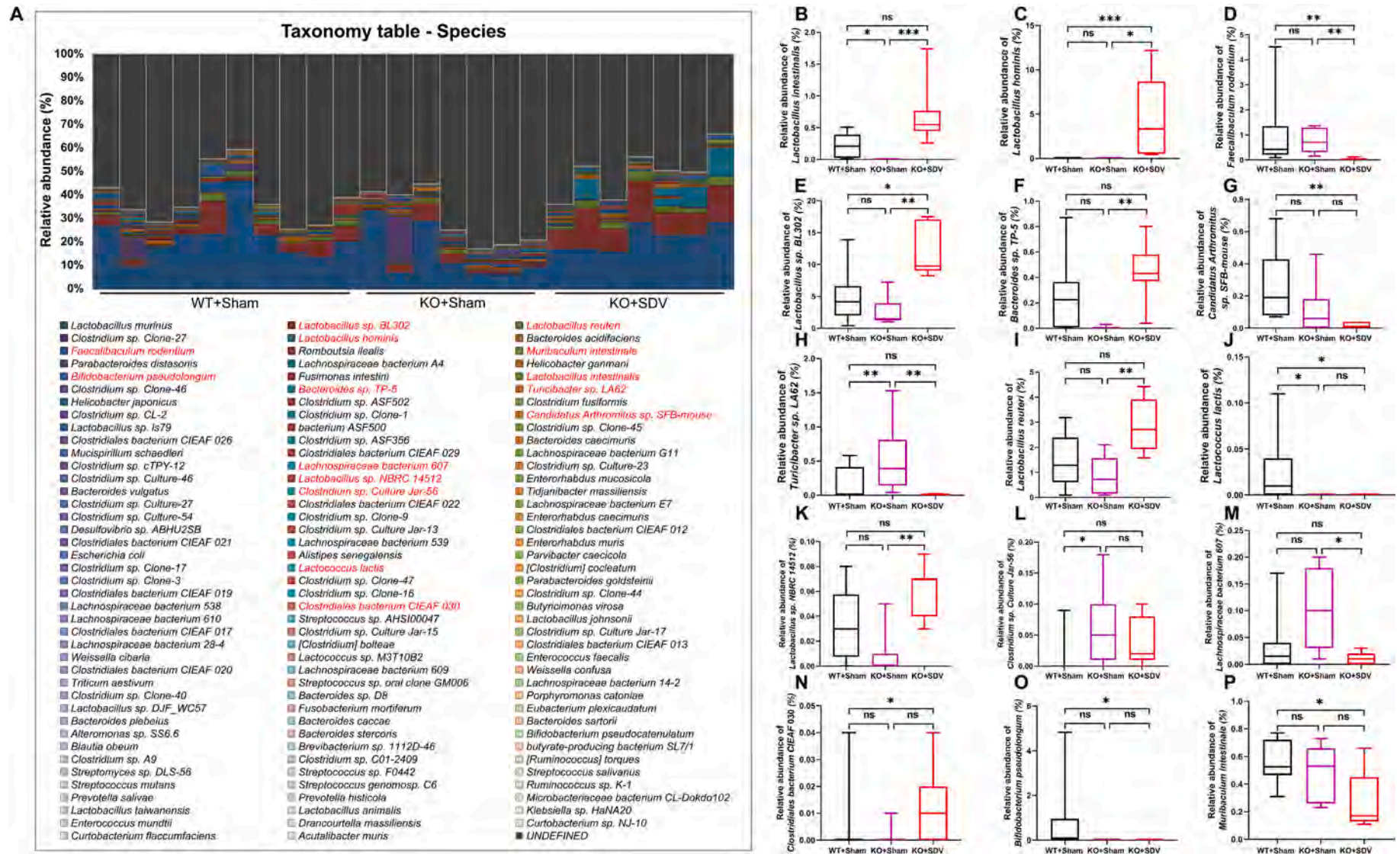


Fig. 6. Effects of bilateral SDV on gut microbiota at the species levels.

(A): Gut bacteria composition at the species level in the three groups. (B): Relative abundance of the species *Lactobacillus intestinalis* (Kruskal-Wallis test, $P = 0.0001$). (C): Relative abundance of the species *Lactobacillus hominis* (Kruskal-Wallis test, $P = 0.0002$). (D): Relative abundance of the species *Faecalibacterium rodentium* (Kruskal-Wallis test, $P = 0.0009$). (E): Relative abundance of the species *Lactobacillus sp. BL302* (Kruskal-Wallis test, $P = 0.0012$). (F): Relative abundance of the species *Bacteroides sp. TP-5* (Kruskal-Wallis test, $P = 0.0018$). (G): Relative abundance of the species *Candidatus Arthromitus sp. SFB-mouse* (Kruskal-Wallis test, $P = 0.0023$). (H): Relative abundance of the species *Turicibacter sp. LA62* (Kruskal-Wallis test, $P = 0.0030$). (I): Relative abundance of the species *Lactobacillus reuteri* (Kruskal-Wallis test, $P = 0.0047$). (J): Relative abundance of the species *Lactococcus lactis* (Kruskal-Wallis test, $P = 0.0053$). (K): Relative abundance of the species *Lactobacillus sp. NBRC 14512* (Kruskal-Wallis test, $P = 0.0088$). (L): Relative abundance of the species *Clostridium sp. Culture Jar-56* (Kruskal-Wallis test, $P = 0.0155$). (M): Relative abundance of the species *Lachnospiraceae bacterium 607* (Kruskal-Wallis test, $P = 0.0155$). (N): Relative abundance of the species *Clostridiales bacterium CIEAF 030* (Kruskal-Wallis test, $P = 0.0214$). (O): Relative abundance of the species *Bifidobacterium pseudolongum* (Kruskal-Wallis test, $P = 0.0245$). (P): Relative abundance of the species *Muribaculum intestinale* (Kruskal-Wallis test, $P = 0.0395$). For all box plots, the middle line in the box addresses the median, the box addresses the interquartile range, and the whisker addresses the most extreme and least values. * $P < 0.05$; ** $P < 0.01$; *** $P < 0.001$. ns: not significant.

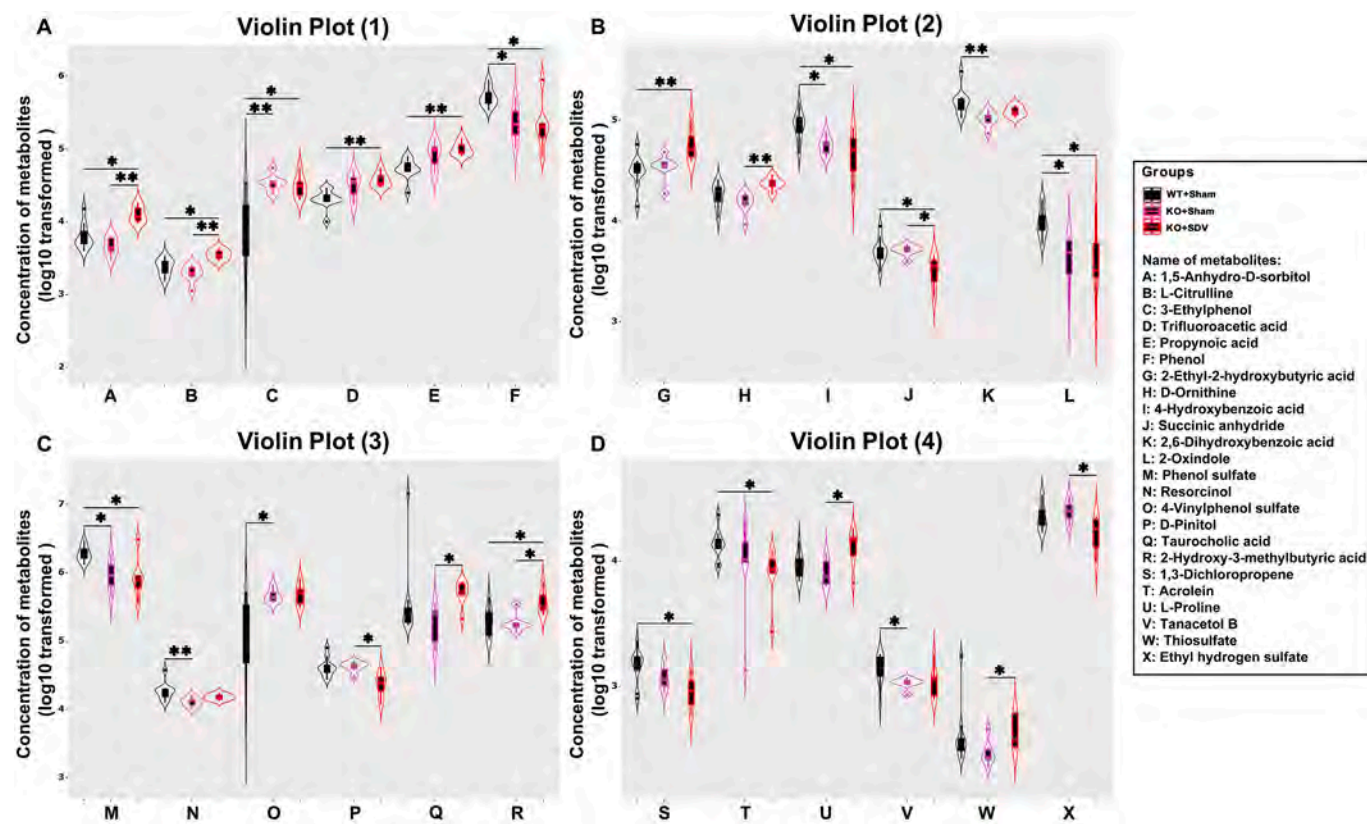


Fig. 7. Effect of bilateral SDV on plasma metabolites. (A): Violin plot showing the changes of 6 kinds of metabolites [1,5-anhydro-D-sorbitol (Kruskal-Wallis test, $P = 0.0016$), L-citrulline (Kruskal-Wallis test, $P = 0.0018$), 3-ethylphenol (Kruskal-Wallis test, $P = 0.0019$), trifluoroacetic acid (Kruskal-Wallis test, $P = 0.0046$), propynoic acid (Kruskal-Wallis test, $P = 0.0046$), phenol (Kruskal-Wallis test, $P = 0.0055$)] among the three groups. (B): Violin plot showing the changes of 6 kinds of metabolites [2-ethyl-2-hydroxybutyric acid (Kruskal-Wallis test, $P = 0.0059$), D-ornithine (Kruskal-Wallis test, $P = 0.0065$), 4-hydroxybenzoic acid (Kruskal-Wallis test, $P = 0.0077$), succinic anhydride (Kruskal-Wallis test, $P = 0.0078$), 2,6-dihydroxybenzoic acid (Kruskal-Wallis test, $P = 0.0080$), 2-oxindole (Kruskal-Wallis test, $P = 0.0080$)] among the three groups. (C): Violin plot showing the changes of 6 kinds of metabolites [phenol sulfate (Kruskal-Wallis test, $P = 0.0080$), resorcinol (Kruskal-Wallis test, $P = 0.0111$), 4-vinylphenol sulfate (Kruskal-Wallis test, $P = 0.0113$), D-pinitol (Kruskal-Wallis test, $P = 0.0122$), taurocholic acid (Kruskal-Wallis test, $P = 0.0129$), 2-hydroxy-3-methylbutyric acid (Kruskal-Wallis test, $P = 0.0145$)] among the three groups. (D): Violin plot showing the changes of 6 kinds of metabolites [1,3-dichloropropene (Kruskal-Wallis test, $P = 0.0203$), acrolein (Kruskal-Wallis test, $P = 0.0209$), L-proline (Kruskal-Wallis test, $P = 0.0245$), tanacetol B (Kruskal-Wallis test, $P = 0.0321$), thiosulfate (Kruskal-Wallis test, $P = 0.0436$), ethyl hydrogen sulfate (Kruskal-Wallis test, $P = 0.0460$)] among the three groups. The X-axis using the letter symbol representing the names of different plasma metabolites, and the Y-axis represents the concentration of various plasma metabolites after log₁₀ transformation. * $P < 0.05$; ** $P < 0.01$; Different colors of violin plots represent the corresponding groups.

factor for the differential expression of structural similarity in microbial communities. We reported that LPS significantly decreased α -diversity and relative abundance of gut microbiota in mice, and that SDV did not cause LPS-induced alterations in α -diversity and relative abundance of gut microbiota in mice (Zhang et al., 2020), suggesting that LPS could cause depression-like behaviors in mice through gut–microbiota–brain axis via subdiaphragmatic vagus nerve. Furthermore, SDV blocked depression-like behaviors in mice after FMT from mice with depression-like behaviors (Pu et al., 2021b; Wang et al., 2020a; Wang et al., 2021). McVey Neufeld et al. (2019) reported that oral treatment with selective serotonin reuptake inhibitor (SSRI: fluoxetine or sertraline) leads to a significant increase in vagal fiber activity, and that blocking vagal signaling from the gut to the brain via SDV abolished antidepressant-like effect of SSRI, suggesting the role of vagus nerve dependent gut–brain axis in the antidepressant effects of SSRIs. From the current data, it is unclear whether subdiaphragmatic vagus nerve is responsible for depression-like phenotypes of *Chrna7* KO mice. A recent study demonstrated that SDV or genetic knock-out of $\alpha 7$ nAChRs abolished the anti-inflammatory actions of famotidine (a histamine 2 receptor antagonist) in mice with LPS-treated cytokine stream (Yang et al., 2022a), suggesting a role of vagus nerve anti-inflammation via $\alpha 7$ nAChRs. Given the crucial role of $\alpha 7$ nAChRs on vagus nerve inflammatory actions

(O'Mahony et al., 2009; Yang et al., 2022a), it is possible that subdiaphragmatic vagus nerve may be responsible for depression-like phenotypes of *Chrna7* KO mice. Taken together, it is likely that gut–microbiota–brain axis via subdiaphragmatic vagus nerve plays an important role in depression-like phenotypes of *Chrna7* KO mice.

At the phylum level, the most abundant phylum *Firmicutes* was significantly increased in KO + SDV group compared to other two groups, suggesting that subdiaphragmatic vagus nerve may affect relative abundance of *Firmicutes* in gastrointestinal tract. At the species level, the relative abundance of *Lactobacillus intestinalis* and *Lactobacillus* sp. *BL302* in KO + SDV group was higher than that of KO + sham group. Furthermore, network analysis showed that these two bacteria were correlated with depression-like phenotypes and reduced synaptic proteins, suggesting a role of these two bacteria in depression. In contrast, the relative abundance of *Turicibacter* sp. *LA62* in KO + SDV group was lower than that of KO + sham group. A network analysis showed that *Turicibacter* sp. *LA62* was also correlated with depression-like phenotypes and reduced synaptic proteins. Collectively, it seems that *Lactobacillus intestinalis*, *Lactobacillus* sp. *BL302*, and *Turicibacter* sp. *LA62* might be associated with depression-like phenotypes although further study is needed.

Using untargeted metabolomics analysis, we found that plasma

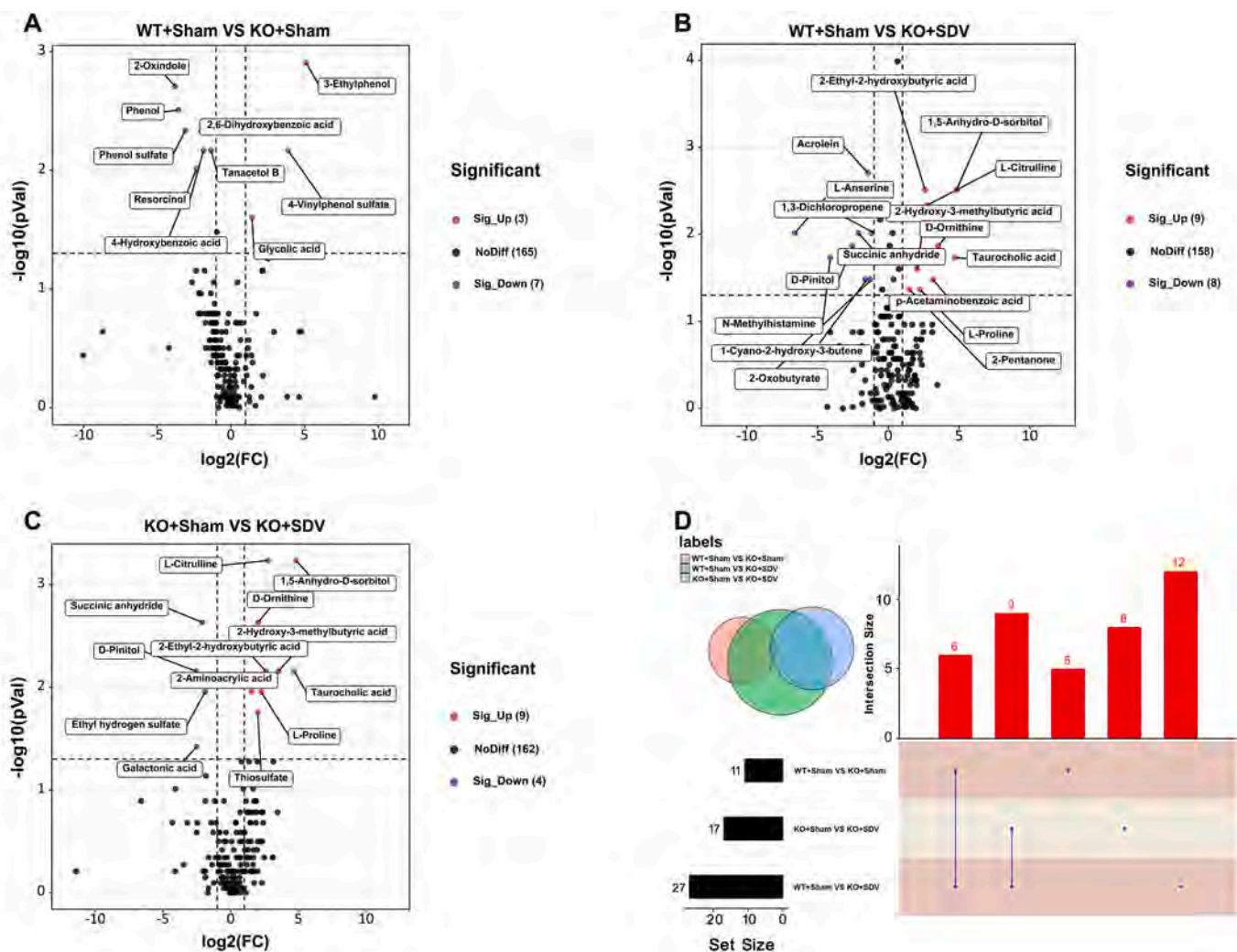


Fig. 8. Differences of plasma metabolites between different experimental groups.

(A): Volcano plot indicating that 3 annotation metabolites were significantly up-regulated, 7 annotation metabolites were significantly down-regulated and 165 annotation metabolites were no differences when comparing the WT + sham group with the KO + sham group. (B): Volcano plot indicating that 9 annotation metabolites were significantly up-regulated, 8 annotation metabolites were significantly down-regulated and 158 annotation metabolites were no differences when comparing the WT + sham group with the KO + SDV group. (C): Volcano plot indicating that 9 annotation metabolites were significantly up-regulated, 4 annotation metabolites were significantly down-regulated and 162 annotation metabolites were no differences when comparing the KO + sham group with the KO + SDV group. The X-axis represents the log₂-transformed values of the FC of plasma metabolite concentration, and the Y-axis represents the -log₁₀-transformed values of P value using the Wilcoxon rank sum test. The horizontal dotted line indicates P = 0.05 and the vertical dotted line indicates FC = ± 2. Metabolites with up-regulated, down-regulated, and no difference were marked in red, purple, and black respectively. (D): UpSet plot listed out that there were 11 kinds of annotated metabolites with statistical differences between the KO + sham group and the KO + SDV group, and 27 kinds of annotated metabolites with statistical differences between the WT + sham group and the KO + SDV group by using the Wilcoxon rank sum test (P < 0.05). In addition, 6 kinds of annotated metabolites showed significant differences between the WT + Sham group and the KO + sham group and between the WT + sham group and the KO + SDV group, and 9 kinds of annotated metabolites showed significant differences between the KO + sham group and the KO + SDV group and between the WT + sham group and the KO + SDV group. Besides, 5 kinds of annotated metabolites showed significant differences only between the WT + sham group and the KO + sham group, 8 kinds of annotated metabolites showed significant differences only between the KO + sham group and the KO + SDV group, 12 kinds of annotated metabolites showed significant differences only between the WT + sham group and the KO + SDV group. (For interpretation of the references to colour in this figure legend, the reader is referred to the web version of this article.)

levels of 1,5-anhydro-D-sorbitol (also known as 1,5-anhydro-D-glucitol), L-citrulline, and taurocholic acid in the KO + SDV group were higher than those of KO + sham group. A network analysis showed that 1,5-anhydro-D-sorbitol was negatively correlated with *Faecalibaculum rodentium*, suggesting that *Faecalibaculum rodentium* may be involved in the synthesis of 1,5-anhydro-D-sorbitol. A report showed that low plasma levels of 1,5-anhydro-D-sorbitol are closely associated with impaired peripheral nerve function and diabetic peripheral neuropathy in patients with type 2 diabetes (Xu et al., 2022), suggesting that lower plasma levels of 1,5-anhydro-D-sorbitol may be a risk factor for diabetic

peripheral neuropathy. L-citrulline is a nitrogen end product produced from glutamine through urea cycle. Blood levels of L-citrulline and L-arginine in unmedicated patients with major depressive disorder (MDD) were significantly lower than healthy controls (Hess et al., 2017). MDD patients had a lower NOS (nitric oxide synthase) activity (L-citrulline/L-arginine ratio) than healthy controls at baseline (Loeb et al., 2020). NOS activity in MDD patients increased significantly after antidepressant treatment (Loeb et al., 2020), suggesting a state biomarker for depression. Furthermore, taurocholic acid (conjugation of cholic acid with taurine) was positively correlated with several bacteria including

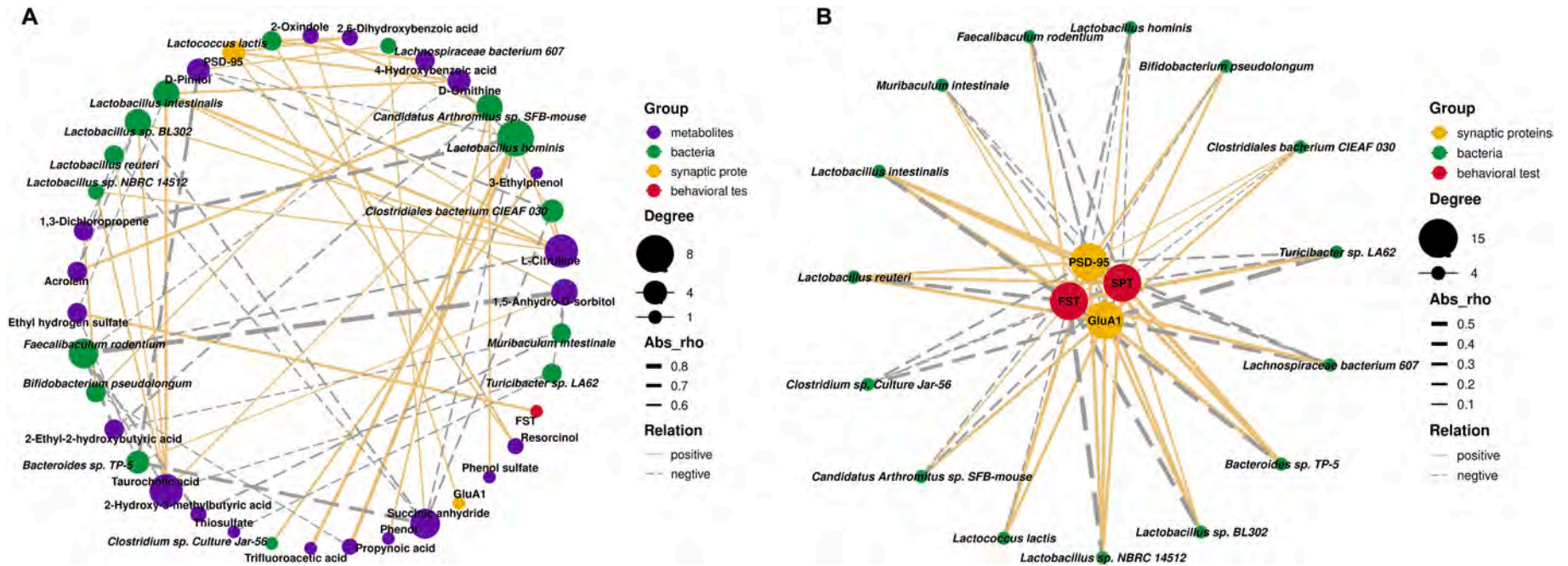


Fig. 9. Correlation network between behavioral data (or synaptic proteins) and microbiota (or metabolites).

(A): A Correlation Network indicating the correlations between the concentrations of plasma metabolites and the gut microbiota at the species level, the results of the behavioral test and the expression of synaptic proteins of mPFC (The threshold was set as $P < 0.05$ and the absolute value of $R \geq 0.5$). The different colors of nodes represent different groups. The sizes of node gradients represent varying degrees of correlation. The thickness of the line represents the absolute value of the correlation coefficient. Solid lines represent positive correlations, dotted lines represent negative correlations). (B): A Correlation Network showed correlations between the relative abundance of gut bacteria at the species level and the results of the behavioral test and the expression of synaptic proteins of mPFC (The threshold was set as $P < 0.05$. The different colors of nodes represent different groups. The sizes of node gradients represent varying degrees of correlation. The thickness of the line represents the absolute value of the correlation coefficient. Solid lines represent positive correlations, dotted lines represent negative correlations).

Lactobacillus intestinalis, suggesting that these bacteria may play a role in the production of taurocholic acid, major bile acid. Interestingly, there was a significant difference in blood levels of taurocholic acid between MDD patients and healthy controls (Bai et al., 2021). Given anti-inflammatory role of taurocholic acid, it is possible that higher levels of taurocholic acid may play a role in antidepressant-like effects of SDV in *Chrna7* KO mice. Succinic anhydride was negatively correlated with *Bacteroides* sp. TP-5 which were associated with depression-like phenotypes. Collectively, it is likely that microbes-derived metabolites may play a role in the antidepressant-like effects of SDV in *Chrna7* KO mice.

A network analysis showed that *Lactobacillus intestinalis*, *Lactobacillus reuteri*, *Turicibacter* sp. LA62, and *Bacteroides* sp. TP-5 were correlated with depression-like behaviors. There are no reports showing the role of *Turicibacter* sp. LA62, and *Bacteroides* sp. TP-5 in depression. We reported that oral ingestion of *Lactobacillus intestinalis* and *Lactobacillus reuteri* caused depression-like phenotypes in antibiotic-treated mice through gut–microbiota–brain axis via subdiaphragmatic vagus nerve (Wang et al., 2020a). Furthermore, we reported that oral ingestion of *Faecalibaculum rodentium* caused depression-like phenotypes in resilient *Ephx2* KO mice through gut–microbiota–brain axis via subdiaphragmatic vagus nerve (Wang et al., 2021). Furthermore, *Faecalibaculum rodentium* was positively correlated with FST data, and negatively correlated with SPT data. These data suggest that *Faecalibaculum rodentium* might play a role in depression-like phenotypes. Collectively, it is likely that these bacteria might play a role in the antidepressant-like effects of SDV in *Chrna7* KO mice although further study is needed.

This study has the one limitation. The current data of this study do not show a direct role of gut microbiota in depression-like phenotypes of *Chrna7* KO mice although a previous study suggests a role of gut microbiota in depression-like phenotypes of *Chrna7* KO mice (Pu et al., 2021b). Further study to identify specific microbiomes which contribute to depression-like phenotypes of *Chrna7* KO mice is needed.

In conclusion, the current data show that SDV blocked depression-like behaviors and reduced synaptic proteins in the mPFC of *Chrna7* KO mice. Therefore, gut–microbiota–brain axis via subdiaphragmatic vagus nerve plays a role in depression-like phenotypes in *Chrna7* KO mice.

Data and code availability

The 16S rRNA sequencing data has been uploaded and saved in the NCBI Sequence Read Archive and is available at the accession number PRJNA845101.

Ethical statement

The experimental protocol of present study was approved by the Chiba University Institutional Animal Care and Use Committee (Permission number 3-399). The experimental mice were all firstly deeply anesthetized with inhaled isoflurane and then rapidly sacrificed by cervical dislocation. All efforts were made to minimize animals suffering.

CRediT authorship contribution statement

Yong Yang: Investigation, Data curation, Formal analysis, Writing – original draft, Writing – review & editing. **Akifumi Eguchi:** Investigation, Data curation, Formal analysis, Writing – review & editing. **Xiayun Wan:** Investigation, Writing – review & editing. **Lijia Chang:** Investigation, Writing – review & editing. **Xingming Wang:** Investigation, Writing – review & editing. **Younge Qu:** Investigation, Writing – review & editing. **Chisato Mori:** Investigation, Funding acquisition, Writing – review & editing. **Kenji Hashimoto:** Conceptualization, Funding acquisition, Writing – original draft, Writing – review & editing.

Declaration of Competing Interest

Dr. Hashimoto is the inventor of filed patent applications on “The use of *R*-ketamine in the treatment of psychiatric diseases”, “(*S*)-norketamine and salt thereof as pharmaceutical”, “*R*-ketamine and derivative thereof as prophylactic or therapeutic agent for neurodegeneration disease or recognition function disorder”, “Preventive or therapeutic agent and pharmaceutical composition for inflammatory diseases or bone diseases”, and “*R*-ketamine and its derivatives as a preventive or therapeutic agent for a neurodevelopmental disorder” by the Chiba University. Dr. Hashimoto has also received speakers' honoraria, consultant fee, or research support from Abbott, Boehringer Ingelheim, Daiichi-Sankyo, Meiji Seika Pharma, Seikagaku Corporation, Dainippon-Sumitomo, Taisho, Otsuka, Murakami Farm and Perception Neuroscience. Other authors declare no conflict of interest.

Data availability

Data will be made available on request.

Acknowledgements

This study was supported by the grant from Japan Society for the Promotion of Science (to K.H., 21H00184, 21H05612), JST OPERA Program Japan (to C.M JPMJOP1831) and unrestricted grant of Yamada Bee Company, Japan (to C.M). Dr. Yong Yang was supported by the Japan China Sasakawa Medical Fellowship (Tokyo, Japan). Dr. Yong Yang and Ms. Xiayun Wan were supported by the Academic Research & Innovation Management Organization of Chiba University (Chiba, Japan).

References

- Andersson, U., Tracey, K.J., 2012. Reflex principles of immunological homeostasis. *Annu. Rev. Immunol.* 30, 313–335. <https://doi.org/10.1146/annurev-immunol-020711-075015>.
- Bai, S., Xie, J., Bai, H., Tian, T., Zou, T., Chen, J.J., 2021. Gut microbiota-derived inflammation-related serum metabolites as potential biomarkers for major depressive disorder. *J. Inflamm. Res.* 14, 3755–3766. <https://doi.org/10.2147/JIR.S324922>.
- Bartoli, F., Misiak, B., Callovini, T., Cavaleri, D., Cioni, R.M., Crocarno, C., Savitz, J.B., Carrà, G., 2021. The kynurenine pathway in bipolar disorder: a meta-analysis on the peripheral blood levels of tryptophan and related metabolites. *Mol. Psychiatry* 26 (7), 3419–3429. <https://doi.org/10.1038/s41380-020-00913-1>.
- Bonaz, B., Bazin, T., Pellissier, S., 2018. The vagus nerve at the interface of the microbiota-gut-brain axis. *Front. Neurosci.* 12, 49. <https://doi.org/10.3389/fnins.2018.00049>.
- Brydges, C.R., Bhattacharyya, S., Dehkordi, S.M., Milanese, Y., Penninx, B., Jansen, R., Kristal, B.S., Han, X., Arnold, M., Kastenmüller, G., Bekhbat, M., Mayberg, H.S., Craighead, W.E., Rush, A.J., Fiehn, O., Dunlop, B.W., Kaddurah-Daouk, R., Mood Disorders Precision Medicine Consortium, 2022. Metabolomic and inflammatory signatures of symptom dimensions in major depression. *Brain Behav. Immun.* 102, 42–52. <https://doi.org/10.1016/j.bbi.2022.02.003>.
- Caso, J.R., MacDowell, K.S., González-Pinto, A., García, S., de Diego-Adeliño, J., Carceller-Sindreu, M., Sarramea, F., Caballero-Villarraso, J., Gracia-García, P., De la Cámara, C., Agüera, L., Gómez-Lus, M.L., Alba, C., Rodríguez, J.M., Leza, J.C., 2021. Gut microbiota, innate immune pathways, and inflammatory control mechanisms in patients with major depressive disorder. *Transl. Psychiatry* 11 (1), 645. <https://doi.org/10.1038/s41398-021-01755-3>.
- Cawthon, C.R., de La Serre, C.B., 2018. Gut bacteria interaction with vagal afferents. *Brain Res.* 1693, 134–139. <https://doi.org/10.1016/j.brainres.2018.01.012>.
- Chang, L., Wei, Y., Hashimoto, K., 2022. Brain-gut-microbiota axis in depression: a historical overview and future directions. *Brain Res. Bull.* 182, 44–56. <https://doi.org/10.1016/j.brainresbull.2022.02.004>.
- Cryan, J.F., O'Riordan, K.J., Cowan, C.S.M., Sandhu, K.V., Bastiaansen, T.F.S., Boehme, M., Codagnone, M.G., Cusotto, S., Fulling, C., Golubeva, A.V., Guzzetta, K. E., Jaggard, M., Long-Smith, C.M., Lyte, J.M., Martin, J.A., Molinero-Perez, A., Moloney, G., Morelli, E., Morillas, E., O'Connor, R., Cruz-Pereira, J.S., Peterson, V.L., Rea, K., Ritz, N.L., Sherwin, E., Spichak, S., Teichman, E.M., van de Wouw, M., Ventura-Silva, A.P., Wallace-Fitzsimons, S.E., Hyland, N., Clarke, G., Dinan, T.G., 2019. The microbiota-gut-brain axis. *Physiol. Rev.* 99 (4), 1877–2013. <https://doi.org/10.1152/physrev.00018.2018>.
- Dani, J.A., 2015. Neuronal nicotinic acetylcholine receptor structure and function and response to nicotine. *Int. Rev. Neurobiol.* 124, 3–19. <https://doi.org/10.1016/bs.inr.2015.07.001>.

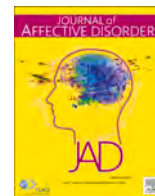
- Dani, J.A., Bertrand, D., 2007. Nicotinic acetylcholine receptors and nicotinic cholinergic mechanisms of the central nervous system. *Annu. Rev. Pharmacol. Toxicol.* 47, 699–729. <https://doi.org/10.1146/annurev.pharmtox.47.120505.105214>.
- Forsythe, P., Bienenstock, J., Kunze, W.A., 2014. Vagal pathways for microbiome-brain-gut axis communication. *Adv. Exp. Med. Biol.* 817, 115–133. https://doi.org/10.1007/978-1-4939-0897-4_5.
- Haroon, E., Raison, C.L., Miller, A.H., 2012. Psychoneuroimmunology meets neuropsychopharmacology: translational implications of the impact of inflammation on behavior. *Neuropsychopharmacology*. 37 (1), 137–162. <https://doi.org/10.1038/npp.2011.205>.
- Hashimoto, K., 2009. Emerging role of glutamate in the pathophysiology of major depressive disorder. *Brain Res. Rev.* 61 (2), 105–123. <https://doi.org/10.1016/j.brainresrev.2009.05.005>.
- Hashimoto, K., 2015. Inflammatory biomarkers as differential predictors of antidepressant response. *Int. J. Mol. Sci.* 16 (4), 7796–7801. <https://doi.org/10.3390/ijms16047796>.
- Hashimoto, K., 2020. Molecular mechanisms of the rapid-acting and long-lasting antidepressant actions of (R)-ketamine. *Biochem. Pharmacol.* 177, 113935 <https://doi.org/10.1016/j.bcp.2020.113935>.
- Hashimoto, K., 2022. Gut–microbiota–brain by bile acids in depression. *Psychiatry Clin. Neurosci.* 76 (7), 281. <https://doi.org/10.1111/pcn.13370>.
- Hess, S., Baker, G., Gyenes, G., Tsuyuki, R., Newman, S., Le Melleo, J.M., 2017. Decreased serum L-arginine and L-citrulline levels in major depression. *Psychopharmacology* 234 (21), 3241–3247. <https://doi.org/10.1007/s00213-017-4712-8>.
- Huang, N., Hua, D., Zhan, G., Li, S., Zhu, B., Jiang, R., Yang, L., Bi, J., Xu, H., Hashimoto, K., Luo, A., Yang, C., 2019. Role of *Actinobacteria* and *Coriobacteriia* in the antidepressant effects of ketamine in an inflammation model of depression. *Pharmacol. Biochem. Behav.* 176, 93–100. <https://doi.org/10.1016/j.pbb.2018.12.001>.
- Jiang, H., Ling, Z., Zhang, Y., Mao, H., Ma, Z., Yin, Y., Wang, W., Tang, W., Tan, Z., Shi, J., Li, L., Ruan, B., 2015. Altered fecal microbiota composition in patients with major depressive disorder. *Brain Behav. Immun.* 48, 186–194. <https://doi.org/10.1016/j.bbi.2015.03.016>.
- Kelly, J.R., Borre, Y., O'Brien, C., Patterson, E., El Aidy, S., Deane, J., Kennedy, P.J., Beers, S., Scott, K., Moloney, G., Hoban, A.E., Scott, L., Fitzgerald, P., Ross, P., Stanton, C., Clarke, G., Cryan, J.F., Dinan, T.G., 2016. Transferring the blues: depression-associated gut microbiota induces neurobehavioural changes in the rat. *J. Psychiatr. Res.* 82, 109–118. <https://doi.org/10.1016/j.jpsychires.2016.07.019>.
- Lei, W., Duan, Z., 2021. Advances in the treatment of cholinergic anti-inflammatory pathways in gastrointestinal diseases by electrical stimulation of vagus nerve. *Digestion* 102 (2), 128–138. <https://doi.org/10.1159/000504474>.
- Li, Z., Lai, J., Zhang, P., Ding, J., Jiang, J., Liu, C., Huang, H., Zhen, H., Xi, C., Sun, Y., Wu, L., Wang, L., Gao, X., Li, Y., Fu, Y., Jie, Z., Li, S., Zhang, D., Chen, Y., Zhu, Y., Lu, S., Lu, J., Wang, D., Zhou, H., Yuan, X., Li, X., Pang, L., Huang, M., Yang, H., Zhang, W., Brix, S., Kristiansen, K., Song, X., Nie, C., Hu, S., 2022. Multi-omics analyses of serum metabolome, gut microbiome and brain function reveal dysregulated microbiota-gut-brain axis in bipolar depression. *Mol. Psychiatry*. <https://doi.org/10.1038/s41380-022-01569-9>.
- Liu, J.J., Wei, Y.B., Strawbridge, R., Bao, Y., Chang, S., Shi, L., Que, J., Gadad, B.S., Trivedi, M.H., Kelseo, J.R., Lu, L., 2020. Peripheral cytokine levels and response to antidepressant treatment in depression: a systematic review and meta-analysis. *Mol. Psychiatry* 25 (2), 339–350. <https://doi.org/10.1038/s41380-019-0474-5>.
- Loeb, E., El Asmar, K., Trabado, S., Gressier, F., Colle, R., Rigal, A., Martin, S., Verstuyft, C., Fève, B., Chanson, P., Becquomont, L., Corruble, E., 2020. Nitric oxide synthase activity in major depressive episodes before and after antidepressant treatment: results of a large case-control treatment study. *Psychol. Med.* 1–10. <https://doi.org/10.1017/S0033291720001749>.
- Lucido, M.J., Bekhbat, M., Goldsmith, D.R., Treadway, M.T., Haroon, E., Felger, J.C., Miller, A.H., 2021. Aiding and abetting anhedonia: impact of inflammation on the brain and pharmacological implications. *Pharmacol. Rev.* 73 (3), 1084–1117. <https://doi.org/10.1124/pharmrev.120.000043>.
- Mac Giollabhui, N., Ng, T.H., Ellman, L.M., Alloy, L.B., 2021. The longitudinal associations of inflammatory biomarkers and depression revisited: systematic review, meta-analysis, and meta-regression. *Mol. Psychiatry* 26 (7), 3302–3314. <https://doi.org/10.1038/s41380-020-00867-4>.
- Martelli, D., McKinley, M.J., McAllen, R.M., 2014. The cholinergic anti-inflammatory pathway: a critical review. *Auton. Neurosci.* 182, 65–69. <https://doi.org/10.1016/j.autneu.2013.12.007>.
- McVey Neufeld, K.A., Bienenstock, J., Bharwani, A., Champagne-Jorgensen, K., Mao, Y., West, C., Liu, Y., Surette, M.G., Kunze, W., Forsythe, P., 2019. Oral selective serotonin reuptake inhibitors activate vagus nerve dependent gut-brain signalling. *Sci. Rep.* 9 (1), 14290. <https://doi.org/10.1038/s41598-019-50807-8>.
- Miller, A.H., Raison, C.L., 2016. The role of inflammation in depression: from evolutionary imperative to modern treatment target. *Nat. Rev. Immunol.* 16 (1), 22–34. <https://doi.org/10.1038/nri.2015.5>.
- Nikolova, V.L., Hall, M.R.B., Hall, L.J., Cleare, A.J., Stone, J.M., Young, A.H., 2021. Perturbations in gut microbiota composition in psychiatric disorders: a review and meta-analysis. *JAMA Psychiatry* 78 (12), 1343–1354. <https://doi.org/10.1001/jamapsychiatry.2021.2573>.
- Olofsson, P.S., Rosas-Ballina, M., Levine, Y.A., Tracey, K.J., 2012. Rethinking inflammation: neural circuits in the regulation of immunity. *Immunol. Rev.* 248 (1), 188–204. <https://doi.org/10.1111/j.1600-065X.2012.01138.x>.
- O'Mahony, C., van der Kleij, H., Bienenstock, J., Shanahan, F., O'Mahony, L., 2009. Loss of vagal anti-inflammatory effect: in vivo visualization and adoptive transfer. *Am. J. Physiol. Regul. Integr. Comp. Physiol.* 297 (4), R1118–R1126. <https://doi.org/10.1152/ajpregu.90904.2008>.
- Park, A.J., Collins, J., Blennerhassett, P.A., Ghia, J.E., Verdu, E.F., Bercik, P., Collins, S.M., 2013. Altered colonic function and microbiota profile in a mouse model of chronic depression. *Neurogastroenterol. Motil.* 25 (9), 733–e575. <https://doi.org/10.1111/nmo.12153>.
- Piovesana, R., Salazar Intriago, M.S., Dini, L., Tata, A.M., 2021. Cholinergic modulation of neuroinflammation: focus on $\alpha 7$ nicotinic receptor. *Int. J. Mol. Sci.* 22 (9), 4912. <https://doi.org/10.3390/ijms22094912>.
- Pu, J., Liu, Y., Zhang, H., Tian, L., Gui, S., Yu, Y., Chen, X., Chen, Y., Yang, L., Ran, Y., Zhong, X., Xu, S., Song, X., Liu, L., Zheng, P., Wang, H., Xie, P., 2021a. An integrated meta-analysis of peripheral blood metabolites and biological functions in major depressive disorder. *Mol. Psychiatry* 26 (8), 4265–4276. <https://doi.org/10.1038/s41380-020-0645-4>.
- Pu, Y., Tan, Y., Qu, Y., Chang, L., Wang, S., Wei, Y., Wang, X., Hashimoto, K., 2021b. A role of the subdiaphragmatic vagus nerve in depression-like phenotypes in mice after fecal microbiota transplantation from *Chrm7* knock-out mice with depression-like phenotypes. *Brain Behav. Immun.* 94, 318–326. <https://doi.org/10.1016/j.bbi.2020.12.032>.
- Pu, Y., Zhang, Q., Tang, Z., Lu, C., Wu, L., Zhong, Y., Chen, Y., Hashimoto, K., Luo, Y., Liu, Y., 2022. Fecal microbiota transplantation from patients with rheumatoid arthritis causes depression-like behaviors in mice through abnormal T cells activation. *Transl. Psychiatry* 12 (1), 223. <https://doi.org/10.1038/s41398-022-01993-z>.
- Qu, Y., Yang, C., Ren, Q., Ma, M., Dong, C., Hashimoto, K., 2017. Comparison of (R)-ketamine and lanicemine on depression-like phenotype and abnormal composition of gut microbiota in a social defeat stress model. *Sci. Rep.* 7 (1), 15725. <https://doi.org/10.1038/s41598-017-16060-7>.
- Sanada, K., Nakajima, S., Kurokawa, S., Barceló-Soler, A., Ikuse, D., Hirata, A., Yoshizawa, A., Tomizawa, Y., Salas-Valero, M., Noda, Y., Mimura, M., Iwanami, A., Kishimoto, T., 2020. Gut microbiota and major depressive disorder: a systematic review and meta-analysis. *J. Affect. Disord.* 266, 1–13. <https://doi.org/10.1016/j.jad.2020.01.102>.
- Schymanski, E.L., Jeon, J., Gulde, R., Fenner, K., Ruff, M., Singer, H.P., Hollender, J., 2014. Identifying small molecules via high resolution mass spectrometry: communicating confidence. *Environ. Sci. Technol.* 48 (4), 2097–2098. <https://doi.org/10.1021/es5002105>.
- Segata, N., Izard, J., Waldron, L., Gevers, D., Miropolsky, L., Garrett, W.S., Huttenhower, C., 2011. Metagenomic biomarker discovery and explanation. *Genome Biol.* 12 (6), R60. <https://doi.org/10.1186/gb-2011-12-6-r60>.
- Shan, J., Hashimoto, K., 2022. Soluble epoxide hydrolase as a therapeutic target for neuropsychiatric disorders. *Int. J. Mol. Sci.* 23 (9), 4951. <https://doi.org/10.3390/ijms23094951>.
- Toenders, Y.J., Laskaris, L., Davey, C.G., Berk, M., Milanese, Y., Lamers, F., Penninx, B.W.J.H., Schmaal, L., 2022. Inflammation and depression in young people: a systematic review and proposed inflammatory pathways. *Mol. Psychiatry* 27 (1), 315–327. <https://doi.org/10.1038/s41380-021-01306-8>.
- Tran, S.M., Mohajeri, M.H., 2021. The role of gut bacterial metabolites in brain development, aging and disease. *Nutrients* 13 (3), 732. <https://doi.org/10.3390/nu13030732>.
- Tsugawa, H., Cajka, T., Kind, T., Ma, Y., Higgins, B., Ikeda, K., Kanazawa, M., VanderGheynst, J., Fiehn, O., Arita, M., 2015. MS-DIAL: data-independent MS/MS deconvolution for comprehensive metabolome analysis. *Nat. Methods* 12 (6), 523–526. <https://doi.org/10.1038/nmeth.3393>.
- Ulloa, L., 2005. The vagus nerve and the nicotinic anti-inflammatory pathway. *Nat. Rev. Drug Discov.* 4 (8), 673–684. <https://doi.org/10.1038/nrd1797>.
- Wan, X., Eguchi, A., Fujita, Y., Ma, L., Wang, X., Yang, Y., Qu, Y., Chang, L., Zhang, J., Mori, C., Hashimoto, K., 2022a. Effects of (R)-ketamine on reduced bone mineral density in ovariectomized mice: a role of gut microbiota. *Neuropharmacol.* 213, 109139. <https://doi.org/10.1016/j.neuropharm.2022.109139>.
- Wan, X., Eguchi, A., Qu, Y., Yang, Y., Chang, L., Shan, J., Mori, C., Hashimoto, K., 2022b. Gut–microbiota–brain axis in the vulnerability to psychosis in adulthood after repeated cannabis exposure during adolescence. *Eur. Arch. Psychiatry Clin. Neurosci.* 272 (7), 1297–1309. <https://doi.org/10.1007/s00406-022-01437-1>.
- Wang, H., Yu, M., Ochani, M., Amella, C.A., Tanovic, M., Susarla, S., Li, J.H., Wang, H., Yang, H., Ulloa, L., Al-Abed, Y., Czura, C.J., Tracey, K.J., 2003. Nicotinic acetylcholine receptor $\alpha 7$ subunit is an essential regulator of inflammation. *Nature*. 421 (6921), 384–388. <https://doi.org/10.1038/nature01339>.
- Wang, S., Ishima, T., Zhang, J., Qu, Y., Chang, L., Pu, Y., Fujita, Y., Tan, Y., Wang, X., Hashimoto, K., 2020a. Ingestion of *Lactobacillus intestinalis* and *Lactobacillus reuteri* causes depression- and anhedonia-like phenotypes in antibiotic-treated mice via the vagus nerve. *J. Neuroinflammation* 17 (1), 241. <https://doi.org/10.1186/s12974-020-01916-z>.
- Wang, S., Qu, Y., Chang, L., Pu, Y., Zhang, K., Hashimoto, K., 2020b. Antibiotic-induced microbiome depletion is associated with resilience in mice after chronic social defeat stress. *J. Affect. Disord.* 260, 448–457. <https://doi.org/10.1016/j.jad.2019.09.064>.
- Wang, S., Ishima, T., Qu, Y., Shan, J., Chang, L., Wei, Y., Zhang, J., Pu, Y., Fujita, Y., Tan, Y., Wang, X., Ma, L., Wan, X., Hammock, B.D., Hashimoto, K., 2021. Ingestion of *Faecalibaculum rodentium* causes depression-like phenotypes in resilient *Ephx2* knock-out mice: a role of brain-gut-microbiota axis via the subdiaphragmatic vagus nerve. *J. Affect. Disord.* 292, 565–573. <https://doi.org/10.1016/j.jad.2021.06.006>.
- Wei, Y., Chang, L., Hashimoto, K., 2022a. Molecular mechanisms underlying the antidepressant actions of arketamine: beyond the NMDA receptor. *Mol. Psychiatry* 27 (1), 559–573. <https://doi.org/10.1038/s41380-021-01121-1>.

- Wei, Y., Wang, T., Liao, L., Fan, X., Chang, L., Hashimoto, K., 2022b. Brain-spleen axis in health and diseases: a review and future perspective. *Brain Res. Bull.* 182, 130–140. <https://doi.org/10.1016/j.brainresbull.2022.02.008>.
- WHO, 2021. Depression. <https://www.who.int/news-room/fact-sheets/default/depression>.
- Wong, M.L., Inserra, A., Lewis, M.D., Mastronardi, C.A., Leong, L., Choo, J., Kentish, S., Xie, P., Morrison, M., Wesselingh, S.L., Rogers, G.B., Licinio, J., 2016. Inflammasome signaling affects anxiety- and depressive-like behavior and gut microbiome composition. *Mol. Psychiatry* 21 (6), 797–805. <https://doi.org/10.1038/mp.2016.46>.
- Wu, Y.J., Wang, L., Ji, C.F., Gu, S.F., Yin, Q., Zuo, J., 2021. The role of $\alpha 7$ nAChR-mediated cholinergic anti-inflammatory pathway in immune cells. *Inflammation*. 44 (3), 821–834. <https://doi.org/10.1007/s10753-020-01396-6>.
- Xu, F., Zhao, L.H., Wang, X.H., Wang, C.H., Yu, C., Zhang, X.L., Ning, L.Y., Huang, H.Y., Su, J.B., Wang, X.Q., 2022. Plasma 1,5-anhydro-D-glucitol is associated with peripheral nerve function and diabetic peripheral neuropathy in patients with type 2 diabetes and mild-to-moderate hyperglycemia. *Diabetol. Metab. Syndr.* 14 (1), 24. <https://doi.org/10.1186/s13098-022-00795-z>.
- Yang, C., Shirayama, Y., Zhang, J.C., Ren, Q., Yao, W., Ma, M., Dong, C., Hashimoto, K., 2015. R-ketamine: a rapid-onset and sustained antidepressant without psychotomimetic side effects. *Transl. Psychiatry* 5 (9), e632. <https://doi.org/10.1038/tp.2015.136>.
- Yang, C., Qu, Y., Fujita, Y., Ren, Q., Ma, M., Dong, C., Hashimoto, K., 2017. Possible role of the gut microbiota-brain axis in the antidepressant effects of (R)-ketamine in a social defeat stress model. *Transl. Psychiatry* 7 (12), 1294. <https://doi.org/10.1038/s41398-017-0031-4>.
- Yang, C., Fang, X., Zhan, G., Huang, N., Li, S., Bi, J., Jiang, R., Yang, L., Miao, L., Zhu, B., Luo, A., Hashimoto, K., 2019. Key role of gut microbiota in anhedonia-like phenotype in rodents with neuropathic pain. *Transl. Psychiatry* 9 (1), 57. <https://doi.org/10.1038/s41398-019-0379-8>.
- Yang, H., George, S.J., Thompson, D.A., Silverman, H.A., Tsaava, T., Tynan, A., Pavlov, V.A., Chang, E.H., Andersson, U., Brines, M., Chavan, S.S., Tracey, K.J., 2022a. Famotidine activates the vagus nerve inflammatory reflex to attenuate cytokine storm. *Mol. Med.* 28 (1), 57. <https://doi.org/10.1186/s10020-022-00483-8>.
- Yang, Y., Ishima, T., Wan, X., Wei, Y., Chang, L., Zhang, J., Qu, Y., Hashimoto, K., 2022b. Microglial depletion and abnormalities in gut microbiota composition and short-chain fatty acids in mice after repeated administration of colony stimulating factor 1 receptor inhibitor PLX5622. *Eur. Arch. Psychiatry Clin. Neurosci.* 272 (3), 483–495. <https://doi.org/10.1007/s00406-021-01325-0>.
- Zhang, J.C., Wu, J., Fujita, Y., Yao, W., Ren, Q., Yang, C., Li, S.X., Shirayama, Y., Hashimoto, K., 2014. Antidepressant effects of TrkB ligands on depression-like behavior and dendritic changes in mice after inflammation. *Int. J. Neuropsychopharmacol.* 18 (4), pyu077. <https://doi.org/10.1093/ijnp/pyu077>.
- Zhang, J.C., Yao, W., Hashimoto, K., 2016a. Brain-derived neurotrophic factor (BDNF)-TrkB signaling in inflammation-related depression and potential therapeutic targets. *Curr. Neuropharmacol.* 14 (7), 721–731. <https://doi.org/10.2174/1570159x146666160119094646>.
- Zhang, J.C., Yao, W., Ren, Q., Yang, C., Dong, C., Ma, M., Wu, J., Hashimoto, K., 2016b. Depression-like phenotype by deletion of $\alpha 7$ nicotinic acetylcholine receptor: role of BDNF-TrkB in nucleus accumbens. *Sci. Rep.* 6, 36705. <https://doi.org/10.1038/srep36705>.
- Zhang, J.C., Yao, W., Dong, C., Ren, Q., Ma, M., Hashimoto, K., 2017. Blockade of interleukin-6 receptor in the periphery promotes rapid and sustained antidepressant actions: a possible role of gut-microbiota-brain axis. *Transl. Psychiatry* 7 (5), e1138. <https://doi.org/10.1038/tp.2017.112>.
- Zhang, K., Fujita, Y., Chang, L., Qu, Y., Pu, Y., Wang, S., Shirayama, Y., Hashimoto, K., 2019. Abnormal composition of gut microbiota is associated with resilience versus susceptibility to inescapable electric stress. *Transl. Psychiatry* 9 (1), 231. <https://doi.org/10.1038/s41398-019-0571-x>.
- Zhang, J., Ma, L., Chang, L., Pu, Y., Qu, Y., Hashimoto, K., 2020. A key role of the subdiaphragmatic vagus nerve in the depression-like phenotype and abnormal composition of gut microbiota in mice after lipopolysaccharide administration. *Transl. Psychiatry* 10 (1), 186. <https://doi.org/10.1038/s41398-020-00878-3>.
- Zheng, P., Zeng, B., Zhou, C., Liu, M., Fang, Z., Xu, X., Zeng, L., Chen, J., Fan, S., Du, X., Zhang, X., Yang, D., Yang, Y., Meng, H., Li, W., Melgiri, N.D., Licinio, J., Wei, H., Xie, P., 2016. Gut microbiome remodeling induces depressive-like behaviors through a pathway mediated by the host's metabolism. *Mol. Psychiatry* 21 (6), 786–796. <https://doi.org/10.1038/mp.2016.44>.



Contents lists available at ScienceDirect

Journal of Affective Disorders

journal homepage: www.elsevier.com/locate/jad

Research paper

Depression-like phenotypes in mice with hepatic ischemia/reperfusion injury: A role of gut–microbiota–liver–brain axis via vagus nerve

Yong Yang^{a,b}, Akifumi Eguchi^c, Xiayun Wan^a, Chisato Mori^{c,d}, Kenji Hashimoto^{a,*}^a Division of Clinical Neuroscience, Chiba University Center for Forensic Mental Health, Chiba 260-8670, Japan^b Department of Neurosurgery, Guizhou Provincial People's Hospital, Guiyang 550002, China^c Department of Sustainable Health Science, Chiba University Center for Preventive Medical Sciences, Chiba 263-8522, Japan^d Department of Bioenvironmental Medicine, Graduate School of Medicine, Chiba University, Chiba 260-8670, Japan

ARTICLE INFO

Keywords:

Arketamine
Depression
Gut microbiota
Liver
Metabolites
Vagus nerve

ABSTRACT

Depression is a frequent symptom in patients with chronic liver disease; however, the mechanisms underlying this association remain unclear. Dysbiosis of gut microbiota plays a critical role in depression through the gut–brain axis via the vagus nerve. In this study, we investigated whether the gut–microbiota–liver–brain axis plays a role in depression-like phenotypes in mice with hepatic ischemia/reperfusion (HI/R) injury via the vagus nerve. Behavioral tests for depression-like behaviors were performed 7 days after sham or HI/R injury surgery. Mice with HI/R injury exhibited splenomegaly, systemic inflammation, depression-like behaviors, reduced expression of synaptic proteins in the prefrontal cortex (PFC), abnormal composition of gut microbiota, and altered blood metabolites and lipids. Furthermore, there were positive or negative correlations between the relative abundance of microbiome and behavioral data or blood metabolites (or lipids). Moreover, subdiaphragmatic vagotomy significantly blocked these changes in mice with HI/R injury. Notably, depression-like phenotypes in mice with HI/R injury were ameliorated after subsequent single injection of the new antidepressant arketamine. The current findings suggest that HI/R injury induces depression-like phenotypes in mice through the gut–microbiota–liver–brain axis via the subdiaphragmatic vagus nerve. Furthermore, arketamine may have therapeutic potential in the treatment of depression in patients with chronic liver disease.

1. Introduction

Chronic liver disease (CLD) is a progressive disorder characterized by the degeneration and regeneration of the liver parenchyma, leading to fibrosis and cirrhosis. The prevalence of depression is higher in patients with CLD than in the general population, suggesting a link between the two disorders (Gutteling et al., 2006; Kronsten et al., 2022; Mullish et al., 2014; Patten et al., 2008). A recent review revealed a high prevalence of depression in patients with CLD, including chronic hepatitis B, chronic hepatitis, alcoholic liver disease, and non-alcoholic fatty liver disease (Huang et al., 2017). Interestingly, signs of psychological distress and depression in patients with cirrhosis are associated with the severity of liver disease (Bianchi et al., 2005). Although depression is a common psychiatric symptom in patients with CLD, the pathogenetic mechanisms underlying this association are not well understood.

Multiple lines of evidence from clinical and pre-clinical studies suggest a role of the gut–microbiota–brain axis in depression (Chang

et al., 2022; Cryan et al., 2019; Jiang et al., 2015; Liu et al., 2023; Sanada et al., 2020; Wei et al., 2022a; Zheng et al., 2016). Notably, the vagus nerve plays an important role in the bidirectional communication between the gut microbiota and the brain (Bonaz et al., 2018; Chang et al., 2022; Forsythe et al., 2014; Hashimoto, 2023a; Wei et al., 2022a). Interestingly, subdiaphragmatic vagotomy (SDV) prevents the onset of depression-like behaviors and changes in the composition of the gut microbiota in mice caused by injection of lipopolysaccharide (LPS) (Zhang et al., 2020) and fecal microbiota transplantation from mice with depression-like phenotypes (Pu et al., 2021; Wang et al., 2020, 2021). Furthermore, SDV blocks depression-like behaviors in *Chrna7* knock-out mice (Yang et al., 2023) and working memory impairment in mice with chronic inflammatory pain (Yue et al., 2023). Taken together, these observations suggest that the gut microbiota–brain axis plays a critical role in depression via the subdiaphragmatic vagus nerve (Chang et al., 2022; Hashimoto, 2023a; Wei et al., 2022a). Kronsten et al. (2022) proposed that gut-mediated systemic inflammation might contribute to

* Corresponding author.

E-mail address: hashimoto@faculty.chiba-u.jp (K. Hashimoto).<https://doi.org/10.1016/j.jad.2023.10.142>

Received 26 May 2023; Received in revised form 14 October 2023; Accepted 22 October 2023

Available online 24 October 2023

0165-0327/© 2023 Elsevier B.V. All rights reserved.

the close relationship between depression and CLD, suggesting abnormalities in the gut–liver–brain axis.

Hepatic ischemia/reperfusion (HI/R) injury causes damage to the liver parenchyma. HI/R injury is a major complication of liver surgery, including liver resection, and liver transplantation (Hirao et al., 2022; Konishi and Lentsch, 2017). Despite technological advances over the last decade, the mechanisms of HI/R injury remain unclear because of the complexity of the underlying pathogenetic processes (Rampes and Ma, 2019). Rodent models of HI/R injury have been widely used; however, there are no reports showing depression-like phenotypes in rodents with HI/R injury. There are also no reports on the role of the gut–liver–brain axis, via the vagus nerve, in rodents with HI/R injury.

Here, we investigated the link between depression and CLD. We evaluated depression-like behaviors in mice with HI/R injury, and we measured blood inflammation, and synaptic proteins in the brain. We also performed 16 s rRNA analysis of feces samples, as well as untargeted metabolomics and lipidomic analyses of plasma samples to examine the role of the gut microbiota–brain axis in the depression-like behaviors. Additionally, we examined the role of the subdiaphragmatic vagus nerve on these depression-like phenotypes by performing SDV. Furthermore, we investigated the effects of the new antidepressant arketamine in mice with HI/R injury since a single dose showed rapid-acting antidepressant-like effects in rodents with depression-like phenotypes (Hashimoto, 2020, 2023a, 2023b; Wei et al., 2022b; Yang et al., 2015, 2019; Zhang et al., 2014, 2022a; Zhang et al., 2023).

2. Materials and methods

2.1. Animals

Male adult C57BL/6Ncr mice were purchased from the Japan SLC Co., Ltd. (Hamamatsu, Shizuoka, Japan). All the experimental mice were aged 9 weeks, body weight 18–28 g. All the experimental mice were acclimatized to standard laboratory conditions (4 or 5/cage), maintain alternating cycles of 12 h of light and 12 h of darkness (lights on from 7:00–19:00), and under constant room temperature of 23 ± 1 °C and controlled humidity of 55 ± 5 %. Animals were given free admittance to chow and water. The experimental protocol of this study was approved by the Chiba University Institutional Animal Care and Use Committee (Permission number: 4–314, 4–375 and 4–438). The experimental mice were deeply anesthetized with inhaled isoflurane and then rapidly sacrificed by cervical dislocation. All efforts were made to minimize animals suffering.

2.2. Reagents

Arketamine [or (R)-ketamine] hydrochloride was prepared as reported previously (Zhang et al., 2014). The dose (10 mg/kg as hydrochloride salt) of arketamine was dissolved in the saline as reported previously (Yang et al., 2015; Zhang et al., 2014). Other reagents were purchased commercially.

2.3. Hepatic ischemia-reperfusion (HI/R) injury

Sham surgery or 70 % HI/R was performed under continuous inhalation anesthesia with 4–5 % isoflurane by using an inhalation small animal anesthesia apparatus (KN-1071 NARCOBIT-E; Natsume Seisakusho, Tokyo, Japan), according to the previous method (Ji et al., 2010, 2013) with a slight modification. Briefly, the arterial/portal vessels to the left and middle lobes of the liver were clamped for 1 h, while preserving blood flow to the right and caudate lobes. There was no vascular occlusion in sham group mice.

2.4. Bilateral subdiaphragmatic vagotomy (SDV)

Bilateral SDV or sham surgery was performed under continuous

inhalation anesthesia with 4–5 % isoflurane using an inhalation small animal anesthesia apparatus (KN-1071 NARCOBIT-E; Natsume Seisakusho, Tokyo, Japan) according to previous methods (Pu et al., 2021; Wang et al., 2020, 2021; Yang et al., 2023; Zhang et al., 2020). During the sham operation, the abdominal wall incision of the same size was made in the same way at the same site. After the dorsal and ventral branches of the subdiaphragmatic vagus nerve were also softly exposed but not cut off. When the HI/R + SDV procedure was performed, the SDV was performed first through the same abdominal approach, followed by the HI/R procedure.

2.5. Behavioral tests

Behavioral tests, including locomotion test (LMT), forced swimming test (FST), and 1 % sucrose preference test (SPT) were performed as reported previously (Pu et al., 2021; Yang et al., 2023).

2.6. Enzyme-linked immunosorbent assay (ELISA)

ELISA kits for the measurement of interleukin-6 (IL-6) (cat number: 88-7064, Invitrogen, Camarillo, CA, USA), and tumor necrosis factor- α (TNF- α) (cat number: 88-7324, Invitrogen, Camarillo, CA, USA) were used.

2.7. Western blotting analysis

Western blotting analysis was performed as previously reported (Yang et al., 2022, 2023). The PFC tissues were homogenized in ice-cold Laemmli lysis buffer. To avoid cross-contamination, each specimen was prepared separately. Then liquid supernatants were collected after centrifugation at $3000 \times g$ (RCF) at 4 °C for 20 min. The total protein concentration extracted from each sample was detected on a spectrophotometer (Molecular Devices Emmax Precision Microplate Reader; Molecular Devices., San Jose, CA, USA) using a DC protein assay kit (Bio-Rad, Hercules, CA, USA). By adding a quarter volume of sample buffer (125 mM Tris-HCl, pH 6.8; 0.1 % bromophenol blue; 4 % sodium dodecyl sulfate; and 10 % β -mercaptoethanol and 20 % glycerol) and Laemmli Lysis buffer in appropriate proportions to balance the total protein concentration of each sample, then incubate them at 95 °C for 10 min.

Considering the size of target protein, we chose 10 % sodium dodecyl sulfate–polyacrylamide gel electrophoresis (SDS-PAGE) (catalog #: 4568125, Mini-PROTEAN TGX™ Stain-Free Gels; Bio-Rad, USA) separated the proteins by gel electrophoresis. Then a Trans-Blot Mini Cell apparatus (Bio-Rad) was used to electrotransfer the target protein onto polyvinylidene difluoride membranes.

Synaptic proteins such as glutamate receptor 1 (AMPA subtype: GluA1: [the α -amino-3-hydroxy-5-methyl-4-isoxazolepropionic acid receptor A1]) and postsynaptic density protein 95 (PSD-95) were decreased in the PFC of mice with depression-like phenotypes (Pu et al., 2021; Wang et al., 2020, 2021; Yang et al., 2023). Ionized calcium-binding adapter molecule 1 (Iba1) is a specific marker for microglia in the brain. For immunodetection, the polyvinylidene difluoride membranes were blocked with blocker [5 % skim milk in TBS + 0.1 % Tween-20 (TBST)] at room temperature for 1 h, the membranes for detecting PSD-95 were incubated with the recommended dilution of the primary antibody against PSD-95 (1:1000, catalog number: 51-6900695, 1 μ g/mL, Invitrogen, Camarillo, CA, USA), while the membranes for detecting Iba1 and β -actin were incubated with the appropriate dilution of the primary antibody against Iba1 (1:1000, catalog number: 016-20001, 1 μ g/mL, FUJIFILM, Tokyo, Japan) and β -actin (1:10,000; catalog number: A5441 Sigma-Aldrich Co., Ltd., St Louis, MO, USA) at 4 °C overnight. The next day, wash the polyvinylidene difluoride membranes in three washes of TBST, 10 min each. Then the polyvinylidene difluoride membranes were selectively incubated with a recommended dilution of labeled secondary antibody [anti-mouse antibody (1:5000, catalog

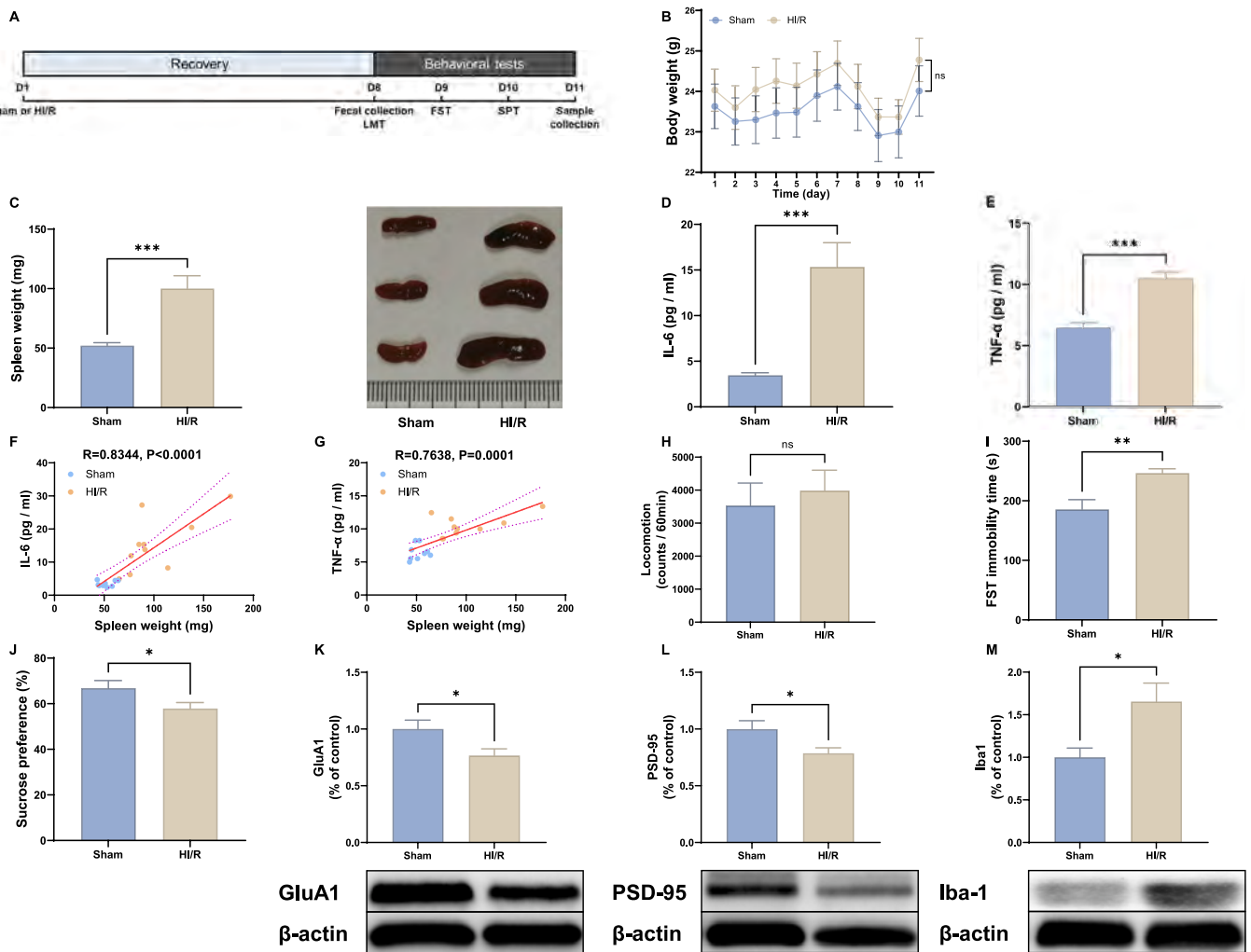


Fig. 1. Depression-like phenotypes in mice with HI/R injury.

(A): Experimental schedule. On day 1, sham or HI/R surgery was performed, and they were recovered 7 days. On day 8, fresh feces samples were collected, and subsequently LMT was performed. FST and 1 % SPT were performed on day 9 and day 10, respectively. On day 11, prefrontal cortex (PFC) and plasma samples were collected. (B): Body weight (repeated measure ANOVA, $F_{(1, 17)} = 0.5576, P = 0.4654$). (C): Spleen weight (unpaired t-test, $t = 4.131, df = 17, P = 0.0007$) and representative photograph of spleen in the two groups. (D): Plasma levels of IL-6 (unpaired t-test, $t = 4.207, df = 17, P = 0.0006$). (E): Plasma levels of TNF- α (unpaired t-test, $t = 6.232, df = 17, P < 0.0001$). (F): There was a positive correlation ($R = 0.8344, P < 0.0001$) between the spleen weight and plasma levels of IL-6 in two groups. (G): There was a positive correlation ($R = 0.7638, P = 0.0001$) between the spleen weight and plasma levels of TNF- α in two groups. (H): locomotion (LMT) (unpaired t-test, $t = 0.4923, df = 17, P = 0.6288$). (I): FST (unpaired t-test, $t = 3.543, df = 17, P = 0.0025$). (J): SPT (unpaired t-test, $t = 2.158, df = 17, P = 0.0455$). (K) Western blot analysis of GluA1 in the PFC (unpaired t-test, $t = 2.403, df = 17, P = 0.0279$) and the representative bands. (L): Western blot analysis of PSD-95 in the PFC (unpaired t-test, $t = 2.473, df = 17, P = 0.0243$) and the representative bands. (M): Western blot analysis of Iba1 in the PFC (unpaired t-test, $t = 2.612, df = 17, P = 0.0182$) and the representative bands. The data are shown as means \pm S.E.M (sham group: $n = 9$, HI/R group: $n = 10$). ANOVA: analysis of variance. ns: not significant; * $P < 0.05$; ** $P < 0.01$; *** $P < 0.001$.

number: NA931, GE Healthcare) or a horseradish peroxidase-conjugated anti-rabbit antibody (1:5000, catalog number: NA934, GE Healthcare)] in 5 % blocking buffer in TBST at room temperature for 1 h. After three final washes in TBST, 10 min each. The bands in the polyvinylidene difluoride membranes were detected using enhanced chemiluminescence plus a Western Blotting Detection system (GE Healthcare Bioscience).

The membranes for detecting GluA1 were incubated in elution buffer (62.5 mM Tris-HCl, pH 6.8, 2 % sodium dodecyl sulfate, and 100 mM β -mercaptoethanol) (preheat in incubator at 60 °C for 10 min, shake 50 times/min) at 60 °C for 30 min and then washed three times (10 min at a time) in TBST. The stripped membranes were incubated with the recommended dilution of primary antibody directed against GluA1 (1:10,000; catalog number: ab31232, Abcam, Cambridge, MA, USA) at 4 °C overnight. The following day, washing the membranes for three times (10 min at a time) in TBST and were incubated with a

recommended dilution of horseradish peroxidase-conjugated anti-rabbit antibody (1:5000, catalog number: NA934, GE Healthcare) for 1 h at room temperature. After three final washes in TBST, 10 min each. The bands in the polyvinylidene difluoride membranes were detected using enhanced chemiluminescence plus a Western Blotting Detection system (GE Healthcare Bioscience). Images were produced using a ChemiDoc™ Touch Imaging System (170-01401; Bio-Rad Laboratories, Hercules, CA, USA), and immunoreactive bands were quantified using Image Lab™3.0 software (Bio-Rad Laboratories).

2.8. Collection of fresh fecal samples and 16S ribosome RNA sequencing

We collected fresh fecal samples from mice before the behavioral test LMT. Subsequently, the experimental workflow including the microbial community DNA extraction, DNA quality control, PCR, product purification, library quality control, sequencing and bioinformatics analysis

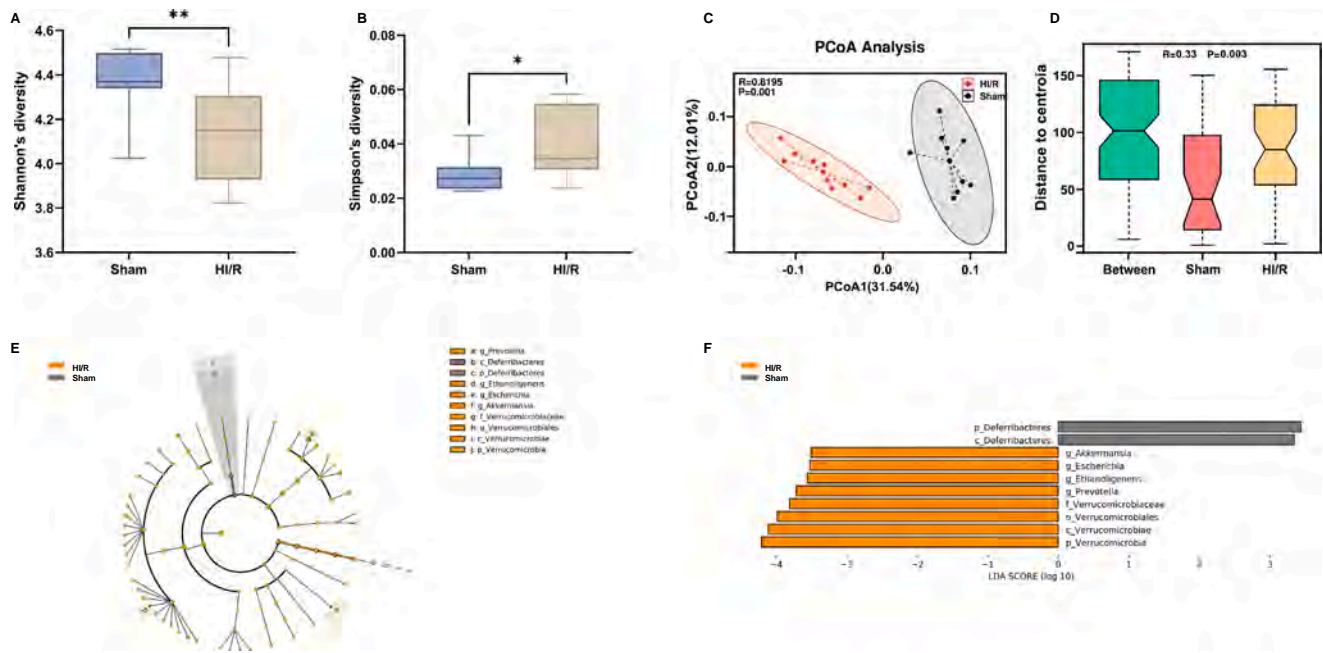


Fig. 2. Abnormal composition of gut microbiota and the LEfSe algorithm in the mice with HI/R injury.

(A): Shannon's diversity (Mann-Whitney test, $P = 0.008$). (B): Simpson's diversity (Mann-Whitney test, $P = 0.022$). (C): PCoA based on OTU level (ANOSIM, Bray-Curtis dissimilarity matrix) ($R = 0.8195$, $P = 0.001$). (D): OTU ANOSIM analysis ($R = 0.33$, $P = 0.003$) ("Between" indicates the difference between groups, and others indicate the difference within each group. R value represents the degree of difference between groups and within groups, ranged from -1 to 1 ; R value >0 indicates that the difference between groups is greater than the difference within the group; R value <0 indicates that the difference within the group is greater than the difference between groups; the larger the absolute value of R value, the greater the relative difference. The lower the P value, the more significant the effect of this difference test. P value <0.05 indicates a significant difference). (E): Functional branching diagram generated from LEfSe showing the differences of the two groups at different taxonomic levels. (F): Histogram representing the enriched taxa with LDA score > 3.3 and $P < 0.05$ obtained from LEfSe of the two groups (p: phylum, c: class, o: order, f: family, g: genus). For all boxplots, the middle line in the box addresses the median, the box addresses the interquartile range, and the whisker addresses the most extreme and least values. * $P < 0.05$; ** $P < 0.01$.

was performed as our previously method (Yang et al., 2023). The 16S ribosome RNA sequencing data has been uploaded and saved in the NCBI Sequence Read Archive and is available at the accession number PRJNA929656.

2.9. Untargeted metabolomic and lipidomic analyses of plasma samples

Untargeted metabolomics profiles from plasma samples were analyzed using ultra-performance liquid chromatography-tandem quadruple time-of-flight mass spectrometry (UPLC-QTOF/MS) technique. The acquisition was operated on an ExionLC™ AD system (SCIEX, Tokyo, Japan) coupled to a X500R QTOF system (SCIEX, Tokyo, Japan), then the metabolomics profiles data was annotated and analyzed as our previously reported (Yang et al., 2023). Untargeted lipidomic analysis of plasma samples were performed using an X500R QTOF system (SCIEX, Tokyo, Japan) operated in positive and negative electrospray mode (AB Sciex, Foster City, CA) coupled with a ExionLC™ AD system (SCIEX, Tokyo, Japan). The lipidomic data processing and analysis were performed as previously reported (Tsugawa et al., 2020).

2.10. Statistical analysis

Statistical analysis of the data was performed using SPSS version 20.0 software (SPSS, Tokyo, Japan). The data were shown as the mean \pm standard error of the mean (S.E.M.). The data of body weight were analyzed using repeated measure analysis of variance (ANOVA), followed by Fisher's least significant difference (LSD) test. The data of spleen weight were analyzed using unpaired *t*-test (for two groups) or two-way ANOVA (for four groups). Data of behavioral tests, pro-inflammatory cytokines, synaptic proteins and microglial marker were analyzed using unpaired *t*-test (for two groups), one-way ANOVA (for

three groups), or two-way ANOVA (for four groups), followed by Fisher's LSD test. The α -diversity of gut microbiota, the abundance of gut microbiota at the species level, metabolites and lipids between the two groups were analyzed using Mann-Whitney test. Bioinformatic analysis of PCoA, LEfSe algorithm of intestinal microbiota, boxplot analysis of metabolomics and correlation networks were all performed by using the OmicStudio tools (<https://www.omicstudio.cn/tool>).

Correlations between spleen weight and the concentrations of pro-inflammatory cytokines were analyzed by using Pearson's correlation analysis. Correlations between the plasma metabolites (or lipids), the intestinal microbiota at species level, depression-like phenotypes, the concentrations of pro-inflammatory cytokines and synaptic proteins (or microglial marker) in the PFC were analyzed using Spearman's correlation analysis. P-value for comparison <0.05 was regarded as significant.

3. Results

3.1. Depression-like phenotypes in mice with HI/R injury

Behavioral tests were performed 7 days after surgery (Fig. 1A). There were no changes in body weight between the two groups (Fig. 1B). The HI/R group showed splenomegaly compared with the sham group (Fig. 1C). Plasma levels of pro-inflammatory cytokines such as interleukin-6 (IL-6) and tumor necrosis factor- α (TNF- α) were higher in the HI/R group than in the sham group (Fig. 1D, E). There were positive correlations between spleen weight and plasma levels of IL-6 and TNF- α (Fig. 1F, G). In the behavioral tests, there were no changes in locomotor activity between the two groups (Fig. 1H). However, the HI/R group showed increased immobility time in the forced swimming test (FST) (Fig. 1I) and reduced sucrose preference in the sucrose preference test

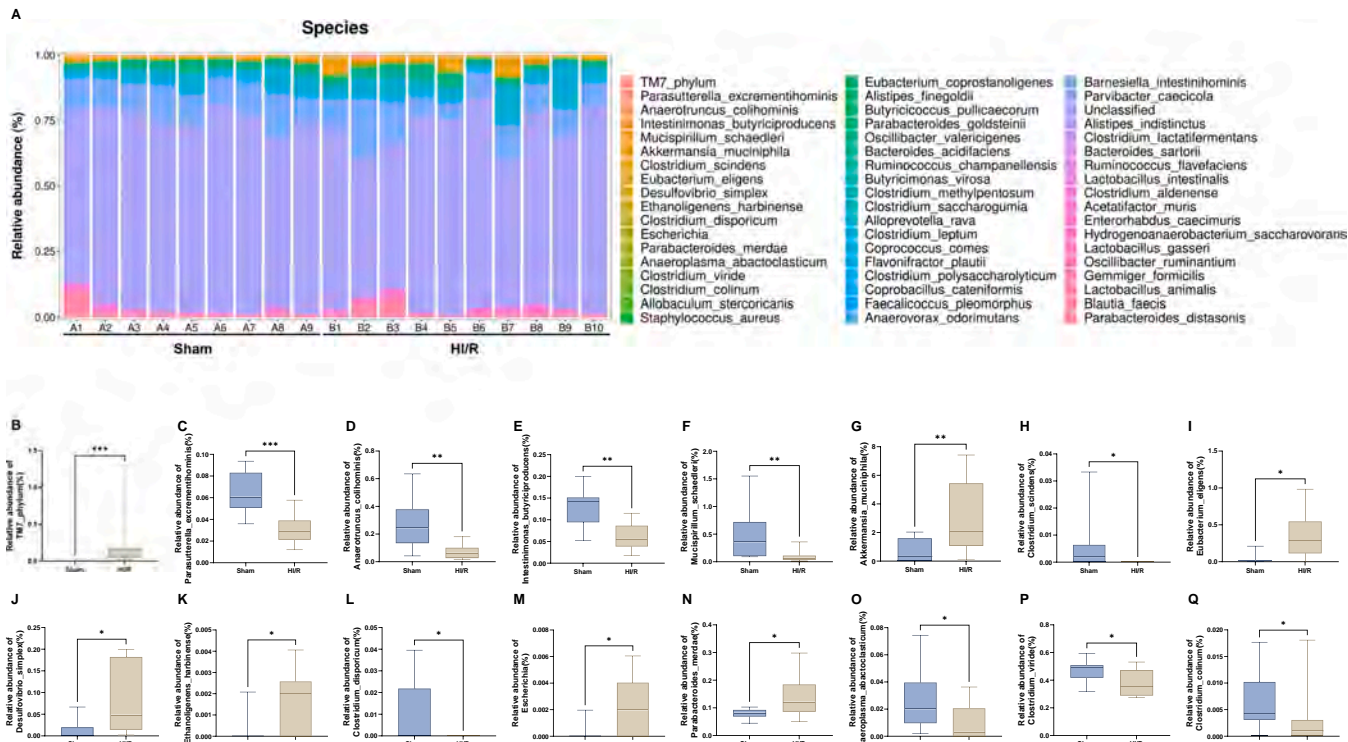


Fig. 3. Effects of HI/R on the gut microbiota at the level of species.

(A): Gut bacteria composition at the species level in the two groups. (B): Relative abundance of the species *TM7_phylum* (Mann-Whitney test, $P < 0.0001$). (C): Relative abundance of the species *Parasutterella_excrementihominis* (Mann-Whitney test, $P = 0.0004$). (D): Relative abundance of the species *Anaerotruncus_colihominis* (Mann-Whitney test, $P = 0.0015$). (E): Relative abundance of the species *Intestinimonas_butyrificiproducens* (Mann-Whitney test, $P = 0.0030$). (F): Relative abundance of the species *Mucispirillum_schaedleri* (Mann-Whitney test, $P = 0.0057$). (G): Relative abundance of the species *Akkermansia_muciniphila* (Mann-Whitney test, $P = 0.0071$). (H): Relative abundance of the species *Clostridium_scindens* (Mann-Whitney test, $P = 0.0108$). (I): Relative abundance of the species *Eubacterium_eligens* (Mann-Whitney test, $P = 0.0101$). (J): Relative abundance of the species *Desulfovibrio_simplex* (Mann-Whitney test, $P = 0.0126$). (K): Relative abundance of the species *Ethanoligenens_harbinense* (Mann-Whitney test, $P = 0.0162$). (L): Relative abundance of the species *Clostridium_disporicum* (Mann-Whitney test, $P = 0.0325$). (M): Relative abundance of the species *Escherichia* (Mann-Whitney test, $P = 0.0257$). (N): Relative abundance of the species *Parabacteroides_merdae* (Mann-Whitney test, $P = 0.0279$). (O): Relative abundance of the species *Anaeroplasm_a_bactoclasticum* (Mann-Whitney test, $P = 0.0267$). (P): Relative abundance of the species *Clostridium_viride* (Mann-Whitney test, $P = 0.0350$). (Q): Relative abundance of the species *Clostridium_colinum* (Mann-Whitney test, $P = 0.0347$). For all boxplots, the middle line in the box addresses the median, the box addresses the interquartile range, and the whisker addresses the most extreme and least values. * $P < 0.05$; ** $P < 0.01$; *** $P < 0.001$.

(SPT) compared with the sham group (Fig. 1J). Furthermore, expression of synaptic proteins (GluA1 and PSD-95) in the prefrontal cortex (PFC) was lower in the HI/R group than in the sham group (Fig. 1K, L). In contrast, levels of Iba1 in the PFC were significantly higher in the HI/R group compared with the sham group (Fig. 1M). These data suggest that mice with HI/R injury have systemic inflammation, reduced expression of synaptic proteins, and microglial activation in the PFC, resulting in depression-like phenotypes.

3.2. Composition of gut microbiota and LEfSe analysis

Examination of α -diversity revealed significant differences in Shannon's diversity and Simpson's diversity indices between the two groups (Fig. 2A, B). The β -diversity of the gut microbiota in the two groups was analyzed by Principal Coordinate Analysis (PCoA). At the operational taxonomic unit (OTU) level, PCoA analysis revealed a significant difference in composition through analysis of similarities (ANOSIM) assessment ($R = 0.8195$, $P = 0.001$) (Fig. 2C). ANOSIM analysis at the OTU level indicated that the difference between the two groups was greater than the differences within the groups ($R = 0.33$, $P = 0.003$) (Fig. 2D).

A cladogram was used to depict the relationship between the biomarker taxa (layers of the cladogram representing different levels, with phylum, class, order, family and genus from inside to outside) generated by LEfSe (linear discrimination analysis effect size) analysis

(Fig. 2E). We identified eight taxonomic biomarkers for the following microbes in the HI/R group: the genus *Akkermansia*, the genus *Escherichia*, the genus *Ethanoligenens*, the genus *Prevotella*, the family *Verrucomicrobiaceae*, the order *Verrucomicrobiales*, the class *Verrucomicrobiae*, and the phylum *Verrucomicrobia* (Fig. 2F). Furthermore, we identified two taxonomic biomarkers, for the class and the phylum *Deferritbacteres* in the sham group (Fig. 2F).

3.3. Gut microbiota at the species level

At the species level, the screen identified 16 bacteria that significantly differed in relative abundance (Fig. 3A). The relative abundances of *TM7_phylum*, *Akkermansia_muciniphila*, *Eubacterium_eligens*, *Desulfovibrio_simplex*, *Ethanoligenens_harbinense*, *Escherichia* and *Parabacteroides_merdae* were significantly higher in the HI/R group compared with the sham group, whereas the relative abundances of *Parasutterella_excrementihominis*, *Anaerotruncus_colihominis*, *Intestinimonas_butyrificiproducens*, *Mucispirillum_schaedleri*, *Clostridium_scindens*, *Clostridium_disporicum*, *Anaeroplasm_a_bactoclasticum*, *Clostridium_viride* and *Clostridium_colinum* were significantly lower in the HI/R group compared with the sham group (Fig. 3B–Q).

3.4. Untargeted metabolomic and lipidomic analyses of plasma samples

To examine the interaction between the gut microbiome and host

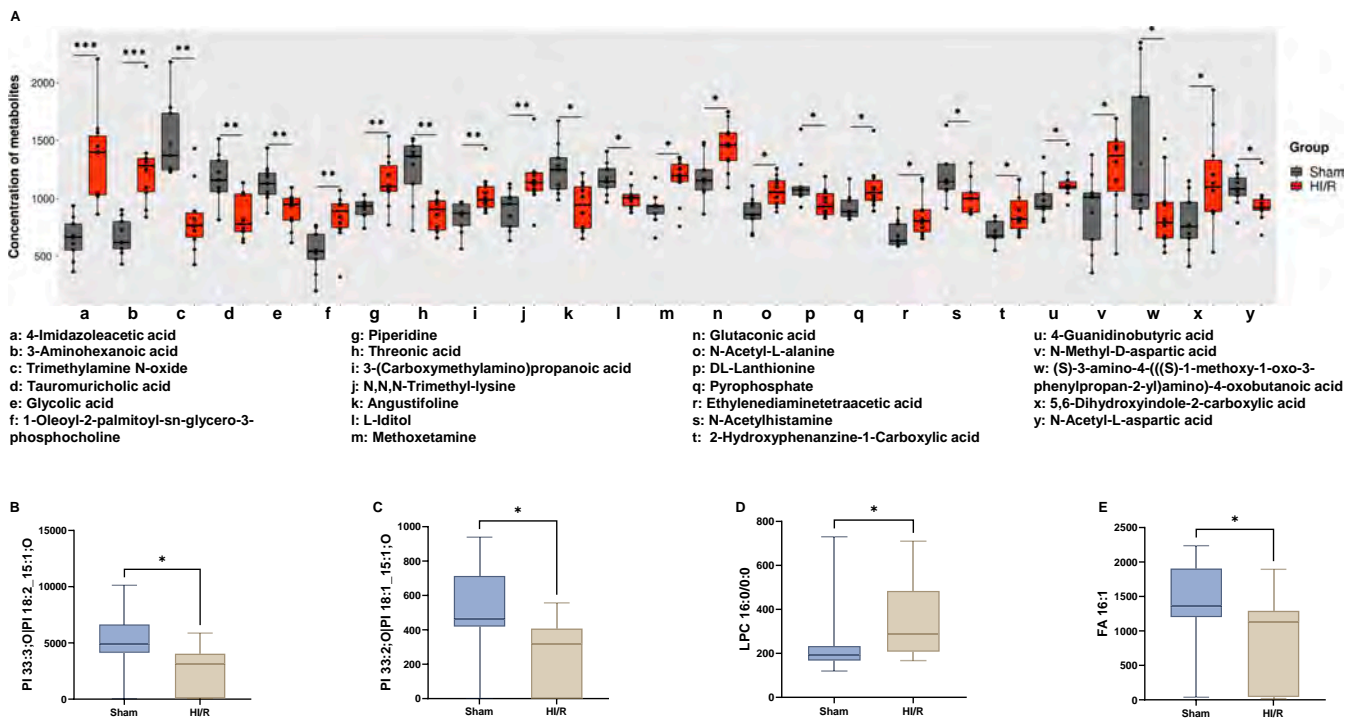


Fig. 4. Untargeted metabolomic and lipidomic analyses of plasma samples in mice with HI/R injury.

(A): Boxplots showing the changes of 25 kinds of metabolites between the two groups. They are listed as follows: 4-imidazoleacetic acid (Mann-Whitney test, $P < 0.0001$), 3-aminohexanoic acid (Mann-Whitney test, $P = 0.0002$), trimethylamine *N*-oxide (Mann-Whitney test, $P = 0.0004$), taurumuricholic acid (Mann-Whitney test, $P = 0.0010$), glycolic acid (Mann-Whitney test, $P = 0.0030$), 1-oleoyl-2-palmitoyl-sn-glycero-3-phosphocholine (Mann-Whitney test, $P = 0.0057$), piperidine (Mann-Whitney test, $P = 0.0057$), threonic acid (Mann-Whitney test, $P = 0.0057$), 3-(carboxymethylamino) propanoic acid (Mann-Whitney test, $P = 0.0076$), *N,N,N*-trimethyl-lysine (Mann-Whitney test, $P = 0.0076$), angustifoline (Mann-Whitney test, $P = 0.0101$), *L*-iditol (Mann-Whitney test, $P = 0.0133$), methoxetamine (Mann-Whitney test, $P = 0.0133$), glutaconic acid (Mann-Whitney test, $P = 0.0172$), *N*-acetyl-*L*-alanine (Mann-Whitney test, $P = 0.0172$), *DL*-lanthionine (Mann-Whitney test, $P = 0.0220$), pyrophosphate (Mann-Whitney test, $P = 0.0220$), ethylenediaminetetraacetic acid (Mann-Whitney test, $P = 0.0279$), *N*-acetylhistamine (Mann-Whitney test, $P = 0.0279$), 2-hydroxyphenazine-1-carboxylic acid (Mann-Whitney test, $P = 0.0350$), 4-guanidinobutyric acid (Mann-Whitney test, $P = 0.0350$), *N*-methyl-*D*-aspartic acid (Mann-Whitney test, $P = 0.0350$), (*S*)-3-amino-4-(((*S*)-1-methoxy-1-oxo-3-phenylpropan-2-yl)amino)-4-oxobutanoic acid (Mann-Whitney test, $P = 0.0435$), 5,6-dihydroxyindole-2-carboxylic acid (Mann-Whitney test, $P = 0.0435$), *N*-acetyl-*L*-aspartic acid (Mann-Whitney test, $P = 0.0435$). The X-axis using the lowercase letter symbol representing the names of different plasma metabolites, and the Y-axis represents the concentration of various plasma metabolites. Different colors of boxplots represent the corresponding groups.

(B) PI 33:3; O|PI 18:2_15:1; O (Mann-Whitney test, $P = 0.0172$). (C) PI 33:2; O|PI 18:1_15:1; O (Mann-Whitney test, $P = 0.0291$). (D) LPC 16:0/0:0 (Mann-Whitney test, $P = 0.035$). (E) FA 16:1 (Mann-Whitney test, $P = 0.0435$). * $P < 0.05$; ** $P < 0.01$; *** $P < 0.001$.

metabolism, we conducted untargeted metabolomic and lipidomic analyses of plasma samples. After quality control and removal of low-abundance peaks, a subset of 214 metabolites was annotated. We identified 25 metabolites that differed significantly between the two groups (Fig. 4A). Furthermore, a subset of 55 lipids was annotated after data processing. We identified 4 significantly different lipids between the two groups (Fig. 4B–E).

3.5. Correlations among the gut microbiota, plasma metabolites/lipids, depression-like phenotypes, plasma pro-inflammatory cytokines, synaptic proteins and Iba1

There were correlations between the plasma metabolites/lipids and the relative abundance of gut microbiota in the two groups, suggesting a close relationship between the two. After screening the data, with a threshold of $P < 0.05$ and an absolute *R*-value of ≥ 0.5 , a Correlation Network was constructed to indicate the relationship between the plasma metabolites/lipids and gut microbiome at the species level, depression-like behaviors, plasma pro-inflammatory cytokines, synaptic proteins and the microglial marker Iba1 in the PFC, all of which significantly differed between the two groups (Fig. 5A). The relative abundance of several microbes was positively or negatively correlated with plasma metabolites such as 4-imidazoleacetic acid, 3-aminohexanoic acid, trimethylamine *N*-oxide, taurumuricholic acid, and glycolic

acid (Fig. 5A). In addition, there were correlations between the plasma metabolites/lipids and the FST data, plasma levels of pro-inflammatory cytokines, synaptic proteins and the microglial marker Iba1 in the PFC (Fig. 5A).

Using the Correlation Network, we investigated correlations between the relative abundance of the gut bacteria and depression-like phenotypes, plasma cytokines, synaptic proteins and Iba1 in the PFC (Fig. 5B). There were also positive or negative correlations between plasma IL-6 or TNF- α and the relative abundance of several species (Fig. 5B). Furthermore, there were positive (or negative) correlations between the FST data and the relative abundance of several species (Fig. 5B). Moreover, there were positive (or negative) correlations between the relative abundance of the species and the levels of synaptic proteins or Iba1 in the PFC (Fig. 5B). These data suggest that several microbiota and metabolites may contribute to systemic inflammation, resulting in microglial activation in the brain and depression-like phenotypes.

3.6. Effects of bilateral SDV in depression-like phenotypes in the HI/R mouse model

Prior research suggests that the subdiaphragmatic vagus nerve could be implicated in depression-like phenotypes in mice (Pu et al., 2021; Wang et al., 2020, 2021; Yang et al., 2023; Zhang et al., 2020). To examine the role of the subdiaphragmatic vagus nerve in the depression-

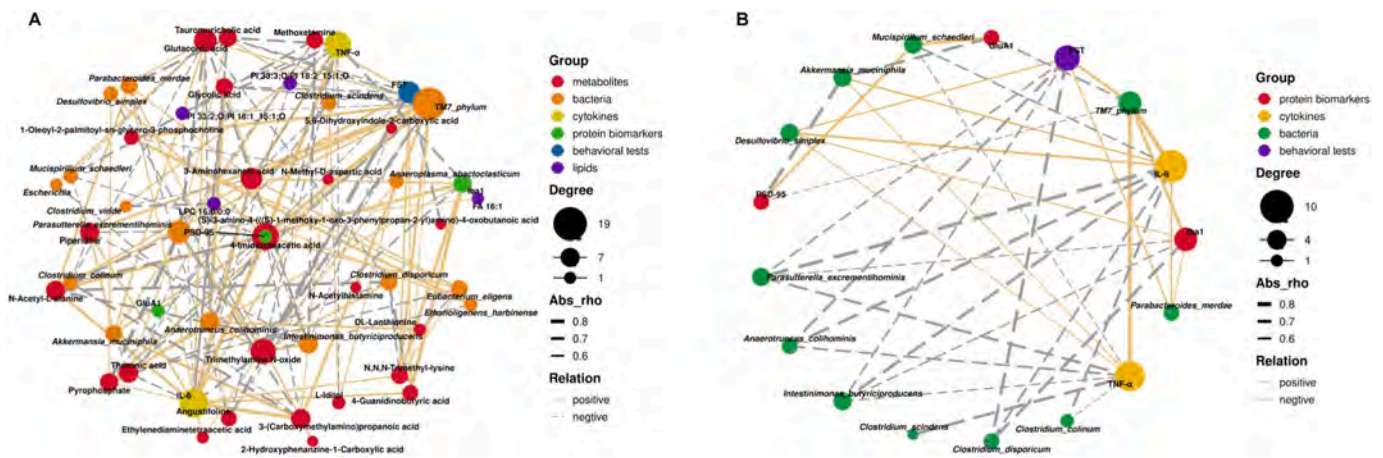


Fig. 5. Correlation network between behavioral data (or synaptic proteins, microglial marker, and pro-inflammatory cytokine) and microbiota (or metabolites and lipids).

(A): A Correlation Network indicating the correlations between the concentrations of plasma metabolites (or lipids) and the gut microbiota at the species level, the results of the behavioral test, the concentrations of pro-inflammatory cytokines, synaptic proteins and microglial marker Iba1 in the PFC. (B): A Correlation Network showed correlations between the relative abundance of gut bacteria at the species level and the results of the behavioral test, the concentrations of pro-inflammatory cytokines, synaptic proteins and microglial marker Iba1 in the PFC. Both the threshold of correlation networks above were set as $P < 0.05$ and the absolute value of $R \geq 0.5$. The different colors of nodes represent different groups. The sizes of node gradients represent varying degrees of correlation. The thickness of the line represents the absolute value of the correlation coefficient. Solid lines represent positive correlations, dotted lines represent negative correlations.

like phenotypes in mice with HI/R injury, we investigated the effects of bilateral SDV (Fig. 6A). Body weights after surgery were significantly changed among the four groups (Fig. 6B). The spleen weights in the HI/R + SDV group were significantly lower than those in the HI/R + sham group (Fig. 6C). Furthermore, plasma levels of IL-6 and TNF- α in the HI/R + SDV group were significantly lower than those in the HI/R + sham group (Fig. 6D, E). There were positive correlations between spleen weight and the plasma concentration of IL-6 or TNF- α among the four groups (Fig. 6F, G).

There were no differences in locomotor activity among the four groups (Fig. 6H). The immobility time in the FST in the HI/R + SDV group was significantly lower than that in the HI/R + sham group (Fig. 6I). In the SPT, sucrose preference in the HI/R + SDV group was significantly higher than that in the HI/R + sham group (Fig. 6J). Furthermore, the expression levels of synaptic proteins (e.g., GluA1 and PSD-95) in the PFC were significantly higher in the HI/R + SDV group compared with the HI/R + sham group (Fig. 6K, L). The expression of Iba1 in the PFC was significantly lower in the HI/R + SDV group than in the HI/R + sham group (Fig. 6M). These data suggest that bilateral SDV blocks depression-like behaviors, increased plasma levels of pro-inflammatory cytokines, altered expressions of synaptic proteins and Iba1 in the PFC of mice with HI/R injury.

3.7. Effects of arketamine on depression-like phenotypes in mice with HI/R injury

We have demonstrated that arketamine could be a rapid-acting antidepressant, devoid of the side effects associated with ketamine (Wei et al., 2022b; Zhang et al., 2022a; Zhang et al., 2023). Here, we examined the effects of a single dose of the new antidepressant arketamine (10 mg/kg, i.p.) in the HI/R model (Fig. 7A). There were no changes in body weight (Fig. 7B) or locomotor activity (Fig. 7C) among the three groups. The immobility time in the FST was significantly greater in the HI/R + saline group compared with the other two groups (Fig. 7D). In the SPT, sucrose preference was significantly lower in the HI/R + saline group compared with the other two groups (Fig. 7E). Arketamine also attenuated the reduced levels of GluA1 and PSD-95 in the PFC of mice with HI/R injury (Fig. 7F, G). A single injection of arketamine significantly attenuated the increase in expression of Iba1 in the PFC of mice with HI/R injury (Fig. 7H). These results suggest that depression-like

phenotypes in mice with HI/R injury are ameliorated by a single dose of arketamine.

4. Discussion

There are a number of major findings of this study. First, mice with HI/R injury had higher blood levels of pro-inflammatory cytokines, reduced expression of synaptic proteins (i.e., GluA1 and PSD-95) and increased expression of Iba1 (indicative of microglial activation) in the PFC, resulting in depression-like phenotypes. Second, there were significant changes in α -diversity and β -diversity in gut microbiota between the two groups. LEfSe analysis identified the genera *Akkermansia*, *Escherichia*, *Ethanoligenens* and *Prevotella* as potential microbial markers in the HI/R group. Furthermore, several species and metabolites/lipids were altered between the two groups. There were also correlations between the relative abundance of several microbes and blood cytokines, depression-like behaviors, or synaptic proteins and the microglia marker in the PFC. Network analysis showed correlations between several microbes and blood metabolites or behavioral indices. Third, SDV prevented splenomegaly, systemic inflammation (the increases in IL-6 and TNF- α), and altered expression of synaptic proteins and Iba1 in the PFC of mice with HI/R injury. Finally, depression-like phenotypes, and altered expressions of GluA1, PSD-95 and Iba1 in the PFC of mice with HI/R injury were improved after a single injection of arketamine. Taken together, these findings suggest that the gut microbiota–liver–brain axis plays a key role in depression-like phenotypes in mice with HI/R injury via the subdiaphragmatic vagus nerve, and that arketamine exhibits a rapid-acting antidepressant-like action in mice with HI/R injury.

It has been reported that LPS-induced splenomegaly is associated with blood levels of pro-inflammatory cytokines (Ma et al., 2022, 2023; Zhang et al., 2020, 2021a, 2021b). In this study, we found a positive correlation between spleen weight and blood levels of pro-inflammatory cytokines in mice. Collectively, these results suggest that HI/R-induced liver injury contributes to systemic inflammation, resulting in splenomegaly and depression-like phenotypes.

Analysis of gut microbiota shows that HI/R injury is a driving factor for the differential expression of microbial communities. At the species level, there were differences in the relative abundance of several microbiota between the two groups. Using untargeted metabolomic and lipidomic analyses, we found that several metabolites/lipids were

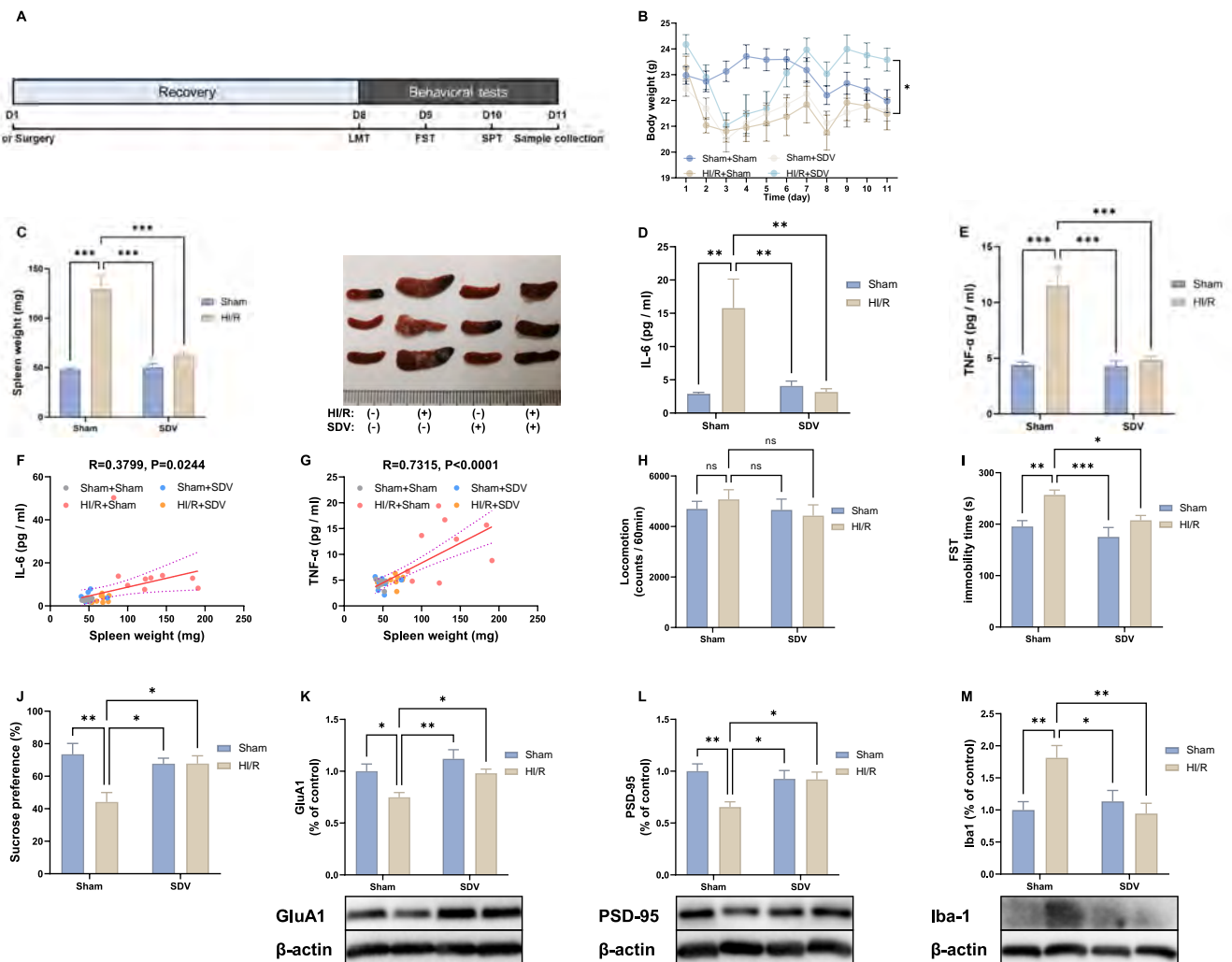


Fig. 6. Effects of bilateral SDV in depression-like phenotypes of mice with HI/R injury. (A): Experimental schedule. On day 1, surgery (HI/R and/or SDV) or sham surgery was performed, and they were recovered 7 days. On day 8, LMT was performed. FST and SPT were performed on day 9 and day 10, respectively. On day 11, PFC and plasma samples were collected. (B): Body weight (repeated measure two-way ANOVA, time: $F_{(3,481, 107.9)} = 23.84, P < 0.0001$; group: $F_{(3,31)} = 2.987, P = 0.0461$; interaction: $F_{(30,310)} = 9.574, P < 0.0001$). (C): Spleen weight (two-way ANOVA, HI/R: $F_{(1,31)} = 20.06, P < 0.0001$; SDV: $F_{(1,31)} = 42.52, P < 0.0001$; Interaction: $F_{(1,31)} = 22.97, P < 0.0001$) and representative photograph of spleen in the four group. (D): Plasma levels of IL-6 (two-way ANOVA, HI/R: $F_{(1,31)} = 6.074, P = 0.0195$; SDV: $F_{(1,31)} = 6.689, P = 0.0146$; Interaction: $F_{(1,31)} = 8.886, P = 0.0056$). (E): Plasma levels of TNF- α (two-way ANOVA, HI/R: $F_{(1,31)} = 11.58, P = 0.0019$; SDV: $F_{(1,31)} = 14.94, P = 0.0005$; Interaction: $F_{(1,31)} = 11.06, P = 0.0023$). (F): There was a positive correlation ($R = 0.3799, P = 0.0244$) between the spleen weight and plasma levels of IL-6 in the four groups. (G): There was a positive correlation ($R = 0.7315, P < 0.0001$) between the spleen weight and plasma levels of TNF- α in the four groups. (H): Locomotion (LMT) (two-way ANOVA, HI/R: $F_{(1,31)} = 0.7289, P = 0.3998$; SDV: $F_{(1,31)} = 0.03425, P = 0.8544$; Interaction: $F_{(1,31)} = 0.5760, P = 0.4536$). (I): FST (two-way ANOVA, HI/R: $F_{(1,31)} = 8.150, P = 0.0076$; SDV: $F_{(1,31)} = 14.68, P = 0.0006$; Interaction: $F_{(1,31)} = 1.430, P = 0.2408$). (J): SPT (two-way ANOVA, HI/R: $F_{(1,31)} = 2.776, P = 0.1058$; SDV: $F_{(1,31)} = 7.544, P = 0.0099$; Interaction: $F_{(1,31)} = 7.634, P = 0.0095$). (K): Western blot analysis of GluA1 in the PFC (two-way ANOVA, HI/R: $F_{(1,31)} = 8.269, P = 0.0072$; SDV: $F_{(1,31)} = 10.23, P = 0.0032$; Interaction: $F_{(1,31)} = 0.8455, P = 0.3649$) and the representative bands. (L): Western blot analysis of PSD-95 in the PFC (two-way ANOVA, HI/R: $F_{(1,31)} = 1.958, P = 0.1716$; SDV: $F_{(1,31)} = 6.524, P = 0.0158$; Interaction: $F_{(1,31)} = 6.101, P = 0.0192$) and the representative bands. (M): Western blot analysis of Iba1 in the PFC (two-way ANOVA, HI/R: $F_{(1,31)} = 4.846, P = 0.0353$; SDV: $F_{(1,31)} = 3.468, P = 0.0721$; Interaction: $F_{(1,31)} = 9.057, P = 0.0052$) and the representative bands. The data are shown as means \pm S.E.M (sham + sham group: $n = 8$, HI/R + sham group: $n = 9$, sham + SDV group: $n = 8$, HI/R + SDV group: $n = 10$). ANOVA: analysis of variance. ns: not significant; * $P < 0.05$; ** $P < 0.01$; *** $P < 0.001$.

altered between the two groups. Network analysis showed that blood levels of metabolites/lipids were correlated with the relative abundance of microbiota, suggesting a role of the microbiome in the synthesis of these metabolites/lipids. Notably, we found correlations between depression-like behaviors and the relative abundances of microbiota, suggesting a role of the gut microbiome in depression. A recent study demonstrated that gut microbiota-derived metabolites play a role in HI/R injury through the modulation of macrophage metabolic reprogramming (Lu et al., 2023). Given the role of gut microbiota in depression (Chang et al., 2022; Liu et al., 2023), it is likely that alterations in the gut microbiota–brain axis, including metabolites and lipids, may play a role

in the depression-like behaviors in mice with HI/R injury.

Previous studies demonstrated that SDV blocks the onset of depression-like behaviors in mice caused by LPS administration (Zhang et al., 2020) or fecal microbiota transplantation from mice with depression-like behaviors (Pu et al., 2021; Wang et al., 2020, 2021). Furthermore, SDV blocks the onset of depression-like behaviors in *Chrna7* knockout mice (Yang et al., 2023) and demyelination in the brain of cuprizone-treated mice (Wang et al., 2023). A study showed a role of the gut–spleen axis, via the subdiaphragmatic vagus nerve, in sleep deprivation-induced aggravation of systemic inflammation in mice after LPS injection (Zhang et al., 2021b). In this study, we found that

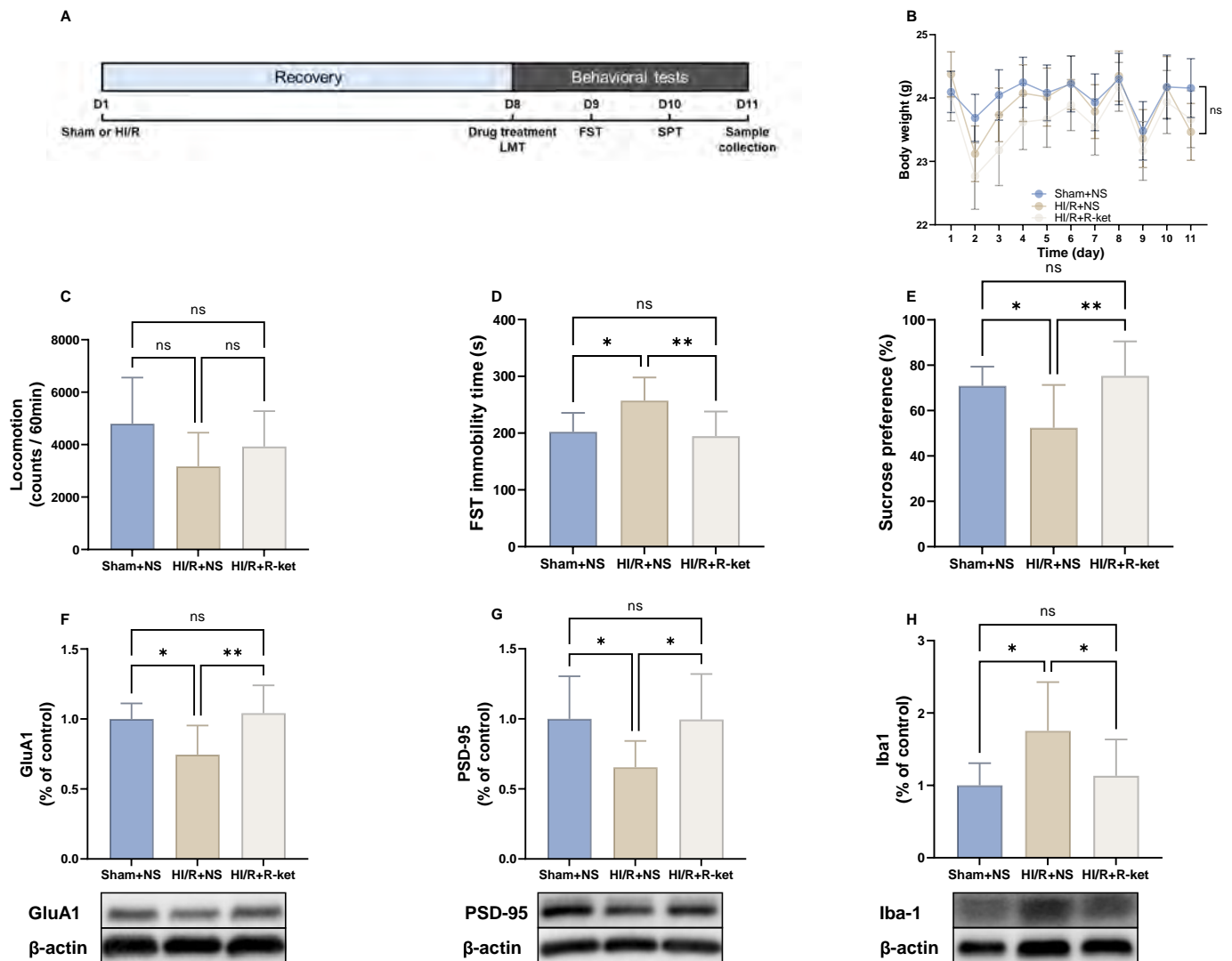


Fig. 7. Effect of new antidepressant arketamine in depression-like phenotypes of mice with HI/R injury.

(A): Experimental schedule. On day 1, sham or HI/R was performed, and they were recovered 7 days. On day 8, normal saline (NS) (10 ml/kg) or arketamine (R-ket) (10 mg/kg) was administered intraperitoneally and subsequently LMT was performed. FST and SPT were performed on day 9 and day 10, respectively. On day 11, prefrontal cortex (PFC) and plasma samples were collected. (B): Body weight (repeated measure ANOVA, $F_{(2, 24)} = 0.2773$, $P = 0.7603$). (C): LMT (one-way ANOVA, $F_{(2, 24)} = 2.728$, $P = 0.0856$). (D): FST (one-way ANOVA, $F_{(2, 24)} = 6.770$, $P = 0.0047$). (E): SPT (one-way ANOVA, $F_{(2, 24)} = 6.034$, $P = 0.0075$). (F): Western blot analysis of GluA1 in the PFC (one-way ANOVA, $F_{(2, 24)} = 7.317$, $P = 0.0033$) and the representative bands. (G): Western blot analysis of PSD-95 in the PFC (one-way ANOVA, $F_{(2, 24)} = 4.538$, $P = 0.0213$) and the representative bands. (H): Western blot analysis of Iba1 in the PFC (one-way ANOVA, $F_{(2, 24)} = 5.422$, $P = 0.0114$) and the representative bands. The data are shown as means \pm S.E.M (Sham + NS group: $n = 9$, HI/R + NS group: $n = 9$, HI/R + arketamine group: $n = 9$). ANOVA: analysis of variance. NS: normal saline. R-ket: Arketamine. ns: not significant; * $P < 0.05$; ** $P < 0.01$.

SDV notably reduced depression-like phenotypes and splenomegaly in mice with HI/R injury by exerting anti-inflammatory effects. Given the role of the gut–liver axis in liver diseases (Albillos et al., 2020; Schwabe and Greten, 2020; Wiest et al., 2017; Zhang et al., 2022b), it is likely that the gut–liver–brain axis, via the subdiaphragmatic vagus nerve, plays a critical role in depression-like phenotypes in mice with HI/R injury. A study underscored the role of the vagus nerve in regulating the systemic inflammatory response to the endotoxin LPS (Borovikova et al., 2000). Given this, SDV might effectively reduce systemic inflammation in this model. Because vagus nerve stimulation (VNS) has potent anti-inflammatory actions (Hashimoto, 2023a, 2023c; Wang et al., 2022), it is likely that VNS might be a potential therapeutic option for patients with CLD.

The robust antidepressant action of the anesthetic ketamine was a serendipitous discovery in the field of psychiatric disorders, producing rapid-acting and sustained antidepressant actions in treatment-resistant patients with depression (Hashimoto, 2022). Accumulating preclinical

data suggest that arketamine, the (*R*)-enantiomer of ketamine, is a safer antidepressant than ketamine or esketamine, the (*S*)-enantiomer of ketamine (Hashimoto, 2020; Wei et al., 2022b; Zhang et al., 2022a; Zhang et al., 2023). Previous studies have reported that arketamine improves depression-like behaviors and altered composition of the gut microbiota in mice with depression-like behaviors (Qu et al., 2017; Wan et al., 2023; Yang et al., 2017), suggesting a role of the gut microbiota–brain axis in the beneficial effects of arketamine (Hashimoto, 2020, 2023b; Hua et al., 2022; Wei et al., 2022b). In this study, we found that arketamine improved depression-like phenotypes in mice with HI/R injury. It is noteworthy that these changes in mice with HI/R injury were ameliorated by a single post-injection of arketamine. Although the mechanisms underlying the effects of arketamine in the HI/R model are currently unclear, it is likely that anti-inflammatory actions via the gut–liver–brain axis may play a role in its beneficial effects. A phase II trial of arketamine (PCN-101) by Perception Neuroscience is currently underway (Zhang et al., 2022a). Therefore, it is of interest to investigate

whether arketamine can improve depression in patients with CLD.

This study has some limitations. First, we did not evaluate the blood levels of alanine aminotransferase (ALT) and aspartate aminotransferase (AST), nor did we conduct H&E staining of the liver 7 days post-surgery. This is because ALT and AST levels typically return to baseline 24 h after surgery (Wu et al., 2011). Second, we focused on the PFC for assessing synaptic protein expression, even though other brain regions, such as hippocampus, are implicated in depression. Third, we did not investigate the effects of fecal microbiota transplantation (FMT) from mice with HI/R injury, which would have provided insights into the role of gut microbiota in depression-like phenotypes. This necessitates future exploration using FMT from mice with HI/R injury. Fourth, the study did not examine the impact of an antibiotic cocktail designed to delete host microbiota, leaving room to further determine the influence of host microbiota in this model. A future study using an antibiotic cocktail is recommended. Finally, we have yet to explore the relationship between the microbiome or metabolites and depression-like phenotypes in mice with HI/R injury. Future research should delve into how these factors potentially influence depression-like phenotypes in this model.

In summary, our findings suggest that the gut microbiota–liver–brain axis, via the subdiaphragmatic vagus nerve, plays a key role in depression-like phenotypes in the HI/R mouse model. Arketamine may have therapeutic potential for depression in patients with CLD.

Financial support

This study was supported by the grant from Japan Society for the Promotion of Science (to K.H., 21H02846, 21H00184, 21H05612), JST OPERA Program Japan (to C.M. JPMJOP1831) and unrestricted grant of Yamada Bee Company, Japan (to C.M.). Dr. Yong Yang was supported by the Japan China Sasakawa Medical Fellowship (Tokyo, Japan). Dr. Yong Yang and Ms. Xiayun Wan were supported by the Academic Research & Innovation Management Organization of Chiba University (Chiba, Japan).

Author statement

YY and KH designed the study. YY, and XW performed the experiments. AE and CM performed metabolomics analysis. YY analyzed the data. YY and KH wrote the manuscript. All authors have read and approved the final manuscript.

CRediT authorship contribution statement

YY and KH performed study concept/design; YY and XW performed animal experiments and data acquisition; AE and CM performed metabolomic and lipidomic analyses; YY and KH drafted manuscript; CM and KH obtained funding; all authors have read/edited the manuscript.

Declaration of competing interest

Dr. Hashimoto is the inventor of filed patent applications on “The use of R-Ketamine in the treatment of psychiatric diseases”, “(S)-norketamine and salt thereof as pharmaceutical”, “R-Ketamine and derivative thereof as prophylactic or therapeutic agent for neurodegeneration disease or recognition function disorder”, “Preventive or therapeutic agent and pharmaceutical composition for inflammatory diseases or bone diseases”, “R-Ketamine and its derivatives as a preventive or therapeutic agent for a neurodevelopmental disorder”, and “Preventive or therapeutic agent and pharmaceutical composition for inflammatory diseases” by the Chiba University. Dr. Hashimoto also declares that he has received research support and consultant from Abbott, Boehringer Ingelheim, Daiichi-Sankyo, Meiji Seika Pharma, Seikagaku Corporation, Sumitomo-Pharma, Taisho, Otsuka, Murakami Farm and Perception Neuroscience. The other authors have no conflict of interest.

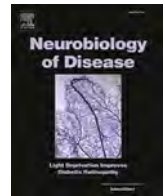
Acknowledgment

We thank Edanz (<https://jp.edanz.com/ac>) for editing a draft of this manuscript.

References

- Albillos, A., de Gottardi, A., Rescigno, M., 2020. The gut-liver axis in liver disease: pathophysiological basis for therapy. *J. Hepatol.* 72 (3), 558–577. <https://doi.org/10.1016/j.jhep.2019.10.003>.
- Bianchi, G., Marchesini, G., Nicolino, F., Graziani, R., Sgarbi, D., Loguercio, C., Abbiati, R., Zoli, M., 2005. Psychological status and depression in patients with liver cirrhosis. *Dig. Liver Dis.* 37 (8), 593–600. <https://doi.org/10.1016/j.dld.2005.01.020>.
- Bonaz, B., Bazin, T., Pellissier, S., 2018. The vagus nerve at the interface of the microbiota-gut-brain axis. *Front. Neurosci.* 12, 49. <https://doi.org/10.3389/fnins.2018.00049>.
- Borovikova, L.V., Ivanova, S., Zhang, M., Yang, H., Botchkina, G.I., Watkins, L.R., Wang, H., Abumrad, N., Eaton, J.W., Tracey, K.J., 2000. Vagus nerve stimulation attenuates the systemic inflammatory response to endotoxin. *Nature* 405 (6785), 458–462. <https://doi.org/10.1038/35013070>.
- Chang, L., Wei, Y., Hashimoto, K., 2022. Brain-gut-microbiota axis in depression: a historical overview and future directions. *Brain Res. Bull.* 182, 44–56. <https://doi.org/10.1016/j.brainresbull.2022.02.004>.
- Cryan, J.F., O’Riordan, K.J., Cowan, C.S.M., Sandhu, K.V., Bastiaansen, T.F.S., Boehme, M., Codagnone, M.G., Cussotto, S., Fulling, C., Golubeva, A.V., Guzzetta, K. E., Jaggari, M., Long-Smith, C.M., Lyte, J.M., Martin, J.A., Molinero-Perez, A., Moloney, G., Morelli, E., Morillas, E., O’Connor, R., Cruz-Pereira, J.S., Peterson, V.L., Rea, K., Ritz, N.L., Sherwin, E., Spichak, S., Teichman, E.M., van de Wouw, M., Ventura-Silva, A.P., Wallace-Fitzsimons, S.E., Hyland, N., Clarke, G., Dinan, T.G., 2019. The microbiota-gut-brain axis. *Physiol. Rev.* 99 (4), 1877–2013. <https://doi.org/10.1152/physrev.00018.2018>.
- Forsythe, P., Bienenstock, J., Kunze, W.A., 2014. Vagal pathways for microbiome-brain-gut axis communication. *Adv. Exp. Med. Biol.* 817, 115–133. https://doi.org/10.1007/978-1-4939-0897-4_5.
- Gutteling, J.J., de Man, R.A., van der Plas, S.M., Schalm, S.W., Busschbach, J.J.V., Darlington, A.S.E., 2006. Determinants of quality of life in chronic liver patients. *Aliment. Pharmacol. Ther.* 23 (11), 1629–1635. <https://doi.org/10.1111/j.1365-2036.2006.02934.x>.
- Hashimoto, K., 2020. Molecular mechanisms of the rapid-acting and long-lasting antidepressant actions of (R)-ketamine. *Biochem. Pharmacol.* 177, 113935. <https://doi.org/10.1016/j.bcp.2020.113935>.
- Hashimoto, K., 2022. Ketamine: anesthetic, psychotomimetic, antidepressant, or anthelmintic? *Mol. Psychiatry* 27 (8), 3116–3118.
- Hashimoto, K., 2023a. Neuroinflammation through the vagus nerve-dependent gut–microbiota–brain axis in treatment-resistant depression. *Prog. Brain Res.* 278, 61–77. <https://doi.org/10.1016/bs.pbr.2023.01.003>.
- Hashimoto, K., 2023b. Arketamine for cognitive impairment in psychiatric disorders. *Eur. Arch. Psychiatry Clin. Neurosci.* 273 (7), 1513–1525. <https://doi.org/10.1007/s00406-023-01570-5>.
- Hashimoto, K., 2023c. Detrimental effects of COVID-19 in the brain and therapeutic options for long COVID: the role of Epstein-Barr virus and the gut-brain axis. *Mol. Psychiatry* (2023 Jul 4). <https://doi.org/10.1038/s41380-023-02161-5>.
- Hirao, H., Nakamura, K., Kupiec-Weglinski, J.W., 2022. Liver ischaemia-reperfusion injury: a new understanding of the role of innate immunity. *Nat. Rev. Gastroenterol. Hepatol.* 19 (4), 239–256. <https://doi.org/10.1038/s41575-021-00549-8>.
- Hua, H., Huang, C., Liu, H., Xu, X., Xu, X., Wu, Z., Liu, C., Wang, Y., Yang, C., 2022. Depression and antidepressant effects of ketamine and its metabolites: the pivotal role of gut microbiota. *Neuropharmacology* 220, 109272. <https://doi.org/10.1016/j.neuropharm.2022.109272>.
- Huang, X., Liu, X., Yu, Y., 2017. Depression and chronic liver diseases: are there shared underlying mechanisms? *Front. Mol. Neurosci.* 10, 134. <https://doi.org/10.3389/fnmol.2017.00134>.
- Ji, H., Shen, X., Gao, F., Ke, B., Freitas, M.C., Uchida, Y., Busuttill, R.W., Zhai, Y., Kupiec-Weglinski, J.W., 2010. Programmed death-1/B7-H1 negative costimulation protects mouse liver against ischemia and reperfusion injury. *Hepatology* 52 (4), 1380–1389. <https://doi.org/10.1002/hep.23843>.
- Ji, H., Zhang, Y., Liu, Y., Shen, X.D., Gao, F., Nguyen, T.T., Busuttill, R.W., Waschek, J.A., Kupiec-Weglinski, J.W., 2013. Vasoactive intestinal peptide attenuates liver ischemia/reperfusion injury in mice via the cyclic adenosine monophosphate-protein kinase a pathway. *Liver Transpl.* 19 (9), 945–956. <https://doi.org/10.1002/lt.23681>.
- Jiang, H., Ling, Z., Zhang, Y., Mao, H., Ma, Z., Yin, Y., Wang, W., Tang, W., Tan, Z., Shi, J., Li, L., Ruan, B., 2015. Altered fecal microbiota composition in patients with major depressive disorder. *Brain Behav. Immun.* 48, 186–194. <https://doi.org/10.1016/j.bbi.2015.03.016>.
- Konishi, T., Lentsch, A.B., 2017. Hepatic ischemia/reperfusion: mechanisms of tissue injury, repair, and regeneration. *Gene Expr.* 17 (4), 277–287. <https://doi.org/10.3727/105221617X15042750874156>.
- Kronsten, V.T., Tranah, T.H., Pariante, C., Shawcross, D.L., 2022. Gut-derived systemic inflammation as a driver of depression in chronic liver disease. *J. Hepatol.* 76 (3), 665–680. <https://doi.org/10.1016/j.jhep.2021.11.008>.

- Liu, L., Wang, H., Chen, X., Zhang, Y., Zhang, H., Xie, P., 2023. Gut microbiota and its metabolites in depression: from pathogenesis to treatment. *EBioMedicine* 90, 104527. <https://doi.org/10.1016/j.ebiom.2023.104527>.
- Lu, T., Li, Q., Lin, W., Zhao, X., Li, F., Ji, J., Zhang, Y., Xu, N., 2023. Gut microbiota-derived glutamine attenuates liver ischemia/reperfusion injury via macrophage metabolic reprogramming. *Cell. Mol. Gastroenterol. Hepatol.* 15 (5), 1255–1275. <https://doi.org/10.1016/j.jcmgh.2023.01.004>.
- Ma, L., Zhang, J., Fujita, Y., Qu, Y., Shan, J., Wan, X., Wang, X., Ishima, T., Kobayashi, K., Wang, L., Hashimoto, K., 2022. Nuclear factor of activated T cells 4 in the prefrontal cortex is required for prophylactic actions of (R)-ketamine. *Transl. Psychiatry* 12 (1), 27. <https://doi.org/10.1038/s41398-022-01803-6>.
- Ma, L., Wang, L., Qu, Y., Wan, X., Hashimoto, K., 2023. A role of splenic heme biosynthesis pathway in the persistent prophylactic actions of arketamine in lipopolysaccharide-treated mice. *Transl. Psychiatry* 13 (1), 269. <https://doi.org/10.1038/s41398-023-02564-6>.
- Mullish, B.H., Kabir, M.S., Thursz, M.R., Dhar, A., 2014. Review article: depression and the use of antidepressants in patients with chronic liver disease or liver transplantation. *Aliment. Pharmacol. Ther.* 40 (8), 880–892. <https://doi.org/10.1111/apt.12925>.
- Patten, S.B., Williams, J.V., Lavorato, D.H., Modgill, G., Jette, N., Eliasziw, M., 2008. Major depression as a risk factor for chronic disease incidence: longitudinal analysis in a general population cohort. *Gen. Hosp. Psychiatry* 30 (5), 407–413. <https://doi.org/10.1016/j.genhosppsych.2008.05.001>.
- Pu, Y., Tan, Y., Qu, Y., Chang, L., Wang, S., Wei, Y., Wang, X., Hashimoto, K., 2021. A role of the subdiaphragmatic vagus nerve in depression-like phenotypes in mice after fecal microbiota transplantation from *Chrna7* knock-out mice with depression-like phenotypes. *Brain Behav. Immun.* 94, 318–326. <https://doi.org/10.1016/j.bbi.2020.12.032>.
- Qu, Y., Yang, C., Ren, Q., Ma, M., Dong, C., Hashimoto, K., 2017. Comparison of (R)-ketamine and lanicemine on depression-like phenotype and abnormal composition of gut microbiota in a social defeat stress model. *Sci. Rep.* 7 (1), 15725. <https://doi.org/10.1038/s41598-017-16060-7>.
- Rampes, S., Ma, D., 2019. Hepatic ischemia-reperfusion injury in liver transplant setting: mechanisms and protective strategies. *J. Biomed. Res.* 33 (4), 221–234. <https://doi.org/10.7555/JBR.32.20180087>.
- Sanada, K., Nakajima, S., Kurokawa, S., Barceló-Soler, A., Ikuse, D., Hirata, A., Yoshizawa, A., Tomizawa, Y., Salas-Valero, M., Noda, Y., Mimura, M., Iwanami, A., Kishimoto, T., 2020. Gut microbiota and major depressive disorder: a systematic review and meta-analysis. *J. Affect. Disord.* 266, 1–13. <https://doi.org/10.1016/j.jpsy.2021.05.009>.
- Schwabe, R.F., Greden, T.F., 2020. Gut microbiome in HCC—mechanisms, diagnosis and therapy. *J. Hepatol.* 72 (2), 230–238. <https://doi.org/10.1016/j.jhep.2019.08.016>.
- Tsugawa, H., Ikeda, K., Takahashi, M., Satoh, A., Mori, Y., Uchino, H., Okahashi, N., Yamada, Y., Tada, I., Bonini, P., Higashi, Y., Okazaki, Y., Zhou, Z., Zhu, Z.J., Koelmel, J., Cajka, T., Fiehn, O., Saito, K., Arita, M., Arita, M., 2020. A lipidome atlas in MS-DIAL 4. *Nat. Biotechnol.* 38 (10), 1159–1163. <https://doi.org/10.1038/s41587-020-0531-2>.
- Wan, X., Eguchi, A., Chang, L., Mori, C., Hashimoto, K., 2023. Beneficial effects of arketamine on the reduced bone mineral density in susceptible mice after chronic social defeat stress: role of the gut-microbiota-bone-brain axis. *Neuropharmacology* 228, 109466. <https://doi.org/10.1016/j.neuropharm.2023.109466>.
- Wang, S., Ishima, T., Zhang, J., Qu, Y., Chang, L., Pu, Y., Fujita, Y., Tan, Y., Wang, X., Hashimoto, K., 2020. Ingestion of *Lactobacillus intestinalis* and *Lactobacillus reuteri* causes depression- and anhedonia-like phenotypes in antibiotic-treated mice via the vagus nerve. *J. Neuroinflammation* 17 (1), 241. <https://doi.org/10.1186/s12974-020-01916-z>.
- Wang, S., Ishima, T., Qu, Y., Shan, J., Chang, L., Wei, Y., Zhang, J., Pu, Y., Fujita, Y., Tan, Y., Wang, X., Ma, L., Wan, X., Hammock, B.D., Hashimoto, K., 2021. Ingestion of *Faecalibaculum rodentium* causes depression-like phenotypes in resilient *Ephx2* knock-out mice: a role of brain-gut-microbiota axis via the subdiaphragmatic vagus nerve. *J. Affect. Disord.* 292, 565–573. <https://doi.org/10.1016/j.jad.2021.06.006>.
- Wang, X., Yang, J., Hashimoto, K., 2022. (R)-ketamine as prophylactic and therapeutic drug for neurological disorders: beyond depression. *Neurosci. Biobehav. Rev.* 139, 104762. <https://doi.org/10.1016/j.neubiorev.2022.104762>.
- Wang, X., Eguchi, A., Yang, Y., Chang, L., Wan, X., Shan, J., Qu, Y., Ma, L., Mori, C., Yang, J., Hashimoto, K., 2023. Key role of the gut-microbiota-brain axis via the subdiaphragmatic vagus nerve in demyelination of the cuprizone-treated mouse brain. *Neurobiol. Dis.* 176, 105951. <https://doi.org/10.1016/j.nbd.2022.105951>.
- Wei, Y., Chang, L., Hashimoto, K., 2022a. Molecular mechanisms underlying the antidepressant actions of arketamine: beyond the NMDA receptor. *Mol. Psychiatry* 27 (1), 559–573. <https://doi.org/10.1038/s41380-021-01121-1>.
- Wei, Y., Wang, T., Liao, L., Fan, X., Chang, L., Hashimoto, K., 2022b. Brain-spleen axis in health and diseases: a review and future perspective. *Brain Res. Bull.* 182, 130–140. <https://doi.org/10.1016/j.brainresbull.2022.02.008>.
- Wiest, R., Albillos, A., Trauner, M., Bajaj, J.S., Jalan, R., 2017. Targeting the gut-liver axis in liver disease. *J. Hepatol.* 67 (5), 1084–1103. <https://doi.org/10.1016/j.jhep.2017.05.007>.
- Wu, C., Xia, Y., Wang, P., Lu, L., Zhang, F., 2011. Triptolide protects mice from ischemia/reperfusion injury by inhibition of IL-17 production. *Int. Immunopharmacol.* 11 (10), 1564–1572. <https://doi.org/10.1016/j.intimp.2011.05.015>.
- Yang, C., Shirayama, Y., Zhang, J.C., Ren, Q., Yao, W., Ma, M., Dong, C., Hashimoto, K., 2015. R-ketamine: a rapid-onset and sustained antidepressant without psychotomimetic side effects. *Transl. Psychiatry* 5 (9), e632. <https://doi.org/10.1038/tp.2015.136>.
- Yang, C., Qu, Y., Fujita, Y., Ren, Q., Ma, M., Dong, C., Hashimoto, K., 2017. Possible role of the gut microbiota-brain axis in the antidepressant effects of (R)-ketamine in a social defeat stress model. *Transl. Psychiatry* 7 (12), 1294. <https://doi.org/10.1038/s41398-017-0031-4>.
- Yang, C., Yang, J., Luo, A., Hashimoto, K., 2019. Molecular and cellular mechanisms underlying the antidepressant effects of ketamine enantiomers and its metabolites. *Transl. Psychiatry* 9 (1), 280. <https://doi.org/10.1038/s41398-019-0624-1>.
- Yang, Y., Ishima, T., Wan, X., Wei, Y., Chang, L., Zhang, J., Qu, Y., Hashimoto, K., 2022. Microglial depletion and abnormalities in gut microbiota composition and short-chain fatty acids in mice after repeated administration of colony stimulating factor 1 receptor inhibitor PLX5622. *Eur. Arch. Psychiatry Clin. Neurosci.* 272 (3), 483–495. <https://doi.org/10.1007/s00406-021-01325-0>.
- Yang, Y., Eguchi, A., Wan, X., Chang, L., Wang, X., Qu, Y., Mori, C., Hashimoto, K., 2023. A role of gut-microbiota-brain axis via subdiaphragmatic vagus nerve in depression-like phenotypes in *Chrna7* knock-out mice. *Prog. Neuropsychopharmacol. Biol. Psychiatry* 120, 110652. <https://doi.org/10.1016/j.pnpbp.2022.110652>.
- Yue, C., Luan, W., Gu, H., Qiu, D., Ding, X., Liu, P., Wang, X., Hashimoto, K., Yang, J.J., 2023. The role of the gut-microbiota-brain axis via the subdiaphragmatic vagus nerve in chronic inflammatory pain and comorbid spatial working memory impairment in complete Freund's adjuvant mice. *J. Psychiatr. Res.* 166, 61–73. <https://doi.org/10.1016/j.jpsy.2023.09.003>.
- Zhang, J.C., Li, S.X., Hashimoto, K., 2014. R (-)-ketamine shows greater potency and longer lasting antidepressant effects than S (+)-ketamine. *Pharmacol. Biochem. Behav.* 116, 137–141. <https://doi.org/10.1016/j.pbb.2013.11.033>.
- Zhang, J., Ma, L., Chang, L., Pu, Y., Qu, Y., Hashimoto, K., 2020. A key role of the subdiaphragmatic vagus nerve in the depression-like phenotype and abnormal composition of gut microbiota in mice after lipopolysaccharide administration. *Transl. Psychiatry* 10 (1), 186. <https://doi.org/10.1038/s41398-020-00878-3>.
- Zhang, J., Ma, L., Wan, X., Shan, J., Qu, Y., Hashimoto, K., 2021a. (R)-ketamine attenuates LPS-induced endotoxin-derived delirium through inhibition of neuroinflammation. *Psychopharmacology (Berl)* 238 (10), 2743–2753. <https://doi.org/10.1007/s00213-021-05889-6>.
- Zhang, Y., Xie, B., Chen, X., Zhang, J., Yuan, S., 2021b. A key role of gut microbiota-vagus nerve/spleen axis in sleep deprivation-mediated aggravation of systemic inflammation after LPS administration. *Life Sci.* 265, 118736. <https://doi.org/10.1016/j.lfs.2020.118736>.
- Zhang, J.C., Yao, W., Hashimoto, K., 2022a. Arketamine, a new rapid-acting antidepressant: a historical review and future directions. *Neuropharmacology* 218, 109219. <https://doi.org/10.1016/j.neuropharm.2022.109219>.
- Zhang, X., Liu, H., Hashimoto, K., Yuan, S., Zhang, J., 2022b. The gut–liver axis in sepsis: interaction mechanisms and therapeutic potential. *Crit. Care* 26 (1), 213. <https://doi.org/10.1186/s13054-022-04090-1>.
- Zhang, K., Yao, Y., Hashimoto, K., 2023. Ketamine and its metabolites: potential as novel treatments for depression. *Neuropharmacology* 222, 109305. <https://doi.org/10.1016/j.neuropharm.2022.109305>.
- Zheng, P., Zeng, B., Zhou, C., Liu, M., Fang, Z., Xu, X., Zeng, L., Chen, J., Fan, S., Du, X., Zhang, X., Yang, D., Wang, Y., Meng, H., Li, W., Melgiri, N.D., Licinio, J., Wei, H., Xie, P., 2016. Gut microbiome remodeling induces depressive-like behaviors through a pathway mediated by the host's metabolism. *Mol. Psychiatry* 21 (6), 786–796. <https://doi.org/10.1038/mp.2016.44>.



Depression-like phenotypes in mice following common bile duct ligation: Insights into the gut–liver–brain axis via the vagus nerve

Yong Yang^{a,b}, Akifumi Eguchi^c, Chisato Mori^{c,d}, Kenji Hashimoto^{a,*}

^a Division of Clinical Neuroscience, Chiba University Center for Forensic Mental Health, Chiba 260-8670, Japan

^b Department of Neurosurgery, Guizhou Provincial People's Hospital, Guiyang 550002, China

^c Department of Sustainable Health Science, Chiba University Center for Preventive Medical Sciences, Chiba 263-8522, Japan

^d Department of Bioenvironmental Medicine, Graduate School of Medicine, Chiba University, Chiba 260-8670, Japan

ARTICLE INFO

Keywords:

Arketamine
Depression
Gut microbiota
Liver cirrhosis
Metabolites
Vagus nerve

ABSTRACT

Depression frequently occurs in patients with liver cirrhosis, yet the reasons for this correlation are not fully understood. Dysbiosis of gut microbiota has been implicated in depression through the gut–brain axis via the vagus nerve. This study explored the potential role of the gut–liver–brain axis via the vagus nerve in depression-like phenotypes in mice with liver cirrhosis. These mice underwent common bile duct ligation (CBDL), a method used to stimulate liver cirrhosis. To assess depression-like behaviors, behavioral tests were conducted 10 days following either sham or CBDL surgeries. The mice with CBDL displayed symptoms such as splenomegaly, elevated plasma levels of interleukin-6 and tumor necrosis factor- α , depression-like behaviors, decreased levels of synaptic proteins in the prefrontal cortex (PFC), disrupted gut microbiota balance, and changes in blood metabolites (or lipids). Additionally, there were positive or negative correlations between the relative abundance of microbiome and behavioral data or blood metabolites (or lipids). Significantly, these changes were reversed in CBDL mice by performing a subdiaphragmatic vagotomy. Intriguingly, depression-like phenotypes in mice with CBDL were improved after a single injection of arketamine, a new antidepressant. These results suggest that CBDL-induced depression-like phenotypes in mice are mediated through the gut–liver–brain axis via the subdiaphragmatic vagus nerve, and that arketamine might offer a new treatment approach for depression in liver cirrhosis patients.

1. Introduction

Liver cirrhosis, characterized by the overaccumulation of extracellular matrix proteins like collagen, is common in most chronic liver diseases (CLDs) (Ginès et al., 2021; Tapper and Parikh, 2023). Depression is frequently observed in liver cirrhosis patients, with its prevalence notably higher than in the general populations, indicating a possible connection between these conditions (Bianchi et al., 2005; Nardelli et al., 2013; Singh et al., 1997). A substantial U.S. population-based study (56,197,690 adults) found a significant association between liver cirrhosis and an increased risk of depression (Abureesh et al., 2022). The exact biological mechanisms linking depression and liver cirrhosis remain elusive. However, liver cirrhosis can induce various physiological changes that might contribute to depression, including hormonal imbalances, immune system dysfunction, and the build-up of neurotoxins that the damaged liver fails to filter effectively (Bonnel

et al., 2011; Kur et al., 2020; Zhou et al., 2014). Notably, the severity of liver disease in patients with cirrhosis correlates with signs of psychological distress and depression (Bianchi et al., 2005). Depression in liver cirrhosis patients is more than a comorbidity; it can influence the liver disease's progression, affecting treatment adherence, lifestyle choices, and overall prognosis. Therefore, treating depression in these patients is essential. Although the interaction between liver cirrhosis and depression is complex and bidirectional, the precise underlying mechanisms are still not fully understood (Huang et al., 2017).

Numerous clinical and pre-clinical studies indicate a significant role of the gut–brain axis, including gut microbiota, in depression (Chang et al., 2022; Cryan et al., 2019; Hashimoto, 2023a, 2023b; Hua et al., 2022; Liu et al., 2023; Sanada et al., 2020; Wei et al., 2022a, 2022b; Zheng et al., 2016). The vagus nerve is key in the two-way communication between the gut microbiota and the brain (Bonaz et al., 2018; Chang et al., 2022; Forsythe et al., 2014; Hashimoto, 2023b, 2023c; Wei

* Corresponding author.

E-mail address: hashimoto@faculty.chiba-u.jp (K. Hashimoto).

<https://doi.org/10.1016/j.nbd.2024.106433>

Received 13 January 2024; Received in revised form 6 February 2024; Accepted 6 February 2024

Available online 7 February 2024

0969-9961/© 2024 The Authors. Published by Elsevier Inc. This is an open access article under the CC BY-NC-ND license (<http://creativecommons.org/licenses/by-nc-nd/4.0/>).

et al., 2022b). Interestingly, subdiaphragmatic vagotomy (SDV) has been shown to prevent depression-like behaviors and alterations in gut microbiota composition in mice following lipopolysaccharide (LPS) administration (Zhang et al., 2020) and fecal microbiota transplantation (FMT) from mice with depression-like phenotypes (Pu et al., 2021; Wang et al., 2020, 2021). Additionally, SDV blocks depression-like behaviors in *Chrna7* knock-out mice (Yang et al., 2023) and in mice with hepatic ischemia/reperfusion (HI/R) injury (Yang et al., 2024), as well as working memory impairment in mice with chronic inflammatory pain (Yue et al., 2023). SDV also blocks the resilience-enhancing effects of the entactogen 3,4-methylenedioxymetamphetamine in mice subjected to chronic restraint stress (Qu et al., 2023a, 2023b), and prevents demyelination in the mouse brain treated with cuprizone (Wang et al., 2023). These studies support the crucial role of the gut–brain axis via the subdiaphragmatic vagus nerve in depression (Chang et al., 2022; Hashimoto, 2023b; Wei et al., 2022a). Kronsten et al. (2022) hypothesized that gut-mediated systemic inflammation might link depression and CLD, indicating potential abnormalities in the gut–liver–brain axis. Furthermore, clinical data highlight significant patterns of gut microbiota dysbiosis in liver cirrhosis patients, which may lead to cognitive impairments and mood disorders (Smith et al., 2023).

Common bile duct ligation (CBDL), a well-established model for studying secondary biliary fibrosis, triggers the proliferation of biliary epithelial cells and oval cells. This proliferation leads to an increase in bile ductules, portal inflammation, and fibrosis, and ultimately results in liver cirrhosis and liver failure (Geerts et al., 2008; Tag et al., 2015; Van Campenhout et al., 2019). While rodent models of CBDL are extensively utilized in research, there have been no studies reported to date that demonstrate depression-like phenotypes in rodents subjected to CBDL. Similarly, the potential role of the gut–liver–brain axis, specifically through the vagus nerve, in rodents with CBDL has not been reported in the literature.

This study aimed to explore the connection between depression and liver cirrhosis. Initially, we assessed depression-like behaviors in mice with CBDL, alongside measuring blood inflammation markers and synaptic proteins in the brain. Secondly, to delve into the gut–liver–brain axis's role in these depression-like behaviors, we conducted 16 s rRNA analysis of feces samples and untargeted metabolomic and lipidomic analyses of plasma samples. Thirdly, we explored the role of the subdiaphragmatic vagus nerve on these depression-like phenotypes by performing SDV. Lastly, we investigated the impact of the novel antidepressant arketamine in mice with CBDL since a single dose showed rapid-acting antidepressant-like effects in rodents with depression-like phenotypes (Hashimoto, 2020, 2022, 2023d; Wei et al., 2022a; Yang et al., 2015, 2019; Zhang et al., 2014, 2022a; Zhang et al., 2023).

2. Materials and methods

2.1. Animals

Male adult C57BL/6Ncr mice, sourced from the Japan SLC Co., Ltd. (Hamamatsu, Shizuoka, Japan), were used in this study. All the experimental mice were aged 9 weeks, body weight 21.5–26.5 g. All the experimental mice were acclimatized to standard laboratory conditions (4 or 5/ cage), maintained alternating cycles of 12 h of light and 12 h of darkness (lights on from 7:00–19:00), and under constant room temperature of 23 ± 1 °C and controlled humidity of $55 \pm 5\%$. Animals were given free admittance to chow and water. The experimental protocol of present study was approved by the Chiba University Institutional Animal Care and Use Committee (Permission numbers 4–312, 4–405 and 4–441). The mice were all firstly deeply anesthetized with inhaled isoflurane and then rapidly sacrificed by cervical dislocation. All efforts were made to minimize animal's suffering.

2.2. Reagents

Arketamine [or (*R*)-ketamine] hydrochloride was prepared as reported previously (Zhang et al., 2014). The dose (10 mg/kg as hydrochloride salt) of arketamine was dissolved in the saline as reported previously (Yang et al., 2015; Yang et al., 2024; Yao et al., 2022). Other reagents were purchased commercially.

2.3. Common bile duct ligation (CBDL)

Sham or CBDL surgeries were performed under continuous inhalation anesthesia with 4–5% isoflurane using an inhalation small animal anesthesia apparatus (KN-1071 NARCOBIT-E; Natsume Seisakusho, Tokyo, Japan), with minor modifications from previous reports (Tag et al., 2015). Briefly, mice were placed in a supine position and, once fully anesthetized, the abdominal operation area was prepared. The skin was disinfected with iodophor. A 1.5 cm median incision was made along the abdominal midline, starting 0.5 cm below the xiphoid process. This incision was gently opened using a Mini incision spreader to expose the liver. The liver tissue was carefully maneuvered upwards with a small cotton ball moistened in saline, aided by a surgical microscope (Leica, Heidelberg, Germany), positioning the ventral side against the diaphragm and making the hilum visible. The small intestine was gently separated to expose the common bile duct. The bile duct was carefully isolated from the adjacent portal vein and hepatic artery using microserrations forceps. A 5–0 suture was placed around the bile duct and secured with two surgical knots, applying increasing traction to ensure effective obstruction without severing the duct. A second ligation was added in the same manner but did not dissect the bile duct in-between. Post-operation, no bleeding or no additional injury was noted. The peritoneal cavity was rinsed with 0.9% NaCl solution, and abdominal organs were gently repositioned. The abdominal incision was sutured in layers using 5–0 surgical silk, maintaining aseptic conditions throughout.

During sham surgeries, an identical abdominal incision was made, and the common bile duct was exposed, but not ligated. All other steps mirrored those of the surgery group.

2.4. Bilateral subdiaphragmatic vagotomy (SDV)

Bilateral SDV or sham surgeries were conducted under continuous inhalation anesthesia with 4–5% isoflurane, using a small animal anesthesia apparatus (KN-1071 NARCOBIT-E; Natsume Seisakusho, Tokyo, Japan), following methods described in previous studies (Pu et al., 2021; Yang et al., 2023, 2024; Zhang et al., 2020). Briefly, mice were placed in a right-side decubitus position. The skin was disinfected with iodophor disinfectant, and sterile tissue was laid down. An incision about 1 cm in length, parallel to the costal arch, was made at 0.5 cm below the left costal arch, starting from the midline alba of abdomen. The incision was gently opened with a Mini incision spreader to expose the underlying liver tissue. The liver was cautiously elevated using a sterilized cotton ball moistened with saline, and under guidance of a surgical microscope (Leica, Heidelberg, Germany), the fascia between the caudate and left lobes of the liver was sharply incised to fully expose the esophagus and surrounding area. The dorsal and ventral branches of the vagus nerve running along the esophagus under the diaphragm were identified and carefully severed. Post-procedure, no bleeding or additional injury to the esophagus, liver, or other organs was observed. The liver tissue was repositioned, and 0.5 ml saline solution was injected into the abdominal cavity. The incision was then sutured in layers using 5–0 surgical silk, ensuring aseptic technique throughout. SDV success was verified by a significant increase in stomach volume on the 14th postoperative day, indicative of vagus nerve innervation loss.

During sham surgeries, an identical abdominal incision was made. The dorsal and ventral branches of the subdiaphragmatic vagus nerve were gently exposed but not severed. No bleeding or additional organ

damage was noted. After repositioning the abdominal organs, 0.5 ml normal saline was injected into the abdominal cavity, and the incision was closed using the same layered suture technique. When combining CBDL + SDV procedures, SDV was performed first via the same abdominal approach, followed by the CBDL procedure.

2.5. Behavioral tests

Behavioral tests, including locomotion test (LMT), forced swimming test (FST), and 1% sucrose preference test (SPT) were performed as reported previously (Yang et al., 2023, 2024) (Fig. 1A).

In order to monitor the locomotor activity of the mice, we adopted an automatic animal movement analysis system (SCANET MV-40; MEL-QUEST Co., Ltd., Toyama, Japan). The cumulative ambulatory activity counts were automatic document continuously over a total stage of 60 min (10 min \times 6 times) after the mice were placed into the experimental cube boxes [33 cm (height) \times 56 cm (width) \times 56 cm (length)]. To avoid experimental interference, the cube boxes were cleaned up during the test interval.

A mouse automated forced-swim apparatus (SCANET MV-40; MEL-QUEST Co., Ltd., Toyama, Japan) was used to perform FST. Mice were placed into an inescapable transparent tank [31 cm (height) \times 23 cm (diameter)] that was filled with tap water at a temperature of $23 \pm 1^\circ\text{C}$ and a depth of 15 cm. Then their escape related mobility behavior was measured immediately. The immobility times were automatic document

and calculated using the analytical software of the apparatus over a total stage of 6 min (1 min \times 6 times).

For 1% SPT, which was carried out in the separate animal's home cage. Each mouse was presented with two dual bearing sipper bottles, one bottle contained tap water, and the second contained a 1% sucrose solution. After 24 h of every mouse exposed to the respective two bottles containing different solutions, replaced the positions of two bottles for each other to lower any confound produced by a side bias. After another 24 h, all food and bottles were deprived lasting 4 h, then performed 1 h exposure to two identical bottles (containing tap water and 1% sucrose solution), which were weighed before and after the exposure period. The 1% sucrose preference was calculated as a percentage of 1% sucrose solution intake weight over the total liquid intake weight.

2.6. Enzyme-linked immunosorbent assay (ELISA)

ELISA kits for the detection of interleukin-6 (IL-6) (cat Number: 88-7064, Invitrogen, Camarillo, CA, USA), and tumor necrosis factor- α (TNF- α) (cat Number: 88-7324, Invitrogen, Camarillo, CA, USA) were used as reported previously (Yang et al., 2024).

2.7. Western blot analysis

Western blot analysis was conducted following the methods described in previous studies (Yang et al., 2022, 2023, 2024). Prefrontal

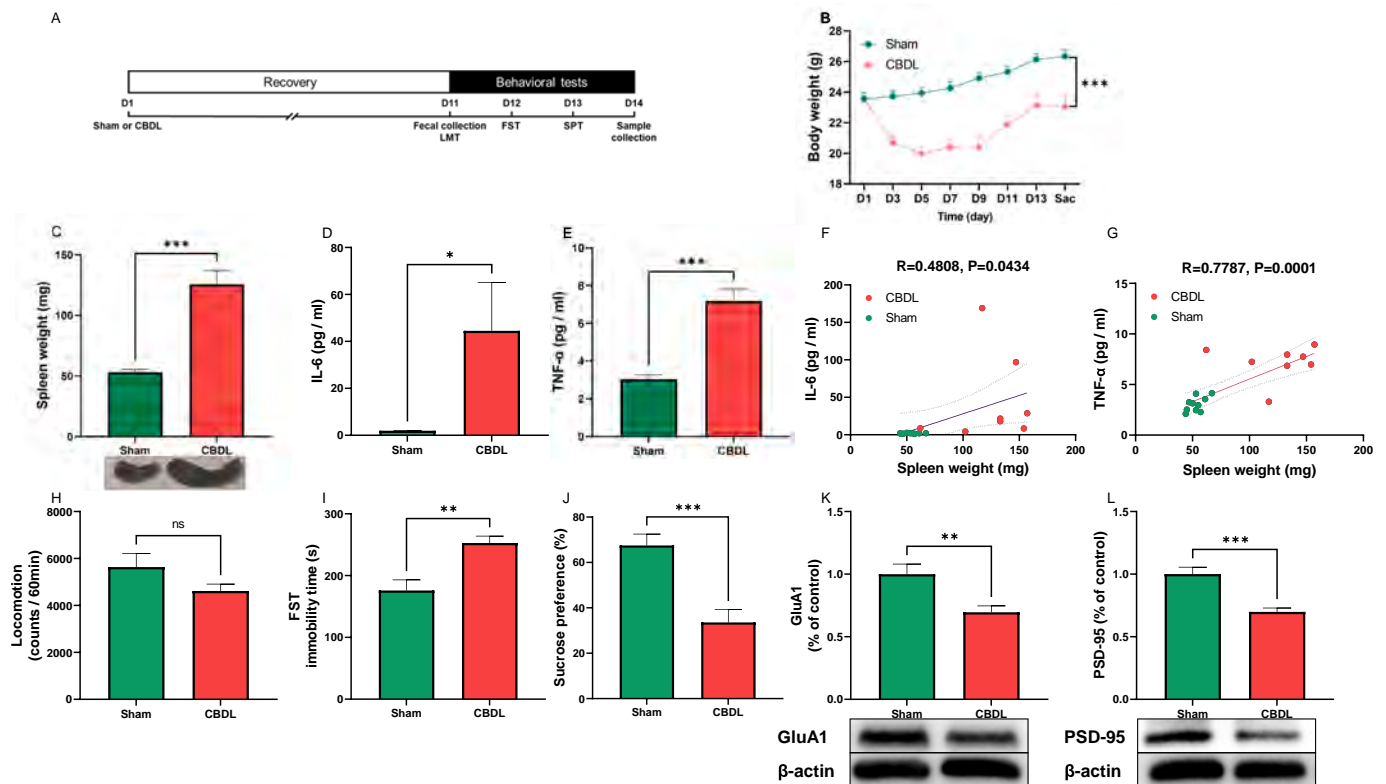


Fig. 1. Depression-like phenotypes in mice with CBDL.

(A): Experimental schedule. On day 1, mice underwent either sham or CBDL surgery. A 10-day recovery period followed. Fresh fecal samples were collected on day 11, and subsequently LMT was performed. FST and 1% SPT were performed on day 12 and day 13, respectively. Prefrontal cortex (PFC) and plasma samples were collected on day 14. (B): Body weight (repeated measure ANOVA, $F_{(1,16)} = 33.08$, $P < 0.001$). (C): Spleen weight (unpaired t -test, $t = 7.050$, $df = 16$, $P < 0.001$) and representative photograph of spleen in the two groups. (D): Plasma levels of IL-6 (unpaired t -test, $t = 2.320$, $df = 16$, $P = 0.0339$). (E): Plasma levels of TNF- α (unpaired t -test, $t = 6.895$, $df = 16$, $P < 0.001$). (F): There was a positive correlation ($R = 0.4808$, $P = 0.0434$) between the spleen weight and plasma levels of IL-6 in two groups. (G): There was a positive correlation ($R = 0.7787$, $P = 0.0001$) between the spleen weight and plasma levels of TNF- α in two groups. (H): locomotion (LMT) (unpaired t -test, $t = 1.446$, $df = 16$, $P = 0.1675$). (I): FST (unpaired t -test, $t = 3.522$, $df = 16$, $P = 0.0028$). (J): SPT (unpaired t -test, $t = 4.495$, $df = 16$, $P = 0.0004$). (K) Western blot analysis of GluA1 in the PFC (unpaired t -test, $t = 2.996$, $df = 16$, $P = 0.0086$) and the representative bands. (L): Western blot analysis of PSD-95 in the PFC (unpaired t -test, $t = 4.396$, $df = 16$, $P = 0.0005$) and the representative bands. The data are shown as means \pm S.E.M (sham group: $n = 10$, CBDL group: $n = 8$). ANOVA: analysis of variance. ns: not significant; * $P < 0.05$; ** $P < 0.01$; *** $P < 0.001$.

cortex (PFC) tissues were homogenized in ice-cold Laemmli lysis buffer, with each specimen processed separately to prevent cross-contamination. After centrifugation at 3000 ×g (RCF) at 4 °C for 20 min, liquid supernatants were collected. The total protein concentration in each sample was measured using a DC protein assay kit (Bio-Rad, Hercules, CA, USA) on a spectrophotometer (Molecular Devices Emax Precision Microplate Reader; Molecular Devices., San Jose, CA, USA). To prepare the samples for electrophoresis, a quarter volume of sample buffer (125 mM Tris-HCl, pH 6.8; 0.1% bromophenol blue; 4% sodium dodecyl sulfate; and 10% β-mercaptoethanol and 20% glycerol) was added to the Laemmli Lysis buffer. The proportions were adjusted to equalize the total protein concentration across samples. These mixtures were then incubated at 95 °C for 10 min. For electrophoresis, we employed 10% sodium dodecyl sulfate–polyacrylamide gel electrophoresis (SDS-PAGE) (catalog #: 4568125, Mini-PROTEAN TGX™ Stain-Free Gels; Bio-Rad, USA), selected based on the size of the target protein. The separated proteins were then transferred onto polyvinylidene difluoride membranes using a trans-Blot Mini Cell apparatus (Bio-Rad).

Synaptic proteins such as glutamate receptor 1 (AMPA subtype: GluA1: [the α-amino-3-hydroxy-5-methyl-4-isoxazolepropionic acid receptor A1]) and postsynaptic density protein 95 (PSD-95) were decreased in the PFC of mice with depression-like phenotypes (Yang et al., 2022, 2023, 2024). For immunodetection, the polyvinylidene difluoride membranes were blocked with blocker [5% skim milk in TBS + 0.1% Tween-20 (TBST)] at room temperature for 1 h, the membranes for detecting PSD-95 were incubated with the recommended dilution of the primary antibody against PSD-95 (1:1000, catalog number: 51–6,900,695, 1 μg/mL, Invitrogen, Camarillo, CA, USA), while the membranes for detecting β-actin were incubated with the appropriate dilution of the primary antibody against β-actin (1:10,000; catalog number: A5441 Sigma-Aldrich Co., Ltd., St Louis, MO, USA) at 4 °C overnight. The next day, wash the polyvinylidene difluoride membranes in three washes of TBST, 10 min each. Then the polyvinylidene difluoride membranes were selectively incubated with a recommended dilution of labeled secondary antibody [anti-mouse antibody (1:5000, catalog number: NA931, GE Healthcare) or a horseradish peroxidase-conjugated anti-rabbit antibody (1:5000, catalog number: NA934, GE Healthcare)] in 5% blocking buffer in TBST at room temperature for 1 h. After three final washes in TBST, 10 min each. The bands in the polyvinylidene difluoride membranes were detected using enhanced chemiluminescence plus a Western Blotting Detection system (GE Healthcare Bioscience).

The membranes for detecting GluA1 were incubated in elution buffer (62.5 mM Tris-HCl, pH 6.8, 2% sodium dodecyl sulfate, and 100 mM β-mercaptoethanol) (preheat in incubator at 60 °C for 10 min, shake 50 times/min) at 60 °C for 30 min and then washed three times (10 min at a time) in TBST. The stripped membranes were incubated with the recommended dilution of primary antibody directed against GluA1 (1:10,000; catalog number: ab31232, Abcam, Cambridge, MA, USA) at 4 °C overnight. The following day, washing the membranes for three times (10 min at a time) in TBST and were incubated with a recommended dilution of horseradish peroxidase-conjugated anti-rabbit antibody (1:5000, catalog number: NA934, GE Healthcare) for 1 h at room temperature. After three final washes in TBST, 10 min each. The bands in the polyvinylidene difluoride membranes were detected using enhanced chemiluminescence plus a Western Blotting Detection system (GE Healthcare Bioscience). Images were produced using a ChemiDoc™ Touch Imaging System (170–01401; Bio-Rad Laboratories, Hercules, CA, USA), and immunoreactive bands were quantified using Image Lab™3.0 software (Bio-Rad Laboratories).

2.8. Collection of fresh fecal samples and 16S ribosome RNA sequencing

We collected fresh fecal samples from mice before the behavioral test of LMT. The subsequent experimental workflow, which included microbial community DNA extraction, DNA quality control, PCR

amplification, product purification, library quality control, sequencing, and bioinformatics analysis, was carried out in accordance with our previously reported methods (Yang et al., 2023, 2024). The 16S ribosome RNA sequencing data has been uploaded to and stored in the NCBI Sequence Read Archive, and can be accessed using the accession number PRJNA929668.

2.9. Untargeted metabolomic and lipidomic analyses of plasma samples

Untargeted metabolomics profiling of plasma samples was conducted using ultra-performance liquid chromatography–tandem quadrupole time-of-flight mass spectrometry (UPLC-QTOF/MS) technique. This process involved an ExionLC™ AD system (SCIEX, Tokyo, Japan) coupled with a X500R QTOF system (SCIEX, Tokyo, Japan). The metabolomics profile data were subsequently annotated and analyzed according to the methods we previously reported (Yang et al., 2024). In parallel, untargeted lipidomic analysis of plasma samples were carried out using an X500R QTOF system (SCIEX, Tokyo, Japan), operated in both positive and negative electrospray ionization modes (AB Sciex, Foster City, CA). This system was also coupled with an ExionLC™ AD system (SCIEX, Tokyo, Japan). The data processing and analysis for this lipidomic study were performed in line with previously established protocols (Tsugawa et al., 2020; Yang et al., 2024).

2.10. Statistical analysis

Statistical analysis of the data was performed using the SPSS version 20.0 software (SPSS, Tokyo, Japan). The data were shown as the mean ± standard error of the mean (S.E.M.). The data of body weight were analyzed using repeated measure analysis of variance (ANOVA), followed by Fisher's least significant difference (LSD) test. The data of spleen weight were analyzed using an unpaired *t*-test (for two groups) or two-way ANOVA (for four groups). Data of behavioral tests, pro-inflammatory cytokines and synaptic proteins were analyzed using unpaired *t*-test (for two groups), one-way ANOVA (for three groups), or two-way ANOVA (for four groups), followed by Fisher's LSD test. The α-diversity of gut microbiota, the abundance of gut microbiota at the species level, metabolites and lipids between the two groups were analyzed using Mann-Whitney test. Bioinformatic analysis of PCoA, LEfSe algorithm of intestinal microbiota, boxplot analysis of metabolomics/lipids and correlation networks were all performed by using the OmicStudio tools (<https://www.omicstudio.cn/tool>).

Correlations between spleen weight and the concentrations of pro-inflammatory cytokines were analyzed by using Pearson's correlation analysis. Correlations between the plasma metabolites (or lipids), the intestinal microbiota at species level, depression-like phenotypes, the concentrations of pro-inflammatory cytokines and synaptic proteins in the PFC were analyzed using Spearman's correlation analysis. *P*-value for comparison <0.05 was regarded as significant.

3. Results

3.1. Depression-like phenotypes in mice with CBDL

Behavioral tests were conducted 11 days post-surgery (Fig. 1A). The CBDL group exhibited a reduction in body weight relative to the sham-operated group (Fig. 1B). The CBDL group presented splenomegaly compared to the sham group (Fig. 1C). In the CBDL group, plasma levels of pro-inflammatory cytokines, including IL-6 and TNF-α, were elevated compared to those in the sham group (Fig. 1D, E). Positive correlations were observed between the weight of the spleen and the plasma levels of IL-6 and TNF-α (Fig. 1F, G). In behavioral tests, no significant differences in locomotor activity were noted between the two groups (Fig. 1H). However, the CBDL group demonstrated increased immobility time in the FST (Fig. 1I) and a decreased sucrose preference in the SPT (Fig. 1J) compared to the sham group. Additionally, levels of synaptic proteins

(GluA1 and PSD-95) in the PFC were lower in the CBDL group than in the sham group (Fig. 1K, L). These findings indicate that mice with CBDL exhibit reduced body weight, splenomegaly, heightened systemic inflammation, and diminished synaptic protein expression in the PFC, which collectively contribute to depression-like phenotypes.

3.2. Effects of CBDL on the composition diversity of gut microbiota

The composition of the intestinal microbiota in both the CBDL group and sham group was examined using both α -diversity and β -diversity metrics. The Mann–Whitney U test showed no significant differences in Observed_otus, Chao, Ace, Shannon's diversity, Simpson's diversity, and Good's coverage between the CBDL and sham groups (Fig. 2A–F). β -diversity in the intestinal microbiota of the two groups was assessed using Principal Coordinate Analysis (PCoA). At the operational taxonomic unit (OTU) level, the PCoA analysis indicated a marked difference in microbiota composition, as shown by analysis of similarities (ANOSIM) ($R = 0.6971$, $P = 0.001$) (Fig. 2G). The ANOSIM at the OTU level suggested that the inter-group differences in microbiota composition were more pronounced than the intra-group variations ($R = 0.691$, $P = 0.001$) (Fig. 2H).

3.3. Effects of CBDL on the LEfSe algorithm of intestinal microbiota

A cladogram was utilized to illustrate the relationship among biomarker taxa identified by LEfSe. This cladogram is structured in layers representing different taxonomic levels: phylum, class, order, family and genus, arranged from the innermost to the outermost layer (Fig. 3A). In the CBDL group, LEfSe analysis identified five taxonomic biomarkers: the phylum *Firmicutes*, the class *Clostridia*, the order *Clostridiales*, the family *Lachnospiraceae* and the genus *Clostridium_XIVa*

(Fig. 3B). Conversely, six taxonomic biomarkers were identified in the sham group, including the phylum *Bacteroidetes*, the class *Bacteroidia*, the order *Bacteroidales*, the family *Porphyromonadaceae* and *Prevotellaceae*, and the genus *Barnesiella* (Fig. 3B).

3.4. Gut microbiota at the species level

At the species level, the analysis revealed 21 bacterial species with significant differences in relative abundance between the groups (Fig. 4A). In the CBDL group, the species *Alistipes_finegoldii*, *Akkermansia_muciniphila*, *Lactobacillus_intestinalis*, *Clostridium_aldenense*, *Allobaculum_stercoricanis*, *Clostridium_methylpentosum*, *Parabacteroides_goldsteini*, *Gemmiger_formicilis*, *Bacteroides_acidifaciens*, *Parabacteroides_distasonii*, and *Clostridium_cocleatum* exhibited significantly higher relative the sham group. Conversely, the species *Alloprevotella_rava*, *Bacteroides_sartorii*, *Parvibacter_caecicola*, *Barnesiella_intestinihominis*, *Butyrivibrio_pullicaeorum*, *Enterorhabdus_caecimuris*, *Leptotrichia_shahii*, *Escherichia*, *Eubacterium_coprostanoligenes* and *Prevotella_baroniae* showed significantly lower relative to the sham group (Fig. 4B–V).

3.5. Untargeted metabolomic and lipidomic analyses of plasma samples

To examine the interaction between the gut microbiome and host metabolic processes, untargeted metabolomic and lipidomic analyses were performed on plasma samples. Following quality control measures and the exclusion of low-abundance peaks, 131 metabolites were successfully annotated. Among these, 29 metabolites were found to have significant differences in abundance between the two groups (Fig. 5A). Additionally, after thorough data processing, 92 lipids were annotated. Of these, 50 lipids showed significant variations in abundance between the two groups (Fig. 5B).

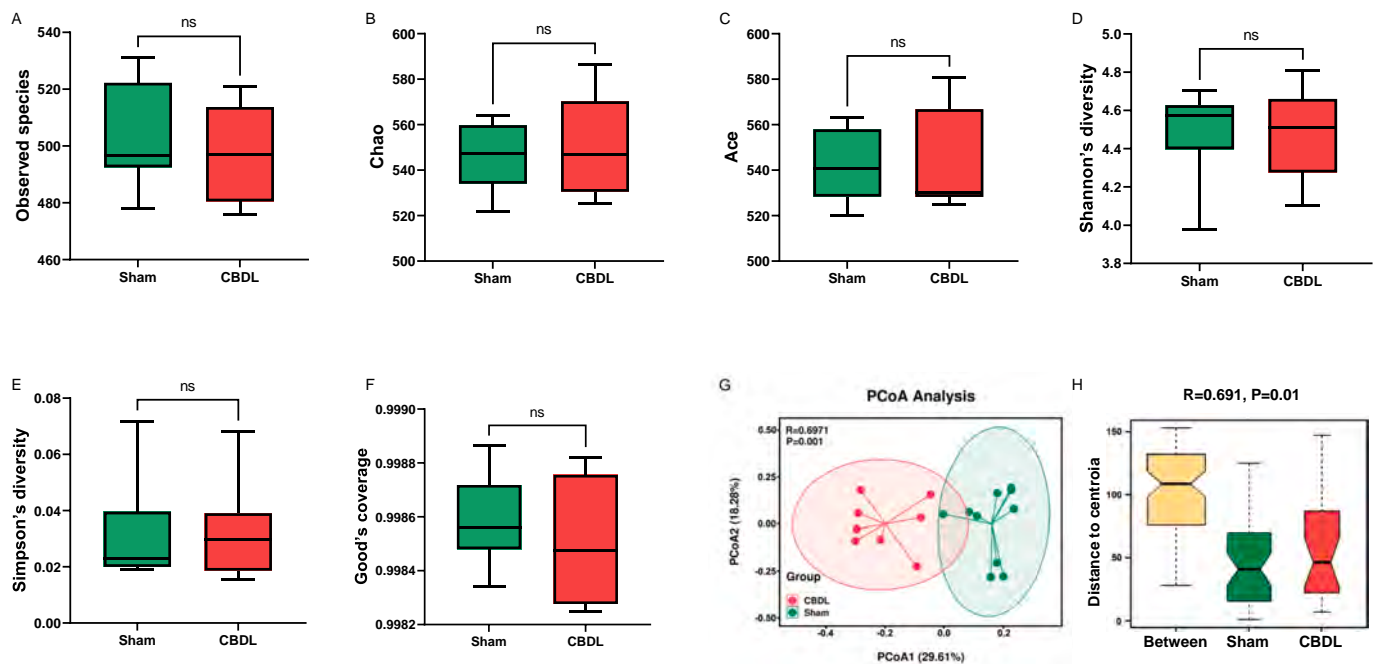


Fig. 2. Effects of CBDL on the diversity of gut microbiota composition.

(A): Observed_species (Mann-Whitney test, $P = 0.594$). (B): Chao (Mann-Whitney test, $P = 0.829$). (C): Ace (Mann-Whitney test, $P = 0.829$). (D): Shannon's diversity (Mann-Whitney test, $P = 0.762$). (E): Simpson's diversity (Mann-Whitney test, $P = 0.897$). (F): Good's coverage (Mann-Whitney test, $P = 0.450$). (G): PCoA based on OTU level (ANOSIM, bray methods) ($R = 0.6971$, $P = 0.001$). (H): OTU ANOSIM analysis ($R = 0.691$, $P = 0.001$). ("Between" indicates the difference between groups, and others indicate the difference within each group. R value represents the degree of difference between groups and within groups, ranged from -1 to 1 ; R value >0 indicates that the difference between groups is greater than the difference within the group; R value <0 indicates that the difference within the group is greater than the difference between groups; the larger the absolute value of R value, the greater the relative difference. The lower the P value, the more significant the effect of this difference test. P value <0.05 indicates a significant difference). For all box plots, the middle line in the box addresses the median, the box addresses the interquartile range, and the whisker addresses the most extreme and least values. ns: not significant.

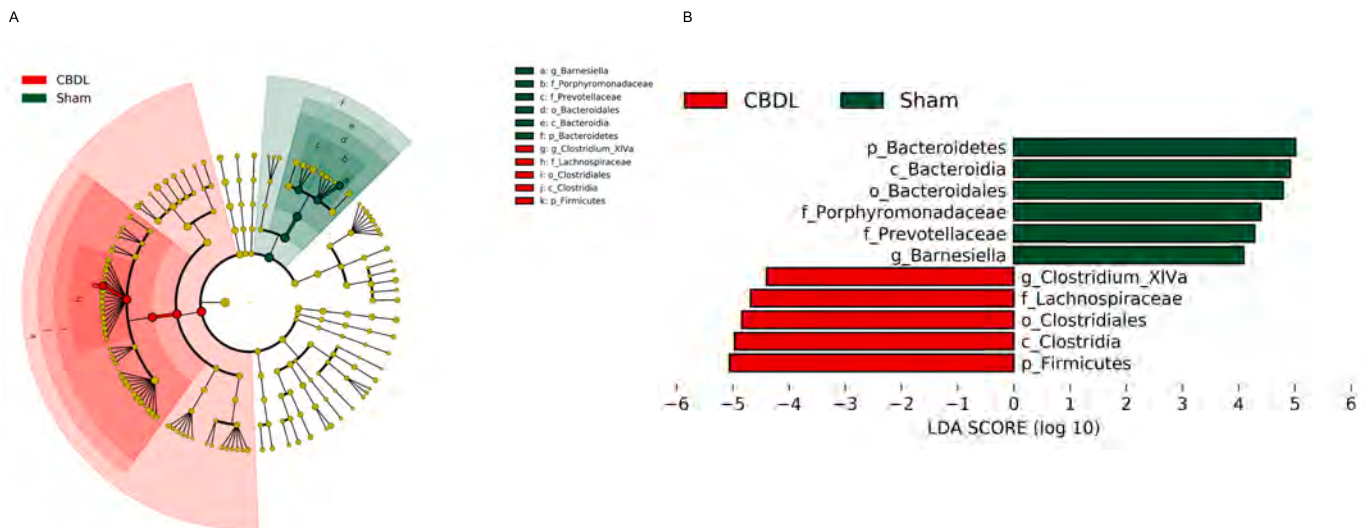


Fig. 3. LefSe analysis for potential bacteria biomarkers of gut microbiota.

(A): Functional branching diagram generated from LefSe showing the differences of the two groups at different taxonomic levels. (B): Histogram representing the enriched taxa with LDA score > 4.0 and $P < 0.05$ obtained from LefSe of the two groups (p: phylum. c: class. o: order. f: family. g: genus).

3.6. Correlations among the gut microbiota, plasma metabolites/lipids, depression-like phenotypes, plasma pro-inflammatory cytokines, and synaptic proteins

Correlations were observed between the plasma metabolites/lipids and the relative abundance of gut microbiota in the two groups, indicating a significant association between them. Through data screening with a threshold of $P < 0.05$ and an absolute R-value of ≥ 0.5 , a Correlation Network was established. This network highlights the connections between the plasma metabolites, gut microbiome at the species level, depression-like behaviors, plasma pro-inflammatory cytokines, and synaptic proteins in the PFC, all of which showed significant differences between the groups (Fig. 6A). The relative abundance of various microbial species was found to be either positively or negatively correlated with 29 plasma metabolites that exhibited significant differences between the groups (Fig. 6A). Moreover, there were notable correlations between plasma metabolites and the behavioral outcomes (SPT and FST), plasma levels of pro-inflammatory cytokines, and synaptic protein concentrations in the PFC (Fig. 6A).

A Correlation Network was developed to illustrate the connections between plasma lipids, gut microbiome at the species level, depression-like behaviors, plasma pro-inflammatory cytokines, and synaptic proteins in the PFC, all of which exhibited significant variations between the two groups (Fig. 6B). Several microbial species demonstrated either positive or negative correlations with various types of plasma lipids (Fig. 6B). Additionally, associations were observed between plasma lipids and the behavioral outcomes (SPT and FST), plasma levels of pro-inflammatory cytokines, and synaptic protein concentrations in the PFC (Fig. 6B).

Using the Correlation Network, the study also explored the relationships between the relative abundance of the gut bacteria and depression-like phenotypes, plasma cytokines, and synaptic proteins in the PFC (Fig. 6C). Notable positive or negative correlations were identified between plasma IL-6 or TNF- α levels and the relative abundance of several bacterial species (Fig. 6C). Furthermore, both positive and negative correlations between the SPT/FST data and the relative abundance of various microbial species (Fig. 6C). Likewise, correlations, either positive or negative, were observed between the abundance of certain species and the levels of synaptic proteins in the PFC (Fig. 6C). These findings suggest a potential role of various microbiota and metabolites in contributing to systemic inflammation, which may lead to

the development of depression-like phenotypes.

3.7. Effects of bilateral SDV in depression-like phenotypes in mice with CBDL

Previous studies indicate a potential role of the subdiaphragmatic vagus nerve in the development of depression-like phenotypes in mice (Pu et al., 2021; Wang et al., 2020, 2021; Yang et al., 2023, 2024; Zhang et al., 2020). To explore the role of the subdiaphragmatic vagus nerve in the depression-like phenotypes in mice with CBDL, we assessed the effects of bilateral SDV (Fig. 7A). Significant variations in body weight were observed among the four groups (Fig. 7B). In the CBDL + SDV group, plasma concentrations of IL-6 and TNF- α were significantly lower than those in the CBDL + sham group (Fig. 7C, D). Locomotor activity did not show any significant differences across the four groups (Fig. 7E). The immobility time in the FST in the CBDL + SDV group was significantly lower than that in the CBDL + sham group (Fig. 7F). In the SPT, sucrose preference was significantly higher in the CBDL + SDV group than that in the CBDL + sham group (Fig. 7G). Additionally, the expression levels of synaptic proteins (e.g., GluA1 and PSD-95) in the PFC were significantly increased in the CBDL + SDV group compared to the CBDL + sham group (Fig. 7H, I). These findings suggest that bilateral SDV may mitigate depression-like behaviors, decrease elevated plasma levels of pro-inflammatory cytokines, normalize altered expressions of synaptic proteins in the PFC of mice subjected to CBDL.

3.8. Effects of arketamine on depression-like phenotypes in mice with CBDL

Arketamine has been proposed as a rapid-acting antidepressant, potentially without the adverse effects commonly associated with ketamine (Wei et al., 2022a; Zhang et al., 2022a, 2022b; Zhang et al., 2023). In this study, we examined the effects of a single dose of arketamine (10 mg/kg, i.p.) in the CBDL model (Fig. 8A). Significant differences in body weight were observed among the three groups (Fig. 8B). The spleen weights in the CBDL + normal saline (NS) group were significantly higher compared to the other two groups (Fig. 8C). No changes in locomotor activity were detected across the three groups (Fig. 8D). The immobility time in the FST was significantly longer in the CBDL + NS group than in the other two groups (Fig. 8E). In the SPT, the sucrose preference was significantly reduced in the CBDL + NS group

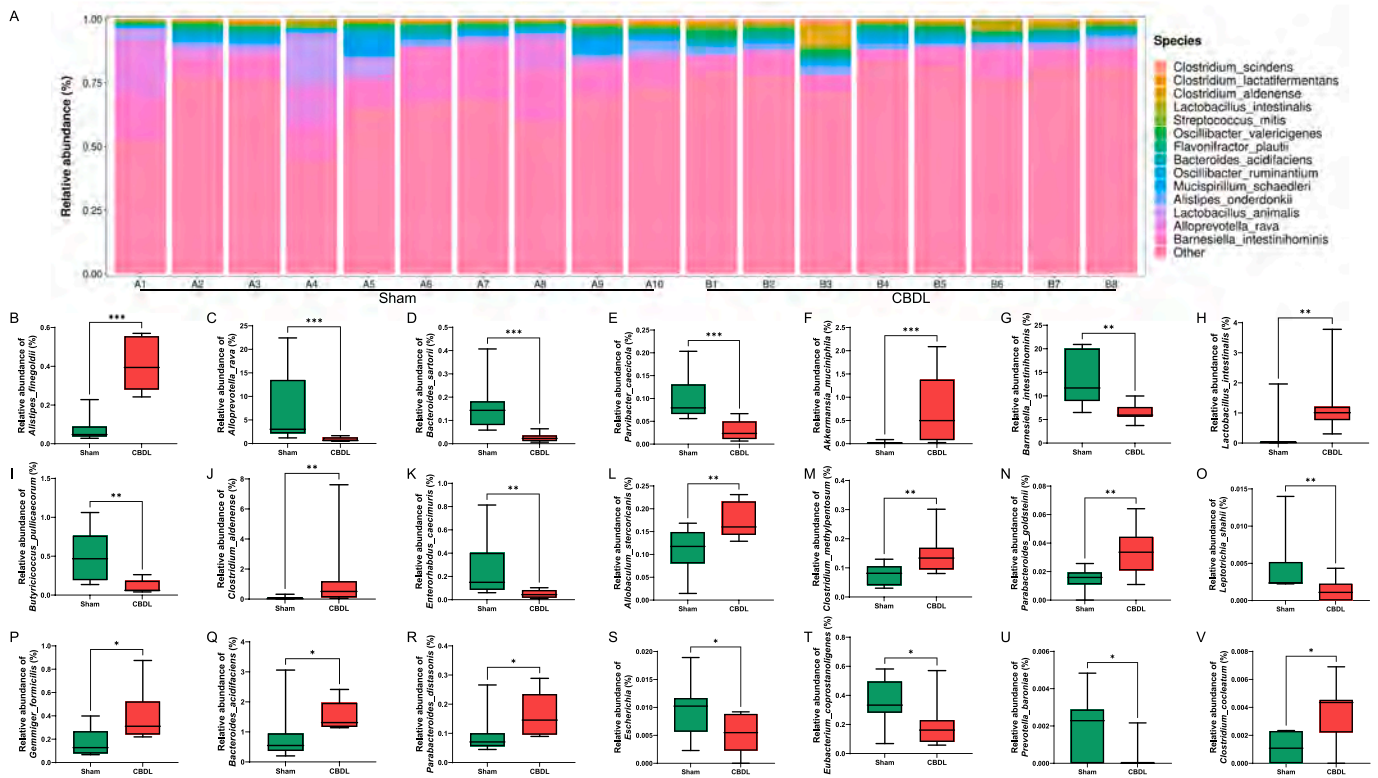


Fig. 4. Effects of CBDL on gut microbiota at the species levels. (A): Gut bacteria composition at the species level in the two groups. (B): Relative abundance of the species *Alistipes_finegoldii* (Mann-Whitney test, $P < 0.0001$). (C): Relative abundance of the species *Alloprevotella_rava* (Mann-Whitney test, $P = 0.0002$). (D): Relative abundance of the species *Bacteroides_sartorii* (Mann-Whitney test, $P = 0.0002$). (E): Relative abundance of the species *Parvibacter_caecicola* (Mann-Whitney test, $P = 0.0002$). (F): Relative abundance of the species *Akkermansia_muciniphila* (Mann-Whitney test, $P = 0.0005$). (G): Relative abundance of the species *Barnesiella_intestinihominis* (Mann-Whitney test, $P = 0.0014$). (H): Relative abundance of the species *Lactobacillus_intestinalis* (Mann-Whitney test, $P = 0.0021$). (I): Relative abundance of the species *Butyrivibrio_furiosus* (Mann-Whitney test, $P = 0.0031$). (J): Relative abundance of the species *Clostridium_aldense* (Mann-Whitney test, $P = 0.0044$). (K): Relative abundance of the species *Enterorhabdus_caecimuris* (Mann-Whitney test, $P = 0.0044$). (L): Relative abundance of the species *Allobaculum_stercoricanis* (Mann-Whitney test, $P = 0.0085$). (M): Relative abundance of the species *Clostridium_methylpentosum* (Mann-Whitney test, $P = 0.0085$). (N): Relative abundance of the species *Parabacteroides_goldsteinii* (Mann-Whitney test, $P = 0.0079$). (O): Relative abundance of the species *Leptotrichia_shahii* (Mann-Whitney test, $P = 0.0117$). (P): Relative abundance of the species *Bacteroides_acidifaciens* (Mann-Whitney test, $P = 0.0155$). (R): Relative abundance of the species *Parabacteroides_distasonis* (Mann-Whitney test, $P = 0.0205$). (S): Relative abundance of the species *Escherichia* (Mann-Whitney test, $P = 0.0266$). (T): Relative abundance of the species *Eubacterium_coprostanoligenes* (Mann-Whitney test, $P = 0.0266$). (U): Relative abundance of the species *Prevotella_baroniae* (Mann-Whitney test, $P = 0.0241$). (V): Relative abundance of the species *Clostridium_cocleatum* (Mann-Whitney test, $P = 0.0261$). For all box plots, the middle line in the box addresses the median, the box addresses the interquartile range, and the whisker addresses the most extreme and least values. * $P < 0.05$; ** $P < 0.01$; *** $P < 0.001$.

compared to the other groups (Fig. 8F). Arketamine also counteracted the decreased levels of GluA1 and PSD-95 in the PFC of mice with CBDL (Fig. 8G, H). These findings indicate that a single administration of arketamine can effectively alleviate depression-like phenotypes in mice subjected to CBDL.

4. Discussion

The major findings of this study are summarized as follows: Firstly, mice subjected to CBDL demonstrated a loss of body weight, splenomegaly, elevated blood levels of pro-inflammatory cytokines, and a reduction in synaptic protein expression (i.e., GluA1 and PSD-95) in the PFC, which contributed to depression-like phenotypes (increased immobility time of FST and decreased sucrose preference of SPT). Secondly, significant alterations in the β -diversity of gut microbiota were observed between the two groups. LEfSe analysis pinpointed the genus *Clostridium_XIa* as a potential microbial marker in the CBDL group. Additionally, notable changes in various species and metabolites were detected between the two groups, with correlations found between the relative abundance of certain microbes and blood cytokines, depression-like behaviors, and synaptic proteins in the PFC. Network analysis

revealed associations between specific microbes, blood metabolites (or lipids), and behavioral indices. Thirdly, SDV effectively prevented splenomegaly, systemic inflammation (characterized by increased IL-6 and TNF- α levels), and alterations in synaptic protein expression in the PFC of CBDL mice. Finally, the administration of a single dose of arketamine ameliorated depression-like phenotypes and reversed the decreased expressions of GluA1 and PSD-95 in the PFC of mice with CBDL. Collectively, these findings suggest a crucial role for the gut–liver–brain axis mediated by the subdiaphragmatic vagus nerve in the development of depression-like phenotypes in mice with CBDL. Additionally, arketamine demonstrated rapid-acting antidepressant-like properties in this model.

Recent studies have indicated a link between LPS-induced splenomegaly and elevated blood levels of pro-inflammatory cytokines such as IL-6 and TNF- α (Ma et al., 2022a, 2022b, 2023; Zhang et al., 2020; Zhang et al., 2021a, 2021b). In this study, we observed a positive correlation between the weight of spleen and the levels of pro-inflammatory cytokines in the blood of mice. Taken together, these findings imply that CBDL surgery may lead to systemic inflammation, which in turn contribute to the development of splenomegaly and depression-like phenotypes.

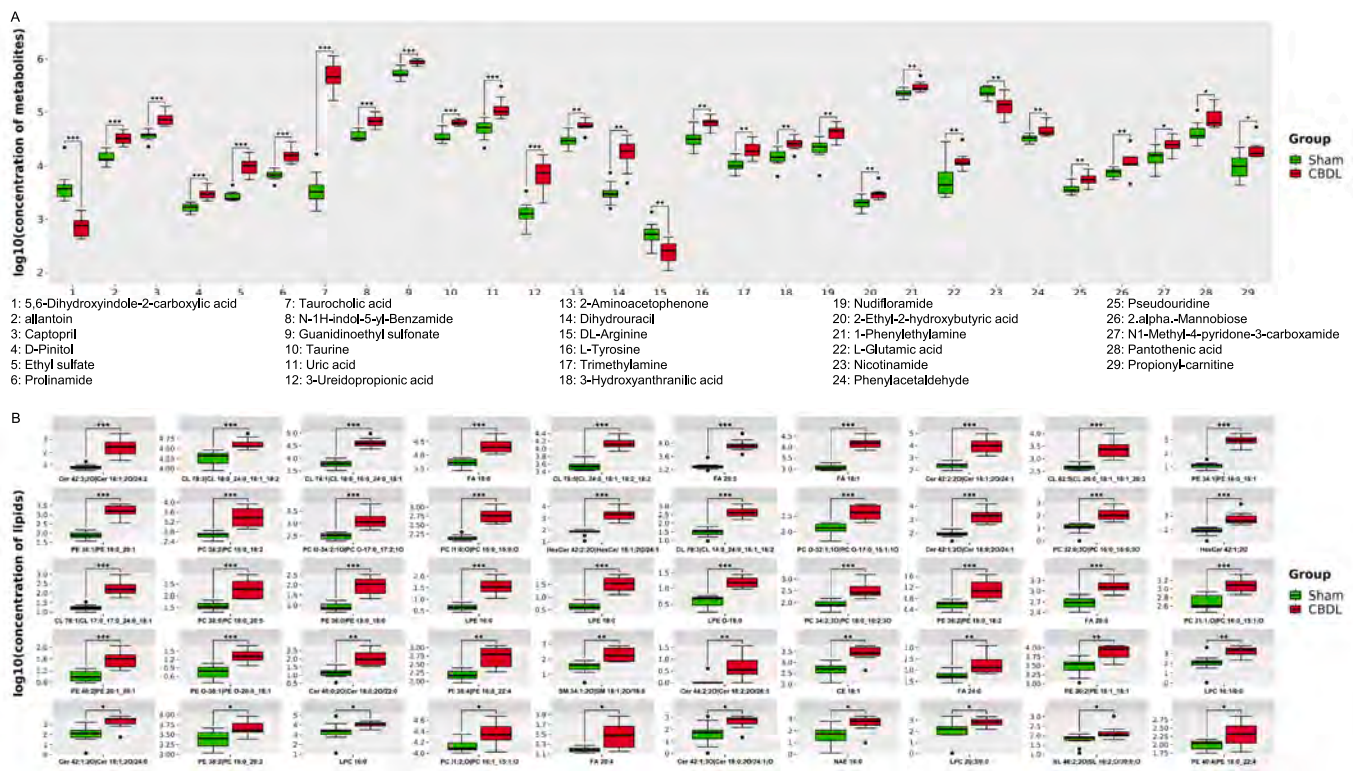


Fig. 5. Untargeted metabolomic and lipidomic analyses of plasma samples in mice with CBDL. (A) Boxplots showing the changes of 29 kinds of metabolites between the two groups. They are listed as follows: 5,6-dihydroxyindole-2-carboxylic acid (Mann-Whitney test, $P < 0.001$), allantoin (Mann-Whitney test, $P < 0.001$), captopril (Mann-Whitney test, $P < 0.001$), D-pinitol (Mann-Whitney test, $P < 0.001$), ethyl sulfate (Mann-Whitney test, $P < 0.001$), prolinamide (Mann-Whitney test, $P < 0.001$), taurocholic acid (Mann-Whitney test, $P < 0.001$), N-1H-indol-5-yl-benzamide (Mann-Whitney test, $P < 0.001$), guanidinoethyl sulfonate (Mann-Whitney test, $P < 0.001$), taurine (Mann-Whitney test, $P < 0.001$), uric acid (Mann-Whitney test, $P < 0.001$), 3-ureidopropionic acid (Mann-Whitney test, $P < 0.001$), 2-aminoacetophenone (Mann-Whitney test, $P = 0.0010$), dihydrouracil (Mann-Whitney test, $P = 0.0010$), DL-arginine (Mann-Whitney test, $P = 0.0014$), L-tyrosine (Mann-Whitney test, $P = 0.0019$), trimethylamine (Mann-Whitney test, $P = 0.0025$), 3-hydroxyanthranilic acid (Mann-Whitney test, $P = 0.0034$), nudifloramide (Mann-Whitney test, $P = 0.0034$), 2-ethyl-2-hydroxybutyric acid (Mann-Whitney test, $P = 0.0045$), 1-phenylethylamine (Mann-Whitney test, $P = 0.0059$), L-glutamic acid (Mann-Whitney test, $P = 0.0059$), nicotinamide (Mann-Whitney test, $P = 0.0059$), phenylacetaldehyde (Mann-Whitney test, $P = 0.0059$), pseudouridine (Mann-Whitney test, $P = 0.0059$), 2.alpha.-mannobiose (Mann-Whitney test, $P = 0.0077$), N1-methyl-4-pyridone-3-carboxamide (Mann-Whitney test, $P = 0.0100$), pantothenic acid (Mann-Whitney test, $P = 0.0100$), propionyl-carnitine (Mann-Whitney test, $P = 0.0100$). The X-axis using the Arabic numerals representing the names of different plasma metabolites, and the Y-axis represents the concentration of various plasma metabolites. Different colors of boxplots represent the corresponding groups. (B) Boxplots showing the changes of 50 kinds of lipids between the two groups. They are listed as follows: Cer 42:3|20|Cer 18:1;20/24:2 (Mann-Whitney test, $P < 0.001$), CL 78:3|CL 18:0 24:0 18:1 18:2 (Mann-Whitney test, $P < 0.001$), CL 74:1|CL 16:0 16:0 24:0 18:1 (Mann-Whitney test, $P < 0.001$), FA 18:0 (Mann-Whitney test, $P < 0.001$), CL 78:5|CL 24:0 18:1 18:2 18:2 (Mann-Whitney test, $P < 0.001$), FA 20:3 (Mann-Whitney test, $P < 0.001$), FA 18:1 (Mann-Whitney test, $P < 0.001$), Cer 42:2|20|Cer 18:1;20/24:1 (Mann-Whitney test, $P < 0.001$), CL 82:5|CL 26:0 18:1 18:1 20:3 (Mann-Whitney test, $P < 0.001$), PE 34:1|PE 16:0 18:1 (Mann-Whitney test, $P < 0.001$), PE 38:1|PE 18:0 20:1 (Mann-Whitney test, $P < 0.001$), PC 36:2|PC 18:0 18:2 (Mann-Whitney test, $P < 0.001$), PC O-34:2;10|PC O-17:0 17:2;10 (Mann-Whitney test, $P < 0.001$), PC 31:0;O|PC 16:0 15:0;O (Mann-Whitney test, $P < 0.001$), HexCer 42:2;20|HexCer 18:1;20/24:1 (Mann-Whitney test, $P < 0.001$), CL 70:3|CL 14:0 24:0 16:1 16:2 (Mann-Whitney test, $P < 0.001$), Cer 42:1;20|Cer 18:0;20/24:1 (Mann-Whitney test, $P < 0.001$), PC 32:0;30|PC 16:0 16:0;30 (Mann-Whitney test, $P < 0.001$), HexCer 42:1;20 (Mann-Whitney test, $P < 0.001$), CL 76:1|CL 17:0 17:0 24:0 18:1 (Mann-Whitney test, $P < 0.001$), PC 38:5|PC 18:0 20:5 (Mann-Whitney test, $P < 0.001$), PE 36:0|PE 18:0 18:0 (Mann-Whitney test, $P < 0.001$), LPE 16:0 (Mann-Whitney test, $P < 0.001$), LPE 18:0 (Mann-Whitney test, $P < 0.001$), LPE O-18:0 (Mann-Whitney test, $P < 0.001$), PC 34:2;30|PC 18:0 16:2;30 (Mann-Whitney test, $P < 0.001$), PE 36:2|PE 18:0 18:2 (Mann-Whitney test, $P < 0.001$), FA 20:5 (Mann-Whitney test, $P < 0.001$), PC 31:1;O|PC 16:0 15:1;O (Mann-Whitney test, $P < 0.001$), PE 40:2|PE 20:1 20:1 (Mann-Whitney test, $P < 0.001$), PE O-38:1|PE O-20:0 18:1 (Mann-Whitney test, $P < 0.001$), Cer 40:0;20|Cer 18:0;20/22:0 (Mann-Whitney test, $P = 0.0010$), PE 38:4|PE 16:0 22:4 (Mann-Whitney test, $P = 0.0014$), SM 34:1;20|SM 18:1;20/16:0 (Mann-Whitney test, $P = 0.0014$), Cer 44:2;20|Cer 18:2;20/26:0 (Mann-Whitney test, $P = 0.0021$), CE 18:1 (Mann-Whitney test, $P = 0.0025$), FA 24:0 (Mann-Whitney test, $P = 0.0045$), PE 36:2|PE 18:1 18:1 (Mann-Whitney test, $P = 0.0059$), LPC 16:1/0:0 (Mann-Whitney test, $P = 0.0059$), Cer 42:1;20|Cer 18:1;20/24:0 (Mann-Whitney test, $P = 0.0100$), PE 38:2|PE 18:0 20:2 (Mann-Whitney test, $P = 0.0129$), LPC 16:0 (Mann-Whitney test, $P = 0.0164$), PC 31:2;O|PC 16:1 15:1;O (Mann-Whitney test, $P = 0.0209$), FA 20:4 (Mann-Whitney test, $P = 0.0209$), Cer 42:1;30|Cer 18:0;20/24:1;O (Mann-Whitney test, $P = 0.0209$), NAE 16:0 (Mann-Whitney test, $P = 0.0209$), LPC 20:3/0:0 (Mann-Whitney test, $P = 0.0330$), SL 46:2;20|SL 16:2;0/30:0;O (Mann-Whitney test, $P = 0.0367$), PE 40:4|PE 18:0 22:4 (Mann-Whitney test, $P = 0.0410$). * $P < 0.05$; ** $P < 0.01$; *** $P < 0.001$.

Analysis of gut microbiota revealed that CBDL significantly influences the variations in microbial community expression. Specifically, at the species level, notable differences in the relative abundance of various microbiota were observed between the two groups. Through comprehensive untargeted metabolomic and lipidomic analyses, we identified distinct changes in several metabolites and lipids across these groups. Network analysis further indicated that the blood levels of these metabolites and lipids are associated with the relative abundance of

certain microbiota, hinting at the microbiome's involvement in their synthesis. Importantly, our findings also include correlations between depression-like behaviors and specific microbiota abundances, underscoring the potential role of the gut microbiome in depression. A previous study reported dysbiosis in gut microbiota and changes in tight junction proteins (i.e., claudin-1, ZO-1) in mice following CBDL (Alaish et al., 2013). Considering the established link between gut microbiota and depression (Chang et al., 2022; Liu et al., 2023), it seems plausible

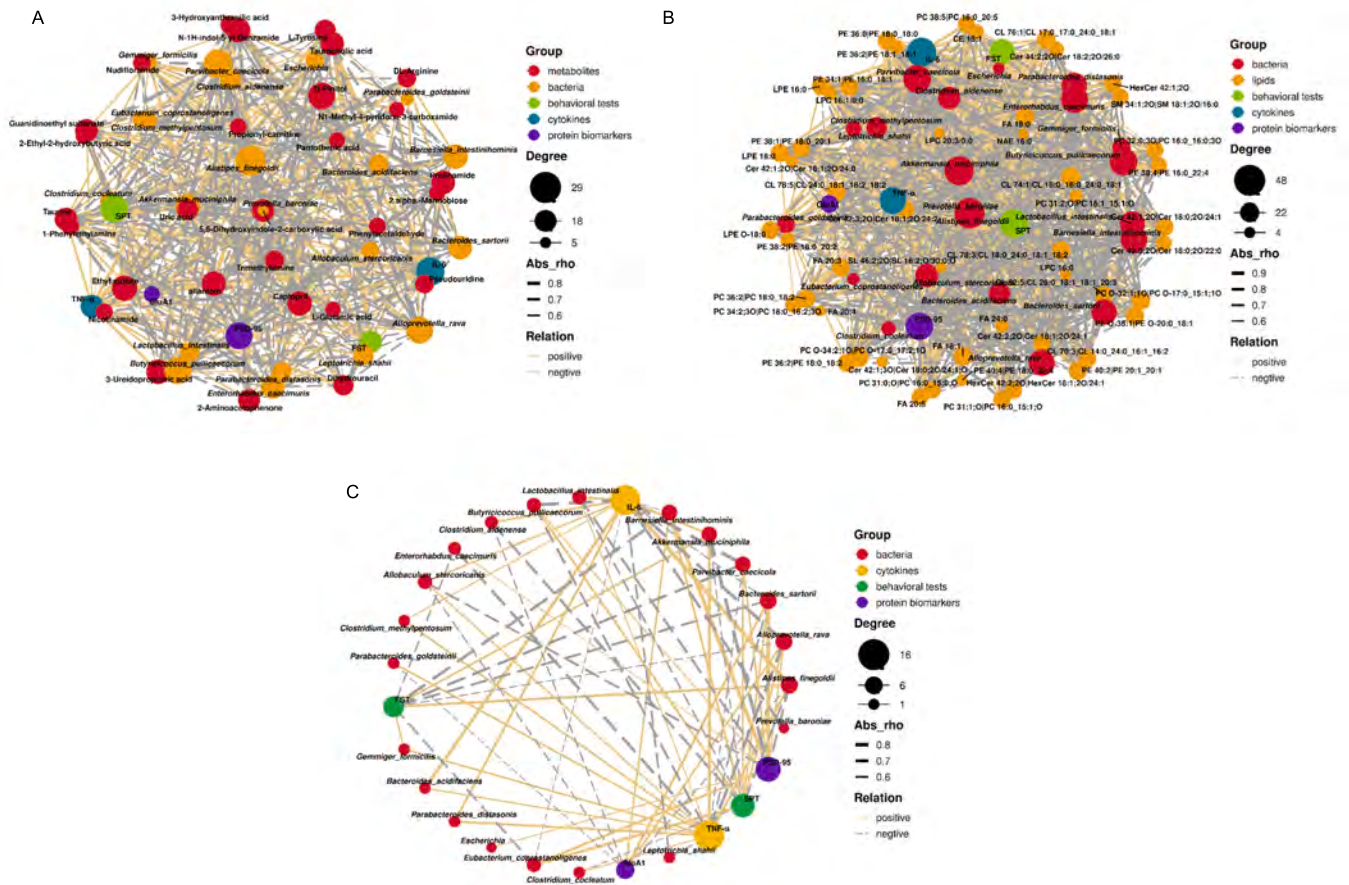


Fig. 6. Correlation network between behavioral data (or synaptic proteins, microglial marker, and pro-inflammatory cytokine) and microbiota (or metabolites and lipids).

(A): A Correlation Network indicating the correlations between the concentrations of plasma metabolites and the gut microbiota at the species level, the results of the behavioral test, the concentrations of pro-inflammatory cytokines and synaptic proteins in the PFC. (B): A Correlation Network indicating the correlations between the concentrations of plasma lipids and the gut microbiota at the species level, the results of the behavioral test, the concentrations of pro-inflammatory cytokines and synaptic proteins in the PFC. (C): A Correlation Network showed correlations between the relative abundance of gut bacteria at the species level and the results of the behavioral test, the concentrations of pro-inflammatory cytokines and synaptic proteins in the PFC. Both the threshold of correlation networks above were set as $P < 0.05$ and the absolute value of $R \geq 0.5$. The different colors of nodes represent different groups. The sizes of node gradients represent varying degrees of correlation. The thickness of the line represents the absolute value of the correlation coefficient. Solid lines represent positive correlations, dotted lines represent negative correlations.

that alterations in the gut–brain axis, including changes in metabolites and lipids, might contribute to the depression-like behaviors in CBDL mice.

Prior research has established that SDV can prevent the onset of depression-like behaviors in mice. This effect was observed following LPS administration (Zhang et al., 2020), as well as after FMT from mice with depression-like behaviors (Pu et al., 2021; Wang et al., 2020, 2021). Additionally, SDV has been effective in preventing depression-like behaviors in *Chrna7* knockout mice (Yang et al., 2023), in mice with HI/R injury (Yang et al., 2024), and in alleviating demyelination in the brains of cuprizone-treated mice (Wang et al., 2023). Another study highlighted the role of the gut–spleen axis, specifically through the subdiaphragmatic vagus nerve, in exacerbating systemic inflammation in mice under sleep deprivation following LPS administration (Zhang et al., 2021b). In our study, we found that SDV effectively alleviated both depression-like phenotypes and splenomegaly in mice with CBDL, indicating a role of the subdiaphragmatic vagus nerve in depression-like behaviors and splenomegaly in these mice. Considering the significance of the gut–liver axis in liver diseases (Albillos et al., 2020; Schwabe and Greten, 2020; Wiest et al., 2017; Zhang et al., 2022b), the

gut–liver–brain axis, likely mediated through the subdiaphragmatic vagus nerve, appears to be crucial in the development of depression-like phenotypes in mice with CBDL. The role of the vagus nerve in modulating the systemic inflammatory response to LPS was also underscored (Borovikova et al., 2000). Given the vagus nerve's role on systemic inflammation, SDV might be an effective strategy in reducing inflammation in this model. Moreover, with vagus nerve stimulation (VNS) known for its potent anti-inflammatory actions (Hashimoto, 2023b, 2023c; Wang et al., 2022), VNS could potentially be a therapeutic option for patients suffering from liver cirrhosis.

The discovery of ketamine's robust antidepressant properties was an unexpected milestone in the treatment of psychiatric disorders, offering rapid and sustained antidepressant actions for treatment-resistant patients with depression (Hashimoto, 2022). Preclinical studies indicate that arketamine, the (R)-enantiomer of ketamine, may be a safer antidepressant alternative compared to ketamine or esketamine, the (S)-enantiomer of ketamine (Hashimoto, 2020, 2023b, 2023d, 2024; Wei et al., 2022a; Zhang et al., 2022a; Zhang et al., 2023). Our earlier research demonstrated that arketamine not only alleviates depression-like behaviors in mice but also modifies the gut microbiota

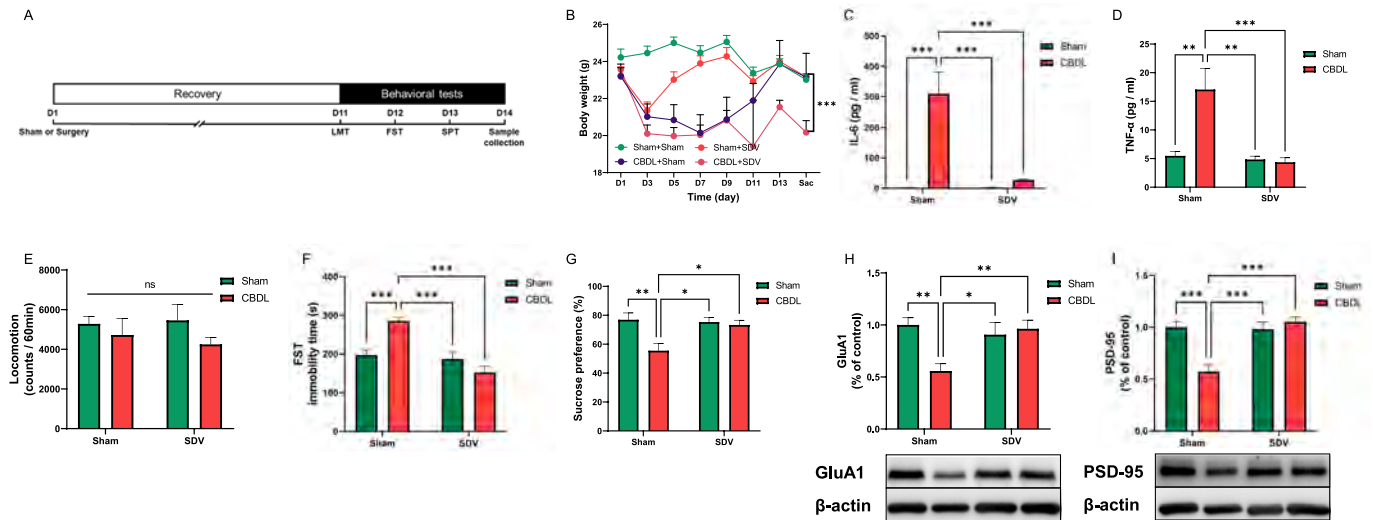


Fig. 7. Effects of bilateral SDV in depression-like phenotypes of mice with CBDL. (A): Experimental schedule. On day 1, surgery (CBDL and/or SDV) or sham surgery was performed, and they were recovered 10 days. On day 11, LMT was performed. FST and SPT were performed on day 12 and day 13, respectively. On day 14, PFC and plasma samples were collected. (B): Body weight (repeated measure two-way ANOVA, time: $F_{(2,135, 53.37)} = 4.169, P = 0.0187$; group: $F_{(3, 25)} = 10.68, P = 0.0001$; interaction: $F_{(21, 175)} = 2.654, P = 0.0003$). (C): Plasma levels of IL-6 (two-way ANOVA, CBDL: $F_{(1, 25)} = 16.44, P = 0.0004$; SDV: $F_{(1, 25)} = 22.86, P < 0.0001$; Interaction: $F_{(1, 25)} = 16.44, P = 0.0004$). (E): Plasma levels of TNF- α (two-way ANOVA, CBDL: $F_{(1, 25)} = 12.01, P = 0.0019$; SDV: $F_{(1, 25)} = 8.348, P = 0.0079$; Interaction: $F_{(1, 25)} = 9.862, P = 0.0043$). (D): Locomotion (LMT) (two-way ANOVA, CBDL: $F_{(1, 25)} = 0.06112, P = 0.8068$; SDV: $F_{(1, 25)} = 2.205, P = 0.1501$; Interaction: $F_{(1, 25)} = 0.2991, P = 0.5893$). (E): FST (two-way ANOVA, CBDL: $F_{(1, 25)} = 25.91, P < 0.0001$; SDV: $F_{(1, 25)} = 3.552, P = 0.0712$; Interaction: $F_{(1, 25)} = 18.73, P = 0.0002$). (F): SPT (two-way ANOVA, CBDL: $F_{(1, 25)} = 3.752, P = 0.0641$; SDV: $F_{(1, 25)} = 7.740, P = 0.0101$; Interaction: $F_{(1, 25)} = 5.314, P = 0.0297$). (G): Western blot analysis of GluA1 in the PFC (two-way ANOVA, CBDL: $F_{(1, 25)} = 3.411, P = 0.0766$; SDV: $F_{(1, 25)} = 5.223, P = 0.0310$; Interaction: $F_{(1, 25)} = 8.779, P = 0.0066$) and the representative bands. (H): Western blot analysis of PSD-95 in the PFC (two-way ANOVA, CBDL: $F_{(1, 25)} = 15.78, P = 0.0005$; SDV: $F_{(1, 25)} = 9.410, P = 0.0051$; Interaction: $F_{(1, 25)} = 18.27, P = 0.0002$) and the representative bands. The data are shown as means \pm S.E.M (sham + sham group: $n = 8$, CBDL + sham group: $n = 7$, sham + SDV group: $n = 6$, CBDL + SDV group: $n = 8$). ANOVA: analysis of variance. ns: not significant; * $P < 0.05$; ** $P < 0.01$; *** $P < 0.001$.

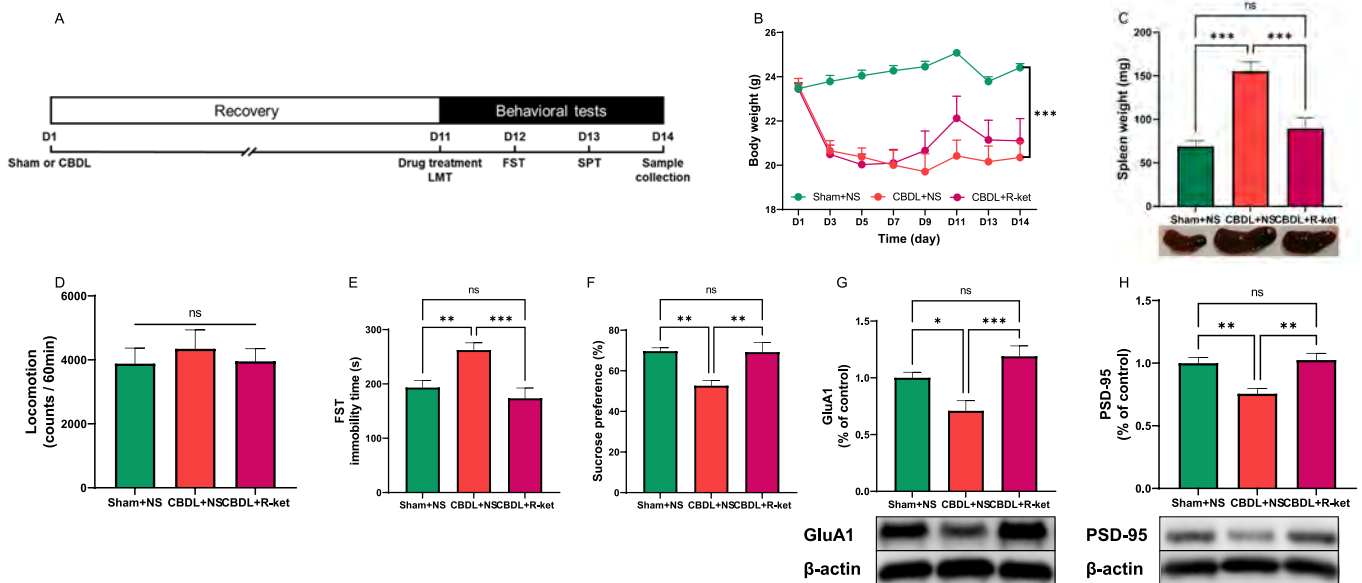


Fig. 8. Effect of new antidepressant arketamine in depression-like phenotypes of mice with CBDL. (A): Experimental schedule. On day 1, sham or CBDL was performed, and they were recovered 10 days. On day 11, normal saline (NS) (10 ml/kg) or arketamine (R-ket) (10 mg/kg) was administered intraperitoneally and subsequently LMT was performed. FST and SPT were performed on day 12 and day 13, respectively. On day 14, prefrontal cortex (PFC) and plasma samples were collected. (B): Body weight (repeated measure ANOVA, $F_{(2, 26)} = 16.89, P < 0.001$). (C): Spleen weight (one-way ANOVA, $F_{(2, 26)} = 20.42, P < 0.001$). (D): LMT (one-way ANOVA, $F_{(2, 26)} = 0.2491, P = 0.7813$). (E): FST (one-way ANOVA, $F_{(2, 26)} = 9.660, P = 0.0007$). (F): SPT (one-way ANOVA, $F_{(2, 26)} = 9.743, P = 0.0007$). (G): Western blot analysis of GluA1 in the PFC (one-way ANOVA, $F_{(2, 26)} = 9.429, P = 0.0008$) and the representative bands. (H): Western blot analysis of PSD-95 in the PFC (one-way ANOVA, $F_{(2, 26)} = 10.26, P = 0.0005$) and the representative bands. The data are shown as means \pm S.E.M (Sham + NS group: $n = 10$, CBDL + NS group: $n = 10$, CBDL + R-ket group: $n = 9$). ANOVA: analysis of variance. NS: normal saline. R-ket: Arketamine. ns: not significant; * $P < 0.05$; ** $P < 0.01$; *** $P < 0.001$.

composition in these models (Qu et al., 2017; Yang et al., 2017). Additionally, we found that arketamine can reverse reduced bone mineral density in mice exposed to stress (Wan et al., 2023) and ovariectomized mice (Wan et al., 2022), acting through the gut-microbiota-bone axis. Considering the crucial role of gut microbiota on bone mineral density (Chen et al., 2023; Ohlsson and Sjögren, 2015), it seems plausible that the gut microbiota–bone axis may play a pivotal role in arketamine's beneficial effects on bone mineral density (Wan et al., 2022, 2023; Wei et al., 2022a). More recently, our studies have shown that a single dose of arketamine can improve depression-like phenotypes in mice with HI/R injury (Yang et al., 2024), as well as in mice with CBDL (this study). Remarkably, these beneficial effects on HI/R injury or CBDL models are attainable with just one post-injection of arketamine. While the precise mechanisms of arketamine's action in the HI/R or CBDL models remain to be fully understood, it is plausible that its anti-inflammatory actions, potentially mediated via the gut–liver–brain axis, play a significant role. The association between depressive symptoms and cognitive decline in patients with liver cirrhosis is well-documented (Pantiga et al., 2003; San Martín-Valenzuela et al., 2020; Stewart et al., 2011). Given the influence of depression and cognitive function on the progression of liver cirrhosis (Mullish et al., 2014; Patten et al., 2008), exploring whether arketamine can alleviate depression in patients with liver cirrhosis presents a compelling area of research.

This study has several limitations. Initially, we were unable to measure the blood levels of alanine aminotransferase and aspartate aminotransferase, as the plasma samples were allocated for metabolomic and lipidomic analyses. Additionally, our research did not include behavioral assessments for cognitive deficits, although a previous study has shown that rats with bile duct ligation can exhibit spatial memory deficits (Huang et al., 2009). Another limitation is our focus solely on the PFC for evaluating synaptic protein expression, despite the known relevance of other brain regions, like the hippocampus, in depression. Furthermore, the study did not examine the potential effects of FMT from mice with CBDL, which could have provided further understanding of the gut microbiota's role in depression-like phenotypes. This area warrants future investigations using FMT from CBDL mice. Lastly, the current research has not yet investigated the connections between the microbiome or metabolites and depression-like phenotypes in CBDL mice. Future studies should aim to elucidate how these factors may contribute to depression-like phenotypes in this model.

In conclusion, our findings indicate that the gut–liver–brain axis, particularly through the subdiaphragmatic vagus nerve, is crucial in the development of depression-like phenotypes in mice following CBDL. Considering the significant role that depression plays in the progression of liver cirrhosis, arketamine emerges as a promising therapeutic candidate for treating depression in patients with this condition.

CRedit authorship contribution statement

Yong Yang: Writing – review & editing, Writing – original draft, Methodology, Investigation, Formal analysis, Data curation, Conceptualization. **Akifumi Eguchi:** Writing – review & editing, Validation, Resources, Methodology, Investigation, Data curation. **Chisato Mori:** Writing – review & editing, Supervision, Resources, Funding acquisition. **Kenji Hashimoto:** Writing – review & editing, Writing – original draft, Supervision, Funding acquisition, Conceptualization.

Declaration of competing interest

Dr. Hashimoto is the inventor of filed patent applications on “The use of R-ketamine in the treatment of psychiatric diseases”, “(S)-norketamine and salt thereof as pharmaceutical”, “R-ketamine and derivative thereof as prophylactic or therapeutic agent for neurodegeneration disease or recognition function disorder”, “Preventive or therapeutic agent and pharmaceutical composition for inflammatory diseases or bone diseases”, and “R-ketamine and its derivatives as a preventive or

therapeutic agent for a neurodevelopmental disorder” by the Chiba University. Dr. Hashimoto has also received speakers' honoraria, consultant fee, or research support from Abbott, Daiichi-Sankyo, Meiji Seika Pharma, Seikagaku Corporation, Dainippon-Sumitomo, Taisho, Otsuka, Murakami Farm and Perception Neuroscience. Other authors declare no conflict of interest.

Data availability

Data will be made available on request.

Acknowledgements

This study was supported by the grants from Japan Society for the Promotion of Science (to K.H., 21H00184, 21H05612, 23 K17634), JST OPERA Program Japan (to C.M. JPMJOP1831) and unrestricted grant of Yamada Bee Company, Japan (to C.M.). Dr. Yong Yang was supported by the Japan China Sasakawa Medical Fellowship (Tokyo, Japan) and JST SPRING (JPMJSP2109).

References

- Abureesh, M., Alkhayyat, M., Abualnadi, I., Badran, R., Henneberry, J.D., Sadiq, W., Novakovic, V., Barkin, R., Barkin, S., Deeb, L.S., 2022. Epidemiology of depressive disorders in patients with liver cirrhosis: a population-based study in the United States. *Prim. Care Compan. CNS Disord.* 24 (1), 20m02889. <https://doi.org/10.4088/PCC.20m02889>.
- Alaish, S.M., Smith, A.D., Timmons, J., Greenspon, J., Eyvazzadeh, D., Murphy, E., Shea-Donahue, T., Cirimotich, S., Mongodin, E., Zhao, A., Fasano, A., Nataro, J.P., Cross, A., 2013. Gut microbiota, tight junction protein expression, intestinal resistance, bacterial translocation and mortality following cholestasis depend on the genetic background of the host. *Gut Microbes* 4 (4), 292–305. <https://doi.org/10.4161/gmic.24706>.
- Albillos, A., de Gottardi, A., Rescigno, M., 2020. The gut-liver axis in liver disease: pathophysiological basis for therapy. *J. Hepatol.* 72 (3), 558–577. <https://doi.org/10.1016/j.jhep.2019.10.003>.
- Bianchi, G., Marchesini, G., Nicolino, F., Graziani, R., Sgarbi, D., Loguercio, C., Abbati, R., Zoli, M., 2005. Psychological status and depression in patients with liver cirrhosis. *Dig. Liver Dis.* 37 (8), 593–600. <https://doi.org/10.1016/j.dld.2005.01.020>.
- Bonaz, B., Bazin, T., Pellissier, S., 2018. The vagus nerve at the interface of the microbiota-gut-brain axis. *Front. Neurosci.* 12, 49. <https://doi.org/10.3389/fnins.2018.00049>.
- Bonnell, A.R., Bunchorntavakul, C., Reddy, K.R., 2011. Immune dysfunction and infections in patients with cirrhosis. *Clin. Gastroenterol. Hepatol.* 9 (9), 727–738. <https://doi.org/10.1016/j.cgh.2011.02.031>.
- Borovikova, L.V., Ivanova, S., Zhang, M., Yang, H., Botchkina, G.I., Watkins, L.R., Wang, H., Abumrad, N., Eaton, J.W., Tracey, K.J., 2000. Vagus nerve stimulation attenuates the systemic inflammatory response to endotoxin. *Nature* 405 (6785), 458–462. <https://doi.org/10.1038/35013070>.
- Chang, L., Wei, Y., Hashimoto, K., 2022. Brain-gut-microbiota axis in depression: a historical overview and future directions. *Brain Res. Bull.* 182, 44–56. <https://doi.org/10.1016/j.brainresbull.2022.02.004>.
- Chen, S., Zhou, G., Han, H., Jin, J., Li, Z., 2023. Causal effects of specific gut microbiota on bone mineral density: a two-sample Mendelian randomization study. *Front. Endocrinol. (Lausanne)* 14, 1178831. <https://doi.org/10.3389/fendo.2023.1178831>.
- Cryan, J.F., O'Riordan, K.J., Cowan, C.S.M., Sandhu, K.V., Bastiaansen, T.F.S., Boehme, M., Codagnone, M.G., Cusotto, S., Furling, C., Golubeva, A.V., Guzzetta, K. E., Jaggar, M., Long-Smith, C.M., Lyte, J.M., Martin, J.A., Molinero-Perez, A., Moloney, G., Morelli, E., Morillas, E., O'Connor, R., Cruz-Pereira, J.S., Peterson, V.L., Rea, K., Ritz, N.L., Sherwin, E., Spichak, S., Teichman, E.M., van de Wouw, M., Ventura-Silva, A.P., Wallace-Fitzsimons, S.E., Hyland, N., Clarke, G., Dinan, T.G., 2019. The microbiota-gut-brain axis. *Physiol. Rev.* 99 (4), 1877–2013. <https://doi.org/10.1152/physrev.00018.2018>.
- Forsythe, P., Bienenstock, J., Kunze, W.A., 2014. Vagal pathways for microbiome-brain-gut axis communication. *Adv. Exp. Med. Biol.* 817, 115–133. https://doi.org/10.1007/978-1-4939-0897-4_5.
- Geerts, A.M., Vanheule, E., Praet, M., Van Vlierberghe, H., De Vos, M., Colle, I., 2008. Comparison of three research models of portal hypertension in mice: macroscopic, histological and portal pressure evaluation. *Int. J. Exp. Pathol.* 89 (4), 251–263. <https://doi.org/10.1111/j.1365-2613.2008.00597.x>.
- Ginès, P., Krag, A., Abaldas, J.G., Solà, E., Fabrellas, N., Kamath, P.S., 2021. Liver cirrhosis. *Lancet* 398 (10308), 1359–1376. [https://doi.org/10.1016/S0140-6736\(21\)01374-X](https://doi.org/10.1016/S0140-6736(21)01374-X).
- Hashimoto, K., 2020. Molecular mechanisms of the rapid-acting and long-lasting antidepressant actions of (R)-ketamine. *Biochem. Pharmacol.* 177, 113935. <https://doi.org/10.1016/j.bcp.2020.113935>.

- Hashimoto, K., 2022. Ketamine: anesthetic, psychotomimetic, antidepressant, or anthelmintic? *Mol. Psychiatry* 27 (8), 3116–3118.
- Hashimoto, K., 2023a. Emerging role of the host microbiome in neuropsychiatric disorders: overview and future directions. *Mol. Psychiatry* 28 (9), 3625–3637. <https://doi.org/10.1038/s41380-023-02287-6>.
- Hashimoto, K., 2023b. Neuroinflammation through the vagus nerve-dependent gut-microbiota-brain axis in treatment-resistant depression. *Prog. Brain Res.* 278, 61–77. <https://doi.org/10.1016/bs.pbr.2023.01.003>.
- Hashimoto, K., 2023c. Detrimental effects of COVID-19 in the brain and therapeutic options for long COVID: the role of Epstein-Barr virus and the gut-brain axis. *Mol. Psychiatry*. <https://doi.org/10.1038/s41380-023-02161-5>, 2023 Jul 4.
- Hashimoto, K., 2023d. Arketamine for cognitive impairment in psychiatric disorders. *Eur. Arch. Psychiatry Clin. Neurosci.* 273 (7), 1513–1525. <https://doi.org/10.1007/s00406-023-01570-5>.
- Hashimoto, K., 2024. Are “mystical experiences” essential for antidepressant actions of ketamine and the classic psychedelics? *Eur. Arch. Psychiatry Clin. Neurosci.* (in press).
- Hua, H., Huang, C., Liu, H., Xu, X., Xu, X., Wu, Z., Liu, C., Wang, Y., Yang, C., 2022. Depression and antidepressant effects of ketamine and its metabolites: the pivotal role of gut microbiota. *Neuropharmacology* 220, 109272. <https://doi.org/10.1016/j.neuropharm.2022.109272>.
- Huang, L.T., Tiao, M.M., Tain, Y.L., Chen, C.C., Hsieh, C.S., 2009. Melatonin ameliorates bile duct ligation-induced systemic oxidative stress and spatial memory deficits in developing rats. *Pediatr. Res.* 65 (2), 176–180. <https://doi.org/10.1203/PDR.0b013e31818d5bc7>.
- Huang, X., Liu, X., Yu, Y., 2017. Depression and chronic liver diseases: are there shared underlying mechanisms? *Front. Mol. Neurosci.* 10, 134. <https://doi.org/10.3389/fnmol.2017.00134>.
- Kronsten, V.T., Tranah, T.H., Pariante, C., Sawcross, D.L., 2022. Gut-derived systemic inflammation as a driver of depression in chronic liver disease. *J. Hepatol.* 76 (3), 665–680. <https://doi.org/10.1016/j.jhep.2021.11.008>.
- Kur, P., Kolasa-Wolosiuk, A., Misiakiewicz-Has, K., Wiszniewska, B., 2020. Sex hormone-dependent physiology and diseases of liver. *Int. J. Environ. Res. Public Health* 17 (8), 2620. <https://doi.org/10.3390/ijerph17082620>.
- Liu, L., Wang, H., Chen, X., Zhang, Y., Zhang, H., Xie, P., 2023. Gut microbiota and its metabolites in depression: from pathogenesis to treatment. *EBioMedicine* 90, 104527. <https://doi.org/10.1016/j.ebiom.2023.104527>.
- Ma, L., Zhang, J., Fujita, Y., Qu, Y., Shan, J., Wan, X., Wang, X., Ishima, T., Kobayashi, K., Wang, L., Hashimoto, K., 2022a. Nuclear factor of activated T cells 4 in the prefrontal cortex is required for prophylactic actions of (R)-ketamine. *Transl. Psychiatry* 12 (1), 27. <https://doi.org/10.1038/s41398-022-01803-6>.
- Ma, L., Zhang, J., Fujita, Y., Shinno-Hashimoto, H., Shan, J., Wan, X., Qu, Y., Chang, L., Wang, X., Hashimoto, K., 2022b. Effects of spleen nerve denervation on depression-like phenotype, systemic inflammation, and abnormal composition of gut microbiota in mice after administration of lipopolysaccharide: a role of brain-spleen axis. *J. Affect. Disord.* 317, 156–165. <https://doi.org/10.1016/j.jad.2022.08.087>.
- Ma, L., Wang, L., Qu, Y., Wan, X., Hashimoto, K., 2023. A role of splenic heme biosynthesis pathway in the persistent prophylactic actions of arketamine in lipopolysaccharide-treated mice. *Transl. Psychiatry* 13 (1), 269. <https://doi.org/10.1038/s41398-023-02564-6>.
- Mullish, B.H., Kabir, M.S., Thursz, M.R., Dhar, A., 2014. Review article: depression and the use of antidepressants in patients with chronic liver disease or liver transplantation. *Aliment. Pharmacol. Ther.* 40 (8), 880–892. <https://doi.org/10.1111/apt.12925>.
- Nardelli, S., Pentassuglio, I., Pasquale, C., Ridola, L., Moscucci, F., Merli, M., Mina, C., Marianetti, M., Frattino, M., Izzo, C., Merkel, C., Riggio, O., 2013. Depression, anxiety and alexithymia symptoms are major determinants of health related quality of life (HRQoL) in cirrhotic patients. *Metab. Brain Dis.* 28 (2), 239–243. <https://doi.org/10.1007/s11011-012-9364-0>.
- Ohlsson, C., Sjögren, K., 2015. Effects of the gut microbiota on bone mass. *Trends Endocrinol. Metab.* 26 (2), 69–74. <https://doi.org/10.1016/j.tem.2014.11.004>.
- Pantiga, C., Rodrigo, L.R., Cuesta, M., Lopez, L., Arias, J.L., 2003. Cognitive deficits in patients with hepatic cirrhosis and in liver transplant recipients. *J. Neuropsychiatr. Clin. Neurosci.* 15 (1), 84–89. <https://doi.org/10.1176/jnp.15.1.84>.
- Patten, S.B., Williams, J.V., Lavorato, D.H., Modgill, G., Jette, N., Eliasziw, M., 2008. Major depression as a risk factor for chronic disease incidence: longitudinal analysis in a general population cohort. *Gen. Hosp. Psychiatry* 30 (5), 407–413. <https://doi.org/10.1016/j.genhosppsych.2008.05.001>.
- Pu, Y., Tan, Y., Qu, Y., Chang, L., Wang, S., Wei, Y., Wang, X., Hashimoto, K., 2021. A role of the subdiaphragmatic vagus nerve in depression-like phenotypes in mice after fecal microbiota transplantation from *Chrna7* knock-out mice with depression-like phenotypes. *Brain Behav. Immun.* 94, 318–326. <https://doi.org/10.1016/j.bbi.2020.12.032>.
- Qu, Y., Yang, C., Ren, Q., Ma, M., Dong, C., Hashimoto, K., 2017. Comparison of (R)-ketamine and lanicemine on depression-like phenotype and abnormal composition of gut microbiota in a social defeat stress model. *Sci. Rep.* 7 (1), 15725. <https://doi.org/10.1038/s41598-017-16060-7>.
- Qu, Y., Eguchi, A., Wan, X., Ma, L., Chang, L., Shan, J., Yang, Y., Mori, C., Hashimoto, K., 2023a. Repeated use of 3,4-methylenedioxymethamphetamine is associated with the resilience in mice after chronic social defeat stress: a role of gut-microbiota-brain axis. *Psychiatry Res.* 320, 115020. <https://doi.org/10.1016/j.psychres.2022.115020>.
- Qu, Y., Eguchi, A., Ma, L., Wan, X., Mori, C., Hashimoto, K., 2023b. Role of the gut-brain axis via the subdiaphragmatic vagus nerve in stress resilience of 3,4-methylenedioxymethamphetamine in mice exposed to chronic restraint stress. *Neurobiol. Dis.* 189, 106348. <https://doi.org/10.1016/j.nbd.2023.106348>.
- San Martín-Valenzuela, C., Borrás-Barrachina, A., Gallego, J.J., Urios, A., Mestre-Salvador, V., Correa-Ghisays, P., Ballester, M.P., Escudero-García, D., Tosca, J., Montón, C., Ríos, M.P., Kosenko, E., Felipe, V., Tabares-Seisdedos, R., Selva-Verá, G., Montoliu, C., 2020. Motor and cognitive performance in patients with liver cirrhosis with minimal hepatic encephalopathy. *J. Clin. Med.* 9 (7), 2154. <https://doi.org/10.3390/jcm9072154>.
- Sanada, K., Nakajima, S., Kurokawa, S., Barceló-Soler, A., Ikuse, D., Hirata, A., Yoshizawa, A., Tomizawa, Y., Salas-Valero, M., Noda, Y., Mimura, M., Iwanami, A., Kishimoto, T., 2020. Gut microbiota and major depressive disorder: a systematic review and meta-analysis. *J. Affect. Disord.* 266, 1–13. <https://doi.org/10.1016/j.jpsychires.2021.05.009>.
- Schwabe, R.F., Greten, T.F., 2020. Gut microbiome in HCC—mechanisms, diagnosis and therapy. *J. Hepatol.* 72 (2), 230–238. <https://doi.org/10.1016/j.jhep.2019.08.016>.
- Singh, N., Gayowski, T., Wagener, M.M., Marino, I.R., 1997. Depression in patients with cirrhosis. Impact on outcome. *Dig. Dis. Sci.* 42 (7), 1421–1427. <https://doi.org/10.1023/a:1018898106656>.
- Smith, M.L., Wade, J.B., Wolstenholme, J., Bajaj, J.S., 2023. Gut microbiota-brain-cirrhosis axis. *Hepatology*. <https://doi.org/10.1097/HEP.0000000000000344>, 2023 Mar 6.
- Stewart, C.A., Enders, F.T., Mitchell, M.M., Felmlee-Devine, D., Smith, G.E., 2011. The cognitive profile of depressed patients with cirrhosis. *Prim. Care Compan. CNS Disord.* 13 (3). <https://doi.org/10.4088/PCC.10m01090>. PCC.10m01090.
- Tag, C.G., Sauer-Lehnen, S., Weiskirchen, S., Borkham-Kamphorst, E., Tolba, R.H., Tacke, F., Weiskirchen, R., 2015. Bile duct ligation in mice: induction of inflammatory liver injury and fibrosis by obstructive cholestasis. *J. Vis. Exp.* 96, e52438. <https://doi.org/10.3791/52438>.
- Tapper, E.B., Parikh, N.D., 2023. Diagnosis and management of cirrhosis and its complications: a review. *JAMA* 329 (18), 1589–1602. <https://doi.org/10.1001/jama.2023.5997>.
- Tsugawa, H., Ikeda, K., Takahashi, M., Satoh, A., Mori, Y., Uchino, H., Okahashi, N., Yamada, Y., Tada, I., Bonini, P., Higashi, Y., Okazaki, Y., Zhou, Z., Zhu, Z.J., Koelme, J., Cajka, T., Fiehn, O., Saito, K., Arita, M., Arita, M., 2020. A lipidome atlas in MS-DIAL 4. *Nat. Biotechnol.* 38 (10), 1159–1163. <https://doi.org/10.1038/s41587-020-0531-2>.
- Van Campenhout, S., Van Vlierberghe, H., Devisscher, L., 2019. Common bile duct ligation as model for secondary biliary cirrhosis. *Methods Mol. Biol.* 1981, 237–247. https://doi.org/10.1007/978-1-4939-9420-5_15.
- Wan, X., Eguchi, A., Fujita, Y., Ma, L., Wang, X., Yang, Y., Qu, Y., Chang, L., Zhang, J., Mori, C., Hashimoto, K., 2022. Effects of (R)-ketamine on reduced bone mineral density in ovarietomized mice: a role of gut microbiota. *Neuropharmacology* 213, 109139. <https://doi.org/10.1016/j.neuropharm.2022.109139>.
- Wan, X., Eguchi, A., Chang, L., Mori, C., Hashimoto, K., 2023. Beneficial effects of arketamine on the reduced bone mineral density in susceptible mice after chronic social defeat stress: role of the gut-microbiota-brain axis. *Neuropharmacology* 228, 109466. <https://doi.org/10.1016/j.neuropharm.2023.109466>.
- Wang, S., Ishima, T., Zhang, J., Qu, Y., Chang, L., Pu, Y., Fujita, Y., Tan, Y., Wang, X., Hashimoto, K., 2020. Ingestion of *Lactobacillus intestinalis* and *Lactobacillus reuteri* causes depression- and anhedonia-like phenotypes in antibiotic-treated mice via the vagus nerve. *J. Neuroinflammation* 17 (1), 241. <https://doi.org/10.1186/s12974-020-01916-z>.
- Wang, S., Ishima, T., Qu, Y., Shan, J., Chang, L., Wei, Y., Zhang, J., Pu, Y., Fujita, Y., Tan, Y., Wang, X., Ma, L., Wan, X., Hammock, B.D., Hashimoto, K., 2021. Ingestion of *Faecalibaculum rodentium* causes depression-like phenotypes in resilient *Ephx2* knock-out mice: a role of brain-gut-microbiota axis via the subdiaphragmatic vagus nerve. *J. Affect. Disord.* 292, 565–573. <https://doi.org/10.1016/j.jad.2021.06.006>.
- Wang, X., Yang, J., Hashimoto, K., 2022. (R)-ketamine as prophylactic and therapeutic drug for neurological disorders: beyond depression. *Neurosci. Biobehav. Rev.* 139, 104762. <https://doi.org/10.1016/j.neubiorev.2022.104762>.
- Wang, X., Eguchi, A., Yang, Y., Chang, L., Wan, X., Shan, J., Qu, Y., Ma, L., Mori, C., Yang, J., Hashimoto, K., 2023. Key role of the gut-microbiota-brain axis via the subdiaphragmatic vagus nerve in demyelination of the cuprizone-treated mouse brain. *Neurobiol. Dis.* 176, 105951. <https://doi.org/10.1016/j.nbd.2022.105951>.
- Wei, Y., Chang, L., Hashimoto, K., 2022a. Molecular mechanisms underlying the antidepressant actions of arketamine: beyond the NMDA receptor. *Mol. Psychiatry* 27 (1), 559–573. <https://doi.org/10.1038/s41380-021-01121-1>.
- Wei, Y., Wang, T., Liao, L., Fan, X., Chang, L., Hashimoto, K., 2022b. Brain-spleen axis in health and diseases: a review and future perspective. *Brain Res. Bull.* 182, 130–140. <https://doi.org/10.1016/j.brainresbull.2022.02.008>.
- Wiest, R., Albillos, A., Trauner, M., Bajaj, J.S., Jalan, R., 2017. Targeting the gut-liver axis in liver disease. *J. Hepatol.* 67 (5), 1084–1103. <https://doi.org/10.1016/j.jhep.2017.05.007>.
- Yang, C., Shirayama, Y., Zhang, J.C., Ren, Q., Yao, W., Ma, M., Dong, C., Hashimoto, K., 2015. R-ketamine: a rapid-onset and sustained antidepressant without psychotomimetic side effects. *Transl. Psychiatry* 5 (9), e632. <https://doi.org/10.1038/tp.2015.136>.
- Yang, C., Qu, Y., Fujita, Y., Ren, Q., Ma, M., Dong, C., Hashimoto, K., 2017. Possible role of the gut microbiota-brain axis in the antidepressant effects of (R)-ketamine in a social defeat stress model. *Transl. Psychiatry* 7 (12), 1294. <https://doi.org/10.1038/s41398-017-0031-4>.
- Yang, C., Yang, J., Luo, A., Hashimoto, K., 2019. Molecular and cellular mechanisms underlying the antidepressant effects of ketamine enantiomers and its metabolites. *Transl. Psychiatry* 9 (1), 280. <https://doi.org/10.1038/s41398-019-0624-1>.
- Yang, Y., Ishima, T., Wan, X., Wei, Y., Chang, L., Zhang, J., Qu, Y., Hashimoto, K., 2022. Microglial depletion and abnormalities in gut microbiota composition and short-chain fatty acids in mice after repeated administration of colony stimulating factor 1

- receptor inhibitor PLX5622. *Eur. Arch. Psychiatry Clin. Neurosci.* 272 (3), 483–495. <https://doi.org/10.1007/s00406-021-01325-0>.
- Yang, Y., Eguchi, A., Wan, X., Chang, L., Wang, X., Qu, Y., Mori, C., Hashimoto, K., 2023. A role of gut-microbiota-brain axis via subdiaphragmatic vagus nerve in depression-like phenotypes in *Chrna7* knock-out mice. *Prog. Neuro-Psychopharmacol. Biol. Psychiatry* 120, 110652. <https://doi.org/10.1016/j.pnpbp.2022.110652>.
- Yang, Y., Eguchi, A., Wan, X., Mori, C., Hashimoto, K., 2024. Depression-like phenotypes in mice with hepatic ischemia/reperfusion injury: a role of gut-microbiota-liver-brain axis via vagus nerve. *J. Affect. Disord.* 345, 157–167. <https://doi.org/10.1016/j.jad.2023.10.142>.
- Yao, W., Cao, Q., Luo, S., He, L., Yang, C., Chen, J., Qi, Q., Hashimoto, K., Zhang, J.C., 2022. Microglial ERK-NRBP1-CREB-BDNF signaling in sustained antidepressant actions of (R)-ketamine. *Mol. Psychiatry* 27 (3), 1618–1629. <https://doi.org/10.1038/s41380-021-01377-7>.
- Yue, C., Luan, W., Gu, H., Qiu, D., Ding, X., Liu, P., Wang, X., Hashimoto, K., Yang, J.J., 2023. The role of the gut-microbiota-brain axis via the subdiaphragmatic vagus nerve in chronic inflammatory pain and comorbid spatial working memory impairment in complete Freund's adjuvant mice. *J. Psychiatr. Res.* 166, 61–73. <https://doi.org/10.1016/j.jpsychires.2023.09.003>.
- Zhang, J., Ma, L., Chang, L., Pu, Y., Qu, Y., Hashimoto, K., 2020. A key role of the subdiaphragmatic vagus nerve in the depression-like phenotype and abnormal composition of gut microbiota in mice after lipopolysaccharide administration. *Transl. Psychiatry* 10 (1), 186. <https://doi.org/10.1038/s41398-020-00878-3>.
- Zhang, J., Ma, L., Wan, X., Shan, J., Qu, Y., Hashimoto, K., 2021a. (R)-ketamine attenuates LPS-induced endotoxin-derived delirium through inhibition of neuroinflammation. *Psychopharmacology* 238 (10), 2743–2753. <https://doi.org/10.1007/s00213-021-05889-6>.
- Zhang, J.C., Li, S.X., Hashimoto, K., 2014. R (–)-ketamine shows greater potency and longer lasting antidepressant effects than S (+)-ketamine. *Pharmacol. Biochem. Behav.* 116, 137–141. <https://doi.org/10.1016/j.pbb.2013.11.033>.
- Zhang, J.C., Yao, W., Hashimoto, K., 2022a. Arketamine, a new rapid-acting antidepressant: a historical review and future directions. *Neuropharmacology* 218, 109219. <https://doi.org/10.1016/j.neuropharm.2022.109219>.
- Zhang, K., Yao, Y., Hashimoto, K., 2023. Ketamine and its metabolites: potential as novel treatments for depression. *Neuropharmacology* 222, 109305. <https://doi.org/10.1016/j.neuropharm.2022.109305>.
- Zhang, X., Liu, H., Hashimoto, K., Yuan, S., Zhang, J., 2022b. The gut–liver axis in sepsis: interaction mechanisms and therapeutic potential. *Crit. Care* 26 (1), 213. <https://doi.org/10.1186/s13054-022-04090-1>.
- Zhang, Y., Xie, B., Chen, X., Zhang, J., Yuan, S., 2021b. A key role of gut microbiota–vagus nerve/spleen axis in sleep deprivation-mediated aggravation of systemic inflammation after LPS administration. *Life Sci.* 265, 118736. <https://doi.org/10.1016/j.lfs.2020.118736>.
- Zheng, P., Zeng, B., Zhou, C., Liu, M., Fang, Z., Xu, X., Zeng, L., Chen, J., Fan, S., Du, X., Zhang, X., Yang, D., Yang, Y., Meng, H., Li, W., Melgiri, N.D., Licinio, J., Wei, H., Xie, P., 2016. Gut microbiome remodeling induces depressive-like behaviors through a pathway mediated by the host's metabolism. *Mol. Psychiatry* 21 (6), 786–796. <https://doi.org/10.1038/mp.2016.44>.
- Zhou, W.C., Zhang, Q.B., Qiao, L., 2014. Pathogenesis of liver cirrhosis. *World J. Gastroenterol.* 20 (23), 7312–7324. <https://doi.org/10.3748/wjg.v20.i23.7312>.

日中笹川医学奨学金制度<学位取得コース>評価書

課程博士：指導教官用



第 44 期

研究者番号：G4404

作成日：2024年3月10日

氏名	蔣 夢恬	JIANG MENG TIAN	性別	F	生年月日	1996/03/15
所属機関（役職）	東京医科歯科大学大学院医歯学総合研究科（大学院生）					
研究先（指導教官）	東京医科歯科大学大学院医歯学総合研究科 口腔機能再構築学講座生体補綴歯科学分野（若林 則幸 教授）					
研究テーマ	暗条件下での血清及び唾液中の二酸化チタンの殺菌効果に及ぼす3種類のイオン性抗菌剤の影響に関する研究 Development of antibacterial dental materials using cation-doped TiO ₂ nanosheet in dark condition					
専攻種別	<input type="checkbox"/> 論文博士			<input checked="" type="checkbox"/> 課程博士		

研究者評価（指導教官記入欄）

成績状況	優 学業成績係数=	取得単位数
		30/30
学生本人が行った研究の概要	研究課題では、優れた抗菌活性を有する新規歯科補綴装置用材料の創製のため、光析出法にて金属ナノ粒子を担持させたチタニアナノシートを開発することを目的としている。本年度は、作製した金属固溶チタニアナノシートのキャラクタリゼーションを、走査型電子顕微鏡、透過型電子顕微鏡、X線回折により解析した。また、電子線散乱による評価を継続している。また、う蝕原性細菌である Streptococcus mutans を用いた抗菌活性を評価した。その結果、銅を固溶したチタニアナノシートの抗菌活性が最も優れていることが明らかとなり、本成果を、国際学会である The 3rd International Symposium on Design & Engineering by Joint Inverse Innovation for Materials Architecture (DEJI2MA-3) と 2024 International Association for Dental, Oral, and Craniofacial Research にて発表を行った。次年度に論文を投稿予定である。	
総合評価	【良かった点】 本年度は、作製した金属固溶チタニアナノシートのキャラクタリゼーションと抗菌活性評価までを行い、十分な研究活動を行ったと評価できる。特に、水熱化学合成法と光析出法を用いた金属固溶チタニアナノシートの合成方法に習熟し、今後、本法を応用した材料開発を遂行できるようになった。また、細菌を用いた抗菌活性評価を独立して遂行可能となった。研究室のチームとも協調性をもって活動することができた。	
	【改善すべき点】 今後、自立した研究者として活躍するためには、得られた実験結果の解釈とその意味を理解することが重要である。また、その結果から今後の検討課題を吟味することが必要であるが、問題点の抽出とその解決策の提案が不十分であることが見受けられた。改善の傾向が見受けられるが、独立した研究者として活躍するためには、今後一層の研鑽が必要である。	
	【今後の展望】 作製した金属ナノ粒子は数 nm サイズのため、学内機器では詳細な解析を行うことができない。そこで次年度は、東京都立産業技術センターにてキャラクタリゼーションを行う予定である。また、歯科材料への応用のため、光触媒活性と抗菌活性の評価を行う予定である。	

学位取得見込	研究は順調に進捗しており、本学が定める学位取得の単位も到達している。次年度は論文の執筆にとりかかり、学術雑誌への投稿を予定しており、十分に学位取得の要件を満たすと考える。
評価者（指導教官名） 若林 則幸	

日中笹川医学奨学金制度(学位取得コース)中間報告書 研究者用



第44期

研究者番号: G4404

作成日: 2024年3月 5 日

氏名	蒋 梦恬	JIANG MENG TIAN	性別	F	生年月日	1996/03/15
所属機関(役職)	東京医科歯科大学大学院医歯学総合研究科(大学院生)					
研究先(指導教官)	東京医科歯科大学大学院医歯学総合研究科 口腔機能再構築学講座生体補綴歯科学分野(若林 則幸 教授)					
研究テーマ	暗条件下での血清及び唾液中の二酸化チタンの殺菌効果に及ぼす3種類のイオン性抗菌剤の影響に関する研究 Development of antibacterial dental materials using cation-doped TiO ₂ nanosheet in dark condition					
専攻種別	論文博士	<input type="checkbox"/>	課程博士	<input checked="" type="checkbox"/>		

1. 研究概要(1)

1) 目的(Goal)

Titania (TiO₂) has antibacterial effects due to its photocatalytic activity and has been applied not only in the industrial field but also in the medical and dental fields. To improve the functions of TiO₂, we have prepared highly-ordered TiO₂ nanosheets (TiO₂ NS) exposing the {001} planes and have shown that they have superior photocatalytic activity compared to conventional titania nanoparticles. In this study, we made silver, copper, and cerium-doped titania nanosheets (Ag/TiO₂ NS, Cu/TiO₂ NS, and Ce/TiO₂ NS) and performed antibacterial tests of these 3 kinds of metal-doped TiO₂ NS to explore the antibacterial effect against *Streptococcus mutans*.

2) 戦略(Approach)

The photodeposition method is based on the photocatalytic property of semiconductor materials afforded by their band gap. Several conditions are needed to enable the photodeposition method. First, the photon energy of the exposure light should be larger than the energy band gap of the semiconductor. When light that has the proper energy level for the band gap of the semiconductor is absorbed, electrons from the valence band can be excited. Second, the reduction potential of the metal ion should be more positive than the conduction band energy level of the semiconductor. Third, the efficient separation and migration of photo-generated electron-hole pairs is necessary. Finally, the semiconductor should act as a template for active sites of metal deposition and have a large surface area. If these four conditions are met, the synthesis of metal/semiconductor nanocomposite by photodeposition method is possible, since nanoscale semiconductor materials have many active sites that have large surface energy due to their morphology. Also, this is a simple and green method since it does not require the addition of chemical reagents or any conditions other than light exposure[1].

3) 材料と方法(Materials and methods)

1. Synthesis of F-TiO₂ NS

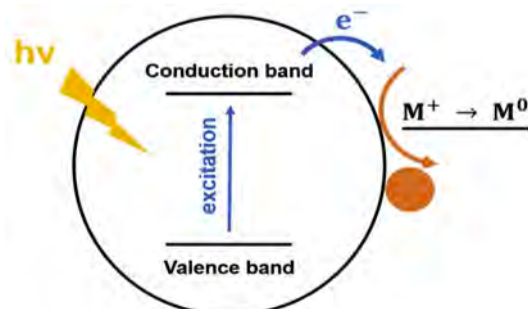
Dissolve 1 g Ammonium hexafluorotitanate into 5 ml of hydrochloric acid (5 M). Add a controlled amount titanium (IV) butoxide to the above solution to make that the total F/Ti molar ratio is 1.0 under strong stirring and white gels formed. The gels are placed into a 50 ml Teflon tube for a 6-hour hydrothermal reaction at 180° C. The products of the hydrothermal reaction are washed with ultrapure water three times and by methanol once, all with subsequent centrifugal separation. The obtained TiO₂ NS were then freeze dried[2,3].

2. Removal of the fluorides from F-TiO₂ NS to produce TiO₂ NS

To attain the removal of the fluorides from the surface, the as-prepared F-TiO₂ NS was washed with 0.1M NaOH (10 mg TiO₂/ml, 2 h under stirring at ~300K). The suspension was then centrifuged (4000rpm, 15min). The paste of TiO₂ NS was recovered by centrifugation and washed by water 3 times (1500mg, 40 ml, 4000 rpm, 15 min) to remove Na⁺ ions from the surface.

Preparation of metal doped TiO₂ NS by photodeposition

For preparation of metal-modified TiO₂ NS, silver nitrate, copper sulfate pentahydrate and cerium nitrate hexahydrate are used as metal precursors. The amount of each metal doped on 1500mg TiO₂ NS is 1.2*10⁻⁴mol, which means that the quantity of silver nitrate, copper sulfate and cerium nitrate is 20.40mg, 30.00mg and 52.08mg respectively.



Schematic diagram of photodeposition method. When light is absorbed in the band gap, electrons from valence band are excited and migrate to reduce metal ions to metal. $h\nu$, light energy; e^- , photoexcited electron; M^+ , metal ion; M^0 , metal.

1. 研究概要 (2)

The weighted TiO₂ NS powder is put into a Pyrex glass tube equipped with a magnetic stirrer, to which 75ml of methanol(99.5%) aqueous solution(50vol%, distilled water) is added. Then, the aqueous solution of metal salt is slowly dropped while being stirred(75ml distilled water). The suspension is gas-sparged (N₂) for 15 min. The tube is photoirradiated for 3 hours for Ag/TiO₂, Cu/TiO₂ and Ce/TiO₂ with magnetic stirring (500rpm) by a 121-W high-pressure mercury lamp under thermostatic control at 298K. The thus-obtained photocatalysts is centrifuged (4000rpm for 30 min), washed three times with methanol and three times with distilled water, and freeze-dried, and then the product is collected for further study[4].

3. Characterization of three composite materials

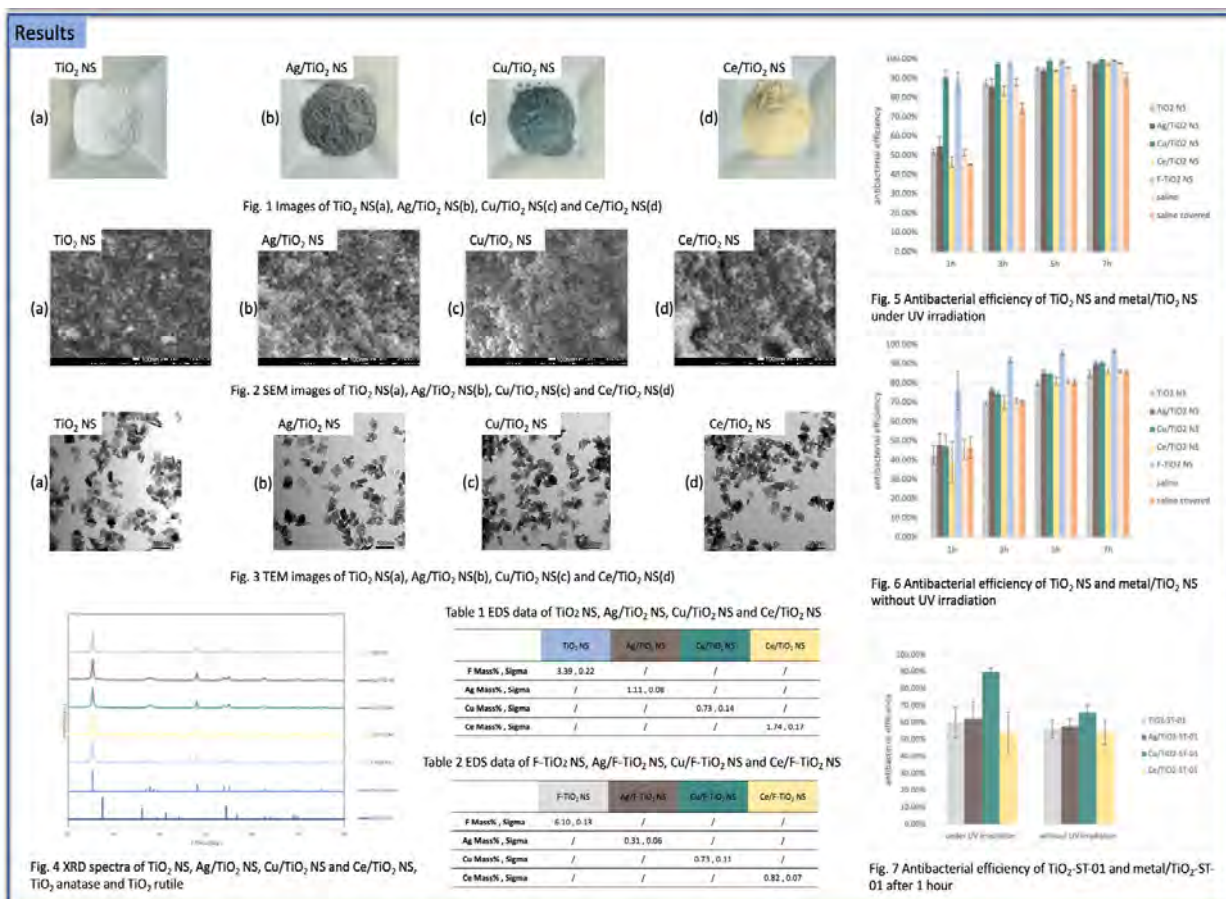
Use X-ray diffractometer, scanning electron microscope, transmittance electron microscope and energy-dispersive X-ray spectrometer to show the crystal structure, morphology and chemical composition of the precipitates. The length and thickness are measured from TEM images.

4. Antibacterial tests against S. mutans

Precultures of S. mutans was grown in ATCC Medium:44 Brain-Heart Infusion (BHI) Broth at 37°C anaerobically (180 rpm). After 18 h, cells are harvested by centrifugation (2200 rpm, 19°C, 5 min), washed twice with 5 ml of saline and resuspended in saline. The density is standardized and adjusted to 0.5 McFarland concentration using a turbidity meter. 9 ml of S. mutans' suspension is poured into the glass bottle with 1 ml metal/TiO₂ or metal/TiO₂-ST-01 or metal/TiO₂-ST-41 saline solution. In addition, two controls were set as 9 ml of S. mutans's suspension with 1 ml saline and one of the glass bottles was covered with aluminum foil.

All experiments are carried out in glass bottles with and without UV irradiation (2.5 mW/cm², 315nm-400nm, 27W) with magnetic stirring (speed 300rpm). At proposed time intervals luminescence was recorded.

4) 実験結果 (Results)



5) 考察 (Discussion)

Ag, Cu and Ce could be doped on titanium dioxide by photodeposition. Ag, Cu and Ce doping by photodeposition could affect the antibacterial efficiency of TiO₂ nanosheets and TiO₂ nanoparticles against Streptococcus mutans.

6) 参考文献 (References)

[1].Lee, Y. et al. Photodeposited metal-semiconductor nanocomposites and their applications. J. Materiomics 4, 83-94 (2018).
 [2].Hayashi, K. et al. Enhanced Antibacterial Property of Facet-Engineered TiO₂ Nanosheet in Presence and Absence of Ultraviolet Irradiation. Materials 13, 78 (2019).
 [3].Tan, Z. et al. Particle size for photocatalytic activity of anatase TiO₂ nanosheets with highly exposed {001} facets. RSC Adv. 3, 19268 (2013).
 [4].Wei, Z. et al. Noble metal-modified octahedral anatase titania particles with enhanced activity for decomposition of chemical and microbiological pollutants. Chem. Eng. J. 318, 121-134 (2017).
 [5].Effects of catalyst preparation method and reaction parameters on the ultrasound assisted Photocatalytic oxidation of reactive yellow 84 dye.

2. 執筆論文 Publication of thesis ※記載した論文を添付してください。Attach all of the papers listed below.

論文名 1 Title	Enhanced Photocatalysis of Electrically Polarized Titania Nanosheets					
掲載誌名 Published journal	nanomaterials					
	2024 年 1 月	14 巻(号)	171 頁 ~	181 頁	言語 Language	English
第1著者名 First author	Tomoyuki Mihara	第2著者名 Second author	Kosuke Nozaki		第3著者名 Third author	Yasuyuki Kowaka
その他著者名 Other authors	Mengtian Jiang , Kimihiro Yamashita, Hiroyuki Miura and Satoshi Ohara					
論文名 2 Title						
掲載誌名 Published journal						
	年 月	巻(号)	頁 ~	頁	言語 Language	
第1著者名 First author		第2著者名 Second author			第3著者名 Third author	
その他著者名 Other authors						
論文名 3 Title						
掲載誌名 Published journal						
	年 月	巻(号)	頁 ~	頁	言語 Language	
第1著者名 First author		第2著者名 Second author			第3著者名 Third author	
その他著者名 Other authors						
論文名 4 Title						
掲載誌名 Published journal						
	年 月	巻(号)	頁 ~	頁	言語 Language	
第1著者名 First author		第2著者名 Second author			第3著者名 Third author	
その他著者名 Other authors						
論文名 5 Title						
掲載誌名 Published journal						
	年 月	巻(号)	頁 ~	頁	言語 Language	
第1著者名 First author		第2著者名 Second author			第3著者名 Third author	
その他著者名 Other authors						

3. 学会発表 Conference presentation ※筆頭演者として総会・国際学会を含む主な学会で発表したものを記載してください

※Describe your presentation as the principal presenter in major academic meetings including general meetings or international meetings

学会名 Conference	International Summer Program 2023, Tokyo Medical and Dental University		
演題 Topic	Development of metal nanoparticle-modified titanium dioxide nanosheets through photodeposition		
開催日 date	2023 年 8 月 1 日	開催地 venue	Tokyo
形式 method	<input type="checkbox"/> 口頭発表 Oral <input checked="" type="checkbox"/> ポスター発表 Poster	言語 Language	<input type="checkbox"/> 日本語 <input checked="" type="checkbox"/> 英語 <input type="checkbox"/> 中国語
共同演者名 Co-presenter	Kosuke Nozaki, Takeshi Ueno, Noriyuki Wakabayashi		
学会名 Conference	The 3rd International Symposium on Design & Engineering by Joint Inverse Innovation for Materials Architecture (DEJI2MA-3)		
演題 Topic	Influence of three kinds of ionic antibacterial agents on the antibacterial effect of titania		
開催日 date	2023 年 10 月 20 日	開催地 venue	Tokyo
形式 method	<input type="checkbox"/> 口頭発表 Oral <input checked="" type="checkbox"/> ポスター発表 Poster	言語 Language	<input type="checkbox"/> 日本語 <input checked="" type="checkbox"/> 英語 <input type="checkbox"/> 中国語
共同演者名 Co-presenter	Kosuke Nozaki, Takeshi Ueno, Satoshi Ohara, Takayuki Mokudai, Noriyuki Wakabayashi		
学会名 Conference			
演題 Topic			
開催日 date	年 月 日	開催地 venue	
形式 method	<input type="checkbox"/> 口頭発表 Oral <input type="checkbox"/> ポスター発表 Poster	言語 Language	<input type="checkbox"/> 日本語 <input type="checkbox"/> 英語 <input type="checkbox"/> 中国語
共同演者名 Co-presenter			
学会名 Conference			
演題 Topic			
開催日 date	年 月 日	開催地 venue	
形式 method	<input type="checkbox"/> 口頭発表 Oral <input type="checkbox"/> ポスター発表 Poster	言語 Language	<input type="checkbox"/> 日本語 <input type="checkbox"/> 英語 <input type="checkbox"/> 中国語
共同演者名 Co-presenter			

4. 受賞(研究業績) Award (Research achievement)

名称 Award name	国名 Country	受賞年 Year of	年 月
名称 Award name	国名 Country	受賞年 Year of	年 月

5. 本研究テーマに関わる他の研究助成金受給 Other research grants concerned with your research theme

受給実績 Receipt record	<input checked="" type="checkbox"/> 有 <input type="checkbox"/> 無
助成機関名称 Funding agency	国立研究開発法人科学技術振興機構次世代研究者挑戦的研究プログラム
助成金名称 Grant name	東京医科歯科大学卓越大学院生制度(II)
受給期間 Supported period	2022 年 4 月 ~ 2025 年 3 月
受給額 Amount received	50万/年 円
受給実績 Receipt record	<input type="checkbox"/> 有 <input type="checkbox"/> 無
助成機関名称 Funding agency	
助成金名称 Grant name	
受給期間 Supported period	年 月 ~ 年 月
受給額 Amount received	円

6. 他の奨学金受給 Another awarded scholarship

受給実績 Receipt record	<input checked="" type="checkbox"/> 有 <input type="checkbox"/> 無
助成機関名称 Funding agency	国立研究開発法人科学技術振興機構次世代研究者挑戦的研究プログラム
奨学金名称 Scholarship name	東京医科歯科大学卓越大学院生制度(II)
受給期間 Supported period	2022 年 4 月 ~ 2025 年 3 月
受給額 Amount received	16万/月 円

7. 研究活動に関する報道発表 Press release concerned with your research activities

※記載した記事を添付してください。Attach a copy of the article described below

報道発表 Press release	<input type="checkbox"/> 有 <input type="checkbox"/> 無	発表年月日 Date of release	
発表機関 Released medium			
発表形式 Release method	・新聞 ・雑誌 ・Web site ・記者発表 ・その他()		
発表タイトル Released title			

8. 本研究テーマに関する特許出願予定 Patent application concerned with your research theme

出願予定 Scheduled	<input type="checkbox"/> 有 <input type="checkbox"/> 無	出願国 Application	
出願内容(概要) Application contents			

9. その他 Others

--

指導責任者(記名) 若林 則幸

Article

Enhanced Photocatalysis of Electrically Polarized Titania Nanosheets

Tomoyuki Mihara ¹, Kosuke Nozaki ^{1,*} , Yasuyuki Kowaka ¹, Mengtian Jiang ¹, Kimihiro Yamashita ¹, Hiroyuki Miura ¹ and Satoshi Ohara ²

¹ Graduate School of Medical and Dental Sciences, Tokyo Medical and Dental University, Bunkyo-ku, Tokyo 113-8549, Japan; t.mihara.fpro@tmd.ac.jp (T.M.); y.kowaka.fpro@tmd.ac.jp (Y.K.); jiang.mt.fpro@tmd.ac.jp (M.J.); yama-k.bcr@tmd.ac.jp (K.Y.); h.miura.fpro@tmd.ac.jp (H.M.)

² New Industry Creation Hatchery Center, Tohoku University, Aoba, Sendai 980-8579, Japan; s.ohara@super-nano.com

* Correspondence: k.nozaki.fpro@tmd.ac.jp; Tel.: +83-5803-5516

Abstract: Titania (TiO₂) nanosheets are crystals with controlled, highly ordered structures that improve the functionality of conventional TiO₂ nanoparticles. Various surface modification methods have been studied to enhance the effectiveness of these materials as photocatalysts. Surface modifications using electrical polarization have attracted considerable attention in recent years because they can improve the function of titania without changing its composition. However, the combination of facet engineering and electrical polarization has not been shown to improve the functionality of TiO₂ nanosheets. In the present study, the dye-degradation performance of polarized TiO₂ nanosheets was evaluated. TiO₂ nanosheets with a F/Ti ratio of 0.3 were synthesized via a hydrothermal method. The crystal morphology and structure were evaluated using transmission electron microscopy and X-ray diffraction. Then, electrical polarization was performed under a DC electric field of 300 V at 300 °C. The polarized material was evaluated using thermally stimulated current measurements. A dye-degradation assay was performed using a methylene blue solution under ultraviolet irradiation. The polarized TiO₂ nanosheets exhibited a dense surface charge and accelerated decolorization. These results indicate that electrical polarization can be used to enhance the photocatalytic activity of TiO₂.

Keywords: TiO₂; surface charge; electrical polarization; photocatalytic activity; dye decolorization



Citation: Mihara, T.; Nozaki, K.; Kowaka, Y.; Jiang, M.; Yamashita, K.; Miura, H.; Ohara, S. Enhanced Photocatalysis of Electrically Polarized Titania Nanosheets. *Nanomaterials* **2024**, *14*, 171. <https://doi.org/10.3390/nano14020171>

Academic Editor: Antonino Gulino

Received: 1 December 2023

Revised: 5 January 2024

Accepted: 5 January 2024

Published: 12 January 2024



Copyright: © 2024 by the authors. Licensee MDPI, Basel, Switzerland. This article is an open access article distributed under the terms and conditions of the Creative Commons Attribution (CC BY) license (<https://creativecommons.org/licenses/by/4.0/>).

1. Introduction

Titania (TiO₂) has been used in industrial applications as well as in the dental field as a denture cleaner and for tooth bleaching because it causes a reduction–oxidation (redox) reaction through photocatalytic activity on its surface [1]. Ultraviolet (UV) irradiation generates electrons and holes on the surface of titania, resulting in the generation of reactive oxygen species (ROS) such as superoxide anions (O₂^{•−}) and hydroxyl radicals (•OH) in the presence of water and oxygen [2]. These oxidizing substances can decompose organic dyes with a higher efficiency than common oxygen molecules [3]. However, the generated electrons and holes recombine within 50 ns, indicating that carriers have a longer lifetime on their surfaces [4].

The photocatalytic activity of titania has been improved using various methods, such as facet engineering [5,6], structure regulation [7], and metal doping [8]. These methods aim to enhance the photocatalytic activity by delaying electron–hole recombination. Especially enhanced photocatalysis has been obtained by designing compact heterojunctions [9]. We previously reported a highly ordered, facet-controlled, anatase-type titania nanosheet (NS) with several {001} planes and found that it had superior photocatalytic activity and antibacterial capability compared to conventional titania nanoparticles [10,11]. Titania NSs with side lengths of 29 nm were synthesized using ammonium hexafluorotitanate

((NH₄)₂TiF₆) and titanium butoxide (Ti(OBu)₄). Fluoride from ammonium hexafluorotitanate inhibits crystal growth of the {001} facet by adhering to its facet, which has a high surface energy. The {001} surface has also been reported to have a higher reactivity site against UV irradiation than the {101} surface, which causes redox reactions on both the {001} and {101} surfaces [12]. These results suggest that facet-engineered titania is crucial for the design of photocatalyst-containing biomaterials. However, decolorization was achieved through decomposition via photocatalytic activity as well as by adsorbing dyes on the titania surface [13].

Dye adsorption is typically regulated by physical forces such as van der Waals forces, hydrogen bonds, polarity, and dipole–dipole interactions [14]. The surface charge also plays a critical role in dye adsorption [15]. Electrical polarization has attracted considerable attention as a promising surface modification method [16–18]. We previously reported the surface modification of bioceramics, including hydroxyapatite, carbonated apatite, β -tricalcium phosphate (TCP), zirconia, bioglasses, and glass ceramics, through the electrical polarization process, which can induce surface charges without any doped elements or coating [19–23]. Although the strong ferroelectric polarization of TiO₂ can be achieved through the conjunction of perovskite-based material layers [24], such as BaTiO₃ and SrTiO₃, for applications in the medical and dental fields, surface modifications without any other impurities are highly recommended.

Electrical polarization also regulates titania's electrical dipole orientation under DC electric fields and a high temperature of approximately 300 to 400 °C and maintains its orientation at room temperature [25]. Electrically polarized titania has been reported to enhance osteoblast-like cell proliferation and differentiation and osteoconductivity [23,25,26]. In previous studies, polarized titania was fabricated using the micro-arc oxidation method, which incorporates calcium and phosphate ions. However, it is unclear whether the dipole orientation of titania without doped elements can be induced using electrical polarization. Concerning metal Ti-oxidated titania, we electrically polarized a thick titania layer on a titanium substrate. Bandyopadhyay et al. also reported that titania nanotubes on Ti can be polarized by electrothermal polarization and are supposed to be a novel biomaterial to promote in vivo osseointegration at an early stage in vivo [27]. It is still unclear whether titania powder can be electrically polarized.

The purpose of this study was to attempt the surface modification of NSs by electrical polarization and evaluate the dye-degradation capability of polarized titania NSs to clarify their functions. TiO₂ NSs with a fluorine-to-titanium molar ratio of 0.3 were hydrothermally synthesized. The crystal structure was characterized using transmission electron microscopy (TEM) and X-ray diffraction (XRD). Subsequently, electrical polarization was performed, and the surface charges were evaluated using thermally stimulated current (TSDC) measurements. The dye-degradation performance of the polarized NS was evaluated using a methylene blue (MB) dye-degradation test. The null hypothesis was that electrical polarization does not enhance the decolorizing performance of TiO₂.

2. Materials and Methods

2.1. Synthesis of Titania Nanosheets

The details of the fabrication process for the titania NSs have been described previously [10]. Briefly, titanium butoxide (Sigma-Aldrich, St. Louis, MO, USA) was added dropwise with stirring to 37% hydrochloric acid (FUJIFILM Wako Pure Chemical Corp., Osaka, Japan) and ammonium hexafluorotitanate (Sigma-Aldrich, St. Louis, MO, USA) at a F/Ti ratio of 0.3. The precursor was transferred to a high-pressure reaction vessel and hydrothermally synthesized at 180 °C for 6 h. The precipitates were sonicated thrice with methanol and twice with distilled water. The precipitates were then freeze-dried to obtain a titania NS using a freeze dryer (FDS-1000, Tokyo Rikakikai Co., Ltd., Tokyo, Japan). Titania nanoparticles (NPs, FUJIFILM Wako Pure Chemical Corp. Osaka, Japan) were used as control materials.

Japan). Titania nanoparticles (NPs, FUJIFILM Wako Pure Chemical Corp. Osaka, Japan) were used as control materials.

2.2. Electrical Polarization

2.2.1. Electrical Polarization

NS and NP powders were poured into an alumina ring with an inner diameter of 10 mm and a depth of 2 mm, sandwiched between platinum foil electrodes, and then electrically polarized under a DC electric field at 300 V/mm and 300 °C for 1 h (P-NS, P-NP) (Figure 1). As the control group, NSs and NPs were subjected to the same process of heating at 300 °C under 0 V/mm (H-NS, H-NP).

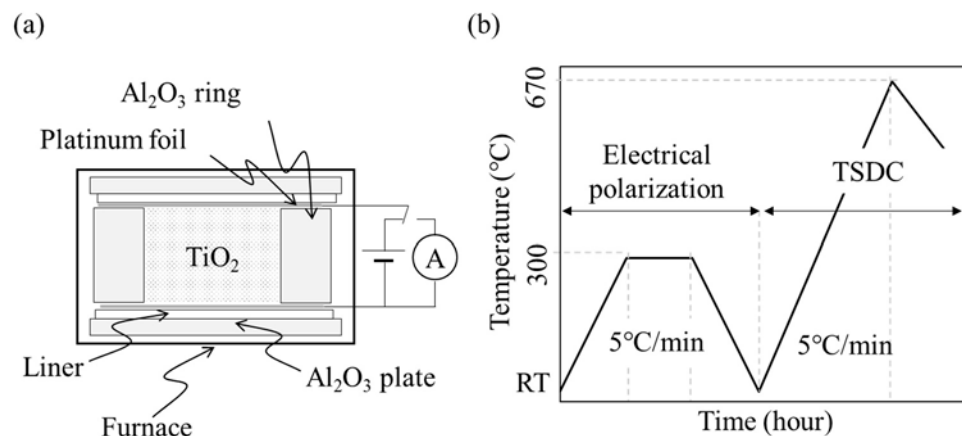


Figure 1. (a) Schematic diagram of sample preparation for electrical polarization. For the thermally polarized sample, a current (J) was prepared for electrical polarization. For the galvanostatic TSDC measurement, the TSDC polarization and TSDC measurement were conducted to a galvanometer. (b) Temperature program for electrical polarization and TSDC measurement procedure.

2.3. Characterization

The crystal morphology and structure of each sample were observed using TEM (JEOL-7000XRS1, JEOL Ltd., Tokyo, Japan) (JEM-1400Flash, JEOL Ltd., Tokyo, Japan). In addition, the phase composition of the sample surface was analyzed in the 2 θ range of 20° to 80° using XRD (D8 advance, Bruker AXS GmbH, Karlsruhe, Germany). Polarized and non-polarized samples were evaluated using TSDC at a temperature increase rate of 5.0 °C/min from room temperature to 670 °C in air after polarization with a galvanometer (6514/J, Tektronix Inc., Tokyo, Japan) (Figure 1) [20–22,26,27]. The stored charge (Q) was calculated from the TSDC spectra using the following equation:

$$Q = \frac{1}{\beta} \int J(T) dT$$

where Q is the stored charge (C/cm²), β is the ramp rate of the temperature (K/s), and J(T) is the depolarized current density (A/cm).

The optical properties of the heated and polarized samples were characterized using UV-visible (UV-vis) spectrophotometer (Jasco M-550, JASCO International Co. Ltd., Tokyo, Japan). The optical bandgap energies (E_g) of the polarized and non-polarized samples were calculated using Tauc plots as previously described [28]. The optical bandgap energies (E_g) of the polarized and non-polarized sample were calculated using Tauc plots, as previously described [28].

2.4. Dye-Degradation Assay

The dye-degradation test using the redox reaction was conducted using a 0.3 mM MB solution. Each sample was mixed with MB at a concentration of 10 mg/mL. The mixed samples were irradiated at 20 °C (NCP2215, Nissinrika Corp., Tokyo, Japan) for 1, 10, 30, 60, 120, 180, 240, or 480 min under UV light (HL100G, Sen special light Source, SEN LIGHTS CORP., Osaka, Japan) at 2.5 mW/cm² (Figure 2). The samples were centrifuged (20,000 × g, 10 min), the supernatant was diluted 10-fold, and the absorbance was measured at 630 nm using a microplate reader (Model680, Bio-Rad Laboratories Inc., Hercules, Berkeley, CA, USA). For the non-irradiated group, the absorbance was measured in the same manner after UV irradiation under the same conditions, shielded with aluminum foil. After obtaining

at 630 nm using a microplate reader (Model680, Bio-Rad Laboratories Berkeley, CA, USA). For the non-irradiated group, the absorbance was measured in the same manner after UV irradiation under the same conditions, shielded with a foil. After obtaining the absorbance at each time point, the rate constant of MB was calculated using the following equation:

the absorbance at each time point, the rate constant of MB degradation was calculated using the following equation:

$$\ln \frac{A_0}{A_t} = k_a t$$

where k_a is a rate constant, A_t is the absorbance of the MB solution at each time, and A_0 is the absorbance after 1 min.

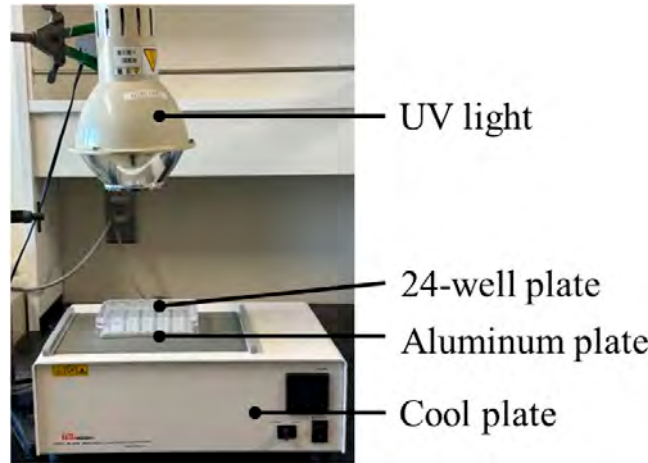


Figure 2. Experimental setup for dye degradation assay. The temperature of the 24-well plate was regulated by a cool plate via an aluminum plate.

2.5. Measurement of ROS

2.5.1. Measurement of ROS
 To measure the ROS generated from the titania samples (P-NS, P-NP, H-NS, and H-NP) under UV irradiation, disodium terephthalate (DTA, Tokyo Kasei Kogyo, Tokyo, Japan) and nitro blue tetrazolium (NBT, Tokyo Kasei Kogyo, Tokyo, Japan) assays were performed. NBT and DTA react with superoxide anions and convert them to formazan and 2-hydroxy terephthalic acid (HTA), respectively [10,29].

The NBT solution was mixed with 4 mg/mL of TiO₂ and irradiated with UV light at 2.5 mW/cm² for 2 h. After irradiation, the solution was centrifuged at 13,000 rpm for 10 min, and the supernatant was discarded. The precipitates were dissolved in dimethyl sulfoxide (DMSO, Fujifilm Wako Pure Chemicals Corporation, Osaka, Japan) and stirred for 10 min. The absorbance was measured at 570 nm using a spectrophotometer.

The NBT solution was mixed with 4 mg/mL of TiO₂ and irradiated with UV light at 2.5 mW/cm² for 2 h. After irradiation, the solution was centrifuged at 13,000 rpm for 10 min, and the supernatant was discarded. The precipitates were dissolved in dimethyl sulfoxide (DMSO, Fujifilm Wako Pure Chemicals Corporation, MA, USA) and stirred for 10 min. The absorbance and fluorescence intensity were measured at 570 nm using a spectrophotometer.

As previously reported [10], the absorbance and fluorescence intensity were converted to the concentrations of superoxide anions and hydroxyl radicals, respectively [30,31].

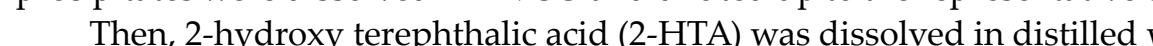
Briefly, a reaction mixture containing riboflavin, methionine, and NBT in potassium phosphate buffer was incubated for 1 h at room temperature. The purple precipitates were dissolved in DMSO and diluted up to the representative concentrations.

Then, 2-hydroxy terephthalic acid (2-HTA) was dissolved in distilled water up to the representative concentrations. The concentration of the hydroxyl radical can be estimated using the following reaction:

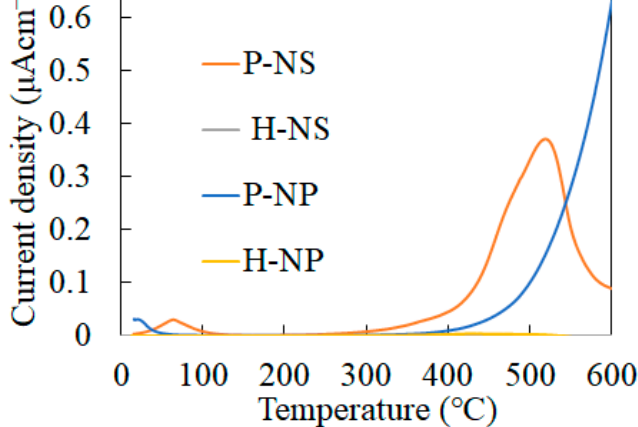


As previously reported [10], the absorbance and fluorescence intensity were converted to the concentrations of superoxide anions and hydroxyl radicals and 2-HTA [30,31]. Briefly, a reaction mixture containing riboflavin, methionine, potassium phosphate buffer was incubated for 1 h at room temperature. The purple precipitates were dissolved in DMSO and diluted up to the representative concentrations.

Then, 2-hydroxy terephthalic acid (2-HTA) was dissolved in distilled water up to the representative concentrations. The concentration of the hydroxyl radical can be estimated using the following reaction:

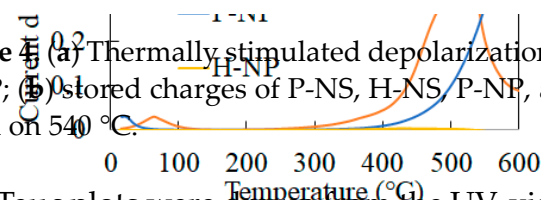


As previously reported [10], the absorbance and fluorescence intensity were converted to the concentrations of superoxide anions and hydroxyl radicals and 2-HTA [30,31]. Briefly, a reaction mixture containing riboflavin, methionine, potassium phosphate buffer was incubated for 1 h at room temperature. The purple precipitates were dissolved in DMSO and diluted up to the representative concentrations.



	Stored charges (µCcm ⁻²)
P-NS	315.4
H-NS	3.2
P-NP	106.4
H-NP	0.9

Figure 4. (a) Thermally stimulated depolarization current (TSDC) spectra of P-NS, H-NS, P-NP, and H-NP; (b) stored charges of P-NS, H-NS, P-NP, and H-NP. The spectra were cut off and calculated based on 540 °C.



	Stored charges (µCcm ⁻²)
P-NS	315.4
H-NS	3.2
P-NP	106.4
H-NP	0.9

Figure 5. (a) Tauc plots and (b) optical bandgap energy of heated and polarized TiO₂ NSs (H-NS and P-NS) and NPs (H-NP and P-NP).

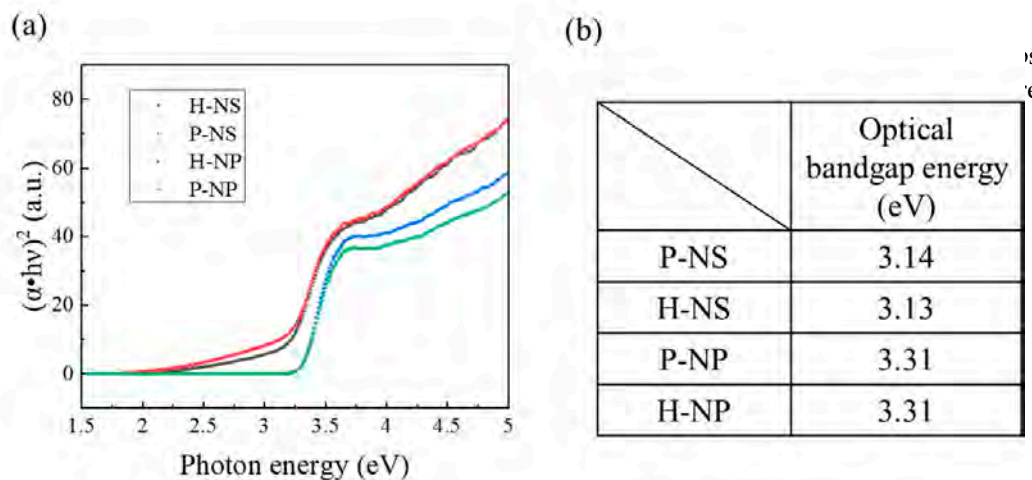


Figure 5. (a) Tauc plots and (b) optical bandgap energy of heated and polarized TiO₂ NSs (H-NS and P-NS) and NPs (H-NP and P-NP).

3.3. Effects of Electrical Polarization on Photocatalytic Properties of Titania Nanosheet

Figure 5. (a) Tauc plots and (b) optical bandgap energy of heated and polarized TiO₂ NSs (H-NS and P-NS) and NPs (H-NP and P-NP).

3.3.1. Production of Hydroxyl Radical and Superoxide Anion under UV Irradiation

The generation of superoxide anions and hydroxyl radicals was evaluated using nitro blue tetrazolium and DTA assays. Because the amount of converted formalin and 2-HTA standard curves, as shown in Figure 6, P-NP showed the highest efficiency in generating superoxide and hydroxyl radicals. The polarized titania also generated more ROS than non-polarized titania.

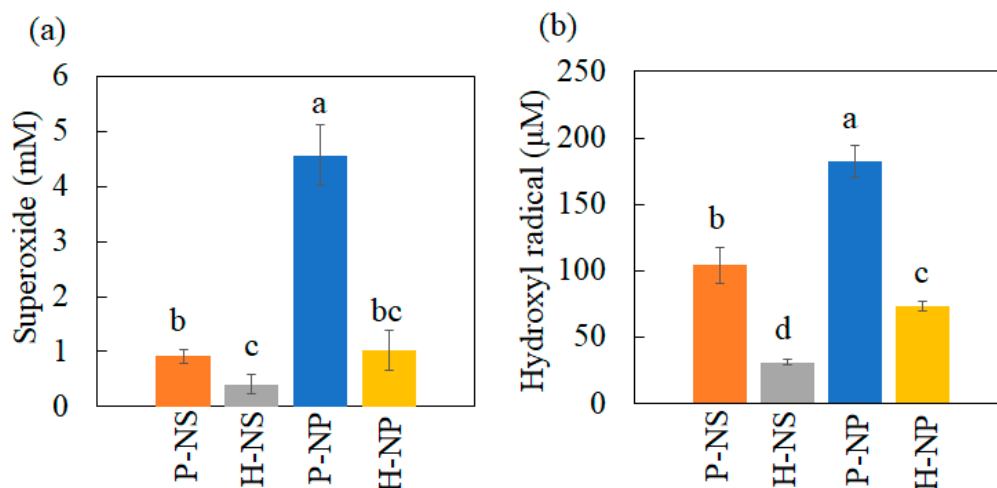


Figure 6. ROS production under UV irradiation. (a) Superoxide anion production and (b) hydroxyl radical production. The different letters show significant differences at $\alpha = 0.05$.

3.3.2. Decolorization Experimental Results

The decolorization of the MB solution with titania without UV irradiation was evaluated at regular intervals. Under UV irradiation, MB decomposed in a time-dependent manner (Figure 7a). P-NS showed the highest dye degradation efficiency after 480 min

evaluated at regular intervals. Under UV irradiation, MB decomposed in a time-dependent manner (Figure 7a). P-NS showed the highest dye degradation efficiency after 480 min (Figure 7a). Electrical polarization enhanced dye degradation in the NS group, but no effect was observed in the NP group. The decolorization of MB without UV irradiation showed no time-dependent changes after 30 min (Figure 7b). However, as significant differences of P-NS, H-NS, P-NP, and H-NP (Figure 7c). The electrical polarization of the significantly enhanced the decolorization compared to non-polarized titania. The calculated rate constant of P-NS was higher than those of H-NS, H-NP, and P-NP (Figure 8). The

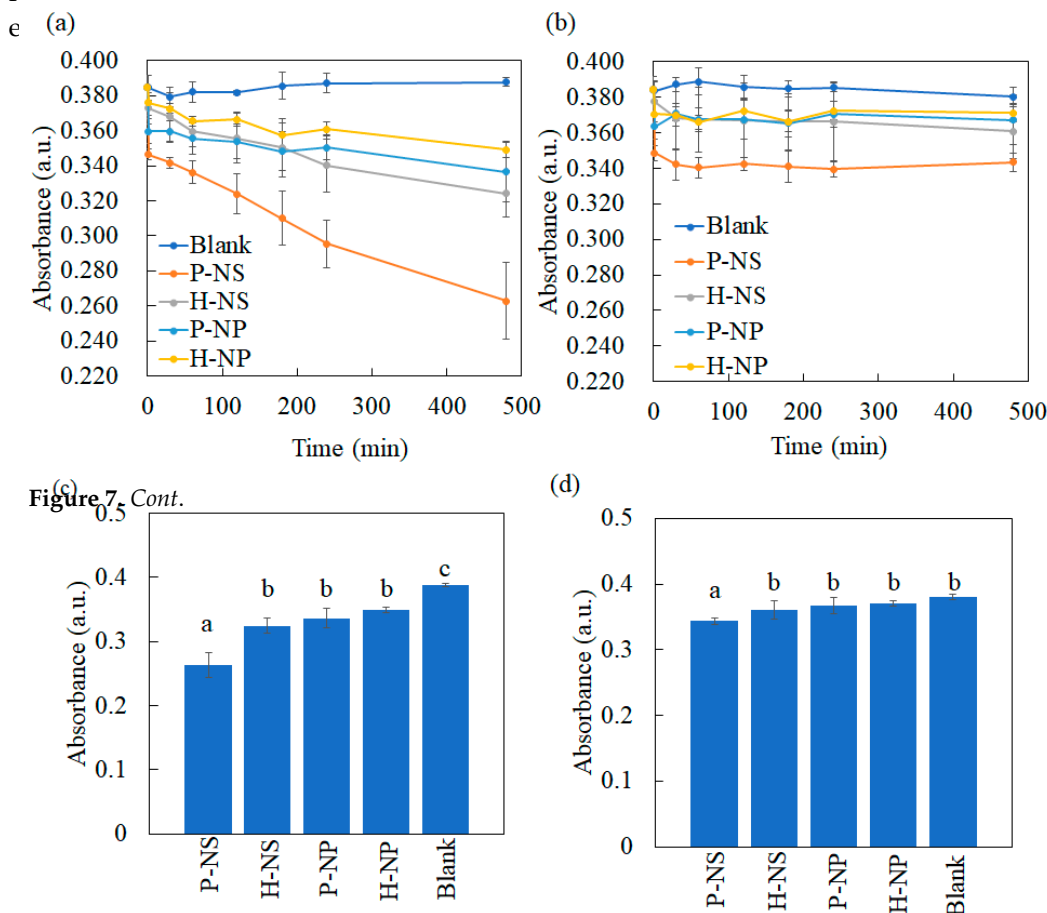


Figure 7. Cont.

Figure 7. Time course plot of the MB decolorization reaction using the prepared titania samples (a) under UV irradiation and (b) in the dark. Multiple comparisons of MB absorbance after 480 min (c)

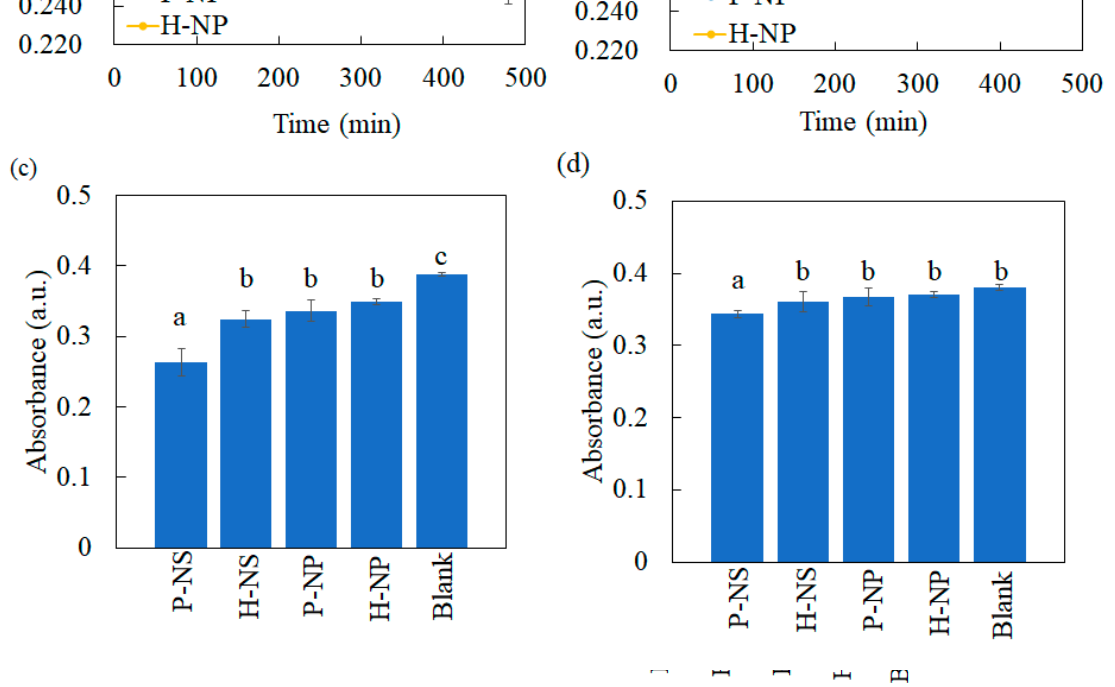


Figure 7. Time course plot of the MB decolorization reaction using the prepared titania samples (a) under UV irradiation and (b) in the dark. Multiple comparisons of MB absorbance after 480 min (c) under UV irradiation and (d) in the dark. Multiple comparison letters show significant differences at $\alpha = 0.05$. The different letters show significant differences at $\alpha = 0.05$.

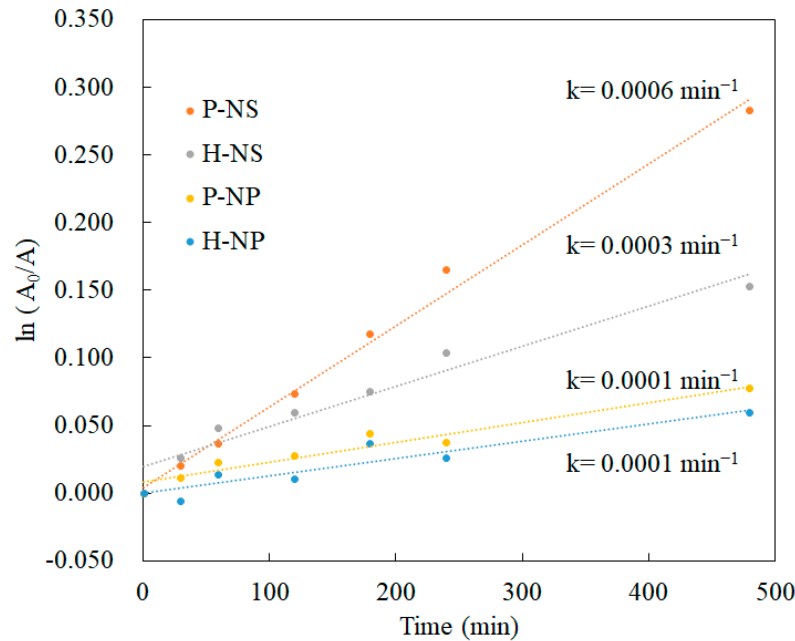


Figure 8. Reaction rate of $\ln(A_0/A)$ of MB under UV irradiation.

4. Discussion

This is the first study to regulate the surface charges of TiO_2 NPs and NSs using the electrical polarization method. We showed enhanced dye-degradation activity of polarized TiO_2 NSs. To modify the degradation performance of TiO_2 , the crystal growth was regulated by supplying F ions during the hydrothermal synthesis using ammonium hexafluorotitanate and titanium butoxide as starting materials with a F/Ti ratio of 0.3. Anatase-type TiO_2 NSs as small as 6.3 nm were obtained. The TiO_2 powder was then electrically polarized by a DC electric field at 300 V/mm and 300 °C for 1 h to control the surface charges. The TSDC results showed that polarized TiO_2 NSs were successfully prepared. Accelerated dye degradation was achieved by P-NS, but not by polarized P-NP. However, superoxide anion and hydroxyl radical generation, detected using NBT and DTA assays, was enhanced by both P-NS and P-NP. From these results, the null hypothesis, which states that electrical polarization does not enhance the decolorizing performance of TiO_2 , was rejected, as P-NS accelerated MB degradation compared to H-NS.

Titania NSs have been reported to have high photocatalytic activity because of the heterojunctions of the {101}/ {001} plane, and they are considered an alternative for titania nanoparticles [32]. We previously synthesized titania NSs with a side length of 6.3 to 445 nm and clarified that the best photocatalytic activity was achieved by titania NSs with a side length of 6.3 nm [28]. In this study, a titania NS with a side length of 6.3 nm was used as a representative substrate for electrical polarization because the single-nanometer-sized titania NS showed the highest dye-degradation performance compared to the other NSs and NPs.

Dipole formation in a crystal structure originates from the orientation of the positive and negative ions. Electrical polarization enables the reorientation of ions at room temperature to be fixed by a constant DC electric field from high to low temperatures without substituting ions. TSDC measurements can evaluate the surface charges as an electric current induced by the relaxation of dipoles through a heating process. The surface charges of TiO₂ NPs and NSs were estimated to be induced by the reorientation of oxygen vacancies and Ti³⁺ because regularly synthesized TiO₂ contains 1% oxygen vacancies [33]. Furthermore, the TiO₂ NSs contained F⁻, not only at the surface, but also in the lattice, substituting for O²⁻ and inducing the reduction of Ti⁴⁺ to Ti³⁺ to compensate for the charges [34]. Hence, P-NS dipoles may be induced by reorienting the oxygen vacancy and F⁻.

In the decolorization experiment, P-NS showed the strongest decolorizing power after 480 min compared with H-NS, P-NP, and H-NP. These results agree with the trend in our previous report showing the better decolorizing capability of NSs compared to that of NPs. Furthermore, electrical polarization accelerated the decolorization of MB by P-NS. The TSDC measurements confirmed that the surface charges of P-NS and P-NP were successfully induced by electrical polarization. Azeez et al. reported that the MB adsorption by TiO₂ NPs was enhanced by the higher surface charges originating from the rich hydroxyl groups [13]. However, this study showed that the adsorption of the MB dye was also enhanced by electrical polarization, inducing surface charges without adding any elements to the surfaces. This study also demonstrated that polarized NSs and NPs induced the production of more superoxide anions and hydroxyl radicals under UV irradiation compared to the non-polarized samples. Although ROS generation can be enhanced by accelerated redox reactions on the surface of TiO₂ by UV irradiation, the optical bandgap energy results indicated that electrical polarization had no influence on the reactivity against UV irradiation. ROS are usually detected by indirect methods using scavengers such as DTA and NBT because of the rapid reactions and decomposition during UV irradiation [2]. This indicates that the polarized TiO₂ accelerated the reaction of DTA and NBT through redox reactions, following the enhanced adsorption of scavengers.

Despite the greater generation of ROS by P-NP and H-NP, the decolorizing effects of P-NS and H-NS were greater than those of P-NP and H-NP. This is because the formation of ROS has been reported to be enhanced by the mixed phase of rutile and anatase [35]. The commercially available NPs used in this study showed a mixed phase of anatase and rutile phases, whereas the NSs showed a single anatase phase. A previous study indicated that the adsorption of MB was enhanced by TiO₂ NSs compared to that by TiO₂ NPs [36], which resulted in accelerated dye degradation by the P-NS.

From the above results, the dye-degradation process by polarized TiO₂ NSs under aqueous conditions was proposed as follows. The adsorption of efficient photons by TiO₂ NSs generated electrons and holes, which resulted in the generation of superoxide anions and hydroxyl radicals. The polarized TiO₂ NSs absorbed more MB dye compared to the polarized TiO₂ NPs, heated TiO₂ NSs, or heated TiO₂ NPs. Oxidation by the generated ROS and direct oxidation by the reaction with holes degraded the MB solution.

5. Conclusions

A facile preparation of TiO₂ NSs using a hydrothermal synthesis with a fluorine/titanium ratio of 0.3 and the modification of surface charges by electrical polarization methods was reported. The synthesized TiO₂ NSs formed a flattened crystal structure with an average side length and thickness of 6.3 nm and 4.9 nm, respectively. TSDC measurements showed a dense surface charge of P-NS and P-NP without changing their morphology or optical properties. The MB degradation assay using P-NS showed an increase in the dye-degradation rate and adsorption efficiency. Furthermore, P-NS and P-NP accelerated the generation of hydroxyl and superoxide anions, respectively. This simple and robust technique can be applied to various ceramic nanocatalysts to manipulate their surface charge and enhance their photocatalytic activity. Considering the enhanced photocatalytic activity of polarized TiO₂ NSs, the band structure of heated and polarized TiO₂ will be further investigated to clarify the mechanisms of enhanced dye degradation.

Author Contributions: Conceptualization, K.N., K.Y. and S.O.; formal analysis, K.N. and T.M.; funding acquisition, K.N., K.Y. and S.O.; investigation, K.N., Y.K. and T.M.; methodology, K.N.; project administration, H.M. and K.N.; resources, S.O.; supervision, K.N., K.Y. and S.O.; validation, K.N., M.J., Y.K. and T.M.; visualization, K.N., T.M., Y.K. and M.J.; writing—original draft, K.N. and T.M.; writing—review and editing, K.Y., K.N., and S.O. All authors have read and agreed to the published version of the manuscript.

Funding: This research was partially funded by the Ministry of Education, Culture, Sports, Science, and Technology of Japan (grant numbers 20K10049, 20K09990, and 23K09269). Part of this research was supported by a Grant-in-Aid for the Cooperative Research Project of Creation of Life Innovation Materials for Interdisciplinary and International Researcher Development from the Ministry of Education, Culture, Sports, Science, and Technology of Japan (MEXT), the Cooperative Research Project of the Research Center for Biomedical Engineering, the Nippon Sheet Glass Foundation for Materials Science and Engineering, and the Iketani Science and Technology Foundation (0311049-A).

Data Availability Statement: Data is contained within the article.

Conflicts of Interest: The authors declare no conflicts of interest.

References

1. Nam, Y.; Lim, J.H.; Ko, K.C.; Lee, J.Y. Photocatalytic activity of TiO₂ nanoparticles: A theoretical aspect. *J. Mater. Chem. A* **2019**, *7*, 13833–13859. [[CrossRef](#)]
2. Nosaka, Y.; Nosaka, A.Y. Generation and detection of reactive oxygen species in photocatalysis. *Chem. Rev.* **2017**, *117*, 11302–11336. [[CrossRef](#)] [[PubMed](#)]
3. Wang, J.; Zhang, Y.Y.; Guo, Y.; Zhang, L.; Xu, R.; Xing, Z.Q.; Wang, S.; Zhang, X. Interaction of bovine serum albumin with acridine orange (CI Basic Orange 14) and its sonodynamic damage under ultrasonic irradiation. *Dye. Pigment.* **2009**, *80*, 271–278. [[CrossRef](#)]
4. Ozawa, K.; Emori, M.; Yamamoto, S.; Yukawa, R.; Yamamoto, S.; Hobara, R.; Fujikawa, K.; Sakama, H.; Matsuda, I. Electron-hole recombination time at TiO₂ single-crystal surfaces: Influence of surface band bending. *J. Phys. Chem. Lett.* **2014**, *5*, 1953–1957. [[CrossRef](#)]
5. Yang, H.G.; Sun, C.H.; Qiao, S.Z.; Zou, J.; Liu, G.; Smith, S.C.; Cheng, H.M.; Lu, G.Q. Anatase TiO₂ single crystals with a large percentage of reactive facets. *Nature* **2008**, *453*, 638–641. [[CrossRef](#)]
6. Liu, X.G.; Dong, G.J.; Li, S.P.; Lu, G.X.; Bi, Y.P. Direct observation of charge separation on anatase TiO₂ crystals with selectively etched {001} facets. *J. Am. Chem. Soc.* **2016**, *138*, 2917–2920. [[CrossRef](#)] [[PubMed](#)]
7. Zhang, C.; Zhou, Y.M.; Bao, J.H.; Fang, J.S.; Zhao, S.; Zhang, Y.W.; Sheng, X.; Chen, W. Structure regulation of ZnS@g-C₃N₄/TiO₂ nanospheres for efficient photocatalytic H₂ production under visible-light irradiation. *Chem. Eng. J.* **2018**, *346*, 226–237. [[CrossRef](#)]
8. Basavarajappa, P.S.; Patil, S.B.; Ganganagappa, N.; Reddy, K.R.; Raghu, A.V.; Reddy, C.V. Recent progress in metal-doped TiO₂, non-metal doped/codoped TiO₂ and TiO₂ nanostructured hybrids for enhanced photocatalysis. *Int. J. Hydrog. Energy* **2020**, *45*, 7764–7778. [[CrossRef](#)]
9. Zhu, X.; Xu, H.; Liu, J.; Bi, C.; Tian, J.; Zong, K.; Wang, B.; Ding, P.; Wang, X.; Chu, P.K.; et al. Stacking Engineering of Heterojunctions in Half-Metallic Carbon Nitride for Efficient CO₂ Photoreduction. *Adv. Sci.* **2023**, *10*, 2307192. [[CrossRef](#)]
10. Tan, Z.Q.; Sato, K.; Takami, S.; Numako, C.; Umetsu, M.; Soga, K.; Nakayama, M.; Sasaki, R.; Tanaka, T.; Ogino, C.; et al. Particle size for photocatalytic activity of anatase TiO₂ nanosheets with highly exposed {001} facets. *RSC Adv.* **2013**, *3*, 19268–19271. [[CrossRef](#)]

11. Hayashi, K.; Nozaki, K.; Tan, Z.Q.; Fujita, K.; Nemoto, R.; Yamashita, K.; Miura, H.; Itaka, K.; Ohara, S. Enhanced antibacterial property of facet-engineered TiO₂ nanosheet in presence and absence of ultraviolet irradiation. *Materials* **2020**, *13*, 78. [[CrossRef](#)]
12. Tachikawa, T.; Yamashita, S.; Majima, T. Evidence for crystal-face-dependent TiO₂ photocatalysis from single-molecule imaging and kinetic analysis. *J. Am. Chem. Soc.* **2011**, *133*, 7197–7204. [[CrossRef](#)] [[PubMed](#)]
13. Azeez, F.; Al-Hetlani, E.; Arafa, M.; Abdelmonem, Y.; Nazeer, A.A.; Amin, M.O.; Madkour, M. The effect of surface charge on photocatalytic degradation of methylene blue dye using chargeable titania nanoparticles. *Sci. Rep.* **2018**, *8*, 7104. [[CrossRef](#)]
14. Yagub, M.T.; Sen, T.K.; Afroze, S.; Ang, H.M. Dye and its removal from aqueous solution by adsorption: A review. *Adv. Colloid Interface Sci.* **2014**, *209*, 172–184. [[CrossRef](#)] [[PubMed](#)]
15. Zhang, R.Z.; Quan, S.; Xia, M.; Wang, Q.; Zhang, W.; Yang, J.M. Effect of surface charge status of amorphous porous coordination polymer particles on the adsorption of organic dyes from an aqueous solution. *J. Colloid Interface Sci.* **2018**, *525*, 54–61. [[CrossRef](#)] [[PubMed](#)]
16. Das, A.; Pamu, D. A comprehensive review on electrical properties of hydroxyapatite based ceramic composites. *Mater. Sci. Eng. C Mater. Biol. Appl.* **2019**, *101*, 539–563. [[CrossRef](#)]
17. Saxena, A.; Kakimoto, K.; Dubey, A.K. Polarization induced dielectric and electrical response of electrovector hydroxyapatite and ferroelectric sodium potassium niobate ceramics. *J. Phys. D* **2020**, *53*, 395402. [[CrossRef](#)]
18. Sans, J.; Arnau, M.; Fontana-Escartín, A.; Turon, P.; Alemán, C. Permanently polarized materials: An approach for designing materials with customized electrical properties. *Chem. Mater.* **2023**, *35*, 3765–3780. [[CrossRef](#)]
19. Yamashita, K.; Oikawa, N.; Umegaki, T. Acceleration and deceleration of bone-like crystal growth on ceramic hydroxyapatite by electric poling. *Chem. Mater.* **1996**, *8*, 2697–2700. [[CrossRef](#)]
20. Ubele-Kalnina, D.; Nakamura, M.; Gross, K.A. Inter-Laboratory Study on Measuring the Surface Charge of Electrically Polarized Hydroxyapatite. *J. Funct. Biomater.* **2023**, *14*, 100. [[CrossRef](#)]
21. Belik, A.A.; Morozov, V.A.; Deyneko, D.V.; Savon, A.E.; Baryshnikova, O.V.; Zhukovskaya, E.S.; Dorbakov, N.G.; Katsuya, Y.; Tanaka, M.; Stefanovich, S.Y.; et al. Antiferroelectric properties and site occupations of R³⁺ cations in Ca₈MgR(PO₄)₇ luminescent host materials. *J. Alloys Compd.* **2017**, *699*, 928–937. [[CrossRef](#)]
22. Metwally, S.; Stachewicz, U. Surface potential and charges impact on cell responses on biomaterials interfaces for medical applications. *Mat. Sci. Eng. C-Mat.* **2019**, *104*, 109883. [[CrossRef](#)] [[PubMed](#)]
23. Verma, A.S.; Singh, A.; Kumar, D.; Dubey, A.K. Electro-mechanical and Polarization-Induced Antibacterial Response of 45S5 Bioglass-Sodium Potassium Niobate Piezoelectric Ceramic Composites. *ACS Biomater. Sci. Eng.* **2020**, *6*, 3055–3069. [[CrossRef](#)] [[PubMed](#)]
24. Li, Y.; Li, J.; Yang, W.; Wang, X. Implementation of ferroelectric materials in photocatalytic and photoelectrochemical water splitting. *Nanoscale Horiz.* **2020**, *5*, 1174–1187. [[CrossRef](#)]
25. Nagai, A.; Yamazaki, Y.; Ma, C.F.; Nozaki, K.; Toyama, T.; Yamashita, K. Response of osteoblast-like MG63 cells to TiO₂ layer prepared by micro-arc oxidation and electric polarization. *J. Eur. Ceram. Soc.* **2012**, *32*, 2647–2652. [[CrossRef](#)]
26. Ma, C.F.; Xiong, X.B.; Li, H.J.; Huang, J.F.; Lu, J.H.; Hu, Z.B. Response of osteoblast to CVIC/C and HA coating on CVIC/C in vitro. *Rare Met. Mater. Eng.* **2004**, *33*, 1274–1277.
27. Bandyopadhyay, A.; Shivaram, A.; Mitra, I.; Bose, S. Electrically polarized TiO₂ nanotubes on Ti implants to enhance early-stage osseointegration. *Acta Biomater.* **2019**, *96*, 686–693. [[CrossRef](#)]
28. Kowaka, Y.; Nozaki, K.; Mihara, T.; Yamashita, K.; Miura, H.; Tan, Z.; Ohara, S. Development of TiO₂ nanosheets with high dye degradation performance by regulating crystal growth. *Materials* **2023**, *16*, 1229. [[CrossRef](#)]
29. Sahni, M.; Locke, B.R. Quantification of hydroxyl radicals produced in aqueous phase pulsed electrical discharge reactors. *Ind. Eng. Chem. Res.* **2006**, *45*, 5819–5825. [[CrossRef](#)]
30. Ishibashi, K.; Fujishima, A.; Watanabe, T.; Hashimoto, K. Quantum yields of active oxidative species formed on TiO₂ photocatalyst. *J. Photochem. Photobiol. A* **2000**, *134*, 139–142. [[CrossRef](#)]
31. Bourmonville, C.F.; Díaz-Ricci, J.C. Quantitative determination of superoxide in plant leaves using a modified NBT staining method. *Phytochem. Anal.* **2011**, *22*, 268–271. [[CrossRef](#)] [[PubMed](#)]
32. Masudy, P.S.; Tanhaei, M.; Farahani, H.D.A.M.; Jianguyong, H. A review on the synthesis of the various types of anatase TiO₂ facets and their applications for photocatalysis. *Katal R. Chem. Eng. J.* **2020**, *384*, 123384.
33. Bi, X.; Du, G.; Kalam, A.; Sun, D.; Yu, Y.; Su, Q.; Xu, B.; Al-Sehemi, A.G. Tuning oxygen vacancy content in TiO₂ nanoparticles to enhance the photocatalytic performance. *Chem. Eng. Sci.* **2021**, *234*, 116440. [[CrossRef](#)]
34. Fu, R.; Wu, Z.; Pan, Z.; Gao, Z.; Li, Z.; Kong, X.; Li, L. Fluorine-Induced Surface Metallization for ammonia Synthesis under Photoexcitation up to 1550 nm. *Angew. Chem. Int. Ed. Engl.* **2021**, *60*, 11173–11179. [[CrossRef](#)]
35. Nosaka, Y.; Nosaka, A. Understanding hydroxyl radical (•OH) generation processes in photocatalysis. *ACS Energy Lett.* **2016**, *1*, 356–359. [[CrossRef](#)]
36. Nakamura, S.; Takeda, H.; Yamashita, K. Proton transport polarization and depolarization of hydroxyapatite ceramics. *J. Appl. Phys.* **2001**, *89*, 5386–5392. [[CrossRef](#)]

Disclaimer/Publisher’s Note: The statements, opinions and data contained in all publications are solely those of the individual author(s) and contributor(s) and not of MDPI and/or the editor(s). MDPI and/or the editor(s) disclaim responsibility for any injury to people or property resulting from any ideas, methods, instructions or products referred to in the content.

日中笹川医学奨学金制度＜学位取得コース＞評価書

課程博士：指導教官用



第 44 期

研究者番号：G4405

作成日：2024年3月10日

氏名	陳曹傑	CHEN CAOJIE	性別	M	生年月日	1984/01/23
所属機関（役職）	慶應義塾大学医学部（大学院生）					
研究先（指導教官）	慶應義塾大学医学部形成外科学教室（貴志 和生 教授）					
研究テーマ	創傷治癒とオートファジーの関係 The relationship between autophagy and wound healing					
専攻種別	<input type="checkbox"/> 論文博士			<input checked="" type="checkbox"/> 課程博士		

研究者評価（指導教官記入欄）

成績状況	良 学業成績係数=	取得単位数
		100%
学生本人が行った研究の概要	オートファジーと創傷治癒、YAP,En-1,mTOR の関係について、in vitro 並びに in vivo のマウスを用いた動物実験を行い、それぞれの関係性について調べた。	
総合評価	【良かった点】 一生懸命研究を行い、解らないところのトラブルシューティングができていた。	
	【改善すべき点】 試問での質疑、応答能力。	
	【今後の展望】 中国に帰り、本研究成果を生かした医師の仕事を行う。	
学位取得見込	あり	
評価者（指導教官名） 貴志和生		

日中笹川医学奨学金制度<学位取得コース>報告書 研究者用



第44期

研究者番号: G4405

作成日: 2024年3月10日

氏名	陈 曹杰	CHEN CAOJIE	性別	M	生年月日 1984/01/23
所属機関(役職)	慶應義塾大学医学部(大学院生)				
研究先(指導教官)	慶應義塾大学医学部形成外科学教室(貴志 和生 教授)				
研究テーマ	創傷治癒とオートファジーの関係 The relationship between autophagy and wound healing				
専攻種別	論文博士	<input type="checkbox"/>	課程博士	<input checked="" type="checkbox"/>	

1. 研究概要(1)

1) 目的(Goal)

Wound repair dysfunction is becoming a major public health issue worldwide. Yes-associated protein (YAP) has previously been reported to be closely related to wound healing, while how YAP accelerates wound healing via regulating autophagy needs to be further probed.

2) 戦略(Approach)

A series of comparative experiments were conducted on skin trauma models to investigate the mechanisms of autophagy and other roles in the trauma healing process.

3) 材料と方法(Materials and methods)

ICR male mice were involved in two independent animal experiments; the mice were randomly allocated into control, autophagy inhibitor (3-MA) (injection), and 3-MA (drip) group or control, si-NC, si-YAP group (8 mice for each). Full-thickness excisional wounds (8 mm) in mice were created by punch to construct an in vivo wound model to observe the effects of autophagy inhibitor (3-MA) (by injection and drip) and si-YAP by electrotransfection.

4) 実験結果(Results)

Firstly, we found that the autophagy inhibitor (3-MA) accelerated wound closure in vivo. Loss-of-function experiments subsequently revealed that YAP knockdown led to increased proliferation and migration of fibroblasts as well as reduced autophagy, resulting in accelerated wound healing. In addition, our results revealed that YAP could positively regulate Engrailed-1 (En1) expression in fibroblasts. En1 knockdown also promoted the proliferation and migration of fibroblasts, meanwhile resulting in increased mammalian target of rapamycin (mTOR) levels and reduced autophagy in fibroblasts.

5) 考察(Discussion)

YAP knockdown repressed autophagy in fibroblasts to accelerate wound closure by regulating the En1/mTOR axis.

6) 参考文献(References)

1. Singer AJ, Clark RA. Cutaneous wound healing. *N Engl J Med* 1999; 341: 738-46.
2. Eming SA, Martin P, Tomic-Canic M. Wound repair and regeneration: mechanisms, signaling, and translation. *Sci Transl Med* 2014; 6: 265sr6.
3. Reed BR, Clark RA. Cutaneous tissue repair: practical implications of current knowledge. II. *J Am Acad Dermatol* 1985; 13: 919-41.
4. Brem H, Tomic-Canic M. Cellular and molecular basis of wound healing in diabetes. *J Clin Invest* 2007; 117: 1219-22.
5. Klionsky DJ. Autophagy: from phenomenology to molecular understanding in less than a decade. *Nat Rev Mol Cell Biol* 2007; 8: 931-7.
6. Ren H, Zhao F, Zhang Q, Huang X, Wang Z. Autophagy and skin wound healing. *Burns Trauma* 2022; 10: tkac003.
7. Qiang L, Yang S, Cui YH, He YY. Keratinocyte autophagy enables the activation of keratinocytes and fibroblasts and facilitates wound healing. *Autophagy* 2021; 17: 2128-43.
8. Mijaljica D, Spada F, Klionsky DJ, Harrison IP. Autophagy is the key to making chronic wounds acute in skin wound healing. *Autophagy* 2023: 1-7.
9. Dey A, Varelas X, Guan KL. Targeting the Hippo pathway in cancer, fibrosis, wound healing and regenerative medicine. *Nat Rev Drug Discov* 2020; 19: 480-94.
10. Wei F, Wang A, Wang Q, Han W, Rong R, Wang L. Plasma endothelial cells-derived extracellular vesicles promote wound healing in diabetes through YAP and the PI3K/Akt/mTOR pathway. *Aging (Albany NY)* 2020; 12: 12002-18.
11. Mascharak S, desJardins-Park HE, Davitt MF, Griffin M, Borrelli MR, Moore AL, Chen K, Duoto B, Chinta M, Foster DS, Shen AH, Januszyk M, Kwon SH, Wernig G, Wan DC, Lorenz HP, Gurtner GC, Longaker MT. Preventing Engrailed-1 activation in fibroblasts yields wound regeneration without scarring. *Science* 2021; 372: eaba2374.

1. 研究概要(2)

12. Györfi AH, Matei AE, Fuchs M, Liang C, Rigau AR, Hong X, Zhu H, Lubber M, Bergmann C, Dees C, Ludolph I, Horch RE, Distler O, Wang J, Bengsch B, Schett G, Kunz M, Distler JHW. Engrailed 1 coordinates cytoskeletal reorganization to induce myofibroblast differentiation. *J Exp Med* 2021; 218: e20201916.
13. Gao Y, Luo C, Rui T, Fan Y, Yao Y, Shen H, Gao C, Wang T, Wang H, Chen X, Zhang J, Li D, Xia C, Li LL, Wang Z, Zhang M, Chen X, Tao L. Autophagy inhibition facilitates wound closure partially dependent on the YAP/IL-33 signaling in a mouse model of skin wound healing. *FASEB J* 2021; 35: e21920.
14. Huo JF, Chen XB. Long noncoding RNA growth arrest-specific 5 facilitates glioma cell sensitivity to cisplatin by suppressing excessive autophagy in an mTOR-dependent manner. *J Cell Biochem* 2019; 120: 6127-36.
15. Qiang L, Sample A, Liu H, Wu X, He YY. Epidermal SIRT1 regulates inflammation, cell migration, and wound healing. *Sci Rep* 2017; 7: 14110.
16. Spiekstra SW, Breetveld M, Rustemeyer T, Scheper RJ, Gibbs S. Wound-healing factors secreted by epidermal keratinocytes and dermal fibroblasts in skin substitutes. *Wound Repair Regen* 2007; 15: 708-17.
17. van Zanten MC, Mistry RM, Suami H, Campbell-Lloyd A, Finkemeyer JP, Piller NB, et al. The Lymphatic Response to Injury with Soft-Tissue Reconstruction in High-Energy Open Tibial Fractures of the Lower Extremity. *Plast Reconstr Surg* 2017; 139: 483-91.
18. Ban E, Jeong S, Park M, Kwon H, Park J, Song EJ, Kim A. Accelerated wound healing in diabetic mice by miRNA-497 and its anti-inflammatory activity. *Biomed Pharmacother* 2020; 121: 109613.
19. Wang F, Zhang C, Dai L, Zhang Y, Wang Y, Hao Y, Ji S, Xu Z, Han N, Chen H, Zhang Q, Nan W. Bafilomycin A1 Accelerates Chronic Refractory Wound Healing in db/db Mice. *Biomed Res Int* 2020; 2020: 6265701.
20. Lawrence J, Nho R. The Role of the Mammalian Target of Rapamycin (mTOR) in Pulmonary Fibrosis. *Int J Mol Sci* 2018; 19: 778.
21. Guo Y, Lin C, Xu P, Wu S, Fu X, Xia W, Yao M. AGEs Induced Autophagy Impairs Cutaneous Wound Healing via Stimulating Macrophage Polarization to M1 in Diabetes. *Sci Rep* 2016; 6: 36416.
22. Shi W, Wu Y, Bian D. p75NTR silencing inhibits proliferation, migration, and extracellular matrix deposition of hypertrophic scar fibroblasts by activating autophagy through inhibiting the PI3K/Akt/mTOR pathway. *Can J Physiol Pharmacol* 2021; 99: 349-59.
23. Schlegelmilch K, Mohseni M, Kirak O, Pruszek J, Rodriguez JR, Zhou D, Kreger BT, Vasioukhin V, Avruch J, Brummelkamp TR, Camargo FD. Yap1 acts downstream of α -catenin to control epidermal proliferation. *Cell* 2011; 144: 782-95.
24. Silvis MR, Kreger BT, Lien WH, Klezovitch O, Rudakova GM, Camargo FD, Lantz DM, Seykora JT, Vasioukhin V. α -catenin is a tumor suppressor that controls cell accumulation by regulating the localization and activity of the transcriptional coactivator Yap1. *Sci Signal* 2011; 4: ra33.
25. Jiang D, Correa-Gallegos D, Christ S, Stefanska A, Liu J, Ramesh P, Rajendran V, De Santis MM, Wagner DE, Rinkevich Y. Two succeeding fibroblastic lineages drive dermal development and the transition from regeneration to scarring. *Nat Cell Biol* 2018; 20: 422-431.
26. Kim YC, Guan KL. mTOR: a pharmacologic target for autophagy regulation. *J Clin Invest* 2015; 125: 25-32.

2. 執筆論文 Publication of thesis ※記載した論文を添付してください。Attach all of the papers listed below.

論文名 1 Title	YAP knockdown repressed autophagy in fibroblasts to accelerate wound healing through regulating En1/mTOR axis					
掲載誌名 Published journal	European Review for Medical and phamacological Sciences					
	2024 年 2 月	28 巻(号)	949 頁 ~	958 頁	言語 Language	English
第1著者名 First author	Chen Caojie	第2著者名 Second author	Kishi Kazuo		第3著者名 Third author	
その他著者名 Other authors						
論文名 2 Title	Single-Cell RNA-seq Analysis Reveals Cellular Functional Heterogeneity in Dermis Between Fibrotic and Regenerative Wound Healing Fates					
掲載誌名 Published journal	Frontiers in Immunology					
	2022 年 5 月	875407 巻(号)	頁 ~	頁	言語 Language	English
第1著者名 First author	Chen Caojie	第2著者名 Second author	Hiroki Kajita		第3著者名 Third author	Kento Takaya
その他著者名 Other authors	Noriko Aramaki-Hattori , Shigeki Sakai , Toru Asou , Kazuo Kishi					
論文名 3 Title						
掲載誌名 Published journal						
	年 月	巻(号)	頁 ~	頁	言語 Language	English
第1著者名 First author		第2著者名 Second author			第3著者名 Third author	
その他著者名 Other authors						
論文名 4 Title						
掲載誌名 Published journal						
	年 月	巻(号)	頁 ~	頁	言語 Language	
第1著者名 First author		第2著者名 Second author			第3著者名 Third author	
その他著者名 Other authors						
論文名 5 Title						
掲載誌名 Published journal						
	年 月	巻(号)	頁 ~	頁	言語 Language	
第1著者名 First author		第2著者名 Second author			第3著者名 Third author	
その他著者名 Other authors						

3. 学会発表 Conference presentation ※筆頭演者として総会・国際学会を含む主な学会で発表したものを記載してください

※Describe your presentation as the principal presenter in major academic meetings including general meetings or international meetin

学会名 Conference					
演題 Topic	オートファジーと創傷治癒の関係				
開催日 date	年	月	日	開催地 venue	Tokyo
形式 method	<input type="checkbox"/> 口頭発表 Oral	<input type="checkbox"/> ポスター発表 Poster	言語 Language	<input type="checkbox"/> 日本語	<input type="checkbox"/> 英語 <input type="checkbox"/> 中国語
共同演者名 Co-presenter					
学会名 Conference					
演題 Topic					
開催日 date	年	月	日	開催地 venue	Tokyo
形式 method	<input type="checkbox"/> 口頭発表 Oral	<input type="checkbox"/> ポスター発表 Poster	言語 Language	<input type="checkbox"/> 日本語 <input checked="" type="checkbox"/> 英語	<input type="checkbox"/> 中国語
共同演者名 Co-presenter					
学会名 Conference					
演題 Topic					
開催日 date	年	月	日	開催地 venue	
形式 method	<input type="checkbox"/> 口頭発表 Oral	<input type="checkbox"/> ポスター発表 Poster	言語 Language	<input type="checkbox"/> 日本語 <input type="checkbox"/> 英語	<input type="checkbox"/> 中国語
共同演者名 Co-presenter					
学会名 Conference					
演題 Topic					
開催日 date	年	月	日	開催地 venue	
形式 method	<input type="checkbox"/> 口頭発表 Oral	<input type="checkbox"/> ポスター発表 Poster	言語 Language	<input type="checkbox"/> 日本語 <input type="checkbox"/> 英語	<input type="checkbox"/> 中国語
共同演者名 Co-presenter					

4. 受賞(研究業績) Award (Research achievement)

名称 Award name	国名 Country		受賞年 Year of award	年	月
	国名 Country		受賞年 Year of award	年	月

5. 本研究テーマに関わる他の研究助成金受給 Other research grants concerned with your resarch theme

受給実績 Receipt record	<input type="checkbox"/> 有 <input type="checkbox"/> 無
助成機関名称 Funding agency	
助成金名称 Grant name	
受給期間 Supported period	年 月 ~ 年 月
受給額 Amount received	円
受給実績 Receipt record	<input type="checkbox"/> 有 <input type="checkbox"/> 無
助成機関名称 Funding agency	
助成金名称 Grant name	
受給期間 Supported period	年 月 ~ 年 月
受給額 Amount received	円

6. 他の奨学金受給 Another awarded scholarship

受給実績 Receipt record	<input type="checkbox"/> 有 <input type="checkbox"/> 無
助成機関名称 Funding agency	
奨学金名称 Scholarship name	
受給期間 Supported period	年 月 ~ 年 月
受給額 Amount received	円

7. 研究活動に関する報道発表 Press release concerned with your research activities

※記載した記事を添付してください。Attach a copy of the article described below

報道発表 Press release	<input type="checkbox"/> 有 <input type="checkbox"/> 無	発表年月日 Date of release	
発表機関 Released medium			
発表形式 Release method	・新聞 ・雑誌 ・Web site ・記者発表 ・その他()		
発表タイトル Released title			

8. 本研究テーマに関する特許出願予定 Patent application concerned with your research theme

出願予定 Scheduled	<input type="checkbox"/> 有 <input type="checkbox"/> 無	出願国 Application	
出願内容(概要) Application contents			

9. その他 Others

--

指導責任者(記名) 貴志 和生

YAP knockdown repressed autophagy in fibroblasts to accelerate wound healing through regulating En1/mTOR axis

C.-J. CHEN, K. KISHI

Department of Plastic and Reconstructive Surgery, Keio University School of Medicine, Tokyo, Japan

Abstract. – OBJECTIVE: Wound repair dysfunction is becoming a major public health issue worldwide. Yes-associated protein (YAP) has previously been reported to be closely related to wound healing, while how YAP accelerates wound healing *via* regulating autophagy needs to be further probed.

MATERIALS AND METHODS: ICR male mice were involved in two independent animal experiments; the mice were randomly allocated into control, autophagy inhibitor (3-MA) (injection), and 3-MA (drip) group or control, si-NC, si-YAP group (8 mice for each). Full-thickness excisional wounds (8 mm) in mice were created by punch to construct an *in vivo* wound model to observe the effects of autophagy inhibitor (3-MA) (by injection and drip) and si-YAP by electrotransfection.

RESULTS: Firstly, we found that the autophagy inhibitor (3-MA) accelerated wound closure *in vivo*. Loss-of-function experiments subsequently revealed that YAP knockdown led to increased proliferation and migration of fibroblasts as well as reduced autophagy, resulting in accelerated wound healing. In addition, our results revealed that YAP could positively regulate Engrailed-1 (En1) expression in fibroblasts. En1 knockdown also promoted the proliferation and migration of fibroblasts, meanwhile resulting in increased mammalian target of rapamycin (mTOR) levels and reduced autophagy in fibroblasts.

CONCLUSIONS: YAP knockdown repressed autophagy in fibroblasts to accelerate wound closure by regulating the En1/mTOR axis.

Key Words:

Wound healing, Autophagy, YAP, Engrailed-1, mTOR.

Abbreviations

Yes-associated protein (YAP); Engrailed-1 (En1); Mammalian target of rapamycin (mTOR); 3-(4, 5-Dimethylthiazolyl)-2, 5-diphenyltetrazolium bromide (MTT); Immunohistochemistry (IHC); Quantitative real-time

polymerase chain reaction (RT-qPCR); Standard deviation, (SD); Analysis of variance (ANOVA); Dulbecco's Modified Eagle Medium (DMEM).

Introduction

Mammalian skin wound healing refers to an evolutionarily conserved process that includes three separated but overlapping stages: hemostasis/inflammatory, proliferative, and remodeling stages to rebuild the skin's barrier function¹. Various cells in the skin, including keratinocytes and fibroblasts, work together to respond rapidly after acute skin injury to restore damaged skin function². Currently, many people, including the elderly, diabetic patients, and patients undergoing chemotherapy or radiotherapy, suffer from wound repair dysfunction, which imposes a huge burden on their lives and health^{3,4}. Therefore, it is urgent and necessary to explore the pathogenesis of wound healing dysfunction. Autophagy, a cellular self-decomposing process for degrading and recycling excess components⁵, is involved in the regulation of wound healing^{6,7}. Autophagy is finely modulated in different stages of wound healing at a precise extent of activity to meet the stage-specific requirements. However, the role of autophagic activity in facilitating wound healing is still controversial. Autophagy, under appropriate conditions, operates as a modulator to monitor and promote timely and proper healing processes. However, any alterations in regulating autophagy can lead to improper activity, resulting in imperfect wound healing, such as persistent chronic wounds and hypertrophic scarring⁸. Importantly, inhibition of autophagy was reported in the literature to facilitate wound healing, of which the underlying mechanism remains largely unknown.

Yes-associated protein (YAP), a transcriptional co-activator of Hippo signaling, functions in tissue regeneration, wound healing and immune regulation⁹. Much evidence^{9,10} has emphasized its function in epidermal development and skin wound repair. As proof, Mascharak et al¹¹ revealed that YAP knockdown could promote fibroblast-induced wound regeneration by repressing engrailed-1 (En1) activation. En1 is a neural-specific transcription factor that functions in regulating the development of many tissues and organs¹². However, the specific mechanism of the YAP/En1 axis in regulating wound healing needs to be revealed. Notably, YAP inhibition was reported¹³ to repress autophagy and accelerate skin wound closure, and the downstream target of En1, the mammalian target of rapamycin (mTOR), is also the core regulator of autophagy^{12,14}. All this evidence suggests that the YAP/En1/mTOR axis is a risk factor affecting wound healing, while its role in regulating autophagy during wound healing is largely unknown.

Based on the above evidence, we speculated that YAP knockdown repressed autophagy in wound healing by regulating the En1/mTOR axis, thereby ameliorating wound healing dysfunction. Our research provided potential therapeutic targets for wound healing dysfunction.

Materials and Methods

Construction of In Vivo Wound Model

The study was carried out between 2021.12 and 2023.8. The ICR male mice (8-10 weeks of age, Sankyo, Tokyo, Japan) were purchased and fed in separate cages. A full-thickness excisional wound (8 mm) in mice was created as previously reported¹⁵. Two independent animal experiments were conducted, and the mice were randomly allocated into the control, 3-MA (injection), and 3-MA (drip) group or control, si-NC, and si-YAP group (8 mice for each). Mice in 3-MA (injection) group, 3-MA (drip) group, and control group were intraperitoneally injected with 3-MA (10 mg/kg, AdipoGen, San Diego, CA, USA), drip 3-MA (10 mM) and drip Phosphate-buffered saline (PBS), respectively, every day after skin injury. For si-YAP experiment, 10 μ L PBS, 10 μ L si-NC and si-YAP (Horizon Discovery, London, UK) with a concentration of 5 mM were mixed with 40 μ L green fluorescent protein (GFP) reporter plasmid with a concentration of 500 mg/L, and then the mixture

was dripped onto the wound edges of mice for electrotransfection by NEPA21 electroporator (NEPA GENE Co. Ltd. Chiba, Japan) using electrodes for *in vivo* experiments. The number of GFP-positive cells on the wound edges was observed and calculated one day after electrotransfection to confirm successful transfection. Wound images were acquired after wounding on days 0, 4, 7, 10 and 14. The wound healing rate was calculated as the percentage of the original wound size using the following formula: (initial area – final area)/initial area \times 100%. On day 10 after the wound injury in the 3-MA experiment, three wound samples were randomly selected from the wounds of three mice in each group. Half of the samples were subjected to western blot experiments, and the other half to immunostaining experiments. On day 10 after the wound injury in the si-YAP experiment, three wound samples were randomly selected from three mice in each group. Half of the samples were subjected to immunostaining experiments, 1/4 of the samples were subjected to RT-qPCR experiments, and the rest 1/4 were subjected to western blot experiments. These mice were sacrificed by cervical dislocation after anesthesia. Then, wound samples were collected from these mice. Our study was approved by the Animal Ethics Committee of Keio University School of Medicine [A2022-128].

Immunohistochemistry (IHC)

The sections (4 μ m in thickness) were prepared. After deparaffinization and antigen retrieval, sections were then blocked and incubated with antibodies against LC3A/B (CST, Danvers, MA, USA, 1:100, 12741), YAP (CST, Danvers, MA, USA, 1:100, 14074) and En1 (Bioss, Woburn, MA, USA, 1:100, bs-11744R-HRP) overnight. The staining of LC3 and YAP was followed by the incubation with the secondary antibody biotinylated goat anti-rabbit (Vector Laboratories, Newark, NJ, USA, 1:500, BA1000) for 1 h. A secondary antibody was not used for staining En1. We used the ABC kit (Vector Laboratories, Newark, NJ, USA) for staining except for En1. The sections were stained with DAB and then counterstained with hematoxylin, dehydrated, and mounted. The images were taken using a microscope. Then, we calculated the proportion of positive cells in the dermis of skin tissue (excluding the epidermis) in the 3 separate fields of view using ImageJ software.

Quantitative Real-Time Polymerase Chain Reaction (RT-qPCR)

Total RNA was extracted with Isogen (Nippongene, Tokyo, Japan). The cDNA was synthesized using the cDNA Synthesis System (BioRad, Hercules, CA, USA). Then, SYBR Qpcr Mix (Toyobo, Tokyo, Japan) was employed for the RT-qPCR assay. *GAPDH* was used as the reference gene for mRNA.

The data was analyzed with $2^{-\Delta\Delta CT}$ method. The primers used in the study were listed as follows (5'-3'):

YAP (F): ACCCTCGTTTTGCCATGAAC
YAP (R): TGTGCTGGGATTGATATTCCGTA
En1 (F): GCACACGTTATTCGGATCG
En1 (R): GCTTGTCCTCCTTCTCGTTCT
GAPDH (F): AGGTCGGTGTGAACGGATTTG
GAPDH (R): GGGGTCGTTGATGGCAACA

Western Blot

Total proteins were extracted using Ristocetin-induced platelet aggregation (RIPA). Qubit Protein Assay Kit (Invitrogen, Carlsbad, CA, USA) was used to quantify the concentration. Proteins were separated using the 10% sodium dodecyl-sulfate polyacrylamide gel electrophoresis (SDS-PAGE) TGX mini gel and further transferred into a Polyvinylidene fluoride (PVDF) membrane (Transblot Turbo, Bio-Rad, Hercules, CA, USA). The membranes were subsequently incubated overnight with antibodies against LC3A/B (CST, Danvers, MA, USA, 1:1000, 12741), YAP (CST, Danvers, MA, USA, 1:1000, 14074), mTOR (Abcam, Waltham, MA, USA, 1:1000, ab134903), β -actin (Abcam, Waltham, MA, USA, 1:5000, ab8226) and En1 (Bioss Inc., Woburn, MA, USA, 1:1000, bs-11744R-HRP). After being washed with PBS-T, membranes were then incubated with the corresponding secondary antibody goat anti-rabbit HRP-linked (CST, Danvers, MA, USA, 1:5000, 7074), goat anti-rabbit HRP-linked (CST, Danvers, MA, USA, 1:5000, 7074), goat anti-rabbit HRP-linked (CST, Danvers, MA, USA, 1:5000, 7074), goat anti-mouse pAb-HRP (MBL, Chiba, Japan, 1:5000, 330) respectively for 60 min. A secondary antibody was not used for the western blot of En1. Protein bands were analyzed by an ECL detection kit (WBULS0100, Millipore, Billerica, MA, USA). Pictures were taken by ImageQuant LAS 4000mini (Cytiva, MA, USA) and then analyzed by ImageJ.

Isolation and Culture of Fibroblasts

ICR male mice (8-10 weeks old) were sacrificed by cervical dislocation after anesthesia. The trunk skin was separated and cut into small pieces in the ultra-clean bench after disinfection with 75% ethanol. After removing blood by rinsing with PBS, the tissues were transferred evenly to cell culture flasks. DMEM complete medium was added to submerge the tissue block in a constant temperature incubator to fully cultivate. After 24 h, DMEM complete medium was added, which was replaced every 3 days. The purified mouse skin fibroblasts were used for subsequent experiments.

Cell Transfection

siRNA of YAP, En1 (si-YAP, si-En1 – Horizon Discovery, London, UK), and their negative controls were transfected into cells using the TransIT-TKO Transfection Reagent (Mirus Bio, Madison, Wisconsin, United States).

3-(4, 5-Dimethylthiazolyl)-2, 5-Diphenyltetrazolium Bromide (MTT) Assay

Cells were seeded in a 96-well plate (2×10^3 cells/well) for 24 h and incubated in 5 mg/mL MTT (MTT Cell Count kit, Nacalai Tesque Inc., Nakagyo-ku, Kyoto, Japan) for 4 h. Then the absorbance at 490 nm was analyzed with a microplate reader (SpectraMax, Molecular Devices, San Jose, CA, USA) after DMSO supplement.

Scratch Assay

Mouse fibroblasts were plated into 6-well plates supplemented with DMEM. An artificial wound was created in the confluent cell monolayer using a 200 μ L pipette tip. Cells were cultured after the removal of the medium. The images were taken at 0 h and 24 h using a microscope. The area was measured without cells in the middle, respectively, by ImageJ, and then the change rate of the area from 0 to 24 hours was calculated using the following formula: (initial area – final area)/initial area \times 100%.

Statistical Analysis

Statistical data was analyzed by SPSS 19.0 (IBM Corp., Armonk, NY, USA) and expressed as means \pm standard deviation (SD). The differences between the two groups were analyzed using Student's *t*-tests. One-way analysis of variance (ANOVA) was performed to assess the differences among multiple groups. *p*-values lower than 0.05 were considered significant.

Results

Autophagy Inhibition Accelerated Wound Closure *In Vivo*

As previously reported¹³, autophagy inhibitor treatment accelerated wound healing *in vivo*. In the current study, it was also observed that the wound healing rate of a skin injury mouse model was significantly increased by 3-MA (autophagy inhibitor) treatment on day 10 (Figure 1A-B). The increased autophagy marker (LC3II/I), YAP, and En1 levels were observed in the skin of control mice, while these changes were partially reversed by 3-MA treatment, resulting in accelerated wound closure and reduced expression of YAP, EN1, and autophagy marker (LC3A/B) in the skin 10 days after injury (Figure 1C-D). Collectively, our results suggested that autophagy inhibition contributed to wound closure *in vivo*.

YAP Knockdown Facilitated Wound Closure *In Vivo*

To probe the role of YAP in wound healing, we induced the knockdown of YAP in the wounds of model mice. It was observed that the wound healing rate was significantly higher in the si-YAP group than in the si-NC group (Figure 2A-B). In addition, YAP knockdown led to reduced YAP and En1 mRNA levels in the skin of model mice 10 days after injury (Figure 2C). Moreover, it was observed that si-YAP transfection resulted in reduced LC3II/I, YAP and En1 levels (Figure 2D). Taken together, YAP knockdown increased the wound healing rate by repressing autophagy.

YAP Knockdown Promoted the Proliferation and Migration of Fibroblasts

Fibroblasts are commonly used cells to study wound healing *in vitro*¹⁶. Herein, we aimed to explore the role of YAP in regulating the proliferation and migration of fibroblasts isolated from mouse skin. Firstly, we induced YAP knockdown in fibroblasts (Figure 3A). As revealed in Figure 3B, cell proliferation of fibroblasts was increased by YAP knockdown (Figure 3C). In addition, it was observed that YAP knockdown led to increased cell migration of fibroblasts (Figure 3D). Moreover, YAP knockdown resulted in reduced protein level of LC3II/I in fibroblasts. In conclusion, YAP knockdown promoted the proliferation and migration of fibroblasts.

YAP Regulated mTOR-Mediated Autophagy in Fibroblasts by Regulation of En1

We first observed that the YAP knockdown resulted in reduced En1 level and increased mTOR level in mouse fibroblasts (Figure 4A). In order to probe the role of En1 in regulating mTOR and autophagy in wound healing, we induced En1 knockdown in fibroblasts by transfecting si-En1 into cells. As demonstrated in Figure 4B, si-En1 transfection resulted in reduced En1 level and increased mTOR level in fibroblasts. Functional experiments subsequently demonstrated that the proliferation (Figure 4C) and migration (Figure 4D) of fibroblasts were promoted by En1 silencing. Additionally, En1 knockdown resulted in reduced LC3II/I level in fibroblasts (Figure 4E). In summary, En1 served as the target of YAP in regulating mTOR-mediated autophagy in fibroblasts, thereby regulating cell proliferation and migration.

Discussion

Skin injury is a common event after accidental trauma¹⁷. Delayed wound healing has always been an important health problem worldwide, especially among diabetic patients and the elderly¹⁸. Wound healing is a complicated process, the specific mechanism of which has not been fully understood. In the current study, it was found that autophagy inhibition promoted wound closure *in vivo*. We subsequently investigated the regulatory mechanisms of autophagy during wound healing *in vitro*; our results revealed that YAP promoted autophagy in fibroblasts and facilitated their migration and proliferation in wound healing by regulating the En1/mTOR axis, providing a potential therapeutic target for wound healing dysfunction.

Autophagy refers to a catabolic process that removes unwanted components *via* lysosomal degradation pathways. Autophagy has been largely reported to be involved in various diseases such as heart disease, cancer, and neurodegeneration, and the function of autophagy in tissue regeneration is intriguing. Our study found that autophagy inhibition could accelerate wound closure *in vivo*, making it a promising target for chronic wound healing. Consistently, several other studies^{13,19,20} also pointed out that autophagy inhibitors accelerated wound healing in normal mice or diabetic wounds. For example, advanced glycation end-

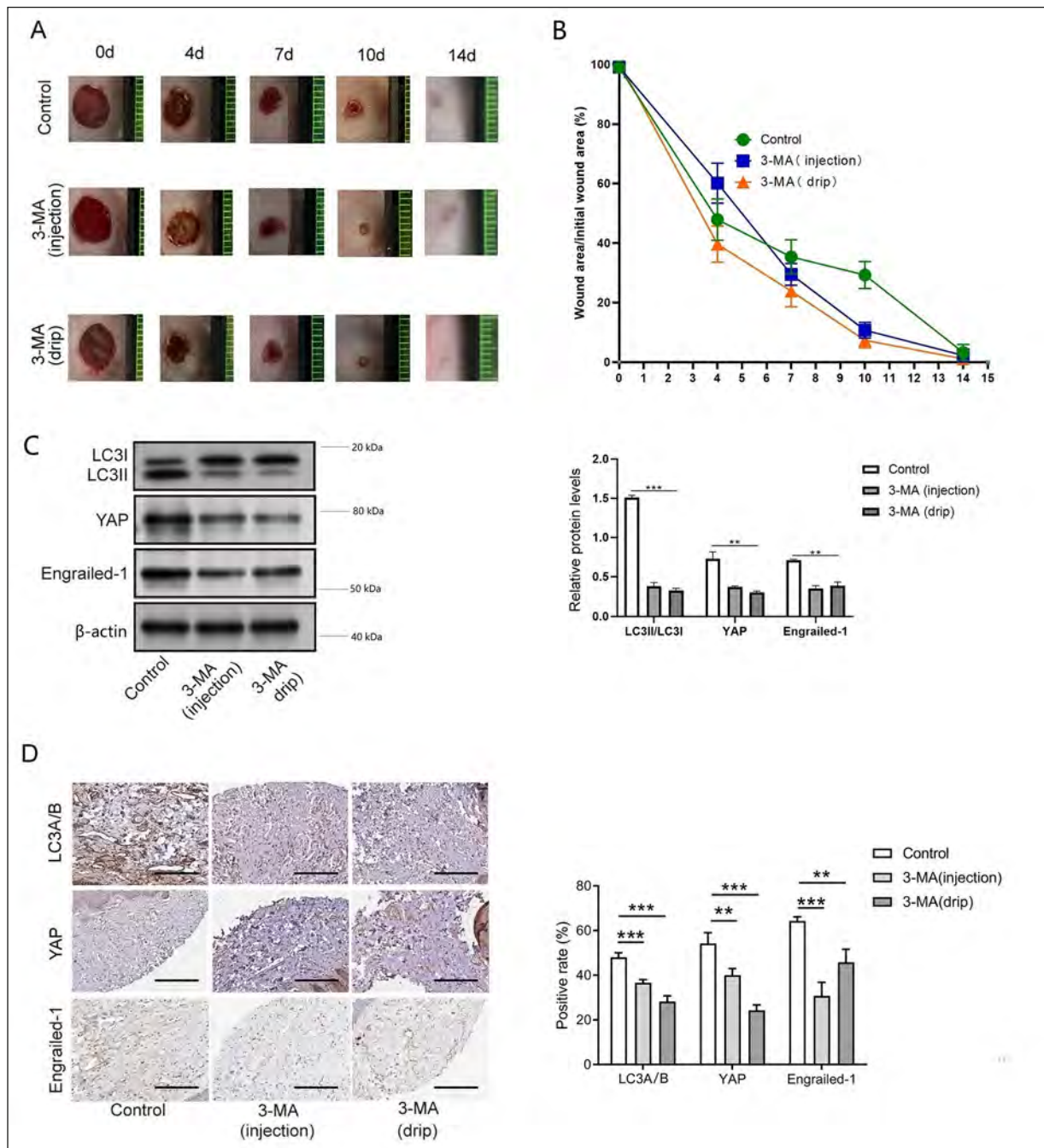


Figure 1. Autophagy inhibition accelerated wound closure *in vivo*. Mice after the skin was injured were subjected to 3-MA. **A-B**, Representative wound healing images, and the wound closures were quantified. **C**, Western blot was employed to evaluate LC3II/I, YAP and En1 levels in skin tissues. **D**, The protein levels of LC3A/B, En1, and YAP in the dermis of skin tissues were detected by IHC (magnification 200×). The solid line represents 100 μm. The measurement data were presented as mean ± SD. N = 5. ***p* < 0.01, ****p* < 0.001.

products (AGEs) can elicit autophagy, modulating macrophage polarization to M1 and impairing wound healing²¹. In addition, excessive autophagy impairs the healing process of diabetic wounds and leads to the formation of hypertrophic scars²². However, some studies^{7,8} also demonstrated that

autophagy may have a positive impact on wound healing. Appropriate hydration can contribute to rapid and efficient wound closure by promoting cell proliferation and migration and extracellular matrix reorganization *via* inducing autophagy⁸. Moreover, autophagy in various types of cells

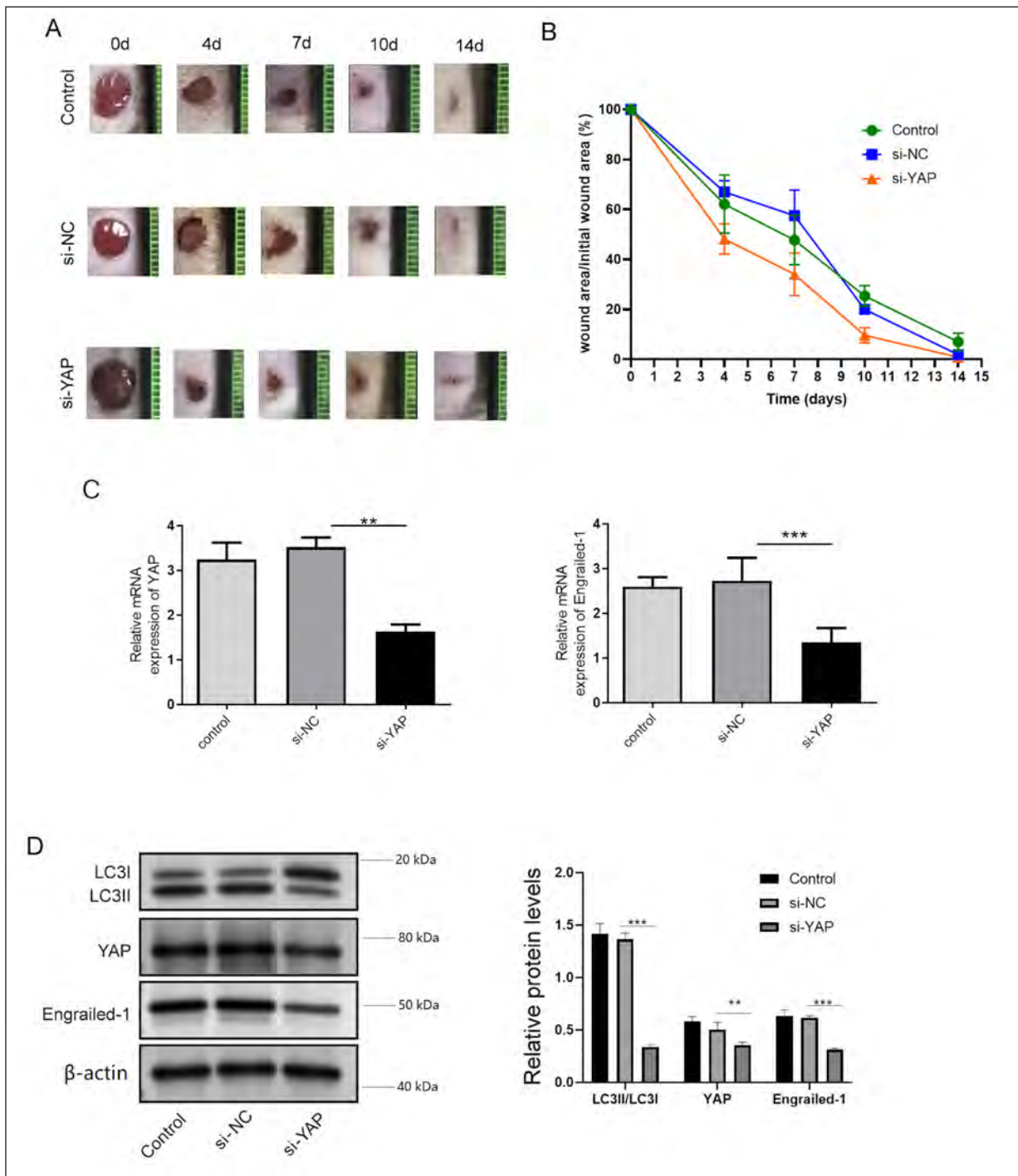


Figure 2. YAP knockdown facilitated wound closure *in vivo*. We electrotransfected si-YAP or si-NC into the wound edges of mice after the skin was injured. **A-B**, Representative wound healing images, and the wound closures were quantified. **C**, RT-qPCR was carried out to determine the mRNA levels of YAP and En1 in skin tissues. **D**, The protein levels of LC3II/I, YAP and En1 levels in skin tissues were detected using western blot. The measurement data were presented as mean \pm SD. N = 5. ** p < 0.01, *** p < 0.001.

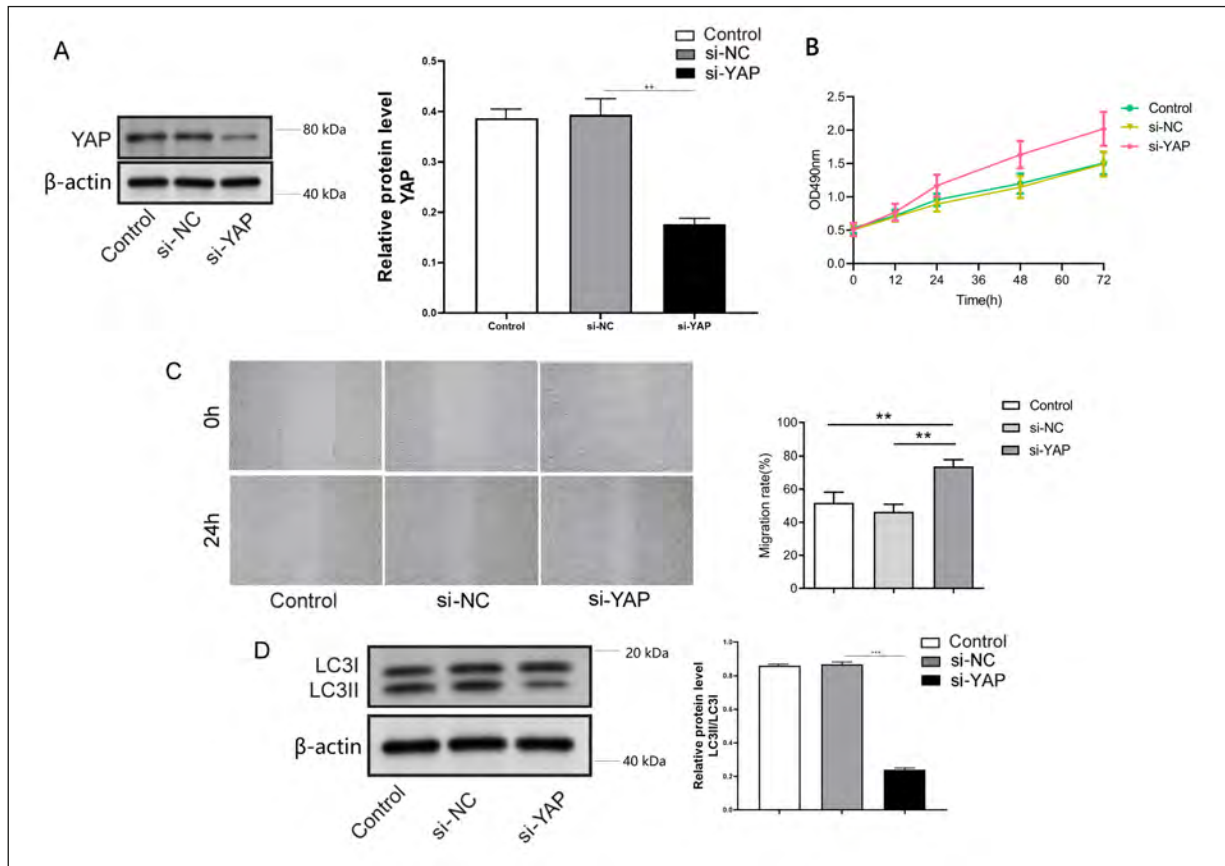


Figure 3. YAP knockdown promoted the proliferation and migration of fibroblasts. We induced YAP knockdown in fibroblasts. **A**, YAP expression was examined by RT-qPCR and western blot. **B**, Cell proliferation was analyzed by MTT assay. **C**, Cell migration was analyzed by scratch assay. **D**, Western blot was employed to evaluate LC3II/I levels. The measurement data were presented as mean \pm SD. All data was obtained from at least three replicate experiments. * $p < 0.05$, ** $p < 0.01$, *** $p < 0.001$.

may cause different results. Qiang et al⁷ showed that epidermal autophagy can facilitate the activation of keratinocytes and fibroblasts and coordinate their interactions, thus enhancing skin repair, whereas we found that autophagy in fibroblasts is a risk factor for wound healing. Hence, autophagy has a dual role in regulating wound healing and can determine different clinical outcomes depending on the tissue or cell in which it occurs⁶. Therefore, future studies should further clarify the exact role of autophagy in different stages of wound healing and develop cell-specific autophagy drugs to promote wound healing.

As above, autophagy is a crucial process for wound healing. However, its underlying molecular mechanism needs to be further elucidated. We found that the YAP/En1/mTOR axis is essential to regulate autophagy in skin wound healing. YAP knockdown repressed autophagy in fibroblasts in wound healing to promote their migration and

proliferation, accelerating wound closure through modulating En/mTOR pathway. As widely described, YAP, as a transcriptional coactivator of the Hippo signaling, plays a critical role in skin wound repair⁹. As proof, ectopic expression of activated YAP mutants or deregulation of upstream regulators of YAP localization resulted in an uncontrolled epidermal injury response^{23,24}. More importantly, it was also previously reported¹¹ that verteporfin (YAP inhibitor) or YAP knockdown could promote wound regeneration with restoration of skin attachment, ultrastructure, and mechanical strength. In agreement with previous results, our study suggested that YAP is a risk factor affecting wound healing, and loss-of-function experiments revealed that YAP knockdown promoted the proliferation and migration of fibroblasts, leading to accelerated wound closure *in vivo* as well as reduced autophagy in wounds. Therefore, the conclusion drawn was that YAP

knockdown accelerated wound healing *in vitro* and *in vivo* by suppressing autophagy in fibroblasts.

As previously described¹¹, YAP inhibition promoted wound regeneration by suppressing En1 activation, indicating that En1 might function as the target of YAP in regulating wound healing. The current study also illustrated that En1 was the downstream target of YAP in regulating wound healing and autophagy. En1 is crucial for tissue regeneration. For instance, in the fetal stage, En1-history-positive fibroblasts possess scarring abilities. Conversely, En1-history-naive fibroblasts drive dermal development and regeneration²⁵. As expected, En1 knockdown can also reduce autophagy in fibroblasts and promote the proliferation and migration of fibroblasts through activation of the mTOR pathway. mTOR, a serine/threonine kinase, is a master regulator of autophagy²⁶. Previous studies²⁶ showed that mTOR activation results in inhibition of autophagy. Col-

lectively, YAP knockdown increased mTOR level by inhibiting En1 expression, thereby repressing autophagy in fibroblasts during wound healing. As a result, YAP can be chosen as a therapeutic target for skin regeneration, and inhibition of YAP can accelerate wound healing.

The major limitation of the present study was lack of clinical validations. The effect of autophagy inhibitor on wound healing needs to be further verified. In addition, the mechanisms underlying how YAP regulates En1/mTOR axis should be further clarified in future studies.

Conclusions

Taken together, YAP knockdown repressed autophagy in fibroblasts and accelerated wound healing by regulating the En1/mTOR axis. Our research provided a hopeful strategy for wound repair dysfunction.

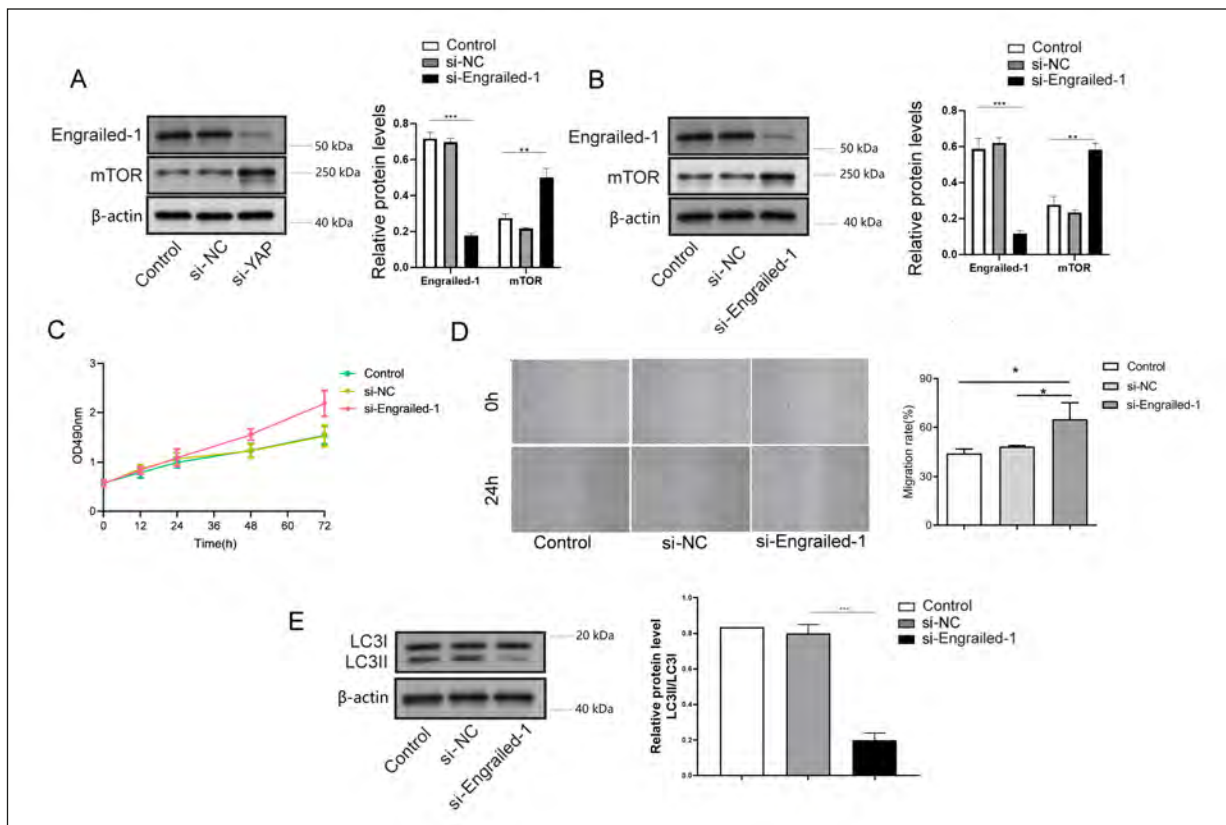


Figure 4. YAP regulated mTOR-mediated autophagy in fibroblasts by regulation of En1. **A**, En1 and mTOR levels in fibroblasts following YAP knockdown were assessed by western blot. We induced En1 knockdown in fibroblasts. **B**, Western blot was conducted to detect En1 and mTOR levels in cells. **C**, MTT assay was carried out to examine cell proliferation. **D**, Cell migration was analyzed by scratch assay. **E**, Western blot was employed to evaluate LC3II/I levels. The measurement data were presented as mean \pm SD. All data was obtained from at least three replicate experiments. * $p < 0.05$, ** $p < 0.01$, *** $p < 0.001$.

Conflict of Interest

All authors agree with the presented findings, have contributed to the work, and declare no conflict of interest.

Funding

This work was supported in part by Japan China Sasakawa Medical Fellowship (2017816).

Ethics Approval

Our study was approved by the Animal Ethics Committee of Keio University School of Medicine [A2022-128].

Data Availability

Data will be made available on request to the corresponding author.

Authors' Contribution

CJC: Conceptualization, Methodology, Software, Data curation, Writing- Original draft preparation, Visualization, Investigation. KK: Conceptualization, Supervision, Writing- Reviewing and Editing.

References

- 1) Singer AJ, Clark RA. Cutaneous wound healing. *N Engl J Med* 1999; 341: 738-746.
- 2) Eming SA, Martin P, Tomic-Canic M. Wound repair and regeneration: mechanisms, signaling, and translation. *Sci Transl Med* 2014; 6: 265sr6.
- 3) Reed BR, Clark RA. Cutaneous tissue repair: practical implications of current knowledge. II. *J Am Acad Dermatol* 1985; 13: 919-941.
- 4) Brem H, Tomic-Canic M. Cellular and molecular basis of wound healing in diabetes. *J Clin Invest* 2007; 117: 1219-1222.
- 5) Klionsky DJ. Autophagy: from phenomenology to molecular understanding in less than a decade. *Nat Rev Mol Cell Biol* 2007; 8: 931-937.
- 6) Ren H, Zhao F, Zhang Q, Huang X, Wang Z. Autophagy and skin wound healing. *Burns Trauma* 2022; 10: tkac003.
- 7) Qiang L, Yang S, Cui YH, He YY. Keratinocyte autophagy enables the activation of keratinocytes and fibroblasts and facilitates wound healing. *Autophagy* 2021; 17: 2128-2143.
- 8) Mijaljica D, Spada F, Klionsky DJ, Harrison IP. Autophagy is the key to making chronic wounds acute in skin wound healing. *Autophagy* 2023; 19: 2578-2584.
- 9) Dey A, Varelas X, Guan KL. Targeting the Hippo pathway in cancer, fibrosis, wound healing and regenerative medicine. *Nat Rev Drug Discov* 2020; 19: 480-494.
- 10) Wei F, Wang A, Wang Q, Han W, Rong R, Wang L. Plasma endothelial cells-derived extracellular vesicles promote wound healing in diabetes through YAP and the PI3K/Akt/mTOR pathway. *Aging (Albany NY)* 2020; 12: 12002-12018.
- 11) Mascharak S, desJardins-Park HE, Davitt MF, Griffin M, Borrelli MR, Moore AL, Chen K, Duoto B, Chinta M, Foster DS, Shen AH, Januszyk M, Kwon SH, Wernig G, Wan DC, Lorenz HP, Gurtner GC, Longaker MT. Preventing Engrailed-1 activation in fibroblasts yields wound regeneration without scarring. *Science* 2021; 372: eaba2374.
- 12) Györfi AH, Matei AE, Fuchs M, Liang C, Rigau AR, Hong X, Zhu H, Lubner M, Bergmann C, Dees C, Ludolph I, Horch RE, Distler O, Wang J, Bengsch B, Schett G, Kunz M, Distler JHW. Engrailed 1 coordinates cytoskeletal reorganization to induce myofibroblast differentiation. *J Exp Med* 2021; 218: e20201916.
- 13) Gao Y, Luo C, Rui T, Fan Y, Yao Y, Shen H, Gao C, Wang T, Wang H, Chen X, Zhang J, Li D, Xia C, Li LL, Wang Z, Zhang M, Chen X, Tao L. Autophagy inhibition facilitates wound closure partially dependent on the YAP/IL-33 signaling in a mouse model of skin wound healing. *FASEB J* 2021; 35: e21920.
- 14) Huo JF, Chen XB. Long noncoding RNA growth arrest-specific 5 facilitates glioma cell sensitivity to cisplatin by suppressing excessive autophagy in an mTOR-dependent manner. *J Cell Biochem* 2019; 120: 6127-6136.
- 15) Qiang L, Sample A, Liu H, Wu X, He YY. Epidermal SIRT1 regulates inflammation, cell migration, and wound healing. *Sci Rep* 2017; 7: 14110.
- 16) Spiekstra SW, Breetveld M, Rustemeyer T, Scheper RJ, Gibbs S. Wound-healing factors secreted by epidermal keratinocytes and dermal fibroblasts in skin substitutes. *Wound Repair Regen* 2007; 15: 708-717.
- 17) van Zanten MC, Mistry RM, Suami H, Campbell-Lloyd A, Finkemeyer JP, Piller NB, Caplash Y. The Lymphatic Response to Injury with Soft-Tissue Reconstruction in High-Energy Open Tibial Fractures of the Lower Extremity. *Plast Reconstr Surg* 2017; 139: 483-491.
- 18) Ban E, Jeong S, Park M, Kwon H, Park J, Song EJ, Kim A. Accelerated wound healing in diabetic mice by miRNA-497 and its anti-inflammatory activity. *Biomed Pharmacother* 2020; 121: 109613.
- 19) Wang F, Zhang C, Dai L, Zhang Y, Wang Y, Hao Y, Ji S, Xu Z, Han N, Chen H, Zhang Q, Nan W. Bafilomycin A1 Accelerates Chronic Refractory Wound Healing in db/db Mice. *Biomed Res Int* 2020; 2020: 6265701.
- 20) Lawrence J, Nho R. The Role of the Mammalian Target of Rapamycin (mTOR) in Pulmonary Fibrosis. *Int J Mol Sci* 2018; 19: 778.
- 21) Guo Y, Lin C, Xu P, Wu S, Fu X, Xia W, Yao M. AGEs Induced Autophagy Impairs Cutaneous Wound Healing via Stimulating Macrophage Polarization to M1 in Diabetes. *Sci Rep* 2016; 6: 36416.

- 22) Shi W, Wu Y, Bian D. p75NTR silencing inhibits proliferation, migration, and extracellular matrix deposition of hypertrophic scar fibroblasts by activating autophagy through inhibiting the PI3K/Akt/mTOR pathway. *Can J Physiol Pharmacol* 2021; 99: 349-359.
- 23) Schlegelmilch K, Mohseni M, Kirak O, Pruszek J, Rodriguez JR, Zhou D, Kreger BT, Vasioukhin V, Avruch J, Brummelkamp TR, Camargo FD. Yap1 acts downstream of α -catenin to control epidermal proliferation. *Cell* 2011; 144: 782-795.
- 24) Silvis MR, Kreger BT, Lien WH, Klezovitch O, Rudakova GM, Camargo FD, Lantz DM, Seykora JT, Vasioukhin V. α -catenin is a tumor suppressor that controls cell accumulation by regulating the localization and activity of the transcriptional coactivator Yap1. *Sci Signal* 2011; 4: ra33.
- 25) Jiang D, Correa-Gallegos D, Christ S, Stefanska A, Liu J, Ramesh P, Rajendran V, De Santis MM, Wagner DE, Rinkevich Y. Two succeeding fibroblastic lineages drive dermal development and the transition from regeneration to scarring. *Nat Cell Biol* 2018; 20: 422-431.
- 26) Kim YC, Guan KL. mTOR: a pharmacologic target for autophagy regulation. *J Clin Invest* 2015; 125: 25-32.



Single-Cell RNA-seq Analysis Reveals Cellular Functional Heterogeneity in Dermis Between Fibrotic and Regenerative Wound Healing Fates

Cao-Jie Chen¹, Hiroki Kajita¹, Kento Takaya¹, Noriko Aramaki-Hattori¹, Shigeki Sakai¹, Toru Asou^{2*} and Kazuo Kishi^{1*}

¹ Department of Plastic and Reconstructive Surgery, Keio University School of Medicine, Tokyo, Japan, ² Department of Plastic Surgery, Tokyo Cosmetic Surgery Clinic, Tokyo, Japan

OPEN ACCESS

Edited by:

Tian Li,
Independent Researcher, Xi'an, China

Reviewed by:

Li-xin Tang,
Chongqing Public Health Medical
Center, China
Zi-chao Li,
Fourth Military Medical University,
China

*Correspondence:

Kazuo Kishi
kkishi@a7.keio.jp
Toru Asou
mori@ideajapan.com

Specialty section:

This article was submitted to
Cancer Immunity
and Immunotherapy,
a section of the journal
Frontiers in Immunology

Received: 14 February 2022

Accepted: 04 April 2022

Published: 17 May 2022

Citation:

Chen C-J, Kajita H, Takaya K,
Aramaki-Hattori N, Sakai S, Asou T
and Kishi K (2022) Single-Cell RNA-
seq Analysis Reveals Cellular
Functional Heterogeneity in Dermis
Between Fibrotic and Regenerative
Wound Healing Fates.
Front. Immunol. 13:875407.
doi: 10.3389/fimmu.2022.875407

Background: Fibrotic scars are common in both human and mouse skin wounds. However, wound-induced hair neogenesis in the murine wounding models often results in regenerative repair response. Herein, we aimed to uncover cellular functional heterogeneity in dermis between fibrotic and regenerative wound healing fates.

Methods: The expression matrix of single-cell RNA sequencing (scRNA-seq) data of fibrotic and regenerative wound dermal cells was filtered, normalized, and scaled; underwent principal components analysis; and further analyzed by Uniform Manifold Approximation and Projection (UMAP) for dimension reduction with the Seurat package. Cell types were annotated, and cell-cell communications were analyzed. The core cell population myofibroblast was identified and the biological functions of ligand and receptor genes between myofibroblast and macrophage were evaluated. Specific genes between fibrotic and regenerative myofibroblast and macrophage were identified. Temporal dynamics of myofibroblast and macrophage were reconstructed with the Monocle tool.

Results: Across dermal cells, there were six cell types, namely, EN1-negative myofibroblasts, EN1-positive myofibroblasts, hematopoietic cells, macrophages, pericytes, and endothelial cells. Ligand and receptor genes between myofibroblasts and macrophages mainly modulated cell proliferation and migration, tube development, and the TGF- β pathway. Specific genes that were differentially expressed in fibrotic compared to regenerative myofibroblasts or macrophages were separately identified. Specific genes between fibrotic and regenerative myofibroblasts were involved in the mRNA metabolic process and organelle organization. Specific genes between fibrotic and regenerative macrophages participated in regulating immunity and phagocytosis. We then observed the underlying evolution of myofibroblasts or macrophages.

Conclusion: Collectively, our findings reveal that myofibroblasts and macrophages may alter the skin wound healing fate through modulating critical signaling pathways.

Keywords: skin wound healing, fibrosis, regeneration, myofibroblast, macrophage, single-cell RNA sequencing

INTRODUCTION

The skin is the organ with the largest surface area in the human body that provides an efficient protective barrier against mechanical injury, microbial pathogens, and trauma (1). The skin's immune system is divided into two structural compartments: epidermis and dermis, both of which contain a plethora of immunocompetent cell types (2). The epidermis is home to the main skin-resident immune cells, Langerhans cells, and melanocytes. Meanwhile, immune-specialized cells like dendritic cells, macrophages, and T cells reside in the dermis (3). The communications within immune populations and the skin environment are critical to the effectiveness of the skin immune system (4). Wound healing is a complex process in the human body, where numerous cell populations with different functions are involved in the stages of hemostasis, inflammatory response, growth, re-epithelialization, and remodeling (5). It is essential to repair the skin after damage (6). Skin wound healing involves three primary phases: inflammation, re-epithelialization, and tissue remodeling (7). Nevertheless, effective therapeutic strategies of accelerating healing and decreasing scarring remain lacking. Single-cell RNA sequencing (scRNA-seq) technology has emerged as an indispensable tool for elucidating cellular phenotype and functional heterogeneity (8). Deciphering the role of each cell type and interactions within cells is of importance to understand the mechanism of normal wound closure (9). Alterations in the microenvironment may influence cellular recruitment or activation, resulting in damaged states of wound healing. ScRNA-seq can be applied for deciphering the cellular changes in chronic wounds and hypertrophic scarring, thereby promoting the development of more effective therapeutic solutions for healing wounds (10). Moreover, in-depth understanding of the differences between fibrotic and regenerative wound healing fates is a prerequisite for developing more effective therapeutic interventions (2). Here, the purpose of this study was to reveal cellular functional heterogeneity in the dermis between fibrotic and regenerative wound healing fates.

MATERIALS AND METHODS

Acquisition of scRNA-seq Profiles

10× genomics scRNA-seq data of regenerative [GSM4213633; large full-thickness excision (1 cm²) allows *de novo* follicle regeneration] and fibrotic (GSM4213632; large wounds lead to hairless scars) wound-induced hair neogenesis (WIHN) wounds of adult 6- or 7-week-old C57Bl/6j mice were curated from the Gene Expression Omnibus (GEO) repository (<https://www.ncbi.nlm.nih.gov/gds/>). The accession number was GSE141814 (11). Regenerative wounds were defined as hair neogenesis, decreased contraction, decreased Wnt and TGF- β signaling activity, and decreased collagen production, while fibrotic wounds were defined as decreased hair neogenesis, increased contraction, increased Wnt and TGF- β signaling activity, and increased collagen production. This dataset was based on the platform of GPL21103 Illumina HiSeq 4000 (*Mus musculus*).

Quality Control

The DropletUtils package (v 3.13) was adopted to read unique molecular identifiers (UMI) count matrix, identify cells from empty droplets, remove barcode-swapped pseudo-cells, and downsample the count matrix (12). The calculateQCMetrics function of the Scater package was used for counting the expression of genes in cells (13). Cells with proportions of mitochondrial genes $\leq 10\%$ and ribosomal genes $\geq 10\%$ were determined for further analysis.

Data Preprocessing and Principal Component Analysis

The expression matrix was normalized with the NormalizeData function of the Seurat package (14). The top 2,000 highly variable genes were screened by the FindVariableFeatures function. Then, expression data were linearly scaled utilizing the ScaleData function. Finally, principal component analysis (PCA) was performed with the RunPCA function based on the 2,000 genes.

Cell Cluster and Annotation

The principal components with large standard deviations were selected. Then, cell clustering analysis was performed using the FindNeighbors and FindClusters function of the Seurat package. With the RunUMAP function, Uniform Manifold Approximation and Projection (UMAP) was carried out for dimension reduction. Cell types were annotated on the basis of the known marker genes.

Identification of Novel Marker Genes

To calculate the differentially expressed genes between each cluster and all other cells, the FindAllMarkers function of the Seurat package was used and novel marker genes were identified according to the following criteria: $|\log \text{fold change (FC)}| \geq 0.1$, the minimum expression ratio of cell population = 0.25, and p -value ≤ 0.05 .

Ligand–Receptor Network Analysis

Based on the ligand–receptor pairs from the previous literature (15), the relationship pairs of receptors and ligands were analyzed based on the marker genes of various cells. Then, a cell–cell communication network was conducted and visualized with the Cytoscape software (16). The core cell population was identified according to the largest number of receptor–ligand pairs in the network. Moreover, the receptor and ligand genes were extracted.

Function Enrichment Analysis

Function enrichment analysis of the indicated genes was carried out utilizing the clusterProfiler package, including Gene Ontology (GO) and Kyoto Encyclopedia of Genes and Genomes (KEGG) pathway analysis (17). GO categories contain biological process, cellular component, and molecular function. Terms with $p < 0.05$ were considered significantly enriched.

Protein–Protein Interaction Analysis

The Search Tool for the Retrieval of Interacting Genes (STRING) database (version 11.0; <https://string-db.org/>) was utilized for

exploring the functional interactions between marker gene-encoded proteins (18). Then, PPI networks were constructed and the top 20 hub genes were identified.

Pseudotime Analysis

Pseudotime analysis was carried out with the Monocle 3 tool (19). Firstly, genes that were expressed in at least 5% of the cells were selected. Then, the `reduceDimension` function was utilized to perform dimensionality reduction analysis, followed by cell cluster with the `clusterCells` function. Afterwards, the `differentialGeneTest` function was adopted to determine candidate genes with differences between the clusters with $p < 0.05$. The dimensionality reduction analysis of the cells was carried out using the `DDRTree` approach and the `reduceDimension` function based on the candidate genes. Through the `orderCells` function, the cells along the quasi-chronological trajectory were sorted and visualized.

Gene Set Variation Analysis

The single-sample gene set enrichment analysis (ssGSEA) function of the Gene Set Variation Analysis (GSVA) package was utilized for comparisons of the differences in GO and KEGG terms between groups (20).

Isolation and Culture of Fibroblasts

C57BL/6 male mice (8–10 weeks old; Sankyo) were used for fibroblast isolation. Briefly, mice were sacrificed by cervical dislocation. The trunk skin was separated in the ultra-clean bench, immersed in 75% ethanol for disinfection, and then cut into small pieces. Blood was removed by rinsing with PBS buffer and transferred evenly to cell culture dishes. DMEM complete medium (Wako) was added to submerge the tissue block that was placed in a constant temperature incubator to fully cultivate. After 24 h, DMEM complete medium was added, which was replaced every 3 days. The mouse skin fibroblasts were purified by the differential adhesion method and were used for subsequent experiments. Our study was approved by the Animal Ethics Committee of Keio University School of Medicine [12090(5)].

Transfection

Using the TransIT-TKO Transfection Reagent (Mirus), siRNA-Engrailed-1 (horizon) and siRNA-control were transfected into fibroblasts in a constant-temperature incubator. Forty-eight hours later, the knockdown effect of siRNA was confirmed by real-time quantitative polymerase-chain reaction (RT-qPCR).

RT-qPCR

Total RNA was extracted from fibroblasts using the Isogen reagent (Nippon Gene) following the manufacturer's instructions. cDNA synthesis was achieved based on the cDNA Synthesis System (Bio-Rad). RT-qPCR was carried out utilizing SYBR Qpcr Mix (Toyobo) on a 7500 Real-Time PCR system (Applied Biosystems). The primer sequences were as follows: EN1, 5'-ACACAACCTGCGATCC TACT-3'(forward) and 5'-GGACGGTCCGAATAGCGTG-3' (reverse); ACTB, 5'-GGC TGTATTCCCCTCCATCG-3'(forward) and 5'-CCAGTTGGTAACAATGCCATGT-3' (reverse). The relative expressions were calculated with the $2^{-\Delta\Delta Ct}$ method.

Wound Healing Assay

Fibroblasts were plated onto a 6-well plate (about 3×10^5 cells/well). When the confluence reached 100%, the fibroblast monolayer was scratched with a 1000- μ l pipette tip. Additionally, detached fibroblasts were removed with serum-free medium. At 0 h and 24 h, the wounded area was photographed.

Statistical Analysis

All statistical analysis was performed using the R language (version 3.6.1) and R Bioconductor packages. $p < 0.05$ indicated statistical significance.

RESULTS

Quality Control of scRNA-seq Data of Fibrotic and Regenerative Wound Dermal Cells

Herein, we collected scRNA data of dermal cells from large skin wounds on day 18 with two distinct healing fates (fibrosis: GSM4213632 or regeneration: GSM4213633) from the GSE141814 dataset. Before analysis, we presented quality control of scRNA data. Barcode rank plots separately depicted the distribution of barcodes in total UMI count for fibrotic and regenerative wound dermal cells (**Supplementary Figures 1A, B**). Knee and inflection points in the barcode rank plots indicated the transition of the total UMI count distribution, which reflected the difference between empty droplets and cell droplets. After filtrating empty droplets, we counted the expression of genes in each cell (**Supplementary Figures 1C, D**). Afterwards, we filtrated out cells with proportions of mitochondrial genes $> 10\%$ and ribosomal genes $< 10\%$ (**Supplementary Figures 1E, F**).

Cell Cluster of Fibrotic and Regenerative Wound Dermal Cells

After normalizing scRNA data, we screened the top 2,000 highly variable genes across fibrotic and regenerative wound dermal cells (**Figure 1A**). Then, scRNA data were linearly scaled and analyzed by dimensionality reduction with PCA. Here, we screened the top two principal components for subsequent analysis (**Figure 1B**). PCA results uncovered the prominent difference between fibrotic and regenerative wound dermal cells (**Figure 1C**). According to the elbow point, we identified the optimal principal components as 8 (**Figure 1D**). Heatmaps depicted the top 20 marker genes in each principal component (**Figure 1E**). With the UMAP method, dermal cells were clustered into 15 clusters (**Figure 1F**). The top ten marker genes of each cell cluster are presented in **Figure 1G**.

Identification of Cell Types and Their Marker Genes Across Fibrotic and Regenerative Wound Dermal Cells

This study attempted to identify cell types across fibrotic and regenerative wound dermal cells. Based on the known marker genes, six cell types were annotated, as follows: EN1-negative

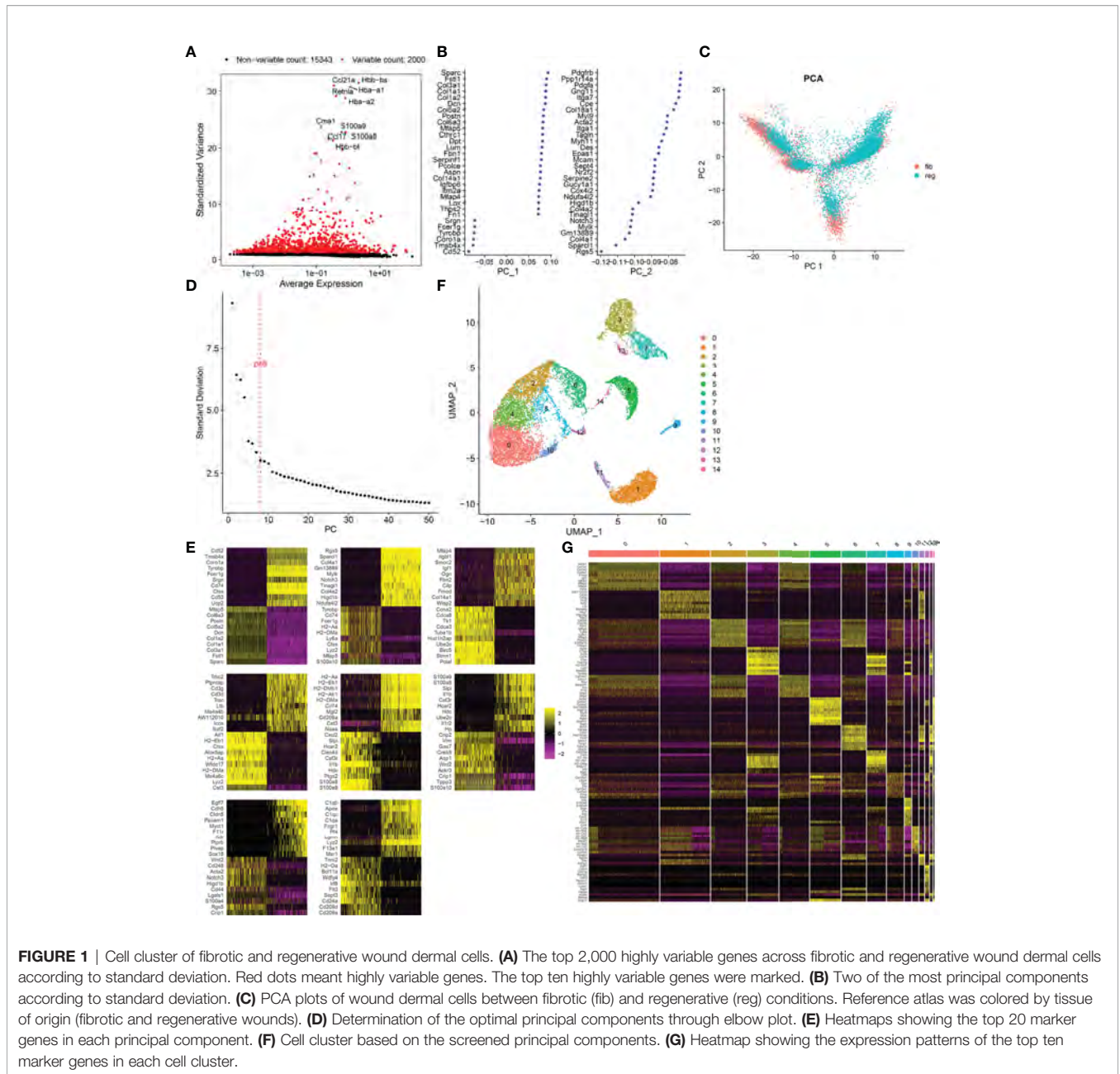


FIGURE 1 | Cell cluster of fibrotic and regenerative wound dermal cells. **(A)** The top 2,000 highly variable genes across fibrotic and regenerative wound dermal cells according to standard deviation. Red dots meant highly variable genes. The top ten highly variable genes were marked. **(B)** Two of the most principal components according to standard deviation. **(C)** PCA plots of wound dermal cells between fibrotic (fib) and regenerative (reg) conditions. Reference atlas was colored by tissue of origin (fibrotic and regenerative wounds). **(D)** Determination of the optimal principal components through elbow plot. **(E)** Heatmaps showing the top 20 marker genes in each principal component. **(F)** Cell cluster based on the screened principal components. **(G)** Heatmap showing the expression patterns of the top ten marker genes in each cell cluster.

myofibroblasts ($n = 6,392$), EN1-positive myofibroblasts ($n = 2,219$), hematopoietic cells ($n = 3,774$), macrophages ($n = 1,461$), pericytes ($n = 1,493$), and endothelial cells ($n = 303$; **Figure 2A**). **Table 1** lists the cell ratio of each cell type. In particular, we noticed the differences in ratios of EN1-negative and -positive myofibroblasts between fibrotic and regenerative wound dermal cells (**Figure 2B**). With $|\log_{2}FC| \geq 0.1$, the minimum expression ratio of cell population = 0.25, and $p\text{-value} \leq 0.05$, we identified novel marker genes in each cell type (**Supplementary Table 1**). The top ten marker genes in each cell type were visualized, as follows: EN1-negative myofibroblasts (Aebp1, Col1a1, Col1a2, Col3a1, Col8a1, Dcn, Eln, Mfap2, Mfap4, and Sparc),

hematopoietic cells (AW112010, Cd3d, Cd3g, Cd52, Hcst, Ltb, Ptprca, Rac2, Srgn, and Trbc2), macrophages (Apoe, C1qb, Ccl9, Cd74, Ctss, Fcer1g, H2-Eb1, Lyz2, Ms4a6c, and Tyrobp), pericytes (Acta2, Col4a1, Col4a2, Gm13889, Higd1b, Myl9, Mylk, Rgs5, Sparc11, and Tagln), EN1-positive myofibroblasts (Birc5, Pclaf, Stnm1, Ube2c, Hist1h2ap, Col5a3, Cks2, Aqp1, Tnfrsf10, and Timp1), and endothelial cells (Egfl7, Cldn5, Cdh5, Ramp2, Ecsr, Pecam1, Cd200, Ltbp4, Aqp1, and Hist1h2ap) (**Figure 2C**). Furthermore, we detected the expression levels of the known marker genes that were used for annotating cell types, as follows: endothelial cells (Cldn5, Pecam1, and Cd74), EN1-negative and -positive myofibroblasts (En1, Col1a1, Dcn, Sfrp4,

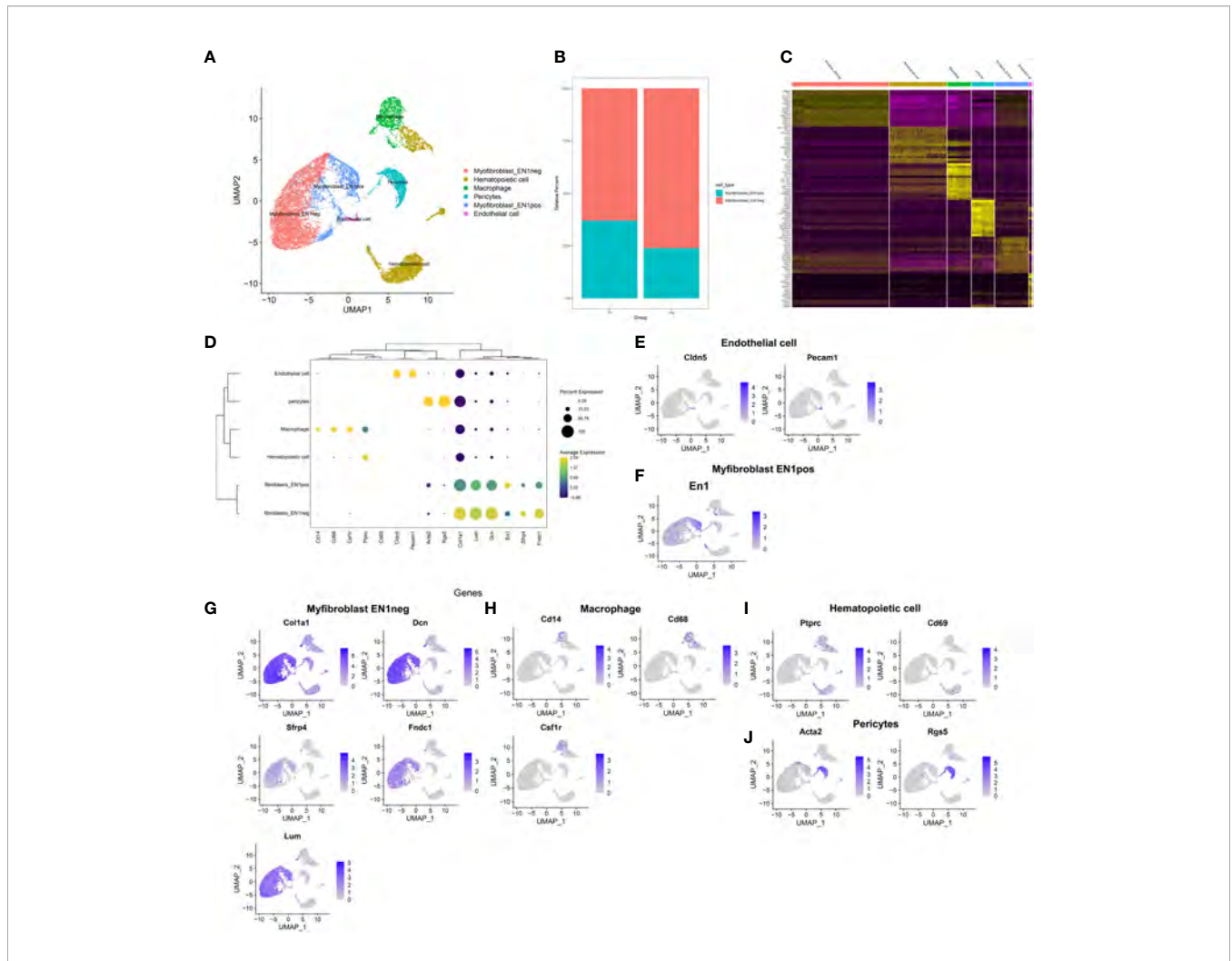


FIGURE 2 | Identification of cell types and their marker genes across fibrotic and regenerative wound dermal cells. **(A)** UMAP plots showing cell types identified by marker genes. Each cell type was colored by a unique color. **(B)** The cell ratio of EN1-negative and -positive myfibroblasts among fibrotic and regenerative wound dermal cells. **(C)** Heatmap visualizing cell-type-specific gene expression patterns. Each column represented the average expression after cells were grouped. **(D)** Integrated analysis showing marker genes across cell types. The size of each circle reflected the percentage of cells in each cell type where the gene was detected, and the color shadow reflected the average expression level within each cell type. **(E–J)** UMAP plots of expression of the marker genes for endothelial cells, EN1-negative and -positive myfibroblasts, macrophages, hematopoietic cells, and pericytes.

TABLE 1 | Cell ratio of each cell type.

Cell type	Group	Count	Total	Ratio
Endothelial cell	Fibrotic	76	5,130	0.014815
Endothelial cell	Regenerative	112	10,512	0.010654
EN1-negative myfibroblasts	Fibrotic	772	5,130	0.150487
EN1-negative myfibroblasts	Regenerative	5,620	10,512	0.534627
EN1-positive myfibroblasts	Fibrotic	454	5,130	0.088499
EN1-positive myfibroblasts	Regenerative	1,765	10,512	0.167903
Hematopoietic cell	Fibrotic	2,439	5,130	0.475439
Hematopoietic cell	Regenerative	1,335	10,512	0.126998
Macrophage	Fibrotic	725	5,130	0.141326
Macrophage	Regenerative	851	10,512	0.080955
Pericytes	Fibrotic	664	5,130	0.129435
Pericytes	Regenerative	829	10,512	0.078862

Fndc1, and Lum), macrophages (Cd14, Cd68, and Csf1r), and hematopoietic cells (Ptpcr, Cd69, Acta2, and Rgs5) (Figures 2D–J).

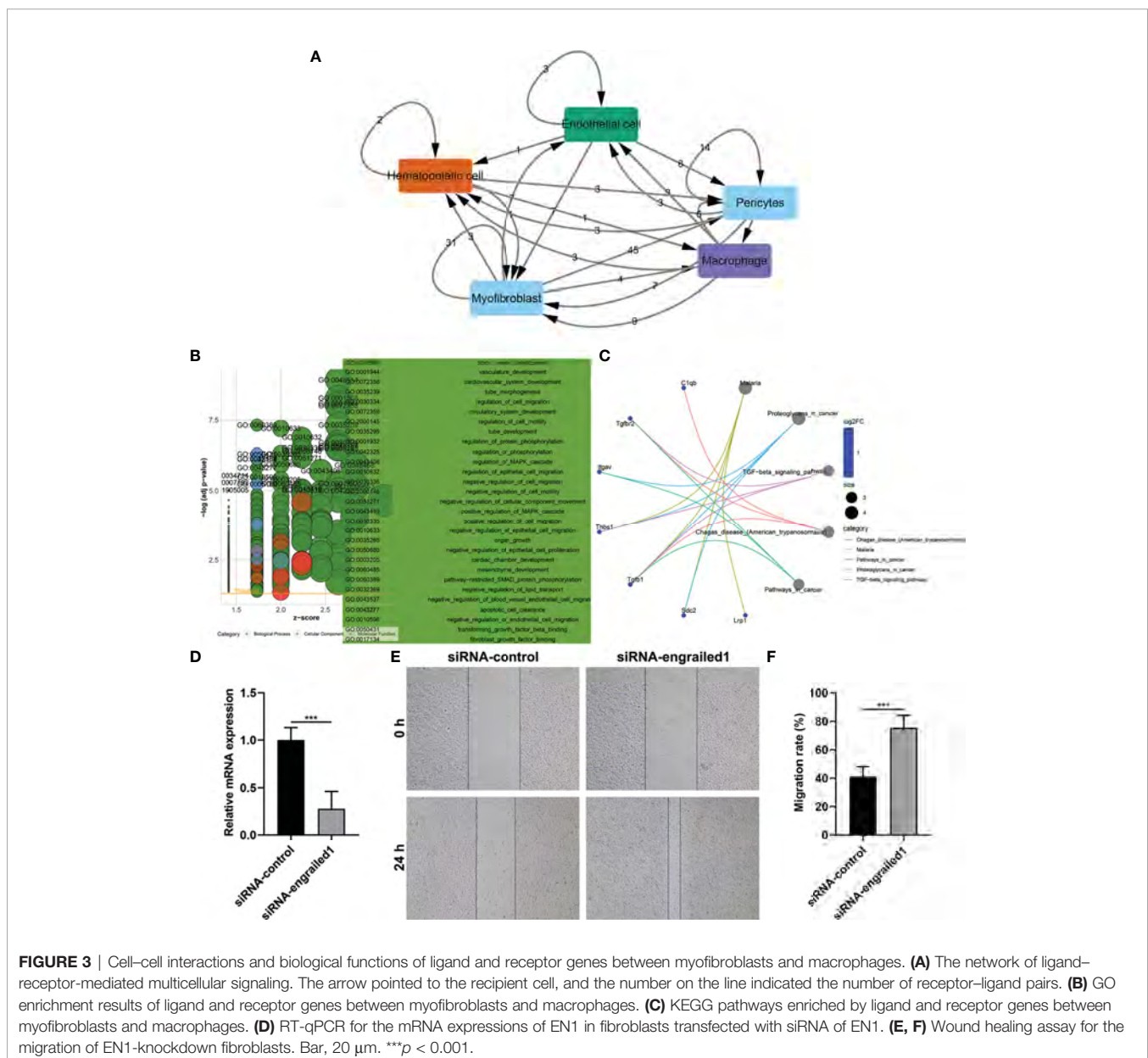
Cell–Cell Interactions Based on Ligand–Receptor Interactions

Wound healing is a complex process that necessitates the collaborative efforts of diverse cell lineages (21). Cell-to-cell communications across diverse cell types thoroughly govern appropriate functions of metazoans as well as widely rely on interactions between secreted ligands and cell-surface receptors. Based on the marker genes, ligand–receptor interactions were matched. The number of ligands/receptors for myofibroblasts, pericytes, endothelial cells, macrophages, and hematopoietic cells

was 114, 91, 32, 28 and 17, respectively (Figure 3A). According to the number of intercellular receptor–ligand pairs, we screened out myofibroblasts as the core cell population.

Biological Functions of Ligand and Receptor Genes Between Myofibroblasts and Macrophages

We further evaluated the biological functions of ligand and receptor genes between myofibroblasts and macrophages. Our results demonstrated that ligand and receptor genes between myofibroblasts and macrophages were mainly involved in tube morphogenesis and development, regulation of cell migration, and motility (Figure 3B). Moreover, we found that the TGF- β signaling pathway was markedly enriched by these



ligand and receptor genes between myfibroblasts and macrophages (Figure 3C).

Knockdown of EN1 Facilitates Fibroblast Migration

We further verified the effects of EN1 on the migration of fibroblasts. Firstly, siRNA against EN1 was designed and transected into fibroblasts. RT-qPCR demonstrated that EN1 mRNA expression was distinctly reduced following siRNA-EN1 transfection (Figure 3D). According to wound healing results, EN1-knockout fibroblasts displayed significantly enhanced migration capacity (Figures 3E, F). Hence, EN1 suppression enabled to facilitate fibroblast migration.

Identification of Specific Genes Between Fibrotic and Regenerative Myfibroblasts and Their Biological Functions

With the cutoffs of $|FC| > 1.2$ and $p < 0.05$, we identified 546 up- and 481 downregulated specific genes in regenerative compared to fibrotic myfibroblasts (Figures 4A–C). Table 2 lists the first 20 up- and downregulated specific genes between regenerative and fibrotic myfibroblasts. As depicted in Figure 4D, we observed that the specific genes markedly participated in

collagen-containing extracellular matrix, posttranscriptional regulation of gene expression, positive regulation of cell migration, mRNA metabolic process, and apoptotic signaling pathway. Moreover, ribosome and thermogenesis were prominently enriched by the specific genes (Figure 4E).

Identification of Specific Genes Between Fibrotic and Regenerative Macrophages and Their Biological Functions

With the cutoffs of $|FC| > 1.2$ and $p < 0.05$, we found that 100 specific genes were significantly upregulated while 197 specific genes were significantly downregulated in regenerative compared to fibrotic macrophages (Figures 5A–C). Table 3 lists the first 20 up- and downregulated specific genes between fibrotic and regenerative macrophages. GO enrichment analysis uncovered that the specific genes were markedly involved in the negative regulation of programmed cell death, the regulation of cell migration, innate immune response and apoptotic signaling pathway, collagen-containing extracellular matrix, the positive regulation of T cell activation, and response to interferon γ (Figure 5D). Moreover, we observed that antigen processing and presentation, pathways in cancer, phagosome, ribosome, and tuberculosis were prominently enriched by the specific genes (Figure 5E).

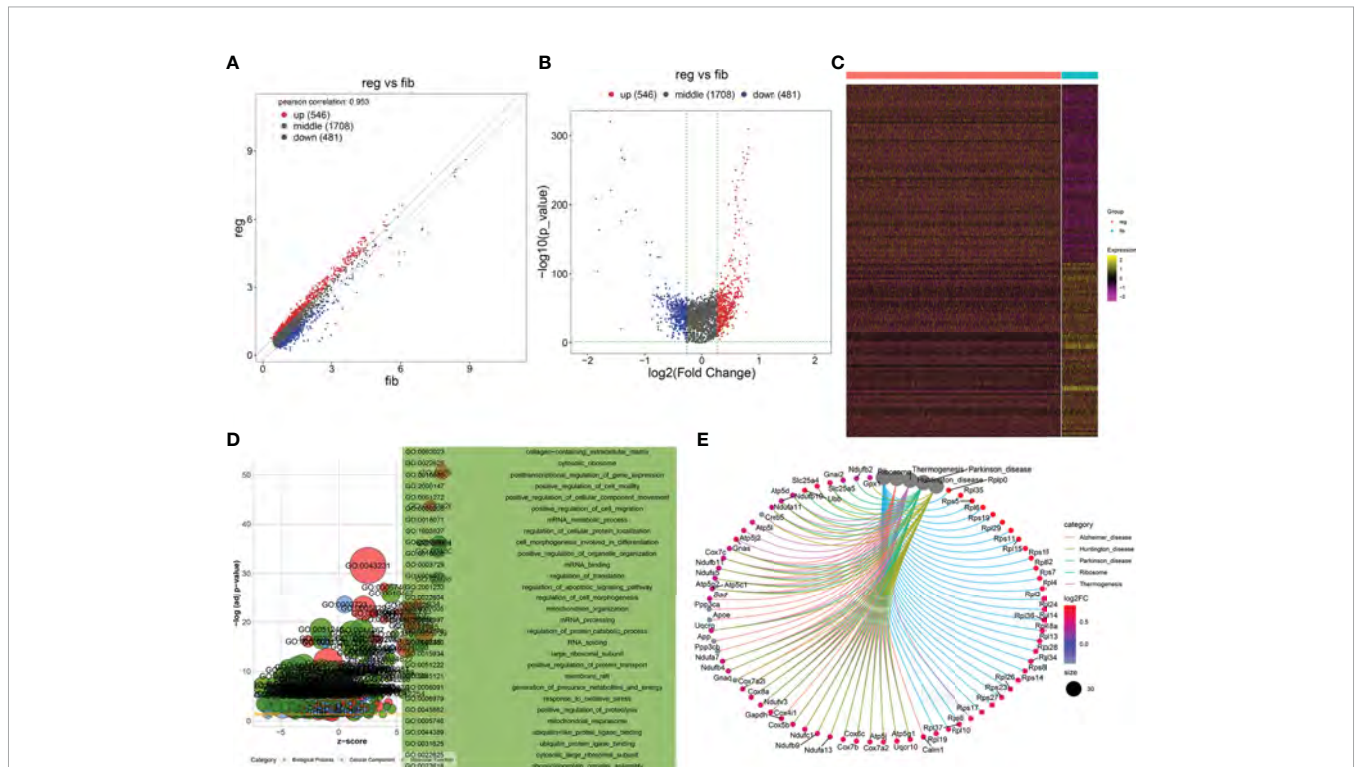


FIGURE 4 | Identification of specific genes between fibrotic and regenerative myfibroblasts and their biological functions. (A, B) Scatter plots and volcano diagram for the up- and downregulated specific genes in regenerative (reg) compared to fibrotic (fib) myfibroblasts. Red dots meant upregulated genes while blue dots meant downregulated genes. (C) Heatmap visualizing the expression patterns of the specific genes in fibrotic and regenerative myfibroblasts. Yellow represented upregulation and purple represented downregulation. (D) GO enrichment results of specific genes that were abnormally expressed between fibrotic and regenerative myfibroblasts. (E) KEGG pathways involved in specific genes that were abnormally expressed between fibrotic and regenerative myfibroblasts.

TABLE 2 | The first 20 up- and downregulated specific genes between fibrotic and regenerative myofibroblasts.

Gene	log2FC	p-value	Q-value	Regenerative	Fibrotic
Rplp0	0.870992	0	0	5.166991	4.295999
Ifitm2	0.843781	1.12E-173	1.94E-169	3.837826	2.994046
Mfap5	0.826158	5.93E-128	1.03E-123	4.591184	3.765026
Lgals1	0.820706	4.86E-284	8.43E-280	6.19352	5.372813
Hist1h2bc	0.81979	4.50E-90	7.81E-86	2.042755	1.222965
Serf2	0.805752	1.37E-310	2.39E-306	4.973459	4.167707
Rpl35	0.801322	0	0	5.164454	4.363133
Rps5	0.795055	5.07E-274	8.79E-270	4.725084	3.930029
Basp1	0.794315	1.55E-93	2.69E-89	2.268422	1.474106
Rpl6	0.792999	4.84E-266	8.40E-262	4.489802	3.696803
Ybx1	0.791379	6.39E-117	1.11E-112	2.98192	2.19054
Rps19	0.790084	0	0	5.198609	4.408525
Ost4	0.782118	2.55E-123	4.42E-119	3.079057	2.296939
Rpl29	0.780779	1.14E-175	1.98E-171	3.875578	3.094799
H19	0.767949	8.58E-45	1.49E-40	3.185378	2.417429
Rps11	0.763653	3.10E-260	5.37E-256	4.655295	3.891641
Rpl15	0.760256	2.28E-207	3.96E-203	4.262648	3.502392
Ifi20	0.758	1.47E-93	2.55E-89	2.397842	1.639842
Ssr4	0.745387	2.11E-101	3.67E-97	2.89302	2.147633
Ubb	0.744921	1.14E-144	1.97E-140	4.529784	3.784862
mt-Nd4l	-2.08112	0	0	0.883721	2.964844
mt-Atp6	-1.85976	0	0	5.349053	7.20881
Hspa1b	-1.85125	4.49E-209	7.79E-205	0.611879	2.463132
mt-Co2	-1.84169	0	0	4.106449	5.948142
AC160336.1	-1.81875	4.98E-104	8.63E-100	0.763221	2.58197
Hspa1a	-1.79337	2.08E-164	3.61E-160	1.385872	3.179244
mt-Nd4	-1.60147	3.51E-321	6.08E-317	3.543676	5.145146
mt-Nd5	-1.59322	2.78E-221	4.83E-217	1.144946	2.738165
mt-Cytb	-1.57454	0	0	4.565919	6.140456
Igfbp2	-1.4162	1.28E-20	2.21E-16	2.045862	3.462061
mt-Nd3	-1.41514	1.13E-177	1.96E-173	1.403288	2.818428
mt-Nd1	-1.4142	4.61E-280	8.00E-276	4.509633	5.923829
mt-Co3	-1.39259	1.24E-268	2.15E-264	5.529273	6.921861
mt-Co1	-1.35374	1.30E-265	2.26E-261	5.598606	6.952347
mt-Nd2	-1.32088	1.81E-190	3.14E-186	2.765453	4.086338
Gm26917	-1.31863	7.03E-191	1.22E-186	0.653702	1.972335
Cd74	-1.15624	2.79E-193	4.84E-189	0.624805	1.781046
Lars2	-0.96874	2.21E-146	3.83E-142	0.232192	1.200933
Luc7l2	-0.91132	1.16E-98	2.01E-94	1.18695	2.098275
Hspg2	-0.90368	3.60E-128	6.24E-124	2.381196	3.284878

PPI Network Analysis of Specific Genes Between Fibrotic and Regenerative Myofibroblasts or Macrophages

With the STRING tool, we probed the interactions between myofibroblast- or macrophage-specific gene-encoded proteins. In **Figure 6A**, there were 616 nodes in the PPI network of myofibroblasts, reflecting the close interactions of myofibroblast-specific gene-encoded proteins. According to degree, the top 20 nodes were identified as hub genes, including Rps27a, Rps11, Rps23, Rps3, Rps5, Rps15a, Rps6, Rps9, Rps13, Rps14, Rps25, Rps3a1, Rps27, Rps8, Rps19, Rps28, Rps7, Rpl8, Rps18, Rpl26, Rpl32, and Rps16, indicating that the above genes were the core of the network. **Figure 6B** depicts the interactions between macrophage-specific gene-encoded proteins. The 20 hub genes were as follows: Uba52, Rps9, Gnb2l1, Rpl27, Rpl38, Rps13, Rps15a, Fau, Rpl18, Rpl30, Rpl35a, Rpl7, Rpl2, Rps24, Rpl13a, Rpl4, Rps10, Rps12, Rps27rt, and Rps2. The above genes deserve in-depth explorations.

Reconstruction of the Temporal Dynamics of Myofibroblast and Macrophage

To investigate the underlying evolution among myofibroblasts and macrophages, this study adopted the Monocle tool to reveal a pseudotemporal ordering for the similarity of cell clusters with developmental lineages. For myofibroblasts, the results clearly demonstrated the uniform development of myofibroblasts from cluster 6 to cluster 10 (**Figure 7A**). The trends of pseudotime-dependent genes along the pseudo-timeline were divided into six cell clusters of myofibroblasts with diverse expression dynamics. Furthermore, we observed that macrophage under fibrotic conditions was in the beginning position of the differentiation process and was sequentially transformed into macrophage under regenerative conditions (**Figure 7B**).

GSVA Between Clusters 6 and 10 of Fibrotic and Regenerative Myofibroblasts

According to the results of pseudotime analysis of myofibroblasts, we carried out GSVA between the initially differentiated cluster 6

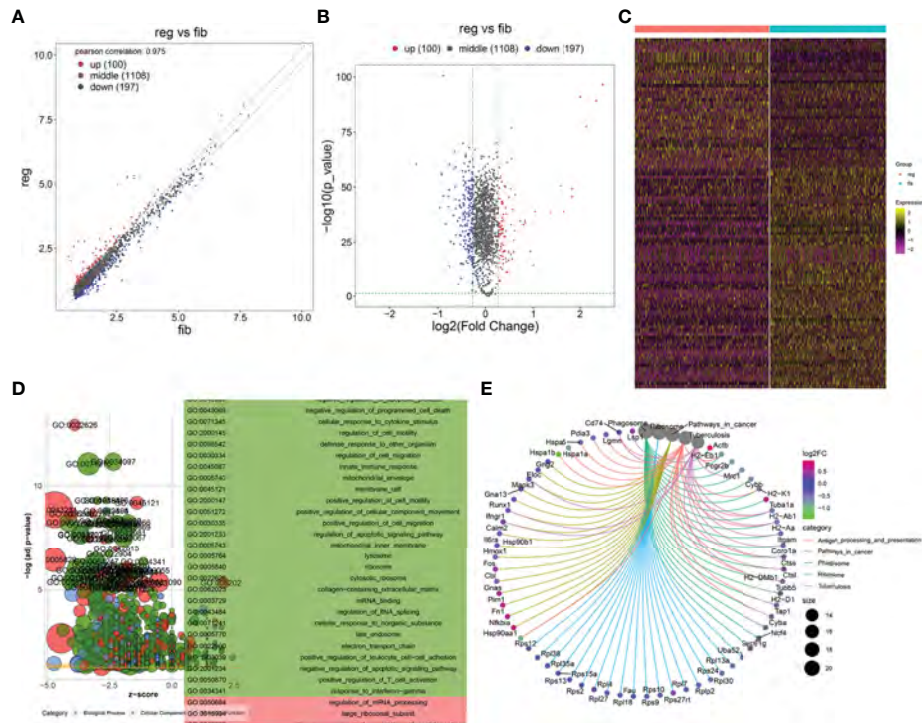


FIGURE 5 | Identification of specific genes between fibrotic and regenerative macrophages and their biological functions. **(A, B)** Scatter plots and volcano diagram showing the up- and downregulated specific genes in regenerative (reg) compared to fibrotic (fib) macrophages. Red dots meant upregulated genes while blue dots meant downregulated genes. **(C)** Heatmap visualizing the expression patterns of the specific genes in fibrotic and regenerative macrophages. Yellow represented upregulation and purple represented downregulation. **(D)** GO enrichment results of specific genes that were abnormally expressed between fibrotic and regenerative macrophages. **(E)** KEGG pathways involved in specific genes that were abnormally expressed between fibrotic and regenerative macrophages.

and the final differentiated cluster 10. Compared with cluster 10 of myofibroblasts in fibrotic and regenerative dermal cells, biological processes such as the metabolic process significantly activated cluster 6 of myofibroblasts in fibrotic and regenerative dermal cells (**Figure 8A**). As depicted in **Figure 8B**, we noticed the prominent activation of cellular components such as mitochondria in cluster 6 of fibrotic and regenerative myofibroblasts in comparison to those in cluster 10. Moreover, we observed that fibrotic and regenerative myofibroblasts in cluster 6 had significantly activated molecular functions like oxidoreductase activity compared with fibrotic and regenerative myofibroblasts in cluster 10 (**Figure 8C**). We also compared the differences in KEGG pathways between clusters. Diverse signaling pathways like metabolic pathways, RNA transport, spliceosome, thermogenesis, oxidative phosphorylation, carbon metabolism, ribosome, cell cycle, protein processing in the endoplasmic reticulum, and biosynthesis of amino acids were prominently activated in fibrotic and regenerative myofibroblasts in cluster 6 compared to those in cluster 10 (**Figure 8D**).

GSVA Between Fibrotic and Regenerative Macrophages

GSVA was also presented between fibrotic and regenerative macrophages. In **Figure 9A**, we determined that biological processes such as the metabolic process and immune response

were markedly activated in fibrotic macrophages compared to regenerative macrophages. The significantly activated cellular components such as the spliceosomal complex, catalytic complex, ribonucleoprotein complex, nuclear lumen, nucleoplasm, nucleolus, cytosol, nucleus, catalytic step 2 spliceosome, chromosome, and protein-containing complex were found in fibrotic macrophages compared with regenerative macrophages (**Figure 9B**). As shown in **Figure 9C**, we investigated the marked activation of molecular functions like RNA binding, ATP binding, mRNA binding, adenylyl ribonucleotide binding, adenylyl nucleotide binding, drug binding, nucleic acid binding, heterocyclic compound binding, organic cyclic compound binding, and ATPase activity in fibrotic macrophages in comparison to regenerative macrophages. Moreover, our results showed that KEGG pathways such as spliceosome, NOD-like receptor signaling pathway, Fc gamma R-mediated phagocytosis, antigen processing and presentation, endocytosis, necroptosis, and natural killer cell-mediated cytotoxicity displayed marked activation in fibrotic macrophages compared to regenerative macrophages (**Figure 9D**).

DISCUSSION

Skin wound healing involves complicated coordinated interactions within cells. Through scRNA-seq data, this study identified six cell

TABLE 3 | The first 20 up- and downregulated specific genes between fibrotic and regenerative macrophages.

Gene name	log2FC	p-value	Q-value	Regenerative	Fibrotic
Sparc	2.474022	3.60E-97	6.24E-93	5.010571	2.536548
Col1a1	2.33817	6.49E-90	1.13E-85	5.266303	2.928133
Col1a2	2.13485	3.01E-78	5.21E-74	5.327119	3.192269
Col3a1	2.005563	1.16E-91	2.01E-87	5.223726	3.218163
Dcn	1.836106	2.30E-46	3.98E-42	2.785851	0.949745
Bgn	1.83586	5.99E-50	1.04E-45	2.600128	0.764269
Fstl1	1.648779	1.28E-39	2.22E-35	2.200177	0.551399
Postn	1.572566	2.54E-51	4.40E-47	2.775437	1.202871
Mfap5	1.370976	2.18E-39	3.79E-35	2.023966	0.65299
Hbb-bs	1.031846	1.21E-39	2.10E-35	2.844128	1.812282
Cxcl2	1.004274	2.60E-15	4.51E-11	3.268016	2.263742
Actb	0.934603	1.46E-21	2.53E-17	7.663418	6.728815
Klf2	0.828223	1.34E-34	2.33E-30	2.497856	1.669632
Timp2	0.824526	1.09E-35	1.89E-31	1.978589	1.154062
Neat1	0.789153	1.13E-33	1.96E-29	2.328203	1.53905
Nfkbia	0.718421	2.88E-35	4.99E-31	2.761737	2.043317
Lgals1	0.61418	3.23E-47	5.60E-43	4.783109	4.168928
Fn1	0.610899	5.21E-31	9.03E-27	3.726565	3.115666
Pim1	0.59329	1.34E-26	2.32E-22	2.966403	2.373113
Cd63	0.592092	2.84E-21	4.92E-17	2.447508	1.855417
Hspa1b	-1.44863	2.08E-61	3.60E-57	1.266466	2.715092
Hsp90aa1	-0.957	1.59E-41	2.76E-37	2.518111	3.475109
Gm26917	-0.91834	3.81E-57	6.61E-53	0.782974	1.701314
Gm42418	-0.91626	1.85E-56	3.20E-52	1.082872	1.999131
Tpt1	-0.89005	3.21E-101	5.57E-97	4.517284	5.40733
mt-Nd5	-0.87923	1.13E-46	1.96E-42	0.858755	1.737986
Hspa1a	-0.83491	4.80E-34	8.32E-30	3.320621	4.155527
mt-Co2	-0.78506	1.59E-46	2.76E-42	3.967573	4.752638
mt-Atp6	-0.77046	5.82E-42	1.01E-37	4.934988	5.70545
Mycbp2	-0.75645	1.65E-49	2.86E-45	0.967289	1.723739
H2-Eb1	-0.75235	6.73E-15	1.17E-10	5.220528	5.972878
Fcgr2b	-0.75221	7.44E-61	1.29E-56	1.801335	2.553547
Mrc1	-0.72837	6.62E-26	1.15E-21	1.012111	1.740482
mt-Nd4l	-0.67023	7.15E-38	1.24E-33	0.682842	1.35307
AC160336.1	-0.65981	5.00E-25	8.66E-21	1.805651	2.465465
Prkcd	-0.6507	2.95E-59	5.12E-55	1.387319	2.038016
Cybb	-0.64225	8.79E-67	1.52E-62	1.99459	2.636836
Tgfb1	-0.63629	6.10E-51	1.06E-46	2.746255	3.382547
H2-K1	-0.62809	3.72E-45	6.44E-41	2.787025	3.415118
Irf5	-0.61724	5.52E-41	9.58E-37	2.037704	2.654947

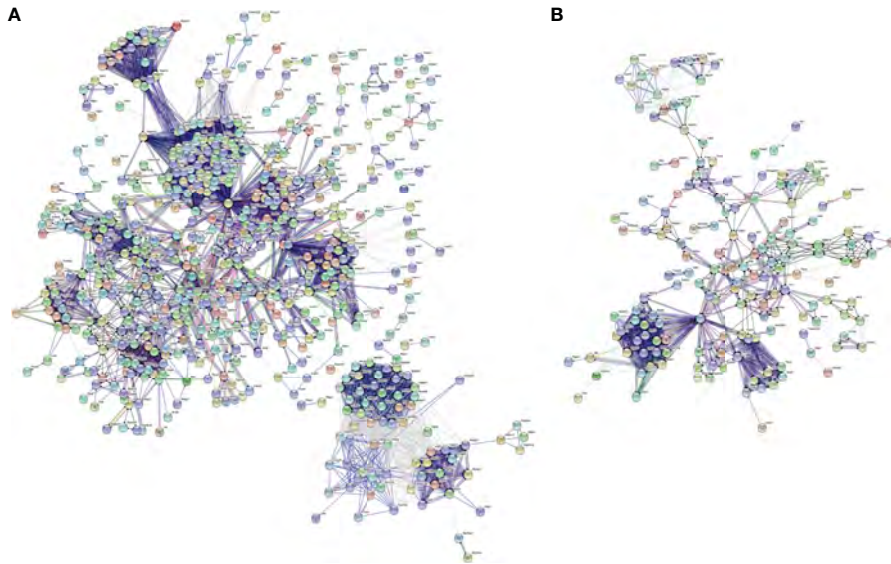


FIGURE 6 | PPI network analysis of specific genes between fibrotic and regenerative myfibroblasts or macrophages. **(A)** The PPI network of specific genes between fibrotic and regenerative myfibroblasts. **(B)** The PPI network of specific genes between fibrotic and regenerative macrophages.

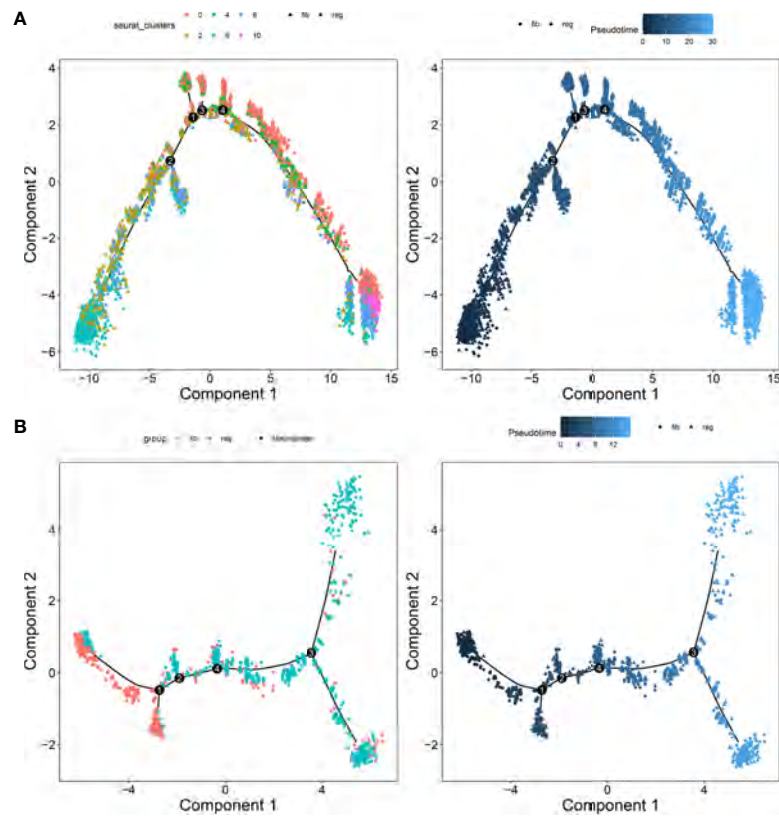


FIGURE 7 | Pseudotime ordering of myfibroblasts and macrophages. **(A)** Myfibroblasts and **(B)** macrophages. Each dot represented one cell and each branch represented one cell state. The left plot was labeled with cell states and the right plot was labeled with developmental time.

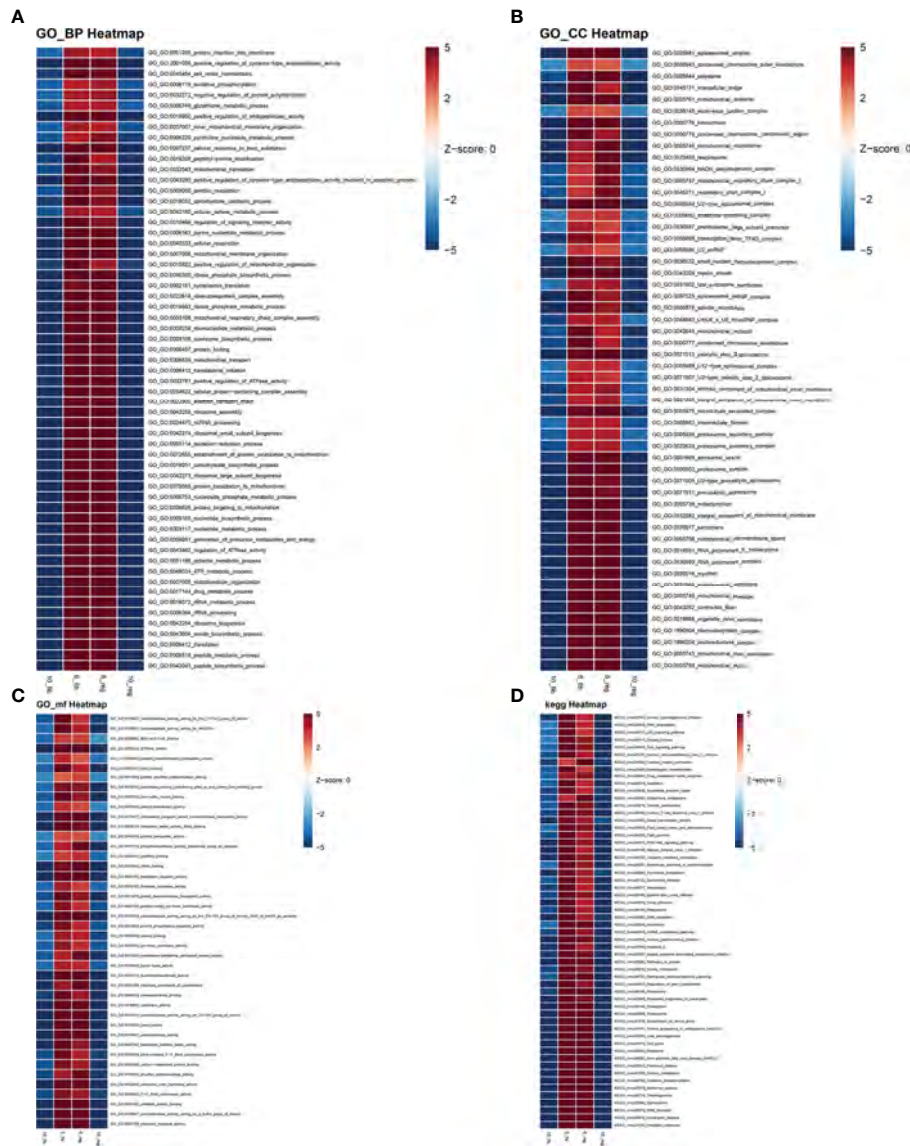
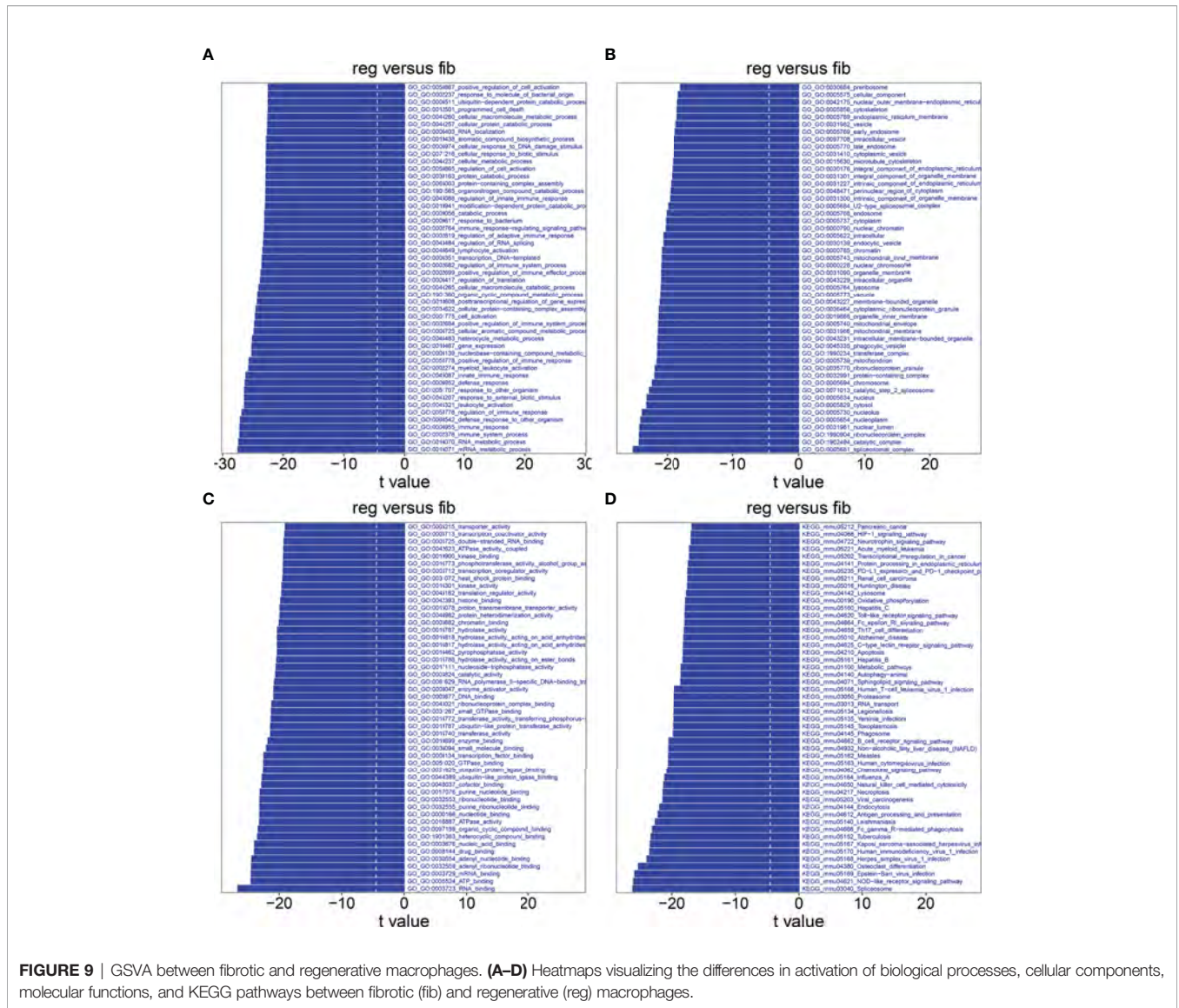


FIGURE 8 | GSEA between clusters 6 and 10 of fibrotic and regenerative myfibroblasts. **(A–D)** Heatmaps showing the differences in activation of biological processes, cellular components, molecular functions, and KEGG pathways between clusters 6 and 10 of fibrotic (fib) and regenerative (reg) myfibroblasts.

populations, namely, EN1-negative myfibroblasts, EN1-positive myfibroblasts, hematopoietic cells, macrophages, pericytes, and endothelial cells, across the dermis. Evidence suggests that EN1-positive fibroblasts are known to function in scarring, and EN1-negative fibroblasts yield wound regeneration. Thus, we used EN1 as a marker to divide the subgroups. Dynamic cellular events after skin injury rely on bidirectional cell–cell communications against effective wound healing (22). Our results demonstrated the cross-talks between myfibroblasts, hematopoietic cells, macrophages, pericytes, and endothelial cells in the dermis based on the ligand–receptor interactions. As per previous studies, CX3CR1 may mediate the recruitment of bone marrow-derived monocytes or macrophages in skin wound healing, thereby releasing profibrotic

as well as angiogenic mediators (23). Moreover, macrophages support proliferation and heterogeneity of myfibroblasts in skin repair (24). Serum endothelial cell-derived extracellular vesicles facilitate diabetic wound healing *via* enhancing myfibroblast proliferation and decreasing senescence (25). Intradermal adipocytes modulate the recruitment of myfibroblasts in skin wound healing (26). Fibroblasts promote NG²⁺ pericyte populations in murine skin development as well as repair (27). On the basis of the above lines of evidence, there were remarkable interplays between diverse cell types during dermis progression. According to the number of ligands and receptors, we identified myfibroblasts as the core cell population. Our function enrichment analyses uncovered that the ligand and receptor



genes between myfibroblasts and macrophages were mainly involved in regulating cell proliferation and migration, tube development, and the TGF-β pathway. The TGF-β signaling pathway plays an important role in the formation of collagen in fibroblasts and myfibroblasts (28). Cytokine TGF-β may induce dermal dendritic cells to express IL-31, thereby activating sensory neurons as well as stimulating wound itching during skin wound healing (29). Hence, targeting the TGF-β pathway is the promising therapeutic intervention to reduce abnormal skin scar formation.

To explore the differences in molecular mechanisms involving myfibroblasts between fibrotic and regenerative wound healing fates, we identified 546 up- and 481 downregulated specific genes in regenerative compared to fibrotic myfibroblasts. This revealed the heterogeneity of myfibroblasts between fibrotic and regenerative wound healing. Our GO and KEGG enrichment analysis uncovered the key biological functions involving the specific genes between fibrotic and regenerative myfibroblasts. As a

result, these specific genes between fibrotic and regenerative myfibroblasts prominently participated in the mRNA metabolic process and organelle organization. Extracellular matrix of connective tissues is synthesized by myfibroblasts that play a critical role in sustaining the structural integrity of various tissues (30).

Skin wound macrophage is an important regulator of skin repair, and its dysfunction may cause chronic and non-healing skin wounds (31). Further analysis identified that 100 specific genes were significantly upregulated while 197 specific genes were significantly downregulated in regenerative compared to fibrotic macrophages. Functional enrichment analysis uncovered that these specific genes between fibrotic and regenerative macrophages primarily participated in regulating inflammatory response, immunity, and phagocytosis. Immunity is the most important function of the skin, which can prevent harmful exposure from the external and internal environment (32).

Furthermore, late wound macrophage phagocytosis of the Wnt inhibitor may induce chronic Wnt activity during fibrotic skin healing (11). Collectively, our findings revealed that the heterogeneity of myofibroblasts or macrophages might determine wound healing fate as regenerative or fibrotic.

CONCLUSION

Taken together, this study uncovered cellular functional heterogeneity in dermis between fibrotic and regenerative wound healing fates. Moreover, myofibroblasts and macrophages may change the skin wound healing fates by modulating critical signaling pathways. Therefore, our data provided an insight into the development of more effective therapeutic interventions for improving healing fates.

DATA AVAILABILITY STATEMENT

The datasets presented in this study can be found in online repositories. The names of the repository/repositories and accession number(s) can be found at: <https://www.ncbi.nlm.nih.gov/>, GSM4213633; <https://www.ncbi.nlm.nih.gov/>, GSM4213632; <https://www.ncbi.nlm.nih.gov/>, GSE141814.

ETHICS STATEMENT

Ethical review and approval were not required for the study on human participants in accordance with the local legislation and institutional requirements. Written informed consent for participation was not required for this study in accordance with the national legislation and the institutional requirements. The animal study was reviewed and approved by Keio University

REFERENCES

- Rajesh A, Stuart G, Real N, Tschirley A, Ahn J, Wise L, et al. Skin Antigen-Presenting Cells and Wound Healing: New Knowledge Gained and Challenges Encountered Using Mouse Depletion Models. *Immunology* (2021) 163(1):98–104. doi: 10.1111/imm.13311
- Griffin DR, Archang MM, Kuan C-H, Weaver WM, Weinstein JS, Feng AC, et al. Activating an Adaptive Immune Response From a Hydrogel Scaffold Imparts Regenerative Wound Healing. *Nat Mater* (2021) 20(4):560–9. doi: 10.1038/s41563-020-00844-w
- Yamaguchi K, Kanno E, Tanno H, Sasaki A, Kitai Y, Miura T, et al. Distinct Roles for Dectin-1 and Dectin-2 in Skin Wound Healing and Neutrophilic Inflammatory Responses. *J Invest Dermatol* (2021) 141(1):164–76.e8. doi: 10.1016/j.jid.2020.04.030
- Chen T-Y, Wen T-K, Dai N-T, Hsu S-H. Cryogel/hydrogel Biomaterials and Acupuncture Combined to Promote Diabetic Skin Wound Healing Through Immunomodulation. *Biomaterials* (2021) 269:120608. doi: 10.1016/j.biomaterials.2020.120608
- Rodrigues M, Kosaric N, Bonham CA, Gurtner GC. Wound Healing: A Cellular Perspective. *Physiol Rev* (2019) 99(1):665–706. doi: 10.1152/physrev.00067.2017

School of Medicine. Written informed consent was not obtained from the individual(s) for the publication of any potentially identifiable images or data included in this article.

AUTHOR CONTRIBUTIONS

C-JC, HK, and KT: conception or design of the work. C-JC, HK, KT, NA-H, SS, TA, and KK: acquisition, analysis, or interpretation of data. C-JC, HK, KT, NA-H, SS, TA, and KK: drafting the manuscript or revising it critically for important intellectual content. All authors contributed to the article and approved the submitted version.

FUNDING

This work was supported in part by Japan China Sasakawa Medical Fellowship (2017816).

SUPPLEMENTARY MATERIAL

The Supplementary Material for this article can be found online at: <https://www.frontiersin.org/articles/10.3389/fimmu.2022.875407/full#supplementary-material>

Supplementary Figure 1 | Quality control of scRNA-seq data of fibrotic and regenerative wound dermal cells. (A, B) Barcode rank plots separately showing the detected knee and inflection points for fibrotic and regenerative wound dermal cells. (C, D) The expression of all genes, ribosomal genes, and mitochondrial genes in each cell was shown for fibrotic and regenerative wound dermal cells. (E, F) The proportions of mitochondrial and ribosomal genes expressed in each cell were counted for fibrotic and regenerative wound dermal cells.

Supplementary Table 1 | The list of novel marker genes identified in each cell type.

- Aragona M, Dekoninck S, Rulands S, Lenglez S, Mascré G, Simons BD, et al. Defining Stem Cell Dynamics and Migration During Wound Healing in Mouse Skin Epidermis. *Nat Commun* (2017) 8:14684. doi: 10.1038/ncomms14684
- Govindaraju P, Todd L, Shetye S, Monslow J, Puré E. CD44-Dependent Inflammation, Fibrogenesis, and Collagenolysis Regulates Extracellular Matrix Remodeling and Tensile Strength During Cutaneous Wound Healing. *Matrix Biol* (2019) 75–6:314–30. doi: 10.1016/j.matbio.2018.06.004
- Haensel D, Jin S, Sun P, Cinco R, Dragan M, Nguyen Q, et al. Defining Epidermal Basal Cell States During Skin Homeostasis and Wound Healing Using Single-Cell Transcriptomics. *Cell Rep* (2020) 30(11):3932–47.e6. doi: 10.1016/j.celrep.2020.02.091
- Theocharidis G, Baltzis D, Roustit M, Tellechea A, Dangwal S, Khetani RS, et al. Integrated Skin Transcriptomics and Serum Multiplex Assays Reveal Novel Mechanisms of Wound Healing in Diabetic Foot Ulcers. *Diabetes* (2020) 69(10):2157–69. doi: 10.2337/db20-0188
- Guerrero-Juarez CF, Dedhia PH, Jin S, Ruiz-Vega R, Ma D, Liu Y, et al. Single-Cell Analysis Reveals Fibroblast Heterogeneity and Myeloid-Derived Adipocyte Progenitors in Murine Skin Wounds. *Nat Commun* (2019) 10(1):650. doi: 10.1038/s41467-018-08247-x
- Gay D, Ghinatti G, Guerrero-Juarez CF, Ferrer RA, Ferri F, Lim CH, et al. Phagocytosis of Wnt Inhibitor SFRP4 by Late Wound Macrophages Drives

- Chronic Wnt Activity for Fibrotic Skin Healing. *Sci Adv* (2020) 6(12): eay3704. doi: 10.1126/sciadv.aay3704
12. Lun ATL, Riesenfeld S, Andrews T, Dao TP, Gomes T, Marioni JC. EmptyDrops: Distinguishing Cells From Empty Droplets in Droplet-Based Single-Cell RNA Sequencing Data. *Genome Biol* (2019) 20(1):63. doi: 10.1186/s13059-019-1662-y
 13. McCarthy DJ, Campbell KR, Lun ATL, Wills QF. Scater: Pre-Processing, Quality Control, Normalization and Visualization of Single-Cell RNA-Seq Data in R. *Bioinformatics* (2017) 33(8):1179–86. doi: 10.1093/bioinformatics/btw777
 14. Butler A, Hoffman P, Smibert P, Papalexi E, Satija R. Integrating Single-Cell Transcriptomic Data Across Different Conditions, Technologies, and Species. *Nat Biotechnol* (2018) 36(5):411–20. doi: 10.1038/nbt.4096
 15. Ramiłowski JA, Goldberg T, Harshbarger J, Kloppmann E, Lizio M, Satagopam VP, et al. A Draft Network of Ligand-Receptor-Mediated Multicellular Signalling in Human. *Nat Commun* (2015) 6:7866. doi: 10.1038/ncomms8866
 16. Doncheva NT, Morris JH, Gorodkin J, Jensen LJ. Cytoscape StringApp: Network Analysis and Visualization of Proteomics Data. *J Proteome Res* (2019) 18(2):623–32. doi: 10.1021/acs.jproteome.8b00702
 17. Yu G, Wang L-G, Han Y, He Q-Y. ClusterProfiler: An R Package for Comparing Biological Themes Among Gene Clusters. *OMICS* (2012) 16(5):284–7. doi: 10.1089/omi.2011.0118
 18. Szklarczyk D, Gable AL, Lyon D, Junge A, Wyder S, Huerta-Cepas J, et al. STRING V11: Protein-Protein Association Networks With Increased Coverage, Supporting Functional Discovery in Genome-Wide Experimental Datasets. *Nucleic Acids Res* (2019) 47(D1):D607–13. doi: 10.1093/nar/gky1131
 19. Cao J, Spielmann M, Qiu X, Huang X, Ibrahim DM, Hill AJ, et al. The Single-Cell Transcriptional Landscape of Mammalian Organogenesis. *Nature* (2019) 566(7745):496–502. doi: 10.1038/s41586-019-0969-x
 20. Hänzelmann S, Castelo R, Guinney J. GSVA: Gene Set Variation Analysis for Microarray and RNA-Seq Data. *BMC Bioinf* (2013) 14:7. doi: 10.1186/1471-2105-14-7
 21. Sorkin M, Huber AK, Hwang C, Carson WF4, Menon R, Li J, et al. Regulation of Heterotopic Ossification by Monocytes in a Mouse Model of Aberrant Wound Healing. *Nat Commun* (2020) 11(1):722. doi: 10.1038/s41467-019-14172-4
 22. Zhou X, Brown BA, Siegel AP, El Masry MS, Zeng X, Song W, et al. Exosome-Mediated Crosstalk Between Keratinocytes and Macrophages in Cutaneous Wound Healing. *ACS Nano* (2020) 14(10):12732–48. doi: 10.1021/acsnano.0c03064
 23. Ishida Y, Gao J-L, Murphy PM. Chemokine Receptor CX3CR1 Mediates Skin Wound Healing by Promoting Macrophage and Fibroblast Accumulation and Function. *J Immunol* (2008) 180(1):569–79. doi: 10.4049/jimmunol.180.1.569
 24. Shook BA, Wasko RR, Rivera-Gonzalez GC, Salazar-Gatzimas E, López-Giráldez F, Dash BC, et al. Myofibroblast Proliferation and Heterogeneity are Supported by Macrophages During Skin Repair. *Science* (2018) 362(6417). doi: 10.1126/science.aar2971
 25. Wei F, Wang A, Wang Q, Han W, Rong R, Wang L, et al. Plasma Endothelial Cells-Derived Extracellular Vesicles Promote Wound Healing in Diabetes Through YAP and the PI3K/Akt/mTOR Pathway. *Aging (Albany NY)* (2020) 12(12):12002–18. doi: 10.18632/aging.103366
 26. Schmidt BA, Horsley V. Intradermal Adipocytes Mediate Fibroblast Recruitment During Skin Wound Healing. *Development* (2013) 140(7):1517–27. doi: 10.1242/dev.087593
 27. Goss G, Rognoni E, Salameti V, Watt FM. Distinct Fibroblast Lineages Give Rise to NG2+ Pericyte Populations in Mouse Skin Development and Repair. *Front Cell Dev Biol* (2021) 9:675080. doi: 10.3389/fcell.2021.675080
 28. Zhang T, Wang X-F, Wang Z-C, Lou D, Fang Q-Q, Hu Y-Y, et al. Current Potential Therapeutic Strategies Targeting the TGF- β /Smad Signaling Pathway To Attenuate Keloid and Hypertrophic Scar Formation. *BioMed Pharmacother* (2020) 129:110287. doi: 10.1016/j.biopha.2020.110287
 29. Xu J, Zanvit P, Hu L, Tseng P-Y, Liu N, Wang F, et al. The Cytokine TGF- β Induces Interleukin-31 Expression From Dermal Dendritic Cells to Activate Sensory Neurons and Stimulate Wound Itching. *Immunity* (2020) 53(2):371–83.e5. doi: 10.1016/j.immuni.2020.06.023
 30. Lynch MD, Watt FM. Fibroblast Heterogeneity: Implications for Human Disease. *J Clin Invest* (2018) 128(1):26–35. doi: 10.1172/JCI93555
 31. Chen H, Shi R, Luo B, Yang X, Qiu L, Xiong J, et al. Macrophage Peroxisome Proliferator-Activated Receptor γ Deficiency Delays Skin Wound Healing Through Impairing Apoptotic Cell Clearance in Mice. *Cell Death Dis* (2015) 6(1):e1597. doi: 10.1038/cddis.2014.544
 32. Matejuk A. Skin Immunity. *Arch Immunol Ther Exp (Warsz)* (2018) 66(1):45–54. doi: 10.1007/s00005-017-0477-3

Conflict of Interest: The authors declare that the research was conducted in the absence of any commercial or financial relationships that could be construed as a potential conflict of interest.

Publisher's Note: All claims expressed in this article are solely those of the authors and do not necessarily represent those of their affiliated organizations, or those of the publisher, the editors and the reviewers. Any product that may be evaluated in this article, or claim that may be made by its manufacturer, is not guaranteed or endorsed by the publisher.

Copyright © 2022 Chen, Kajita, Takaya, Aramaki-Hattori, Sakai, Asou and Kishi. This is an open-access article distributed under the terms of the Creative Commons Attribution License (CC BY). The use, distribution or reproduction in other forums is permitted, provided the original author(s) and the copyright owner(s) are credited and that the original publication in this journal is cited, in accordance with accepted academic practice. No use, distribution or reproduction is permitted which does not comply with these terms.

日中笹川医学奨学金制度<学位取得コース>評価書

論文博士：指導教官用



第 44 期

研究者番号：G4406

作成日：2024年3月10日

氏名	趙 宏波	ZHAO HONGBO	性別	M	生年月日	1980/10/11
所属機関（役職）	中国医学科学院肿瘤医院深圳医院胸外科（副主任醫師）					
研究先（指導教官）	東海大学医学部消化器外科上部消化管グループ（小柳 和夫 教授）					
研究テーマ	食道癌術後縫合不全に対する ICG 蛍光イメージング法の有用性の検討 To investigate the value of Indocyanine Green Fluorescence Imaging (ICGFI) in preventing postoperative anastomotic leakage after esophagectomy					
専攻種別	<input checked="" type="checkbox"/> 論文博士			<input type="checkbox"/> 課程博士		

研究者評価（指導教官記入欄）

成績状況	(優) 良 可 不可	取得単位数
		取得単位数 / 取得すべき単位数総数
学生本人が行った研究の概要		タイトル：食道癌術後縫合不全に対する ICG 蛍光イメージング法の有用性の検討 概要：食道癌再建胃管血流は縫合不全に関与する因子の一つである。われわれはこれまでに胃管血流速度の遅延が縫合不全に関与することを報告してきた。本研究では胃管作成時の切離線の違いが血流速度と縫合不全に関連するかどうかを検討した。結果として、右胃大網動静脈を温存することにより血流速度が速くなり、術後の縫合不全が減少することが分かった。現在、論文を作成し投稿中である。
総合評価		【良かった点】 研究を熱心に行い論文作成まで終了した。 消化器外科グループのスタッフとも良好なコミュニケーションを図り、病棟回診や手術見学なども積極的に行った。
		【改善すべき点】 コロナ感染症の影響もあったと考えるが、もう少し交流の輪が広がるとさらに有意義であったと考えられる。
		【今後の展望】 本研究は食道癌術後の合併症回避において汎用性が高い。今後も研究継続が可能であるので、さらに研究を深めて後進の指導にもあたってほしい。
学位取得見込		論文作成は済み現在、投稿中である。 Accept が得られたところで学位申請を行う見込みである。
評価者（指導教官名） 小柳 和夫		

日中笹川医学奨学金制度<学位取得コース>報告書

研究者用



第44期

研究者番号: G4406

作成日: 2024年2月 18 日

氏名	赵宏波	ZHAO HONGBO	性別	M	生年月日	1980/10/11
所属機関(役職)	中国医学科学院肿瘤医院深圳医院胸外科(副主任醫師)					
研究先(指導教官)	東海大学医学部消化器外科上部消化管グループ(小柳 和夫 教授)					
研究テーマ	食道癌術後縫合不全に対するICG蛍光イメージング法の有用性の検討 To investigate the value of Indocyanine Green Fluorescence Imaging (ICGFI) in preventing postoperative anastomotic leakage after esophagectomy					
専攻種別	論文博士	<input checked="" type="checkbox"/>	課程博士	<input type="checkbox"/>		

1. 研究概要(1)

1) 目的 (Goal) This study aimed to investigate the effectiveness of a modified incision line on the lesser curvature for gastric conduit formation during esophagectomy in enhancing the perfusion of gastric conduit as determined by indocyanine green fluorescence imaging, and reducing the incidence of anastomotic leakage.

2) 戦略 (Approach) & 3) 材料と方法 (Materials and methods) 272 patients who underwent esophagectomy at our institute between 2014 and 2022 were enrolled in this study. These patients were divided based on two different types of cutlines on lesser curvature: Conventional group (n = 141) followed the traditional cutline, and Current group (n = 131) adopted a modified cutline. Gastric conduit perfusion was assessed by ICG fluorescence imaging and clinical outcomes after esophagectomy were evaluated.

4) 実験結果 (Results): The distance from pylorus to the cutline was significantly longer in Current group compared with Conventional group (median: 9.0 cm vs. 5.0 cm, $p < 0.001$). The blood flow speed in gastric conduit wall was significantly higher in Current group than in Conventional group (median: 2.81 cm/sec vs. 2.54 cm/sec, $p = 0.001$). Furthermore, anastomotic leakage was significantly lower ($p = 0.024$) and hospital stay was significantly shorter ($p < 0.001$) in Current group compared with Conventional group. Multivariate analysis identified blood flow speed in the gastric conduit wall as the only variable significantly associated with anastomotic leakage. Conclusions: ICG fluorescence imaging is a feasible, reliable method for assessment of gastric conduit perfusion. Modified lesser curvature cutline could enhance gastric conduit perfusion, promote blood circulation around anastomotic site, and reduce the risk of anastomotic leakage after esophagectomy.

5) 考察 (Discussion) In this study, we investigated the effectiveness of using a modified cutline on the gastric lesser curvature during esophagectomy to reduce the incidence of postoperative anastomotic leakage. The blood flow speed in the gastric conduit wall increased significantly with the use of the modified cutline on the gastric lesser curvature to preserve the entire RGA, thus, our proposed modification of the cutline resulted in improved perfusion of the gastric conduit. Furthermore, our findings revealed a significant reduction of anastomotic leakage for patients in which the modified cutline was performed. These findings further indicate the feasibility and reliability of ICG fluorescence imaging for intraoperative assessment of gastric conduit perfusion and suggest that modifying the lesser curvature cutline to preserve the entire RGA could be a promising strategy to minimize the risk of anastomotic leakage after esophagectomy.

Ischemia of the gastric conduit at the anastomotic site is widely acknowledged as a significant predisposing factor for anastomotic leakage. Early endoscopic assessments after esophagectomy have indicated that anastomotic defects predominantly occur in the region between the remaining esophagus and the proximal end of the longitudinal gastric staple line. In addition, unlike the greater curvature, which receives relatively higher blood flow from the right gastroepiploic artery, the lesser curvature side of the formed gastric conduit often lacks adequate arterial supply. These findings are also in accordance with clinical observations and prompt us to consider strategies to enhance blood perfusion in the gastric wall with the use of ICG fluorescence imaging.

The importance of preserving the right gastroepiploic artery for forming the gastric conduit is widely recognized in surgical practice, while handling of the RGA is currently not standardized and is mostly based on individual surgeons' preferences. In general, the fully intact stomach and wider gastric tube exhibit adequate vascularization, whereas a narrow gastric tube tends to show poor vascularization, particularly at the anastomosis site. In narrow gastric tubes, the right gastroepiploic artery is the only feeding artery (23,24). Furthermore, narrower gastric tubes may be associated with a wide disruption of the broad microscopic network of capillaries and arterioles in the submucosa of the lesser curvature. A larger width of the gastric conduit has been demonstrated as being significantly associated with improved gastric conduit perfusion and reduced risk of anastomotic leaks. Assuming that the length of the gastric conduit allows for sufficient anastomosis, preserving the RGA, which also allows retention of the right gastric vein, may be essential for maintaining adequate blood supply and improving the venous drainage for the gastric conduit wall based on its anatomical distribution and microvascular connections.

We adopted the strategy of preserving the entire RGA with a 3.5 cm width gastric conduit and verified its potential impact on the perfusion of the gastric conduit assessed by intraoperative ICG fluorescence imaging and the clinical outcomes. Our results revealed that adoption of a modified cutline on the gastric lesser curvature resulted in a significant increase in the distance from the pylorus to the cutline and a significantly shorter length of the gastric conduit as compared with that of the conventional cutline. However, we found that all of the preserved gastric conduits were sufficiently long to be pulled up to the neck for completion of the standard anastomosis in the area of ICG fluorescence imaging. We also found that preservation of the entire RGA led to a significantly improved blood flow speed within the gastric conduit, especially in the gastric wall. Furthermore, there was a positive correlation between improvement of the blood flow speed in the gastroepiploic artery and that in the gastric conduit wall. Some studies have demonstrated the existence of a correlation between the inflow and outflow of blood in the gastric conduit. For example, severe venous congestion in the gastric conduit could lead to a reduction in the inflow. We concluded from the above results that adoption of the modified strategy for gastric conduit formation led to significantly improved blood perfusion throughout the gastric conduit. Notably, preservation of the entire RGA resulted in a significantly lower incidence of anastomotic leakage and shorter hospital stays. We also found a significant negative correlation between anastomotic leakage and the blood flow speed in the gastric conduit wall. This is consistent with the theoretical expectation of a reduced incidence of anastomotic leakage after esophagectomy and shorter hospital stays with improved gastric conduit perfusion.

1. 研究概要(2)

Multivariable logistic regression analysis using data from the entire cohort identified the blood flow speed in the gastric conduit wall as the only variable showing a significant association with the risk of postoperative anastomotic leakage. A blood flow speed of ≤ 2.19 cm/s in the gastric conduit was found as a significant independent predictor for anastomotic leakage. This cutoff value for the blood flow speed in the gastric conduit was consistent with that reported from a previous study conducted in 2023, but higher than the cutoff values determined in two previous studies. In the first study, conducted in 2016, we determined a cutoff value of 1.76 cm/s, while in the second study, conducted in 2020, we determined a cutoff value of 2.07 cm/s. We speculate that in the first study, the small sample size could have limited our determination of the cutoff value, while in the second study, in which a significant number of patients with systemic atherosclerosis were included, systemic atherosclerosis could have impacted the microvascular perfusion of the capillary vessels of the gastric conduit, resulting in a lower calculated cutoff value. We propose to further explore the appropriate cutoff value for the blood flow speed in the gastric conduit wall to reduce the risk of anastomotic leakage in future studies.

There were several limitations of our study. First, the study was a retrospective investigation conducted at a single center, which may limit the generalizability of the results. Second, the difference in the periods in which the surgeries were performed could have introduced some bias. All patients who underwent surgery by the conventional method were operated before 2019, while all patients who underwent surgery by the modified method were operated after 2019. Third, a significant portion of anastomoses in our patient cohort were hand-sewn, and it has been found that a relatively short gastric conduit is sufficient when manual anastomosis is performed as compared with other anastomosis methods. Therefore, surgeons who prefer using other anastomosis methods than the manual method should interpret the results of our present study with caution.

In conclusion, it is feasible and reliable to assess gastric conduit perfusion intraoperatively by ICG fluorescence imaging with appropriate parameter settings. Moreover, preservation of the entire RGA during gastric conduit formation led to significantly improved vascular perfusion and reduced risk of anastomotic leakage after esophagectomy. Thus, this modified strategy for lesser curvature incision should be considered as the standard for handling the lesser curvature during esophagectomy with gastric conduit reconstruction.

6)参考文献(References)

1. Moody S, Senkin S, Islam SMA, Wang J, Nasrollahzadeh D, Cortez Cardoso Penha R, et al. Mutational signatures in esophageal squamous cell carcinoma from eight countries with varying incidence. *Nat Genet.* 2021 Nov;53(11):1553-63.
2. Kitagawa Y, Uno T, Oyama T, Kato K, Kato H, Kawakubo H, et al. Esophageal cancer practice guidelines 2017 edited by the Japan Esophageal Society: part 1. *Esophagus.* 2019 Jan;16(1):1-24.
3. Fabbi M, Hagens ERC, van Berge Henegouwen MI, Gisbertz SS. Anastomotic leakage after esophagectomy for esophageal cancer: definitions, diagnostics, and treatment. *Dis Esophagus.* 2021 Jan 11;34(1).
4. Takeuchi H, Miyata H, Gotoh M, Kitagawa Y, Baba H, Kimura W, et al. A risk model for esophagectomy using data of 5354 patients included in a Japanese nationwide web-based database. *Ann Surg.* 2014;260(2):259-66.
5. Koyanagi K, Ozawa S, Ninomiya Y, Oguma J, Kazuno A, Yatabe K, et al. Association between indocyanine green fluorescence blood flow speed in the gastric conduit wall and superior mesenteric artery calcification: predictive significance for anastomotic leakage after esophagectomy. *Esophagus.* 2021 Apr 1;18(2):248-57.
6. Ninomiya Y, Koyanagi K, Ozawa S, Oguma J, Kazuno A, Yatabe K, et al. Predictive impact of the thoracic inlet space on ICG fluorescence blood flow speed in the gastric conduit wall and anastomotic leakage after esophagectomy. *Esophagus.* 2023 Jan 1;20(1):81-8.
7. Koyanagi K, Ozawa S, Ninomiya Y, Yatabe K, Higuchi T, Yamamoto M, et al. Indocyanine green fluorescence imaging for evaluating blood flow in the reconstructed conduit after esophageal cancer surgery. *Vol. 52, Surgery Today.* Springer; 2022. p. 369-76.
8. Koyanagi K, Ozawa S, Oguma J, Kazuno A, Yamazaki Y, Ninomiya Y, et al. Blood flow speed of the gastric conduit assessed by indocyanine green fluorescence: New predictive evaluation of anastomotic leakage after esophagectomy. *Medicine (United States).* 2016 Jul 1;95(30).
9. Ishikawa Y, Breuler C, Chang AC, Lin J, Orringer MB, Lynch WR, et al. Quantitative perfusion assessment of gastric conduit with indocyanine green dye to predict anastomotic leak after esophagectomy. *Diseases of the Esophagus.* 2022 May 1;35(5).
10. Yoshimi F, Asato Y, Ikeda S, Okamoto K, Komuro Y, Imura J, et al. Using the supercharge technique to additionally revascularize the gastric tube after a subtotal esophagectomy for esophageal cancer. *Am J Surg.* 2006 Feb;191(2):284-7.
11. Ikeda Y, Niimi M, Kan S, Shatari T, Takami H, Kodaira S. Clinical significance of tissue blood flow during esophagectomy by laser doppler flowmetry. *J Thorac Cardiovasc Surg.* 2001 Dec;122(6):1101-6.
12. Ladak F, Dang JT, Switzer N, Mocanu V, Tian C, Birch D, et al. Indocyanine green for the prevention of anastomotic leaks following esophagectomy: a meta-analysis. *Vol. 33, Surgical Endoscopy.* Springer New York LLC; 2019. p. 384-94.
13. Polom K, Murawa D, Rho YS, Nowaczyk P, Hünerbein M, Murawa P. Current trends and emerging future of indocyanine green usage in surgery and oncology: a literature review. *Cancer.* 2011 Nov 1;117(21):4812-22.
14. Nishikawa K, Fujita T, Yuda M, Tanaka Y, Matsumoto A, Tanishima Y, et al. Quantitative assessment of blood flow in the gastric conduit with thermal imaging for esophageal reconstruction. *Ann Surg.* 2020 Jun 1;271(6):1087-94.
15. Thammineedi SR, Patnaik SC, Saksena AR, Ramalingam PR, Nusrath S. The utility of indocyanine green angiography in the assessment of perfusion of gastric conduit and proximal esophageal stump against visual assessment in patients undergoing esophagectomy: a prospective study. *Indian J Surg Oncol.* 2020 Dec 1;11(4):684-91.
16. Ng CSH, Ong BH, Chao YK, Wright GM, Sekine Y, Wong I, et al. Use of indocyanine green fluorescence imaging in thoracic and esophageal surgery. *Ann Thorac Surg.* 2023 Apr;115(4):1068-76.

1. 研究概要(3)

17. Kitagawa H, Namikawa T, Iwabu J, Yokota K, Uemura S, Munekage M, et al. Correlation between indocyanine green visualization time in the gastric tube and postoperative endoscopic assessment of the anastomosis after esophageal surgery. *Surg Today*. 2020 Nov 1;50(11):1375–82.
18. Jansen SM, de Bruin DM, van Berge Henegouwen MI, Strackee SD, Veelo DP, van Leeuwen TG, et al. Optical techniques for perfusion monitoring of the gastric tube after esophagectomy: a review of technologies and thresholds. *Dis Esophagus*. 2018 Jun 1;31(6).
19. Åkesson O, Heyman I, Johansson J, Rissler P, Falkenback D. Early endoscopic assessment after esophagectomy can predict anastomotic complications: a novel scoring system. *Surg Endosc*. 2022 Mar 1;36(3):1903–9.
20. Page RD, Asmat A, McShane J, Russell GN, Pennefather SH. Routine endoscopy to detect anastomotic leakage after esophagectomy. *Annals of Thoracic Surgery*. 2013 Jan;95(1):292–8.
21. Fujiwara H, Nakajima Y, Kawada K, Tokairin Y, Miyawaki Y, Okada T, et al. Endoscopic assessment 1 day after esophagectomy for predicting cervical esophagogastric anastomosis-relating complications. *Surg Endosc*. 2016 Apr 1;30(4):1564–71.
22. Kobayashi S, Kanetaka K, Yoneda A, Yamaguchi N, Kobayashi K, Nagata Y, et al. Endoscopic mucosal ischemic index for predicting anastomotic complications after esophagectomy: a prospective cohort study. *Langenbecks Arch Surg*. 2023 Jan 17;408(1):37.
23. Pierie JPEN, De Graaf PW, Van Vroonhoven TJM V, Obertopf H. The vascularization of a gastric tube as a substitute for the esophagus is affected by its diameter.
24. Liebermann-Meffert DM, Meier R, Siewert JR. Vascular anatomy of the gastric tube used for esophageal reconstruction. *Ann Thorac Surg*. 1992 Dec;54(6):1110–5.
25. Mingol-Navarro F, Ballester-Pla N, Jimenez-Rosellon R. Ischaemic conditioning of the stomach previous to esophageal surgery. *J Thorac Dis*. 2019 Apr;11(Suppl 5):S663–74.
26. Pather K, Deladisma AM, Guerrier C, Kriley IR, Awad ZT. Indocyanine green perfusion assessment of the gastric conduit in minimally invasive Ivor Lewis esophagectomy. *Surg Endosc*. 2022 Feb 1;36(2):896–903.

Esophageal squamous cell carcinoma (ESCC) is a serious health concern, particularly in regions like Japan and China where incidence rates are notably high. One of the most perilous complications that can arise after surgical removal of the esophagus, known as esophagectomy, is anastomotic leakage. This complication occurs when the connection between the remaining esophagus and the newly created gastric conduit fails to seal properly, leading to leakage of digestive fluids and potentially severe infections. Preventing such leaks is vital and has thus become a focal point in the field of esophageal surgery research.

To address this issue, surgeons have turned to the use of Indocyanine green (ICG) fluorescence during surgery. ICG is a fluorescent dye that, when injected into the bloodstream, emits light that can be detected by special cameras. This technology allows surgeons to evaluate the blood supply at the anastomosis site—a crucial factor in successful healing and prevention of leaks. By ensuring adequate blood flow to the area, surgical techniques can be refined to enhance the perfusion of the gastric conduit, which is the section of the stomach that is connected to the esophagus during reconstruction.

ICG fluorescence-guided surgeries have demonstrated promising results in reducing anastomotic leakage rates. Building on this potential, the study in question explored the effectiveness of a specific surgical modification: altering the incision line on the lesser curvature during the formation of the gastric conduit. The rationale behind this modification is that by changing the angle or position of the cut, one might improve blood flow to the area, thereby boosting the overall perfusion.

The study involved a retrospective analysis of 272 patients who underwent esophagectomy procedures between 2014 and 2022. These patients were divided into two groups based on the type of cutline used for their gastric conduit formation: the conventional group, which followed traditional surgical guidelines, and the current group, which implemented the modified cutline approach.

Using ICG fluorescence imaging, the researchers assessed the perfusion of the gastric conduit in both groups. They also monitored postoperative outcomes, including the rate of anastomotic leakage and the duration of hospital stays. The data revealed that the current group, with the modified cutline, had several advantages over the conventional group. Notably, this group exhibited a longer distance from the pylorus to the cutline, which was associated with significantly higher blood flow speeds within the wall of the gastric conduit. Furthermore, the rate of anastomotic leakage was significantly reduced, and patients in this group tended to have shorter hospital stays compared to those in the conventional group.

Multivariate analysis confirmed that increased blood flow speed in the gastric conduit wall was significantly linked to a reduced risk of leakage. This finding underscores the importance of adequate blood supply in preventing anastomotic leaks and suggests that the modified cutline technique could play a pivotal role in enhancing surgical outcomes.

In conclusion, the study provides evidence that ICG fluorescence imaging is a reliable method for assessing perfusion during esophageal surgeries. The modified cutline technique on the lesser curvature for gastric conduit formation appears to improve perfusion, enhance blood circulation around the anastomosis site, and reduce the likelihood of postoperative leaks. Such findings could lead to changes in surgical practices aimed at minimizing the risk of anastomotic leakage and improving patient recovery times.

2. 執筆論文 Publication of thesis ※記載した論文を添付してください。Attach all of the papers listed below.

論文名 1 Title	Modification of the Lesser Curvature Incision Line Enhanced Gastric Conduit Perfusion as Determined by Indocyanine Green Fluorescence Imaging and Decreased the Incidence of Anastomotic Leakage Following Esophagectomy(Under review).					
掲載誌名 Published journal						
	年	月	巻(号)	頁 ~	頁	言語 Language
第1著者名 First author	Hongbo Zhao		第2著者名 Second author	Kazuo Koyanagi1, MD, PhD		第3著者名 Third author
第3著者名 Third author	Yamato Ninomiya					
その他著者名 Other authors	Akihito Kazuno MD, PhD, Miho Yamamoto, MD, PhD, Yoshiaki Shoji, MD, PhD, Kentaro Yatabe, MD, PhD, Kohei Kanamori MD, PhD, Kohei Tajima, MD, Masaki Mori					
論文名 2 Title	Effective Postoperative Surveillance Protocol after Thoracoscopic Esophagectomy Focusing on Symptoms in Patients with Esophageal Cancer.					
掲載誌名 Published journal	Journal of the American College of Surgeons					
	2023 年	Nov 月	237(5) 巻(号)	771 頁 ~	778 頁	言語 Language
第1著者名 First author	Kohei Tajima1, MD		第2著者名 Second author	uo Koyanagi1, MD, PhD, FA		第3著者名 Third author
第3著者名 Third author	Shoji Ozawa1, MD, PhD, FAC					
その他著者名 Other authors	Akihito Kazuno1, MD, PhD, Miho Yamamoto, MD, PhD, Yoshiaki Shoji, MD, PhD, Kentaro Yatabe, MD, PhD, Kohei Kanamori, MD, PhD, Hongbo Zhao, MD, PhD, Masaki					
論文名 3 Title	Perioperative outcomes of neoadjuvant chemotherapy plus camrelizumab compared with chemotherapy alone and chemoradiotherapy for locally advanced esophageal squamous cell cancer. Front Immunol.					
掲載誌名 Published journal	Frontiers in Immunology					
	2023 年	Feb 月	7;14:1066527 巻(号)	頁 ~	頁	言語 Language
第1著者名 First author	Baihua Zhang,Hongbo Zhao		第2著者名 Second author	Xun Wu		第3著者名 Third author
第3著者名 Third author	Lianghui Gong					
その他著者名 Other authors	Desong Yang1,XuLi, Xiaoyan Chen, Jigang Li, Wenxiang Wang, Jie Wu1 and Qin Xiao					
論文名 4 Title						
掲載誌名 Published journal						
	年	月	巻(号)	頁 ~	頁	言語 Language
第1著者名 First author			第2著者名 Second author			第3著者名 Third author
第3著者名 Third author						
その他著者名 Other authors						
論文名 5 Title						
掲載誌名 Published journal						
	年	月	巻(号)	頁 ~	頁	言語 Language
第1著者名 First author			第2著者名 Second author			第3著者名 Third author
第3著者名 Third author						
その他著者名 Other authors						

3. 学会発表 Conference presentation ※筆頭演者として総会・国際学会を含む主な学会で発表したものを記載してください

※Describe your presentation as the principal presenter in major academic meetings including general meetings or international meetin

学会名 Conference					
演題 Topic					
開催日 date	年	月	日	開催地 venue	
形式 method	<input type="checkbox"/> 口頭発表 Oral	<input type="checkbox"/> ポスター発表 Poster	言語 Language	<input type="checkbox"/> 日本語	<input type="checkbox"/> 英語 <input type="checkbox"/> 中国語
共同演者名 Co-presenter					
学会名 Conference					
演題 Topic					
開催日 date	年	月	日	開催地 venue	
形式 method	<input type="checkbox"/> 口頭発表 Oral	<input type="checkbox"/> ポスター発表 Poster	言語 Language	<input type="checkbox"/> 日本語	<input type="checkbox"/> 英語 <input type="checkbox"/> 中国語
共同演者名 Co-presenter					
学会名 Conference					
演題 Topic					
開催日 date	年	月	日	開催地 venue	
形式 method	<input type="checkbox"/> 口頭発表 Oral	<input type="checkbox"/> ポスター発表 Poster	言語 Language	<input type="checkbox"/> 日本語	<input type="checkbox"/> 英語 <input type="checkbox"/> 中国語
共同演者名 Co-presenter					
学会名 Conference					
演題 Topic					
開催日 date	年	月	日	開催地 venue	
形式 method	<input type="checkbox"/> 口頭発表 Oral	<input type="checkbox"/> ポスター発表 Poster	言語 Language	<input type="checkbox"/> 日本語	<input type="checkbox"/> 英語 <input type="checkbox"/> 中国語
共同演者名 Co-presenter					

4. 受賞(研究業績) Award (Research achievement)

名称 Award name	国名 Country		受賞年 Year of award	年	月
	国名 Country		受賞年 Year of award	年	月

5. 本研究テーマに関わる他の研究助成金受給 Other research grants concerned with your research theme

受給実績 Receipt record	<input type="checkbox"/> 有 <input type="checkbox"/> 無
助成機関名称 Funding agency	
助成金名称 Grant name	
受給期間 Supported period	年 月 ~ 年 月
受給額 Amount received	円
受給実績 Receipt record	<input type="checkbox"/> 有 <input type="checkbox"/> 無
助成機関名称 Funding agency	
助成金名称 Grant name	
受給期間 Supported period	年 月 ~ 年 月
受給額 Amount received	円

6. 他の奨学金受給 Another awarded scholarship

受給実績 Receipt record	<input type="checkbox"/> 有 <input type="checkbox"/> 無
助成機関名称 Funding agency	
奨学金名称 Scholarship name	
受給期間 Supported period	年 月 ~ 年 月
受給額 Amount received	円

7. 研究活動に関する報道発表 Press release concerned with your research activities

※記載した記事を添付してください。Attach a copy of the article described below

報道発表 Press release	<input type="checkbox"/> 有 <input type="checkbox"/> 無	発表年月日 Date of release	
発表機関 Released medium			
発表形式 Release method	・新聞 ・雑誌 ・Web site ・記者発表 ・その他()		
発表タイトル Released title			

8. 本研究テーマに関する特許出願予定 Patent application concerned with your research theme

出願予定 Scheduled	<input type="checkbox"/> 有 <input type="checkbox"/> 無	出願国 Application	
出願内容(概要) Application contents			

9. その他 Others

--

指導責任者(記名) 小柳 和夫



OPEN ACCESS

EDITED BY

Zhihao Lu,
Beijing Cancer Hospital, Peking University,
China

REVIEWED BY

Kezhou Zhu,
Life Sciences Institute, University of
Michigan, United States
Tong Wu,
Purdue University Indianapolis,
United States

*CORRESPONDENCE

Jie Wu

✉ wujie@hnca.org.cn

Qin Xiao

✉ xiaoqin2501@hnca.org.cn

[†]These authors have contributed
equally to this work and share
first authorship

SPECIALTY SECTION

This article was submitted to
Cancer Immunity
and Immunotherapy,
a section of the journal
Frontiers in Immunology

RECEIVED 11 October 2022

ACCEPTED 25 January 2023

PUBLISHED 07 February 2023

CITATION

Zhang B, Zhao H, Wu X, Gong L, Yang D,
Li X, Chen X, Li J, Wang W, Wu J and
Xiao Q (2023) Perioperative outcomes of
neoadjuvant chemotherapy plus
camrelizumab compared with
chemotherapy alone and
chemoradiotherapy for locally advanced
esophageal squamous cell cancer.
Front. Immunol. 14:1066527.
doi: 10.3389/fimmu.2023.1066527

COPYRIGHT

© 2023 Zhang, Zhao, Wu, Gong, Yang, Li,
Chen, Li, Wang, Wu and Xiao. This is an
open-access article distributed under the
terms of the [Creative Commons Attribution
License \(CC BY\)](https://creativecommons.org/licenses/by/4.0/). The use, distribution or
reproduction in other forums is permitted,
provided the original author(s) and the
copyright owner(s) are credited and that
the original publication in this journal is
cited, in accordance with accepted
academic practice. No use, distribution or
reproduction is permitted which does not
comply with these terms.

Perioperative outcomes of neoadjuvant chemotherapy plus camrelizumab compared with chemotherapy alone and chemoradiotherapy for locally advanced esophageal squamous cell cancer

Baihua Zhang^{1†}, Hongbo Zhao^{2†}, Xun Wu¹, Lianghai Gong¹,
Desong Yang¹, Xu Li¹, Xiaoyan Chen³, Jigang Li³,
Wenxiang Wang¹, Jie Wu^{1*} and Qin Xiao^{4*}

¹The Second Department of Thoracic Surgery, Hunan Clinical Medical Research Center of Accurate Diagnosis and Treatment for Esophageal Carcinoma, Hunan Cancer Hospital and The Affiliated Cancer Hospital of Xiangya School of Medicine, Central South University, Changsha, China, ²Department of Thoracic Surgery, National Cancer Center/National Clinical Research Center for Cancer/Cancer Hospital and Shenzhen Hospital, Chinese Academy of Medical Sciences and Peking Union Medical College, Shenzhen, China, ³Department of Pathology, Hunan Cancer Hospital and The Affiliated Cancer Hospital of Xiangya School of Medicine, Central South University, Changsha, China, ⁴Key Laboratory of Translational Radiation Oncology, Hunan Province, The First Department of Thoracic Radiation Oncology, Hunan Cancer Hospital, The Affiliated Cancer Hospital of Xiangya School of Medicine, Central South University, Changsha, Hunan, China

Purpose: Neoadjuvant chemoimmunotherapy (nCIT) is becoming a new therapeutic frontier for resectable esophageal squamous cell carcinoma (ESCC); however, crucial details and technical know-how regarding surgical techniques and the perioperative challenges following nCIT remain poorly understood. The study investigated and compared the advantages and disadvantages of esophagectomy following nCIT with neoadjuvant chemotherapy (nCT) and chemoradiotherapy (nCRT).

Methods: We retrospectively analyzed data of patients initially diagnosed with resectable ESCC at clinical stage T2-4N+ and received neoadjuvant therapy followed by esophagectomy at the Hunan Cancer Hospital between October 2014 and February 2021. Patients were divided into three groups according to neoadjuvant treatment: (i) nCIT; (ii) nCT; and (iii) nCRT.

Results: There were 34 patients in the nCIT group, 97 in the nCT group, and 31 in the nCRT group. Compared with nCT, nCIT followed by esophagectomy achieved higher pathological complete response (pCR; 29.0% versus 4.1%, $p < 0.001$) and major pathological response (MPR; 52.9% versus 16.5%, $p < 0.001$) rates, more resected lymph nodes during surgery (25.06 ± 7.62 versus 20.64 ± 9.68 , $p = 0.009$), less intraoperative blood loss (200.00 ± 73.86 versus 266.49 ± 176.29 mL, $p = 0.035$), and comparable results in other perioperative parameters. Compared with nCRT, nCIT achieved similar pCR (29.0% versus 25.8%) and MPR (52.9% versus 51.6%, $p = 0.862$) rates, with significantly more lymph nodes resected

during surgery (25.06 ± 7.62 versus 16.94 ± 7.24 , $p < 0.001$), shorter operation time (267.79 ± 50.67 versus 306.32 ± 79.92 min, $p = 0.022$), less intraoperative blood loss (200.00 ± 73.86 versus 264.53 ± 139.76 mL, $p = 0.022$), and fewer ICU admissions after surgery (29.4% versus 80.6%, $p < 0.001$). Regarding perioperative adverse events and complications, no significant statistical differences were detected between the nCIT and the nCT or nCRT groups. The 3-year overall survival rate after nCIT was 73.3%, slightly higher than 46.1% after nCT and 39.7% after nCRT, with no statistically significant differences ($p = 0.883$).

Conclusions: This clinical analysis showed that nCIT is safe and feasible, with satisfactory pCR and MPR rates. Esophagectomy following nCIT has several perioperative advantages over nCT and nCRT, with comparable perioperative morbidity and mortality. The long-term survival benefits after nCIT still requires further investigation.

KEYWORDS

neoadjuvant therapy, programmed cell death protein-1 inhibitors, immunotherapy, esophagectomy, neoadjuvant chemoradiotherapy, esophageal squamous cell carcinoma

Introduction

In 2020, esophageal carcinoma was the seventh most prevalent cancer and sixth leading cause of cancer-related death worldwide (1). The predominant esophageal cancer subtype in Asia is esophageal squamous cell carcinoma (ESCC) (2). ESCC accounts for over 84% of newly diagnosed esophageal cancers annually (3, 4). Surgical resection remains the gold standard for patients with locally advanced resectable ESCC. However, studies have shown that local recurrence and distant metastasis occur in approximately 33% of patients who receive surgery alone (5, 6). Thus, ESCC treatment is challenging and requires a multidisciplinary approach to improve the surgical therapeutic effect in locally advanced resectable disease.

Following the launch of a new era in immunotherapy (including programmed cell death-ligand 1 [PD-L1] and programmed cell death protein-1 [PD-1] inhibitors), further exploration of neoadjuvant immunotherapy alone or combined with chemotherapy or chemoradiotherapy is expected to further improve the therapeutic effect in locally advanced resectable ESCC. In a recent systematic review including 27 phase 2 or 3 clinical trials with 815 patients, the pooled pathological complete response (pCR) rate was 32.4% in ESCC after neoadjuvant chemoimmunotherapy (nCIT), with the pooled incidence of treatment-related severe adverse events of 26.9% (7). Zhu et al. reported that neoadjuvant immunochemoradiotherapy could not improve the pCR rate than neoadjuvant chemoradiotherapy (nCRT) for ESCC, but significantly increased the risk of severe adverse events (8). Another multicenter retrospective study that included 370 ESCC patients showed that the pCR rates of mono-immunotherapy, nCIT, and nCRT plus immunotherapy were 12.1%, 25.5%, and 42.3%, respectively (9). Hence, neoadjuvant PD-1/PD-L1 inhibitors in combination with chemotherapy or chemoradiotherapy are becoming a new therapeutic frontier for resectable ESCC with promising clinical outcomes. However, long-term follow-up are warranted to validate the survival benefits of nCIT or nCRT plus immunotherapy.

Camrelizumab is a PD-1 inhibitor produced in China by Jiangsu Hengrui Pharmaceuticals Co, Ltd. (Lianyungang, China). The ESCORT-1st study showed that first-line camrelizumab plus chemotherapy could achieve better disease control and long-term survival in advanced ESCC than chemotherapy alone (10). Several prospective phase-II clinical trials have also demonstrated that after neoadjuvant chemotherapy plus camrelizumab (nCIT) for ESCC, pCR rates ranged from 24.1% to 42.5%, with major pathological response (MPR) rates of between 45% and 68.8% (11–14). However, these sample sizes were small, and only a few studies reported survival results. Additionally, crucial details and technical know-how regarding the surgical techniques and perioperative challenges following nCIT are still poorly understood.

In the present study, we retrospectively reviewed the perioperative outcomes of esophagectomy following nCIT to compare it with surgery after nCT and nCRT. This study aimed to investigate the potential advantages and disadvantages of esophagectomy after nCIT.

Patients and methods

Inclusion and exclusion criteria

This is a retrospective, single-center, observational study. Patients initially diagnosed with resectable ESCC at clinical stages T2-4N+ (American Joint Committee on Cancer, 8th edition) and received neoadjuvant therapy followed by curative-intent surgery between October 2014 and February 2021 at the Hunan Cancer Hospital were recruited. The Eastern Cooperative Oncology Group's performance status of all patients was 0 or 1. Patients were included on the basis of the following criteria; (1): only squamous cell carcinoma components; (2); thoracic ESCC; (3); patients who received neoadjuvant chemotherapy (nCT), nCIT (only camrelizumab), or nCRT followed by esophagectomy; and (4) the

chemotherapy regimens only consisted of paclitaxel and platinum. The exclusion criteria were as follows; (1): pathological non-squamous cell carcinoma components; (2); patients with unresectable primary tumors, more than seven lymph node metastases (N3), or distant metastasis (M1) before neoadjuvant treatment; (3); patients with previous cancer type(s) or other concurrent malignant tumors; (4); patients that received other forms of treatment before surgery; and (5) incomplete medical records.

All clinical data were obtained from medical records and retrospectively analyzed. This study was conducted per the Declaration of Helsinki (as revised in 2013). The Ethics Committee of Hunan Cancer Hospital approved this study (No. 2022097), and patients' written informed consent was obtained.

Neoadjuvant treatment modalities

Patients were retrospectively divided into three groups according to the neoadjuvant treatment modality they received; (1): the nCT group, including patients who received one to four cycles of paclitaxel combined with platinum chemotherapy (21 days per cycle); (2); the nCIT group, including patients who received conventional chemotherapy (1–4 cycles of paclitaxel and platinum) and camrelizumab (200 mg) on the first day of each cycle; and (3) the nCRT group, including patients who received concurrent chemotherapy (1–4 cycles of paclitaxel and platinum) and radiotherapy (6-MV X-ray, 39.6–45.0 Gy/1.8–2.0 Gy/f) before esophagectomy.

Surgery and adjuvant therapy

Generally, patients would receive a tumor re-evaluation within 2 to 6 weeks after the last neoadjuvant treatment cycle. Following multidisciplinary discussion, a curative-intent surgical resection was immediately performed when the tumor was considered operable. Overall, esophagectomy with the stomach as the esophageal substitute and cervical or thoracic anastomosis were performed in all patients, while experienced surgeons regularly conducted a standard 2-field lymphadenectomy. Cervical lymphadenectomy (3-field) was performed only when lymph node metastasis was suspected in the neck region.

Adjuvant treatments were then performed on the basis of pathological tumor stage and each patient's recovery condition. After multidisciplinary discussion, postoperative chemoradiotherapy or chemotherapy alone might be recommended for patients with ypN + or palliative resection. In the nCIT group, adjuvant therapy with camrelizumab might be recommended for 1 year after surgery.

Outcome measures and follow-up

As reported in previous studies (15, 16), pCR was defined as no viable tumor cells in the resected specimen. In contrast, MPR was defined as <10% viable residual tumor cells detected in the specimen. Pathological responses were evaluated independently by two

experienced pathologists. Treatment-related adverse events (TRAEs) were graded as per the National Cancer Institute Common Terminology Criteria for Adverse Events (CTCAE) version 5.0. Weight loss at initial diagnosis was defined as weight loss detected within six months before the diagnosis of ESCC. Operation time was calculated from incision to wound closure.

Radiographic evaluations were conducted every 3 months for the first 2 years after surgery, and then every 6 months thereafter. Whenever recurrence was suspected, rebiopsy and/or 18F-FDG positron emission tomography-computed tomography (PET-CT) or both were performed to identify the possible recurrence.

Statistical analysis

The primary endpoint was the MPR rate, and the secondary endpoints were the pCR, perioperative morbidity, and 3-year OS rates. OS was defined as the time (in months) from surgery to the date of death or the last follow-up. Survival analyses were calculated and compared using Kaplan–Meier curves and the log-rank test.

Differences in clinicopathological features between groups were calculated using the chi-square (χ^2) test or *t*-test. SPSS software 23.0 (IBM Corp., Armonk, NY, USA) was used to perform all statistical analyses. A *p*-value <0.05 (two-sided) was considered to be statistically significant.

Results

Overview of patient cohorts

Between October 2014 and February 2021, 194 patients were screened for eligibility. Eventually, 162 patients were enrolled for further analysis (34 patients in the nCIT group, 97 in the nCT group, and 31 in the nCRT group) (Figure 1). All 162 patients in the study finished one to four cycles of neoadjuvant therapy. As summarized in Table 1, the enrolled patients in the nCIT group have a mean age of 60.68 ± 7.44 years old and predominantly consisted of males (91.2%), which were consistent with the nCT and nCRT groups. No significant differences were detected between the nCIT and the nCT or nCRT groups in other baseline characteristics, including cigarette consumption, alcohol abuse, weight loss at initial diagnosis, body mass index, tumor location, tumor length, cN, and pathological differentiation. However, the cT4 percentage in the nCIT group was 35.3%, which was significantly higher than in the nCT group (16.5%, $p=0.021$) but comparable to that in the nCRT group (19.4%, $p=0.238$).

Perioperative outcomes

All patients successfully received esophagectomy and most achieved radical resection with no significant statistical differences (Table 2). The time interval between final neoadjuvant therapy and surgery in the nCIT group was 35.91 ± 6.76 days, which was significantly longer than in the nCT group (32.70 ± 7.56 days, $p=0.024$) but shorter than in the nCRT group (41.87 ± 10.60 days,

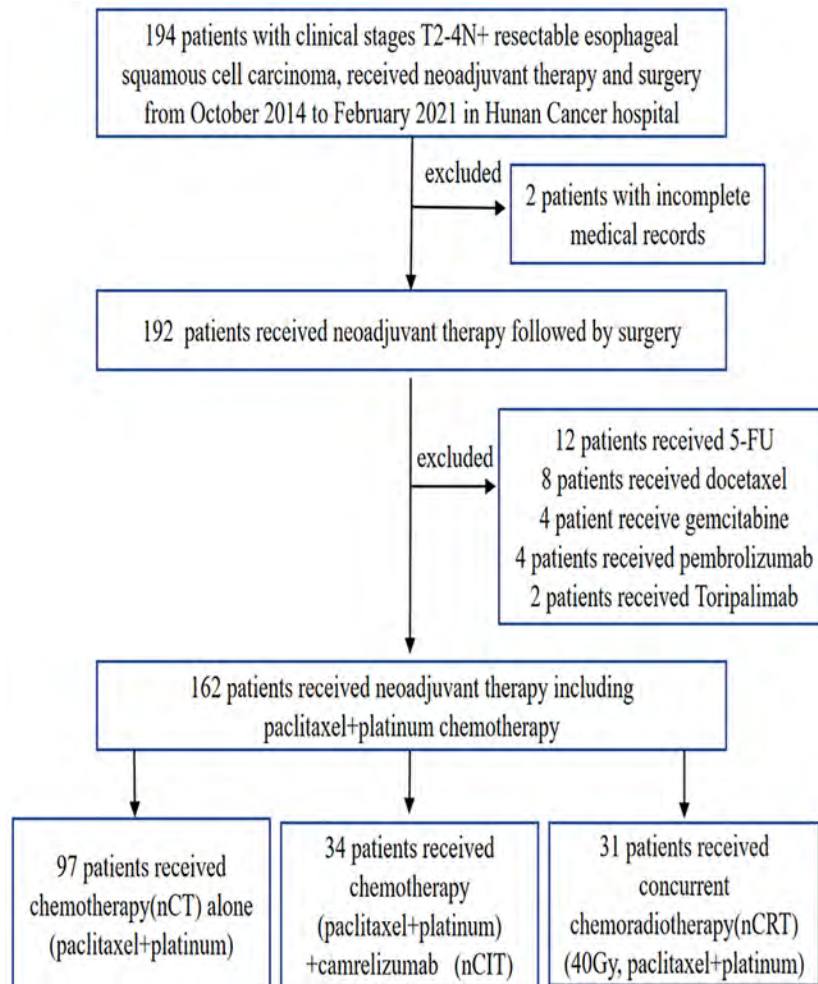


FIGURE 1
Patient selection flowchart.

$p=0.010$). Patients in the nCIT group (267.79 ± 50.67 min) required a shorter operation time than those in the nCRT group (306.32 ± 79.92 min, $p=0.022$). Meanwhile, no significant difference was detected between the nCIT and nCT groups (291.40 ± 71.48 min, $p=0.078$). Additionally, intraoperative blood loss in the nCIT group (200.00 ± 73.86 mL) was less than in the nCT (266.49 ± 176.29 mL, $p=0.035$) and nCRT (264.53 ± 139.76 mL, $p=0.022$) groups. Notably, 2-field lymphadenectomy was the principal method for lymph node resection in all groups. However, the average number of resected lymph nodes in the nCIT group (25.06 ± 7.62) was significantly higher than in the other two groups ($p=0.009$, $p<0.001$, respectively).

Three-incisional esophagectomy with anastomosis in the neck was the principal surgery in all three groups. As summarized in Table 2, no significant differences were detected between the groups in the total drainage after operation, duration of chest tube, and hospital stay after surgery. The frequency of ICU stay after surgery in the nCIT group (29.4%) was comparable with that in the nCT group (32.0%, $p=0.783$) but significantly lower than in the nCRT group (80.6%, $p<0.001$).

Pathological efficacy

In the pathological analysis after surgery, MPR was observed in 18 patients in the nCIT group (52.9%), including nine primary tumor pCRs (26.4%) (8 T0N0 [23.5%], 1 T0N+ [2.9%]), and nine patients (26.5%) had 1% to 10% viable residual tumor cells detected in the specimens. In the nCT group, MPR was achieved in 16 patients (16.5%), including four primary tumor pCRs (4.1%) (3 T0N0 [3.1%], 1 T0N+ [1.0%]), which was significantly lower than in the nCIT group ($p<0.001$). In the nCRT group, 16 patients (51.6%) achieved MPR, including eight primary tumor pCRs (25.8%) (7 T0N0 [22.6%], 1 T0N+ [3.2%]), which was similar to the nCIT group ($p=0.862$).

Accordingly, the ypT0-2 percentage in the nCIT group (67.6%) was also significantly higher than in the nCT group (39.2%, $p=0.004$) but similar to the nCRT group (58.1%, $p=0.424$). No significant differences were detected between the groups for other pathological parameters including ypN stage, ypTNM stage, positive lymph node number, and lymphovascular invasion (LVI), or perineural invasion. After surgery, approximately half of the patients received adjuvant

TABLE 1 Clinical characteristics for ESCC patients received neoadjuvant therapy.

Variables	nCIT (n=34)	nCT (n=97)	P value	nCIT (n=34)	nCRT (n=31)	P value
Age						
Mean \pm SD ^a , y	60.68 \pm 7.44	60.08 \pm 7.78	0.699	60.68 \pm 7.44	57.23 \pm 6.79	0.056
Gender						
Male	31 (91.2)	94 (96.9)	0.169	31 (91.2)	30 (96.8)	0.348
Female	3 (8.8)	3 (3.1)		3 (8.8)	1 (3.2)	
Cigarette consumption						
Former/current	30 (88.2)	86 (88.7)	0.947	30 (88.2)	27 (87.1)	0.889
No	4 (11.8)	11 (11.3)		4 (11.8)	4 (12.9)	
Alcohol abuse						
Former/current	28 (82.4)	78 (80.4)	0.804	28 (82.4)	29 (93.5)	0.170
No	6 (17.6)	19 (19.6)		6 (17.6)	2 (6.5)	
Weight loss at initial diagnosis						
Yes	21 (61.8)	50 (51.5)	0.303	21 (61.8)	15 (48.4)	0.279
No	13 (38.2)	47 (48.5)		13 (38.2)	16 (51.6)	
BMI index						
Mean \pm SD ^a	21.82 \pm 2.74	21.35 \pm 3.17	0.442	21.82 \pm 2.74	21.77 \pm 1.91	0.932
Tumor location						
Upper thoracic	3 (8.8)	10 (10.3)	0.642	3 (8.8)	4 (12.9)	0.169
Middle thoracic	11 (32.4)	39 (40.2)		11 (32.4)	16 (51.6)	
Lower thoracic	20 (58.8)	48 (49.5)		20 (58.8)	11 (35.5)	
Tumor length before treatment						
Mean \pm SD ^a , cm	5.36 \pm 1.81	5.11 \pm 1.89	0.512	5.36 \pm 1.81	5.21 \pm 1.72	0.736
cT						
T2/3	22 (64.7)	81 (83.5)	0.021	22 (64.7)	25 (80.6)	0.151
T4	12 (35.3)	16 (16.5)		12 (35.3)	6 (19.4)	
cN						
N1	17 (50.0)	59 (60.8)	0.271	17 (50.0)	11 (35.5)	0.238
N2	17 (50.0)	38 (39.2)		17 (50.0)	20 (64.5)	
Pathological differentiation						
Poor/moderate	27 (79.4)	70 (72.2)	0.407	27 (79.4)	27 (87.1)	0.409
Well	7 (20.6)	27 (27.8)		7 (20.6)	4 (12.9)	

^aVariables were described by mean (x) and standard deviation (s).

ESCC, esophageal squamous cell carcinoma; cT, clinical T stage before treatment; cN, clinical N stage before treatment; nCT, neoadjuvant chemotherapy; nCIT, neoadjuvant chemotherapy plus Camrelizumab; nCRT, neoadjuvant chemoradiotherapy.

therapy, with no statistically significant difference observed among the three groups.

Perioperative adverse events and complications

The adverse events related to neoadjuvant therapy are summarized in Table 3. The frequency of adverse events in the

nCIT group was 47.1%, which was comparable with the nCT and nCRT groups. Regarding CTCAE grade, the frequency of severe adverse events (grade III/IV) in the nCIT group was 25.0%, which was similar to the 16.2% and 41.1% in the nCT and nCRT groups, respectively. No deaths related to neoadjuvant therapy (CTCAE grade V) were observed in any group. As to the adverse event types, myelosuppression and erythra were the principal events in the nCIT group, which was different from that of myelosuppression and gastrointestinal react in the nCT group ($p=0.002$).

TABLE 2 The perioperative outcomes of esophagectomy after neoadjuvant therapy.

Variables	nCIT (n=34)	nCT (n=97)	P value	nCIT (n=34)	nCRT (n=31)	P value
Interval days						
$x \pm s^a$ (day)	35.91 \pm 6.76	32.70 \pm 7.56	0.024	35.91 \pm 6.76	41.87 \pm 10.60	0.010
Surgical radicality						
Radical	33 (97.1)	89 (91.8)	0.293	33 (97.1)	29 (93.5)	0.500
Palliative	1 (2.9)	8 (8.2)		1 (2.9)	2 (6.5)	
Operation time						
$x \pm s^a$ (min)	267.79 \pm 50.67	291.40 \pm 71.48	0.078	267.79 \pm 50.67	306.32 \pm 79.92	0.022
Intraoperative blood loss						
$x \pm s^a$ (ml)	200.00 \pm 73.86	266.49 \pm 176.29	0.035	200.00 \pm 73.86	264.53 \pm 139.76	0.022
Extent of lymph node resection						
2-field	34 (100.0)	96 (99.0)	0.552	34 (100.0)	30 (96.8)	0.291
3-field	0	1 (1.0)		0	1 (3.2)	
Resected lymph nodes number						
$x \pm s^a$	25.06 \pm 7.62	20.64 \pm 9.68	0.009	25.06 \pm 7.62	16.94 \pm 7.24	< 0.001
Anastomosis position						
Neck	33 (97.1)	90 (92.8)	0.370	33 (97.1)	26 (83.9)	0.067
Thoracic	1 (2.9)	7 (7.2)		1 (2.9)	5 (16.1)	
Total drainage after operation						
$x \pm s^a$ (ml)	1925.29 \pm 2239.05	2476.25 \pm 3335.70	0.285	1925.29 \pm 2239.05	3664.35 \pm 6581.08	0.151
Duration of chest tube						
$x \pm s^a$ (day)	8.00 \pm 4.70	8.78 \pm 3.47	0.378	8.00 \pm 4.70	11.42 \pm 19.98	0.336
ICU stay after surgery						
Yes	10 (29.4)	31 (32.0)	0.783	10 (29.4)	25 (80.6)	< 0.001
No	24 (70.6)	66 (68.0)		24 (70.6)	6 (19.4)	
Hospital stays after surgery						
$x \pm s^a$ (day)	12.76 \pm 7.30	12.27 \pm 4.71	0.713	12.76 \pm 7.30	15.65 \pm 19.38	0.423
Pathological response						
MPR	18 (52.9)	16 (16.5)	< 0.001	18 (52.9)	16 (51.6)	0.862
PR	9 (26.5)	48 (49.5)		9 (26.5)	7 (22.6)	
SD/PD	7 (20.6)	33 (34.0)		7 (20.6)	8 (25.8)	
ypT stage						
T0-2	23 (67.6)	38 (39.2)	0.004	23 (67.6)	18 (58.1)	0.424
T3-4	11 (32.4)	59 (60.8)		11 (32.4)	13 (41.9)	
ypN stage						
N-	20 (58.8)	45 (46.4)	0.212	20 (58.8)	18 (58.1)	0.951
N+	14 (41.2)	52 (53.6)		14 (41.2)	13 (41.9)	
ypTNM stage						

(Continued)

TABLE 2 Continued

Variables	nCIT (n=34)	nCT (n=97)	P value	nCIT (n=34)	nCRT (n=31)	P value
0-II	22 (64.7)	45 (46.4)	0.179	22 (64.7)	20 (64.5)	0.839
III	9 (26.5)	41 (42.3)		9 (26.5)	7 (22.6)	
IVA	3 (8.8)	11 (11.3)		3 (8.8)	4 (12.9)	
Positive lymph nodes number						
$\bar{x} \pm s^a$	1.32 \pm 2.43	1.51 \pm 2.36	0.707	1.32 \pm 2.43	1.06 \pm 1.98	0.642
LVI/perineural invasion						
Yes	6 (17.6)	14 (14.4)	0.654	6 (17.6)	2 (6.5)	0.170
No	28 (82.4)	83 (85.6)		28 (82.4)	29 (93.5)	
Adjuvant therapy						
Yes	20 (58.8)	46 (47.4)	0.253	20 (58.8)	15 (48.4)	0.399
No	14 (41.2)	51 (52.6)		14 (41.2)	16 (51.6)	

^aVariables were described by mean (\bar{x}) and standard deviation (s).

nCIT, neoadjuvant chemotherapy plus Camrelizumab; nCT, neoadjuvant chemotherapy; nCRT, neoadjuvant chemoradiotherapy; Interval days, interval days between final neoadjuvant therapy and surgery; ypT, pathological T stage after neoadjuvant therapy; ypN, pathological N stage after neoadjuvant therapy; ypTNM, pathological TNM stage after neoadjuvant therapy; ICU, intensive care unit; LVI, lymphovascular invasion; MPR, major pathological response; PR, partial response; SD, stable disease; PD, progressive disease.

Postoperative complications related to surgery within 30 days occurred in 17 patients (50.0%) in the nCIT group, approximately 37 patients (38.1%) in the nCT group, and 13 patients (41.9%, $p=0.227$) in the nCRT group ($p=0.515$) (Table 4). The principal complications included pulmonary complications, anastomotic leakage, hoarseness, and cardiac complications, and these were unrelated to the neoadjuvant therapeutic modality. One patient in the nCIT group received

a reoperation within 30 days due to diaphragmatic hernia and chyle, four patients in the nCT group due to anastomotic leakage or tracheostomy, and one patient in the nCRT group due to intrathoracic anastomotic leakage.

Only one patient suffered from sudden death, which was 11 days after surgery, and the patient was in the nCT group. The 90-day mortality rate was 8.8% in the nCIT group, and 7.2% in the nCT group ($p=0.761$), while no deaths within 90 days were observed in the

TABLE 3 The adverse events of neoadjuvant therapy.

Variables	nCIT (n=34)	nCT (n=97)	P value	nCIT (n=34)	nCRT (n=31)	P value
Adverse events						
Yes	16 (47.1)	37 (38.1)	0.362	16 (47.1)	17 (54.8)	0.531
No	18 (52.9)	60 (61.9)		18 (52.9)	14 (45.2)	
CTCAE grade						
Any grade	N=16	N=37		N=16	N=17	
I	6 (37.5)	15 (40.5)	0.765	6 (37.5)	4 (23.5)	0.596
II	6 (37.5)	16 (43.2)	0.877	6 (37.5)	6 (35.3)	0.859
III	2 (12.5)	3 (8.1)	0.465	2 (12.5)	4 (23.5)	0.329
IV	2 (12.5)	3 (8.1)	0.465	2 (12.5)	3 (17.6)	0.566
V	0	0		0	0	
Adverse event types						
Myelosuppression	7 (43.8)	18 (48.6)	0.002	7 (43.8)	12 (70.6)	0.129
Erythra	7 (43.8)	1 (2.7)		7 (43.8)	1 (5.9)	
Hepatic dysfunction	1 (6.3)	4 (10.8)		1 (6.3)	1 (5.9)	
Gastrointestinal react	1 (6.3)	12 (32.4)		1 (6.3)	2 (11.8)	
Renal dysfunction	0	2 (5.49)		0	1 (5.9)	

nCT, neoadjuvant chemotherapy; nCIT, neoadjuvant chemotherapy plus Camrelizumab; nCRT, neoadjuvant chemoradiotherapy; CTCAE, Common Terminology Criteria for Adverse Events (version 5.0).

TABLE 4 Perioperative complications within 30 days after surgery and mortality.

Variables	nCIT (n=34)	nCT (n=97)	P value	nCIT (n=34)	nCRT (n=31)	P value
Postoperative complications						
Yes	17 (50.0)	37 (38.1)	0.227	17 (50.0)	13 (41.9)	0.515
No	17 (50.0)	58 (61.9)		17 (50.0)	18 (58.1)	
Complication types	n=17	n=37		n=17	n=13	
Hoarseness	2 (11.8)	6 (16.2)		2 (11.8)	1 (7.7)	
Pulmonary complications	7 (41.7)	10 (27.0)		7 (41.7)	3 (23.1)	
Cardiac complications	2 (11.8)	1 (2.7)		2 (11.8)	2 (15.4)	
Chyle	1 (5.9)	3 (8.1)		1 (5.9)	0	
Anastomotic leakage	2 (11.8)	8 (21.6)		2 (11.8)	4 (30.8)	
Gastric and intestinal complications	1 (5.9)	3 (8.1)		1 (5.9)	0	
Other complications	2 (11.8)	6 (16.2)		2 (11.8)	3 (23.1)	
Reoperation in 30 days						
No	33 (97.1)	93 (95.9)	0.757	33 (97.1)	30 (96.8)	0.947
Yes	1 (2.9)	4 (4.1)		1 (2.9)	1 (3.2)	
30-day mortality						
No	34 (100.0)	96 (99.0)	0.552	34 (100.0)	31 (100.0)	1.000
Yes	0	1 (1.0)		0	0	
90-day mortality						
No	31 (91.2)	90 (92.8)	0.761	31 (91.2)	31 (100.0)	0.09
Yes	3 (8.8)	7 (7.2)		3 (8.8)	0	

nCT, neoadjuvant chemotherapy; nCIT, neoadjuvant chemotherapy plus Camrelizumab; nCRT, neoadjuvant chemoradiotherapy.

nCRT group. No statistically significant difference was found between the nCIT and nCRT groups ($p=0.09$).

Overall survival and analysis of prognostic factors

Until July 30, 2022, the median follow-up of the entire cohort was 20.45 months, with a range of 0.36 to 84.76 months. In the nCIT group, the 1- and 3-year OS rates were 82.4% and 73.3%, respectively, which were not significantly different from the nCT group (77.3% and 46.1%, respectively) and the nCRT group (83.9% and 39.7%, respectively) (Figure 2A, $p=0.883$). Furthermore, the 3-year OS for patients who achieved MPR was 68.7%, which was significantly higher than 46.3% for partial responders and 23.8% for those with stable/progressive disease (Figure 2B, $p<0.001$). Patients who achieved radical esophagectomy attained a much better 3-year OS rate than those who achieved palliative surgery (49.7% versus 0%, Figure 2C, $p<0.001$). In the analysis of postoperative pathological stage, patients with stage ypN- achieved a 3-year OS of 60.6%, which was longer than the 29.0% for patients with ypN+ (Figure 2D, $p<0.001$). Further analysis showed that patients with earlier ypT0-2 and yp0-II staged disease also had better long-term survival rates (Figures 2E, F, $p<0.001$).

Interestingly, the 3-year OS rate of patients with weight loss at initial diagnosis was 38.7%, which was significantly shorter than the 55.8% for patients without weight loss ($p=0.032$). Additionally, the 3-year OS for patients without LVI/perineural invasion was 48.3%, which was longer than the 33.8% for patients with LVI/perineural invasion ($p=0.022$). However, age, sex, body mass index, tumor length at initial diagnosis, tumor location, pathological differentiation, and adjuvant systemic therapy were not significantly correlated with OS in univariate Cox analysis (Table 5).

In the multivariate analysis, which included significant factors identified by univariate analysis, only surgical radicality (hazard ratio [HR]: 5.882, 95% confidence interval [CI]: 2.799–12.359, $p<0.001$), pathological response (HR: 1.493, 95% CI: 1.040–2.143, $p=0.030$), and ypN stage (HR: 2.100, 95% CI: 1.245–3.542, $p=0.005$) were found to be independent prognostic factors for OS other than neoadjuvant modality (Table 5).

Discussion

This study described potential intraoperative technical challenges after nCIT and compared them with other neoadjuvant treatment modalities including nCT and nCRT. Compared with nCT, nCIT followed by esophagectomy achieved higher pCR and MPR rates,

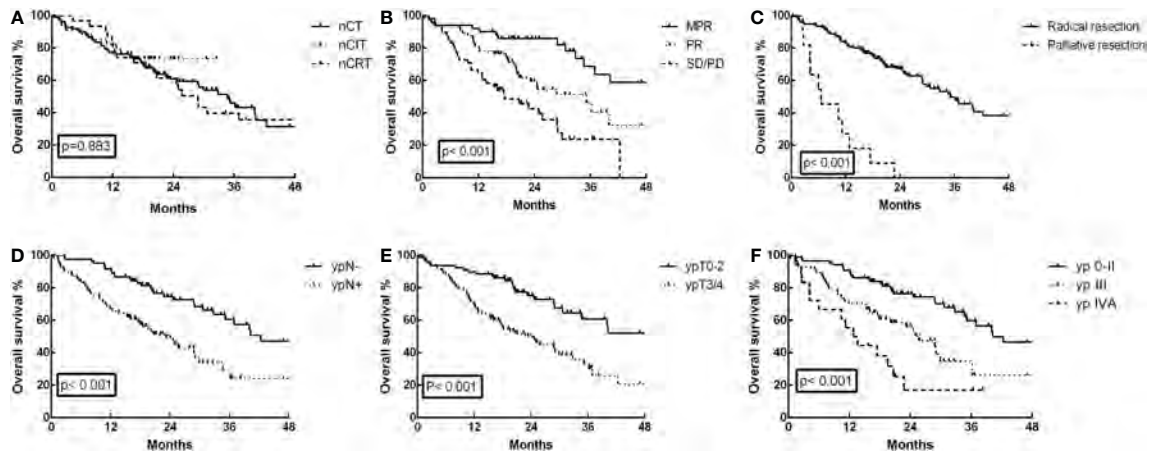


FIGURE 2
Overall survival (OS) curves for the 162 ESCC patients. (A) OS was not significantly different in the neoadjuvant chemoimmunotherapy (nCIT) group compared with the neoadjuvant chemotherapy (nCT) and neoadjuvant chemoradiotherapy (nCRT) groups ($p=0.883$). (B) OS was significantly increased for patients who achieved major pathological response (MPR) compared with those who achieved partial response (PR) and stable disease (SD)/progressive disease (PD) ($p<0.001$). (C) OS was increased for patients who achieved radical esophagectomy compared with those who achieved palliative surgery ($p<0.001$). (D) OS was increased in patients with stage ypN- compared with those who had stage ypN+ ($p<0.001$). (E) OS was increased in patients with stage ypT0-2 compared with those who had stage ypT3/4 ($p<0.001$). (F) OS was increased in patients with stage yp0-II compared with those who had stage ypIII and ypIVA ($p<0.001$).

more resected lymph nodes during surgery, less intraoperative blood loss, and comparable results in other perioperative parameters. Compared with nCRT, nCIT achieved similar pCR and MPR rates, significantly more resected lymph nodes during surgery, shorter operation time, less intraoperative blood loss, and less frequent ICU stays after surgery. Regarding postoperative complications, no

significant statistical difference was detected between the nCIT and the nCT or nCRT groups.

Over the past decade, there have been lingering controversies concerning the effects of neoadjuvant chemotherapy (nCT), chemoradiotherapy (nCRT), and immunotherapy for ESCC. There is still no convincing evidence to prove which neoadjuvant

TABLE 5 Univariate and multivariate analysis of OS for 162 ESCC patients treated with surgery following neoadjuvant therapy.

Characteristics	Univariate		Multivariate	
	HR (95% CI)	P	HR (95% CI)	P
Age (y): < 60 vs ≥ 60	1.039 (0.660-1.634)	0.870		
Gender: Male vs Female	0.564 (0.138-2.299)	0.424		
Weight loss at initial diagnosis: Yes vs No	1.679 (1.047-2.692)	0.032*		
BMI index: < 22 vs ≥ 22	0.870 (0.545-1.390)	0.561		
Tumor length at initial diagnosis: <5 vs ≥ 5 cm	0.981 (0.620-1.553)	0.936		
Tumor location: Lower vs Upper/middle	1.250 (0.793-1.972)	0.337		
Pathological differentiation: Poor/moderate vs Well	1.170 (0.673-2.035)	0.579		
Surgical radicality: Palliative vs Radical	7.415 (3.765-14.605)	<0.001*	5.882 (2.799-12.359)	<0.001
Pathological response: SD(PD) vs PR vs MPR(CR)	2.090 (1.533-2.849)	<0.001*	1.493 (1.040-2.143)	0.030
ypT stage: ypT3-4 vs ypT0-2	2.555 (1.569-4.161)	<0.001*		
ypN stage: ypN+ vs ypN-	2.601 (1.615-4.190)	<0.001*	2.100 (1.245-3.542)	0.005
ypTNM stage: IVA vs III vs 0-II	1.588 (1.300-1.939)	<0.001*		
LVI/perineural invasion: Yes vs No	2.026 (1.105-3.715)	0.022*		
Neoadjuvant therapeutic modality: nCRT vs nCIT vs nCT	0.990 (0.872-1.125)	0.883		
Adjuvant systemic therapy: Yes vs No	0.957(0.606-1.511)	0.849		

*Factors included into multivariate analysis.

ESCC, esophageal squamous cell carcinoma; OS, overall survival; nCIT, neoadjuvant chemotherapy plus Camrelizumab; nCT, neoadjuvant chemotherapy; nCRT, neoadjuvant chemoradiotherapy; ypT, pathological T stage after neoadjuvant therapy; ypN, pathological N stage after neoadjuvant therapy; ypTNM, pathological TNM stage after neoadjuvant therapy; vs, versus; HR, hazard ratio; CI, confidence interval.

therapeutic modality is best for locally advanced resectable ESCC. Pathological responses including pCR and MPR have been considered as principal surrogate endpoints to evaluate the therapeutic efficacy of different neoadjuvant treatments. Previous large-scale randomized clinical trials have reported that nCRT could achieve higher pCR rates (43.2-49%) than nCT (3.8-10.7%) in ESCC, but nCRT might have more postoperative complications and higher postoperative mortality, with no identified overall survival differences (4, 17–24). Therefore, in Western countries, many institutions have adopted nCRT followed by esophagectomy, but globally, many other countries support nCT alone (4, 25).

In this study, the pCR rate for the primary tumor was 26.4%, and the MPR rate was 52.9% after nCIT, consistent with previous reports (9, 11, 12, 26–30). However, after nCT for ESCC, the pCR rate in previous studies is usually between 3.8% and 10.7% (23, 24, 31), which is close to the 4.1% for the primary tumor in this study and significantly lower than the results for nCIT. In contrast, the pCR rate for nCRT has reached approximately 28.9% to 49% in previous studies, which is slightly better than the 25.8% in this study (21, 24, 31–33). Xu et al. demonstrated that the pCR rate was comparable between nCIT and nCRT (29.8% vs 34.0%), with no significant differences in the incidence of postoperative complications and 30-day mortality (34). Thus, this study showed that ESCC might achieve better therapeutic efficacy from nCIT and nCRT on the basis of pCR and MPR results.

Although the pathological efficacy was better for nCIT and nCRT, controversies concerning the long-term survival results remained. Previous prospective trials on esophageal cancer, including JCOG9907, OEO2, CROSS, and NEOCRTEC5010 have demonstrated that nCT or nCRT can achieve better OS results than surgery alone or postoperative chemotherapy (20, 21, 32, 35). Nonetheless, survival differences between different neoadjuvant therapeutic modalities have not been clarified. Klevebro et al. and Wang et al. showed that nCRT could result in a higher pCR rate than nCT, but with no significant survival benefits (24, 31). Another study showed no significant differences in the 5-year OS or the 5-year relapse-free survival (RFS) rates between nCRT and nCT (36). Two separate meta-analyses also reported that nCRT did not show significant long-term survival benefits as nCT (37, 38). In this study, the 1-year OS rate in the nCIT group were 82.4%, consistent with the 1-year OS of between 87.6% and 92.8% in previous reports (29, 39), but not significantly different from nCT (77.3%) and nCRT (83.9%). In a few propensity score matching analyses, the 1-year OS rate in the nCIT group was 94.5-95.7%, slightly better than 84.8% in the nCT group and 86.2% in the nCRT group, but with no significant statistical differences (40, 41). Although no statistically significant difference was observed in our data, the 3-year OS after nCIT was 73.3%, slightly higher than 46.1% after nCT and 39.7% after nCRT. However, the sample size and follow-up time in the present study were too limited to report mature OS results. Therefore, the survival benefit after nCIT in locally advanced resectable ESCC still requires further investigation. Furthermore, as previously reported (4, 36, 42), our further analysis showed that radical esophagectomy, MPR, and ypN0 (no lymph node metastasis) were independent favorable prognostic factors for OS after neoadjuvant therapy. As to adjuvant therapy, approximately half of the patients received adjuvant therapy in each group, and no statistically significant difference was observed

among the three groups. No survival difference was observed between patients received adjuvant therapy or not in our analysis.

This study also highlighted advantages for esophagectomy, as nCIT had more lymph nodes resected and less intraoperative blood loss compared with nCT. During our surgery, tumor and metastatic lymph nodes regression was more significant in the nCIT group than in the nCT group, facilitating lymph node clearance and reducing operation times. Qiao et al. also reported that patients who received nCIT had more lymph nodes cleared during surgery than those who received nCT (34 vs. 30, $p < 0.001$), with comparable incidence of complications (23). Furthermore, when compared with nCRT, esophagectomy after nCIT also achieved more resected lymph nodes, shorter operation times, less intraoperative blood loss, and less frequent ICU stays after surgery. Based on our surgical experience, mild or moderate tissue adhesions were more frequently observed in the nCIT group compared to the nCRT group, which might help reduce the intraoperative difficulties. In certain propensity score matching analyses by Hong et al. and Xiao et al, esophagectomy after nCIT required shorter operative times, and dissected more lymph nodes than after nCRT (41, 43). Cheng et al. also reported that the nCIT group had minimal intraoperative blood loss, shorter operative times, and fewer perioperative complications than the nCRT group (37). However, the extent of lymph node resection and positive lymph node numbers after nCIT were similar to after nCT and nCRT in this study. Regarding other perioperative parameters such as radical resection rate and several postoperative recovery parameters, no significant differences were detected among the three groups.

Perioperative morbidity and mortality are the principal concerns in surgical treatment following neoadjuvant therapy. This study detected no significant statistical differences in the CTCAE grade related to neoadjuvant therapy and postoperative complication types among the three groups. Thus, the addition of camrelizumab to nCT did not increase morbidity or mortality. Additionally, another study by Qiao et al. showed that the total incidence of adverse events during nCIT was lower (77.1%) than nCT (91.7%, $p = 0.003$) (23). As reported in previous studies (26, 30), pneumonia was the most prevalent major 30-day postoperative complication in this study. Other common complications included hoarseness, cardiac complication, and anastomotic leakage. Fortunately, no treatment- or surgery-related deaths were observed within 30 days after esophagectomy in this study, except for one sudden death in the nCT group, proving that esophagectomy following nCIT is safe and feasible.

Some limitations are apparent in this study. First, selection biases were inevitable between groups due to the limited sample size and the retrospective design. For example, the cT4 percentage in the nCIT group was 35.3%, which was significantly higher than in the nCT group. Second, the follow-up and recurrences data are insufficient to report mature OS and disease-free survival results. Third, each neoadjuvant therapy might have specific benefits for patient subgroups. The information on predictive biomarkers for therapeutic efficacy, such as PD-L1 expression, was absent in the present study. Therefore, the problem remains with selecting optimal patients who might benefit from different therapeutic modalities. Hence, more prospective phase III clinical trials with larger sample sizes and multiple centers should be conducted to identify the advantages and disadvantages of each neoadjuvant therapy in locally advanced resectable ESCC.

Conclusion

In conclusion, this real-world analysis showed that nCIT is safe and feasible, with satisfactory pCR and MPR rates. Esophagectomy following nCIT achieved several perioperative advantages over nCT and nCRT, with comparable perioperative morbidity and mortality. Although the 3-year OS after nCIT is slightly higher, the long-term survival benefits still require further investigation.

Data availability statement

The original contributions presented in the study are included in the article/supplementary material. Further inquiries can be directed to the corresponding authors.

Ethics statement

The studies involving human participants were reviewed and approved by The Ethics Committee of Hunan Cancer Hospital (No. 2022097). The patients/participants provided their written informed consent to participate in this study.

Author contributions

(I) Conception and design: BZ, QX, W, JW, XW, HZ. (II) Administrative support: BZ, QX. (III) Provision of study materials or patients: BZ, JW, DY, XL, WW, QX, XW, HZ, LG, XC, JL. (IV) Collection and assembly of data: BZ, JW, QX, XW, HZ, LG. (V) Data analysis and interpretation: BZ, QX. (VI) Manuscript writing: all

References

- Sung H, Ferlay J, Siegel RL, Laversanne M, Soerjomataram I, Jemal A, et al. Global cancer statistics 2020: GLOBOCAN estimates of incidence and mortality worldwide for 36 cancers in 185 countries. *CA: Cancer J Clin* (2021) 71(3):209–49. doi: 10.3322/caac.21660
- Pennathur A, Gibson MK, Jobe BA, Luketich JD. Oesophageal carcinoma. *Lancet* (2013) 381(9864):400–12. doi: 10.1016/S0140-6736(12)60643-6
- Arnold M, Ferlay J, van Berge Henegouwen MI, Soerjomataram I. Global burden of oesophageal and gastric cancer by histology and subsite in 2018. *Gut* (2020) 69(9):1564–71. doi: 10.1136/gutjnl-2020-321600
- Leng XF, Daiko H, Han YT, Mao YS. Optimal preoperative neoadjuvant therapy for resectable locally advanced esophageal squamous cell carcinoma. *Ann New York Acad Sci* (2020) 1482(1):213–24. doi: 10.1111/nyas.14508
- Demarest CT, Chang AC. The landmark series: Multimodal therapy for esophageal cancer. *Ann Surg Oncol* (2021) 28(6):3375–82. doi: 10.1245/s10434-020-09565-5
- Yang H, Liu H, Chen Y, Zhu C, Fang W, Yu Z, et al. Long-term efficacy of neoadjuvant chemoradiotherapy plus surgery for the treatment of locally advanced esophageal squamous cell carcinoma: The NEOCRTEC5010 randomized clinical trial. *JAMA Surg* (2021) 156(8):721–9. doi: 10.1001/jamasurg.2021.2373
- Ge F, Huo Z, Cai X, Hu Q, Chen W, Lin G, et al. Evaluation of clinical and safety outcomes of neoadjuvant immunotherapy combined with chemotherapy for patients with resectable esophageal cancer: A systematic review and meta-analysis. *JAMA Net Open* (2022) 5(11):e2239778. doi: 10.1001/jamanetworkopen.2022.39778
- Zhu J, Leng X, Gao B, Wang B, Zhang H, Wu L, et al. Efficacy and safety of neoadjuvant immunotherapy in resectable esophageal or gastroesophageal junction carcinoma: A pooled analysis of prospective clinical trials. *Front Immunol* (2022) 13:1041233. doi: 10.3389/fimmu.2022.1041233
- Yang Y, Tan L, Hu J, Li Y, Mao Y, Tian Z, et al. Safety and efficacy of neoadjuvant treatment with immune checkpoint inhibitors in esophageal cancer: Real-world multicenter retrospective study in China. *Dis esophagus* (2022) 35(11):doac031. doi: 10.1093/dote/doac031
- Luo H, Lu J, Bai Y, Mao T, Wang J, Fan Q, et al. Effect of camrelizumab vs placebo added to chemotherapy on survival and progression-free survival in patients with advanced or metastatic esophageal squamous cell carcinoma: The ESCORT-1st randomized clinical trial. *Jama* (2021) 326(10):916–25. doi: 10.1001/jama.2021.12836
- Liu J, Yang Y, Liu Z, Fu X, Cai X, Li H, et al. Multicenter, single-arm, phase II trial of camrelizumab and chemotherapy as neoadjuvant treatment for locally advanced esophageal squamous cell carcinoma. *J Immunother Cancer* (2022) 10(3):e004291. doi: 10.1136/jitc-2021-004291
- Liu J, Li J, Lin W, Shao D, Depypere L, Zhang Z, et al. Neoadjuvant camrelizumab plus chemotherapy for resectable, locally advanced esophageal squamous cell carcinoma (NIC-ESCC2019): A multicenter, phase 2 study. *Int J Cancer*. (2022) 151(1):128–37. doi: 10.1002/ijc.33976
- Yang P, Zhou X, Yang X, Wang Y, Sun T, Feng S, et al. Neoadjuvant camrelizumab plus chemotherapy in treating locally advanced esophageal squamous cell carcinoma patients: a pilot study. *World J Surg Oncol* (2021) 19(1):333. doi: 10.1186/s12957-021-02446-5
- Yang W, Xing X, Yeung SJ, Wang S, Chen W, Bao Y, et al. Neoadjuvant programmed cell death 1 blockade combined with chemotherapy for resectable esophageal squamous cell carcinoma. *J Immunother Cancer* (2022) 10(1):e003497. doi: 10.1136/jitc-2021-003497
- Zhang B, Xiao H, Pu X, Zhou C, Yang D, Li X, et al. A real-world comparison between neoadjuvant chemoimmunotherapy and chemotherapy alone for resectable non-small cell lung cancer. *Cancer Med* (2022) 12(1):274–86. doi: 10.1002/cam4.4889

authors. (VII) Final approval of manuscript: all authors. All authors contributed to the article and approved the submitted version.

Funding

This study was supported in part by the Hunan Natural Science Foundation (2021JJ70105), Innovation Guide Program of Medical Technology in Hunan Province (2020SK51111), National Cancer Center Climbing Fund (NCC201918A01), and Changsha Science and Technology Project (kq1901079).

Acknowledgments

We thank James P. Mahaffey, PhD, from Liwen Bianji (Edanz) (www.liwenbianji.cn) for editing the English text of this manuscript.

Conflict of interest

The authors declare that the research was conducted in the absence of any commercial or financial relationships that could be construed as a potential conflict of interest.

Publisher's note

All claims expressed in this article are solely those of the authors and do not necessarily represent those of their affiliated organizations, or those of the publisher, the editors and the reviewers. Any product that may be evaluated in this article, or claim that may be made by its manufacturer, is not guaranteed or endorsed by the publisher.

16. Cottrell TR, Thompson ED, Forde PM, Stein JE, Duffield AS, Anagnostou V, et al. Pathologic features of response to neoadjuvant anti-PD-1 in resected non-small-cell lung carcinoma: A proposal for quantitative immune-related pathologic response criteria (irPRC). *Ann Oncol* (2018) 29(8):1853–60. doi: 10.1093/annonc/mdy218
17. Mariette C, Dahan L, Mornex F, Maillard E, Thomas PA, Meunier B, et al. Surgery alone versus chemoradiotherapy followed by surgery for stage I and II esophageal cancer: Final analysis of randomized controlled phase III trial FFCO 9901. *J Clin Oncol* (2014) 32(23):2416–22. doi: 10.1200/JCO.2013.53.6532
18. Chan KKW, Saluja R, Delos Santos K, Lien K, Shah K, Cramarossa GA, et al. Neoadjuvant treatments for locally advanced, resectable esophageal cancer: A network meta-analysis. *Int J Cancer*. (2018) 143(2):430–7. doi: 10.1002/ijc.31312
19. Zheng Y, Liu XB, Sun HB, Xu J, Shen S, Ba YF, et al. A phase III study on neoadjuvant chemotherapy versus neoadjuvant toripalimab plus chemotherapy for locally advanced esophageal squamous cell carcinoma: Henan cancer hospital thoracic oncology group 1909 (HCHTOG1909). *Ann Trans Med* (2021) 9(1):73. doi: 10.21037/atm-20-5404
20. Ando N, Kato H, Igaki H, Shinoda M, Ozawa S, Shimizu H, et al. A randomized trial comparing postoperative adjuvant chemotherapy with cisplatin and 5-fluorouracil versus preoperative chemotherapy for localized advanced squamous cell carcinoma of the thoracic esophagus (JCOG9907). *Ann Surg Oncol* (2012) 19(1):68–74. doi: 10.1245/s10434-011-2049-9
21. Yang H, Liu H, Chen Y, Zhu C, Fang W, Yu Z, et al. Neoadjuvant chemoradiotherapy followed by surgery versus surgery alone for locally advanced squamous cell carcinoma of the esophagus (NEOCRTEC5010): A phase III multicenter, randomized, open-label clinical trial. *J Clin Oncol* (2018) 36(27):2796–803. doi: 10.1200/JCO.2018.79.1483
22. van Hagen P, Hulshof MC, van Lanschot JJ, Steyerberg EW, van Berge Henegouwen MI, Wijnhoven BP, et al. Preoperative chemoradiotherapy for esophageal or junctional cancer. *New Engl J Med* (2012) 366(22):2074–84. doi: 10.1056/NEJMoa1112088
23. Qiao Y, Zhao C, Li X, Zhao J, Huang Q, Ding Z, et al. Efficacy and safety of camrelizumab in combination with neoadjuvant chemotherapy for ESCC and its impact on esophagectomy. *Front Immunol* (2022) 13:953229. doi: 10.3389/fimmu.2022.953229
24. Wang H, Tang H, Fang Y, Tan L, Yin J, Shen Y, et al. Morbidity and mortality of patients who underwent minimally invasive esophagectomy after neoadjuvant chemoradiotherapy vs neoadjuvant chemotherapy for locally advanced esophageal squamous cell carcinoma: A randomized clinical trial. *JAMA Surg* (2021) 156(5):444–51. doi: 10.1001/jamasurg.2021.0133
25. Shah MA, Kennedy EB, Catenacci DV, Deighton DC, Goodman KA, Malhotra NK, et al. Treatment of locally advanced esophageal carcinoma: ASCO guideline. *J Clin Oncol* (2020) 38(23):2677–94. doi: 10.1200/JCO.20.00866
26. Zhang Z, Hong ZN, Xie S, Lin W, Lin Y, Zhu J, et al. Neoadjuvant sintilimab plus chemotherapy for locally advanced esophageal squamous cell carcinoma: A single-arm, single-center, phase 2 trial (ESONICT-1). *Ann Trans Med* (2021) 9(21):1623. doi: 10.21037/atm-21-5381
27. Xing W, Zhao L, Zheng Y, Liu B, Liu X, Li T, et al. The sequence of chemotherapy and toripalimab might influence the efficacy of neoadjuvant chemioimmunotherapy in locally advanced esophageal squamous cell cancer—a phase II study. *Front Immunol* (2021) 12:772450. doi: 10.3389/fimmu.2021.772450
28. Yan X, Duan H, Ni Y, Zhou Y, Wang X, Qi H, et al. Tislelizumab combined with chemotherapy as neoadjuvant therapy for surgically resectable esophageal cancer: A prospective, single-arm, phase II study (TD-NICE). *Int J Surg (London England)*. (2022) 103:106680. doi: 10.1016/j.ijsu.2022.106680
29. Chen F, Qiu L, Mu Y, Sun S, Yuan Y, Shang P, et al. Neoadjuvant chemoradiotherapy with camrelizumab in patients with locally advanced esophageal squamous cell carcinoma. *Front Surg* (2022) 9:893372. doi: 10.3389/fsurg.2022.893372
30. Gu YM, Shang QX, Zhang HL, Yang YS, Wang WP, Yuan Y, et al. Safety and feasibility of esophagectomy following neoadjuvant immunotherapy combined with chemotherapy for esophageal squamous cell carcinoma. *Front Surg* (2022) 9:851745. doi: 10.3389/fsurg.2022.851745
31. Klevebro F, Alexandersson von Döbeln G, Wang N, Johnsen G, Jacobsen AB, Friesland S, et al. A randomized clinical trial of neoadjuvant chemotherapy versus neoadjuvant chemoradiotherapy for cancer of the oesophagus or gastro-oesophageal junction. *Ann Oncol* (2016) 27(4):660–7. doi: 10.1093/annonc/mdw010
32. Shapiro J, van Lanschot JJB, Hulshof M, van Hagen P, van Berge Henegouwen MI, Wijnhoven BPL, et al. Neoadjuvant chemoradiotherapy plus surgery versus surgery alone for oesophageal or junctional cancer (CROSS): Long-term results of a randomised controlled trial. *Lancet Oncol* (2015) 16(9):1090–8. doi: 10.1016/S1470-2045(15)00040-6
33. Chao YK, Chen HS, Wang BY, Hsu PK, Liu CC, Wu SC. Factors associated with survival in patients with oesophageal cancer who achieve pathological complete response after chemoradiotherapy: A nationwide population-based study. *Eur J cardio-thoracic Surg* (2017) 51(1):155–9. doi: 10.1093/ejcts/ezw246
34. Xu L, Wei XF, Li CJ, Yang ZY, Yu YK, Li HM, et al. Pathologic responses and surgical outcomes after neoadjuvant immunotherapy versus neoadjuvant chemoradiotherapy in patients with locally advanced esophageal squamous cell carcinoma. *Front Immunol* (2022) 13:1052542. doi: 10.3389/fimmu.2022.1052542
35. Allum WH, Stenning SP, Bancewicz J, Clark PI, Langley RE. Long-term results of a randomized trial of surgery with or without preoperative chemotherapy in esophageal cancer. *J Clin Oncol* (2009) 27(30):5062–7. doi: 10.1200/JCO.2009.22.2083
36. Zhang G, Zhang C, Sun N, Xue L, Yang Z, Fang L, et al. Neoadjuvant chemoradiotherapy versus neoadjuvant chemotherapy for the treatment of esophageal squamous cell carcinoma: A propensity score-matched study from the national cancer center in China. *J Cancer Res Clin Oncol* (2022) 148(4):943–54. doi: 10.1007/s00432-021-03659-7
37. Jing SW, Qin JJ, Liu Q, Zhai C, Wu YJ, Cheng YJ, et al. Comparison of neoadjuvant chemoradiotherapy and neoadjuvant chemotherapy for esophageal cancer: A meta-analysis. *Future Oncol (London England)*. (2019) 15(20):2413–22. doi: 10.2217/fon-2019-0024
38. Han J, Wang Z, Liu C. Survival and complications after neoadjuvant chemotherapy or chemoradiotherapy for esophageal cancer: a meta-analysis. *Future Oncol (London England)*. (2021) 17(17):2257–74. doi: 10.2217/fon-2021-0021
39. Yin GQ, Li ZL, Li D. The safety and efficacy of neoadjuvant camrelizumab plus chemotherapy in patients with locally advanced esophageal squamous cell carcinoma: A retrospective study. *Cancer Manage Res* (2022) 14:2133–41. doi: 10.2147/CMAR.S358620
40. Jing SW, Zhai C, Zhang W, He M, Liu QY, Yao JF, et al. Comparison of neoadjuvant immunotherapy plus chemotherapy versus chemotherapy alone for patients with locally advanced esophageal squamous cell carcinoma: A propensity score matching. *Front Immunol* (2022) 13:970534. doi: 10.3389/fimmu.2022.970534
41. Xiao X, Yang YS, Zeng XX, Shang QX, Luan SY, Zhou JF, et al. The comparisons of neoadjuvant chemoimmunotherapy versus chemoradiotherapy for oesophageal squamous cancer. *Eur J cardio-thoracic Surg* (2022) 62(1):ezac341. doi: 10.1093/ejcts/ezac341
42. Leng X, He W, Yang H, Chen Y, Zhu C, Fang W, et al. Prognostic impact of postoperative lymph node metastases after neoadjuvant chemoradiotherapy for locally advanced squamous cell carcinoma of esophagus: From the results of NEOCRTEC5010, a randomized multicenter study. *Ann Surg* (2021) 274(6):e1022–e9. doi: 10.1097/SLA.00000000000003727
43. Hong ZN, Gao L, Weng K, Huang Z, Han W, Kang M. Safety and feasibility of esophagectomy following combined immunotherapy and chemotherapy for locally advanced esophageal squamous cell carcinoma: A propensity score matching analysis. *Front Immunol* (2022) 13:836338. doi: 10.3389/fimmu.2022.836338

Journal of the American College of Surgeons Publish Ahead of Print

DOI: 10.1097/XCS.0000000000000801

**Effective Postoperative Surveillance Protocol after Thoracoscopic Esophagectomy
Focusing on Symptoms in Patients with Esophageal Cancer**

Kohei Tajima¹, MD, Kazuo Koyanagi¹, MD, PhD, FACS, Soji Ozawa¹, MD, PhD, FACS,
Akihito Kazuno¹, MD, PhD, Miho Yamamoto¹, MD, PhD, Yoshiaki Shoji¹, MD, PhD,
Kentaro Yatabe¹, MD, PhD, Kohei Kanamori¹, MD, PhD, Hongbo Zhao¹, MD, PhD, Masaki
Mori¹, MD, PhD, FACS

¹Department of Gastroenterological Surgery, Tokai University School of Medicine, Isehara,
Japan

Disclosure Information: Nothing to disclose.

Presented at the 75th Annual meeting of the Japan Esophageal Society, Tokyo, Japan, July
2021, the 29th Japan Digestive Disease Week Meeting, Kobe, Japan,
November 2021, and the 122nd Annual Congress of the Japan Surgical Society, Kumamoto,
Japan, April 2022.

Correspondence address: Soji Ozawa, MD, FACS, PhD, Department of Gastroenterological
Surgery, Tokai University School of Medicine, 143, Shimokasuya, Isehara, Kanagawa,
Japan, 259-1193, (e-mail: soji888@gmail.com)

Brief title: Surveillance Protocol after Esophagectomy

Abstract

Background: The optimal postoperative surveillance protocol after esophagectomy for patients with esophageal cancer has still not been established. We investigated the risk factors for recurrence of esophageal cancer to devise an appropriate surveillance protocol. Furthermore, we focused on the appearance/worsening of symptoms to determine if additional imaging examinations should be performed.

Methods: We enrolled 416 patients with esophageal and esophagogastric junctional cancer who had undergone thoracoscopic esophagectomy at Tokai University Hospital. Outpatient visits for the patients are usually scheduled at least 4 times per year with CT imaging and blood biochemical examination. We evaluated the time to recurrence after esophagectomy, especially the correlation of this parameter with the appearance/worsening of symptoms during the postoperative outpatient follow-up.

Results: Of the 416 patients, recurrence occurred in 127 patients (30.5%). The median time to recurrence was 6 months after esophagectomy; recurrence occurred within 24 months in 112 patients (88%), and 51 of these patients (40%) developed some new symptom(s) (symptomatic group) prior to the diagnosis of recurrence. The number of patients who developed recurrence within 6 months was significantly higher in the symptomatic group as compared with that in the asymptomatic group (66.7% vs. 46.0%, $p=0.02$). The overall survival in the symptomatic group was significantly shorter than that in the asymptomatic group ($p<0.001$).

Conclusions: We advocate an effective surveillance protocol depending on the appearance/worsening of symptoms to diagnose recurrence of esophageal cancer; we recommend routine imaging examinations every 6 months and clinical outpatient follow-up at even shorter intervals for the first 24 months after esophagectomy.

Abbreviations

MIE = minimally invasive esophagectomy

PET-CT = positron emission tomography-CT

UICC = the Union for International Cancer Control

TNM = Tumor-Node-Metastasis

ICS = intercostal space

OS = overall survival

ASA-PS = Anesthesiologists physical status

ICIs = immune checkpoint inhibitors

Keywords: surveillance, symptom, esophageal cancer, thoracoscopic esophagectomy, recurrence, outpatient

ACCEPTED

Introduction

Esophageal cancer was ranked seventh in terms of the cancer incidence and sixth in terms of the cancer mortality worldwide in 2020¹. The highest regional incidence rates are reported from East Asia for both men and women. The histology in the majority is squamous cell carcinoma. Despite the advances in the diagnostic methods, surgical procedures, and multidisciplinary treatment approaches, the prognosis of esophageal cancer remains unsatisfactory². The reported rate of recurrence of esophageal cancer after radical esophagectomy is 29%-43%³⁻⁵. Moreover, as recurrence after esophagectomy is observed within two years after surgery in almost all cases, an appropriate postoperative clinical surveillance protocol is recommended even for patients undergoing curative esophagectomy.

On the other hand, very few patients develop recurrence later than three years after radical esophagectomy. Follow-up intervals and frequency of imaging examinations after esophagectomy may need to be adjusted depending on the time elapsed after the surgery. According to a nationwide survey conducted in Japan, most hospitals usually require their patients to visit the outpatient department at least four times a year during the first two years after curative resection and at least twice a year in the third and subsequent years; however, no consensus has been established yet⁶. The National Comprehensive Cancer Network Guidelines recommend follow-up at the outpatient clinic for medical history taking and physical examination every 3-6 months for 1-2 years, and every 6-12 months for 3-5 years after curative esophagectomy⁷. However, the frequencies of imaging examinations are not clearly specified, and these are performed as needed. Frequent imaging tests are not recommended for the diagnosis of recurrence, not only owing to a lack evidence of improved prognosis, but may also lead to unnecessary radiation exposure of the patients and increased healthcare costs. On the other hand, outpatient visits enable communication between the patient and physician and establishment of a positive patient-physician relationship, which

improves patient satisfaction and plays an important role in cancer treatment^{8,9}. To date, few studies have discussed establishment of an appropriate surveillance protocol after esophagectomy for esophageal cancer. Therefore, no appropriate postoperative surveillance protocol has been defined yet, and patients are often followed up empirically at each institution.

The purpose of this study was to clarify the risk factors for recurrence for esophageal cancer and the influence of the risk factors on the timing of recurrence, in order to devise an appropriate postoperative surveillance protocol, including the optimal intervals for outpatient visits and frequencies of imaging examinations. We assessed the long-term outcomes in esophageal cancer patients who had undergone minimally invasive esophagectomy (MIE) at our high-volume center (single-institution study). Notably, we focused on the appearance/worsening of symptoms in the patients with recurrence to determine if additional imaging examinations are needed, because the postoperative appearance/worsening of symptoms could be a marker of systemic tumor recurrence and influence the survival.

Methods

Patients

This was a single-center retrospective cohort study of patients with esophageal and esophagogastric junctional cancer conducted at the Tokai University Hospital. We enrolled a total of 416 patients who had undergone thoracoscopic esophagectomy with two- or three-field lymph node dissection for esophageal cancer between January 2010 and December 2019 at our hospital. Patients with R1 or R2 were excluded from the study as cases in which radical curative resection was not possible. The median observation period was 39 months. We conducted this retrospective study with the approval of the Institution Review Board of Tokai University Hospital (20R-346).

Tumor staging

Clinical staging investigations in this study included upper gastrointestinal endoscopy, upper gastrointestinal series, computed tomography (CT) of the neck, chest and abdomen, and positron emission tomography-CT (PET-CT).

Tumor staging was based on the Union for International Cancer Control (UICC) Tumor-Node-Metastasis (TNM) grading system, 8th edition. In principle, preoperative chemotherapy was administered to patients with cStage II or more advanced cancer. Patients with supraclavicular lymph node metastasis were indicated for esophagectomy with lymph node dissection including the supraclavicular lymph nodes. Histopathological diagnosis of the resected tumors was performed according to the Japanese Classification of Esophageal Cancer, 11th Edition¹⁰.

Surgical procedure

MIE was first introduced at our hospital in 2009, and has several advantages over open thoracic esophagectomy¹¹⁻¹⁴. Our standard surgical procedure for patients with esophageal cancer is MIE, except in patients in whom unilateral ventilation is expected to be difficult and those who have intense adhesions within the thoracic cavity.

We performed MIE with the patient in prone position, in which the gravity in the thoracic cavity and the CO₂ pneumothorax push down the organs in the middle mediastinum, affording a wide surgical field¹⁵. It is also beneficial in terms of ergonomics for the surgeon's stance, pulmonary gas exchange in the patient, and avoidance of direct lung injury¹⁶. The patient is placed in a prone position, with the right arm raised over the head. The surgeon, assistant, and endoscopist stand on the right side of the patient and watch the video monitor placed on the opposite side. At first, a 12-mm trocar is inserted into the seventh intercostal space (ICS) between the inferior scapular angle line and posterior axillary line, and a pneumothorax in the right chest is induced using CO₂ gas. The thoracic cavity is examined to

identify any pleural adhesions, and a 12-mm trocar is inserted into the ninth ICS on the inferior scapular angle line for inserting the flexible thoracoscope. Another 12-mm trocar is inserted into the fifth ICS on the posterior axillary line. Five-millimeter trocars are then inserted into the seventh ICS on the middle axillary line, and the third ICS on the middle axillary line. First, the anterior mediastinal pleura of the esophagus is incised, and the trachea and heart are shifted downward, to make the dissection between the esophagus and middle mediastinal organs much easier. Next, dissection is performed between the esophagus and the vertebra or descending aorta. The esophagus is finally mobilized from the thoracic inlet along with the peri-esophageal mediastinal lymph nodes.

Postoperative follow-up

All esophageal cancer patients are followed up after radical esophagectomy at the outpatient gastrointestinal surgical care. Outpatient visits are scheduled at least 4 times a year at first. In principle, blood samples are drawn at each visit, and CT imaging from the neck to the pelvis is performed every 3 months. Further outpatient and imaging examinations are scheduled as needed depending on the appearance/worsening of symptoms in the patients. We evaluated the patients at the postoperative outpatient clinic for the appearance/worsening of symptoms.

Statistical analysis

The overall survival (OS) of the patients overall was calculated by the Kaplan- Meier method, and the difference in the OS between the recurrence group and no- recurrence group was analyzed using the log-rank test. Next, the clinicopathological factors were compared between the recurrence and no-recurrence group, and the risk factors for recurrence were examined. The length of time from the date of esophagectomy to the date of diagnosis of recurrence was defined as the time to recurrence, and the relationship between the time to recurrence and risk factors for recurrence or symptoms at recurrence were also examined.

Differences between the two groups were analyzed using the Mann-Whitney *U* test for continuous variables and the χ^2 test or Fisher's exact test for categorical variables. Survival curves were drawn using the Kaplan-Meier method. P values of less than 0.05 were considered as denoting significance. All the analyzes were performed using the statistical software package IBM SPSS statistics 26 (IBM Japan, Tokyo, Japan).

Results

Characteristics of the patients

Of the 416 patients, 357 (86%) were male and 59 (14%) were female (Supplemental Digital Content 1, <http://links.lww.com/JACS/A287>). The median age was 68 years, and the median BMI was 21.6. The American Society of Anesthesiologists physical status (ASA-PS) was 2 in 361 patients (87%). The most common frequent tumor location was the middle esophagus (225 patients, 54%), followed by the lower and upper esophagus. The most common histological type was squamous cell carcinoma (365 patients, 88%). According to the TNM classification, the pStage was classified as I in 139 patients (33%), II in 99 patients (24%), and III in 101 patients (24%). Preoperative treatment was administered in 181 patients (43%) and postoperative complications were observed in 239 patients (57%). Of the 416 patients, 127 (31%) were diagnosed as having recurrence.

Comparison between the recurrence and no-recurrence groups

Comparison of characteristics between the recurrence group (127 patients) and no-recurrence group (289 patients) revealed that mean age ($p=0.02$) and BMI ($p=0.008$) were lower in the recurrence group (Supplemental Digital Content 1, <http://links.lww.com/JACS/A287>). The no-recurrence group was more likely to have pT1, pN0, pM0, or pStage I disease as compared with the recurrence group ($p<0.001$). Preoperative treatment was administered more frequently in the recurrence group than in the no-recurrence group ($p<0.001$). The median OS in the overall study cohort was 104 months (Supplemental Digital Content 2,

<http://links.lww.com/JACS/A287>). The median OS in the recurrence group was 24 months. The 5-year OS rate in the recurrence group was 13%, which was shorter than that of 78% in the no-recurrence group ($p < 0.001$), indicating the very poor prognosis in the recurrence group (Supplemental Digital Content 3, <http://links.lww.com/JACS/A287>).

Time to recurrence

The recurrence rate by stage was 0% in patients with pStage 0 disease, 11% in patients with pStage I disease, 22% in patients with pStage II disease, 48% in patients with pStage III disease, and 72% in patients with pStage IV disease. The recurrence rate was lower in patients with Stage I and Stage II disease and higher in patients with Stage III and Stage IV disease. The median time to recurrence in the recurrence groups was 6 months. In 88% of cases with recurrence, the recurrence occurred within 24 months, and in 95% of cases, the recurrence occurred within 36 months after esophagectomy. In all of the cases with recurrence, the recurrence occurred within 60 months after the surgery (Fig. 1a). The median time to recurrence by stage was 18 months in patients with pStage I disease, 7 months in patients with pStage II disease, 5 months in patients with pStage III disease, and 4 months in patients with pStage IV disease (Supplemental Digital content 4, <http://links.lww.com/JACS/A287>). More than 90% of patients with Stage III/Stage IV disease developed recurrence within 24 months after esophagectomy. pStage I patients showed a lower recurrence rate as well as a longer to time to recurrence as compared with pStage III and pStage IV patients.

Sites of recurrence

Among the 127 patients with recurrence, lymph nodes ($n=90$, 70%) were the most common recurrent organ, followed by the lungs ($n=31$, 24%), liver ($n=27$, 21%), and bones ($n=13$, 10%) (include duplicate data). All of the recurrent patients with bone metastasis had simultaneous metastasis in other organs. Rare sites of recurrence were the skin (3%),

cerebellum (0.7%), and adrenal glands (3%). There was no difference in the survival duration after diagnosis of recurrence or in the time to recurrence between patients with and without lymph node recurrence (Supplemental Digital Content 5 a,b, <http://links.lww.com/JACS/A287>). The time to recurrence and survival after diagnosis of recurrence also did not differ significantly between patients with and without lung recurrence (Supplemental Digital Content 5 c,d, <http://links.lww.com/JACS/A287>). Patients with liver recurrence tended to have a shorter time to recurrence than those without liver recurrence ($p=0.05$). Of the patients with liver recurrence, the recurrence developed within 12 months after esophagectomy in 80% of cases and within 24 months in all cases (Supplemental Digital Content 5e, <http://links.lww.com/JACS/A287>). The prognosis of patients with liver recurrence was poor, with a median survival time after recurrence of 9 months ($p=0.002$) (Supplemental Digital Content 5f, <http://links.lww.com/JACS/A287>). The time to recurrence in patients with bone recurrence did not differ significantly as compared with that in patients with non-bone recurrence (Supplemental Digital Content 5g, <http://links.lww.com/JACS/A287>). However, the prognosis of patients with bone recurrence was poor, with a median survival time after recurrence of only 4 months ($p=0.003$) (Supplemental Digital Content 5h, <http://links.lww.com/JACS/A287>).

Number of recurrence sites

Of the 127 patients in the recurrence group, 77 (61%) showed single-organ recurrence (Table 1), while the remaining 39% showed simultaneous recurrence in multiple organs. The higher the number of recurrence sites, the poorer the prognosis of the patients (Supplemental Digital Content 6, <http://links.lww.com/JACS/A287>).

Symptoms at recurrence

Among the 127 patients with recurrence, 51 (40%) complained of some symptom(s) prior to the diagnosis of recurrence. In 66% of the patients with symptoms (symptomatic group), the

recurrence occurred within 6 months after the surgery. On the other hand, recurrence occurred within 6 months after the surgery only in 46.0% ($p=0.02$) of the patients without symptoms (asymptomatic group). The time to recurrence in the symptomatic group tended to be shorter than that in the asymptomatic group (median: 5 months vs. 7 months; $p=0.08$) (Fig. 1b). The main type of symptom at the recurrence was investigated in 51 patients in the symptomatic group. The most common symptom was pain, followed by respiratory symptom, fatigue, lump, and digestive symptom (Table 2). Further, the time to recurrence was significantly longer for the patients with pain compared to the patients with symptoms other than pain such as respiratory symptoms, fatigue, lump, and digestive symptoms (median: 9 months vs. 4 months; $p=0.042$, Fig. 2). In the examination of the relationship between the site of initial recurrence and the presence of symptoms at recurrence, there was no significant difference in the percentage of patients with symptoms among patients with lymph node, liver or lung recurrence, but the percentage of patients with symptoms was higher in the patients with bone recurrence ($p=0.006$) (Table 3). The median OS was 14 months in the symptomatic group and 33 months in the asymptomatic group, with a worse prognosis in the patient group with symptoms at recurrence ($p<0.001$) (Fig. 1c). Patients with symptoms at recurrence had a worse median survival after recurrence than the patients without symptoms at recurrence (median: 5 months vs. 22 months; $p<0.0001$) (Fig. 1d).

Discussion

This study was conducted to devise an appropriate postoperative surveillance protocol for patients with esophageal cancer undergoing radical esophagectomy. Of all the patients who developed recurrence after the surgery, the recurrence occurred within 24 months of the surgery in 88% of patients. The median time to recurrence was 6 months in the recurrence group and 5 months in the patients of this group with symptoms at recurrence. Routine outpatient follow-up with imaging studies is necessary at least every 6 months for up to 24

months after esophagectomy, and additional studies should be considered according to the symptoms of the patients. The frequency of imaging studies could possibly be reduced after 24 months from surgery.

The time to recurrence decreased as the pathological stage of the disease increased. This result was similar to previously published reports by Lindenmann et al. and Hiyoshi et al.^{17,18}. On the other hand, the presence/absence of preoperative treatment had no influence on the time to recurrence. In more than 80% of all patients with recurrence, the recurrence developed within 24 months after the esophagectomy. These results suggest that periodic follow-up is required within 24 months after radical resection, regardless of the tumor stage and treatment administration prior to surgery. As there were no cases of recurrence later than 60 months after esophagectomy, systematic follow-up to detect recurrence may not be necessary in long-term survivors later than 5 years after esophageal cancer surgery.

With regard to the initial site of recurrence, lymph nodes were the most common site of recurrence, consistent with previous reports¹⁹⁻²³. Patients with liver recurrence had a poor prognosis, even if the recurrence was localized within the liver. This may be because multiple intrahepatic recurrences are often detected in patients with liver recurrence and less responsive to any chemotherapy, as previously reported^{19,24}. Bone recurrence often occurs together with recurrences in other organs, which could explain why patients with bone metastases show a relatively poor prognosis.

With regard to the number of organ sites with recurrence, single-organ recurrence was the most common, accounting for 77 cases (61%). Lymph node recurrence accounted for 49 cases (63%) of all the cases with single-organ recurrence. In many of the patients with lymph node recurrence, the recurrence was limited to the local area nodes and to a limited number of nodes. In recent years, oligo-recurrence, in which a small number of metastatic recurrences are found in a limited number of organs, has attracted attention. In this study also, lymph

node recurrence was frequently observed in patients with oligo- recurrence (data not shown), and chemoradiotherapy or surgical resection could possibly be performed as radical treatment in such cases. On the other hand, the prognosis was poorer in patients with simultaneous recurrences in multiple organs, and the greater the number of organ sites of recurrence, the poorer the prognosis. All patients with bone recurrence in this study also had recurrence(s) in other organs, which could explain the poor prognosis in patients with bone recurrence.

In this study to devise an appropriate surveillance protocol for patients with esophageal cancer after MIE, we focused on the occurrence/worsening of symptoms at recurrence. Among all patients with recurrence, 51 patients (40%) complained of some symptom(s) prior to the diagnosis of recurrence. The time to recurrence in the group with symptoms at the time of recurrence was 5 months, which was shorter than in the group that reported no symptoms at the diagnosis of recurrence. The most common symptom at the recurrence was pain, followed by respiratory symptom, fatigue, lump, and digestive symptom. The time to recurrence was 3-4.5 months in the group with symptoms other than pain. These results suggest that it is important to enquire about the presence/absence of new/worsening symptoms and the type of symptoms, particularly respiratory symptoms, fatigue, lump or digestive symptoms, at the time of the outpatient follow-up visits. In patients with symptoms at recurrence, not only the time to recurrence was shorter, but also the survival time after recurrence was shorter. All patients with bone metastasis had simultaneous metastases in other organs, and the symptoms in patients with bone metastases were related to both bone and other organ recurrence. Shortened survival of the patients with bone metastases was caused by multiple organ recurrence.

In this study, we demonstrated the existence of a correlation between a shorter time to recurrence and the development/worsening of symptoms after MIE, therefore, medical examination at the outpatient clinic should be frequently performed in patients with

symptoms. Furthermore, imaging studies should be performed as needed. Additional examinations should be performed promptly for the patients developing respiratory symptoms, fatigue, lump, or digestive symptoms, especially in the early postoperative period. On the other hand, the time to recurrence in the group without any symptom(s) at recurrence was 7 months. Therefore, routine imaging tests should be performed at least every 6 months even in patients without any symptoms. Based on these findings, we propose that a combination of outpatient follow-up at least every 3 months and imaging examinations every 6 months until 24 months after curative esophagectomy for esophageal cancer as an effective surveillance method. It is important to mention that imaging examinations should be promptly performed to check for tumor recurrence in patients reporting symptoms at the time of the outpatient follow-up consultation.

None of the patients included in the present study received immune checkpoint inhibitors (ICIs) as adjuvant therapy. Most of the patients had also not received ICIs as 2nd or further line therapy. ICI therapy has been reported effective as adjuvant therapy after radical resection and also as 1st line treatment in patients with unresectable locally advanced or recurrent esophageal cancer²⁵⁻²⁷. Therefore, further investigation of an effective surveillance protocol for patients who have received adjuvant ICI therapy is warranted.

This study had several advantages and limitations. The first of the advantages was that all of the patients had undergone thoracoscopic esophagectomy, so that there was little bias arising from the technique used for the surgery in the current study. Second, our institution has extensive experience in thoracoscopic esophagectomy and this study was conducted in patients who received treatment with an already established surgical technique. Third, almost all patients with Stage II and Stage III cancer had routinely received neoadjuvant chemotherapy, so that there was little preoperative treatment bias.

The first limitation was that our study was conducted retrospectively at a single institution, and large prospective multicenter studies are needed to establish an optimal postoperative surveillance protocol for patients with esophageal cancer after radical esophagectomy. The second limitation of our study was that squamous cell carcinoma was predominant among the cases enrolled in the study, so that the results may not be extrapolatable to patients with esophageal adenocarcinoma. This is an issue for future study.

Conclusions

We advocate an effective surveillance protocol focused on the occurrence/worsening of patient symptoms for early detection of recurrence in patients with esophageal cancer who have undergone radical resection; we recommend routine imaging examinations every 6 months and outpatient care at even shorter intervals for the first 24 months after esophagectomy. We believe that this surveillance protocol may enable early therapeutic intervention and improvement of the prognosis in esophageal cancer patients with disease recurrence after surgery.

References

1. Sung H, Ferlay J, Siegel RL, Laversanne M, et al. Global cancer statistics 2020: GLOBOCAN estimates of incidence and mortality worldwide for 36 cancers in 185 countries. *CA Cancer J Clin* 2021; **71**: 209-249.
2. Koyanagi K, Kanamori K, Ninomiya Y, et al. Progress in multimodal treatment for advanced esophageal squamous cell carcinoma: Results of multi-institutional trials conducted in Japan. *Cancers* 2021; **13**: 51.
3. Sugiyama M, Morita M, Yoshida R, et al. Patterns and time of recurrence after complete resection of esophageal cancer. *Surg Today* 2012; **42**: 752-758
4. Lou F, Sima CS, Adusumilli PS, Bains MS, et al. Esophageal cancer recurrence patterns and implications for surveillance. *J Thorac Oncol* 2013; **8**: 1558-1562
5. Kunisaki C, Makino H, Takagawa R, et al. Surgical outcomes in esophageal cancer patients with tumor recurrence after curative esophagectomy. *J Gastrointest Surg* 2008; **12**: 802-810
6. Toh Y, Kitagawa Y, Kuwano H, et al. A nation-wide survey of follow-up strategies for esophageal cancer patients after a curative esophagectomy or a complete response by definitive chemoradiotherapy in Japan. *Esophagus* 2016; **13**: 173-181.
7. NCCN clinical practice guidelines in oncology – Esophageal and Esophagogastric Junction Cancers 2022.
<https://www.nccn.org/patients/guidelines/content/PDF/esophageal-patient.pdf>
8. Zachariae R, Pedersen CG, Jensen AB, et al. Association of perceived physician communication style with patient satisfaction, distress, cancer-related self-efficacy, and perceived control over the disease. *Br J Cancer* 2003; **88**: 658-65

9. Bernacki R, Paladino J, Neville BA, et al. Effect of the serious illness care program in outpatient oncology: A cluster randomized clinical trial. *JAMA Intern Med* 2019; **179**: 751-759
10. Japan Esophageal Society. Japanese classification of esophageal cancer, 11th edition: part II and III. *Esophagus* 2017; **14**: 37-65
11. Cushieri A, Shimi S, Banting S. Endoscopic oesophagectomy through a right thoracoscopic approach. *J R Coll Surg Edinb* 1992; **37**: 7-11.
12. Biere SS, van Berge Henegouwen MI, et al. Minimally invasive versus open oesophagectomy for patients with oesophageal cancer: a multicentre, open-label, randomised controlled trial. *Lancet* 2012; **379**: 1887-1892.
13. Straatman J, van der Wielen N, Cuesta MA, et al. Minimally invasive versus open esophageal resection: three-year follow-up of the previously reported randomized controlled trial: the TIME Trial. *Ann Surg* 2017; **266**: 232-236.
14. Osugi H, Takemura M, Higashino M, et al. A comparison of video-assisted thoracoscopic oesophagectomy and radical lymph node dissection for squamous cell cancer of the oesophagus with open operation. *Br J Surg* 2003; **90**: 108- 113.
15. Ozawa S, Ito E, Kazuno A, Chino O, et al. Thoracoscopic esophagectomy while in a prone position for esophageal cancer: a preceding anterior approach method. *Surg Endosc* 2013; **27**: 40–47.
16. Koyanagi K, Ozawa S, Tachimori Y. Minimally invasive esophagectomy performed with performed with the patient in a prone position: a systematic review. *Surg Today* 2016; **46**: 275–284.
17. Lindenmann J, Fediuk M, Fink-Neuboeck N, et al. Hazard curves for tumor recurrence and tumor-related death following esophagectomy for esophageal cancer. *Cancers* 2020; **12**: 2066.

18. Hiyoshi Y, Yoshida N, Watanabe M, et al. Late recurrence after radical resection of esophageal cancer *World J Surg*. 2016; **40**: 913– 920.
19. Miyata H, Yamasaki M, Kurokawa Y, et al. Survival factors in patients with recurrence after curative resection of esophageal squamous cell carcinomas. *Ann Surg Oncol* 2011; **18**: 3353–3361.
20. Bhansali MS, Fujita H, Kakegawa T, et al. Pattern of recurrence after extended radical esophagectomy with three-field lymph node dissection for squamous cell carcinoma in the thoracic esophagus. *World J Surg* 1997; **21**: 275-281.
21. Yamashita K, Watanabe M, Mine S, et al. Patterns and Outcomes of Recurrent Esophageal Cancer After Curative Esophagectomy. *World J Surg* 2017; **41**: 2337-2344.
22. Morinaga T, Iwatsuki M, Yamashita K, et al. Oligometastatic recurrence as a prognostic factor after curative resection of esophageal squamous cell carcinoma. *Surg Today* 2021; **51**: 798-806.
23. Sugiyama M, Morita M, Yoshida R, et al. Patterns and time of recurrence after complete resection of esophageal cancer. *Surg Today* 2012; **42**: 752-758.
24. Nobel TB, Sihag S, Xing X, Eljalby M, et al. Oligometastases after curative esophagectomy are not one size fits all. *Ann Thorac Surg* 2021; **112**: 1775- 1781.
25. Kelly RJ, Ajani JA, Kuzdzal J, et al. Adjuvant nivolumab in resected esophageal or gastroesophageal junction cancer. *N Engl J Med* 2021; **384**: 1191-1203.
26. Doki Y, Ajani JA, Kato K, et al. Nivolumab combination therapy in advanced esophageal squamous-cell carcinoma. *N Engl J Med* 2022; **386**: 449-462.
27. Sun JM, Shen L, Shah MA, et al. Pembrolizumab plus chemotherapy versus chemotherapy alone for first-line treatment of advanced oesophageal cancer (KEYNOTE-590): a randomised, placebo-controlled, phase 3 study. *Lancet* 2021; **398**: 759-771.

Figure legend

Figure 1. Time to recurrence and survival after recurrence in patients with symptom or without symptom. (A) Time to recurrence (all patients with recurrence); (B) time to recurrence; (C) overall survival; (D) survival after recurrence

Figure 2. Time to recurrence in patients with pain or with other symptoms (respiratory symptoms, fatigue, lump or digestive symptoms)

ACCEPTED

Table 1. Number Of Recurrent Organs at Diagnosis of Recurrence

Number of recurrent organs	Patients with recurrence, n (%)
1	77 (61)
2	28 (22)
3	13 (10)
4	7 (6)
5	1 (1)
6	1 (1)
Total	127 (100)

ACCEPTED

Table 2. Type Of Symptoms and Time After Surgery in the Symptomatic Group

Symptom	Data, n (%), (n=51)	Time after surgery, mo
Pain	17 (33)	8
Respiratory	12 (23)	4
Fatigue	9 (18)	4
Lump	7 (14)	3
Digestive	6 (12)	4.5

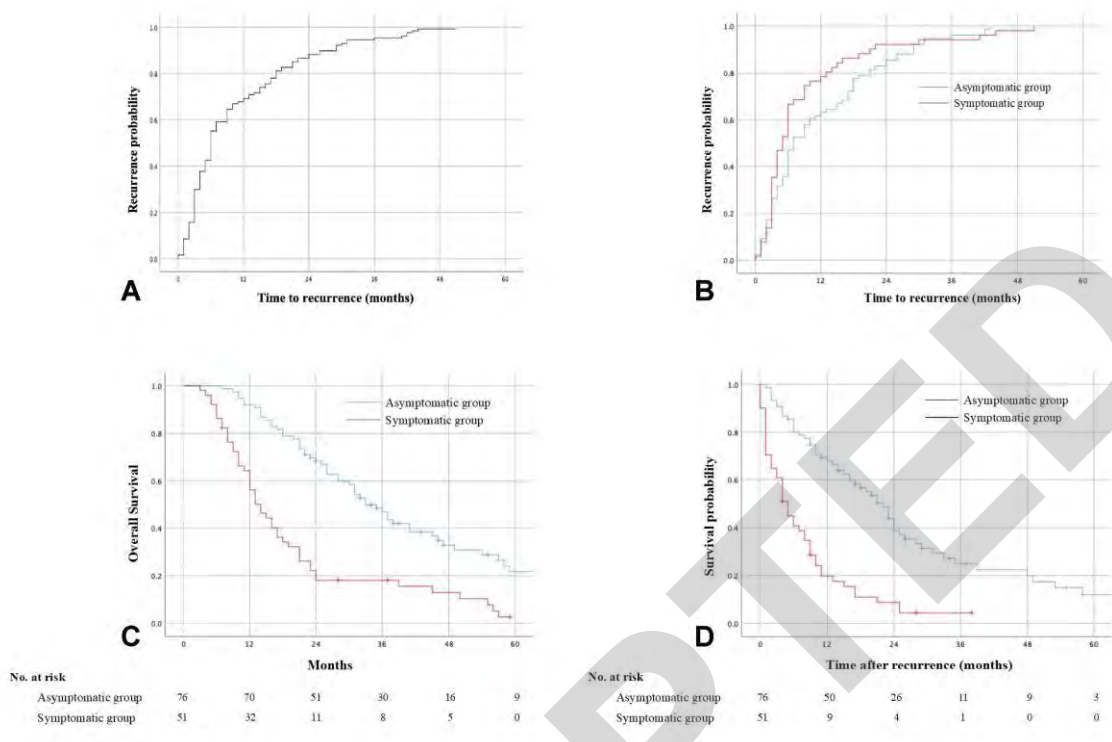
ACCEPTED

Table 3. Comparison of Symptoms at Recurrence According to Organs

Site of recurrence	Symptoms, n (N=51)	No symptom, n (N=76)	p Value*
Lymph node, n			
Yes	39	51	0.320
No	12	25	
Liver, n			
Yes	10	17	0.826
No	41	59	
Lung, n			
Yes	15	16	0.299
No	36	60	
Bone, n			
Yes	10	3	0.006
No	41	73	
Other, n			
Yes	25	14	<0.001
No	26	62	

* χ^2 test or Fisher's exact test

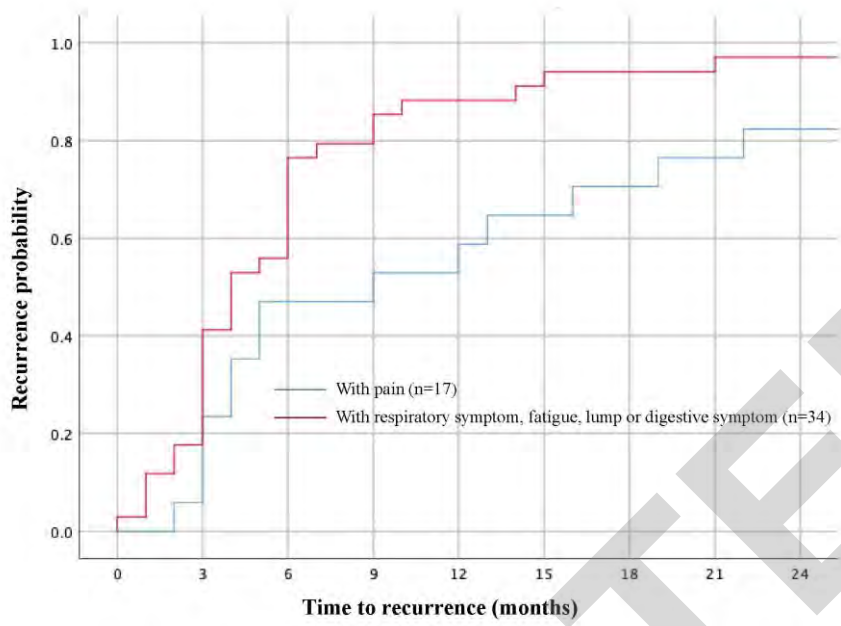
Figure 1



Downloaded from http://journals.lww.com/journals by BHDMEFPHKAV1ZEUm1IQNda+kJLHEZgbsIHod4XMMIOncY WCX1AWWnyQP/ID3I3D00dFy7T7vSF4C3YCA/OAV/pDDa8KKGKVV0Ymy+78= on 08/15/2023

ACCEPTED

Figure 2



ACCEPTED

日中笹川医学奨学金制度<学位取得コース>評価書

課程博士：指導教官用



第 44 期

研究者番号：G4407

作成日：2024年3月10日

氏名	周英	ZHOU YING	性別	F	生年月日	1983/11/10
所属機関（役職）	金沢大学大学院人間社会環境研究科（博士後期課程大学院生）					
研究先（指導教官）	金沢大学大学院人間社会環境研究科人間社会環境学専攻（堤敦朗教授）					
研究テーマ	日本における精神科医療通訳者の実態と心理的体験 Actual situation and psychological experiences of psychiatric interpreters in Japan					
専攻種別	<input type="checkbox"/> 論文博士			<input checked="" type="checkbox"/> 課程博士		

研究者評価（指導教官記入欄）

成績状況	<input checked="" type="checkbox"/> 優 <input type="checkbox"/> 良 <input type="checkbox"/> 可 <input type="checkbox"/> 不可 学業成績係数=	取得単位数
		取得単位数=19／取得すべき単位総数=16
学生本人が行った研究の概要	多くの外国人が日本に在留しているが、在日外国人医療に関する病院や診療所における課題は少なくない。その中で、医療通訳者に求められている役割は大きい。しかし、日本では医療通訳が国家資格として確立されておらず、その多くがボランティアベースで取り組まれているのが現実である。医療の現場に医学を修めていない医療通訳者が入ることでその質の担保や危険性が指摘されている。また、医療の現場では死産や癌の告知、余命の説明や抗がん剤による治療など、精神的に負担の大きい内容の通訳を強いられることがある。特に、医療通訳の中でも精神科医療通訳は、一般身体の医療通訳以上に様々な心理的な影響を受けていることが報告されている。したがって、精神科医療通訳を含む医療通訳の受ける心理的体験と心理的影響を究明する必要がある。研究では17人の医療通訳者を対象に、半構造化インタビューを行なった。質的記述的研究法で分析した結果、10の「サブカテゴリー」と4つの「カテゴリー」を抽出した。それぞれ【阻害要因】（[制約]、[困難な経験]、[感情的な疲弊]からなる）、【促進要因】（[保証]、[承認]、[やりがい]からなる）、【医療通訳者の資質】（[情熱と奉仕の精神]、[対処と適応]からなる）と【専門的基盤への追求】（[体制整備への要望]、[医療通訳としての専門性]からなる）である。	
総合評価	【良かった点】 日本の精神科医療通訳者の実態と心理的体験はこれまで研究されなかった。そういう意味では価値のある研究だといえる。医療通訳の背景、歴史、海外と日本の状況などを漏れなく紹介し、精神科医療通訳者の実態の調査を展開するための土台を作った。研究結果を既存理論との比較もあり、自身のオリジナリティを出している。精神科医療通訳者の実態が究明され、医療通訳者への注目、支援、こころのケアなどのニーズも言及され、今後の政策改善につながると期待される。	
	【改善すべき点】 テーマは日本にとどまらないグローバルな課題である。よって、今後は英語での論文執筆および国際誌への投稿に挑戦してほしい	
	【今後の展望】 今後はさらなる大きいサンプルサイズで、量的研究法を用いて、研究結果を検証したり、発展させたりすることを期待される。博士論文執筆の過程で、基本的な研究実施のための素養や能力を身につけており、大いに活躍できると思う。	

学位取得見込	2024年3月に取得が決定している。
評価者（指導教官名） 堤 敦朗	

日中笹川医学奨学金制度<学位取得コース>報告書 研究者用



第44期

研究者番号: G4407

作成日: 2024年3月5日

氏名	周英	ZHOU YING	性別	F	生年月日	1983/11/10
所属機関(役職)	金沢大学大学院人間社会環境研究科(大学院生)					
研究先(指導教官)	金沢大学大学院人間社会環境研究科人間社会環境学専攻(堤 敦朗 教授)					
研究テーマ	日本における精神科医療通訳者の実態と心理的体験 Actual situation and psychological experiences of psychiatric interpreters in Japan					
専攻種別	論文博士	<input type="checkbox"/>	課程博士	<input checked="" type="checkbox"/>		

1. 研究概要(1)

1) 目的 (Goal)

多くの外国人が日本に在留しているが、在日外国人医療に関する病院や診療所における課題は少なくない。その中で、医療通訳者に求められている役割は大きい。しかし、日本では医療通訳が国家資格として確立されておらず、その多くがボランティアベースで取り組まれているのが現実である。医療の現場に医学を修めていない医療通訳者が入ることでその質の担保や危険性が指摘されている。また、医療の現場では死産や癌の告知、余命の説明や抗がん剤による治療など、精神的に負担の大きい内容の通訳を強いられることがある。特に、医療通訳の中でも精神科医療通訳は、一般身体医療通訳以上に様々な心理的影響を受けていることが報告されている。したがって、精神科医療通訳を含む医療通訳の受ける心理的体験と心理的影響を究明する必要がある。

2) 戦略 (Approach)

- 半構造化インタビューによってデータを収集した。「リサーチクエスション」は以下のとおりである。
- ・医療通訳という職業に関連する精神的苦痛、性質、程度とはどういったものか。
 - ・精神科医療通訳は一般身体医療通訳と比べて、通訳によって受ける心理的影響または精神的苦痛は何か特徴があるのか。
 - ・通訳者が実施している対処法は何か。
 - ・支援や監督体制について、どう考えているか。

3) 材料と方法 (Materials and methods)

調査は2022年9月から2023年5月にかけて、複数の通訳派遣団体および医療通訳が配置されている病院の協力を得て実施した。本調査は金沢大学人間社会研究域倫理審査委員会より承認を受けた(承認番号: 2022-31)。日本における精神科医療通訳の実態と心理的体験に関する研究は存在しない。そのため、この主観的体験を明らかにするためには、質的記述的研究デザインが適切だと判断した。作成した逐語録に基づき、文節の意味の内容を検討し、コード化、サブカテゴリー化、カテゴリー化した。

4) 実験結果 (Results)

本研究では、2件以上の精神科医療通訳の経験を持ち、3年以上の医療通訳経験者であることである。または、精神科の経験がなくても、10年以上の医療通訳の経験者の方を対象とした。最終的に17名に半構造化面接を行なった。分析の結果、一次コード600個前後、二次コード97個、サブカテゴリー10個が抽出され、4つのカテゴリーを生成した。

日本における医療通訳者は、社会的に認識されず、守られず、サポートを受けていないなどの【制約】をされながら、暴力などの【困難な経験】をし、ネガティブな感情を抱くなど【感情的な疲弊】を体験する一方、派遣機関や病院の自らの工夫でのサポートとなる【保証】を受け、患者や医療関係者に【承認】をされ、【やりがい】を感じて、医療通訳の仕事に励んでいる。そもそも、日本で活躍している医療通訳者の多くは【情熱と奉仕の精神】を持ち、医療通訳の仕事をしていくうちに、自分磨きを常に行い、難しい場面への【対処と適応】を考える。しかし、自分の素質や努力だけでは不足するとも気づき、【体制整備への要望】を持ち、【医療通訳としての専門性】を確立したいとも思っている。

【促進要因】と【医療通訳者の資質】がそれぞれ【阻害要因】と拮抗関係にあった。困難な状況などの【阻害要因】は重圧のようなものだが、情熱と奉仕の精神を持つ【医療通訳者の素質】や、やりがいなどの【促進要因】が基盤となっており、バランスが取れるように支えている。特に【医療通訳者の資質】がバランスを保持するための基盤の中核に存在していた。すなわち、困難な状況がありながらも、【促進要因】と【医療通訳者の資質】がパワーとなり、重圧である【阻害要因】に対抗している。しかし、このバランスが取れている状態が決して丈夫なものや持続可能なものではない。これに気づいている医療通訳者たちはより確固たるバランスを求めめるために、【専門的基盤への追求】をする。この三者が拮抗している関係の切り口が【専門的基盤への追求】であると考える。

5) 考察 (Discussion)

・制約

医療通訳者たちは、暴力などの【困難な経験】をし、ネガティブな感情を抱くなど【感情的な疲弊】を体験し、全体的にみて、日本における医療通訳者が未だに社会的に認識されず、守られず、サポートを受けていないなどの【制約】を受けている。これは日本の外国人政策および外国人の地位に関係するものではないかと考える。

日本はアメリカなどと比較して移民の数が少なく、移民に対する姿勢が消極的であると言える。移民政策には外国人の出入国を扱う「出入国管理政策」と入国した外国人を生活者として社会に受け入れる「社会統合政策」がある。日本は移民に消極的であるから、外国人の社会統合を任されたのは地方自治体で、実際に現場で外国人の生活支援を担っているのはNPOやボランティアの市民である。このように医療通訳のような外国人の生活支援を担う専門職へのサポートを担うのもNPOやボランティアであることが現状である。

さらに、(医療通訳者を含む)コミュニティ通訳者はマイナーな言語を扱うことが多く、サービス提供の対象者もマイノリティの人たちで、社会の辺縁に置かれる外国人たちである。どの言語を使い、誰のために通訳するかによって、通訳者のステータスが決まる。このような背景で、(医療通訳者を含む)コミュニティ通訳者の社会的ステータスが低く認識されているのである。

・体験

本研究では、精神科医療通訳者を含む医療通訳者の悲しみ、辛さ、不安、心配、動揺などのネガティブな感情と二次的トラウマ体験が確認された。これは先行研究と一致している。また、難民への対応の特段の難しさと心情の複雑さを確認でき、難民への対応が日本や海外に関わらず医療通訳者にとって困難な体験になりやすいことが示唆された。さらに、日本における医療通訳者が感じる苦痛の多くは時間が経つに連れ、気分転換などにより軽減をしていくことが確認でき、先行研究と一致した。

ネガティブな感情以外に、本研究では医療通訳者の達成感、感謝の気持ちなどのポジティブな感情も確認できた。これは海外のプロフェッショナルの医療通訳者と対照的に、日本の医療通訳者のほとんどはボランティアで活動している。ボランティアでも一つの専門分野を成り立たせるパワーとエネルギーは日本における医療通訳者の身で確認できた。

・精神科

本研究で精神科の通訳は困難であると調査で確認できた。場面的に、「暴力（言語的または身体的）をふるう患者の通訳」、「自殺行為のあった患者の通訳」、「患者が拘束される保護室に入る必要」、「強制入院の患者への対応」、「患者と家族が敵対し、通訳をそれぞれの味方にさせようとする板挟み状態」、「通訳によって、自分のキャラクターを変える患者」、「急に連絡が途切れる患者」などがあり、通訳者たちは身構えたり、気を使ったり、戸惑ったりする。内容的には、精神科は「患者が支離滅裂な内容を話す」、「主訴が診断基準で、難しい」、「抽象的な内容で、伝わるかどうか心配」、「ブライバシーが特に重視される領域で、事前に資料がもらえず、準備しにくい」など、対応の難しさが伺えた。通訳者たちの心理に関して、「怖い」、「自分を責める」、「動揺」、「戸惑い」、「共感しすぎて二次受傷を受ける」などが確認でき、さらに「患者への配慮」も確認できた。例えば、「患者は鬱で通訳依頼をするのも精一杯で、他は望まない」とか、「精神科患者を社会全体でサポートすべき」とか、「母語で自分の心情を語れない患者は大変だ」とかである。また、精神科で医療通訳をする際に、特に気をつけなければならないのは「距離感（頼りにされすぎ問題）」、「言葉の加減、ニュアンス」などがある。精神科対応として、「傾聴」、「安心させる態度」、「優しい言葉」、「患者の言葉を真に受けない」、「割り切る」、「言葉尻を取れないようにする」、「言葉のやり取りを意識して訳す」、「補って訳す」、「ありえない話をありえないまま訳す」、「精神科にはアドホック通訳が厳禁」、「患者に寄り添い、患者の立場にたつ」などが確認できた。また、精神科医療通訳をやって、肯定的な側面もあった。「精神科に興味がある」、「勉強になって、役に立った」、「知ることで、動揺や怖さを克服する」、「医者が患者の行動を見ているので、それほど言葉が必要でない時もある」、「精神的な病気の患者さんを病院が待たせないで、待ち時間が少ない」などがあった。

・レジリエンス理論との照合

ネガティブな経験をした人が必ずしもネガティブな影響を受けるとは限らない。[制約]を受け、[困難な経験]をし、[感情的な疲弊]があるが、回復して適応できるようになるパワーとエネルギーが医療通訳者の身に見られた。または、回復でき適応できる医療通訳者しか残れない現実があるとも言えよう。

レジリエンスは多くの分野で研究されるが、統一された定義はない。平野によると、「レジリエンスとは心理的な傷つきや落ち込みから立ち直る回復力のこと」であり、持って生まれた気質と関連の強い「資質的レジリエンス要因」と、後天的に身につけていきやすい「獲得的レジリエンス要因」に分けた。

レジリエンスに関する記述は医療通訳者の身でも確認できた。【阻害要因】の状況下で、【医療通訳者の資質】（「情熱と奉仕の精神」と「対処と適応」）を発揮して、「逆境」を乗り越えた。レジリエンス研究における「逆境」とは「困難・不幸・トラウマに結びつくひどい苦難や苦悩」、あるいは広範に「日常生活の中に埋め込まれた些末な混乱を含む」である。本研究での【阻害要因】となる【制約】、【困難な経験】、「感情的な疲弊」を医療通訳者にとっての「逆境」とみなすことができる。このような「逆境」を医療通訳者たちは乗り越え、心理的社会的良好な状態を維持でき適応的に生活している。彼らのこのような適応する過程・能力・結果のことをレジリエンスとすることができる。

・提案

医療通訳の市場という点では、通訳者は不利な状況に置かれる。しかも、医療通訳者利用サービスの財源が不安定で、外国人患者自身が支払う受益者負担、地方自治体や医療機関が負担する、各種助成金によるなど、ケースバイケースである。このように市場原理がうまく働かない分野においては、政府が介入すべきだと思われる。中村によると、医療通訳サービスをどのように組み込むかという課題に取り組む必要がある。健康保険法の診療報酬算定方法に医療通訳者加算などの形で医療通訳サービスを組み込むことにより、医療通訳者という存在を制度化することが可能になるという。

また、医療通訳を対象にする研修に関して、厚労省は「医療通訳育成カリキュラム基準」や「テキスト」を作成して提示するが、研修時間や具体的な研修内容は自治体や各NPO団体に任せているのが現状である。今後、国家レベルの統一研修、統一教材および統一の試験ができれば、医療通訳者の質の確保が可能になるだろう。

最後に、医療通訳者は医療通訳の仕事によって、【困難な経験】をし、【感情的な疲弊】になることが本研究で確認された。医療通訳者へのフォローアップは一部の派遣団体NPOや病院機関で見られるが、全ての医療通訳者がフォローされ、精神的なケアを受けられるとは言い難い。医療通訳者向けのカウンセリング制度の確立も必要であると思われる。これは医療通訳者たちへのエンパワーメントにもなると思われる。

・限界と課題

本研究の限界について述べる。1点目として、対象者に偏りがある可能性がある。本研究は、研究目的に賛同してインタビューに答えてくださった方の体験から分析した結果であり、インタビューを拒否した者とは違った体験をしている可能性がある。2点目として、本研究の対象者の選定に、年齢、言語、性別に関して多様性に限界がある。3点目として、本研究では精神科クリニックなど精神科に特化する医療通訳の方へのインタビューができなかった。

しかし、日本では、医療通訳者、精神科医療通訳者の実態や心理的体験に関する研究は極めて少ないため、医療通訳者たちの語りは、今後の体制整備、研修、支援への示唆を得る上で、重要な意義があったと考えられる。

今後の課題について述べる。本研究では、対象者の偏りがあったため、今後は若い世代の医療通訳者、少数言語の医療通訳者、男性の医療通訳者、および精神科クリニックに所属する精神科に特化した医療通訳者の方へアクセスをすることが必要である。また、本研究は、質的研究でベースとなるモデル図を作成したが、今後は量的研究を用いて、日本全国にいる医療通訳者を対象に、結果の検証をより大きいサンプルサイズでしていくことが求められる。

6) 参考文献 (References)

・中村安秀：医療通訳士の必要性と重要性 ―外国人に対する保健医療の現状と課題―。(中村安秀, 南谷かおり編) 医

療通訳という仕事 ―ことばと文化の壁を超えて―, 3-19, 大阪大学出版会, 大阪 (2013) など多数。

(紙面の関係で詳細を省略、添付ファイルの博士論文をご参考に)

2. 執筆論文 Publication of thesis ※記載した論文を添付してください。Attach all of the papers listed below.

論文名 1 Title	精神科医療通訳の「患者擁護」について					
掲載誌名 Published journal	日中医学					
	2022 年 11 月	Vol.37 No.3 巻(号)	29/59 頁 ~	33/62 頁	言語 Language	日本語/中国語
第1著者名 First author	周英	第2著者名 Second author	堤敦朗		第3著者名 Third author	
その他著者名 Other authors						
論文名 2 Title						
掲載誌名 Published journal						
	年 月	巻(号)	頁 ~	頁	言語 Language	
第1著者名 First author		第2著者名 Second author			第3著者名 Third author	
その他著者名 Other authors						
論文名 3 Title						
掲載誌名 Published journal						
	年 月	巻(号)	頁 ~	頁	言語 Language	
第1著者名 First author		第2著者名 Second author			第3著者名 Third author	
その他著者名 Other authors						
論文名 4 Title						
掲載誌名 Published journal						
	年 月	巻(号)	頁 ~	頁	言語 Language	
第1著者名 First author		第2著者名 Second author			第3著者名 Third author	
その他著者名 Other authors						
論文名 5 Title						
掲載誌名 Published journal						
	年 月	巻(号)	頁 ~	頁	言語 Language	
第1著者名 First author		第2著者名 Second author			第3著者名 Third author	
その他著者名 Other authors						

3. 学会発表 Conference presentation ※筆頭演者として総会・国際学会を含む主な学会で発表したものを記載してくだ

※Describe your presentation as the principal presenter in major academic meetings including general meetings or international me

学会名 Conference	第29回多文化間精神医学会学術総会			
演題 Topic	日本における医療通訳(特に精神科医療通訳)が受ける心理的影響に関する研究:質的研究			
開催日 date	2023 年 1 月 20 日	開催地 venue	滋賀県大津市	
形式 method	<input checked="" type="checkbox"/> 口頭発表 Oral <input type="checkbox"/> ポスター発表 Poster	言語 Language	<input checked="" type="checkbox"/> 日本語 <input type="checkbox"/> 英語 <input type="checkbox"/> 中国語	
共同演者名 Co-presenter	堤敦朗			
学会名 Conference				
演題 Topic				
開催日 date	年 月 日	開催地 venue		
形式 method	<input type="checkbox"/> 口頭発表 Oral <input type="checkbox"/> ポスター発表 Poster	言語 Language	<input type="checkbox"/> 日本語 <input type="checkbox"/> 英語 <input type="checkbox"/> 中国語	
共同演者名 Co-presenter				
学会名 Conference				
演題 Topic				
開催日 date	年 月 日	開催地 venue		
形式 method	<input type="checkbox"/> 口頭発表 Oral <input type="checkbox"/> ポスター発表 Poster	言語 Language	<input type="checkbox"/> 日本語 <input type="checkbox"/> 英語 <input type="checkbox"/> 中国語	
共同演者名 Co-presenter				
学会名 Conference				
演題 Topic				
開催日 date	年 月 日	開催地 venue		
形式 method	<input type="checkbox"/> 口頭発表 Oral <input type="checkbox"/> ポスター発表 Poster	言語 Language	<input type="checkbox"/> 日本語 <input type="checkbox"/> 英語 <input type="checkbox"/> 中国語	
共同演者名 Co-presenter				

4. 受賞(研究業績) Award (Research achievement)

名称 Award name	国名 Country		受賞年 Year of	年 月
	国名 Country		受賞年 Year of	年 月

5. 本研究テーマに関わる他の研究助成金受給 Other research grants concerned with your research theme

受給実績 Receipt record	<input type="checkbox"/> 有 <input checked="" type="checkbox"/> 無
助成機関名称 Funding agency	
助成金名称 Grant name	
受給期間 Supported period	年 月 ~ 年 月
受給額 Amount received	円
受給実績 Receipt record	<input type="checkbox"/> 有 <input checked="" type="checkbox"/> 無
助成機関名称 Funding agency	
助成金名称 Grant name	
受給期間 Supported period	年 月 ~ 年 月
受給額 Amount received	円

6. 他の奨学金受給 Another awarded scholarship

受給実績 Receipt record	<input type="checkbox"/> 有 <input checked="" type="checkbox"/> 無
助成機関名称 Funding agency	
奨学金名称 Scholarship name	
受給期間 Supported period	年 月 ~ 年 月
受給額 Amount received	円

7. 研究活動に関する報道発表 Press release concerned with your research activities

※記載した記事を添付してください。Attach a copy of the article described below

報道発表 Press release	<input type="checkbox"/> 有 <input checked="" type="checkbox"/> 無	発表年月日 Date of release	
発表機関 Released medium			
発表形式 Release method	・新聞 ・雑誌 ・Web site ・記者発表 ・その他()		
発表タイトル Released title			

8. 本研究テーマに関する特許出願予定 Patent application concerned with your research theme

出願予定 Scheduled	<input type="checkbox"/> 有 <input checked="" type="checkbox"/> 無	出願国 Application	
出願内容(概要) Application contents			

9. その他 Others

--

指導責任者(記名) 堤 敦朗

精神科医療通訳の「患者擁護」について

“Patient Advocacy” for Psychiatric Interpreters

金沢大学人間社会環境研究科 博士後期課程

周 英
堤 敦朗

金沢大学融合研究域 教授

【Abstract】

Globalization has facilitated international travel, and the number of non-native patients receiving psychiatric services in Japan is increasing. Consequently, differences in language and culture have become the biggest issues faced by psychiatric institutions. Therefore, psychiatric interpreters are expected to play a major role. Studies have indicated that medical interpreters require advocacy, especially in psychiatric settings. This article clarifies what is meant by the term “advocacy” and why it is required in psychiatric interpretation.

【Key words】

Psychiatric interpreters, Advocacy, Community interpreters

はじめに

世界規模でグローバル化が進み、人々の国境を跨ぐ移動が容易となっている。出入国在留管理庁^[1]によると、2020年6月末に日本における在留外国人数は288万5904人で、日本の総人口のおよそ2%を占めている。

日本全国の精神医療機関に対して実施された「精神医療機関における外国人患者受入の現状と課題把握に関する調査」^[2]（2020年3月）で、精神医療機関を受診する外国人患者の対応には多くの施設が苦慮していて、その背景に「言語面」や「文化的」背景が存在すること、また日本にいる外国人に対応するために「同意書および告知文書」の多言語版の作成や精神保健福祉法の早急な整備など、精神科医療における外国人患者の受け入れ環境の整備の必要性などが認識された。

このような状況下において、医療通訳が大きな役割を担うことができる。「言葉」の問題に関して、「心の病を患うと、外国語能力が極端に落ちる」「母語以外で自分の内面を語ることは難しい」^[3] ことがあるため、医療通訳が間に立つと、患者が母語で病状や心境などを語るができる。さらに「文化」の問題に関しては、両方の文化を知る医療通訳者がいる場合、文化の違いによる理解の差に気づき、適度な範囲内で補足説明をすることで医師と患者の間の意思疎通がよりスムーズになり、医師の病状把握や患者の安心感につながる事が期待できる。

本稿では、精神科の医師と患者の間に立つ医療通訳者のことを「精神科医療通訳」とする。「精神科医療通訳」は「一般身体医療通訳」と区別するために名づけたもので、既存の固有名詞ではない。また、医療通訳は「コミュニティ通訳」の一種であるため、医療通訳を論ずるにあたり、まずコミュニティ通訳について論ずる必要がある。

コミュニティ通訳とは

通訳の種類分類方法には大きく分けて2つある。一つは通訳の手法で分類する方法であり、「同時通訳」「逐次通訳」「ウィスパリング通訳」がある。もう一つは目的によって分類する方法であり、「会議通訳」「エンターテインメント通訳」「ビジネス通訳」「放送通訳」「コミュニティ通訳」「通訳ガイド」などがある¹⁾。

本稿で取り扱う「コミュニティ通訳」とは、在住外国人が専門職と話す時に使う通訳であり、具体的には「医療通訳」「司法通訳」「行政通訳」「教育通訳」などが挙げられる^[4]。これらの異なるタイプの通訳者は異文化の媒介者として意思疎通のための役割を果たす点においては同じだが、通訳者が置かれている環境がそれぞれ異なるため、通訳に求められる「言葉の伝達」以外の要素が異なってくる。例えば、「司法通訳」は中立性が極端に求められる^[5]のに対し、医療通訳は医師と患者のつなぎ役として患者の擁護をする必要がある^[6]。

精神科医療通訳の特殊性

医療通訳の役割を決定するいくつかの要素の一つに「医療科の特質」がある。

精神科医療の特質は、精神科医が患者の「行動・振る舞い」「認知能力」「コミュニケーション能力」を確認して診断をする点にある。これらの要素を判断するために、Turner^[7]は患者の話し方の要素、すなわち「構文」「語順」「語彙の整合性」「言葉の

脱落」「文化や宗教との整合性」「母国語での言語能力」の6つに注目すべきだと述べている。

つまり精神科医療における医療通訳では、患者の話す言葉の構文や語順の自然さ、不自然さを再現し、語彙の選択や整合性に問題があればそれも再現し、患者が話す事柄がその所属する文化や宗教において適切なものであるかも説明し、さらには通訳するだけではわからない患者の母国語での言語能力の評価を行うことまでもが求められるのである。精神科医療において医療通訳は、辻褄の合わないものは辻褄の合わないまま通訳して、その説明も求められる^[8]。例えば、統合失調症の幻覚妄想状態の患者がいるとする。統合失調症患者の最も重要な障害は思考障害で、精神科医が患者の訴えを聞いても、思考に論理の飛躍があるため、話の脈絡がうまくつかめず、理解不能であったりする。構文や語順の崩れ、語彙の整合性の不具合、言葉の脱落、自分自身で新しい言葉を作るという言語新作もみられる^[6]。しかし、通訳者はそのまま通訳し、その内容についても説明しなければならない。

さらに、上述の6つの要素を再現するには「機械的な通訳」では足りないため、事前に医師と通訳者が打ち合わせを行う必要がある。Turnerが診察前の打ち合わせ項目として「患者の医療背景」「患者の文化背景」「医療通訳の役割」「異文化問題への対処法」そして「中断方法」を提起している。さらに診察後の確認項目として、「診断に重要な要素の確認」と「通訳者の精神状態の把握」を指摘している^[7]。

事前の打ち合わせに関して、精神科医の阿部先生は、通訳者と患者が行うことも必要だと指摘する^[6]。診察をスムーズに進めるためには、患者が受

¹⁾ 通訳の分類法は国や地域、ひいては通訳派遣会社などによって違うため、上記の分類法は、状況や場面によって呼称が変わる場合がある。

診に至った背景を通訳者が事前に聞き取っておく必要があり、そのため通訳者は、精神科医療に関する医学的知識をある程度有しておく必要がある。また、医師と通訳者の事前打ち合わせと比較して、患者と通訳者の事前打ち合わせは、患者に通訳者が自分の味方であると感じさせやすいため、患者と通訳者の信頼構築につながる可能性がある。

精神科医療において同じ通訳者が担当することがより良いと考えられている。同じ通訳が継続的に担当すると患者と通訳者の間に個人的な関係が生まれ、「中立的」な立場が取りにくくなる懸念もあるが、他方で同じ通訳者が担当することで、前述した6つの要素に精通しやすくなり、患者との信頼関係の構築が容易になるメリットもある。その結果、診断に必要な要素を効率よく、正確に伝えることが可能になる^[8]。

したがって、精神科医療以外の医療における通訳は主に身体疾患に関わる医学的な知識が求められるが、精神医療における通訳は、精神疾患の症状、診断名や精神医療制度などに関する専門的知識が求められる。また、精神科医と患者の心をつなぐ理解者として位置づけられなければならないため、語学力以外に文化の理解や患者の擁護が求められる^[8]。

精神医療の通訳者に求められる専門性とは、精神疾患名とその疾患の概念、精神症状、診断方法、治療法、薬物の効用と副作用、治療経過、予後と精神医療制度の知識を指す。さらに、診察室で患者と精神科医をつなぐ通訳者として、自分の感情をできるだけ排除し、習得した知識を用いて両者の橋渡しをすることである。そのためには、両者の表情に気を配り、患者の苦悩や文化社会的背景を理解し、それぞれの感情と会話を正確な訳語で適切に伝え、患者と精神科医が通訳内容に対して同じ解釈をしているかを見抜いて、両者のつながりに揺るぎなく位置することが求められる^[6]。

精神科医療通訳の「患者擁護」とは

日本看護協会^[9]によると、「患者擁護」=アドボカシー (advocacy) とは権利擁護や代弁などという意味であり、看護実践において看護職は、患者のアドボケーター (権利擁護者、代弁者) として患者の権利を擁護し、患者の価値や信念に最も近い決定ができるように援助し、さらに患者の人間としての尊厳、プライバシーなどを尊重しなければならないという。

通訳の立場での「患者擁護」の定義について、国際的な規定やアメリカ、日本の規定、また専門家の見解を以下に示す。

- ・ 国際医療通訳者協会^[10] (IMIA: International Medical Interpreters Association) は医療通訳者の行動に関する倫理規定を策定した。倫理規程においては「通訳者は、患者の権利を擁護する役割、および情報伝達のために適切かつ必要な場合に限り、専門的な判断力で、異文化間の仲介者として医療提供者と患者に文化の違いや慣行を説明する役割を担う。」との記述がある。
- ・ 全米医療通訳協議会^[11] (NCIHC) は2004年7月に「全米医療通訳倫理規定」を発表した。この規定で「患者擁護」について「患者の健康、福利、あるいは尊厳が危険にさらされている場合、通訳者は、アドボケーター (擁護者) としてふるまうことを正当化されるかもしれない。アドボカシー (擁護的行為) とは、健康上の良い結果を支援するという意図を伴い、コミュニケーション促進の範囲を超えて、個人のために行われる行為であると理解される。擁護は、状況を慎重に思慮深く分析した後に、そして、他のより介入的でない手段によって問題が解決されなかった場合にのみ、行われるべきである。」

と示している。

- ・ 日本における規程に関して、厚生労働省の「医療通訳」^[12] テキストでは、権利擁護（アドボカシー）に関して「権利擁護（アドボカシー）とは患者が生命の尊厳や危機にさらされている場合には、適切な知識と判断によって権利擁護を果たすことである。」と示している。さらに、「通訳者が権利擁護を行うことは、通訳者の役割を超えており、すべきではないと禁止している国もあるが、本基準では、医療通訳においては、適切な状況分析をした上で、患者の安全や生命が脅かされる、危機にさらされている場合に限り、本来の医療通訳者としての役割から外れて、権利擁護のための行動を取ることができる」と付け加えている。
- ・ 専門家は通訳者の「患者擁護」について、飯田^[13]は「医療通訳士は患者と医療従事者の言葉と文化、置かれる状況を理解するから、全ての人に適切な医療サービスが提供されるよう尽力することが求められ、患者擁護ができる。」、また「権利の擁護は医療通訳士が直接的代理や代行を行うことでなく、患者が自らの権利を確保し回復して行くための支援を行うこと」と述べている。
- ・ エレーラ・ルルデス^[14]は「患者擁護」について、「外国人の患者などが言葉の壁によって自分を語れない（自身を代弁できない）場合、通訳士は「救済者」として手を差し伸べる」、「日本に暮らす外国人の社会的・経済的状況を把握したり、患者のわずかな顔の表情から文化的、家族的、個人的な状況を読み取ったりして必要な擁護を行う」、「通訳士は外国人に対する情報提供者（情報源）の役割を担っている。患者は通訳士に対して色々な期待を寄せているが、通訳者は、いつ直接介入すべきか、いつ他者に援

助を求めるべきかについて判断しなければならない」、「通訳士という仕事は、良心的で粘り強く、過保護にならない程度の暖かさを持った尊敬されるような対人援助である」と述べている。

以上の倫理規定および専門家の観点を踏まえ、通訳者の立場における「患者擁護」は「患者が危険にさらされ、他の介入的な手段がない場合にのみ行って良いという極めて稀な行為だ」と一部に認識されている一方、「通訳者が患者を観察し、患者が危険にさらされている場合には、患者の権利が尊重されるように患者の代弁者になったり、文化の理解者として患者と医者との間の文化的なギャップを埋めたり、情報提供者になったり、患者のために他の人に助けを求めたりして患者の回復を支援することである」と暫定的に定義づけることもできる。

終わりに

精神科医療通訳の特殊性と「患者擁護」の定義について論じた。しかし、実際の現場で精神科医療通訳をしている医療通訳者たちは「患者擁護」をどのように認識・実行しているのか、また実行する際の課題の有無に関して、引き続き研究をしていきたい。

謝辞

本研究は、日中笹川医学奨学金の助成を受けたものです。この奨学金制度により、私は研究活動に専念することができています。ご支援いただいた方々に厚く御礼申し上げます。

引用文献：

- [1] 出入国在留管理庁 在留外国人統計（旧登録外国人統計）統計表 https://www.moj.go.jp/isa/policies/statistics/toukei_ichiran_touroku.html（アクセス日：2022年3月1日）
- [2] 厚生労働省課題 令和元年度障害者総合福祉推進事業精神医療機関における外国人患者受入の現状と課題把握に関する調査 <https://www.mhlw.go.jp/content/12200000/000672477.pdf>（アクセス日：2022年3月1日）
- [3] 阿部裕 多文化精神医療 鹿児島：ラグーナ出版：2019
- [4] 村松紀子 「コミュニティ活動における医療通訳士の役割」『医療通訳士という仕事』大阪：大阪大学出版社：2013：76
- [5] 長尾ひろみ 「医療通訳の職業倫理規定」『医療通訳入門』東京：松柏社：2007 29-46
- [6] 阿部裕 精神医療におけるコミュニティ通訳の必要性 シリーズ多言語・多文化協働実践研究 16 2013：105-113
- [7] Turner G Onsite Mental Health Interpreting A workshop for Professional Interpreters from MMHA's NT forum
- [8] 押見貴之 精神医療における医療通訳 こころと文化 2009：8巻：108-113
- [9] 日本看護協会 看護実践情報 臨床倫理のアプローチ <https://www.nurse.or.jp/nursing/practice/rinri/text/basic/approach/index.html>（アクセス日：2022年3月1日）
- [10] IMIA Code of Ethics <https://www.imiaweb.org/code/default.asp>（アクセス日：2022年3月1日）
IMIA 倫理規定（日本語訳） <https://www.imiaweb.org/uploads/pages/393.pdf>（アクセス日：2022年3月1日）
- [11] 全米医療通訳倫理規定 https://www.migrationpolicy.org/sites/default/files/language_portal/ANationalCodeofEthicsforInterpretersinHealthCareinJapanese_0.pdf（アクセス日：2022年3月1日）
- [12] 厚生労働省 医療通訳に関する資料 テキスト「医療通訳」 <https://www.mhlw.go.jp/content/10800000/000385181.pdf> アクセス日：2022年3月1日
- [13] 飯田奈美子 「医療通訳士倫理規定を読み解く」『医療通訳士という仕事』大阪：大阪大学出版社：2013：33-47
- [14] エレーラ・ルルデス 「外国人患者から見た医療通訳士の役割」『医療通訳士という仕事』大阪：大阪大学出版社：2013：89-97

◆ 著者連絡先 ◆

周 英

金沢大学人間社会環境研究科 博士後期課程

E-mail：11431984@qq.com

精神科医疗口译的“患者拥护”

“Patient Advocacy” for Psychiatric Interpreters

金泽大学人间社会环境研究科 博士后期课程

周 英

金泽大学融合研究域 教授

堤 敦朗

【Abstract】

Globalization has facilitated international travel, and the number of non-native patients receiving psychiatric services in Japan is increasing. Consequently, differences in language and culture have become the biggest issues faced by psychiatric institutions. Therefore, psychiatric interpreters are expected to play a major role. Studies have indicated that medical interpreters require advocacy, especially in psychiatric settings. This article clarifies what is meant by the term “advocacy” and why it is required in psychiatric interpretation.

【Key words】

Psychiatric interpreters, Advocacy, Community interpreters

前 言

全球化正在世界范围进行，人们可以更容易的在世界各地移动。根据日本出入国在留管理厅^[1]的数据显示，截至2020年6月底，在日本的外国人人数为288万5904人，约占日本总人口的2%。

根据以日本全国范围的精神科医疗机构为对象开展的“精神科医疗机构接收外国人患者的现状和问题把握的相关调查”^[2]（2020年3月）显示，许多精神科医疗机构在接诊外国患者时感到困惑，并表示其原因在于“语言”和“文化”的不同。为了更好地应对在日本的外国患者，有必要准备更多种语言版本的“知情同意书和告知文件”，尽早完善精神保健福祉法，以改善对外国患者的接收环境。

在这样的大背景下，医疗口译员可以发挥重要作用。在“语言”的问题上，由于“当一个人患有精神疾病时，他的外语能力会极大降低。”“使用母语之外

的语言来谈论自己内心感受是很困难的”^[3]，所以医疗口译员可以帮助患者使用母语来谈论自己的病情和感受。此外，在“文化”方面，可以预见，了解两种文化的医疗口译员更明白文化差异造成的理解偏差，并能在合理的范围内提供补充说明，从而使医生和患者之间的沟通更加顺畅，使医生更好的了解患者病情并使患者更为放心。

在本文中，将介于精神科医生和患者之间的医疗口译员称为“精神科医疗口译”。它并非固定术语，是为了与“一般身体类医疗口译”区分，才冠以此名。医疗口译是“社区口译”的一种，在探讨医疗口译之前，需要首先认识什么是社区口译。

什么是社区口译

口译主要有两种分类。一种是按照翻译方式，可分为“同声传译”、“交替传译”和“耳语翻译”。另

一种是按照翻译目的划分。主要类别包括“会议口译”、“娱乐口译”、“商务口译”、“广播口译”、“社区口译”和“导游口译”等¹。

而本文所涉及的“社区口译”是指居住在日本的外国居民与专职人员交谈时所使用的口译。具体包括“医疗口译”、“司法口译”、“行政口译”和“教育口译”^[4]。这些不同类型的口译员作为不同文化间的中介，发挥促进沟通的作用方面是相同的，但由于口译员所处的环境不同，所以对他们除了“语言传播”之外的素质要求也不同。比如，“司法口译”被要求必须极为中立^[5]，而与此相对，医疗口译则更需要口译员作为医生与患者之间的纽带，对患者进行拥护^[6]。

精神科医疗口译的特殊性

有几个要素决定了医疗口译的实际作用，其中之一是“医疗部门的特质”。

精神科医学的特殊性在于医生诊断时需要考虑患者的“行动和行为”、“认知能力”以及“沟通能力”。Turner^[7]认为，精神科医生需要关注患者的表达，即“句法”、“词序”、“词汇的一致性”、“单词的遗漏”、“与文化和宗教的一致性”、“母语的语言能力”这六要素。

也就是说，精神科医疗口译，需要在翻译中再现实出患者所表达的语言的句法和词序是否自然，如果词汇的选择和一致性方面出现问题也应将其体现在翻译中，并对患者所说的事由是否与其所属的文化与宗教相契合进行说明。并且，因为仅靠翻译无法评估患者的母语水平，口译员还需要对其母语能力进行评价。也就是说，精神科医疗口译如果遇到患者的话语不合常理不合逻辑，也应该使用不合常理不合逻辑的方式进行翻译^[8]。例如，假设有一位精神分裂症的患者出

现幻觉和妄想。由于精神分裂症患者最严重的问题是思维障碍，所以精神科医生即使倾听了患者的主诉，但由于病人的思维具有跳跃性，无法掌握其言语脉络，从而导致患者的话语无法理解。除了句法和词序的混乱之外，还可能出现词汇的不一致以及单词的遗漏和患者自身创造出新语言的语言创新现象^[6]。但是，出现这样的情况时，口译员必须如实翻译，并对这些情况进行解释说明。

此外，由于“机械翻译”不足以再现上述六个要素，所以需要医生与口译员进行事前沟通确认。Turner提出了“患者的就医经历”、“患者的文化背景”、“医疗口译的作用”、“跨文化问题的处理方法”以及“如何打断”来作为检查前的沟通项目。并认为，就诊后应该“确认诊断过程中的重要要素”和“把握口译员的精神状态”^[7]。

但是，关于事前沟通确认，精神科的阿部医生认为应该由口译员和患者来进行事前沟通^[6]。为使诊疗能够顺利进行，口译员需要事先听取患者的就诊背景，因此，口译员需要具备一定的精神科方面的医学知识。此外，与医生和口译员的事前沟通确认相比，患者与口译员的事前沟通确认能让患者更容易产生口译员是站在自己一方的感觉，从而更容易的建立双方之间的信任关系。

在精神科医疗中由同一位口译员来持续负责被认为是更为理想的。但也有人担心，同一位口译员持续负责会使患者和译员之间形成个人关系，从而很难保持“中立”立场。但另一方面，同一位口译员负责的好处在于更容易把握上述六要素，并更容易与患者建立信任关系，从而能够更高效准确的传递诊断所需的要素信息^[8]。

因此，精神科医疗之外的医疗口译主要需要掌握与身体疾病相关的医学知识。而精神科医疗口译，则需要具备精神疾病的症状、诊断名称和精神保健系统

¹ 由于各国、各地区以及各口译派遣机构对口译员的分类不同，上述分类法在不同的情况和场合下会有不同的叫法。

的专业知识。此外，他们还必须是精神科医生与患者心灵之间的理解纽带。除了语言能力之外，还需要有文化的理解和对患者的拥护^[8]。

精神科医疗口译需要具备的专业素质，是指精神疾病的名称及其概念、精神疾病的症状、诊断方法、治疗方法、药物效益和副作用、治疗过程、预后和精神疾病医疗系统的相关知识。此外，作为诊疗室中患者与精神科医生的桥梁，口译员需要尽量不受自己情绪的影响，用所掌握的知识为二者的沟通作出努力。为此，需要既注意双方的面部表情，又理解患者的苦恼和文化社会背景，并用正确的语言恰当地传达每一次情绪和对话，观察患者和精神科医生对翻译内容是否有相同的理解，坚定地置身于两者的沟通之中^[6]。

精神科医疗口译的“患者拥护”是什么

根据日本护理协会^[9]的说法，“患者拥护”= advocacy 有权利拥护和代言等意思。在护理实践中，护士作为患者的 advocator（权利拥护者、代言人），需要维护患者的权利，帮助患者做出最接近他们价值观和信念的决定，并确保患者作为人的尊严和隐私得到尊重。

从口译员的角度来看，“患者拥护”意味着什么？本节将探讨国际和美国、日本的规定，以及专家的意见。

- 首先，国际医疗口译员协会^[10]（IMIA：International Medical Interpreters Association）为医疗口译员的行为制定了一套道德准则。其中，“口译员有责任维护患者的权利，为了传递信息在合适并必须这样做的情况下，利用他们的专业判断，作为跨文化的中介人士来向医疗服务提供者和患者解释文化和习惯差异。”
- 全美医疗口译委员会^[11]（NCIHC）于2004年7月

发布了“全美医疗口译道德准则”。准则对“患者拥护”的定义如下。当“病人的健康、福祉或尊严受到威胁时，口译员可以充当 advocator（拥护者）。Advocacy（拥护行为）被理解为，有支持形成积极的健康方面的结果的意图，并超越了促进沟通的范畴，为了个人而发生的行为。这种拥护行为，必须要在对情况深思熟虑之后，并且仅在其他非介入类手段无法解决问题的情况下才能使用。”

- 日本的情况，可以参考厚生劳动省的“医疗口译”^[12]教材。该教材中关于权利拥护（Advocacy）提供了如下措辞。“权利拥护（Advocacy）是在患者的生命尊严受到威胁时，使用恰当的知识来判断来保护他们权利的行为。”还进一步指出，“口译员的权利拥护行为，超出了口译员的职责范围，有些国家禁止口译员的这一行为。但本准则中规定，医疗口译在对情况进行恰当分析的基础上，仅在患者的安全和生命受到威胁，处于危险中时，才可以偏离原有的医疗口译的职责，来采取权利拥护的行为。”
- 专家们对口译员的患者拥护的解释则如下所示。饭田^[13]认为，“医疗口译员了解患者和医护人员语言和文化的差异，以及他们所处的环境，因此他们应致力于向所有人提供合适的医疗服务，并能够进行患者拥护行为。”他/她还指出，“权利拥护不是医疗口译员直接代理或代行，而是协助患者争取和恢复自己的权利。”
- Lourdes Herrera^[14]对“患者拥护”提出了以下观点。“当外国患者因语言障碍而无法为自己说话（无法为自己代言）时，口译员会像“救援者”一样伸出援手”，“需要通过了解生活在日本的外国人的社会和经济状况，并从患者的细微面部表情来读取其文化、家庭和个人情况，提供必要的拥护行为。”“口译员还扮演着向外国人提供信息（信息来源）的角色。患者对口译员有诸多

期待，但口译员必须判断应该何时直接干预，何时寻求他人的帮助。”“口译这份工作，应该是善良和坚持的，并且是令人尊重的援助过程，既给予一定程度上的温暖，又不会过度保护。”

总结上述道德规范和专家意见，虽然部分观点认为口译员所做出的“患者拥护”是“只有在患者处于危险境地，并在没有其他可干预的手段时才能采取的及其罕见的行为。”但作者希望暂且将其定义为“口译员观察患者，当患者处于危险境地时，需要成为患者的代言人以确保患者的权利得到尊重，还需要作为文化的理解者来弥补患者和医护之间的文化差异，以及作为信息提供者，或者作为支持者为患者寻求他人的帮助来协助患者康复”。

结 论

本文探讨了精神科医疗口译的特殊性和“患者拥护”的定义。然而，在实际临床中，从事精神科医疗口译的口译员们究竟如何看待和实践“患者拥护”，以及在实践过程中是否有困难之处。这些将会成为作者未来的研究课题。

鸣 谢

这项研究得到了中日笹川医学奖学金的资助。奖学金帮助我全身心投入到研究活动中。在此我表示衷心的感谢。

引用文献：

- [1] 出入国在留管理厅 在留外国人统计（旧登录外国人统计）统计表
https://www.moj.go.jp/isa/policies/statistics/toukei_ichiran_touroku.html（访问时间：2022年3月1日）
- [2] 厚生劳动省课题 令和元年度残疾人综合福祉推进事业

精神科医疗机构接收外国人患者的现状和问题把握的相关调查 <https://www.mhlw.go.jp/content/12200000/000672477.pdf>（访问时间：2022年3月1日）

- [3] 阿部裕 多文化精神医疗 鹿儿岛：Laguna 出版：2019
- [4] 村松纪子“社区活动中医疗口译员的作用”《医疗口译这份工作》大阪：大阪大学出版社：2013：76
- [5] 长尾 Hiromi “医疗口译的职业伦理规定”《医疗口译入门》东京：松柏社：2007 29-46
- [6] 阿部裕 精神医疗领域中社区口译的必要性 Series 多语言和多文化合作实践研究 16 2013：105-113
- [7] Turner G Onsite Mental Health Interpreting A workshop for Professional Interpreters from MMHA’s NT forum
- [8] 押见贵之 精神医疗中的医疗口译 心与文化 2009：8卷：108-113
- [9] 日本护理协会 护理实践信息 临床伦理方法 <https://www.nurse.or.jp/nursing/practice/rinri/text/basic/approach/index.html>（访问时间：2022年3月1日）
- [10] IMIA Code of Ethics <https://www.imiaweb.org/code/default.asp>（访问时间：2022年3月1日）
 IMIA 伦理规定（日语翻译版）<https://www.imiaweb.org/uploads/pages/393.pdf>（访问时间：2022年3月1日）
- [11] 全美医疗口译伦理规定 https://www.migrationpolicy.org/sites/default/files/language_portal/ANationalCodeofEthicsforInterpretersinHealthCareinJapanese_0.pdf（访问时间：2022年3月1日）
- [12] 厚生劳动省 与医疗口译相关的资料 课本《医疗口译》<https://www.mhlw.go.jp/content/10800000/000385181.pdf>（访问时间：2022年3月1日）
- [13] 饭田奈美子“医疗口译员伦理规定解读”《论医疗口译这份工作》大阪：大阪大学出版社：2013：33-47
- [14] Lourdes Herrera“从外国患者的角度看医疗口译的作用”《论医疗口译这份工作》大阪：大阪大学出版社：2013：89-97

◆ 著者联系方法 ◆

周 英

金泽大学人间社会环境研究科 博士后期课程

E-mail：11431984@qq.com

日中笹川医学奨学金制度<学位取得コース>評価書

課程博士：指導教官用



第 44 期

研究者番号：G4408

作成日：2024年3月1日

氏名	劉天驕	LIU TIANJIAO	性別	M	生年月日	1995/03/10
所属機関(役職)	成都市婦女兒童中心醫院醫務部(幹事)					
研究先(指導教官)	京都大学大学院 医学研究科遺伝医学講座分子遺伝学分野(篠原 隆司 教授)					
研究テーマ	α-Klotho を要因とする老化過程における精子幹細胞の微小環境制御 The study on the molecular mechanism of α-Klotho' s regulation of spermatogonial stem cell niche during aging					
専攻種別	<input type="checkbox"/> 論文博士			<input checked="" type="checkbox"/> 課程博士		

研究者評価(指導教官記入欄)

成績状況	良 学業成績係数=	取得単位数
		取得単位数 30 / 取得すべき単位数総数 30
学生本人が行った研究の概要	劉天驕さんは老化が精子形成に及ぼす影響を調べるため、老化モデルである α-Klotho ノックアウトマウスの解析を行いました。このマウスの精巣においてテストステロンの産生の低下と、血液精巣閉鎖を形成する分子の発現の低下していることを見出し、これらが精子形成の破綻に関わっている可能性を示唆する結果を得ました。また、テストステロンを皮下に埋め込み、もしくは皮下注射にて連続投与し、精巣や他の臓器に与える影響を調べました。	
総合評価	【良かった点】 実験手技は着実に増え、日本語は入学時より上達し読み書きに関してはかなり改善されました。	
	【改善すべき点】 日本語の会話の能力はまだ低く、研究室の他のメンバーとのコミュニケーションができていません。 研究に関しては、実験がうまくいかないなど問題が生じた時に自分で解決法を探す態度がまだできていません。	
	【今後の展望】 実験はできるようになりましたが、今後は研究の進め方や、問題が生じた時の対処法など、自立して研究に取り組んでいけるようになるかどうか大きな課題だと思われます。	
学位取得見込	奨学金支援終了後3年以内に日本の博士学位を取得できる見込みです。	
評価者(指導教官名) 篠原 隆司		

日中笹川医学奨学金制度<学位取得コース>報告書 研究者用



第44期

研究者番号: G4408

作成日: 2024年3月 12 日

氏名	刘 天骄	LIU TIANJIAO	性別	M	生年月日	1995/03/10
所属機関(役職)	成都市妇女儿童中心医院婦人科(医師)					
研究先(指導教官)	京都大学大学院 医学研究科遺伝医学講座分子遺伝学分野(篠原 隆司 教授)					
研究テーマ	α -Klothoを要因とする老化過程における精子幹細胞の微小環境制御 The study on the molecular mechanism of α -Klotho's regulation of spermatogonial stem cell niche during aging					
専攻種別	論文博士	<input checked="" type="checkbox"/>	課程博士	<input type="checkbox"/>		
1. 研究概要(1) 1) 目的(Goal) Aging is an urgent sociomedical issue which greatly threatens the fertility of population in many societies, especially in the developed countries and regions. It was reported that advanced paternal age brings higher risks of the pre-mature birth, low Apgar scores or admission to a neonatal intensive care department of newborns. The paternal age also improves the incidence rate of multiple congenital defects such as heart malformations as well as oral, palate and lip cleft. In addition, many mental disorders like autism, schizophrenia, bipolar disorder, low intelligence capacity were also more frequently observed with advanced father's age. ¹ The spermatogonial stem cells (SSCs), a rare subpopulation of the spermatogonia, are tasked to self-renew actively to sustain the SSC reservoir and give rise to progenitors poised for eventually differentiating into sperms ² . Spermatogonial stem cell (SSC) transplantation is regarded as a promising technique for treating the infertility of male survivors from cancer therapies before sexual maturation. The SSC transplantation, which reintroduces the SSCs into the seminiferous tubules of recipient's testis, can initiate their spermatogenesis and enable the production of their own biological children. The aging of SSCs is always accompanied by impaired proliferation, epigenetic abnormalities, altered metabolism and even the loss of sperm-forming function ³ , hampering the scientific utilization of SSCs' versatility a lot. The serial transplantation of SSCs into young testes, which enabled the longer than lifetime proliferation of SSCs and also proved their strong proliferation ability ⁴ . This evidence indicated that the SSCs have a unique mode of aging which is likely caused by the deteriorated niche, a protective region for stem cells with surrounding stromal cells. The Klotho gene is a critical gene in regulating phosphate metabolism and senescence. Mice deficient in α -Klotho not only have a phosphate metabolism dysfunction and hyperphosphatemia due to the impaired urinary phosphate excretion but also show apparent and multiple phenotypes of premature aging, including slower growth, smaller body size, atrophy of multiple organs, vascular calcification, sarcopenia, cardiac hypertrophy and fibrosis, osteopenia, emphysematous lung, hearing impairment, cognitive defects and shortened lifespan. ⁵ Its abnormal expression and functioning was recently found play an essential role in the premature placental senescence and malformation caused by advanced maternal age. ⁶ However, its regulation on the aging of male fertility has not been reported yet. This study aims to investigate the molecular mechanism of Klotho's regulation on the senescence of spermatogonial stem cells and their niche.						
2) 戦略(Approach) (1) investigate the spermatogonial stem cell niche of Klotho testis using immunostaining (2) functional analysis of the blood testicular barrier (BTB) of Klotho testis (3) exogenous supplement of testosterone into Klotho KO male mice and investigate its lifespan, spermatogonial stem cell niche and spermatogenesis						
3) 材料と方法(Materials and methods) (1) Animal: All the experimental protocols including animals were granted by the Institutional Animal Care and Use Committee of Kyoto University. The Klotho-deficient mice were produced by crossing the heterozygous Klotho +/- male and female mice. (2) Testosterone injection: 0.45mg per 0.1ml olive oil were subcutaneously injected into the Klotho KO male mice twice a week since 6 week old. (3) Biotin intrusion experiment: A total volume of 10 μ l 7.5mg/ml biotin was injected into each testis when the Klotho-deficient mice turned 10-week-old after anesthesia. Half hour after the injection, the mice were sacrificed, and the testes were removed and processed for immunostaining of Biotin. (4) Macroscopic and histological analysis of testes: Implanted mice were killed at the age of 12 weeks (4 weeks post-implantation). The testes were kept intact in cold PBS and observed under macroscopy. The testes and epididymis were fixed in 10% neutral-buffered formalin and embedded in paraffin blocks. Slides were stained with hematoxylin and eosin and checked for histological analysis						

(5) Immunostaining: Testes were fixed in 4% paraformaldehyde for 2 h at 4° C, and embedded in Tissue-Tek OCT compound (Sakura Finetek, Tokyo, Japan) before cryosectioning. Cryo-sections of 6 μ m thickness were then prepared. The tissue were then treated with 0.1% Triton-X and sodium citrate in phosphate-buffered saline (PBS) for permeabilization. Donkey serum diluted at 10 fold in PBS were applied onto the slide for blocking. The tissues were treated with first antibodies in 4 degree overnight, then incubated with second antibodies in room temperature for 1 hour after washing with PBS. Hoechst were diluted at 1:300 ratio in PBS and then dropped onto the slides and kept for 10 minutes for counter staining.

(6) Serum collection and Enzyme linked immunosorbent assay (ELISA): The blood from the carotid artery of mice will be collected during scarification. The blood would be kept in 4 degree overnight. The serum was collected after centrifugation at 1200rpm for 30min and cryopreserved in -80 degree. The ELISA will be performed for detecting the concentration of testosterone according to producer's protocol.

4) 実験結果 (Results)

We firstly examined the expression of Claudin 3, 5 and 11, as well as the key enzymes of testosterone synthesis (CYP17A1 and HSD3B) in the testes of Klotho KO and WT mice. We noticed that Cldn3 (0.004 ± 0.001 vs. 0.045 ± 0.008 $\mu\text{m}^2/\mu\text{m}$, $p < 0.001$), Cldn11 (0.006 ± 0.017 vs. 0.025 ± 0.006 $\mu\text{m}^2/\mu\text{m}$, $p = 0.01$), and CYP17A1 (0.112 ± 0.112 vs. 58.27 ± 9.82 μm^2 , $p = 0.0005$) are remarkably lower in Klotho KO testes in comparison with the WT, but the expressions of HSD3B and Cldn5 are comparable in both groups. These results imply the impaired BTB and testosterone metabolism in Klotho-deficient testis. Then we performed the Biotin intrusion experiment on the 10 weeks old Klotho KO mice and WT mice's testes ($n = 4$) to confirm whether there is a functional defect of BTB in Klotho KO testes. A total volume of 10 μl 7.5mg/ml biotin was injected into each testis. We observed that the majority of seminiferous tubules in Klotho KO mice's testes are notably more penetrated by biotin, while almost no biotin intrusion could be found in the WT testes ($88.89 \pm 4.54\%$ vs. $6.25 \pm 3.61\%$, $p < 0.0001$). We also detected the mRNA level of Klotho- α in the testes of CTL and W mice (5 Weeks old, $n = 3$) using qPCR. The result shows that α -Klotho's expression in W mice testes is significantly lower than the control group (1.023 ± 0.031 vs. 0.457 ± 0.062 , $p = 0.0012$).

Previous results showed the impaired testosterone metabolism and tight junction between Sertoli cells in Klotho KO testes. As previous studies showed that testosterone could rescue the incomplete tight junction between Sertoli cells and ameliorated the phenotype of aging, we hypothesized that the malfunctioning and lower expression of cldn3 and cldn11 in Klotho KO testes were caused by the lower level of testosterone. We also supplemented the testosterone into Klotho-deficient mice to rescue its fertility. To verify the feasibility of such technique, we treated 4 Klotho KO mice per group with testosterone or pure olive oil respectively. After 6 weeks of injection, we noticed that the external genital organ of the testosterone group became bigger. As we investigate the testosterone and olive oil treated Klotho KO by immunofluorescence, we found that the testosterone-treated Klotho deficient mice not only had a comparable level of Cldn5 as compared with the cholesterol group, but also showed increased level of Cldn3, Cldn11, as well as the GFRA1, Ki67 Positive GFRA1, and PNA, indicating that the testosterone treatment might not only repaired the BTB, but also facilitated its spermatogenesis. In consistent with these findings, the macroscopic and histological investigation of testosterone and cholesterol treated testes and the pathological examination of their epididymis also showed that the testosterone treatment had notably increased the size and weight of Klotho KO testis and facilitated the maturation of sperm in the epididymis compared with the olive oil group.

5) 考察 (Discussion)

We previously reported the intrinsic senescence model of SSC via Jnk-mediated glycolysis activation using long-term cultured SSCs. We noticed that aged SSCs proliferate faster than young SSCs and showed enhanced glycolytic activity, but still kept euploidy and exhibited stable androgenetic imprinting patterns with robust SSC activity, though having shortened telomeres. In consistency with this, the investigation of Klotho-deficient mice model also showed hyperactivation of JNK and enhanced glycolysis. We also reported the significantly smaller size, fewer PNA⁺ tubules, increased proliferation of ZBTB16⁺ cells, and enhanced level of 53BP1 expression in Klotho KO testis.

Although many phenotypes of Klotho-deficient testis were described in our previous work, the detailed molecular mechanism of Klotho's regulation on the spermatogonial stem cell niche and spermatogenesis has not been clearly elucidated. In present study, we observed the impaired testosterone metabolism, functional and structural defects of blood testicular barrier in the Klotho-KO testis, which could be rescued by the exogenous supplement of testosterone. To our surprise, the 4-week implantation of testosterone (from 8 weeks to 12 weeks) not only repaired the BTB of Klotho-deficient testis but also recovered their spermatogenesis. These findings indicated the potential existence of the Klotho-testosterone-BTB pathway. To verify such hypothesis, we plan to perform western blot in our future study. In addition, we would also endeavor to explore the underlying molecular mechanism in detail.

6) 参考文献 (References)

- 1 Janeczko, D., Hołowczuk, M., Orzeł, A., Klatka, B. & Semczuk, A. Paternal age is affected by genetic abnormalities, perinatal complications and mental health of the offspring. *Biomed Rep* 12, 83–88, doi:10.3892/br.2019.1266 (2020).
- 2 Takashima, S. & Shinohara, T. Culture and transplantation of spermatogonial stem cells. *Stem Cell Res* 29, 46–55, doi:10.1016/j.scr.2018.03.006 (2018).
- 3 Schultz, M. B. & Sinclair, D. A. When stem cells grow old: phenotypes and mechanisms of stem cell aging. *Development* 143, doi:10.1242/dev.130633 (2016).
- 4 Ryu, B.-Y., Orwig, K. E., Oatley, J. M., Avarbock, M. R. & Brinster, R. L. Effects of aging and niche microenvironment on spermatogonial stem cell self-renewal. *Stem Cells* 24, 1505–1511 (2006).
- 5 Kuro-O, M. The Klotho proteins in health and disease. *Nat Rev Nephrol* 15, 27–44, doi:10.1038/s41581-018-0078-3 (2019).
- 6 Chen, Z. et al. Advanced maternal age causes premature placental senescence and malformation via dysregulated α -Klotho expression in trophoblasts. *Aging Cell* 20, e13417, doi:10.1111/acel.13417 (2021).

2. 執筆論文 Publication of thesis ※記載した論文を添付してください。Attach all of the papers listed below.

論文名 1 Title	Current perception of transvaginal natural orifice transluminal endoscopic surgery among Chinese female gynecological medical staff					
掲載誌名 Published journal	Asian journal of surgery					
	2022 年 12 月	45 卷(号)	2947 頁 ~	2950 頁	言語 Language	English
第1著者名 First author	Tianjiao Liu	第2著者名 Second author	Dan Feng		第3著者名 Third author	Xin Li
その他著者名 Other authors						
論文名 2 Title	Potential resolution of placenta previa from the 28th-to the 36th-week of pregnancy: A retrospective longitudinal cohort study.					
掲載誌名 Published journal	Placenta					
	2022 年 8 月	126 卷(号)	164 頁 ~	170 頁	言語 Language	English
第1著者名 First author	Xiong Wen	第2著者名 Second author	Xin Li		第3著者名 Third author	Tianjiao Liu
その他著者名 Other authors	Rui Ding, Linbo Cheng, Dan Feng, Duan Duan, Mi Su, Yalan Li, Xiao Yang, Sumei Wei					
論文名 3 Title	Repeated transvaginal natural orifice transluminal endoscopic surgery: An initial Chinese experience					
掲載誌名 Published journal	The Journal of Obstetrics and Gynaecology Research					
	2023 年 8 月	49 卷(号)	2501 頁 ~	2508 頁	言語 Language	English
第1著者名 First author	Dan Feng	第2著者名 Second author	Tianjiao Liu		第3著者名 Third author	Xin Li
その他著者名 Other authors	Jieru Peng, Lu Huang, Li He					
論文名 4 Title	Perioperative outcomes of and predictors for conversion from transvaginal natural orifice transluminal endoscopic tubal surgeries: A retrospective cohort study of 619 patients.					
掲載誌名 Published journal	International Journal of Gynaecology and Obstetrics					
	2023 年 1 月	161 卷(号)	803 頁 ~	811 頁	言語 Language	English
第1著者名 First author	Dan Feng	第2著者名 Second author	Li He		第3著者名 Third author	Xin Li
その他著者名 Other authors	Qiang Zhang, Jieru Peng, Lu Huang, Tianjiao Liu, Yonghong Lin					
論文名 5 Title	Transvaginal natural orifice endoscopic surgery for tubal ectopic pregnancy: A more suitable surgical approach for enhanced recovery after surgery					
掲載誌名 Published journal	Heliyon					
	2024 年 1 月	- 卷(号)	- 頁 ~	- 頁	言語 Language	English
第1著者名 First author	Ying Liu	第2著者名 Second author	Xin Li		第3著者名 Third author	Tianjiao Liu
その他著者名 Other authors	Aijie Xie, Xian Wu, Yujian Jia, Xiaoyan Liao, Wei Cheng, Hui Wang, Fangyuan Zhong, Lijuan Xu, Juan Huang, Siqin					

3. 学会発表 Conference presentation ※筆頭演者として総会・国際学会を含む主な学会で発表したものを記載してくだ

※Describe your presentation as the principal presenter in major academic meetings including general meetings or international me

学会名 Conference				
演題 Topic				
開催日 date	年	月	日	開催地 venue
形式 method	<input type="checkbox"/> 口頭発表 Oral	<input type="checkbox"/> ポスター発表 Poster	言語 Language	<input type="checkbox"/> 日本語 <input checked="" type="checkbox"/> 英語 <input type="checkbox"/> 中国語
共同演者名 Co-presenter				
学会名 Conference				
演題 Topic				
開催日 date	年	月	日	開催地 venue
形式 method	<input type="checkbox"/> 口頭発表 Oral	<input type="checkbox"/> ポスター発表 Poster	言語 Language	<input type="checkbox"/> 日本語 <input type="checkbox"/> 英語 <input type="checkbox"/> 中国語
共同演者名 Co-presenter				
学会名 Conference				
演題 Topic				
開催日 date	年	月	日	開催地 venue
形式 method	<input type="checkbox"/> 口頭発表 Oral	<input type="checkbox"/> ポスター発表 Poster	言語 Language	<input type="checkbox"/> 日本語 <input type="checkbox"/> 英語 <input type="checkbox"/> 中国語
共同演者名 Co-presenter				
学会名 Conference				
演題 Topic				
開催日 date	年	月	日	開催地 venue
形式 method	<input type="checkbox"/> 口頭発表 Oral	<input type="checkbox"/> ポスター発表 Poster	言語 Language	<input type="checkbox"/> 日本語 <input type="checkbox"/> 英語 <input type="checkbox"/> 中国語
共同演者名 Co-presenter				

4. 受賞(研究業績) Award (Research achievement)

名称 Award name	国名 Country		受賞年 Year of	年	月
	国名 Country		受賞年 Year of	年	月

5. 本研究テーマに関わる他の研究助成金受給 Other research grants concerned with your research theme

受給実績 Receipt record	<input checked="" type="checkbox"/> 有 <input type="checkbox"/> 無
助成機関名称 Funding agency	成都市婦女児童中心医院
助成金名称 Grant name	成都市婦女児童中心医院英才計画第3期
受給期間 Supported period	2024 年 1 月 ~ 2025 年 12 月
受給額 Amount received	4,000,000 円
受給実績 Receipt record	<input type="checkbox"/> 有 <input type="checkbox"/> 無
助成機関名称 Funding agency	
助成金名称 Grant name	
受給期間 Supported period	年 月 ~ 年 月
受給額 Amount received	円

6. 他の奨学金受給 Another awarded scholarship

受給実績 Receipt record	<input type="checkbox"/> 有 <input checked="" type="checkbox"/> 無
助成機関名称 Funding agency	
奨学金名称 Scholarship name	
受給期間 Supported period	年 月 ~ 年 月
受給額 Amount received	円

7. 研究活動に関する報道発表 Press release concerned with your research activities

※記載した記事を添付してください。Attach a copy of the article described below

報道発表 Press release	<input type="checkbox"/> 有 <input checked="" type="checkbox"/> 無	発表年月日 Date of release	
発表機関 Released medium			
発表形式 Release method	・新聞 ・雑誌 ・Web site ・記者発表 ・その他()		
発表タイトル Released title			

8. 本研究テーマに関する特許出願予定 Patent application concerned with your research theme

出願予定 Scheduled	<input type="checkbox"/> 有 <input checked="" type="checkbox"/> 無	出願国 Application	
出願内容(概要) Application contents			

9. その他 Others

--

指導責任者(記名) 篠原 隆司



Letter to Editor

Current perception of transvaginal natural orifice transluminal endoscopic surgery among Chinese female gynecological medical staff



Keywords:

Transvaginal natural orifice transluminal endoscopic surgery
 Female medical staff
 Minimally invasive surgery
 Laparoendoscopy
 Online questionnaire

To the editor,

Natural orifice transluminal endoscopic surgery (NOTES) is a novel minimally invasive surgical (MIS) concept for performing endoscopic procedures via natural orifices.¹ Its feasibility for human clinical application was initially proven by transgastric appendectomy surgery conducted in 2003.² Since then, NOTES has developed rapidly, and surgeons have explored its use through other orifices, such as the intestinal tract and vagina. Notably, transvaginal NOTES (vNOTES) has been shown to outperform many other NOTES approaches due to the availability of greater operative space and easier removal of resected tissues, thus it has become increasingly popular for peritoneal surgeries, especially gynecologic laparoendoscopy, despite some reservations regarding the procedure.³

Theoretically, the acceptance of and preference for vNOTES can vary remarkably among patients and healthcare workers from different cultural, ethnic, and socioeconomic backgrounds, and it can be also expected to change with the development of endoscopic techniques and instruments. In the Western world, several surveys on patients and medical workers have investigated their

perceptions of the vNOTES procedure and yielded paradoxical results.⁴ However, after the introduction of vNOTES in mainland China seven years ago, its familiarity among the public and acceptance among mainland Chinese medical professionals has rarely been reported.⁵ Since healthcare workers' perception and awareness of such novel MIS procedures is probably a prerequisite for its recommendation and popularization, and female medical staff can provide insights from gynecological patients' perspective in hypothetical scenarios, we conducted a citywide online questionnaire survey in Chengdu, China, to investigate Chinese female gynecological health workers' current perceptions of vNOTES and to identify potential factors that contribute to their preference for vNOTES.

In our study, 523 gynecologists and 482 nurses completed the questionnaire. The majority (92.6%) had a positive attitude toward vNOTES. The “prefer vNOTES” group included a much lower proportion of respondents finishing postgraduate education than the “did not prefer vNOTES” group (11.0% vs. 25.7%, $p = 0.003$). They also included significantly more respondents having heard of the vNOTES procedure (83.9% vs. 68.9%, $p = 0.001$) and a strikingly higher proportion of members who had participated in vNOTES training courses (47.1% vs. 11.8%, $p = 0.029$). A significantly higher proportion of participants opted for vNOTES for reasons like safety (73.9% vs. 23.0%, $p < 0.001$), effectiveness (70.8% vs. 25.7%, $p < 0.001$), postsurgical cosmesis (93.7% vs. 73.0%, $p < 0.001$) and less postprocedural pain (71.1% vs. 47.3%, $p < 0.001$) than those in the “did not prefer vNOTES” group (shown in Table 1). Logistic regression revealed that concerns regarding postprocedural cosmesis (odds ratio (OR) = 3.239, $p < 0.001$) and prior awareness of vNOTES (OR = 2.271, $p = 0.004$) were significant predictors of preference for vNOTES, whereas those with higher education levels had a negative coefficient for vNOTES preference (OR = 0.549, $p = 0.003$) (see Fig. 1).

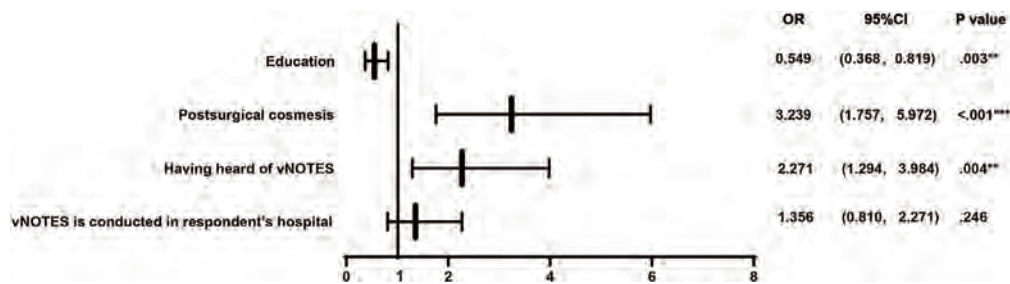


Fig. 1. Logistic regression model for factors that made vNOTES preferable. NOTE: ** $p < .01$, *** $p < .001$. Abbreviations: vNOTES, transvaginal natural orifice transluminal endoscopic surgery.

<https://doi.org/10.1016/j.asjsur.2022.06.117>

1015-9584/© 2022 Asian Surgical Association and Taiwan Robotic Surgery Association. Publishing services by Elsevier B.V. This is an open access article under the CC BY-NC-ND license (<http://creativecommons.org/licenses/by-nc-nd/4.0/>).

Table 1
Subject characteristics and attitudes toward vNOTES in “prefer for vNOTES” group versus “not prefer for vNOTES” group.

Subject characteristics	prefer vNOTES	not prefer vNOTES	X ²	P value
	n = 931(92.6%)	n = 74 (7.4%)		
Age group (years old)			2.871	0.580
20-30	258(27.7%)	22 (29.7%)		
31-40	394(42.3%)	36 (48.6%)		
41-50	204 (21.9%)	13 (17.6%)		
51-60	70 (7.5%)	3 (4.1%)		
≥61	5 (0.5%)	0(0%)		
Occupation			2.462	0.117
Gynecologist	478 (51.3%)	45 (60.8%)		
Nurse	453 (48.7%)	29 (39.2%)		
Educational background			13.762	0.003**
College	203 (21.8%)	14 (18.9%)		
Bachelor	625 (67.1%)	41 (55.4%)		
Master	97 (10.4%)	18 (24.3%)		
Doctoral	6 (0.6%)	1 (1.4%)		
Occupational title			2.271	0.518
Elementary	313 (33.6%)	24 (32.4%)		
Intermediate	354 (38.0%)	27 (36.5%)		
Senior	241 (25.9%)	19 (25.7%)		
Others	23 (2.5%)	4 (5.4%)		
The level of hospital you working for			3.203	0.361
Tertiary A	591 (63.5%)	54 (73.0%)		
Tertiary B	167 (17.9%)	8 (10.8%)		
Secondary A	96 (10.3%)	7 (9.5%)		
Secondary B	77 (8.3%)	5 (6.8%)		
How many years have you practiced medicine?			4.135	0.388
≤3	117 (12.6%)	13 (17.6%)		
3-5	92 (9.9%)	8 (10.8%)		
5-10	200 (21.5%)	16 (21.6%)		
10-20	297 (31.9%)	26 (35.1%)		
≥20	225 (24.2%)	11 (14.9%)		
Have you ever experienced laparoscopic surgery or examination			2.430	0.119
Yes	182 (19.5%)	9(12.2%)		
No	749 (80.5%)	65 (87.8%)		
Have you experienced laparotomy?			2.208	0.137
Yes	397(42.6%)	25 (33.8%)		
No	534 (57.4%)	49 (66.2%)		
Do you have child or children?			1.583	0.208
Yes	804 (93.1%)	60 (81.1%)		
No	127 (13.6%)	14 (18.9%)		
Attitude toward vNOTES				
Do you think postsurgical cosmesis is as important as safety for gynecologic surgery?			21.215	<0.001***
Yes	862 (92.6%)	57 (77.0%)		
No	69 (7.4%)	17 (23.0%)		
Have you ever heard of laparoendoscopic single site surgery?			0.698	0.404
Yes	867 (93.1%)	67 (90.5%)		
No	64 (6.9%)	7 (9.5%)		
(Q10)Have you heard of transvaginal natural orifice transluminal endoscopic surgery (vNOTES)?			10.779	0.001**
Yes	781 (83.9%)	51(68.9%)		
Never	150(16.1%)	23 (31.1%)		
If your answer to Q10 is yes, how do you know about it?	n = 781	n = 51		
Academic conference	488 (62.5%)	25 (49.0%)	3.671	0.055
Training courses	368 (47.1%)	16 (11.8%)	4.776	0.029*
Reading literatures	413 (52.9%)	29 (56.9%)	0.305	0.580
Heard from colleagues	496 (63.5%)	33 (64.7%)	0.057	0.811
Relatives and friends received vNOTES	119 (15.2%)	6 (11.8%)	0.452	0.501
Is vNOTES conducted in your hospital?			4.014	0.045*
Yes	490 (52.6%)	30 (40.5%)		
No	441 (47.4%)	44 (59.5%)		
What is the acceptable complication incidence rate of vNOTES for you to replace the conventional laparoendoscopic gynecologic surgery? (The incidence rate for surgical complications of laparoendoscopy is 0%–3%)			10.220	0.006**
0%–3%	626 (67.2%)	37 (50.0%)		
3%–6%	200 (21.5%)	27 (36.5%)		
6%–9%	105 (11.3%)	10 (13.5%)		
Are you willing to undergo vNOTES (if diagnosed with indication) or recommend it to relatives/friends/families?			84.902	<0.001***
Yes	688 (73.9%)	17 (23.0%)		
No	243 (26.1%)	57 (77.0%)		
If you are a patient or a family member of a patient, for what reason(s) you would prefer to undergo vNOTES (multiple options)?				
Safe	688 (73.9%)	17 (23.0%)	84.902	<0.001***

Table 1 (continued)

Subject characteristics	prefer vNOTES	not prefer vNOTES	X ²	P value
	n = 931(92.6%)	n = 74 (7.4%)		
Effective	659 (70.8%)	19 (25.7%)	63.546	<0.001***
Cosmetic/scarless	874 (93.9%)	54 (73.0%)	42.344	<0.001***
No pain or painless	662 (71.1%)	35 (47.3%)	18.283	<0.001***
Other reasons	6 (0.6%)	9 (12.2%)	61.852	<0.001***
If you are a patient or a family member of a patient, refuse to undergo vNOTES may for (multiple options)?				
Worried about its potential impact on sexual life	210 (22.6%)	27 (36.5%)	7.382	0.007**
Worried about its potential impact on pregnancy and childbirth	193 (20.7%)	29 (39.2%)	13.572	<0.001***
Worried about the failure of the operation	273 (29.3%)	27 (36.5%)	1.680	0.195
Worried about surgical complications	334 (35.9%)	43 (58.1%)	14.455	<0.001***
Other reasons	10 (1.1%)	11 (14.9%)	63.725	<0.001***
Do you think age is a major factor for choosing vNOTES or recommending it to friends and relatives?			3.272	0.070
Yes	330 (35.4%)	34 (45.9%)		
No	601 (64.6%)	40 (54.1%)		
If your answer is yes, what do you think is the most appropriate age for vNOTES	n = 330	n = 34	9.656	0.008**
20–40	227 (68.8%)	16 (47.1%)		
41–55	84 (25.4%)	12 (25.5%)		
>55	19 (5.8%)	6 (17.6%)		
(Q22) Do you think finish childbirth or not is a major factor in the surgical selection of vNOTES or the recommendation of it to your family and friends' choice?			1.002	0.317
Yes	348 (37.4%)	32 (43.2%)		
No	583 (62.6%)	42 (56.8%)		
If your answer to Q22 is yes, do you think you should finish childbirth before undergoing vNOTES?	n = 342	n = 32	0.021	0.885
Yes	265 (77.5%)	24 (75.0%)		
No	83 (22.5%)	8 (25.0%)		
Gynecologists' perspective of vNOTES				
	Prefer vNOTES n = 495	Not prefer vNOTES n = 42	X ²	P value
Would you like to conduct vNOTES in your department?			20.148	<0.001***
Yes	485 (98.0%)	36 (85.7%)		
No	10 (2.0%)	6 (14.3%)		
Do you think the prospect of vNOTES is good?			61.310	<0.001***
Yes	474 (95.8%)	27 (64.3%)		
No	21 (4.2%)	15 (35.7%)		
What do you think make it difficult to popularize vNOTES (multiple options)?				
Difficulty in establishment of surgical platform	294(59.4%)	25(59.5%)	0.002	1.000
Restricted operative visualization	388(78.4%)	38(90.4%)	3.452	0.063
The chopstick effect of single-port laparoscopy makes it difficult to perform vNOTES	376(76.0%)	24(57.1%)	7.213	0.007**
Low acceptance rate among patients	99(20.0%)	12(28.5%)	1.735	0.188
Higher operative cost	201(40.6%)	9(21.4%)	5.979	0.014*
Other-----	10(2.0%)	0(0%)	0.865	0.352
Gynecologists' perspective of vNOTES				
	Prefer vNOTES n = 495	Not prefer vNOTES n = 42	X ²	P value
Would you like to conduct vNOTES in your department?			20.148	<0.001***
Yes	485 (98.0%)	36 (85.7%)		
No	10 (2.0%)	6 (14.3%)		
Do you think the prospect of vNOTES is good?			61.310	<0.001***
Yes	474 (95.8%)	27 (64.3%)		
No	21 (4.2%)	15 (35.7%)		
What do you think make it difficult to popularize vNOTES (multiple options)?				
Difficulty in establishment of surgical platform	294(59.4%)	25(59.5%)	0.002	1.000
Restricted operative visualization	388(78.4%)	38(90.4%)	3.452	0.063
The chopstick effect of single-port laparoscopy makes it difficult to perform vNOTES	376(76.0%)	24(57.1%)	7.213	0.007**
Low acceptance rate among patients	99(20.0%)	12(28.5%)	1.735	0.188
Higher operative cost	201(40.6%)	9(21.4%)	5.979	0.014*
Other-----	10(2.0%)	0(0%)	0.865	0.352

In conclusion, the majority of surveyed female gynecologic healthcare workers had a supportive attitude toward vNOTES. Prior awareness and evaluation of surgical cosmesis had a positive influence on the surgical preference for vNOTES. However, concerns about its impact on sexual life, pregnancy, and childbirth still exist.

Funding

This study was funded by Chengdu High-level Key Clinical Specialty Construction Project, Chengdu Municipal Health Commission Project (No.2021215), Fifth Round of Chengdu Municipal Science and Technology Research Program (No.2021-YF05-00627-SN), and Japan China Sasakawa Medical Fellowship.

Data availability statement

Data of this study can be obtained from the corresponding author upon reasonable request.

Author contributions

Dan Feng conceptualized the study and formulated the questionnaire. Tianjiao Liu, Dan Feng, and Xin Li drafted and revised the manuscript. Tianjiao Liu and Xin Li also participated in statistical analyses. Li He supervised this study and critically reviewed the manuscript.

Declaration of competing interest

The authors declared no conflicts of interest related to this article.

Acknowledgment

We thank all the gynecologists and nurses who participated in our survey.

Appendix A. Supplementary data

Supplementary data to this article can be found online at <https://doi.org/10.1016/j.asjsur.2022.06.117>.

References

1. Rattner D, Kalloo A. ASGE/SAGES working group on natural orifice transluminal

- endoscopic surgery. *Surg Endosc*. 2006;20(2):329–333. October 2005.
2. Rao GV, Reddy DN, Banerjee R. NOTES: human experience. *Gastrointest Endosc Clin N Am*. 2008;18(2).
3. Kho RM. vNOTES: is it the panacea we are all hoping for? *J Minim Invasive Gynecol*. 2021;28(6):1146–1147.
4. Gerntke CI, Kersten JF, Schön G, Mann O, Stark M, Benhidjeb T. Women's perception of transvaginal natural orifice transluminal endoscopic surgery (NOTES): results of a survey of female medical staff and literature review. *Surg Innovat*. 2016;23(2):201–211.
5. Fei YF, Fei L, Salazar M, Renton DB, Hazey JW. Transvaginal surgery: do women want it? *J Laparoendosc Adv Surg Tech*. 2014;24(10):676–683.

Tianjiao Liu¹, Dan Feng¹

The Department of Gynecology of Chengdu Women's and Children's Central Hospital, School of Medicine, University of Electronic Science and Technology of China, Chengdu, People's Republic of China

Xin Li¹

The Department of Obstetrics of Chengdu Women's and Children's Central Hospital, School of Medicine, University of Electronic Science and Technology of China, Chengdu, People's Republic of China

Li He*

The Department of Gynecology of Chengdu Women's and Children's Central Hospital, School of Medicine, University of Electronic Science and Technology of China, Chengdu, People's Republic of China

* Corresponding author. No.1617, Riyue Avenue, Chengdu, Sichuan, 610091, China.

E-mail address: helisichuan@163.com (L. He).

9 March 2022

Available online 2 July 2022

¹ These authors contributed equally to this work.



Contents lists available at ScienceDirect

Asian Journal of Surgery

journal homepage: www.e-asianjournalsurgery.com

Letter to Editor

Current perception of transvaginal natural orifice transluminal endoscopic surgery among Chinese female gynecological medical staff



Keywords:

Transvaginal natural orifice transluminal endoscopic surgery
 Female medical staff
 Minimally invasive surgery
 Laparoendoscopy
 Online questionnaire

To the editor,

Natural orifice transluminal endoscopic surgery (NOTES) is a novel minimally invasive surgical (MIS) concept for performing endoscopic procedures via natural orifices.¹ Its feasibility for human clinical application was initially proven by transgastric appendectomy surgery conducted in 2003.² Since then, NOTES has developed rapidly, and surgeons have explored its use through other orifices, such as the intestinal tract and vagina. Notably, transvaginal NOTES (vNOTES) has been shown to outperform many other NOTES approaches due to the availability of greater operative space and easier removal of resected tissues, thus it has become increasingly popular for peritoneal surgeries, especially gynecologic laparoendoscopy, despite some reservations regarding the procedure.³

Theoretically, the acceptance of and preference for vNOTES can vary remarkably among patients and healthcare workers from different cultural, ethnic, and socioeconomic backgrounds, and it can be also expected to change with the development of endoscopic techniques and instruments. In the Western world, several surveys on patients and medical workers have investigated their

perceptions of the vNOTES procedure and yielded paradoxical results.⁴ However, after the introduction of vNOTES in mainland China seven years ago, its familiarity among the public and acceptance among mainland Chinese medical professionals has rarely been reported.⁵ Since healthcare workers' perception and awareness of such novel MIS procedures is probably a prerequisite for its recommendation and popularization, and female medical staff can provide insights from gynecological patients' perspective in hypothetical scenarios, we conducted a citywide online questionnaire survey in Chengdu, China, to investigate Chinese female gynecological health workers' current perceptions of vNOTES and to identify potential factors that contribute to their preference for vNOTES.

In our study, 523 gynecologists and 482 nurses completed the questionnaire. The majority (92.6%) had a positive attitude toward vNOTES. The “prefer vNOTES” group included a much lower proportion of respondents finishing postgraduate education than the “did not prefer vNOTES” group (11.0% vs. 25.7%, $p = 0.003$). They also included significantly more respondents having heard of the vNOTES procedure (83.9% vs. 68.9%, $p = 0.001$) and a strikingly higher proportion of members who had participated in vNOTES training courses (47.1% vs. 11.8%, $p = 0.029$). A significantly higher proportion of participants opted for vNOTES for reasons like safety (73.9% vs. 23.0%, $p < 0.001$), effectiveness (70.8% vs. 25.7%, $p < 0.001$), postsurgical cosmesis (93.7% vs. 73.0%, $p < 0.001$) and less postprocedural pain (71.1% vs. 47.3%, $p < 0.001$) than those in the “did not prefer vNOTES” group (shown in Table 1). Logistic regression revealed that concerns regarding postprocedural cosmesis (odds ratio (OR) = 3.239, $p < 0.001$) and prior awareness of vNOTES (OR = 2.271, $p = 0.004$) were significant predictors of preference for vNOTES, whereas those with higher education levels had a negative coefficient for vNOTES preference (OR = 0.549, $p = 0.003$) (see Fig. 1).

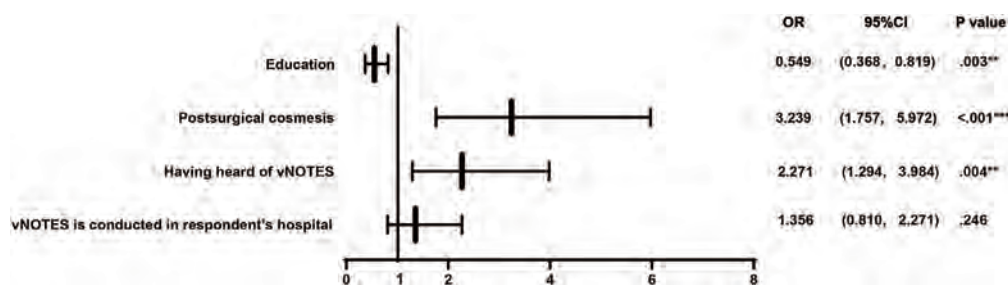


Fig. 1. Logistic regression model for factors that made vNOTES preferable. NOTE: ** $p < .01$, *** $p < .001$. Abbreviations: vNOTES, transvaginal natural orifice transluminal endoscopic surgery.

<https://doi.org/10.1016/j.asjsur.2022.06.117>

1015-9584/© 2022 Asian Surgical Association and Taiwan Robotic Surgery Association. Publishing services by Elsevier B.V. This is an open access article under the CC BY-NC-ND license (<http://creativecommons.org/licenses/by-nc-nd/4.0/>).

Table 1
Subject characteristics and attitudes toward vNOTES in “prefer for vNOTES” group versus “not prefer for vNOTES” group.

Subject characteristics	prefer vNOTES	not prefer vNOTES	X ²	P value
	n = 931(92.6%)	n = 74 (7.4%)		
Age group (years old)			2.871	0.580
20-30	258(27.7%)	22 (29.7%)		
31-40	394(42.3%)	36 (48.6%)		
41-50	204 (21.9%)	13 (17.6%)		
51-60	70 (7.5%)	3 (4.1%)		
≥61	5 (0.5%)	0(0%)		
Occupation			2.462	0.117
Gynecologist	478 (51.3%)	45 (60.8%)		
Nurse	453 (48.7%)	29 (39.2%)		
Educational background			13.762	0.003**
College	203 (21.8%)	14 (18.9%)		
Bachelor	625 (67.1%)	41 (55.4%)		
Master	97 (10.4%)	18 (24.3%)		
Doctoral	6 (0.6%)	1 (1.4%)		
Occupational title			2.271	0.518
Elementary	313 (33.6%)	24 (32.4%)		
Intermediate	354 (38.0%)	27 (36.5%)		
Senior	241 (25.9%)	19 (25.7%)		
Others	23 (2.5%)	4 (5.4%)		
The level of hospital you working for			3.203	0.361
Tertiary A	591 (63.5%)	54 (73.0%)		
Tertiary B	167 (17.9%)	8 (10.8%)		
Secondary A	96 (10.3%)	7 (9.5%)		
Secondary B	77 (8.3%)	5 (6.8%)		
How many years have you practiced medicine?			4.135	0.388
≤3	117 (12.6%)	13 (17.6%)		
3-5	92 (9.9%)	8 (10.8%)		
5-10	200 (21.5%)	16 (21.6%)		
10-20	297 (31.9%)	26 (35.1%)		
≥20	225 (24.2%)	11 (14.9%)		
Have you ever experienced laparoscopic surgery or examination			2.430	0.119
Yes	182 (19.5%)	9(12.2%)		
No	749 (80.5%)	65 (87.8%)		
Have you experienced laparotomy?			2.208	0.137
Yes	397(42.6%)	25 (33.8%)		
No	534 (57.4%)	49 (66.2%)		
Do you have child or children?			1.583	0.208
Yes	804 (93.1%)	60 (81.1%)		
No	127 (13.6%)	14 (18.9%)		
Attitude toward vNOTES				
Do you think postsurgical cosmesis is as important as safety for gynecologic surgery?			21.215	<0.001***
Yes	862 (92.6%)	57 (77.0%)		
No	69 (7.4%)	17 (23.0%)		
Have you ever heard of laparoendoscopic single site surgery?			0.698	0.404
Yes	867 (93.1%)	67 (90.5%)		
No	64 (6.9%)	7 (9.5%)		
(Q10)Have you heard of transvaginal natural orifice transluminal endoscopic surgery (vNOTES)?			10.779	0.001**
Yes	781 (83.9%)	51(68.9%)		
Never	150(16.1%)	23 (31.1%)		
If your answer to Q10 is yes, how do you know about it?	n = 781	n = 51		
Academic conference	488 (62.5%)	25 (49.0%)	3.671	0.055
Training courses	368 (47.1%)	16 (11.8%)	4.776	0.029*
Reading literatures	413 (52.9%)	29 (56.9%)	0.305	0.580
Heard from colleagues	496 (63.5%)	33 (64.7%)	0.057	0.811
Relatives and friends received vNOTES	119 (15.2%)	6 (11.8%)	0.452	0.501
Is vNOTES conducted in your hospital?			4.014	0.045*
Yes	490 (52.6%)	30 (40.5%)		
No	441 (47.4%)	44 (59.5%)		
What is the acceptable complication incidence rate of vNOTES for you to replace the conventional laparoendoscopic gynecologic surgery? (The incidence rate for surgical complications of laparoendoscopy is 0%–3%)			10.220	0.006**
0%–3%	626 (67.2%)	37 (50.0%)		
3%–6%	200 (21.5%)	27 (36.5%)		
6%–9%	105 (11.3%)	10 (13.5%)		
Are you willing to undergo vNOTES (if diagnosed with indication) or recommend it to relatives/friends/families?			84.902	<0.001***
Yes	688 (73.9%)	17 (23.0%)		
No	243 (26.1%)	57 (77.0%)		
If you are a patient or a family member of a patient, for what reason(s) you would prefer to undergo vNOTES (multiple options)?				
Safe	688 (73.9%)	17 (23.0%)	84.902	<0.001***

Table 1 (continued)

Subject characteristics	prefer vNOTES	not prefer vNOTES	X ²	P value
	n = 931(92.6%)	n = 74 (7.4%)		
Effective	659 (70.8%)	19 (25.7%)	63.546	<0.001***
Cosmetic/scarless	874 (93.9%)	54 (73.0%)	42.344	<0.001***
No pain or painless	662 (71.1%)	35 (47.3%)	18.283	<0.001***
Other reasons	6 (0.6%)	9 (12.2%)	61.852	<0.001***
If you are a patient or a family member of a patient, refuse to undergo vNOTES may for (multiple options)?				
Worried about its potential impact on sexual life	210 (22.6%)	27 (36.5%)	7.382	0.007**
Worried about its potential impact on pregnancy and childbirth	193 (20.7%)	29 (39.2%)	13.572	<0.001***
Worried about the failure of the operation	273 (29.3%)	27 (36.5%)	1.680	0.195
Worried about surgical complications	334 (35.9%)	43 (58.1%)	14.455	<0.001***
Other reasons	10 (1.1%)	11 (14.9%)	63.725	<0.001***
Do you think age is a major factor for choosing vNOTES or recommending it to friends and relatives?			3.272	0.070
Yes	330 (35.4%)	34 (45.9%)		
No	601 (64.6%)	40 (54.1%)		
If your answer is yes, what do you think is the most appropriate age for vNOTES	n = 330	n = 34	9.656	0.008**
20-40	227 (68.8%)	16 (47.1%)		
41-55	84 (25.4%)	12 (25.5%)		
>55	19 (5.8%)	6 (17.6%)		
(Q22) Do you think finish childbirth or not is a major factor in the surgical selection of vNOTES or the recommendation of it to your family and friends' choice?			1.002	0.317
Yes	348 (37.4%)	32 (43.2%)		
No	583 (62.6%)	42 (56.8%)		
If your answer to Q22 is yes, do you think you should finish childbirth before undergoing vNOTES?	n = 342	n = 32	0.021	0.885
Yes	265 (77.5%)	24 (75.0%)		
No	83 (22.5%)	8 (25.0%)		
Gynecologists' perspective of vNOTES				
	Prefer vNOTES n = 495	Not prefer vNOTES n = 42	X ²	P value
Would you like to conduct vNOTES in your department?			20.148	<0.001***
Yes	485 (98.0%)	36 (85.7%)		
No	10 (2.0%)	6 (14.3%)		
Do you think the prospect of vNOTES is good?			61.310	<0.001***
Yes	474 (95.8%)	27 (64.3%)		
No	21 (4.2%)	15 (35.7%)		
What do you think make it difficult to popularize vNOTES (multiple options)?				
Difficulty in establishment of surgical platform	294(59.4%)	25(59.5%)	0.002	1.000
Restricted operative visualization	388(78.4%)	38(90.4%)	3.452	0.063
The chopstick effect of single-port laparoscopy makes it difficult to perform vNOTES	376(76.0%)	24(57.1%)	7.213	0.007**
Low acceptance rate among patients	99(20.0%)	12(28.5%)	1.735	0.188
Higher operative cost	201(40.6%)	9(21.4%)	5.979	0.014*
Other-----	10(2.0%)	0(0%)	0.865	0.352
Gynecologists' perspective of vNOTES				
	Prefer vNOTES n = 495	Not prefer vNOTES n = 42	X ²	P value
Would you like to conduct vNOTES in your department?			20.148	<0.001***
Yes	485 (98.0%)	36 (85.7%)		
No	10 (2.0%)	6 (14.3%)		
Do you think the prospect of vNOTES is good?			61.310	<0.001***
Yes	474 (95.8%)	27 (64.3%)		
No	21 (4.2%)	15 (35.7%)		
What do you think make it difficult to popularize vNOTES (multiple options)?				
Difficulty in establishment of surgical platform	294(59.4%)	25(59.5%)	0.002	1.000
Restricted operative visualization	388(78.4%)	38(90.4%)	3.452	0.063
The chopstick effect of single-port laparoscopy makes it difficult to perform vNOTES	376(76.0%)	24(57.1%)	7.213	0.007**
Low acceptance rate among patients	99(20.0%)	12(28.5%)	1.735	0.188
Higher operative cost	201(40.6%)	9(21.4%)	5.979	0.014*
Other-----	10(2.0%)	0(0%)	0.865	0.352

In conclusion, the majority of surveyed female gynecologic healthcare workers had a supportive attitude toward vNOTES. Prior awareness and evaluation of surgical cosmesis had a positive influence on the surgical preference for vNOTES. However, concerns about its impact on sexual life, pregnancy, and childbirth still exist.

Funding

This study was funded by Chengdu High-level Key Clinical Specialty Construction Project, Chengdu Municipal Health Commission Project (No.2021215), Fifth Round of Chengdu Municipal Science and Technology Research Program (No.2021-YF05-00627-SN), and Japan China Sasakawa Medical Fellowship.

Data availability statement

Data of this study can be obtained from the corresponding author upon reasonable request.

Author contributions

Dan Feng conceptualized the study and formulated the questionnaire. Tianjiao Liu, Dan Feng, and Xin Li drafted and revised the manuscript. Tianjiao Liu and Xin Li also participated in statistical analyses. Li He supervised this study and critically reviewed the manuscript.

Declaration of competing interest

The authors declared no conflicts of interest related to this article.

Acknowledgment

We thank all the gynecologists and nurses who participated in our survey.

Appendix A. Supplementary data

Supplementary data to this article can be found online at <https://doi.org/10.1016/j.asjsur.2022.06.117>.

References

1. Rattner D, Kalloo A. ASGE/SAGES working group on natural orifice transluminal

- endoscopic surgery. *Surg Endosc*. 2006;20(2):329–333. October 2005.
2. Rao GV, Reddy DN, Banerjee R. NOTES: human experience. *Gastrointest Endosc Clin N Am*. 2008;18(2).
3. Kho RM. vNOTES: is it the panacea we are all hoping for? *J Minim Invasive Gynecol*. 2021;28(6):1146–1147.
4. Gerntke CI, Kersten JF, Schön G, Mann O, Stark M, Benhidjeb T. Women's perception of transvaginal natural orifice transluminal endoscopic surgery (NOTES): results of a survey of female medical staff and literature review. *Surg Innovat*. 2016;23(2):201–211.
5. Fei YF, Fei L, Salazar M, Renton DB, Hazey JW. Transvaginal surgery: do women want it? *J Laparoendosc Adv Surg Tech*. 2014;24(10):676–683.

Tianjiao Liu¹, Dan Feng¹

The Department of Gynecology of Chengdu Women's and Children's Central Hospital, School of Medicine, University of Electronic Science and Technology of China, Chengdu, People's Republic of China

Xin Li¹

The Department of Obstetrics of Chengdu Women's and Children's Central Hospital, School of Medicine, University of Electronic Science and Technology of China, Chengdu, People's Republic of China

Li He*

The Department of Gynecology of Chengdu Women's and Children's Central Hospital, School of Medicine, University of Electronic Science and Technology of China, Chengdu, People's Republic of China

* Corresponding author. No.1617, Riyue Avenue, Chengdu, Sichuan, 610091, China.

E-mail address: helisichuan@163.com (L. He).

9 March 2022

Available online 2 July 2022

¹ These authors contributed equally to this work.



ORIGINAL ARTICLE

Repeated transvaginal natural orifice transluminal endoscopic surgery: An initial Chinese experience

Dan Feng¹ | Tianjiao Liu¹ | Xin Li¹ | Jieru Peng² | Lu Huang¹ | Li He¹

¹Department of Gynecology, Chengdu Women's and Children's Central Hospital, School of Medicine, University of Electronic Science and Technology of China, Chengdu, China

²Medical Administrative Department, Chengdu Women's and Children's Central Hospital, School of Medicine, University of Electronic Science and Technology of China, Chengdu, China

Correspondence

Li He, Department of Gynecology, Chengdu Women's and Children's Central Hospital, School of Medicine, University of Electronic Science and Technology of China, No. 1617, Riyue Avenue, Chengdu 610091, China.
Email: helisichuan@163.com

Funding information

Chengdu High-level Key Clinical Specialty Construction Project; Chengdu Municipal Health Commission Project, Grant/Award Number: 2021215; Fifth Round of Chengdu Municipal Science and Technology Research Program, Grant/Award Number: 2021-YF05-00627-SN; Japan China Sasakawa Medical Fellowship Program; Chengdu Municipal Medical Research Project in 2023

Abstract

Aims: To investigate the perioperative outcomes and sexual function of patients undergoing repeated transvaginal natural orifice transluminal endoscopic surgery (vNOTES).

Methods: We retrieved the records of patients who underwent vNOTES twice at our institute between April 2019 and December 2022 and analyzed their baseline information and perioperative complications, and compared the pre- and postoperative sexual function of both vNOTES.

Results: Patients' mean age and body mass index were 29.00 ± 3.59 and 30.4 ± 4.00 years and 21.89 ± 3.69 and 22.76 ± 3.88 kg/m², respectively, when receiving the first and second vNOTES. Ectopic pregnancy was the most frequent indication for vNOTES, with 7 cases in the first vNOTES and 11 cases in repeated vNOTES. The interval between the two vNOTESs ranged from 9 days to 38 months. The operation duration (63.33 ± 13.71 vs. 67.33 ± 22.51 min, $p = 0.723$), intraoperative estimated blood loss (32.00 ± 20.42 vs. 30.00 ± 9.26 mL, $p = 0.429$), and duration of postoperative hospital stay (2.20 ± 0.56 vs. 2.40 ± 0.51 days, $p = 0.082$) of both vNOTESs were comparable. No significant differences were found in any of the domains in the comparison of pre-first and post-first vNOTES, pre-second and post-second vNOTES, and pre-first and post-second vNOTES female sexual function index. None of the patients delivered after the second vNOTES.

Conclusion: Repeated vNOTES is safe and feasible. No significant change in the patients' sexual function was found in our cohort after the first and second vNOTES.

KEYWORDS

culdotomy, female sexual function index, incision complications, perioperative complications

INTRODUCTION

Natural orifice transluminal endoscopic surgery (NOTES) uses natural orifices such as the stomach, urethra, rectum, and vagina to access the body cavity and targeted organs. With the development of endoscopic techniques, NOTES has been proven clinically feasible and has achieved better surgical outcomes, especially in averting visible skin scars.¹ However, because of technical difficulties and specific morbidities, most NOTES approaches require highly skilled hands and careful preoperative examination and consultation; thus, they have not gained popularity as expected.²

NOTES performed transvaginally, hereinafter abbreviated as vNOTES, has avoided many demerits of other NOTES. It enables shorter access to the peritoneum and urogenital organs, easier retrieval of large and hard specimens, closure of the incision under direct view, and the use of rigid endoscopes. It also reportedly outperforms other endoscopic techniques because of its better cosmetic outcomes, less pain and intraoperative bleeding, and faster recovery.³ Therefore, vNOTES has been increasingly used to treat benign gynecological diseases.

Although many studies have demonstrated the feasibility and safety of vNOTES for better short-term surgical outcomes compared to other endoscopic techniques,^{4,5} evidence supporting its repeatability is still lacking.^{6,7} Considering that it was not fully elucidated whether the second

Dan Feng, Tianjiao Liu, and Xin Li contributed equally to this study.

vNOTES can be successfully performed without severe adverse surgical outcomes and it is possible that the repeated colpotomy in the second vNOTES might cause undesirable impairment to patients' sexual function and vaginal delivery, research on repeated vNOTES' impact on these issues is desperately needed to fill the knowledge gap.⁶ To this end, this case series retrieved all the 15 repeated vNOTES for benign gynecological indications performed at our institute in recent years and compared the postoperative outcomes and pre- and postoperative sexual function of both vNOTESs, hoping to prove the feasibility and safety of repeated vNOTES.

METHODS

Study design

This is a retrospective study, which investigated a series of patients who underwent vNOTES twice at our institute between April 2019 and December 2022 and analyzed their baseline information (age, education, ethnicity, body mass index [BMI], gravidity and parity history, abdominopelvic surgical history, and comorbidities) and perioperative outcomes (time to establish the surgical entrance, operation duration, intraoperative pelvic adhesion [categorized based on the grading system issued by the American Society for Reproductive Medicine, ASRM], estimated intraoperative blood loss, volume of blood transfusion, pre- and postoperative hemoglobin levels, postoperative pain score [Visual Analog Scale, VAS] of the first to third postoperative days,⁸ and intraoperative complications, including surgical conversion) of both vNOTESs. The VAS consists of a 10 cm-long line with both ends representing the extremes of pain intensity (from painless to extremely painful). The time to establish surgical entrance was defined as the sum of the time taken to expose the cervical part of the vagina and posterior vaginal fornix by clamping, incise the posterior vaginal fornix, and insert the disposable tractor. In addition, when patients were about to undergo vNOTES, their preoperative sexual functions were surveyed using the Female Sexual Function Index (FSFI) scale after obtaining their written consent forms during the preoperative assessment. Postoperative sexual function data were collected 3–6 months after vNOTES. The intervals between the vNOTESs were calculated and recorded. The patients' postoperative childbirth status was also followed up until the end of the study.

Inclusion and exclusion criteria

At our institute, we had similar inclusion and exclusion criteria for the first and second vNOTES, except that the patient requiring the second vNOTES must have a surgical history of a first vNOTES. The inclusion criteria for

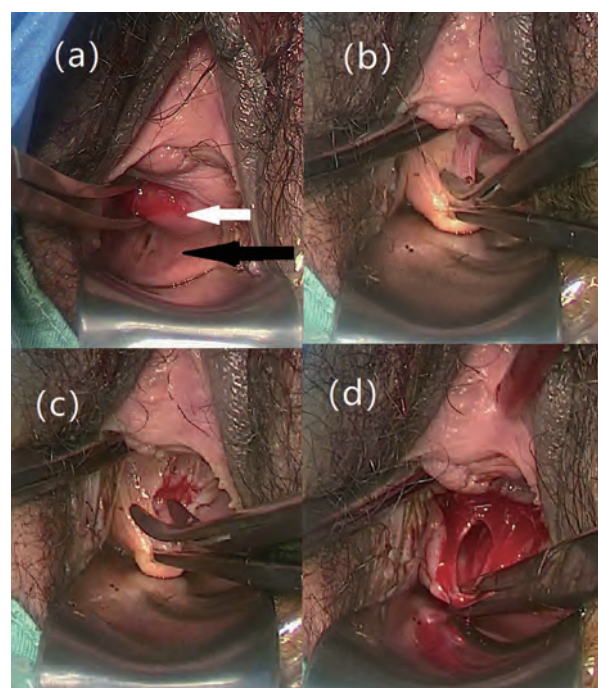


FIGURE 1 Critical steps in establishing the surgical platform of second transvaginal natural orifice transluminal endoscopic surgery (vNOTES). (a) Mucous wrinkles on the posterior vaginal fornix. (b–d) Entering the pelvic cavity through the previous incision.

vNOTES were: (i) laparoscopic surgery was needed for benign gynecological indications; (ii) patients showed willingness to undergo vNOTES. The exclusion criteria for vNOTES were as follows: (i) history of rectal surgery, severe pelvic inflammation, and pelvic radiotherapy; (ii) signs of suspected rectovaginal endometriosis, malignant tumors, or severe pelvic adhesions in preoperative examinations; (iii) not yet experienced sexual intercourse; (iv) not suitable to receive transvaginal surgery due to the risk of infection, including vaginal infections, or massive pelvic hemorrhage potentially necessitating autotransfusion; and, (v) myoma on the lateral wall or posterior and anterior wall of the uterus.

Surgical procedures

The vNOTES approaches in the present study were similar to those described in previous publications, with incisions of both first and second vNOTES made on the posterior vaginal fornix.^{9–12} All surgeries were performed by the same group of highly experienced surgeons. By the end of vNOTES, an anti-cohesive reagent (Gynecare Interceed [Johnson & Johnson, New Jersey, the United States]), was applied if the patient was willing to receive anti-cohesive treatment. The surgical incisions were closed by continuous suturing of both layers of the vaginal wall and peritoneum using a 2–0 absorbable suture. For the second vNOTES, there are two noteworthy

TABLE 1 Patients' baseline information.

Case no.	Age (year) ^a	Age (year) ^b	BMI (kg/m ²) ^a	BMI (kg/m ²) ^b	Gravity ^a	Gravity ^b	Parity ^a	Parity ^b	Vaginal delivery ^a	Vaginal delivery ^b	Cesarean section ^a	Cesarean section ^b
1	25	28	21.6	27.0	0	2	0	0	0	0	0	0
2	26	27	18.5	18.9	1	2	0	0	0	0	0	0
3	35	37	26.7	27.0	1	3	0	0	0	0	0	0
4	26	26	19.3	19.3	2	2	0	0	0	0	0	0
5	30	32	17.1	17.9	3	4	0	0	0	0	0	0
6	30	33	24.0	25.1	7	8	0	0	0	0	0	0
7	25	26	27.0	28.0	2	3	0	0	0	0	0	0
8	26	26	19.1	20.3	0	1	0	0	0	0	0	0
9	26	26	19.8	19.8	1	2	0	0	0	0	0	0
10	31	33	26.0	25.7	4	5	1	1	0	0	1	1
11	36	37	21.2	21.8	3	3	1	1	0	0	1	1
12	30	33	20.3	20.1	3	3	2	2	2	2	0	0
13	27	28	19.5	19.7	0	0	0	0	0	0	0	0
14	29	30	19.2	21.1	1	2	0	0	0	0	0	0
15	33	34	29.0	29.7	5	5	1	1	1	1	0	0
Average	29.00 ± 3.59	30.4 ± 4.00	21.89 ± 3.69	22.76 ± 3.88								

Abbreviation: vNOTES, transvaginal natural orifice transluminal endoscopic surgery.

^aCharacteristics of 1st vNOTES.

^bCharacteristics of 2nd vNOTES.

points (shown in Figure 1): (1) Before performing the culdotomy for establishing the surgical platform of the second vNOTES, special mucous wrinkles on the posterior vaginal fornix, caused by the previous incision and suture, could be easily noticed (Figure 1a); (2) Due to the narrow surgical safe zone of the posterior fornix, we accessed the pelvic cavity via a previous incision located 0.5 cm below the cervicovaginal junction or in the same location as the mucous wrinkles (Figure 1b–d).

FSFI

The FSFI is a validated and widely applied scale with a maximum obtainable score of 95. It comprises 19 questions involving six domains of female sexual experience, including libido, arousal, lubrication, orgasm, satisfaction, and pain.¹³ A score lower than 26.5 indicates impaired sexual function.¹⁴ The score of each domain is determined by the sum of all items in that domain multiplied by the domain factor (desire, 0.6; arousal, 0.3; lubrication, 0.3; orgasm, 0.4; satisfaction, 0.4; pain, 0.4). The overall score is the sum of the six domain scores.

Statistical analysis

SPSS version 25.0 (IBM Corporation, Armonk, NY) and GraphPad Prism (version 9.0.0, GraphPad Software, San Diego, CA) were used for statistical analyses of the present study. Paired Student's *t*-test was performed for each patient's pre- and postoperative FSFI scores of the first and second vNOTESs. Statistical significance was defined as a *p*-value lower than 0.05.

RESULTS

Patients' baseline characteristics

During the study period, there were approximately 3000 patients who underwent their first vNOTES. Among them, 21 patients were initially considered for a second vNOTES, but 6 cases (5 cases of tubal pregnancy and massive pelvic hemorrhage and 1 case of a potentially malignant indication) underwent transumbilical laparoendoscopic single site surgery instead. As a result, there were 15 patients who were willing to undergo a second vNOTES in light of their satisfactory cosmetic outcomes and painless experience in the first vNOTES. Their socio-demographic characteristics are given in Table 1. Their mean age during the first and second vNOTES was 29.00 ± 3.59 and 30.4 ± 4.00 years, respectively. The mean values of their BMI when receiving the first and second vNOTES were 21.89 ± 3.69 and 22.76 ± 3.88 kg/m². Three patients had never experienced pregnancy before their first vNOTES. This number decreased to one

after the second vNOTES. Most patients (11/15) were nulliparous at the time of the first vNOTES. One case had induced labor at the 20th gestational week because of fetal anomalies during the interval between both vNOTES. None of the patients delivered after the second vNOTES. Among the remaining four cases, one patient had experienced vaginal delivery once, one had delivered vaginally twice, and the other two had undergone cesarean section once.

Surgical outcomes of first and second vNOTES

Subsequently, we summarized the clinicopathological characteristics of both the vNOTESs (Table 2). Ectopic pregnancy was the most frequent indication for vNOTES, with 7 cases during the first vNOTES and 11 during the second, followed by ovarian teratoma, with 5 cases during the first vNOTES. The interval between both vNOTES approaches ranged from 9 days to 38 months, with case 4 complicated by persistent ectopic pregnancy after vNOTES salpingostomy, and thus received a vNOTES salpingectomy on the 9th postoperative day. Their postoperative VAS score also remained stable, with only case no. 8 experiencing slightly increased VAS score after the second vNOTES (2 and 1 on the first and second postoperative day of the first vNOTES, respectively vs. 3, 2, and 1 on postoperative Day 1, 2, and 3, respectively). Intriguingly, this patient did not experience any perioperative or postoperative complications during the follow-up, even though the surgical interval was remarkably short. No other perioperative complications were found in either vNOTES among the patients. We also noticed slightly exacerbated intraoperative pelvic adhesion during the first vNOTES in cases 3, 6, and 12, which correspondingly increased the difficulty of repeated vNOTES but did not lead to any surgical conversion. In addition, none of the cases had any postoperative incision complications such as hernia, polypi, or granuloma. The operation duration (63.33 ± 13.71 vs. 67.33 ± 22.51 min, $p = 0.429$), intraoperative estimated blood loss (32.00 ± 20.42 vs. 30.00 ± 9.26 , $p = 0.723$), and postoperative hospital stay (2.20 ± 0.56 vs. 2.40 ± 0.51 , $p = 0.082$) of both vNOTESs were also comparable. However, we noticed a prolonged surgical duration in cases 3, 10, 12, and 15. Moreover, the matched samples *t*-test revealed that the second vNOTES needed a significantly longer time to establish the surgical entrance (3.53 ± 1.36 vs. 4.73 ± 1.58 , $p = 0.023$). Noteworthy, three patients were pregnant at the end of the study period.

Pre- and postoperative sexual function of the first and second vNOTES

The domain and overall scores of the patients' pre- and postoperative FSFI for both vNOTES are listed in Table 3 as mean \pm standard error. We only recorded case 4's pre-first and post-second vNOTES FSFI (due to the

TABLE 2 Clinicopathological features of the first and second vNOTES.

Case no.	Surgical type ^a	Interval between both vNOTES, days	Indication ^a	Indication ^b	Time to reach the abdominal cavity, min		Operation duration, min ^b
					abdominal cavity, min ^a	the abdominal cavity, min ^b	
1	Right ovarian cystectomy	787	Right ovarian teratoma(5 cm)	Left ampullary pregnancy	7	5	50
2	Left ovarian cystectomy	152	Left ovarian teratoma(5.5 cm)	Left ampullary pregnancy	3	4	35
3	Bilateral tubal ligation	283	Infertility; IVF	Infertility; IVF	5	8	105
4	Left Salpingostomy	9	Left ampullary pregnancy	Persistent Ectopic Pregnancy	3	5	40
5	Right salpingostomy	546	Right ampullary pregnancy	Right ampullary pregnancy	2	4	50
6	Left salpingostomy	891	Left ampullary pregnancy	Left ampullary pregnancy	2	6	75
7	Right salpingostomy	692	Right ampullary pregnancy	Left ampullary pregnancy	3	6	80
8	Left ovarian cystectomy	290	Left ovarian teratoma (6.5 cm)	Right ampullary pregnancy	3	4	60
9	Bilateral neosalpingostomy + right ovarian cystectomy	136	Secondary infertility + Right ovarian teratoma (5 cm)	Right ampullary pregnancy	4	6	90
10	Left salpingostomy	940	Left ampullary pregnancy	Right ampullary pregnancy	5	3	70
11	Myomectomy	406	posterior Uterine myoma	Left ampullary pregnancy	3	4	60
12	Right ovarian cystectomy	1156	Right ovarian teratoma (2.0 cm)	Right ovarian mucinous cystadenoma (2.0 cm)	4	3	95
13	Neosalpingostomy + hydrotubation	184	Left hydrosalpinx	Infertility, IVF	3	3	50
14	Right salpingostomy	84	Right tubal pregnancy	Right ampullary pregnancy	2	3	50
15	Left tubal ligation	231	Left hydrosalpinx	Left Hydrosalpinx	4	7	100
Average		452.47 ± 359.00			3.53 ± 1.36	4.73 ± 1.58	63.33 ± 13.71
P-value					0.023 ^c	0.429 ^c	67.33 ± 22.51

Case no.	Intraoperative estimated blood loss ^a	Intraoperative estimated blood loss ^b	Perioperative complications ^a	Perioperative complications ^b	Postoperative complications ^a	Postoperative complications ^b	VAS score of first 3 postoperative days ^b		Hospital stay ^b
							days ^a	days ^b	
1	30	30	—	—	—	—	1/0	1/1	2
2	30	20	—	—	—	—	1/1	1/1	2
3	20	50	—	—	—	—	2/2/0	2/1/0	3
4	30	20	—	—	Persistent Ectopic Pregnancy	—	1/0	1/1	2
5	20	20	—	—	—	—	2/0	3/1	2
6	20	30	—	—	—	—	2/2/0	2/2/0	3
7	20	30	—	—	—	—	2/1	1/1	2
8	20	30	—	—	—	—	1	2/1	2

(Continues)

TABLE 2 (Continued)

Case no.	Intraoperative estimated blood loss ^a	Intraoperative estimated blood loss ^b	Perioperative complications ^a	Perioperative complications ^b	Postoperative complications ^a	Postoperative complications ^b	VAS score of first 3 postoperative days ^a	VAS score of first 3 postoperative days ^b	Hospital stay ^a	Hospital stay ^b
9	50	50	—	—	—	—	2/1	2/1	2	2
10	20	30	—	—	—	—	1/1	2/1	2	2
11	100	30	—	—	—	—	2/1/0	2/1/1	3	3
12	30	30	—	—	—	—	2/1/0	2/2/0	3	3
13	30	20	—	—	—	—	1/1	2/1	2	2
14	30	30	—	—	—	—	2/2/0	3/1/0	3	3
15	30	30	—	—	—	—	2/0	2/1/0	2	3
Average	32.00 ± 20.42	30.00 ± 9.26	—	—	—	—			2.20 ± 0.56	2.40 ± 0.13
<i>P</i> -value	0.723 ^c								0.082 ^c	

Abbreviations: IVF, in vitro fertilization; VAS, Visual Analogue Scale; vNOTES, transvaginal natural orifice transluminal endoscopic surgery.

^aCharacteristics of 1st vNOTES.

^bCharacteristics of 2nd vNOTES.

^cMatched samples *t*-test.

short surgical interval) and case 15's pre- and post-first vNOTES FSFI (received the surgery 1 month before drafting); all the remaining cases were surveyed all four time points. Three comparisons were conducted between (1) the pre- and postoperative FSFI scores of the first vNOTES, (2) the pre- and postoperative FSFI of the second vNOTES, and (3) the pre-first and post-second vNOTES FSFI. We noticed a slightly lower score in the pain domain of pre- and postoperative FSFI for repeated vNOTES compared to those for the first vNOTES (pre-first vNOTES: 4.96 ± 0.78 ; post-first vNOTES: 4.82 ± 0.79 ; pre-second vNOTES: 4.45 ± 1.39 ; post-second vNOTES: 4.43 ± 1.36). Such difference was also observed in the overall scores (pre-first vNOTES: 24.52 ± 2.44 ; post-first vNOTES: 24.23 ± 2.15 ; pre-second vNOTES: 22.43 ± 6.50 ; post-second vNOTES: 4.43 ± 1.36). However, no significant differences were found in any of the domains or overall scores between the three comparisons.

DISCUSSION

With the unprecedented development of minimally invasive surgical techniques and equipment, the vNOTES approach has gained increasing popularity in general surgery, urology and gynecology. Meanwhile, whether vNOTES can be performed repeatedly has become a huge concern among gynecologists and endoscopists.^{6,7,15,16} Some experts are of the opinion that the re-entry via the culdotomy of previous vNOTES should be avoided,¹⁶ while the clinical evidence supporting such an opinion is still lacking. Traditional laparoendoscopy can easily enter the abdominal cavity through the previous entrance and use new trocar sites on the abdominal walls. However, owing to the limited operative safety zone of the vaginal fornix, the second vNOTES requires a re-incision of the previous incision to establish the surgical access, which may cause potential incisional complications and impact patients' sexual life and childbirth.

To date, reports regarding repeated vNOTES are scarce. The first and only study discussing the feasibility of a second vNOTES complete hysterectomy among patients who underwent the first vNOTES adnexectomy mainly focused on the surgical complications of the second vNOTES and included only 11 patients, most of whom were already in their peri- or postmenopausal period.⁶ Evidence of the safety and impact of repeated non-hysterectomy vNOTES on childbirth and sexual quality of life is still lacking.

vNOTES is an emerging minimally invasive surgical technique, which has not been widely performed worldwide. It has been conducted in our institute for only 4 years.¹⁷ We have performed 3000 cases of vNOTES so far, but because not many patients would suffer from another benign gynecological disease in such a short

TABLE 3 FSFI domain scores before and 3 month after 1st and 2nd vNOTES.

Domain	Pre-1st vNOTES	Post-1st vNOTES	<i>P</i> -value ^a	Pre-2nd vNOTES	Post-2nd vNOTES	<i>P</i> -value ^b	<i>P</i> -value ^c
Desire	3.44 ± 0.66	3.28 ± 0.59	0.164	3.04 ± 0.55	3.13 ± 0.48	0.336	0.365
Arousal	3.04 ± 0.61	3.06 ± 0.62	0.991	3.00 ± 0.70	2.98 ± 0.75	0.752	0.302
Lubrication	4.60 ± 0.71	4.52 ± 0.69	0.573	4.52 ± 0.72	4.67 ± 0.69	0.221	0.221
Orgasm	4.13 ± 0.78	4.16 ± 0.84	0.670	4.14 ± 0.73	4.09 ± 0.63	0.435	0.551
Satisfaction	4.35 ± 0.67	4.40 ± 0.77	0.334	4.51 ± 0.62	4.31 ± 0.59	0.187	0.477
Pain	4.96 ± 0.78	4.82 ± 0.79	0.151	4.45 ± 1.39	4.43 ± 1.36	0.583	0.328
Overall	24.52 ± 2.44	24.23 ± 2.15	0.272	22.43 ± 6.50	22.33 ± 6.49	0.566	0.250

Abbreviations: FSFI, female sexual function index; vNOTES, transvaginal natural orifice transluminal endoscopic surgery.

^aComparison between the pre- and postoperative FSFI scores of the 1st vNOTES.

^bComparison between the pre- and postoperative FSFI scores of the 2nd vNOTES.

^cComparison between the pre-first and post-second vNOTES FSFI.

period after the first vNOTES, we did not have many patients who underwent a second vNOTES. Thus, we only had a few cases of repeated vNOTES, making the study on the repeatability of vNOTES challenging.

There were several intriguing findings regarding the second vNOTES in our study. The postoperative VAS score of both vNOTESs were similar, with only 1 patient having a slightly increased VAS score. We speculate that it might be due to the scarce distribution of nerves in the posterior vaginal fornix, which is also one of the most notable minimal invasive features of the vNOTES technique. There was no significant difference in the operative duration between both vNOTESs in our 15 cases, despite several cases experiencing longer surgical duration in the second vNOTES. We conclude that the prolonged surgical duration experienced by several cases might be caused by more severe pelvic adhesions or lesser surgical experience of the second surgeon. The significantly longer time needed to establish the surgical entrance in the second vNOTES may be caused by a less clear anatomical structure as a result of the first vNOTES.

Since transvaginal access could be accomplished through the posterior or anterior vaginal fornix and even the vaginal residue after the complete hysterectomy, the repeated vNOTES could be categorized into the following situations: (1) vNOTES complete hysterectomy following the first vNOTES via culdotomy in the posterior or anterior vaginal fornix; (2) both vNOTES performed through culdotomy in the posterior vaginal fornix; and (3) both vNOTES established via the anterior vaginal fornix. In clinical practice, the first two situations are the overwhelming majority. Only one publication has explored the feasibility of the first scenario of repeated vNOTES.⁶ In our study, all vNOTESs of the 15 cases, regardless of whether they were performed initially or later, were conducted through posterior fornix culdotomy. Our perioperative findings showed no aggravation of postoperative pelvic adhesion and a comparable incidence rate of surgical complications as the first vNOTES, indicating that repeated vNOTES may be a safe and feasible surgical alternative for patients with a history of posterior fornix entrance vNOTES.

No evidence has been found on the impact of the second vNOTES on patients' sexual well-being so far. Some previously published studies have shown no significant difference in patients' FSFI between vNOTES and conventional laparoscopic opportunistic bilateral salpingectomy.¹⁸ Consistent with this, the 15 cases in our study also had comparable FSFI domain and overall scores, regardless of vNOTES. One potential explanation is that most somatic vaginal innervation is distributed in the distal and anterior parts of the vaginal walls and bypasses the posterior vaginal fornix, thus making the culdotomy, even the repeat culdotomy, least deleterious to sexual function.^{19,20}

Regarding the impact of vNOTES on childbirth, several cases of successful vaginal delivery among patients who underwent the first vNOTES, including ovarian cystectomy, tubal ligation, and myomectomy, have been reported, primarily revealing the relative safety of vNOTES concerning childbirth.^{21,22} However, no evidence of the impact of repeated vNOTES on childbirth has been reported in the literature. Unfortunately, due to the relatively short postoperative follow-up period and small cohort size in our study, after the second vNOTES, none of the patients had delivered vaginally or via cesarean section.

Although several limitations of the current study might hinder the generalizability of our findings, including the small cohort size, various surgical intervals, the potential selection bias, and the fact that the patients have not yet undergone childbirth after the second vNOTES, this case series first reported the sexual functions of patients who underwent vNOTES twice and found no significant change in FSFI and comparable incidence rate of perioperative complications between these two vNOTES. This might be helpful for the minimally invasive surgical approach selection for patients who undergo vNOTES once. Our study provides evidence that the second vNOTES could be successfully conducted without overt impact on patients' postoperative outcomes and sexual function. However, a larger sample size and longer follow-up period are needed to investigate the influence of vNOTES and repeated vNOTES on childbirth.

To sum up, we provide preliminarily evidence that repeated non-hysterectomy vNOTES, which has a comparable incidence rate of perioperative complications

and insignificant impact on patients' sexual function, is safe and feasible.

CONFLICT OF INTEREST STATEMENT

The authors declare no conflict of interest for this article.

DATA AVAILABILITY STATEMENT

The data that support the findings of this study are openly available in Figshare at <http://doi.org/10.6084/m9.figshare.23608890>, Reference number 23.

ETHICS STATEMENT

This study was approved by the ethics committee of our institute (CWCCH-2021122). All information retrieval and questionnaire surveys were conducted with the written consent of each patient. For privacy concerns, their identifiable characteristics were not transcribed from the Hospital Information System.

ORCID

Dan Feng  <https://orcid.org/0000-0002-7324-1548>

Tianjiao Liu  <https://orcid.org/0000-0001-8279-5924>

Xin Li  <https://orcid.org/0000-0002-6734-9034>

Li He  <https://orcid.org/0000-0002-9716-2457>

REFERENCES


- Gauderer MW, Ponsky JL, Izant RJ. Gastrostomy without laparotomy: a percutaneous endoscopic technique. *J Pediatr Surg.* 1980;15(6):872–5.
- Atallah S, Martin-Perez B, Keller D, Burke J, Hunter L. Natural-orifice transluminal endoscopic surgery. *Br J Surg.* 2015;102(2):e73–92. <https://doi.org/10.1002/bjs.9710>
- Brandão P, Almeida A, Ramôa P. vNOTES for adnexal procedures. *J Obstet Gynaecol.* 2021;41(7):1134–8. <https://doi.org/10.1080/01443615.2020.1841124>
- Baekelandt J, de Mulder PA, le Roy I, Mathieu C, Laenen A, Enzlin P, et al. Adnexectomy by vaginal natural orifice transluminal endoscopic surgery versus laparoscopy: results of a first randomised controlled trial (NOTABLE trial). *BJOG.* 2021;128(11):1782–91. <https://doi.org/10.1111/1471-0528.16838>
- Baekelandt JF, de Mulder PA, le Roy I, Mathieu C, Laenen A, Enzlin P, et al. Hysterectomy by transvaginal natural orifice transluminal endoscopic surgery versus laparoscopy as a day-care procedure: a randomised controlled trial. *BJOG.* 2019;126(1):105–13. <https://doi.org/10.1111/1471-0528.15504>
- Nulens K, van Genechten I, Baekelandt J. Repeat vaginal natural orifice transluminal endoscopic surgery: a first feasibility study. *Gynecol Obstet Invest.* 2021;86(1–2):117–22. <https://doi.org/10.1159/000513403>
- Perretta S, Vix M, Dallemagne B, Nassif J, Donatelli G, Marescaux J. Video. Repeated transvaginal notes: is it possible? *Surg Endosc.* 2012;26(2):565. <https://doi.org/10.1007/s00464-011-1923-7>
- Ferreira-Valente MA, Pais-Ribeiro JL, Jensen MP. Validity of four pain intensity rating scales. *Pain.* 2011;152(10):2399–404. <https://doi.org/10.1016/j.pain.2011.07.005>
- Chen X, Liu H, Sun D, Zhang JJ, Fan Q, Shi H, et al. Transvaginal natural orifice transluminal endoscopic surgery for tubal pregnancy and a device innovation from our institution. *J Minim Invasive Gynecol.* 2019;26(1):169–74. <https://doi.org/10.1016/j.jmig.2018.05.013>
- Huang L, Lin Y-H, Yang Y, Gong Z-L, He L. Comparative analysis of vaginal natural orifice transluminal endoscopic surgery versus transumbilical laparoendoscopic single-site surgery in ovarian cystectomy. *J Obstet Gynaecol Res.* 2021;47(2):757–64. <https://doi.org/10.1111/jog.14603>
- Baekelandt J, Vercammen J. IMELDA transvaginal approach to ectopic pregnancy: diagnosis by transvaginal hydrolaparoscopy and treatment by transvaginal natural orifice transluminal endoscopic surgery. *Fertil Steril.* 2017;107(1):e1–2. <https://doi.org/10.1016/j.fertnstert.2016.09.024>
- Lee C-L, Wu K-Y, Su H, Ueng S-H, Yen C-F. Transvaginal natural-orifice transluminal endoscopic surgery (NOTES) in adnexal procedures. *J Minim Invasive Gynecol.* 2012;19(4):509–13. <https://doi.org/10.1016/j.jmig.2012.02.005>
- Rosen R, Brown C, Heiman J, Leiblum S, Meston C, Shabsigh R, et al. The female sexual function index (FSFI): a multidimensional self-report instrument for the assessment of female sexual function. *J Sex Marital Ther.* 2000;26(2):191–208.
- Gerstenberger EP, Rosen RC, Brewer JV, Meston CM, Brotto LA, Wiegel M, et al. Sexual desire and the female sexual function index (FSFI): a sexual desire cutpoint for clinical interpretation of the FSFI in women with and without hypoactive sexual desire disorder. *J Sex Med.* 2010;7(9):3096–103. <https://doi.org/10.1111/j.1743-6109.2010.01871.x>
- Reddy H, Kim SW, Plewniak K. Applications of vaginal natural orifice transluminal endoscopic surgery (vNOTES) in gynecologic surgery. *Curr Opin Obstet Gynecol.* 2022;34(4):220–6. <https://doi.org/10.1097/GCO.0000000000000799>
- Baekelandt J, Noori N, Hofmann L, Mansoor A, Kapurbandara S. Standardised step by step approach to adnexectomy by vaginal natural orifice transluminal endoscopic surgery. *Eur J Obstet Gynecol Reprod Biol.* 2022;274:160–5. <https://doi.org/10.1016/j.ejogrb.2022.05.021>
- Huang L, Feng D, Gu D-X, Lin YH, Gong ZL, Liu DD, et al. Transvaginal natural orifice transluminal endoscopic surgery in gynecological procedure: experience of a women's and children's medical center from China. *J Obstet Gynaecol Res.* 2022;48(11):2926–34. <https://doi.org/10.1111/jog.15402>
- Yassa M, Kaya C, Kalafat E, Tekin AB, Karakas S, Mutlu MA, et al. The comparison of transvaginal natural orifice transluminal endoscopic surgery and conventional laparoscopy in opportunistic bilateral salpingectomy for permanent female sterilization. *J Minim Invasive Gynecol.* 2022;29(2):257–64. <https://doi.org/10.1016/j.jmig.2021.08.009.e1>
- Solomon D, Lentz R, Duffy AJ, Bell RL, Roberts KE. Female sexual function after pure transvaginal appendectomy: a cohort study. *J Gastrointest Surg.* 2012;16(1):183–7. <https://doi.org/10.1007/s11605-011-1706-4>
- Tunuguntla HSGR, Gousse AE. Female sexual dysfunction following vaginal surgery: myth or reality? *Curr Urol Rep.* 2004;5(5):403–11.
- Feng D, He L. Pregnancy and childbirth after transvaginal natural orifice transluminal endoscopic surgery for benign gynecological diseases. *Int J Gynaecol Obstet.* 2021;155:551–2. <https://doi.org/10.1002/ijgo.13820>
- Thomaidis P, Weltermann NJ, Seefeldt CS, Richards DC, Sauerwald A, Heiss MM, et al. Transvaginal hybrid-NOTES procedures-do they have a negative impact on pregnancy and delivery? *Langenbecks Arch Surg.* 2021;406(6):2045–52. <https://doi.org/10.1007/s00423-021-02105-z>
- Dan Feng TL, Xin L, Jieru P, Lu H, Li H. Supplementary file of repeated vNOTES. Figshare (Accessed 30 June 2023). <http://doi.org/10.6084/m9.figshare.23608890>.

How to cite this article: Feng D, Liu T, Li X, Peng J, Huang L, He L. Repeated transvaginal natural orifice transluminal endoscopic surgery: An initial Chinese experience. *J Obstet Gynaecol Res.* 2023;49(10):2501–8. <https://doi.org/10.1111/jog.15757>

CLINICAL ARTICLE

Gynecology

Perioperative outcomes of and predictors for conversion from transvaginal natural orifice transluminal endoscopic tubal surgeries: A retrospective cohort study of 619 patients

Dan Feng¹  | Li He¹  | Xin Li¹  | Qiang Zhang¹ | Jieru Peng² | Lu Huang¹ | Tianjiao Liu¹  | Yonghong Lin¹ 

¹Department of Gynecology, Chengdu Women's and Children's Central Hospital, School of Medicine, University of Electronic Science and Technology of China, Chengdu, People's Republic of China

²Medical Administrative Department, Chengdu Women's and Children's Central Hospital, School of Medicine, University of Electronic Science and Technology of China, Chengdu, People's Republic of China

Correspondence

Yonghong Lin, Department of Gynecology, Chengdu Women's and Children's Central Hospital, School of Medicine, University of Electronic Science and Technology of China, No.1617, Riyue Avenue, Chengdu, Sichuan, 611731, People's Republic of China.

Email: linyhcd2011@163.com

Funding information

Chengdu High-level Key Clinical Specialty Construction Project; Sichuan Provincial Medical Association Project, Grant/Award Number: S19085; the Chengdu Municipal Health Commission Project, Grant/Award Number: 2021215; the Japan-China Sasakawa Medical Fellowship Program

Abstract

Objective: To assess the perioperative outcomes of vNOTES tubal surgeries and to identify predictors of surgical conversion.

Methods: A single-center retrospective cohort study was performed on 619 patients who underwent vNOTES tubal surgeries in our institute from December 2018 to October 2021. Patients were categorized into “converted” or “non-converted” groups based on whether conversion occurred. *t*-test and χ^2 test were performed on demographic and clinicopathologic data to compare their perioperative outcomes. Logistic regression was built to identify predictors for surgical conversions.

Results: The conversion and complication rates of the vNOTES tubal surgeries in the present study were 3.07% and 4.85%, respectively. The “converted group” has a significantly higher percentage of patients with severe pelvic adhesions (9/19 [47.4%]) and pelvic endometriosis (2/19 [10.5%]), which significantly predicates surgical conversion. The “converted group” also had a longer duration of surgery (140.94 ± 88.73 min, $P = 0.002$) and an increased proportion of “converted from vNOTES” patients experienced more than 50 ml of intraoperative blood loss (7/19 [36.9%]). Four patients had intraoperative rectal injuries, and no Clavien–Dindo III–V postoperative complications occurred.

Conclusion: vNOTES tubal surgeries are safe due to low conversion and complication rates. Severe pelvic adhesion and endometriosis are predictors for surgical conversions.

KEYWORDS

intraoperative conversion, risk factors, surgical complication, surgical outcomes, tubal operation, vNOTES

1 | INTRODUCTION

The development and progress of surgical technology over recent decades have led us to adopt many minimally invasive surgical (MIS) options. Natural orifice transluminal endoscopic surgery (NOTES), a

novel MIS concept of accessing the abdominal cavity through natural orifices, has created an innovative, less painful, and scarless surgical alternative to conventional laparoscopy in recent years.¹ Because of the anatomical features of the vagina, transvaginal NOTES (vNOTES) allow easy access to the female internal genital

Dan Feng, Li He, Xin Li and Tianjiao Liu contributed equally to this work.

© 2023 International Federation of Gynecology and Obstetrics.

organs and safe closure of the incision, making them increasingly popular and frequently utilized in the field of gynecology.²

Although vNOTES was proved clinically feasible in 2007,³ it still lacks adequate evidence demonstrating its safety and ineligible risk factors for surgical conversions. However, the rate of complications and intraoperative conversion to other approaches, along with the effectiveness of disease treatment, are the most important immediate judgment criteria for the safety and feasibility of novel procedures like vNOTES. Due to their relatively lower complexity, tubal operations such as ligation, salpingostomy, chromoperturbation, and resection are always the first choice of novice gynecologists learning the vNOTES technique. Additionally, none of the existing publications regarding these vNOTES tubal surgeries presents a sample size larger than 20 patients.⁴ More solid clinical evidence is thus required for better surgical recommendation and consultation of vNOTES.^{5,6} Considering that, understanding why vNOTES tubal surgeries were converted is important and could help gynecologists to make better preoperative decisions. Here we retrospectively reviewed 619 vNOTES tubal surgeries in our institute to investigate the perioperative outcomes, especially surgical conversions, and to identify predictors for conversion.

2 | MATERIALS AND METHODS

2.1 | Study design

This retrospective study analyzed the data on the postoperative outcomes of 619 patients who underwent vNOTES tubal surgeries, mainly for treating ectopic tubal pregnancy, hydrosalpinx, or infertility, in the Department of Gynecology of Chengdu Women's and Children's Central Hospital (CWCCH), Chengdu, People's Republic of China, from December 2018 to October 2021 (Figure 1). In our center, patients who underwent vNOTES tubal surgeries all met following criteria: (1) laparoscopic surgery was required for tubal pathology; (2) patients were willing to receive vNOTES, although the following patients were excluded: (i) those with a history of rectal surgery, severe pelvic inflammatory disease, or pelvic radiotherapy; (ii) patients suspected of rectovaginal endometriosis, malignant tumors, or severe pelvic adhesions; (iii) and those who had not had sexual intercourse.⁷⁻⁹ A 1-month routine follow-up was carried out to investigate patients' short-term postoperative outcomes. Given the relatively narrow operative space, restricted visualization, and technical difficulty associated with vNOTES for delicate suturing in neosalpingostomy and tubal anastomosis for natural conception, these tubal surgeries were rarely conducted transvaginally in our institute. Based on whether vNOTES was converted to other approaches or not, the patients were grouped into "converted from vNOTES" ($n = 19$) and "non-converted vNOTES" ($n = 600$), respectively. Following that, statistical analyses were carried out to compare the postoperative outcomes of the groups and identify the risk factors for surgical conversion.

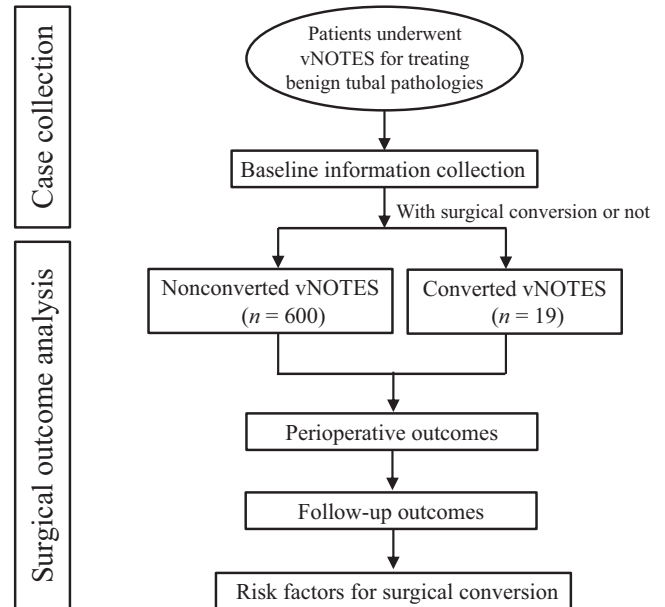


FIGURE 1 Flow diagram of present study.

2.2 | Surgical procedures

The vNOTES tubal surgical technique and instruments used for the present study have been previously described.^{4,9-11} A detailed gynecological physical examination and ultrasonography were performed during the preoperative examination and assessment to rule out severe pelvic adhesion. The surgical procedures involved in the present study included tubal salpingostomy, salpingectomy, tubal ligation, and several instances of chromoperturbation. In the present study, 33 surgeons performed vNOTES tubal procedures and were classified as second-line and third-line surgeons based on their years of experience. There are 21 second-line surgeons in our center, each of whom has at least 10 years of operating experience and has performed more than 500 laparoscopies, including about 30 instances of vNOTES, and 12 third-line surgeons, each of whom has at least 20 years of operating experience and has performed more than 1000 laparoscopies, including more than 60 instances of vNOTES. First-line surgeons (with less than 10 years of operating experience) were regarded as relatively inexperienced and were not permitted to perform the vNOTES surgery as chief operators in our institute; thus they were not included. From the day that vNOTES was performed to the third postoperative day, the Visual Analogue Scale (VAS) was applied to each patient to measure their postoperative pain daily.

2.3 | Baseline information and perioperative characteristics of the patients

We included patients' sociodemographics, such as age, ethnicity, body mass index (BMI, calculated as weight in kilograms divided by the square of height in meters), gravidity, parity, and surgical or gestational histories, as their baseline characteristics. We also

gathered their clinicopathologic characteristics, such as a history of previous abdominal or pelvic surgeries and the presence of uterine pathology, endometriosis or pelvic adhesion, and classified them using consensus criteria, with some modifications due to the relatively narrow field of visualization in the case of vNOTES.^{12,13} The perioperative features of the patients, such as operative duration, postoperative hospital stay, postoperative fever, volume of estimated blood loss, and postoperative pain scores, were also collected. The surgical conversion implied converting a vNOTES procedure to an open abdominal (OA) surgery, transumbilical laparoendoscopic single port (LESS), or conventional multiport laparoscopy (MPL) procedure. The Clavien–Dindo (CD) classification method was applied to categorize the postoperative complications of each surgical patient.¹⁴ We also calculated the uterine volume using the formula for the volume of a prolate ellipsoid, $V = 0.52 \times \text{maximum length} \times \text{anteroposterior diameter} \times \text{transverse diameter}$, for analyzing the uterine size's role in the surgical conversion of vNOTES tubal surgeries.¹⁵

2.4 | Ethics statement

The present study was approved by the Ethics Committee of the CWCCH, and written informed consent was obtained from all patients during their admission. After retrieving the data from the HIS, all personally identifiable information about the patients was deleted.

2.5 | Statistical analyses

All data were analyzed with SPSS version 25 (IBM). The continuous variables were presented as mean \pm standard deviation (SD) and analyzed using a two-sample *t*-test or Mann–Whitney *U*-test as appropriate. The categorical variables were expressed as numbers and percentages and compared using the χ^2 or Fisher exact test unless stated otherwise. A logistic regression was built to determine the predictors for surgical conversion, and the results were presented in the form of odds ratios and 95% confidence intervals (CIs). A *P*-value of less than 0.05 was considered statistically significant.

3 | RESULTS

3.1 | Overall profile of patient cohort

Of the 619 patients included in the present study, only 19 (3.07%) experienced surgical conversion from vNOTES (Table 1), and no patient was lost during the 1-month postoperative follow-up. The entire study cohort included 403 salpingectomies, 49 tubal ligations, including 20 neosalpingostomies, 138 salpingostomies, and 29 tubal chromoperturbations, of which six and three of these

procedures were combined with fimbrioplasty and neosalpingostomy, respectively.

3.2 | Demographic and clinicopathologic features of the patients

Both patient groups, “non-converted vNOTES” and “converted from vNOTES,” displayed similar distributions in terms of mean age (31.45 ± 5.53 years vs. 32.42 ± 7.44 years, $P = 0.458$), BMI (21.66 ± 3.15 vs. 20.48 ± 2.46 , $P = 0.107$), and proportion of Han Chinese ethnicity (578/600 [96.3%] vs. 19/19 [100%], $P = 0.395$). Statistically significant differences were also absent in terms of gravidity, parity, cumulative cesarean sections, and previous pelvic or abdominal surgeries between the patients in the groups. The distribution of different procedures between these two groups was also similar, with the majority having undergone salpingectomy (390/600 [65.0%] vs. 13/19 [68.4%], $P = 0.890$). In addition, the proportions of different classes of surgeons conducting the procedures in both groups were also similar, with 256/600 (42.7%) versus 9/19 (47.4%) surgeries performed by second-line surgeons and 344/600 (57.3%) versus 10/19 (52.6%) surgeries performed by third-line gynecologists ($P = 0.683$). Besides, these two groups also had similar uterine volumes (56.47 ± 31.32 vs. 54.14 ± 23.96 , $P = 0.748$) and compositions of concurrent uterine pathologies (myoma 26/600 [4.3%] vs. 1/19 [5.3%]; adenomyoma 7/600 [1.2%] vs. 0, $P = 0.879$).

Notably, the converted group had a significantly lower proportion of patients who underwent vNOTES for treating ectopic pregnancy (370/600 [61.7%] vs. 9/19 [47.4%]) and a bigger proportion for treating tubal hydrosalpinx (191/600 [32.3%] vs. 8/19 [42.1%], $P = 0.036$). A higher percentage of patients in the converted vNOTES group had severe pelvic adhesions (9/19 [47.4%] vs. 0/600 [0.0%], $P < 0.001$) and endometriosis (2/19 [10.5%] vs. 10/600 [1.7%], $P < 0.001$). Additionally, the patients in this group underwent a significantly longer duration of surgery than did the non-converted vNOTES patients (140.94 ± 88.73 min vs. 67.22 ± 27.50 min, $P = 0.002$). The postoperative outcomes of the patients in these two groups also differed significantly. Although the patients between the groups displayed no significant difference in the postoperative pain score for three consecutive days, a significantly larger percentage of patients in the converted vNOTES group stayed hospitalized for longer than a week post-surgery (6/19 [31.6%] vs. 11/600 [1.8%], $P < 0.001$). In addition, a higher proportion of patients in the converted vNOTES group had lost more than an estimated 50 ml of blood intraoperatively (7/19 [36.9%] vs. 17/600 [2.9%], $P < 0.001$).

The perioperative complications in our cohort are listed in Table 2. There were four cases of rectal injury in our cohort, including one full-thickness rectal injury in both groups and two seromuscular injuries in the “converted vNOTES” group. In the non-converted case of full-thickness rectal injury, the surgeon successfully repaired the injured rectum and completed the whole

TABLE 1 Demographics and clinical characteristics of patients who underwent vNOTES tubal surgery without versus with surgical conversions.

Characteristics	Non-converted vNOTES (n = 600 [96.9%])	Converted from vNOTES (n = 19 [3.1%])	P-value
Age (year)	31.45 ± 5.53	32.42 ± 7.44	0.458
BMI ^a	21.66 ± 3.15	20.48 ± 2.46	0.107
Ethnicity			0.395
Han Chinese	578 (96.3%)	19 (100.0%)	
Minority groups	22 (3.7%)	0	
Gravidity			0.609
0	96 (16.0%)	2 (10.5%)	
1	137 (22.8%)	6 (31.6%)	
≥2	367 (61.2%)	11 (57.9%)	
Parity			0.973
0	323 (53.8%)	10 (52.6%)	
1	207 (34.5%)	7 (36.8%)	
≥2	70 (11.7%)	2 (10.5%)	
Cesarean section			0.518
0	480 (80.0%)	17 (89.5%)	
1	96 (16.0%)	2 (10.5%)	
≥2	24 (4.0%)	0	
Vaginal delivery			0.210
0	439 (73.2%)	11 (57.9%)	
1	121 (20.1%)	7 (36.8%)	
≥2	40 (6.7%)	1 (5.3%)	
Previous pelvic or abdominal surgery			0.145
0	354 (59.0%)	15 (78.9%)	
1	177 (29.5%)	4 (21.1%)	
≥2	69 (11.5%)	0	
Chief complaint			0.016
Ectopic pregnancy	371 (62.6%)	9 (47.4%)	
Infertility	28 (4.7%)	1 (5.3%)	
Tubal hydrosalpinx	199 (32.3%)	8 (42.1%)	
Fallopian tube abscess	2 (0.3%)	1 (5.3%)	
Types of tubal surgery			0.890
Salpingostomy	135 (22.5%)	3 (15.8%)	
Salpingectomy	390 (65.0%)	13 (68.4%)	
Tubal ligation	47 (7.8%)	2 (10.5%)	
Chromopertubation	19 (3.2%)	1 (5.3%)	
Chromopertubation combined with fimbrioplasty or neosalpingostomy	9 (1.5%)	0	
Surgeon type			0.683
Second-line	256 (42.7%)	9 (47.4%)	
Third-line	344 (57.3%)	10 (52.6%)	
Uterine volume (cm ³) ^b	56.47 ± 31.32	54.14 ± 23.96	0.748
Concurrent uterine pathology			0.879
None	567 (94.5%)	18 (94.7%)	
Myoma	26 (4.3%)	1 (5.3%)	

TABLE 1 (Continued)

Characteristics	Non-converted vNOTES (n = 600 [96.9%])	Converted from vNOTES (n = 19 [3.1%])	P-value
Adenomyoma	7 (1.2%)	0	
Presence of pelvic adhesions			<0.001
None	155 (25.8%)	4 (21.1%)	
Mild or moderate	445 (74.2%)	6 (31.6%)	
Severe	0	9 (47.4%)	
Presence of pelvic endometriosis			<0.001
Deep endometriosis	0 (0.0%)	2 (10.5%)	
Ovarian endometriosis	6 (1.0%)	0 (0.0%)	
Superficial endometriosis	4 (0.7%)	0 (0.0%)	
None	590 (98.3%)	17 (89.5%)	
Surgical duration (min)	67.22 ± 27.50	140.94 ± 88.73	0.002
Estimated intraoperative blood loss (ml)			<0.001
≤50	583 (97.2%)	12 (63.2%)	
≤100	12 (2.0%)	5 (26.3%)	
≤200	1 (0.2%)	1 (5.3%)	
>200	4 (0.7%)	1 (5.3%)	
Postoperative complications (Clavien–Dindo classification)			0.241
None	576 (96.0%)	17 (89.4)	
I	17 (2.8%)	1 (5.3%)	
II	7 (1.2%)	1 (5.3%)	
III–V	0 (0.0%)	0 (0.0%)	
Postoperative pain score ^c			
Day 0	2.86 ± 0.43	2.95 ± 0.23	0.129
Day 1	2.33 ± 0.69	2.53 ± 0.61	0.225
Day 2	1.49 ± 0.66	1.63 ± 0.68	0.346
Day 3	0.90 ± 0.58	1.16 ± 0.69	0.055
Postoperative hospitalization duration (day)			<0.001
<3	433 (72.2%)	10 (52.6%)	
3–7	156 (26.0%)	3 (15.8%)	
>7	11 (1.8%)	6 (31.6%)	

^aBody mass index (calculated as weight in kilograms divided by the square of height in meters).

^bUterine volume was calculated using the formula for the volume of prolate ellipsoid: $V = 0.52 \times \text{maximum length} \times \text{anteroposterior diameter} \times \text{transverse diameter}$.

^cVisual Analogue Scale (VAS).

procedure in a vNOTES manner. Furthermore, we displayed the more detailed distribution of postoperative complications according to the CD classification (Table 2). The incidence rates of CD I–IV complications in our cohort were 18/619 (2.91%) for CD I, 8/619 (1.29%) for CD II, and zero for CD III and CD IV, respectively. For the CD I complications, there were seven cases of vomiting, four of fever, two of pain (requiring a painkiller), one of wound bleeding, two cases of anemia (requiring iron supplements), and two cases of urinary retention requiring catheterization. As for the CD II complications, all six cases of postoperative pelvic infection occurred in the non-converted vNOTES group, and both groups had one patient with ileus.

3.3 | Risk factors for surgical conversion

For further identification of the risk factors dictating the conversion from vNOTES tubal surgery in our cohort, we performed a logistic regression analysis on the factors relevant to the surgical conversions, including BMI, history of vaginal delivery, history of abdominopelvic surgery, uterine volume, the presence of pelvic adhesion, and endometriosis (Table 3). We found that the presence of severe pelvic adhesion and endometriosis significantly increased the chance of surgical conversion from vNOTES. Patients with severe pelvic adhesion were more than 14 times as likely to be converted to MPL or LESS in comparison with those without pelvic adhesion (adjusted odds ratio [OR] 14.87,

TABLE 2 Perioperative complications of vNOTES tubal surgery.

Complications	Non-converted vNOTES (n = 600)	Converted from vNOTES (n = 19)	All cases (n = 619)
Intraoperative complications	1	3	4 (0.65%)
Full-thickness rectal injury	1 (0.17%)	1 (5.26%)	
Rectal seromuscular injury	0	2 (10.53%)	
Postoperative complications			
CD I	17 (2.83%)	1 (5.26%)	18 (2.91%)
Vomiting	7 (1.17%)	0	7 (1.13%)
Fever (without treatment with antibiotics)	3 (0.50%)	1 (5.26%)	4 (0.65%)
Pain	2 (0.32%)	0	2 (0.32%)
Wound bleeding	1 (0.16%)	0	1 (0.16%)
Anemia requiring iron supply	2 (0.33%)	0	2 (0.32%)
Urinary retention	2 (0.33%)	0	1 (0.16%)
CD II	7 (1.17%)	1 (5.26%)	8 (1.29%)
Postoperative acute pelvic inflammatory disease	6 (1.00%)	0	6 (0.97%)
Incomplete ileus	1 (0.16%)	1 (5.26%)	2 (0.32%)
CD III-V	0	0	0
Total	25 (4.17%)	5 (26.32%)	30 (4.85%)

Abbreviation: CD, Clavien–Dindo classification.

TABLE 3 Logistic regression analysis of risk factors for conversion of vNOTES tubal surgeries.

Variable	P-value	Adjusted OR (95%CI)
BMI ^a	0.421	0.91 (0.75–1.14)
History of vaginal delivery	0.417	1.40 (0.64–3.16)
History of abdominopelvic surgery	0.347	0.60 (0.23–1.76)
Uterine size	0.745	0.99 (0.98–1.01)
Presence of mild or moderate pelvic adhesion	0.582	1.71 (0.19–18.56)
Presence of severe pelvic adhesion	<0.001	14.87 (5.63–40.16)
Presence of endometriosis	<0.001	14.63 (3.93–56.84)

Abbreviations: CI, confidence interval; OR, odds ratio; vNOTES, transvaginal natural orifice transluminal endoscopic surgery.

^aBody mass index (calculated as weight in kilograms divided by the square of height in meters).

95% CI 5.63–40.16, $P < 0.001$). In addition, the presence of endometriosis also significantly increased the chance of surgical conversion from vNOTES (adjusted OR 14.63, 95% CI 3.93–56.84, $P < 0.001$).

3.4 | Clinical characteristics of patients with surgical conversion

We present the major clinicopathologic features of all 19 patients who underwent surgical conversion in Table 4. Generally speaking,

there were two major indications for these conversions, including: (1) failure in entering the abdominal cavity through the posterior vaginal fornix (8 patients); and (2) the procedures could not be completed in a vNOTES manner after the surgical platform had been established (11 patients). For the rectum and posterior uterine wall adhere to each other tightly, thus sealing the posterior fornix. As for the second indication, there were four different situations of surgical conversion, including interstitial tubal pregnancy (2 cases, 18.18%), abnormal location of the fallopian tube (2 cases, 18.18%), an unexpected malignant intraoperative finding (1 case, 9.09%), and serious pelvic adhesions that made it hard to expose the pathological tubes (6 cases, 54.55%). Of note, all three converted rectal injuries were found in patients with the first indication. The planned procedures were one chromopertubation, two tubal ligations, three tubal salpingotomies, and 13 salpingectomies. Two procedures were converted to conventional MPL, and the remaining 17 were converted to the LESS approach. Nine second-line and 10 third-line surgeons performed these surgeries.

4 | DISCUSSION

Lee et al.¹¹ were the first to report on the clinical application of vNOTES in the treatment of ectopic pregnancy. Nowadays, vNOTES is a basic MIS procedure that is frequently performed by novice surgeons learning this MIS technique. Although vNOTES is associated with several desirable postoperative outcomes, including better cosmetic satisfaction, quicker recovery, and less postoperative pain,¹⁶ clinical evidence proving its safety and feasibility is still lacking.⁵ The majority of previous studies on vNOTES have failed to document a

TABLE 4 Key clinicopathological features of patients who underwent surgical conversion in attempted vNOTES tubal surgery.

Patient no.	Type of vNOTES tubal surgery	Age (years)	BMI ^a	Entered the abdominal cavity in a vNOTES manner or not	Presence of pelvic endometriosis	Converted to:	Cause of conversion	Perioperative complication
1	Salpingostomy	29	21.5	Yes	None	LESS	Unpredicted malignance: ovarian dysgerminoma (2 cm)	None
2	Salpingostomy	35	25.0	Yes	None	LESS	Severe pelvic adhesion	None
3	Salpingectomy	28	22.6	Yes	None	LESS	Abnormal location of fallopian tube: the fimbriated extremity as adhered to the anterior wall of uterus	None
4	Salpingectomy	42	22.4	Yes	None	MPL	Severe pelvic adhesion	None
5	Salpingectomy	25	22.0	Yes	None	LESS	Interstitial pregnancy	None
6	Salpingectomy	31	18.9	Yes	None	LESS	Abnormal location of fallopian tube: left fallopian tube was adhered to left round ligament	None
7	Salpingectomy	32	18.4	Yes	None	LESS	Interstitial pregnancy	None
8	Salpingectomy	56	17.6	Yes	None	LESS	Severe pelvic adhesion	None
9	Salpingectomy	28	21.2	Yes	None	LESS	Severe pelvic adhesion	None
10	Tubal ligation	37	21.1	Yes	None	LESS	Severe pelvic adhesion	None
11	Salpingectomy	32	20.8	Yes	None	LESS	Severe pelvic adhesion	None
12	Salpingectomy	31	22.5	No	None	MPL	Severe pelvic adhesion and injury of adjacent organs	Rectal seromuscular injury
13	Tubal ligation	40	25.3	No	None	LESS	Severe pelvic adhesion and injury of adjacent organs	Rectal seromuscular injury
14	Salpingectomy	34	18.8	No	None	LESS	Severe pelvic adhesion	Incomplete ileus
15	Salpingectomy	30	19.5	No	Yes	LESS	Severe pelvic adhesion	None
16	Tubal hydrotubation	25	19.1	No	None	LESS	Severe pelvic adhesion	None
17	Salpingectomy	27	17.7	No	Yes	LESS	The pelvic endometriosis caused adhesion in the Douglas pouch	Full-thickness rectal injury
18	Salpingostomy	26	17.4	No	None	LESS	Severe pelvic adhesion	None
19	Salpingectomy	28	17.3	No	None	LESS	Severe pelvic adhesion	None

Abbreviations: LESS, laparoscopic single port; MPL, multiport laparoscopy; vNOTES, transvaginal natural orifice transluminal endoscopic surgery.

^aBody mass index (calculated as weight in kilograms divided by the square of height in meters).

large enough sample size and detailed perioperative data, and have rarely focused on the aspects of surgical conversion either,^{4,10,17,18} making their conclusions questionable.^{5,6}

The present study first reported the risk factors for the surgical conversion of vNOTES tubal surgeries. Our regression analysis revealed that patients with endometriosis and severe pelvic adhesions had a significantly higher chance of undergoing surgical conversion from vNOTES. Many previous studies also indicated that vNOTES is contraindicated in patients with severe pelvic adhesions, which significantly increase the risk of rectal injury.^{11,18} This is probably because endometriosis and severe pelvic adhesion can result in adhesion formation in the pouch of Douglas, blocking the entry site of vNOTES and causing the surgical conversion.¹⁹ Despite performing detailed preoperative gynecological examinations on patients to avoid such risks, we were still confronted with several cases of "latent" or unpredictable severe pelvic adhesions, making it difficult to enter the abdominal cavity during surgery or resulting in accidentally injury to the rectum of the patient. Some of these patients did not have any prior events of severe pelvic adhesion based on their medical histories and pelvic examinations. However, this does not rule out the use of vNOTES in the treatment of patients with pelvic adhesion. Many studies have reported the detection of Douglas cul-de-sac obliteration and deep endometriosis using medical imaging, especially ultrasonography, which could aid in reducing surgical conversion of vNOTES in our future clinical practice.²⁰⁻²² In the present study itself, patients who were diagnosed with mild or moderate pelvic adhesion were successfully operated on with vNOTES and rarely converted to the OA, MPL, or transumbilical LESS approach.

We also found that factors such as BMI, and history of vaginal delivery or abdominopelvic surgery, including cesarean section, did not increase the risk of surgical conversion. Our findings were almost consistent with a newly published consensus on the safe implementation of vNOTES, which held the view that a previous cesarean section and a high BMI (>30) were not contraindications for vNOTES.⁷ Many other publications have also shown that the vNOTES approach is advantageous for patients with obesity, as surgeons can easily access the pelvic cavity in a transvaginal manner using endoscopic instruments and extract the resected tissue through the vaginal tract.^{11,23,24}

The complication rate in our cohort is comparable to that of a recently published study on vNOTES with a large sample size (4.85% vs. 3.9%), in which all the 1000 surgeries were performed by a high-volume vNOTES expert,²⁵ but the conversion rate of the present study is higher than that study (3.07% vs. 0.4%). We reason that it is because we had a more diverse composition of surgeons, the majority of whom have a much lower caseload and more years' experience of conducting vNOTES than the expert in the other study. The most serious perioperative complication in the present study was rectal injury. There were two full-thickness and two seromuscular rectal injuries. Of these, one full-thickness injury was repaired via vNOTES and the remaining three were converted into MPL or LESS.

In the present study, we attempted to provide solid clinical evidence about the perioperative complications, especially surgical

conversions, of vNOTES tubal surgeries. One of the strengths of the present study is its large sample size. Furthermore, variables such as the primary outcome and incidence of conversion are well documented in the medical records and are not simply subject to interpretation. However, there are a few inherent limitations to the study design. Besides, we only performed a 1-month follow-up, which was relatively short, and did not get long-term postoperative complications data, such as deep dyspareunia and incision granulomas. Another limitation is that the present study only investigated vNOTES complications in treating tubal pathology, which restricted the generalization of our findings to other procedures such as cystectomies, myomectomies, hysterectomies, and oophorectomies. Furthermore, our data were retrospectively collected, which might have introduced information bias and the possibility of data misclassification.

5 | CONCLUSION

vNOTES tubal surgeries are safe due to their low conversion and complication rates. Their surgical conversions are dictated by severe pelvic adhesion and endometriosis.

AUTHOR CONTRIBUTIONS

Dan Feng conceptualized this project. Dan Feng, Li He, and Qiang Zhang completed the data collection. Tianjiao Liu, Dan Feng, and Xin Li drafted the manuscript. Tianjiao Liu, Xin Li, Qiang Zhang, and Jieru Peng participated in the statistical analysis. Li He and Yonghong Lin supervised the project. All the authors contributed substantially to critical revisions of the manuscript.

ACKNOWLEDGMENTS

We gratefully thank the Chengdu High-level Key Clinical Specialty Construction Project, the Chengdu Municipal Health Commission Project (Grant number: 2021215), the Fifth Round of the Chengdu Municipal Science and Technology Research Program (grant number: 2021-YF05-00627-SN), Sichuan Provincial Medical Association Project (grant number: S19085) and the Japan-China Sasakawa Medical Fellowship Program for providing financial support of present study.

CONFLICT OF INTEREST

The authors have no conflicts of interest.

DATA AVAILABILITY STATEMENT

Research data are not shared.

ORCID

Dan Feng  <https://orcid.org/0000-0002-7324-1548>

Li He  <https://orcid.org/0000-0002-9716-2457>

Xin Li  <https://orcid.org/0000-0002-6734-9034>

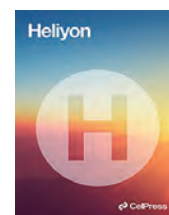
Tianjiao Liu  <https://orcid.org/0000-0001-8279-5924>

Yonghong Lin  <https://orcid.org/0000-0001-7566-8732>

REFERENCES

- Moreira-Pinto J, Lima E, Correia-Pinto J, Rolanda C. Natural orifice transluminal endoscopic surgery: a review. *World J Gastroenterol*. 2011;17(33):3795-3801. doi:10.3748/wjg.v17.i33.3795
- Yoshiki N. Review of transvaginal natural orifice transluminal endoscopic surgery in gynecology. *Gynecol Minim Invasive Ther*. 2017;6(1):1-5. doi:10.1016/j.gmit.2016.11.007
- Zorrón R, Filgueiras M, Maggioni LC, Pombo L, Lopes Carvalho G, Lacerda OA. NOTES. Transvaginal cholecystectomy: report of the first case. *Surg Innov*. 2007;14(4):279-283. doi:10.1177/1553350607311090
- Chen X, Liu H, Sun D, et al. Transvaginal natural orifice transluminal endoscopic surgery for tubal pregnancy and a device innovation from our institution. *J Minim Invasive Gynecol*. 2019;26(1):169-174. doi:10.1016/j.jmig.2018.05.013
- Kho RM. vNOTES: is it the panacea we are all hoping for? *J Minim Invasive Gynecol*. 2021;28(6):1146-1147. doi:10.1016/j.jmig.2021.04.012
- Becerra Garcia FC, Romo-Medrano Mora KE. Our perception of "Women's positive perception of transvaginal NOTES surgery": let the voices be heard, not just counted. *Surg Endosc*. 2010;24(5):1226-1228. doi:10.1007/s00464-009-0750-6
- Kapurubandara S, Lowenstein L, Salvay H, Herijgers A, King J, Baekelandt J. Consensus on safe implementation of vaginal natural orifice transluminal endoscopic surgery (vNOTES). *Eur J Obstet Gynecol Reprod Biol*. 2021;263:216-222. doi:10.1016/j.ejogrb.2021.06.019
- Huang L, He L, Zhang L, et al. Application of the prone position in myomectomy by transvaginal natural orifice transluminal endoscopic surgery. *Wideochir Inne Tech Maloinwazyjne*. 2021;16(1):234-242. doi:10.5114/wiitm.2020.95397
- Huang L, Lin Y-H, Yang Y, Gong Z-L, He L. Comparative analysis of vaginal natural orifice transluminal endoscopic surgery versus transumbilical laparoendoscopic single-site surgery in ovarian cystectomy. *J Obstet Gynaecol Res*. 2021;47(2):757-764. doi:10.1111/jog.14603
- Baekelandt J, Vercammen J. IMELDA transvaginal approach to ectopic pregnancy: diagnosis by transvaginal hydrolaparoscopy and treatment by transvaginal natural orifice transluminal endoscopic surgery. *Fertil Steril*. 2017;107(1):e1-e2. doi:10.1016/j.fertnstert.2016.09.024
- Lee C-L, Wu K-Y, Su H, Ueng S-H, Yen C-F. Transvaginal natural-orifice transluminal endoscopic surgery (NOTES) in adnexal procedures. *J Minim Invasive Gynecol*. 2012;19(4):509-513. doi:10.1016/j.jmig.2012.02.005
- Johnson NP, Hummelshoj L, Adamson GD, et al. World endometriosis society consensus on the classification of endometriosis. *Hum Reprod*. 2017;32(2):315-324. doi:10.1093/humrep/dew293
- Mettler L, Hucke J, Bojahr B, Tinneberg HR, Leyland N, Avelar R. A safety and efficacy study of a resorbable hydrogel for reduction of post-operative adhesions following myomectomy. *Hum Reprod*. 2008;23(5):1093-1100. doi:10.1093/humrep/den080
- Dindo D, Demartines N, Clavien P-A. Classification of surgical complications: a new proposal with evaluation in a cohort of 6336 patients and results of a survey. *Ann Surg*. 2004;240(2):205-213.
- Goldstein SR, Horii SC, Snyder JR, Raghavendra BN, Subramanyam B. Estimation of nonpregnant uterine volume based on a nomogram of gravid uterine volume: its value in gynecologic uterine abnormalities. *Obstet Gynecol*. 1988;72(1):86-90.
- Li C-B, Hua K-Q. Transvaginal natural orifice transluminal endoscopic surgery (vNOTES) in gynecologic surgeries: a systematic review. *Asian J Surg*. 2020;43(1):44-51. doi:10.1016/j.asjsur.2019.07.014
- Liu J, Bardawil E, Lin Q, et al. Transvaginal natural orifice transluminal endoscopic surgery tubal reanastomosis: a novel route for tubal surgery. *Fertil Steril*. 2018;110(1):182. doi:10.1016/j.fertnstert.2018.02.139
- Xu B, Liu Y, Ying X, Fan Z. Transvaginal endoscopic surgery for tubal ectopic pregnancy. *JSLs*. 2014;18(1):76-82. doi:10.4293/108680813X13693422519875
- Cranney R, Condous G, Reid S. An update on the diagnosis, surgical management, and fertility outcomes for women with endometrioma. *Acta Obstet Gynecol Scand*. 2017;96(6):633-643. doi:10.1111/aogs.13114
- Reid S, Condous G. Transvaginal sonographic sliding sign: accurate prediction of pouch of Douglas obliteration. *Ultrasound Obstet Gynecol*. 2013;41(6):605-607. doi:10.1002/uog.12469
- Leonardi M, Martins WP, Espada M, Georgousopoulou E, Condous G. Prevalence of negative sliding sign representing pouch of Douglas obliteration during pelvic transvaginal ultrasound for any indication. *Ultrasound Obstet Gynecol*. 2020;56(6):928-933. doi:10.1002/uog.22023
- Arion K, Aksoy T, Allaire C, et al. Prediction of pouch of Douglas obliteration: point-of-care ultrasound versus pelvic examination. *J Minim Invasive Gynecol*. 2019;26(5):928-934. doi:10.1016/j.jmig.2018.09.777
- Lee C-L, Wu K-Y, Su H, Wu P-J, Han C-M, Yen C-F. Hysterectomy by transvaginal natural orifice transluminal endoscopic surgery (NOTES): a series of 137 patients. *J Minim Invasive Gynecol*. 2014;21(5):818-824. doi:10.1016/j.jmig.2014.03.011
- Kaya C, Yıldız Ş, Alay İ, Aslan Ö, Aydinler İE, Yaşar L. The comparison of surgical outcomes following laparoscopic hysterectomy and vNOTES hysterectomy in obese patients. *J Invest Surg*. 2022;35(4):862-867. doi:10.1080/08941939.2021.1927262
- Baekelandt J, Kapurubandara S. Benign Gynaecological procedures by vaginal natural orifice transluminal endoscopic surgery (vNOTES): complication data from a series of 1000 patients. *Eur J Obstet Gynecol Reprod Biol*. 2021;256:221-224. doi:10.1016/j.ejogrb.2020.10.059

How to cite this article: Feng D, He L, Li X, et al. Perioperative outcomes of and predictors for conversion from transvaginal natural orifice transluminal endoscopic tubal surgeries: A retrospective cohort study of 619 patients. *Int J Gynecol Obstet*. 2023;161:803-811. doi:10.1002/ijgo.14653



Research article

Transvaginal natural orifice endoscopic surgery for tubal ectopic pregnancy: A more suitable surgical approach for enhanced recovery after surgery

Ying Liu ^{a,1}, Xin Li ^{a,*}, Tianjiao Liu ^{a,1}, Aijie Xie ^a, Xian Wu ^a, Yujian Jia ^a, Xiaoyan Liao ^a, Wei Cheng ^a, Hui Wang ^a, Fangyuan Zhong ^a, Lijuan Xu ^a, Juan Huang ^a, Siqin Xiu ^a, Zhongzhi Li ^b, Yalan Li ^c, Xue Xiao ^{d,**}, Yonghong Lin ^{a,***}, Xiaoqin Gan ^{a,****}

^a Department of Gynecology and Obstetrics, Chengdu Women's and Children's Central Hospital, School of Medicine, University of Electronic Science and Technology of China, Chengdu, 611731, China

^b Department of Gynecology and Obstetrics, Chongqing University Fuling Hospital, Chongqing, 408099, China

^c Psychiatry Department, Psychosomatic Medical Center, The Fourth People's Hospital of Chengdu, Chengdu, 610036, China

^d Department of Gynecology and Obstetrics, West China Second University Hospital, Sichuan University, Chengdu, 610041, China

ARTICLE INFO

Keywords:

Enhanced recovery after surgery
Salpingectomy
Salpingostomy
Laparoscopic
Transvaginal natural orifice endoscopic surgery
Tubal pregnancy

ABSTRACT

Objective: We aimed to determine the safety of Vaginal natural orifice transluminal endoscopic surgery (vNOTES) in terms of the Enhanced Recovery after Surgery (ERAS) concept for tubal pregnancy surgery and provide a detailed process of vNOTES for tubal pregnancy surgery, including experience and key points for surgeons performing this procedure.

Methods: The Longitudinal Vaginal Natural Orifice Transluminal Endoscopic Surgery Study (LovNOTESS), which was conducted in Chengdu, China. A total of 219 patients who underwent tubal ectopic pregnancy surgery between September 2021 and March 2022. The patients underwent salpingectomy or salpingostomy using transumbilical laparoscopic single-site surgery (LESS) or vNOTES, according to their preferences. This study prospectively collected perioperative and one-year follow-up data on tubal pregnancy outcomes after vNOTES and compared them with those after LESS.

Results: The vNOTES group showed a shorter surgical duration, hospitalization duration, and postoperative exhaust time and a lower analgesic medication usage rate, but it showed a higher surgical conversion rate. The vNOTES approach reduced the postoperative exhaust time by

* Corresponding author. Chengdu Women's and Children's Central Hospital, 1617 Riyue Avenue, Qingyang District, Chengdu, 611731, Sichuan, China.

** Corresponding author. West China Second University Hospital, Sichuan University, No. 20, Block 3, Renmin Road, Chengdu, 610041, China.

*** Corresponding author. Chengdu Women's and Children's Central Hospital, 1617 Riyue Avenue, Qingyang District, Chengdu, 611731, Sichuan, China.

**** Corresponding author. Chengdu Women's and Children's Central Hospital, 1617 Riyue Avenue, Qingyang District, Chengdu, 611731, Sichuan, China.

E-mail addresses: 554989333@qq.com (Y. Liu), xinlicwch@163.com (X. Li), xiaoxuesc@aliyun.com (X. Xiao), linyhcd2011@163.com (Y. Lin), amandine2021@163.com (X. Gan).

¹ These authors contributed equally to this work.

<https://doi.org/10.1016/j.heliyon.2024.e24945>

Received 18 October 2023; Received in revised form 13 January 2024; Accepted 17 January 2024

Available online 20 January 2024

2405-8440/© 2024 Published by Elsevier Ltd. This is an open access article under the CC BY-NC-ND license (<http://creativecommons.org/licenses/by-nc-nd/4.0/>).

approximately 9 h (95% confidence interval [CI]: $-11.93, -5.57$ h, $p < .001$) and the risk of postoperative analgesic drug use by 77% (odds ratio, 0.23; 95% CI: 0.10, 0.61, $p = .023$).

Conclusion: vNOTES can shorten the exhaust time and duration of hospitalization, reduce postoperative pain, and avoid surface surgical scars in tubal pregnancy surgeries, consistent with the ERAS concept. However, more comprehensive preoperative evaluation of patients who choose vNOTES is required to reduce the occurrence of intraoperative conversion.

Trial registration: ChiCTR2100053483.

1. Introduction

Ectopic pregnancy involves implantation of the zygote outside the uterine cavity, and tubal pregnancy is the most common form of ectopic pregnancy [1]. Although the incidence rate of tubal pregnancies is only approximately 0.5%–2.3% [2,3], it is the main cause of early pregnancy death [4,5]. Stable and ruptured tubal pregnancies are primarily treated using surgical procedures, which are divided into salpingostomies and salpingectomies [6,7].

Tubal pregnancy surgeries are routinely performed as daycare surgeries at our department because of the minor surgical damage. While the conventional surgical approach is transumbilical laparoendoscopic single-site surgery (LESS), vaginal natural orifice transluminal endoscopic surgery (vNOTES) has recently emerged as an option [8–11]. The growing relevance of the Enhanced Recovery after Surgery (ERAS) concept requires surgeons to continuously refine their surgical skills to ensure less surgery-related damage and pain, shorter hospital stays, and earlier return to normal life [12–14]. In comparison with LESS, vNOTES shows milder postoperative pain, faster anal exhaust, and complete absence of surface scars, consistent with the concept of ERAS [15–19]. Although the feasibility of vNOTES for tubal pregnancy surgery has been reported, data regarding its safety are limited [8]. Considering its anatomical specificity, this approach may cause damage to adjacent organs such as the bladder or rectum [16,20,21], indicating the need to investigate the safety of vNOTES in tubal pregnancy surgery in terms of the ERAS concept.

Therefore, this study prospectively collected and compared perioperative and one-year follow-up data on tubal pregnancies treated using vNOTES and LESS. Using these data, we aimed to determine the safety of vNOTES in terms of the ERAS concept for tubal pregnancy surgery and provide detailed insights regarding vNOTES for tubal pregnancy surgery, including important considerations for surgeons performing this procedure.

2. Materials and methods

2.1. Study design and participants

This study was based on the Longitudinal Vaginal Natural Orifice Transluminal Endoscopic Surgery Study (LovNOTESS), which was conducted in Chengdu, China (China Clinical Trials Registry ChiCTR2200059282), and was approved by the Institutional Review Board of Chengdu Women and Children's Central Hospital (No. 202130). This subgroup study prospectively collected perioperative and one-year follow-up data of patients with tubal pregnancy who were willing to undergo surgical treatment between September 2021 and March 2022. This study only recruited patients with stable vital signs, and patients suspected of significant abdominal bleeding or hemorrhagic shock underwent emergency surgery. Meanwhile, this study excluded patients with absolute or relative contraindications to vNOTES, such as suspected vaginal infections, severe pelvic adhesions, fallopian tube ovarian abscesses, endometriosis, malignancy, intrauterine pregnancy, potential interstitial ectopic pregnancy (through preoperative ultrasound examination [22]) or sacrouterine nodularity. After informing the patient in detail about the risks associated with the surgery and providing written informed consent, the patient underwent salpingectomy or salpingostomy using LESS or vNOTES according to their preferences. In tubal pregnancies, suspected vaginal infections, severe pelvic adhesions, or lesions located in the interstitial part of the fallopian tubes are contraindications for vNOTES.

2.2. Data collection

The patients' perioperative data were collected from the hospital's electronic medical record system, including data related to the patients' age, duration of amenorrhea, body mass index (BMI), fertility history, previous abdominal surgery, surgical method, surgical approach, maximum diameter of the mass, preoperative and postoperative blood human chorionic gonadotropin (HCG) levels, operation time, pelvic adhesions, surgical conversion, postoperative exhaust time, length of hospital stay, and perioperative complications. The operative time was measured from the time the incision was made to the end of suturing. Postoperative recovery data included the time from the end of the surgery to the first postoperative activity, urination, feeding, and exhaust. For salpingectomy, outpatient follow-up assessments were performed 1 week after surgery and 1 month thereafter; for salpingostomy, patients were required to undergo weekly blood HCG tests until they showed negative results.

2.3. Standard surgical procedures for transumbilical LESS and vNOTES under ERAS

For all patients, the routine procedure for ERAS was as follows: patients fasted for >8 h after consuming fried or fatty foods or

meats, >6 h after consuming light meals or milk, and >2 h after drinking water. Urinary catheters were not routinely placed during surgery. After waking up from anesthesia, the patient was asked to eat light food as soon as possible and get out of bed as soon as possible. For patients who experienced no specific discomfort, discharge was routinely performed on the same day or in the morning after surgery (within 24 h of admission). After discharge, patients were given a 24-h online phone number to contact the doctors in case of adverse events.

All surgeries were performed by the same qualified surgeons in accordance with the same surgical procedures. Patients emptied their bladder before surgery and received an intravenous infusion of 1-g cefazoline 30 min before surgery to prevent infection. The patient was assisted in the lithotomy position and administered general anesthesia. Before performing vNOTES, cervical forceps were used to pull the cervix to ensure good cervical and uterine activity. For vNOTES, the specific operating steps are as follows: 1) The vaginal retractor exposes the cervix, and 2 Allis forceps are used to pull the cervix outward and upward to expose the posterior vaginal fornix; 2. Make a 2 cm transverse incision at the midpoint of the posterior vaginal fornix, cut the whole thickness of the vaginal wall, and then use tissue scissors to separate the tissue to reach the peritoneum; 3) Cut the peritoneum and extend the incision toward 4 and 8 o'clock in the vagina; 4) A disposable double-ring multi-instrument access port (Beijing Aerospace Kadi Technology Development Institute, HK-TH-60.4TY) was inserted into the pelvic cavity through the incision. For the LESS procedure, an incision was made at the navel. The next steps were same in all groups and followed: Pneumoperitoneum was created up to 14 mmHg of CO2 insufflation and a 10-mm 30-degree rigid laparoscope (Karl Storz GmbH & Co. KG, Tuttlingen, Germany) was used for visualization.

2.4. Standard surgical procedures for salpingostomy or salpingectomy

For salpingostomy, an incision was made on the opposite side of the fallopian tube mesentery, at the most prominent point of the pregnancy mass. Bipolar electrocoagulation was performed to create an electrocoagulation band along the long axis of the fallopian tube. The fallopian tube was placed inside a specimen bag to prevent the villi from flowing into the abdominal cavity. Electrocoagulation hooks or scissors were used to cut longitudinally along the long axis of the affected fallopian tube, with a slightly shorter incision length than the pregnancy mass. Non-invasive forceps were used to lift the incision edge of the fallopian tube wall, stretch into a 5-mm flushing suction device along the tube wall into the lumen, use water pressure to separate the villi and blood clots from the tube wall, and drive the villi and blood clots to completely discharge from the incision under water flow. If the villi and blood clots adhered tightly to the tube wall and could not be completely separated by water pressure, non-invasive grasping forceps were used to gently pull the villi tissue and continue to separate the villi from the base of the tube wall under water pressure. The lumen of the fallopian tube was rinsed repeatedly with an NaCl solution to ensure the absence of residual villous tissue. The wound surface of the Fallopian

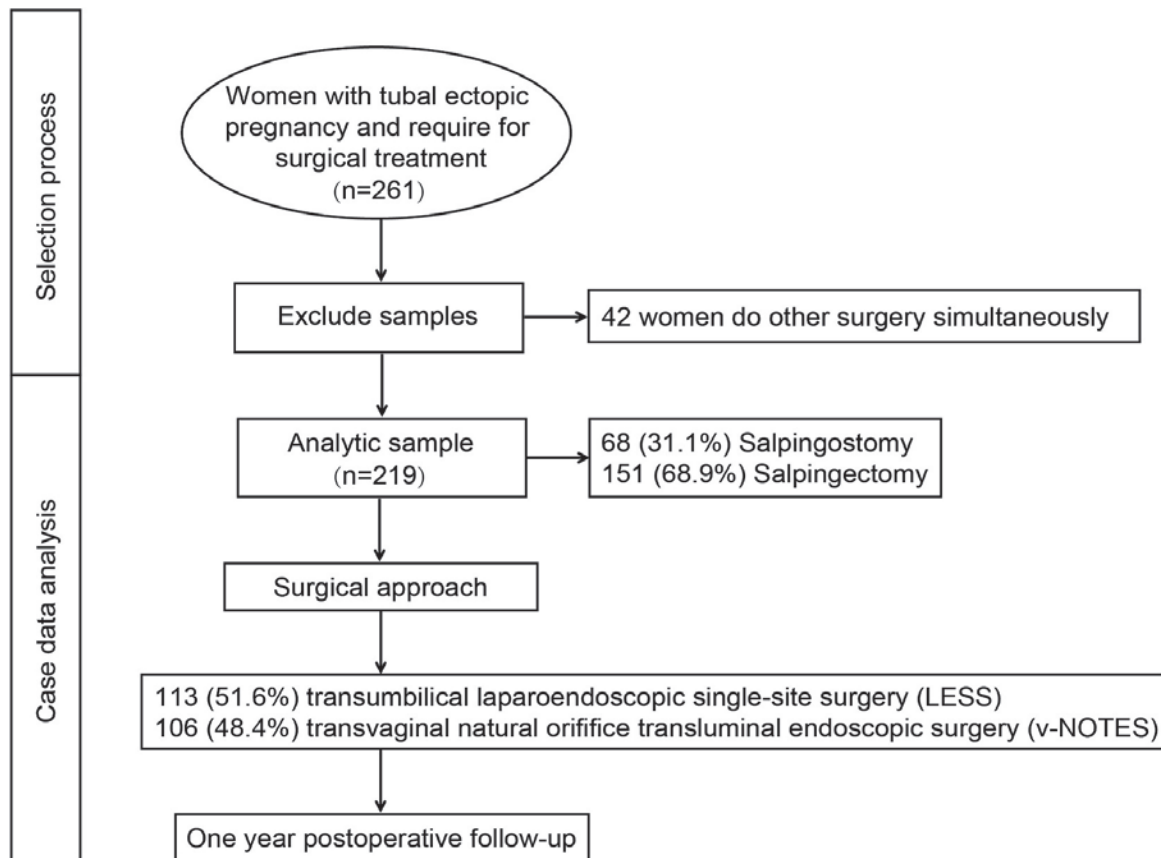


Fig. 1. Selection process for this study.

tube was opened or sutured discontinuously to the mucosal layer.

For salpingectomy, the fimbriated extremity of the fallopian gland was lifted with non-invasive forceps, the mesosalpinx was coagulated with bipolar electrocoagulation, and the mesosalpinx was gradually cut to the isthmus of the oviduct with scissors. After bipolar electrocoagulation of the interstitial part of the fallopian tube, scissors were used to cut the fallopian tube at the electrocoagulation site, and the wound was electrocoagulated to stop the bleeding.

All surgeons and surgical team members follow standardized operating procedures to complete the learning curve [23] and achieve proficiency. If intraoperative injury of large vessels, important organs or bleeding >800 ml, the surgical method will be changed. vNOTES is generally converted to transabdominal single-port laparoscopic surgery, and single-port laparoscopic surgery is converted to multi-ports surgery. Immediately convert to open surgery if there is a life-threatening vascular injury.

The abdominal and vaginal wound were closed with 2-0 absorbed suture and 2-0 barbed absorbable suture respectively. If the patient feels significant pain after surgery, 10 ml of ibuprofen will be given as a single oral analgesic. Use again after 4–6 h if necessary.

2.5. Statistical analysis

SPSS software (version 27.0; IBM Corp., Armonk, NY, USA) were used to perform the all statistical analyses. Fisher's exact or Chi-square tests were used to analyze categorical data, reporting as counts (percentages). The mean \pm standard deviation values of continuous variables were evaluated via Student's t-test and least significant difference Student's t-test. Multivariate linear regression analysis was used to detect the factors influencing intraoperative bleeding, duration of surgery, and postoperative exhaust time. Binary logistic regression was used to analyze the associations between preoperative characteristics and postoperative analgesic medication usage. Covariates were selected according to the different variables in the univariate analysis and factors that were reported to affect the dependent variable in previous studies. All statistical significance was set at $P < .05$ with two-tailed tests.

3. Results

The selection process for the study population is illustrated in Fig. 1. Initially, 261 patients with tubal ectopic pregnancies who were willing to undergo surgical treatment were recruited for the study. After excluding patients who underwent other surgeries simultaneously, the final analysis included 219 patients, of whom 106 (48.4%) underwent vNOTES and 113 (51.6%) underwent LESS. The average age of the patients, duration of amenorrhea, and BMI at recruitment were 31.40 ± 5.45 years, 31.40 ± 5.45 days, and 21.28 ± 3.16 kg/m², respectively. Among these patients, 159 (72.6%) had a history of artificial dilation and curettage abortion, 115 (52.5%) had undergone abdominal surgery, and 30 (13.7%) had a previous ectopic pregnancy. Among the 219 patients, 68 (31.1%) chose salpingostomy and 151 (68.9%) chose salpingectomy (Table 1).

No statistically significant differences were observed in the demographic characteristics of the patients in the LESS and vNOTES groups. Patients in the vNOTES group showed a shorter duration of surgery and hospitalization, a shorter postoperative exhaust time, and a lower analgesic medication use rate, but had a higher surgical conversion rate (Table 2). The reasons for surgical conversion in four cases in the vNOTES group were as follows: the procedure was beyond the scope of the surgical instrument due to adhesion of the fallopian tube to the lateral wall of the pelvic cavity in one case; difficulty stopping bleeding due to the proximity of the mass to the uterine part in one case; and difficulty entering the pelvic cavity due to pelvic adhesions in two cases. All four of these patients were transferred to the LESS group. Perioperative complications in the LESS group included persistent ectopic pregnancy after surgery in one patient, poor incision healing in one patient, and postoperative fever and one patient had; in contrast, perioperative complications in the vNOTES group included persistent ectopic pregnancy after surgery in one patient, postoperative pelvic hemorrhage in one patient, and postoperative fever in two patients had. All patients recovered after undergoing conservative treatment and were discharged without re-surgery.

The volume of intraoperative bleeding can be indirectly used as an indicator of surgical injury, and was further analyzed using

Table 1
Description of the patients demographic characteristics and operation types.

Variables	Total
Patients	219
Age (year)	31.40 ± 5.45
BMI (kg/m ²)	21.28 ± 3.16
Duration of amenorrhea (day)	47.90 ± 10.45
History of abdominal surgery	115 (52.5%)
History of D & C artificial abortion	159 (72.6%)
History of ectopic pregnancy	30 (13.7%)
Surgical approach	
LESS	113 (51.6%)
v-NOTES	106 (48.4%)
Surgical type	
Salpingostomy	68 (31.1%)
Salpingectomy	151 (68.9%)

BMI: body mass index, v-NOTES: vaginal natural orifice transluminal endoscopic surgery, LESS: laparoendoscopic single-site surgery.

Table 2
Description of the patient characteristics by surgical approaches.

Variables	LESS	v-NOTES	P-value
Patients	N = 113	N = 106	
Age (year)	31.60 ± 4.98	31.24 ± 5.86	0.735 ^a
BMI (kg/m ²)	21.38 ± 3.41	21.20 ± 2.97	0.769 ^a
Duration of amenorrhea (day)	46.92 ± 7.95	48.67 ± 12.15	0.374 ^a
History of abdominal surgery	60 (53.1%)	55 (51.9%)	0.756 ^b
Max diameter of mass (cm)	2.94 ± 1.32	2.78 ± 1.19	0.493 ^a
Preoperative HCG (mIU/ml)	2861.12 ± 5765.42	3004.95 ± 5647.45	0.897 ^a
D&C artificial abortion	73 (64.6%)	86 (81.1%)	0.787 ^b
History of ectopic pregnancy	17 (15.0%)	13 (12.2%)	0.293 ^b
Emergency surgery	4 (3.5%)	5 (4.7%)	0.702 ^c
Surgical type			0.215 ^b
Salpingostomy	38 (33.6%)	30 (28.3%)	
Salpingectomy	75 (66.4%)	76 (71.7%)	
Operative information			
Duration of surgery (min)	59.53 ± 21.35	55.94 ± 17.06	0.230 ^a
Bleeding volume (ml)	22.19 ± 31.01	18.02 ± 15.39	0.370 ^a
Pelvic adhesion	35 (31.0%)	32 (30.2%)	0.846 ^b
Surgical conversion	0 (0%)	4 (3.8%)	0.026 ^c
Post-Operative information			
Hemoglobin difference (g/L)	15.65 ± 9.43	13.71 ± 9.23	0.387 ^a
Hospital stay (day)	1.03 ± 0.18	0.60 ± 0.13	0.041 ^a
Exhaust time (hour)	6.05 ± 4.89	4.84 ± 3.90	0.204 ^a
Analgesic medication use	26 (23.9%)	8 (7.6%)	<0.001 ^b
Perioperative complications	3 (2.7%)	4 (3.8%)	0.776 ^c

BMI: body mass index, v-NOTES: vaginal natural orifice transluminal endoscopic surgery, LESS: laparoendoscopic single-site surgery, HCG: human chorionic gonadotropin, D&C: Dilation and Curettage.

^a Average and standard deviation. Student's *t*-Test.

^b Number (percentage). Chi-squared Test.

^c Number (percentage). Fisher Exact Test.

multiple linear regression. The results showed that the amount of intraoperative bleeding was positively correlated with surgical conversion and pelvic adhesions. The bleeding volume increased by approximately 29 mL in cases involving surgical conversion (95% confidence interval [CI]: 17.56, 39.73 mL, *p* = .019) and 19 mL for each 1-grade increase in pelvic adhesion (95% CI: 7.08, 27.39 mL, *p* = .043) (Table 3).

The factors influencing operation time were further analyzed using multiple linear regression, and the results showed that operation duration was correlated with BMI, surgical type, surgical conversion, and pelvic adhesion (Fig. 2A). Salpingostomy, surgical conversion, and each grade of pelvic adhesion increased the operation duration by approximately 10 min (95% CI: 1.24, 18.22 min, *p* = .025), 32 min (95% CI: 16.83, 46.17 min, *p* = .037), and 9 min (95% CI: 5.33, 13.39 min, *p* = .012), respectively (Fig. 2B). Interestingly, the operation duration also increased by approximately 1.4 min when BMI increased by 1 kg/m² (95% CI: 0.24, 2.59 min, *p* = .019).

Early postoperative anal exhaust indicates faster recovery of gastrointestinal function. Multiple linear regression analysis was conducted to investigate the factors influencing postoperative anal exhaust time, and the results showed that exhaust time was correlated with BMI, surgical approach, and pelvic adhesions (Table 4). A 1-kg/m² increase in BMI and an increase one 1 grade in

Table 3
Association between perioperative characteristics and volume of intraoperative bleeding.

Variables	Beta	95% CI	P-value	VIF
R ² = 0.360				
Age (year)	0.09	(-0.87,1.06)	0.849	1.29
BMI (kg/m ²)	-0.25	(-1.86,1.36)	0.760	1.21
Surgical approach (vNOTES)	-5.62	(-15.08,3.84)	0.242	1.04
Surgical type (Salpingostomy)	2.49	(-9.14,14.11)	0.672	1.36
Surgical transfer	28.64	(17.56,39.73)	0.019	1.13
History of abdominal surgery	-2.15	(-7.45,3.15)	0.423	1.15
Duration of amenorrhea	-0.02	(-0.51,0.46)	0.929	1.19
Max diameter of mass	-0.35	(-4.15,3.45)	0.855	1.04
Preoperative HCG	0.01	(0,0.02)	0.146	1.16
Emergency surgery	2.16	(-4.49,8.81)	0.588	1.06
Pelvic adhesion	19.24	(7.08,31.39)	0.043	1.10
Duration of surgery	0.19	(-0.08,0.46)	0.166	1.28
Surgeon	-3.60	(-11.39,4.19)	0.361	1.22

BMI: body mass index, v-NOTES: vaginal natural orifice transluminal endoscopic surgery, HCG: human chorionic gonadotropin.

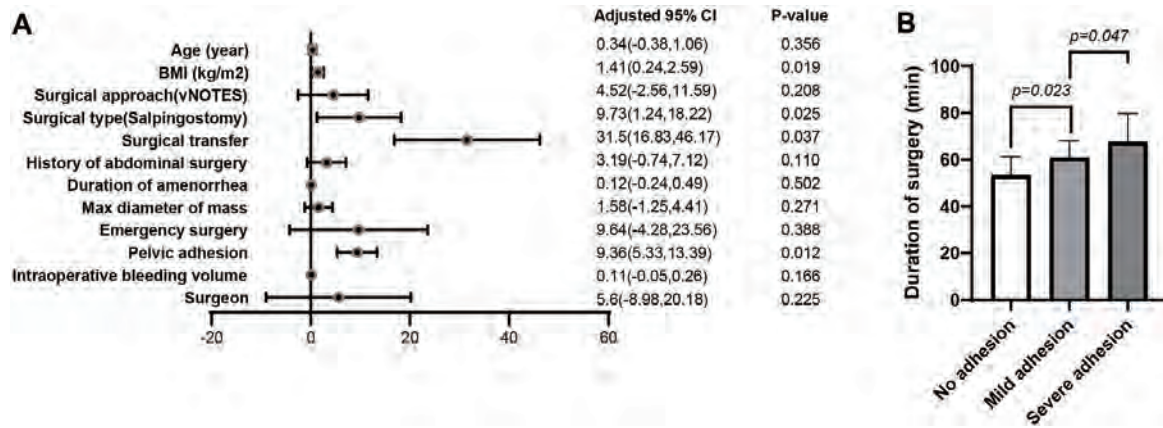


Fig. 2. The influence of surgical characteristics on the operation duration. (A) Multiple linear regression showed that the operation duration was correlated with BMI, surgical type, surgical conversion, and pelvic adhesion. Salpingostomy, surgical conversion, and each grade of pelvic adhesion increased the operation duration by approximately 10 min (95% confidence interval [CI]: 1.24, 18.22 min; $p = .025$), 32 min (95% CI: 16.83, 46.17 min; $p = .037$), and 9 min (95% CI: 5.33, 13.39 min; $p = .012$), respectively. Interestingly, the operation duration increased by approximately 1.4 min when BMI increased by 1 kg/m² (95% CI: 0.24, 2.59 min, $p = .019$). (B) The groups with no adhesions, mild adhesions, and severe adhesions showed significant differences in the duration of surgery.

pelvic adhesion increased the exhaust time by 0.6 h (95% CI: 0.26, 0.85 h, $p = .027$) and 6.7 h (95% CI: 2.90, 10.57 h, $p = .019$), respectively. Notably, the vNOTES approach reduced the postoperative exhaust time by approximately 9 h (95% CI: -11.93, -5.57 h, $p < .001$).

Analgesics are not routinely used after surgery, and patients actively requesting the use of analgesics may be experiencing greater pain and discomfort. The factors influencing postoperative analgesic drug use were analyzed using binary logistic regression, and the results showed that analgesic drug use was correlated with the surgical approach, surgical conversion, and duration of surgery (Table 5). Surgical conversion increased the risk of postoperative analgesic drug use by 102% (odds ratio [OR]: 2.02, 95% CI: 1.34, 3.56, $p = .025$), while vNOTES decreased the risk by 77% (OR:0.23, 95% CI: 0.10, 0.61, $p = .023$). Moreover, the risk of postoperative analgesic drug use increased by 3% when the duration of surgery increased by 1 min (OR:1.03, 95% CI: 1.01, 1.12, $p = .037$).

The patient’s fertility history was followed-up by phone one year after surgery. In the salpingostomy group, more patients chose contraception, mostly because of concerns regarding the recurrence of ectopic pregnancy. In this group, patients planning to conceive had a higher natural conception rate and risk of recurrent tubal pregnancy, and lower rates of infertility or conception through assisted reproductive technologies (Supplementary Table 1).

4. Discussion

Our results showed that vNOTES shortened the exhaust time and hospital stay, reduced postoperative pain, and helped avoid surface surgical scars, consistent with ERAS requirements. In this prospective study, we compared the perioperative characteristics of tubal pregnancy surgery using LESS and vNOTES in terms of the ERAS requirements and collected data on fertility one year after surgery. In addition, the advantages and disadvantages of vNOTES in relation to the ERAS requirements for tubal pregnancy surgery are discussed in detail, providing a theoretical basis for the further development of vNOTES.

The vNOTES and LESS approaches showed no significant differences in intraoperative bleeding, surgical duration, or postoperative

Table 4
Association between postoperative exhaust time and perioperative characteristics.

Variables	Beta	95% CI	P-value	VIF
$R^2 = 0.607$				
Age (year)	-0.01	(-0.33,0.32)	0.963	1.32
BMI (kg/m ²)	0.56	(0.26,0.85)	0.027	1.14
Surgical approach (vNOTES)	-8.75	(-11.93,-5.57)	<0.001	1.07
Surgical type (Salpingostomy)	-2.19	(-5.92,1.55)	0.249	1.28
Surgical transfer	5.68	(-18.31,29.66)	0.201	1.21
History of abdominal surgery	1.31	(-0.64,3.25)	0.187	1.43
Max diameter of mass	0.63	(-0.63,1.88)	0.325	1.04
Emergency surgery	0.42	(-5.55,6.39)	0.889	1.35
Pelvic adhesion	6.73	(2.90,10.57)	0.019	1.16
Intraoperative bleeding volume	-0.03	(-0.09,0.04)	0.415	1.07
Duration of surgery	-0.02	(-0.10,0.07)	0.715	1.22
Surgeon	-0.45	(-1.60,0.71)	0.443	1.12

BMI: body mass index, v-NOTES: vaginal natural orifice transluminal endoscopic surgery.

Table 5

Association between postoperative analgesic medication use and perioperative characteristics.

Variables	Exp(B)	95% CI	P-value
Age (year)	0.94	(0.85,1.02)	0.177
BMI (kg/m ²)	1.01	(0.86,1.18)	0.901
Surgical approach (vNOTES)	0.23	(0.10,0.61)	0.023
Surgical type (Salpingostomy)	1.02	(0.71,1.44)	0.916
Surgical transfer	2.02	(1.34,3.56)	0.025
History of abdominal surgery	0.68	(0.02,1.38)	0.826
Duration of amenorrhea	1.47	(0.89,2.43)	0.128
Max diameter of mass	0.97	(0.92,1.02)	0.255
Emergency surgery	1.29	(0.02,2.31)	0.256
Pelvic adhesion	0.56	(0.03,1.32)	0.545
Postoperative exhaust time	1.02	(0.97,1.06)	0.212
Intraoperative bleeding volume	1.00	(0.98,1.02)	0.791
Duration of surgery	1.03	(1.01,1.12)	0.037
Surgeon	1.45	(0.27,2.02)	0.109

BMI: body mass index, v-NOTES: vaginal natural orifice transluminal endoscopic surgery.

complication rates, indicating that the vNOTES approach is safe and feasible. However, the surgical conversion rate of 3.8% in the vNOTES group was much higher than that in the LESS group (0%). These conversions were primarily attributable to adhesions and the presence of the mass in the uterine part. In such cases, continued surgery under vNOTES may cause damage to neighboring organs; consequently, these patients were converted to LESS. Thus, surgeons should conduct a more comprehensive preoperative evaluation of the patients selected for vNOTES. A history of dysmenorrhea or previous pelvic surgery, difficult uterine activity, and tenderness of sacral ligament nodules may provide important clues for screening of severe pelvic adhesions [24,25]. In addition, vaginal ultrasound can be used for real-time assessment of the sliding of the uterus on the anterior wall of the rectum. If these evaluations indicate severe pelvic adhesions, the vNOTES approach should be avoided. Notably, the lesion was in the uterine part in one case. Due to failure to reach the uterine fundus, the patient underwent transumbilical single-port laparoscopy for hemostasis. This reflects the limitations of vNOTES that for lesions in the uterine fundus, vNOTES is difficult to perform surgery due to limitations in field of view and instrument range. We believe that a combination of these methods can effectively avoid the complications associated with inappropriate patient selection.

In this cohort, the incidence of complications was 3.2%, slightly higher than that associated with LESS in previous studies [21, 26–30]. Among the cases showing complications, two involved persistent ectopic pregnancies, accounting for 2.9% of salpingostomy cases, which was similar to the corresponding percentage reported in previous studies [31,32]. Both patients recovered and were discharged from the hospital after methotrexate administration following surgery, and neither patient required re-surgery. Moreover, the surgical duration in the vNOTES group was shorter than that in the LESS group, although the difference was not statistically significant. This may be due to the smaller chopstick effect caused by the lesion being closer to the platform [33–35]. Our experience suggests that salpingostomy and ovarian cystectomy are more convenient to perform using vNOTES because the lesion site is directly located in front of the approach [36,37].

The timing of postoperative anal exhaust as a part of the discharge evaluation criteria is crucial for evaluating the ERAS mode [38, 39]. In our cohort, the postoperative exhaust time was shorter in the vNOTES group than in the LESS group, which is consistent with previous studies [40]. The vNOTES procedure was performed in the pelvic area, and showed little effect on the upper abdomen. After entering the pelvis, the first step is to push the small intestine into the abdominal cavity, after which the intestine will not be touched again, thereby minimizing intestinal irritation. Additionally, because the vNOTES incision is made in the vaginal vault, this site is insensitive to cutting pain caused by visceral nerve innervation. Lighter postoperative pain encourages patients to get out of the bed early after surgery, which can also promote gastrointestinal recovery and facilitate earlier exhaust [41,42].

The ERAS concept requires less damage to patients, faster postoperative recovery, greater patient comfort, and an earlier return to normal life activities [43–45]. The findings of this study imply that vNOTES is not inferior to or is even more suitable than LESS in terms of the ERAS concept. Moreover, vNOTES offers the advantage of completely eliminating surface scars, making it aesthetically pleasing. However, in patients who choose vNOTES, a more comprehensive preoperative evaluation is required to reduce the occurrence of intraoperative conversion.

The follow-up assessments of the patients' fertility status one year after surgery yielded noteworthy findings. Among the patients who chose salpingostomy because of reproductive reasons, 61.8% chose continuous contraception because of concerns regarding another ectopic pregnancy. However, patients who undergo salpingectomy have fewer options for contraception because they don't have to worry about ectopic pregnancy happening again in the affected fallopian tubes. This situation may also be caused by informed notification from physicians during the perioperative period. As for patients who choose salpingostomy, physicians usually recommend strict contraception for 3–6 months and inform them that the affected fallopian tube will increase the risk of ectopic pregnancy again after surgery. This may increase the psychological pressure on patients, leading them to choose long-term contraception. Although patients undergoing salpingostomy have a slightly higher natural conception rate, they also have a 15.4% chance of recurrent tubal pregnancy. Therefore, further studies are needed to determine which surgical method is the best choice for women with reproductive needs.

The strengths of this study include its prospective design and professional participants. The patients were included on the basis of

strict inclusion and exclusion criteria and a surgical procedure, ensuring a high degree of consistency in demographic characteristics between the two groups. This study compared the perioperative characteristics of the two most advanced surgical methods for tubal pregnancy surgery and preliminarily confirmed the safety and effectiveness of vNOTES for this procedure. In addition, a relatively comprehensive experimental design was implemented by prospectively collecting follow-up data from patients at 1 week, 1 month, and 1 year after surgery.

This pilot study strengthened our understanding of the safety of vNOTES during tubal pregnancy. However, this study had some limitations. First, the sample size of this study was relatively smaller than that of similar studies using Multi-port and LESS. Second, the limitations of the vNOTES technique are the chopstick effect (lack of triangulation resulting from the use of the conventional equipment) and the limited experience of the surgeons. Before performing vNOTES surgery, we suggest that all surgeons and surgical team members should follow standardized operating procedures to complete the learning curve [23]. Third, although this study shows that vNOTES can promote ERAS in patients, it is necessary to grasp the indications of this approach to reduce the occurrence of complications and surgical conversions. Four, since this study is not a randomized clinical trial, we are unable to specify surgical procedures for patients. After fully informing the advantages and disadvantages of the two surgeries, the final decision is based on the patient's wishes. Therefore, in this process, some potential bias factors may be added, which may affect the choice of surgical methods for patients. Five, if there is a conventional surgical group as the control group, it can indeed better demonstrate the advantages of vNOTES. However, due to the fact that our hospital no longer performs routine open surgery and Multi-port laparoscopic surgery except for some large uterine fibroids or malignant tumor surgeries, we do not have enough data as a control. Six, vNOTES has been widely used in gynecology for only 5 years, and the patients in this study were followed-up for only 1 year. Longer follow-up periods with more patients can improve our understanding of the short- and long-term complications of vNOTES and their potential influence on sexual function and fertility. Therefore, large-scale multicenter studies involving more patients, longer time periods, and more types of surgery are needed to further promote the widespread use of vNOTES in the field of gynecology.

5. Conclusions

Our results indicated that vNOTES could shorten the exhaust time and hospital stay, reduce postoperative pain, and avoid surface surgical scars, consistent with the ERAS concept. Thus, vNOTES may be more suitable for ERAS than LESS. However, in patients who choose vNOTES, a more comprehensive preoperative evaluation is required to reduce the occurrence of intraoperative conversion. With the further popularization of minimally invasive and scar free surgery, vNOTES will inevitably achieve longer-term development. Therefore, more and higher quality research is needed to demonstrate its advantages and promote its rapid development.

Capsule

To reflect the safety of vaginal natural orifice transluminal endoscopic surgery (vNOTES) in terms of the Enhanced Recovery after Surgery (ERAS) concept for tubal pregnancy surgery and provide a detailed process of vNOTES for tubal pregnancy surgery, including experience and key points for surgeons performing this procedure.

Funding

Financial support for this study was provided by the Sichuan Provincial Department of Science and Technology (2023YFS0219 and 2023YFS0228), Chengdu Science and Technology Bureau (No: 2021-YF0500530-SN) and the Chengdu Municipal Health Commission (No: 2021074, 2022441, 2023261, 2023413 and 2023475). The funding agencies did not have any role in the design of the study; collection, analysis, and interpretation of data; or in writing the manuscript.

Attestation statement

The subjects in this trial have not concomitantly been involved in other randomized trials. Data regarding any of the subjects in the study has not been previously published unless specified. Data will be made available to the editors of the journal for review or query upon request.

IRB approval

This study was approved by the Institutional Review Board of Chengdu Women and Children's Central Hospital (No. 202130) on June 14, 2021.

Data availability

The datasets generated and analyzed during the current study are not publicly available because of our ongoing prospective study but are available from the corresponding author upon reasonable request.

CRediT authorship contribution statement

Ying Liu: Writing – original draft. **Xin Li:** Writing – original draft. **Tianjiao Liu:** Writing – original draft. **Aijie Xie:** Writing – original draft. **Xian Wu:** Writing – original draft. **Yujian Jia:** Writing – original draft. **Xiaoyan Liao:** Writing – original draft. **Wei Cheng:** Writing – original draft. **Hui Wang:** Writing – original draft. **Fangyuan Zhong:** Writing – original draft. **Lijuan Xu:** Writing – original draft. **Juan Huang:** Writing – original draft. **Siqin Xiu:** Writing – original draft. **Zhongzhi Li:** Writing – original draft. **Yalan Li:** Writing – original draft. **Xue Xiao:** Writing – review & editing, Writing – original draft, Funding acquisition. **Yonghong Lin:** Writing – original draft. **Xiaoqin Gan:** Writing – original draft.

Declaration of competing interest

The authors declare that they have no known competing financial interests or personal relationships that could have appeared to influence the work reported in this paper.

Acknowledgements

The authors would like to thank all participants and researchers who contributed to this cohort study.

Appendix A. Supplementary data

Supplementary data to this article can be found online at <https://doi.org/10.1016/j.heliyon.2024.e24945>.

References

- [1] Y.T. Shen, Y.Y. Yang, P.G. Zhang, L.M. He, R.H. Che, Z. Li, W. Lu, Tubal ectopic pregnancy: a retrospective cohort study on clinical characteristics, treatment options and reproductive outcomes within 5 years, *Arch. Gynecol. Obstet.* 306 (6) (2022) 2055–2062.
- [2] K. Tamai, T. Koyama, K. Togashi, MR features of ectopic pregnancy, *Eur. Radiol.* 17 (12) (2007) 3236–3246.
- [3] G. Oron, T. Tulandi, A pragmatic and evidence-based management of ectopic pregnancy, *J. Minim. Invasive Gynecol.* 20 (4) (2013) 446–454.
- [4] P. Cheng, X.H. Yang, Preservation of the fallopian tube in ectopic tubal pregnancy. An analysis of the outcome of two laparoscopic surgical approaches, *Ann. Ital. Chir.* 93 (2022) 241–247.
- [5] E. Nedopekina, S. Escura, T. Cobo, S.R. Hansson, J.M. Martinez, F. Figueras, M. Lopez, Conservative treatment in non-tubal ectopic pregnancy and predictors of treatment failure, *Eur. J. Obstet. Gynecol. Reprod. Biol.* 257 (2021) 6–10.
- [6] E. Eghbali, M. Azari, A. Jafarizadeh, S. Alihosseini, Spontaneous bilateral tubal ectopic pregnancy preoperatively diagnosed by the ultrasound: a case report, *BMC Pregnancy Childbirth* 23 (1) (2023) 125.
- [7] P. Torok, A. Naem, S. Csehely, V. Chiantera, Z. Sleiman, A.S. Lagana, Reproductive outcomes after expectant and surgical management for tubal pregnancy: a retrospective study, *Minim Invasive Ther. Allied Technol.* (2023) 1–9.
- [8] B. Xu, Y. Liu, X. Ying, Z. Fan, Transvaginal endoscopic surgery for tubal ectopic pregnancy, *J. Soc. Laparoendosc. Surg.* 18 (1) (2014) 76–82.
- [9] Y.W. Kim, B.J. Park, T.E. Kim, D.Y. Ro, Single-port laparoscopic salpingectomy for surgical treatment of tubal pregnancy: comparison with multi-port laparoscopic salpingectomy, *Int. J. Med. Sci.* 10 (8) (2013) 1073–1078.
- [10] G. Ozceltik, D. Simsek, I. Hortu, A.O. Yeniel, I.M. Itil, Transvaginal natural orifice transluminal endoscopic surgery for ectopic pregnancy, *J. Obstet. Gynaecol. Res.* 48 (3) (2022) 843–849.
- [11] G. Ozceltik, A.O. Yeniel, A.O. Atay, I.M. Itil, Transvaginal natural orifice transluminal endoscopic surgery for tubal stump pregnancy, *J. Minim. Invasive Gynecol.* 28 (4) (2021) 750–751.
- [12] J. Ripolles-Melchor, A. Abad-Motos, M. Bruna-Esteban, M. Garcia-Nebreda, I. Otero-Martinez, O.A. Fernandez, M.P. Tormos-Perez, G. Paseiro-Crespo, R. Garcia-Alvarez, M. Am-O, et al., Association between use of enhanced recovery after surgery protocols and postoperative complications after gastric surgery for cancer (POWER 4): a nationwide, prospective multicentre study, *Cir. Esp. (Engl. Ed.)* (2023).
- [13] G. Nelson, C. Fotopoulou, J. Taylor, G. Glaser, J. Bakkum-Gamez, L.A. Meyer, R. Stone, G. Mena, K.M. Elias, A.D. Altman, et al., Enhanced recovery after surgery (ERAS(R)) society guidelines for gynecologic oncology: addressing implementation challenges - 2023 update, *Gynecol. Oncol.* 173 (2023) 58–67.
- [14] J. Gillet, L. Morgado, A. Hamy, C. Casa, S. Mucci, F. Drissi, P. Le Naoures, J.F. Hamel, A. Venara, Does stoma modify compliance with enhanced recovery after surgery programs? Results of a cohort study, *Int. J. Colorectal Dis.* 38 (1) (2023) 100.
- [15] J. Baekelandt, L. Matak, M. Merckx, S. Housmans, J. Deprest, T. Tollens, Posterior rectus fascia prolapse (PREFAP) repair: a new native tissue approach to pelvic organ prolapse via vaginal natural orifice transluminal endoscopic surgery, *Arch. Gynecol. Obstet.* (2023).
- [16] L. Mereu, B. Pecorino, M. Ferrara, M. Siniscalchi, G. Garraffa, M.G. D'Agate, P. Scollo, Cumulative sum analysis of learning curve process for vaginal natural orifice transluminal endoscopic surgery (V-notes) hysterectomy, *J. Minim. Invasive Gynecol.* (2023).
- [17] V.T. Lerner, G. May, C.B. Iglesia, Vaginal natural orifice transluminal endoscopic surgery revolution: the next frontier in gynecologic minimally invasive surgery, *J. Soc. Laparoendosc. Surg.* 27 (1) (2023).
- [18] L. Huang, J. Yu, Y. Li, Z.L. Gong, D. Feng, L. He, Y.H. Lin, Transvaginal natural orifice transluminal endoscopic surgery versus conventional vaginal surgery for sacrospinous ligament fixation of apical compartment prolapse: a retrospective analysis, *BMC Surg.* 23 (1) (2023) 24.
- [19] J. Jung, J.J. Noh, J. Jeon, C.S. Chang, T.J. Kim, Comparison of surgical outcomes of adnexectomy by vaginal natural orifice transluminal endoscopic surgery (vNOTES) versus single-port access (SPA) surgery, *J. Personalized Med.* 12 (12) (2022).
- [20] J. Zhang, Y. Dai, J. Leng, L. Zhu, J. Lang, D. Sun, Hysterectomy and bilateral adnexectomy using transvaginal natural orifice transluminal endoscopic surgery: the role of multichannel abdominal PORT and vaginal support ring, *J. Obstet. Gynaecol. Res.* 47 (7) (2021) 2521–2528.
- [21] M.S. Kim, J.J. Noh, T.J. Kim, Hysterectomy and adnexal procedures by vaginal natural orifice transluminal endoscopic surgery (VNH): initial findings from a Korean surgeon, *Front. Med. (Lausanne)* 7 (2020) 583147.
- [22] M. Elsherbiny, E.T. Lim, K. Ma, Interstitial ectopic pregnancy: laparoscopic cornuostomy, *J. Minim. Invasive Gynecol.* 30 (6) (2023) 439–440.
- [23] L. Huang, L. He, L. Huang, X. Gan, Y. Lin, Z. Xiong, Learning curve analysis of transvaginal natural orifice transluminal endoscopic hysterectomy combined under the standard operating procedure, *Int. J. Gynaecol. Obstet.* 159 (3) (2022) 689–695.
- [24] M. Hui, C. Schwartzburg, A. Bhalwal, Utility of vaginal natural orifice transluminal endoscopic surgery for permanent sterilization after failed attempt at bilateral tubal ligation at the time of previous cesarean section, *J. Minim. Invasive Gynecol.* 29 (10) (2022) 1138–1139.

- [25] X. Guan, E. Bardawil, J. Liu, R. Kho, Transvaginal natural orifice transluminal endoscopic surgery as a rescue for total vaginal hysterectomy, *J. Minim. Invasive Gynecol.* 25 (7) (2018) 1135–1136.
- [26] A. Kale, E. Mağ, G. Basol, E.C. Gundogdu, Y. Aboalhasan, G. Yildiz, B. Kuru, E. Kale, T. Usta, M. Altintas, et al., A new and alternative route: transvaginal natural orifice transluminal endoscopic scarless surgery (vaginal natural orifice transluminal endoscopic surgery) for class 2 and class 3 obese patients suffering from benign and malignant gynecologic pathologies, *Surg. Innovat.* 29 (6) (2022) 730–741.
- [27] I. Tavano, S. Housmans, J. Bosteels, J. Baekelandt, Pregnancy outcome after vaginal natural orifice transluminal endoscopic surgery, a first retrospective observational cohort study, *Gynecol. Obstet. Invest.* 86 (5) (2021) 432–437.
- [28] K. Nulens, R. Kempenaers, J. Baekelandt, Hysterectomy via vaginal Natural Orifice Transluminal Endoscopic Surgery in virgin patients: a first feasibility study, *J. Obstet. Gynaecol.* 42 (1) (2022) 116–121.
- [29] K. Nulens, I. Van Genechten, J. Baekelandt, Repeat vaginal natural orifice transluminal endoscopic surgery: a first feasibility study, *Gynecol. Obstet. Invest.* 86 (1–2) (2021) 117–122.
- [30] L. Huang, Y.H. Lin, Y. Yang, Z.L. Gong, L. He, Comparative analysis of vaginal natural orifice transluminal endoscopic surgery versus transumbilical laparoendoscopic single-site surgery in ovarian cystectomy, *J. Obstet. Gynaecol. Res.* 47 (2) (2021) 757–764.
- [31] E. Wall-Wieler, C.L. Shover, J.M. Hah, S.L. Carmichael, A.J. Butwick, Opioid prescription and persistent opioid use after ectopic pregnancy, *Obstet. Gynecol.* 136 (3) (2020) 548–555.
- [32] S. Akira, Y. Negishi, T. Abe, M. Ichikawa, T. Takeshita, Prophylactic intratubal injection of methotrexate after linear salpingostomy for prevention of persistent ectopic pregnancy, *J. Obstet. Gynaecol. Res.* 34 (5) (2008) 885–889.
- [33] T. Benhidjeb, I. Benhidjeb, M. Stark, S. Kreisel, M. Kruger, J. Pfitzenmaier, J. Schulte am Esch, Women's perception of transgastric and transvaginal natural orifice transluminal endoscopic surgery (NOTES) - impact of medical education, stage of life and cross-cultural aspects, *Int. J. Womens Health* 14 (2022) 1881–1895.
- [34] M.L. Interdonato, P. Scollo, T. Bignardi, F. Massimello, M. Ferrara, G. Donatiello, M. Caretto, P. Mannella, B. Pecorino, M.G. Meroni, et al., Hysterectomy by transvaginal natural orifice transluminal endoscopic surgery: an Italian initial experience, *Front. Med. (Lausanne)* 9 (2022) 1018232.
- [35] A.B. Tekin, M. Yassa, C. Kaya, D. Budak, P.B. Ilter, M.A. Mutlu, C. Usta, O.S. Gunkaya, E. Yavuz, N. Tug, Implementing the transvaginal natural orifice transluminal endoscopic surgery (vNOTES) "first" strategy in benign gynecological surgeries, *Arch. Gynecol. Obstet.* 307 (4) (2023) 1007–1013.
- [36] Y. Jung, A. Rattanaburi, O. Kim, J.H. Park, K.H. Lee, A simple gasless direct suturing technique to achieve ovarian hemostasis during transvaginal natural orifice transluminal endoscopic surgery ovarian cystectomy, *J. Laparoendosc. Adv. Surg. Tech.* 31 (9) (2021) 1046–1050.
- [37] C.B. Li, K.Q. Hua, Transvaginal natural orifice transluminal endoscopic surgery (vNOTES) in gynecologic surgeries: a systematic review, *Asian J. Surg.* 43 (1) (2020) 44–51.
- [38] J. Chen, A.L. Luo, L. Yang, W. Wang, X. Zhou, M. Yang, Nutrition management by a multidisciplinary team for prevention of nutritional deficits and morbidity following esophagectomy, *Braz. J. Med. Biol. Res.* 56 (2023) e12421.
- [39] Z. Wang, Q. Xia, A. Li, Q. Lv, Comparison of the effects of endoscopic submucosal dissection and laparoscopic distal radical surgery on the rehabilitation and quality of life of patients with early gastric cancer, *Am. J. Transl. Res.* 15 (3) (2023) 2183–2190.
- [40] Q. Hou, X. Li, L. Huang, Y. Xiong, D. Feng, Q. Zhang, X. Zeng, Y. Yang, T. Liu, Y. Li, et al., Transvaginal natural orifice endoscopic surgery for myomectomy: can it be a conventional surgery? *Front. Surg.* 9 (2022) 1013918.
- [41] X. Lv, C. Li, M. Tang, D. Yuan, Y. Zhong, Y. Xie, Study of the effect of pain on postoperative rehabilitation of patients with uterine malignant tumor, *Front. Surg.* 9 (2022) 1052800.
- [42] N. Zhang, J. Miao, Q. Zheng, The effect of nursing intervention on patients with inguinal hernia and its influence on self-management ability, *Contrast Media Mol. Imaging* 2022 (2022) 4965709.
- [43] Z. Lin, C. Yang, Y. Wang, M. Yan, H. Zheng, Comparison of prolonged postoperative ileus between laparoscopic right and left colectomy under enhanced recovery after surgery: a propensity score matching analysis, *World J. Surg. Oncol.* 20 (1) (2022) 68.
- [44] N. Kugelman, O. Lavie, N. Cohen, M. Schmidt, A. Reuveni, L. Ostrovsky, H. Dabah, Y. Segev, Enhanced recovery after surgery is feasible and beneficial and should be the standard in major gynecological surgeries, *Isr. Med. Assoc. J.* 23 (11) (2021) 725–730.
- [45] O.I. Tkachenko, S.H. Chetverikov, O.V. Bondar, V.Y. Maksymovskiy, M. Chetverikov, V.V. Chetverikova-Ovchynnyk, Implementation of the enhanced recovery after surgery protocol for patients with peritoneal carcinomatosis undergoing cytoreductive surgery and hyperthermic intraperitoneal chemoperfusion, *Contemp. Oncol.* 25 (2) (2021) 133–139.

日中笹川医学奨学金制度<学位取得コース>評価書

課程博士：指導教官用



第 44 期

研究者番号：G4409

作成日：2024年3月7日

氏名	馬 快	MA KUAI	性別	F	生年月日	1993/08/25
所属機関（役職）	大阪大学大学院医学系研究科（大学院生）					
研究先（指導教官）	大阪大学大学院医学系研究科腎臓内科学（猪阪 善隆 教授） 国立成育医療研究センター研究所 RI 管理室/移植免疫研究室（李 小康 室長）					
研究テーマ	腎移植における腎臓線維化発生機序の解明と新規治療法の開発に関する研究 Elucidation of the mechanism and development of new therapeutic methods for renal fibrosis after kidney transplantation					
専攻種別	<input type="checkbox"/> 論文博士			<input checked="" type="checkbox"/> 課程博士		

研究者評価（指導教官記入欄）

成績状況	優 学業成績係数=95	取得単位数
		30/30
学生本人が行った研究の概要	腎臓の線維化は、ほとんどの慢性腎臓病の特徴である。腎線維化の動物モデルでは、マウスの左尿管を結紮する一側尿管閉塞(UUO)より確立され、広く基礎研究に使用されている。一方、5-アミノレブリン酸(5-ALA)は、ヘムやプロトポルフィリン IX(PpIX)の重要な前駆体である。我々これまでの研究で、ヘムオキシゲナーゼ(HO)-1の発現が5-ALAとクエン酸第一鉄(SFC)により増強されることを明らかにした。本研究では、UUOによって誘発されたマウスの腎線維化および炎症に対する5-ALAおよびSFCの保護効果を検証した。	
総合評価	【良かった点】 腎線維化のマウスモデルを確立することができた。評価項目として、病理学、血清学と関連遺伝子のmRNAとタンパク質発現の実験系も併せて確立した。また、5-ALAおよびSFCマウスへ投与の実験で、その効果が示した。	
	【改善すべき点】 5-ALAおよびSFCを用いたマウスへ投与後の効果の作用機序がまだ不明な点があるため、引き続き、検証する必要がある。	
	【今後の展望】 上記腎線維化のマウスモデルを用いて、5-ALAおよびSFCの投与での治療評価及びその作用機序を解明することで、将来臨床への応用に目指したい。	
学位取得見込	学位取得見込み	
評価者（李 小康）		

日中笹川医学奨学金制度<学位取得コース>報告書 研究者用



第44期

研究者番号: G4409

作成日:2024年3月7日

氏名	马快	MA KUAI	性別	F	生年月日	1993/08/25
所属機関(役職)	大阪大学大学院医学系研究科(大学院生)					
研究先(指導教官)	大阪大学大学院医学系研究科腎臓内科学(猪阪 善隆 教授) 国立成育医療研究センター研究所RI管理室/移植免疫研究室(李 小康 室長)					
研究テーマ	腎移植における腎臓線維化発生機序の解明と新規治療法の開発に関する研究 Elucidation of the mechanism and development of new therapeutic methods for renal fibrosis after kidney transplantation					
専攻種別	論文博士	<input type="checkbox"/>	課程博士	<input checked="" type="checkbox"/>		

1) 目的(Goal)

Renal fibrosis is the hallmark of most progressive kidney diseases. Unilateral ureteral obstruction (UUO), the ligation of the ureter, most commonly the left ureter, has been widely used to establish animal models of renal fibrosis [1]. 5-aminoacetylacrylic acid (5-ALA), a key precursor of heme and protoporphyrin IX (PpIX), is catalyzed in animal cells by mitochondrial aminoacetylacrylic synthetase using glycine and succinyl-coA [2]. Previous studies demonstrated that heme oxygenase (HO)-1 expression was up-regulated by 5-ALA and sodium ferrous citrate (SFC) [2-5]. HO-1 is known to be a rate determining enzyme in heme metabolism that produces bilirubin and carbon monoxide, which were demonstrated to act as anti-inflammatory factors. The present study aimed to investigate the protective effect of 5-ALA and SFC against UUO-induced renal fibrosis and inflammation in mice.

2) 戦略(Approach)

In present study, we used 5-ALA and SFC to treat UUO-induced renal fibrosis and inflammation. For that purpose, mice were randomly divided into five treatment groups: Naive group, 7d UUO model group, 7d UUO + 5ALA/SFC group, 14d UUO model group, 14d UUO + 5ALA/SFC group. 5ALA/SFC was administered to the mice for 7 or 14 days following UUO. At the sampling days, blood and kidney tissue samples were collected for evaluation. Renal tissue was harvested and fixed in 10% formalin or optimal cutting temperature compound for histological examination. For the biochemical and molecular expression assessments, kidney tissues were immediately frozen and stored at 80° C until analysis.

3) 材料と方法(Materials and methods)

(1) Animals and unilateral ureteral obstruction model

Specific-pathogen-free inbred male C57BL/6J (B6/J; H-2kb) mice, 8-10 weeks old, were purchased from Japan SLC, Inc. (Shizuoka, Japan). All mice received humane care in accordance with the guidelines of the Animal Use and Care Committee of the National Research Institute for Child Health and Development, Tokyo, Japan (Permission number: A2009-010-C14). All mouse experiments conformed to the National Institutes of Health guidelines for the care and use of laboratory animals. The UUO model was estimated as follows. The abdominal cavity of mice was opened through the left abdominal incision. The left ureter of mice was bluntly separated and double-ligated with 4-0 sutures in the middle and upper 1/3, and the abdominal cavity was closed by layered suture.

(2) Reagents

5-ALA hydrochloride (SBI Pharmaceuticals Co., Ltd., Tokyo, Japan) and SFC (Fe²⁺) (Eisai Food & Chemical Co., Ltd., Tokyo, Japan) were dissolved in distilled water (DW) at a molar ratio of 5-ALA:SFC of 1:0.5. SFC was diluted in 100mg/kg 5-ALA solution immediately prior to administration.

(3) Treatment protocol

All mice were given adaptive feeding for one week and randomly divided into four groups: Naive group, UUO (7d) group, UUO + 5-ALA/SFC (7d) group, UUO (14d) group and UUO + 5-ALA/SFC (14d) group. 5-ALA/SFC was administered via daily gavage at a dose of 100 mg/kg for 7 and 14 days, respectively. Afterwards, blood, spleen and renal tissues were collected for subsequent experiments on day7 and day14.

(4) Serum biochemical analyses

Serum was collected from whole-blood samples after standing for 30 minutes at 37° C and centrifuged at 3000 g for 20 minutes at 4° C. The samples were then measured for the blood urea nitrogen (BUN) and serum creatinine (Cr) concentrations with a commercially available kit (Fujifilm, Tokyo, Japan) and an automatic biochemical analyzer (DRI-CHEM 3500i; Fujifilm) according to the manufacturer's instructions.

(5) Histology and histopathological analyses

Renal 5-μm-thick sections were prepared and subjected to staining with hematoxylin and eosin (HE) (Muto Pure Chemicals, Tokyo, Japan) for morphological analyses. Slides were then examined by light microscopy (OLYMPUS, Tokyo, Japan).

(6) Masson's trichrome staining, Sirius red staining

The degree of renal tissue injury was evaluated by Masson's trichrome staining. The kidney tissues were fixed in 4% paraformaldehyde, embedded in paraffin, and sliced into 4-μm paraffin sections. Then, sections were treated in xylene, dehydrated with graded ethanol, and stained with Masson (Sigma-Aldrich; Merck KGaA). After staining, the sections were dehydrated with 70 and 90% ethanol. Slides observed with an optical microscope (Olympus, Tokyo, Japan). Histological results were quantified using the WinRoof 7.4 software program (Mitani Corporation, Tokyo, Japan).

1. 研究概要 (2)(7) Immunohistochemical analysis

(8) RNA purification and quantitative RT-PCR

(9) Western blotting

(10) Statistical analyses

4) 実験結果 (Results)

(1) 5-ALA/SFC reduced UUO-induced renal dysfunction and tubulointerstitial injury

To determine whether 5-ALA/SFC treatment improves the outcome in acute kidney injury (AKI) and subsequent renal fibrosis, we set up a rodent model of unilateral ureteral obstruction (UUO). Mice were treated with 5-ALA/SFC or acted as controls on day 7 and 14 (Fig. 1A). Blood samples were measured for the blood urea nitrogen (BUN) and serum creatinine (Cr) concentrations with a commercially available kit (Fujifilm, Tokyo, Japan) and an automatic biochemical analyzer (DRI-CHEM 3500i; Fujifilm) according to the manufacturer's instructions. Compared with naive group, serum BUN in UUO model group on day7 and day14 increased significantly ($p < 0.001$ and $p < 0.0001$, respectively). 5-ALA/SFC treatment decreased the levels of BUN on day7 and day14 ($p < 0.01$ and $p < 0.0001$, respectively). The levels of Cr also down-regulated markedly by 5-ALA/SFC administration on day14 ($p < 0.05$) but had no significant differences on day7 (Fig. 1B). Kidneys of the UUO side and naive group were harvested for histopathology on day 7 and day 14. Hematoxylin and eosin (H&E) staining showed that 5-ALA/SFC attenuated tubular atrophy, tubular dilatation and inflammatory cell infiltration.

(2) 5-ALA/SFC exerted protective effects against inflammation

Renal mRNA expression of inflammatory cytokine-related genes, particularly tumor necrosis factor- α (TNF- α), inducible nitric oxide synthase (iNOS), interferon- γ (IFN- γ), interleukin-1 beta (IL-1 β), IL-17, C-C motif chemokine ligand 2 (CCL2), CCL5, CD11c and C-C chemokine receptor type 2 (CCR2), were significantly higher in UUO group on day7 and day14. In contrast, the expression of TNF- α , IL-1 β , CCL2, CCL5, IL-17, iNOS and CCR2 was lower in the 7d_A/S group than in the 7d_control group ($p < 0.01$, $p < 0.05$ and $p < 0.01$, respectively). The IFN- γ expression was down-regulated as well but without a significant difference. After the administration of 5-ALA/SFC for 7 days, TNF- α and IL-1 β showed notable reductions in expression ($p < 0.01$ and $p < 0.01$, respectively). The infiltration of neutrophils in liver was assessed using chloroacetate esterase staining of liver specimens.

(3) 5-ALA/SFC exerted anti-apoptotic effects.

The mRNA expression of apoptosis-related molecules, particularly Bcl-2-associated X (Bax), caspase-1, caspase-3 and NF- κ B, was markedly up-regulated in the 7d_control group compared with Naïve group ($p < 0.05$, $p < 0.0001$, $p < 0.001$ and $p < 0.0001$, respectively). The mRNA expression of Bax, caspase-1, caspase-3, caspase-9 and NF- κ B showed a significant decrease ($p < 0.05$) in the 7d_A/S group on day7 but had no significant differences on day14. Furthermore, the mRNA expression of Bcl-2 in the 7d_A/S group was markedly up-regulated on day7 ($p < 0.05$).

To confirm the anti-apoptosis effect of 5-ALA/SFC, we measured the protein levels of Bax and NF- κ B in renal tissues in the Naïve group, 14d_control group and 14d_A/S group by Western blotting. After a densitometric analysis of the signals, we found that the expression of Bax and NF- κ B was significantly reduced by the treatment of 5-ALA/SFC ($p < 0.05$ and $p < 0.05$, respectively).

(4) 5-ALA/SFC mitigated UUO-induced tubulointerstitial fibrosis

Picro-Sirius red staining and Masson's trichrome (MT) staining showed markedly decreased tubulointerstitial fibrosis in the 5-ALA/SFC treated group on day 7 and day 14. We then performed IHC staining to evaluate kidney fibrosis. Tubules were surrounded by expanded interstitium with abundant interstitial collagen I and α -SMA. 5-ALA/SFC treatment suppressed tubulointerstitial fibrosis on day 7 and day 14 dramatically.

RT-PCR revealed that 5-ALA/SFC significantly reduced mRNA expression of PDGF, TIMP-1, TIMP-2, Col1 α 1, Col5 α 3, MMP9 and α -SMA. To confirm the anti-fibrosis effect of 5-ALA/SFC, we measured the protein levels of TGF- β , Col1 α 1 and α -SMA in renal tissues in the Naïve group, 14d_control group and 14d_A/S group by Western blotting. After a densitometric analysis of the signals, we found that the expression of TGF- β , Col1 α 1 and α -SMA was significantly reduced by the treatment of 5-ALA/SFC ($p < 0.01$, $p < 0.01$ and $p < 0.001$, respectively).

(5) 5-ALA/SFC promotes renal proliferation through activation of the ERK signaling pathway

To further characterize 5-ALA/SFC-induced renal proliferation, we analyzed the expression and activation of p44 ERK1 and p42 ERK2. This analysis revealed that 5-ALA/SFC significantly increased the levels of phosphorylated (activated) ERK1/2 on day 14.

5) 考察 (Discussion)

5-ALA/SFC is a very promising treatment of renal diseases and the rational use of it will solve many problems clinically.

6) 参考文献 (References)

1 Bai Y, Wang W, Yin P, Gao J, Na L, Sun Y, Wang Z, Zhang Z, Zhao C. Ruxolitinib Alleviates Renal Interstitial Fibrosis in UUO Mice. *INT J BIOL SCI* 2020 2020-01-20; 16(2): 194-203.

2 Fujino M, Nishio Y, Ito H, Tanaka T, Li XK. 5-Aminolevulinic acid regulates the inflammatory response and alloimmune reaction. *INT IMMUNOPHARMACOL* 2016 2016-08-01; 37: 71-78.

3 Liu C, Zhu P, Fujino M, Zhu S, Ito H, Takahashi K, Nakajima M, Tanaka T, Zhuang J, Li XK. 5-ALA/SFC Attenuated Binge Alcohol-Induced Gut Leakiness and Inflammatory Liver Disease in HIV Transgenic Rats. *ALCOHOL CLIN EXP RES* 2019 2019-08-01; 43(8): 1651-1661.

4 Hu X, Que W, Hirano H, Wang Z, Nozawa N, Ishii T, Ishizuka M, Ito H, Takahashi K, Nakajima M, Tanaka T, Zhu P, Guo WZ, Li XK. 5-Aminolevulinic acid/sodium ferrous citrate enhanced the antitumor effects of programmed cell death-ligand 1 blockade by regulation of exhausted T cell metabolism in a melanoma model. *CANCER SCI* 2021 2021-07-01; 112(7): 2652-2663.

5 Negoro H, Chatziantonio C, Razaque MS. Therapeutic potential of 5-aminolevulinic acid and sodiumferrous citrate for viral insults: relevance to the COVID-19 crisis. *EXPERT REV ANTI-INFE* 2022 2022-05-01; 20(5): 657-661.

2. 執筆論文 Publication of thesis ※記載した論文を添付してください。Attach all of the papers listed below.

論文名 1 Title	Combinations of anti-GITR antibody and CD28 superagonist ameliorated dextran sodium sulfate-induced mouse colitis.					
掲載誌名 Published journal	Clin Exp Immunol					
	2022 年 6 月	208(3) 巻(号)	340 頁 ~	350 頁	言語 Language	English
第1著者名 First author	Kuai Ma	第2著者名 Second author	Weitao Que	第3著者名 Third author	Xin Hu	
その他著者名 Other authors	Wen-Zhi Guo, Liang Zhong, Daisuke Ueda, Er-Li Gu, Xiao-Kang Li					
論文名 2 Title	A Mesenchymal-Epithelial Transition Factor-Agonistic Antibody Accelerates Cirrhotic Liver Regeneration and Improves Mouse Survival Following Partial Hepatectomy					
掲載誌名 Published journal	Liver Transpl.					
	2022 年 5 月	28(5) 巻(号)	782 頁 ~	793 頁	言語 Language	English
第1著者名 First author	Kuai Ma	第2著者名 Second author	Weitao Que	第3著者名 Third author	Xin Hu	
その他著者名 Other authors	Wen-Zhi Guo, Er-Li Gu, Liang Zhong, Virginia Morello, Manuela Cazzanti, Paolo Michieli, Terumi Takahara, Xiao-Kang Li					
論文名 3 Title	Combinations of anti-GITR antibody and CD28 superagonist induce permanent allograft acceptance by generating type 1 regulatory T cells.					
掲載誌名 Published journal	Sci Adv.					
	2022 年 8 月	(31)eabo4413巻(号)	頁 ~	頁	言語 Language	English
第1著者名 First author	Weitao Que	第2著者名 Second author	Kuai Ma	第3著者名 Third author	Xin Hu	
その他著者名 Other authors	Wen-Zhi Guo, Xiao-Kang Li					
論文名 4 Title	Coral calcium carried hydrogen ameliorates the severity of non-alcoholic steatohepatitis induced by a choline deficient high carbohydrate fat-free diet in elderly rats.					
掲載誌名 Published journal	Sci Rep.					
	2023 年 6 月	13(1):11646. 巻(号)	頁 ~	頁	言語 Language	English
第1著者名 First author	Kuai Ma	第2著者名 Second author	Xin Hu	第3著者名 Third author	Keiki Nambu	
その他著者名 Other authors	Daisuke Ueda, Naotsugu Ichimaru, Masayuki Fujino, Xiao-Kang Li					
論文名 5 Title						
掲載誌名 Published journal						
	年 月	巻(号)	頁 ~	頁	言語 Language	
第1著者名 First author		第2著者名 Second author		第3著者名 Third author		
その他著者名 Other authors						

3. 学会発表 Conference presentation ※筆頭演者として総会・国際学会を含む主な学会で発表したものを記載してください。
 ※Describe your presentation as the principal presenter in major academic meetings including general meetings or international meeting

学会名 Conference	第58回日本移植学会総会			
演題 Topic	Combinations of anti-GITR antibody and CD28 superagonist generated type 1 regulatory T cells			
開催日 date	2022 年 10 月 14 日	開催地 venue	名古屋	
形式 method	<input checked="" type="checkbox"/> 口頭発表 Oral	<input type="checkbox"/> ポスター発表 Poster	言語 Language	<input type="checkbox"/> 日本語 <input checked="" type="checkbox"/> 英語 <input type="checkbox"/> 中国語
共同演者名 Co-presenter	Weitao Que, Xin Hu, Xiao-Kang Li			
学会名 Conference				
演題 Topic				
開催日 date	年 月 日	開催地 venue		
形式 method	<input type="checkbox"/> 口頭発表 Oral	<input type="checkbox"/> ポスター発表 Poster	言語 Language	<input type="checkbox"/> 日本語 <input type="checkbox"/> 英語 <input type="checkbox"/> 中国語
共同演者名 Co-presenter				
学会名 Conference				
演題 Topic				
開催日 date	年 月 日	開催地 venue		
形式 method	<input type="checkbox"/> 口頭発表 Oral	<input type="checkbox"/> ポスター発表 Poster	言語 Language	<input type="checkbox"/> 日本語 <input type="checkbox"/> 英語 <input type="checkbox"/> 中国語
共同演者名 Co-presenter				
学会名 Conference				
演題 Topic				
開催日 date	年 月 日	開催地 venue		
形式 method	<input type="checkbox"/> 口頭発表 Oral	<input type="checkbox"/> ポスター発表 Poster	言語 Language	<input type="checkbox"/> 日本語 <input type="checkbox"/> 英語 <input type="checkbox"/> 中国語
共同演者名 Co-presenter				
学会名 Conference				
演題 Topic				
開催日 date	年 月 日	開催地 venue		
形式 method	<input type="checkbox"/> 口頭発表 Oral	<input type="checkbox"/> ポスター発表 Poster	言語 Language	<input type="checkbox"/> 日本語 <input type="checkbox"/> 英語 <input type="checkbox"/> 中国語
共同演者名 Co-presenter				

4. 受賞(研究業績) Award (Research achievement)

名称 Award name	国名 Country		受賞年 Year of award	年 月
	国名 Country		受賞年 Year of award	年 月

5. 本研究テーマに関わる他の研究助成金受給 Other research grants concerned with your research theme

受給実績 Receipt record	<input type="checkbox"/> 有 <input checked="" type="checkbox"/> 無
助成機関名称 Funding agency	
助成金名称 Grant name	
受給期間 Supported period	年 月 ~ 年 月
受給額 Amount received	円
受給実績 Receipt record	<input type="checkbox"/> 有 <input checked="" type="checkbox"/> 無
助成機関名称 Funding agency	
助成金名称 Grant name	
受給期間 Supported period	年 月 ~ 年 月
受給額 Amount received	円

6. 他の奨学金受給 Another awarded scholarship

受給実績 Receipt record	<input checked="" type="checkbox"/> 有 <input type="checkbox"/> 無
助成機関名称 Funding agency	中国国家留学基金管理委員会
奨学金名称 Scholarship name	国家建設高水平大学公派研究生項目
受給期間 Supported period	2020 年 12 月 ~ 2024 年 12 月
受給額 Amount received	8,160,000 円

7. 研究活動に関する報道発表 Press release concerned with your research activities

※記載した記事を添付してください。Attach a copy of the article described below

報道発表 Press release	<input type="checkbox"/> 有 <input checked="" type="checkbox"/> 無	発表年月日 Date of release	
発表機関 Released medium			
発表形式 Release method	・新聞 ・雑誌 ・Web site ・記者発表 ・その他()		
発表タイトル Released title			

8. 本研究テーマに関する特許出願予定 Patent application concerned with your research theme

出願予定 Scheduled	<input type="checkbox"/> 有 <input checked="" type="checkbox"/> 無	出願国 Application	
出願内容(概要) Application contents			

9. その他 Others

--

指導責任者(記名) 李 小康

Research Article

Combinations of anti-GITR antibody and CD28 superagonist ameliorated dextran sodium sulfate-induced mouse colitis

Kuai Ma^{1,2}, Weitao Que², Xin Hu², Wen-Zhi Guo³, Liang Zhong⁴, Daisuke Ueda⁵, Er-li Gu¹, and Xiao-Kang Li^{*2,3} 

¹Department of Gastroenterology and Hepatology, Jing'an District Central Hospital, Jing'an Branch of Huashan Hospital, Fudan University, Shanghai, China

²Division of Transplantation Immunology, National Research Institute for Child Health and Development, Tokyo, Japan

³Department of Hepatobiliary and Pancreatic Surgery, The First Affiliated Hospital of Zhengzhou University, Zhengzhou, China

⁴Department of Gastroenterology, Huashan Hospital, Fudan University, Shanghai, China

⁵Division of Hepato-Pancreato-Biliary Surgery and Transplantation, Department of Surgery, Kyoto University Graduate School of Medicine, Kyoto, Japan

*Correspondence: Xiao-Kang Li, Division of Transplantation Immunology, National Research Institute for Child Health and Development, 2-10-1 Okura, Setagaya-ku, Tokyo 157-8535 Japan. Tel: +81 3 3416 0181; Fax: +81 3 3417 2864; E-mail: ri-k@ncchd.go.jp

Abstract

Ulcerative colitis (UC) is one of the two main forms of inflammatory bowel disease (IBD) and is an idiopathic, chronic inflammatory disease of the colonic mucosa with an unclear etiology. Interleukin (IL)-10 has been reported to play a crucial role in the maintenance of immune homeostasis in the intestinal environment. Type 1 regulatory T (Tr1) cells are a subset of CD4⁺Foxp3⁻ T cells able to secrete high amounts of IL-10 with potent immunosuppressive properties. In this study, we found that the combination of anti-GITR antibody (G3c) and CD28 superagonist (D665) treatment stimulated the generation of a large amount of Tr1 cells. Furthermore, G3c/D665 treatment not only significantly relieved severe mucosal damage but also reduced the incidence of colonic shortening, weight loss, and hematochezia. Dextran sodium sulfate (DSS) upregulated the mRNA levels of IL-6, IL-1 β , IL-17, IL-12, tumor necrosis factor- α , C-C chemokine receptor type 5, and Bax in splenic lymphocytes (SPLs) and colon tissues, while G3c/D665 treatment conversely inhibited the increase in mRNA levels of these genes. In addition, G3c/D665 treatment altered the proportion of CD4⁺ and CD8⁺ T cells and increased CD4⁺CD25⁺Foxp3⁺ regulatory T cells in SPLs, mesenteric lymph nodes (MLNs), and lamina propria lymphocytes (LPLs). Thus, the combination of G3c and D665 treatment showed efficacy against DSS-induced UC in mice by inducing a large amount of Tr1 cell generation via the musculoaponeurotic fibrosarcoma pathways *in vivo* and relieving inflammatory responses both systemically and locally.

Keywords: anti-GITR antibody, CD28 superagonist, dextran sulfate sodium, inflammatory bowel disease, type 1 regulatory T cells

Abbreviations: Ahr: Aryl hydrocarbon receptors; APCs: activated antigen-presenting cells; CTLs: cytotoxic T cells; CTLA-4: cytotoxic T lymphocyte antigen 4; DSS: dextran sodium sulfate; Ebi3: EBV-induced gene 3; Egr2: early growth response 2; Eomes: eomesodermin; FCM: flow cytometry; GITR: glucocorticoid-induced tumor necrosis factor receptor-related protein; IBD: inflammatory bowel disease; IL: Interleukin; Irf4: Interferon regulatory factor 4; LPLs: lamina propria lymphocytes; Maf: musculoaponeurotic fibrosarcoma; MLNs: mesenteric lymph nodes; PBS: phosphate-buffered saline; Prdm1: PR domain zinc finger protein 1; RT-PCR: real-time polymerase chain reaction; SPLs: splenic lymphocytes; Tbx21: T-box transcription factor 21; TCR: T-cell receptor; Teff: effector T cell; TGF- β : transforming growth factor beta; TLR: Toll-like receptor; Tregs: regulatory T cells; Tr1: Type 1 regulatory T; UC: ulcerative colitis.

Introduction

Ulcerative colitis (UC) is a type of inflammatory bowel disease (IBD) characterized by chronic and repeated episodes of enteropathy with symptoms of abdominal pain, severe diarrhea, rectal bleeding, tenesmus, and extraintestinal manifestation [1]. Although the etiology and pathogenesis of UC are complicated and remain uncertain, studies have demonstrated that UC is closely related to the imbalance in mucosal immunity and changes in the colonic barrier [2]. Previous studies showed that the oral administration of dextran sodium sulfate (DSS) in mice induced colitis with clinical symptoms

and histopathological features markedly similar to those of human UC [3]. Therefore, the DSS-induced mouse model has been widely used to assess the effects of therapeutic manipulation of UC. At present, there is no cure for UC, and the main treatments for this disorder remain glucocorticosteroids and immunosuppressive agents. More effective and viable therapies with fewer side effects are thus urgently needed [4].

In recent years, cellular therapies have been explored in various immune-mediated inflammatory diseases (IMIDs), including IBD [5, 6]. The immune system maintains peripheral tolerance and downregulates unwanted inflammatory

Received 14 March 2022; Revised 14 April 2022; Accepted for publication 2 May 2022

© The Author(s) 2022. Published by Oxford University Press on behalf of the British Society for Immunology. All rights reserved.

For permissions, please e-mail: journals.permissions@oup.com

responses through specialized subpopulations of T cells, namely regulatory T cells (Tregs). The two best-characterized subsets of CD4⁺ Tregs are CD25⁺Foxp3⁺CD4⁺ T cells and IL-10-producing Foxp3⁺CD4⁺ T cells, Type 1 regulatory T (Tr1) cells [7]. Foxp3⁺ Tregs are characterized by the constitutive expression of the transcription factor forkhead box protein 3 (Foxp3) and the expression of the IL-2 receptor α -chain (CD25) [8]. Tr1 cells represent a subset of CD4⁺Foxp3⁻ T cells able to suppress colitogenic T cell responses mainly through the production of high amounts of the cytokine IL-10 with potent immunosuppressive properties [9]. IL-10 has been reported to play a crucial role in the maintenance of the intestinal microbe-immune homeostasis [10]. In addition to CD25⁺Foxp3⁺ Tregs, Tr1 cells are potential candidates for cellular therapy in mucosal diseases [5]. Previous studies have reported that Tr1 cells can be generated from murine and human CD4⁺ T cells *in vitro* [11, 12], but no effective pharmacological approaches have been able to expand antigen-specific or disease-specific Tr1 cells *in vivo*. In the present study, we found that combinations of anti-GITR antibody (G3c) and CD28 superagonist (D665) treatment induced large amounts of IL-10/IFN- γ -co-producing CD4⁺Foxp3⁻ Tr1 cells in mice. Furthermore, Tr1 cells contribute to the immunomodulatory effect of protecting against colitis via the high production of IL-10.

In the present study, we determined the protective role of the combinations of G3c and D665 treatment on DSS-induced UC in mice by evaluating the disease activity index (DAI), colon lengths, and pathological changes. To clarify the variation in the proportion and phenotype of immune cells after G3c/D665 treatment, we performed a flow cytometry (FCM) analysis with splenic lymphocytes (SPLs), mesenteric lymph nodes (MLNs), and colon lamina propria lymphocytes (LPLs). Furthermore, cytokine levels were detected by real-time polymerase chain reaction (RT-PCR). The key role of Tr1 cells in G3c/D665 treatment against UC was further elucidated.

Materials and methods

Animal model

Male C57BL/6JmSLc (B6/J; H-2k^b) mice 8–10 weeks old, purchased from Shizuoka Laboratory Animal Center (Shizuoka, Japan), were maintained under specific-pathogen-free conditions in a feeding room with automatically controlled light and temperature according to the guidelines of the Institutional Animal Care and Use Committee. All animal procedures were authorized by the National Research Institute for Child Health and Development (permission no. A2009-010-C12).

Mice were randomized into three groups: a naïve group, a 3.5% DSS-control group and a 3.5% DSS + G3c/D665-treated group. Acute colitis of mice was induced with 3.5% DSS (molecular weight, 36 000–50 000; MP Biomedicals, Irvine, CA) for 5 days followed by *ad libitum* drinking water for 3 days. The DSS solutions were dissolved in sterile, distilled water, and prepared fresh every other day. Mice were given a single dose of D665, 1 mg/mice on day 0 and a single dose of G3c, 1 mg/mice on day 3 via intraperitoneal injection as a treated group. G3c and D665 antibodies were purified from the supernatant of hybridomas, gifts from J. Shimizu, Kyoto University, Japan and Dr T. Hunig, University of Wurzburg, respectively. Naïve mice received free water during the study period. Body weight and the DAI were evaluated daily during the colitis induction and recovery phases of the experiment [13]. After mice were sacrificed on day 8, the entire colon was removed from the caecum to the anus, and the colon length was measured as an indirect marker of inflammation.

The DAI

The body weight of mice in each group was recorded daily, as well as the stool consistency and the presence of occult or gross blood per rectum during the experimental period. These parameters were respectively scored by one trained observer blinded to the protocol, and the DAI was calculated as reported previously (Table 1) [14].

Histology and histological scoring

The entire colon was washed with phosphate-buffered saline (PBS), and the distal colon was fixed in 10% formaldehyde solution for 48 h and embedded in paraffin for histological analyses. Sections of the colon (4-mm thick) were prepared and subjected to staining with hematoxylin and eosin (H&E; Muto Pure Chemicals, Osaka, Japan) for morphological analyses. Slides were then examined by light microscopy (OLYMPUS, Tokyo, Japan) in a blinded fashion to assess the inflammation state and blindly scored using a previously published grading system (Table 2) [15].

Table 1: Disease activity index (DAI) scoring.

Score	Weight loss (%)	Stool consistency	Rectal bleeding
0	< 1	Normal	Negative hemocult test
1	1-5		
2	5-10	Loose stools	Positive hemocult test
3	10-20		
4	>20	Diarrhea	Gross bleeding

Table 2: Histological injury scoring.

Score	Severity of inflammation	Depth of injury	Crypt damage
0	None	None	None
1	Slight	Mucosal	Basal 1/3 damaged
2	Moderate	Mucosal and submucosal	Basal 2/3 damaged
3	Severe	Transmural	Only surface epithelium intact
4			Entire crypt and epithelium lost

Cell preparation and the flow cytometry analysis

Lymphocyte types among SPLs, MLNs, and LPLs were detected by the LSRFortessa system (BD Biosciences, Franklin Lakes, NJ). Cells were subjected to live/dead staining (Thermo Fisher Scientific, Cleveland, OH) for labeling dead cells and blocked with anti-CD16/CD32 Fc Block antibody to prevent non-specific antibody binding. The following antibodies were purchased from BioLegend (San Diego, CA) and used in the flow cytometry analysis: BV405 anti-mouse CD45 mAb, PE/CF594 anti-mouse CD3 mAb, AF700 anti-mouse CD4 mAb, APC/Cy7 anti-mouse CD4 mAb, AF700 anti-mouse CD8 mAb, and APC/Cy7 anti-mouse CD25 mAb. For intracellular staining, cells were fixed and permeabilized using the transcription factor staining buffer set (eBioscience, San Diego, CA), and then intracellular Foxp3 staining was performed using FITC anti-mouse Foxp3 mAb (eBioscience), PE/Cy7 anti-mouse IFN- γ mAb, APC anti-mouse CTLA-4 mAb, and PE anti-mouse IL-10 mAb purchased from BioLegend. For intracellular cytokine staining, cells were stimulated with 50 ng/ml phorbol 12-myristate 13-acetate (BD Golgi Plug™), 1 mM ionomycin (Sigma-Aldrich, St. Louis, MO), and Brefeldin A (eBioscience) in complete medium for 4 h, followed by surface and intracellular staining. The stained cells were analyzed with the FlowJo software program (Version 10.5.0; BD Biosciences).

Total mRNA preparation and quantitative RT-PCR (qRT-PCR)

Total mRNA was extracted from frozen SPLs, MLNs, and colon tissues using a RNeasy Mini Kit (Qiagen, Valencia, CA). Each 0.8- μ g aliquot of mRNA was reverse-transcribed to cDNA using a Prime Script RT reagent Kit (RR037A; Takara, Shiga, Japan). qRT-PCR was performed by the SYBR® Green system using an Applied Biosystem PRISM7900 apparatus (Thermo Fisher Scientific). The PCR cycle conditions for the SYBR® Green system were 50 °C for 2 min, 95 °C for 2 min, 45 cycles of 95 °C for 15 s, and 60 °C for 60 s. The comparative cycle threshold (Ct)

method was used to determine the relative gene expression, and the results of target genes (Table 3) were normalized by subtracting the Ct value of 18S rRNA, with the fold change calculated by comparative CT.

Western blot analyses

In brief, frozen SPLs in three groups were homogenized in RIPA buffer containing 1% protease inhibitor cocktail-1 and 1% protease inhibitor cocktail-2 (Sigma-Aldrich) followed by centrifugation in a microfuge at top speed for 30 min. Protein concentrations were assayed using Bio-Rad Protein Assay (Bio-Rad, Hercules, CA). Samples were separated by electrophoresis on 10% polyacrylamide gels and transferred to Immobilon-PVDF (Bio-Rad). After brief incubation with 5% non-fat milk to block non-specific binding, membranes were exposed overnight at 4 °C to specific musculoaponeurotic fibrosarcoma (Maf) (Cell Signaling Technology, Danvers, MA). Maf activity was quantified by a laser densitometric analysis of the radiographic film using the ImageJ software program (NIH, Bethesda, MD).

Statistical analyses

The GraphPad Prism 9 software program (GraphPad, San Diego, CA) was used to calculate statistical significance. A two-way analysis of variance (ANOVA) method and one-way ANOVA method were used to compare the three groups. Data are expressed as the mean \pm SD. A value of $P < 0.05$ was considered to be statistically significant (* $P < 0.05$; ** $P < 0.01$; *** $P < 0.001$; **** $P < 0.0001$).

Results

G3c/D665 treatment exhibited the potential to attenuate DSS-induced colitis in mice

We evaluated the potential therapeutic effect of G3c/D665 on a DSS-induced mouse colitis model that had been established by orally feeding 3.5% DSS for 5 consecutive days and water

Table 3: Primer sequences for real-time qPCR.

Gene	Forward Primer (5'~3')	Reverse Primer (3'~5')
Prdm1	CCCTCATCGGTGAAGTCTA	ACGTAGCGCATCCAGTTG
Eomes	GCGCATGTTTCCTTTCTTGAG	GGTCGGCCAGAACCCTTC
Egr2	GCCAAGGCCGTAGACAAAATC	CCACTCCGTTTCATCTGGTCA
Tbx21	AGCAAGGACGGCGAATGTT	GGGTGGACATATAAGCGGTTT
Ahr	AGCCGGTGCAGAAAACAGTAA	AGGCGGTCTAACTCTGTGTTT
TGF- β	ATCCTGTCCAACTAAGGCTCG	ACCTCTTTAGCATAGTAGTCCGC
Foxp3	CACCCAGGAAAGACAGCAACC	GCAAGAGCTCTTGCCATTGA
Maf	GCAGAGACACGTCCTGGAGTGC	CGAGCTTGGCCCTGCAACTAGC
TNF- α	AAGCCTGTAGCCCACGTCGTA	GGCACCCTAGTTGGTTGTCTTTG
IL-1 β	ACCTTCCAGGATGAGGACATGA	AACGTCACACACCAGCAGGTTA
Bax	GGCTGCTTGTCTGGATCCAA	ATGGTCACTGTCTGCCATGTG
CCR-5	GACATCCGTTCCCCCTACAAG	TCACGCTCTTCAGCTTTTTGCAG
IL-6	GGCGGATCGGATGTTGTGAT	GGACCCCAGACAATCGGTTG
IL-12	AGCACGGCAGCAGAATAAA	CTCCACCTGTGAGTTCTTCAAA
IL-17	CAGCAGCGATCATCCCTCAAAG	CAGGACCAGGATCTCTTGCTG
IL-10	GCTCTTACTGACTGGCATGAG	CGCAGCTCTAGGAGCATGTG
18S	ACATCGACCTACCAAGAGG	TCCCATCCTTCACATCCTTC

for 3 days. As expected, mice in the 3.5% DSS-control group lost more body weight and exhibited shorter colon lengths and higher DAI scores than the naïve and G3c/D665-treated groups. The improvement of symptoms, such as colonic shortening, weight loss, and hematochezia, in mice treated with G3c/D665 was significant. The colon tissue sections in naïve mice showed no signs of inflammation, while those in the control group showed distortion of crypts, loss of goblet cells, inflammatory cell infiltration, and severe mucosal damage. In contrast, G3c/D665 treatment obviously improved the pathological changes (Fig. 1A). The colons from G3c/D665-treated DSS-colitis mice were relatively normal, exhibiting only slight evidence of inflammatory cell infiltration. These findings were also quantitatively evaluated by a histopathological analysis and scored using a previously published grading system (Fig. 1B). Taken together, these findings indicate that the combination of G3c/D665 treatment effectively attenuated DSS-induced colitis in mice.

G3c/D665 treatment substantially suppressed inflammatory and apoptotic responses in colitis mice

To understand the anti-inflammatory effect of the combinations of G3c/D665 treatment in DSS-induced colitis in mice, we measured the mRNA levels of pro-inflammatory and apoptotic cytokines and chemokines in colon tissues and spleen lymphocytes. The results show that the mRNA levels

of pro-inflammatory cytokines (such as TNF- α , IL-6, IL-1 β , IL-17, and IL-12), pro-inflammatory chemokines (such as CCR-5) and apoptotic factors (such as Bax) were significantly increased in mice in the control group. However, the increase in these cytokines and chemokines was reduced by G3c/D665 treatment in colon tissues (Fig. 2A). In spleen lymphocytes, the mRNA levels of pro-inflammatory cytokines, such as TNF- α , IL-6, IL-1 β , and IL-12, were significantly reduced in the G3c/D665-treated group as well (Fig. 2B). Our data indicated that G3c/D665 treatment conferred profound protection against DSS-induced colitis in association with reduced inflammatory and apoptotic responses, alleviated tissue damage, and the maintenance of intestinal integrity and functionality.

G3c/D665 treatment altered the proportion of CD4⁺ and CD8⁺ T cells in SPLs, MLNs, and LPLs.

To clarify the variation in the number and/or phenotype of immune cells after G3c/D665 treatment, we performed an FCM analysis with SPLs, MLNs, and LPLs. Previous studies have shown that CD8⁺ cytotoxic T cells play a vital role in inducing relapsing colitis [16]. As shown in Fig. 3, in the present study, the proportion of CD8⁺ cytotoxic T cells among SPLs ($P < 0.0001$) and MLNs ($P < 0.05$) was significantly downregulated by the combinations of G3c and D665 treatment compared to the control group, whereas there was no significant change in the LPLs. Furthermore, SPLs, MLNs,

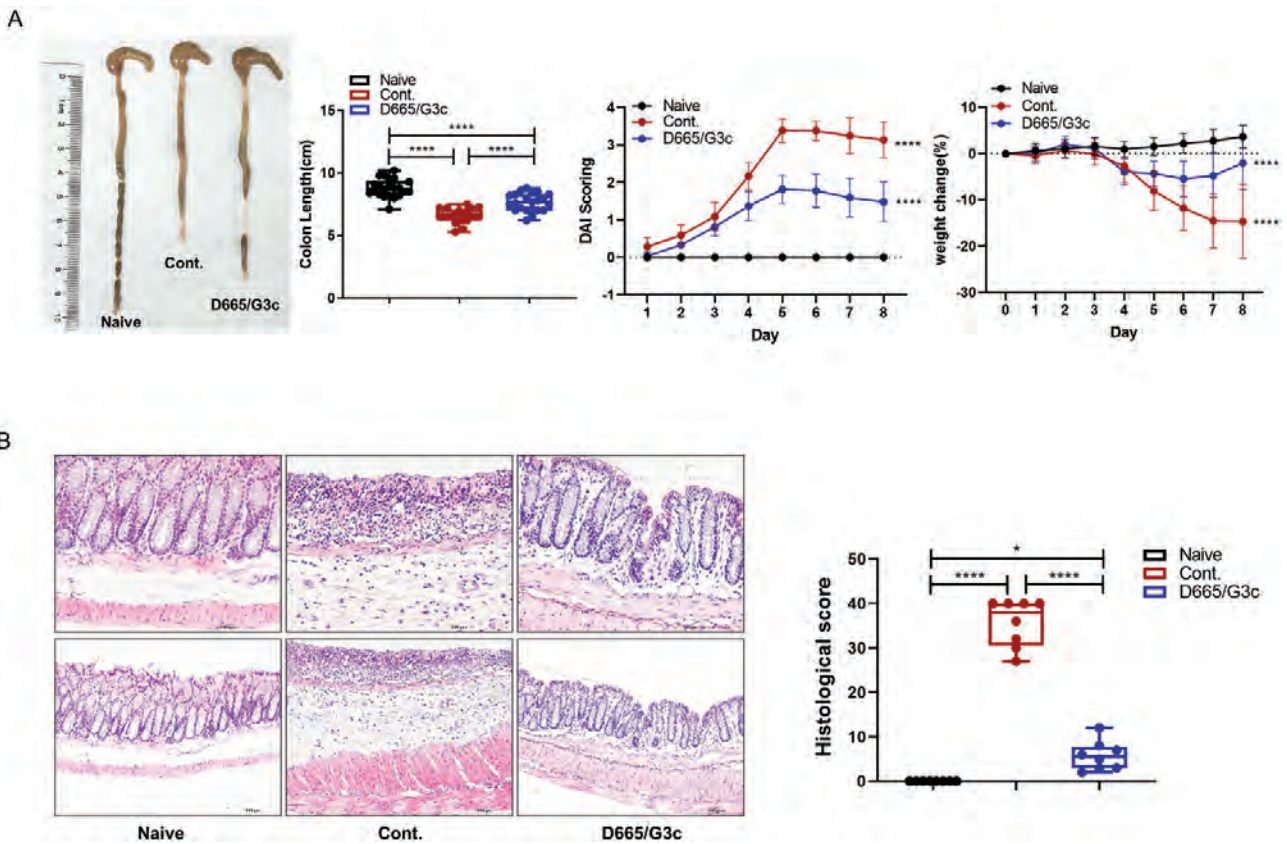


Figure 1: G3c/D665 treatment attenuated DSS-induced damage of colon. (A) The colon gross appearance and length analysis of mice are shown. The DAI of mice and the weight change (%) of mice are also presented. (B) Hematoxylin and eosin (HE) staining of colon specimens in the three groups. Substantial monocyte infiltration, mucosa erosion, goblet cell arrangement disorder, and reduction were seen in the colon specimens of the 3.5% DSS-control group. A Hematoxylin and eosin (HE) analysis of the colon specimens is shown (scale bars = 100 and 200 μ m). Each bar represents the mean \pm SD. * $P < 0.05$, **** $P < 0.0001$.

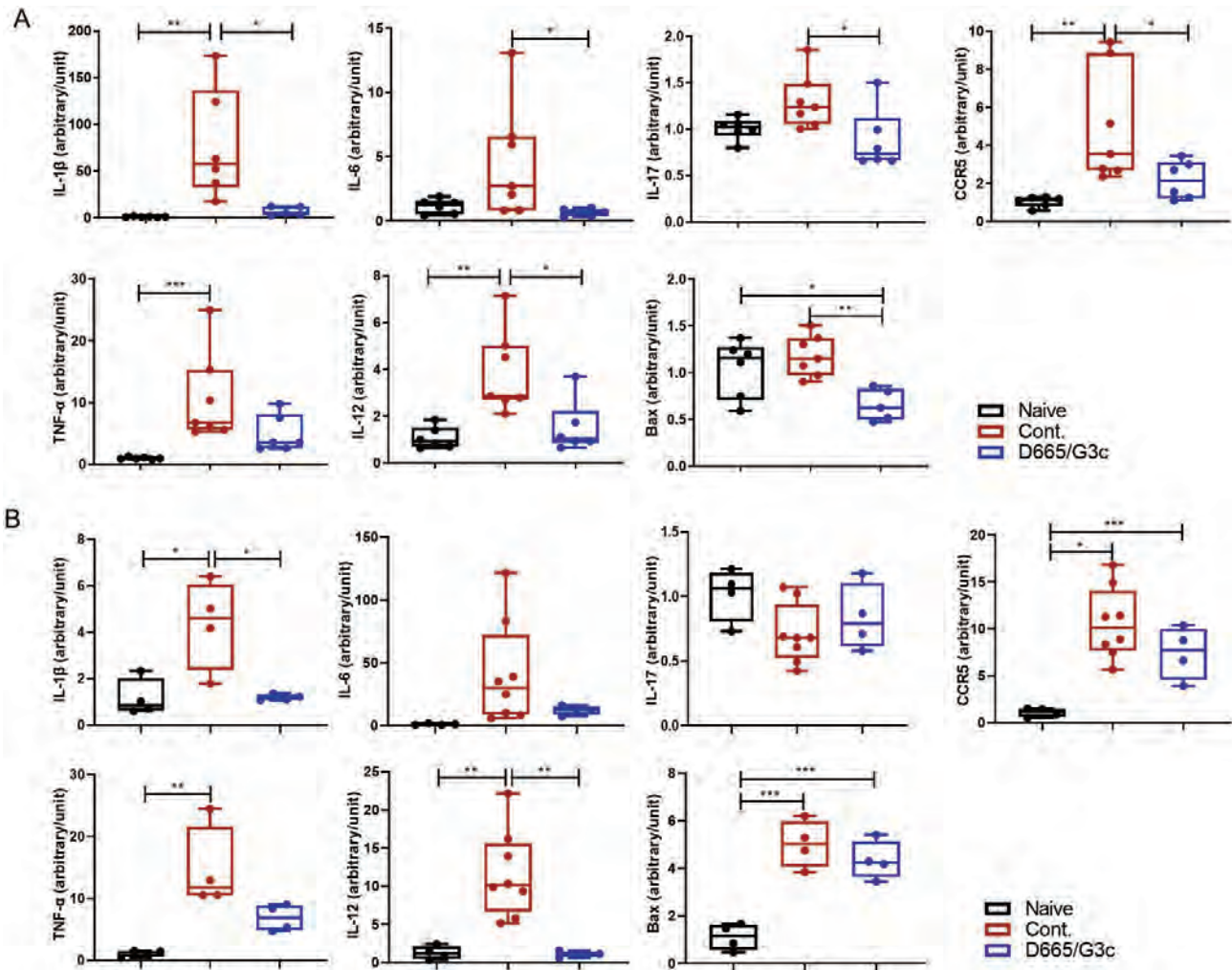


Figure 2: G3c/D665 treatment reduced the mRNA expression of inflammatory and apoptosis cytokine-related genes. (A) Homogenates of colon tissues were analyzed by qRT-PCR as described in the materials and methods. The mRNA expression of inflammatory cytokines-related genes, particularly IL-1 β , IL-6, IL-12, IL-17, and CCR-5, was significantly lower in the G3c/D665-treated group than in the control group. The mRNA expression of apoptosis-related gene, such as Bax, was reduced in the G3c/D665-treated group. (B) SPLs were analyzed by qRT-PCR as well. Compared with the control group, the mRNA expression of inflammatory and apoptosis cytokine-related genes, such as IL-1 β , IL-12, and Bcl-2, was reduced in the G3c/D665-treated group. Values are expressed as arbitrary units (mean \pm SD). * P < 0.05, ** P < 0.01, *** P < 0.001.

and LPLs in the G3c/D665 group showed an apparent increase in the proportion of CD4⁺ T cells compared with the control group.

G3c/D665 treatment led to CD4⁺CD25⁺Foxp3⁺ Treg expansion in DSS-induced colitis

Tregs are a unique subpopulation of CD4⁺ T cells that play pivotal roles in maintaining immune tolerance, improving the inflammatory intestinal environment, and conferring therapeutic benefits for colitis [17, 18], so we evaluated the population of CD4⁺CD25⁺Foxp3⁺ Tregs in SPLs, MLNs, and LPLs among the three groups.

Our analysis showed that the percentage of CD4⁺CD25⁺Foxp3⁺ Tregs in the G3c/D665-treated group was markedly higher than in the other two groups (Fig. 4A, B). Although the combination of G3c and D665 treatment generated a large number of CD4⁺CD25⁺Foxp3⁺ Tregs according to the FCM analysis, the mRNA expression of Foxp3 gene was not significantly increased in the G3c/D665 group (Supplementary Fig. S1). Both the T cell

protein cytotoxic T lymphocyte antigen 4 (CTLA-4) pathway and CD4⁺CD25⁺Foxp3⁺ Tregs are essential for maintaining control of immune homeostasis [19]. We further analyzed CTLA-4 and found that CD4⁺CD25⁺Foxp3⁺ Tregs significantly expressed CTLA-4 in the SPLs, MLNs, and LPLs of the three groups (Fig. 4C, D).

G3c/D665 treatment increased the proportion of Tr1 cells in DSS-induced mouse colitis

Tr1 cells are characterized by their high IL-10-producing capacity and the ability to inhibit T cell responses and colitis [11]. Therefore, we performed an FCM analysis to gain insight into the expression of IL-10⁺Foxp3⁻ Tr1 cells and IL-10⁺IFN- γ ⁻ Tr1 cells gated from CD4⁺ T cells. Our result showed that the combinations of G3c and D665 treatment generated large amounts of IL-10⁺Foxp3⁻ Tr1 cells and IL-10⁺IFN- γ ⁻ Tr1 cells in the three different lymphocyte types (Fig. 5). To identify the expression of Tr1-related transcription factors (TFs), we extracted TFs known to regulate Tr1 differentiation, including early growth response 2 (Egr2), Aryl hydrocarbon receptors

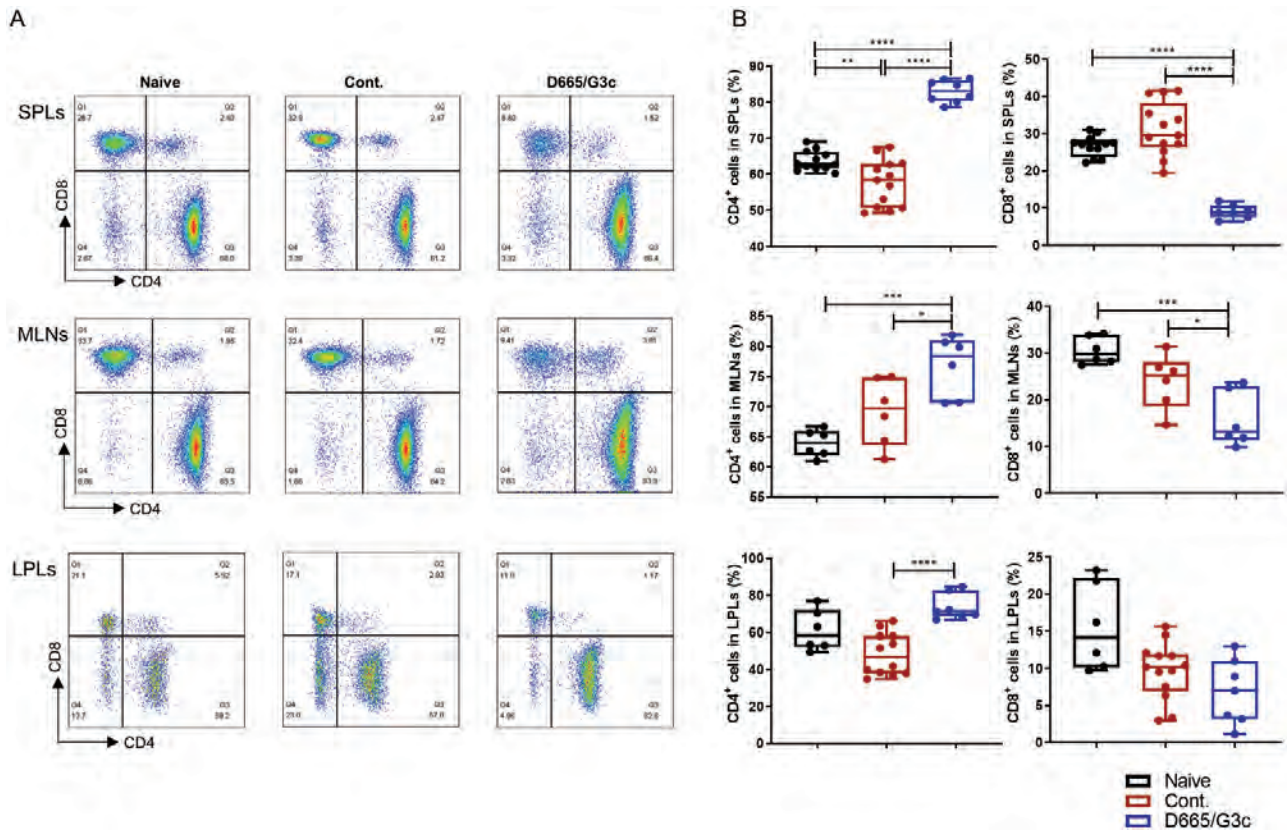


Figure 3: G3c/D665 treatment increased the proportion of CD4⁺ T cells in SPLs, MLNs, and LPLs. (A) A representative FCM analysis assessing the expression of CD8⁺ and CD4⁺ T cells gated on CD3⁺ T cells in SPLs, MLNs, and LPLs of three groups. (B) The proportion of CD4⁺ T cells was significantly increased in the G3c/D665-treated group compared to the control group in SPLs, MLNs, and LPLs. The proportion of CD8⁺ T cells was significantly reduced in the G3c/D665-treated group compared to the 3.5% DSS group in SPLs and MLNs. Data are expressed as the mean ± SD. **P* < 0.05, ***P* < 0.01, ****P* < 0.001, *****P* < 0.0001.

(Ahr), T-box transcription factor 21 (Tbx21), Eomesodermin (Eomes), PR domain zinc finger protein 1 (Prdm1), transforming growth factor beta (TGF-β), and Maf (Fig. 6, Supplementary Fig. S1). Of these, the mRNA expression of the Prdm1 and Eomes genes was markedly upregulated in the MLNs of the G3c/D665-treated group but showed no significant difference in SPLs or LPLs. In contrast, the mRNA expression of the Ahr gene was shown to be downregulated in MLNs, SPLs, and LPLs of the G3c/D665-treated group, while the Tbx21, Egr2, and TGF-β mRNA expression did not increase as well Supplementary (Fig. S1). The mRNA expression of IL-10 was significantly increased in the SPLs of the G3c/D665-treated group but did not differ markedly among the three groups in MLNs or LPLs. Interestingly, the protein expression of Maf was increased in the SPLs of the G3c/D665-treated group (Fig. 6D) according to Western blotting, but its mRNA expression was not upregulated in any of the three lymphocyte species according to RT-PCR (Supplementary Fig. S1).

Discussion

UC has become a global public health threat, UC patients suffer from a poor quality of life, increased risk of colorectal cancer, and morbidity/mortality associated with colectomy performed for possible symptomatic relief [20]. Despite recent advances and the development of biological therapies, no drugs provide sustained remission of UC at present [21].

Due to substantial advances in our understanding of the biology of regulatory immune cells, novel cell-based therapies to dampen or prevent undesired immune responses in multiple immune diseases, including UC, have been developed. In previous studies on cell therapies for IBD, increased attention has been paid to the use of Foxp3⁺ Tregs, but there have been few studies on Tr1 cells. Our study showed that Tr1 cells also have several functional properties that may make them particularly well-suited for treating UC or other inflammatory intestinal diseases.

D665 is a unique class of CD28-superagonist monoclonal antibody that has been reported to be capable of activating T cells without overt stimulation of the T-cell receptor (TCR) and selectively activating Tregs in rodents, suggesting an option for the treatment of autoimmune and inflammatory diseases [22]. Glucocorticoid-induced tumor necrosis factor receptor-related protein (GITR) is a transmembrane protein expressed on the surface of multiple types of immune cells and acts as a co-activating molecule that promotes the function of effector T cells and the expansion of Tregs, making it an attractive target for immunotherapy [23, 24]. The important role of GITR in immune system regulation has attracted a lot of attention for immunotherapeutic treatment of cancers and autoimmune diseases and resulted in the development of anti-GITR antibodies [25, 26]. G3c is an anti-GITR antibody that can recognize GITR and have strong co-stimulatory activity for both Tregs and responder T cells [27]. In our previous trials, we found that the use of D665 alone expanded Foxp3⁺

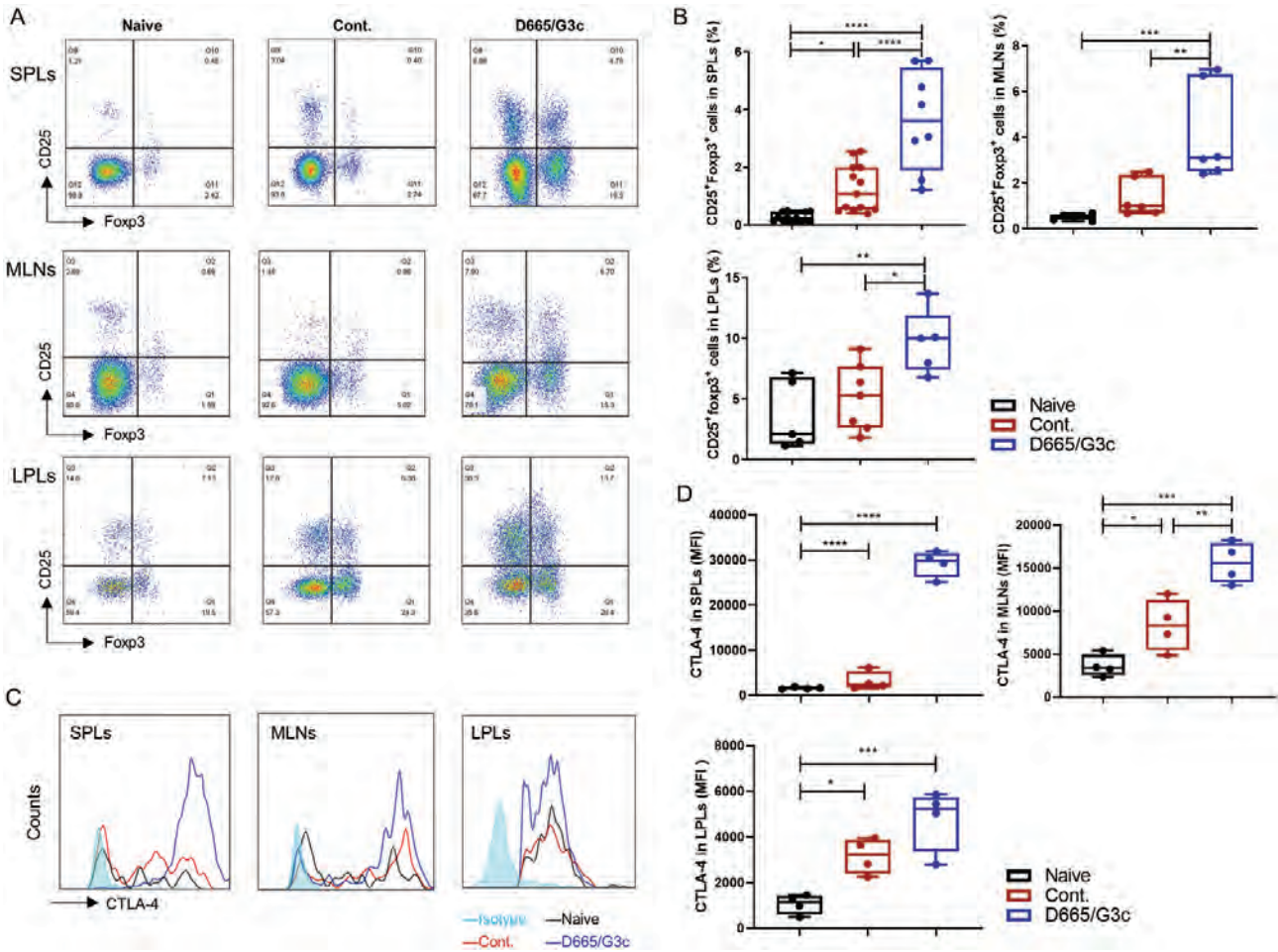


Figure 4: G3c/D665 treatment increased the proportion of CD4⁺CD25⁺Foxp3⁺ Tregs in SPLs, MLNs, and LPLs. (A) A representative FCM analysis assessing the expression of CD4⁺CD25⁺Foxp3⁺ Tregs gated on CD4⁺ T cells in the SPLs, MLNs, and LPLs of the three groups. (B) The proportion of Tregs was significantly increased in the G3c/D665-treated group compared to the control group among SPLs, MLNs, and LPLs. (C–D) A representative FCM analysis assessing the MFI of CTLA-4 expression in the SPLs, MLNs, and LPLs of the three groups gated from CD4⁺CD25⁺Foxp3⁺ Tregs. Data are expressed as the mean ± SD. **P* < 0.05, ***P* < 0.01, ****P* < 0.001, *****P* < 0.0001.

Tregs, whereas the single-use of G3c could not generate Tregs. In our data, D665 potentially expanded Tregs, and the GITR-targeting G3c application further enforced the expansion of Tregs. Large amounts of Tr1 cells were generated after D665 and G3c treatments. G3c played an important role in the induction of Tr1 cells based on D665 treatment. Interestingly, injecting G3c before D665 did not have this effect as well.

To understand the protective effects of G3c/D665 on DSS-induced colitis, mice that had received DSS were given a single dose of D665 1 mg/mice on day 0 and a single dose of G3c 1 mg/mice on day 3 by intraperitoneal injection. This G3c/D665 treatment markedly ameliorated the severity of DSS-induced colitis by inhibiting various pathological manifestations, such as colonic shortening, weight loss, intestinal bleeding, and diarrhea, resulting in a significant reduction in the DAI of the treatment group compared with the non-treated group (Fig. 1A). Furthermore, the degree of mucosal inflammation was markedly improved in mice given G3c/D665 treatment, with observations of decreased mucosal lesions, decreased inflammatory infiltration, and crypt damage microscopically (Fig. 1B).

A hallmark of UC is the dysregulated activation of inflammatory cytokines and components of signaling pathways

[28]. Aberrant activation of the immune response and uncontrolled production of inflammatory cytokines has been proven to cause disruption of intestinal barriers, disturbance of intestinal homeostasis, and extensive mucosal injury and inflammation, leading to the development of UC. In response to the commensal microbiota and Toll-like receptor (TLR) signaling, activated antigen-presenting cells (APCs) in the inflamed mucosa of UC produce large amounts of pro-inflammatory cytokines, such as IL-1β, IL-6, IL-12, and TNF-α [28–30]. CCR-5 is a chemokine receptor predominantly expressed on the surface of Th1 polarized T cells and plays an important role in T cell-mediated tissue damage [31]. IL-17 was reported to mediate pro-inflammatory functions including the upregulation of TNF-α, IL-1β, and IL-6 and the recruitment of neutrophils to induce tissue destruction in IBD [28]. In our study, the mRNA levels of pro-inflammatory cytokines (such as TNF-α, IL-6, IL-1β, IL-17, and IL-12), pro-inflammatory chemokines (such as CCR-5), and apoptotic factors (such as Bax) were significantly upregulated in mice in the DSS-control group, as expected (Fig. 2). These indicators were downregulated after treatment, suggesting that G3c/D665 has a significant inhibitory effect on intestinal inflammation and cell necrosis.

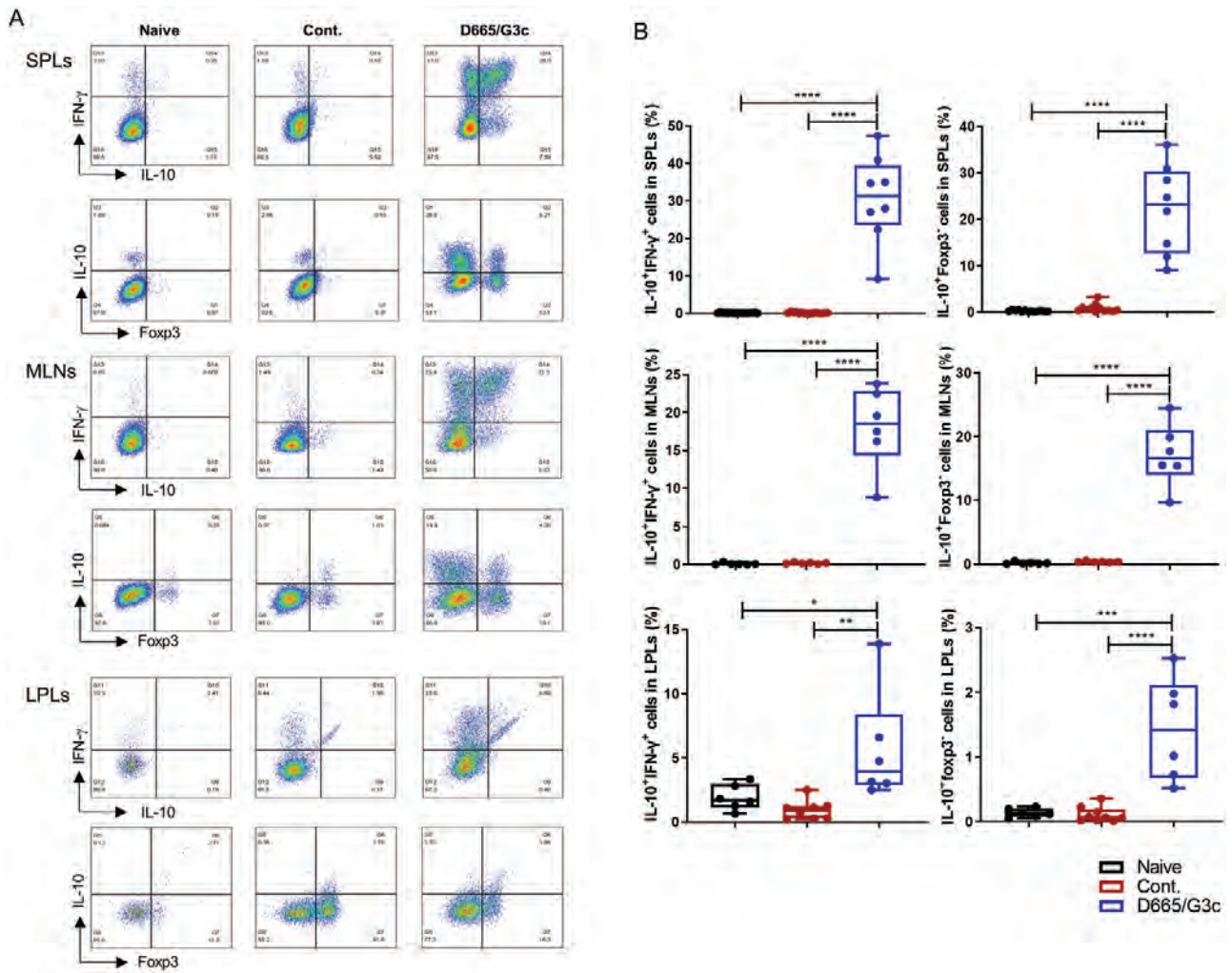


Figure 5: G3c/D665 treatment increased the proportion of IL-10⁺IFN-g⁺Tr1 cells and IL-10⁺Foxp3⁺ Tr1 cells in SPLs, MLNs, and LPLs. (A) A representative FCM analysis assessing the proportion of IL-10⁺IFN-g⁺ Tr1 and IL-10⁺Foxp3⁺ Tr1 cells gated on CD4⁺ T cells among the SPLs, MLNs, and LPLs of the three groups. (B) The proportion of IL-10⁺IFN-g⁺ Tr1 cells and IL-10⁺Foxp3⁺ Tr1 cells was significantly increased in the G3c/D665-treated group compared to the control group among SPLs, MLNs, and LPLs. Data are expressed as the mean \pm SD. *P < 0.05, **P < 0.01, ***P < 0.001, ****P < 0.0001.

Previous studies have reported that colitis was prevented by *in vivo* antibody depletion of CD8⁺ T cells but not by that of CD4⁺ T cells. CD8⁺ cytotoxic T cells (CTLs) induce relapsing colitis in normal mice, and the cytolytic function of CD8⁺ CTLs against epithelial cells may initiate the intestinal inflammatory process [16]. Our FCM data showed that CD8⁺ CTLs were significantly downregulated by G3c/D665 treatment in SPLs and MLNs, whereas there were no significant differences between these two groups in LPLs (Fig. 3). G3c/D665 treatment obviously altered the proportion of CD8⁺ CTLs and CD4⁺ T cells, and the proportion of CD4⁺ T cells in SPLs, MLNs, and LPLs of G3c/D665 group was significantly higher than that in the control group. These results suggest an important role of CD8⁺ CTLs as initiators of colitis and that G3c/D665 treatment can improve colitis by modulating CD4⁺ T cell and CD8⁺ CTL production by modulating systemic or local immunity.

Intestinal mucosal damage caused by UC is associated with mucosal T-cell dysfunction, the imbalance between pro-inflammatory and anti-inflammatory cytokines, and cellular inflammation [28, 32, 33]. CD4⁺CD25⁺Foxp3⁺ Tregs play a critical role in the maintenance of self-tolerance and control

of autoimmune diseases and offer a therapeutic option in cases of inflammatory colitis [17, 34, 35]. To clarify the protective activity of G3c/D665 treatment in DSS-colitis, the CD4⁺CD25⁺Foxp3⁺ Treg population was evaluated by FCM. In our study, the combination of G3c and D665 treatment led to the expansion of CD4⁺CD25⁺Foxp3⁺ Tregs in the spleen and MLNs and LPLs of DSS-induced colitis mice (Fig. 4A, B). Cytotoxic T lymphocyte antigen 4 (CTLA-4) (also called CD152) is a key regulator of adaptive immune responses and an inhibitory relative of the T cell co-stimulatory molecule CD28, which has an immunoregulatory function of suppressing the T cell response [36, 37]. Tregs and CTLA-4 have complementary and largely overlapping mechanisms of immune tolerance, and Tregs commonly use CTLA-4 to effect suppression [19]. Our results showed that CD4⁺CD25⁺Foxp3⁺ Tregs significantly expressed CTLA-4 in both SPLs and MLNs, with increased CTLA-4 levels in LPLs, but there was no statistical significance (Fig. 4C, D), indicating that the combination therapy of G3c and D665 partly played a role in the treatment of colitis through Foxp3⁺ Tregs and CTLA-4.

Tr1 cells regulate responses of both naïve and memory T cells and control inflammasome activity *in vivo* and *in*

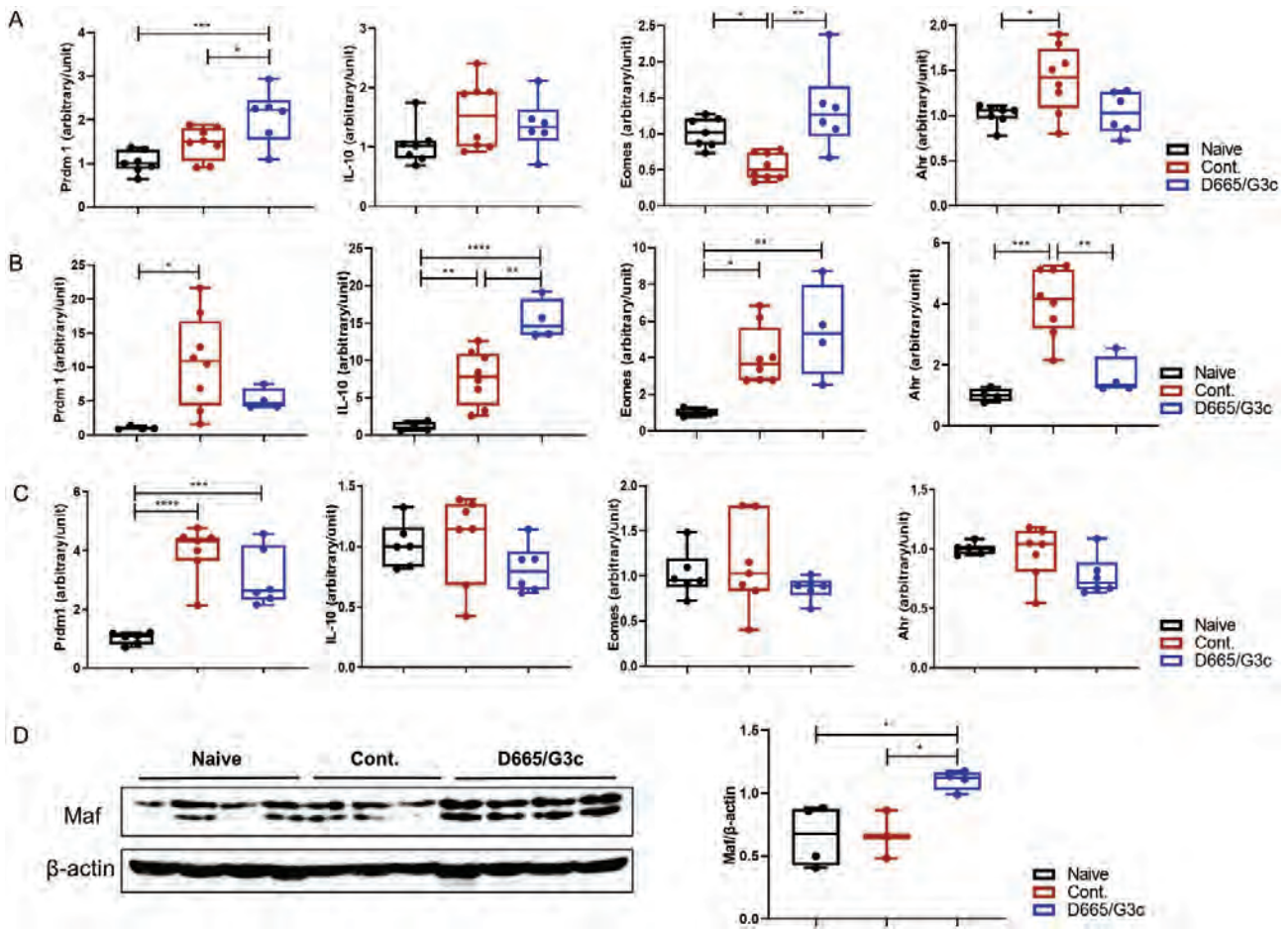


Figure 6: G3c/D665 treatment altered the mRNA expression and protein levels of Tr1 cell-related genes. MLNs (A), SPLs (B) and colon tissues (C) were analyzed by qRT-PCR as described in the materials and methods. The mRNA expression of Tr1 cell-related genes, particularly Prdm1, IL-10, Eomes, and Ahr is shown. (D). A Western blot analysis of the Maf of the SPLs in the three group is shown. Data are expressed as the mean \pm SD. * $P < 0.05$, ** $P < 0.01$, *** $P < 0.001$, **** $P < 0.0001$.

vitro, mainly through the secretion of the immunosuppressive cytokine IL-10 [12]. IL-10 is an anti-inflammatory and immune regulatory cytokine that plays a key role in maintaining immune homeostasis in the gut environment [11, 38]. Furthermore, Tr1 cells have been reported to have a unique ability to promote the development of intestinal goblet cells and repair the epithelial cell barrier function, supporting their use as a cell-based therapy for modulating intestinal inflammation [11]. Previous studies have reported that D665 was able to induce the expansion of CD4⁺Foxp3⁺ Tregs *in vivo*, but it has not been reported to induce Tr1 cells thus far [22, 34, 39]. The application of G3c following D665 in our study mediated the expansion of Tregs and the generation of a large number of Tr1 cells. Based on these findings, along with the evidence that aberrant Tregs function and dysregulated control of epithelial homeostasis induce spontaneous intestinal inflammation in gene-knockout mice deficient for IL-10 [40], we hypothesized that Tr1 cells might have unique advantages over CD4⁺Foxp3⁺ Tregs in controlling colitis. Our studies showed that the combination of G3c and D665 induced the generation of large amounts of IL-10/IFN- γ -co-producing CD4⁺Foxp3⁺ Tr1 cells *in vivo*, and the proliferation of Tr1 cells was much greater than that of CD4⁺CD25⁺Foxp3⁺ Tregs (Fig. 4). Human Tr1-like

cells reportedly express the Eomes gene, a T-box transcription factor that controls the cytotoxic functions of CD8⁺ CTLs and NK cells [41]. Another important transcriptional regulator, Prdm1, has also been shown to promote IL-10 production by Tr1 cells [42]. We assessed the expression of these Tr1 cell-related TFs and found that the mRNA expression of the Prdm1 and Eomes genes was markedly upregulated in MLNs of the G3c/D665-treated group (Fig. 6). A previous study revealed that Maf acted as a growth factor for Tr1 cell development and was critical for IL-10 secretion since IL-27-induced Tr1 cell differentiation was defective in Maf^{-/-} mice [43, 44]. The protein expression of Maf was significantly increased in the SPLs of the G3c/D665-treated group, suggesting that G3c/D665 treatment may promote the generation of Tr1 cells through the Maf pathway.

In a clinical trial in 2006, CD28 superagonist (TGN1412) was reported to result in the instantaneous arrest and uncontrolled T cell activation with cytokine storm [45], but it was later clear that dose-reduction could preferentially address Tregs in humans [46]. The further development of CD28 superagonist (TAB08) has been resumed and is now being evaluated in a phase II study. A previous study has reported that using D665 alone on DSS-induced colitis weakly induced

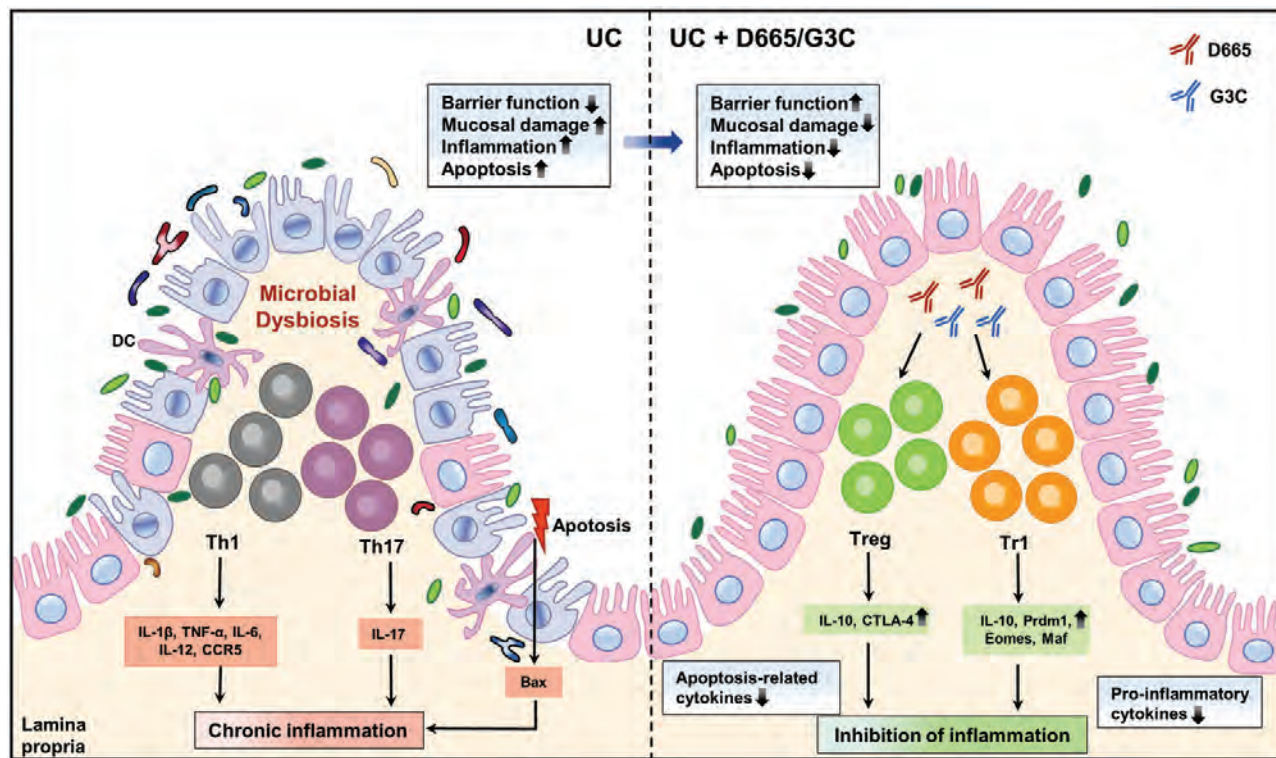


Figure 7: Immune mechanism of G3c/D665 in the treatment of UC. In UC, the intestinal barrier is disrupted, the mucosa is severely damaged, and the balance of intestinal microflora is dysregulated. In the colonic lamina propria, Th1 cells release many pro-inflammatory cytokines, such as IL-1 β , TNF- α , IL-6, IL-12, and CCR-5, while Th17 cells release IL-17. The release of apoptotic factor, such as Bax, is also increased in UC. G3c and D665 treatment expands Tregs and Tr1 cells, thereby increasing the release of anti-inflammatory cytokines and decreasing the release of pro-inflammatory cytokines and apoptotic factors. Tregs release IL-10 and CTLA-4, while Tr1 cells release IL-10, Prdm1, Eomes, and Maf. After the administration of G3c and D665, the intestinal barrier is restored, mucosal damage is repaired, and colitis is improved.

the levels of IL-2 and IFN- γ in the spleen and colon but did not result in pathophysiologically relevant levels of cytokine storm [34]. we have not observed any signs of the disorders in the G3c/D665 treated mice with DSS-induced colitis.

Taken together, our data demonstrated that the combination of G3c and D665 treatment targets Tr1 cell generation *in vivo* to reduce the colon damage in DSS-induced mouse colitis by secreting a large amount of IL-10, maintaining and enhancing their regulatory functions (Fig. 7). This represents a major advance towards the therapeutic use of Tr1 cells as cellular therapy and supports the potential of the combination of G3c and D665 as a new auspicious therapeutic option for treating UC in the clinic. Furthermore, harnessing the suppressive potential of Tr1 cells may have important implications for cell therapy of autoimmune, autoinflammatory, and transplantation-related diseases.

Supplementary data

Supplementary data is available at *Clinical and Experimental Immunology* online.

Acknowledgements

The authors are grateful to thank Miss Sato for her invaluable technical assistance. This study was supported by research grants from the Grants of Ministry of Education, Culture, Sports, Science, and Technology of Japan (Grants-in-Aid 17H04277).

Conflicts of interest

All authors of this manuscript have no conflicts of interest to disclose as described by *Clinical and Experimental Immunology*.

Author contributions

KM, WTQ, XH, WZG, LZ, DU, ELG, and XKL conceived and designed the project; KM acquired the data; KM, WTQ, XH, WZG, LZ, DU, ELG, and XKL analyzed and interpreted the data; KM and XKL wrote the paper. All authors read and approved the final manuscript.

Clinical trial registration

Not applicable.

Ethical approval

Mice were cared for in accordance with the National Research Institute for Child Health and Development guidelines on laboratory animal welfare (permission no. A2009-010-C12). The animal research adheres to the ARRIVE guidelines.

Data availability

Data are available upon reasonable request.

References

- Ordas I, Eckmann L, Talamini M, et al. Ulcerative colitis. *Lancet* 2012, 380, 1606–19.
- Geremia A, Biancheri P, Allan P, et al. Innate and adaptive immunity in inflammatory bowel disease. *Autoimmun Rev* 2014, 13, 3–10.
- Chassaing B, Aitken JD, Malleshappa M, et al. Dextran sulfate sodium (DSS)-induced colitis in mice. *Curr Protoc Immunol* 2014, 104, 15–25.
- Cao H, Liu J, Shen P, et al. Protective effect of naringin on DSS-induced ulcerative colitis in mice. *J Agric Food Chem* 2018, 66, 13133–40.
- Cassinotti A, Passamonti F, Segato S. Cell therapy in inflammatory bowel disease. *Pharmacol Res* 2021, 163, 105247.
- Negi S, Saini S, Tandel N, et al. Translating treg therapy for inflammatory bowel disease in humanized mice. *Cells-Basel* 2021, 10, 1847.
- Roncarolo MG, Gregori S, Bacchetta R, et al. The biology of T regulatory type 1 cells and their therapeutic application in immune-mediated diseases. *Immunity* 2018, 49, 1004–19.
- Rudensky AY. Regulatory T cells and Foxp3. *Immunol Rev* 2011, 241, 260–8.
- Andolfi G, Foustieri G, Rossetti M, et al. Enforced IL-10 expression confers type 1 regulatory T cell (Tr1) phenotype and function to human CD4(+) T cells. *Mol Ther* 2012, 20, 1778–90.
- Neumann C, Scheffold A, Rutz S. Functions and regulation of T cell-derived interleukin-10. *Semin Immunol* 2019, 44, 101344.
- Cook L, Stahl M, Han X, et al. Suppressive and gut-reparative functions of human type 1 T regulatory cells. *Gastroenterology* 2019, 157, 1584–98.
- Battaglia M, Gregori S, Bacchetta R, et al. Tr1 cells: from discovery to their clinical application. *Semin Immunol* 2006, 18, 120–7.
- Hidalgo-Cantabrana C, Algeri F, Rodriguez-Nogales A, et al. Effect of aropy exopolysaccharide-producing *Bifidobacterium animalis* subsp. *lactis* strain orally administered on DSS-induced colitis mice model. *Front Microbiol* 2016, 7, 868.
- Cooper HS, Murthy SN, Shah RS, et al. Clinicopathologic study of dextran sulfate sodium experimental murine colitis. *Lab Invest* 1993, 69, 238–49.
- Dieleman LA, Palmén MJ, Akol H, et al. Chronic experimental colitis induced by dextran sulphate sodium (DSS) is characterized by Th1 and Th2 cytokines. *Clin Exp Immunol* 1998, 114, 385–91.
- Nancey S, Holvoet S, Graber I, et al. CD8+ cytotoxic T cells induce relapsing colitis in normal mice. *Gastroenterology* 2006, 131, 485–96.
- Fan L, Qi Y, Qu S, et al. *B. adolescentis* ameliorates chronic colitis by regulating Treg/Th2 response and gut microbiota remodeling. *Gut Microbes* 2021, 13, 1–17.
- Clough JN, Omer OS, Tasker S, et al. Regulatory T-cell therapy in Crohn's disease: challenges and advances. *Gut* 2020, 69, 942–52.
- Walker LS. Treg and CTLA-4: two intertwining pathways to immune tolerance. *J Autoimmun* 2013, 45, 49–57.
- Miao Z, Chen L, Feng H, et al. Baitouweng decoction ameliorates ulcerative colitis in mice partially attributed to regulating Th17/Treg balance and restoring intestinal epithelial barrier. *Front Pharmacol* 2020, 11, 531117.
- Nunes NS, Chandran P, Sundby M, et al. Therapeutic ultrasound attenuates DSS-induced colitis through the cholinergic anti-inflammatory pathway. *EBioMedicine* 2019, 45, 495–510.
- Langenhorst D, Tabares P, Gulde T, et al. Self-recognition sensitizes mouse and human regulatory T cells to low-dose CD28 superagonist stimulation. *Front Immunol* 2017, 8, 1985.
- Riccardi C, Ronchetti S, Nocentini G. Glucocorticoid-induced TNFR-related gene (GITR) as a therapeutic target for immunotherapy. *Expert Opin Ther Targets* 2018, 22, 783–97.
- Zappasodi R, Sirard C, Li Y, et al. Rational design of anti-GITR-based combination immunotherapy. *Nat Med* 2019, 25, 759–66.
- He C, Maniyar RR, Avraham Y, et al. Therapeutic antibody activation of the glucocorticoid-induced TNF receptor by a clustering mechanism. *Sci Adv* 2022, 8, m4552.
- Petrillo MG, Ronchetti S, Ricci E, et al. GITR+ regulatory T cells in the treatment of autoimmune diseases. *Autoimmun Rev* 2015, 14, 117–26.
- Nishioka T, Nishida E, Iida R, et al. In vivo expansion of CD4+Foxp3+ regulatory T cells mediated by GITR molecules. *Immunol Lett* 2008, 121, 97–104.
- Neurath MF. Cytokines in inflammatory bowel disease. *Nat Rev Immunol* 2014, 14, 329–42.
- Ng SC, Benjamin JL, McCarthy NE, et al. Relationship between human intestinal dendritic cells, gut microbiota, and disease activity in Crohn's disease. *Inflamm Bowel Dis* 2011, 17, 2027–37.
- Moschen AR, Tilg H, Raine T. IL-12, IL-23 and IL-17 in IBD: immunobiology and therapeutic targeting. *Nat Rev Gastroenterol Hepatol* 2019, 16, 185–96.
- Turner JE, Steinmetz OM, Stahl RA, et al. Targeting of Th1-associated chemokine receptors CXCR3 and CCR5 as therapeutic strategy for inflammatory diseases. *Mini Rev Med Chem* 2007, 7, 1089–96.
- Maynard CL, Weaver CT. Intestinal effector T cells in health and disease. *Immunity* 2009, 31, 389–400.
- Larabi A, Barnich N, Nguyen H. New insights into the interplay between autophagy, gut microbiota and inflammatory responses in IBD. *Autophagy* 2020, 16, 38–51.
- Chen J, Xie L, Toyama S, et al. The effects of Foxp3-expressing regulatory T cells expanded with CD28 superagonist antibody in DSS-induced mice colitis. *Int Immunopharmacol* 2011, 11, 610–7.
- Xu M, Duan XY, Chen QY, et al. Effect of compound sophorae decoction on dextran sodium sulfate (DSS)-induced colitis in mice by regulating Th17/Treg cell balance. *Biomed Pharmacother* 2019, 109, 2396–408.
- Rowshanravan B, Halliday N, Sansom DM. CTLA-4: a moving target in immunotherapy. *Blood* 2018, 131, 58–67.
- Hansel TT, Kropshofer H, Singer T, et al. The safety and side effects of monoclonal antibodies. *Nat Rev Drug Discov* 2010, 9, 325–38.
- Schmitt H, Ulmschneider J, Billmeier U, et al. The TLR9 agonist cobitolimod induces IL10-producing wound healing macrophages and regulatory T cells in ulcerative colitis. *J Crohns Colitis* 2020, 14, 508–24.
- Schmidt T, Willenborg S, Hunig T, et al. Induction of T regulatory cells by the superagonistic anti-CD28 antibody D665 leads to decreased pathogenic IgG autoantibodies against desmoglein 3 in a HLA-transgenic mouse model of pemphigus vulgaris. *Exp Dermatol* 2016, 25, 293–8.
- Matharu KS, Mizoguchi E, Cotoner CA, et al. Toll-like receptor 4-mediated regulation of spontaneous *Helicobacter*-dependent colitis in IL-10-deficient mice. *Gastroenterology* 2009, 137, 1380–90.e1.
- Gruarin P, Maglie S, De Simone M, et al. Eomesodermin controls a unique differentiation program in human IL-10 and IFN-gamma coproducing regulatory T cells. *Eur J Immunol* 2019, 49, 96–111.
- Montes DOM, Kumar R, de Labastida RF, et al. Blimp-1-dependent IL-10 production by Tr1 cells regulates TNF-mediated tissue pathology. *PLoS Pathog* 2016, 12, e1005398.
- Pot C, Jin H, Awasthi A, et al. Cutting edge: IL-27 induces the transcription factor c-Maf, cytokine IL-21, and the costimulatory receptor ICOS that coordinately act together to promote differentiation of IL-10-producing Tr1 cells. *J Immunol* 2009, 183, 797–801.
- Pot C, Apetoh L, Kuchroo VK. Type 1 regulatory T cells (Tr1) in autoimmunity. *Semin Immunol* 2011, 23, 202–8.
- Sundqvist KG. CD28 Superagonist shock and blockage of motogenic T cell cascade. *Front Immunol* 2021, 12, 670864.
- Hunig T. The rise and fall of the CD28 superagonist TGN1412 and its return as TAB08: a personal account. *FEBS J* 2016, 283, 3325–34.

A Mesenchymal-epithelial transition factor-Agonistic Antibody Accelerates Cirrhotic Liver Regeneration and Improves Mouse Survival Following Partial Hepatectomy

Kuai Ma,^{1,2} Weitao Que,¹ Xin Hu,¹ Wen-Zhi Guo,³ Er-li Gu,² Liang Zhong,⁴ Virginia Morello,⁵ Manuela Cazzanti,⁵ Paolo Michieli,^{5,6} Terumi Takahara,⁷ and Xiao-Kang Li^{1,3}

¹Division of Transplantation Immunology, National Research Institute for Child Health and Development, Tokyo, Japan; ²Department of Gastroenterology and Hepatology, Jing'an District Central Hospital, Jing'an Branch of Huashan Hospital, Fudan University, Shanghai, China; ³Department of Hepatobiliary and Pancreatic Surgery, The First Affiliated Hospital of Zhengzhou University, Zhengzhou, China; ⁴Department of Gastroenterology, Huashan Hospital, Fudan University, Shanghai, China; ⁵AgomAb Therapeutics NV, Gent, Belgium; ⁶Molecular Biotechnology Center, University of Torino Medical School, Torino, Italy; and ⁷Third Department of Internal Medicine, University of Toyama, Toyama, Japan

Small-for-size syndrome (SFSS) is a common complication following partial liver transplantation and extended hepatectomy. SFSS is characterized by postoperative liver dysfunction caused by insufficient regenerative capacity and portal hyperperfusion and is more frequent in patients with preexisting liver disease. We explored the effect of the Mesenchymal-epithelial transition factor (MET)-agonistic antibody 71D6 on liver regeneration and functional recovery in a mouse model of SFSS. Male C57/BL6 mice were exposed to repeated carbon tetrachloride injections for 10 weeks and then randomized into 2 arms receiving 3 mg/kg 71D6 or a control immunoglobulin G (IgG). At 2 days after the randomization, the mice were subjected to 70% hepatectomy. Mouse survival was recorded up to 28 days after hepatectomy. Satellite animals were euthanized at different time points to analyze liver regeneration, fibrosis, and inflammation. Serum 71D6 administration significantly decreased mouse mortality consequent to insufficient regeneration of the cirrhotic liver. Analysis of liver specimens in satellite animals revealed that 71D6 promoted powerful activation of the extracellular signal-regulated kinase pathway and accelerated liver regeneration, characterized by increased liver-to-body weight, augmented mitotic index, and higher serum albumin levels. Moreover, 71D6 accelerated the resolution of hepatic fibrosis as measured by picrosirius red, desmin, and α -smooth muscle actin staining, and suppressed liver infiltration by macrophages as measured by CD68 and F4/80 staining. Analysis of gene expression by reverse-transcription polymerase chain reaction confirmed that 71D6 administration suppressed the expression of key profibrotic genes, including platelet-derived growth factor, tissue inhibitor of metalloproteinase 3, and transforming growth factor- β 1, and of key proinflammatory genes, including tumor necrosis factor- α , interleukin-1 β , chemokine (C-C motif) ligand 3, and chemokine (C-C motif) ligand 5. These results suggest that activating the MET pathway via an hepatocyte growth factor-mimetic antibody may be beneficial in patients with SFSS and possibly other types of acute and chronic liver disorders.

Liver Transplantation 0 1–12 2021 AASLD.

Received April 12, 2021; accepted September 10, 2021.

Small-for-size syndrome (SFSS) is a common yet underrecognized complication following partial liver

transplantation and extended hepatectomy.⁽¹⁾ It is characterized by postoperative liver dysfunction caused by insufficient regenerative capacity and portal hyperperfusion and is more frequent in patients with preexisting liver disease.⁽²⁾ Approximately one-third of liver transplant recipients who develop early graft failure qualify for SFSS. Small-for-size liver grafts show delayed and impaired regeneration⁽³⁾ and have greater risks of failure

Abbreviations: agomAbs, agonistic monoclonal antibodies; α -SMA, α -smooth muscle actin; a.u., arbitrary units; CCL3, chemokine (C-C motif) ligand 3; CCl4, carbon tetrachloride; CCL5, chemokine (C-C motif) ligand 5; ELISA, enzyme-linked immunosorbent assay; ERK,

including microcirculatory damage, inflammatory injury, and accelerated acute rejection, leading to liver failure with associated coagulopathy, ascites, prolonged cholestasis, and encephalopathy. Because of the persistent organ shortage, living donor liver transplantation is becoming the most viable option for patients with end-stage liver disease. Donor safety always comes first in living donor liver transplantation, and there is a growing momentum for the increased use of small-for-size grafts in association with hepato-regenerative therapies.^(4,5)

Hepatocyte growth factor (HGF) is a pleiotropic cytokine of mesenchymal origin that plays a key role in organ regeneration.⁽⁶⁾ Its high-affinity receptor, the MET

tyrosine kinase, is mainly expressed by epithelial and endothelial cells, but it is also present on some immune cells as well as in various types of myofibroblasts.⁽⁷⁾ In the liver, HGF is typically secreted by hepatic stellate cells (HSCs) and plays a key role in hepatic regeneration. Following injury, increased HGF secretion initiates a repair program that limits cell damage, ensures hepatocyte regeneration, inhibits myofibroblast hyperproliferation, and suppresses inflammation, restoring liver function.⁽⁸⁾

Despite the broad therapeutic potential of HGF in liver diseases, its translation to the clinic has been challenging. In fact, HGF does not display ideal drug-like properties: its very short plasma half-life (a few minutes) causes an unfavorable pharmacokinetics because of its high avidity for the extracellular matrix, it has a poor biodistribution; it needs proteolytic activation to acquire biological activity, and once activated it is unstable; lastly, its industrial manufacture is difficult and costly. To overcome the limitations of HGF and to generate a drug that could effectively promote liver regeneration in patients, we generated a series of anti-MET agonistic monoclonal antibodies (“agomAbs”) that bind to MET at high affinity and determine MET activation, mimicking the biochemical and biological activity of HGF. AgomAbs combine the powerful therapeutic potential of HGF with the excellent pharmacokinetic, pharmacodynamic, and manufacturing properties of antibodies.

In this study, we explored the therapeutic potential of 71D6, a fully agonistic anti-MET antibody that cross-reacts with rodent, nonhuman primate, and human MET in a mouse model of SFSS.

Materials and Methods

SERUM 71D6 ANTIBODY GENERATION AND CHARACTERIZATION

Serum 71D6 was generated by immunization of *Llama glama* using the SIMPLE antibody platform.⁽⁹⁾ A detailed description of its generation and characterization has been published previously.⁽¹⁰⁾ Binding of 71D6 to MET and HGF-mediated and 71D6-mediated MET autophosphorylation and analysis of MET downstream signaling were performed as described.⁽¹⁰⁾

ANIMAL MODEL

Mouse procedures were authorized by the National Research Institute for Child Health and Development

extracellular signal-regulated kinase; H & E, hematoxylin-eosin; HGF, hepatocyte growth factor; hMET, human mesenchymal-epithelial transition factor; HSCs, hepatic stellate cells; IgG, immunoglobulin G; IgG1, immunoglobulin G1; IL-1 β , interleukin-1 β ; IP, intraperitoneally; IV, intravenously; mMET, mouse mesenchymal-epithelial transition factor; mRNA, messenger RNA; N/A, Not applicable; PCNA, proliferating cell nuclear antigen; PDGF, platelet-derived growth factor; PSR, picosirius red; qRT-PCR, quantitative reverse-transcription polymerase chain reaction; RT-PCR, reverse-transcription polymerase chain reaction; SD, standard deviation; SFSS, small-for-size syndrome; TIMP3, tissue inhibitor of metalloproteinase 3; TNF- α , tumor necrosis factor- α .

Address reprint requests to Paolo Michieli, Ph.D., Molecular Biotechnology Center, University of Torino Medical School, Via Nizza 52, I-10126 Torino, Italy. Telephone: +39 11 670 64 99; E-mail: paolo.michieli@unito.it

Address reprint requests to Terumi Takahara, M.D., Ph.D., Third Department of Internal Medicine, University of Toyama, 2630 Sugitani, Toyama, 930-0194 Japan. Telephone: +81 76-434-502; E-mail: terutaka-tym@umin.ac.jp

Address reprint requests to Xiao-Kang Li, M.D., Ph.D., Division of Transplantation Immunology, National Research Institute for Child Health and Development, 2-10-1 Okura, Setagaya-ku, Tokyo, 157-8535 Japan. Telephone: +81-3-3416-0181; FAX: +81-3-3417-2864; E-mail: ri-k@nchd.go.jp

This study was supported in part by the Ministry of Education, Culture, Sports, Science and Technology of Japan (Grants-in-Aid 16K11064, 24/17H04277, and 18K08558), the National Center for Child Health and Development (Grant 29-09), and Science and Technology Innovation Talents in Henan Universities (no. 19HASTTT003).

Manuela Cazzanti, Paolo Michieli, and Virginia Morello consult for, own stock in, and are employed by AgomAb Therapeutics NV.

Copyright © 2021 The Authors. Liver Transplantation published by Wiley Periodicals LLC on behalf of American Association for the Study of Liver Diseases. This is an open access article under the terms of the Creative Commons Attribution-NonCommercial-NoDerivs License, which permits use and distribution in any medium, provided the original work is properly cited, the use is non-commercial and no modifications or adaptations are made.

View this article online at wileyonlinelibrary.com.

DOI 10.1002/lt.26301

(permission no. A2014-010-C06). The 8-week-old male C57BL/6JmsSLc mice (Shizuoka Laboratory Animal Center, Shizuoka, Japan) were subjected to repeated subcutaneous injection of 10% carbon tetrachloride (CCl₄; Wako) dissolved in olive oil (100 µL/mouse) twice a week for 10 weeks. On the day of the last CCl₄ administration, the mice were randomized into 2 arms receiving 3 mg/kg of 71D6 or a control antibody against the F glycoprotein of respiratory syncytial virus⁽¹¹⁾ (both in the mouse immunoglobulin G1 [IgG1] format). At 2 days after randomization, all of the mice were subjected to 70% hepatectomy by removal of the anterior 2 lobes and posterior left lobe. The 71D6 or control IgG were administered intraperitoneally (IP) at a dose of 3 mg/kg 2 days before hepatectomy and at days 0, 2, 4, 6, 8, 10, and 12. Mice recruited in the trial included main study animals and satellite animals. The spontaneous survival rate of the main study animals was recorded from days 0 to 28. Satellite animals (3 mice per group) were euthanized at 3, 7, and 28 days after hepatectomy. Serum and liver samples were stored at -80°C.

SERUM BIOCHEMICAL MEASUREMENTS

Serum was collected from whole-blood samples after standing for 30 minutes at 37°C and then centrifuged at 1800g for 25 minutes at 4°C. Serum samples were then analyzed for serum albumin concentrations using a commercially available kit (Fujifilm) and an automatic biochemical analyzer (DRI-CHEM 3500i; Fujifilm) according to the manufacturer's instructions. Serum HGF concentration was measured using the mouse/rat HGF Quantikine enzyme-linked immunosorbent assay (ELISA) kit (R&D Systems). Serum 71D6 concentration was determined by ELISA as described.⁽¹⁰⁾

HISTOPATHOLOGICAL AND IMMUNOHISTOCHEMICAL EXAMINATION

Both the liver portion extracted at the time of hepatectomy and that collected at autopsy were processed for histopathological examination. Liver tissues were fixed in 10% formalin for 48 hours, routinely processed, and sliced into sections of 4 µm in thickness. For detection of liver fibrosis, sections were stained with picosirius red (PSR; Sigma-Aldrich), anti-α-smooth muscle actin (α-SMA) antibodies (AbCam) and anti-desmin antibodies (Boehringer). For detection of macrophage

infiltration, sections were stained with antibodies against CD68 (AbCam) and F4/80 (AbCam). For detection of liver proliferation, sections were stained with anti-proliferating cell nuclear antigen (PCNA) antibodies (Dako). Sections were also stained with hematoxylin-eosin (H & E) and periodic acid-Schiff (both from Sigma-Aldrich). After staining, specimens were photographed under a microscope (Olympus). Histological and immunohistochemical results were quantified using WinRoof 7.4 software (Mitani Corporation).

TOTAL MESSENGER RNA PREPARATION AND QUANTITATIVE REVERSE-TRANSCRIPTION POLYMERASE CHAIN REACTION ANALYSIS

Total messenger RNA (mRNA) was extracted from frozen liver tissues using RNeasy Mini Kit (Qiagen). Each 0.8 µg aliquot of mRNA was reverse transcribed to complementary DNA using a Prime Script reverse-transcription (RT) reagent kit (RR037A; Takara). Quantitative reverse-transcription polymerase chain reaction (qRT-PCR) was performed using the SYBR Green system or the primer/probe set system (primer sequences are listed in Table 1) the Applied Biosystem PRISM7900 apparatus (Thermo Fisher Scientific) is a machine which is used to do RT-PCR. The PCR cycle conditions for the SYBR Green system were 95°C for 3 minutes, 45 cycles of 95°C for 3 seconds, and 60°C for 30 seconds. The PCR cycle conditions for the primer/probe set system were 50°C for 2 minutes, 95°C for 15 minutes, 40 cycles of 95°C for 30 seconds, 60°C for 1 minute, and 25°C for 2 minutes. The comparative threshold cycle (ΔΔCt) method was used for determining relative gene expression, and the results of target genes (including fibrosis-related genes and inflammation-related genes) were normalized by subtracting *18S* expression values.

IN VIVO ANALYSIS OF EXTRACELLULAR SIGNAL-REGULATED KINASE ACTIVATION

Frozen liver tissue was homogenized in radio immunoprecipitation assay buffer containing 1% protease inhibitor cocktail-1 and 1% protease inhibitor cocktail-2 (Sigma-Aldrich) followed by centrifugation in a microfuge at top speed for 30 minutes. Protein concentrations were assayed using a Protein Assay kit (Bio-Rad). Samples were separated by electrophoresis on

TABLE 1. Primers and Probes Used in This Study

Genes (PCR)	Forward (5'-3')	Reverse (5'-3')	Probe
<i>TIMP3</i> (SYBR Green)	CACAAAGTTGCACAGTCCTG	TTTGTGCGCTCAAGCTAGA	N/A
<i>PDGF</i> (SYBR Green)	TACAGTTGCACTCCCAGGAAT	CTTCCAGTTGACAGTCCGCA	N/A
<i>TGF-β</i> (SYBR Green)	ATCCTGTCCAACTAAGGCTCG	ACCTCTTAGCATAGTAGTCCGC	N/A
<i>TNF-α</i> (SYBR Green)	AAGCCTGTAGCCACGTCGTA	GGCACCAGTGTGGTTGTCTTTG	N/A
<i>CCL5</i> (SYBR Green)	TGCCCTCACCATCATCCTCACT	GGCGGTTCCCTCGAGTGACA	N/A
<i>IL-1β</i> (SYBR Green)	ACCTCCAGGATGAGGACATGA	AACGTCACACACCAGCAGGTTA	N/A
<i>18S</i> (SYBR Green)	ATGAGTCCACTTTAAATCCTTTAACGA	CTTTAATATACGCTATTGGAGCTGGAA	N/A
<i>CCL3</i> (Taqman)	ACCCAGGTCTCTTTGGAGTCAGCGCA	TCCCAGCCAGGTGTCAATTTTC	AGGCATTGAGTCCAGGTGAG
<i>18S</i> (Taqman)	ATCCATTGGAGGGCAAGTCTGGTGC	ATGAGTCCACTTTAAATCCTTTAACGA	CTTTAATATACGCTATTGGAGGCTGGAA

NOTE: Liver-specific expression of profibrotic and proinflammatory genes determined by SYBR green PCR or Taqman PCR as indicated in the table. N/A, Not applicable.

10% polyacrylamide gels and transferred to Immobilon (Bio-Rad) polyvinylidene fluoride. After brief incubation with 5% nonfat milk to block nonspecific binding, membranes were exposed overnight at 4°C to specific phosphorylated anti-p44/p42 extracellular signal-regulated kinase (ERK) antibodies (Cell Signaling Technology). Membranes were washed and exposed to alkaline phosphatase-conjugated secondary antibodies and visualized by incubation in 5% nonfat milk. Phosphorylated p44/p42 ERK activity was quantified by laser densitometric analysis of the radiographic film using ImageJ software (National Institutes of Health, Bethesda, MD).

STATISTICAL ANALYSIS

Prism7 software (GraphPad, San Diego, CA) was used to calculate statistical significance. A 2-way analysis of variance method and Student *t* test method were used for comparisons between groups. Survival rate analysis was performed using a log-rank (Cox-Mantel) test. Data are expressed as mean ± standard deviation (SD). A value of *P* < 0.05 was considered to be statistically significant.

Results

SERUM 71D6 BINDS TO MET AT HIGH AFFINITY AND PROMOTES MET ACTIVATION, MIMICKING HGF

HGF-mimetic, agonistic anti-MET antibodies were generated by immunization of *L. glama* using the SIMPLE antibody platform.⁽⁹⁾ Their biochemical

and biological characterizations have been published previously.⁽¹⁰⁾ Among these molecules, which include both partial and full agonists of MET, serum 71D6 represents the most potent fully agonistic antibody. Serum 71D6 was produced as a chimera between variable llama regions and human or mouse IgG1/λ constant regions. Serum 71D6 bound to either the human MET (hMET) or mouse MET (mMET) extracellular domain with the concentration for 50% of maximal effect in the picomolar range (Fig. 1A). Stimulation of immortalized mouse liver cells with 71D6 or HGF resulted in a similar dose-dependent activation of MET and of its downstream signaling (Fig. 1B). An overlapping pattern of MET activation and signaling was observed in MET-expressing human epithelial cells of various origin (not shown).

SYSTEMIC 71D6 ADMINISTRATION RESULTS IN BIOLOGICALLY SIGNIFICANT PLASMA LEVELS

The pharmacokinetic properties of 71D6 were tested in various mouse strains using various routes of administration. In all studies, increasing doses of the antibody were delivered as a single bolus, and antibody levels in plasma were determined at different time points using a MET-based ELISA assay. Table 2 shows the results obtained in a representative study conducted by IP injection. Serum 71D6 concentration reached a peak 8 hours after injection (65 nM at 1 mg/kg and 2638 nM at 30 mg/kg). After 2 days, plasma 71D6 levels showed only a minor deflection (38 nM at 1 mg/kg and 2466 nM at 30 mg/kg). After 8 days, all dose levels except the lowest were still detectable

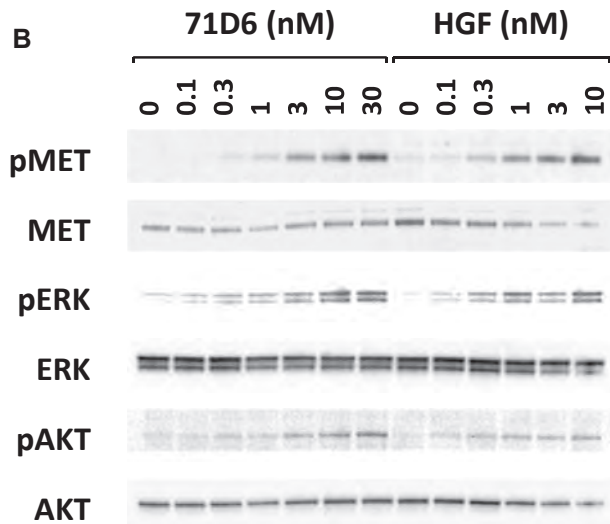
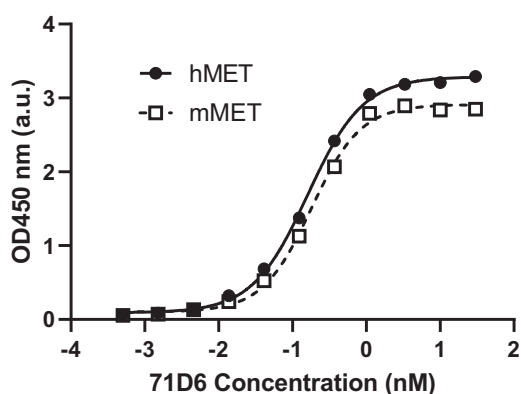
A Binding to MET Extracellular Domain

FIG. 1. 71D6 binds to MET at high affinity and elicits MET activation and downstream signaling, mimicking HGF function. (A) 71D6 binding to hMET or mMET extracellular domain was analyzed by ELISA (a.u.). (B) MET activation and downstream signaling induced by HGF or 71D6 was studied in human mouse MLP29 liver precursor cells. Cell lysates were analyzed by Western blotting using antibodies specific for the phosphorylated forms of MET, ERK, and AKT (pMET, pERK and pAKT) as well as antibodies against total MET, ERK, and AKT.

and well in the nanomolar range. Based on these data, the mean plasma half-life of 71D6 corresponded to approximately 5 days (note that recombinant HGF has a half-life of a few minutes in both rodents⁽¹²⁾ and humans).⁽¹³⁾ Considering that in normal, healthy mice endogenous HGF plasma levels range from 1 to 10 pM⁽¹⁴⁾ and that in the MET phosphorylation assays shown in Fig. 1B both HGF and 71D6 reached saturation at about 10 nM, the concentrations reached

following IP injections of 71D6 shown in Table 2 are certainly relevant from a biologic viewpoint.

SERUM 71D6 DISPLAYS A POTENT HEPATOTROPHIC ACTIVITY IN MICE

The biological effects of 71D6 administration were compared with those of recombinant HGF *in vivo*. In a first experiment, a single bolus of 1 mg/kg of either 71D6 or HGF was administered intravenously (IV) to adult Balb-c mice. Liver-to-body weight ratio and serum albumin levels were measured 4 and 10 days later. As shown in Fig. 2A, 71D6 administration resulted in a marked increase in liver weight both at day 4 (91%) and at day 10 (42%). In contrast, recombinant HGF administration promoted only a minor increase in liver weight (20% at day 4 and 0% at day 10). Serum albumin levels, expression of the synthetic activity of the liver, were invariably higher in the 71D6-treated mice, confirming the superior potency of the antibody. In a second experiment, we aimed at compensating the shorter half-life of HGF with more frequent administration. Because of the challenge of IV injecting the same animals multiple times, IP injection was preferred. Mice were injected IP with either a single bolus of 1 mg/kg 71D6 or with 1 mg/kg recombinant HGF every 12 hours for 5 days. Mice were euthanized at day 6 and subjected to the same analysis as noted previously. Even when administered more frequently, HGF could not match the potent hepatotrophic activity of 71D6. In fact, mice injected with a single bolus of 71D6 displayed a 70% larger liver compared with controls, whereas animals injected repeatedly with HGF showed a modest 10% increase in liver weight (Fig. 2B). Similarly, 71D6 injection resulted in 121% higher albumin levels compared with controls, whereas HGF injection increased serum albumin secretion by 52%. Therefore, 71D6 elicits a significantly more potent hepatotrophic effect in mice compared with recombinant HGF.

SERUM 71D6 PROMOTES LIVER REGENERATION AND INCREASES SURVIVAL IN MICE UNDERGOING CCl₄ INJURY AND PARTIAL HEPATECTOMY

Prompted by the previous results, we evaluated the therapeutic effect of 71D6 on liver regeneration in a

TABLE 2. Pharmacokinetic Properties of 71D6

Dose (mg/kg)	Maximum Concentration (nM)	Day 2 Concentration (nM)	Day 8 Concentration (nM)
1	65 ± 3	38 ± 6	0 ± 0
3	271 ± 56	249 ± 70	17 ± 12
10	1265 ± 270	1062 ± 114	257 ± 27
30	2638 ± 327	2466 ± 494	446 ± 45

NOTE: 71D6 concentration in plasma was determined at different time points following IP injection of different dose levels of antibody as a single bolus. Values represent the mean ± standard deviation of at least 3 biological replicates.

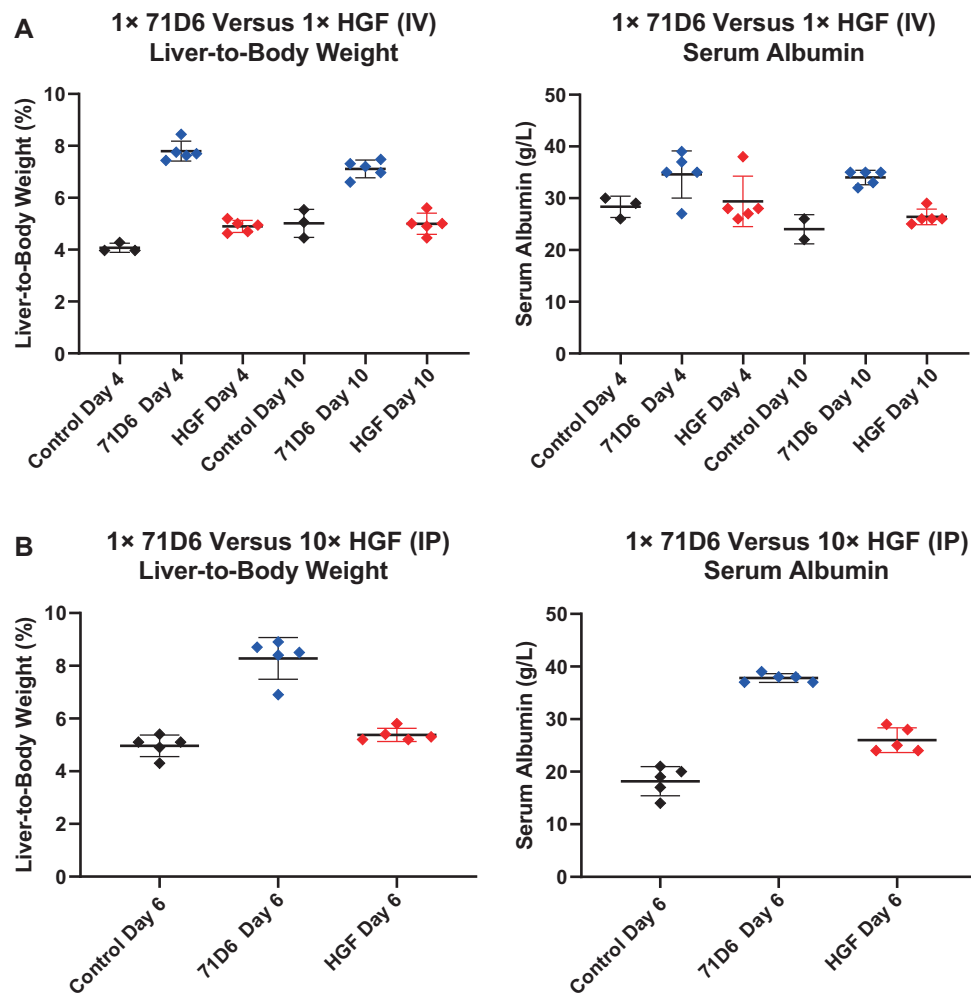


FIG. 2. 71D6 displays a potent hepatotrophic activity in mice. (A) A single 1 mg/kg bolus of 71D6 or human recombinant HGF was injected IV into adult Balb-c mice, and the liver-to-body weight and serum albumin levels were determined 4 and 8 days afterward. (B) A single 1 mg/kg bolus of 71D6 or multiple doses (10 over 5 days) of 1 mg/kg recombinant human HGF were injected IP into adult Balb-c mice. Liver-to-body weight and serum albumin levels were determined 6 days after the first injection. Black represents control group. Red represents HGF group. Blue represents 71D6 group.

mouse model of SFSS. This model reproduces the impaired regenerative capacity of the liver in patients with cirrhosis or other hepatic diseases. Mice were subjected to chronic CCl4 intoxication for 10 weeks and then

randomized into 2 arms receiving either 3 mg/kg 71D6 or a control IgG1. At 3 days after randomization, all mice were subjected to 70% hepatectomy. Mouse survival was recorded up to 28 days after hepatectomy.

Satellite animals were euthanized at different time points to analyze liver regeneration, fibrosis, and inflammation. This hepatectomy model typically presents high mortality within 4 days after surgery. Remarkably, the survival rate observed in the 71D6-treated group was significantly higher than that observed in the control group ($P = 0.03$). Although only 5 of 24 mice (21%) in the control group survived for 28 days after hepatectomy, 7 of 13 71D6-treated mice (54%) were alive at the end of the experiment (Fig. 3A). As shown in Fig. 3B, 71D6 also accelerated body weight recovery following surgery compared with controls ($P < 0.001$). Liver weight was also evaluated upon autopsy of satellite animals at various time intervals. As shown in Fig. 3C, 71D6 significantly increased the liver-to-body weight ratio at most time points analyzed (days 1 and 3, $P < 0.05$; day 7, nonsignificant; day 28, $P < 0.001$).

Consistent with these findings, serum albumin levels in 71D6-treated animals increased (Fig. 3D) and showed a significant difference with the control group starting on day 7 ($P < 0.01$) and reaching a peak on day 28 ($P < 0.01$). These data indicate that 71D6 treatment promotes liver regeneration and accelerates recovery of liver function after partial hepatectomy.

SERUM 71D6 PROMOTES HEPATIC PROLIFERATION FOLLOWING HEPATECTOMY THROUGH ACTIVATION OF THE ERK SIGNALING PATHWAY

Hepatocyte proliferation following hepatectomy was assessed by staining liver sections with anti-PCNA

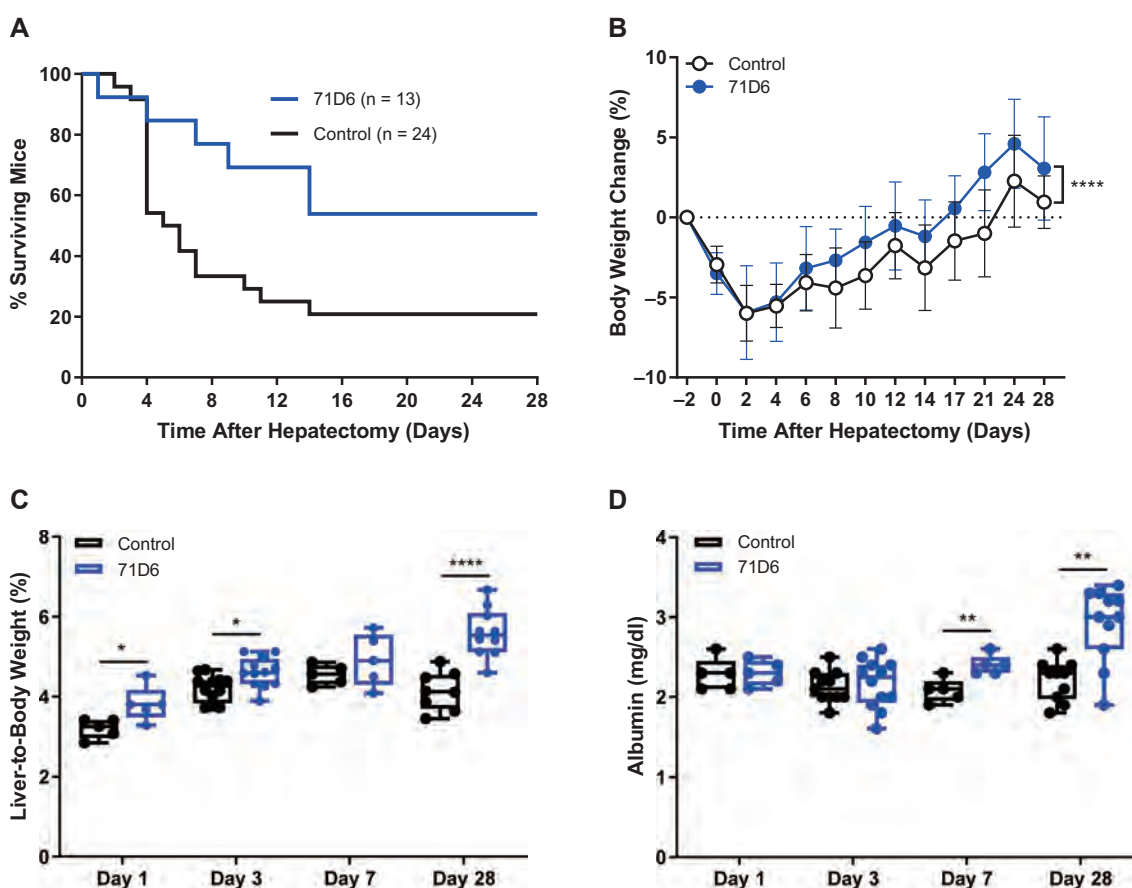


FIG. 3. 71D6 promotes liver regeneration and increases survival in mice undergoing CCl₄ injury and partial hepatectomy. (A) Kaplan-Meier curve analysis of mouse survival ($P = 0.03$). (B) Body weight change over time (mean \pm SD) ($P < 0.001$). (C) Liver-to-body weight over time (days 1 and 3, $P < 0.05$; day 7, nonsignificant; day 28, $P < 0.001$). (D) Serum albumin levels over time (days 1 and 3, nonsignificant; day 7, $P < 0.01$; day 28, $P < 0.01$).

antibodies. As shown in Fig. 4A, the number of PCNA-positive cells was higher in the 71D6-treated group starting at day 3 and peaking at day 28. To further characterize 71D6-induced liver proliferation, we analyzed the expression and activation of p44 ERK1 and p42 ERK2, a key event in the postinjury liver regeneration program.⁽¹⁵⁾ This analysis revealed that 71D6 significantly increased the levels of phosphorylated (activated) ERK1/2 on both day 3 and day 28 following hepatectomy (Fig. 4B). Activation of ERK1/2 directly correlated with PCNA expression, suggesting that 71D6 stimulates activation of ERK1/2 in the remnant liver, resulting in accelerated hepatic regeneration. Notably, however, no ERK1/2 activation was detected in control animals despite hepatectomy typically inducing spontaneous liver regeneration within a few days. This could be attributed to, and is consistent with, the impaired regenerative capacity of a cirrhotic liver. To cast light onto the mechanism underlying this regenerative impairment, we analyzed serum HGF levels in posthepatectomy mice as well as in healthy, naïve animals. This analysis revealed that posthepatectomy mice

treated with the control IgG protein displayed only a marginal increase in HGF levels compared with naïve mice (Fig. 3C). Interestingly, serum HGF levels were slightly higher in the 71D6 group, probably because of larger liver mass and/or increased hepatic function. In any case, serum HGF levels were confined to the picomolar range, whereas 71D6 levels measured in the same samples remained well above MET saturating levels for the entire duration of the study (full activation of MET is reached with 10 nM 71D6). These results explain the absence of ERK activation and the poor liver regeneration observed in the control group on one hand and justify the superior regenerative ability of the animals treated with 71D6 on the other hand.

SERUM 71D6 AMELIORATES HEPATIC FIBROSIS AFTER PARTIAL HEPATECTOMY ON CIRRHOTIC BACKGROUND

Sections of livers harvested from satellite animals were stained with H & E, PSR, and antibodies against

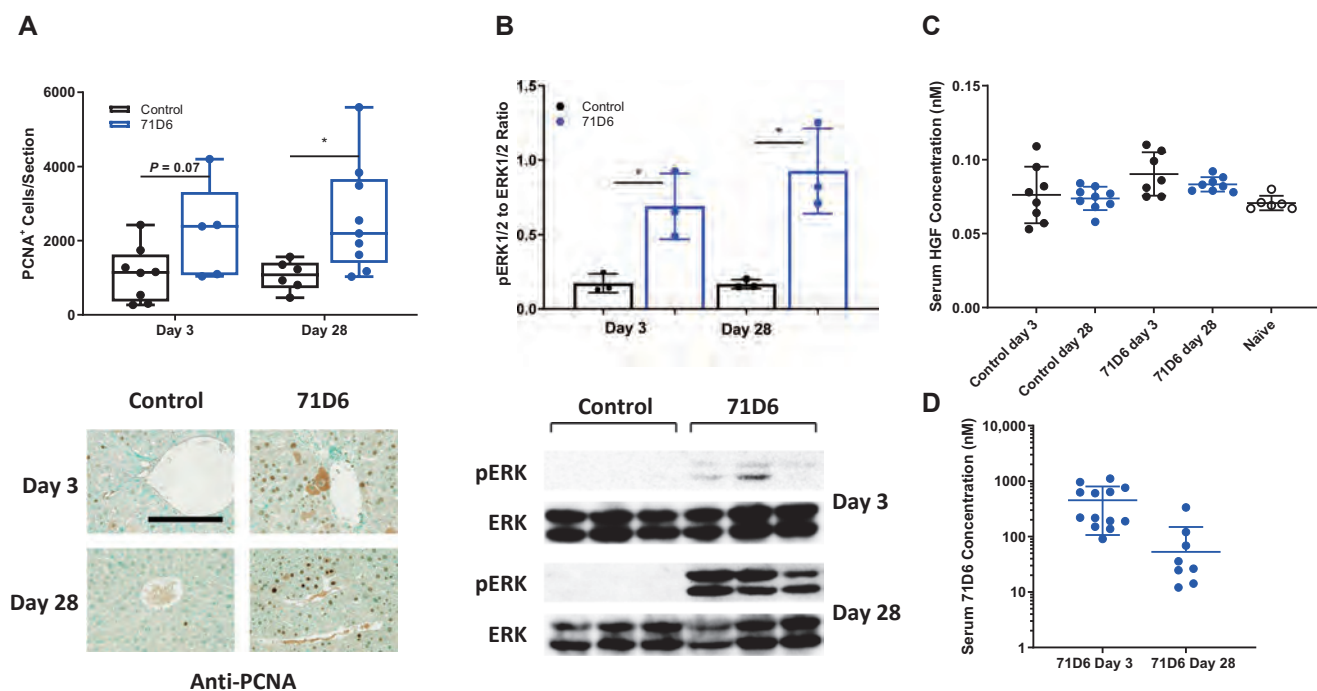


FIG. 4. 71D6 promotes hepatic proliferation following hepatectomy of cirrhotic mice through activation of the ERK signaling pathway. (A) Hepatic proliferation is expressed as the number of PCNA-positive cells per liver section analyzed. Representative images are shown below the graph. The bar is 250 μ M. (B) The levels of phosphorylated and total ERK1/2 (p44/p42) were determined by Western blot analysis of liver samples. The ratio between phosphorylated ERK1/2 and total ERK1/2 was determined by densitometric analysis. (C) Serum HGF levels in mice of the control and 71D6 groups as well as in healthy, naïve animals were determined by ELISA. (D) Serum 71D6 levels in mice of the 71D6 group were determined by ELISA.

desmin or α -SMA. Liver specimens of the control group showed consistent formation of thin fibrotic septa at the portal and central areas on day 3. Although milder, fibrosis was still present at day 28. Control liver sections also displayed high density of myofibroblasts. In contrast, liver specimens of the 71D6 group showed significantly milder signs of fibrosis and a reduced presence of myofibroblasts already at day 3. Liver fibrosis was quantified and expressed as the percentage of PSR-positive area (Fig. 5A), number of desmin-positive cells (Fig. 5B), and percentage of α -SMA-positive area (Fig. 5C). To further strengthen these results, the expression of fibrosis-related genes was analyzed by quantitative RT-PCR. This analysis revealed that 71D6 significantly reduced mRNA expression of platelet-derived growth factor (*PDGF*), tissue inhibitor of metalloproteinase 3 (*TIMP3*), and transforming growth factor β 1 (*TGF- β 1*), which are involved in collagen deposition and activation of HSCs (Fig. 5D). Together, these results suggest that in mice subjected to CC14 treatment and partial hepatectomy,

the agonistic anti-MET antibody 71D6 effectively accelerates the regression of hepatic fibrosis by inhibiting the activation of multiple fibrogenic pathways.

SERUM 71D6 REDUCES MACROPHAGE INFILTRATION IN THE REGENERATING LIVER

Liver specimens extracted at autopsy were analyzed by immunohistochemistry using antibodies against F4/80 and CD68. The number of cells positive for F4/80 ($P < 0.05$; Fig. 6A) and CD68 ($P < 0.0001$; Fig. 6B) was significantly lower in the 71D6 group compared with the control group on day 28. Consistent with histological findings, mRNA levels of inflammatory cytokine genes (tumor necrosis factor α [*TNF- α*], interleukin 1β [*IL1 β*], chemokine [C-C motif] ligand 3 [*CCL3*], and chemokine [C-C motif] ligand 5 [*CCL5*]) were significantly lower in the liver homogenates of 71D6-treated mice compared with control mice on day 28 ($P < 0.05$; Fig. 6C).

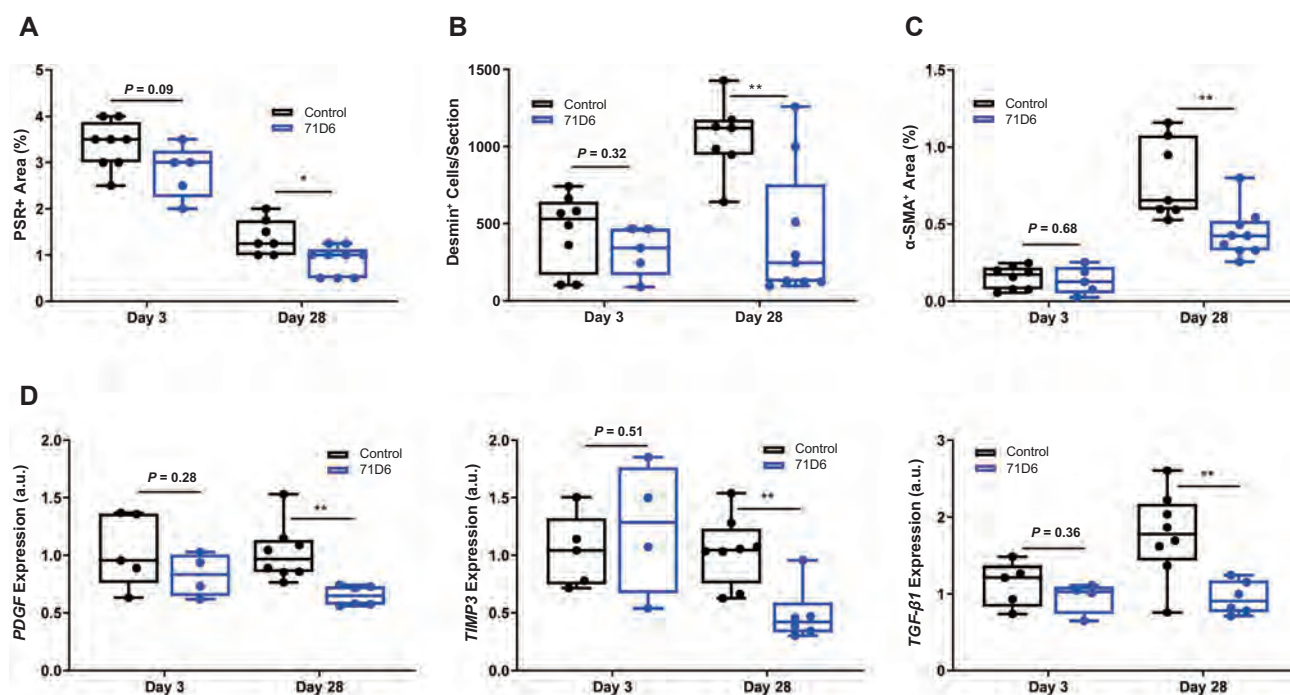


FIG. 5. 71D6 ameliorates hepatic fibrosis after partial hepatectomy on cirrhotic background. (A) Liver sections were stained with PSR. Data are expressed as percentage of PSR-positive area. (B) Liver sections were stained with anti-desmin antibodies. Data are expressed as number of desmin-positive cells per section analyzed. (C) Liver sections were stained with anti- α -SMA antibodies. Data are expressed as percentage of α -SMA-positive area. (D) Liver specimens were analyzed by RT-PCR to determine the levels of *PDGF*, *TGF- β 1*, and *TIMP3* expression. Data are expressed as a.u.

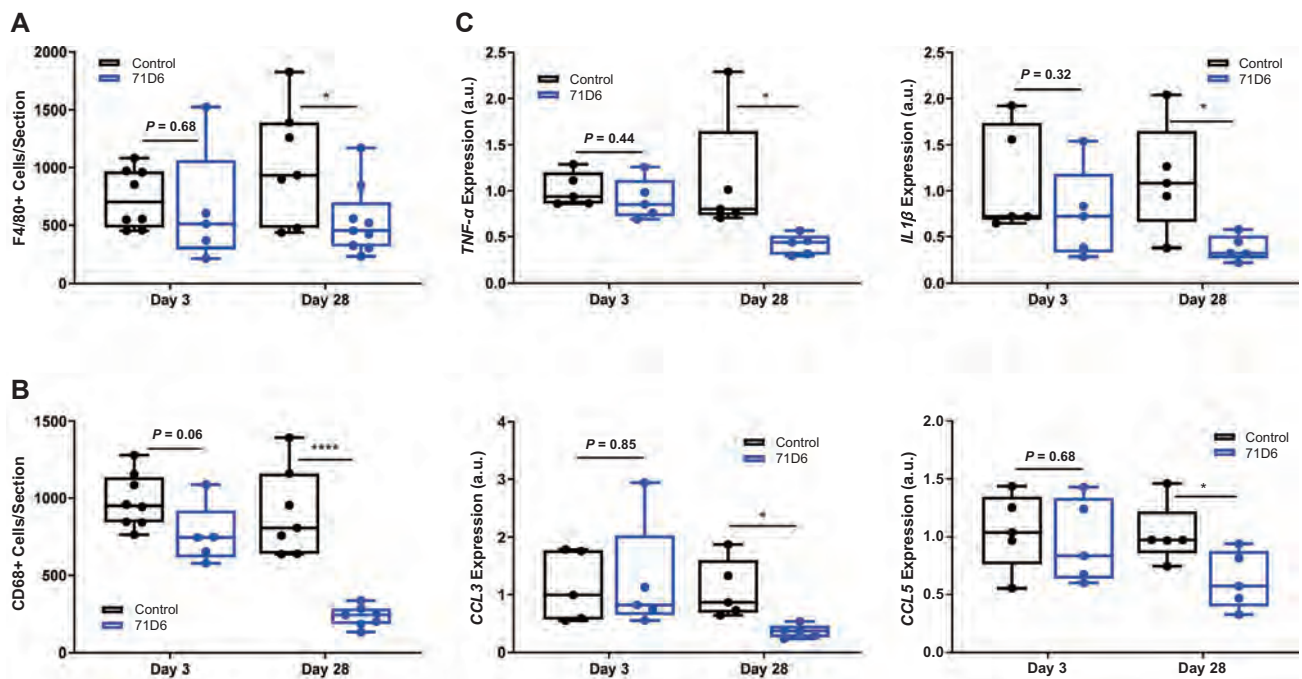


FIG. 6. 71D6 reduces macrophage infiltration in the regenerating liver. (A) Liver sections were stained with anti-F4/80 antibodies. Data are expressed as number of F4/80-positive cells per section analyzed. (B) Liver sections were stained with anti-CD68 antibodies. Data are expressed as number of CD68-positive cells per section analyzed. (C) Liver specimens were analyzed by RT-PCR to determine the levels of *TNF-α*, *IL1β*, *CCL3*, and *CCL5* expression. Data are expressed as a.u.

Discussion

Liver failure is prone to occur after liver transplantation or extended resection when the size and function of the remnant liver is unable to meet the metabolic demand of the patient. SFSS limits the use of living donor and split-liver transplants, and lifesaving large resections of tumors or nonmalignant lesions may be limited by concerns of postsurgical liver failure. Furthermore, SFSS is analogous to end-stage liver disease where the functional liver mass no longer meets metabolic demand. Therefore, there is a major need for effective therapies capable of enhancing and accelerating liver regeneration.

Most studies evaluating regenerative therapies take advantage of the 70% hepatectomy model in mice or rats. In this model, 70% of the liver, usually the median and left lateral lobes, is surgically removed. In response to this, the remnant liver enlarges until it restores normal mass and function. Although the liver has a remarkable potential for regeneration, this regenerative capacity becomes impaired with serious

liver fibrosis.⁽¹⁶⁾ The transition of quiescent HSCs to activated, scar-forming, myofibroblast-like cells leads to excessive extracellular matrix synthesis.^(17,18) This abnormal scar formation in the liver has been shown to hold back hepatocyte proliferation. In the present study, we studied a newly developed agonistic anti-MET antibody that increased hepatocyte proliferation after partial hepatectomy in mice with CCl₄-induced liver disease.

Following 70% hepatectomy, both hepatocytes and nonparenchymal cells are activated and integrate multiple signals originating from immune, hormonal, and metabolic networks to induce liver regeneration.⁽¹⁹⁾ Within this process, the activation of HGF/MET signaling pathway has been demonstrated to be 1 of the essential mechanisms that lead hepatocytes into the cell cycle after hepatectomy.⁽²⁰⁾ Following resection, HGF protein levels in plasma typically rise,⁽²¹⁾ but liver fibrosis is known to prevent this process. The lack of HGF induction on a cirrhotic background was fully confirmed in our study (Fig. 4C). To circumvent defective endogenous HGF activation, we employed

the 71D6 agonistic anti-MET antibody. When bound by 71D6, the MET receptor dimerizes and becomes phosphorylated on tyrosine residues to initiate MET downstream signaling (Fig. 1).

The results presented here indicate that liver-to-body weight ratio increased very slowly in the control group, whereas it increased markedly and constantly in the 71D6-treated group (Fig. 3). Quantitative analysis of PCNA immunostaining also confirmed that the agonistic anti-MET antibody potently promotes hepatocyte proliferation (Fig. 4A). We also clarified the involvement of the ERK1/2 signaling pathway in this hepato-proliferative effect. It is known that the Ras/Raf/MEK/ERK cascade has the ability to lead to cellular responses, including proliferation. The ERK1/2 signaling pathway can also regulate the hepatocyte proliferative response during the regeneration of normal liver.⁽²²⁾ Our Western blot results showed that 71D6 strongly activated ERK p44/p42, closely reflecting the high levels of PCNA expression (Fig. 4B). Our results clearly show that 71D6 has the ability to mimic HGF signaling in vivo, including activation of downstream kinases and promotion of hepatocyte proliferation. However, in contrast to HGF, 71D6 is very stable in vivo (Table 2) and displays superior pharmacodynamic properties (Fig. 2). These results highlight the therapeutic potential of 71D6 in liver regeneration.

Liver fibrosis is an inadequate wound-healing response to chronic liver injury and is characterized by the excessive deposition and reduced degradation of the extracellular matrix. Excessive accumulation of extracellular matrix alters the hepatic architecture to progress to liver fibrosis, and if not prevented it may eventually lead to cirrhosis and even liver cancer. Our study provides evidence that 71D6 treatment leads to a significantly lower degree of collagen, desmin, and α -SMA compared with controls (Fig. 5A,B). This is explained by the direct inhibition of multiple fibrogenic pathways including those controlled by *PDGF*, *TIMP3*, and *TGF- β 1* (Fig. 5C). These data support the hypothesis that 71D6 has the ability to antagonize TGF- β 1 directly so as to reduce liver fibrosis and improve liver regeneration.⁽²³⁾

Furthermore, our study showed that 71D6 also inhibited the infiltration of inflammatory cells into the liver. In fact, the number of F4/80-positive and CD68-positive cells in the 71D6 group was significantly lower than that observed in the control group (Fig. 6A,B). Consistent with these findings, qRT-PCR analysis revealed that the expressions of proinflammatory

cytokines and chemokines such as TNF- α , IL1 β , CCL3, and CCL5 were much lower in the liver homogenates of 71D6-treated mice compared with control animals (Fig. 6C).

Thus, not only does 71D6 overcome the inability of a cirrhotic liver to regenerate following hepatectomy, but it also achieves faster resolution of fibrosis and the effective suppression of inflammation. Together, these results suggest that activating the MET pathway via an HGF-mimetic antibody may be beneficial in patients with SFSS and possibly other types of acute and chronic liver disorders.

Acknowledgments: The authors thank Philippe Wiesel for critically reading the manuscript, Luca Rossi for in vivo work, Damiana Sattanino for assay setup, and the entire AgomAb team for continuous support.

REFERENCES

- 1) Riddiough GE, Christophi C, Jones RM, Muralidharan V, Perini MV. A systematic review of small for size syndrome after major hepatectomy and liver transplantation. *HPB* 2020;22:487-496.
- 2) Masuda Y, Yoshizawa K, Ohno Y, Mita A, Shimizu A, Soejima Y. Small-for-size syndrome in liver transplantation: definition, pathophysiology and management. *Hepatobiliary Pancreat Dis Int* 2020;19:334-341.
- 3) Zhong Z, Schwabe RF, Kai Y, He L, Yang L, Bunzendahl H, et al. Liver regeneration is suppressed in small-for-size liver grafts after transplantation: involvement of c-Jun N-terminal kinase, cyclin D1, and defective energy supply. *Transplantation* 2006;82:241-250.
- 4) Greenbaum LE, Ukomadu C, Tchorz JS. Clinical translation of liver regeneration therapies: a conceptual road map. *Biochem Pharmacol* 2020;175:113847.
- 5) Forbes SJ, Newsome PN. Liver regeneration—mechanisms and models to clinical application. *Nat Rev Gastroenterol Hepatol* 2016;13:473-485.
- 6) Nakamura T, Mizuno S. The discovery of hepatocyte growth factor (HGF) and its significance for cell biology, life sciences and clinical medicine. *Proc Jpn Acad Ser B Phys Biol Sci* 2010;86:588-610.
- 7) Matsumoto K, Funakoshi H, Takahashi H, Sakai K. HGF-Met pathway in regeneration and drug discovery. *Biomedicines* 2014;2:275-300.
- 8) Nakamura T, Sakai K, Nakamura T, Matsumoto K. Hepatocyte growth factor twenty years on: much more than a growth factor. *J Gastroenterol Hepatol* 2011;26(suppl 1):188-202.
- 9) Klarenbeek A, Blanchetot C, Schragel G, Sadi AS, Ongenaes N, Hemrika W, et al. Combining somatic mutations present in different in vivo affinity-matured antibodies isolated from immunized *Lama glama* yields ultra-potent antibody therapeutics. *Protein Eng Des Sel* 2016;29:123-133.
- 10) Michieli P. Anti-Met antibodies and uses thereof. European patent application EP 3475302 A1 2019. <https://www.lens.org/lens/patent/062-815-545-734-095>.
- 11) Cingoz O. Motavizumab. *mAbs* 2009;1:439-442.
- 12) Ido A, Moriuchi A, Kim I, Numata M, Nagata-Tsubouchi Y, Hasuike S, et al. Pharmacokinetic study of recombinant human

- hepatocyte growth factor administered in a bolus intravenously or via portal vein. *Hepato Res* 2004;30:175-181.
- 13) Ido A, Moriuchi A, Numata M, Murayama T, Teramukai S, Marusawa H, et al. Safety and pharmacokinetics of recombinant human hepatocyte growth factor (rh-HGF) in patients with fulminant hepatitis: a phase I/II clinical trial, following preclinical studies to ensure safety. *J Transl Med* 2011;9:55.
 - 14) Xue F, Takahara T, Yata Y, Minemura M, Morioka CY, Takahara S, et al. Attenuated acute liver injury in mice by naked hepatocyte growth factor gene transfer into skeletal muscle with electroporation. *Gut* 2002;50:558-562.
 - 15) Tao Y, Wang M, Chen E, Tang H. Liver regeneration: analysis of the main relevant signaling molecules. *Mediators Inflamm* 2017;2017:4256352.
 - 16) Chan A, Kow A, Hibi T, Di Benedetto F, Serrablo A. Liver resection in cirrhotic liver: are there any limits? *Int J Surg* 2020;82S:109-114.
 - 17) Issa R, Zhou X, Trim N, Millward-Sadler H, Krane S, Benyon C, Iredale J. Mutation in collagen-1 that confers resistance to the action of collagenase results in failure of recovery from CCl4-induced liver fibrosis, persistence of activated hepatic stellate cells, and diminished hepatocyte regeneration. *FASEB J* 2003;17:47-49.
 - 18) Henderson NC, Forbes SJ. Hepatic fibrogenesis: from within and outwith. *Toxicology* 2008;254:130-135.
 - 19) Yagi S, Hirata M, Miyachi Y, Uemoto S. Liver regeneration after hepatectomy and partial liver transplantation. *Int J Mol Sci* 2020;21:8414.
 - 20) Thorgeirsson SS. The central role of the c-Met pathway in rebuilding the liver. *Gut* 2012;61:1105-1106.
 - 21) Eguchi S, Yanaga K, Okudaira S, Sugiyama N, Miyamoto S, Furui J, Kanematsu T. Changes in serum levels of hepatocyte growth factor in patients undergoing adult-to-adult living-donor liver transplantation. *Transplantation* 2003;76:1769-1770.
 - 22) Chen XG, Xu CS, Liu YM. Involvement of ERK1/2 signaling in proliferation of eight liver cell types during hepatic regeneration in rats. *Genet Mol Res* 2013;12:665-677.
 - 23) Fabregat I, Moreno-Cáceres J, Sánchez A, Dooley S, Dewidar B, Giannelli G, ten Dijke P. TGF- β signalling and liver disease. *FEBS J* 2016;283:2219-2232.

A Mesenchymal-epithelial transition factor-Agonistic Antibody Accelerates Cirrhotic Liver Regeneration and Improves Mouse Survival Following Partial Hepatectomy

Kuai Ma,^{1,2} Weitao Que,¹ Xin Hu,¹ Wen-Zhi Guo,³ Er-li Gu,² Liang Zhong,⁴ Virginia Morello,⁵ Manuela Cazzanti,⁵ Paolo Michieli,^{5,6} Terumi Takahara,⁷ and Xiao-Kang Li^{1,3}

¹Division of Transplantation Immunology, National Research Institute for Child Health and Development, Tokyo, Japan; ²Department of Gastroenterology and Hepatology, Jing'an District Central Hospital, Jing'an Branch of Huashan Hospital, Fudan University, Shanghai, China; ³Department of Hepatobiliary and Pancreatic Surgery, The First Affiliated Hospital of Zhengzhou University, Zhengzhou, China; ⁴Department of Gastroenterology, Huashan Hospital, Fudan University, Shanghai, China; ⁵AgomAb Therapeutics NV, Gent, Belgium; ⁶Molecular Biotechnology Center, University of Torino Medical School, Torino, Italy; and ⁷Third Department of Internal Medicine, University of Toyama, Toyama, Japan

Small-for-size syndrome (SFSS) is a common complication following partial liver transplantation and extended hepatectomy. SFSS is characterized by postoperative liver dysfunction caused by insufficient regenerative capacity and portal hyperperfusion and is more frequent in patients with preexisting liver disease. We explored the effect of the Mesenchymal-epithelial transition factor (MET)-agonistic antibody 71D6 on liver regeneration and functional recovery in a mouse model of SFSS. Male C57/BL6 mice were exposed to repeated carbon tetrachloride injections for 10 weeks and then randomized into 2 arms receiving 3 mg/kg 71D6 or a control immunoglobulin G (IgG). At 2 days after the randomization, the mice were subjected to 70% hepatectomy. Mouse survival was recorded up to 28 days after hepatectomy. Satellite animals were euthanized at different time points to analyze liver regeneration, fibrosis, and inflammation. Serum 71D6 administration significantly decreased mouse mortality consequent to insufficient regeneration of the cirrhotic liver. Analysis of liver specimens in satellite animals revealed that 71D6 promoted powerful activation of the extracellular signal-regulated kinase pathway and accelerated liver regeneration, characterized by increased liver-to-body weight, augmented mitotic index, and higher serum albumin levels. Moreover, 71D6 accelerated the resolution of hepatic fibrosis as measured by picrosirius red, desmin, and α -smooth muscle actin staining, and suppressed liver infiltration by macrophages as measured by CD68 and F4/80 staining. Analysis of gene expression by reverse-transcription polymerase chain reaction confirmed that 71D6 administration suppressed the expression of key profibrotic genes, including platelet-derived growth factor, tissue inhibitor of metalloproteinase 3, and transforming growth factor- β 1, and of key proinflammatory genes, including tumor necrosis factor- α , interleukin-1 β , chemokine (C-C motif) ligand 3, and chemokine (C-C motif) ligand 5. These results suggest that activating the MET pathway via an hepatocyte growth factor-mimetic antibody may be beneficial in patients with SFSS and possibly other types of acute and chronic liver disorders.

Liver Transplantation 0 1–12 2021 AASLD.

Received April 12, 2021; accepted September 10, 2021.

Small-for-size syndrome (SFSS) is a common yet underrecognized complication following partial liver

transplantation and extended hepatectomy.⁽¹⁾ It is characterized by postoperative liver dysfunction caused by insufficient regenerative capacity and portal hyperperfusion and is more frequent in patients with preexisting liver disease.⁽²⁾ Approximately one-third of liver transplant recipients who develop early graft failure qualify for SFSS. Small-for-size liver grafts show delayed and impaired regeneration⁽³⁾ and have greater risks of failure

Abbreviations: agomAbs, agonistic monoclonal antibodies; α -SMA, α -smooth muscle actin; a.u., arbitrary units; CCL3, chemokine (C-C motif) ligand 3; CCl4, carbon tetrachloride; CCL5, chemokine (C-C motif) ligand 5; ELISA, enzyme-linked immunosorbent assay; ERK,

including microcirculatory damage, inflammatory injury, and accelerated acute rejection, leading to liver failure with associated coagulopathy, ascites, prolonged cholestasis, and encephalopathy. Because of the persistent organ shortage, living donor liver transplantation is becoming the most viable option for patients with end-stage liver disease. Donor safety always comes first in living donor liver transplantation, and there is a growing momentum for the increased use of small-for-size grafts in association with hepato-regenerative therapies.^(4,5)

Hepatocyte growth factor (HGF) is a pleiotropic cytokine of mesenchymal origin that plays a key role in organ regeneration.⁽⁶⁾ Its high-affinity receptor, the MET

tyrosine kinase, is mainly expressed by epithelial and endothelial cells, but it is also present on some immune cells as well as in various types of myofibroblasts.⁽⁷⁾ In the liver, HGF is typically secreted by hepatic stellate cells (HSCs) and plays a key role in hepatic regeneration. Following injury, increased HGF secretion initiates a repair program that limits cell damage, ensures hepatocyte regeneration, inhibits myofibroblast hyperproliferation, and suppresses inflammation, restoring liver function.⁽⁸⁾

Despite the broad therapeutic potential of HGF in liver diseases, its translation to the clinic has been challenging. In fact, HGF does not display ideal drug-like properties: its very short plasma half-life (a few minutes) causes an unfavorable pharmacokinetics because of its high avidity for the extracellular matrix, it has a poor biodistribution; it needs proteolytic activation to acquire biological activity, and once activated it is unstable; lastly, its industrial manufacture is difficult and costly. To overcome the limitations of HGF and to generate a drug that could effectively promote liver regeneration in patients, we generated a series of anti-MET agonistic monoclonal antibodies (“agomAbs”) that bind to MET at high affinity and determine MET activation, mimicking the biochemical and biological activity of HGF. AgomAbs combine the powerful therapeutic potential of HGF with the excellent pharmacokinetic, pharmacodynamic, and manufacturing properties of antibodies.

In this study, we explored the therapeutic potential of 71D6, a fully agonistic anti-MET antibody that cross-reacts with rodent, nonhuman primate, and human MET in a mouse model of SFSS.

Materials and Methods

SERUM 71D6 ANTIBODY GENERATION AND CHARACTERIZATION

Serum 71D6 was generated by immunization of *Llama glama* using the SIMPLE antibody platform.⁽⁹⁾ A detailed description of its generation and characterization has been published previously.⁽¹⁰⁾ Binding of 71D6 to MET and HGF-mediated and 71D6-mediated MET autophosphorylation and analysis of MET downstream signaling were performed as described.⁽¹⁰⁾

ANIMAL MODEL

Mouse procedures were authorized by the National Research Institute for Child Health and Development

extracellular signal-regulated kinase; H & E, hematoxylin-eosin; HGF, hepatocyte growth factor; hMET, human mesenchymal-epithelial transition factor; HSCs, hepatic stellate cells; IgG, immunoglobulin G; IgG1, immunoglobulin G1; IL-1 β , interleukin-1 β ; IP, intraperitoneally; IV, intravenously; mMET, mouse mesenchymal-epithelial transition factor; mRNA, messenger RNA; N/A, Not applicable; PCNA, proliferating cell nuclear antigen; PDGF, platelet-derived growth factor; PSR, picosirius red; qRT-PCR, quantitative reverse-transcription polymerase chain reaction; RT-PCR, reverse-transcription polymerase chain reaction; SD, standard deviation; SFSS, small-for-size syndrome; TIMP3, tissue inhibitor of metalloproteinase 3; TNF- α , tumor necrosis factor- α .

Address reprint requests to Paolo Michieli, Ph.D., Molecular Biotechnology Center, University of Torino Medical School, Via Nizza 52, I-10126 Torino, Italy. Telephone: +39 11 670 64 99; E-mail: paolo.michieli@unito.it

Address reprint requests to Terumi Takahara, M.D., Ph.D., Third Department of Internal Medicine, University of Toyama, 2630 Sugitani, Toyama, 930-0194 Japan. Telephone: +81 76-434-502; E-mail: terutaka-ty@umin.ac.jp

Address reprint requests to Xiao-Kang Li, M.D., Ph.D., Division of Transplantation Immunology, National Research Institute for Child Health and Development, 2-10-1 Okura, Setagaya-ku, Tokyo, 157-8535 Japan. Telephone: +81-3-3416-0181; FAX: +81-3-3417-2864; E-mail: ri-k@nchd.go.jp

This study was supported in part by the Ministry of Education, Culture, Sports, Science and Technology of Japan (Grants-in-Aid 16K11064, 24/17H04277, and 18K08558), the National Center for Child Health and Development (Grant 29-09), and Science and Technology Innovation Talents in Henan Universities (no. 19HASTTT003).

Manuela Cazzanti, Paolo Michieli, and Virginia Morello consult for, own stock in, and are employed by AgomAb Therapeutics NV.

Copyright © 2021 The Authors. Liver Transplantation published by Wiley Periodicals LLC on behalf of American Association for the Study of Liver Diseases. This is an open access article under the terms of the Creative Commons Attribution-NonCommercial-NoDerivs License, which permits use and distribution in any medium, provided the original work is properly cited, the use is non-commercial and no modifications or adaptations are made.

View this article online at wileyonlinelibrary.com.

DOI 10.1002/lt.26301

(permission no. A2014-010-C06). The 8-week-old male C57BL/6JmsSLc mice (Shizuoka Laboratory Animal Center, Shizuoka, Japan) were subjected to repeated subcutaneous injection of 10% carbon tetrachloride (CCl₄; Wako) dissolved in olive oil (100 µL/mouse) twice a week for 10 weeks. On the day of the last CCl₄ administration, the mice were randomized into 2 arms receiving 3 mg/kg of 71D6 or a control antibody against the F glycoprotein of respiratory syncytial virus⁽¹¹⁾ (both in the mouse immunoglobulin G1 [IgG1] format). At 2 days after randomization, all of the mice were subjected to 70% hepatectomy by removal of the anterior 2 lobes and posterior left lobe. The 71D6 or control IgG were administered intraperitoneally (IP) at a dose of 3 mg/kg 2 days before hepatectomy and at days 0, 2, 4, 6, 8, 10, and 12. Mice recruited in the trial included main study animals and satellite animals. The spontaneous survival rate of the main study animals was recorded from days 0 to 28. Satellite animals (3 mice per group) were euthanized at 3, 7, and 28 days after hepatectomy. Serum and liver samples were stored at -80°C.

SERUM BIOCHEMICAL MEASUREMENTS

Serum was collected from whole-blood samples after standing for 30 minutes at 37°C and then centrifuged at 1800g for 25 minutes at 4°C. Serum samples were then analyzed for serum albumin concentrations using a commercially available kit (Fujifilm) and an automatic biochemical analyzer (DRI-CHEM 3500i; Fujifilm) according to the manufacturer's instructions. Serum HGF concentration was measured using the mouse/rat HGF Quantikine enzyme-linked immunosorbent assay (ELISA) kit (R&D Systems). Serum 71D6 concentration was determined by ELISA as described.⁽¹⁰⁾

HISTOPATHOLOGICAL AND IMMUNOHISTOCHEMICAL EXAMINATION

Both the liver portion extracted at the time of hepatectomy and that collected at autopsy were processed for histopathological examination. Liver tissues were fixed in 10% formalin for 48 hours, routinely processed, and sliced into sections of 4 µm in thickness. For detection of liver fibrosis, sections were stained with picosirius red (PSR; Sigma-Aldrich), anti-α-smooth muscle actin (α-SMA) antibodies (AbCam) and anti-desmin antibodies (Boehringer). For detection of macrophage

infiltration, sections were stained with antibodies against CD68 (AbCam) and F4/80 (AbCam). For detection of liver proliferation, sections were stained with anti-proliferating cell nuclear antigen (PCNA) antibodies (Dako). Sections were also stained with hematoxylin-eosin (H & E) and periodic acid-Schiff (both from Sigma-Aldrich). After staining, specimens were photographed under a microscope (Olympus). Histological and immunohistochemical results were quantified using WinRoof 7.4 software (Mitani Corporation).

TOTAL MESSENGER RNA PREPARATION AND QUANTITATIVE REVERSE-TRANSCRIPTION POLYMERASE CHAIN REACTION ANALYSIS

Total messenger RNA (mRNA) was extracted from frozen liver tissues using RNeasy Mini Kit (Qiagen). Each 0.8 µg aliquot of mRNA was reverse transcribed to complementary DNA using a Prime Script reverse-transcription (RT) reagent kit (RR037A; Takara). Quantitative reverse-transcription polymerase chain reaction (qRT-PCR) was performed using the SYBR Green system or the primer/probe set system (primer sequences are listed in Table 1) the Applied Biosystem PRISM7900 apparatus (Thermo Fisher Scientific) is a machine which is used to do RT-PCR. The PCR cycle conditions for the SYBR Green system were 95°C for 3 minutes, 45 cycles of 95°C for 3 seconds, and 60°C for 30 seconds. The PCR cycle conditions for the primer/probe set system were 50°C for 2 minutes, 95°C for 15 minutes, 40 cycles of 95°C for 30 seconds, 60°C for 1 minute, and 25°C for 2 minutes. The comparative threshold cycle (ΔΔCt) method was used for determining relative gene expression, and the results of target genes (including fibrosis-related genes and inflammation-related genes) were normalized by subtracting *18S* expression values.

IN VIVO ANALYSIS OF EXTRACELLULAR SIGNAL-REGULATED KINASE ACTIVATION

Frozen liver tissue was homogenized in radio immunoprecipitation assay buffer containing 1% protease inhibitor cocktail-1 and 1% protease inhibitor cocktail-2 (Sigma-Aldrich) followed by centrifugation in a microfuge at top speed for 30 minutes. Protein concentrations were assayed using a Protein Assay kit (Bio-Rad). Samples were separated by electrophoresis on

TABLE 1. Primers and Probes Used in This Study

Genes (PCR)	Forward (5'-3')	Reverse (5'-3')	Probe
<i>TIMP3</i> (SYBR Green)	CACAAAGTTGCACAGTCCTG	TTTGTGCGCTCAAGCTAGA	N/A
<i>PDGF</i> (SYBR Green)	TACAGTTGCACTCCCAGGAAT	CTTCCAGTTGACAGTCCGCA	N/A
<i>TGF-β</i> (SYBR Green)	ATCCTGTCCAACTAAGGCTCG	ACCTCTTAGCATAGTAGTCCGC	N/A
<i>TNF-α</i> (SYBR Green)	AAGCCTGTAGCCACGTCGTA	GGCACCAGTAGTTGGTTGTCTTTG	N/A
<i>CCL5</i> (SYBR Green)	TGCCCTCACCATCATCCTCACT	GGCGGTTCCCTCGAGTGACA	N/A
<i>IL-1β</i> (SYBR Green)	ACCTCCAGGATGAGGACATGA	AACGTCACACACCAGCAGGTTA	N/A
<i>18S</i> (SYBR Green)	ATGAGTCCACTTTAAATCCTTTAACGA	CTTTAATATACGCTATTGGAGCTGGAA	N/A
<i>CCL3</i> (Taqman)	ACCCAGGTCTCTTTGGAGTCAGCGCA	TCCCAGCCAGGTGTCAATTTTC	AGGCATTCAAGTCCAGGTCCAG
<i>18S</i> (Taqman)	ATCCATTGGAGGGCAAGTCTGGTGC	ATGAGTCCACTTTAAATCCTTTAACGA	CTTTAATATACGCTATTGGAGGCTGGAA

NOTE: Liver-specific expression of profibrotic and proinflammatory genes determined by SYBR green PCR or Taqman PCR as indicated in the table. N/A, Not applicable.

10% polyacrylamide gels and transferred to Immobilon (Bio-Rad) polyvinylidene fluoride. After brief incubation with 5% nonfat milk to block nonspecific binding, membranes were exposed overnight at 4°C to specific phosphorylated anti-p44/p42 extracellular signal-regulated kinase (ERK) antibodies (Cell Signaling Technology). Membranes were washed and exposed to alkaline phosphatase-conjugated secondary antibodies and visualized by incubation in 5% nonfat milk. Phosphorylated p44/p42 ERK activity was quantified by laser densitometric analysis of the radiographic film using ImageJ software (National Institutes of Health, Bethesda, MD).

STATISTICAL ANALYSIS

Prism7 software (GraphPad, San Diego, CA) was used to calculate statistical significance. A 2-way analysis of variance method and Student *t* test method were used for comparisons between groups. Survival rate analysis was performed using a log-rank (Cox-Mantel) test. Data are expressed as mean ± standard deviation (SD). A value of *P* < 0.05 was considered to be statistically significant.

Results

SERUM 71D6 BINDS TO MET AT HIGH AFFINITY AND PROMOTES MET ACTIVATION, MIMICKING HGF

HGF-mimetic, agonistic anti-MET antibodies were generated by immunization of *L. glama* using the SIMPLE antibody platform.⁽⁹⁾ Their biochemical

and biological characterizations have been published previously.⁽¹⁰⁾ Among these molecules, which include both partial and full agonists of MET, serum 71D6 represents the most potent fully agonistic antibody. Serum 71D6 was produced as a chimera between variable llama regions and human or mouse IgG1/λ constant regions. Serum 71D6 bound to either the human MET (hMET) or mouse MET (mMET) extracellular domain with the concentration for 50% of maximal effect in the picomolar range (Fig. 1A). Stimulation of immortalized mouse liver cells with 71D6 or HGF resulted in a similar dose-dependent activation of MET and of its downstream signaling (Fig. 1B). An overlapping pattern of MET activation and signaling was observed in MET-expressing human epithelial cells of various origin (not shown).

SYSTEMIC 71D6 ADMINISTRATION RESULTS IN BIOLOGICALLY SIGNIFICANT PLASMA LEVELS

The pharmacokinetic properties of 71D6 were tested in various mouse strains using various routes of administration. In all studies, increasing doses of the antibody were delivered as a single bolus, and antibody levels in plasma were determined at different time points using a MET-based ELISA assay. Table 2 shows the results obtained in a representative study conducted by IP injection. Serum 71D6 concentration reached a peak 8 hours after injection (65 nM at 1 mg/kg and 2638 nM at 30 mg/kg). After 2 days, plasma 71D6 levels showed only a minor deflection (38 nM at 1 mg/kg and 2466 nM at 30 mg/kg). After 8 days, all dose levels except the lowest were still detectable

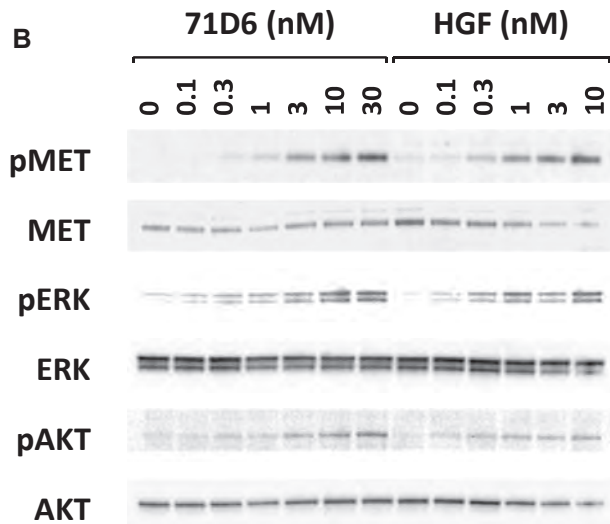
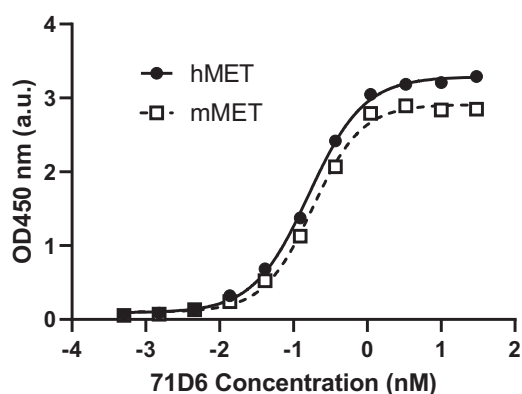
A Binding to MET Extracellular Domain

FIG. 1. 71D6 binds to MET at high affinity and elicits MET activation and downstream signaling, mimicking HGF function. (A) 71D6 binding to hMET or mMET extracellular domain was analyzed by ELISA (a.u.). (B) MET activation and downstream signaling induced by HGF or 71D6 was studied in human mouse MLP29 liver precursor cells. Cell lysates were analyzed by Western blotting using antibodies specific for the phosphorylated forms of MET, ERK, and AKT (pMET, pERK and pAKT) as well as antibodies against total MET, ERK, and AKT.

and well in the nanomolar range. Based on these data, the mean plasma half-life of 71D6 corresponded to approximately 5 days (note that recombinant HGF has a half-life of a few minutes in both rodents⁽¹²⁾ and humans).⁽¹³⁾ Considering that in normal, healthy mice endogenous HGF plasma levels range from 1 to 10 pM⁽¹⁴⁾ and that in the MET phosphorylation assays shown in Fig. 1B both HGF and 71D6 reached saturation at about 10 nM, the concentrations reached

following IP injections of 71D6 shown in Table 2 are certainly relevant from a biologic viewpoint.

SERUM 71D6 DISPLAYS A POTENT HEPATOTROPHIC ACTIVITY IN MICE

The biological effects of 71D6 administration were compared with those of recombinant HGF *in vivo*. In a first experiment, a single bolus of 1 mg/kg of either 71D6 or HGF was administered intravenously (IV) to adult Balb-c mice. Liver-to-body weight ratio and serum albumin levels were measured 4 and 10 days later. As shown in Fig. 2A, 71D6 administration resulted in a marked increase in liver weight both at day 4 (91%) and at day 10 (42%). In contrast, recombinant HGF administration promoted only a minor increase in liver weight (20% at day 4 and 0% at day 10). Serum albumin levels, expression of the synthetic activity of the liver, were invariably higher in the 71D6-treated mice, confirming the superior potency of the antibody. In a second experiment, we aimed at compensating the shorter half-life of HGF with more frequent administration. Because of the challenge of IV injecting the same animals multiple times, IP injection was preferred. Mice were injected IP with either a single bolus of 1 mg/kg 71D6 or with 1 mg/kg recombinant HGF every 12 hours for 5 days. Mice were euthanized at day 6 and subjected to the same analysis as noted previously. Even when administered more frequently, HGF could not match the potent hepatotrophic activity of 71D6. In fact, mice injected with a single bolus of 71D6 displayed a 70% larger liver compared with controls, whereas animals injected repeatedly with HGF showed a modest 10% increase in liver weight (Fig. 2B). Similarly, 71D6 injection resulted in 121% higher albumin levels compared with controls, whereas HGF injection increased serum albumin secretion by 52%. Therefore, 71D6 elicits a significantly more potent hepatotrophic effect in mice compared with recombinant HGF.

SERUM 71D6 PROMOTES LIVER REGENERATION AND INCREASES SURVIVAL IN MICE UNDERGOING CCl₄ INJURY AND PARTIAL HEPATECTOMY

Prompted by the previous results, we evaluated the therapeutic effect of 71D6 on liver regeneration in a

TABLE 2. Pharmacokinetic Properties of 71D6

Dose (mg/kg)	Maximum Concentration (nM)	Day 2 Concentration (nM)	Day 8 Concentration (nM)
1	65 ± 3	38 ± 6	0 ± 0
3	271 ± 56	249 ± 70	17 ± 12
10	1265 ± 270	1062 ± 114	257 ± 27
30	2638 ± 327	2466 ± 494	446 ± 45

NOTE: 71D6 concentration in plasma was determined at different time points following IP injection of different dose levels of antibody as a single bolus. Values represent the mean ± standard deviation of at least 3 biological replicates.

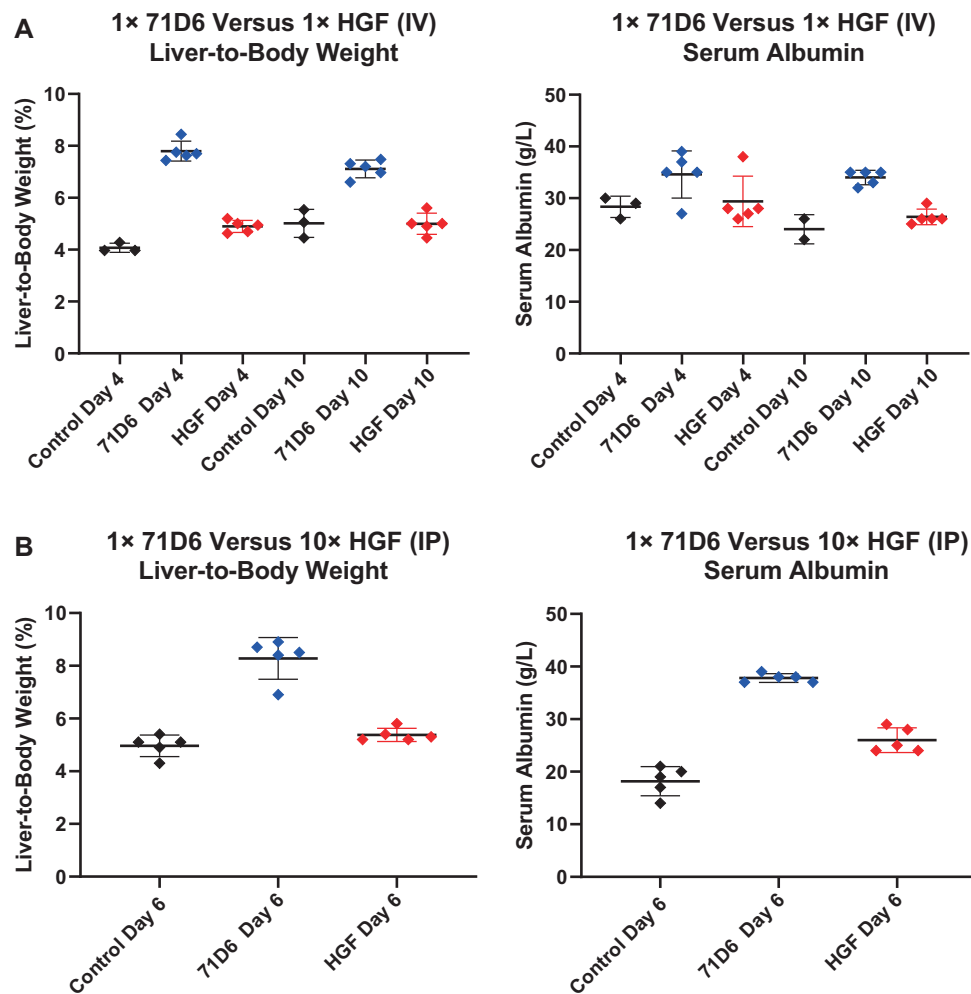


FIG. 2. 71D6 displays a potent hepatotrophic activity in mice. (A) A single 1 mg/kg bolus of 71D6 or human recombinant HGF was injected IV into adult Balb-c mice, and the liver-to-body weight and serum albumin levels were determined 4 and 8 days afterward. (B) A single 1 mg/kg bolus of 71D6 or multiple doses (10 over 5 days) of 1 mg/kg recombinant human HGF were injected IP into adult Balb-c mice. Liver-to-body weight and serum albumin levels were determined 6 days after the first injection. Black represents control group. Red represents HGF group. Blue represents 71D6 group.

mouse model of SFSS. This model reproduces the impaired regenerative capacity of the liver in patients with cirrhosis or other hepatic diseases. Mice were subjected to chronic CCl4 intoxication for 10 weeks and then

randomized into 2 arms receiving either 3 mg/kg 71D6 or a control IgG1. At 3 days after randomization, all mice were subjected to 70% hepatectomy. Mouse survival was recorded up to 28 days after hepatectomy.

Satellite animals were euthanized at different time points to analyze liver regeneration, fibrosis, and inflammation. This hepatectomy model typically presents high mortality within 4 days after surgery. Remarkably, the survival rate observed in the 71D6-treated group was significantly higher than that observed in the control group ($P = 0.03$). Although only 5 of 24 mice (21%) in the control group survived for 28 days after hepatectomy, 7 of 13 71D6-treated mice (54%) were alive at the end of the experiment (Fig. 3A). As shown in Fig. 3B, 71D6 also accelerated body weight recovery following surgery compared with controls ($P < 0.001$). Liver weight was also evaluated upon autopsy of satellite animals at various time intervals. As shown in Fig. 3C, 71D6 significantly increased the liver-to-body weight ratio at most time points analyzed (days 1 and 3, $P < 0.05$; day 7, nonsignificant; day 28, $P < 0.001$).

Consistent with these findings, serum albumin levels in 71D6-treated animals increased (Fig. 3D) and showed a significant difference with the control group starting on day 7 ($P < 0.01$) and reaching a peak on day 28 ($P < 0.01$). These data indicate that 71D6 treatment promotes liver regeneration and accelerates recovery of liver function after partial hepatectomy.

SERUM 71D6 PROMOTES HEPATIC PROLIFERATION FOLLOWING HEPATECTOMY THROUGH ACTIVATION OF THE ERK SIGNALING PATHWAY

Hepatocyte proliferation following hepatectomy was assessed by staining liver sections with anti-PCNA

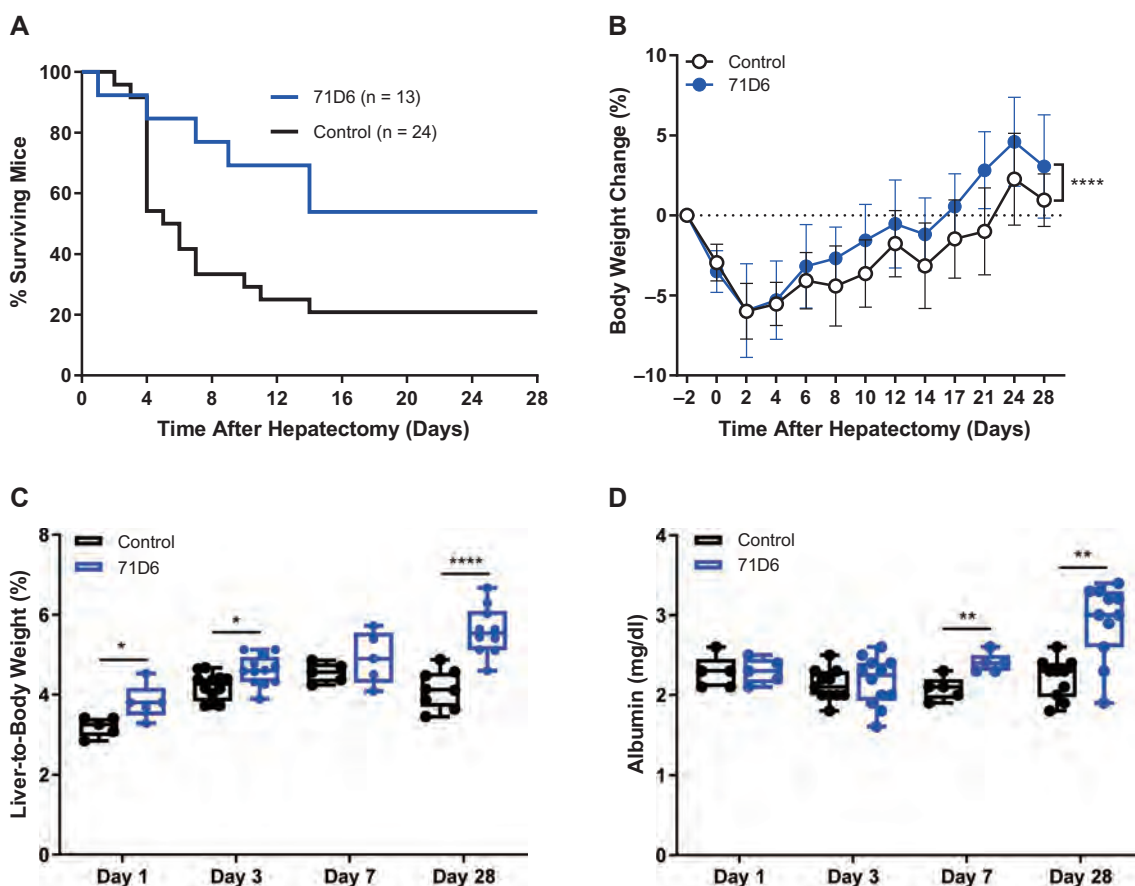


FIG. 3. 71D6 promotes liver regeneration and increases survival in mice undergoing CCl₄ injury and partial hepatectomy. (A) Kaplan-Meier curve analysis of mouse survival ($P = 0.03$). (B) Body weight change over time (mean \pm SD) ($P < 0.001$). (C) Liver-to-body weight over time (days 1 and 3, $P < 0.05$; day 7, nonsignificant; day 28, $P < 0.001$). (D) Serum albumin levels over time (days 1 and 3, nonsignificant; day 7, $P < 0.01$; day 28, $P < 0.01$).

antibodies. As shown in Fig. 4A, the number of PCNA-positive cells was higher in the 71D6-treated group starting at day 3 and peaking at day 28. To further characterize 71D6-induced liver proliferation, we analyzed the expression and activation of p44 ERK1 and p42 ERK2, a key event in the postinjury liver regeneration program.⁽¹⁵⁾ This analysis revealed that 71D6 significantly increased the levels of phosphorylated (activated) ERK1/2 on both day 3 and day 28 following hepatectomy (Fig. 4B). Activation of ERK1/2 directly correlated with PCNA expression, suggesting that 71D6 stimulates activation of ERK1/2 in the remnant liver, resulting in accelerated hepatic regeneration. Notably, however, no ERK1/2 activation was detected in control animals despite hepatectomy typically inducing spontaneous liver regeneration within a few days. This could be attributed to, and is consistent with, the impaired regenerative capacity of a cirrhotic liver. To cast light onto the mechanism underlying this regenerative impairment, we analyzed serum HGF levels in posthepatectomy mice as well as in healthy, naïve animals. This analysis revealed that posthepatectomy mice

treated with the control IgG protein displayed only a marginal increase in HGF levels compared with naïve mice (Fig. 3C). Interestingly, serum HGF levels were slightly higher in the 71D6 group, probably because of larger liver mass and/or increased hepatic function. In any case, serum HGF levels were confined to the picomolar range, whereas 71D6 levels measured in the same samples remained well above MET saturating levels for the entire duration of the study (full activation of MET is reached with 10 nM 71D6). These results explain the absence of ERK activation and the poor liver regeneration observed in the control group on one hand and justify the superior regenerative ability of the animals treated with 71D6 on the other hand.

SERUM 71D6 AMELIORATES HEPATIC FIBROSIS AFTER PARTIAL HEPATECTOMY ON CIRRHOTIC BACKGROUND

Sections of livers harvested from satellite animals were stained with H & E, PSR, and antibodies against

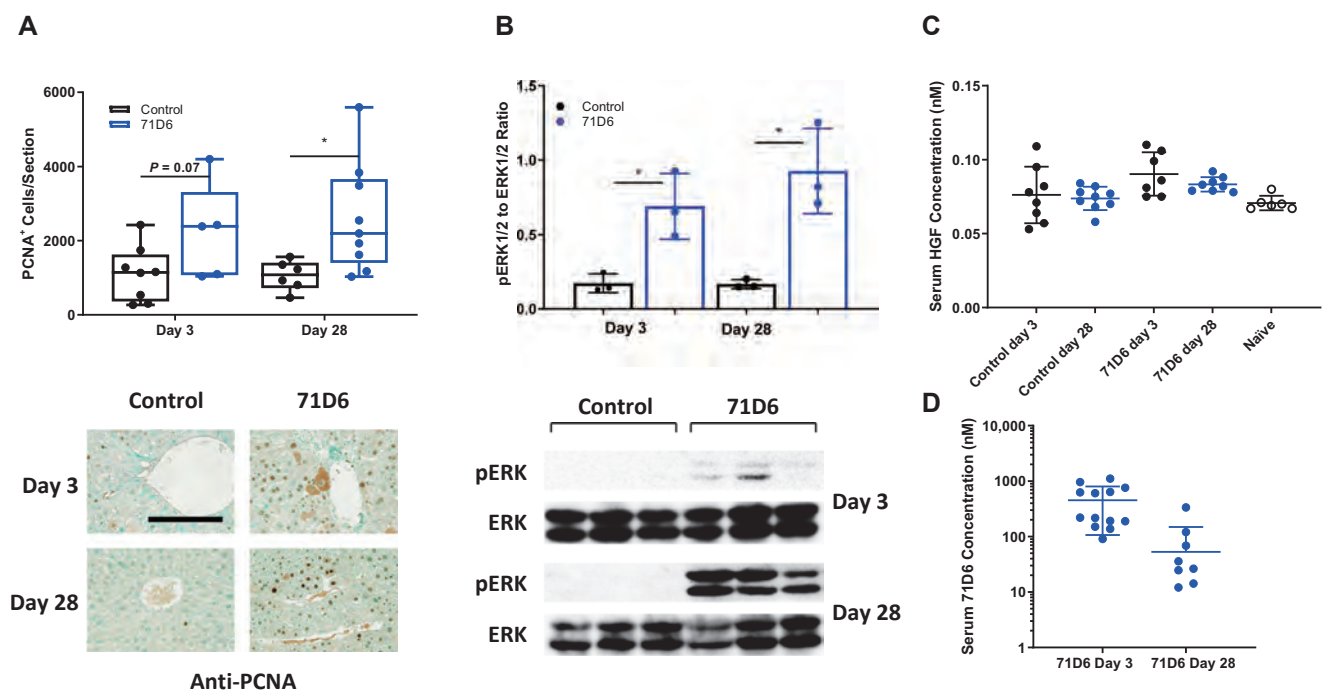


FIG. 4. 71D6 promotes hepatic proliferation following hepatectomy of cirrhotic mice through activation of the ERK signaling pathway. (A) Hepatic proliferation is expressed as the number of PCNA-positive cells per liver section analyzed. Representative images are shown below the graph. The bar is 250 μ M. (B) The levels of phosphorylated and total ERK1/2 (p44/p42) were determined by Western blot analysis of liver samples. The ratio between phosphorylated ERK1/2 and total ERK1/2 was determined by densitometric analysis. (C) Serum HGF levels in mice of the control and 71D6 groups as well as in healthy, naïve animals were determined by ELISA. (D) Serum 71D6 levels in mice of the 71D6 group were determined by ELISA.

desmin or α -SMA. Liver specimens of the control group showed consistent formation of thin fibrotic septa at the portal and central areas on day 3. Although milder, fibrosis was still present at day 28. Control liver sections also displayed high density of myofibroblasts. In contrast, liver specimens of the 71D6 group showed significantly milder signs of fibrosis and a reduced presence of myofibroblasts already at day 3. Liver fibrosis was quantified and expressed as the percentage of PSR-positive area (Fig. 5A), number of desmin-positive cells (Fig. 5B), and percentage of α -SMA-positive area (Fig. 5C). To further strengthen these results, the expression of fibrosis-related genes was analyzed by quantitative RT-PCR. This analysis revealed that 71D6 significantly reduced mRNA expression of platelet-derived growth factor (*PDGF*), tissue inhibitor of metalloproteinase 3 (*TIMP3*), and transforming growth factor β 1 (*TGF- β 1*), which are involved in collagen deposition and activation of HSCs (Fig. 5D). Together, these results suggest that in mice subjected to CC14 treatment and partial hepatectomy,

the agonistic anti-MET antibody 71D6 effectively accelerates the regression of hepatic fibrosis by inhibiting the activation of multiple fibrogenic pathways.

SERUM 71D6 REDUCES MACROPHAGE INFILTRATION IN THE REGENERATING LIVER

Liver specimens extracted at autopsy were analyzed by immunohistochemistry using antibodies against F4/80 and CD68. The number of cells positive for F4/80 ($P < 0.05$; Fig. 6A) and CD68 ($P < 0.0001$; Fig. 6B) was significantly lower in the 71D6 group compared with the control group on day 28. Consistent with histological findings, mRNA levels of inflammatory cytokine genes (tumor necrosis factor α [*TNF- α*], interleukin 1 β [*IL1 β*], chemokine [C-C motif] ligand 3 [*CCL3*], and chemokine [C-C motif] ligand 5 [*CCL5*]) were significantly lower in the liver homogenates of 71D6-treated mice compared with control mice on day 28 ($P < 0.05$; Fig. 6C).

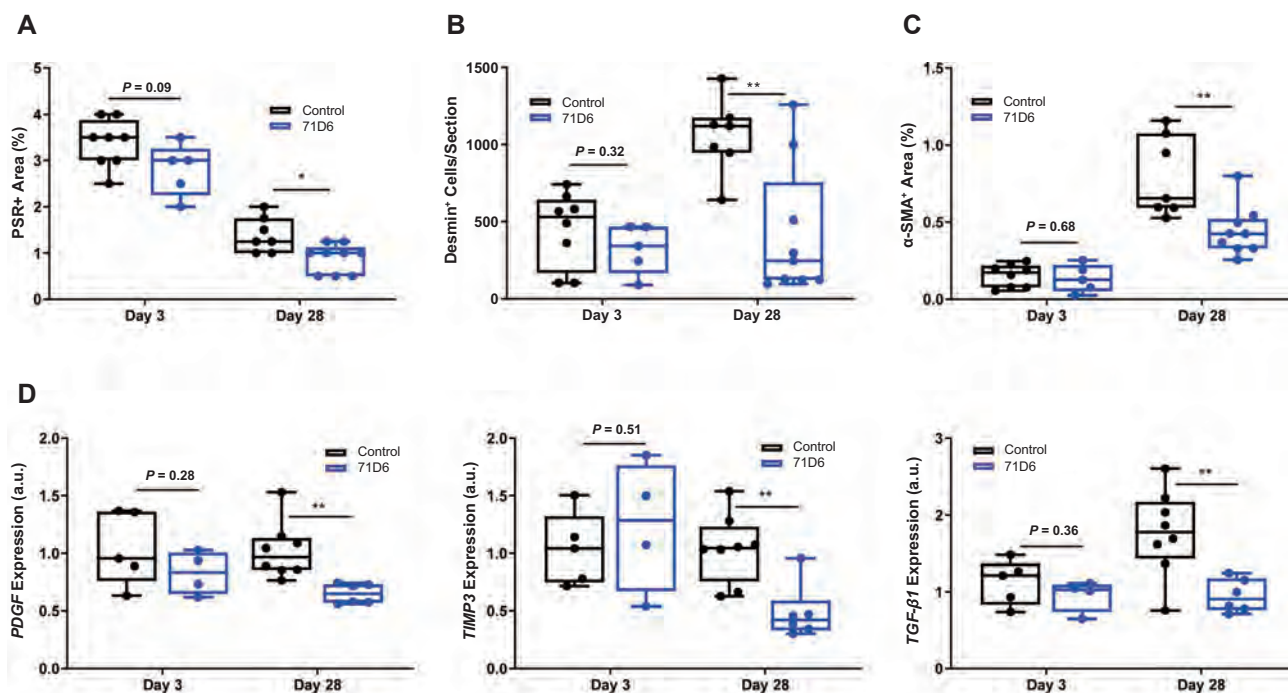


FIG. 5. 71D6 ameliorates hepatic fibrosis after partial hepatectomy on cirrhotic background. (A) Liver sections were stained with PSR. Data are expressed as percentage of PSR-positive area. (B) Liver sections were stained with anti-desmin antibodies. Data are expressed as number of desmin-positive cells per section analyzed. (C) Liver sections were stained with anti- α -SMA antibodies. Data are expressed as percentage of α -SMA-positive area. (D) Liver specimens were analyzed by RT-PCR to determine the levels of *PDGF*, *TGF- β 1*, and *TIMP3* expression. Data are expressed as a.u.

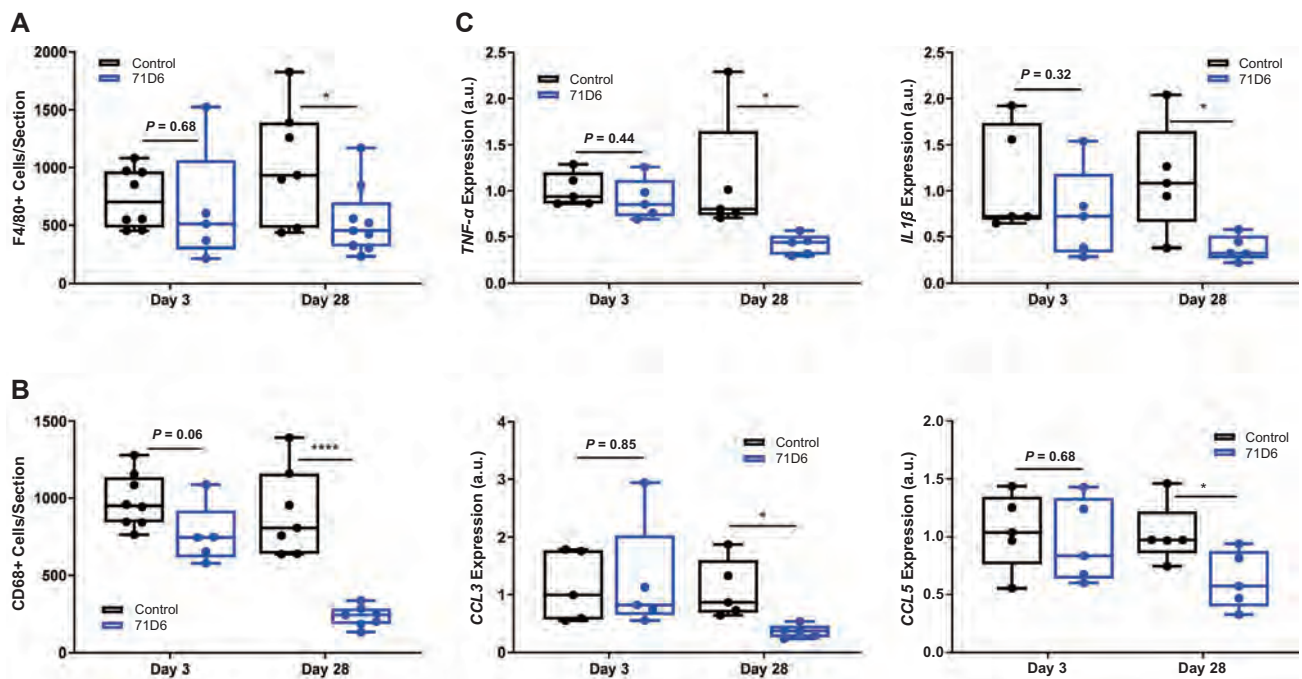


FIG. 6. 71D6 reduces macrophage infiltration in the regenerating liver. (A) Liver sections were stained with anti-F4/80 antibodies. Data are expressed as number of F4/80-positive cells per section analyzed. (B) Liver sections were stained with anti-CD68 antibodies. Data are expressed as number of CD68-positive cells per section analyzed. (C) Liver specimens were analyzed by RT-PCR to determine the levels of *TNF- α* , *IL1 β* , *CCL3*, and *CCL5* expression. Data are expressed as a.u.

Discussion

Liver failure is prone to occur after liver transplantation or extended resection when the size and function of the remnant liver is unable to meet the metabolic demand of the patient. SFSS limits the use of living donor and split-liver transplants, and lifesaving large resections of tumors or nonmalignant lesions may be limited by concerns of postsurgical liver failure. Furthermore, SFSS is analogous to end-stage liver disease where the functional liver mass no longer meets metabolic demand. Therefore, there is a major need for effective therapies capable of enhancing and accelerating liver regeneration.

Most studies evaluating regenerative therapies take advantage of the 70% hepatectomy model in mice or rats. In this model, 70% of the liver, usually the median and left lateral lobes, is surgically removed. In response to this, the remnant liver enlarges until it restores normal mass and function. Although the liver has a remarkable potential for regeneration, this regenerative capacity becomes impaired with serious

liver fibrosis.⁽¹⁶⁾ The transition of quiescent HSCs to activated, scar-forming, myofibroblast-like cells leads to excessive extracellular matrix synthesis.^(17,18) This abnormal scar formation in the liver has been shown to hold back hepatocyte proliferation. In the present study, we studied a newly developed agonistic anti-MET antibody that increased hepatocyte proliferation after partial hepatectomy in mice with CCl₄-induced liver disease.

Following 70% hepatectomy, both hepatocytes and nonparenchymal cells are activated and integrate multiple signals originating from immune, hormonal, and metabolic networks to induce liver regeneration.⁽¹⁹⁾ Within this process, the activation of HGF/MET signaling pathway has been demonstrated to be 1 of the essential mechanisms that lead hepatocytes into the cell cycle after hepatectomy.⁽²⁰⁾ Following resection, HGF protein levels in plasma typically rise,⁽²¹⁾ but liver fibrosis is known to prevent this process. The lack of HGF induction on a cirrhotic background was fully confirmed in our study (Fig. 4C). To circumvent defective endogenous HGF activation, we employed

the 71D6 agonistic anti-MET antibody. When bound by 71D6, the MET receptor dimerizes and becomes phosphorylated on tyrosine residues to initiate MET downstream signaling (Fig. 1).

The results presented here indicate that liver-to-body weight ratio increased very slowly in the control group, whereas it increased markedly and constantly in the 71D6-treated group (Fig. 3). Quantitative analysis of PCNA immunostaining also confirmed that the agonistic anti-MET antibody potently promotes hepatocyte proliferation (Fig. 4A). We also clarified the involvement of the ERK1/2 signaling pathway in this hepato-proliferative effect. It is known that the Ras/Raf/MEK/ERK cascade has the ability to lead to cellular responses, including proliferation. The ERK1/2 signaling pathway can also regulate the hepatocyte proliferative response during the regeneration of normal liver.⁽²²⁾ Our Western blot results showed that 71D6 strongly activated ERK p44/p42, closely reflecting the high levels of PCNA expression (Fig. 4B). Our results clearly show that 71D6 has the ability to mimic HGF signaling in vivo, including activation of downstream kinases and promotion of hepatocyte proliferation. However, in contrast to HGF, 71D6 is very stable in vivo (Table 2) and displays superior pharmacodynamic properties (Fig. 2). These results highlight the therapeutic potential of 71D6 in liver regeneration.

Liver fibrosis is an inadequate wound-healing response to chronic liver injury and is characterized by the excessive deposition and reduced degradation of the extracellular matrix. Excessive accumulation of extracellular matrix alters the hepatic architecture to progress to liver fibrosis, and if not prevented it may eventually lead to cirrhosis and even liver cancer. Our study provides evidence that 71D6 treatment leads to a significantly lower degree of collagen, desmin, and α -SMA compared with controls (Fig. 5A,B). This is explained by the direct inhibition of multiple fibrogenic pathways including those controlled by *PDGF*, *TIMP3*, and *TGF- β 1* (Fig. 5C). These data support the hypothesis that 71D6 has the ability to antagonize TGF- β 1 directly so as to reduce liver fibrosis and improve liver regeneration.⁽²³⁾

Furthermore, our study showed that 71D6 also inhibited the infiltration of inflammatory cells into the liver. In fact, the number of F4/80-positive and CD68-positive cells in the 71D6 group was significantly lower than that observed in the control group (Fig. 6A,B). Consistent with these findings, qRT-PCR analysis revealed that the expressions of proinflammatory

cytokines and chemokines such as TNF- α , IL1 β , CCL3, and CCL5 were much lower in the liver homogenates of 71D6-treated mice compared with control animals (Fig. 6C).

Thus, not only does 71D6 overcome the inability of a cirrhotic liver to regenerate following hepatectomy, but it also achieves faster resolution of fibrosis and the effective suppression of inflammation. Together, these results suggest that activating the MET pathway via an HGF-mimetic antibody may be beneficial in patients with SFSS and possibly other types of acute and chronic liver disorders.

Acknowledgments: The authors thank Philippe Wiesel for critically reading the manuscript, Luca Rossi for in vivo work, Damiana Sattanino for assay setup, and the entire AgomAb team for continuous support.

REFERENCES

- 1) Riddiough GE, Christophi C, Jones RM, Muralidharan V, Perini MV. A systematic review of small for size syndrome after major hepatectomy and liver transplantation. *HPB* 2020;22:487-496.
- 2) Masuda Y, Yoshizawa K, Ohno Y, Mita A, Shimizu A, Soejima Y. Small-for-size syndrome in liver transplantation: definition, pathophysiology and management. *Hepatobiliary Pancreat Dis Int* 2020;19:334-341.
- 3) Zhong Z, Schwabe RF, Kai Y, He L, Yang L, Bunzendahl H, et al. Liver regeneration is suppressed in small-for-size liver grafts after transplantation: involvement of c-Jun N-terminal kinase, cyclin D1, and defective energy supply. *Transplantation* 2006;82:241-250.
- 4) Greenbaum LE, Ukomadu C, Tchorz JS. Clinical translation of liver regeneration therapies: a conceptual road map. *Biochem Pharmacol* 2020;175:113847.
- 5) Forbes SJ, Newsome PN. Liver regeneration—mechanisms and models to clinical application. *Nat Rev Gastroenterol Hepatol* 2016;13:473-485.
- 6) Nakamura T, Mizuno S. The discovery of hepatocyte growth factor (HGF) and its significance for cell biology, life sciences and clinical medicine. *Proc Jpn Acad Ser B Phys Biol Sci* 2010;86:588-610.
- 7) Matsumoto K, Funakoshi H, Takahashi H, Sakai K. HGF-Met pathway in regeneration and drug discovery. *Biomedicines* 2014;2:275-300.
- 8) Nakamura T, Sakai K, Nakamura T, Matsumoto K. Hepatocyte growth factor twenty years on: much more than a growth factor. *J Gastroenterol Hepatol* 2011;26(suppl 1):188-202.
- 9) Klarenbeek A, Blanchetot C, Schragel G, Sadi AS, Ongenaes N, Hemrika W, et al. Combining somatic mutations present in different in vivo affinity-matured antibodies isolated from immunized *Lama glama* yields ultra-potent antibody therapeutics. *Protein Eng Des Sel* 2016;29:123-133.
- 10) Michieli P. Anti-Met antibodies and uses thereof. European patent application EP 3475302 A1 2019. <https://www.lens.org/lens/patent/062-815-545-734-095>.
- 11) Cingoz O. Motavizumab. *mAbs* 2009;1:439-442.
- 12) Ido A, Moriuchi A, Kim I, Numata M, Nagata-Tsubouchi Y, Hasuike S, et al. Pharmacokinetic study of recombinant human

hepatocyte growth factor administered in a bolus intravenously or via portal vein. *Hepatol Res* 2004;30:175-181.

- 13) Ido A, Moriuchi A, Numata M, Murayama T, Teramukai S, Marusawa H, et al. Safety and pharmacokinetics of recombinant human hepatocyte growth factor (rh-HGF) in patients with fulminant hepatitis: a phase I/II clinical trial, following preclinical studies to ensure safety. *J Transl Med* 2011;9:55.
- 14) Xue F, Takahara T, Yata Y, Minemura M, Morioka CY, Takahara S, et al. Attenuated acute liver injury in mice by naked hepatocyte growth factor gene transfer into skeletal muscle with electroporation. *Gut* 2002;50:558-562.
- 15) Tao Y, Wang M, Chen E, Tang H. Liver regeneration: analysis of the main relevant signaling molecules. *Mediators Inflamm* 2017;2017:4256352.
- 16) Chan A, Kow A, Hibi T, Di Benedetto F, Serrablo A. Liver resection in cirrhotic liver: are there any limits? *Int J Surg* 2020;82S:109-114.
- 17) Issa R, Zhou X, Trim N, Millward-Sadler H, Krane S, Benyon C, Iredale J. Mutation in collagen-1 that confers resistance to the action of collagenase results in failure of recovery from CCl4-induced liver fibrosis, persistence of activated hepatic stellate cells, and diminished hepatocyte regeneration. *FASEB J* 2003;17:47-49.
- 18) Henderson NC, Forbes SJ. Hepatic fibrogenesis: from within and outwith. *Toxicology* 2008;254:130-135.
- 19) Yagi S, Hirata M, Miyachi Y, Uemoto S. Liver regeneration after hepatectomy and partial liver transplantation. *Int J Mol Sci* 2020;21:8414.
- 20) Thorgeirsson SS. The central role of the c-Met pathway in rebuilding the liver. *Gut* 2012;61:1105-1106.
- 21) Eguchi S, Yanaga K, Okudaira S, Sugiyama N, Miyamoto S, Furui J, Kanematsu T. Changes in serum levels of hepatocyte growth factor in patients undergoing adult-to-adult living-donor liver transplantation. *Transplantation* 2003;76:1769-1770.
- 22) Chen XG, Xu CS, Liu YM. Involvement of ERK1/2 signaling in proliferation of eight liver cell types during hepatic regeneration in rats. *Genet Mol Res* 2013;12:665-677.
- 23) Fabregat I, Moreno-Cáceres J, Sánchez A, Dooley S, Dewidar B, Giannelli G, ten Dijke P. TGF- β signalling and liver disease. *FEBS J* 2016;283:2219-2232.



OPEN

Coral calcium carried hydrogen ameliorates the severity of non-alcoholic steatohepatitis induced by a choline deficient high carbohydrate fat-free diet in elderly rats

Kuai Ma¹, Xin Hu¹, Keiki Nambu², Daisuke Ueda³, Naotsugu Ichimaru⁴, Masayuki Fujino^{1,5}✉ & Xiao-Kang Li¹✉

Hydrogen has been reported to act as an antioxidant, anti-apoptosis and anti-inflammatory agent. Coral calcium carried hydrogen (G2-SUIISO) is a safer and more convenient form of hydrogen agent than others. The mechanism underlying the hepatoprotective effects of G2-SUIISO using an elderly non-alcoholic steatohepatitis (NASH) rat model was investigated. Two days after fasting, six-month-old elderly male F344/NSlc rats were given a choline deficient high carbohydrate fat-free (CDHCFF) diet from day 0 to day 3 as CDHCFF control group, and then switched to a normal diet from days 4 to 7 with or without 300 mg/kg G2-SUIISO. Rats in each group were finally being sacrificed on day 3 or day 7. In the CDHCFF diet group, G2-SUIISO decreased the liver weight-to-body weight ratio, the serum AST, ALT, total cholesterol levels, inflammatory infiltration, pro-inflammatory cytokine expression and lipid droplets with inhibiting lipogenic pathways by reducing sterol regulatory element-binding protein-1c, acetyl-CoA carboxylase and fatty acid synthase gene expression compared with the CDHCFF diet alone. G2-SUIISO had beneficial effects of anti-apoptosis as well the down-regulation of pro-apoptotic molecules including NF- κ B, caspase-3, caspase-9 and Bax. These findings suggest that G2-SUIISO treatment exerts a significant hepatoprotective effect against steatosis, inflammation and apoptosis in elderly NASH rats.

Abbreviations

ACC	Acetyl-CoA carboxylase
ALT	Alanine transaminase
AST	Aspartate transaminase
Bax	Bcl-2-associated X
CCR2	C-C chemokine receptor type 2
CDHCFF	Choline deficient high carbohydrate fat-free
FAS	Fatty acid synthase
FFAs	Free fatty acids
G2-SUIISO	Coral calcium carried hydrogen G2
HCC	Hepatocellular carcinoma
H ₂	Hydrogen
HSCs	Hepatic stellate cells

¹Division of Transplantation Immunology, National Research Institute for Child Health and Development, 2-10-1 Okura, Setagaya-ku, Tokyo 157-8535, Japan. ²Acche Corporation, Tokyo, Japan. ³Division of Hepato-Pancreato-Biliary Surgery and Transplantation, Department of Surgery, Kyoto University Graduate School of Medicine, Kyoto, Japan. ⁴Department of Urology, Kinki Central Hospital, Hyogo, Japan. ⁵Management Department of Biosafety, Laboratory Animal, and Pathogen Bank, National Institute of Infectious Diseases, 1-23-1, Toyama, Shinjuku-ku, Tokyo 162-8640, Japan. ✉email: mfujino-kkr@umin.ac.jp; ri-k@ncchd.go.jp

IL-6	Interleukin 6
IL-1 β	Interleukin-1 beta
IFN- γ	Interferon-gamma
iNOS	Inducible nitric oxide synthase
LDs	Lipid droplets
mRNA	Messenger RNA
NASH	Non-alcoholic steatohepatitis
NAFLD	Non-alcoholic fatty liver disease
NF κ B	Nuclear factor- κ B
OB-R	Leptin receptor
OPN	Osteopontin
ROS	Reactive oxygen species
RT-PCR	Real time-polymerase chain reaction
SREBP-1c	Sterol regulatory element-binding protein-1c
TC	Total cholesterol
TNF- α	Tumor necrosis factor-alpha

Non-alcoholic fatty liver disease (NAFLD) is the most common chronic liver disorder associated with metabolic dysfunction and is a leading cause of cirrhosis and hepatocellular carcinoma (HCC) with a global prevalence of 25%¹. It usually develops in the absence of excessive alcohol consumption and is associated with an unhealthy diet and lack of physical activity. Non-alcoholic steatohepatitis (NASH) is a progressive form of NAFLD, characterized by chronic inflammation and hepatocyte injury due to fat accumulation². A community-based study found that fatty liver is prevalent in the elderly population, with a prevalence of over 40%³.

Aging is a complex phenomenon characterized by the gradual decline of the tissue and organ function accompanying the irreversible age-related loss of viability. Impairment of the liver function and development of NAFLD are common among the elderly⁴. Accumulating evidence has pointed out that the process of aging itself markedly increases the prevalence of metabolic syndrome in humans, reportedly being a risk factor of NAFLD⁵, as it predisposes individuals to hepatic functional and structural impairment and metabolic risk. Oxidative stress is considered the primary cause of general aging as well as diseases associated with aging, especially metabolic diseases⁶. Oxidative stress, lipotoxicity and inflammation⁷ have been shown to play central roles in the development and progression of NAFLD. Furthermore, the progressively increased production of reactive oxygen species (ROS) during the aging process contributes to the accumulation of lipids, particularly cholesterol, in the liver of elderly individuals⁸.

Molecular hydrogen (H₂) was previously reported to act as an antioxidant for preventive and therapeutic applications by selectively alleviating cytotoxic oxygen radicals without affecting other ROS⁹. Previous studies have reported that H₂ functions as an antioxidant, anti-apoptosis and anti-inflammatory agent in many animal models and human clinical studies¹⁰. Among these studies, H₂ administration can be roughly divided into inhaling H₂ gas, drinking H₂ dissolved water and injecting H₂ dissolved saline¹¹. In our present study, we used coral calcium carried hydrogen (G2-SUIISO), which is a safer and more convenient form of H₂ agent than others, as the source of H₂. In general, H₂ cannot be kept in supplements as-is. Coral powder was therefore selected as the material to convey H₂, and we employed a unique method to successfully immobilize H₂ on the surface of the carrier coral calcium. When the coral calcium enters the body, hydrogen is generated upon contact with moisture.

The present study investigated the potential effects of G2-SUIISO with the goal of evaluating whether or not G2-SUIISO could attenuate the severity of NASH induced by a choline deficient high carbohydrate fat-free (CDHCFF) diet in elderly rats.

Results

G2-SUIISO attenuated CDHCFF-induced nonalcoholic steatohepatitis. As shown in Fig. 1B and Supplementary Fig. 3A, the liver weight-to-body weight ratio in the 3d_control group was significantly higher ($p < 0.0001$) than that in the Naïve group, while this value was lower ($p < 0.01$) in the 3d_G2 group. Furthermore, the liver weight-to-body weight ratio in the 7d_G2 group was down-regulated ($p < 0.05$) compared with the 7d_control group as well. The above results suggested that CDHCFF administration resulted in liver enlargement, and going back to eating normal diet again with G2-SUIISO treatment significantly attenuated this CDHCFF-induced liver enlargement.

NASH is characterized as the excessive accumulation of TC in lipid droplets (LDs) in hepatocytes, and ALT and AST activities are important biomarkers of liver damage or diseases⁸. G2-SUIISO significantly reduced the serum ALT, AST and TC levels in elderly NASH rats (Fig. 1C). The serum ALT and AST levels both notably differed between the 3d_control group and 3d_G2 group ($p < 0.001$), indicating that a CDHCFF diet caused severe hepatocellular injury in rats. Compared with the 3d_control group, the serum ALT and AST levels in the 3d_G2 group were markedly decreased. In addition, the serum TC levels were higher in the 3d/7d_control group than in the 3d/7d_G2 group ($p < 0.05$ and $p < 0.05$, respectively) suggesting that G2-SUIISO had notable effects of attenuating CDHCFF-induced NASH. In contrast, serum triglyceride (TG) was significantly decreased by CDHCFF diet and G2-SUIISO treatment showed comparable concentrations (Supplementary Fig. 3B). Based on the HE staining of liver specimens in Fig. 1D, we observed that the normal liver showed a clear and homogeneous texture, while the CDHCFF groups developed hepatocyte steatosis, ballooning and inflammatory cell infiltration on day 3 that was relieved on day 7. Compared with the CDHCFF diet groups, hepatocyte ballooning and steatosis in rat specimens were clearly reduced in the G2-SUIISO groups on days 3 and 7 (Fig. 1E, $p < 0.001$, $p < 0.001$, respectively), suggesting that G2-SUIISO ameliorated hepatic steatosis in NASH rats.

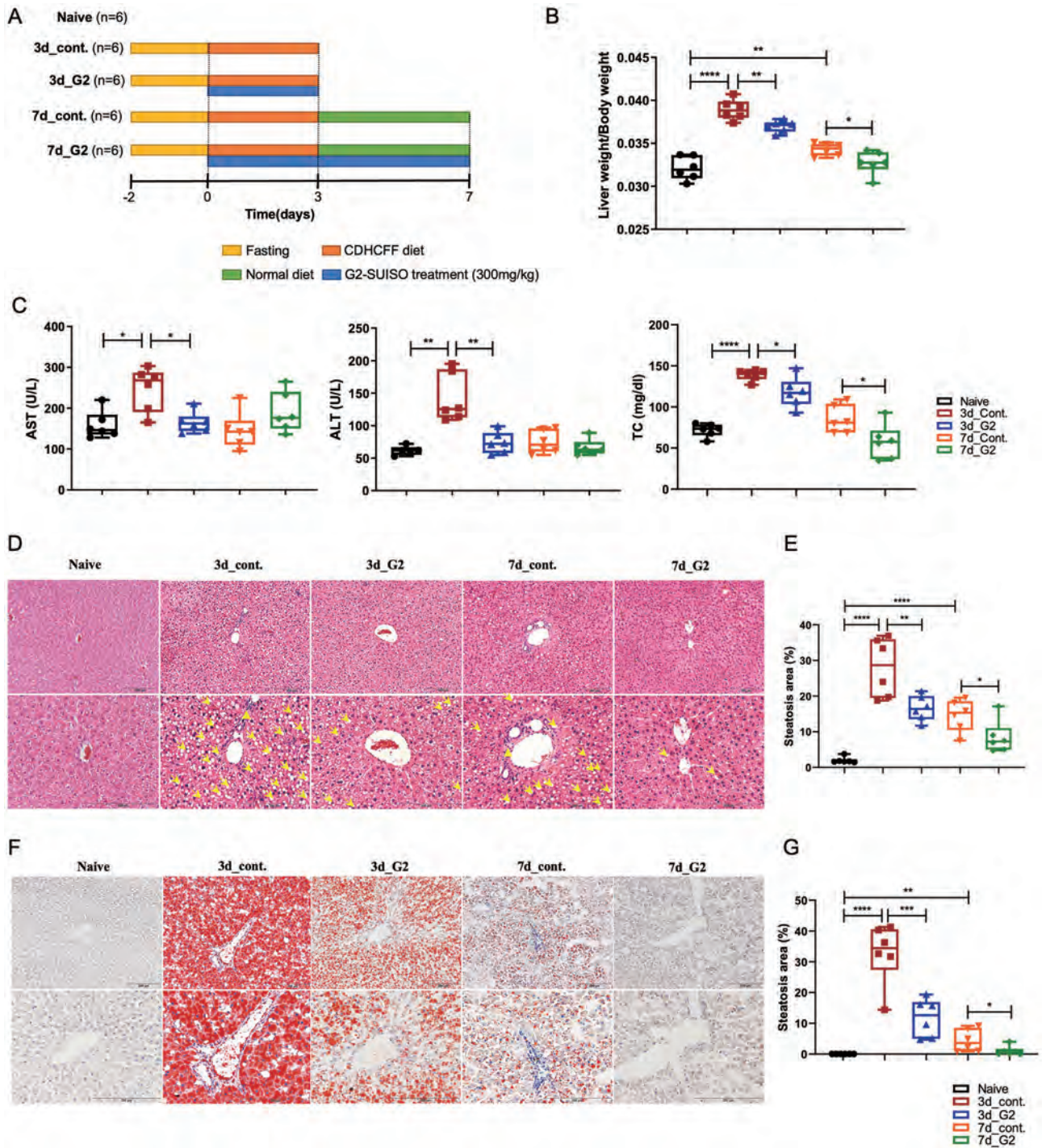


Figure 1. G2-SUIISO attenuated CDHCFE-induced nonalcoholic steatohepatitis. (A) The experimental design and timeline of the groups was shown. (B) The liver weight-to-body weight ratio in the five groups is shown. (C) G2-SUIISO treatment significantly reduced serum ALT, AST and TC levels in NASH rats. (D) Hematoxylin and eosin (HE) staining of liver specimens in different groups suggested that G2-SUIISO improved hepatic steatosis in NAFLD rats. The yellow triangle represents the area of inflammatory cell infiltration. White vacuoles showed lipids (yellow arrow) in HE staining (magnification $\times 100$ & $\times 200$). (E) An analysis of the HE staining of fatty liver specimens is shown. Each bar represents the mean \pm SD. (F) Liver sections of five groups were stained by Oil Red O solution. Red areas showed lipids in Oil Red O staining (magnification $\times 100$ & $\times 200$). (G) An analysis of the Oil Red O staining of fatty liver specimens is shown. Each bar represents the mean \pm SD; * $p < 0.05$, ** $p < 0.01$, *** $p < 0.001$, **** $p < 0.0001$.

To further explore the protective effects of G2-SUIISO on reducing steatosis in elderly NASH rats, liver sections from the five groups were subjected to Oil red O staining, which was used to measure fat loading in the hepatocytes. Based on Fig. 1F, we can see that G2-SUIISO decreased intracellular lipid deposition in the livers of the CDHCFF group. A histological analysis of Oil Red O staining revealed a significant increase in intracellular lipid deposition in the livers of the 3d_CDHCFF group and 7d_CDHCFF group ($p < 0.0001$ and $p < 0.01$, respectively) (Fig. 1G). Numbers of LDs were markedly reduced in the livers of G2-SUIISO-treated mice on days 3 and 7 ($p < 0.001$ and $p < 0.05$, respectively).

G2-SUIISO exerted protective effects against inflammation. Among cytokine-related to the progression of NASH, tumor necrosis factor-alpha (TNF- α) plays a pivotal role in the inflammatory pathogenesis of NASH¹². As shown in Fig. 2A, hepatic mRNA expression of inflammatory cytokine-related genes, particularly TNF- α , inducible nitric oxide synthase (iNOS), osteopontin (OPN), interferon-gamma (IFN- γ), interleukin-1 beta (IL-1 β), IL-6 and C-C chemokine receptor type 2 (CCR2), were significantly higher following administration of an CDHCFF diet. In contrast, the expression of TNF- α , iNOS and CCR2 was lower in the 3d_G2 group than in the 3d_control group ($p < 0.01$, $p < 0.05$ and $p < 0.01$, respectively). The IFN- γ , OPN, IL-1 β and IL-6 expression was down-regulated as well but without a significant difference. After the administration of G2-SUIISO for 7 days, TNF- α and IL-1 β showed notable reductions in expression ($p < 0.01$ and $p < 0.01$, respectively). The infiltration of neutrophils in liver was assessed using chloroacetate esterase staining of liver specimens. The hepatic expression of neutrophils was significantly increased in the CDHCFF diet control group compared with Naïve group on days 3 and 7 ($p < 0.05$ and $p < 0.05$, respectively) (Fig. 2B,C). Following the administration of G2-SUIISO, the neutrophil numbers in NASH liver specimens were reduced on days 3 and 7 ($p < 0.05$ and $p < 0.05$, respectively), and only a few scattered inflammatory foci were observed compared with

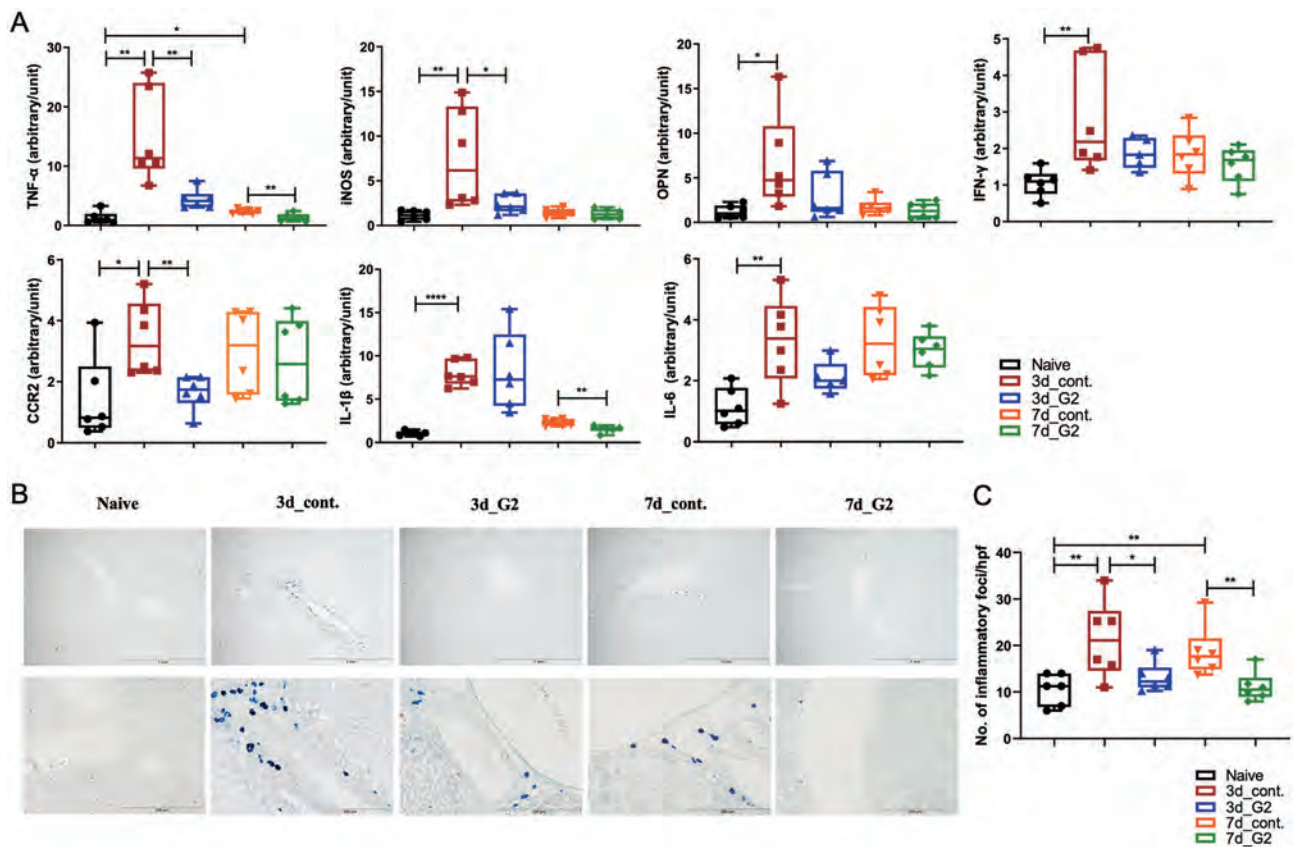


Figure 2. G2-SUIISO reduced the mRNA expression of inflammatory cytokine-related genes. (A) Homogenates of liver tissues were analyzed by qRT-PCR, as described in the Materials and Methods. The mRNA expression of inflammatory cytokine-related genes, particularly TNF- α , iNOS and CCR2, was significantly lower in the 3d_G2 group than in the 3d_control group. The mRNA expression of inflammatory cytokine-related genes, such as IFN- γ , OPN, IL-1 β and IL-6, tended to be down-regulated following G2-SUIISO treatment. Values are expressed as the mean \pm SD in arbitrary units; * $p < 0.05$, ** $p < 0.01$, **** $p < 0.0001$. (B) Chloroacetate esterase staining of liver specimens with inflammatory foci in the five groups is shown (magnification $\times 40$ & $\times 200$). (C) Analysis results of chloroacetate esterase staining of fatty liver specimens are shown. A total of 4 high power fields (hpf) ($\times 40$) were randomly selected from each liver specimens ($n = 5$), and the number of inflammatory foci was counted. The data are expressed as the cell number/high-power field. Each bar represents the mean \pm SD; * $p < 0.05$.

the control group. In addition, the infiltration of T cells and macrophages in the liver was also analyzed using CD3 and ED1 monoclonal antibody. Both expressions in the liver specimens were increased in the 3d_CDHCFF group compared to the Naïve group ($p < 0.01$ and $p < 0.01$, respectively), and G2-SUIISO treatment decreased the infiltration of CD3- and ED1-positive cells (Supplementary Fig. 2). Taken together, these findings suggested that G2-SUIISO might prevent inflammation and inflammatory cell infiltration in the NASH elderly model liver.

G2-SUIISO exerted anti-apoptotic effects. Previous studies have reported that increased hepatocyte apoptosis may play an important role in controlling the development of NASH¹³. As shown in Fig. 3A, the mRNA expression of apoptosis-related molecules, particularly Bax, caspase-1, caspase-3 and NF- κ B, was markedly up-regulated in the 3d_CDHCFF control group compared with Naïve group ($p < 0.0001$, $p < 0.001$, $p < 0.0001$ and $p < 0.0001$, respectively). The mRNA expression of Bax showed a significant decrease ($p < 0.05$) in the 7d_G2 group, and that of caspase-1, caspase-3 and NF- κ B showed decreasing trend. Furthermore, the mRNA expression of caspase-3 in the 3d_G2 group showed decreasing trend compared with the 3d_control group.

To confirm the anti-apoptosis effect of G2-SUIISO, we measured the protein levels of caspase-1, caspase-3, caspase-9 and NF- κ B in liver tissues in the Naïve group, 3d_control group and 3d_G2 group by Western blotting (Fig. 3B). After a densitometric analysis of the signals, we found that the expression of caspase-3, caspase-9 and NF- κ B was significantly reduced by the treatment of G2-SUIISO ($p < 0.05$, $p < 0.01$ and $p < 0.05$, respectively), whereas the caspase-1 expression showed no significant difference from before treatment.

G2-SUIISO reduced steatosis in CDHCFF-induced NASH. As a pathological analysis showed that G2-SUIISO reduced the lipid deposition caused by an CDHCFF diet in the liver (Fig. 1C–F), the mRNA expression of fatty acid uptake- and lipid metabolism-related cytokine-related genes in the five groups, particularly leptin receptor (OB-R), fatty acid synthase (FAS) and acetylCoA carboxylase (ACC), as well as sterol regulatory element-binding protein-1c (SREBP-1c) was measured. In Fig. 4, the mRNA expression of the OB-R, ACC and FAS genes increased significantly in the 3d_CDHCFF control group compared with the Naïve group ($p < 0.001$, $p < 0.0001$ and $p < 0.0001$, respectively). The SREBP-1c gene expression in the 3d_CDHCFF control group also showed an increasing trend but without significance. G2-SUIISO markedly down-regulated the expression of OB-R compared with the 3d_CDHCFF control group ($p < 0.05$) and tended to down-regulate the expression of ACC and SERBP-1c. After 7 days of G2-SUIISO administration, the mRNA expression of SREBP-1c, ACC

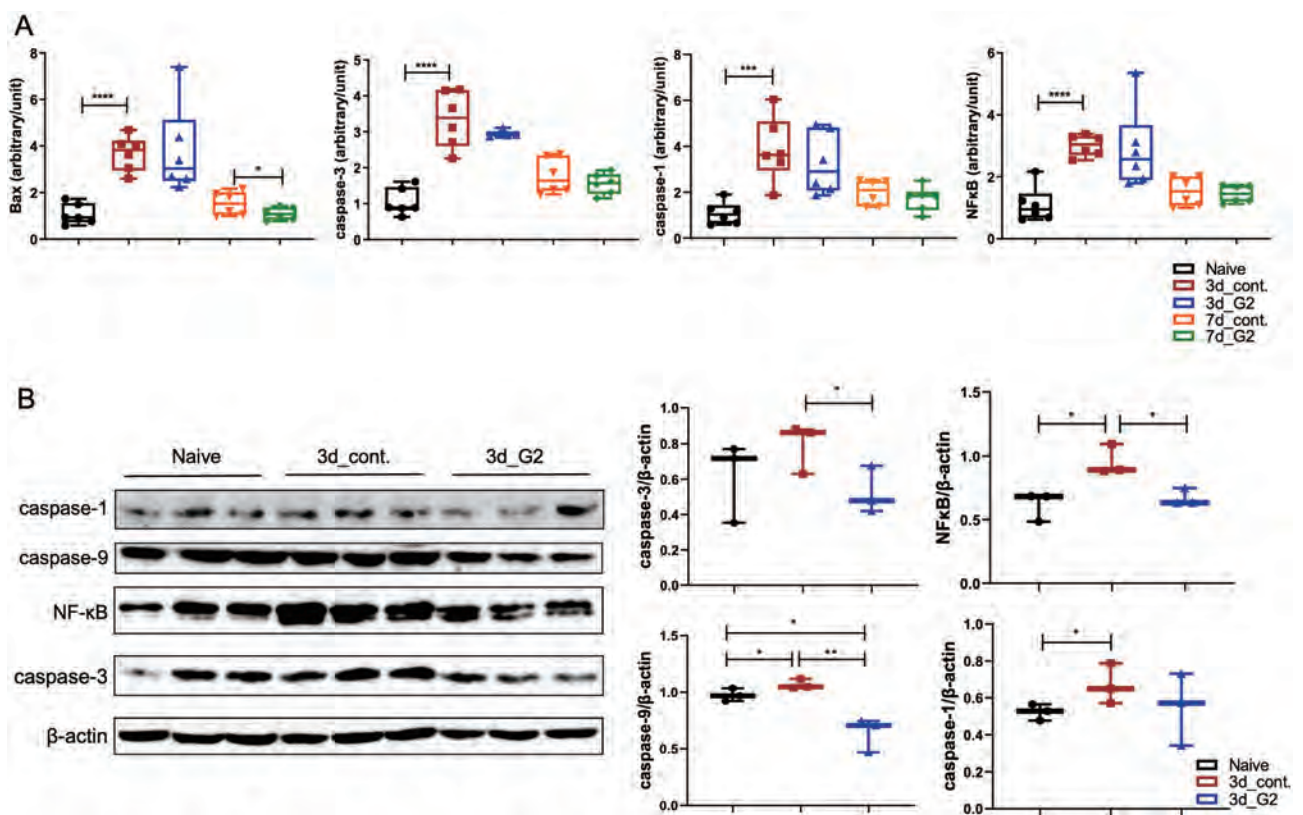


Figure 3. G2-SUIISO reduced the mRNA expression of apoptotic molecules. (A) The mRNA expression of apoptosis-related genes in the five groups, particularly Bax, caspase-1, caspase-3 and NF- κ B, is shown. (B) Results of a Western blot analysis of caspase-1, caspase-3, caspase-9 and NF- κ B levels in the liver tissue of the Naïve group, 3d_control group and 3d_G2 group are shown. Data are expressed as the mean \pm SD; * $p < 0.05$, ** $p < 0.01$, *** $p < 0.001$, **** $p < 0.0001$.

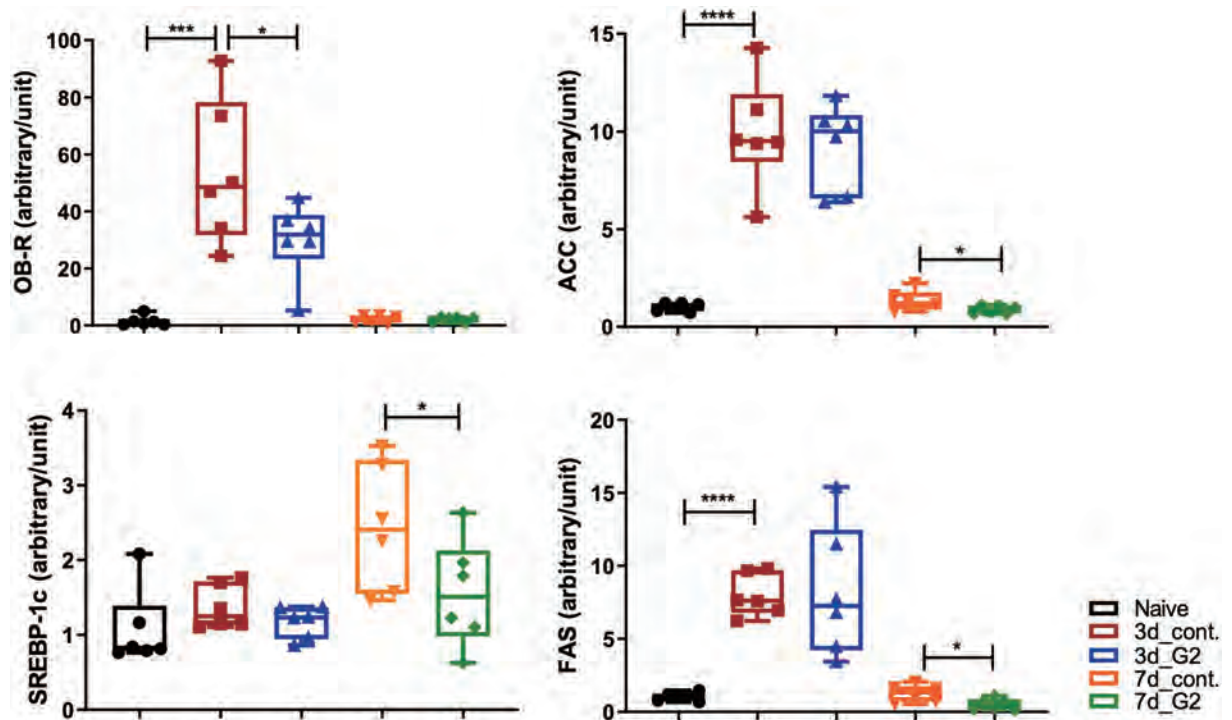


Figure 4. G2-SUISO reduced hepatocyte steatosis in CDHCF diet-induced nonalcoholic steatohepatitis rat. The mRNA expression of fatty acid uptake- and lipid metabolism-related genes in the five groups, particularly leptin receptor (OB-R), fatty acid synthase (FAS) and acetylCoA carboxylase (ACC), as well as sterol regulatory element-binding protein-1c (SREBP-1c) are shown. Data are expressed as the mean \pm SD; * p < 0.05, ** p < 0.01, *** p < 0.001, **** p < 0.0001.

and FAS showed significant reductions (p < 0.05, p < 0.05 and p < 0.05, respectively). Furthermore, the mRNA expression of cholesterol metabolism genes, such as sterol regulatory element binding protein-2 (SREBP-2) or hydroxymethyl-glutaryl-CoA reductase (HMGCR) genes was increased by CDHCF diet and G2-SUISO treatment showed the trend of decrease of the expression of these mRNA expression (Supplementary Fig. 3C).

Discussion

The prevalence of NAFLD has increased significantly in parallel with increasing rates of obesity, now being the most common cause of chronic liver disease worldwide¹⁴. NAFLD is reported to be a heterogeneous disease with a high prevalence in elderly patients, characterized by the accumulation of TG and fatty acids in hepatocytes¹⁵. Compared with younger groups, NAFLD in the elderly may carry a more substantial burden of hepatic and extra-hepatic manifestations and complications¹⁶. Indeed, in our NASH model, aged rats showed more severe hepatitis when fed an CDHCF diet than young rats (Supplementary Fig. 1). H₂ has been reported to act as a therapeutic antioxidant by selectively reducing cytotoxic oxygen radicals, potentially leading to therapeutic effects in a variety of diseases, such as ischemia–reperfusion injury, colitis, NASH and aging-related diseases^{9,17–20}. G2-SUISO is widely used in dietary supplement products (https://acche.co.jp/supplement/items_platinum/) as a safe and effective form of antioxidant with minimal side effects. This study demonstrated the promising potential effects of G2-SUISO in a rat elderly model of NASH.

In this study, we used a CDHCF diet, which is one of the useful methods, to generate our NASH rat model^{21,22}. As expected, CDHCF diet-fed rats exhibited increased adipose tissue weights and liver weight-to-body weight ratios compared to the Naïve group (Fig. 1). In addition, the liver pathology summarized the major features of human NASH, including steatosis, ballooning degeneration and inflammation. With this model, the hepatic lipogenic/inflammation/apoptosis gene expression and serum biochemical markers, such as AST, ALT and TC, attenuation by G2-SUISO showed convincing results for estimating the effect of the drug in our research. Oxidative stress and inflammation are the main components that contribute to the pathogenesis of NASH. It is widely acknowledged that TNF- α expression increases in cases of obesity and plays a major role in the inflammatory pathogenesis of NASH²³. Enrichment of innate immune cells and increased inflammation are hallmarks of NASH. Increasing evidence supports that neutrophils play a key role in the onset of NASH, and histological findings from human liver biopsies suggest that enhanced infiltration of neutrophils is one of the key histological features of NASH^{24,25}. Activation of the transcription factor NF- κ B also results in production of key chemokines for neutrophil recruitment²⁶. Steatosis is reported to lead to increased signaling of the transcription factor NF- κ B, which can induce the production of pro-inflammatory mediators, such as TNF- α , IL-6 and IL-1 β ²⁷. In addition, these pro-inflammatory cytokines contribute to the recruitment and activation of Kupffer cells to mediate inflammation in NASH. In our study, the mRNA expression of TNF- α significantly

decreased following the administration of G2-SUIISO to our rat NASH model (Fig. 2). The expression of other pro-inflammatory mediators, including IFN- γ , OPN, IL-1 β , CCR2, iNOS and IL-6, was markedly increased under CDHCF diet. Following G2-SUIISO treatment, most of these cytokines showed a down-regulated trend, suggesting that G2-SUIISO might have an anti-inflammatory effect. As shown in Fig. 3, down-regulation of NF- κ B by G2-SUIISO is one of the possible reason for the reduction of pro-inflammatory molecules, while the mechanism of NF- κ B suppression by H₂ is still unclear²⁸. Other reasons may include induction of anti-inflammatory molecules. The trend toward enhanced mRNA expression of HO-1 was observed by G2-SUIISO administration (data not shown) and several studies demonstrated that HO-1 inhibit NF- κ B^{29–31}.

Previous studies have reported that cell death, including apoptosis, seems to play a vital role in the progression of NASH¹³. Apoptotic hepatocytes stimulate immune cells and hepatic stellate cells (HSCs) to progress to NASH and fibrosis through the production of inflammasomes and cytokines. NF- κ B is a master regulator of inflammation and cell death in the development of various liver diseases, such as NAFLD, hepatocellular injury, liver fibrosis and HCC³². The activation of NF- κ B in Kupffer cells or infiltrating monocytes is pro-inflammatory and induces the expression of death ligands, such as TNF- α ³³. Caspases are related to the induction of apoptosis, which is a mode of cell death regulated by homeostasis, supporting the coordinated demolition and clearance of aging and damaged cells³⁴. Bax belongs to the Bcl-2 protein family, and its pro-apoptotic function has been confirmed in many studies³⁵. The expression of these pro-apoptotic molecules was significantly up-regulated in the CDHCF diet control group on day 3 (Fig. 3). The administration of G2-SUIISO then down-regulated the pro-apoptosis molecules, such as NF- κ B and caspases, on day 3 according to our Western blot analyses. These findings suggest that G2-SUIISO may prevent apoptosis in the NASH model liver by inhibiting the expression of pro-apoptotic molecules.

In the present study, G2-SUIISO attenuated lipid accumulation in CDHCF-induced NASH in elderly rats. The reverse alterations in the hepatic lipid accumulation can be explained by the effects of G2-SUIISO on lipid metabolism. Previous studies have shown that the excessive hepatic accumulation of TG and FFAs induces hepatic steatosis^{36,37}. The present study demonstrated that treatment with G2-SUIISO ameliorated the lipid accumulation in the liver of CDHCF diet rats via the modulation of lipid metabolism-related molecules. The hepatic uptake of fatty acids is thought to occur via several mechanisms, including a transporter-mediated mechanism. In patients with NAFLD, the hepatic expression of fatty acid synthesis genes and fatty acid oxidation-related genes is up-regulated. ACC catalyzes the production of malonyl-CoA and is a major building block for de novo lipogenesis, promoting the oxidation of FFAs³⁸. SREBP-1c is a transcription factor that is a major regulator of FAS and other lipogenic proteins and is essential for the utilization and storage of glucose carbon³⁹. It regulates the onset of the lipogenic program and is able to bind to the promoters of several lipogenesis enzyme genes and induce their expression⁴⁰. The activity of the SREBP-1c/FAS pathway was previously shown to be markedly elevated and to contribute to the progression of hepatic steatosis in NASH mice⁴¹. Our present findings showed that G2-SUIISO significantly down-regulated SREBP-1c, FAS and ACC expression (Fig. 4), indicating that G2-SUIISO protects NASH rats from the SREBP-1c/FAS pathway. In this study, serum TG remained reduced after 2 days of fasting and feeding the CDHCF diet, with comparable concentrations with/without G2-SUIISO (Supplementary Fig. 3B). Previous study demonstrated that serum TG concentration was decreased after 2 days fasting but gradually increase after refeeding²¹. The reason why serum triglyceride levels are not increased by the CDHCF diet is still unclear, but one possible reason may be due to the use of rats of different species and ages in this study.

As shown in Fig. 5, hepatic FFAs in the liver were increased after feeding a CDHCF diet and accounted for the majority of the lipid accumulation, which can trigger NASH^{42,43}. Excessive consumption and dietary abnormalities (such as consuming a CDHCF diet after fasting) is related to oxidative stress in various tissues, including vessels, adipose tissues and the liver, and is consequent to disease development. Normally, oxidative stress, such as ROS, is continuously generated within cells but is counterbalanced by the antioxidant system to defend the body from cellular or tissue damage⁴⁴. In the progression of aging and lipogenesis, an imbalance of oxidant synthesis and antioxidants is the major contributor to the pathogenesis of NASH, leading to liver injury and hepatocyte deterioration⁴⁵.

Antioxidants have been suggested to be beneficial for health promotion and disease prevention. Chemiluminescence emission in vitro has been used to verify that H₂ can scavenge ROS markedly⁴⁶. Our results confirmed that the administration of G2-SUIISO, a proven safe and convenient antioxidant, improved NASH in our elderly rat model, probably due to its antioxidant activity. Hepatic and general serum marker levels including the liver weight-to-body weight ratio, AST and ALT were all improved, while FFA uptake-related, inflammatory and pro-apoptosis molecules were suppressed in the NASH liver by administration of G2-SUIISO. The beneficial effects of G2-SUIISO against hepatic steatosis in NASH elderly rats may be exerted through the inhibition of lipogenesis pathways by reducing SREBP-1c, ACC and FAS expression, thereby causing a reduction in the hepatic fat accumulation and a significant decrease in TC levels in serum. Overall, these results indicate that G2-SUIISO represents a simple and novel therapeutic strategy for NASH and NAFLD. Previous studies also showed that H₂ therapy is a very promising treatment of liver diseases and the rational use of it has already solved many problems clinically⁴⁷. However, the current clinical delivery method of H₂ is not very convenient, and G2-SUIISO can be made into capsules to solve this problem and facilitate H₂ administration.

Methods

Manufacturing method of G2-SUIISO. The original method of coral calcium carried hydrogen was described previously^{48,49}. The coral powder containing calcium carbonate was sealed into a pressure vessel, and gas with a concentration of 100% (vol) H₂ was circulated at a rate of 5 L/min at a temperature of 800 °C and pressure of 0.8 MPa, treated at a high temperature for 1 h. At 300 °C and 0.8 MPa, H₂ gas concentration of 100% (vol)

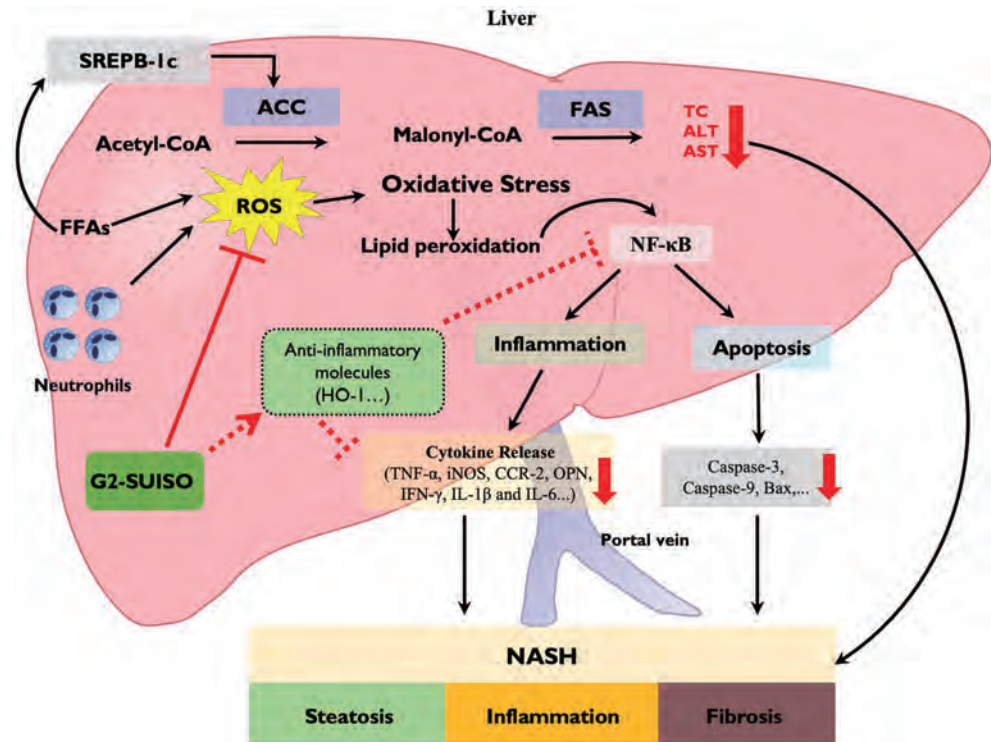


Figure 5. Schematic hypothesis of the mechanisms underlying the effects of G2-SUIISO for treating nonalcoholic steatohepatitis. The beneficial effect of G2-SUIISO against hepatic steatosis in NASH elderly rats may occur through the inhibition of lipogenesis pathways by reducing SREBP-1c, ACC and FAS gene expression, thereby causing a reduction in the hepatic fat accumulation and a significant decrease in total cholesterol (TC) levels in serum. The administration of G2-SUIISO can decrease lipid peroxidation and pro-inflammatory cytokines, such as TNF- α , iNOS, CCR-2, OPN, IL-1 β and IL-6, which modulate liver damage in CDHCF diet-fed rats. G2-SUIISO might also up-regulated anti-inflammatory molecules, such as HO-1, which suppressed NF- κ B and inflammatory cytokine expression. G2-SUIISO is therefore able to reduce the activities of AST and ALT in the serum of NASH elderly rats. Furthermore, G2-SUIISO was found to exert anti-apoptotic effects as well by down-regulating pro-apoptotic molecules, such as caspase-9, caspase-3 and Bax via down-regulation of NF- κ B. Overall, this study provides evidence for the beneficial effects of G2-SUIISO in reversing the progression of NASH in elderly rats.

was circulated at a speed of 5 L/min and treated at a low temperature for 4 h. Finally, hydrogen powder with an average particle size of about 10 μ m was obtained by grinding.

Animal model. Six-month-old elderly male F344/NSlc rats (450–500 g) were purchased from Shizuoka Laboratory Animal Center (Shizuoka, Japan) and housed in a feeding room with automatically controlled light and temperature according to the guidelines of the Institutional Animal Care and Use Committee. All animal procedures were authorized by the National Research Institute for Child Health and Development (Permission No. A2020-004-C01-M01).

An acute NASH model was originally developed in 1997²¹ and is currently used in the field of fatty liver research with minor modification^{22,50–52}. As early as three days after starting the CDHCF diet, rats may develop hepatic inflammation. In our study, acute NASH in a rat model was induced by fasting for two days followed by feeding a CDHCF diet for three days. Rats in the present study were randomized into five groups as shown in Fig. 1A and as follows: (1) Naïve group (n = 6): rats received a normal diet and were gavaged with distilled water; (2) CDHCF control group on day 3 (3d_cont.) (n = 6): rats were fed an CDHCF diet from days 0 to 3 and then sacrificed on day 3; (3) CDHCF + G2-SUIISO-treated group on day 3 (3d_G2) (n = 6): rats had NASH induced, were gavaged with 300 mg/kg G2-SUIISO from days 0 to 3, and then were sacrificed on day 3; (4) CDHCF control group on day 7 (7d_cont.) (n = 6): rats were fed an CDHCF diet from days 0 to 3, switched to a normal diet from days 4 to 7, and then were sacrificed on day 7; (5) CDHCF + G2-SUIISO-treated group on day 7 (7d_G2) (n = 6): rats were fed an CDHCF diet from days 0 to 3 and then switched to a normal diet from days 4 to 7. At the same time, rats were gavaged with 300 mg/kg G2-SUIISO from days 0 to 7 before finally being sacrificed on day 7. At sacrifice, blood was collected, the liver weight-to-body weight ratio was measured, and the entire liver was removed for further analyses.

Serum biochemical analyses. Serum was collected from whole-blood samples after standing for 30 min at 37 °C and centrifuged at 3000 g for 20 min at 4 °C. The samples were then measured for the AST, ALT, TC and TG concentrations with a commercially available kit (Fujifilm, Tokyo, Japan) and an automatic biochemical analyzer (DRI-CHEM 3500i; Fujifilm) according to the manufacturer's instructions.

Histology and histopathological analyses. Liver tissues were cut and fixed in 10% formaldehyde solution for 48 h and embedded in paraffin for histological analysis. Sections of liver 4- μ m-thick were prepared and subjected to staining with hematoxylin and eosin (HE) (Muto Pure Chemicals, Tokyo, Japan) for morphological analyses to evaluate hepatocyte steatosis, ballooning and inflammatory cell infiltration. For another assessment of inflammatory cell infiltration, the quantification of neutrophils in liver specimens was stained using the Naphthol AS-D Chloroacetate Esterase Staining Kit (Muto Pure Chemicals). Slides were then examined by light microscopy (OLYMPUS, Tokyo, Japan) in a blind fashion to assess the inflammation state. Histological results were quantified using the WinRoof 7.4 software program (Mitani Corporation, Tokyo, Japan) as described previously⁵³.

Oil Red O staining. The frozen liver samples with optimal cutting temperature were cryo-sectioned at 5 μ m with a cryostat and then stained with Oil Red O working solution (Muto Pure Chemicals) for TG and FFA staining to evaluate hepatocyte steatosis⁵⁴. Results were quantified using the WinRoof 7.4 software program (Mitani Corporation) as well.

Immunohistochemical examinations. Immunohistochemical staining was performed on frozen sections using mouse anti-rat ED1 monoclonal antibody (Bio-Rad, Hercules, CA, USA) and Purified mouse anti-rat CD3 monoclonal antibody (BD Biosciences, San Diego, CA) as described previously⁵⁵.

Total mRNA preparation and quantitative reverse transcription polymerase chain reaction (qRT-PCR). Total mRNA was extracted from liver tissues using an RNeasy Mini Kit (Qiagen, Valencia, CA, USA). Each 0.8- μ g aliquot of mRNA was reverse-transcribed to cDNA using a Prime Script RT reagent Kit (RR037A; Takara, Shiga, Japan). qRT-PCR was performed by the SYBR[®] Green system using an Applied Biosystem PRISM7900 apparatus (Thermo Fisher Scientific, Waltham, MA, USA). The PCR cycle conditions for the SYBR[®] Green system were 50 °C for 2 min, 95 °C for 2 min, 45 cycles of 95 °C for 15 s and 60 °C for 60 s. The comparative cycle threshold (CT) method was used to determine the relative gene expression. The results of target genes (Table 1) were normalized by subtracting the CT value of 18S expression. The fold change was calculated by a comparative CT method as described previously⁵⁶.

Genes	Forward (5'-3')	Reverse (5'-3')	
SYBR green PCR system			
IFN- γ	GAAAGCCTAGAAAGTCTGAAGAAC	GCACCGACTCCTTTCCGCTTCCT	
IL-6	TGATGGATGCTTCCAAACTG	GAGCATTGGAAGTTGGGGTA	
IL-1 β	CACCTTCTTTTCTTCATCTTTG	GTCGTTGCTTGCTCTCCTTGTA	
CCR2	TTCTGGGCTCACTATGCTGC	AAGGGCCACAAGTATGCTGA	
Bax	CCAGGACGCATCCACCAAGAAGC	TGCCACACGGAAGAAGACCTCTCG	
Caspase-1	GTGTTGCAGATAATGAGGGC	AAGGTCCTGAGGGCAAAGAG	
Caspase-3	GGACCTGTGGACCTGAAAAA	GCATGCCATATCATCGTCAG	
Bcl-2	GGATGACTTCTCTCGTCGCTACCGT	ATCCCTGAAGAGTTCCTCCACCAC	
NF κ B	GCATGCCATATCATCGTCAG	TGCTTCTCTCCCAGGAATA	
OB-R	TGCCTTGGAGGACTATGGGT	AGCCCCCTCAAAGACGAAG	
ACC	GCCTTCTCTGACAAACGAG	TCCATACGCCTGAAACATGA	
SREBP-1c	TGGATTGCACATTGAAGACAT	GCTCCTCTTGATTCCAGGC	
FAS	CAGCTGTCAGTGTAAGAAACATGTC	AGCTCACGTGCAGTTAATTGTG	
HMGCR	CCCAGCCTACAAACTGGAAA	CCATTGGCACCTGGTACTCT	
SREBP-2	AGACTTGGTCATGGGGACAG	GGGGAGACATCAGAAGGACA	
18S	ATGAGTCCACTTTAAATCCTTTAACGA	CTTTAATATACGCTATTGGAGCTGGAA	
Genes	Forward (5'-3')	Reverse (5'-3')	Probe
Taqman probe PCR			
TNF- α	AATGGGCTCCCTCTCATCAGT	ACGGGCTTGTCACTCGAGTT	CCAGACCCTCACACTCAGATCATCTTCTCA
iNOS	GGACATTAACAACAACGTGGAGAA	AACCATTTTGATGCTTGTGACTCTT	TGCTATTTCCCAGCCCAACAACACAGG
OPN	CAAAGTCCAGGAGTTCCCTGTT	CTCTTATGCGGGAGGTGA	TGATGAACAGTATCCCGATGCCACAGAT
18S	ATCCATTGGAGGGCAAGTCTGGTGC	ATGAGTCCACTTTAAATCCTTTAACGA	CTTTAATATACGCTATTGGAGGCTGGAA

Table 1. Primer sequences and probes used in this study.

Western blot analyses. Western blot analysis was performed as described previously²⁰. In brief, frozen liver tissues in the five groups were homogenized in RIPA buffer containing 1% protease inhibitor cocktail-1 and 1% protease inhibitor cocktail-2 (Sigma-Aldrich, St. Louis, MO, USA) followed by centrifugation in a microfuge at top speed for 30 min. Protein concentrations were assayed using a Bio-Rad Protein Assay (Bio-Rad). Samples were separated by electrophoresis on 10% polyacrylamide gels and transferred to Immobilon-PVDF (Bio-Rad). The membranes corresponding to the molecule of interest were cut out prior to hybridization with the antibody. After brief incubation with 5% non-fat milk to block non-specific binding, membranes were exposed overnight at 4 °C to specific caspase-1, caspase-3, caspase-9 and nuclear factor- κ B (NF- κ B). Protein expression was quantified by a laser densitometric analysis of the radiographic film using the ImageJ software program (NIH, Bethesda, MD, USA). The protein normalization was performed using β -actin as internal loading control.

Statistical analyses. The GraphPad Prism 9 software program (GraphPad, San Diego, CA, USA) was used to calculate statistical significance. Student's *t*-test was used for unpaired data. Data are expressed as the mean \pm standard deviation (SD). A value of $p < 0.05$ was considered to be statistically significant ($*p < 0.05$; $**p < 0.01$; $***p < 0.001$; $****p < 0.0001$).

Data availability

The datasets that support the findings of this study are available from the corresponding author on reasonable request.

Received: 27 March 2023; Accepted: 16 July 2023

Published online: 19 July 2023

References

- Powell, E. E., Wong, V. W. & Rinella, M. Non-alcoholic fatty liver disease. *Lancet* **397**, 2212–2224. [https://doi.org/10.1016/S0140-6736\(20\)32511-3](https://doi.org/10.1016/S0140-6736(20)32511-3) (2021).
- Frailie, J. M., Palliyil, S., Barelle, C., Porter, A. J. & Kovaleva, M. Non-alcoholic steatohepatitis (NASH)—a review of a crowded clinical landscape, driven by a complex disease. *Drug Des. Dev. Ther.* **15**, 3997–4009. <https://doi.org/10.2147/DDDT.S315724> (2021).
- Chen, T. P., Lai, M., Lin, W. Y., Huang, K. C. & Yang, K. C. Metabolic profiles and fibrosis of nonalcoholic fatty liver disease in the elderly: A community-based study. *J. Gastroenterol. Hepatol.* **35**, 1636–1643. <https://doi.org/10.1111/jgh.15073> (2020).
- Yang, J. *et al.* Oxidative stress and non-alcoholic fatty liver disease: Effects of omega-3 fatty acid supplementation. *Nutrients* <https://doi.org/10.3390/nu11040872> (2019).
- Sheedfar, F., Di Biase, S., Koonen, D. & Vinciguerra, M. Liver diseases and aging: Friends or foes?. *Aging Cell* **12**, 950–954. <https://doi.org/10.1111/acel.12128> (2013).
- Finkel, T. & Holbrook, N. J. Oxidants, oxidative stress and the biology of ageing. *Nature* **408**, 239–247. <https://doi.org/10.1038/35041687> (2000).
- Chen, Z., Tian, R., She, Z., Cai, J. & Li, H. Role of oxidative stress in the pathogenesis of nonalcoholic fatty liver disease. *Free Radic. Biol. Med.* **152**, 116–141. <https://doi.org/10.1016/j.freeradbiomed.2020.02.025> (2020).
- Gao, Y. *et al.* Exercise and dietary intervention ameliorate high-fat diet-induced NAFLD and liver aging by inducing lipophagy. *Redox Biol.* **36**, 101635. <https://doi.org/10.1016/j.redox.2020.101635> (2020).
- Ohsawa, I. *et al.* Hydrogen acts as a therapeutic antioxidant by selectively reducing cytotoxic oxygen radicals. *Nat. Med.* **13**, 688–694. <https://doi.org/10.1038/nm1577> (2007).
- Hu, Q. *et al.* Molecular hydrogen: A potential radioprotective agent. *Biomed. Pharmacother.* **130**, 110589. <https://doi.org/10.1016/j.biopha.2020.110589> (2020).
- Iketani, M. & Ohsawa, I. Molecular hydrogen as a neuroprotective agent. *Curr. Neuropharmacol.* **15**, 324–331. <https://doi.org/10.2174/1570159x14666160607205417> (2017).
- Wigg, A. J. *et al.* The role of small intestinal bacterial overgrowth, intestinal permeability, endotoxaemia, and tumour necrosis factor alpha in the pathogenesis of non-alcoholic steatohepatitis. *Gut* **48**, 206–211. <https://doi.org/10.1136/gut.48.2.206> (2001).
- Kanda, T. *et al.* Apoptosis and non-alcoholic fatty liver diseases. *World J. Gastroenterol.* **24**, 2661–2672. <https://doi.org/10.3748/wjg.v24.i25.2661> (2018).
- Wang, X. J. & Malhi, H. Nonalcoholic fatty liver disease. *Ann. Intern. Med.* **169**, ITC65–ITC80. <https://doi.org/10.7326/AITC201811060> (2018).
- Noureddin, M. *et al.* Clinical and histological determinants of nonalcoholic steatohepatitis and advanced fibrosis in elderly patients. *Hepatology* **58**, 1644–1654. <https://doi.org/10.1002/hep.26465> (2013).
- Bertolotti, M. *et al.* Nonalcoholic fatty liver disease and aging: epidemiology to management. *World J. Gastroenterol.* **20**, 14185–14204. <https://doi.org/10.3748/wjg.v20.i39.14185> (2014).
- Nie, C. *et al.* Hydrogen gas inhalation alleviates myocardial ischemia-reperfusion injury by the inhibition of oxidative stress and NLRP3-mediated pyroptosis in rats. *Life Sci.* **272**, 119248. <https://doi.org/10.1016/j.lfs.2021.119248> (2021).
- Fu, Z., Zhang, J. & Zhang, Y. Role of molecular hydrogen in ageing and ageing-related diseases. *Oxid. Med. Cell Longev.* **2022**, 2249749. <https://doi.org/10.1155/2022/2249749> (2022).
- LeBaron, T. W. *et al.* Molecular hydrogen is comparable to sulfasalazine as a treatment for DSS-induced colitis in mice. *EXCLI J.* **20**, 1106–1117. <https://doi.org/10.17179/excli2021-3762> (2021).
- Li, S. W. *et al.* Hydrogen-rich water protects against liver injury in nonalcoholic steatohepatitis through HO-1 enhancement via IL-10 and Sirt1 signaling. *Am. J. Physiol. Gastrointest. Liver Physiol.* **320**, G450–G463. <https://doi.org/10.1152/ajpgi.00158.2020> (2021).
- Delzenne, N. M., Hernaux, N. A. & Taper, H. S. A new model of acute liver steatosis induced in rats by fasting followed by refeeding a high carbohydrate-fat free diet. Biochemical and morphological analysis. *J. Hepatol.* **26**, 880–885. [https://doi.org/10.1016/S0168-8278\(97\)80256-5](https://doi.org/10.1016/S0168-8278(97)80256-5) (1997).
- Nagai, K. *et al.* Impact of venous-systemic oxygen persufflation with nitric oxide gas on steatotic grafts after partial orthotopic liver transplantation in rats. *Transplantation* **95**, 78–84. <https://doi.org/10.1097/TP.0b013e318277e2d1> (2013).
- Machado, M. V. & Diehl, A. M. Pathogenesis of nonalcoholic steatohepatitis. *Gastroenterology* **150**, 1769–1777. <https://doi.org/10.1053/j.gastro.2016.02.066> (2016).
- Cho, Y. & Szabo, G. Two faces of neutrophils in liver disease development and progression. *Hepatology* **74**, 503–512. <https://doi.org/10.1002/hep.31680> (2021).
- Wu, L. *et al.* The role of neutrophils in innate immunity-driven nonalcoholic steatohepatitis: Lessons learned and future promise. *Hepatol. Int.* **14**, 652–666. <https://doi.org/10.1007/s12072-020-10081-7> (2020).

26. Ishida, Y. *et al.* Opposite roles of neutrophils and macrophages in the pathogenesis of acetaminophen-induced acute liver injury. *Eur. J. Immunol.* **36**, 1028–1038. <https://doi.org/10.1002/eji.200535261> (2006).
27. Cobbina, E. & Akhlaghi, F. Non-alcoholic fatty liver disease (NAFLD)—pathogenesis, classification, and effect on drug metabolizing enzymes and transporters. *Drug Metab. Rev.* **49**, 197–211. <https://doi.org/10.1080/03602532.2017.1293683> (2017).
28. Russell, G., Nenov, A., Kisher, H. & Hancock, J. T. Molecular hydrogen as medicine: An assessment of administration methods. *Hydrogen* **2**, 444–460 (2021).
29. Yang, H. *et al.* Heme oxygenase-1 inhibits the proliferation of hepatic stellate cells by activating PPAR γ and suppressing NF- κ B. *Comput. Math. Methods Med.* **2022**, 8920861. <https://doi.org/10.1155/2022/8920861> (2022).
30. Bellezza, I. *et al.* Inhibition of NF- κ B nuclear translocation via HO-1 activation underlies α -tocopheryl succinate toxicity. *J. Nutr. Biochem.* **23**, 1583–1591. <https://doi.org/10.1016/j.jnutbio.2011.10.012> (2012).
31. Gao, W. *et al.* Dissecting the crosstalk between Nrf2 and NF- κ B response pathways in drug-induced toxicity. *Front. Cell Dev. Biol.* <https://doi.org/10.3389/fcell.2021.809952> (2022).
32. Luedde, T. & Schwabe, R. F. NF- κ B in the liver—linking injury, fibrosis and hepatocellular carcinoma. *Nat. Rev. Gastroenterol. Hepatol.* **8**, 108–118. <https://doi.org/10.1038/nrgastro.2010.213> (2011).
33. Ricchi, M. *et al.* Differential effect of oleic and palmitic acid on lipid accumulation and apoptosis in cultured hepatocytes. *J. Gastroenterol. Hepatol.* **24**, 830–840. <https://doi.org/10.1111/j.1440-1746.2008.05733.x> (2009).
34. Van Opdenbosch, N. & Lamkanfi, M. Caspases in cell death, inflammation, and disease. *Immunity* **50**, 1352–1364. <https://doi.org/10.1016/j.immuni.2019.05.020> (2019).
35. Guo, M. *et al.* Bax functions as coelomocyte apoptosis regulator in the sea cucumber *Apostichopus japonicus*. *Dev. Comp. Immunol.* **102**, 103490. <https://doi.org/10.1016/j.dci.2019.103490> (2020).
36. Choi, S. S. & Diehl, A. M. Hepatic triglyceride synthesis and nonalcoholic fatty liver disease. *Curr. Opin. Lipidol.* **19**, 295–300. <https://doi.org/10.1097/MOL.0b013e3282ff5e55> (2008).
37. Ong, K. T., Mashek, M. T., Bu, S. Y., Greenberg, A. S. & Mashek, D. G. Adipose triglyceride lipase is a major hepatic lipase that regulates triacylglycerol turnover and fatty acid signaling and partitioning. *Hepatology* **53**, 116–126. <https://doi.org/10.1002/hep.24006> (2011).
38. Fang, K. *et al.* Diosgenin ameliorates palmitic acid-induced lipid accumulation via AMPK/ACC/CPT-1A and SREBP-1c/FAS signaling pathways in LO2 cells. *BMC Complement Altern. Med.* **19**, 255. <https://doi.org/10.1186/s12906-019-2671-9> (2019).
39. Moon, Y. S. & Ali, S. Possible mechanisms for the equilibrium of ACC and role of ACC deaminase-producing bacteria. *Appl. Microbiol. Biotechnol.* **106**, 877–887. <https://doi.org/10.1007/s00253-022-11772-x> (2022).
40. Stoeckman, A. K. & Towle, H. C. The role of SREBP-1c in nutritional regulation of lipogenic enzyme gene expression. *J. Biol. Chem.* **277**, 27029–27035. <https://doi.org/10.1074/jbc.M202638200> (2002).
41. An, J. P. *et al.* Anti-hepatic steatosis activity of *Sicyos angulatus* extract in high-fat diet-fed mice and chemical profiling study using UHPLC-qTOF-MS/MS spectrometry. *Phytomedicine* **63**, 152999. <https://doi.org/10.1016/j.phymed.2019.152999> (2019).
42. Puri, P. *et al.* A lipidomic analysis of nonalcoholic fatty liver disease. *Hepatology* **46**, 1081–1090. <https://doi.org/10.1002/hep.21763> (2007).
43. Bechmann, L. P. *et al.* The interaction of hepatic lipid and glucose metabolism in liver diseases. *J. Hepatol.* **56**, 952–964. <https://doi.org/10.1016/j.jhep.2011.08.025> (2012).
44. Vona, R., Gambardella, L., Cittadini, C., Straface, E. & Pietraforte, D. Biomarkers of oxidative stress in metabolic syndrome and associated diseases. *Oxid. Med. Cell Longev.* **2019**, 8267234. <https://doi.org/10.1155/2019/8267234> (2019).
45. Oseini, A. M. & Sanyal, A. J. Therapies in non-alcoholic steatohepatitis (NASH). *Liver Int.* **37**(Suppl 1), 97–103. <https://doi.org/10.1111/liv.13302> (2017).
46. Deenin, W., Malakul, W., Boonsong, T., Phoungpetchara, I. & Tunsophon, S. Papaya improves non-alcoholic fatty liver disease in obese rats by attenuating oxidative stress, inflammation and lipogenic gene expression. *World J. Hepatol.* **13**, 315–327. <https://doi.org/10.4254/wjh.v13.i3.315> (2021).
47. Shi, J., Duncan, B. & Kuang, X. Hydrogen treatment: A novel option in liver diseases. *Clin. Med. (Lond.)* **21**, e223–e227. <https://doi.org/10.7861/clinmed.2020-0370> (2021).
48. Okuda, R. *et al.* Evaluation of released amount of hydrogen after high pressure hydrogen loading in carbonate. *Results Eng.* **4**, 100047. <https://doi.org/10.1016/j.rineng.2019.100047> (2019).
49. Li, H. *et al.* Hydrogen adsorption and desorption characteristics of heat-treated calcium carbonate derived from Akoya-Pearl-Oyster nacre. *J. Environ. Chem. Eng.* **8**, 103983. <https://doi.org/10.1016/j.jece.2020.103983> (2020).
50. Minor, T., Akbar, S., Tolba, R. & Dombrowski, F. Cold preservation of fatty liver grafts: prevention of functional and ultrastructural impairments by venous oxygen persufflation. *J. Hepatol.* **32**, 105–111. [https://doi.org/10.1016/s0168-8278\(00\)80196-8](https://doi.org/10.1016/s0168-8278(00)80196-8) (2000).
51. Miyachi, Y. *et al.* Etiology of liver steatosis influences the severity of ischemia/reperfusion injury and survival after liver transplantation in rats. *Liver Transpl.* **26**, 1504–1515. <https://doi.org/10.1002/lt.25814> (2020).
52. Okamura, Y. *et al.* Impact of subnormothermic machine perfusion preservation in severely steatotic rat livers: A detailed assessment in an isolated setting. *Am. J. Transpl.* **17**, 1204–1215. <https://doi.org/10.1111/ajt.14110> (2017).
53. Liu, C. *et al.* 5-ALA/SFC attenuated binge alcohol-induced gut leakiness and inflammatory liver disease in HIV transgenic rats. *Alcohol Clin. Exp. Res.* **43**, 1651–1661. <https://doi.org/10.1111/acer.14117> (2019).
54. Li, S. *et al.* Astaxanthin prevents ischemia-reperfusion injury of the steatotic liver in mice. *PLoS ONE* **12**, e0187810. <https://doi.org/10.1371/journal.pone.0187810> (2017).
55. Kawasaki, M. *et al.* Inducible liver injury in the transgenic rat by expressing liver-specific suicide gene. *Biochem. Biophys. Res. Commun.* **311**, 920–928. <https://doi.org/10.1016/j.bbrc.2003.10.085> (2003).
56. Zhao, J. *et al.* Monotherapy with anti-CD70 antibody causes long-term mouse cardiac allograft acceptance with induction of tolerogenic dendritic cells. *Front. Immunol.* **11**, 555996. <https://doi.org/10.3389/fimmu.2020.555996> (2020).

Acknowledgements

This study was supported by research grants from the Grant of Ministry of Education, Culture, Sports, Science and Technology of Japan (Grants-in-Aid 21K08634) and a Grant from the National Center for Child Health and Development (31-02).

Author contributions

X.K.L. conceptualized the study and all authors contributed to the study design. Data collection was conducted by K.M. The preparation of the research materials and data analysis were conducted by K.M., M.F., and X.K.L. Results and interpretations of the study data were discussed by all authors. The first draft of the manuscript was written by K.M., and all authors commented on earlier versions of the manuscript. All authors read and approved the final manuscript.

Competing interests

The authors declare no competing interests.

Additional information

Supplementary Information The online version contains supplementary material available at <https://doi.org/10.1038/s41598-023-38856-6>.

Correspondence and requests for materials should be addressed to M.F. or X.-K.L.

Reprints and permissions information is available at www.nature.com/reprints.

Publisher's note Springer Nature remains neutral with regard to jurisdictional claims in published maps and institutional affiliations.



Open Access This article is licensed under a Creative Commons Attribution 4.0 International License, which permits use, sharing, adaptation, distribution and reproduction in any medium or format, as long as you give appropriate credit to the original author(s) and the source, provide a link to the Creative Commons licence, and indicate if changes were made. The images or other third party material in this article are included in the article's Creative Commons licence, unless indicated otherwise in a credit line to the material. If material is not included in the article's Creative Commons licence and your intended use is not permitted by statutory regulation or exceeds the permitted use, you will need to obtain permission directly from the copyright holder. To view a copy of this licence, visit <http://creativecommons.org/licenses/by/4.0/>.

© The Author(s) 2023

日中笹川医学奨学金制度<学位取得コース>評価書

課程博士：指導教官



第 44 期

研究者番号：G4410

作成日：2024年3月10日

氏名	徐勇	XU YONG	性別	M	生年月日	1990/05/04
所属機関（役職）	長崎大学大学院医歯薬学総合研究科（大学院生）					
研究先（指導教官）	長崎大学原爆後障害医療研究所幹細胞生物学研究分野（原研幹細胞）（李桃生 教授）					
研究テーマ	ニカラベンによる間葉系幹細胞の放射線損傷の軽減 Nicaraven for attenuating the radiation-induced damage of Mesenchymal stem(stromal) cells					
専攻種別	<input type="checkbox"/> 論文博士			<input checked="" type="checkbox"/> 課程博士		

研究者評価（指導教官記入欄）

成績状況	優良	取得単位数
		早期卒業修了（既に学位取得）
学生本人が行った研究の概要	胸部の放射線がん治療に伴う肺傷害のメカニズムを解明し、新たな予防・治療の開発である。また、人工呼吸管理について、酸素吸入や換気量が肺傷害に与える影響を動物実験で調べている。	
総合評価	【良かった点】 ものごとを真摯に取り組み、研究も順調に進み、既に研究成果を出し、これまでに第一著者として論文3本を国際学術誌に採択・掲載された。昨年10月に、早期終了し医学博士の学位を取得した。	
	【改善すべき点】 特になし	
	【今後の展望】 既に学位を取得され、中国で就職した。	
学位取得見込	昨年10月に、早期卒業修了し、博士学位を取得された	
評価者（指導教官名）		李桃生

日中笹川医学奨学金制度<学位取得コース>報告書 研究者用



第44期

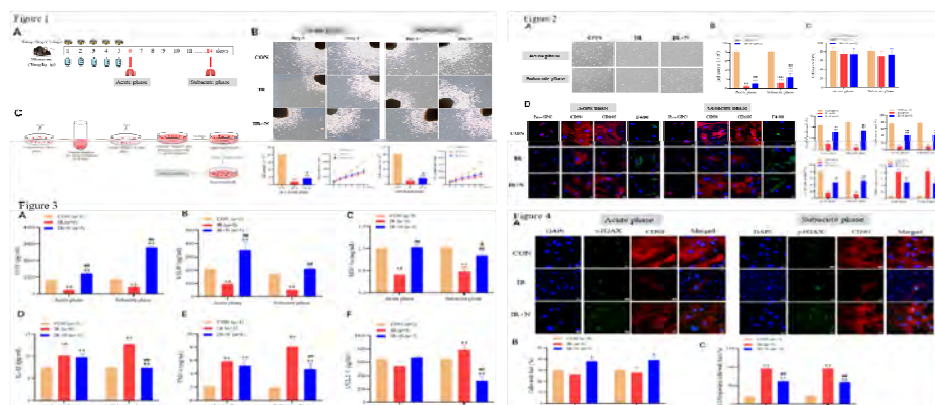
研究者番号: G4410

作成日: 2024年3月 10 日

氏名	徐 勇	XU YONG	性別	M	生年月日	1990/05/04
所属機関(役職)	長崎大学大学院医歯薬学総合研究科(大学院生)					
研究先(指導教官)	長崎大学原爆後障害医療研究所幹細胞生物学研究分野(原研幹細胞)(李 桃生 教授)					
研究テーマ	ニカラベンによる基質細胞の放射線損傷の軽減 Nicaraven attenuates radiation-induced injury of stromal cells in lungs					
専攻種別	論文博士	<input type="checkbox"/>	課程博士	<input checked="" type="checkbox"/>		
<p>1. 研究概要(1)</p> <p>1) 目的(Goal)</p> <p>i. To investigate whether nicaraven can attenuate radiation-induced injury of lung stromal cells (LSCs).</p> <p>ii. To understand the relevant molecular mechanisms on nicaraven for attenuating radiation-induced injury of LSCs.</p> <p>2) 戦略(Approach)</p> <p>C57BL/6 mice (9-week old) were exposed to 6 Gy X-ray thoracic radiation per day for 5 days (cumulative dose of 30 Gy) and nicaraven (50 mg/kg) or saline was injected intraperitoneally in 5 min after each radiation exposure. At 6 day (acute phase) or 14 days (subacute phase), we collected lung tissues and cultured as “explants” to grow LSCs, and further evaluated the quality and quantity of LSCs.</p> <p>3) 材料と方法(Materials and methods)</p> <p>1. Ex vivo expansion of LSCs from mouse lung tissue “explants”.</p> <p>MSCs were expanded using a method as previously described (Figure 1B).</p> <p>2. Detection of characterization of LSCs.</p> <p>IF staining was performed to detect the expression levels of CD90, CD105, Pro-SPC, F4/80 in LSCs.</p> <p>3. Evaluation of DNA damage of LSCs.</p> <p>To evaluate the DNA damage of LSCs, the expression levels of γ-H2AX and CD90 were estimated by immunostaining.</p> <p>4. Evaluation of paracrine mechanisms of LSCs.</p> <p>ELISA was used to detect the growth factors of HGF, VEGF, SDF-1α and inflammatory factors of IL-1β, CCL2, TNF-1α in conditioned medium from the supernatants of one passaged LSCs.</p> <p>4) 実験結果(Results)</p> <p>4.1 Nicaraven attenuates radiation-induced changes on the number and phenotype of LSCs</p> <p>We sacrificed mice and took lung tissue for experiments at the acute and subacute phases (Figure 1A). Our data showed that the irradiated lungs produced a significantly lower number of LSCs compared to healthy lungs after culture at the acute and subacute phases, which was significantly mitigated by nicaraven administration. To examine whether ionizing radiation would change the phenotypic characterization of LSCs. Of the acute phase, compared to the CON group, these LSCs in the IR group expressed significantly lower Pro-SPC, CD90, and CD105 ($p < 0.01$; Figure 2D); but higher F4/80 ($p < 0.01$; Figure 2D). However, LSCs in the IR+N group significantly expressed higher Pro-SPC, CD90, CD105 ($p < 0.01$; Figure 2D), and lower F4/80 ($p < 0.01$; Figure 2D) than that of the IR group. Of the subacute phase, LSCs in the IR group also showed lower expression of Pro-SPC, CD90, CD105 ($p < 0.01$; Figure 2D), but higher expression of F4/80 ($p < 0.01$; Figure 2D) than that of the CON group. However, LSCs in the IR+N group expressed significantly higher Pro-SPC, CD90, and CD105 ($p < 0.01$; Figure 2D) but lower F4/80 ($p < 0.01$; Figure 2D) compared to the IR group.</p> <p>4.2 Nicaraven significantly attenuates radiation-induced changes in the factors production of LSCs</p> <p>We examined the levels of related cytokines in the conditioned medium. Compared with these LSCs from the healthy lungs, LSCs from the irradiated lungs produced significantly less HGF, VEGF, and SDF-1α in the conditioned medium ($p < 0.01$). However, all these changes of HGF, VEGF, and SDF-1α released by LSCs from the irradiated lungs were significantly mitigated by nicaraven administration at the acute and subacute phases ($p < 0.01$). We detected the contents of IL-1β, TNF-α, and CCL2 in the conditioned medium. Compared with the healthy controls, the contents of IL-1β and TNF-α released by LSCs from irradiated lungs were significantly increased in the conditioned medium ($p < 0.01$), which were partially mitigated by nicaraven administration at the acute phase. Similarly, LSCs from irradiated lungs at the subacute phase produced more IL-1β, TNF-α, and CCL2 in the conditioned medium ($p < 0.01$) but significantly attenuated by nicaraven administration ($p < 0.01$).</p>						

4.3 Nicaraven significantly attenuates radiation-induced DNA damage of CD90-positive LSCs

Immunofluorescence staining was performed to detect the formation of γ -H2AX foci in LSCs (Figure 4A). Quantitative data showed that the percentage of γ -H2AX-positive LSCs was not significantly changed in the IR group than the CON group. However, the percentage of γ -H2AX-positive LSCs was significantly higher in the IR+N group compared to the IR group at the acute and subacute phases ($p < 0.05$; Figure 4B). We further detected the formation of γ -H2AX foci in CD90-positive LSCs. Quantitative data indicated that the percentage of γ -H2AX foci in CD90-positive LSCs was significantly higher in the IR group compared to the CON group, at either the acute phase ($p < 0.01$; Figure 4C) or the subacute phase ($p < 0.01$; Figure 4C). Interestingly, the percentage of CD90-positive LSCs with γ -H2AX foci was significantly lower in the IR+N group compared to the IR group, at either the acute ($p < 0.01$; Figure 4C) and subacute ($p < 0.01$; Figure 4C) phases. These results indicated that nicaraven administration significantly reduced radiation-induced DNA damage of CD90-positive LSCs.



5) 考察 (Discussion)

The use of radiation therapy to treat cancer inevitably involves exposure of normal tissues. Which can damage tissue homeostasis. Mesenchymal stromal cells (MSCs) residing in the lung are highly susceptible to radiation and are known to play critical roles in tissue homeostasis. In this study, we tried to primarily MSCs from lung tissues “explants” and then investigated whether nicaraven can attenuate the radiation-induced injury of MSCs, mainly focusing the quantity and quality of MSCs after nicaraven administrations. Our data indicated that nicaraven administration significantly restored the outgrowth of MSCs and their altered phenotypes caused by radiation exposure, clearly attenuated the radiation-induced DNA damage of MSCs. Besides these, nicaraven administration significantly increased the production of HGF, VEGF, SDF-1 α , IL-6 and decreased the levels of TNF- α , CCL2 in the conditioned medium, suggesting the effectiveness of nicaraven for attenuating radiation-induced injury of MSCs.

High ionizing radiation induces directly DNA double-strand breaks and triggers the release of ROS. The level of ROS overwhelms can cause DNA damage. Nicaraven has been well recognized on radical-specific scavenging properties and can attenuate radiation-induced DNA damage of lung tissue cells. we herein found that nicaraven can attenuate DNA damage of lung cells, especially the CD90-positive mesenchymal stromal cells.

Repair of damaged tissues is a fundamental biological mechanism that allows the ordered replacement of dead or damaged cells after injury. Over the last few decades, advances have been reported in the use of mesenchymal stromal cells (MSCs) for lung tissue repair and regeneration. MSCs are highly metabolically active and their secretome gives rise to the same effects commonly described for the cells themselves. MSCs not only replace damaged lung epithelial cells but also promote tissue repair through the secretion of chemokines, cytokines, growth factors and paracrine molecules.

Indeed, there are some limitations in this study. First, we only investigated the radiation-induced injury in lung stromal cells, a mixed cell population, because all types of stromal cells could be outgrew naturally from lung tissue “explants”. Secondly, we were interested to detect the quality of CD90- or CD105-positive resident mesenchymal stem cells, but it is technically difficult for us to get enough pure CD90- or CD105-positive cells from the lungs of mice for experiments, especially the irradiated lungs.

6) 参考文献 (References)

- Henry E, Cores J, Hensley MT, Anthony S et.al. Adult Lung Spheroid Cells Contain Progenitor Cells and Mediate Regeneration in Rodents With Bleomycin-Induced Pulmonary Fibrosis. *Stem Cells Transl Med.* 2015 Nov;4(11):1265-74.
- Sveiven SN, Nordgren TM. Lung-resident mesenchymal stromal cells are tissue-specific regulators of lung homeostasis. *Am J Physiol Lung Cell Mol Physiol.* 2020 Aug 1;319(2):L197-L210.
- Wynn TA. Integrating mechanisms of pulmonary fibrosis. *J Exp Med.* 2011 Jul 4;208(7):1339-50.
- Chen Y, Liu X, Tong Z. Mesenchymal Stem Cells in Radiation-Induced Pulmonary Fibrosis: Future Prospects. *Cells.* 2022 Dec 20;12(1):6.
- Wang LK, Wu TJ, Hong JH et.al. Radiation Induces Pulmonary Fibrosis by Promoting the Fibrogenic Differentiation of Alveolar Stem Cells. *Stem Cells Int.* 2020 Sep 29;2020:6312053.
- Zanoni M, Cortesi M, Zamagni A et.al. The Role of Mesenchymal Stem Cells in Radiation-Induced Lung Fibrosis. *Int J Mol Sci.* 2019 Aug 8;20(16):3876.

2. 執筆論文 Publication of thesis ※記載した論文を添付してください。Attach all of the papers listed below.

論文名 1 Title	Hyperoxia but not high tidal volume contributes to ventilator-induced lung injury in healthy mice					
掲載誌名 Published journal	BMC Pulmonary medicine					
	2023 年 9 月	23(1) 巻(号)	154 頁 ~	頁	言語 Language	English
第1著者名 First author	Yong Xu	第2著者名 Second author	Yu Li		第3著者名 Third author	Da Zhai
その他著者名 Other authors	Reiko Sekiya; Chen Yan; Keiichi Jingu; Tao-Sheng Li					
論文名 2 Title	Optimization on the dose and time of nicaraven administration for mitigating the side effects of radiotherapy in a preclinical tumor-bearing mouse model					
掲載誌名 Published journal	Therapeutic Advances in Respiratory Disease					
	2022 年 12 月	16 巻(号)	頁 ~	頁	言語 Language	English
第1著者名 First author	Yong Xu	第2著者名 Second author	Lina Abdelghany		第3著者名 Third author	Reiko Sekiya
その他著者名 Other authors	Da Zhai; Keiichi Jingu; Tao-Sheng Li					
論文名 3 Title	Nicaraven mitigates radiation-induced lung injury by downregulating the NF- κ B and TGF- β /Smad pathways to suppress the inflammatory response					
掲載誌名 Published journal	Journal of Radiation Research					
	2022 年 3 月	63(2) 巻(号)	158 頁 ~	167 頁	言語 Language	English
第1著者名 First author	Yong Xu	第2著者名 Second author	Da Zhai		第3著者名 Third author	Shinji Goto
その他著者名 Other authors	Xu Zhang; Keiichi Jingu; Tao-Sheng Li					
論文名 4 Title	Nicaraven Exerts a Limited Effect on Radiation-Induced Inhibition of Tumor Growth in a Subcutaneous Murine Tumor Model					
掲載誌名 Published journal	Radiation Research					
	2023 年 10 月	200(4) 巻(号)	382 頁 ~	388 頁	言語 Language	English
第1著者名 First author	Lina Abdelghany	第2著者名 Second author	Yong Xu		第3著者名 Third author	Reiko Sekiya
その他著者名 Other authors	Chen Yan; Keiichi Jingu; Tao-Sheng Li					
論文名 5 Title	Hydrostatic pressure stabilizes HIF-1 α expression in cancer cells to protect against oxidative damage during metastasis					
掲載誌名 Published journal	Oncology Reports					
	2021 年 10 月	46(4) 巻(号)	211 頁 ~	頁	言語 Language	English
第1著者名 First author	Da Zhai	第2著者名 Second author	Yong Xu		第3著者名 Third author	Lina Abdelghany
その他著者名 Other authors	Xu Zhang; Jingyan Liang; Shuohua Zhang; Changying Guo; Tao-Sheng Li					
論文名 6 Title	Ex Vivo Hydrostatic Pressure Loading of Atrial Tissues Activates Profibrotic Transcription via TGF- β Signal Pathway					
掲載誌名 Published journal	International Heart Journal					
	2022 年 3 月	63(2) 巻(号)	367 頁 ~	374 頁	言語 Language	English
第1著者名 First author	Xu Zhang	第2著者名 Second author	Yousuf Yassouf		第3著者名 Third author	Kai Huang
その他著者名 Other authors	Yong Xu, Zi-Sheng Huang, Da Zhai, Reiko Sekiya, Ke-Xiang Liu, Tao-Sheng Li					

3. 学会発表 Conference presentation ※筆頭演者として総会・国際学会を含む主な学会で発表したものを記載してください

※Describe your presentation as the principal presenter in major academic meetings including general meetings or international meetin

学会名 Conference	The radiation Disaster Medical Science 5th International Symposium		
演題 Topic	Nicaraven for attenuating radiation-induced lung injury		
開催日 date	2021 年 2 月 17 日	開催地 venue	Online
形式 method	<input type="checkbox"/> 口頭発表 Oral <input checked="" type="checkbox"/> ポスター発表 Poster	言語 Language	<input type="checkbox"/> 日本語 <input checked="" type="checkbox"/> 英語 <input type="checkbox"/> 中国語
共同演者名 Co-presenter	None		
学会名 Conference	日本放射線影響学会第65回大会		
演題 Topic	Nicaraven attenuates radiation-induced lung injury by suppressing inflammatory response.		
開催日 date	2022 年 9 月 17 日	開催地 venue	大阪公立大学
形式 method	<input type="checkbox"/> 口頭発表 Oral <input checked="" type="checkbox"/> ポスター発表 Poster	言語 Language	<input type="checkbox"/> 日本語 <input checked="" type="checkbox"/> 英語 <input type="checkbox"/> 中国語
共同演者名 Co-presenter	None		
学会名 Conference			
演題 Topic			
開催日 date	年 月 日	開催地 venue	
形式 method	<input type="checkbox"/> 口頭発表 Oral <input type="checkbox"/> ポスター発表 Poster	言語 Language	<input type="checkbox"/> 日本語 <input type="checkbox"/> 英語 <input type="checkbox"/> 中国語
共同演者名 Co-presenter			
学会名 Conference			
演題 Topic			
開催日 date	年 月 日	開催地 venue	
形式 method	<input type="checkbox"/> 口頭発表 Oral <input type="checkbox"/> ポスター発表 Poster	言語 Language	<input type="checkbox"/> 日本語 <input type="checkbox"/> 英語 <input type="checkbox"/> 中国語
共同演者名 Co-presenter			

4. 受賞(研究業績) Award (Research achievement)

名称 Award name	国名 Country	受賞年 Year of award	年 月
名称 Award name	国名 Country	受賞年 Year of award	年 月

5. 本研究テーマに関わる他の研究助成金受給 Other research grants concerned with your research theme

受給実績 Receipt record	<input type="checkbox"/> 有 <input type="checkbox"/> 無
助成機関名称 Funding agency	
助成金名称 Grant name	
受給期間 Supported period	年 月 ~ 年 月
受給額 Amount received	円
受給実績 Receipt record	<input type="checkbox"/> 有 <input type="checkbox"/> 無
助成機関名称 Funding agency	
助成金名称 Grant name	
受給期間 Supported period	年 月 ~ 年 月
受給額 Amount received	円

6. 他の奨学金受給 Another awarded scholarship

受給実績 Receipt record	<input checked="" type="checkbox"/> 有 <input type="checkbox"/> 無
助成機関名称 Funding agency	Nagasaki University
奨学金名称 Scholarship name	Maeda Saeko Memorial Scholarship
受給期間 Supported period	2021 年 4 月 ~ 2022 年 4 月
受給額 Amount received	600,000 円

7. 研究活動に関する報道発表 Press release concerned with your research activities

※記載した記事を添付してください。Attach a copy of the article described below

報道発表 Press release	<input type="checkbox"/> 有 <input type="checkbox"/> 無	発表年月日 Date of release	
発表機関 Released medium			
発表形式 Release method	・新聞 ・雑誌 ・Web site ・記者発表 ・その他()		
発表タイトル Released title			

8. 本研究テーマに関する特許出願予定 Patent application concerned with your research theme

出願予定 Scheduled	<input type="checkbox"/> 有 <input type="checkbox"/> 無	出願国 Application	
出願内容(概要) Application contents			

9. その他 Others

--

指導責任者(記名) 李 桃生

RESEARCH

Open Access



Hyperoxia but not high tidal volume contributes to ventilator-induced lung injury in healthy mice

Yong Xu^{1,2}, Yu Li³, Da Zhai^{1,2}, Chen Yan^{1,2}, Jingyan Liang⁴, Taiga Ichinomiya⁵, Tetsuya Hara⁵, Chiaki Inadomi^{5*} and Tao-Sheng Li^{1,2*}

Abstract

Background Mechanical ventilation is a supportive therapy used to maintain respiratory function in several clinical and surgical cases but is always accompanied by lung injury risk due to improper treatment. We investigated how tidal volume and oxygen delivery would contribute independently or synergistically to ventilator-induced lung injury (VILI).

Methods Under general anesthesia and tracheal intubation, healthy female C57BL/6 N mice (9 weeks old) were randomly ventilated for 2 h by standard (7 ml/kg) or high (14 ml/kg) tidal volume at positive end-expiratory pressure (PEEP) of 2 cmH₂O, with room air, 50% O₂ (moderate hyperoxia), or 100% O₂ (severe hyperoxia); respectively. Mice were sacrificed 4 h after mechanical ventilation, and lung tissues were collected for experimental assessments on lung injury.

Results Compared with the healthy control, severe hyperoxia ventilation by either standard or high tidal volume resulted in significantly higher wet-to-dry lung weight ratio and higher levels of IL-1 β and 8-OHdG in the lungs. However, moderate hyperoxia ventilation, even by high tidal volume did not significantly increase the levels of IL-1 β and 8-OHdG in the lungs. Western blot analysis showed that the expression of RhoA, ROCK1, MLC2, and p-MLC2 was not significantly induced in the ventilated lungs, even by high tidal volume at 2 cmH₂O PEEP.

Conclusion Severe hyperoxia ventilation causes inflammatory response and oxidative damage in mechanically ventilated lungs, while high tidal volume ventilation at a reasonable PEEP possibly does not cause VILI.

Keywords Mechanical ventilation, Tidal volume, Oxidative damage, Inflammatory response, Mechanotransduction

*Correspondence:

Chiaki Inadomi
inadomic@nagasaki-u.ac.jp
Tao-Sheng Li
litaoshe@nagasaki-u.ac.jp

¹ Department of Stem Cell Biology, Atomic Bomb Disease Institute, Nagasaki University, 1-12-4 Sakamoto, Nagasaki 852-8523, Japan

² Department of Stem Cell Biology, Nagasaki University Graduate School of Biomedical Sciences, 1-12-4 Sakamoto, Nagasaki 852-8523, Japan

³ Department of Anesthesiology, The Second Affiliated Hospital of Nanchang University, Nanchang City 330006, Jiangxi Province, China

⁴ Institute of Translational Medicine, Medical College, Yangzhou University, Yangzhou 225000, Jiangsu, P.R. China

⁵ Department of Anesthesiology and Intensive Care Medicine, Nagasaki University Graduate School of Biomedical Sciences, 1-7-1 Sakamoto, Nagasaki 852-8501, Japan



© The Author(s) 2023. **Open Access** This article is licensed under a Creative Commons Attribution 4.0 International License, which permits use, sharing, adaptation, distribution and reproduction in any medium or format, as long as you give appropriate credit to the original author(s) and the source, provide a link to the Creative Commons licence, and indicate if changes were made. The images or other third party material in this article are included in the article's Creative Commons licence, unless indicated otherwise in a credit line to the material. If material is not included in the article's Creative Commons licence and your intended use is not permitted by statutory regulation or exceeds the permitted use, you will need to obtain permission directly from the copyright holder. To view a copy of this licence, visit <http://creativecommons.org/licenses/by/4.0/>. The Creative Commons Public Domain Dedication waiver (<http://creativecommons.org/publicdomain/zero/1.0/>) applies to the data made available in this article, unless otherwise stated in a credit line to the data.

Introduction

Every year over 800,000 critically ill patients require mechanical ventilation in the United States [1]. Although mechanical ventilation provides essential life support, can also induce or aggravate lung injury by causing ventilator-induced lung injury (VILI) [2]. Mechanical ventilation strategies for reducing VILI in patients with apparent pulmonary diseases are well known: low tidal volume to limit overdistention, optimal oxygen level to prevent hyperoxia, and high positive end-expiratory pressure (PEEP) to prevent injury from low lung volume (atelectrauma) and alveolar collapse [3–5]. Mechanical ventilation is also often applied to patients with shock [6, 7], general anesthesia cases [8], respiratory arrest [9], and so on. Previous studies have attempted to optimize tidal volume and oxygen level to alleviate VILI in patients without apparent pulmonary diseases [3, 10–12]. However, the optimal mechanical ventilation strategy for cases without apparent pulmonary diseases is still uncertain.

Excessive high tidal volume ventilation can result in oxidative stress-induced damage, recruitment of neutrophils, and local release of inflammatory mediators in lungs [13, 14]. VILI involves direct tissue damage due to high mechanical stretch and indirect tissue damage by transducing mechanical stress to activate specific intracellular pathways involved in “mechanotransduction” in lung cells. Previous studies have demonstrated the critical role of mechanotransduction signaling pathways, mainly including Rho-associated protein kinase (ROCK) signaling pathway in VILI. Rho GTPases are signaling G proteins that are distributed across the lower surface of the cell and regulate cytoskeletal dynamics by controlling actin polymerization and myosin II-mediated contraction [15, 16].

Oxygen administration is important for preventing or correcting hypoxemia. Exposure to hyperoxia is a recognized cause of lung injury, producing histopathologic changes similar to those seen in VILI, including oxidative stress and inflammatory response [17–19]. Oxidative damage is mediated by reactive oxygen species (free radicals) derived directly from molecular oxygen. The accumulation of free hydroxyl radicals and peroxynitrite results in the oxidation of proteins and peroxidation of membrane lipids and nucleic acids [20, 21]. Despite the near-ubiquitous concomitant use of mechanical ventilation and oxygen delivery, little is known about the independent and synergistic effects of tidal volume and oxygen delivery on VILI underlying healthy lungs.

In this study, we purposed to investigate how tidal volume and oxygen delivery would independently or synergistically contribute to VILI, mainly focusing on the inflammatory response and oxidative damage in the lungs.

Materials and methods

Animals

Nine weeks old female C57BL/6 N mice (19–22 g, CLEA, Japan) were used for the study. Mice were housed in a pathogen-free room with a controlled environment under a 12-h light-dark cycle and maintained on laboratory chow, with free access to food and water as previously described [22]. This study was approved by the Institutional Animal Care and Use Committee of Nagasaki University (No.1608251335-12). All animal procedures were performed in accordance with institutional and national guidelines.

Mechanical ventilation protocol

Mice were anesthetized with intraperitoneal injection of domitor (0.75 mg/kg), midazolam (4 mg/kg), vetorphale (5 mg/kg), and then orotracheally intubated with a 20 g intravenous indwelling catheter and attached to a mini ventilator (MiniVent Type 845, Harvard Apparatus, USA). Mice were randomized to be ventilated by standard tidal volume (7 ml/kg) [23, 24] or high tidal volume (14 ml/kg); respectively with room air (21% O₂), 50% O₂ (FIO₂=0.5, moderate hyperoxia), or 100% O₂ (FIO₂=1.0, severe hyperoxia) for 2 h (Fig. 1A). The ventilation rate was 120 breaths/min. We used 2 cmH₂O PEEP in the official experiments, but high tidal volume ventilation with room air (21% O₂) at 10 cm and 20 cmH₂O PEEP were also tested for inducing lung injury. Non-ventilated mice under general anesthesia with spontaneous breathing were used as controls and were kept on spontaneous breathing for 6 h before being sacrificed. Body temperature was maintained using a 37 °C heating pad.

Tissue sampling

Mice were sacrificed at 4 h after mechanical ventilation (Fig. 1A). After flushing with PBS via right ventricle to remove the blood, the lungs were extracted and weighed. The left lobe was fixed with 4% paraformaldehyde for paraffin sections. The right superior lobe was used for measuring the wet-to-dry lung weight ratio. The other lobes of the right lung tissue samples were stored under –80 °C, and used for other experimental analyses.

Lung wet-to-dry weight ratio

The wet-to-dry lung weight ratio is widely used as a parameter for the assessment of pulmonary edema. The freshly extracted lung tissue sample of the right superior lobe was weighed and recorded as the wet weight. After the incubation in an oven at 80 °C for 24 h, the dried tissue sample was weighed and recorded as dry weight. The wet-to-dry lung weight ratio was calculated.

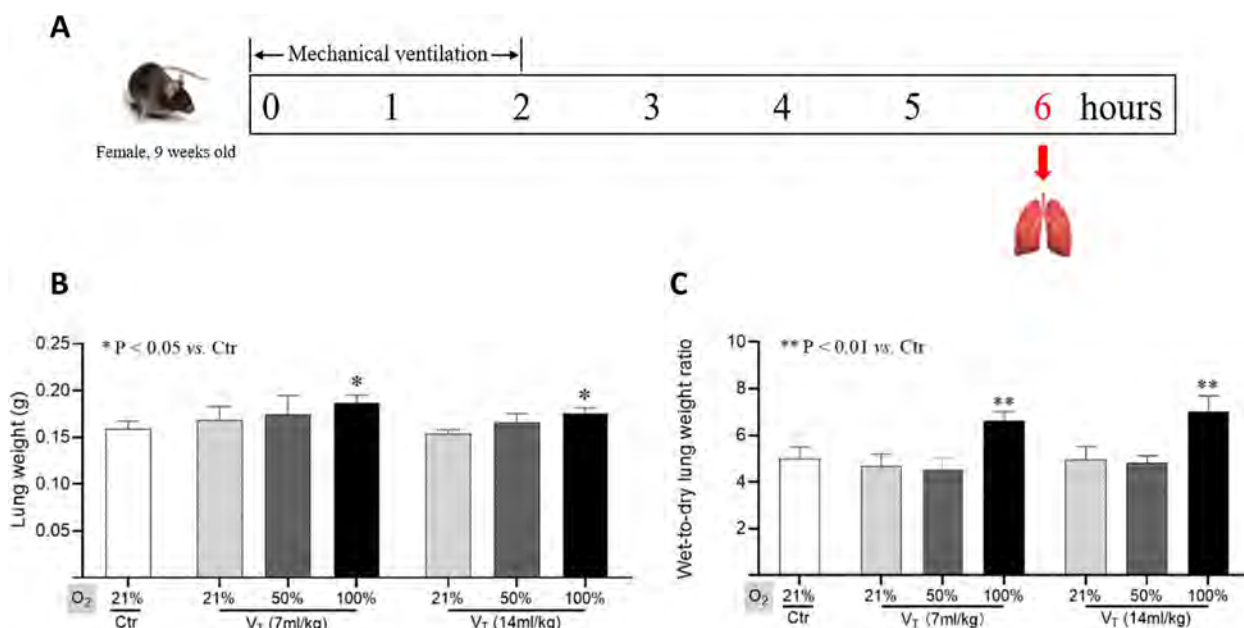


Fig. 1 Lung weight and wet-to-dry lung weight ratio. **A.** Schematic diagram about the experimental timeline. Lung weight (**B**) and wet-to-dry lung weight ratio (**C**) are shown. Data are represented as the means ± SD, n = 3~5 in each group. *p < 0.05, **p < 0.01 vs. Ctr group. V_T: tidal volume

Immunohistochemical analysis

The oxidative injury of the lungs was detected by immunohistochemical analysis as previously described [22]. Briefly, paraffin sections of 5-µm-thick were deparaffinized and rehydrated. After antigen retrieval and blocking, sections were incubated with anti-mouse 8-OHdG antibody (1:100 dilution, Santa Cruz) overnight at 4°C, and followed by the appropriate fluorescent-conjugated secondary antibodies at 25 °C for 60 min. The nuclei were stained with 4, 6-diamidino-2-phenylindole (DAPI) (1:1000 dilution, Life technologies). The positive staining was examined under fluorescence microscope (FV10CW3, OLYMPUS). The percentage of 8-OHdG-positive cells was calculated from 12 randomly selected fields of view (6 fields/slide in 2 slides) and used for statistical analysis.

ELISA

To evaluate the inflammatory response, ELISA kits (R&D Systems) were used to detect the contents of transforming growth factor β1 (TGF-β1) and interleukin-1beta (IL-1β) in lung tissue lysates as previously described [25]. Briefly, the lung tissues were homogenized using Multi-beads shocker® and added to the T-PER reagent (Thermo Fisher Scientific) consisting of proteinase and dephosphorylation inhibitors (Thermo Fisher Scientific). Lung tissue lysates (100 µg protein) were added to each well and measured following the manufacturer’s instructions. The optical density was measured at 450 nm

using a microplate reader (Multiskan Fc, Thermo Fisher Scientific).

RT-qPCR analysis

RT-qPCR was performed to evaluate the gene expression of *Rhoa*, *Rock1*, *Rock2*, *Tgfb1* and *Actb*. Briefly, total RNA was isolated from the lung tissues using Quick-RNATMMicroPrep Kit (Zymo Research, Irvine, CA, USA). RNA concentration and purity were measured by a NanoDrop2000 spectrophotometer (Thermo-Fisher Scientific, Wal-tham, MA, USA) and 1.25 µg RNA was reverse-transcribed using the SuperScript™ VILO™ cDNA Synthesis Kit (Thermo-Fisher Scientific). Quantitative PCR was carried out with the SYBR Green real-time PCR Master Mix (Toyobo, Osaka, Japan). The reactions were performed on a CFX96™ real-time PCR System (Bio-Rad). The gene expression was normalized by housekeeping gene *Actb*. Primers were the following: *Rhoa* (Forward: 5'- TGCTTGCTCATA GTCTTCA-3'; Reverse:5'-CCAACTCTACCTGCTTCC -3'); *Rock1* (Forward: 5'- AGC TTT TGTTGG CAA TCA GC -3'; Reverse:5'- ACT TTC CTGCAA GCT TTT ATC CA -3'); *Rock2* (Forward: 5'- CAGTCC CTG GGT AGT TCA GC -3'; Reverse:5'- GCCTGG CAT ATA CTCCATC-3'); *Tgfb1* (Forward:5'-ATTCTGCGCT TACCTTG-3'; Reverse:5'-CTGTATTCCGCTCTCCTTG G-3'); *Actb* (Forward:5'-GCACCACACTTCTACAA -3'; Reverse:5'-TACGACCAGAGGCATACA-3').

Western blot

Western blot was performed as previously described [22]. Total proteins (30 ug) from lung tissue were separated by SDS-PAGE gels and then transferred to 0.22-μm PVDF membranes (Bio-Rad). After blocking, the membranes were incubated with primary antibodies against RhoA (1:1000 dilution; cat. no. 2117s; CST), ROCK1 (1:1000 dilution; ab156284; Abcam), MLC2 (1:1000 dilution; cat. no. 3672s; CST), p-MLC2 (1:1000 dilution; cat. no. 3671s; CST), 8-OHdG (1:500 dilution; sc-393,871; Santa Cruz), or α-Tubulin (1:1000 dilution; cat. no. 3873 S; CST) overnight at 4°C, respectively; followed by the appropriate horseradish peroxidase-conjugated secondary antibodies (Dako). The expression was visualized using an enhanced chemiluminescence detection kit (Thermo Scientific). Semiquantitative analysis was done using ImageQuant LAS 4000 mini (GE Healthcare Life Sciences). Additional file 1 is the original WB image in the manuscript.

Statistical analysis

Statistical analysis was performed as previously described [25]. All the values were presented as the mean ± SD. For comparison of multiple sets of data, one-way analysis of variance (ANOVA) followed by Tukey’s test (Dr. SPSS II, Chicago, IL) was used for statistical analyses. All analyses were carried out with the SPSS19.0 statistical software (IBM SPSS Co., USA). A *p*-value less than 0.05 was accepted as significant.

Results

Mechanical ventilation with severe hyperoxia at 2 cmH₂O PEEP significantly induces lung injury

All mice survived in the official experiments (Fig. 1A). Our data showed that lung weight in severe hyperoxia ventilation with standard or high tidal volume were increased significantly (*p* < 0.05 vs. control; Fig. 1B).

Similarly, severe hyperoxia ventilation significantly increased the wet-to-dry lung weight ratio, regardless of standard or high tidal volume (*p* < 0.01 vs. control; Fig. 1C).

ELISA was performed to detect the levels of IL-1β and TGF-β1. IL-1β level in the lungs was significantly increased by severe hyperoxia ventilation with either standard or high tidal volume (*p* < 0.05 or *p* < 0.01 vs. control; Fig. 2A). However, moderate hyperoxia ventilation, even by high tidal volume for 2 h did not significantly increase the IL-1β level in lungs (Fig. 2A). Consistent with previous study [26], TGF-β1 level was not significantly changed in the ventilated lungs compared with the control (Fig. 2B).

Oxidative stress can damage macromolecules such as DNA, lipids, and proteins, and 8-OHdG is a marker of oxidative damage to DNA and RNA [27]. Immunohistochemical analysis of lung tissues showed that severe hyperoxia, not moderate hyperoxia ventilation with high or standard tidal volume significantly increased the expression of 8-OHdG in the lungs (*p* < 0.01 vs. control; Fig. 3A). Moreover, Western blot also confirmed the enhancement of 8-OHdG in the ventilated lungs with severe hyperoxia (*p* < 0.01 vs. control; Fig. 3B).

Relatively high tidal volume ventilation at 2 cmH₂O PEEP does not clearly induce lung injury

Previous studies have reported that excessive high tidal volume (> 25 ml/kg) ventilation can independently lead to lung injury [4, 28]. In this study, a relatively high tidal volume (14 ml/kg, double of standard) ventilation at 2 cmH₂O PEEP for 2 h did not significantly increase the wet-to-dry lung weights ratio, as well as the levels of IL-1β and 8-OHdG in the lungs (Figs. 2 and 3). This suggests inconspicuous damage in the lungs.

We further tried to evaluate whether high tidal volume ventilation induced the activation of mechanotransduction signaling in the lungs. Western blot analysis showed that the expression of RhoA, ROCK1,

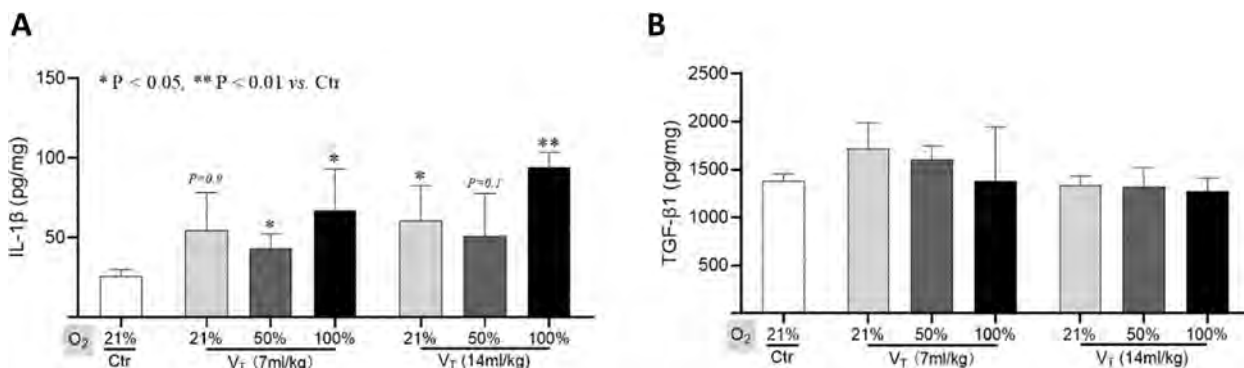


Fig. 2 The levels of IL-1β and TGF-β1 in lung tissues. ELISA data on the levels of IL-1β (A) and TGF-β1 (B) in lungs are shown. Data are represented as the means ± SD, n = 3 ~ 5 in each group. **p* < 0.05, ***p* < 0.01 vs. Ctr group. V_T: tidal volume

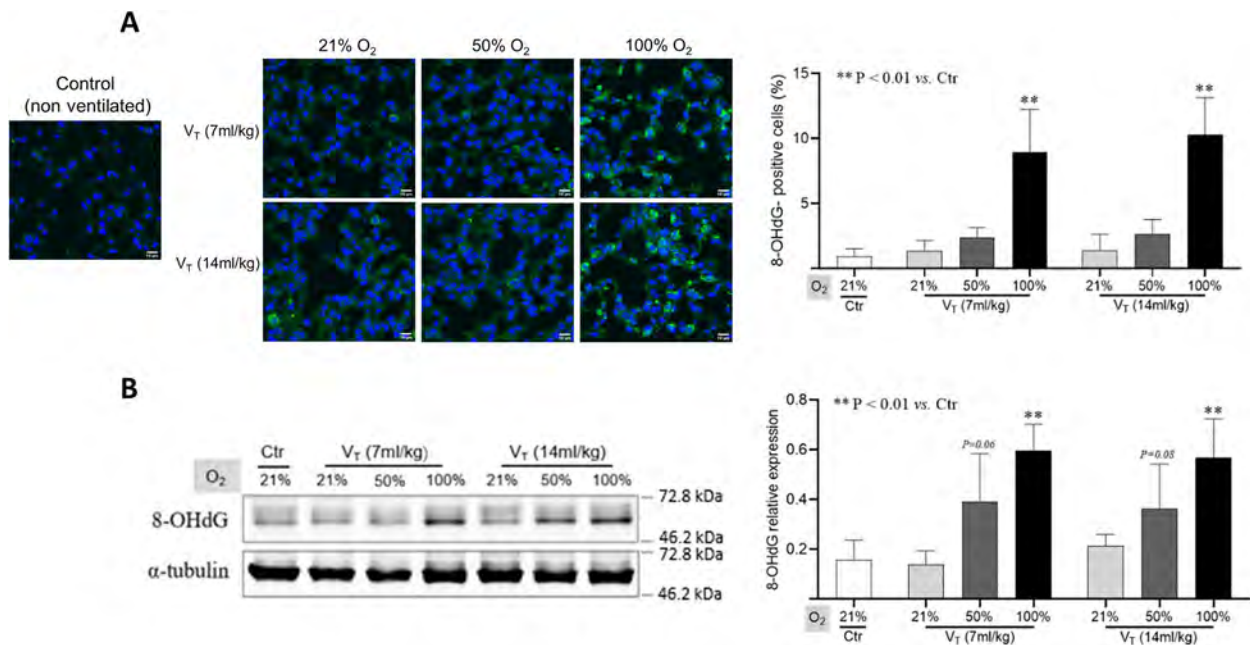


Fig. 3 The expression of 8-OHdG in lung tissues. **A** Representative confocal images (left) and quantitative data (right) of 8-OHdG-positive cells in lung tissues. **B** Representative blots (left) and quantitative data (right) on the expression of 8-OHdG in lungs. Data are normalized to α -tubulin and represented as the means \pm SD, $n = 3 \sim 5$ in each group. $**p < 0.01$ vs. Ctr group. V_T: tidal volume. Additional file 1 is the original WB image in the manuscript

MLC2, and p-MLC2 was not significantly increased in the ventilated lungs even by high tidal volume at 2 cmH₂O PEEP (Fig. 4). RT-qPCR analysis also confirmed that the expression of *Rhoa*, *Rock1*, *Rock2*, and *Tgfb1* was not significantly enhanced in the ventilated lungs (Fig. 5).

Maintaining some amount of PEEP is essential for patients receiving mechanical ventilation [29]. Because our data showed a non-injurious setting for high tidal volume ventilation at 2 cmH₂O PEEP, we then tested

whether VILI would be detectable clearly at higher PEEP. Mice were assigned to be ventilated with high tidal volume (14 ml/kg) with room air at 10 or 20 cmH₂O PEEP for 2 h. All mice survived well during mechanical ventilation, but one mouse died at 1 h after mechanical ventilation at 20 cmH₂O PEEP. Our data showed that high tidal volume ventilation at 10 or 20 cmH₂O PEEP resulted in higher wet-to-dry lung weight ratio and enhanced the expression of IL-1 β , TGF- β 1, and 8-OHdG in the lungs (Supplementary Fig. 1). However, the expression of *Rhoa*,

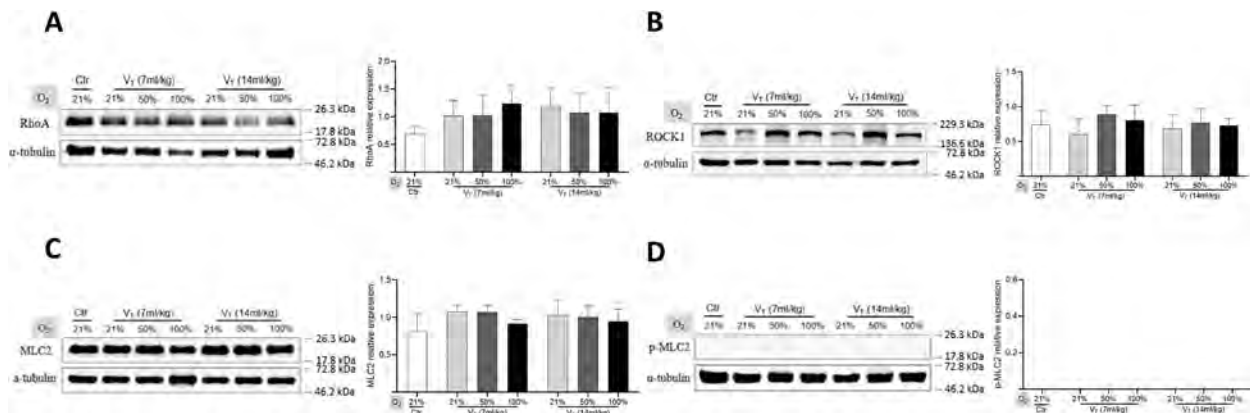


Fig. 4 Western blot analysis on the expression of RhoA, ROCK1, MLC2, and p-MLC2 in lungs. Representative blots (left) and quantitative data (right) on the expression of RhoA (**A**), ROCK1 (**B**), MLC2 (**C**), and p-MLC2 (**D**). Data are normalized to α -tubulin and represented as the means \pm SD, $n = 3 \sim 5$ in each group. V_T: tidal volume. Additional file 1 is the original WB image in the manuscript

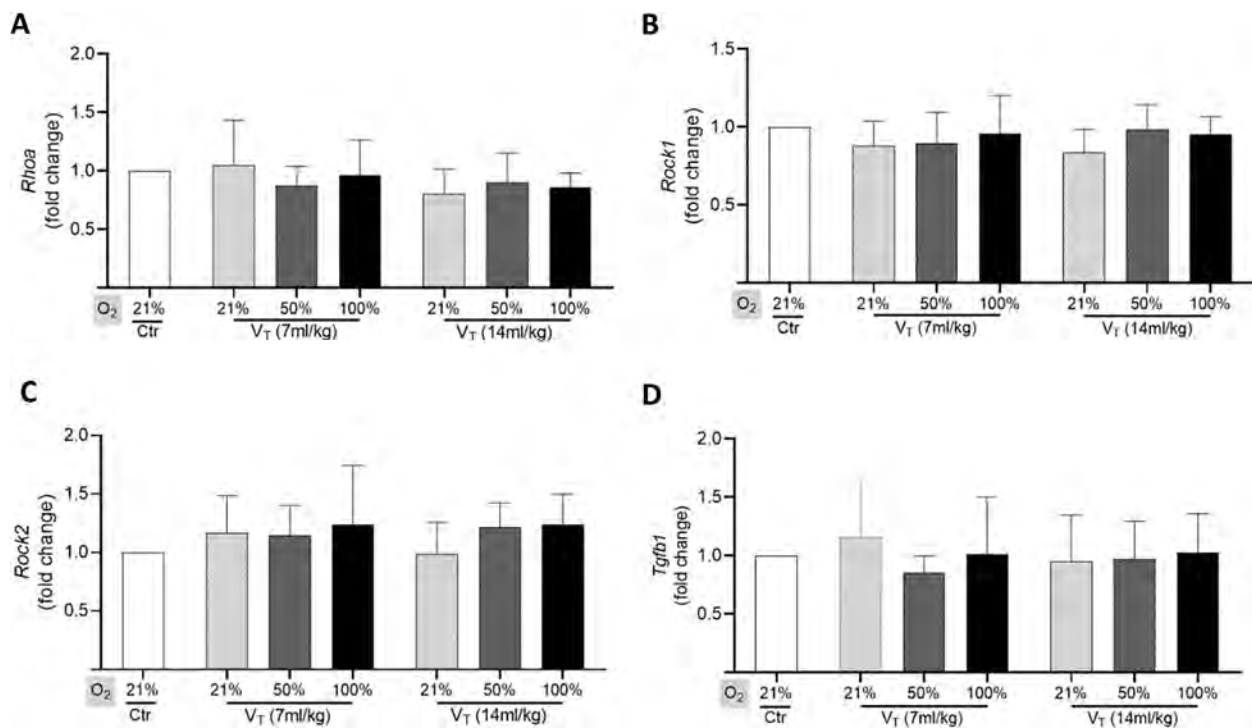


Fig. 5 RT-PCR analysis on the expression of *Rhoa*, *Rock1*, *Rock2*, and *Tgfb1* in lungs. Quantitative RT-PCR data shows the relative expression of *Rhoa* (A), *Rock1* (B), *Rock2* (C), and *Tgfb1* (D) in lungs. Data are represented as the means \pm SD, $n=3\sim 5$ in each group. V_T : tidal volume

Rock1, and *Rock2* in the lungs kept stable or even slightly decreased at 4 h after high tidal volume ventilation at 10 or 20 cmH₂O PEEP (Supplementary Fig. 2).

Discussion

Mechanical ventilation-associated lung injury is a common clinical complication in critically ill patients. Unequivocal evidence suggests that excessive mechanical ventilation and hyperoxia have the potential to aggravate and precipitate lung injury in patients without apparent pulmonary diseases [3, 10–12]. In this study, we also found that severe hyperoxia ventilation clearly induced lung injury. In contrast, lung injury was not clearly detectable with moderate hyperoxia ventilation with a relatively high tidal volume at 2 cmH₂O PEEP.

The levels of oxygen commonly used clinically, ranging from 50 to 100% in one atmosphere, are potentially toxic, and these patients risk exacerbation of underlying lung injury. Previous studies have demonstrated that hyperoxia augments lung injury from excessive high tidal volume ventilation in rabbits [30], in rats [31], and in ex vivo mouse lungs [32]. Although the tolerances to oxygen toxicity may be a little different between mice and human beings, healthy mice are still commonly used for experimental investigation of

VILI. In this study, severe hyperoxia (100% O₂) ventilation for 2 h significantly increased the wet-to-dry lung weight ratio, as well as IL-1 β and 8-OHdG levels in the lungs, suggesting VILI. However, moderate hyperoxia (50% O₂) ventilation did not significantly induce lung injury, even with high tidal volume. Moreover, we did not detect significant changes in TGF- β 1 expression. We speculated that mechanical ventilation with relative high tidal volume (14 ml/kg) at 2 cmH₂O PEEP for 2 h might not be able to activate the TGF- β signaling pathway [26].

According to previous studies [28, 30], excessive high tidal volume (> 25ml/kg) ventilation is associated with the increased release of inflammatory cytokines and exacerbated oxidative damage. As this study is purposed to investigate VILI in patients without apparent pulmonary diseases, we only tested a relatively high tidal volume (14 ml/kg, double of standard). Based on the levels of IL-1 β , TGF- β 1 and 8-OHdG in the lungs, high tidal volume ventilation with air or moderate hyperoxia at 2 cmH₂O PEEP for 2 h did not clearly induce serious injuries to the lungs. As shown in the supplemental data, to confirm that the negative data would not be a technical problem of assessment, we used several mice to test high tidal volume ventilation

with room air at very high PEEP. Our data showed that high tidal volume ventilation with room air at very high PEEP (> 10 cmH₂O) increased the levels of IL-1 β , TGF- β 1, and 8-OHdG in lungs, indicating VILI. Therefore, short-term ventilation with high tidal volume (14 ml/kg) at a low/physiological level of PEEP will be harmless.

In conditions of excessive mechanical overdistension, animal models have shown different signaling pathways involved in the induction of lung injury through mechanical transduction, including RhoA/ROCK signaling, and the MLC phosphorylation of downstream targets of ROCK [15, 16]. Although a relatively high tidal volume (14 ml/kg) ventilation did not cause obvious lung injury in our study, we were still interested to know about the activation of the mechanotransduction signalings in the lungs. Unexpectedly, the expression of RhoA, ROCK1, MLC2, and p-MLC2 was not significantly changed in the lungs ventilated with a relatively high tidal volume at 2 cmH₂O PEEP. Furthermore, the expression of *Rhoa*, *Rock1*, and *Rock2* in the lungs even slightly decreased at 4 h after high tidal volume ventilation at 10 or 20 cmH₂O PEEP, although lung injuries were clearly detectable. Several reasons can be considered about the “inactivation” of mechanotransduction signalings in lungs in our study. Firstly, it is difficult to detect changes in the expression of RhoA, ROCK, and MLC2 in lungs [33, 34]. Secondly, we collected the lung tissues at 4 h after mechanical ventilation administration, which might be not a suitable time window for sensitive detection about the changes of p-MLC2 according to previous reports [35, 36]. Thirdly, the anesthetic midazolam we used is a common central muscle relaxant, which might interfere with the activation of mechanotransduction signaling.

There are some limitations in our study. Firstly, it is necessary to include experimental groups of spontaneous breathing with high F_{IO2} for validating the oxygen toxicity to the lungs. Secondly, as this study was originally designed to investigate the synergistic effect of high tidal volume and hyperoxia in VILI, we only evaluated the inflammatory response by IL-1 β and TGF- β levels. Thirdly, we were also not able to include more reliable parameters on VILI definition, such as respiratory mechanics and histological findings.

Conclusions

Severe hyperoxia ventilation causes inflammatory response and oxidative damage in mechanically ventilated lungs, while high tidal volume ventilation at a reasonable PEEP possibly does not cause VILI.

Supplementary Information

The online version contains supplementary material available at <https://doi.org/10.1186/s12890-023-02626-x>.

Additional file 1.

Acknowledgements

Not applicable.

Authors' contributions

TSL and CI contributed to the conception and design of the study. YX performed the experiments and acquired the data. TSL, YX, YL, DZ, CY, JYL, TI, TH, and CI analyzed and interpreted the data. YX drafted the manuscript and prepared figures. TSL, YX, YL, and DZ critically revised the manuscript for important intellectual content. TSL and CI confirmed the authenticity of all the raw data. All authors read and approved the final version of the manuscript.

Funding

Not applicable.

Availability of data and materials

The datasets used and/or analyzed during the current study are available from the corresponding author on reasonable request.

Declarations

Ethics approval and consent to participate

The animal experiments were approved by the Institutional Animal Care and Use Committee of Nagasaki University (approval no.1608251335-12). We confirmed that all experiments were performed in accordance with relevant guidelines and regulations. And we ensured that manuscript reporting adhered to the ARRIVE guidelines (<https://arriveguidelines.org>) for the reporting of animal experiments.

Consent for publication

Not applicable.

Competing interests

The authors declare no competing interests.

Received: 28 May 2023 Accepted: 31 August 2023

Published online: 20 September 2023

References

- Supinski GS, Callahan LA. Diaphragm weakness in mechanically ventilated critically ill patients. *Crit Care*. 2013;17(3):R120.
- Henderson WR, Chen L, Amato MBP, Brochard LJ. Fifty years of Research in ARDS. *Respiratory mechanics in Acute Respiratory Distress Syndrome*. *Am J Respir Crit Care Med*. 2017;196(7):822–33.
- Gajic O, Dara SI, Mendez JL, Adesanya AO, Festic E, Caples SM, Rana R, St Sauver JL, Lymp JF, Afessa B, Hubmayr RD. Ventilator-associated lung injury in patients without acute lung injury at the onset of mechanical ventilation. *Crit Care Med*. 2004;32(9):1817–24.
- Slutsky AS, Ranieri VM. Ventilator-induced lung injury. *N Engl J Med*. 2013;369(22):2126–36.
- Futier E, Constantin JM, Paugam-Burtz C, Pascal J, Eurin M, Neuschwander A, Marret E, Beaussier M, Gutton C, Lefrant JY, Allaouchiche B, Verzilli D, Leone M, De Jong A, Bazin JE, Pereira B, Jaber S, IMPROVE Study Group. A trial of intraoperative low-tidal-volume ventilation in abdominal surgery. *N Engl J Med*. 2013;369(5):428–37.
- Alviar CL, Rico-Mesa JS, Morrow DA, Thiele H, Miller PE, Maselli DJ, van Diepen S. Positive pressure ventilation in cardiogenic shock: review of the evidence and practical advice for patients with mechanical circulatory support. *Can J Cardiol*. 2020;36(2):300–12.

7. Joffroy R, Saade A, Pegat-Toquet A, Philippe P, Carli P, Vivien B. Pre-hospital mechanical ventilation in septic shock patients. *Am J Emerg Med.* 2019;37(10):1860–3.
8. Guay J, Ochroch EA, Kopp S. Intraoperative use of low volume ventilation to decrease postoperative mortality, mechanical ventilation, lengths of stay and lung injury in adults without acute lung injury. *Cochrane Database Syst Rev.* 2018;7(7):CD011151.
9. Khoury A, De Luca A, Sall FS, Pazart L, Capellier G. Ventilation feedback device for manual ventilation in simulated respiratory arrest: a crossover manikin study. *Scand J Trauma Resusc Emerg Med.* 2019;27(1):93.
10. Serpa Neto A, Cardoso SO, Manetta JA, Pereira VG, Espósito DC, Pasqualucci Mde O, Damasceno MC, Schultz MJ. Association between use of lung-protective ventilation with lower tidal volumes and clinical outcomes among patients without acute respiratory distress syndrome: a meta-analysis. *JAMA.* 2012;308(16):1651–9.
11. Determann RM, Royakkers A, Wolthuis EK, Vlaar AP, Choi G, Paulus F, Hofstra JJ, de Graaff MJ, Korevaar JC, Schultz MJ. Ventilation with lower tidal volumes as compared with conventional tidal volumes for patients without acute lung injury: a preventive randomized controlled trial. *Crit Care.* 2010;14(1):R1.
12. Wongsurakiat P, Pierson DJ, Rubenfeld GD. Changing pattern of ventilator settings in patients without acute lung injury: changes over 11 years in a single institution. *Chest.* 2004;126(4):1281–91.
13. Chapman KE, Sinclair SE, Zhuang D, Hassid A, Desai LP, Waters CM. Cyclic mechanical strain increases reactive oxygen species production in pulmonary epithelial cells. *Am J Physiol Lung Cell Mol Physiol.* 2005;289(5):L834–41.
14. Davidovich N, DiPaolo BC, Lawrence GG, Chhour P, Yehya N, Margulies SS. Cyclic stretch-induced oxidative stress increases pulmonary alveolar epithelial permeability. *Am J Respir Cell Mol Biol.* 2013;49(1):156–64.
15. Marchioni A, Tonelli R, Cerri S, Castaniere I, Andrisani D, Gozzi F, Bruzzi G, Manicardi L, Moretti A, Demurtas J, Baroncini S, Andreani A, Cappiello GF, Busani S, Fantini R, Tabbi L, Samarelli AV, Clini E. Pulmonary Stretch and Lung Mechanotransduction: implications for progression in the fibrotic lung. *Int J Mol Sci.* 2021;22(12):6443.
16. Tschumperlin DJ, Ligresti G, Hilscher MB, Shah VH. Mechanosensing and fibrosis. *J Clin Invest.* 2018;128(1):74–84.
17. Matute-Bello G, Frevert CW, Martin TR. Animal models of acute lung injury. *Am J Physiol Lung Cell Mol Physiol.* 2008;295(3):L379–99.
18. Choi WI, Quinn DA, Park KM, Moufarrej RK, Jafari B, Syrkinina O, Bonventre JV, Hales CA. Systemic microvascular leak in an in vivo rat model of ventilator-induced lung injury. *Am J Respir Crit Care Med.* 2003;167(12):1627–32.
19. Held HD, Boettcher S, Hamann L, Uhlig S. Ventilation-induced chemokine and cytokine release is associated with activation of nuclear factor- κ B and is blocked by steroids. *Am J Respir Crit Care Med.* 2001;163(3 Pt 1):711–6.
20. Nakane M. Biological effects of the oxygen molecule in critically ill patients. *J Intensive Care.* 2020;8(1):95.
21. Auten RL, Davis JM. Oxygen toxicity and reactive oxygen species: the devil is in the details. *Pediatr Res.* 2009;66(2):121–7.
22. Xu Y, Zhai D, Goto S, Zhang X, Jingu K, Li TS. Nicaraven mitigates radiation-induced lung injury by downregulating the NF- κ B and TGF- β /Smad pathways to suppress the inflammatory response. *J Radiat Res.* 2022;63(2):158–65.
23. Dreyfuss D, Soler P, Saumon G. Mechanical ventilation-induced pulmonary edema. Interaction with previous lung alterations. *Am J Respir Crit Care Med.* 1995;151(5):1568–75.
24. Wolthuis EK, Vlaar AP, Choi G, Roelofs JJ, Juffermans NP, Schultz MJ. Mechanical ventilation using non-injurious ventilation settings causes lung injury in the absence of pre-existing lung injury in healthy mice. *Crit Care.* 2009;13(1):R1.
25. Yan C, Luo L, Urata Y, Goto S, Li TS. Nicaraven reduces cancer metastasis to irradiated lungs by decreasing CCL8 and macrophage recruitment. *Cancer Lett.* 2018;418:204–10.
26. Cabrera-Benítez NE, Parotto M, Post M, Han B, Spieth PM, Cheng WE, Valladares F, Villar J, Liu M, Sato M, Zhang H, Slutsky AS. Mechanical stress induces lung fibrosis by epithelial-mesenchymal transition. *Crit Care Med.* 2012;40(2):510–7.
27. Helbock HJ, Beckman KB, Ames BN. 8-Hydroxydeoxyguanosine and 8-hydroxyguanine as biomarkers of oxidative DNA damage. *Methods Enzymol.* 1999;300:156–66.
28. Amatullah H, Maron-Gutierrez T, Shan Y, Gupta S, Tsoporis JN, Varkouhi AK, Teixeira Monteiro AP, He X, Yin J, Marshall JC, Rocco PRM, Zhang H, Kuebler WM, Dos Santos CC. Protective function of DJ-1/PARK7 in lipopolysaccharide and ventilator-induced acute lung injury. *Redox Biol.* 2021;38:101796.
29. Mercat A, Richard JC, Vielle B, Jaber S, Osman D, Diehl JL, Lefrant JY, Prat G, Richecoeur J, Nieszkowska A, Gervais C, Baudot J, Bouadma L, Brochard L. Expiratory pressure (Express) Study Group. Positive end-expiratory pressure setting in adults with acute lung injury and acute respiratory distress syndrome: a randomized controlled trial. *JAMA.* 2008;299(6):646–55.
30. Sinclair SE, Altemeier WA, Matute-Bello G, Chi EY. Augmented lung injury due to interaction between hyperoxia and mechanical ventilation. *Crit Care Med.* 2004;32(12):2496–501.
31. Cooper JA Jr, Fuller JM, McMinn KM, Culbreth RR. Modulation of monocyte chemotactic protein-1 production by hyperoxia: importance of RNA stability in control of cytokine production. *Am J Respir Cell Mol Biol.* 1998;18(4):521–5.
32. Bailey TC, Martin EL, Zhao L, Veldhuizen RA. High oxygen concentrations predispose mouse lungs to the deleterious effects of high stretch ventilation. *J Appl Physiol.* 2003;94(3):975–82.
33. Gawlak G, Tian Y, O'Donnell JJ 3rd, Tian X, Birukova AA, Birukov KG. Paxillin mediates stretch-induced rho signaling and endothelial permeability via assembly of paxillin-p42/44MAPK-GEF-H1 complex. *FASEB J.* 2014;28(7):3249–60.
34. Zhang Y, Jiang L, Huang T, Lu D, Song Y, Wang L, Gao J. Mechanosensitive cation channel Piezo1 contributes to ventilator-induced lung injury by activating RhoA/ROCK1 in rats. *Respir Res.* 2021;22(1):250.
35. Bárány K, Ledvora RF, Mougios V, Bárány M. Stretch-induced myosin light chain phosphorylation and stretch-release-induced tension development in arterial smooth muscle. *J Biol Chem.* 1985;260(11):7126–30.
36. Lee E, Liu Z, Nguyen N, Nairn AC, Chang AN. Myosin light chain phosphatase catalytic subunit dephosphorylates cardiac myosin via mechanisms dependent and independent of the MYPT regulatory subunits. *J Biol Chem.* 2022;298(9):102296.

Publisher's Note

Springer Nature remains neutral with regard to jurisdictional claims in published maps and institutional affiliations.

Ready to submit your research? Choose BMC and benefit from:

- fast, convenient online submission
- thorough peer review by experienced researchers in your field
- rapid publication on acceptance
- support for research data, including large and complex data types
- gold Open Access which fosters wider collaboration and increased citations
- maximum visibility for your research: over 100M website views per year

At BMC, research is always in progress.

Learn more biomedcentral.com/submissions



Optimization on the dose and time of nicaraven administration for mitigating the side effects of radiotherapy in a preclinical tumor-bearing mouse model

Yong Xu, Lina Abdelghany, Reiko Sekiya, Da Zhai, Keiichi Jingu and Tao-Sheng Li 

Abstract

Objective: Radiation-induced lung injury (RILI) is one of the serious complications of radiotherapy. We have recently demonstrated that nicaraven can effectively mitigate RILI in healthy mice. Here, we further tried to optimize the dose and time of nicaraven administration for alleviating the side effects of radiotherapy in tumor-bearing mice.

Methods and results: A subcutaneous tumor model was established in the back of the chest in C57BL/6N mice by injecting Lewis lung cancer cells. Therapeutic thoracic irradiations were done, and placebo or different doses of nicaraven (20, 50, 100 mg/kg) were administered intraperitoneally pre-irradiation (at almost 5–10 min before irradiation) or post-irradiation (within 5 min after irradiation). Mice that received radiotherapy and nicaraven were sacrificed on the 30th day, but control mice were sacrificed on the 15th day. Serum and lung tissues were collected for evaluation. Nicaraven significantly decreased the level of CCL8, but did not clearly change the levels of 8-OHdG, TGF- β , IL-1 β , and IL-6 in serum. Besides these, nicaraven effectively decreased the levels of TGF- β , IL-1 β , and SOD2 in the lungs, especially by post-irradiation administration with the dose of 20 mg/kg. Although there was no significant difference, the expression of SOD1, 53BP1, and caspase 3 was detected lower in the lungs of mice received nicaraven post-irradiation than that of pre-irradiation.

Conclusion: According to our data, the administration of nicaraven at a relatively low dose soon after radiotherapy will be recommended for attenuating the side effects of radiotherapy.

Keywords: DNA damage, fibrosis, inflammatory response, lung injury, radiation

Received: 2 April 2022; revised manuscript accepted: 20 October 2022.

Introduction

Radiotherapy is an essential tool for the treatment of intrathoracic malignancies, including lung, breast, and esophageal cancers.^{1,2} Exposure of healthy tissues to radiation and the toxicity it causes often limits its effectiveness and decreases the survival benefit of radiotherapy. Beyond the systemic side effects, radiation-induced lung injury (RILI) is a serious obstacle to patients receiving radiotherapy for thoracic malignant tumors.^{3,4} RILI occurs in 5–20% of lung cancer patients receiving radiotherapy, which may lead to the discontinuation of treatment. However,

there are still no effective drugs and protective strategies to prevent radiation side effects in cancer patients undergoing radiotherapy.

It is well known that ionizing radiation induces directly DNA double-strand breaks and triggers the release of ROS.⁵ The level of ROS overwhelms can cause oxidative damage to DNA, lipids, and proteins.⁶ Although radiotherapy is a local therapy, it has systemic effects mainly influencing immune and inflammation processes.⁷ Moreover, it has been demonstrated that radiation-induced injuries to tissue cells can promote

Ther Adv Respir Dis

2022, Vol. 16: 1–10

DOI: 10.1177/
17534666221137277

© The Author(s), 2022.

Article reuse guidelines:
sagepub.com/journals-
permissions

Correspondence to:
Tao-Sheng Li
Department of Stem
Cell Biology, Atomic
Bomb Disease Institute,
Nagasaki University, 1-12-
4 Sakamoto, Nagasaki
852-8523, Japan.

Department of Stem Cell
Biology, Graduate School
of Biomedical Sciences,
Nagasaki University,
Nagasaki, Japan
litaoshe@nagasaki-u.ac.jp

Yong Xu
Lina Abdelghany
Da Zhai
Department of Stem
Cell Biology, Atomic
Bomb Disease Institute,
Nagasaki University,
Nagasaki, Japan

Department of Stem Cell
Biology, Graduate School
of Biomedical Sciences,
Nagasaki University,
Nagasaki, Japan

Reiko Sekiya
Department of Stem
Cell Biology, Atomic
Bomb Disease Institute,
Nagasaki University,
Nagasaki, Japan

Keiichi Jingu
Department of Radiation
Oncology, Graduate School
of Medicine, Tohoku
University, Sendai, Japan

the release of a multitude of inflammatory cytokines and chemokines, which indirectly contribute to the consequent damage to cells and tissues and eventually culminate in fibrotic changes.^{8–10} Therefore, the scavenging of ROS and the suppression of the inflammatory response are thought to be potential pharmacological interventions for mitigating the side effects of radiotherapy.

Many past studies have challenged to develop radioprotective agents. Thiol-synthetic compounds, such as amifostine has been approved to use clinically for protecting against radiation injury, however, amifostine has the disadvantages of toxicity and limited route of administration in the clinic.¹¹ Nitrogen oxides, such as Tempol, have also been tested as a radioprotectant, but its application is limited due to problems on producing hypotension and increasing heart rate.¹² Some natural antioxidants, such as vitamin E and selenium have also shown radioprotective effects, but the benefit of antioxidants for cancer radiotherapy is asked to be further confirmed because of the probable effect on radiosensitivity of cancer cells.^{12,13} Therefore, there is still required to develop an ideal agent for mitigating the side effects of radiotherapy for cancer patients.

Nicaraven, a chemically synthesized hydroxyl radical-specific scavenger,¹⁴ has previously been reported to protect against radiation-induced cell death.^{14,15} Nicaraven can also reduce the radiation-induced recruitment of macrophages and neutrophils into irradiated lungs.¹⁶ Moreover, we have recently demonstrated that nicaraven can also effectively protect against RILI by suppressing the inflammatory response.¹⁷ To further develop for clinical application, we herein aim to optimize the dose and time of nicaraven administration for attenuating the side effects of radiotherapy.

Using a preclinical tumor-bearing mice model, we administered different doses of nicaraven, before or soon after thoracic irradiations. We then evaluated the systemic side effects and RILI, mainly by focusing on oxidative stress and inflammatory responses. According to our experimental data, the administration of nicaraven at a relatively low dose soon after radiotherapy will be recommended for attenuating the side effects of radiotherapy.

Materials and methods

Cancer cells and animals

Mouse Lewis lung cancer (LLC) cells were used for the experiments. The cells were maintained in DMEM (FUJIFILM Wako Pure Chemical Corporation), supplemented with 10% fetal bovine serum (Cytiva) and 1% penicillin/streptomycin (Gibco; Thermo Fisher Scientific, Inc.), and cultured at 37°C in a humidified incubator with 5% CO₂.

Male C57BL/6N mice (8 weeks old) were used for the study. Mice were housed in a pathogen-free room with a controlled environment under a 12-h light-dark cycle and maintained on laboratory chow, with free access to food and water. This study was approved by the Institutional Animal Care and Use Committee of Nagasaki University (No.1608251335-12). All animal procedures were performed in accordance with institutional and national guidelines.

Tumor-bearing mouse model, radiotherapy, and nicaraven administration

To match the pathological status of cancer patients, we used a preclinical tumor-bearing model for the experiment. Briefly, mice were subcutaneously inoculated with 5×10^5 LLC cells/0.1 ml of saline in the back of the chest. At 10 days after cancer cell inoculation, mice had randomly received radiotherapy and nicaraven administration as indicated in Figure 1(a). Considering the common clinical radiotherapy regimen for lung cancer and breast cancer,^{18,19} thoracic irradiations (including the heart and lungs) were delivered to mice at a dosage rate of 1.0084 Gy/min (200 kV, 15 mA, 5 mm Al filtration, ISOVOLT TITAN320, General Electric Company, United States). Mice were intraperitoneally injected with 0 (placebo), 20, 50, 100 mg/kg nicaraven pre-irradiation (almost 5–10 min before irradiation) or post-irradiation (within 5 min after irradiation), respectively. Six mice without irradiation exposure were used as control ($n = 6$, Control group).

We measured the body weights of mice every other day. Mice that received radiotherapy and nicaraven were sacrificed on the 30th day, but the control mice were sacrificed on the 15th day. To collect serum, we took the blood from the inferior vena cava of mice under general anesthesia before

sacrifice. Lung tissues were then excised and weighed. The collected serum and lung tissue samples were stored under -80°C , and used for experimental evaluations as follows.

ELISA

We measured the concentrations of 8-oxo-29-deoxyguanosine (8-OHdG), a marker of DNA oxidation in serum using an ELISA kit (Nikken SEIL Corporation, Shizuoka, Japan) according to the manufacturer's instructions. The mean values of duplicate assays with each sample were used for the statistical analyses.

ELISA kits (R&D Systems) were used to detect the contents of transforming growth factor β (TGF- β), interleukin-1beta (IL-1 β), interleukin-6 (IL-6), C-C Motif Chemokine Ligand 8 (CCL8) in serum and lung tissues according to the manufacturer's instructions. Briefly, the lung tissues were homogenized using Multi-beads shocker[®] and added to the T-PER reagent (Thermo Fisher Scientific) consisting of proteinase and dephosphorylation inhibitors (Thermo Fisher Scientific). Then, lung lysates and serum were added to each well and measured per the manufacturer's instructions. The optical density of each well was measured at 450 nm using a microplate reader (Multiskan Fc, Thermo Fisher Scientific).

Western blot

Western blot was performed as previously described.²⁰ Briefly, total protein from the lung tissues was separated by SDS-PAGE gels and then transferred to 0.22- μm PVDF membranes (Bio-Rad). After blocking, the membranes were incubated with primary antibodies against SOD1 (1:500 dilution; cat. no. sc11407; Santa Cruz), SOD2 (1:500 dilution; cat. no. sc30080; Santa Cruz), β -actin (1:1,000 dilution; cat. no. 8457S; CST), 53BP1 (1:1,000 dilution; cat. no. ab36823; Abcam), caspase 3 (1:1,000 dilution; cat. no. 9662; CST), α -SMA (1:1,000 dilution; cat. no. 19245S; CST), collagen I (1:1,000 dilution; cat. no. ab34710; Abcam), or α -Tubulin (1:1,000 dilution; cat. no. 3873S; CST) overnight at 4°C , respectively, followed by the appropriate horseradish peroxidase-conjugated secondary antibodies (Dako). The expression was visualized using an enhanced chemiluminescence detection kit (Thermo Scientific). Semiquantitative analysis

was done using ImageQuant LAS 4000 mini (GE Healthcare Life Sciences).

Statistical analysis

All the values were presented as the mean \pm SD. For comparison of multiple sets of data, one-way analysis of variance (ANOVA) followed by Tukey's test (Dr. SPSS II, Chicago, IL) was used for statistical analyses. All analyses were carried out with the SPSS19.0 statistical software (IBM SPSS Co., USA). A p -value less than 0.05 was accepted as significant.

Results

Nicaraven for mitigating the systemic side effects of radiotherapy is not very clearly detectable in tumor-bearing mice under our experimental treatment regimens

Mice had well tolerated the therapeutic regimens, but two mice in the post-irradiation administration with the dose of 20 mL/kg group died on the 9th and 10th days, and one mouse in the placebo group died on the 19th day during the follow-period (Figure 1(a)). Thoracic irradiation was delivered to mice using lead shielding sheets, and we found the death of mice at the next morning after radiation exposure. Radiation exposure to the brain stem may happen even only 1-mm positioning error. As a single 6 Gy exposure to the brain stem can kill some mice,²¹ we speculated the death of mice should be an error exposure to the brain due to some positioning or shadowing problems of mice during thoracic exposure. The body weights of mice in all groups were decreased temporarily during radiotherapy, but tended to increase a few days after the stopping of irradiation exposures (Figure 1(b)). There was no significant difference on the body weight changes of mice among groups. Compared with the control mice, the lung weights were slightly increased in mice received placebo treatment after radiotherapy. However, the lung weights showed significantly lower in mice received nicaraven post-irradiation than that of placebo treatment ($p < 0.05$, Figure 1(c)).

ELISA was performed to detect the levels of 8-OHdG, TGF- β , IL-1 β , IL-6, CCL8 in serum. The level of 8-OHdG in serum was not significantly different among groups (Figure 2(a)). However, the serum level of 8-OHdG was

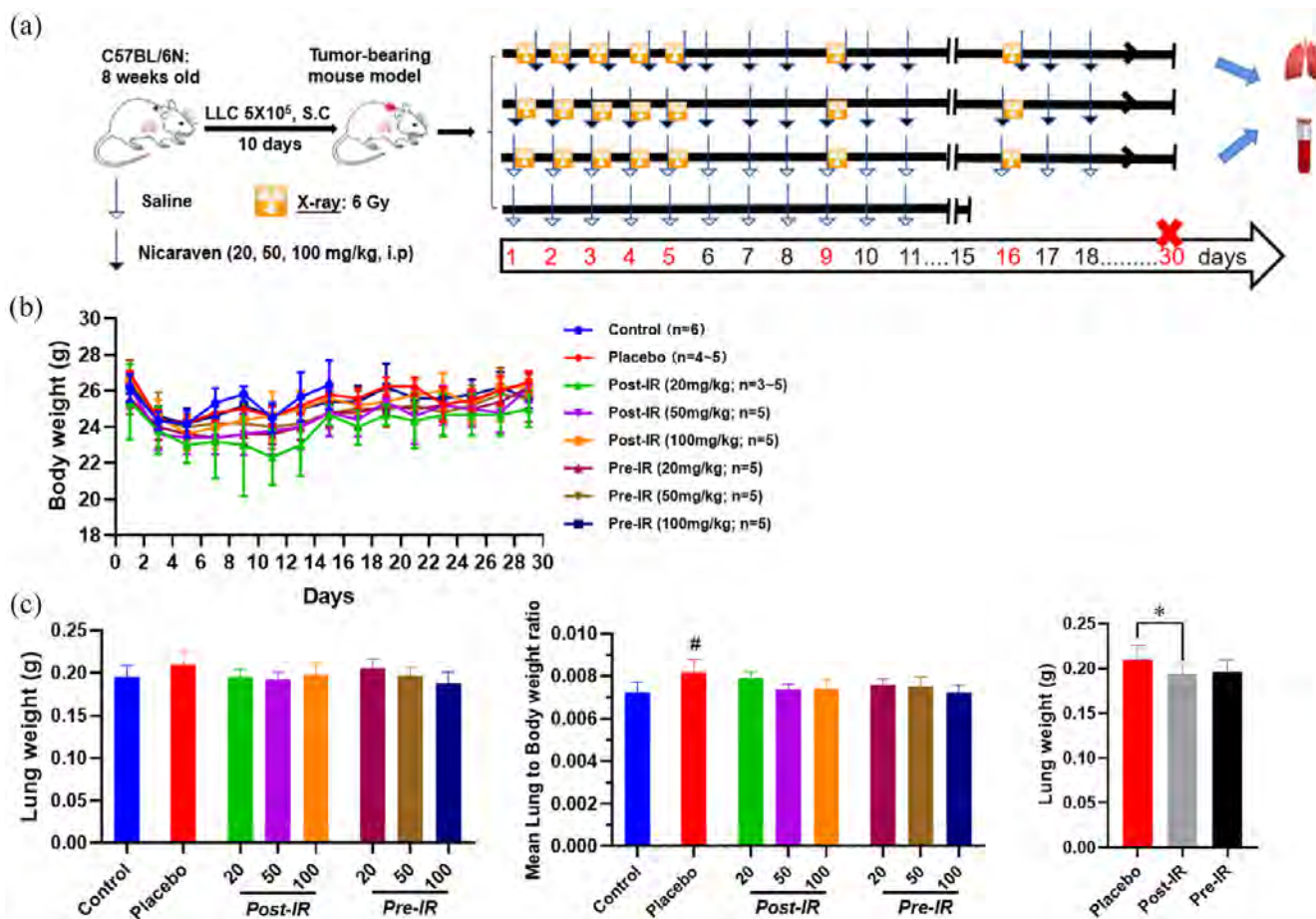


Figure 1. Changes of body weight and lung weight in mice. (a) Schematic diagram about the experimental timeline and protocol. (b) Quantitative data on the changes of body weights through 30 days. (c) Quantitative data on the changes of lung weight and lung to body weight ratio in mice. Data are represented as the means \pm SD, $n=3-6$ in per group. # $p < 0.05$ versus Control group, * $p < 0.05$ versus Placebo group. IR, irradiation; Post-IR, post-irradiation; Pre-IR, pre-irradiation.

detected significantly lower in mice received nicaraven post-irradiation than that of pre-irradiation ($p < 0.05$, Figure 2(a)). Our results also showed that the administration of nicaraven with any dose before or after irradiation did not clearly change the levels of TGF- β , IL-1 β , IL-6 in serum. However, the level of CCL8 in serum was significantly lower in mice received nicaraven either post-irradiation or pre-irradiation when compared with mice received placebo treatment ($p < 0.05$, Figure 2(e)).

The administration of nicaraven at a relatively low dose after radiotherapy shows partial attenuation of RILI in a preclinical tumor-bearing mouse model

To evaluate the inflammatory responses in lungs, ELISA analysis indicated that the TGF- β level in

lungs was slightly increased in mice received placebo treatment after thoracic radiation, but was effectively attenuated by post-irradiation administration with 20 mg/kg nicaraven ($p < 0.05$, Figure 3(a)). Similarly, the IL-1 β level in the lungs was also increased in mice that received placebo treatment after thoracic radiation, but significantly decreased by post-irradiation administration with 20 or 50 mg/kg nicaraven ($p < 0.05$, Figure 3(b)). Strangely, it seems that post-irradiation administration with relatively lower doses of nicaraven more effectively alleviates the enhancement of TGF- β and IL-1 β in lung tissues. However, the levels of IL-6 and CCL8 in the lungs were not significantly different among all groups (Figure 3(c), (d)).

The expression of SOD1 in lungs was detected higher by Western blot in the placebo group than

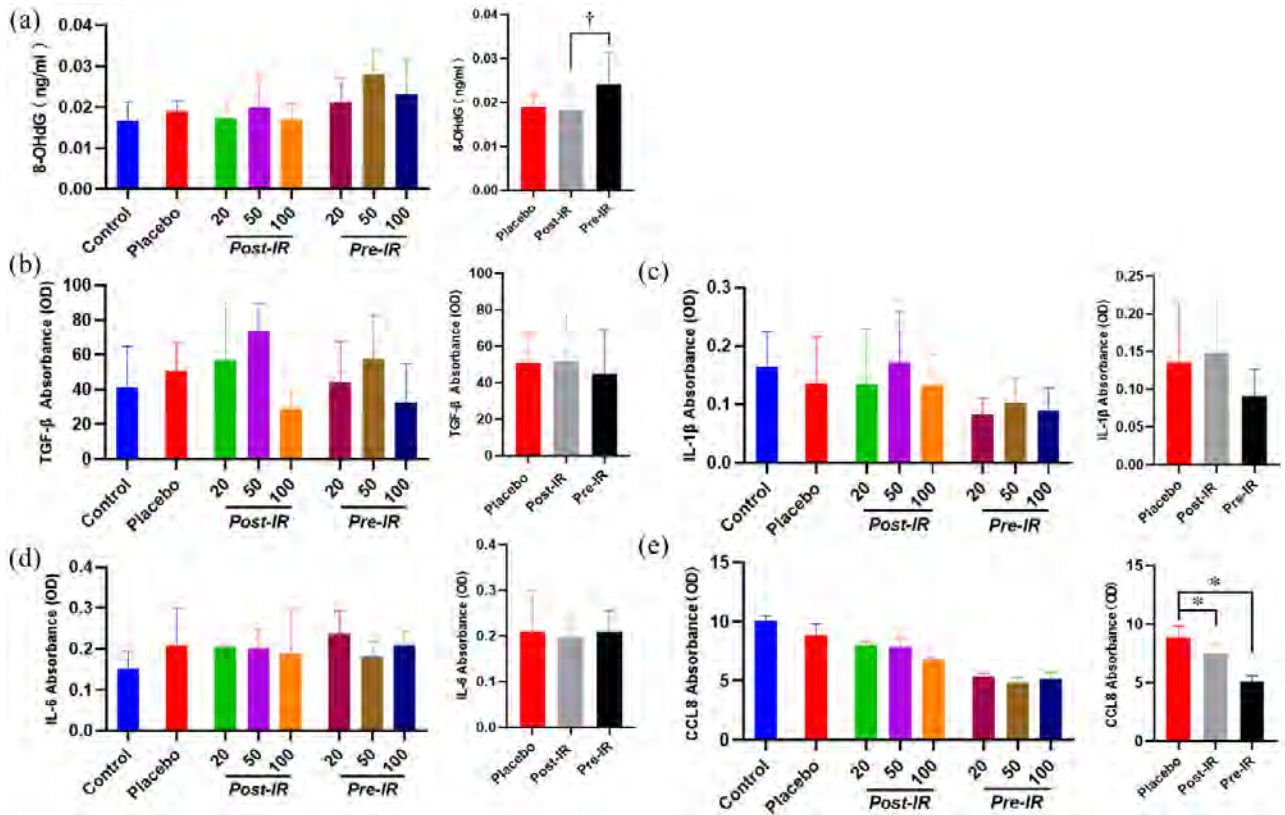


Figure 2. The effect of nicaraven on levels of 8-OHdG and inflammatory factors in serum. Quantitative data on the levels of 8-OHdG (a), TGF-β (b), IL-1β (c), IL-6 (d), CCL8 (e). Data are represented as the means ± SD, *n*=3-6 in per group. **p* < 0.05 versus Placebo group, †*p* < 0.05 versus post-IR group. IR: irradiation; Post-IR: post-irradiation; Pre-IR: pre-irradiation.

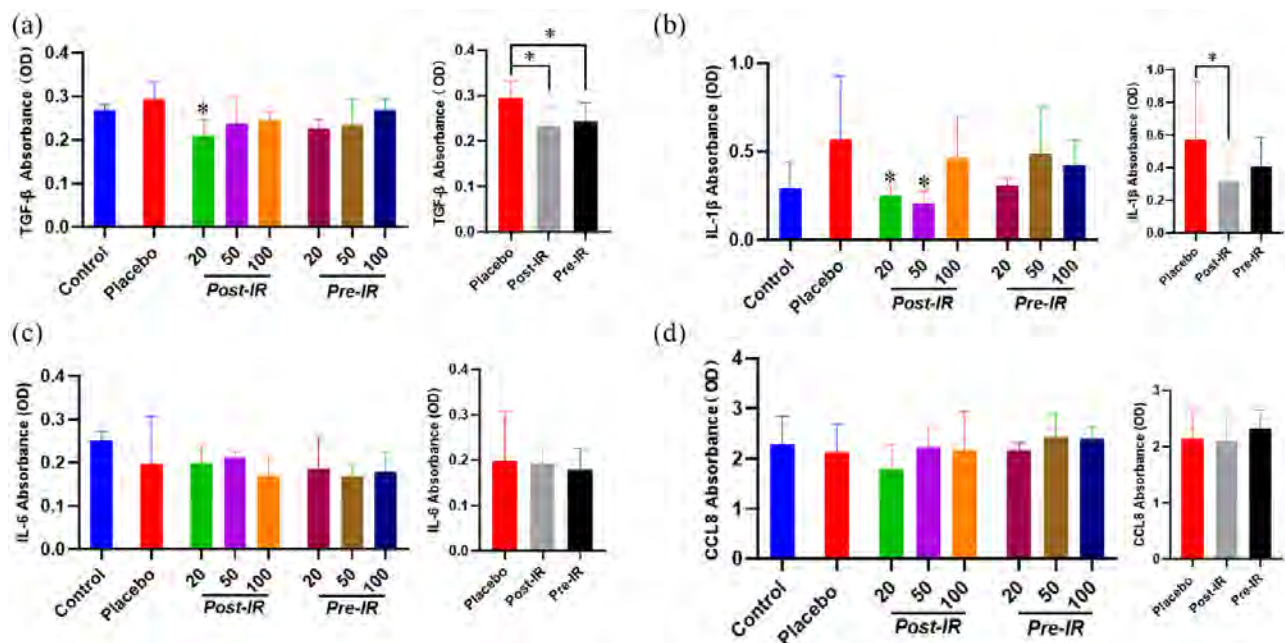


Figure 3. ELISA analysis on the inflammatory response in irradiated lungs. Quantitative data on the levels of TGF-β (a), IL-1β (b), IL-6 (c), CCL8 (d) in irradiated lung tissues were shown. Data are represented as the means ± SD, *n*=3-6 in per group. **p* < 0.05 versus Placebo group. IR: irradiation; Post-IR: post-irradiation; Pre-IR: pre-irradiation.

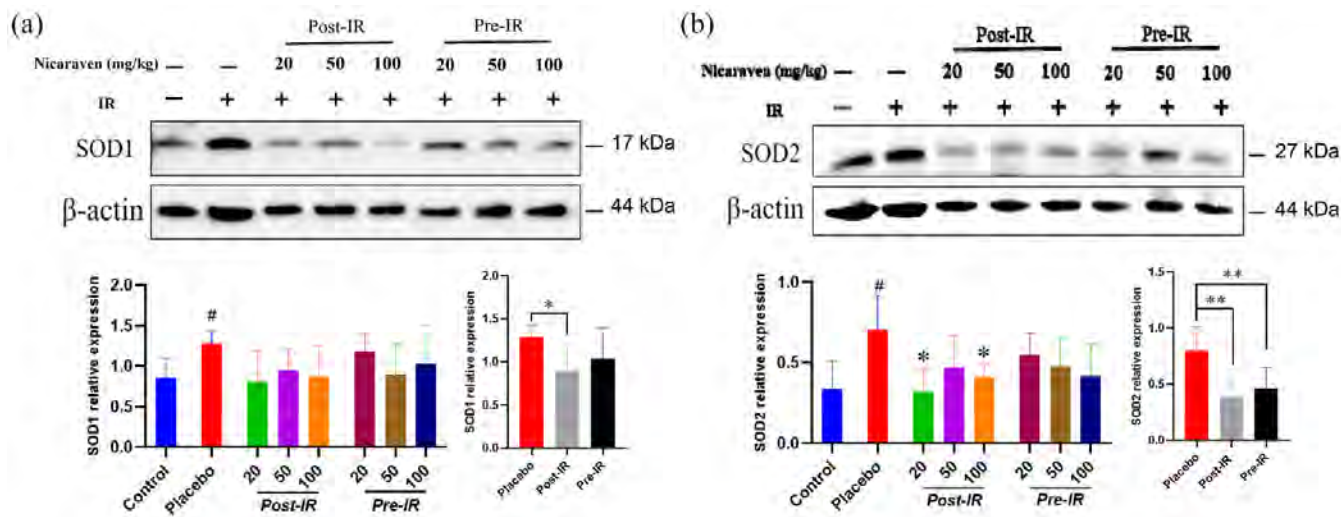


Figure 4. Nicaraven on attenuating oxidative response in irradiated lungs. Representative blots (up), and quantitative data (down) on the expression of SOD1 (a), SOD2 (b). Data are represented as the means \pm SD, $n=3-6$ in per group. # $p < 0.05$ versus Control group, * $p < 0.05$, ** $p < 0.01$ versus Placebo group. IR: irradiation; Post-IR: post-irradiation; Pre-IR: pre-irradiation.

the control group ($p < 0.05$, Figure 4(a)). Although there was no significant difference among all groups (Figure 4(a)), the increased expression of SOD1 in the lungs was effectively attenuated by post-irradiation administration ($p < 0.05$, Figure 4(a)). The expression of SOD2 was also significantly increased in the placebo group, but the increased expression of SOD2 was clearly decreased by post-irradiation administration with 20 or 100 mg/kg nicaraven ($p < 0.05$, Figure 4(b)). The enhanced expression of SOD2 in the lungs was effectively decreased by either post-irradiation or pre-irradiation administration ($p < 0.01$, Figure 4(b)).

We also measured the expression of 53BP1, a marker for DNA damage in lungs by Western blot. Post-irradiation administration of nicaraven showed to slightly decrease the 53BP1 expression in lungs (Figure 5(a)). Caspase 3 has been considered a key effector in inducing cell apoptosis. Compared with the control group without irradiation, Western blot analysis showed a significant enhancement on the expression of caspase 3 in lungs of mice from the placebo group ($p < 0.05$, Figure 5(b)), but the enhanced expression of caspase 3 in irradiated lungs was effectively attenuated only by post-irradiation administration of nicaraven ($p < 0.05$, Figure 5(b)).

We finally investigated the expression of α -SMA and collagen I, the common markers of fibrosis in lungs. Compared with the control group, Western blot analysis showed higher expression of α -SMA and collagen I in lungs of mice from the placebo group (Figure 6). Although there was no significant difference among groups, the enhanced expression of α -SMA and collagen I in irradiated lungs was partially attenuated in mice that received post-irradiation administration of nicaraven (Figure 6).

Discussion

Radiotherapy for cancer is known to accompany side effects, which may lead to the discontinuation of treatment and decrease the quality of life of patients.²² In this study, we investigated the optimal dose and time of nicaraven administration for attenuating the side effects of radiotherapy in tumor-bearing mice. We could not clearly detect significant changes on body weight and the levels of inflammatory cytokines in serum. However, nicaraven administration, especially with a relatively lower dose at the time soon after thoracic irradiations partially decreased the levels of TGF- β , IL-1 β , SOD1, SOD2, and caspase 3 in lungs, suggesting the effectiveness of nicaraven for attenuating the side effects of radiotherapy.

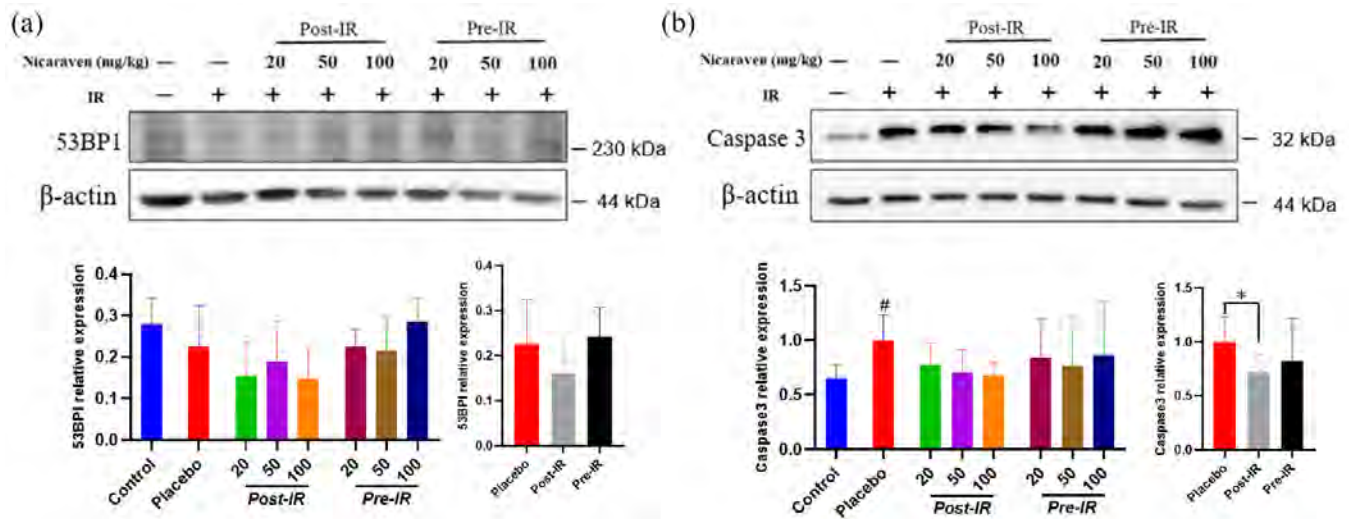


Figure 5. Western blot analysis on the expression of the DNA damage and cell apoptosis in irradiated lungs. Representative blots (up) and quantitative data (down) on the expression of 53BP1 (a), caspase 3 (b). Data are normalized to β -actin. Data are represented as the means \pm SD, $n=3-6$ in per group. [#] $p < 0.05$ versus Control group, * $p < 0.05$ versus Placebo group. IR: irradiation; Post-IR: post-irradiation; Pre-IR: pre-irradiation.

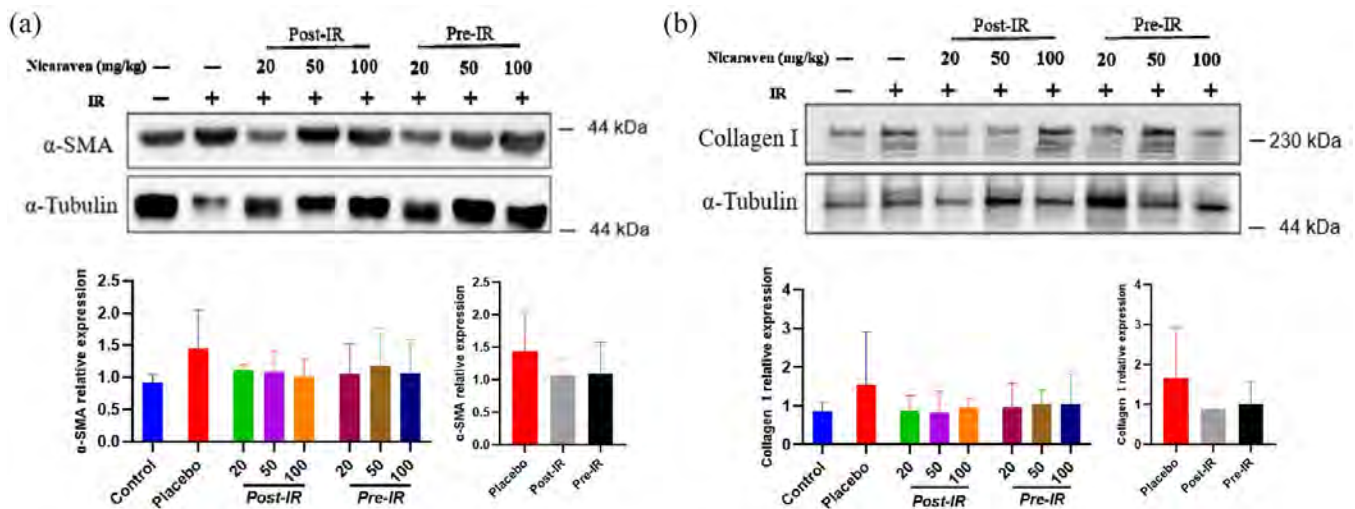


Figure 6. The fibrotic changes in irradiated lungs. Representative blots (up) and quantitative data (down) on the expression of α -SMA (a), collagen I (b) were shown. Data are normalized to α -Tubulin. Data are represented as the means \pm SD, $n=3-6$ in per group. IR: irradiation; Post-IR: post-irradiation; Pre-IR: pre-irradiation.

Nicaraven has been well recognized on radical-specific scavenging property.¹⁴ The 8-OHdG, an oxidized nucleoside of DNA has been frequently used as a marker for detecting oxidative stress.²³ However, consistent with our previous study,²⁴ nicaraven administration did not effectively decrease the level of 8-OHdG in serum in this study.

Radiation exposure results in the release of pro-inflammatory cytokines and chemokines.⁸⁻¹⁰ Radiation-induced systemic and local inflammatory responses can be detected in the blood by an increased level of circulatory cytokines and the activation of immune cells.^{7,25} However, we found that nicaraven administration did not significantly change the levels of TGF- β , IL-1 β , and IL-6 in

serum. Several reasons can be considered for it. First, the sample number in each group was too small to detect a statistical significance. Second, the initial sizes of tumors were widely varied among animals and groups, which also resulted in large variations in measuring data. Third, we collected lungs and serum at 14 days after the last irradiation, which will be not a suitable time window for sensitive detection about the changes of 8-OHdG and inflammatory factors in serum. Otherwise, tumor-secreted factors might also be considered to affect the levels of cytokines and chemokines in serum,²⁶ but we did not find significant correlations between tumor weights and the levels of systemic inflammatory factors (data not shown).

Increasing evidence has shown that the release of a multitude of cytokines in response to radiation exposure can contribute to the damage to the cells/tissues.²² Previous studies have demonstrated that RILI could be alleviated by blocking pro-inflammatory factors.^{27,28} In this study, we observed that nicaraven partially attenuated the enhanced expression of TGF- β and IL-1 β in the lungs, especially by post-irradiation administration with relatively low doses. We have not yet found a clear reason why post-irradiation administration with relatively lower doses of nicaraven even more effectively alleviates the enhancement of TGF- β and IL-1 β in the irradiated lungs. Previous studies have well documented the harmless of nicaraven at the dose of 100 mg/kg in mice.²⁹ As VEGF level may increase in tumor-bearing mice, it is a possibility that a high dose of nicaraven increases the permeability of alveolar capillaries and cause edema of lungs in these tumor-bearing mice.

SOD1 and SOD2 are antioxidant enzymes, but their expression generally increases in response to oxidative stresses and various types of injuries.⁶ Nicaraven partially attenuated the enhanced expression of SOD1 and SOD2 in irradiated lungs, especially by post-irradiation administration. Radiation can directly lead to cell death and apoptosis.^{4,17} Nicaraven also partially decreased the expression of 53BP1 and caspase 3 in irradiated lungs, especially by post-irradiation administration. The main manifestations of the late stage of RILI are fibroblast proliferation and collagen deposition.²⁵ Post-irradiation administration of nicaraven partially decreased the expression of α -SMA and collagen I in irradiated lungs.

This study has several limitations. First, we did not perform histopathological analysis on lungs. Second, we only used male mice for the experiment, but gender difference may affect radiation-induced outcomes.^{30,31} Third, we could not provide data on the 8-OHdG level in lungs because of our technical mistake. Otherwise, due to the small sample size and large individual variation, there was no statistically significance on the expression of α -SMA and collagen I in lungs among groups. Although we have already planned a phase I-II clinical trial in esophageal cancer patients who receiving radiotherapy, the benefit of nicaraven administration will be needed to be further confirmed before clinical application for cancer radiotherapy.

According to our experimental evaluations in a preclinical tumor-bearing mouse model, nicaraven seems to effectively attenuate the side effects of radiotherapy. As nicaraven has a very limited effect on the growth of established tumors,¹⁶ nicaraven may be useful for mitigating the side effects of radiotherapy in cancer patients, and post-irradiation administration with a relatively low dose will be highly recommended.

Declarations

Ethics approval and consent to participate

The animal experiments were approved by the Institutional Animal Care and Use Committee of Nagasaki University (Approval no.1608251335-12) and all animal procedures were performed in accordance with institutional and national guidelines.

Consent for publication

The authors give their consent for publication.

Author contributions

Yong Xu: Data curation; Investigation; Methodology; Writing – original draft; Writing – review & editing.

Lina Abdelghany: Data curation; Investigation; Writing – review & editing.

Reiko Sekiya: Data curation; Investigation.

Da Zhai: Data curation; Writing – review & editing.

Keiichi Jingu: Conceptualization.

Tao-Sheng Li: Conceptualization; Data curation; Investigation; Methodology; Resources; Supervision; Writing – review & editing.

Acknowledgements

None.

Funding

The authors disclosed receipt of the following financial support for the research, authorship, and/or publication of this article: This study was mainly supported by the Japan Agency for Medical Research and Development (JP201m0203081), a Grant-in-Aid from the Ministry of Education, Science, Sports, Culture and Technology, Japan. The funder played no role in the study design, data collection, and analysis, decision to publish, or manuscript preparation.

Competing interests

The authors declared no potential conflicts of interest with respect to the research, authorship, and/or publication of this article.

Availability of data and materials

The datasets used and/or analyzed during the current study are available from the corresponding author on reasonable request.

ORCID iD

Tao-Sheng Li  <https://orcid.org/0000-0002-7653-8873>

References

- Giuranno L, Jent J, De Ruyscher D, *et al.* Radiation-induced lung injury (RILI). *Front Oncol* 2019; 9: 877.
- Kim H, Park SH, Han SY, *et al.* LXA4-FPR2 signaling regulates radiation-induced pulmonary fibrosis via crosstalk with TGF- β /Smad signaling. *Cell Death Dis* 2020; 11: 653.
- Bickelhaupt S, Erbel C, Timke C, *et al.* Effects of CTGF blockade on attenuation and reversal of radiation-induced pulmonary fibrosis. *J Natl Cancer Inst* 2017; 109: 8.
- McBride WH and Schae D. Radiation-induced tissue damage and response. *J Pathol* 2020; 250: 647–655.
- Huang L, Snyder AR and Morgan WF. Radiation-induced genomic instability and its implications for radiation carcinogenesis. *Oncogene* 2003; 22: 5848–5854.
- Nakane M. Biological effects of the oxygen molecule in critically ill patients. *J Intensive Care* 2020; 8: 95.
- Formenti SC and Demaria S. Systemic effects of local radiotherapy. *Lancet Oncol* 2009; 10: 718–726.
- Jin H, Yoo Y, Kim Y, *et al.* Radiation-induced lung fibrosis: preclinical animal models and therapeutic strategies. *Cancers (Basel)* 2020; 12: 1561.
- Kainthola A, Haritwal T, Tiwari M, *et al.* Immunological aspect of radiation-induced pneumonitis, current treatment strategies, and future prospects. *Front Immunol* 2017; 8: 506.
- Im J, Lawrence J, Seelig D, *et al.* FoxM1-dependent RAD51 and BRCA2 signaling protects idiopathic pulmonary fibrosis fibroblasts from radiation-induced cell death. *Cell Death Dis* 2018; 9: 584.
- Weiss JF and Landauer MR. History and development of radiation-protective agents. *Int J Radiat Biol* 2009; 85: 539–573.
- Hahn SM, Krishna MC, DeLuca AM, *et al.* Evaluation of the hydroxylamine Tempol-H as an in vivo radioprotector. *Free Radic Biol Med* 2000; 28: 953–958.
- Hosseinimehr SJ. Trends in the development of radioprotective agents. *Drug Discov Today* 2007; 12: 794–805.
- Akimoto T. Quantitative analysis of the kinetic constant of the reaction of N, N -propylenedinitinamide with the hydroxyl radical using dimethyl sulfoxide and deduction of its structure in chloroform. *Chem Pharm Bull (Tokyo)* 2000; 48: 467–476.
- Watanabe M, Akiyama N, Sekine H, *et al.* Inhibition of poly (ADP-ribose) polymerase as a protective effect of nicaraven in ionizing radiation- and ara-C-induced cell death. *Anticancer Res* 2006; 26(5A): 3421–3427.
- Yan C, Luo L, Urata Y, *et al.* Nicaraven reduces cancer metastasis to irradiated lungs by decreasing CCL8 and macrophage recruitment. *Cancer Lett* 2018; 418: 204–210.
- Xu Y, Zhai D, Goto S, *et al.* Nicaraven mitigates radiation-induced lung injury by downregulating the NF- κ B and TGF- β /Smad pathways to suppress the inflammatory response. *J Radiat Res* 2022; 2022; rrab112.
- Kepka L and Socha J. Dose and fractionation schedules in radiotherapy for non-small cell lung cancer. *Transl Lung Cancer Res* 2021; 10: 1969–1982.
- Shah BA, Xiao J, Oh C, *et al.* Five-fraction prone accelerated partial breast irradiation: long-term

- oncologic, dosimetric, and cosmetic outcome. *Pract Radiat Oncol* 2022; 12: 106–112.
20. Doi H, Kitajima Y, Luo L, *et al.* Potency of umbilical cord blood- and Wharton's jelly-derived mesenchymal stem cells for scarless wound healing. *Sci Rep* 2016; 6: 18844.
 21. Yang L, Yang J, Li G, *et al.* Pathophysiological responses in rat and mouse models of radiation-induced brain injury. *Mol Neurobiol* 2017; 54: 1022–1032.
 22. Hanania AN, Mainwaring W, Ghebre YT, *et al.* Radiation-induced lung injury: assessment and management. *Chest* 2019; 156: 150–162.
 23. Valavanidis A, Vlachogianni T and Fiotakis C. 8-hydroxy-2'-deoxyguanosine (8-OHdG): a critical biomarker of oxidative stress and carcinogenesis. *J Environ Sci Health C Environ Carcinog Ecotoxicol Rev* 2009; 27: 120–139.
 24. Kawakatsu M, Urata Y, Imai R, *et al.* Nicaraven attenuates radiation-induced injury in hematopoietic stem/progenitor cells in mice. *PLoS ONE* 2013; 8: e60023.
 25. Mavragani IV, Laskaratou DA, Frey B, *et al.* Key mechanisms involved in ionizing radiation-induced systemic effects. A current review. *Toxicol Res (Camb)* 2015; 5: 12–33.
 26. Singh M, Tian XJ, Donnenberg VS, *et al.* Targeting the temporal dynamics of hypoxia-induced tumor-secreted factors halts tumor migration. *Cancer Res* 2019; 79: 2962–2977.
 27. Li W, Lu L, Liu B, *et al.* Effects of phycocyanin on pulmonary and gut microbiota in a radiation-induced pulmonary fibrosis model. *Biomed Pharmacother* 2020; 132: 110826.
 28. Chen B, Na F, Yang H, *et al.* Ethyl pyruvate alleviates radiation-induced lung injury in mice. *Biomed Pharmacother* 2017; 92: 468–478.
 29. Zhang X, Moriwaki T, Kawabata T, *et al.* Nicaraven attenuates postoperative systemic inflammatory responses-induced tumor metastasis. *Ann Surg Oncol* 2020; 27: 1068–1074.
 30. Özdemir BC, Csajka C, Dotto GP, *et al.* Sex differences in efficacy and toxicity of systemic treatments: an undervalued issue in the era of precision oncology. *J Clin Oncol* 2018; 36: 2680–2683.
 31. Narendran N, Luzhna L and Kovalchuk O. Sex difference of radiation response in occupational and accidental exposure. *Front Genet* 2019; 10: 260.

Nicaraven mitigates radiation-induced lung injury by downregulating the NF- κ B and TGF- β /Smad pathways to suppress the inflammatory response

Yong Xu^{1,2}, Da Zhai^{1,2}, Shinji Goto^{1,2}, Xu Zhang^{1,2}, Keiichi Jingu³ and Tao-Sheng Li^{1,2,*}

¹Department of Stem Cell Biology, Atomic Bomb Disease Institute, Nagasaki University, Nagasaki 852-8523, Japan

²Department of Stem Cell Biology, Nagasaki University Graduate School of Biomedical Sciences, 1-12-4 Sakamoto, Nagasaki 852-8523, Japan

³Department of Radiation Oncology, Graduate School of Medicine, Tohoku University, Sendai 980-8574, Japan.

*Corresponding author: Department of Stem Cell Biology, Atomic Bomb Disease Institute, Nagasaki University, 1-12-4 Sakamoto, Nagasaki 852-8523, Japan. Tel: +81-95-819-7099; Fax: +81-95-819-7100, E-mail: litaoshe@nagasaki-u.ac.jp

(Received 23 June 2021; revised 16 August 2021; editorial decision 29 October 2021)

ABSTRACT

Radiation-induced lung injury (RILI) is commonly observed in patients receiving radiotherapy, and clinical prevention and treatment remain difficult. We investigated the effect and mechanism of nicaraven for mitigating RILI. C57BL/6 N mice (12-week-old) were treated daily with 6 Gy X-ray thoracic radiation for 5 days in sequences (cumulative dose of 30 Gy), and nicaraven (50 mg/kg) or placebo was injected intraperitoneally in 10 min after each radiation exposure. Mice were sacrificed and lung tissues were collected for experimental assessments at the next day (acute phase) or 100 days (chronic phase) after the last radiation exposure. Of the acute phase, immunohistochemical analysis of lung tissues showed that radiation significantly induced DNA damage of the lung cells, increased the number of Sca-1⁺ stem cells, and induced the recruitment of CD11c⁺, F4/80⁺ and CD206⁺ inflammatory cells. However, all these changes in the irradiated lungs were effectively mitigated by nicaraven administration. Western blot analysis showed that nicaraven administration effectively attenuated the radiation-induced upregulation of NF- κ B, TGF- β , and pSmad2 in lungs. Of the chronic phase, nicaraven administration effectively attenuated the radiation-induced enhancement of α -SMA expression and collagen deposition in lungs. In conclusion we find that nicaraven can effectively mitigate RILI by downregulating NF- κ B and TGF- β /pSmad2 pathways to suppress the inflammatory response in the irradiated lungs.

Keywords: radiation; DNA damage; lung injury; inflammatory response

INTRODUCTION

Radiotherapy is used for cancer treatment, but exposure to high doses of ionizing radiation also damages the normal tissue cells [1, 2]. Radiation-induced lung injury (RILI), including acute pneumonitis and chronic pulmonary fibrosis, is frequently observed in patients receiving thoracic radiotherapy. It is estimated that RILI occurs in 13–37% of lung cancer patients undergoing curative radiotherapy, which may limit the dose of radiotherapy and affect the quality of life [3]. Currently, the pathogenesis of RILI has not yet been fully understood, and there is no effective drug in the clinic.

It is known that high dose ionizing radiation leads to DNA double-strand breaks [4]. DNA damage contributes to oxidative stress, vascular damage, and inflammation. Pneumonitis develops within hours

or days after high dose irradiation exposure, and is accompanied by an increased capillary permeability and the accumulation of inflammatory cells in lungs [5–7]. The recruited inflammatory cells secrete profibrotic cytokines to activate the resident fibroblasts, which finally leads to an excessive collagen production and deposition in the interstitial space of lungs [8–10].

NF- κ B (nuclear factor kappa B) is an important regulator of inflammatory response. The NF- κ B signaling pathway is known to be activated following radiation exposure [11]. TGF- β /Smad signaling pathway also deeply involves in RILI [12, 13]. Thoracic irradiation causes a continuous increase of TGF- β ₁ in plasma, which is a predictor of radiation pneumonitis after radiotherapy [14]. The activation of TGF- β induces the conversion of fibroblasts into myofibroblasts, the elevated

expression of α -smooth muscle actin (α -SMA), and the synthesis of extracellular matrix proteins such as collagen [15, 16]. Therefore, targeting these pathways can be a potential strategy for mitigating RILI.

Nicaraven, a hydroxyl free radical scavenger [17], has previously been demonstrated to protect against the radiation-induced cell death [18, 19]. We have also recently found that the administration of nicaraven to mice soon after high dose γ -ray exposure attenuates the radiation-induced injury of hematopoietic stem/progenitor cells, which is more likely associated with anti-inflammatory effect rather than radical scavenging [20, 21]. Moreover, nicaraven can reduce the radiation-induced recruitment of macrophages and neutrophils into lungs [22]. Therefore, we speculate that nicaraven may effectively mitigate RILI, at least partly by inhibiting inflammatory response through NF- κ B and TGF- β /Smad signaling pathways [23].

By exposing the lungs of adult mice to 30 Gy X-ray, we investigated the effect and mechanism of nicaraven for mitigating RILI. Our results showed that nicaraven administration significantly reduced the DNA damage of lung tissue (stem) cells, inhibited the radiation-induced recruitment of CD11c⁺, F4/80⁺ and CD206⁺ inflammatory cells in lungs at the acute phase, and also mitigated the radiation-induced enhancement of α -SMA and partly decreased the fibrotic area in the irradiated lungs at the chronic phase.

MATERIALS AND METHODS

Animals

Male C57BL/6 N mice (12-week-old; CLEA, Japan) were used for study. Mice were housed in pathogen-free room with a controlled environment under a 12 h light–dark cycle, with free access to food and water. This study was approved by the Institutional Animal Care and Use Committee of Nagasaki University (No.1608251335-12). All animal procedures were performed in accordance with institutional and national guidelines.

Thoracic radiation exposure and nicaraven administration

The RILI model was established as previously described [24]. Briefly, mice were treated daily with 6 Gy X-ray thoracic radiation for 5 days in sequences (cumulative dose of 30 Gy) at a dose rate of 1.0084 Gy/min (200 kV, 15 mA, 5 mm Al filtration, ISOVOLT TITAN320, General Electric Company, United States) (Supplementary Fig. 1A). Nicaraven (50 mg/kg; n = 6, IR + N group) or placebo (n = 6, IR group) was injected intraperitoneally to mice within 10 min after each radiation exposure, and we continued the daily injections for 5 additional days after the last radiation exposure (Supplementary Fig. 1A). Age-matched mice without radiation exposure were used as control (n = 6, CON group). The body weights of mice were recorded once a week. We sacrificed the mice the next day (Acute phase) or the 100th day (Chronic phase) after the last exposure (Supplementary Fig. 1A). At the end of follow-up, mice were euthanized under general anesthesia by severing the aorta to remove the blood. Lung tissues were excised and weighed, and then collected for experimental evaluations as follows.

Immunohistochemical analysis

The DNA damage in lung tissue (stem) cells was detected by immunohistochemical analysis. Briefly, lungs were fixed in 4% paraformaldehyde, and paraffin sections of 6- μ m-thick were deparaffinized and rehydrated. After antigen retrieval and blocking, sections were incubated with rabbit anti-mouse γ -H2AX antibody (1:400 dilution, Abcam) and rat anti-mouse Sca-1 antibody (1:200 dilution, Abcam) overnight at 4°C, and followed by the appropriate fluorescent-conjugated secondary antibodies at 25°C for 60 min. The nuclei were stained with 4, 6-diamidino-2-phenylindole (DAPI) (1:1000 dilution, Life technologies). The positive staining was examined under fluorescence microscope (FV10CW3, OLYMPUS).

The recruitment of inflammatory cells was detected by immunostaining with mouse anti-mouse CD11c antibody (1:150 dilution, Abcam), rat anti-mouse F4/80 antibody (1:100 dilution, Abcam), goat anti-mouse CD206 antibody (1:200 dilution, R&D Systems) overnight at 4°C, and followed by the appropriate Alexa fluorescent-conjugated secondary antibodies (1:400 dilution, Invitrogen), respectively. The nuclei were stained with DAPI. The positive staining was examined under fluorescence microscope (FV10CW3, OLYMPUS).

For quantitative analysis, we counted the positively stained cells in 12 images from two separated independent sections of each lung tissue sample. The number of positively stained cells in each lung tissue sample was normalized by the number of nuclei, and the average value per field (image) from each lung tissue sample was used for statistical analysis.

Masson's trichrome staining

To detect the fibrotic change in lungs, Masson's trichrome staining was performed according to the manufacturer's protocol (Sigma-Aldrich, St. Louis, MO, USA). The stained sections were mounted and then imaged using a microscope (Biorevo BZ-9000; Keyence Japan, Osaka, Japan). The fibrotic area was quantified by measuring the positively stained area using the Image-Pro Plus software (version 5.1.2, Media Cybernetics Inc, Carlsbad, CA, USA), and expressed as a percentage of the total area. The average value from 12 images randomly selected from two separated slides for each lung tissue sample was used for statistical analysis.

Western blot

Western blot was performed as previously described [25]. Briefly, lung tissue sample was homogenized using Multi-beads shocker and added to the T-PER reagent (Thermo Fisher Scientific) consisting of proteinase and dephosphorylation inhibitors (Thermo Fisher Scientific). Total tissue protein purified from lungs were separated by SDS-PAGE gels and then transferred to 0.22- μ m PVDF membranes (Bio-Rad). After blocking, the membranes were incubated with primary antibodies against NF- κ B p65 (1:500 dilution, Abcam), I κ B α (1:1000 dilution, CST), TGF- β (1:1000 dilution, Abcam), pSmad2 (1:1000 dilution, Abcam), α -Tubulin (1:1000 dilution, CST), or GAPDH (1:1000 dilution, Abcam), respectively; and followed by the appropriate horseradish peroxidase-conjugated secondary antibodies (Dako). The expression was visualized using an enhanced chemiluminescence detection kit (Thermo Scientific).

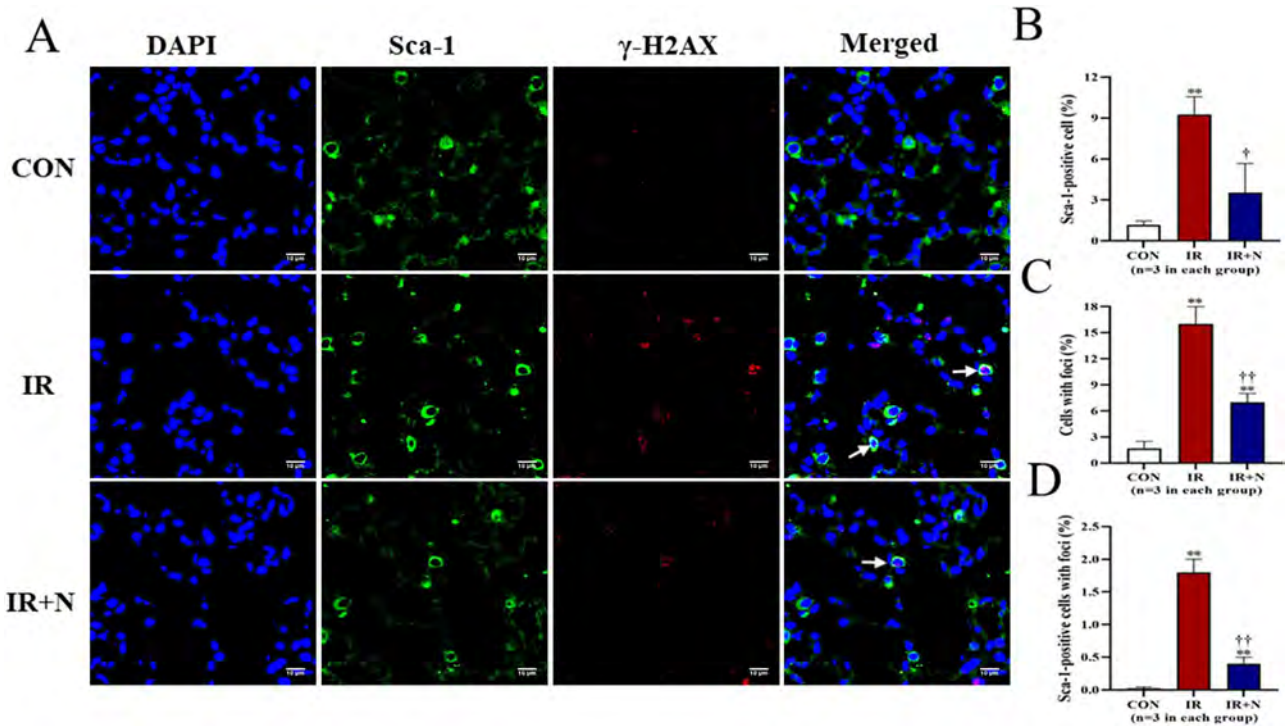


Fig. 1. The DNA damage of lung tissue cells at the acute phase after treatments. (A) Representative confocal images show the expression of Sca-1 and γ -H2AX in lung tissue cells. Quantitative data on the number of Sca-1⁺ stem cells (B), the total cells with γ -H2AX foci formation (C), and the Sca-1⁺ stem cells with γ -H2AX foci formation (D, Arrows) are shown. Scale bars: 10 μ m. The nuclei were stained with DAPI. Data are represented as means \pm SD. ** p < 0.01 vs CON group, + p < 0.05, ++ p < 0.01 vs IR group. CON: Control, IR: Radiation, IR + N: Radiation+Nicaraven.

Semiquantitative analysis was done using ImageQuant LAS 4000 mini (GE Healthcare Life Sciences).

Statistical analysis

All the values were presented as mean \pm SD. For comparison of multiple sets of data, one-way analysis of variance (ANOVA) followed by Tukey's test (Dr. SPSS II, Chicago, IL) was used. For comparison of two sets of data, an unpaired two-tailed t -test was used. All analysis was carried out with the SPSS19.0 statistical software (IBM SPSS Co., USA). A p -value less than 0.05 was accepted as significant.

RESULTS

Nicaraven significantly reduced the radiation-induced DNA damage of lung tissue (stem) cells at the acute phase.

All mice survived after treatments and during the follow-up period. The body weights of the mice were decreased temporarily soon after radiation exposure, but tended to increase approximately 10 days after radiation exposure. Although the body weights of mice between IR group and IR + N group were not significantly different, they were significantly lower than the age-matched non-irradiated mice in the CON group (p < 0.05, Supplementary Fig. 1B). Moreover, the lung weights of mice were not significantly different among all groups at either the acute phase or the chronic phase (Supplementary Fig. 1C).

Immunohistochemistry was performed to evaluate the expression of Sca-1 and γ -H2AX in lung tissue cells at the acute phase (Fig. 1A). Compared to CON group, the number of Sca-1⁺ stem cells was significantly increased in the IR group ($9.27 \pm 1.30\%$ vs $1.17 \pm 0.29\%$, p < 0.01; Fig. 1B). However, the increased number of Sca-1⁺ stem cells in irradiated lungs was significantly attenuated by nicaraven administration ($3.53 \pm 2.15\%$, p < 0.05 vs IR group; Fig. 1B).

The formation of γ -H2AX foci in nuclei of lung tissue cells was dramatically increased in the IR group, but was mildly changed in the IR + N group (Fig. 1A). Quantitative data also indicated that the percentage of γ -H2AX-positive cells was significantly less in the IR + N group than the IR group ($16.27 \pm 2.05\%$ vs $7.13 \pm 0.91\%$, p < 0.01; Fig. 1C). Moreover, we tried to evaluate the formation of γ -H2AX foci in Sca-1⁺ stem cells. Interestingly, the number of Sca-1⁺ stem cells with γ -H2AX foci was more effectively decreased in the IR + N group compared to the IR group ($1.93 \pm 0.51\%$ vs $0.35 \pm 0.19\%$, p < 0.01; Fig. 1D). These results indicate that nicaraven administration can reduce the radiation-induced DNA damage in lung tissue cells, especially in these Sca-1⁺ stem cells.

Nicaraven effectively decreased the radiation-induced recruitment of inflammatory cells into lungs.

According to our previous studies [20, 21], nicaraven protects tissue (stem) cells against radiation injury by inhibiting

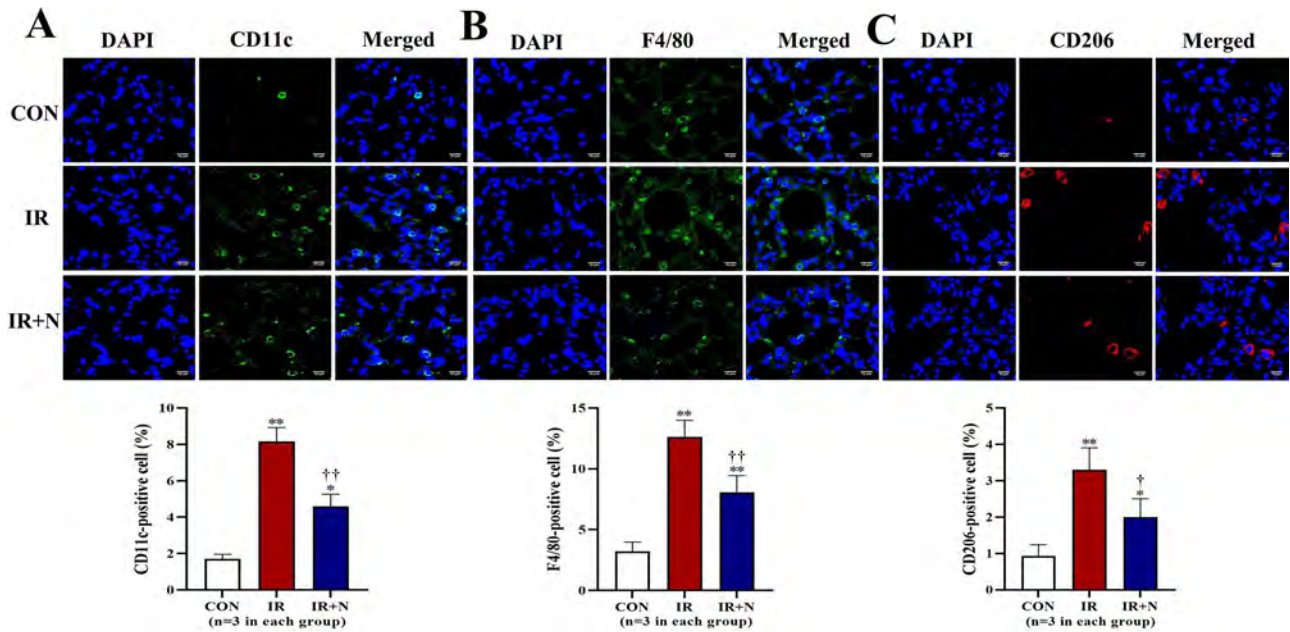


Fig. 2. Immunohistochemical detection of inflammatory cells in lungs at the acute phase after treatments. Representative confocal images (upper) and quantitative data (lower) show the CD11c⁺ cells (A), F4/80⁺ cells (B), and CD206⁺ cells (C) in lungs. Scale bars: 10 μ m. The nuclei were stained with DAPI. Data are represented as means \pm SD. * p < 0.05, ** p < 0.01 vs CON group, † p < 0.05, †† p < 0.01 vs IR group. CON: Control, IR: Radiation, IR + N: Radiation+Nicaraven.

inflammatory response. Therefore, immunohistochemical analysis was performed to detect the inflammatory cells in lungs. The number of CD11c⁺ monocytes and F4/80⁺ macrophages was significantly higher in the IR group than the CON group (p < 0.01, Fig. 2A and B). However, nicaraven administration significantly reduced the recruitment of CD11c⁺ monocytes ($8.23 \pm 0.75\%$ vs $4.61 \pm 0.65\%$, p < 0.01; Fig. 2A) and F4/80⁺ macrophages ($12.63 \pm 1.36\%$ vs $8.07 \pm 1.38\%$, p < 0.01; Fig. 2B) into irradiated lungs. Similarly, the number of M2 macrophages (CD206⁺) was also significantly higher in irradiated lungs than that of non-irradiated lungs (p < 0.01, Fig. 2C). Interestingly, nicaraven administration significantly decreased the CD206⁺ macrophages in irradiated lungs ($3.3 \pm 0.61\%$ vs $2.1 \pm 0.53\%$, p < 0.05; Fig. 2C).

Nicaraven significantly attenuated the radiation-induced upregulation of NF- κ B and TGF- β in lungs

To further understand the molecular mechanism of nicaraven on mitigating RILI, we investigated the expression of NF- κ B and I κ B α (inhibitor of NF- κ B) in lungs at the acute phase. Compared to the CON group, the IR group showed a significant enhancement on the expression of NF- κ B (p < 0.05, Fig. 3A). However, the enhanced expression of NF- κ B in irradiated lungs was effectively attenuated by nicaraven administration (p = 0.09, Fig. 3A). In contrast, the expression of total I κ B α was significantly decreased in irradiated lungs (p < 0.01 vs CON group, Fig. 3B), which was effectively attenuated by nicaraven administration (p < 0.01 vs IR group, Fig. 3B). We also investigated the expression of TGF- β and pSmad2 in irradiated lungs at the acute phase (Fig. 3C and D). The irradiated lungs showed a

significant upregulation of TGF- β and pSmad2 (p < 0.05 vs CON group, Fig. 3C and D), but was effectively attenuated by nicaraven administration (p < 0.05 vs IR group, Fig. 3C and D).

Nicaraven clearly attenuated the radiation-induced enhancement of α -SMA and partially reduced the fibrotic area in irradiated lungs at the chronic phase

We further investigated the expression of α -SMA and collagen deposition in irradiated lungs at the chronic phase. Western blot indicated an enhanced expression of α -SMA in the irradiated lungs (p < 0.05 vs CON group, Fig. 4A), but the enhanced expression of α -SMA in irradiated lungs was completely attenuated by nicaraven administration (Fig. 4A). Similarly, Masson's trichrome staining showed that the fibrotic area in lungs was significantly higher in the IR group than the CON group (p < 0.05, Fig. 4B). However, nicaraven administration tended to only partially reduce the fibrotic area in irradiated lungs ($6.24 \pm 0.64\%$ vs $5.14 \pm 0.51\%$, p = 0.08; Fig. 4B).

DISCUSSION

This study was proposed to investigate the potential effect and underlying mechanism of nicaraven on mitigating RILI. Our experimental data revealed that nicaraven administration not only reduced the DNA damage (γ -H2AX foci formation) of lung tissue (stem) cells, but also inhibited the recruitment of macrophages and neutrophils into irradiated lungs at the acute phase. Nicaraven administration also significantly attenuated the radiation-induced enhancement of TGF- β and NF- κ B, and partially reduced the fibrotic area in irradiated lungs at the chronic phase.

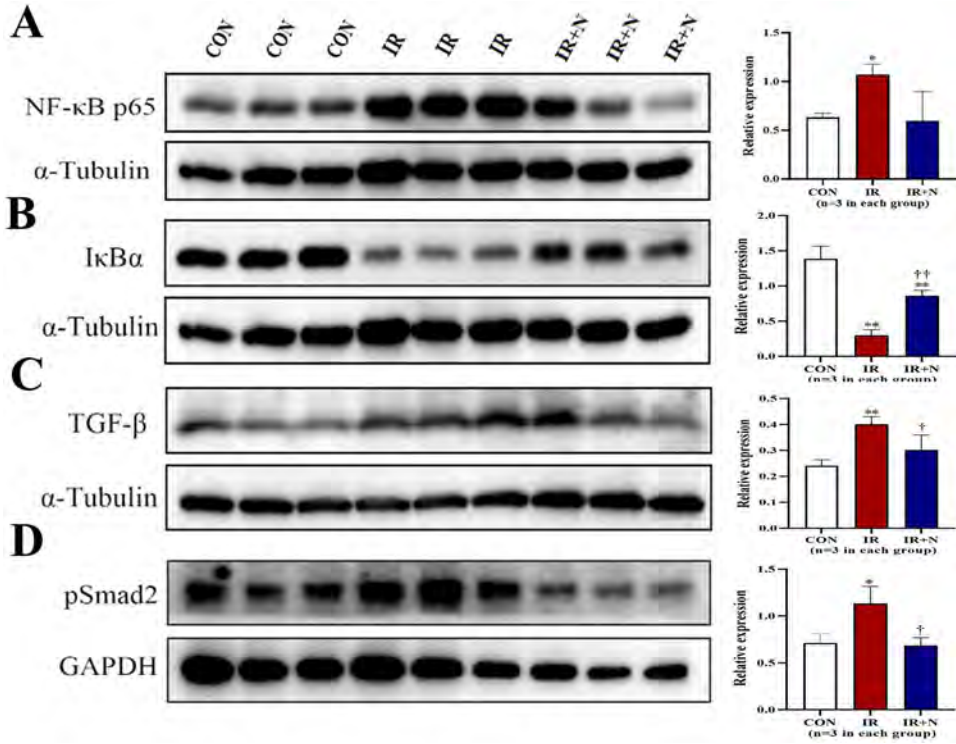


Fig. 3. Western blot analysis on the expression of NF-κB, IκBα, TGF-β, and pSmad2 in lungs. Representative blots (left) and quantitative data (right) on the expression of NF-κB p65 (A), IκBα (B), TGF-β (C), pSmad2 (D) in lungs are shown. Data are normalized to α-Tubulin or GAPDH, and represented as means ± SD. *p < 0.05, **p < 0.01 vs CON group, †p < 0.05, ††p < 0.01 vs IR group. CON: Control, IR: Radiation, IR + N: Radiation+Nicaraven.

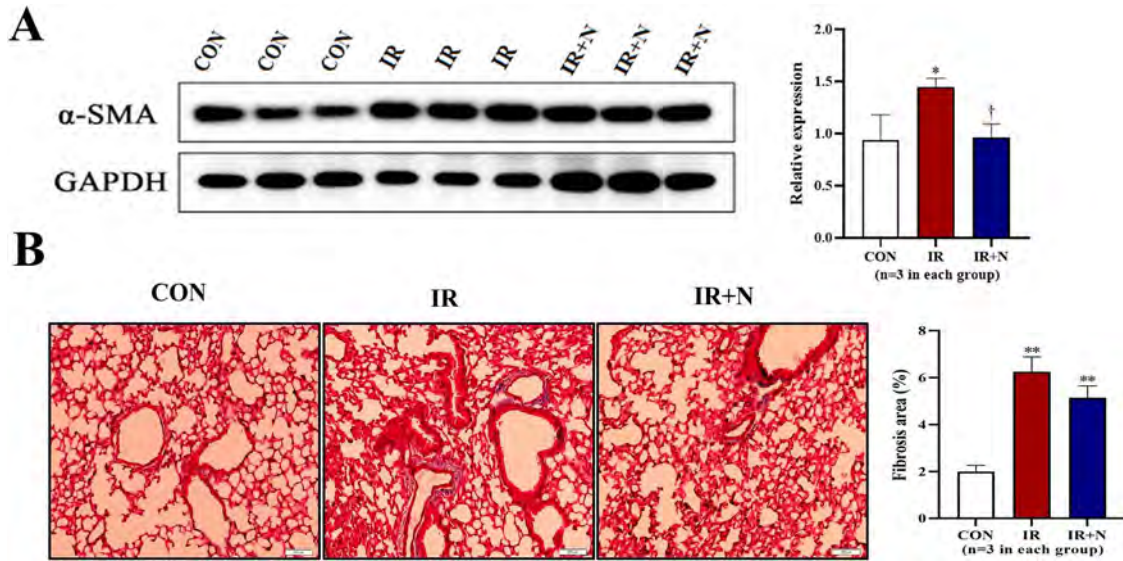


Fig. 4. The fibrotic changes in lungs at the chronic phase after treatments. (A) Representative blots (left) and quantitative data (right) on the expression of α-SMA in lungs are shown. (B) Representative images (left) and quantitative data (right) of Masson's trichrome staining on the fibrotic area in lungs are shown. Scale bars: 200 μm. Data are represented as means ± SD. *p < 0.05, **p < 0.01 vs CON group, †p < 0.05 vs IR group. CON: Control, IR: Radiation, IR + N: Radiation+Nicaraven.

Nicaraven is known as a powerful radical scavenger that effectively protects various tissues and organs against injuries, particularly for ischemia–reperfusion injury in the brain [26–28]. Considering the well-recognized antioxidative property and the potential anti-inflammatory effect of nicaraven, we evaluated the probable role of nicaraven on mitigating RILI.

The exposure to high levels of ionizing radiation leads to DNA double-strand breaks, which elicit cell death or stochastic change [4]. Stem cells are known to play critical role in tissue homeostasis, while ionizing radiation exposure can disrupt the tissue homeostasis. Alveolar epithelium is composed of two cell types: Type I cells account for 95% of the gas exchange surface area, and type II cells can transform into type I cells and have the ability to repair alveoli. Sca-1-positive cells are identified as a population of alveolar type II cells with progenitor cell properties [29]. It has also been demonstrated that the proliferation of Sca-1-positive cells increases during the alveolar epithelial repair phase [29, 30]. In this study, the number of Sca-1-positive cells were exactly increased in irradiated lungs at the acute phase, suggesting the probable role of Sca-1-positive cells for repairing the injured lungs after high dose irradiation. Nicaraven administration showed to reduce the DNA damage of lung tissue cells, especially in these Sca-1-positive cells at the acute phase, which indirectly indicates the protective effect of nicaraven on RILI.

Various chemokines/cytokines are known to be increased in organs/tissues exposed to high dose irradiation, which in turn induces the recruitment of inflammatory cells at the acute phase. The recruited inflammatory cells play a key role in the pathogenesis of RILI [31, 32], because inflammatory cascade is known to promote fibroblast proliferation and collagen deposition [33]. In responding to high dose radiation exposure, the recruitment of monocytes/immune cells (CD11c⁺) into lung tissue plays critical pathophysiological role on RILI. Among the recruited monocytes/immune cells, macrophages (F4/80⁺) represent an important profibrogenic initiator/mediator, but M2 macrophages (CD206⁺) are thought to be an anti-inflammatory phenotype of macrophages. In this study, we found that the recruitment of monocytes/immune cells, including the M2 macrophages was significantly increased in the irradiated lungs. Consistent with previous reports [22, 34], the administration of nicaraven inhibited significantly the recruitment of monocytes into the irradiated lungs. It will be better to understand the precise role of especial subpopulation of inflammatory cells, such as the M2 macrophages in lungs using genetically modified animals. However, the purpose of this study was designed to examine the potency of nicaraven for attenuating RILI through an anti-inflammatory mechanism, we used a wild-type mice rather than the genetically modified mice for experiments.

TGF- β is one of the most critical master regulators on promoting acute inflammation and chronic fibrosis in lungs [12–16]. Previous studies have demonstrated that radiation exposure activates TGF- β /Smad signaling pathway to initiate the inflammatory response, induce the proliferation and activation of fibroblasts, and enhance the synthesis of matrix proteins [35, 36]. Therefore, the inhibition of TGF- β /Smad signaling pathway may effectively mitigate RILI. In this study, nicaraven administration exactly downregulated the expression of TGF- β and pSmad2 in irradiated lungs at the acute phase.

NF- κ B has emerged as a ubiquitous factor involved in the regulation of numerous critical processes, including immune [37], inflammation response [38], cell apoptosis [39], and cell proliferation [40]. While in an inactivated state, NF- κ B is located in the cytosol complexed with the inhibitory protein I κ B α . Radiation exposure can activate NF- κ B signaling pathway. Radiation exposure activates the kinase IKK, which in turn phosphorylates I κ B α and results in ubiquitin-dependent degradation [11, 38, 40]. Dysregulation of NF- κ B signaling can lead to inflammation, autoimmune disease and cancer [41]. In this study, nicaraven administration effectively downregulated the expression of NF- κ B, suggesting the involvement of NF- κ B pathway in the protective effect of nicaraven to RILI.

Generally, although nicaraven administration only tended to partially reduce the fibrotic area in the irradiated lungs, many other parameters, such as the expression of α -SMA was more sensitively and clearly changed. As the activated fibroblasts (α -SMA⁺) are generally thought to be the predominant source of collagen-producing cells, the inhibition on α -SMA expression in irradiated lungs by nicaraven administration suggested the probable benefit of nicaraven for attenuating the development of fibrotic change in irradiated lungs at the chronic phase. In summary, nicaraven administration effectively protected the RILI, likely by suppressing inflammatory response through the NF- κ B and TGF- β /Smad signaling pathways. Nicaraven could be a potential drug for mitigating RILI.

SUPPLEMENTARY DATA

Supplementary data is available at *RADRES Journal* online.

ACKNOWLEDGEMENTS

This study was supported by the Agency for Medical Research and Development under Grant Number JP20lm0203081. The funder played no role in study design, data collection and analysis, decision to publish, or manuscript preparation.

CONFLICT OF INTEREST

The authors indicate no potential conflicts of interest.

REFERENCES

1. Bentzen SM. Preventing or reducing late side effects of radiation therapy: radiobiology meets molecular pathology. *Nat Rev Cancer* 2006;6:702–13.
2. McBride WH, Schae D. Radiation-induced tissue damage and response. *J Pathol* 2020;250:647–55.
3. Rodrigues G, Lock M, D'Souza D et al. Prediction of radiation pneumonitis by dose volume histogram parameters in lung cancer—a systematic review. *Radiother Oncol* 2004;71:127–38.
4. Huang L, Snyder AR, Morgan WF. Radiation-induced genomic instability and its implications for radiation carcinogenesis. *Oncogene* 2003;22:5848–54.
5. Hanania AN, Mainwaring W, Ghebre YT et al. Radiation-induced lung injury: assessment and management. *Chest* 2019;156:150–62.

6. Giuranno L, Ient J, De Ruyscher D et al. Radiation-induced lung injury (RILI). *Front Oncol* 2019;9:877.
7. Kim H, Park SH, Han SY et al. LXA4-FPR2 signaling regulates radiation-induced pulmonary fibrosis via crosstalk with TGF- β /Smad signaling. *Cell Death Dis* 2020;11:653.
8. Jin H, Yoo Y, Kim Y et al. Radiation-induced lung fibrosis: pre-clinical animal models and therapeutic strategies. *Cancers (Basel)* 2020;12:1561.
9. Kainthola A, Haritwal T, Tiwari M et al. Immunological aspect of radiation-induced pneumonitis, current treatment strategies, and future prospects. *Front Immunol* 2017;8:506.
10. Im J, Lawrence J, Seelig D et al. FoxM1-dependent RAD51 and BRCA2 signaling protects idiopathic pulmonary fibrosis fibroblasts from radiation-induced cell death. *Cell Death Dis* 2018;9:584.
11. Devary Y, Rosette C, DiDonato JA et al. NF-kappa B activation by ultraviolet light not dependent on a nuclear signal. *Science* 1993;261:1442–5.
12. Madani I, De Ruyck K, Goeminne H et al. Predicting risk of radiation-induced lung injury. *J Thorac Oncol* 2007;2:864–74.
13. Fleckenstein K, Gauter-Fleckenstein B, Jackson IL et al. Using biological markers to predict risk of radiation injury. *Semin Radiat Oncol* 2007;17:89–98.
14. Anscher MS, Kong FM, Andrews K et al. Plasma transforming growth factor beta1 as a predictor of radiation pneumonitis. *Int J Radiat Oncol Biol Phys* 1998;41:1029–35.
15. Singh V, Torricelli AA, Nayeb-Hashemi N et al. Mouse strain variation in SMA(+) myofibroblast development after corneal injury. *Exp Eye Res* 2013;115:27–30.
16. Tatler AL, Jenkins G. TGF- β activation and lung fibrosis. *Proc Am Thorac Soc* 2012;9:130–6.
17. Akimoto T. Quantitative analysis of the kinetic constant of the reaction of N,N'-propylenedini-cotinamide with the hydroxyl radical using dimethyl sulfoxide and deduction of its structure in chloroform. *Chem Pharm Bull(Tokyo)* 2000;48:467–76.
18. Mori Y, Takashima H, Seo H et al. Experimental studies on Nicaraven as radioprotector-free radical scavenging effect and the inhibition of the cellular injury. *Nihon Igaku Hoshasen Gakkai Zasshi* 1993;53:704–12.
19. Watanabe M, Akiyama N, Sekine H et al. Inhibition of poly (ADP-ribose) polymerase as a protective effect of nicaraven in ionizing radiation- and ara-C-induced cell death. *Anticancer Res* 2006;26:3421–7.
20. Zingarelli B, Scott GS, Hake P et al. Effects of nicaraven on nitric oxide-related pathways and in shock and inflammation. *Shock* 2000;13:126–34.
21. Masana Y, Yoshimine T, Fujita T et al. Reaction of microglial cells and macrophages after cortical incision in rats: effect of a synthesized free radical scavenger, (+/-)-N,N'-propylenedinitocotinamide (AVS). *Neurosci Res* 1995;23:217–21.
22. Yan C, Luo L, Urata Y et al. Nicaraven reduces cancer metastasis to irradiated lungs by decreasing CCL8 and macrophage recruitment. *Cancer Lett* 2018;418:204–10.
23. Lin H, Wu X, Yang Y et al. Nicaraven inhibits TNF α -induced endothelial activation and inflammation through suppressing NF- κ B signaling pathway. *Can J Physiol Pharmacol* 2021;99:803–11.
24. Citrin DE, Shankavaram U, Horton JA et al. Role of type II pneumocyte senescence in radiation-induced lung fibrosis. *J Natl Cancer Inst* 2013;105:1474–84.
25. Doi H, Kitajima Y, Luo L et al. Potency of umbilical cord blood- and Wharton's jelly-derived mesenchymal stem cells for scarless wound healing. *Sci Rep* 2016;6:18844.
26. Asano T, Johshita H, Koide T et al. Amelioration of ischaemic cerebral oedema by a free radical scavenger, AVS: 1,2-bis(nicotinamido)-propane. An experimental study using a regional ischaemia model in cats. *Neurol Res* 1984;6:163–8.
27. Asano T, Takakura K, Sano K et al. Effects of a hydroxyl radical scavenger on delayed ischemic neurological deficits following aneurysmal subarachnoid hemorrhage: results of a multicenter, placebo-controlled double-blind trial. *J Neurosurg* 1996;84:792–803.
28. Imperatore C, Germanò A, d'Avella D et al. Effects of the radical scavenger AVS on behavioral and BBB changes after experimental subarachnoid hemorrhage. *Life Sci* 2000;66:779–90.
29. Liu Y, Kumar VS, Zhang W et al. Activation of type II cells into regenerative stem cell antigen-1(+) cells during alveolar repair. *Am J Respir Cell Mol Biol* 2015;53:113–24.
30. Liu Y, Sadikot RT, Adami GR et al. FoxM1 mediates the progenitor function of type II epithelial cells in repairing alveolar injury induced by *Pseudomonas aeruginosa*. *J Exp Med* 2011;208:1473–84.
31. Johnston CJ, Williams JP, Elder A et al. Inflammatory cell recruitment following thoracic irradiation. *Exp Lung Res* 2004;30:369–82.
32. Mezziani L, Deutsch E, Mondini M. Macrophages in radiation injury: a new therapeutic target. *Onco Targets Ther* 2018;7:e1494488.
33. Boothe DL, Coplowitz S, Greenwood E et al. Transforming growth factor β -1 (TGF- β 1) is a serum biomarker of radiation induced fibrosis in patients treated with intracavitary accelerated partial breast irradiation: preliminary results of a prospective study. *Int J Radiat Oncol Biol Phys* 2013;87:1030–6.
34. Zhang X, Moriwaki T, Kawabata T et al. Nicaraven attenuates postoperative systemic inflammatory responses-induced tumor metastasis. *Ann Surg Oncol* 2020;27:1068–74.
35. Meng XM, Nikolic-Paterson DJ, Lan HY. TGF- β : the master regulator of fibrosis. *Nat Rev Nephrol* 2016;12:325–38.
36. Samarakoon R, Overstreet JM, Higgins PJ. TGF- β signaling in tissue fibrosis: redox controls, target genes and therapeutic opportunities. *Cell Signal* 2013;25:264–8.
37. Baeuerle PA, Henkel T. Function and activation of NF-kappa B in the immune system. *Annu Rev Immunol* 1994;12:141–79.
38. Barnes PJ, Karin M. Nuclear factor-kappaB: a pivotal transcription factor in chronic inflammatory diseases. *N Engl J Med* 1997;336:1066–71.
39. Bours V, Bonizzi G, Bentires-Alj M et al. NF-kappaB activation in response to toxic and therapeutical agents: role in inflammation and cancer treatment. *Toxicology* 2000;153:27–38.

40. Karin M, Cao Y, Greten FR et al. NF-kappaB in cancer: from innocent bystander to major culprit. *Nat Rev Cancer* 2002;2: 301–10.
41. Yu H, Lin L, Zhang Z et al. Targeting NF- κ B pathway for the therapy of diseases: mechanism and clinical study. *Signal Transduct Target Ther* 2020;5:209.

Nicaraven Exerts a Limited Effect on Radiation-Induced Inhibition of Tumor Growth in a Subcutaneous Murine Tumor Model

Authors: Abdelghany, Lina, Xu, Yong, Sekiya, Reiko, Yan, Chen, Jingu, Keiichi, et al.

Source: Radiation Research, 200(4) : 382-388

Published By: Radiation Research Society

URL: <https://doi.org/10.1667/RADE-22-00212.1>

BioOne Complete (complete.BioOne.org) is a full-text database of 200 subscribed and open-access titles in the biological, ecological, and environmental sciences published by nonprofit societies, associations, museums, institutions, and presses.

Your use of this PDF, the BioOne Complete website, and all posted and associated content indicates your acceptance of BioOne's Terms of Use, available at www.bioone.org/terms-of-use.

Usage of BioOne Complete content is strictly limited to personal, educational, and non-commercial use. Commercial inquiries or rights and permissions requests should be directed to the individual publisher as copyright holder.

BioOne sees sustainable scholarly publishing as an inherently collaborative enterprise connecting authors, nonprofit publishers, academic institutions, research libraries, and research funders in the common goal of maximizing access to critical research.

Nicaraven Exerts a Limited Effect on Radiation-Induced Inhibition of Tumor Growth in a Subcutaneous Murine Tumor Model

Lina Abdelghany,^{a,b} Yong Xu,^{a,b} Reiko Sekiya,^{a,b} Chen Yan,^{a,b} Keiichi Jingu,^c Tao-Sheng Li^{a,b,1}

^aDepartment of Stem Cell Biology, Atomic Bomb Disease Institute, Nagasaki University, 1-12-4 Sakamoto, Nagasaki 852-8523, Japan; ^bDepartment of Stem Cell Biology, Nagasaki University Graduate School of Biomedical Sciences, 1-12-4 Sakamoto, Nagasaki 852-8523, Japan; ^cDepartment of Radiation Oncology, Graduate School of Medicine, Tohoku University, Sendai, Japan

Abdelghany L, Xu Y, Sekiya R, Yan C, Jingu K, Li T-S. Nicaraven Exerts a Limited Effect on Radiation-Induced Inhibition of Tumor Growth in a Subcutaneous Murine Tumor Model. *Radiat Res.* 200, 382–388 (2023).

Nicaraven selectively protects normal tissue from radiation-induced injury. To further develop the clinical application of nicaraven for mitigating the side effects of cancer radiotherapy, we investigated the potential effect of nicaraven administration in radiation-induced inhibition of tumor growth. A subcutaneous tumor model was established in mice by the injection of Lewis lung cancer cells at the back of the chest. X-ray radiation was delivered to the thoracic area and different doses of nicaraven (0, 20, 50, 100 mg/kg) were administered intraperitoneally pre- or post-irradiation. The tumor size was measured every other day. Mice were euthanized on day 30, and the tumor weight and the levels of cytokines in tumor tissue were measured. Pre- or post-irradiation administration of nicaraven up to a dose of 100 mg/kg did not significantly diminish the radiation-induced inhibition of tumor growth, but post-irradiation administration of 20 and 50 mg/kg nicaraven resulted in relatively lower tumor weight. The levels of IL-1 β , IL-6, IL-10, MCP-1, MIP-2a, TGF- β ₁, VEGF, p53, p21, cyclin D1 and caspase-3 in tumor tissue did not change by nicaraven administration and were not significantly associated with the tumor weights. According to our experimental data, nicaraven will not significantly diminish the radiation-induced inhibition of tumor growth, even with pre-irradiation administration at a high dose. © 2023 by Radiation Research Society

INTRODUCTION

For many years, radiotherapy has played a momentous role in cancer treatment with curative intent or as an adjuvant modality with chemotherapy or surgery (1). Additionally, radiotherapy is used as a palliative remedy to relieve symptoms in non-malignant and malignant disorders (2). However, many patients experience radiation-induced adverse

effects due to radiation exposure to the surrounding normal tissue (3).

Two main mechanisms cause radiation-induced tissue toxicity: direct DNA damage and the generation of reactive oxygen species (ROS) (4). Furthermore, water molecule ionization produces ROS and nitrogen species that make up 60% of the total damage imposed (5). ROS also provokes inflammation and immune responses, a serious and common complication after exposure to radiation (6). Although some traditional agents have a protective effect on the surrounding normal tissue, they may diminish the radiosensitivity of cancer cells (7). Development of a new agent that selectively protects the normal tissue from radiation-induced injury is needed for clinical application in cancer patients who are receiving radiotherapy.

Nicaraven, a small molecule, originally recognized as a free radical scavenger that is well known to protect normal tissue from ischemia-reperfusion injury (8). We have recently found the protective effect of nicaraven on normal tissue against radiation injury, which is more likely associated with an anti-inflammatory effect rather than the free radical scavenging effect (9–11). We have further confirmed that nicaraven shows a very limited effect on the growth of established tumors in mice (12, 13). Due to the selective radioprotection to normal tissue, nicaraven would be beneficial for cancer patients who are receiving radiotherapy.

Using a tumor-bearing mice model, we administered different doses of nicaraven pre- or post-irradiation. We monitored the tumor growth every other day and measured the levels of inflammatory cytokines/chemokines in tumor tissue. According to our data, nicaraven will not significantly diminish the radiation-induced inhibition of tumor growth.

MATERIALS AND METHODS

Cell Line

The Lewis lung carcinoma cells were grown in DMEM (FUJIFILM Wako) supplemented with 10% fetal bovine serum (Gibco) and 1% streptomycin/penicillin (Gibco), at 37°C in a 5% CO₂ incubator. Cells with almost 80% confluent were harvested for the establishment of a tumor model in mice.

¹Tao-Sheng Li, MD, PhD., Department of Stem Cell Biology, Atomic Bomb Disease Institute, Nagasaki University, 1-12-4 Sakamoto, Nagasaki 852-8523, Japan; email: litaoshe@nagasaki-u.ac.jp.

Mouse Tumor Model

We used 8-week-old male C57BL/6N mice (CLEA Japan Inc., Tokyo, Japan) for the experiment. To establish a tumor model, 5×10^5 cancer cells in 0.1 mL saline solution were injected subcutaneously into the interscapular fat pad of each mouse, at the back of the chest. This study was approved by the Institutional Animal Care and Use Committee of our University (No. 1608251335-12). All experimental procedures were performed by institutional and national guidelines.

Irradiation and Nicaraven Administration Regimens

At 10 days after cancer cell injection, a total of 41 mice were randomly divided into 8 groups, and different treatments were performed as illustrated in Fig. 1A.

For irradiations, general anesthesia was induced in tumor-bearing mice by intraperitoneal injection with an anesthesia cocktail. Thoracic irradiations were delivered to mice by shielding them with a specially designed lead apparatus, which allows a regional delivery of radiation to the tumor nodule in the back of the chest. X-ray radiation was delivered (200 kV, 15 mA, 5 mm aluminum filtration, ISOVOLT TITAN320, General Electric Company), at a dose rate of 1.0084 Gy/min.

Mice were intraperitoneally injected with 20, 50, or 100 mg/kg nicaraven pre-irradiation (about 5 min before exposure) or post-irradiation (within 5 minutes after exposure) ($n = 5$ in each group). For placebo control, mice received radiation treatment but were given saline injection only (placebo group, $n = 5$). In addition, we also included a control group ($n = 6$), in which the mice received neither radiation nor nicaraven administration. The tumor size was monitored by measuring the tumor dimensions using Vernier calipers every other day. Tumor volumes were calculated as: volume (mm^3) = length \times width²/2.

Enzyme-linked Immunosorbent Assay (ELISA)

The tumor tissues were collected after mice euthanasia, and tumor weight was measured. The levels of cytokines/chemokines (IL-1 β , IL-6, IL-10, MCP-1, MIP-2a, TGF- β_1 , and VEGF) were measured by commercial ELISA kits (R&D Systems) according to the instructions of the manufacturer. The tumor tissues were homogenized in a T-PER reagent containing proteinase and phosphatase inhibitors (Thermo Fisher Scientific) using Multi-beads shocker[®]. The optical density of each well was measured at 450 nm using a microplate reader (iMark[™] Microplate Reader; Bio-Rad Laboratories).

Western Blotting

The tissue lysates were heated at 95°C for 5 min, then loaded on an SDS-PAGE gel and transferred to PVDF membrane (Bio-Rad Laboratories). Membranes were probed with primary antibodies against p53 (1:1,000 dilution; cat. no. 2524s; Cell Signaling Technology), p21 (1:1000 dilution; cat. no. 37543; Cell Signaling Technology), caspase 3 (1:1,000 dilution; cat. no. 14220; Cell Signaling Technology), cyclin D1 (1:1000 dilution; cat. no. 2978; Cell Signaling Technology), and β -actin (1:1,000 dilution; cat. no. HRP-66009; Proteintech), at 4°C overnight or 25°C for 1 h. Followed by horseradish peroxidase-conjugated anti-rabbit secondary antibody (Cell Signaling Technology) for 1 h at 25°C, the expression was visualized using an ECL detection kit (SuperSignal West Femto, ThermoFisher Scientific). The blots were detected using ImageQuant LAS 4000 Mini biomolecular imager (Cytiva) and analyzed by ImageJ 2.1.0 software (National Institutes of Health).

Statistical Analysis

Results are expressed as means \pm SD. Statistical differences among groups were determined using a one-way analysis of variance (ANOVA) followed by Dunnett's multiple comparison test. Correlations between cytokine levels and tumor weights were assessed using Pearson's correlation analysis (GraphPad Prism 8.0 software).

RESULTS

Neither Pre-Irradiation nor Post-Irradiation Administration of Nicaraven up to 100 mg/kg Diminishes the Radiation-Induced Inhibition of Tumor Growth

As shown in Fig. 1 on the therapeutic regimens, different treatments were started when a subcutaneous tumor nodule was formed in the back of the chest of mice. As the standard regimen of radiation treatment (14), daily 6 Gy thoracic irradiation was delivered to mice for 5 consecutive days. The tumor nodule grew quickly in non-irradiated controls, and we terminated the follow-up on day 15 for mice of the control group due to the large tumor nodules (Fig. 1A). According to the measured tumor size (Fig. 1B), tumor growth was almost stopped after the daily 6 Gy irradiation for 5 days. As the size of the tumor nodule did not decrease after the first round of radiotherapy, we decided to deliver an additional 6 Gy thoracic irradiation on day 9. The tumor size was still slowly increasing during the follow-up. To further confirm that nicaraven administration would not diminish the radiotherapy-induced inhibition of tumor growth, another 6 Gy thoracic irradiation was delivered to mice again on day 16 (Fig. 1A). We finally terminated the follow-up for all groups on day 30.

The radiation-induced inhibition of tumor growth during the follow-up period was almost not affected by nicaraven administration with different doses given either pre- or post-irradiation (Fig. 1B). Compared to the placebo, the mean change of the tumor volume was slightly decreased only by the post-irradiation administration with 20 and 50 mg/kg nicaraven.

At the endpoint of follow-up, we euthanized the mice and extracted the tumor tissues (Fig. 1C). The tumor sizes varied largely even in the same group, and the tumor weight was much higher in the control group without radiation treatment than in other groups that received radiation. Interestingly, the tumor weight was not significantly different among all groups that received thoracic irradiation, whether the mice were given placebo treatment or nicaraven administration with different doses at different timing (Fig. 1D). Moreover, a simple and direct comparison between pre- or post-irradiation groups also showed that the radiation-induced inhibition of tumor growth was not significantly affected by the timing of nicaraven administration (Fig. 1E).

Nicaraven Administration did not Significantly Change the Levels of IL-1 β , IL-6, IL-10, MCP-1, MIP-2a, TGF- β_1 , VEGF, p53, p21, Caspase-3 and Cyclin D1 in the Tumors

Previous studies have demonstrated the anti-inflammatory effect of nicaraven (11, 15). Therefore, we measured the levels of IL-1 β , IL-6, IL-10, MCP-1, MIP-2a, and TGF- β_1 in tumor tissue by ELISA. As shown in Fig. 2, the levels of IL-1 β , MCP-1, MIP-2a, and TGF- β_1 in tumors were not significantly different among all groups, although the level of IL-6 was slightly decreased in 20 and 50 mg/kg pre-irradiation compared to placebo (Fig. 2B). Furthermore, IL-10 was

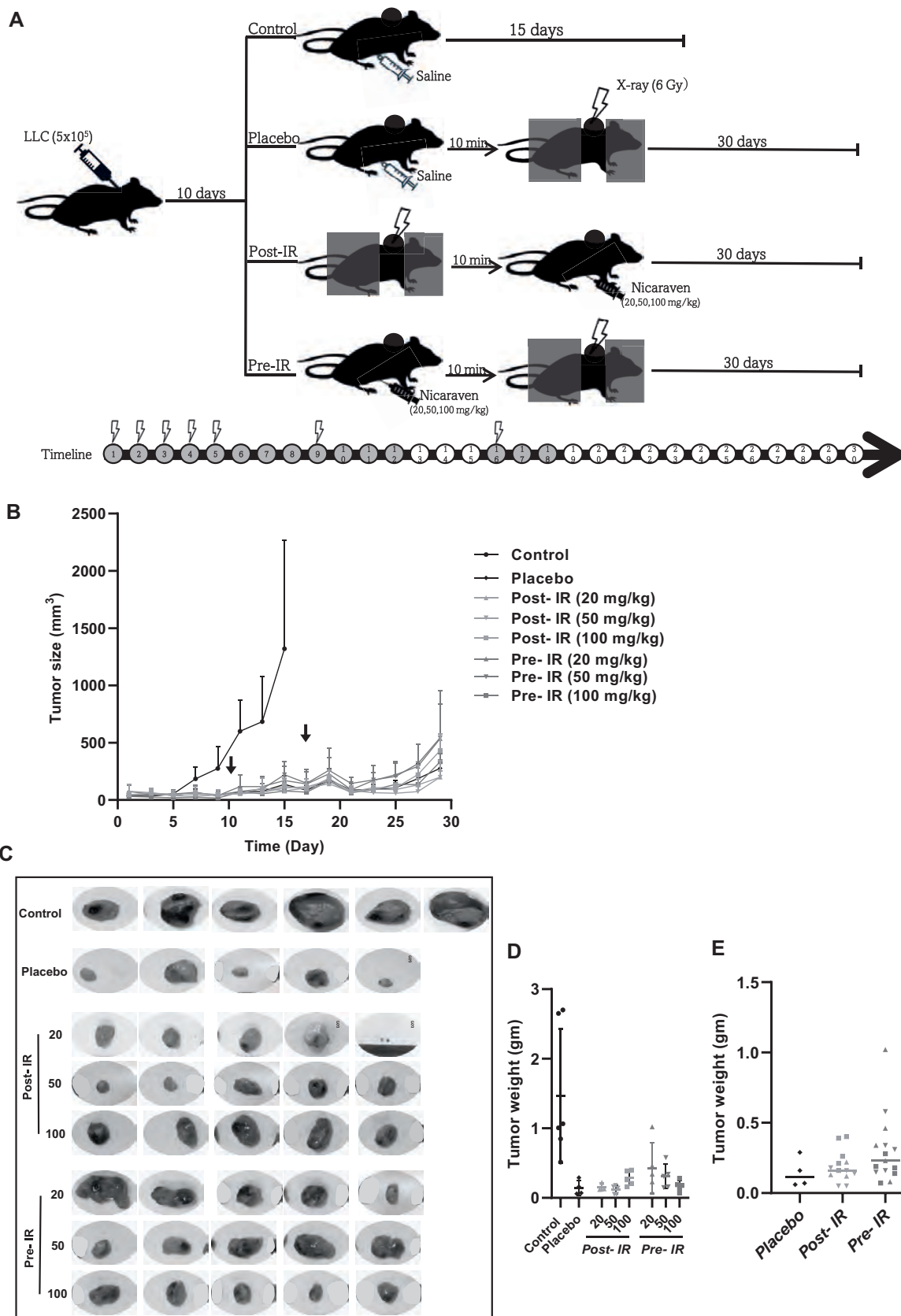


FIG. 1. Changes in tumor size and weight in mice. Panel A: Schematic diagram of the experimental timeline and therapeutic regimens. Panel B: Quantitative data on the changes in tumor size. Panels C–E: The excised tumors and tumor weight at the endpoint are shown. Data are represented as the means \pm SD, $n = 3\text{--}5$ per group. IR: irradiation; Post-IR: post-irradiation; Pre-IR: pre-irradiation. §: mouse death during the follow-up.

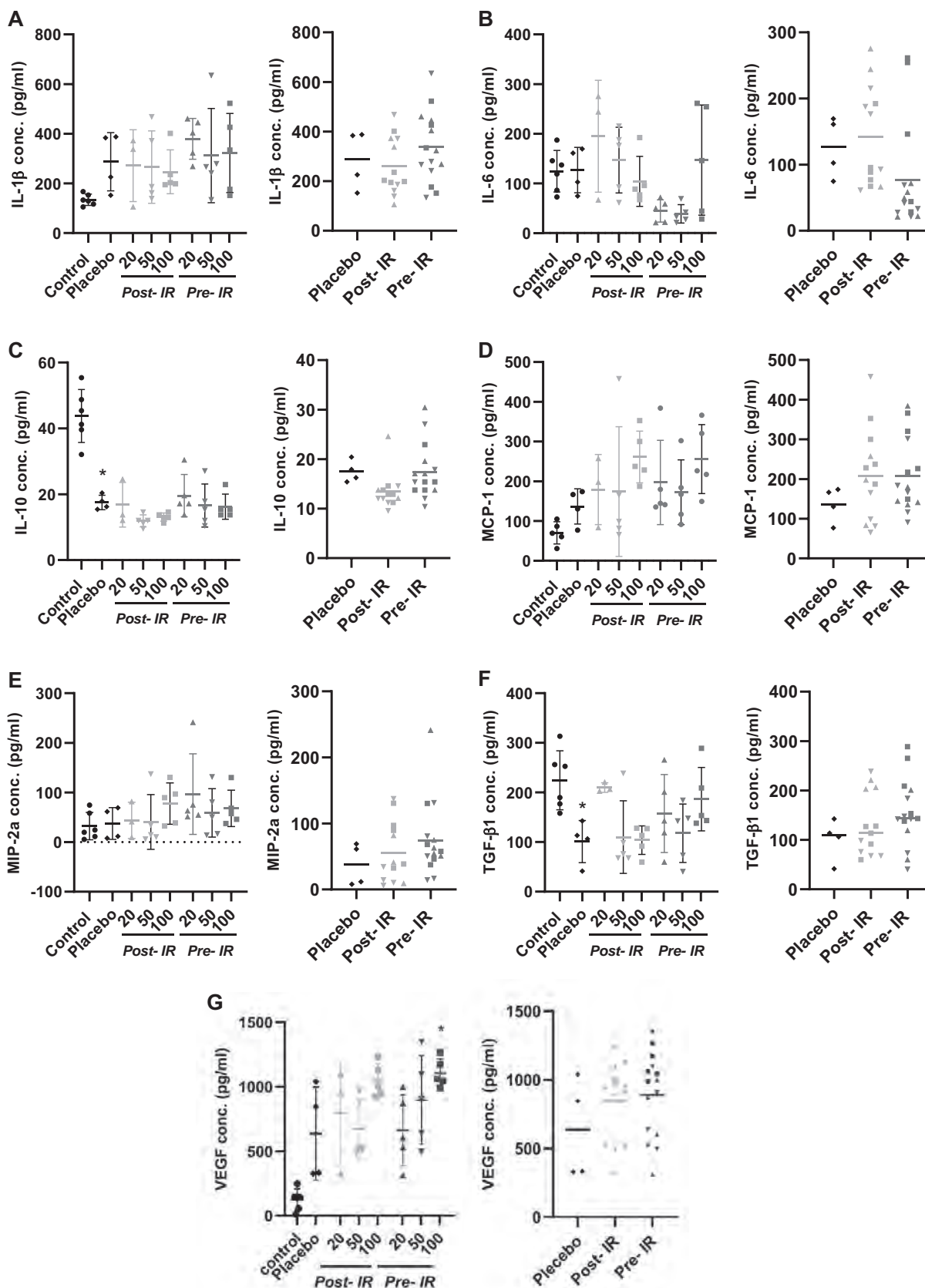


FIG. 2. ELISA analysis on the inflammatory cytokines in the tumors. Quantitative data on the levels of IL-1 β (panel A), IL-6 (panel B), IL-10 (panel C), MCP-1 (panel D), MIP-2a (panel E), TGF- β ₁ (panel F), and VEGF (panel G) in the excised tumor tissue samples are shown. Data are represented as the means \pm SD, n = 3–5 per group. IR: irradiation; Post-IR: post-irradiation; Pre-IR: pre-irradiation.

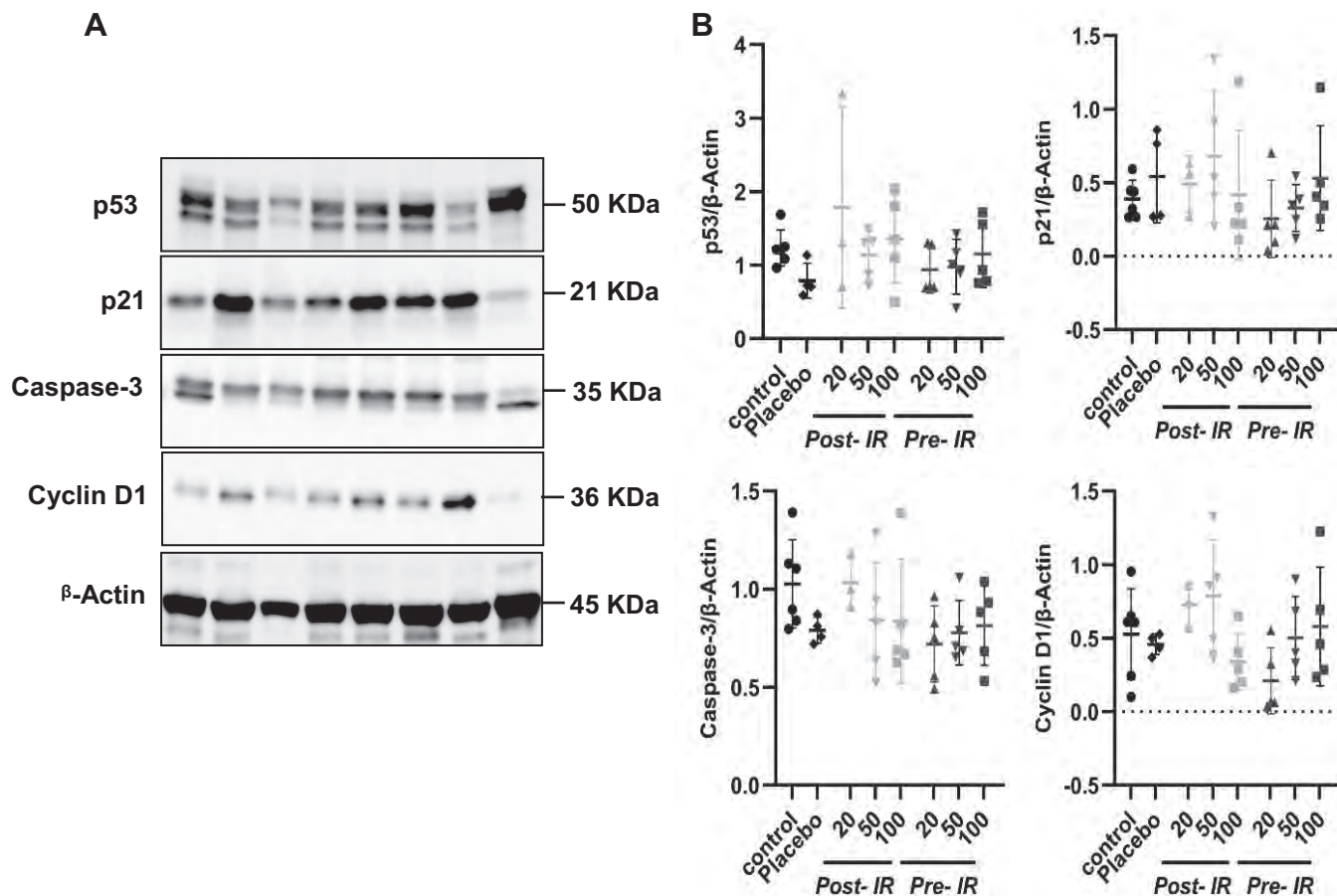


FIG. 3. Western blot for detecting the expression of the apoptotic markers. Representative images (panel A) and semi-quantification data (panel B) show the expression of p53, p21, caspase-3 and cyclin D1 in the tumor extracts.

slightly decreased by post-irradiation nicaraven administration at the doses of 50 and 100 mg/kg (Fig. 2C). Otherwise, the levels of IL-1 β , IL-6, IL-10, MCP-1, MIP-2a, and TGF- β ₁ in the tumors were not significantly correlated with the tumor weights (Supplementary Table S1;² <https://doi.org/10.1667/RADE-22-00212.1.S1>). We also measured the VEGF level in tumors and did not find significant difference among all groups (Fig. 2G).

To further evaluate the apoptosis, we measured the expression of p53, p21, caspase-3 and cyclin D1 in tumors by Western blot. Nicaraven administration did not significantly change the expression of p53, p21, caspase-3 and cyclin D1 in tumors (Fig. 3).

DISCUSSION

Radiotherapy for many types of malignant tumors has proven satisfactory in inhibiting tumor growth (16–18). To obtain better outcomes of radiotherapy, it is still asked to reduce the early and late side effects, as well as to increase tumor response (19, 20). Multiple approaches,

such as the use of radio-protectors (pre-radiotherapy) or radio-mitigators (during or immediately post-radiotherapy) have been tested clinically to reduce the side effects of radiotherapy (21–29). However, there is still no clear evidence of how the approaches affect the sensitivity of cancer cells to radiation.

The side effect of cancer patients receiving radiotherapy is dependent on several parameters, such as the tumor location (30), the dose, and irradiated volume (31). Therefore, radiation-induced toxicity to normal tissue should be evaluated in tumor-bearing models using clinically relevant combination-treatment schedules and surrogate endpoints (32). However, most studies in animals have delivered single dose irradiation rather than clinically relevant fractionated irradiation (33). In this study, we established a tumor on the back of the chest of the mice. To design a clinically relevant radiation treatment regimen, thoracic radiation treatment was delivered to the tumor-bearing mice in 5 fractions (6 Gy/day for 5 days) for a cycle of standard treatment at first and were given two additional doses of 6 Gy thoracic irradiation according to the status of tumor growth. Our data showed that nicaraven administration with different doses either pre- or post-irradiation did not diminish the radiation-induced inhibition of tumor growth.

² Editor's note. The online version of this article (DOI: <https://doi.org/10.1667/RADE-22-00212.1>) contains supplementary information that is available to all authorized users.

Exposure to radiation generates ROS that provokes DNA damage and death to both the cancer cells and the surrounding normal tissue (34). Hence, some free radical scavenging radio-protectors greatly decrease the effect of radiation in inhibiting tumor growth (20). Nicaraven is originally known as a free radical scavenger (35); however, our past studies have demonstrated that nicaraven barely changes the ROS levels on different types of cells (10). Therefore, it is not surprising to us the minimal effect that nicaraven has in radiation-induced inhibition of tumor growth as shown in our study.

It has been reported that hypo-fractionated radiation converts “cold” tumors to “hot” inflammatory tumors by releasing pro-inflammatory factors (36). Since nicaraven has shown an anti-inflammatory effect (11, 15), we measured the levels of several cytokines/chemokines in the tumors. We found that the levels of IL-1 β , IL-6, IL-10, MCP-1, MIP-2a, TGF- β ₁, VEGF, p53, p21, caspase-3 and cyclin D1 in tumor tissues did not significantly change by nicaraven administration and radiotherapy. The pharmacokinetics of nicaraven have been carefully conducted by Chugai Pharmaceutical Co., Ltd. Nicaraven shows a quick (few minutes) adequate whole-body distribution after injection and a short half-life (1.2–1.4 h) in murine. As we collected the tumor tissues almost 2 weeks after the last nicaraven administration, it would not be the optimal time window for detection.

In summary, it seems that nicaraven has a very limited effect on the sensitivity of radiotherapy to established tumors. According to the results from this experimental study, post-irradiation administration of nicaraven at low doses will be recommended. However, randomized controlled trials are needed to further confirm the benefit of nicaraven administration for cancer patients who are receiving radiotherapy.

SUPPLEMENTARY TABLES

Correlations between the levels of cytokines in tumor tissues and the tumor weights at the endpoint.

ACKNOWLEDGMENTS

This study was supported by Japan Agency for Medical Research and Development, a Grant-in-Aid from the Ministry of Education, Science, Sports, Culture and Technology, Japan. All data are included in the paper and/or the Supplementary Material.

Received: November 28, 2022; accepted: August 3, 2023; published online: September 13, 2023

REFERENCES

- Bradley JD, Paulus R, Komaki R, Masters G, Blumenschein G, Schild S, et al. Standard-dose versus high-dose conformal radiotherapy with concurrent and consolidation carboplatin plus paclitaxel with or without cetuximab for patients with stage IIIA or IIIB non-small-cell lung cancer (RTOG 0617): a randomised, two-by-two phase 3 study. *The Lancet Oncology*. 2015 Feb; 16(2):187–99.

- Seegenschmiedt MH, Micke O, Muecke R; German Cooperative Group on Radiotherapy for Non-malignant Diseases (GCG-BD). Radiotherapy for non-malignant disorders: state of the art and update of the evidence-based practice guidelines. *The British journal of radiology*. 2015 Jul; 88(1051):20150080.
- Trott KR, Herrmann T, Kasper M. Target cells in radiation pneumopathy. *International journal of radiation oncology*. 2004 Feb; 58(2):463–9.
- Jack CI, Cottier B, Jackson MJ, Cassapi L, Fraser WD, Hind CR. Indicators of free radical activity in patients developing radiation pneumonitis. *International journal of radiation oncology*. 1996 Jan; 34(1):149–54.
- Terasaki Y, Ohsawa I, Terasaki M, Takahashi M, Kunugi S, Dedong K, et al. Hydrogen therapy attenuates irradiation-induced lung damage by reducing oxidative stress. *American journal of physiology Lung cellular and molecular physiology*. 2011 Oct; 301(4): 415–26.
- Kim SR, Kim DI, Kim SH, Lee H, Lee KS, Cho SH, et al. NLRP3 inflammasome activation by mitochondrial ROS in bronchial epithelial cells is required for allergic inflammation. *Cell Death & Disease*. 2014 Oct; 5(10):e1498.
- Giuranno L, Ient J, De Ruyscher D, Vooijs MA. Radiation-Induced Lung Injury (RILI). *Frontiers in Oncology*. 2019 Sep; 9(6):1–16.
- Alam Mohd S, Ku K, Hashimoto M, Nosaka S, Saitoh Y, Yamauchi M, et al. Hydroxyl radical scavenging effect of nicaraven in myocardial and coronary endothelial preservation and reperfusion injury. *Cardiovascular Research*. 1997 Mar; 33(3):686–92.
- Ali H, Galal O, Urata Y, Goto S, Guo C, Luo L, et al. The potential benefits of nicaraven to protect against radiation-induced injury in hematopoietic stem/progenitor cells with relative low dose exposures. *Biochemical and Biophysical Research Communications*. 2014 Sep; 452(3):548–53.
- Kawakatsu M, Urata Y, Imai R, Goto S, Ono Y, Nishida N, et al. Nicaraven Attenuates Radiation-Induced Injury in Hematopoietic Stem/Progenitor Cells in Mice. *PloS one* 2013 Mar; 8(3):1–7.
- Yan C, Luo L, Urata Y, Goto S, Li TS. Nicaraven reduces cancer metastasis to irradiated lungs by decreasing CCL8 and macrophage recruitment. *Cancer Letters*. 2018 Apr; 418:204–10.
- Yan C, Luo L, Urata Y, Goto S, Guo C, Li TS. Nicaraven, a Potential Radioprotective Agent, has Very Limited Effects on the Survival of Cancer Cells and the Growth of Established Tumors. *Radiation research*. 2017 Feb; 3 45:339–45.
- Abdelghany L, Zhang X, Kawabata T, Goto S, El-Mahdy N, Jingu K, et al. Nicaraven prevents the fast growth of inflamed tumors by an anti-inflammatory mechanism. *Medical oncology*. 2021 Nov; 39(1):7.
- Qu MX, Murrell DH, Millman B, Palma DA, Louie A V. Dose Escalation in 5-Fraction Palliative Thoracic Radiotherapy: A Feasibility and Safety Planning Study. *International Journal of Radiation Oncology*. 2019 Sep; 105(1):E586–7.
- Lin H, Wu X, Yang Y, Wang Z, Huang W, Wang LF, et al. Nicaraven inhibits TNF α -induced endothelial activation and inflammation through suppressing NF- κ B signaling pathway. *Canadian journal of physiology and pharmacology*. 2021 Aug; 99(8):803–811.
- Vinod SK, Hau E. Radiotherapy treatment for lung cancer: Current status and future directions. *Respirology*. 2020 Nov; 25 Suppl 2: S61–71.
- Vordermark D. Radiotherapy of Cervical Cancer. *Oncology research and treatment*. 2016; 39(9):516–20.
- Hennequin C, Barillot I, Azria D, Belkacemi Y, Bollet M, Chauvet B, et al. [Radiotherapy of breast cancer]. *Cancer radiotherapie*. 2016 Sep; 20 Supp 1:S139–46.
- Farhood B, Goradel NH, Mortezaee K, Khanlarkhani N, Salehi E, Nashtaei MS, et al. Melatonin as an adjuvant in radiotherapy for radioprotection and radiosensitization. *Clinical & translational oncology*. 2019 Mar; 21(3):268–79.

20. Zakeri K, Narayanan D, Vikram B, Evans G, Coleman CN, Prasanna PGS. Decreasing the Toxicity of Radiation Therapy: Radioprotectors and Radiomitigators Being Developed by the National Cancer Institute Through Small Business Innovation Research Contracts. *International journal of radiation oncology*. 2019 May; 104(1):188–96.
21. Arroyo-Hernández M, Maldonado F, Lozano-Ruiz F, Muñoz-Montaño W, Nuñez-Baez M, Arrieta O. Radiation-induced lung injury: current evidence. *BMC Pulmonary Medicine*. 2021 Jan; 21(1):1–12.
22. Antonadou D, Coliarakis N, Synodinou M, Athanassiou H, Kouveli A, Verigos C, et al. Randomized phase III trial of radiation treatment +/- amifostine in patients with advanced-stage lung cancer. *International journal of radiation oncology*. 2001 Nov; 51(4):915–22.
23. Para AE, Bezjak A, Yeung IWT, Van Dyk J, Hill RP. Effects of genistein following fractionated lung irradiation in mice. *Radiotherapy and oncology*. 2009 Sep; 92(3):500–10.
24. Vujaskovic Z, Batinic-Haberle I, Rabbani ZN, fu Feng Q, Kang SK, Spasojevic I, et al. A small molecular weight catalytic metalloporphyrin antioxidant with superoxide dismutase (SOD) mimetic properties protects lungs from radiation-induced injury. *Free radical biology & medicine*. 2002 Sep; 33(6):857–63.
25. Rube CE, Wilfert F, Uthe D, Schmid KW, Knoop R, Willich N, et al. Modulation of radiation-induced tumour necrosis factor alpha (TNF-alpha) expression in the lung tissue by pentoxifylline. *Radiotherapy and oncology*. 2002 Aug; 64(2):177–87.
26. Sun Y, Du YJ, Zhao H, Zhang GX, Sun N, Li XJ. Protective effects of ulinastatin and methylprednisolone against radiation-induced lung injury in mice. *Journal of radiation research*. 2016 Sep; 57(5):505–11.
27. Bao P, Gao W, Li S, Zhang L, Qu S, Wu C, et al. Effect of pretreatment with high-dose ulinastatin in preventing radiation-induced pulmonary injury in rats. *European journal of pharmacology*. 2009 Jan; 603(1–3):114–9.
28. Prasanna PGS, Stone HB, Wong RS, Capala J, Bernhard EJ, Vikram B, et al. Normal tissue protection for improving radiotherapy: Where are the Gaps? *Translational cancer research*. 2012 Jun; 1(1):35–48.
29. Tsai JR, Liu PL, Chen YH, Chou SH, Cheng YJ, Hwang JJ, et al. Curcumin Inhibits Non-Small Cell Lung Cancer Cells Metastasis through the Adiponectin/NF-kb/MMPs Signaling Pathway. *PloS one*. 2015; 10(12):e0144462.
30. Vogelius IR, Bentzen SM. A literature-based meta-analysis of clinical risk factors for development of radiation induced pneumonitis. *Acta oncologica*. 2012 Nov; 51(8):975–83.
31. Leprieur EG, Fernandez D, Chatellier G, Klotz S, Giraud P, Durdux C. Acute radiation pneumonitis after conformational radiotherapy for non small cell lung cancer: clinical, dosimetric, and associated-treatment risk factors. *Journal of cancer research and therapeutics*. 2013 Jul- Sep; 9(3):447–51.
32. Dabjan MB, Buck CM, Jackson IL, Vujaskovic Z, Marples B, Down JD. A survey of changing trends in modelling radiation lung injury in mice: bringing out the good, the bad, and the uncertain. *Laboratory investigation; a journal of technical methods and pathology*. 2016 Sep; 96(9):936–49.
33. Paun A, Haston CK. Genomic and genome-wide association of susceptibility to radiation-induced fibrotic lung disease in mice. *Radiotherapy and oncology*. 2012 Dec; 105(3):350–7.
34. Lee SY, Jeong EK, Ju MK, Jeon HM, Kim MY, Kim CH, et al. Induction of metastasis, cancer stem cell phenotype, and oncogenic metabolism in cancer cells by ionizing radiation. *Molecular cancer*. 2017 Jan; 16(1):10.
35. Watanabe M, Akiyama N, Sekine H, Mori M, Manome Y. Inhibition of poly (ADP-ribose) polymerase as a protective effect of nicaraven in ionizing radiation- and ara-C-induced cell death. *Anticancer Research*. 2006 Sep- Oct; 26(5 A):3421–7.
36. Formenti SC, Rudqvist NP, Golden E, Cooper B, Wennerberg E, Lhuillier C, et al. Radiotherapy induces responses of lung cancer to CTLA-4 blockade. *Nature medicine*. 2018 Dec; 24(12):1845–51.

Hydrostatic pressure stabilizes HIF-1 α expression in cancer cells to protect against oxidative damage during metastasis

DA ZHAI^{1,2}, YONG XU^{1,2}, LINA ABDELGHANY^{1,2,3}, XU ZHANG^{1,2}, JINGYAN LIANG⁴,
SHOUHUA ZHANG⁵, CHANGYING GUO⁶ and TAO-SHENG LI^{1,2}

¹Department of Stem Cell Biology, Atomic Bomb Disease Institute, Nagasaki University; ²Department of Stem Cell Biology, Nagasaki University Graduate School of Biomedical Sciences, Nagasaki 852-8523, Japan; ³Department of Pharmacology and Toxicology, Faculty of Pharmacy, Tanta University, Tanta 31527, Egypt; ⁴Institute of Translational Medicine, Medical College, Yangzhou University, Yangzhou, Jiangsu 225000; ⁵Department of General Surgery, Jiangxi Provincial Children's Hospital; ⁶Department of Thoracic Surgery, Jiangxi Cancer Hospital, Nanchang, Jiangxi 330000, P.R. China

Received November 6, 2020; Accepted April 23, 2021

DOI: 10.3892/or.2021.8162

Abstract. The tissue microenvironment is known to play a pivotal role in cancer metastasis. Interstitial fluid hydrostatic pressure generally increases along with the rapid growth of malignant tumors. The aim of the present study was to investigate the role and relevant mechanism of elevated hydrostatic pressure in promoting the metastasis of cancer cells. Using a commercial device, Lewis lung cancer (LLC) cells were exposed to 50 mmHg hydrostatic pressure (HP) for 24 h. The survival time and morphology of the cells did not notably change; however, the results from a PCR array revealed the upregulation of numerous metastasis-promoting genes (*Hgf*, *Cdh11* and *Ephb2*) and the downregulation of metastasis suppressing genes (*Kiss1*, *Syk* and *Htatip2*). In addition, compared with that in the control, the cells which had undergone exposure to 50 mmHg HP showed significantly higher protein expression level of HIF-1 α and the antioxidant enzymes, SOD1 and SOD2, as well as improved tolerance to oxidative stress ($P < 0.05$ vs. control). Following an intravenous injection of the LLC cells into healthy mice, to induce lung metastasis, it was found that the exposure of the LLC cells to 50 mmHg HP for 24 h, prior to injection into the mice, resulted in higher cell survival/retention in the lungs 24 h later and also resulted in more metastatic tumor lesions 4 weeks later ($P < 0.05$ vs. control). Further investigation is required to confirm the molecular mechanism; however, the results from the present study suggested that elevated interstitial fluid HP in malignant tumors may promote the metastasis of cancer cells by stabilizing HIF-1 α expression to defend against oxidative damage.

Introduction

Metastasis occurs in ~90% of malignant tumors and is the leading cause of cancer-associated mortality in patients with cancer worldwide (1,2). A number of biological factors and multiple signaling pathways, such as epithelial-mesenchymal transition, resistance to apoptosis and angiogenesis have been associated with the complex processes of metastasis (3); however, a novel approach for effectively controlling tumor metastasis is still required.

Metastasis is defined as cancer cells leaving the original tumor mass and disseminating to other parts of the body via the bloodstream or lymphatic system. Therefore, the metastatic process represents a multi-step event (3). For example, remote hematogenous metastasis requires the cancer cells to successfully pass through the following steps: i) Transendothelial migration into the vessel (known as intravasation); ii) survival in the circulatory system; iii) attachment to the vessel wall and transendothelial migration out of the vessel (known as extravasation) and iv) eventually live and propagate at the distal site (4,5). All of these steps are accompanied with a change in the surrounding microenvironment, with various biomechanical forces and oxidative stress (6); therefore, metastasis can be a stressful and inefficient event to the cancer cell (7).

Biomechanical forces have been demonstrated to play critical roles in regulating cell migration and proliferation (8,9). With the rapid advancement of mechanobiology in recent years, it has become a hot topic for understanding how biomechanical forces mediate malignant tumor progression (2,8). Beyond the mechanical stress during metastatic processes, it is also well-known that elevated interstitial fluid hydrostatic pressure (HP) occurs in solid tumors (10,11). Higher interstitial fluid HP in tumor mass has been demonstrated to be associated with a worse prognosis in patients with head and neck cancer (12). Furthermore, the exposure of cancer cells to 20 mmHg HP has been demonstrated to accelerate cell motility (8). However, it is not clear whether and how the elevation of interstitial fluid HP in tumor mass promotes the metastasis of cancer cells.

Correspondence to: Professor Tao-Sheng Li, Department of Stem Cell Biology, Atomic Bomb Disease Institute, Nagasaki University, 1-12-4 Sakamoto, Nagasaki 852-8523, Japan
E-mail: litaoshe@nagasaki-u.ac.jp

Key words: hydrostatic pressure, HIF-1 α , metastasis, oxidative stress, adhesion

Notably, it has recently been reported that cyclical mechanical force can induce the stabilization of HIF-1 α and upregulate the protein expression level of CXCL2 in monocytes (13). HIF-1 α is well-known as a master upstream regulator of oxidative stress, metabolism and DNA repair of cells (14-16). Therefore, we hypothesized that elevated interstitial fluid HP in a rapid growing malignant tumor may stabilize HIF-1 α to promote the metastasis of cancer cells.

In the present study, mouse Lewis lung carcinoma (LLC) cells were exposed to 50 mmHg HP for 24 h, then the role of HP on the metastatic property of these cells was investigated using both *in vitro* and *in vivo* experiments.

Materials and methods

Cells and animals. The LLC cells (LL/2) were used for the experiments. The cells were maintained in DMEM (FUJIFILM Wako Pure Chemical Corporation), supplemented with 10% fetal bovine serum (Cytiva) and 1% penicillin/streptomycin (Gibco; Thermo Fisher Scientific, Inc.), and cultured at 37°C in a humidified incubator with 5% CO₂.

A total of 19, male C57BL/6 mice (10-12 weeks old; weight, 23-25 g; CLEA Japan, Inc.) were used for the *in vivo* study. The mice were kept in specific, pathogen-free conditions and were allowed free access to food and water under a controlled temperature (24±1°C) with 55% humidity in a 12-h light/dark cycle. The animal experiments were approved by the Institutional Animal Care and Use Committee of Nagasaki University (approval no. 1608251335-11). All the animal procedures were performed in accordance with institutional and national guidelines. At the end of the experiments, the mice were administered with general anesthesia using an intraperitoneal injection of mixed anesthetics (0.75 mg/kg medetomidine, 4 mg/kg midazolam and 5 mg/kg butorphanol) and sacrificed by severing the abdominal aorta for blood removal. The removal of vital organs (lung tissue) was used as confirmation of the death of the mice following sacrifice.

HP stimulation. HP was induced in the LLC cells using a pneumatic pressurizing system (Strex, Inc.). Briefly, the LLC cells were seeded in 60 mm diameter Petri dishes (1×10⁵ cells/dish) and cultured for 36 h to form an adherent monolayer. The culture dishes were then randomly selected to move into a sealed chamber in which 50 mmHg HP was stably applied using the pneumatic pressurizing system and kept for 24 h (HP group). The culture dishes without HP exposure were used as the control (CON group).

Cell morphology observation and cell count. Cell morphology was observed under a light microscope (IX71S8F-3; Olympus Corporation) at x200 magnification, 24 h following HP exposure. Then, the cells were collected as a single cell suspension to measure the total cell number using a TC20™ Automated Cell Counter (Bio-Rad Laboratories, Inc.).

Reverse transcription (RT)² Profiler™ PCR array. To investigate the mRNA expression level of genes associated with metastasis, RNA was isolated from the cells using a Quick-RNA™ MicroPrep kit (Zymo Research Corp.). The

concentration of RNA was measured using a NanoDrop® 2000 spectrophotometer (Thermo Fisher Scientific, Inc.). Then, 1 μ g RNA was used to generate cDNA using the RT² First Strand kit (Qiagen Corporation), at 25°C for 10 min, 42°C for 60 min, then 85°C for 5 min. Mouse Tumor Metastasis RT² Profiler™ PCR array (cat. no. 330231; Qiagen Corporation) was used with a RT² SYBR-Green Master mix, according to the manufacturer's instructions and a Roche LightCycler 480 machine (Roche Diagnostics). The array contained a total of 84 genes associated with metastasis. The genes included in the assay were also defined by biological function by the manufacturer. The fold change in expression to the control was calculated using a web-based data analysis program (<https://geneglobe.qiagen.com/jp/analyze>). Among the 5 available housekeeping genes (*Actb*, *B2m*, *Gapdh*, *Gusb* and *Hsp90ab1*) in the array, *Actb*, *Gusb* and *Hsp90ab1* were automatically selected as the optimal set of internal control for normalization.

Adhesion assay. To evaluate the adhesion ability, the cells from both the HP and CON groups were harvested as single cell suspensions. Freshly harvested cells (5×10⁴ cells in 5 ml DMEM) were seeded onto a 25-cm² Collagen I-coated Flask (Thermo Fisher Scientific, Inc.). Following incubation for 60 min, the unattached cells were gently removed by washing with PBS twice. The number of adherent cells was counted under a light microscope at x200 magnification. The average cell count from >20 randomly selected fields was used for statistical analysis.

Western blot analysis. The protein expression level of HIF-1 α , SOD1 and SOD2 was evaluated using western blot analysis, as previously described (17). Total protein from the cells was extracted using 1X RIPA buffer (FUJIFILM Wako Pure Chemical Corporation) and the concentration was detected using a BCA assay. A total of 30 μ g protein from each sample was separated using 10-12% SDS-PAGE, then transferred to 0.2- μ m PVDF membranes (Bio-Rad Laboratories, Inc.). After blocking with 5% skimmed milk for 1 h at room temperature, the membranes were incubated with primary antibodies against HIF-1 α (1:250 dilution; cat. no. ab1; room temperature for 2 h; Abcam), SOD1 (1:500 dilution; cat. no. sc11407; overnight at 4°C; Santa Cruz Biotechnology, Inc.), SOD2 (1:500 dilution; cat. no. sc30080; overnight at 4°C; Santa Cruz Biotechnology, Inc.) and β -actin (1:1,000 dilution; cat. no. 8457S; overnight at 4°C; Cell Signaling Technology, Inc.), followed by incubation with horseradish peroxidase-conjugated secondary antibodies (rabbit anti-mouse, 1:1,000 dilution; cat. no. P026002; goat anti-rabbit, 1:1,000 dilution; cat. no. P044801) (both from Dako; Agilent Technologies, Inc.) at room temperature for 1 h. The expression level was visualized using an enhanced chemiluminescence detection kit (Thermo Fisher Scientific, Inc.). Semi-quantitative analysis was done using ImageQuant LAS 4000 mini detection system (v1.0; GE Healthcare Life Sciences).

Evaluation of oxidative stress tolerance. To evaluate oxidative stress tolerance, the cells from both groups were treated with 0, 20 or 50 μ M hydrogen peroxide (H₂O₂) in PBS at 37°C for 2 h. The apoptotic cells were stained with Annexin V-FITC, while the necrotic cells were labelled with PI using an

Annexin V-FITC Apoptosis Detection Kit (Abcam). The cells without staining were used as negative control. Quantitative flow cytometry analysis was performed using a FACSVerse™ flow cytometer and analyzed using BD FACSuite Software (v1.2 Suite 1.0.2) (both from BD Biosciences).

In addition, intracellular reactive oxygen species (ROS) was detected in the cells. Briefly, the cells from both groups were treated with 0, 20 or 50 μM H_2O_2 in PBS at 37°C for 1 h, then incubated with 10 μM general oxidative stress indicator (CM-H2DCFDA; Invitrogen; Thermo Fisher Scientific, Inc.) for another 30 min in the dark. Cells without staining were used as a negative control. The accumulation of intracellular ROS was measured by fluorescence intensity using a FACSVerse™ flow cytometer (BD Biosciences) and analyzed using BD FACSuite Software (v1.2 Suite 1.0.2) (both from BD Biosciences).

Experimental lung cancer metastasis model. To evaluate the metastatic potency, experimental lung cancer metastasis was induced in mice using an intravenous injection of LLC cells (5×10^5 cells in 0.5 ml saline) from the HP (n=6) and the CON (n=7) groups. A total of 4 weeks after the cells were injected into the mice, all the mice were sacrificed as aforementioned. Removal of lung tissue was used for both confirmation of mice death and experimental evaluation. Excised lung tissue was weighed and the number of tumor lesions on the lung surface was counted. For the mice that spontaneously died during the 4-week follow-up period, the date of death was recorded and the lung tissue samples were collected for evaluation. Statistical analysis of the overall survival rate of the mice was also determined.

Immunohistochemical staining. The cell proliferation and microvessel density in the metastatic lesions of the lungs was detected using immunohistochemistry staining. The lungs were fixed in 4% paraformaldehyde for 24 h, at 4°C, and paraffin-embedded sections (6- μm thick) were deparaffinized and rehydrated (xylene, 2x3 min washes; xylene 1:1 with 100% ethanol, 3 min; 100% ethanol, 2x3 min washes; 95% ethanol, 3 min; 70% ethanol, 3 min; 50% ethanol, 3 min; running cold tap water to rinse). After blocking with 1% BSA in PBS (Sigma-Aldrich; Merck KGaA), the sections were incubated with rabbit anti-mouse Ki67 antibody (cat. no. ab16667; 1:100 dilution;) and rabbit anti-mouse CD31 antibody (cat. no. ab28394; 1:150 dilution) (both from Abcam) overnight at 4°C, followed by incubation with the Alexa fluorescent 546-conjugated goat anti rabbit IgG(H+L) secondary antibody (cat. no. A11013; 1:350 dilution; Invitrogen; Thermo Fisher Scientific, Inc.) at room temperature for 1 h. Nuclei were stained with 4, 6-diamidino-2-phenylindole (DAPI; cat. no. D21490; Thermo Fisher Scientific, Inc.) at room temperature for 5 min. Positive staining was examined under a fluorescent microscope (FV10C-W3; Olympus Corporation). The percentage of Ki67-positive cells was calculated from 10 randomly selected fields of view (5 fields/slide in 2 slides) and used for statistical analysis. The CD31-positive stained structures were counted as microvessels and the average number of microvessels counted from 10 randomly selected fields of view (5 fields/slide in 2 slides) was used for statistical analysis.

PKH26 red fluorescent cell labeling. To evaluate the survival/retention of the LLC cells in the lungs of the mice, the cells were labelled with a PKH26 Red Fluorescent Cell Linker kit (Sigma-Aldrich; Merck KGaA). Briefly, the cells were incubated with 2 μM PKH26 dye for 5 min at room temperature, as the manufacturer's recommendations. Then, the mice were intravenously injected with the PKH26-labelled cells (1×10^6 cells in 0.5 ml saline) from the HP (n=3) and the CON (n=3) groups. The mice were sacrificed 24 h following the injection and the lung tissue samples were collected. Cryosections (8- μm thick) of the lung tissues were used for the direct detection of PKH26-labelled LLC cells under a fluorescent microscope (FV10C-W3; Olympus Corporation).

Statistical analysis. The data are presented as the mean \pm SD. Statistical significance between two groups was determined using an unpaired t-test (SPSS; v20.0; IBM Corp.). The survival of the mice was analyzed using a Kaplan-Meier curve and statistical significance was determined using the log-rank test (GraphPad Prism; v8.0.1; GraphPad Software, Inc.). $P < 0.05$ was used to indicate a statistically significant difference.

Results

Exposure of the LLC cells to 50 mmHg HP altered the mRNA expression level of numerous genes associated with metastasis. Firstly, the mRNA expression level of genes associated with metastasis was analyzed between the HP and CON groups. The RT² Profiler™ PCR array revealed that numerous genes were up- or downregulated, with a >1.3-fold difference in the HP group compared with that in the CON group (Table SI). The top 10 up- or downregulated genes are shown in Fig. 1A. Within the top 10 upregulated genes, the upregulation of several adhesion molecules was found, including *Cdh1*, *Cdh11* and *Fnl1* (Fig. 1B). In addition, the upregulation of numerous metastasis-promoting genes, such as *Hgf*, *Cdh11* and *Ephb2*, was also found. Within the top 10 downregulated genes, metastasis suppressors, including *Kiss1*, *Syk* and *Htatip2*, were frequently detected (Fig. 1B). The overall change in the gene expression profile indicated the potential role of HP in enhancing metastatic properties of the LLC cells.

HP exposure enhances the adhesion property of the LLC cells. The exposure of the LLC cells to 50 mmHg HP for 24 h did not induce notable morphological changes (Fig. 2A). The total number of harvested cells was also comparable between the groups ($P=0.70$; Fig. 2A), indicating a limited effect of 50 mmHg HP exposure on cell growth.

As the PCR array data indicated the upregulation of numerous adhesion molecules, the adhesion property of the cells was investigated. It was found that the exposure to 50 mmHg HP significantly increased the number of adherent cells on a collagen I-coated flask ($P < 0.05$; Fig. 2B).

HP exposure increases the protein expression level of HIF-1 α and antioxidant enzymes in the LLC cells. HIF-1 α , a master regulator of the cellular adaptive response to hypoxia, is known to play critical roles in metabolic reprogramming (16) and metastasis (14) in cancer cells. Western blot analysis showed

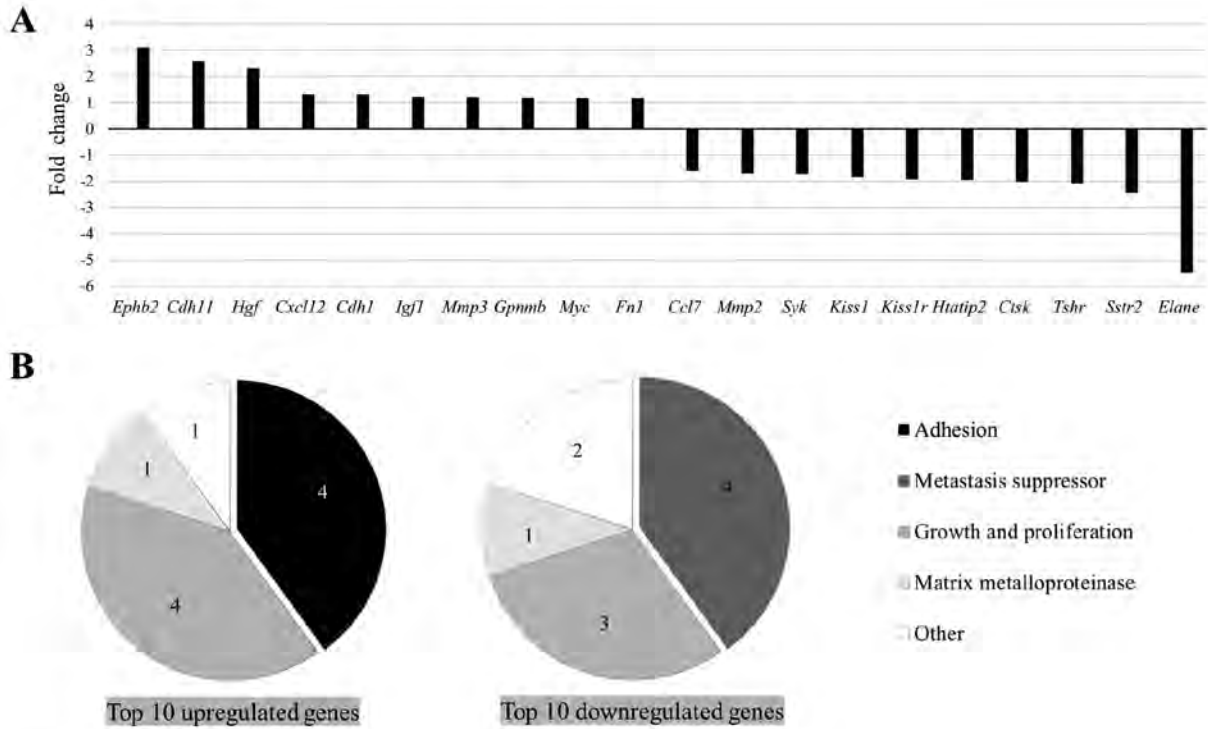


Figure 1. Change in the mRNA expression level of genes in the Lewis lung cancer cells following treatment with or without 50 mmHg HP for 24 h. The mRNA expression level of metastasis-related genes was measured using a reverse transcription² Profiler™ PCR array. The data are presented as the fold change in the cells with HP compared with that in the CON. The top 10 up- and downregulated genes are according to the (A) fold change and (B) the biological functional categories of the genes. HP, hydrostatic pressure exposure; CON, control.

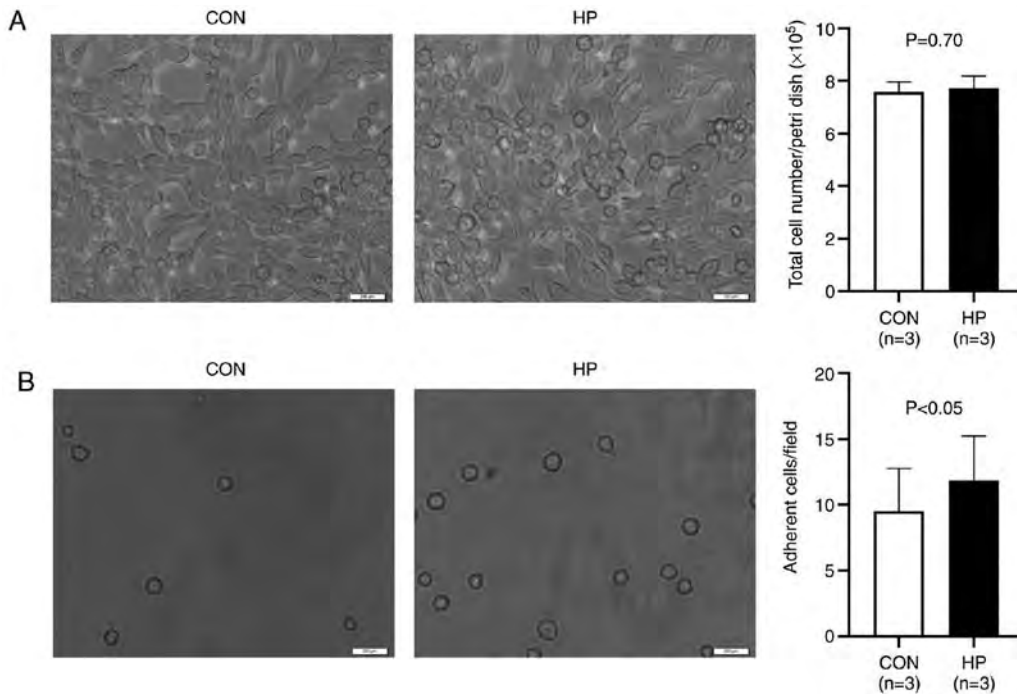


Figure 2. Survival and adhesion property of the Lewis lung cancer cells following treatment with or without 50 mmHg HP for 24 h. (A) Representative images of cell morphology under a phase-contrast microscope (left) and quantitative analysis of the total number of surviving cells per petri dish (right). (B) Representative images (left) and quantitative data (right) of the adherent cells in collagen I-coated flasks. Scale bar, 200 μ m. The data are presented as the mean \pm SD from 3 independent experiments. HP, hydrostatic pressure exposure; CON, control.

that the protein expression level of HIF-1 α was significantly increased in cells exposed to 50 mmHg HP for 24 h (P<0.01; Fig. 3A).

The protein expression level of the antioxidant enzymes, SOD1 and SOD2, which are HIF-1 α downstream signals (18,19), was also investigated. As expected, the exposure

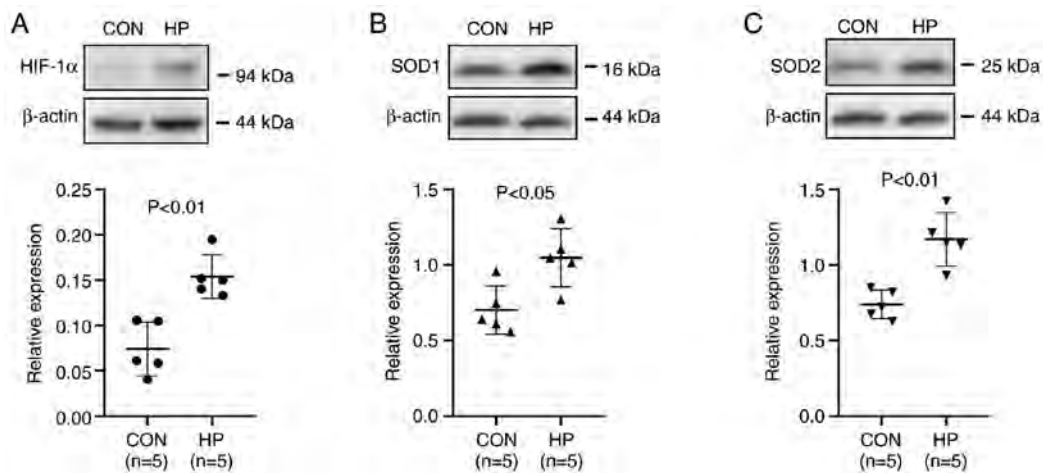


Figure 3. Protein expression level of HIF-1 α , SOD1 and SOD2 is increased following exposure of the LLC cells to 50 mmHg HP for 24 h. Representative blots and semi-quantitative analysis of the protein expression level of (A) HIF-1 α , (B) SOD1 and (C) SOD2 in the LLC cells following treatment with or without 50 mmHg HP for 24 h. The data are presented as the mean \pm SD from 5 independent experiments. HP, hydrostatic pressure; CON, control; LLC, Lewis lung cancer.

of the cells to 50 mmHg HP for 24 h also significantly upregulated the protein expression level of SOD1 and SOD2 ($P<0.05$; Fig. 3B and C).

HP exposure induces the tolerance of the LLC cells to oxidative stress. In addition, the oxidative stress tolerance of the cells was investigated *in vitro*. Cell necrosis, under 20 or 50 μ M H₂O₂ treatment was significantly reduced in the LLC cells pretreated with 50 mmHg for 24 h ($P<0.05$; Fig. 4A); however, the percentage of apoptotic cells was not significantly different between the 2 groups treated with 20 or 50 μ M H₂O₂ ($P=0.26$ and $P=0.45$, respectively; Fig. 4A).

The intracellular ROS level at the baseline (without H₂O₂ stimulation) was detected at comparable levels between the HP and CON groups (Fig. 4B). Unexpectedly, 1-h stimulation with 20 or 50 μ M H₂O₂ notably decreased the ROS accumulation in the LLC cells without pretreatment with 50 mmHg HP compared with that at baseline (Fig. 4B). By contrast, after 1-h stimulation with 20 μ M H₂O₂, the ROS accumulation was slightly increased in the LLC cells pretreated with 50 mmHg HP compared with that at baseline. We hypothesized that the less intracellular ROS accumulation in the LLC cells without HP exposure was due to the severe cell damage or cell death, rather than the resistance to oxidative stress.

HP exposure promotes the metastasis of the LLC cells to the lungs. To evaluate the metastatic potency *in vivo*, the LLC cells were intravenously injected into healthy adult mice. Compared with that in the mice that received LLC cells without HP exposure, significantly worse survival was observed in the mice that received LLC cells pretreated with 50 mmHg HP ($P<0.05$; Fig. 5A). All the mice were killed 4 weeks following the injection of the cells and the maximum percentage body weight loss observed was 9.3%. There were significantly more metastatic tumor lesions in the lungs of the mice in the HP group compared with that in the CON group ($P<0.05$; Fig. 5B and C). The weight of the lung tissue was also significantly higher in the HP group compared with that in the CON group ($P<0.05$; Fig. 5D). These data suggested that HP exposure promoted the metastasis of the LLC cells to the lungs.

To further understand the mechanism involved, the LLC cells were labelled with PKH26 before intravenous injection into the mice, then the survival/retention of the cells in the lungs was analyzed 24 h later. As expected, more LLC cells (or cell clusters) were detected in the lungs from mice in the HP group compared with that in the CON group (Fig. 6A), suggesting an improved survival/retention of the LLC cells by pretreatment with 50 mmHg HP.

Cell proliferation and neovascularization in the metastatic lesions was also analyzed using immunostaining. The percentage of Ki67-positive cells was not significantly different between the HP and CON groups ($P=0.20$; Fig. 6B). However, the density of the CD31-positive microvessels in the metastatic lesions was significantly higher in the HP group compared with that in the CON group ($P<0.05$; Fig. 6C).

Discussion

Various mechanical forces within the microenvironment of the tumor mass have been reported to play critical roles in the progression of malignant tumors (2). Owing to the hyper-permeability of immature capillaries, the elevation of the interstitial fluid HP could be commonly induced by the presence of excess fluid accumulation within malignant tumors (20,21). A previous study has reported that HP may drive breast cancer cells toward a more invasive phenotype (9); however, the precise role and relevant mechanism of the mechanical forces in mediating metastasis is still not well understood.

To investigate the role of HP on the metastatic property of cancer cells, the LLC cells were exposed to 50 mmHg HP to mimic the *in vivo* tumor microenvironment, then the mRNA expression level of genes associated with tumor metastasis was analyzed. A PCR array indicated noticeable changes, including the upregulation of metastasis promoters (*Hgf*, *Cdh11* and *Ephb2*) and the downregulation of metastasis suppressors (*Kiss1*, *Syk* and *Htatip2*) in the LLC cells following exposure to 50 mmHg HP for 24 h. The most upregulated gene, *Ephb2*, has been demonstrated to modulate the metastatic phenotype (22) and induce angiogenesis (23). The most down-regulated gene, *Elane*, has been demonstrated to modulate

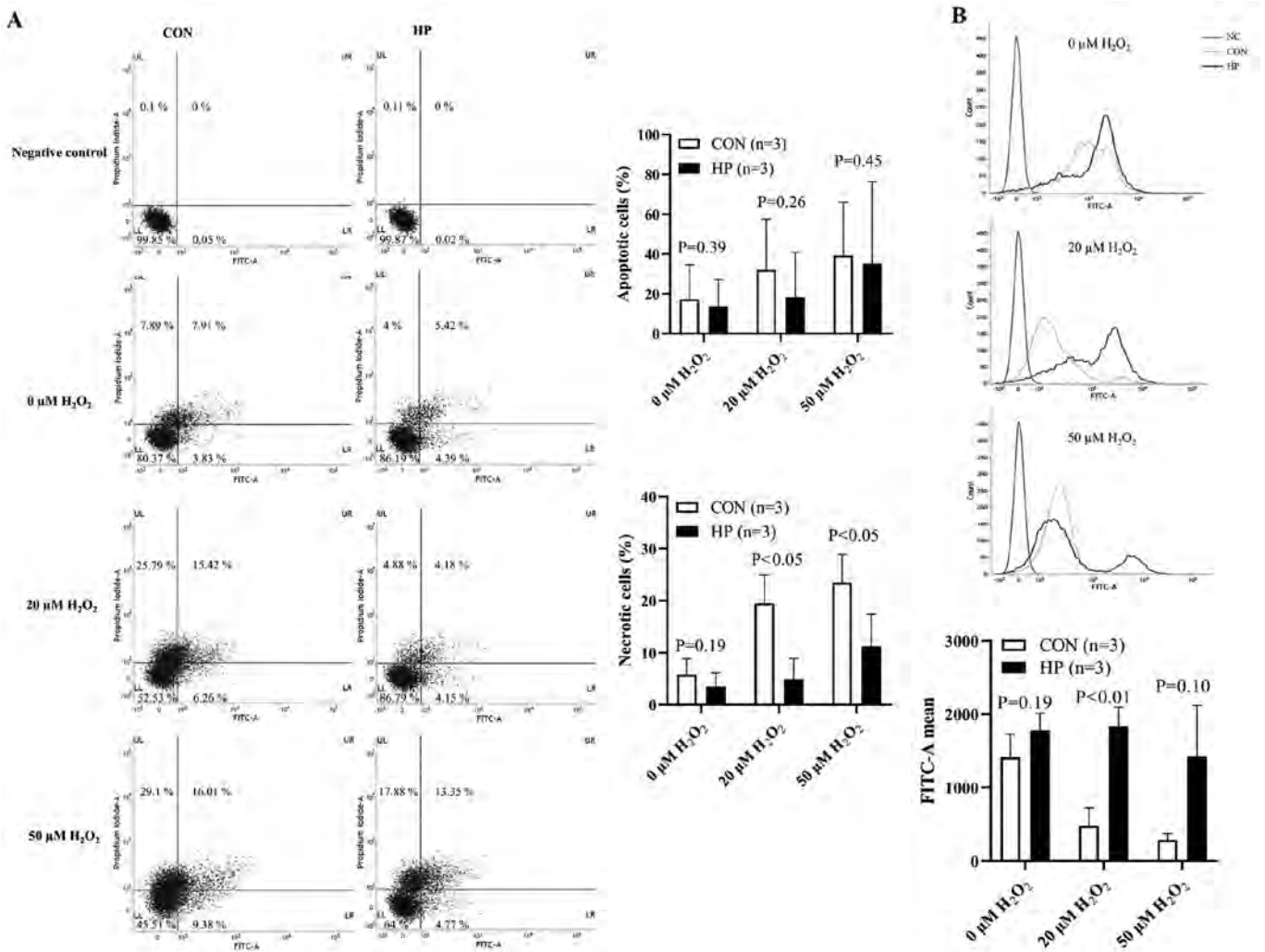


Figure 4. Tolerance of the LLC cells to oxidative stress. The LLC cells were treated with or without 50 mmHg HP and with 0, 20 and 50 $\mu\text{M H}_2\text{O}_2$. The apoptotic/necrotic cells and intracellular ROS was subsequently detected using flow cytometry. (A) Representative flow cytometry plots (left) and quantitative data (right) of the number of apoptotic and necrotic cells. (B) Representative histograms (upper) and quantitative data (lower) of the mean intensity of the intracellular ROS levels. The data are presented as the mean \pm SD from three independent experiments. HP, hydrostatic pressure; CON, control; LLC, Lewis lung cancer; ROS, reactive oxygen species; H_2O_2 , hydrogen peroxide.

neutrophil expression, inflammation and repair (24). Using an experimental lung metastasis model in mice, it was further confirmed that the LLC cells pretreated with 50 mmHg HP developed a significantly higher number of tumor metastasis lesions in the lungs. These data suggested that an elevated interstitial fluid HP in a rapidly growing malignant tumor may enhance the metastatic property of cancer cells.

Additional experiments were performed to further understand how HP enhanced the metastatic property of the LLC cells from different aspects, according to the multi-step processes of hematogenous metastasis. It is well-known that cancer cells enter the circulation system and are exposed to hyperoxic arterial blood for hematogenous metastasis (6). Accumulating evidence suggests that oxidative stress kills most of the circulating cancer cells, resulting in a very poor efficiency of metastasis (6,7). Therefore, oxidative stress tolerance is essential for the successful metastasis of cancer cells. HIF-1 α is well-known as an important mediator of metabolism reprogramming of cancer cells by regulating antioxidant enzymes and antioxidant properties (25). Notably, it has been recently demonstrated that cyclic mechanical force stabilizes HIF-1 α by reducing protein

degradation (13). Consistently, the results from the present study showed the upregulation of HIF-1 α protein expression level in the LLC cells following exposure to 50 mmHg HP for 24 h. In addition, the protein expression level of the antioxidant enzymes, SOD1 and SOD2, the direct downstream targets of HIF-1 α (18,19), were also significantly increased in cells exposed to 50 mmHg HP. This could contribute to enhancing antioxidant capacity of cancer cells for remote hematogenous metastasis. Consistent with the upregulation of various adhesion molecules, the exposure to 50 mmHg HP also enhanced the adhesion property of the LLC cells, as shown by the results of the *in vitro* adhesion and the *in vivo* cell tracking assays.

HIFs are heterodimeric proteins composed of HIF- α and HIF-1 β subunits. HIF-1 α is an O_2 -regulated subunit, while HIF-1 β is a constitutively expressed subunit (26). The protein expression level of HIF-1 α has been reported to be overexpressed in numerous malignant tumors, including lung, prostate, breast and colon carcinomas (27,28). It has been demonstrated that the enhanced protein expression level of HIF-1 α was associated with poor prognosis in patients with breast, oropharyngeal and prostate cancer (29-31). As a master regulator of cellular response

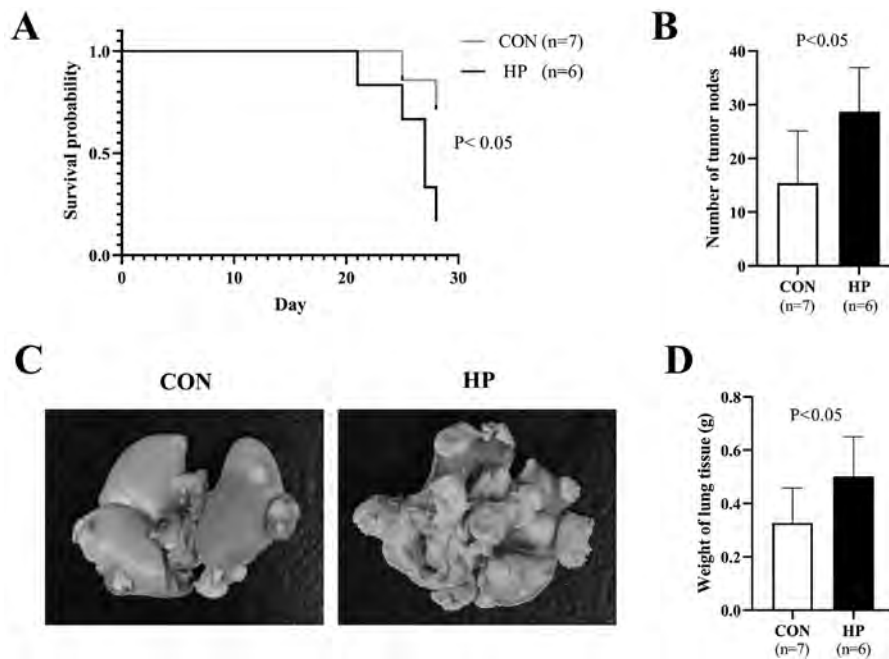


Figure 5. Experimental lung metastasis model in healthy adult mice. The Lewis lung cancer cells were treated with or without 50 mmHg HP and were intravenously injected into the mice, then lung metastasis was evaluated 4 weeks later. (A) Kaplan-Meier curves show the survival probability of the mice. (B) Quantitative data and (C) representative images of tumor metastasis lesions on the surface of lungs. (D) The weight of lung tissues. The data are presented as the mean \pm SD. HP, hydrostatic pressure; CON, control.

to hypoxia, HIF-1 can induce the transcription of several genes involved in angiogenesis, cell proliferation and cell metabolism (15,32). One of the most popularly recognized downstream genes of HIF-1 is vascular endothelial growth factor (VEGF), which is known to induce angiogenesis for the rapid growth of malignant tumors (33). VEGF, originally named as vascular permeability factor, was first identified as a tumor-secreted factor, which increases vascular permeability and promotes the accumulation of ascite fluid (21). Considering the hyper-permeability of microvessels in the tumor (34), it is reasonable to hypothesize that an excess accumulation of exudate in the interstitial space contributes, at least in part, to the increase of the interstitial fluid HP in the tumor mass. As a result, elevated HP may stabilize HIF-1 α , which thereby induces VEGF and antioxidant enzymes to accelerate the growth and metastasis of malignant tumors.

There is a caution in *Cellosaurus* that the LLC cells (LL/2) could be identical to 3LL cells. It is reported that LL/2 cell line could be identical to 3LL cell line because both of them are from mouse Lewis lung carcinoma and show the same biological characteristics. Therefore, this will not affect the conclusion of the present study.

A total of 4 weeks after the cells were injected into the mice was used as the humane endpoint, based on clinical signs (reduced intake and activity) and pathophysiological changes (weight loss >20%). During the follow-up for 4 weeks, the progression of tumor metastasis in the lungs of the mice was not directly monitored; however, it was indirectly monitored by observing the clinical signs (intake and activity) and pathophysiological changes (weight loss) of mice.

For the 7 mice that died spontaneously, prior to the end of the 4-week follow-up time in the lung metastasis mice model, it was confirmed that the 7 mice did not die from lung metastasis-induced respiratory failure or systemic cachexia.

We hypothesized that the cause of spontaneous death may be due to another cause, based on the following: i) There were no signs of severe clinical symptoms in the 7 mice following daily monitoring; ii) based on the assessment of the exercised lungs, there were fewer metastatic lesions in the lungs of the 7 mice; iii) according to the examination of the 7 mice after sacrifice, there was no serious bleeding, inflammation or purulent secretions in the body, no notable signs of metastasis or organ necrosis was found in the chest cavity or in any of the other organs and no obvious occurrence of cachexia was found.

The present study has several limitations. First, a single cell line was used and the cells were only exposed to 50 mmHg HP for all the experiments. This is due to the following reasons: i) The present study was designed to examine whether an elevated HP could promote the metastasis of cancer cells; ii) the C57BL/6 mice were used for *in vivo* experiments and the LLC cell line is the most reproducible syngeneic model for evaluating lung metastasis to date (35); iii) interstitial fluid pressure in solid malignant tumors could be elevated to ~30 mmHg HP (12,36) and iv) the exposure of the LLC cells to 50 mmHg HP altered the mRNA expression level of genes associated with metastasis; however, higher pressure (100 mmHg) induced cell death and cell debris production (data not shown). Therefore, further experiments are required to exposure different cancer cell lines with different HPs. Second, the PCR array was not repeated due to a limited budget. In addition, the fold-change result may also have greater variations if P > 0.05; therefore, it is important to have a sufficient number of biological replicates to validate the array data. However, a mixture of RNA samples was used from three independent experiments to generate the cDNA for a single PCR array in each group. Therefore, the PCR array data was expressed as the average level in 3 samples from each group. Third, further interventional experiments, such as the interference of the HIF-1 α signaling

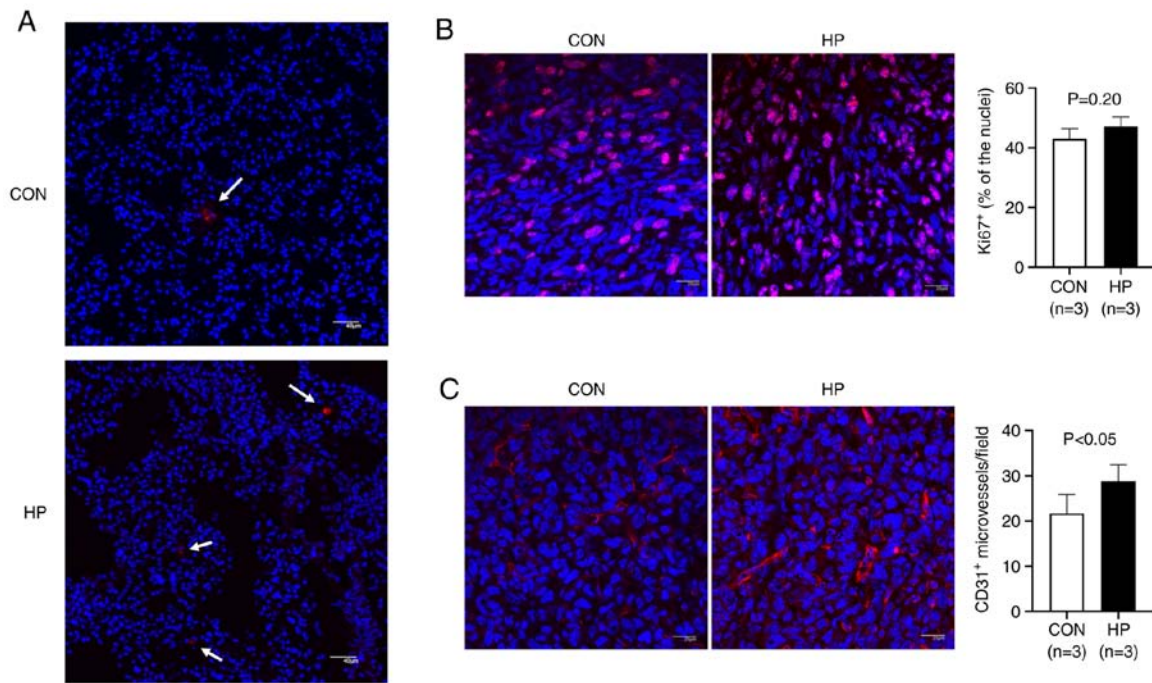


Figure 6. Survival/retention of the LLC cells and immunostaining analysis of proliferating cells and microvessels in the metastatic lesions. The LLC cells were treated with or without 50 mmHg HP, then intravenously injected into the mice. (A) Representative confocal microscopy images of the survival/retention of the PKH26-labelled cells or cell clusters (arrows) in the lungs, 24 h following injection. Scale bar, 40 μ m. (B) Representative images (left) and quantitative data (right) of the Ki67-positive proliferative cells in the metastatic lesions in lungs. Scale bar, 20 μ m. (C) Representative images (left) and quantitative data (right) of the CD31-positive microvessels in the metastatic lesions in the lungs. Scale bar, 20 μ m. The nuclei were stained with DAPI. The data are presented as the mean \pm SD. HP, hydrostatic pressure; CON, control; LLC, Lewis lung cancer.

pathway was not performed, as silencing HIF-1 α alone would change cell biological properties. Furthermore, multiple factors, including the increase in mRNA expression level of HIF-1 α and adhesion molecules could be involved in the HP-induced cancer cell metastasis; therefore, a genetic intervention approach to directly confirm the role of HIF-1 α was not performed in the present study. Forth, Annexin V-positive apoptotic cells were only analyzed using flow cytometry and the expression level of other apoptotic proteins, such as the caspase family, can also be used to indicate apoptosis. In addition, a colony-forming assay was not included, as the potential role of HP in cancer cell metastasis, rather than tumorigenesis and tumor growth was the aim of the present study.

From the results in the present study, an elevated HP in rapidly growing malignant tumors may enhance the metastatic potency of cancer cells via complex mechanisms, including the increase in the mRNA expression level of adhesion molecules to improve cell adhesion and the stabilization of HIF-1 α to induce the expression of antioxidant enzymes to defend against oxidative damage during metastasis (Fig. 7). It is critical to elucidate the comprehensive molecular mechanisms underlying the stabilization of HIF-1 α by HP in further investigations.

Acknowledgements

Not applicable.

Funding

This study was supported in part by a Grant-in-Aid from the Ministry of Education, Science, Sports, Culture and

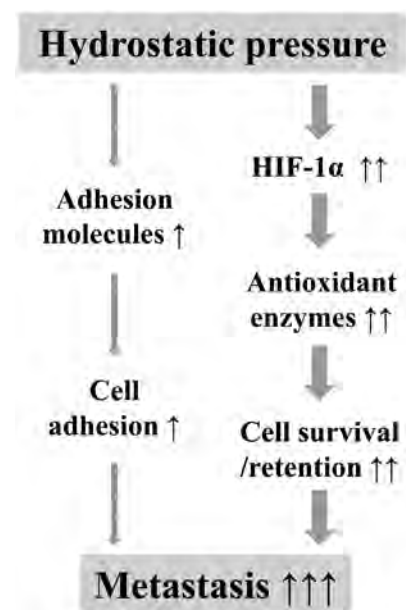


Figure 7. Schematic diagram of hydrostatic pressure induced metastasis of cancer cells. An elevated hydrostatic pressure in malignant tumors may enhance the metastatic potency of cancer cells by i) increasing the mRNA expression level of adhesion molecules to improve cell adhesion, and ii) stabilizing HIF-1 α to induce the expression of antioxidant enzymes to protect against oxidative damage.

Technology, Japan (grant no. 17H04265), the Collaborative Research Program of the Atomic-bomb Disease Institute of Nagasaki University and the Japan China Sasakawa Medical Fellowship.

Availability of data and materials

The datasets used and/or analyzed during the current study are available from the corresponding author on reasonable request.

Author's contributions

All the authors contributed to the conception and design of the study. DZ, YX and LA performed the experiments and acquired the data. TSL, DZ, YX, LA and XZ analyzed and interpreted the data. DZ and SZ drafted the manuscript. TSL, JL and CG critically revised the manuscript for important intellectual content. TSL and DZ confirmed the authenticity of all the raw data. All authors read and approved the final version of the manuscript.

Ethics approval and consent to participate

The animal experiments were approved by the Institutional Animal Care and Use Committee of Nagasaki University (approval no. 1608251335-11) and all animal procedures were performed in accordance with institutional and national guidelines.

Patient consent for publication

Not applicable.

Competing interests

The authors declare that they have no competing interests.

References

- Brabletz T, Lyden D, Steeg PS and Werb Z: Roadblocks to translational advances on metastasis research. *Nat Med* 19: 1104-1109, 2013.
- Bregenzler ME, Horst EN, Mehta P, Novak CM, Repetto T and Mehta G: The role of cancer stem cells and mechanical forces in ovarian cancer metastasis. *Cancers* 11: 1008, 2019.
- Eccles SA and Welch DR: Metastasis: Recent discoveries and novel treatment strategies. *Lancet* 369: 1742-1757, 2007.
- Fidler IJ: The pathogenesis of cancer metastasis: The 'seed and soil' hypothesis revisited. *Nat Rev Cancer* 3: 453-458, 2003.
- Zijl FV, Krupitza G and Mikulits W: Initial steps of metastasis: Cell invasion and endothelial transmigration. *Mutat Res* 728: 23-34, 2011.
- Piskounova E, Agathocleous M, Murphy MM, Hu Z, Huddleston SE, Zhao Z, Leitch AM, Johnson TM, DeBerardinis RJ and Morrison SJ: Oxidative stress inhibits distant metastasis by human melanoma cells. *Nature* 527: 186-191, 2015.
- Vanharanta S and Massague J: Origins of metastatic traits. *Cancer Cell* 24: 410-421, 2013.
- Kao YC, Jheng JR, Pan HJ, Liao WY, Lee CH and Kuo PL: Elevated hydrostatic pressure enhances the motility and enlarges the size of the lung cancer cells through aquaporin upregulation mediated by caveolin-1 and ERK1/2 signaling. *Oncogene* 36: 863-874, 2017.
- Tse JM, Cheng G, Tyrrell JA, Wilcox-Adelman SA, Boucher Y, Jain RK and Munn LL: Mechanical compression drives cancer cells toward invasive phenotype. *Proc Natl Acad Sci USA* 109: 911-916, 2012.
- Less JR, Posner MC, Boucher Y, Borochovitz D, Wolmark N and Jain RK: Interstitial hypertension in human breast and colorectal tumors. *Cancer Res* 52: 6371-6374, 1992.
- Nathan SS, DiResta GR, Casas-Ganem JE, Hoang BH, Sowers R, Yang R, Huvos AG, Gorlick R and Healey JH: Elevated physiologic tumor pressure promotes proliferation and chemosensitivity in human osteosarcoma. *Clin Cancer Res* 11: 2389-2397, 2005.
- Gutmann R, Leunig M, Feyh J, Goetz AE, Messmer K, Kastanbauer E and Jain RK: Interstitial hypertension in head and neck tumors in patients: Correlation with tumor size. *Cancer Res* 52: 1993-1995, 1992.
- Solis AG, Bielecki P, Steach HR, Sharma L, Harman CC, Yun S, de Zoete MR, Warnock JN, To SDF, York AG, *et al*: Mechanosensation of cyclical force by PIEZO1 is essential for innate immunity. *Nature* 573: 69-74, 2019.
- Rankin EB, Nam JM and Giaccia AJ: Hypoxia: Signaling the metastatic cascade. *Trends Cancer* 2: 295-304, 2016.
- Semenza GL: Hypoxia-inducible factors in physiology and medicine. *Cell* 148: 399-408, 2012.
- Semenza GL: Regulation of cancer cell metabolism by hypoxia-inducible factor 1. *Semin Cancer Biol* 19: 12-16, 2009.
- Urata Y, Goto S, Luo L, Doi H, Kitajima Y, Masuda S, Ono Y and Li TS: Enhanced Nox1 expression and oxidative stress resistance in c-kit-positive hematopoietic stem/progenitor cells. *Biochem Biophys Res Commun* 454: 376-380, 2014.
- Hu XQ, Song R and Zhang L: Effect of oxidative stress on the estrogen-NOS-NO-KCa channel pathway in uteroplacental dysfunction: Its implication in pregnancy complications. *Oxid Med Cell Longev* 2019: 9194269, 2019.
- Novak S, Drenjancevic I, Vukovic R, Kellermayer Z, Cosic A, Tolusic Levak M, Balogh P, Culo F and Mihalj M: Anti-inflammatory effects of hyperbaric oxygenation during DSS-induced colitis in BALB/c mice include changes in gene expression of HIF-1 α , proinflammatory cytokines, and antioxidative enzymes. *Mediators Inflamm* 2016: 7141430, 2016.
- Jain RK, Martin JD and Stylianopoulos T: The role of mechanical forces in tumor growth and therapy. *Annu Rev Biomed Eng* 16: 321-346, 2014.
- Senger DR, Galli SJ, Dvorak AM, Perruzzi CA, Harvey VS and Dvorak HF: Tumor cells secrete a vascular permeability factor that promotes accumulation of ascites fluid. *Science* 219: 983-985, 1983.
- Liu YL, Horning AM, Lieberman B, Kim M, Lin CK, Hung CN, Chou CW, Wang CM, Lin CL, Kirma NB, *et al*: Spatial EGFR dynamics and metastatic phenotypes modulated by upregulated EphB2 and Src pathways in advanced prostate cancer. *Cancers (Basel)* 11: 1910, 2019.
- Sato S, Vasaikar S, Eskaros A, Kim Y, Lewis JS, Zhang B, Zijlstra A and Weaver AM: EPHB2 carried on small extracellular vesicles induces tumor angiogenesis via activation of ephrin reverse signaling. *JCI Insight* 4: e132447, 2019.
- Makaryan V, Zeidler C, Bolyard AA, Skokowa J, Rodger E, Kelley ML, Boxer LA, Bonilla MA, Newburger PE, Shimamura A, *et al*: The diversity of mutations and clinical outcomes for ELANE-associated neutropenia. *Curr Opin Hematol* 22: 3-11, 2015.
- Nakashima R, Goto Y, Koyasu S, Kobayashi M, Morinibu A, Yoshimura M, Hiraoka M, Hammond EM and Harada H: UCHL1-HIF-1 axis-mediated antioxidant property of cancer cells as a therapeutic target for radiosensitization. *Sci Rep* 7: 6879, 2017.
- Semenza GL: Pharmacologic targeting of hypoxia-inducible factors. *Annu Rev Pharmacol Toxicol* 59: 379-403, 2019.
- Zhong H, De Marzo AM, Laughner E, Lim M, Hilton DA, Zagzag D, Buechler P, Isaacs WB, Semenza GL and Simons JW: Overexpression of hypoxia-inducible factor 1 α in common human cancers and their metastases. *Cancer Res* 59: 5830-5835, 1999.
- Talks KL, Turley H, Gatter KC, Maxwell PH, Pugh CW, Ratcliffe PJ and Harris AL: The expression and distribution of the hypoxia-inducible factors HIF-1 α and HIF-2 α in normal human tissues, cancers, and tumor-associated macrophages. *Am J Pathol* 157: 411-421, 2000.
- Generali D, Berruti A, Brizzi MP, Campo L, Bonardi S, Wigfield S, Bersiga A, Allevi G, Milani M, Aguggini S, *et al*: Hypoxia-inducible factor-1 α expression predicts a poor response to primary chemoendocrine therapy and disease-free survival in primary human breast cancer. *Clin Cancer Res* 12: 4562-4568, 2006.
- Aebersold DM, Burri P, Beer KT, Laissue J, Djonov V, Greiner RH and Semenza GL: Expression of hypoxia-inducible factor-1 α : A novel predictive and prognostic parameter in the radiotherapy of oropharyngeal cancer. *Cancer Res* 61: 2911-2916, 2001.
- Nanni S, Benvenuti V, Grasselli A, Priolo C, Aiello A, Mattiussi S, Colussi C, Lirangi V, Illi B, D'Eletto M, *et al*: Endothelial NOS, estrogen receptor beta, and HIFs cooperate in the activation of a prognostic transcriptional pattern in aggressive human prostate cancer. *J Clin Invest* 119: 1093-1108, 2009.

32. Semenza GL: Defining the role of hypoxia-inducible factor 1 in cancer biology and therapeutics. *Oncogene* 29: 625-634, 2010.
33. Apte RS, Chen DS and Ferrara N: VEGF in signaling and disease: Beyond discovery and development. *Cell* 176: 1248-1264, 2019.
34. Dvorak HF: Vascular permeability factor/vascular endothelial growth factor: A critical cytokine in tumor angiogenesis and a potential target for diagnosis and therapy. *J Clin Oncol* 20: 4368-4380, 2002.
35. Kellar A, Egan C and Morris D: Preclinical murine models for lung cancer: Clinical trial applications. *Biomed Res Int* 2015: 621324, 2015.
36. Mori T, Koga T, Shibata H, Ikeda K, Shiraishi K, Suzuki M and Iyama K: Interstitial fluid pressure correlates clinicopathological factors of lung cancer. *Ann Thorac Cardiovasc Surg* 21: 201-208, 2015.

***Ex Vivo* Hydrostatic Pressure Loading of Atrial Tissues Activates Profibrotic Transcription via TGF- β Signal Pathway**

Xu Zhang,^{1,2} Mhd, Yousuf Yassouf,^{1,2} Kai Huang,^{1,2} Yong Xu,^{1,2} Zi-Sheng Huang,^{1,2}, Da Zhai,^{1,2}, Reiko Sekiya,^{1,2}, Ke-Xiang Liu,³ MD and Tao-Sheng Li,^{1,2} MD

Summary

Excessive mechanical stress causes fibrosis-related atrial arrhythmia. Herein, we tried to investigate the mechanism of atrial fibrogenesis in response to mechanical stress by *ex vivo* approach. We collected atrial tissues from mice and then cultured them as “explants” under atmospheric pressure (AP group) or 50 mmHg hydrostatic pressure loading (HP group) conditions. Pathway-specific PCR array analysis on the expression of fibrosis-related genes indicated that the loading of atrial tissues to 50 mmHg for 24 hours extensively upregulated a series of profibrotic genes. qRT-PCR data also showed that loading atrial tissues to 50 mmHg enhanced *Rhoa*, *Rock2*, and *Thbs1* expression at different time points. Interestingly, the enhanced expression of *Thbs1* at 1 hour declined at 6-24 hours and then increased again at 72 hours. In contrast, an enhanced expression of *Tgfb1* was observed at 72 hours. In contrast, daily loading to 50 mmHg for 3 hours significantly accelerated the outgrowth of mesenchymal stem-like stromal cells from atrial tissues; however, we did not observe significant phenotypic changes in these outgrowing cells. Our *ex vivo* experimental data clearly show the induction of profibrotic transcription of atrial tissues by HP loading, which confirms the common pathological feature of atrial fibrosis following pressure overload.

(Int Heart J 2022; 63: 367-374)

Key words: Mechanical stress, Mechanotransduction, Fibrogenesis, Arrhythmia

Atrial arrhythmia, such as atrial fibrillation (AF), whose treatment remains thorny, is the most common rhythm disturbance encountered in the clinical setting.¹ The most common pathogenesis of AF is atrial fibrosis. Many studies already reported that excessive mechanical stresses play critical role in atrial fibrosis development.²⁻⁴ Although various profibrotic signals, especially the transforming growth factor- β (TGF- β), can induce interstitial fibrogenesis, the question remains to further clarify the molecular and cellular mechanisms of atrial fibrosis in response to mechanical stresses.

Mechanotransduction, the process of cells that sense the mechanical force from the microenvironment through mechanosensing receptors and then translate mechanical stress into biochemical signals, plays vital roles in tissue cell homeostasis and pathology, such as fibrogenesis.⁵ TGF- β signaling pathway is the core in mechanotransduction of cardiac fibrosis. Additionally, as an essential signal isoform, TGF- β_1 induces the expression of profibrotic genes through the canonical signaling pathway with activation of Smad2/3, or through noncanonical signaling

pathways with activation of RhoA and its downstream kinase ROCK.⁶ As a multicomponent target, RhoA/ROCK signaling is known to involve in cardiac fibrosis.⁷ Thrombospondin-1 (TSP-1), another member of the TGF- β superfamily, can also be excessively induced in response to various stresses or tissue damage.⁸

Mechanical stresses modulate many aspects of cell function, such as proliferation and differentiation, from single cells to pattern formation in whole organisms.⁹ Stromal cells within the defined tissues/organs are known to be the key player of fibrogenesis. Using a mouse unilateral ureteral obstruction model, we recently demonstrated that renal stromal cells shift to profibrogenic phenotype.¹⁰ Thus, we reasonably speculate the fibrotic phenotypic shifting of atrial stromal cells in response to excessive mechanical stresses, but direct experimental evidence is needed.

By *ex vivo* loading mouse atrial tissues to 50 mmHg HP, a kind of mechanical compressive stresses, we investigated the dynamic changes on the expression of fibrosis-related genes and the biological properties of stromal

From the ¹Department of Stem Cell Biology, Nagasaki University Graduate School of Biomedical Sciences, Nagasaki, Japan, ²Department of Stem Cell Biology, Atomic Bomb Disease Institute, Nagasaki University, Nagasaki, Japan and ³Department of Cardiovascular Surgery, The Second Hospital of Jilin University, Jilin, China.

This study was mainly supported by a Grant-in-Aid for the Ministry of Education, Science, Sports, Culture and Technology of Japan and the Collaborative Research Program of the Atomic Bomb Disease Institute of Nagasaki University.

Address for correspondence: Tao-Sheng Li, MD, Department of Stem Cell Biology, Atomic Bomb Disease Institute, Nagasaki University, 1-12-4 Sakamoto, Nagasaki, Nagasaki 852-8523, Japan. E-mail: litaoshe@nagasaki-u.ac.jp

Received for publication August 10, 2021. Revised and accepted November 8, 2021.

Released in advance online on J-STAGE March 15, 2022.

doi: 10.1536/ihj.21-481

All rights reserved by the International Heart Journal Association.

cells.

Methods

Experimental animals: C57BL/6 male mice (9-12 weeks old, CLEA, Japan) were used in this study. All experiments were approved by the Institutional Animal Care and Use Committee of Nagasaki University (No.1608251335-9), and animal procedures were performed following institutional and national guidelines.

Ex vivo culture of atrial tissues as “explants”: The *ex vivo* culture of atrial tissues as “explants” was performed as described previously,¹¹ with a few modifications. Briefly, mice were administered general anesthesia by an intraperitoneal injection of mixed anesthetic (0.75 mg/kg medetomidine, 4 mg/kg midazolam, 5 mg/kg butorphanol). Next, atrial tissues were collected into 6-cm dishes with 2 mL PBS and then minced into small fragments (almost 1 mm × 1 mm) using a surgical knife under zoom stereomicroscope (Olympus SZ61). Then, the minced tissue fragments were moved onto 6-cm culture dishes coated with 15 µg/mL fibronectin (CORNING) for culturing as “explants.” We used Iscove’s Modified Dulbecco’s Medium with the supplement of 10% fetal bovine serum (HyClone, Thermo Scientific), 1% penicillin/streptomycin (Wako), and all culture was performed at 37°C in a humidified incubator under 5% CO₂ and 95% air.

Hydrostatic pressure loading: We loaded the atrial “explants” to 50 mmHg hydrostatic pressure (HP group), by using a set of commercial devices (STREX, Inc.). Of which, gas from the incubator flowed continuously into a closed container to keep the HP at 50 mmHg while maintaining the same temperature, humidity, and CO₂ level as the incubator. As a control, the atrial “explants” were kept in a common CO₂ incubator with AP.

Mouse fibrotic pathway-specific PCR array analysis: To compare the expression of fibrosis-related genes between HP and AP groups, we mixed an equal amount of RNA from three independent mice atrial tissue samples of each group for PCR array analysis. Briefly, total RNA was purified by using Quick-RNA™ Microprep Kit (ZYMO RESEARCH). The RNA concentration was determined using a NanoDrop 2000 spectrophotometer (Thermo Fisher Scientific), and 1 µg of RNA was used to generate cDNA using the RT² First Strand Kit (Qiagen). The mouse fibrosis RT² Profiler PCR array was performed according to the manufacturer’s instructions (#330231 PAMM-120ZA, Qiagen). This PCR array profiles 84 key genes involved in dysregulated tissue remodeling during the repair and healing of wounds. Roche®LightCycler®480 was used to performing the PCR procedure. Qiagen’s online web analysis tool was utilized to analyze the data. *B2m* and *Hsp90ab1* were used as reference genes. The fold changes of gene expression were calculated by determining the ratio of HP group to AP group.

qRT-PCR: To investigate the time-course dynamics of the transcription on *Rhoa*, *Rock1*, *Rock2*, *Tgfb1*, and *Thbs1* in atrial tissues following HP loading, we collected atrial “explants” at 1, 6, 24, and 72 hours ($n = 3$, at each time point for both groups) after the initiation of culture, and we purified total RNA as described above. For qRT-PCR,

the first-strand cDNA was synthesized with SuperScript™ VILO™ MasterMix (Invitrogen) according to the manufacturer’s recommendations, and the RT-PCR was performed using THUNDERBIRD® SYBR® qPCR MIX (TOYOBO) with the CFX96™ Real Time System (BIORAD). The gene expression was normalized by house-keeping gene *B2m*. Primers used for qPCR were the following: *Rhoa* (Forward: 5'- AGC TTG TGG TAA GAC ATG CTT G -3', Reverse:5'- GTG TCC CAT AAA GCC AAC TCT AC -3'); *Rock1* (Forward: 5'- AGC TTT TGT TGG CAA TCA GC -3', Reverse:5'- ACT TTC CTG CAA GCT TTT ATC CA -3'); *Rock2* (Forward: 5'- CAG TCC CTG GGT AGT TCA GC -3', Reverse:5'- GCC TGG CAT ATA CTC CAT C -3'); *Tgfb1* (Forward:5'-CTG CGC TTG CAG AGA TTA AA-3', Reverse:5'-GAA AGC CCT GTA TTC CGT CT-3'); *Thbs1* (Forward:5'-GGA ACG GAA AGA CAA CAC TG-3', Reverse:5'-AGT TGA GCC CGG TCC TCT TG-3').

Monitoring the outgrowth of stromal cells from atrial tissues: To further investigate the effect of HP loading on stromal cells, atrial tissues from mice were collected into 6-cm dish and minced into small fragments as described above. Then, the minced tissue fragments were randomly moved onto fibronectin-coated 6-cm dishes (a total of 40 pieces of minced tissue fragments/dish) and then cultured as “explants” with daily loading to 50 mmHg for 3 hours (HP group) or without pressure loading (AP group). The outgrowth of stromal cells from atrial “explants” was observed every other day, and we counted the number of “explants” with cell outgrowth at different time points (Supplemental Table I). The number of “explants” with cell outgrowth was divided by the total number of seeded “explants” at each time point, and then, the percentiles were used to draw the cell growth curves. Next, we collected the outgrowth cells at 12 days after the initiation of culture, and the total number of outgrowth cells was counted using a NucleoCounter cell-counting device (ChemoMetecA/S, Denmark). Three independent experiments were performed ($n = 3$ for both AP and HP groups).

Immunofluorescence staining: We also investigated the expression of CD105, CD90, and α -SMA in the outgrowth cells by immunofluorescence staining as described previously.¹⁰ Briefly, the first-passaged outgrowth cells were cultured in 8-well chamber slides (1 × 10⁴ /well, Lab-Tek, Thermo Scientific Nunc) coated with 15 µg/mL fibronectin (CORNING). Next, the cells were fixed with 4% paraformaldehyde phosphate buffer solution (Wako). After blocking, the cells were incubated with rabbit anti-mouse CD90 antibody (1:50 dilution, Abcam), rabbit anti-mouse CD105 antibody (1:50 dilution, Abcam), or rabbit anti-mouse α -SMA antibody (1:100 dilution, Abcam), respectively. Positive staining was detected using Alexa Fluorescent 546 goat antirabbit Ig (1:400 dilution, Dako) secondary antibody. The nuclei were stained with 4',6-diamidino-2-phenylindole (DAPI, Thermo Scientific). The immunofluorescence was examined under a microscope (FV10CW3, Olympus). We counted the positively stained cells or measured mean intensity in ten images of each experiment. The percentage of positive cells or mean intensity from three independent experiments was used for

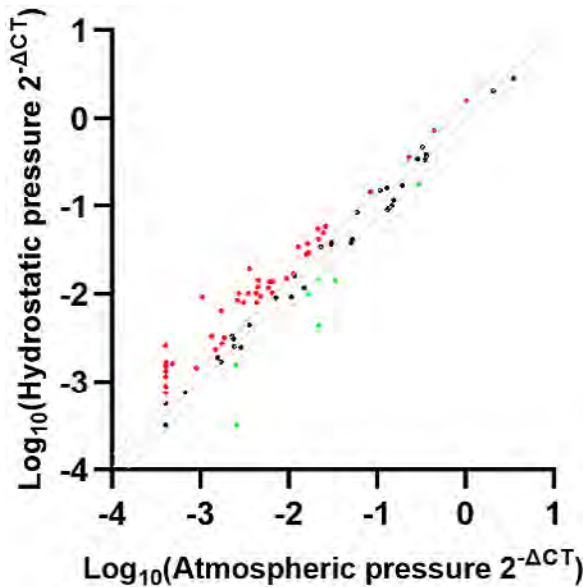


Figure 1. PCR array analysis on the expression of fibrosis-related genes in atrial tissues after 24 hours culture under 50 mmHg HP and AP. The scatter plots describe the relative expression between groups. Genes with more than 1.5-fold upregulation (red dots) and downregulation (green dots) are highlighted.

statistical analysis.

Statistical analysis: All the values were presented as the mean \pm SD. For comparison of multiple sets of data, one-way analysis of variance followed by Tukey’s test (Dr. SPSS II, Chicago, IL) was used for statistical analyses. For comparison of two sets of data, unpaired two-tailed t-test was used for statistical analyses. All analyses were carried out with the SPSS19.0 statistical software (IBM SPSS Co., USA). A *P*-value of less than 0.05 was accepted as significant.

Results

Loading the atrial tissues to 50 mmHg prevalently upregulated the expression of profibrotic genes: We first screened the overall changes in the expression of fibrosis-related genes in atrial “explants” loaded with 50 mmHg HP using the mouse RT² Profiler PCR array (Supplemental Table II). A scatter plot showed that 24 hours loading of atrial tissues to 50 mmHg upregulated many fibrosis-related genes by more than 1.5-fold (Figure 1), although a few genes showed a downregulation by more than 1.5-fold. We further categorized these genes according to their biological functions (Figure 2A) and noticed that these genes that functionally related to the ECM and cell adhesion molecules (Figure 2B), Inflammatory cytokines and chemokines (Figure 2C), TGF- β superfamily members (Figure 2D), Transcription factors (Figure 2E), and growth factors (Figure 2F) were widely upregulated.

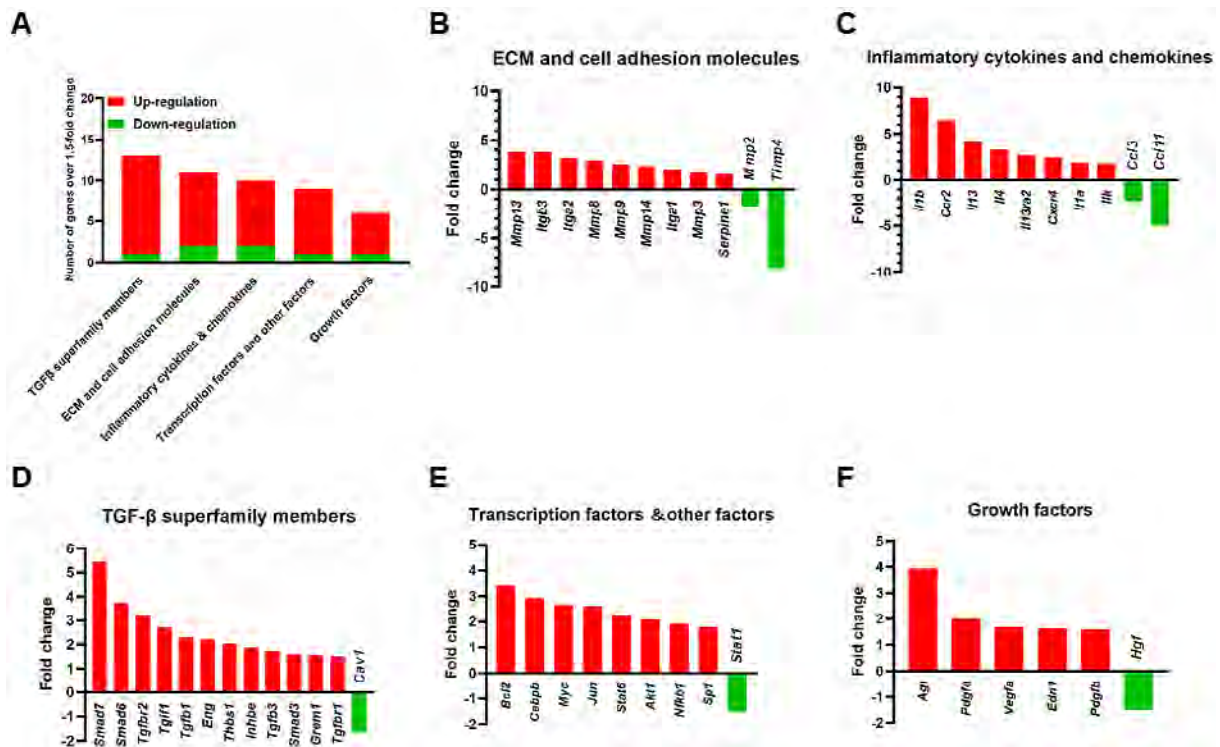


Figure 2. The functional categorization on the fibrosis-related genes included in PCR array analysis. **A:** The number of genes that upregulated and downregulated over 1.5-fold in atrial tissues after 24 hours culture under 50 mmHg HP. **B-F:** Data are also presented by dividing these genes into different categorizations according to their biological functions. Fold change of each gene functionally belongs to ECM and cell adhesion molecules (**B**), inflammatory cytokines and chemokines (**C**), TGF- β superfamily members (**D**), transcription factors (**E**), and growth factors (**F**).

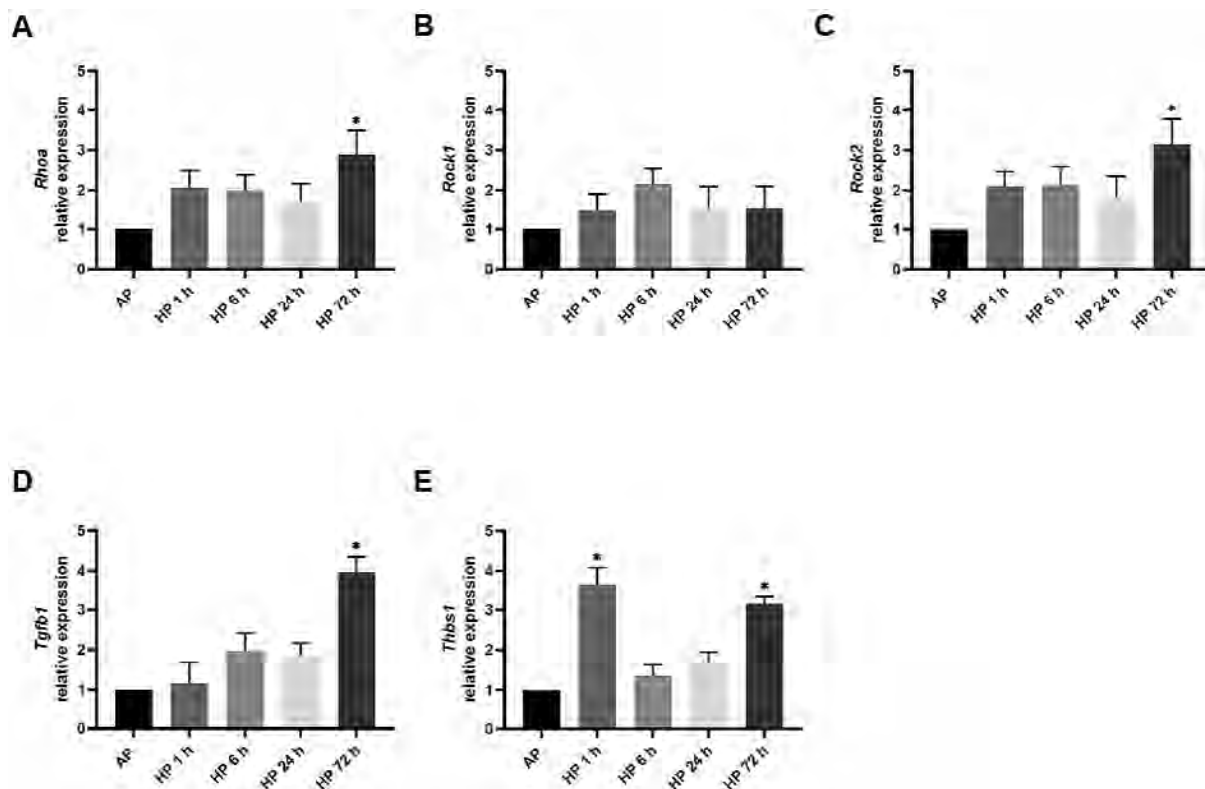


Figure 3. Time-course dynamics on the expression of *Rhoa*, *Rock1*, *Rock2*, *Tgfb1*, and *Thbs1* in atrial tissues followed by *ex vivo* loading to 50 mmHg HP. Quantitative RT-PCR data shows the relative expression of *Rhoa* (A), *Rock1* (B), *Rock2* (C), *Tgfb1* (D), and *Thbs1* (E) at 0, 1, 6, 24, 72 hours after culture. Data are represented by three independent experiments at each time point. * $P < 0.01$ versus AP group. AP indicates atmosphere pressure; and HP, hydrostatic pressure.

Loading the atrial tissues to 50 mmHg activated the TGF- β signaling pathway: Based on the changes of the PCR fibrosis array, we found that TGF- β is the most affected pathway; thus, we tried to check the dynamics of mechanotransduction in response to HP through this pathway. We loaded the atrial tissues with either 0 or 50 mmHg for 1, 6, 24, and 72 hours. Then, we evaluated the gene expression of *Rhoa*, *Rock1*, *Rock2*, *Tgfb1*, and *Thbs1* at each time point. Our qRT-PCR data showed that, as a mechanosensitive multicomponent target of TGF- β non-canonical signaling pathways, the expression of *Rhoa* and *Rock2* was significantly enhanced at 72 hours by 50 mmHg loading ($P < 0.01$, Figure 3A, C). However, as another downstream target of *Rhoa*, the expression of *Rock1* was not changed much at any time point following 50 mmHg loading (Figure 3B). Interestingly, the expression of *Thbs1* was quickly induced at 1 hour, but it declined at 6-24 hours, and then increased again at 72 hours after 50 mmHg loading (Figure 3E). In contrast, the expression of *Tgfb1* was not induced at the early time windows, but it was robustly enhanced at 72 hours after 50 mmHg loading ($P < 0.01$, Figure 3D).

Daily loading of the atrial tissues to 50 mmHg accelerated the outgrowth of stromal cells: The outgrowth of fibroblast-like stromal cells from atrial “explants” was observed mostly at 3-5 days after the initiation of culture, but the outgrowth cells from some “explants” in the HP

group could be observed even at the second day of culture (Figure 4A). By plotting the percentiles of “explants” with cell outgrowth, we found that the cell outgrowth from “explants” was significantly earlier in HP group than AP group (Figure 4B). Next, we harvested all the outgrowth cells 12 days after the initiation of culture, and the total number of outgrowth cells was also significantly increased by daily loading the atrial tissue to 50 mmHg for 3 hours ($P = 0.03$, Figure 4C).

Further, we investigated the phenotypic characteristics of these cells that outgrew from atrial “explants” by immunostaining on the expression of CD90, CD105, and α -SMA (Figure 5). Extensive expression of CD90 and CD105 (almost 90%) was observed in these outgrowth cells (Figure 5A, B), suggesting a mesenchymal stem cell-like phenotype. Although the expression of α -SMA tended to slightly increase in these outgrowth cells from the HP group, no significant difference was found between groups ($P = 0.07$, Figure 5C).

Discussion

Clinical practice and animal experiments indicate that pressure overload-induced atrial fibrosis and remodeling play a vital role in the pathology of rhythm disturbance.¹²⁾ In addition to endothelial cells undergoing additional shear stress, cardiac tissue is mainly exposed to mechani-

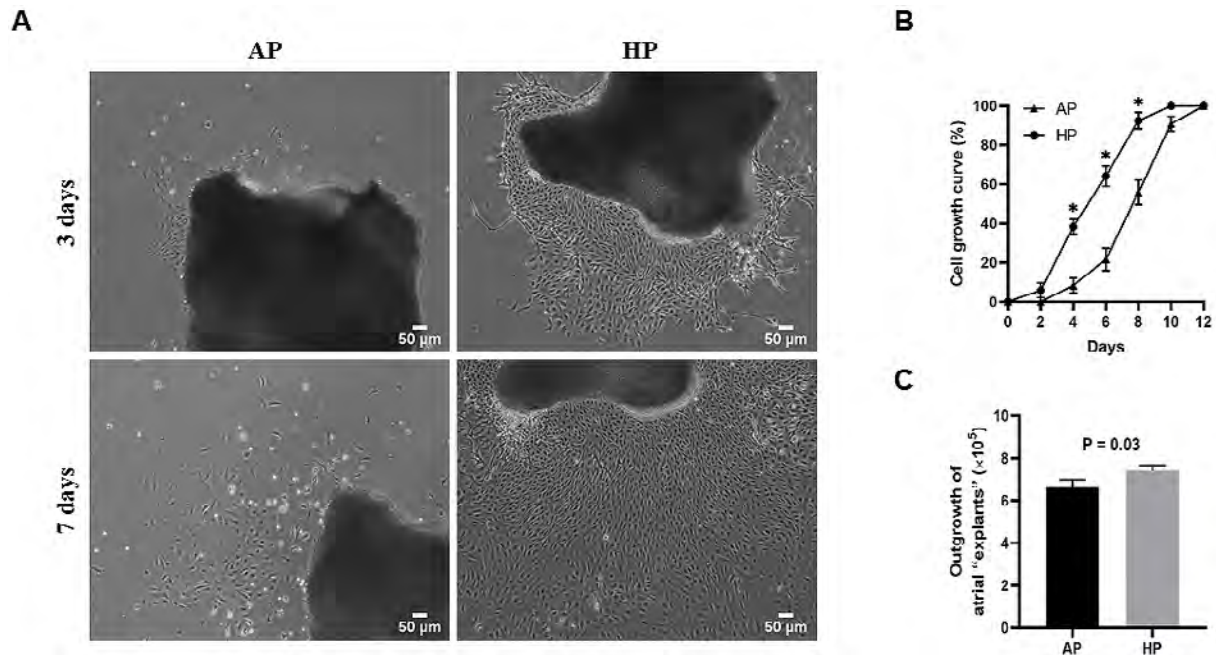


Figure 4. The outgrowth of stromal cells from atrial tissues with daily *ex vivo* loading to 50 mmHg HP for 3 hours. **A:** Representative images show the cells outgrowing from the atrial “explants” at 3 and 7 days after initiation of culture. **B:** The curve lines appear the percentiles of “explants” with cell outgrowing at different time points after the initiation of culture. **C:** The total number of outgrowth cells harvested at 12 days after the initiation of culture. Data are represented by three independent experiments. * $P < 0.05$ versus AP group. AP indicates atmospheric pressure; and HP, hydrostatic pressure.

cal compression stress. It is well known that mechanical stretch induces profibrotic fibroblast phenotypes, which is thought to promote the development of AF.^{13,14} Recent studies also showed that HP involves in atrial remodeling.^{15,16} However, the molecular and cellular mechanisms of atrial fibrosis in response to HP have not yet been well understood.

By *ex vivo* loading the atrial tissues from healthy mice to 50 mmHg HP, we confirmed the extensive enhancement on the expression of profibrotic genes. We further functionally classified these genes according to RT² Profiler PCR array manufacturer’s instructions. Among these genes associated with ECM and cell adhesion molecules, the most upregulated genes were integrin and matrix metalloproteinase (MMP) family members. Indeed, previous studies showed that mechanical stress increases the mechanosensitive integrin subunit and induces the expression of *Mmp8*, *Mmp9*, and *Mmp13* in fibroblasts.¹⁷⁻¹⁹ Mechanical stress can also induce the expression of transcription factors associated with inflammatory response and tissue remodeling, such as *Myc*, *Jun*, *Nfkb*.^{20,21} Coincidentally, the loading of atrial tissues to HP also enhanced the expression of many transcription factors known as the master regulators of inflammatory cytokines and growth factors in our study. A computer biology model applied in a recent study demonstrated that the mechanosignaling network in the heart can be started from the mechanosensing step by several mechanosensors, such as integrin and angiotensin receptor, then induces the activation of multiple signaling cascades, such as TGF- β and RhoA/ROCK pathway, and finally alters the transcrip-

tion of related genes to induce remodeling.²²

TGF- β signal pathway is considered as the core in mechanotransduction of fibrogenesis in response to pressure overload to the heart. As an important signal isoform, TGF- β_1 can trigger the activation of cardiac fibroblasts, induce profibrotic genes through the canonical signaling pathway with activation of Smad2/3, or the noncanonical signaling pathways with activation of Rho/ROCK.⁶ Recent studies further demonstrated that intermittent compressive force induces TGF- β_1 expression in human periodontal fibroblasts.^{23,24} As a branch of TGF- β noncanonical signaling pathways, Rho/ROCK signaling plays a crucial role in various cellular processes, such as cell proliferation and migration. ROCK2 is known to be involved in angiotensin II-induced cardiac hypertrophy, and ROCK2-deficient mice are resistant to pressure overload-induced cardiac hypertrophy.^{26,27} Moreover, a recent study further demonstrated that specific ROCK2 deficiency in cardiac fibroblasts protects the heart from angiotensin II-induced cardiac fibrosis.²⁸ Consistent with these previous studies, our data supported the mechanotransductive role of RhoA/ROCK2 in cardiac fibrosis. Although it has also been reported that the potential role of ROCK1 in the heart in response to mechanical stress,²⁹ we did not find the induction of ROCK1 in atrial tissues by *ex vivo* loading to 50 mmHg within 72 hours follow-up. We speculate that the mechanical stress threshold may be higher for inducing ROCK1 compared to ROCK2.

TSP-1, a mechanosensitive multi-functional matricellular protein of the TGF- β superfamily, has been identified to play a major role in cardiac fibrosis, mainly by ac-

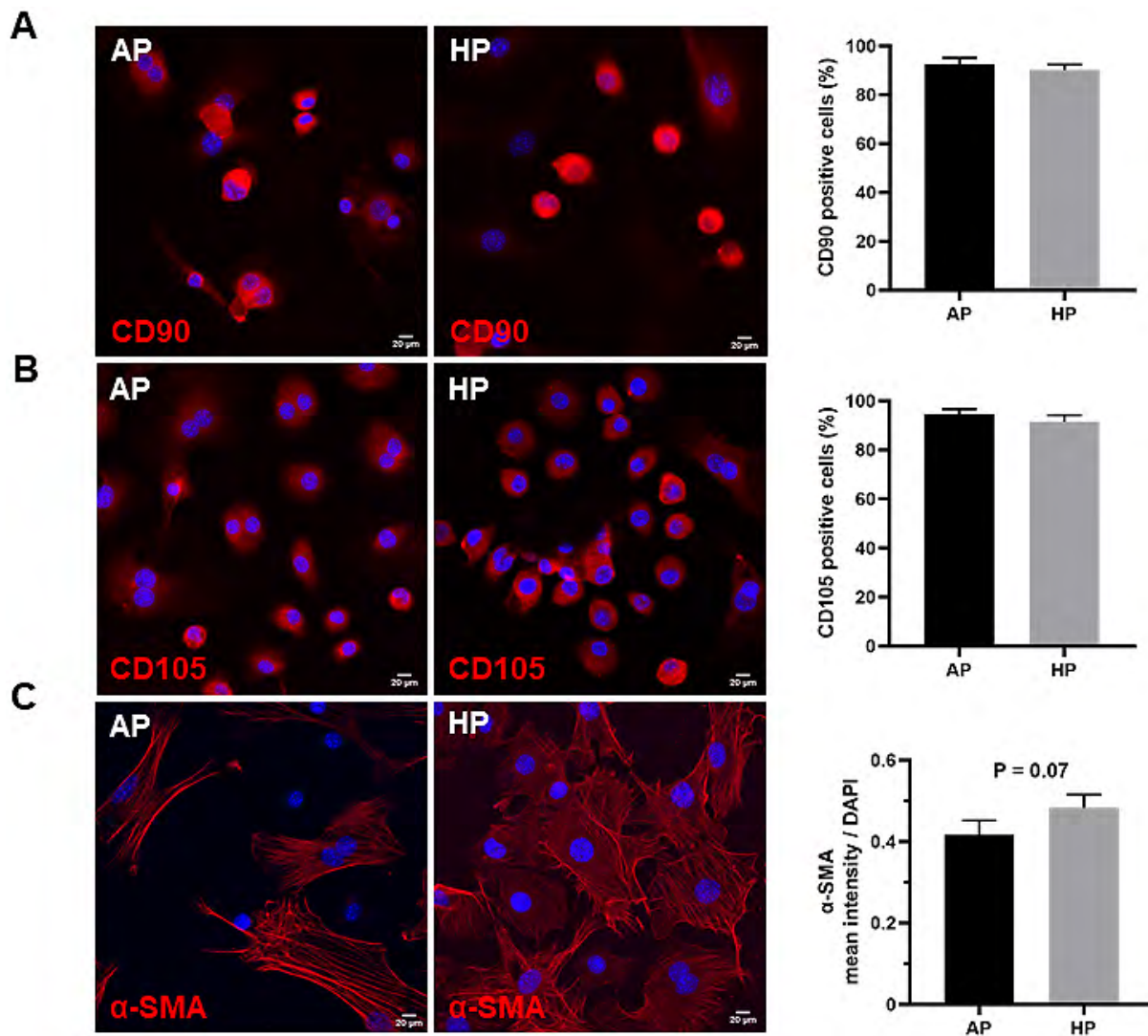


Figure 5. Immunocytochemical analysis on the expression of CD90, CD105, and α -SMA in the outgrowth cells. Representative images (left) and quantitative bar graph data (right) show the expression of CD90 (A), CD105 (B), and α -SMA (C) in the outgrowth cells from atrial “explants.” Scale bar: 20 μ m. AP indicates atmospheric pressure; and HP, hydrostatic pressure.

tivating the TGF- β isoforms, which in turn induces TSP-1 expression.³⁰⁻³²⁾ A recent study in mice demonstrated that TSP-1 deletion leads to the maladaptive remodeling of the aorta in response to pressure overload,³³⁾ suggesting the protective role of TSP-1 in response to mechanical stress. Interestingly, our data showed that *ex vivo* loading atrial tissues to 50 mmHg quickly induced the expression of *Thbs1*; however, the expression of *Thbs1* increased again at 72 hours after the loading to 50 mmHg. The biphasic changes of TSP-1 in response to mechanical stress may represent dual roles of TSP-1 in the heart. In other words, instead of the cardioprotection about the increased TSP-1 soon after suffering from mechanical stresses, a delayed increase of TSP-1 may promote fibrogenesis in the heart with a persistent pressure overload. As we purified total RNA from the outgrowth cells together with the “explants” for the qRT-PCR analysis, data from our study reflected the comprehensive response of atrial tissues to HP.

Stromal cells, such as fibroblasts, within the defined tissues/organs, are known to be the key player of fibrogenesis. A recent study demonstrated that the increased stretch force or matrix stiffness promotes the proliferation and activation of cardiac fibroblasts.¹⁴⁾ Based on our observational data, HP loading accelerated the cell outgrowth from “explants” (Figure 3B) and increased the yield of outgrowth cells (Figure 4C), suggesting the potential role of stromal cells in the atrial fibrosis in response to pressure overload. Although we did not further evaluate the regulatory role of RhoA, ROCKs, and TSP-1 on outgrowth cells at a protein level, the upregulated mRNA expression suggests the probable role on the proliferation, migration, and other biological characteristics of resident stromal cells in response to HP.

We previously reported that cardiac-derived mesenchymal stem-like cells positively express CD90 and CD105, two markers commonly used for detecting mesen-

chymal stem stromal cells.³⁴⁾ The extensive expression of CD105 and CD90 in these outgrowth cells suggests the mesenchymal stem-like cell characteristics. Although researchers previously reported the heterogeneity on the expression of CD90 in cardiac-derived stromal cells from human beings,³⁵⁾ HP loading barely changed the expression of CD90 and CD105 in outgrowth cells in this study. As we did not evaluate the proliferative activity in this study, whether HP loading could change the proliferation of stromal cells is kept unknown. Researchers recently reported that the exposure of human cardiac fibroblasts to 200 mmHg for 8 hours significantly suppresses α -SMA expression.³⁶⁾ Unexpectedly, as a typical marker of myofibroblasts, the expression of α -SMA was not significantly induced in response to loading of atrial tissues to 50 mmHg. The magnitude and duration of HP and the difference in experimental methods might affect the phenotypic shift of stromal cells.

This study exhibits some limitations. First, PCR array analysis was performed only once by using a mixture of RNA from three independent samples. Second, due to the tiny size of mouse atrial tissues, we could not collect enough protein to perform Western blotting analysis for further confirming the relevant molecular mechanism on our findings. Third, we only used 50 mmHg HP for all experiments, and optimizing the experimental conditions in future studies is necessary.

Conclusion

Our data showed the induction of profibrotic transcription of atrial tissues by HP loading, likely by activating TGF- β signal pathway and stromal cells. Data from the *ex vivo* experimental approach provided indirect evidence on the common pathological features of atrial fibrosis following pressure overload.

Disclosure

Conflicts of interest: The authors declare no competing financial interests.

References

1. Kirchhof P. The future of atrial fibrillation management: Integrated care and stratified therapy. *Lancet* 2017; 390: 1873-87.
2. Travers JG, Kamal FA, Robbins J, Yutzey KE, Blaxall BC. Cardiac fibrosis: The fibroblast awakens. *Circ Res* 2016; 118: 1021-40.
3. Creemers EE, Pinto YM. Molecular mechanisms that control interstitial fibrosis in the pressure-overloaded heart. *Cardiovasc Res* 2011; 89: 265-72.
4. Yuan J, Liu H, Gao W, *et al.* MicroRNA-378 suppresses myocardial fibrosis through a paracrine mechanism at the early stage of cardiac hypertrophy following mechanical stress. *Theranostics* 2018; 8: 2565-82.
5. Romani P, Valcarcel-Jimenez L, Frezza C, Dupont S. Crosstalk between mechanotransduction and metabolism. *Nat Rev Mol Cell Biol* 2021; 22: 22-38.
6. Dobaczewski M, Chen W, Frangogiannis NG. Transforming growth factor (TGF)-beta signaling in cardiac remodeling. *J Mol Cell Cardiol* 2011; 51: 600-6.

7. Shimizu T, Liao JK. Rho kinases and cardiac remodeling. *Circ J* 2016; 80: 1491-8.
8. Yamashiro Y, Thang BQ, Shin SJ, *et al.* Role of Thrombospondin-1 in mechanotransduction and development of thoracic aortic aneurysm in mouse and humans. *Circ Res* 2018; 123: 660-72.
9. Mennens SFB, van den Dries K, Cambi A. Role for mechanotransduction in macrophage and dendritic cell immunobiology. *Results Probl Cell Differ* 2017; 62: 209-42.
10. Peng YH, Xiao J, Yan C, Luo L, Li TS. Potential role of the resident mesenchymal stem-like cells in renal fibrogenesis after ureteral obstruction. *Stem Cells Int* 2019; 2019: 2543171.
11. Luo L, Yan C, Urata Y, *et al.* Dose-dependency and reversibility of radiation-induced injury in cardiac explant-derived cells of mice. *Sci Rep* 2017; 7: 40959.
12. Saucerman JJ, Tan PM, Buchholz KS, McCulloch AD, Omens JH. Mechanical regulation of gene expression in cardiac myocytes and fibroblasts. *Nat Rev Cardiol* 2019; 16: 361-78.
13. Yoshida K, Ulfarsson M, Oral H, *et al.* Left atrial pressure and dominant frequency of atrial fibrillation in humans. *Heart Rhythm* 2011; 8: 181-7.
14. Herum KM, Choppe J, Kumar A, Engler AJ, McCulloch AD. Mechanical regulation of cardiac fibroblast profibrotic phenotypes. *Mol Biol Cell* 2017; 28: 1871-82.
15. Wei W, Rao F, Liu F, *et al.* Involvement of Smad3 pathway in atrial fibrosis induced by elevated hydrostatic pressure. *J Cell Physiol* 2018; 233: 4981-9.
16. Li X, Deng CY, Xue YM, *et al.* High hydrostatic pressure induces atrial electrical remodeling through angiotensin upregulation mediating FAK/Src pathway activation. *J Mol Cell Cardiol* 2020; 140: 10-21.
17. Hannafin JA, Attia EA, Henshaw R, Warren RF, Bhargava MM. Effect of cyclic strain and plating matrix on cell proliferation and integrin expression by ligament fibroblasts. *J Orthop Res* 2006; 24: 149-58.
18. Takahashi I, Nishimura M, Onodera K, *et al.* Expression of MMP-8 and MMP-13 genes in the periodontal ligament during tooth movement in rats. *J Dent Res* 2003; 82: 646-51.
19. Fujisawa T, Hattori T, Takahashi K, Kuboki T, Yamashita A, Takigawa M. Cyclic mechanical stress induces extracellular matrix degradation in cultured chondrocytes via gene expression of matrix metalloproteinases and interleukin-1. *J Biochem* 1999; 125: 966-75.
20. Olson AK, Ledee D, Iwamoto K, *et al.* C-Myc induced compensated cardiac hypertrophy increases free fatty acid utilization for the citric acid cycle. *J Mol Cell Cardiol* 2013; 55: 156-64.
21. Manabe I, Shindo T, Nagai R. Gene expression in fibroblasts and fibrosis: Involvement in cardiac hypertrophy. *Circ Res* 2002; 91: 1103-13.
22. Tan PM, Buchholz KS, Omens JH, McCulloch AD, Saucerman JJ. Predictive model identifies key network regulators of cardiomyocyte mechano-signaling. *PLoS Comput Biol* 2017; 13: e1005854.
23. Manokawinchoke J, Pavasant P, Sawangmake C, *et al.* Intermittent compressive force promotes osteogenic differentiation in human periodontal ligament cells by regulating the transforming growth factor-beta pathway. *Cell Death Dis* 2019; 10: 761.
24. Manokawinchoke J, Limjeerajarus N, Limjeerajarus C, Sas-travaha P, Everts V, Pavasant P. Mechanical force-induced TGF β 1 increases expression of SOST/POSTN by hPDL cells. *J Dent Res* 2015; 94: 983-9.
25. Burridge K, Monaghan-Benson E, Graham DM. Mechanotransduction: From the cell surface to the nucleus via RhoA. *Philos Trans R Soc Lond B Biol Sci* 2019; 374: 20180229.
26. Sunamura S, Satoh K, Kurosawa R, *et al.* Different roles of myocardial ROCK1 and ROCK2 in cardiac dysfunction and postcapillary pulmonary hypertension in mice. *Proc Natl Acad Sci USA* 2018; 115: E7129-38.
27. Okamoto R, Li Y, Noma K, *et al.* FHL2 prevents cardiac hypertrophy in mice with cardiac-specific deletion of ROCK2.

- FASEB J 2013; 27: 1439-49.
28. Shimizu T, Narang N, Chen P, *et al.* Fibroblast deletion of ROCK2 attenuates cardiac hypertrophy, fibrosis, and diastolic dysfunction. *JCI Insight* 2017; 2: e93187.
 29. Zhang YM, Bo J, Taffet GE, *et al.* Targeted deletion of ROCK1 protects the heart against pressure overload by inhibiting reactive fibrosis. *FASEB J* 2006; 20: 916-25.
 30. Murphy-Ullrich JE, Suto MJ. Thrombospondin-1 regulation of latent TGF-beta activation: A therapeutic target for fibrotic disease. *Matrix Biol* 2018; 68: 28-43.
 31. Krishna SM, Golledge J. The role of thrombospondin-1 in cardiovascular health and pathology. *Int J Cardiol* 2013; 168: 692-706.
 32. Zhao C, Isenberg JS, Popel AS. Transcriptional and post-transcriptional regulation of Thrombospondin-1 expression: A computational model. *PLOS Comput Biol* 2017; 13: e1005272.
 33. Yamashiro Y, Thang BQ, Ramirez K, *et al.* Matrix mechanotransduction mediated by thrombospondin-1/integrin/YAP in the vascular remodeling. *Proc Natl Acad Sci USA* 2020; 117: 9896-905.
 34. Li TS, Cheng K, Malliaras K, *et al.* Direct comparison of different stem cell types and subpopulations reveals superior paracrine potency and myocardial repair efficacy with cardiosphere-derived cells. *J Am Coll Cardiol* 2012; 59: 942-53.
 35. Cheng K, Malliaras K, Smith RR, *et al.* Human cardiosphere-derived cells from advanced heart failure patients exhibit augmented functional potency in myocardial repair. *JACC Heart Fail* 2014; 2: 49-61.
 36. Tanaka R, Umemura M, Narikawa M, *et al.* Hydrostatic pressure suppresses fibrotic changes via Akt/GSK-3 signaling in human cardiac fibroblasts. *Physiol Rep* 2018; 6: e13687.

Supplemental Files

Supplemental Tables I, II

Please see supplemental files; <https://doi.org/10.1536/ihj.21-481>

日中笹川医学奨学金制度<学位取得コース>評価書

課程博士：指導教官用



第 44 期

研究者番号：G4411

作成日：2024年3月11日

氏名	李佩霖	LI PEILIN	性別	M	生年月日	1994/08/21
所属機関（役職）	長崎大学大学院医歯薬学総合研究科（大学院生）					
研究先（指導教官）	長崎大学大学院医歯薬学総合研究科医療学専攻移植・消化器外科学（江口 晋 教授）					
研究テーマ	小分子誘導肝前駆細胞（CLiP）からの3D胆管形成 3D bile duct formation from small molecule induced liver progenitor cells (CLiPs)					
専攻種別	<input type="checkbox"/> 論文博士			<input checked="" type="checkbox"/> 課程博士		

研究者評価（指導教官記入欄）

成績状況	優 良 可 不可 学業成績係数=	取得単位数
		取得単位数／取得すべき単位数総数 27
学生本人が行った研究の概要	He mainly conducted research on chemically induced bile duct differentiation of liver progenitor cells. Liver cells isolated from human liver have bidirectional differentiation potential after reprogramming with a combination of chemical molecules. Using this progenitor cell for differentiation, the bile duct system was established in vitro, and combined with mature liver cells, the in vitro bile duct-hepatocyte system was established, which can be used for in vitro drug and metabolic analysis. In addition, the other studies include the generation of the hepatobiliary organoids in vitro, pharmacological treatment of small intestinal drug injury, and the use of hepatobiliary organoids for microplastic metabolic analysis.	
総合評価	【良かった点】 He works hard in research and could conduct multiple studies well, discovering problems and solving them in his research.	
	【改善すべき点】 Communicate more and improve Japanese.	
	【今後の展望】 I hope him to achieve better results in research and learn more skills in clinical practice after graduation.	
学位取得見込	He could get the Ph. D degree in Sep. 2024 and graduate earlier.	
評価者（指導教官名） Susumu Eguchi, MD, PhD		

日中笹川医学奨学金制度＜学位取得コース＞報告書 研究者用



第44期

研究者番号: G4411

作成日: 2024年3月 02 日

氏名	李 佩霖	LI PEILIN	性別	M	生年月日 1994/08/21
所属機関(役職)	長崎大学大学院医歯薬学総合研究科(大学院生)				
研究先(指導教官)	長崎大学大学院医歯薬学総合研究科医療学専攻移植・消化器外科学(江口 晋 教授)				
研究テーマ	小分子誘導肝前駆細胞(CLiP)からの3D胆管形成 3D bile duct formation from small molecule induced liver progenitor cells(CLiPs)				
専攻種別	論文博士	<input type="checkbox"/>	課程博士	<input checked="" type="checkbox"/>	
<p>1. 研究概要(1)</p> <p>1) 目的(Goal)</p> <p>2) 戦略(Approach)</p> <p>3) 材料と方法(Materials and methods)</p> <p>4) 実験結果(Results)</p> <p>5) 考察(Discussion)</p> <p>6) 参考文献(References)</p> <p>1. Purpose: To form the three-dimensional bile duct structure and integrated duct-hepatocyte tissue from human CLiPs.</p> <p>2. Backgrounds: The integrity of liver cell function depends on the integrity of the total triad. Portal triads are composed of three major tubes. Branches of the hepatic artery carry oxygenated blood to the hepatocytes, while branches of the portal vein carry blood with nutrients from the small intestine. The bile duct carries bile products away from the hepatocytes to the larger ducts and gall bladder. Therefore, it is necessary to form the structure including the material supply and metabolic waste discharge in regenerative liver tissue so that the hepatic tissue can maintain completed hepatic function for a long term. Herein, we have been able to successfully use rat CLiPs (a small chemical-induced liver progenitor cells developed by Dr. Katsuda) to induce 3D bile duct structure. If we want to form human liver tissue including bile duct and vascular, we have to establish the human 3D bile duct, but we have not yet completed the differentiation of human CLiPs into 3D bile duct structure. Therefore, we need to use human CLIP to induce 3D bile duct.</p> <p>3. Method: 1. Human CLiPs were induced to form 3D bile duct structure in 3D culture system: MEF cell as feeder cell and Matrigel provides with 3D environment. 2. BIM (bile duct induced medium) combine with growth factors (HGF and EGF) would be investigated. Result: 1. Phase image and RT-qPCR showed that the FAC can successfully induce cryohepatocytes to human CLiPs. 2. Inducing human CLiPs to cholangiocytes and formation of the 3D bile duct structures: the combination of MEF feeder cells and Matrigel can induce the human CLiPs to cholangiocytes and form some 3D bile duct structure, which had positive expressions of biliary genes and concentration of Rhodamine123 in BIM medium with HGF. 3. The BIM+HGF had higher efficiency for the formation of the bile duct from hCLiPs compared with the other conditions. 4. The integrated bile-hepatocyte tissue expressed the bile acid transporter proteins and accumulated CLF into biliary lumen from the culture medium via hepatocytes canaliculi. 4. Summary: we formed the functional bile duct from hCLiPs induced from hMHs by molecules combination with FBS. These hCLiPs expressed typical HPCs markers EpCAM, KRT-19, SOX-9, CD133 and gradually downregulated hMHs markers ALB, CYP7A1, and HNF4A during induction. These purified hCLiPs were then used to induce the generation of a 3D bile duct-like structure with lumens in a 3D culture environment with MEF. The bile duct expressed typical biliary epithelial cell markers CK-7, GGT1, CFTR and EpCAM and it had the ability to transport the bile-like substance rhodamine 123 into the lumen of the bile duct. Subsequently, bile ducts were co-cultured with hMHs for two days and bile salt analogues, CLF, were transported into bile duct and aggregate within the lumen from culture medium through the hMHs. The integrated tissue expressed the bile bile canaliculi marker and transporter protein.</p>					

1. 研究概要(2)

- 1.Tanimizu N, Nakamura Y, Ichinohe N, et al. Hepatic biliary epithelial cells acquire epithelial integrity but lose plasticity to differentiate into hepatocytes in vitro during development. *J Cell Sci.* 2013;126:5239–46. doi:10.1242/jcs.133082
- 2.O'Hara SP, Tabibian JH, Splinter PL, et al. The dynamic biliary epithelia: molecules, pathways, and disease. *J Hepatol.* 2013;58:575–82. doi:10.1016/j.jhep.2012.10.011
- 3.Alpini G, McGill JM, LaRusso NF. The pathobiology of biliary epithelia. *Hepatology.* 2002;35:1256–68. doi:https://doi.org/10.1053/jhep.2002.33541
- 4.Cao W, Chen K, Bolkestein M, et al. Dynamics of Proliferative and Quiescent Stem Cells in Liver Homeostasis and Injury. *Gastroenterology.* 2017;153:1133–47. doi:10.1053/j.gastro.2017.07.006
- 5.Strazzabosco M, Fabris L, Spirli C. Pathophysiology of cholangiopathies. *J Clin Gastroenterol.* 2005;39:S90–S102. doi:10.1097/01.mcg.0000155549.29643.ad
- 6.Lazaridis KN, LaRusso NF. The Cholangiopathies. *Mayo Clin Proc.* 2015;90:791–800. doi:10.1016/j.mayocp.2015.03.017
- 7.Buisson EM, Jeong J, Kim HJ, et al. Regenerative Medicine of the Bile Duct: Beyond the Myth. *Int J Stem Cells.* 2019;12:183–94. doi:10.15283/ijsc18055
- 8.Huang Y, Sakai Y, Hara T, et al. Bioengineering of a CLiP-derived tubular biliary-duct-like structure for bile transport in vitro. *Biotechnol Bioeng.* 2021;118:2572–84. doi:10.1002/bit.27773
- 9.Yan J, Tai Y, Zhou H. Culture of Mouse Liver Ductal Organoids. *Methods Mol Biol.* 2022;2455:117–29. doi:10.1007/978-1-0716-2128-8_11
- 10.Wang Z, Faria J, van der Laan LJW, et al. Human Cholangiocytes Form a Polarized and Functional Bile Duct on Hollow Fiber Membranes. *Front Bioeng Biotechnol.* 2022;10:868857. doi:10.3389/fbioe.2022.868857

1.The intrahepatic bile ducts (BDs) play an important role in the modification and transport of bile, and the integration between the BD and hepatocytes is the basis of the liver function. However, the lack of a source of cholangiocytes limits in vitro research. The aim of the present study was to establish three-dimensional BDs combined with human mature hepatocytes (hMHs) in vitro using chemically induced human liver progenitor cells (hCLiPs) derived from hMHs. In this study, we formed functional BDs from hCLiPs using hepatocyte growth factor and extracellular matrix. BDs expressed the typical biliary markers CK-7, GGT1, CFTR and EpCAM and were able to transport the bile-like substance rhodamine 123 into the lumen. The established three-dimensional BDs were cocultured with hMHs. These cells were able to bind to the BDs, and the bile acid analog CLF was transported from the culture medium through the hMHs and accumulated in the lumen of the BDs. The BDs generated from the hCLiPs showed a BD function and a physiological system (e.g., the transport of bile within the liver) when they were connected to the hMHs. We present a novel in vitro three-dimensional BD combined with hMHs for study, drug screening and the therapeutic modulation of the cholangiocyte function.

2.Biliary tubular-hepatocyte system accumulates polystyrene microplastic (PS-MP)-induced hepatotoxicity and mitigate through bile extraction.

Background: Microplastic particles are ubiquitous in daily life and can bioaccumulate in the liver via the hepatic-intestinal axis through dietary sources. The presence of microplastics has been associated with liver abnormalities, particularly in lipid metabolism, and has been documented in nonalcoholic steatohepatitis (NASH). Animal studies have demonstrated that bioaccumulation of microplastics can also lead to abnormalities in lipid and bile metabolism in the liver. However, there is currently no available data on the accumulation and metabolic pathways of microplastics in the liver. The in vitro model is an effective tool for investigating liver diseases and metabolism. To address this gap, we propose to study the metabolism of polystyrene microplastics (PS-MP) in the liver using an in vitro tissue model of bile duct-hepatocytes.

Method:

- 1.Establish an in vitro biliary tubular-hepatocyte tissue with the biliary and hepatic functions. (Confirm the characteristic of the tissue by proteins (IF and IHC), gene expressions (Rt-qPCR) and function assay (Rhodamine 123 and CLF))
- 2.Expose the hepatic tissue with the PS-MP for 1 hours, 24 hours and 48 hours. In order to confirm the hepatotoxicity of the exposing to the PS-MP, the markers of the liver metabolism would be detected, as well as the hepatotoxicity markers.
- 3.The bile efflux would affect the extraction of the PS-MP in the liver, the bile acid and cholesterol transporters inhibition and stimulation experiments would be carried out.

Results:

- 1.The biliary tubular-hepatocyte tissue from the rat CLiPs was successful, which have the functions of the bile transportation and the hepatocyte.
- 2.The human hepatic organoid from human CLiPs was established at the same time and the hepatic organoid contain the biliary tubular structure and the mature hepatocytes. The hepatic organoid also up-take the PS-MP and it seems to be transported into the bile duct. The YAC-HO absorbing the PS-MP cause the hepatotoxicity.
- 3.UDCA facilitates the excretion of the PS-MP excretion into bile ducts and attenuates hepatotoxicity.

2. 執筆論文 Publication of thesis ※記載した論文を添付してください。Attach all of the papers listed below.

論文名 1 Title	Therapeutic effect and mechanism of Daikenchuto in a model of methotrexate-induced acute small intestinal mucositis					
掲載誌名 Published journal	PLOS ONE					
	2023 年 3 月	18 巻(号)	028362	頁 ~	頁	言語 Language English
第1著者名 First author	Peilin Li	第2著者名 Second author	Yusuke Inoue		第3著者名 Third author	Daisuke Miyamoto
その他著者名 Other authors	Toshiyuki Adachi, Satomi Okada, Tomohiko Adachi, Akihiko Soyama, Masaaki Hidaka, Kengo Kanetaka, Shinichiro Ito, Daichi Sadatomi, Sachiko Mogami, Naoki Fujitsuka, Weili Gu, Susumu Eguchi					
論文名 2 Title	Three-dimensional human bile duct formation from chemically induced human liver progenitor cells					
掲載誌名 Published journal	Frontiers in Bioengineering and Biotechnology					
	2023 年 8 月	11 巻(号)		頁 ~	頁	言語 Language English
第1著者名 First author	Li, Peilin	第2著者名 Second author	Miyamoto, Daisuke		第3著者名 Third author	Huang, Yu
その他著者名 Other authors	Adachi Tomohiko, Hidaka Masaaki, Hara Takano, Soyama Akihiko, Matsushima Hajime, Imamura Hajime, Kanetaka Kengo, Gu Weili, Eguchi, Susumu					
論文名 3 Title	Feasibility of Organ Transportation by a Drone: An Experimental Study Using a Rat Model					
掲載誌名 Published journal	Transplantation Proceedings					
	2023 年 9 月	巻(号)		頁 ~	頁	言語 Language English
第1著者名 First author	Enjoji, Takahiro	第2著者名 Second author	Soyama, Akihiko		第3著者名 Third author	Fukumoto, Masayuki
その他著者名 Other authors	Peilin, Li Matsuguma, Kunihito Imamura, Hajime Maruya, Yasuhiro Hara, Takanobu Matsushima, Hajime Kugiyama, Tota Adachi, Tomohiko Hidaka, Masaaki Hamamoto, Sho Takashima, Shiro Maeda, Takahiro Kanetaka, Kengo					
論文名 4 Title						
掲載誌名 Published journal						
	年 月	巻(号)		頁 ~	頁	言語 Language
第1著者名 First author		第2著者名 Second author			第3著者名 Third author	
その他著者名 Other authors						
論文名 5 Title						
掲載誌名 Published journal						
	年 月	巻(号)		頁 ~	頁	言語 Language
第1著者名 First author		第2著者名 Second author			第3著者名 Third author	
その他著者名 Other authors						

3. 学会発表 Conference presentation ※筆頭演者として総会・国際学会を含む主な学会で発表したものを記載してくだ

※Describe your presentation as the principal presenter in major academic meetings including general meetings or international me

学会名 Conference	The 67th Annual Congress of International College of Surgeons Japan Section		
演題 Topic	An animal model of methotrexate-induced acute intestinal mucositis for drug therapy		
開催日 date	2022 年 6 月 4 日	開催地 venue	Tokyo
形式 method	<input checked="" type="checkbox"/> 口頭発表 Oral <input type="checkbox"/> ポスター発表 Poster	言語 Language	<input type="checkbox"/> 日本語 <input checked="" type="checkbox"/> 英語 <input type="checkbox"/> 中国語
共同演者名 Co-presenter	Peilin Li, Yusuke Inoue, Daisuke Miyamoto, Akihiko Soyama, Tomohiko Adachi, Kazuma Kobayashi, Shinichiro Ito, Masaaki Hidaka, Kengo Kanetaka, Susumu Eguchi		
学会名 Conference	Digestive Disease Week 2023; Session: AGA Basic Mechanisms of Tissue Injury, Repair and Fibrosis		
演題 Topic	Therapeutic effect and mechanism of Daikenchuto in a model of methotrexate-induced acute small intestinal mucositis		
開催日 date	2023 年 5 月 6 日	開催地 venue	Chicago
形式 method	<input type="checkbox"/> 口頭発表 Oral <input checked="" type="checkbox"/> ポスター発表 Poster	言語 Language	<input type="checkbox"/> 日本語 <input checked="" type="checkbox"/> 英語 <input type="checkbox"/> 中国語
共同演者名 Co-presenter	Peilin Li, Yusuke Inoue, Daisuke Miyamoto, Akihiko Soyama, Tomohiko Adachi, Kazuma Kobayashi, Shinichiro Ito, Masaaki Hidaka, Kengo Kanetaka, Susumu Eguchi		
学会名 Conference	The 68th Annual Congress of International College of Surgeons Japan Section		
演題 Topic	A life-saving case report of hemolytic uremic syndrome by performing subtotal colorectal resection		
開催日 date	2023 年 6 月 10 日	開催地 venue	Tokyo
形式 method	<input checked="" type="checkbox"/> 口頭発表 Oral <input type="checkbox"/> ポスター発表 Poster	言語 Language	<input type="checkbox"/> 日本語 <input checked="" type="checkbox"/> 英語 <input type="checkbox"/> 中国語
共同演者名 Co-presenter	Peilin Li; Toshiyuki Adachi; Yusuke Inoue; Satomi Okada; Akihiko Soyama; Tomohiko Adachi; Kazuma Kobayashi; Masaaki Hidaka; Kengo Kanetaka;		
学会名 Conference			
演題 Topic			
開催日 date	年 月 日	開催地 venue	
形式 method	<input type="checkbox"/> 口頭発表 Oral <input type="checkbox"/> ポスター発表 Poster	言語 Language	<input type="checkbox"/> 日本語 <input type="checkbox"/> 英語 <input type="checkbox"/> 中国語
共同演者名 Co-presenter			

4. 受賞(研究業績) Award (Research achievement)

名称 Award name	国名 Country	受賞年 Year of	年 月
名称 Award name	国名 Country	受賞年 Year of	年 月

5. 本研究テーマに関わる他の研究助成金受給 Other research grants concerned with your research theme

受給実績 Receipt record	<input checked="" type="checkbox"/> 有 <input type="checkbox"/> 無
助成機関名称 Funding agency	
助成金名称 Grant name	
受給期間 Supported period	年 月 ~ 年 月
受給額 Amount received	円
受給実績 Receipt record	<input type="checkbox"/> 有 <input type="checkbox"/> 無
助成機関名称 Funding agency	Japanese Society of Gastroenterology
助成金名称 Grant name	JSGE (Japanese Society of Gastroenterology) Overseas Young Physician Study/Training Grant System 2023
受給期間 Supported period	2023 年 4 月 ~ 2024 年 3 月
受給額 Amount received	500,000 円

6. 他の奨学金受給 Another awarded scholarship

受給実績 Receipt record	<input checked="" type="checkbox"/> 有 <input type="checkbox"/> 無
助成機関名称 Funding agency	Nagasaki University
奨学金名称 Scholarship name	2023 Nagasaki University Special Research Student Scholarship
受給期間 Supported period	2023 年 4 月 ~ 2024 年 3 月
受給額 Amount received	600,000 円

7. 研究活動に関する報道発表 Press release concerned with your research activities

※記載した記事を添付してください。Attach a copy of the article described below

報道発表 Press release	<input type="checkbox"/> 有 <input type="checkbox"/> 無	発表年月日 Date of release	
発表機関 Released medium			
発表形式 Release method	・新聞 ・雑誌 ・Web site ・記者発表 ・その他()		
発表タイトル Released title			

8. 本研究テーマに関する特許出願予定 Patent application concerned with your research theme

出願予定 Scheduled	<input type="checkbox"/> 有 <input type="checkbox"/> 無	出願国 Application	
出願内容(概要) Application contents			

9. その他 Others

--

指導責任者(記名) 江口 晋



Feasibility of Organ Transportation by a Drone: An Experimental Study Using a Rat Model

Takahiro Enjoji^a, Akihiko Soyama^{a*}, Masayuki Fukumoto^a, Li Peilin^a, Kunihiro Matsuguma^a, Hajime Imamura^a, Yasuhiro Maruya^a, Takanobu Hara^a, Hajime Matsushima^a, Tota Kugiyama^a, Tomohiko Adachi^a, Masaaki Hidaka^a, Sho Hamamoto^b, Shiro Takashima^c, Takahiro Maeda^d, Kengo Kanetaka^a, and Susumu Eguchi^a

^aDepartment of Surgery, Nagasaki University Graduate School of Biomedical Sciences, Nagasaki, Japan; ^bSoraya Inc., Nagasaki, Japan; ^cAll Nippon Airways Company Limited (ANA) Holdings Inc., Tokyo, Japan; and ^dDepartment of General Medicine, Nagasaki University Graduate School of Biomedical Sciences, Nagasaki, Japan

ABSTRACT

Background. Recently, the successful delivery of organs for transplantation using drones was reported. We investigated the influence of transportation by drones on the quality of liver grafts using a rat model.

Methods. Livers of 12 rats (8 and 32 weeks old) were divided into 2 groups of six. Livers were split into 2 parts and allocated to the drone or control groups (both n = 12). The drone experiment was conducted between islands in Nagasaki Prefecture, Japan. The distance between the islands was 12 km. Livers of the drone group were transported by a multicopter at a speed of 30 km/40 km/h over 60 m above sea level. Transported liver quality was analyzed by histology, and biochemistry data were compared between groups.

Results. Cold ischemia time did not differ between groups (902 min and 909 min, respectively). There were no differences in macroscopic findings regarding coloration and damage between groups. Aspartate aminotransferase (AST), alanine aminotransferase (ALT), and alkaline phosphatase (ALP) in preservation fluid were graft weight-corrected and compared, and no significant differences were found between groups: AST/g (4.61 vs 4.81 IU/L), ALT/g (2.78 vs 2.92 IU/L), and ALP/g (39.1 vs 37.0 IU/L). Immunochemical staining showed no significant difference between groups for terminal deoxynucleotidyl transferase dUTP nick and labeling staining (141 vs 113 cells), CD163 (818 vs 870 cells), and TNF- α (1.25 vs 1.41 scores).

Conclusions. The simulation experiment of organ transport for transplantation by drones was successfully conducted. There were no differences in the quality of livers transported by drones or other means. Further studies including large-animal experiments could lead to future clinical applications.

IN transplantation medicine, the graft ischemic time has a significant effect on outcomes [1–3]. Therefore, it is very important to plan for more appropriate logistics of organ transportation. In Japan, current organ transportation often involves chartered aircraft or helicopters for heart transplants, whereas other organs are often transported using public transport. Thus, the organ transportation system is based on a complex network comprising public transport, private transport, and medical workers in transplantation medicine [4].

If public transport is used, time adjustments are necessary because of the use of scheduled flights. In addition, there is a risk that traffic congestion will affect transportation. Therefore, the timing of organ transplants is often dependent on public transport.

*Address correspondence to Akihiko Soyama, MD, PhD, Nagasaki University Graduate School of Biomedical Sciences, 171, Sakamoto, 852-8501, Nagasaki, Japan. E-mail: soyama@nagasaki-u.ac.jp

The accumulation of time resulting from this complex network can make transplantation impossible [5]. In recent years, pilot clinical studies of organ delivery by unmanned aerial systems were reported to solve these problems [6,7]. Unmanned aerial systems enable faster organ transplantation through smoother connections to aircraft and time saving by avoiding traffic jams [8,9]. They also improve access to transplantation in various situations, such as when major roads are closed to traffic due to accidents or disasters. The availability of unmanned aerial systems may also have the advantage of reducing the risk of accidents associated with the transport of organs for transplantation by transplant physicians and transplant-related staff.

There have been no reports of organ transportation by drones in Japan. In this study, we conducted an experiment to test the feasibility of transplant organ transportation by drones in Japan, using an animal model in cooperation with local governments and companies.

MATERIAL AND METHODS

Animal Model

Livers were obtained from model rats at the Nagasaki University Animal Research Facility (approval number: 211202-1). Twelve male Wistar rats (six 8-week-old and 6 32-week-old rats) were set up as models. Whole livers from model rats were obtained and University of Wisconsin (UW) solution was administered in 40 mL–50 mL flushes through the portal vein to perfuse the liver. The livers were split into 2 parts, weighed, grouped into drone and control groups, and then packed in accordance with the protocol of the Japanese Society for Transplantation (1st layer: 100 mL of UW solution, 2nd layer: 100 mL of saline solution, 3rd layer: no solution). Packed livers were stored in a cold container with ice. The above operations were performed on 12 rats per group. The rats were transported to the drone experiment site by a high-speed jetfoil and car.

Drone Transport Experiment

The experiment was conducted between Fukue Island and Hisaka Island, Goto City. The drone used was a multicopter type with a payload capacity of 5 kg and a maximum flight speed of 10 m/s (Fig 1). The livers in the drone group were transported by drone over a distance of approximately 12 km, whereas those in the control group were transported by high-speed



Fig 1. The six-winged multicopter drone used in this study.

vessel and car. Management and decision-making related to drones, such as drone operation and route determination, were carried out by a team of drone specialists. The criteria for the drone used in this study to be deemed flight-worthy was set at a maximum wind speed of 10 m/sec, and it flew along a predetermined route using autonomous navigation. The drone's position was constantly monitored using a Global Positioning System, and it was programmed to switch to manual control in case of any abnormalities. The transportation time and temperature inside the containers during transportation were recorded. After the transportation experiment between the islands was completed, specimens were transported to the Nagasaki University Experimental Facility by high-speed vessel and car, and the specimens were processed.

Biochemical Examination in Preservation Solution

The UW solution (packing layer 1) was collected after transport, stored at -30°C , and measured for aspartate aminotransferase (AST), alanine aminotransferase (ALT), and alkaline phosphatase (ALP) enzyme activities, which were evaluated as values per liver weight.

Histopathological Analyses

Liver tissues were processed for optical microscopy. For this, specimens were fixed in 4% formaldehyde for 48 hr–72 hr, encased in paraffin, and 5 μm -thick sections were prepared. Hematoxylin-eosin (HE) staining and immunohistochemical (IHC) staining were performed. Immunohistochemical staining was performed with Dako Target Retrieval Solution, Tris/EDTA solution (pH = 9.0), Dako REAL Peroxidase-Blocking Solution (Cat. No. S2023, Agilent Technologies, Santa Clara, CA), Protein Block Serum-Free Ready-to-use (Cat. No. X0909), Dako REAL Antibody Diluent (Cat. No. S2022), and Dako REAL EnVision/HRP secondary antibodies, Rabbit/Mouse (Cat. No. K5007). These procedures were performed in accordance with the protocol provided by Dako. After visualization with diaminobenzidine, the sections were counterstained with hematoxylin. The stained specimens were observed using an Olympus BX53 microscope (Olympus, Tokyo, Japan). The primary antibodies used were as follows: rabbit anti-CD163 antibody (Cat. ab182422, Abcam Inc., Cambridge, MA; 1:500) and anti-TNF- α antibody (Cat. ab220210, Abcam Inc.; 1/500).

Terminal deoxynucleotidyl transferase dUTP nick and labeling (TUNEL) staining was performed using a TUNEL Assay kit (Cat. ab206386, Abcam Inc., Cambridge, MA) in accordance with the manufacturer's instructions.

Histopathological and TUNEL staining evaluation. Hematoxylin-eosin staining was evaluated on the basis of the number of cases with findings of necrosis caused by external damage, balloon-like hepatocytes, and edema.

CD163 and TUNEL staining were evaluated quantitatively by counting the number of positive cells in 5 randomly selected fields of view ($\times 200$). TNF- α was evaluated semiquantitatively by scoring on a 4-point scale (0–3) as follows: 0: no expression, 1: mild overexpression, <25% of hepatocytes, 2: moderate overexpression, 25%–50% of hepatocytes, and 3: high overexpression, >50% of hepatocytes.

Statistical Analysis

The data for continuous variables were expressed as means with standard deviation. Data of biochemical, histopathological, and TUNEL staining data were analyzed by two-tailed *t* test using JMP Pro (SAS Institute Inc., Cary, NC). A *P* value <.05 was considered statistically significant.

Table 1. Liver Weight and Cold Ischemia Time in Each Group

	Drone		Control		P value
	Young	Old	Young	Old	
Age in weeks					
Number of samples	6	6	6	6	-
Liver weight(g)	4.3±0.2	6.9±0.5	9.3±0.4	14.8±2.3	<.01
CIT(min)	895±32	909±26	903±34	915±29	.57

RESULTS

Liver Weight and Cold Ischemic Time

The drone and control groups each consisted of 6 young rat livers and 6 old rat livers. The lighter weight split livers were assigned to the drone group. The mean liver weight was 4.3 ± 0.17 g for young rats and 6.9 ± 0.45 g for old rats in the drone group, and 9.3 ± 0.4 g for young rats and 14.8 ± 2.3 g for old rats in the control group. The mean cold ischemic time was 894 ± 32 min for young rat livers and 909 ± 26 min for old rat livers in the drone group, and 903 ± 34 min for young rat livers and 915 ± 29 min for old rat livers in the control group (Table 1). There was no significant difference in cold ischemia time between the drone and control groups (P = .57).

Temperature inside the container during transport. The outside temperature during the experiment was 12°C-16°C. The temperature inside the container in the drone group was maintained at 0°C-5°C and did not vary depending on the method of transportation (Fig 2).

Biochemical examination of preserved solution samples. The values of AST, ALT, and ALP (per liver weight) in the stored solution of the drone and control groups were AST/g: 4.61 ± 3.06 vs 4.84 ± 1.52 (P = .81), ALT/g: 2.78 ± 2.32 vs 2.92 ± 1.04 (P = .85), and LDH/g: 39.1 ± 31.1 vs 37.0 ± 7.6 (P = .82), respectively (Table 2). There were no significant differences in the AST/g, ALT/g, and ALP/g in the preserved solution between the 2 groups.

Macroscopic findings. Macroscopic findings of the livers after transportation are shown in Fig 3. There were no differences in the macroscopic findings of livers from both groups based on necrosis, color change, or external damage.

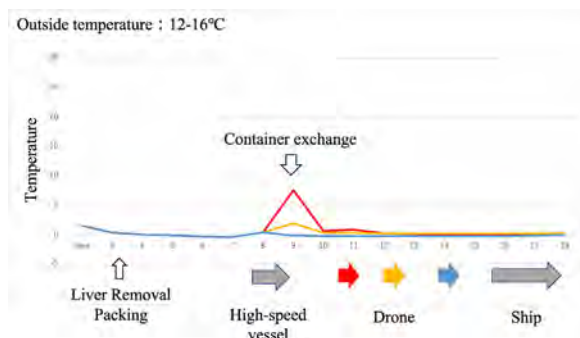


Fig 2. Temperature inside the container. The temperature inside the containers remained constant regardless of the transfer method.

Table 2. Biochemical Analysis

	Drone	Control	P value
AST/g	4.6±3.0	4.8±1.5	.81
ALT/g	2.8±2.3	2.9±1.0	.85
LDH/g	39.1±31.1	37.0±7.6	.82

HE staining. The results of HE staining are shown in Fig 4. There were no findings of necrosis caused by external damage, ballooning hepatocytes, or edema in any of the livers, and no findings suggestive of effects from drone transportation.

TUNEL staining and immunochemical staining. The results of TUNEL staining and immunochemical staining are shown in Fig 5. TUNEL staining showed that the mean quantitative values of the drone and control groups were 141 ± 274 vs 113 ± 211 cells (P = .78), and there was no significant difference between the 2 groups in the assessment of apoptosis. There were no significant differences in the number of Kupffer cells (818 ± 92 vs 870 ± 77 cells; P = .14) or inflammatory markers (CD163 and TNF-α) (1.25 ± 0.45 vs 1.41 ± 0.51 scores; P = .4).

DISCUSSION

An organ transportation experiment was conducted using a drone to transport rat livers. Temperatures were maintained at a constant level during transport, and no adverse effects of drone transportation were observed regarding the physiological or pathologic evaluation of the specimens. There was no significant effect on livers, confirming the safety of organ transportation by drones.

Regarding the current organ transportation system, there are various time issues associated with the use of public transport.

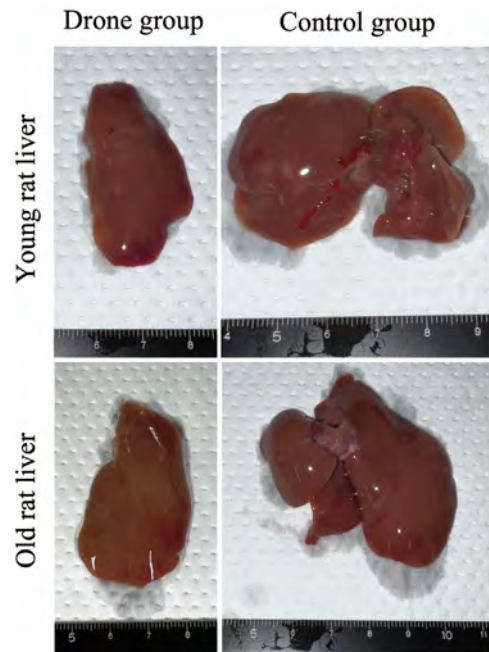


Fig 3. Macroscopic analysis of livers. There were no obvious findings of necrosis, color change, or external damage.

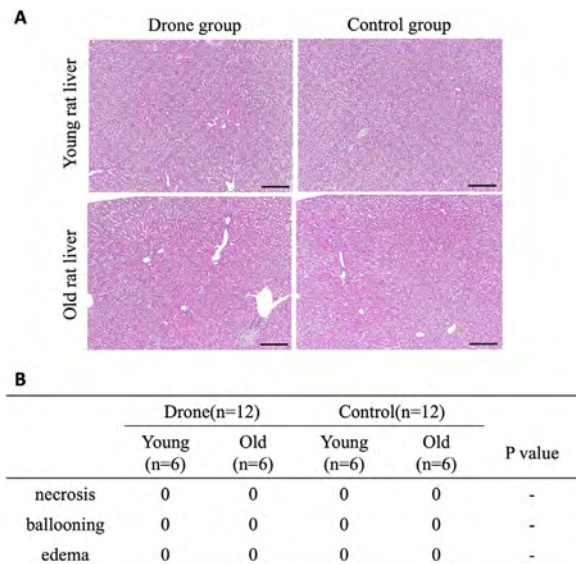


Fig 4. Hematoxylin-eosin (HE) staining. There were no cases of necrosis caused by external influences, balloon-like hepatocytes, or edema. Scale bar, 200 μ m.

For example, staff transporting organs may have to wait because of traffic congestion or lose time because of limited numbers of flights. If drones can be used as a means of organ transportation, they can avoid traffic congestion and connections to scheduled flights in the shortest possible time by taking over the responsibility of transporting the organs from the hospital to the airport. As a result, the cold ischemia time could be shortened. In addition, if future improvements in drone performance enable long-distance, stable flights and direct inter-hospital transport, organ transport will be possible without relying on aircraft time, and further cold ischemia time reduction can be expected.

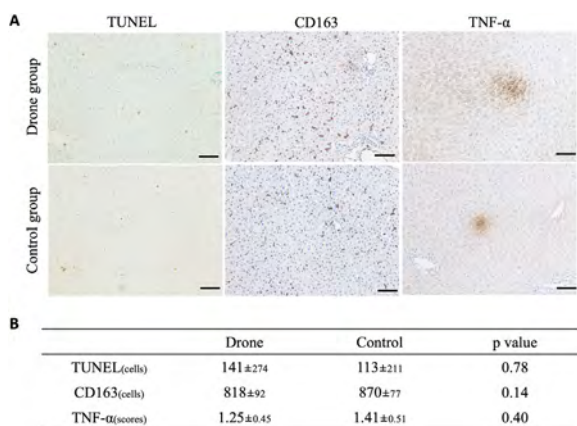


Fig 5. Terminal deoxynucleotidyl transferase dUTP nick and labeling (TUNEL) staining and immunochemical analyses. TUNEL staining and immunochemical staining in young rat livers are shown. No significant differences in staining were found between the drone and control groups. Scale bars, 100 μ m.

Transplant medicine is considered a high-risk procedure in medicine. In 2007, 6 members of the University of Michigan organ transplantation team died during lung transportation [10]. In Japan in 2020, an organ removal team from the University of Tokyo crash-landed while transporting a heart by helicopter, resulting in serious injuries [11]. Thus, the current organ transportation system puts transplantation teams at risk of being involved in accidents. We think that unmanned drones can perform part of this transportation, thereby reducing the risk of accidents to the transplantation team.

In December 2022, the Japanese Civil Aeronautics Law was revised to allow unobserved flights in manned areas if certain conditions are met [12]. This may lead to increased opportunities for drones to be used in the future for the transportation of pharmaceuticals and medical materials, in addition to the delivery of food and other goods. This study provides basic data for considering the feasibility of organ transportation using drones in future transplantation medicine.

Regarding the temperature management of organs during transportation, currently drones do not have temperature control capabilities. Therefore, in this study, we placed a temperature logger inside the container storing the organs and checked the temperature with the logger after landing. Currently, even with conventional means of organ transportation, continuous temperature monitoring is not being conducted. Therefore, if continuous temperature monitoring becomes necessary for organ transportation by drones in the future, the development of a temperature management system would also be required.

The drone used in this study had a maximum payload capacity of 5 kg and was tested using livers from rats. A drone that can withstand a weight of about 10 kg is needed to transport grafted human livers in actual clinical practice. In addition, this experiment involved air transport by a drone over a distance of approximately 12 km. The longest distance achieved in recent drone-based organ transport experiments is approximately 14 km [6,7,13,14]. The safety of long-distance transportation using drones is still not fully understood. In terms of drone logistics, initially focusing on short-distance usage is desirable. Specifically, using drones for transportation between hospitals in urban areas or between hospitals and airports is a viable approach. This allows for the avoidance of risks associated with traffic congestion, disasters, and issues on roads, while enabling smooth connections to limited scheduled flights or charter aircraft. With the future improvement of drone performance and establishment of further safety measures in drone transport, it is anticipated that direct transportation between distant hospitals will become possible. This opens up opportunities for additional research in this field.

In conclusion, this study showed the feasibility of rat organ transport by a drone. Further simulation of organ delivery using larger organs may lead to the clinical use of drones in the future.

DATA AVAILABILITY

All data generated or analyzed during this study are included in this article. Further inquiries can be directed to the corresponding author.

DECLARATION OF COMPETING INTEREST

All the authors declare no known competing financial interests or personal relationships that could have appeared to influence the work reported in this paper.

ACKNOWLEDGMENTS

We thank J. Ludovic Croxford, PhD, from Edanz (<https://jp.edanz.com/ac>) for editing a draft of this manuscript.

REFERENCES

- [1] Wiesner RH, Demetris AJ, Belle SH, Seaberg EC, Lake JR, Zetterman RK, et al. Acute hepatic allograft rejection: incidence, risk factors, and impact on outcome. *Hepatology* 1998;28:638–45.
- [2] Busuttil RW, Farmer DG, Yersiz H, Hiatt JR, McDiarmid SV, Goldstein LI, et al. Analysis of long-term outcomes of 3200 liver transplantations over two decades: a single-center experience. *Ann Surg* 2005;241:905–16; discussion 916–8.
- [3] Totsuka E, Fung JJ, Lee MC, Ishii T, Umehara M, Makino Y, et al. Influence of cold ischemia time and graft transport distance on postoperative outcome in human liver transplantation. *Surg Today* 2002;32:792–9.
- [4] Chow EK, DiBrito S, Luo X, Wickliffe CE, Massie AB, Locke JE, et al. Long cold ischemia times in same hospital deceased donor transplants. *Transplantation* 2018;102:471–7.
- [5] Stewart DE, Kucheryavaya AY, Klassen DK, Turgeon NA, Formica RN, Aeder MI. Changes in deceased donor kidney transplantation one year after KAS implementation. *Am J Transpl* 2016;16:1834–47.
- [6] Scalea JR, Pucciarella T, Talaie T, Restaino S, Drachenberg CB, Alexander C, et al. Successful implementation of unmanned aircraft use for delivery of a human organ for transplantation. *Ann Surg* 2021;274:e282–8.
- [7] Scalea JR, Restaino S, Scassero M, Blankenship G, Bartlett ST, Wereley N. An initial investigation of Unmanned Aircraft Systems (UAS) and real-time organ status measurement for transporting human organs. *IEEE J Transl Eng Health Med* 2018;6:4000107.
- [8] Handford C, Reeves F, Parker P. Prospective use of unmanned aerial vehicles for military medical evacuation in future conflicts. *J R Army Med Corps* 2018;164:293–6.
- [9] Lin CA, Shah K, Mauntel LCC, Shah SA. Drone delivery of medications: review of the landscape and legal considerations. *Am J Health Syst Pharm* 2018;75:153–8.
- [10] Englesbe MJ, Merion RM. The riskiest job in medicine: transplant surgeons and organ procurement travel. *Am J Transplant* 2009;9:2406–15.
- [11] Kotekawa T, Rikimaru S. The Asahi Shimbun. Copter carrying donated heart crash-lands in Fukushima, <https://www.asahi.com/ajw/articles/13094525>; 2020 [accessed 28.01.23].
- [12] MILT Japan. Unmanned aircraft level 4 flight portal site, <https://www.mlit.go.jp/koku/level4/>; 2022 [accessed 28.01.23].
- [13] Conny B, Amy L, Sarah Sonn. Mission GO. MissionGO & Minnesota team transports world's first human pancreas via unmanned aircraft, <https://www.globenewswire.com/news-release/2021/05/11/2227226/0/en/MissionGO-Minnesota-Team-Transports-World-s-First-Human-Pancreas-via-Unmanned-Aircraft.html>; 2021 [accessed 05.07.23].
- [14] Adrianna R. USA TODAY. Drone carries human kidney over Las Vegas desert in what could be the future of organ transportation, <https://www.usatoday.com/story/news/health/2020/09/28/drone-used-transport-human-kidney-airport-las-vegas-nevada/3528614001/>; 2020 [accessed 05.07.2023].

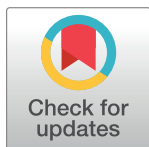
RESEARCH ARTICLE

Therapeutic effect and mechanism of Daikenchuto in a model of methotrexate-induced acute small intestinal mucositis

Peilin Li^{1,2}, Yusuke Inoue¹, Daisuke Miyamoto¹, Toshiyuki Adachi¹, Satomi Okada¹, Tomohiko Adachi¹, Akihiko Soyama¹, Masaaki Hidaka¹, Kengo Kanetaka¹, Shinichiro Ito¹, Daichi Sadatomi³, Sachiko Mogami³, Naoki Fujitsuka³, Weili Gu², Susumu Eguchi^{1*}

1 Department of Surgery, Nagasaki University Graduate School of Biomedical Sciences, Nagasaki, Japan, **2** Department of Surgery, Guangzhou First People's Hospital, School of Medicine, South China University of Technology, Guangzhou, Guangdong, China, **3** Tsumura Kampo Research Laboratories, 2 Tsumura Advanced Technology Research, Tsumura & Co., Ibaraki, Japan

* sueguchi@nagasaki-u.ac.jp



OPEN ACCESS

Citation: Li P, Inoue Y, Miyamoto D, Adachi T, Okada S, Adachi T, et al. (2023) Therapeutic effect and mechanism of Daikenchuto in a model of methotrexate-induced acute small intestinal mucositis. PLoS ONE 18(3): e0283626. <https://doi.org/10.1371/journal.pone.0283626>

Editor: Muhammad Shahid Riaz Rajoka, University of Maryland Baltimore, UNITED STATES

Received: January 11, 2023

Accepted: March 13, 2023

Published: March 30, 2023

Copyright: © 2023 Li et al. This is an open access article distributed under the terms of the [Creative Commons Attribution License](https://creativecommons.org/licenses/by/4.0/), which permits unrestricted use, distribution, and reproduction in any medium, provided the original author and source are credited.

Data Availability Statement: All relevant data are within the paper and its [Supporting Information](#) files.

Funding: This experiment was supported by Tsumura Kampo Research Laboratories, Tsumura & Co. The funder had no role in study design, data collection and analysis, decision to publish, or preparation of the manuscript.

Competing interests: The authors of Peilin Li, Yusuke Inoue, Daisuke Miyamoto, Toshiyuki Adachi, Satomi Okada, Tomohiko Adachi, Akihiko

Abstract

Background

Daikenchuto (DKT) has positive therapeutic effects on improving various gastrointestinal disorders. The present study investigated whether or not DKT has a potential therapeutic effect on chemotherapy-induced acute small intestinal mucositis (CIM) in a rat model.

Methods

Intraperitoneal injection of 10 mg/kg methotrexate (MTX) every 3 days for a total of 3 doses was used for induction of CIM in a rat model. The MTX and DKT-MTX groups were injected with MTX as above from the first day, and the DKT-MTX and DKT groups were administered 2.7% DKT via the diet at the same time. The rats were euthanized on day 15.

Results

The DKT-MTX group showed an improvement in the body weight and conditions of gastrointestinal disorders as well as increased levels of diamine oxidase in plasma and in the small intestinal villi. The pathology results showed that small intestinal mucosal injury in the DKT-MTX group was less severe than that in the MTX group. Immunohistochemistry for myeloperoxidase and malondialdehyde and quantitative real-time polymerase chain reaction (RT-qPCR) for TGF- β 1 and HIF-1 α showed that DKT attenuated peroxidative damage. The crypts in the DKT-MTX group contained more Ki-67-positive cells than MTX group. The zonula occluden-1 and claudin-3 results showed that DKT promoted repair of the mucosal barrier. RT-qPCR for the amino acid transporters EAAT3 and BO+AT also confirmed that DKT promoted mucosal repair and thus promoted nutrient absorption.

Soyama, Masaaki Hidaka, Kengo Kanetaka, Shinichiro Ito and Susumu Eguchi received a research grant from Tsumura & Co. Daichi Sadatomi, Naoki Fujitsuka and Sachiko Mogami are employed by Tsumura & Co. All authors who took part in this study promised to avoid conflicts of interest (even superficial ones) with the company and the research process, and the results conformed to the research specification. All authors undertook to ensure that the personal conduct of all participants was in accordance with the guidelines and to report appropriately when there is a potential for any actual or potential conflict. All the other authors declared no competing interests. The funder provided support in the form of salaries for Daichi Sadatomi, Naoki Fujitsuka and Sachiko Mogami, but did not have any additional role in the study design, data collection and analysis, decision to publish, or preparation of the manuscript. The specific roles of these authors are articulated in the 'author contributions' section.

Conclusion

DKT protected against MTX-induced CIM in a rat model by reducing inflammation, stimulating cell proliferation, and stabilizing the mucosal barrier.

Introduction

Intestinal mucositis (IM) is a common and debilitating side effect of chemotherapy that manifests due to the inability of chemotherapy drugs to differentiate between normal and tumor cells, with the intestinal epithelial cells rapidly proliferating cells and often becoming the target of attack during chemotherapy treatments [1]. Chemotherapy-induced IM (CIM) occurs in as many as 25%-75% of cancer patients receiving different chemotherapy, leading to diarrhea, a decreased quality of life, treatment intolerance resulting in discontinuation, and even death [2]. Due to the complex and diverse clinical symptoms of CIM and the importance of the reducing this toxic complication of chemotherapy, developing new ways to alleviate or prevent CIM is important.

Methotrexate (MTX), a structural analogue of folic acid, is one of the most widely used therapeutic agents for the treatment of the tumors, malignant hematological disorders, and autoimmune diseases [3]. MTX causes inhibition of growth and repair activities of epithelium and mucosa where the dividing and proliferating activities are increased, inducing CIM, which is the main reason for limiting further use of this drug or prompting its use [4].

Daikenchuto (DKT) is a traditional Japanese medicine (Kampo) originally described in a Chinese classic article and independently developed in Japan. It is a mixture of extract powders from dried Japanese pepper, processed ginger, ginseng radix, and malt sugar powder and is reported to have the effects of improving gastrointestinal motility, activating anti-inflammatory, increasing intestinal blood flow, and altering the intestinal microbiome [5,6]. The main mechanism underlying the DKT-mediated contraction and improvement of gastrointestinal motility is modulation of intestinal contraction and relaxation via the release of acetylcholine, nitric oxide, releasing of acetylcholine from cholinergic nerves stimulated by 5-HT₃R and 5-HT₄R and other excitatory neurotransmitters [7,8]. The anti-inflammatory effect of DKT are attributed to the fact that DKT manages the downregulation of cyclooxygenase 2 (COX-2), the upregulation of endogenous adrenomedullin (ADM), and the suppression of eosinophil infiltration [9]. The regulation of intestinal blood flow by DKT is achieved by stimulating epithelial transient receptor potential ankyrin 1 (TRPA1) to induce endogenous ADM release [10]. Recent studies have suggested that DKT can alter the gut microbiota, thereby improving long-lasting dysbiosis and gastrointestinal dysfunction after bowel or liver surgery [11].

In addition to these effects, Wada et al. also demonstrated that DKT enhanced anastomotic healing via an anti-inflammatory effect and increased blood flow after intestinal surgery in rats [12]. DKT has been widely used clinically in patients with gastrointestinal symptoms, such as postoperative intestinal obstruction, inflammatory bowel disease, abdominal pain, and pain accompanied by abdominal flatulence [13–15]. DKT improves gastrointestinal motility disorders and reduces serum C-reactive protein levels in patients with grade B liver injury after hepatectomy and is an effective treatment after hepatectomy for hepatocellular carcinoma [16]. A previous report showed that DKT can suppress the adverse effects associated with irinotecan hydrochloride, an anticancer agent with debilitating side effect of severe diarrhea, and improve the function of tight junction proteins, including zonula occluden-1 (ZO-1), occludin and claudin-4 [17].

The lack of relevant medication for CIM is usually only alleviated by reducing the dose of chemotherapy drugs or stopping chemotherapy, and there is a lack of relevant drugs for complementary or supplementary treatment. Based on existing experiments and recent studies on DKT, we hypothesized that DKT could improve CIM through the above mechanisms. Therefore, the present study investigated whether or not DKT could improve CIM and promote recovery from CIM.

Methods

Animal

Male *Sprague-Dawley rats* (6 weeks, 160–190 g; CLEA Japan Inc., Tokyo, Japan) were used in this study. They were bred and housed at the rat facility in standard rat cages exposing to 12-h light-dark cycles and allowed *ad libitum* access to water and rat chow.

All animal experiments were conducted according to protocols approved by the institutional animal care committee of Nagasaki University and all methods were performed in accordance with the relevant guidelines and regulations of Nagasaki University. The study was reported in accordance with ARRIVE guidelines.

Experimental protocol

All animals were divided randomly into 4 groups: the control group (Col, $n = 5$), MTX-induced model group (MTX, $n = 5$), DKT treatment group (DKT-MTX, $n = 5$), and DKT-only group (DKT, $n = 5$). In the MTX and DKT-MTX groups, MTX was administered (10 mg/kg every 3 days, 3 times total) with intraperitoneal injection. In the MTX-DKT and DKT groups, DKT at 2.7% of the total mass (Tsumura & Co., Tokyo, Japan) mixed in the feed (CE-2 feed; CLEA Japan Inc.) was administered orally from the beginning of the administration of MTX, while the other two groups received non-DKT CE-2 feed. In the control group, the rats were intraperitoneally injected with the same volume of normal saline at the same time.

All rats had their body weight measured every three days. All surviving rats were euthanized by cutting the vena cava to induce exsanguination after abdominal collection of all of the small intestinal tissues under deep isoflurane (Wako Pure Chemical, Osaka, Japan) respiratory anesthesia (All-in-one Anesthetizer, Muromachi Kikai CO. LTD, Japan).

Intestinal histology

The rats were sacrificed under anesthesia at day 15, and the small intestinal tissues were collected immediately. The rat small intestinal tissue was fixed with 4% paraformaldehyde phosphate-buffered solution (PBS; Wako Pure Chemical, Osaka, Japan) for 3 days. Fixed tissues were embedded in paraffin, cut into 5- μm sections, and deparaffinized for standard histological staining with hematoxylin and eosin (HE). HE sections were evaluated blindly for intestinal inflammation, which comprised crypt length, architecture and abscesses, loss of goblet cells, tissue damage, and infiltration of leukocytes and neutrophils.

For immunohistochemistry staining, tissue sections of the small intestines were stained for claudin-3, ZO-1, neutrophil myeloperoxidase (MPO), malondialdehyde (MDA), Ki-67 and diamine oxidase (DAO) (The antibody information were attached to [S1 Table](#)). The percentage of total area of the small intestinal sections was measured using image J Software analysis at least 10 positions.

Quantitative real-time polymerase chain reaction (qRT-PCR)

Tissue samples were acquired at defined time point for mRNA extraction using spin columns according to the manufacturer's instructions (NucleoSpin RNA II; Macherey-Nagel, Duren, Germany). cDNA was synthesized from total RNA using a high-capacity cDNA reverse transcription kit (Applied Biosystems, Tokyo, Japan). In brief, PCR amplification was performed followed by Applied Biosystems (Taq-man was attached to [S2 Table](#)). The gene expression was normalized to that of GAPDH (control intestinal tissue was set as 1.0), and the mRNA expression was determined using the comparative cycle time ($\Delta\Delta C_t$) method.

Determination of plasma DAO activity by an enzyme-linked immunosorbent assay (ELISA)

Plasma of rats was separated in a refrigerated centrifuge and stored at -20°C before determination of the DAO activity using the rat diamine oxidase ELISA Kit (FineTest; ER0895, Wuhan, China) according to the manufacturer's instructions. The DAO activity was calculated according to a standard curve and presented in units/L.

Statistical analyses

At least five rats were used for all experimental groups. The Data of RT-qPCR are represented as mean \pm standard error of the mean from three biological replicates for each sample, while the mRNA sample would be collected at least three samples. The percentage contribution of positivity of IHC was calculated for at least 10 positions by image J Software (ImageJ 1.53k, NIH, USA). The data were expressed as the mean \pm standard error of the mean (S.E.M). Statistical analyses were carried out with the GraphPad Prism software program (GraphPad Software, Inc., California, USA) using a one-way analysis of variance (ANOVA), t-test, or an analysis of variance with repeated measures when appropriate. The survival rate of the rats was shown with Log-rank (Mantel-Cox) test. Asterisks (*) indicate significant differences (* $P < 0.05$, ** $P < 0.01$, by t-test or one-way ANOVA).

Results

DKT can enhance the body weight recovery and ameliorate the symptoms of IM induced by MTX

MTX was used for induction of CIM, and the optimum dose and frequency (10 mg/kg every 3 days, 3 times total) of MTX to induce CIM was determined. The DKT treatment experiment was performed according to the diagram ([Fig 1A](#)). According to the lectures and the recommend dose for patients, 2.7% of the total mass mixed in the feed was administered orally from the beginning of the administration of MTX [18]. The body weight of the rats in the MTX and DKT-MTX groups decreased over time, compared with control group, but after day 12, the body weight of the rats in the DKT-MTX group significantly increased ([Fig 1B](#)). The changes in food intake were similar to those of the body weight, with rats in both the DKT-MTX and MTX groups showing reductions after the administration of MTX, compared to the control group, although values gradually increased in DKT-MTX group after day 12 ([Fig 1C](#)). There was also no significant difference in the survival rate between the MTX group and the DKT-MTX group on day 15 ([Fig 1D](#)).

The MTX group had severe diarrhea by day 15, while the rats in the DKT-MTX group had only slightly soft stool. When the small intestine was observed after euthanasia and opening, the small intestine in the MTX group was observed to be relatively pale in appearance ([Fig 1E](#)). Pathologic changes in the small intestine would be described in detail below.

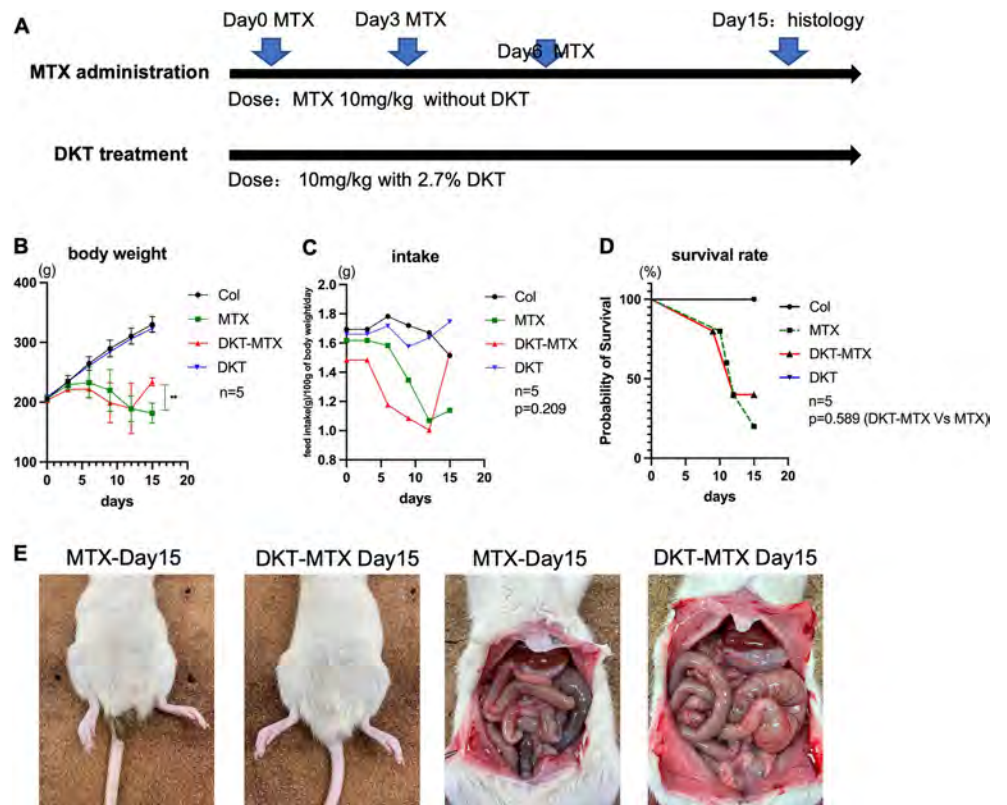


Fig 1. DKT enhanced the body weight recovery and ameliorated the symptoms of IM induced by MTX. (A) The experiment was performed according to the diagram. (B) The body weight of the rats was shown. Data are represented as mean \pm standard error of the mean. One-way ANOVA test, followed by Tukey's multiple comparison test for day15, ns>0.05, **p < 0.001. (C) The food intake of the rats was shown. Data are represented as mean only, Student-t test for day 15 data, DKT-MTX Vs MTX, p = 0.209. (D) The survival rate of the rats in all groups was shown. Log-rank (Mantel-Cox) test, p value = 0.5890. (E) The rats in the DKT-MTX group had no obvious diarrhea, and the intestinal walls of the rats in the MTX group were thinned.

<https://doi.org/10.1371/journal.pone.0283626.g001>

DKT attenuated MTX-induced inflammation and mucosal damage in the small intestinal mucosa

Pathological and inflammation-related factors were used to evaluate the inflammation of the small intestinal mucosa and the therapeutic effect of DKT on acute CIM. HE staining showed that the MTX group had degeneration and vacuolization of the surface and crypt epithelium and villus structure in the jejunum, the digestion and dissolution of epithelial structures, and bleeding and edema in the lamina propria in the ileum. The DKT-MTX group showed the degeneration and vacuolization of the surface and crypt epithelium and villus structure in the jejunum and ileum. There were no marked changes in the control or DKT group (Fig 2A).

Immunohistochemical (IHC) staining for MPO and MDA showed that the DKT-MTX group had a lower percentage contribution of positivity than the MTX group in the jejunum and ileum, although there was no significant difference in the MDA in the jejunum (Fig 2B–2D). RT-qPCR showed that the expression of inflammation-related mRNA of TGF- β 1 was up-regulated in the small intestine of the MTX group, compared with the DKT-MTX and control groups; however, there were no significant changes in the HIF-1 α levels in any groups after DKT treatment (Fig 2E).

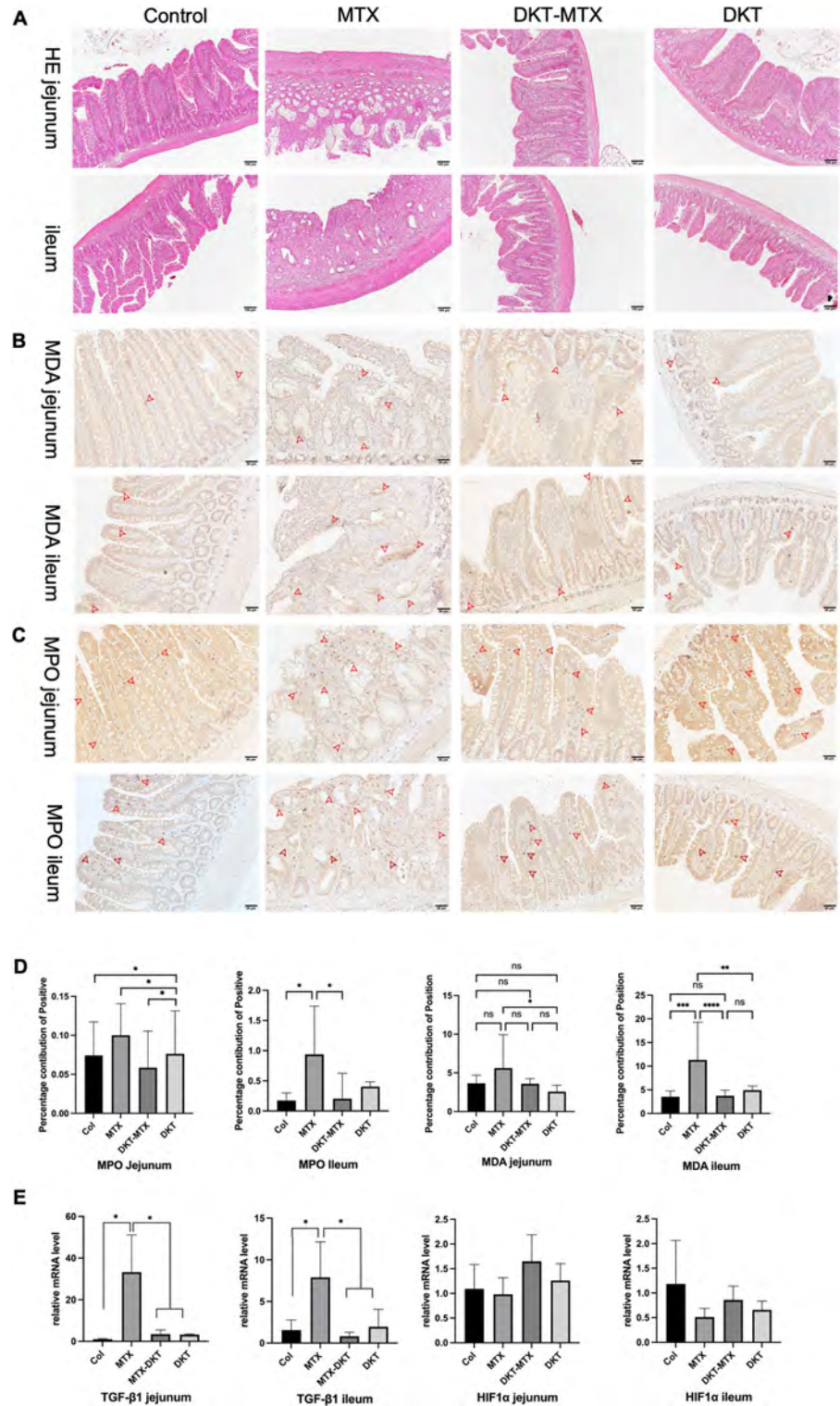


Fig 2. DKT attenuated MTX-induced inflammation and mucosal damage in the small intestinal mucosa. (A) HE staining showed the structural changes in all groups. Scale bar = 100 μ m. (B, C, D) The immunohistochemistry results showed a lower percentage contribution of positivity for (D) MDA (B) and MPO (C) in the jejunum and ileum of the DKT-MTX group than in those of the MTX group. For each criterion, the percentage contribution of positivity was calculated for at least 10 positions. Scale bar = 50 μ m. Data are represented as mean \pm standard error of the mean. One-way ANOVA test, ns>0.05, *p < 0.05. (E) RT-qPCR showed the expression of inflammation-related mRNA of TGF-

$\beta 1$ and HIF-1 α in the four groups. Values were determined relative to GAPDH and presented as fold-change relative to the control group. Data are represented as mean \pm standard error of the mean from three biological replicates. One-way ANOVA test, ns >0.05, *p <0.05.

<https://doi.org/10.1371/journal.pone.0283626.g002>

DKT enhanced small intestinal crypt cell proliferation after administration of MTX

MTX induced small intestinal mucosal epithelial injury by inhibiting the proliferation of small intestinal mucosal crypt cells, which resulted in the suspension of small intestinal mucosal renewal. IHC staining for Ki-67 of the small intestinal tissue was used to evaluate the cell proliferation in the crypts and epithelia of the small intestinal mucosa, which could reflect the repair of the mucosa [19]. After treatment with DKT in the CIM models, the small intestinal mucosal crypts in the DKT-MTX group contained more Ki-67-positive cells than the MTX group (Fig 3A). Positive area counting using the image J software program (NIH, Wisconsin, USA) showed that the DKT-MTX group had a higher percentage contribution of Ki-67 positivity than the MTX group in crypts (Fig 3B). Normal villous crypt ratio (V/C) is 3 to 5:1 [20]. After the rats in the DKT-MTX group were administered with DKT, the small intestinal V/C ratio in the DKT-MTX group was significantly higher than that in the MTX group, which was close to 3 (Fig 3C).

DKT promoted the repair of the mucosal barrier and nutrient absorption functions

DAO can reflect the degree the mucositis induced by MTX. In DKT treatment experiments, the DAO level was decreased in both the MTX and DKT-MTX groups, compared with the control group but gradually recovered after 12 days in the DKT-MTX group (Fig 4A). IHC staining also showed the positions and relative level of DAO in the jejunum and ileum, with statistically significant differences being noted in the jejunum and ileum between the DKT-MTX and MTX groups (Fig 4B and 4C).

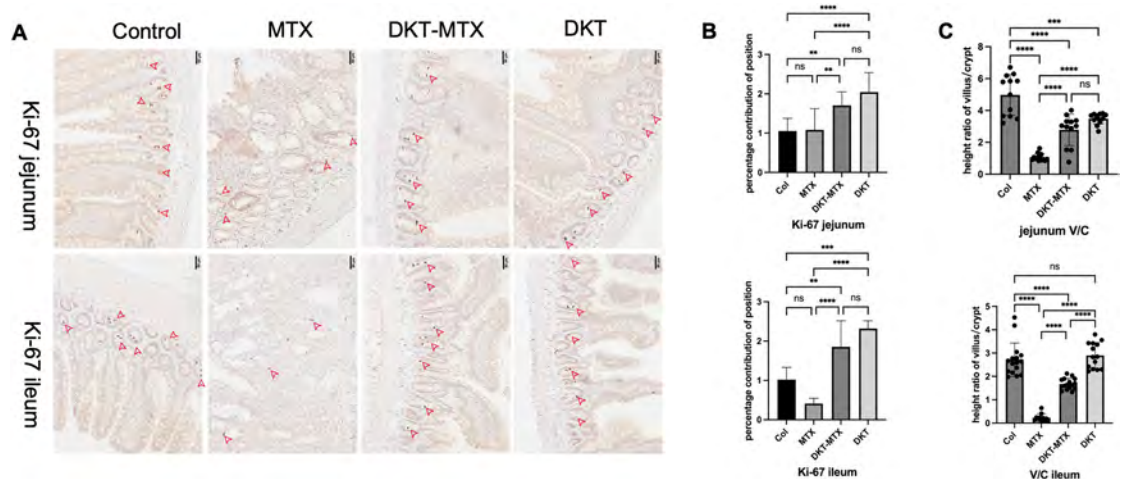


Fig 3. DKT enhanced the small intestinal crypt cell proliferation after the administration of MTX. (A) Immunohistochemical results showed that the small intestinal mucosal crypts in the DKT-MTX group contained more Ki-67-positive cells than the MTX group. (B) The DKT-MTX group had a higher percentage contribution of Ki-67 positivity than the MTX group. Scale bar = 50 μ m. For each criterion, the percentage contribution of Ki-67 positivity was calculated for at least 10 positions using image J software. (C) The high ratio of villus to crypt was measured by image J software. Data are represented as mean \pm standard error of the mean. One-way ANOVA test, ns >0.05, *p <0.05.

<https://doi.org/10.1371/journal.pone.0283626.g003>

To investigate the effect of DKT on the repair of the mucosal barrier function in MTX-induced IM, we examined the ZO-1 protein level in the intestinal tissue by immunofluorescence staining. ZO-1 was predominantly localized along the apical membrane of the intestinal villi in the control, DKT-MTX, and DKT groups. In contrast, a reduction in ZO-1 immunostaining was observed along the apical membrane of the intestinal villi, especially along the ileum, in the MTX group (Fig 4D). Additionally, the tight junction related factor associated to the intestinal permeability, claudin-3, was also investigated. The MTX-treated rats in the MTX group had decreased claudin-3 protein density in the intestinal mucosa, especially in the ileum. The DKT-MTX group had higher claudin-3 protein density in the intestinal mucosa of the rats compared with the MTX group (Fig 4E).

To investigate the effect of DKT on the repair of nutrient absorption function in MTX-induced IM, we examined the expression of genes related to the amino acid transport-related proteins excitatory amino acid transporter 3 (EAAT3) and broad neutral amino acid transporter (BO+AT) in the small intestinal mucosa. The relative gene expression of EAAT3 and BO+AT in the DKT-MTX group was significantly higher than that in the MTX group, especially in the jejunum (Fig 4F).

Discussion

IM is a common side effect of chemotherapy, and with the increasing number of cancer diagnoses and the prevalence of chemotherapy drug use, chemotherapy-associated mucositis has become increasingly common. MTX, as an anti-cancer drug widely used for leukemia and other malignancies, is a structural analogue of folic acid that can inhibit the metabolism of folic acid by competitively inhibiting dihydrofolate reductase, thereby inhibiting the *de novo* synthesis of purines and pyrimidines [21]. Over the past few decades, MTX has been successfully used alone or in combination with other drugs to treat various cancers and autoimmune diseases [22]. Unfortunately, however, due to its multi-organ toxicity, especially in the gastrointestinal system, the therapeutic potential of MTX can be reduced, with the drug typically having to be ceased in response to bone marrow toxicity, cardiotoxicity, nephrotoxicity, and liver toxicity [23,24]. Damage to the gastrointestinal mucosa following MTX treatment in cancer patients includes villus shortening and fusion, epithelial atrophy, crypt loss, inflammatory infiltration of the lamina propria, goblet cell depletion, and barrier dysfunction due to loss of mucosal integrity and reduced nutrient absorption [25].

MTX-induced IM not only causes direct damage by DNA copy inhibition but also induces inflammation and the generation of reactive oxygen species (ROS) [26]. A study has demonstrated that MPO and MDA levels are increased after treatment with MTX, suggesting the possible participation of neutrophil infiltration and ROS in MTX-induced IM [26]. In the present study, we found that levels of MPO, a marker of neutrophil accumulation and infiltration during intestinal mucosa damage, were increased in the epithelial mucosa of rats with IM induced by MTX. Kolli et al. also reported that oxidants such as MDA, which is a product of lipid peroxidation, were increased in MTX-induced small IM [27]. MPO is also an enzyme with peroxidative damage secreted by neutrophils after neutrophil, and it also causes peroxidative damage to tissues. According to our results, oral administration of DKT can inhibit the inflammatory process and ROS damage, as evidenced by the fact that DKT can reduce the production of MPO and MDA.

In addition to peroxidation-related factors, growth factors secreted from mucosa also played a role in this process. TGF- β 1 and HIF-1 α were reported to protect intestinal integrity [28,29]. The mRNA level of TGF- β 1 in the DKT-MTX group was higher than that in the control group on day 15, but it was lower in the jejunum and ileum than in the MTX group. This

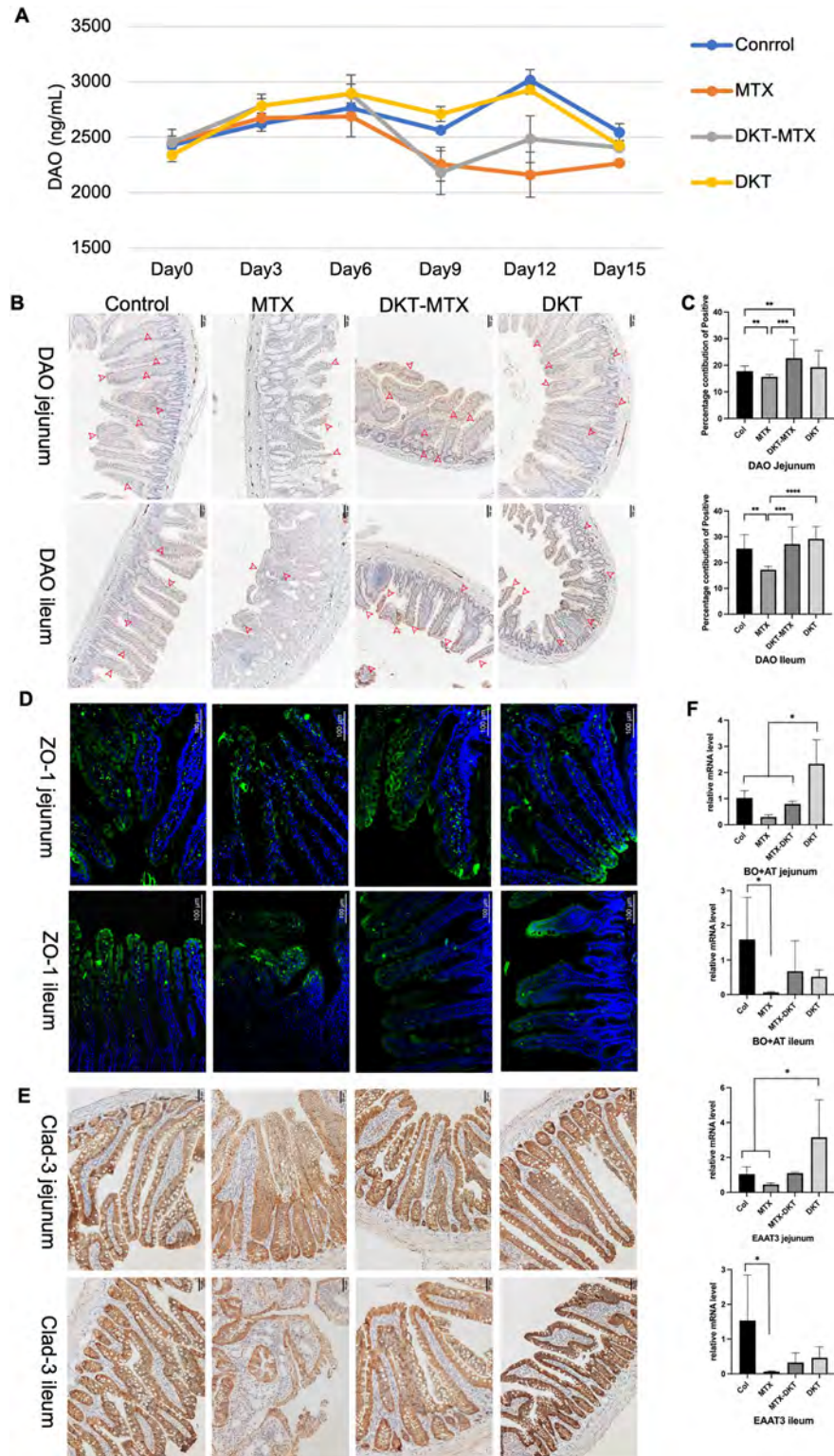


Fig 4. DKT promoted the repair of the mucosal barrier and nutrient absorption functions. (A) The plasma DAO level in the control, MTX, DKT-MTX, and DKT groups. The DAO level decreased in both the MTX and DKT-MTX groups compared with the control group but gradually recovered after day 9 in the DKT-MTX group. Units: ng/ml; DAO, diamine oxidase. (B) Immunohistochemical staining shows the positions and relative level of DAO in the jejunum and ileum of the control, MTX, DKT-MTX, and DKT groups, and (C) the percentage contributions of

positivity are shown. Scale bar = 100 μ m. For each criterion, the percentage contribution of positivity was calculated for at least 10 positions. Data are represented as mean \pm standard error of the mean. One-way ANOVA tests: ns>0.05, *p <0.05. (D) Immunofluorescence staining with the anti-Zo-1 antibody showed the expression and positions of the tight junction protein Zo-1. Bar = 100 μ m, Zo-1, zonula occludens-1. (E) The tight junction related claudin-3 protein associated to the intestinal permeability was investigated by IHC staining. Scale bar = 50 μ m (F) RT-qPCR showed the relative mRNA levels of BO+AT and EAAT3 in the jejunum and ileum. Values were determined relative to GAPDH and presented as fold-change relative to the control group. Data are represented as mean \pm standard error of the mean from three biological replicates. One-way ANOVA: ns>0.05, *p <0.05. EAAT3: Excitatory amino acid transporter 3; BO+AT: Broad neutral amino acid transporter.

<https://doi.org/10.1371/journal.pone.0283626.g004>

method of mucosal repair was also verified in another experiment of DKT in the treatment of intestinal injury repair in rats [12].

The changes in the level and localization of ZO-1 induced by MTX may lead to disorder of the barrier function, which leads to increased intestinal permeability, resulting in intestinal mucosal barrier dysfunction [30]. ZO-1, as a tight junction scaffold protein, has been shown to render structure firmness and impermeability to the junction and functions as a link between occludin and actin, which are the major elements in the structure of the barrier of the small intestine [31]. However, Kuo et al. reported that the tight junction protein ZO-1 was dispensable for the barrier function but critical for intestinal mucosal repair [32]. Furthermore, redistribution of this tight junction function along the lateral plasma membrane sustained the epithelial barrier during cell shedding [33]. In the present study, an immunohistochemical analysis revealed that ZO-1 was predominantly localized along the apical membrane of the intestinal villi in the control and DKT groups. DKT has the potential to promote the expression of ZO-1 in the small intestinal mucosa epithelium to facilitate the repair of tight junctions and improve the mucosal nutrient absorption. These results were also confirmed by the immunostaining of the claudin-3.

The expression of genes related to the amino acid transport-related proteins EAAT3 and BO+AT was up-regulated after the administration of DKT in the DKT-MTX group. A prospective study of the effects of DKT on the blood flow in the superior mesenteric artery and portal vein (PV) reported that DKT may modulate the SMA and PV blood flows by acting on intestinal micro-vessels [34]. The absorption of nutrients around the ileocecal region was related to the blood flow of the intestine and PV. A prospective open-labeled randomized exploratory study also demonstrated that DKT can improve the perioperative nutritional status of patients with colorectal cancer [35].

DAO is a highly active intracellular enzyme in the upper villi of the human and mammalian small intestinal mucosa that plays a role in the metabolism of histamine and various polyamines [36]. Plasma DAO activity was reported to be associated with the degree of small intestinal injury and had potential utility for measuring mucositis during chemotherapy [36,37]. A previous study showed that an increase of DAO activity in the intestine of mature rats leads to an increase in the degree of DAO activity in plasma [38]. In contrast, intestinal mucosal damage caused by hypertonic sodium sulfate solution or atrophy caused by a low-fiber diet reduces plasma DAO activity [39]. In the present study, with the occurrence of MTX-induced IM, the DAO content in rat plasma decreased, and with the onset of gastrointestinal tract symptoms aggravated and reduced to a lower level. In the DKT-MTX group, as DKT promoted the recovery of rat mucosa, the serum content of DAO was also increased. The IHC results also confirmed that the rat small intestinal mucosal epithelial villi of the DKT-MTX group contained higher DAO levels in the mature apical membrane than that in MTX group.

DKT is mainly composed of dried Japanese pepper extract, ginger extract, and ginseng extract. Ginger can reportedly improve ileum damage caused by MTX, shortened villus fusion, inflammatory cell infiltration, and goblet cell depletion [40]. As one of the main components

of DKT, ginger extract has been verified to have a variety of intestinal effects, including anti-inflammatory and antioxidative effects in ulcerative colitis [41]. The mechanism underlying the restoration of the intestinal barrier function by ginger extract involves the increased expression of ZO-1 and claudin-1 protein [42]. Regarding dried Japanese pepper extract (*Zanthoxylum fructus*), there have been articles reporting that *Zanthoxylum fructus* extract inhibits the reduction in mast cell activation by inhibiting sphingosine kinase 1, mainly reducing the release of inflammatory mediators [43]. In research on DKT, it is reported that DKT depolarizes the pacemaker potential of Cajal interstitial cells in an internal or external Ca^{2+} -dependent manner by stimulating the 5-HT₄ and muscarinic M₃ receptors. Its main ingredients are ginseng and ginger root, which help DKT regulate the activity of the intestine and reduce the dysfunction of the small intestine [44]. Some researchers have screened cytoprotective agents against MTX-induced cell genotoxicity from among biologically active phytochemicals and found that agents, such as Siberian ginseng and curcumin have cytoprotective effects [45]. Total ginsenosides was reported to promote intestinal epithelial cell proliferation, presumably via the regulation of the cell cycle and of the expression of proliferation-related proteins by polyamines [46]. Specifically, DKT appears to be less effective in reducing rat mortality due to severe mucosal necrosis but shows marked efficacy in another aspect, such as reducing injury and promoting mucosal repair, as well as improving symptoms. Furthermore, DKT may also have some efficacy against chronic mucositis of the small intestine, so a further investigation regarding chronic mucositis in the clinical setting or as a daily disease will be needed in the future, with particular focus on the therapeutic effect of DKT on chronic mucositis of the small intestine.

In conclusion, DKT may be able to protect against MTX-induced acute small intestinal mucosal injury in a rat model via anti-peroxidation, stimulating cell proliferation, and stabilizing the mucosal barrier. Although DKT comprise numerous chemically diverse compounds with multi-target effects, it has been shown to be able to protect and treat intestinal injury, regardless of administration as a single component or a mixture of multiple components.

Supporting information

S1 Table. List of the first and secondary antibodies in the experiments.

(DOCX)

S2 Table. List of the Taq-man primer of Rt-PCR performed in the experiments.

(DOCX)

Author Contributions

Conceptualization: Peilin Li, Yusuke Inoue.

Data curation: Peilin Li, Daisuke Miyamoto, Satomi Okada, Masaaki Hidaka.

Formal analysis: Peilin Li, Yusuke Inoue, Toshiyuki Adachi, Satomi Okada, Tomohiko Adachi, Kengo Kanetaka, Shinichiro Ito, Weili Gu.

Investigation: Peilin Li.

Methodology: Peilin Li.

Project administration: Peilin Li, Akihiko Soyama, Susumu Eguchi.

Resources: Peilin Li, Daichi Sadatomi, Sachiko Mogami, Naoki Fujitsuka.

Software: Peilin Li.

Supervision: Susumu Eguchi.

Writing – original draft: Peilin Li.

References

1. Dahlgren D, Sjöblom M, Hellström PM, Lennernäs H. Chemotherapeutics-Induced Intestinal Mucositis: Pathophysiology and Potential Treatment Strategies. *Front Pharmacol*. 2021; 12:681417. <https://doi.org/10.3389/fphar.2021.681417> PMID: 34017262
2. Peterson DE, Boers-Doets CB, Bensadoun RJ, Herrstedt J, Committee EG. Management of oral and gastrointestinal mucosal injury: ESMO Clinical Practice Guidelines for diagnosis, treatment, and follow-up. *Ann Oncol*. 2015; 26 Suppl 5:v139–51. <https://doi.org/10.1093/annonc/mdv202> PMID: 26142468
3. Abolmaali SS, Tamaddon AM, Dinarvand R. A review of therapeutic challenges and achievements of methotrexate delivery systems for treatment of cancer and rheumatoid arthritis. *Cancer Chemother Pharmacol*. 2013; 71(5):1115–30. <https://doi.org/10.1007/s00280-012-2062-0> PMID: 23292116
4. Tsukada T, Nakano T, Miyata T, Sasaki S. Life-Threatening Gastrointestinal Mucosal Necrosis during Methotrexate Treatment for Rheumatoid Arthritis. *Case Rep Gastroenterol*. 2013; 7(3):470–5. <https://doi.org/10.1159/000356817> PMID: 24348319
5. Manabe N, Camilleri M, Rao A, Wong BS, Burton D, Busciglio I, et al. Effect of daikenchuto (TU-100) on gastrointestinal and colonic transit in humans. *American journal of physiology Gastrointestinal and liver physiology*. 2010; 298(6):G970–5. <https://doi.org/10.1152/ajpgi.00043.2010> PMID: 20378829
6. Wada Y, Nishiyama M, Uehara H, Sato K, Hamamoto Y, Ogihara H, et al. Microbiome biomarkers associated with the gut contraction response elicited by the Japanese traditional medicine daikenchuto. *Gene*. 2022; 826:146262. <https://doi.org/10.1016/j.gene.2022.146262> PMID: 35257788
7. Kikuchi D, Shibata C, Imoto H, Naitoh T, Miura K, Unno M. Intragastric Dai-Kenchu-To, a Japanese herbal medicine, stimulates colonic motility via transient receptor potential cation channel subfamily V member 1 in dogs. *Tohoku J Exp Med*. 2013; 230(4):197–204. <https://doi.org/10.1620/tjem.230.197> PMID: 23892797
8. Nagano T, Itoh H, Takeyama M. Effects of Dai-kenchu-to on levels of 5-hydroxytryptamine (serotonin) and vasoactive intestinal peptides in human plasma. *Biol Pharm Bull*. 2000; 23(3):352–3. <https://doi.org/10.1248/bpb.23.352> PMID: 10726893
9. Kogure Y, Kanda H, Wang S, Hao Y, Li J, Yamamoto S, et al. Daikenchuto attenuates visceral pain and suppresses eosinophil infiltration in inflammatory bowel disease in murine models. *JGH Open*. 2020; 4(6):1146–54. <https://doi.org/10.1002/jgh3.12410> PMID: 33319050
10. Kono T, Kaneko A, Omiya Y, Ohbuchi K, Ohno N, Yamamoto M. Epithelial transient receptor potential ankyrin 1 (TRPA1)-dependent adrenomedullin upregulates blood flow in rat small intestine. *American journal of physiology Gastrointestinal and liver physiology*. 2013; 304(4):G428–36. <https://doi.org/10.1152/ajpgi.00356.2012> PMID: 23275609
11. Sasaki K, Sasaki D, Sasaki K, Nishidono Y, Yamamori A, Tanaka K, et al. Growth stimulation of Bifidobacterium from human colon using daikenchuto in an in vitro model of human intestinal microbiota. *Sci Rep*. 2021; 11(1):4580. <https://doi.org/10.1038/s41598-021-84167-z> PMID: 33633259
12. Wada T, Kawada K, Hirai K, Toda K, Iwamoto M, Hasegawa S, et al. Enhanced anastomotic healing by Daikenchuto (TJ-100) in rats. *Sci Rep*. 2018; 8(1):1091. <https://doi.org/10.1038/s41598-018-19550-4> PMID: 29348453
13. Eguchi S, Hidaka M, Soyama A, Hara T, Kugiyama T, Hamada T, et al. A Pilot Study Evaluating the Effectiveness and Safety of Daikenchuto (TJ-100) for the Treatment of Postoperative Abdominal Pain or Bloating in Patients Undergoing Hepatectomy: Study Protocol for a Randomized, Open, Controlled Trial. *Kurume Med J*. 2021; 66(3):169–74. <https://doi.org/10.2739/kurumemedj.MS663005> PMID: 34373384
14. Ohbe H, Jo T, Matsui H, Fushimi K, Yasunaga H. Effect of Daikenchuto for Mechanically Ventilated Patients With Enteral Feeding Intolerance: A Propensity Score-Matched Analysis Using a Nationwide Administrative Inpatient Database. *JPEN J Parenter Enteral Nutr*. 2021; 45(8):1703–13. <https://doi.org/10.1002/jpen.2076> PMID: 33483948
15. Kono T, Maejima T, Ono Y, Ito T, Furukawa S, Nishiyama M, et al. Distinct effects of TU-100 (daikenchuto) on long-lasting dysbiosis in the small intestine in patients with colorectal cancer and inflammatory bowel disease. *Gene*. 2022; 820:146266. <https://doi.org/10.1016/j.gene.2022.146266> PMID: 35134471
16. Shimada M, Morine Y, Nagano H, Hatano E, Kaiho T, Miyazaki M, et al. Effect of TU-100, a traditional Japanese medicine, administered after hepatic resection in patients with liver cancer: a multi-center, phase III trial (JFMC40-1001). *Int J Clin Oncol*. 2015; 20(1):95–104. <https://doi.org/10.1007/s10147-014-0678-2> PMID: 24595550

17. Takasu C, Yismaw WG, Kurita N, Yoshikawa K, Kashihara H, Kono T, et al. TU-100 exerts a protective effect against bacterial translocation by maintaining the tight junction. *Surg Today*. 2017; 47(10):1287–94. <https://doi.org/10.1007/s00595-017-1518-6> PMID: 28421347
18. Kong L, Hoshi N, Watanabe D, Yamada Y, Yasutomi E, Adachi S, et al. Effect of Daikenchuto On Spontaneous Intestinal Tumors in Apc(Min/+) Mice. *Kobe J Med Sci*. 2021; 66(4):E139–E48. PMID: 33994517
19. Potten CS, Booth C, Tudor GL, Booth D, Brady G, Hurley P, et al. Identification of a putative intestinal stem cell and early lineage marker; musashi-1. *Differentiation*. 2003; 71(1):28–41. <https://doi.org/10.1046/j.1432-0436.2003.700603.x> PMID: 12558601
20. Serra S, Jani PA. An approach to duodenal biopsies. *J Clin Pathol*. 2006; 59(11):1133–50. <https://doi.org/10.1136/jcp.2005.031260> PMID: 16679353
21. Schmiegelow K. Advances in individual prediction of methotrexate toxicity: a review. *Br J Haematol*. 2009; 146(5):489–503. <https://doi.org/10.1111/j.1365-2141.2009.07765.x> PMID: 19538530
22. Paci A, Veal G, Bardin C, Levêque D, Widmer N, Beijnen J, et al. Review of therapeutic drug monitoring of anticancer drugs part 1—cytotoxics. *Eur J Cancer*. 2014; 50(12):2010–9. <https://doi.org/10.1016/j.ejca.2014.04.014> PMID: 24889915
23. Morsy MA, Ibrahim SA, Amin EF, Kamel MY, Rifaai RA, Hassan MK. Curcumin ameliorates methotrexate-induced nephrotoxicity in rats. *Adv Pharmacol Sci*. 2013; 2013:387071. <https://doi.org/10.1155/2013/387071> PMID: 24381587
24. Perez-Verdia A, Angulo F, Hardwicke FL, Nugent KM. Acute cardiac toxicity associated with high-dose intravenous methotrexate therapy: case report and review of the literature. *Pharmacotherapy*. 2005; 25(9):1271–6. <https://doi.org/10.1592/phco.2005.25.9.1271> PMID: 16164401
25. Maiguma T, Hayashi Y, Ueshima S, Kaji H, Egawa T, Chayama K, et al. Relationship between oral mucositis and high-dose methotrexate therapy in pediatric acute lymphoblastic leukemia. *Int J Clin Pharmacol Ther*. 2008; 46(11):584–90. <https://doi.org/10.5414/cpp46584> PMID: 19000557
26. Kolli VK, Abraham P, Rabi S. Methotrexate-induced nitrosative stress may play a critical role in small intestinal damage in the rat. *Arch Toxicol*. 2008; 82(10):763–70. <https://doi.org/10.1007/s00204-008-0287-9> PMID: 18253714
27. Kolli VK, Abraham P, Isaac B, Kasthuri N. Preclinical efficacy of melatonin to reduce methotrexate-induced oxidative stress and small intestinal damage in rats. *Digestive diseases and sciences*. 2013; 58(4):959–69. <https://doi.org/10.1007/s10620-012-2437-4> PMID: 23053903
28. Saeedi BJ, Kao DJ, Kitzenberg DA, Dobrinskikh E, Schwisow KD, Masterson JC, et al. HIF-dependent regulation of claudin-1 is central to intestinal epithelial tight junction integrity. *Mol Biol Cell*. 2015; 26(12):2252–62. <https://doi.org/10.1091/mbc.E14-07-1194> PMID: 25904334
29. Xiao K, Cao S, Jiao L, Song Z, Lu J, Hu C. TGF- β 1 protects intestinal integrity and influences Smads and MAPK signal pathways in IPEC-J2 after TNF- α challenge. *Innate Immun*. 2017; 23(3):276–84.
30. Hamada K, Shitara Y, Sekine S, Horie T. Zonula Occludens-1 alterations and enhanced intestinal permeability in methotrexate-treated rats. *Cancer Chemother Pharmacol*. 2010; 66(6):1031–8. <https://doi.org/10.1007/s00280-010-1253-9> PMID: 20119715
31. Buckley A, Turner JR. Cell Biology of Tight Junction Barrier Regulation and Mucosal Disease. *Cold Spring Harb Perspect Biol*. 2018; 10(1). <https://doi.org/10.1101/cshperspect.a029314> PMID: 28507021
32. Kuo WT, Zuo L, Odenwald MA, Madha S, Singh G, Gurniak CB, et al. The Tight Junction Protein ZO-1 Is Dispensable for Barrier Function but Critical for Effective Mucosal Repair. *Gastroenterology*. 2021; 161(6):1924–39. <https://doi.org/10.1053/j.gastro.2021.08.047> PMID: 34478742
33. Guan Y, Watson AJ, Marchiando AM, Bradford E, Shen L, Turner JR, et al. Redistribution of the tight junction protein ZO-1 during physiological shedding of mouse intestinal epithelial cells. *Am J Physiol Cell Physiol*. 2011; 300(6):C1404–14. <https://doi.org/10.1152/ajpcell.00270.2010> PMID: 21346149
34. Watanabe S, Inoue M, Miyata M, Boda H. A prospective study of Daikenchuto on superior mesenteric artery and portal venous blood flows in extremely low birthweight infants. *Research Square*; 2022.
35. Fujita F, Torashima Y, Inoue Y, Ito S, Kobayashi K, Kanetaka K, et al. Daikenchuto improved perioperative nutritional status of the patients with colorectal cancer: A prospective open-labeled randomized exploratory study. *Interv Med Appl Sci*. 2019; 11(2):84–8. <https://doi.org/10.1556/1646.11.2019.13> PMID: 32148910
36. Luk GD, Bayless TM, Baylin SB. Plasma postheparin diamine oxidase. Sensitive provocative test for quantitating length of acute intestinal mucosal injury in the rat. *The Journal of clinical investigation*. 1983; 71(5):1308–15. <https://doi.org/10.1172/jci110881> PMID: 6406546
37. Fukudome I, Kobayashi M, Dabanaka K, Maeda H, Okamoto K, Okabayashi T, et al. Diamine oxidase as a marker of intestinal mucosal injury and the effect of soluble dietary fiber on gastrointestinal tract

- toxicity after intravenous 5-fluorouracil treatment in rats. *Med Mol Morphol*. 2014; 47(2):100–7. <https://doi.org/10.1007/s00795-013-0055-7> PMID: 24005798
38. Luk GD, Bayless TM, Baylin SB. Diamine oxidase (histaminase). A circulating marker for rat intestinal mucosal maturation and integrity. *The Journal of clinical investigation*. 1980; 66(1):66–70. <https://doi.org/10.1172/JCI109836> PMID: 6772669
 39. Nakao M, Ogura Y, Satake S, Ito I, Iguchi A, Takagi K, et al. Usefulness of soluble dietary fiber for the treatment of diarrhea during enteral nutrition in elderly patients. *Nutrition*. 2002; 18(1):35–9. [https://doi.org/10.1016/s0899-9007\(01\)00715-8](https://doi.org/10.1016/s0899-9007(01)00715-8) PMID: 11827762
 40. Abdul-Hamid M, Salah M. Intervention of ginger or propolis ameliorates methotrexate-induced ileum toxicity. *Toxicol Ind Health*. 2016; 32(2):313–22. <https://doi.org/10.1177/0748233713500833> PMID: 24097362
 41. Shin JK, Park JH, Kim KS, Kang TH, Kim HS. Antiulcer Activity of Steamed Ginger Extract against Ethanol/HCl-Induced Gastric Mucosal Injury in Rats. *Molecules*. 2020; 25(20). <https://doi.org/10.3390/molecules25204663> PMID: 33066164
 42. Guo XX, Zhang YD, Wang TC, Wang XL, Xu YY, Wang Y, et al. Ginger and 6-gingerol prevent lipopolysaccharide-induced intestinal barrier damage and liver injury in mice. *J Sci Food Agric*. 2022; 102(3):1066–75. <https://doi.org/10.1002/jsfa.11442> PMID: 34309869
 43. Wang X, Kageyama-Yahara N, Hayashi S, Yamamoto T, Kadowaki M. Sphingosine kinase-1-dependent and -independent inhibitory effects of zanthoxyl fructus to attenuate the activation of mucosal mast cells and ameliorate food allergies in mice. *Evid Based Complement Alternat Med*. 2012; 2012:862743. <https://doi.org/10.1155/2012/862743> PMID: 22719791
 44. Kim H, Kim HJ, Yang D, Jung MH, Kim BJ. Depolarizing Effects of Daikenchuto on Interstitial Cells of Cajal from Mouse Small Intestine. *Pharmacogn Mag*. 2017; 13(49):141–7. <https://doi.org/10.4103/0973-1296.196312> PMID: 28216898
 45. Gu S, Wu Y, Yang J. Screening of cytoprotectors against methotrexate-induced cytogenotoxicity from bioactive phytochemicals. *PeerJ*. 2016; 4:e1983. <https://doi.org/10.7717/peerj.1983> PMID: 27190706
 46. Zhu Y, Wang A, Li R, Zhu H, Hu L, Chen W. Total ginsenosides promote the IEC-6 cell proliferation via affecting the regulatory mechanism mediated by polyamines. *Saudi Pharm J*. 2021; 29(10):1223–32. <https://doi.org/10.1016/j.jsps.2021.09.007> PMID: 34744477



OPEN ACCESS

EDITED BY

Nic Davis Leipzig,
University of Akron, United States

REVIEWED BY

Delilah Hendriks,
Hubrecht Institute (KNAW), Netherlands
Soon Seng Ng,
Imperial College London,
United Kingdom

*CORRESPONDENCE

Susumu Eguchi,
✉ sueguchi@nagasaki-u.ac.jp

RECEIVED 29 June 2023

ACCEPTED 10 August 2023

PUBLISHED 21 August 2023

CITATION

Li P, Miyamoto D, Huang Y, Adachi T, Hidaka M, Hara T, Soyama A, Matsushima H, Imamura H, Kanetaka K, Gu W and Eguchi S (2023), Three-dimensional human bile duct formation from chemically induced human liver progenitor cells. *Front. Bioeng. Biotechnol.* 11:1249769. doi: 10.3389/fbioe.2023.1249769

COPYRIGHT

© 2023 Li, Miyamoto, Huang, Adachi, Hidaka, Hara, Soyama, Matsushima, Imamura, Kanetaka, Gu and Eguchi. This is an open-access article distributed under the terms of the [Creative Commons Attribution License \(CC BY\)](https://creativecommons.org/licenses/by/4.0/). The use, distribution or reproduction in other forums is permitted, provided the original author(s) and the copyright owner(s) are credited and that the original publication in this journal is cited, in accordance with accepted academic practice. No use, distribution or reproduction is permitted which does not comply with these terms.

Three-dimensional human bile duct formation from chemically induced human liver progenitor cells

Peilin Li^{1,2}, Daisuke Miyamoto¹, Yu Huang^{1,2}, Tomohiko Adachi¹, Masaaki Hidaka¹, Takanobu Hara¹, Akihiko Soyama¹, Hajime Matsushima¹, Hajime Imamura¹, Kengo Kanetaka¹, Weili Gu² and Susumu Eguchi^{1*}

¹Department of Surgery, Nagasaki University Graduate School of Biomedical Sciences, Nagasaki, Japan,

²Department of Surgery, Guangzhou First People's Hospital, School of Medicine, South China University of Technology, Guangzhou, Guangdong, China

Background: The intrahepatic bile ducts (BDs) play an important role in the modification and transport of bile, and the integration between the BD and hepatocytes is the basis of the liver function. However, the lack of a source of cholangiocytes limits *in vitro* research. The aim of the present study was to establish three-dimensional BDs combined with human mature hepatocytes (hMHs) *in vitro* using chemically induced human liver progenitor cells (hCLiPs) derived from hMHs.

Methods: In this study, we formed functional BDs from hCLiPs using hepatocyte growth factor and extracellular matrix. BDs expressed the typical biliary markers CK-7, GGT1, CFTR and EpCAM and were able to transport the bile-like substance rhodamine 123 into the lumen. The established three-dimensional BDs were cocultured with hMHs. These cells were able to bind to the BDs, and the bile acid analog CLF was transported from the culture medium through the hMHs and accumulated in the lumen of the BDs. The BDs generated from the hCLiPs showed a BD function and a physiological system (e.g., the transport of bile within the liver) when they were connected to the hMHs.

Conclusion: We present a novel *in vitro* three-dimensional BD combined with hMHs for study, drug screening and the therapeutic modulation of the cholangiocyte function.

KEYWORDS

chemically induced progenitor cell, cholangiocyte, bile duct regeneration, bile canaliculi, hepatic organoid

1 Introduction

The liver consists of two types of endodermal epithelial cells, hepatocytes, and biliary epithelial cells (BECs), termed cholangiocytes, which differentiate from hepatoblasts during development (Tanimizu et al., 2013; O'Hara et al., 2013). The BECs form bile ducts (BDs) that connect the liver and the intestine to secrete bile, which is generated in hepatocytes, into the intestine (Alpini et al., 2002). BECs modify and transport the bile produced by hepatocytes so that they can protect the liver from bile-induced damage (O'Hara et al.,

2013). The homeostasis of the connection between the BDs and the hepatocytes is therefore crucial for maintaining a normal liver function and preventing liver damage or disease (Cao et al., 2017). Functional impairment of BECs and the transportation of bile acids play an essential role in the development of various types of biliary disorders and liver failure, which can eventually only be treated by liver transplantation (Strazzabosco et al., 2005). However, the physiology and pathophysiology of cholangiopathies have not yet been fully elucidated (Strazzabosco et al., 2005; Lazaridis and LaRusso, 2015). This is mainly due to the lack of relevant *in vivo* and *in vitro* models for the study of biliary tract development, cholangiopathies and drug assays, especially for bile transport and drainage between BECs and hepatocytes in humans. The shortage of the cell source also limits the *in vitro* study of human BECs (hBECs) and the three-dimensional structural function of the BD (Buisson et al., 2019).

It has been proven to be feasible to use isolated BECs or stem cells as a source to establish a three-dimensional biliary network *in vitro* by bioengineering methods (Ramli et al., 2020; Huang et al., 2021; Sato et al., 2021; Roos et al., 2022; Wang et al., 2022; Yan et al., 2022). Currently, there has been significant improvement in the generation of functional hepatocytes from induced pluripotent stem cells (iPSCs). Several *in vitro* models of human hepatic disease have been established based on iPSCs (Olgasi et al., 2020; Kim et al., 2022; Park et al., 2022; Xu et al., 2022). Some researchers have also used chemically induced pluripotent stem cells to build various hepatocyte and cholangiocyte organoids (Si-Tayeb et al., 2010; Chen et al., 2018; Aizarani et al., 2019; Ramli et al., 2020; Wang et al., 2020; Carberry et al., 2022). Although there has been significant success in the induction of BECs and BD cysts from animal cell sources, the induction of human three-dimensional BDs (hBDs) has not fully progressed (Huang et al., 2020; Ramli et al., 2020; Huang et al., 2021). iPSCs or liver progenitor cells (LPCs) constitute BD epithelial cells, spheroids and biliary tubules in different cultural environments needed the different combinations of growth factors (Tanimizu et al., 2007; Tian et al., 2016). However, iPSCs with altered gene sequences and the isolation of BECs with limited sources still have limited clinical applications, although BECs and biliary organoids have shown great value in the treatment of biliary disease (Sampaziotis et al., 2021; Velazquez and Ebrahimkhani, 2021). Additionally, the present studies of BDs constructed *in vitro* usually ignore the relationship between BDs and hepatocytes. Hepatotoxicity studies based on hepatocytes are basically studies of the hepatocyte culture models or cystic hepatic organoids (Li et al., 2022; Park et al., 2022). Cystic organoids contain BECs and hepatocytes and exhibit corresponding characteristic cell functions. The multicellular tissue of BD combined with hepatocytes is a hepatic organoid that can represent the physiological state.

Katsuda et al. used a small molecule cocktail to chemically induce rodent mature hepatocyte (rMH) dedifferentiation into chemically-induced liver progenitor cells (CLiPs) with bidirectional differentiation potential of MHs and BECs, and on this basis, they and other researchers developed methods for human MHs (hMHs) (Katsuda et al., 2017; Katsuda et al., 2019; Kim et al., 2019). Human CLiPs (hCLiPs), chemically induced from hMHs, offer an appreciated cell source for regenerative medicine (Katsuda et al., 2019). The dilative and proliferative ability and bidirectional

differentiation potential of hCLiPs bring considerable prospects for the treatment of end-stage liver disease. Huang et al. established biliary duct-like structure integrated hepatocyte tissues from rCLiPs, providing an excellent *in vitro* model for hepatobiliary disease research but not for humans (Huang et al., 2020; Huang et al., 2021). The BD-hepatocyte connected tissue as a cocultured organoid model provides a model for studying the integrated BD-hepatocyte and hepatocyte-cholangiopathy *in vitro*, which can be used to study the transport of bile and establish *in vitro* disease models.

In this study, the primary aim was to utilize hCLiPs to establish functional hepatic tissue with a three-dimensional BD connected to the hMHs. The connected tissue exhibits both structural and functional characteristics similar to BD-hepatocyte transporters and bile canaliculi. The interconnected tissue was capable of performing the crucial functions of bile transportation, collection, and delivery.

2 Methods

2.1 Cell culture and conversion

Human Cryo-Hepatocytes (CHHs) (Lot.416, Corning, Woburn, MA, United States) were seeded into collagen type-I-coated dishes (Asahi Techno Glass, Tokyo, Japan) at a density of 2×10^4 cells/cm² in STIM medium to promote attachment to the plate surface. The STIM medium was a hepatocyte culture media kit with 10 ng/μL epidermal growth factor (EGF) containing 1x penicillin–streptomycin–glutamine (100X) (Gibco™, Tokyo, Japan) and 10% fetal bovine serum (FBS, Gibco™, Tokyo, Japan). Four hours later, the culture medium was changed to small chemically reprogrammed culture medium. The small chemical reprogramming culture medium was DMEM/F12 containing 2.4 g/L NaHCO₃ and L-glutamine (Life Technologies, Tokyo, Japan) and supplemented with 5 mM HEPES, 30 mg/L L-proline, 0.05% BSA, 10 ng/mL EGF (all from Sigma–Aldrich Japan, Tokyo, Japan), insulin–transferrin–serine (ITS)-X (Life Technologies, Tokyo, Japan), 10–7 M dexamethasone (Dex) (Fuji Pharma Co. Ltd., Tokyo, Japan), 10 mM nicotinamide (Sigma–Aldrich, Tokyo, Japan), 1 mM ascorbic acid-2 phosphate (Wako Pure Chemical, Osaka, Japan), 100 U/mL penicillin, and 100 mg/mL streptomycin (Life Technologies, Tokyo, Japan) in addition to two small chemical molecules of 0.5 μM A-83-01 (Wako Pure Chemical, Osaka, Japan), 3 μM CHIR99021 (A10199, AdooQ BioScience, Irvine, CA, United States) and 10% FBS, which would be called FAC medium. The culture medium was changed 1 day after seeding and every two/3 days thereafter. It takes 14–16 days to generate hCLiPs at up to 90% confluence from CHHs.

2.2 Removal of fibroblasts and subculture of hCLiPs

The cultured cells reached $\geq 90\%$ confluence and were treated with TrypLE Express (Life Technologies, Tokyo, Japan) for 15–20 min. The hCLiPs were expanded with an equivalent volume of preculture medium, and the cells were transferred to a 15 mL conical tube and centrifuged at 220 g for 5 min. The cell pellet was resuspended in 5 mL of culture medium, and the total number of cells and percent viability were determined using a

hemocytometer. The isolated hCLiPs were seeded onto gelatin-coated culture plates (Asahi Techno Glass, Tokyo, Japan) at a density of 5.0×10^4 cells/cm² and incubated for 60 min. The cells in the medium were isolated and seeded onto collagen-coated plates at a density of 5.0×10^4 cells/cm² and incubated for 10 min. After 10 min, the cells were isolated and seeded onto collagen-coated plates at a density of 1.0×10^4 cells/cm². The cells seeded onto the third collagen-coated plates achieved an appreciable purity. This method was derived from the published patent [JP2020-162551 (P2020-162551A)].

2.3 Human BD formation from hCLiPs

BDs were differentiated and formed from hCLiPs as previously reported (Huang et al., 2021). Briefly, 1–2 days before collecting the hCLiP suspension, we used embryonic fibroblast feeder cells (MEFs) (Cat #PMEF-N, Merck Millipore, Billerica, MA United States) to form an MEF feeder layer by seeding $1\text{--}2 \times 10^5$ cells on collagen-coated 12-well plates (approximately 3×10^4 cells/cm²) in DMEM containing 10% FBS. We plated the dissociated hCLiP suspension onto the MEF feeder layer at a density of $4\text{--}5 \times 10^5$ cells/well (1.2×10^5 cells/cm²) in FAC medium for cell attachment for 1 day. Thereafter, we replaced the medium with BEC induction medium (BIM), which was mTeSR™1 Complete Kit (Catalog #85850, STEMCELL Technologies, Tokyo, Japan), including mTeSR™1 basal medium supplemented with TeSR™1 5X supplement, with the addition three small chemical molecules of 10 μM Y-27632, 0.5 μM A-83-01, 3 μM CHIR99021, hepatocyte growth factor (HGF, Sigma–Aldrich Japan, Tokyo, Japan) and EGF, every 2 days for 6 days, followed by BIM supplemented with 2% growth factor reduced Matrigel (Catalog 354230, Corning, Bedford, United States) for an additional 6–10 days, to facilitate the maturation of BECs and the formation of biliary structures.

2.4 Integrated BD structure to human hepatocytes

We plated CHHs onto three-dimensional BD at a density of 1×10^5 cells/12-well plate (2.5×10^4 cells/cm²) for 1 day in hepatocyte-defined medium (Catalog 05449, Corning, Bedford, United States) supplemented with 10 μg/mL EGF and 10% FBS. We then replaced it with BIM supplemented with 2% Matrigel for another 2–4 days. The BD was automatically attached with hepatocytes with bile canaliculi to the biliary cells.

2.5 Gene expression analysis by quantitative reverse-transcription polymerase chain reaction (qRT–PCR)

Samples were cultured in dishes under various conditions, and mRNA was extracted using a spin column (NucleoSpin RNA II; Macherey-Nagel, Düren, Germany). Synthesis of cDNA was performed using a high-capacity cDNA reverse transcription kit (Applied Biosystems, Tokyo, Japan). Samples were then stored at -20°C until their analysis by polymerase chain reaction (PCR),

which was performed using an Applied Biosystems StepOne Plus Real-time PCR System with TaqMan Gene Expression Assay Kits (Applied Biosystems, Tokyo, Japan) according to the manufacturer's instructions. Briefly, PCR mixtures contained 1 μL of cDNA, 1 μL of TaqMan Gene Expression Assay probe, 5 μL of TaqMan Fast Advanced Master Mix (both from Applied Biosystems), and 13 μL of nuclease-free water. All TaqMan gene primers are listed in [Supplementary Table S1](#). The thermocycling conditions were 95°C for 20 s followed by 40 cycles of 95°C for 1 s and 60°C for 20 s. Expression levels were quantified using the comparative cycle time method. Cycle threshold (Ct) values were automatically determined by the Applied Biosystems StepOne Plus Real-Time PCR System, and fold changes in gene expression were calculated by the $2^{(-\Delta\Delta\text{CT})}$ method. Expression levels were normalized to those of the housekeeping gene and internal control glyceraldehyde 3-phosphate dehydrogenase (GAPDH).

2.6 Immunofluorescence

Cultured cells were fixed with 4% paraformaldehyde in phosphate-buffered saline (PBS) (Wako Pure Chemical, Osaka, Japan) for 10 min. Fixed samples were then incubated in 0.1% Triton X-100 (Sigma–Aldrich, Tokyo, Japan) in PBS for 10 min and blocked in PBS containing 1% BSA for 1 h at room temperature. The cells were then incubated with primary antibodies diluted in PBS+1% BSA at 4°C overnight. After washing with PBS three times, they were incubated with appropriate secondary antibodies diluted in PBS+1% BSA for 2 h. All primary and secondary antibodies are listed in [Supplementary Table S2](#). Nuclei were stained with 4',6-diamidino-2-phenylindole (DAPI) (DOJINDO, Kumamoto, Japan) for 30 min. They were washed for three times in PBS up to 30–60 min. Fluorescence and bright-field images were captured using a microscope (Ti-U and C-HGFI, Nikon, Tokyo, Japan).

2.7 Rhodamine 123 assay

The rhodamine 123 assay was performed. We incubated the cells with Hanks' balanced salt solution (HBSS) containing 100 μM rhodamine 123 (both from Sigma–Aldrich, Tokyo, Japan) for 30 min at 37°C and washed them with HBSS twice. To inhibit the transporter activity of multidrug-resistance protein 1 (Mdr1), we incubated the cells with 20 μM verapamil (Tokyo Chemical Industry Co., Ltd. Tokyo, Japan) at 37°C for 2 h before adding rhodamine 123. Fluorescence and bright-field images were captured using a microscope (Ti-U and C-HGFI, Nikon, Tokyo, Japan).

2.8 Definition of the biliary lumen by cell-tracking staining

Because of the functionality of the hCLiP-derived biliary-duct-like structures, they were able to metabolize a cell-tracking dye to ascertain the extent of the biliary lumen. Therefore, we used the sequential cell-tracking staining method to determine the tubular lumen in the induced biliary duct structures. Briefly, the induced

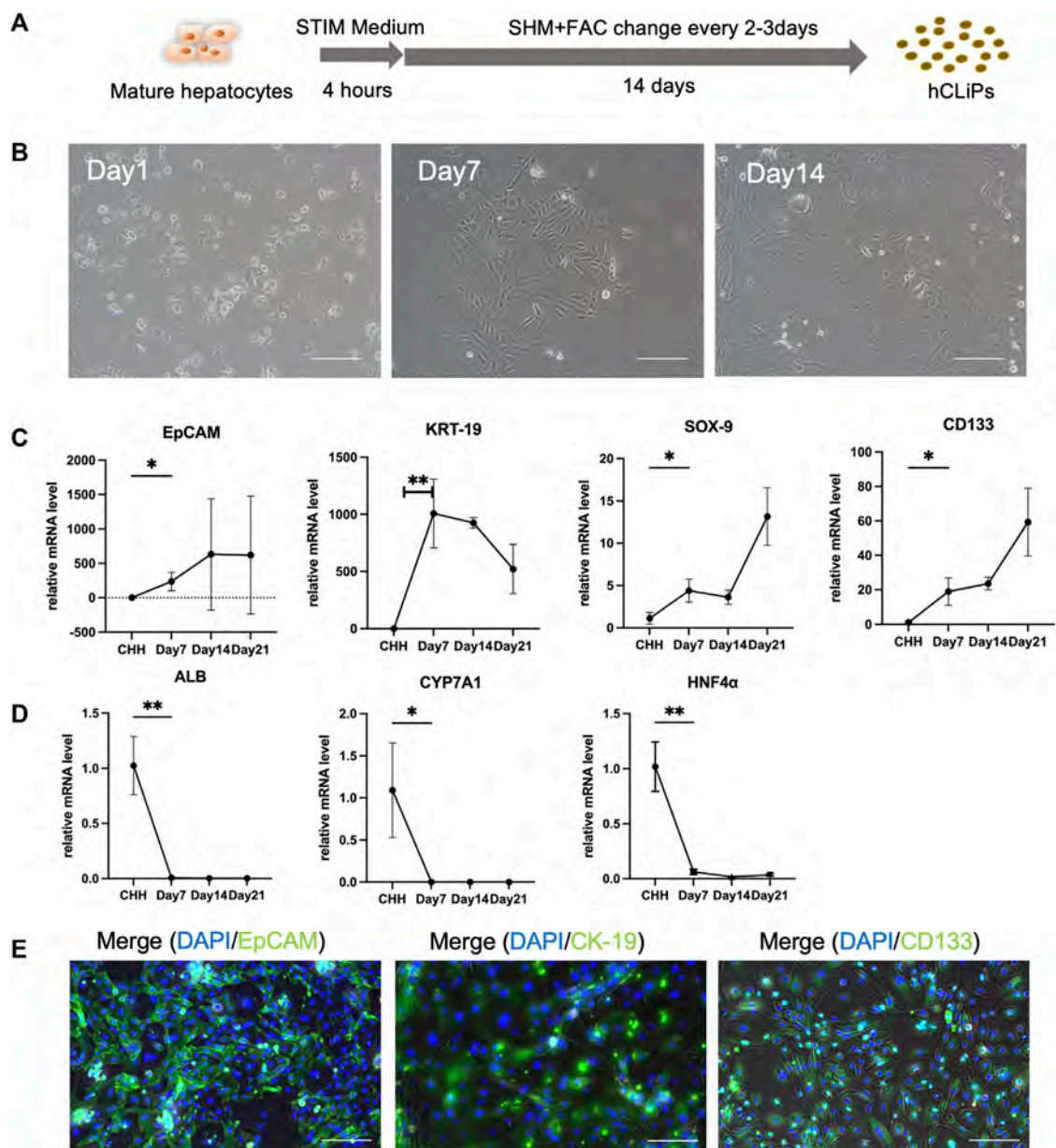


FIGURE 1

FAC medium converted human cryohepatocytes into hepatic progenitor cells. (A) FAC medium could induce human mature hepatocytes (MHs) into chemically induced liver progenitor cells (hCLiPs). (B) The morphology of the MHs gradually changed during 2 weeks of FAC culture. Scale bar = 100 μ m. (C, D) RT-qPCR analysis showed that the hepatic progenitor cell (LPC)-related markers EpCAM, KRT-19, SOX-9, and CD133 gradually increased ($n = 3-6$), while the MH markers ALB, CYP7A1, and HNF-4 α gradually decreased, which indicated that MHs were transferred to the hCLiP ($n = 3-6$). Data represent the mean values. Student's t-test, * $p < 0.05$, ** $p < 0.01$. (E) Immunofluorescence staining of transformed cells was performed on day 14, and the cells expressed the LPC-related markers EpCAM, CK-19, and CD133. Scale bar = 200 μ m.

biliary structures were incubated with 100 μ M rhodamine 123 dye for 10 min at 37°C. Subsequently, the biliary-duct-like structures were cultured in BIM-2 medium (BIM-1 supplemented with 2% Matrigel) for 48 h, followed by incubation with 10 μ M cell tracker orange (CTO, C34551; Invitrogen, Tokyo, Japan) dye for 10 min at 37°C. After washing twice with HBSS, images were captured using a microscope (Ti-U and C-HGFI, Nikon, Tokyo, Japan).

2.9 Cholyl-lysyl-fluorescein (CLF) dye assay

We loaded the cells with 1 μ M CLF (Corning Life Sciences, Bedford, United States) for 30 min at 37°C and washed them twice with HBSS. We observed the cells and captured images using a confocal microscope. We replaced the cell medium with BIM medium to keep the cells alive for an extended period.

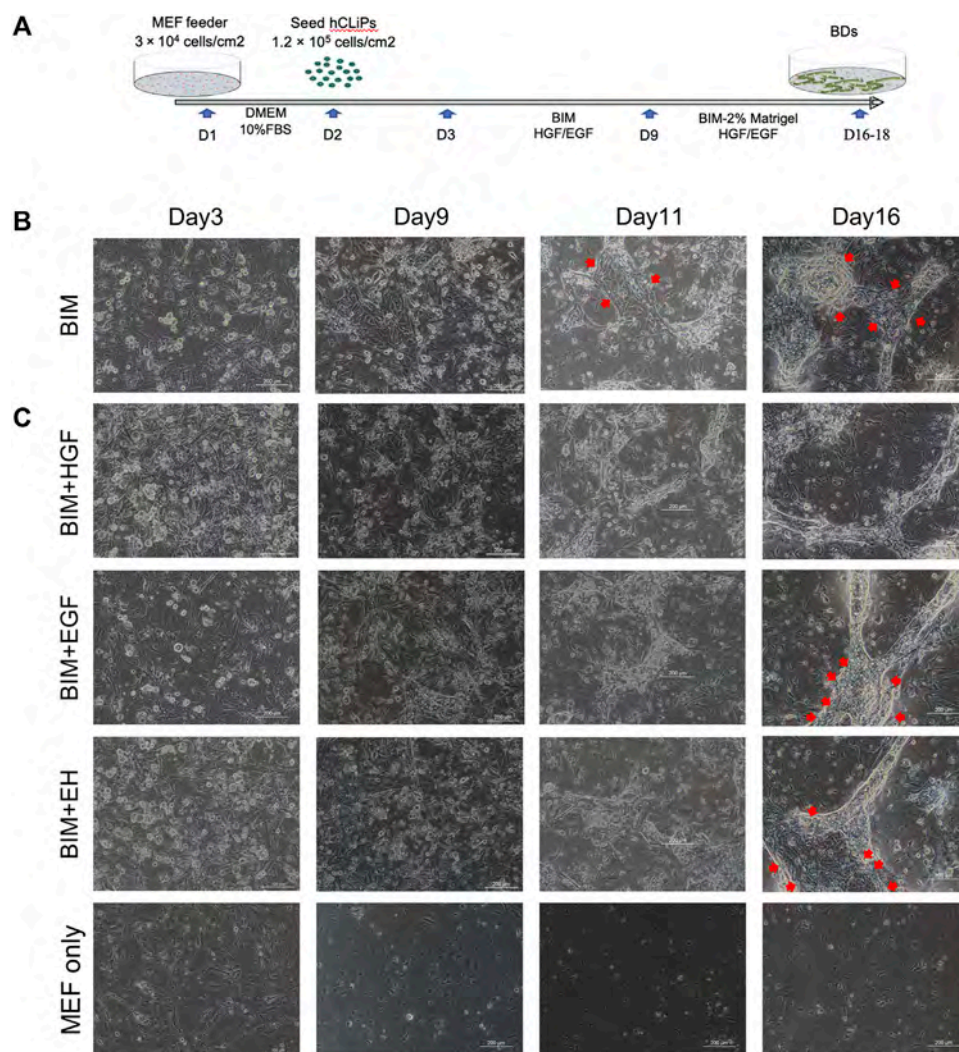


FIGURE 2

HGF promoted bile duct (BD) formation in three-dimensional culture. (A) Embryonic fibroblast feeder cells (MEFs) were used as a layer, and Matrigel was used to construct a three-dimensional culture environment as extracellular matrix (ECM) to induce the hCLiPs to create three-dimensional BDs in a two-step method. (B) The bile duct-induced medium (BIM) to induce BD from hCLiP was inefficient (the red arrow shows the untransformed cells). Scale bar = 200 μm . (C) In BIM, BIM + EGF, and BIM + EH, BDs were mixed with pieces of hCLiPs or transformed BECs, while BIM with HGF was more effective for forming BDs. Scale bar = 200 μm .

2.10 Statistical analysis

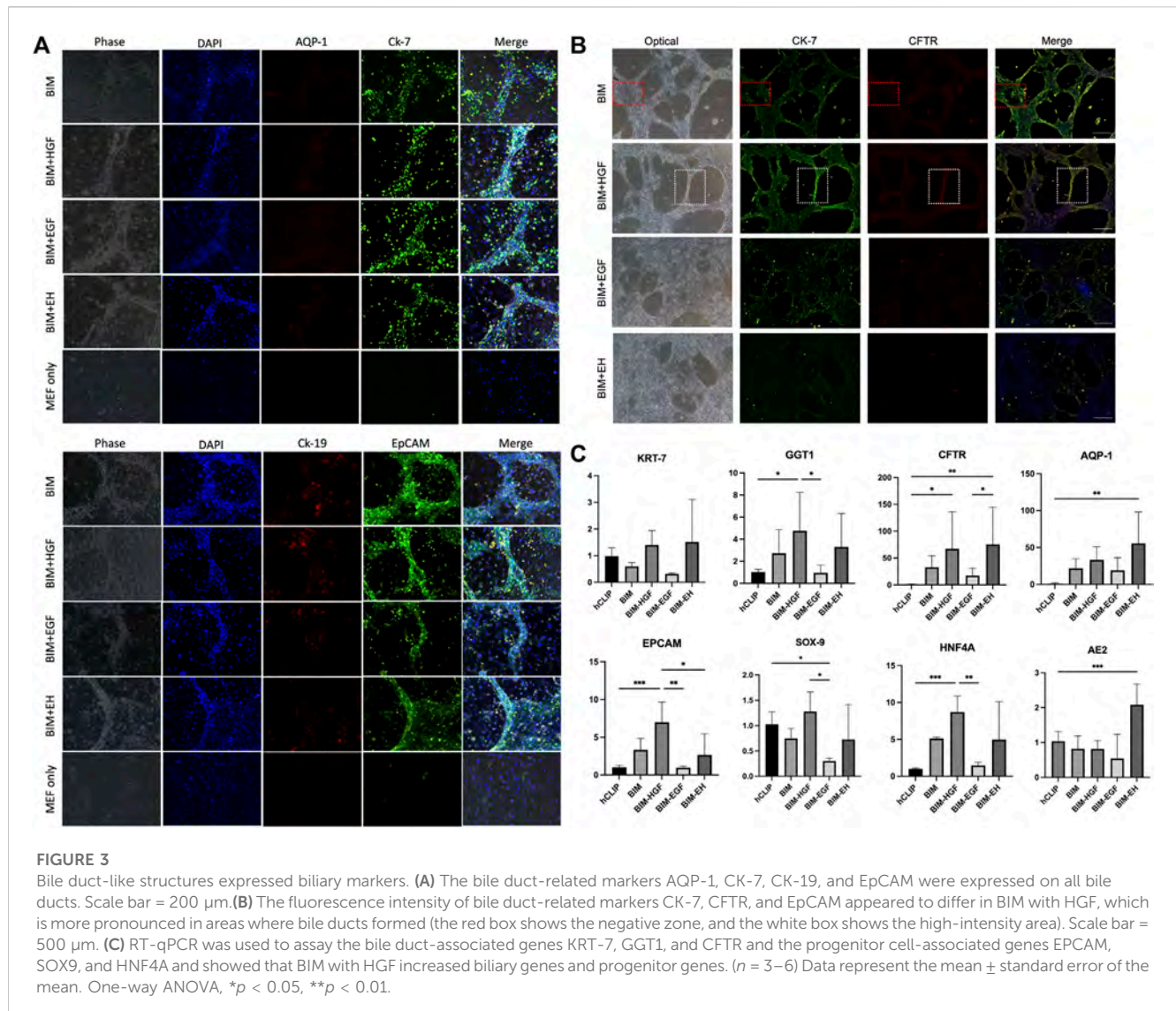
Statistical analyses were performed, and graphs were made using GraphPad Prism 8.0 (GraphPad Software Inc., San Diego, CA, United States). Data were analyzed by Student's *t*-test or a one-way ANOVA. Details of the statistical analyses and the associated values are described in the respective figure legends.

3 Results

3.1 FAC medium converted human cryo-hepatocytes into hepatic progenitor cells

The transformed cells, CHH, were utilized in the experiments and showed significant morphological changes after just 3 days of culture. Notably, the transformed cells displayed a higher capacity for

proliferation compared to primary hepatocytes, achieving approximately 90% confluence within 14 days of culture (Figures 1A, B). Additionally, the proliferation of fibroblasts on the heterogeneous culture plate could be observed (Supplementary Figures S1A, B). The mRNAs of the transformed cells were extracted, and RT-qPCR was used to analyze the gene expression of the hepatocytes and LPCs. The results of Rt-qPCR confirmed that in transformed cells, the expression of LPC-related genes, including EpCAM, KRT-19, SOX-9, and CD133 (Figure 1C), and fibroblast-related genes, including ACTA2, TGF- β 2 and MMP2, was gradually upregulated (Supplementary Figure S1C), while the relative gene expression of Alb, CYP7A1 and HNF4 α in MHs was gradually downregulated (Figure 1D). Moreover, the transformed cells expressed the LPC protein markers EpCAM, CK-19 and CD133, while the heterogeneous cells expressed the α -SMA protein (Figure 1E; Supplementary Figure S1C). The data suggested that these transformed cells converted from CHH by a small molecule cocktail with FAC medium were LPCs.



3.2 HGF promoted BD formation in three-dimensional culture

Three-dimensional BD formation was induced by a two-step method in a three-dimensional environment established with MEFs and Matrigel (Figure 2A). Since the direct use of BIM to induce BDs from hCLiPs was not efficient (Figure 2B), we introduced the growth factors HGF and EGF as supplements of BIM. (Tanimizu et al., 2007; Anzai et al., 2016; Kim et al., 2019). In heterogeneous cell culture dishes that induce hepatic progenitor cells, it is imperative to remove a large number of mixed fibrotic cells (Singh et al., 2013). It has been previously reported that many fibrotic cells produced during the induction of MHs are isolated using different culture medium (Miyoshi et al., 2022). When using hCLiPs to generate BDs, fibroblasts affect the formation of BD due to the rapid proliferation of fibroblasts (Supplementary Figure S2A), and the hCLiPs were enriched in purity without damage by multiple subcultures (Supplementary Figure S3A-C). BIM with HGF or EGF could generate BDs in 3D culture earlier (Day 11) in

comparison to BIM alone. BIM with HGF was more effective in inducing the transformation of hCLiPs into BECs and the formation of BD tubular structures. In BIM, BIM with EGF, BIM with EH, BD were mixed with pieces of hCLiPs or transformed BECs (Figure 2C).

All four groups were subjected to immunofluorescence microscopy to determine whether the induced biliary-like structure was the BD structure. AQP-1, CK-7, CK-19, and EpCAM (BD-related markers) were expressed on all BDs (Figure 3A), but the fluorescence intensity of CK-7, CFTR, and EpCAM appeared to differ. This was more pronounced in areas where BDs formed (Figure 3B; Supplementary Figures S4). As described above, BD-associated proteins are more pronounced in regions of BD-like formation, and the condition of 3D culture supply with HGF is more helpful in inducing hCLiPs to form 3D BDs. This was also confirmed by RT-qPCR results for BD-associated genes (KRT-7, GGT1, and CFTR) and progenitor cell-associated genes (EPCAM, SOX9, and HNF4A) (Figure 3C).

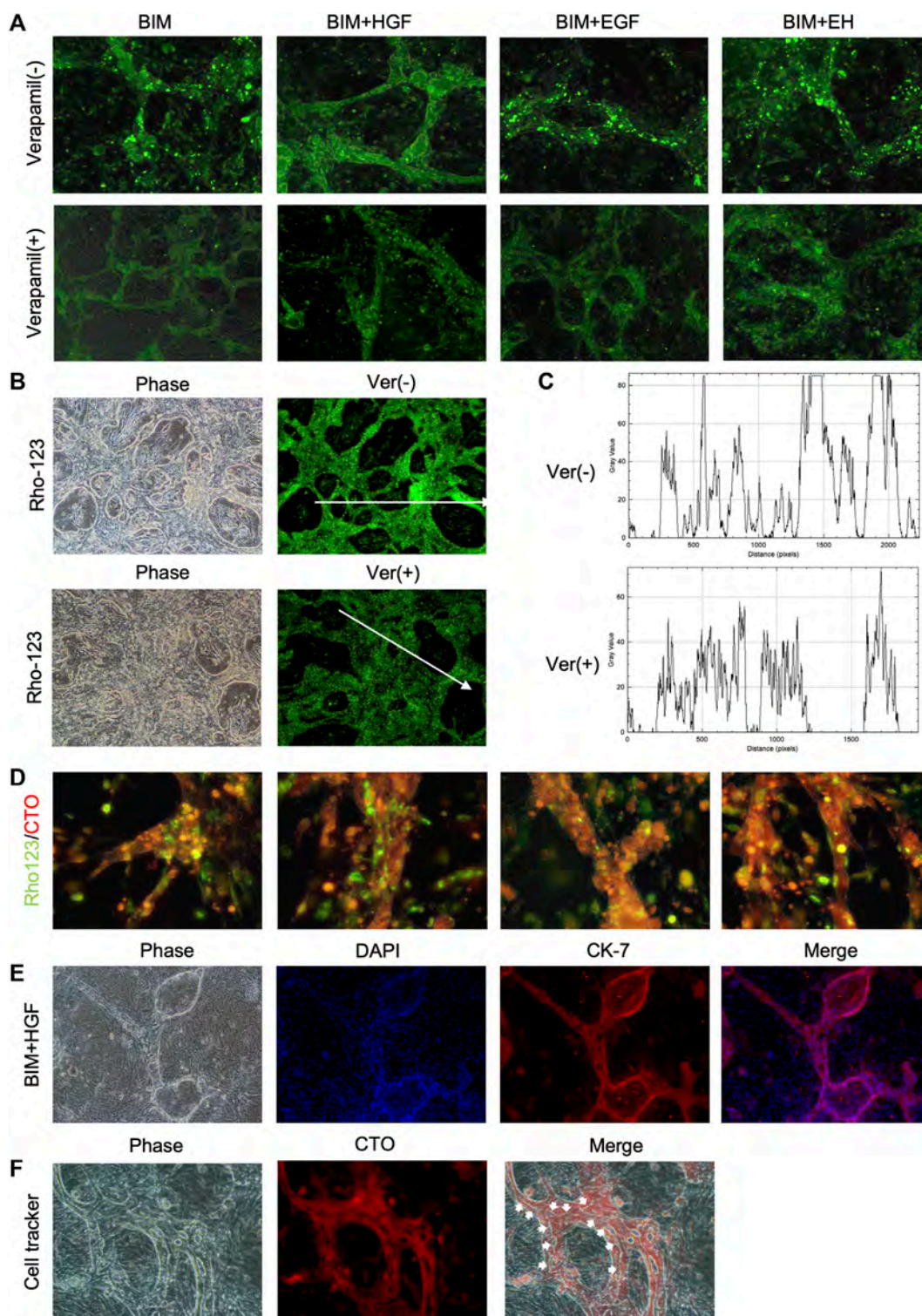
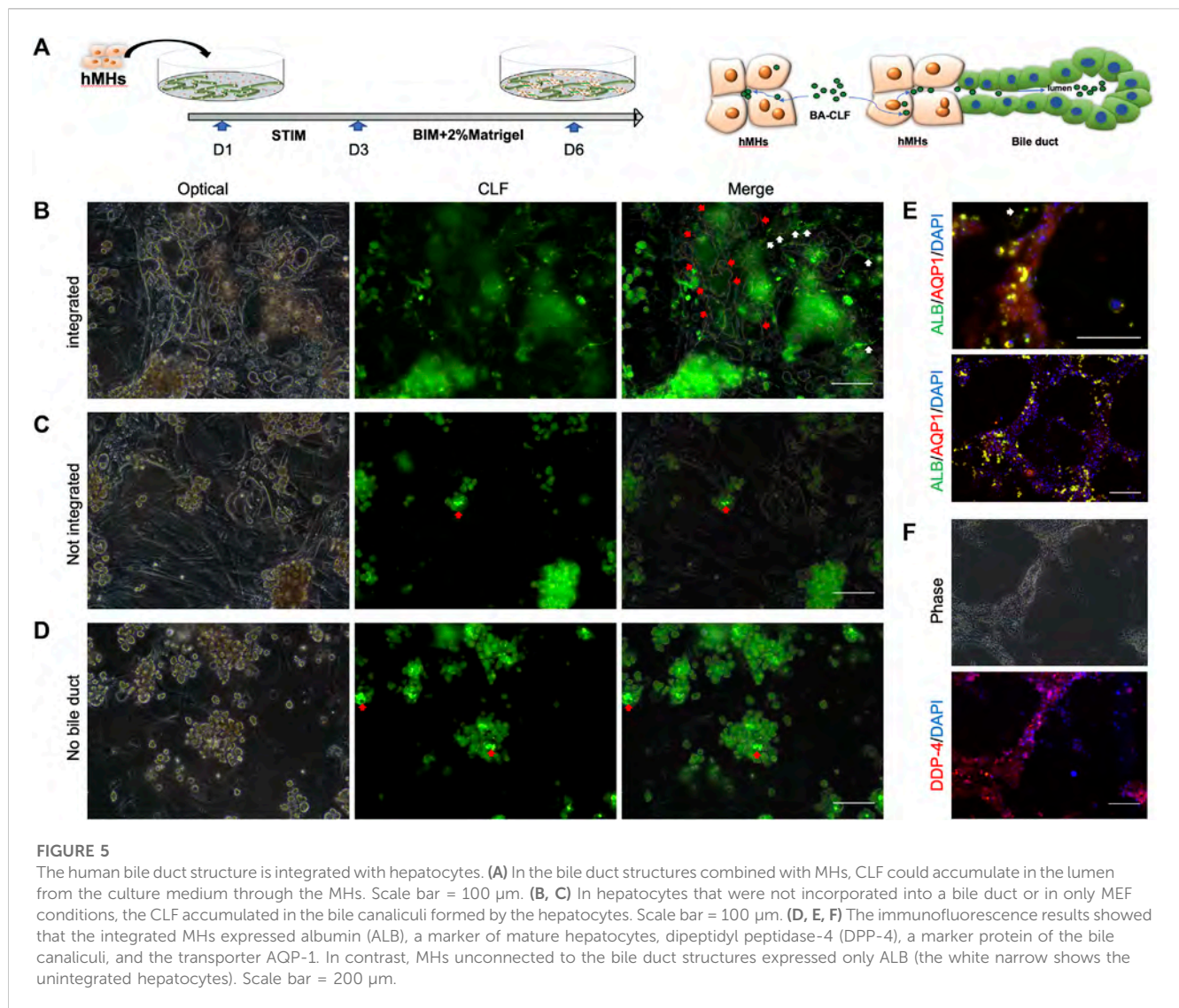


FIGURE 4

The function of the bile duct structure induced by hCLiPs resembles the biliary function. **(A)** Rhodamine-123 was transported into the BEC and accumulated in the lumen of the biliary duct structures. This could be inhibited by the MDR-1 inhibitor verapamil. **(B, C)** Rhodamine-123 was transported into the BEC and accumulated in the lumen of the biliary duct structures in BIM + HGF group, fluorescence intensity along the line was evaluated by ImageJ. **(D)** To further illustrate the presence of lumen in the bile ducts, after 24 h of staining Rhodamine-123, the dye was taken up by bile duct cells for 30 min using a cell tracker orange. **(E, F)** In the BIM + HGF group, CK-7 showed the structure of the bile duct, and cell-tracker staining analysis (30 min) of the bile duct in the BIM + HGF group showed the lumen in the bile duct.



3.3 The functionality of the BD structure induced by hCLiPs resembled the biliary function

The functionality of the BD structure was assessed by determining multidrug resistance protein-1 (MDR1) activity, which was evaluated by the ability to transfer rhodamine-123 into the lumen. Rhodamine-123 was transported into the BECs and then accumulated in the lumen of the BD (Figure 4A). In contrast, as the MDR-1 transporter inhibitor, verapamil prevented rhodamine-123 from accumulating in the lumen of the BD, confirming the functional MDR-1 transport activity in the BD (Figure 4A). The bile duct uptake of rhodamine-123 in BIM + HGF group was further examined, and the bile duct uptake of rhodamine-123 could be inhibited by verapamil (Figures 4B, C). To further illustrate the presence of lumen in the BD, after 24 h of staining with rhodamine-123, the dye was taken up by BECs for 30 min using a cell-tracker, and BIM + HGF could be seen to have a more pronounced cavity when viewed under a fluorescence

microscope (Figure 4D). In the BIM + HGF group, CK-7 showed the structure of the bile duct with cysts, and 30 min cell-tracker orange staining analysis in the BIM + HGF group showed the lumen in the bile duct in the BIM + HGF group (Figures 4E, F). These results suggested that BIM supplied with HGF could induce the formation of a functional BD with a lumen from hCLiPs.

3.4 The human BD structure is integrated with hepatocytes

The intrahepatic BD forms a complex three-dimensional network configured by cholangiocytes. The BD is responsible for bile acid collection and transplantation from the bile canaliculi among hepatocytes in the *in vivo* hepatic system. To investigate whether the BD structure induced by hCLiPs could collect bile acid from bile canaliculi and hepatocytes, we seeded human hepatocytes into the BD system generated from

hCLiPs for 1 day in STIM and 3 days in BIM with HGF, which allowed hepatocytes to integrate into the BD (Figure 5A). Choly-l-Lysyl-Fluorescein (CLF) is a fluorescent bile salt derivative that is being developed as an agent for determining the *in vivo* liver function and *in vitro* hepatocyte function (Milkiewicz et al., 2000; de Waart et al., 2010; Huang et al., 2021). BD integrated with hepatocyte tissue could accumulate CLF in the lumen of the BD (Figure 5B). In contrast, the hepatocytes, which did not incorporate BD, accumulated CLF in the bile canaliculi formed by the hepatocytes (Figure 5C). The accumulation of CLF in the bile canaliculi of hepatocytes under MEF-only conditions also confirmed this finding (Figure 5D). Subsequently, immunofluorescence staining of BD-integrated MHs was performed, and the results showed that these MHs expressed albumin (ALB), dipeptidyl peptidase-4 (DPP-4), a marker protein of the bile canaliculi, and the transporter AQP-1 (Figures 5E, F). In contrast, MHs unconnected to the BD expressed only ALB (Figure 5E). The above results showed that the BD integrated the hMH and was able to transport the CLF from the MHs into the BD lumen.

4 Discussion

A combination of small molecules could convert MHs into LPCs, which had an unlimited self-renewal capacity and could be induced to differentiate into both MHs and BECs (Katsuda et al., 2017; Katsuda et al., 2019; Kim et al., 2019). In this study, we present a novel *in vitro* three-dimensional BD formed by hCLiPs induced from hMHs, which could combine with hMHs as an integrated tissue with the complete biliary function of the accumulation of the bile analog. This tissue represents a model of the human hepatic organoid that is close to the condition *in vivo*. These results demonstrate the functional properties of BECs and the physiological nature of bile transport in the liver, providing a valuable tool for the study of bile transport and metabolism and related diseases. In addition, this tissue-engineered model holds promise for the development of *in vitro* disease models and drug screening.

Previous studies have explored the use of human BECs *in vitro*; however, their practical application has been limited by a number of factors. The low proportion of BECs in the liver, difficulties in isolation, scarcity of donors, and ethical concerns have all hindered the direct utilization of BECs (Katayanagi et al., 1998; Chen et al., 2018; Huang et al., 2020). The use of small molecules to induce mature cell dedifferentiation has gained increased attention in recent times. Small molecule cocktails do not alter the genetic sequence of the cell, which is different from iPSCs, but instead manipulates the cell fate through alterations in the cell's epigenetics, offering a straightforward and highly controllable approach (Knyazer et al., 2021; Guan et al., 2022; Hou et al., 2022; Pan et al., 2022). For instance, the three-dimensional BD generated from hCLiPs demonstrated *in vitro* properties that resembled those of intrahepatic BDs, including the transport of the bile analogs CLF and rhodamine-123. Ramli et al. demonstrated the generation of a human hepatic organoid from iPSCs, in which the cells underwent progressive differentiation

into hepatocytes and cholangiocytes within approximately 50 days of culture (Ramli et al., 2020).

When isolating mature hepatocytes by two-step perfusion using collagenase, fibrous cells, BD cells and other nonparenchymal cells are always mixed because of the heterogeneity of liver cells (Zhang et al., 2016; Aizarani et al., 2019). Induction cultures are often heterogeneous because of the presence of undifferentiated derivatives and nonparenchymal cells, thereby introducing variability, potential immunogenicity, and problems in directed differentiation (Singh et al., 2013; Miyoshi et al., 2022). When FAC medium induced hepatocyte dedifferentiation, fibroblast cells with strong growth ability grew on P0, gained a growth advantage during the passage process and interfered with the proliferation of hCLiPs after passaging, as shown in the supplemental data. When BDs were induced with hCLiPs without the removal of fibroblasts, the growth of BDs was inhibited by the massive proliferation of fibroblasts during induction. The fibroblast cells from FAC culture caused a high background and limited the growth space. In heterogeneous cell culture dishes that induce hepatic progenitor cells, it is particularly important to remove a large number of mixed fibrotic cells (Singh et al., 2013). The properties of stem cells themselves, which differ in their adhesion to different extracellular matrices, are generally weaker than those of fibrotic cells that are capable of secreting collagen (Wang et al., 2016; Aizarani et al., 2019). Stem cells do not inherently attach to the general surface, and there must be some functionalized surface to facilitate adhesion (Lam and Longaker, 2012). It has been previously reported that a large number of fibrotic cells produced during hepatoprostocyte induction are isolated using different culture media (Miyoshi et al., 2022). It seems feasible to select an appropriate adhesion surface for the separation of different cells, especially stem cells and fibrotic cells with large differences in adhesion ability (Wang et al., 2016). The collagen-coated dish can provide a proper adhesion surface for hCLiPs, but for the gelatin-coated dish, its adhesion ability is significantly weaker than that of ordinary fibroblasts, at least in the adhesion time (Miyoshi et al., 2022). After the one-time fibroblast cell removal procedure, the cells in the final collagen-coated dish were mainly EpCAM-positive cells, with only a small number of Desmin-positive cells. The cells in the gelatin dish were almost all Desmin-positive cells, with few EpCAM-positive cells.

When we attempted to use BIM, which was successfully used for rat BD formation in other studies, to induce directed differentiation of hCLiPs into BECs and subsequently construct three-dimensional BD with medium supplemented with Matrigel, the efficiency of BIM was found to be low (Figure 3) (Huang et al., 2021). The growth factors HGF and EGF were introduced into BIM to improve this situation. Other studies have confirmed that these growth factors promote the induction of three-dimensional BD, especially HGF, which can induce the tubular formation of BDs (Tanimizu et al., 2007; Anzai et al., 2016; Tian et al., 2016; Kim et al., 2019). Dong et al. summarized that the components of liver organoids, including R-spondin-1, forskolin, Wnt, EGF, fibroblast growth factor (FGF), HGF, and TGF- β inhibitors, promote the differentiation of LPCs into BECs. Tanimizu et al. demonstrated that PI3K activated by EGF in combination with HGF promoted proliferation during cyst morphogenesis, and tubular or cyst formation depended on the percentage of Matrigel in the total gel volume. According to some

studies, hepatocyte growth factor (HGF) can promote the tube formation of endothelial cells and ductal structure formation of BD cells in three-dimensional culture conditions (Saiki et al., 2006; Tian et al., 2016). HGF can also stimulate the proliferation and differentiation of hepatocytes and induce the formation of hepatocyte-derived biliary epithelium *in vitro* (Limaye et al., 2008; Rose et al., 2021; Tanimizu et al., 2021). The biological responses of scatter, growth, and branching morphogenesis mediated by the HGF receptor are triggered by tyrosine phosphorylation of a single multifunctional docking site located in the carboxy-terminal tail of the receptor (Ponzetto et al., 1994; Boccaccio et al., 1998). The study demonstrated that the HGF receptor binds and phosphorylates Stat-3 and that the ensuing nuclear signaling is required to trigger differentiation for branching morphogenesis (Boccaccio et al., 1998). While HGF, EGF, and the combination of the two induce the transdifferentiation of hepatocytes to BECs, hepatocyte-to-BEC transdifferentiation is regulated by HGF and EGF receptors, and PI3 kinase-mediated signaling independent of AKT is a crucial component of the transdifferentiation process (Limaye et al., 2008). The activation of HGF-Met signaling induces diverse morphogenetic responses, including the formation of branching tubules, cell scattering, and invasion (Birchmeier et al., 2003; Christensen et al., 2005). Therefore, HGF may have a positive effect on BD formation *in vitro* and in three-dimensional culture. Moreover, the LPCs developed cysts with the central lumen in 40% Matrigel, and a lower percentage of Matrigel would form tubular structures (Tanimizu et al., 2007). Tian et al. reported that they had efficiently and controllably generated two-dimensional and three-dimensional BD from iPSC-derived spheroids. The three-dimensional BD structures were formed under control by HGF and EGF in a three-dimensional ECM constructed by Matrigel (Tian et al., 2016). Based on these findings, we compared the efficiency of HGF, EGF, and the combination of the two, and they could promote formation during tubular morphogenesis, but HGF only seemed more efficient. In another similar hCLiPs, Kim et al. reported that hCLiPs formed a tube-like branching morphology using BEC differentiation medium consisting of DMEM/F12 medium containing 10% FBS and 20 ng/mL HGF in a three-dimensional culture constructed with collagen gel (Kim et al., 2019). Indeed, the growth factors used in different culture systems and stem cells are different. Nevertheless, it is undeniable that EGF and HGF are culture components that can be considered to form tubular BD.

Bile is secreted from hepatocytes, extracted into bile canaliculi formed by hepatocytes and subsequently delivered to the intrahepatic BDs, where it is modified by BECs. The BECs form the intrahepatic BD and extrahepatic BD, which complete the modification, secretion, transportation, accumulation, and discharge of bile (Reshetnyak, 2013). Huang et al. and Katsuda et al. demonstrated that they generated rat BD or integrated tubule-hepatocyte tissues *in vitro* that could transport CLF, rhodamine 123 or fluorescein diacetate (Katsuda et al., 2017; Huang et al., 2021). This is the first reported instance of a tissue connection between the human tubular BD and hepatocytes and presents an excellent opportunity to develop an organoid model for studying diseases related to human biliary hepatocytes. *In vitro*, the functionality of the BD was assessed by determining MDR1 activity, which was evaluated by the ability to transfer rhodamine-123 into the lumen.

The BD could collect rhodamine-123 in the BECs, which could accumulate in the lumen, and this could be inhibited by verapamil. Additionally, the P-gp transport function was evaluated by the active transport of rhodamine 123, and verapamil was also an inhibitor of the P-gp function (Wang et al., 2022). Milkiewicz et al. demonstrated that the transportation of CLF is mediated by ATP binding cassette subfamily C members 2 and 3 (ABCC2, 3), which encode canalicular multispecific organic anion transporters 2 and 3 (MRP2/3) (Milkiewicz et al., 2000). The bile canaliculi formed by the MHs without connecting BDs were also observed collecting CLF, while it was reported that this phenomenon was not observed in either the BEC monolayer or the BD without hepatocytes (Huang et al., 2021). Therefore, we speculated that the bile canaliculi formed by the MHs formed a connection with BD and had the ability to transport the bile analog CLF. Subsequent immunofluorescence experiments also confirmed the presence of AQP-1 and DPP-4 proteins between the MHs and the BD, which are also bile transportation-related proteins. In conclusion, the connection of the MHs to the BD provided a microstructural basis for the excretion of bile.

Overall, this study provides a promising avenue for establishing a novel *in vitro* system that combines hMHs and BD using HGF and Matrigel. The functional BD, generated from the hCLiPs, displayed characteristics of BDs and were able to accumulate a bile analog, demonstrating their biliary function. By coculturing and connecting hMHs and functional BD, researchers can study various physiological and pathophysiological conditions and evaluate drug responses. The future study of the establishment of disease models from this model could provide a valuable tool for drug development and understanding disease mechanisms.

Data availability statement

The original contributions presented in the study are included in the article/[Supplementary Material](#), further inquiries can be directed to the corresponding author.

Ethics statement

Ethical approval was not required for the studies on humans in accordance with the local legislation and institutional requirements because only commercially available established cell lines were used. Ethical approval was not required for the studies on animals in accordance with the local legislation and institutional requirements because only commercially available established cell lines were used.

Author contributions

PL designed the research study, performed experiments and data interpretation, and wrote the manuscript. DM and YH contributed to the data analysis. SE gave final approval of the manuscript. All authors contributed to the article and approved the submitted version.

Funding

This study was supported in part by the Japan China Sasakawa Medical Fellowship. This study was supported in part by the Grant-in-Aid for Scientific Research (21K08598).

Conflict of interest

The authors declare that the research was conducted in the absence of any commercial or financial relationships that could be construed as a potential conflict of interest.

Publisher's note

All claims expressed in this article are solely those of the authors and do not necessarily represent those of their affiliated organizations, or those of the publisher, the editors and the reviewers. Any product that may be evaluated in this article, or claim that may be made by its manufacturer, is not guaranteed or endorsed by the publisher.

Supplementary material

The Supplementary Material for this article can be found online at: <https://www.frontiersin.org/articles/10.3389/fbioe.2023.1249769/full#supplementary-material>

References

- Aizarani, N., Saviano, A., Sagar, M., Maily, L., Durand, S., Herman, J. S., et al. (2019). A human liver cell atlas reveals heterogeneity and epithelial progenitors. *Nature* 572, 199–204. doi:10.1038/s41586-019-1373-2
- Alpini, G., McGill, J. M., and LaRusso, N. F. (2002). The pathobiology of biliary epithelia. *Hepatology* 35, 1256–1268. doi:10.1053/jhep.2002.33541
- Anzai, K., Chikada, H., Tsunoyama, K., Ida, K., Kagawa, T., Inagaki, Y., et al. (2016). Foetal hepatic progenitor cells assume a cholangiocytic cell phenotype during two-dimensional pre-culture. *Sci. Rep.* 6, 28283. doi:10.1038/srep28283
- Birchmeier, C., Birchmeier, W., Gherardi, E., and Vande Woude, G. F. (2003). Metastasis, motility and more. *Nat. Rev. Mol. Cell. Biol.* 4, 915–925. doi:10.1038/nrm1261
- Boccaccio, C., Andò, M., Tamagnone, L., Bardelli, A., Michieli, P., Battistini, C., et al. (1998). Induction of epithelial tubules by growth factor HGF depends on the STAT pathway. *Nature* 391, 285–288. doi:10.1038/34657
- Buisson, E. M., Jeong, J., Kim, H. J., and Choi, D. (2019). Regenerative medicine of the bile duct: beyond the myth. *Int. J. Stem Cells* 12, 183–194. doi:10.15283/ijsc18055
- Cao, W., Chen, K., Bolkestein, M., Yin, Y., Versteegen, M. M., Bijvelds, M. J., et al. (2017). Dynamics of proliferative and quiescent stem cells in liver homeostasis and injury. *Gastroenterology* 153, 1133–1147. doi:10.1053/j.gastro.2017.07.006
- Carberry, C. K., Ferguson, S. S., Beltran, A. S., Fry, R. C., and Rager, J. E. (2022). Using liver models generated from human-induced pluripotent stem cells (iPSCs) for evaluating chemical-induced modifications and disease across liver developmental stages. *Toxicol. Vitro* 83, 105412. doi:10.1016/j.tiv.2022.105412
- Chen, C., Jochems, P. G. M., Salz, L., Schneeberger, K., Penning, L. C., van de Graaf, S. F. J., et al. (2018). Bioengineered bile ducts recapitulate key cholangiocyte functions. *Biofabrication* 10, 034103. doi:10.1088/1758-5090/aac8fd
- Christensen, J. G., Burrows, J., and Salgia, R. (2005). c-Met as a target for human cancer and characterization of inhibitors for therapeutic intervention. *Cancer Lett.* 225, 1–26. doi:10.1016/j.canlet.2004.09.044
- de Waart, D. R., Häusler, S., Vlaming, M. L., Kunne, C., Hänggi, E., Gruss, H. J., et al. (2010). Hepatic transport mechanisms of choly-L-lysyl-fluorescein. *J. Pharmacol. Exp. Ther.* 334, 78–86. doi:10.1124/jpet.110.166991
- Guan, J., Wang, G., Wang, J., Zhang, Z., Fu, Y., Cheng, L., et al. (2022). Chemical reprogramming of human somatic cells to pluripotent stem cells. *Nature* 605, 325–331. doi:10.1038/s41586-022-04593-5
- Hou, X., Ma, S., Fan, W., Li, F., Xu, M., Yang, C., et al. (2022). Chemically defined and small molecules-based generation of sinoatrial node-like cells. *Stem Cell. Res. Ther.* 13, 158. doi:10.1186/s13287-022-02834-y
- Huang, Y., Sakai, Y., Hara, T., Katsuda, T., Ochiya, T., Gu, W., et al. (2021). Bioengineering of a CLiP-derived tubular biliary-duct-like structure for bile transport *in vitro*. *Biotechnol. Bioeng.* 118, 2572–2584. doi:10.1002/bit.27773
- Huang, Y., Sakai, Y., Hara, T., Katsuda, T., Ochiya, T., Gu, W. L., et al. (2020). Differentiation of chemically induced liver progenitor cells to cholangiocytes: investigation of the optimal conditions. *J. Biosci. Bioeng.* 130, 545–552. doi:10.1016/j.jbiosc.2020.07.009
- Katayanagi, K., Kono, N., and Nakanuma, Y. (1998). Isolation, culture and characterization of biliary epithelial cells from different anatomical levels of the intrahepatic and extrahepatic biliary tree from a mouse. *Liver* 18, 90–98. doi:10.1111/j.1600-0676.1998.tb00133.x
- Katsuda, T., Kawamata, M., Hagiwara, K., Takahashi, R. u., Yamamoto, Y., Camargo, F. D., et al. (2017). Conversion of terminally committed hepatocytes to culturable bipotent progenitor cells with regenerative capacity. *Cell. Stem Cell.* 20, 41–55. doi:10.1016/j.stem.2016.10.007
- Katsuda, T., Matsuzaki, J., Yamaguchi, T., Yamada, Y., Prieto-Vila, M., Hosaka, K., et al. (2019). Generation of human hepatic progenitor cells with regenerative and metabolic capacities from primary hepatocytes. *Elife* 8, e47313. doi:10.7554/eLife.47313
- Kim, H., Im, I., Jeon, J. S., Kang, E. H., Lee, H. A., Jo, S., et al. (2022). Development of human pluripotent stem cell-derived hepatic organoids as an alternative model for drug safety assessment. *Biomaterials* 286, 121575. doi:10.1016/j.biomaterials.2022.121575
- Kim, Y., Kang, K., Lee, S. B., Seo, D., Yoon, S., Kim, S. J., et al. (2019). Small molecule-mediated reprogramming of human hepatocytes into bipotent progenitor cells. *J. Hepatol.* 70, 97–107. doi:10.1016/j.jhep.2018.09.007
- Knyazer, A., Bunu, G., Toren, D., Mrcica, T. B., Segev, Y., Wolfson, M., et al. (2021). Small molecules for cell reprogramming: a systems biology analysis. *Aging (Albany NY)* 13, 25739–25762. doi:10.18632/aging.203791
- Lam, M. T., and Longaker, M. T. (2012). Comparison of several attachment methods for human iPS, embryonic and adipose-derived stem cells for tissue engineering. *J. Tissue Eng. Regen. Med.* 6 (Suppl. 3), s80–s86. doi:10.1002/term.1499
- Lazaridis, K. N., and LaRusso, N. F. (2015). The cholangiopathies. *Mayo Clin. Proc.* 90, 791–800. doi:10.1016/j.mayocp.2015.03.017

SUPPLEMENTARY FIGURE S1

It was necessary to remove the fibroblast cells mixed with the hCLiPs. (A) The fibroblast cells would increase during the induction of hCLiPs by FAC medium. Scale bar = 500 μ m. (B) If the fibroblast cells mixed in the culture dish were not removed, the fibroblast cells with rapid proliferation ability would overgrow in the culture dish after passaging. (C) Fibroblast-related genes, including ACTA2, TGF- β 2, and MMP2, were gradually upregulated during induction. ($n = 3-6$) Data represent the mean \pm standard error of the mean. One-way ANOVA, * $p < 0.01$. (D) Heterogeneous cells expressed the EpCAM and α -SMA proteins. Scale bar = 200 μ m.

SUPPLEMENTARY FIGURE S2

The fibroblast cells proliferated rapidly in a 3D culture environment, making it difficult to form or fragment 3D bile ducts. Scale bar = 500 μ m.

SUPPLEMENTARY FIGURE S3

The hCLiPs were enriched in purity without damage by multiple subcultures. (A) Multiple subcultures were utilized to remove mixed fibroblast cells in the suspension of hCLiP. (B) Immunofluorescence staining of collagen dish-2 and a gelatin dish on day 8. Conversely to the gelatin dishes, fewer Desmin-positive cells were observed in Collagen dish-2 and most cells were EpCAM-positive. (C) RT-qPCR results showed that the fibrosis related genes ACTA2, TGF- β 2, and MMP2 were more highly expressed in the fiber cells of the gelatin dishes than in the hCLiPs of collagen dish-2, while the LPC marker genes EpCAM, SOX-9, and CD133 were more highly expressed in the hCLiPs. Data represent the mean \pm standard error of the mean. Student's t test, * $p < 0.05$, * $p < 0.01$.

SUPPLEMENTARY FIGURE S4

The immunofluorescence results showed that the EpCAM protein was expressed in the area of bile duct formation, while the EpCAM protein expression was lower in cells that failed to form tubular structures in the BIM+EGF and BIM+EH groups.

- Li, M., Gong, J., Gao, L., Zou, T., Kang, J., and Xu, H. (2022). Advanced human developmental toxicity and teratogenicity assessment using human organoid models. *Ecotoxicol. Environ. Saf.* 235, 113429. doi:10.1016/j.ecoenv.2022.113429
- Limaye, P. B., Bowen, W. C., Orr, A. V., Luo, J., Tseng, G. C., and Michalopoulos, G. K. (2008). Mechanisms of hepatocyte growth factor-mediated and epidermal growth factor-mediated signaling in transdifferentiation of rat hepatocytes to biliary epithelium. *Hepatology* 47, 1702–1713. doi:10.1002/hep.22221
- Milkiewicz, P., Saksena, S., Cardenas, T., Mills, C. O., and Elias, E. (2000). Plasma elimination of cholyl-lysyl-fluorescein (CLF): a pilot study in patients with liver cirrhosis. *Liver* 20, 330–334. doi:10.1034/j.1600-0676.2000.020004330.x
- Miyoshi, T., Hidaka, M., Miyamoto, D., Sakai, Y., Murakami, S., Huang, Y., et al. (2022). Successful induction of human chemically induced liver progenitors with small molecules from damaged liver. *J. Gastroenterol.* 57, 441–452. doi:10.1007/s00535-022-01869-5
- O'Hara, S. P., Tabibian, J. H., Splinter, P. L., and LaRusso, N. F. (2013). The dynamic biliary epithelia: molecules, pathways, and disease. *J. Hepatol.* 58, 575–582. doi:10.1016/j.jhep.2012.10.011
- Olgasi, C., Cucci, A., and Follenzi, A. (2020). iPSC-derived liver organoids: a journey from drug screening, to disease modeling, arriving to regenerative medicine. *Int. J. Mol. Sci.* 21, 6215. doi:10.3390/ijms21176215
- Pan, T., Wang, N., Zhang, J., Yang, F., Chen, Y., Zhuang, Y., et al. (2022). Efficiently generate functional hepatic cells from human pluripotent stem cells by complete small-molecule strategy. *Stem Cell. Res. Ther.* 13, 159. doi:10.1186/s13287-022-02831-1
- Park, Y., Thadasina, D., Bolujo, I., Isidan, A., Cross-Najafi, A. A., Lopez, K., et al. (2022). Three-dimensional organoids as a model to study nonalcoholic fatty liver disease. *Semin. Liver Dis.* 42, 423–433. doi:10.1055/a-1934-5588
- Ponzetto, C., Bardelli, A., Zhen, Z., Maina, F., dalla Zonca, P., Giordano, S., et al. (1994). A multifunctional docking site mediates signaling and transformation by the hepatocyte growth factor/scatter factor receptor family. *Cell* 77, 261–271. doi:10.1016/0092-8674(94)90318-2
- Ramli, M. N. B., Lim, Y. S., Koe, C. T., Demircioglu, D., Tng, W., Gonzales, K. A. U., et al. (2020). Human pluripotent stem cell-derived organoids as models of liver disease. *Gastroenterology* 159, 1471–1486.e12. doi:10.1053/j.gastro.2020.06.010
- Reshetnyak, V. I. (2013). Physiological and molecular biochemical mechanisms of bile formation. *World J. Gastroenterol.* 19, 7341–7360. doi:10.3748/wjg.v19.i42.7341
- Roos, F. J. M., van Tienderen, G. S., Wu, H., Bordeu, I., Vinke, D., Albarinos, L. M., et al. (2022). Human branching cholangiocyte organoids recapitulate functional bile duct formation. *Cell. Stem Cell.* 29, 776–794.e13. doi:10.1016/j.stem.2022.04.011
- Rose, S., Ezan, F., Cuvellier, M., Bruyère, A., Legagneux, V., Langouët, S., et al. (2021). Generation of proliferating human adult hepatocytes using optimized 3D culture conditions. *Sci. Rep.* 11, 515. doi:10.1038/s41598-020-80019-4
- Saiki, A., Watanabe, F., Murano, T., Miyashita, Y., and Shirai, K. (2006). Hepatocyte growth factor secreted by cultured adipocytes promotes tube formation of vascular endothelial cells *in vitro*. *Int. J. Obes. (Lond)* 30, 1676–1684. doi:10.1038/sj.ijo.0803316
- Sampaziotis, F., Muraro, D., Tysoe, O. C., Sawiak, S., Beach, T. E., Godfrey, E. M., et al. (2021). Cholangiocyte organoids can repair bile ducts after transplantation in the human liver. *Science* 371, 839–846. doi:10.1126/science.aaz6964
- Sato, K., Zhang, W., Safarikia, S., Isidan, A., Chen, A. M., Li, P., et al. (2021). Organoids and spheroids as models for studying cholestatic liver injury and cholangiocarcinoma. *Hepatology* 74, 491–502. doi:10.1002/hep.31653
- Si-Tayeb, K., Lemaigre, F. P., and Duncan, S. A. (2010). Organogenesis and development of the liver. *Dev. Cell.* 18, 175–189. doi:10.1016/j.devcel.2010.01.011
- Singh, A., Suri, S., Lee, T., Chilton, J. M., Cooke, M. T., Chen, W., et al. (2013). Adhesion strength-based, label-free isolation of human pluripotent stem cells. *Nat. Methods* 10, 438–444. doi:10.1038/nmeth.2437
- Strazzabosco, M., Fabris, L., and Spirli, C. (2005). Pathophysiology of cholangiopathies. *J. Clin. Gastroenterol.* 39, S90–S102. doi:10.1097/01.mcg.0000155549.29643.ad
- Tanimizu, N., Ichinohe, N., Sasaki, Y., Itoh, T., Sudo, R., Yamaguchi, T., et al. (2021). Generation of functional liver organoids on combining hepatocytes and cholangiocytes with hepatobiliary connections *ex vivo*. *Nat. Commun.* 12, 3390. doi:10.1038/s41467-021-23575-1
- Tanimizu, N., Miyajima, A., and Mostov, K. E. (2007). Liver progenitor cells develop cholangiocyte-type epithelial polarity in three-dimensional culture. *Mol. Biol. Cell.* 18, 1472–1479. doi:10.1091/mbc.e06-09-0848
- Tanimizu, N., Nakamura, Y., Ichinohe, N., Mizuguchi, T., Hirata, K., and Mitaka, T. (2013). Hepatic biliary epithelial cells acquire epithelial integrity but lose plasticity to differentiate into hepatocytes *in vitro* during development. *J. Cell. Sci.* 126, 5239–5246. doi:10.1242/jcs.133082
- Tian, L., Deshmukh, A., Ye, Z., and Jang, Y. Y. (2016). Efficient and controlled generation of 2D and 3D bile duct tissue from human pluripotent stem cell-derived spheroids. *Stem Cell. Rev. Rep.* 12, 500–508. doi:10.1007/s12015-016-9657-5
- Velazquez, J. J., and Ebrahimkhani, M. R. (2021). Cholangiocyte organoids as a cell source for biliary repair. *Transpl. Int.* 34, 999–1001. doi:10.1111/tri.13902
- Wang, X., Ni, C., Jiang, N., Wei, J., Liang, J., Zhao, B., et al. (2020). Generation of liver bipotential organoids with a small-molecule cocktail. *J. Mol. Cell. Biol.* 12, 618–629. doi:10.1093/jmcb/mjaa010
- Wang, Y., Zhang, W., Yuan, J., and Shen, J. (2016). Differences in cytocompatibility between collagen, gelatin and keratin. *Mater. Sci. Eng. C Mater. Biol. Appl.* 59, 30–34. doi:10.1016/j.msec.2015.09.093
- Wang, Z., Faria, J., van der Laan, L. J. W., Penning, L. C., Masereeuw, R., and Spee, B. (2022). Human cholangiocytes form a polarized and functional bile duct on hollow fiber membranes. *Front. Bioeng. Biotechnol.* 10, 868857. doi:10.3389/fbioe.2022.868857
- Xu, X., Jiang, S., Gu, L., Li, B., Xu, F., Li, C., et al. (2022). High-throughput bioengineering of homogenous and functional human-induced pluripotent stem cells-derived liver organoids via micropatterning technique. *Front. Bioeng. Biotechnol.* 10, 937595. doi:10.3389/fbioe.2022.937595
- Yan, J., Tai, Y., and Zhou, H. (2022). Culture of mouse liver ductal organoids. *Methods Mol. Biol.* 2455, 117–129. doi:10.1007/978-1-0716-2128-8_11
- Zhang, C. Y., Yuan, W. G., He, P., Lei, J. H., and Wang, C. X. (2016). Liver fibrosis and hepatic stellate cells: etiology, pathological hallmarks and therapeutic targets. *World J. Gastroenterol.* 22, 10512–10522. doi:10.3748/wjg.v22.i48.10512

公益財団法人日中医学協会
T E L 03-5829-9123
F A X 03-3866-9080
E-MAIL iryo@jpcnma.or.jp
〒101-0032 東京都千代田区岩本町 1-4-3
住 泉 K M ビル 6 階
URL : <https://www.jpcnma.or.jp/>